Lecture Notes in Civil Engineering

A. Rama Mohan Rao · K. Ramanjaneyulu
Editors

Recent Advances in Structural Engineering, Volume 1

Select Proceedings of SEC 2016

Springer

Lecture Notes in Civil Engineering

Volume 11

Lecture Notes in Civil Engineering (LNCE) publishes the latest developments in Civil Engineering - quickly, informally and in top quality. Though original research reported in proceedings and post-proceedings represents the core of LNCE, edited volumes of exceptionally high quality and interest may also be considered for publication. Volumes published in LNCE embrace all aspects and subfields of, as well as new challenges in, Civil Engineering. Topics in the series include:

- Construction and Structural Mechanics
- Building Materials
- Concrete, Steel and Timber Structures
- Geotechnical Engineering
- Earthquake Engineering
- Coastal Engineering
- Hydraulics, Hydrology and Water Resources Engineering
- Environmental Engineering and Sustainability
- Structural Health and Monitoring
- Surveying and Geographical Information Systems
- Heating, Ventilation and Air Conditioning (HVAC)
- Transportation and Traffic
- Risk Analysis
- Safety and Security

To submit a proposal or request further information, please contact the appropriate Springer Editor:

- Mr. Pierpaolo Riva at pierpaolo.riva@springer.com (Europe and Americas);
- Ms. Swati Meherishi at swati.meherishi@springer.com (India);
- Ms. Li Shen at li.shen@springer.com (China);
- Dr. Loyola D'Silva at loyola.dsilva@springer.com (Southeast Asia and Australia/NZ).

More information about this series at http://www.springer.com/series/15087

A. Rama Mohan Rao · K. Ramanjaneyulu
Editors

Recent Advances in Structural Engineering, Volume 1

Select Proceedings of SEC 2016

Springer

Editors
A. Rama Mohan Rao
Structural Health Monitoring Laboratory
CSIR-Structural Engineering Research Centre
Chennai, Tamil Nadu
India

K. Ramanjaneyulu
Advanced Concrete Testing & Evaluation Laboratory (ACTEL)
CSIR-Structural Engineering Research Centre
Chennai, Tamil Nadu
India

ISSN 2366-2557 ISSN 2366-2565 (electronic)
Lecture Notes in Civil Engineering
ISBN 978-981-13-0361-6 ISBN 978-981-13-0362-3 (eBook)
https://doi.org/10.1007/978-981-13-0362-3

Library of Congress Control Number: 2018939461

Printed on acid-free paper

This Springer imprint is published by the registered company Springer Nature Singapore Pte Ltd.
The registered company address is: 152 Beach Road, #21-01/04 Gateway East, Singapore 189721, Singapore

Preface

The Tenth Structural Engineering Convention 2016 (SEC-2016) was organized by CSIR-Structural Engineering Research Centre jointly with IIT Madras and Anna University, Chennai, during 21–23 December 2016 at CSIR-SERC, Chennai, India. SEC-2016 provided a common platform for professional structural engineers, academicians and researchers in the broad fields of engineering mechanics and structural engineering to exchange ideas for enriching the research and development activities in the area of structural engineering.

The papers contributed in this convention are a reflection of the diverse research activities in this area and represent the recent developments and futuristic trends in the fundamental understanding of behaviour of materials and structures, computational structural mechanics, structural health monitoring, mitigation strategies against natural hazards, performance- and durability-based design methodologies, repair and retrofit methods, and technologies for sustainable development. More than four hundred delegates from research organizations, academia and industry participated and presented their papers, making this conference a real great success. All the papers presented are double-blind peer-reviewed.

This lecture series in Civil Engineering with the theme of *Recent Advances in Structural Engineering* is brought out in two volumes and contains the select papers presented in SEC-2016. This volume (Volume 1) contains 92 contributions in the following parts:

Part I Analysis and Design of Concrete Structures
Part II Analysis and Design of Steel Structures
Part III Computational Structural Mechanics
Part IV New Building Materials for Sustainable Construction
Part V Mitigation of Structures against Natural Hazards
Part VI Structural Health Monitoring

We believe that the collection of papers included in this volume will contribute to scientific developments in the field of structural engineering in a global sense and will be a useful reference work for the academicians, researchers and also most

importantly the student community pursuing research in the area of structural engineering.

The success of the conference, SEC-2016, was due to the collective efforts of a large number of individuals, members of the various organizing committees and sponsors. We should take this opportunity to thank all of them for making SEC-2016 a great success. We would like to especially thank all the reviewers, the majority of them from CSIR-SERC who have spent their quality time for reviewing more than five hundred papers received.

Chennai, India

A. Rama Mohan Rao
K. Ramanjaneyulu

Contents

Part I Analysis and Design of Concrete Structures

Analysis and Design of Tabletop Foundation for Turbine Generators 3
Siddhartha Bhattacharya

Effect of Infill Wall Stiffness on Seismic Analysis of High-Rise Building Resting on Sloping Ground 19
Kolasani Rajasekhar and Maganti Janardhana

Effect of Pile Layout and Pile Cap Thickness on Load Distribution in Piles 35
Meenu Sharma

Reaction Response of Horizontally Curved and Skewed Concrete Box-Girder Bridges 49
Tanmay Gupta and Manoj Kumar

Performance Estimation of Solid and Punched Shear Wall Buildings with Two Modelling Techniques 61
Juturu Swetha, Onkar G. Kumbhar and Ratnesh Kumar

Effect of Modeling Assumptions on Seismic Performance of RC Building 73
Onkar G. Kumbhar and Ratnesh Kumar

Robust Optimal Design of Buried Reinforced Concrete Pipe in Trenchless Construction Under Bounded Type Uncertainty Considering Seismic Load 85
S. Mukherjee, P. K. Shaw, G. Datta, S. Bhattacharjya and S. Ghosh

Numerical Study on Flexural Capacity of Biaxial Hollow Slab 97
R. Sagadevan and B. Nageswara Rao

Issues on Design Shear Strength of RC Deep Beams 107
J. Leon Raj and G. Appa Rao

Detailing of Stirrup Reinforcement Along the Span and Across the Width of Reinforced Concrete Beams 119
D. S. R. Murty and G. Papa Rao

Pylon Shape Analysis of Cable-Stayed Bridges 133
R. Sharath and R. K. Ingle

Evaluation of Minimum Flexural Reinforcement in Design of Reinforced Concrete Beams 145
H. E. Nagesh and G. Appa Rao

Various Aspects of Detailing of Reinforcement in Two-Pile Cap Concrete 157
Murty Sree Rama Chandra Devalraju and Dinakar Pedapenki

Comparative Study of Flat Slab-Column Connection Techniques for Seismic Loading 171
Aastha Mahajan, Ratnesh Kumar and Onkar G. Kumbhar

Comparative Study of 1D and 2D Simulation Models of Hollow RC Bridge Columns Under Reversed Cyclic Loads 183
Vijay Kumar Polimeru, Abhideep Sahu and Arghadeep Laskar

Comparative Study of Different Foundation and Sidewall Systems for Large Storage Tanks 193
T. Pavan Kumar, G. Papa Rao and P. Veerabhadra Rao

Influence of Shear Core Curtailment on the Structural Response of Core-Wall Structures 207
Nishant Rathi, G. Muthukumar and Manoj Kumar

Location of Balance Points on Design and Actual *P–M* Interaction Curve for RC Sections 217
Piyush Mehta, Sumit Kumar, Vikash Kumar, Sunil Bandawala and Kaustubh Dasgupta

Effect of Skewness on Shear Lag Effect in RC Box-Girder Bridges 233
Manoj Kumar, Nitin Gulhane and Tanmay Gupta

Stress in Unbonded Tendons for Post-tensioned Concrete Members—Assessment of Prediction Equations and Experimental Investigation 247
R. Manisekar and K. Saravana Kumar

Biaxial Effects in Unreinforced Masonry (URM) Load-Bearing Walls 263
Jacob Alex Kollerathu and Arun Menon

Bond Performance of Pretensioned Concrete Systems 277
Prabha Mohandoss, Sriram K. Kompella and Radhakrishna G. Pillai

Part II Analysis and Design of Steel Structures

Comparative Study of Fire-Resistant Design of Steel Structures as per IS800:2007, AS4100:1998, AISC360:2010 and EN1993-1-2 289
Dhara Shah and Janak Shah

Effects of Column-to-Beam Strength Ratio on Behaviour of Beam-to-Column Moment Joints 303
Arnav Anuj Kasar, S. D. Bharti, M. K. Shrimali and Rupen Goswami

Moment–Rotation Response for Semi-rigid Connections 313
Venkatesh Patnana, A. Y. Vyavahare and Laxmikant M. Gupta

Semi-elliptical LDSS Hollow Stub Columns Under Axial Compression 327
Tekcham Gishan Singh and Konjengbam Darunkumar Singh

Assessment of Load Carrying Capacity of Thin-Webbed Castellated Beam 339
A. Cyril Thomas and K. Baskar

Evaluation of Seismic Performance of Steel Plate Shear Walls Arranged in Staggered Configuration 351
Abhishek Verma and Dipti Ranjan Sahoo

Identification of Semi-rigid Joints in Steel Frame Structures Using Vibration-Based Technique 363
Joy Pal and Sauvik Banerjee

Identification of Parameter of Truss Structure by Limited Static Strain Measurement 375
Debasish Bandyopadhyay, Sumit Saha and Tanvir Sohail

TWLIGHT-IITM—A Computational Utility for Elastic Buckling Stress Predictions of Cold-Formed Steel Elements 389
S. S. Ajeesh and S. Arul Jayachandran

Part III Computational Structural Mechanics

Improved Sparse High-Dimensional Model Representation Based on Least Absolute Shrinkage and Selection Operator 405
Tanmoy Chatterjee and Rajib Chowdhury

Reliability-Based Design Optimization—A Hybrid PCFE-Based Approach 419
Souvik Chakraborty and Rajib Chowdhury

Numerical Modeling of Spalling in High Strength Concrete at High Temperature 431
Patnayakuni Ravi Prakash and Gaurav Srivastava

A Study on Finite Element Modelling of Acoustic Emission Waveforms in Composite and Sandwich Plates 441
Sanjay Sengupta, Pijush Topdar and Aloke Kumar Datta

HDMR-Based Bayesian Structural System Identification 453
O. A. Shereena and B. Nageswara Rao

Adaptive Metamodel-Based Efficient Robust Design Optimization of Offshore Structure Under Wave Loading 465
Gaurav Datta, Soumya Bhattacharjya and Subrata Chakraborty

Shear Strength of Semi-corrugated Webbed Beam 477
Anjaly J. Pillai and Laxmikant M. Gupta

Failure Analysis of Composite Cylindrical Shells Using Continuum Damage Mechanics 487
Maharshi Kintada and Arbind Kumar Singh

Prediction of Compressive Strength of Concrete: Machine Learning Approaches 503
Dipro Dutta and Sudhirkumar V. Barai

Numerical Study of the Effect of Boundary Conditions on Buckling Behaviour of Flat Oval LDSS Stub Column Under Axial Compression 515
Khwairakpam Sachidananda and Konjengbam Darunkumar Singh

Two-Dimensional Mesoscale Compressive Damage Analysis of CT Images of a Concrete Cube 525
S. Vinay Kumar and Nirjhar Dhang

Flutter Reliability Studies of a Swept Back Plate 537
G. Shanthini, A. C. Pankaj and M. Manjuprasad

Nonlinear Static Analysis of Offshore J-Lay Risers Using Finite Element Method 551
S. Madhuri, B. Narendra Kumar and K. Venkateswara Rao

Estimation of Modal Characteristics of a Reduced-Order Fluid–Structure Interaction System 563
Hridya P. Lal, W. Dheelibun Remigius, Sayan Gupta and Sunetra Sarkar

A Simple NURBS Finite Element for 2D Sloshing Analysis 577
Mrityunjoy Mandal and Shaikh Jahangir Hossain

Numerical Study on Cyclic Response of Self-centering Steel Buckling-Restrained Braces 589
Ahmad Fayeq Ghowsi, Amanollah Faqiri and Dipti Ranjan Sahoo

Computational Modelling of Cement Hydration to Evaluate the Mechanical and Transport Properties 599
B. S. Sindu, S. Radha Meenaloshini and Saptarshi Sasmal

Three-Dimensional Analytical Solution for FGM Plate with Varying Material Properties in In-plane Directions Using Extended Kantorovich Method 611
Poonam Kumari and Agyapal Singh

Effect of Support Settlement on the Behaviour of Stone Masonry Arch Bridge 623
T. P. Vijayalekshmi and Job Thomas

Part IV New Building Materials for Sustainable Construction

Experimental Studies on Physical Properties and Strength Response of Construction and Demolition Wastes 635
Ashok Kumar Suluguru, Arkamitra Kar, Anasua GuhaRay and Naveen James

Combined Effect of Steel Fibers with Ferrochrome Slag on Hardened Concrete 647
Rohit Shah and Tribikram Mohanty

An Experimental Investigation to Determine the Properties of Fly Ash Based Geopolymers as per Indian Standards 657
Suman Saha and C. Rajasekaran

Impact Response of Paver Blocks with Waste Tyre Crumb Rubber 669
R. Bharathi Murugan, E. Rama Sai and C. Natarajan

AAC Block Masonry with Ready Mix Mortar—An Experimental and Numerical Analysis 681
Deepa Doddamani and Mangala Keshava

Effect of Addition of Fly Ash and Superplasticizer on Ultra-fine Slag Based Geopolymer Mortar 693
Sulaem Musaddiq Laskar and Sudip Talukdar

Carbonation, Shrinkage and Long-Term Studies on Recycled Aggregate Concrete 703
V. Bhashya and B. H. Bharatkumar

Mechanical Properties of PVA and Polyester Fibers Based Engineered Cementitious Composites 715
S. B. Singh and Pankaj Munjal

A Correlation Study Between Lime Reactivity Strength Test and Calorimeter for Different SCMs 729
Anuj Parashar, Vineet Shah, Geetika Mishra and Shashank Bishnoi

Effects of Steel Fibre on Self-Compacting Concrete with Fly Ash 737
Gaurav Udgata and Ashoke Kumar Rath

Investigation on Characteristics of *Spinacia oleracea* as an Innovative Internal Curing Agent in Combination with Self-compacting Admixtures 747
G. S. Rampradheep, M. Sivaraja, M. Geetha, R. Saranya, R. Sathish, V. Vignesh, G. Kavin, K. Gayathiri, M. Balaji and R. Divya

Recycled Aggregate Concrete: Particle Packing Method (PPM) of Mix Design Approach 759
Subhasis Pradhan, Shailendra Kumar and Sudhirkumar V. Barai

Durability of Fly Ash Added Reinforced Concrete in Chloride and Composite Chloride–Sulfate Environment 773
Arya Anuj Jee and Bulu Pradhan

Study on Strength Reduction Factor of Blended Concrete Exposed to Seawater 787
T. Jena and K. C. Panda

Influence of Fly Ash and Silpozz on the Concrete Containing Crusher Dust as Sand Replacement Material 803
S. Jena and K. C. Panda

Behaviour of RC Structural Elements with Laced Reinforcement 817
V. Sai Venkata Ramanjaneyulu and G. Papa Rao

Influence of Metakaolin and Silpozz on Development of High-Strength Concrete 827
P. Sarangi and K. C. Panda

Influence of Particle Packing Method on Sustainable Concrete Using Fly Ash and Recycled Aggregates 841
Sushree Sunayana and Sudhirkumar V. Barai

Glass Fibre Reinforced Gypsum Panels for Sustainable Construction 855
S. R. Gouri Krishna, Philip Cherian, Devdas Menon and A. Meher Prasad

A Study on the Strength and Performance of Geopolymer Concrete Subjected to Elevated Temperatures 869
G. Mallikarjuna Rao, T. D. Gunneswara Rao, M. Siva Nagi Reddy and D. Rama Seshu

Degradation Kinetics of Cement-Based Materials in Citric Acid 891
K. P. Ramaswamy and Manu Santhanam

Influence of Blended Cement on the Fresh Properties of Self-compacting Concrete Incorporating Recycled Aggregate 907
Ranganathan Senthamilselvi and Purushothaman Revathi

Flow Characteristics of Polymer-Modified Sisal Fibre-Reinforced Mortar 921
Sriraman Priyadharshini and Gudimella Ramakrishna

Steel Fibres as a Partial Shear Reinforcement in Self-compacting Concrete 935
K. Praveen and S. Venkateswara Rao

On the Toughness Characterization of Fibre- Reinforced Concrete Using Notched Beam Tests 947
Sujatha Jose and Ravindra Gettu

Investigations on Aggregate Reactivity in Geopolymer Concrete 961
B. Singh and G. Ishwarya

Bond Behaviour of Recycled Aggregate Concrete 971
M. Surya, P. Lakshmy and V. V. L. K. Rao

Durability and In Situ Performance Evaluation of Sustainable Recycled Aggregate Concrete Using Fluorogypsum as Cementitious Binder 985
Monalisa Behera, A. K. Minocha, S. K. Bhattacharyya and Rajesh Deoliya

Shear Behaviour of Glass Fibre-Reinforced Geopolymer Concrete 999
K. Nithyapriya, K. Subramanian, X. John Britto and M. P. Muthuraj

Part V Mitigation of Structures Against Natural Hazards

The Effect of Macroroughness in Front of Building for Tsunami Pressure Dissipation—A Numerical Study 1013
D. Ghosh, A. K. Mittal, S. K. Bhattacharyya and S. Behera

Performance of Base-Isolated Building Frame for Extreme Earthquakes 1025
M. Bhandari, S. D. Bharti, M. K. Shrimali and T. K. Datta

Analytical Seismic Fragility Analysis of Existing Building Frame in Northeast India 1037
S. Mukherjee, S. Ghosh, S. Ghosh and S. Chakraborty

Seismic Vulnerability Assessment of Open Ground Storey Buildings 1051
G. V. Rama Rao, N. Gopalakrishnan and K. Sathish Kumar

Cyclic Behavior of Retrofitted-Reinforced Concrete Coupling Beams 1063
Romanbabu M. Oinam, P. C. Ashwin Kumar, Dipti Ranjan Sahoo and Kaushik Maran

Part VI Structural Health Monitoring

Nonlinear System Identification of Breathing Crack Using Empirical Slow-Flow Model 1075
J. Prawin and A. Rama Mohan Rao

Analytical Investigations on Structural Damage Identification Using Torsional Wave Propagation 1087
K. Varun Kumar, T. Jothi Saravanan, N. Gopalakrishnan and K. M. Mini

Damage Assessment in Composites Using Frequency Discrimination of Acoustic Emission Signals 1097
Sanjay Sengupta, Aloke Kumar Datta and Pijush Topdar

Handling Environmental and Operational Variations in Structural Health Monitoring 1111
K. Lakshmi and A. Rama Mohan Rao

Influence of Curing on Acoustic Emission Characteristics of Plain Concrete Subjected to Uniaxial Compression 1123
Richa Priyadarshi, Isha Narsaria, K. P. Sreejaya and R. Vidya Sagar

Size-Dependent Wave Propagation Response in Nanoscale Beams Using Spectral Finite Element Method Incorporating Surface Energy Effects 1135
N. Khandelwal and S. Kapuria

Reconstruction of Faulty Sensor Data in Time Domain 1149
A. Rama Mohan Rao, K. Lakshmi and Harshil Khimesara

A Novel Method for Vibration-Based Damage Detection in Structures Using Marginal Hilbert Spectrum 1161
Timir Baran Roy, Srishti Banerji, Soraj Kumar Panigrahi, Ajay Chourasia, Lucia Tirca and Ashutosh Bagchi

About the Editors

Dr. A. Rama Mohan Rao obtained his doctoral degree on high-performance computing techniques for nonlinear dynamic analysis from the Indian Institute of Science, Bangalore. He joined CSIR-SERC, Chennai, as a scientist in 1989 (after working nearly for a decade in the design and construction sector) and rose to the position of chief scientist. Currently, he heads the Structural Health Monitoring Laboratory, CSIR-SERC. He is also a Professor at the Academy of Scientific and Innovative Research (AcSIR) and has taught several advanced courses for M.Tech. and Ph.D. students. He was co-editor of the *Journal of Structural Engineering* from 2004 to 2007 and was an editorial board member for all the International Conferences on Parallel, Distributed, Grid and Cloud Computing for Engineering (PARENG 2009–2017) held in various European locations between 2009 and 2017. His research interests include computational structural mechanics; high-performance computing; structural system identification, control and health monitoring; nature-inspired computing, systems engineering; and combinatorial optimization. He has authored more than 95 peer-reviewed papers spread over 45 journals as well as 90 conference papers and several technical reports related to sponsored research and consultancy projects. He is a life member of several professional bodies and was awarded a UNDP fellowship for the year 1994–1995. He was a member of the team that won the CSIR Technology Prize in 1999 for scientific contributions to the development of advanced computational methodologies, modelling techniques and software for analysis and design of complex structures. He has also received an award for "excellence in high-performance cluster computing" from Sun Microsystems in February 2004. He was also a Visiting Research Scientist at the University of Berkeley, California, USA; Cornell University, Ithaca, USA; and Swansea University, UK, in 1994–1995.

Dr. K. Ramanjaneyulu graduated from the Regional Engineering College, Warangal (now NIT Warangal), and obtained his postgraduate degree in structural engineering from the Indian Institute of Science, Bangalore. He obtained his doctoral degree in structural engineering on stability behaviour of wind-loaded natural draught cooling tower shells from the IIT Madras in 1992. He joined SERC,

Madras, as a scientist in 1989 and rose to the position of chief scientist. He currently heads the Advanced Concrete Testing & Evaluation Laboratory (ACTEL), CSIR-SERC. He is also a Professor at the Academy of Scientific and Innovative Research (AcSIR). His research interests include the behaviour of reinforced concrete structures; analysis and design of special structures such as bridges and cooling tower shells; blast-resistant design of structures; nonlinear finite element analysis of reinforced concrete plate and shell structures; and structural health assessment and management of bridges. He has published over 80 papers in refereed national/international journals and over 100 papers at international and national conferences/seminars.

Part I
Analysis and Design of Concrete Structures

Analysis and Design of Tabletop Foundation for Turbine Generators

Siddhartha Bhattacharya

Abstract The paper illustrates through a practical example the step-by-step procedure adopted in designing a tabletop foundation supported on piles for a steam turbine generator with operating speed of 60 Hz. Finite element model of the tabletop foundation is generated in ANSYS. Analysis results are used to perform the static design checks. Dynamic analysis is performed to check for resonance and allowable amplitude limits of the foundation as specified by machine vendor.

Keywords Steam turbine generator foundation · Finite element
Static analysis · Dynamic analysis

1 General Introduction

Steam turbine generators (STG) and combustion turbine generator (CTG) are used in almost all modern petrochemical, LNG plants, and power plant facilities. Reinforced concrete tabletop foundations are required to support these high-speed rotating heavy machineries and are one of the most critical and challenging structures on any industrial project. Because of the complexity in the analysis and design of this type of a machine foundation, several modern analysis techniques are adopted to predict its exact behavior under sustained vibrating loads and to extract the results to perform the reinforced concrete design. Static and dynamic analysis is carried on with two different stiffness values for piles and material elasticity for concrete. The basic intent is to ensure that resonance does not take place under any circumstances and the amplitudes of vibration remain within allowable limits as specified by the vendor. The paper explains in detail, through a practical example problem, the step-by-step methods involved in the analysis and design of a tabletop foundation for a steam turbine generator operating at a speed of 60 Hz.

S. Bhattacharya (✉)
Bechtel India Pvt. Ltd, 244-245 Udyog Vihar, Phase IV, Gurgaon, Haryana, India
e-mail: sbhattac@bechtel.com

A. Rama Mohan Rao and K. Ramanjaneyulu (eds.), *Recent Advances in Structural Engineering, Volume 1*, Lecture Notes in Civil Engineering 11,
https://doi.org/10.1007/978-981-13-0362-3_1

2 Foundation Geometry

The STG pedestal supports a steam turbine machine which consists of one low-pressure turbine, one HP/LP (HP—high pressure; LP—low pressure) turbine, and one generator. All of the equipment are located at the operating deck. The layout of the operating deck is determined by the footprint of the machines. The condenser located beneath the low-pressure turbine is supported directly on the condenser piers that are sitting on the pedestal base mat.

The STG pedestal foundation is a massive concrete frame structure consisting of a 30.5 m × 12.0 m in plan and 2.4 m thick operating deck (also known as tabletop) supported by eight columns, all of which are supported by a 32.4 m × 14.4 m in plan and 2.3 m thick base mat on piles. The top elevation of the tabletop is 11.85 m above the top of the base mat. Columns are located at 150 mm within the edges of the tabletop to facilitate rebar placement. There are three openings in the tabletop for the connections of various pipes and equipment to the underside of the steam turbine generator. A general view of the STG foundation is shown in Fig. 1. Pile arrangement is shown in Fig. 2. The number of piles is calculated based on a manual estimate of the number of piles required to resist the vertical and lateral loads under operating and seismic conditions. Labels are used to identify the

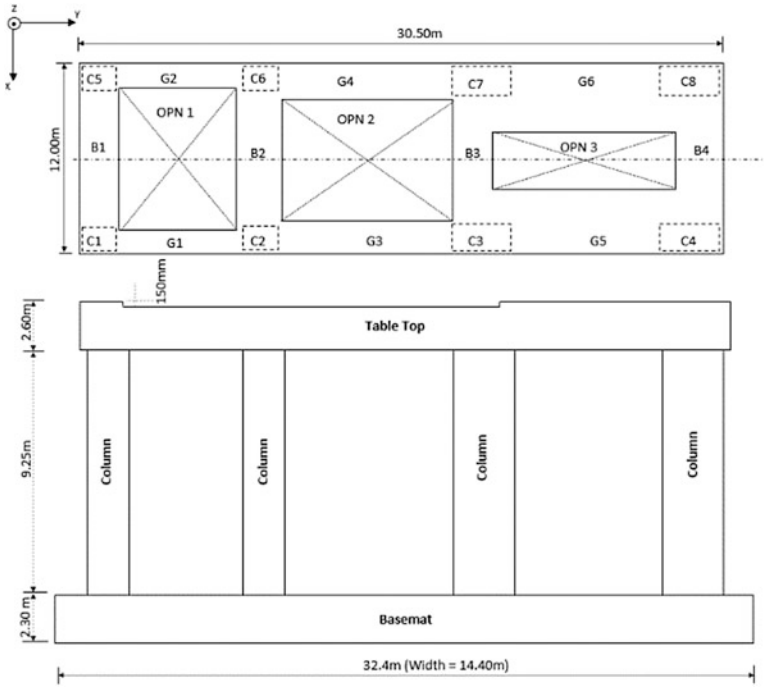

Fig. 1 Geometric details of STG foundation

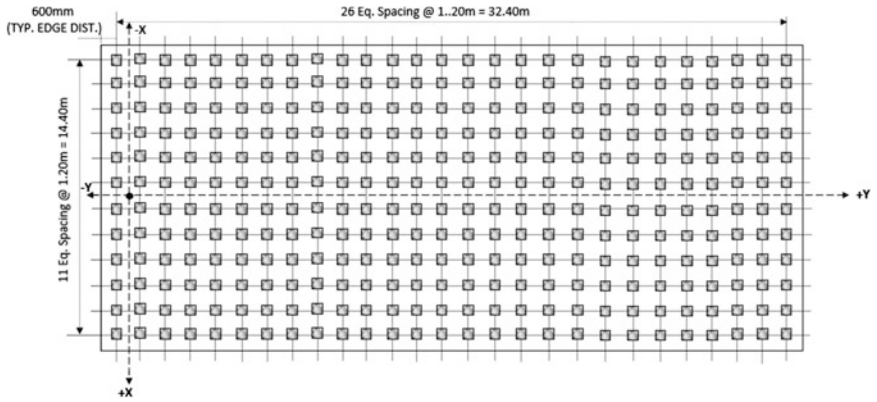

Fig. 2 Pile layout plan

Table 1 Geometric properties of the foundation

Member		*H* (m)	*B* (m)
Columns	C1–C5	2.10	2.10
	C2–C6	2.10	2.10
	C3–C7	2.75	2.10
	C4-C8	2.75	2.10
Girders/beams	G1–G2	2.45	2.45
	G3–G4	2.45	3.00
	G5–G6	2.60	4.00
	B1	2.45	2.06
	B2	2.45	1.65
	B3	2.45	1.85
	B4	2.60	2.75

different structural elements. The elements in the longitudinal direction are referred to as girders and the transverse elements are identified as beams. In the same way, vertical elements are referred to as columns. Table 1 shows the dimension details of the structural components.

3 Finite Element Model

Based on the initial sizing, as specified above, a 3-D solid finite element model is created to assess the behavior of the STG foundation. 10-noded tetrahedral element (SOLID92) is created in ANSYS for generating the mesh for the entire model. SOLID92 element has a quadratic displacement behavior and is well suited to

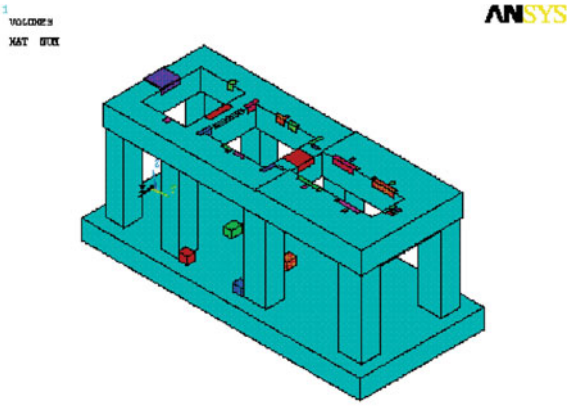

Fig. 3 ANSYS model of the tabletop foundation

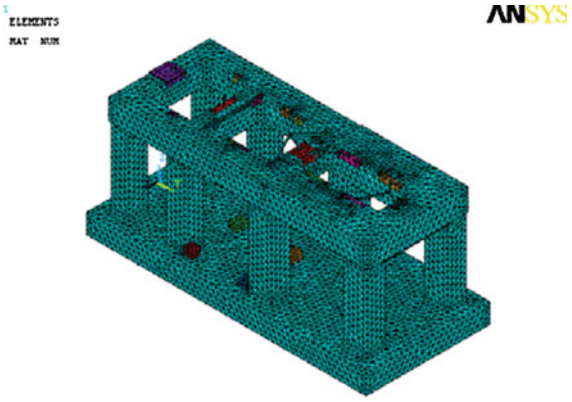

Fig. 4 Meshed model of the tabletop foundation

model irregular meshes. The foundation piles are modeled as springs at each pile locations with two horizontal and one vertical stiffness using spring–damper elements (COMBIN14). The solid model is presented in Fig. 3, and meshed model is presented in Fig. 4. For dynamic analysis, machine mass is modeled at each sole plate location by adjusting the mass density of the embed volumes at each sole plate location using the formula

$$\rho_i = \rho_c + \frac{W_{\mathrm{mi}}}{V_i} \tag{1}$$

where ρ_i is the density assigned to the contact volume, ρ_c is the density of reinforced concrete, and W_{mi} is the machine mass acting on the contact volume V_i. This approach is used for purposes of both dynamic and static analyses. Other machine loads are applied by dividing the loads by total number of nodes within the

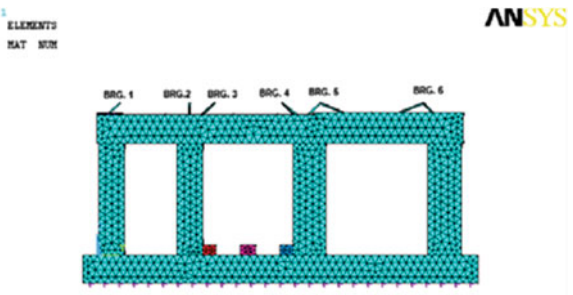

Fig. 5 Meshed model showing bearings

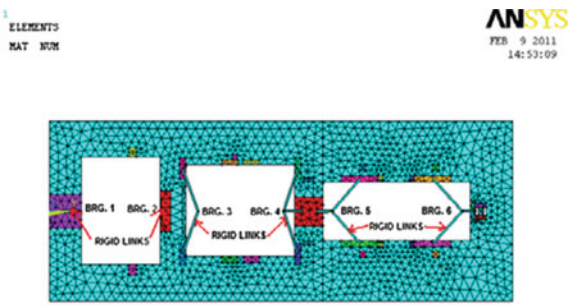

Fig. 6 Meshed model showing bearings and rigid links

corresponding designated volume. The six bearing locations are modeled as nodes at the shaft level of the machine and are connected to the center of sole plates with very stiff axial beam elements. The sole plates are modeled in a way that the center of the plate is a master node and all other nodes on the plate are slaves. This is done to simulate the rigid behavior of the plates (Fig. 6).

4 Loads and Load Combinations

Loads and load combinations are adopted as per the specifications from vendor, standard industry practice, and relevant ASCE and ACI codal provisions. In general, the following loads are adopted in analyzing and designing the STG foundation:

(a) Dead load (DL)
(b) Live load (LL)
(c) Thermal load (TL)
(d) Vacuum load (VL)
(e) Normal torque load (TN)
(f) Emergency torque load (TE)

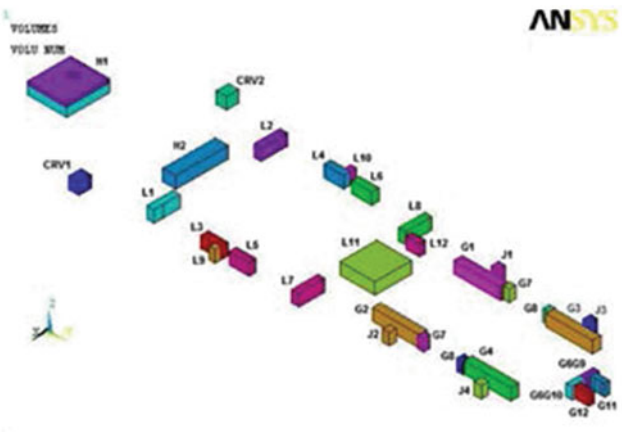

Fig. 7 Volumes for load points and sole plate ID

(g) Jacking post load (JP)
(h) Bowed rotor accidental load (BR)
(i) Loss of bucket load (LB)
(j) Unbalanced load (UNL)
(k) Condenser flooding load (CF)
(l) Wind load (WL)
(m) Seismic load (EL)
(n) Non-sliding load (NSL)

These loads are applied as uniformly distributed nodal loads in the loading volumes at sole plate locations. Such loading volumes are shown in Fig. 7.

The load combinations adopted for checking the capacity of pile foundations are as follows:

(a) DL + LL
(b) DL + LL ± 0.7EL
(c) 0.6DL ± 0.7LL
(d) DL + LL + TN + UNL
(e) DL + LL + TN + 0.7EL + UNL
(f) DL ± NSL + TN
(g) DL + TL
(h) DL + TN ± BR
(i) DL + JP
(j) DL + CF

The load combinations adopted for static check and reinforced concrete design of the foundation are as follows:

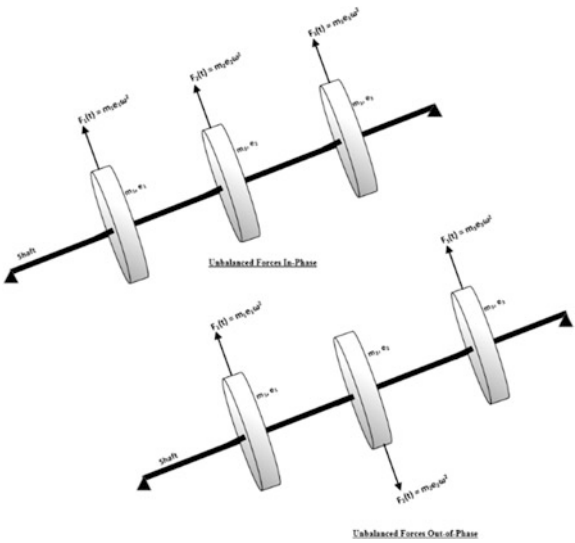

Fig. 8 Unbalanced loads at bearing locations

(a) 1.4DL
(b) 1.2DL + 1.6LL
(c) 1.2DL + LL ± EL
(d) 0.9DL ± EL
(e) 1.4DL + 1.4VL
(f) 1.2DL + 1.6LL + 1.2VL ± 1.6TL + 1.6TN + 1.6UNL
(g) 1.2DL + LL + 1.2VL + TN ± EL + UNL
(h) DL + VL ± NSL + TN
(i) DL + VL + TN
(j) DL + VL + TN ± BR
(k) DL + VL + TN ± LB
(l) DL + JP
(m) DL + CF

The most important thing to note in these combinations is that the unbalanced load and bowed rotor accidental loads need to be considered in both vertical and horizontal directions one at a time. For seismic load, both horizontal, vertical and orthogonal loading directions need to be considered simultaneously with full contribution from one direction along with 30% contribution from orthogonal directions (Fig. 8).

5 Static Serviceability Check

Misalignment tolerance matrix (MTM) deflection criteria check is the most importance static acceptance criteria for an STG foundation. This check is performed to ensure that the turbine generator foundation is rigid enough to assure correct bearing alignment during its operating condition. The checks are performed as per vendor provided guidelines in order to ensure that the foundation meets the criteria for the proper functioning of the machine. The MTM defines the percentage of available misalignment that is consumed at a given bearing due to a displacement at another bearing. It can be described as an "Influence Coefficient Approach". The deflections that may result from various loadings on the foundation after initial alignment are calculated. These deflections are then multiplied by the influence coefficient as provided by the vendor to calculate the response at a particular bearing location due to deflection at other bearing locations. In Fig. 5, if R_3' is the initial response at bearing location 2 and y_1, y_2, y_3, y_4, y_5, and y_6 be the deflections at bearing locations with influence coefficient C_1, C_2, C_3, C_4, C_5, and C_6, then the resultant response (R_3) at bearing location 2 will be

$$R_3 = R_3' + C_1 y_1 + C_2 y_2 + C_3 y_3 + C_4 y_4 + C_5 y_5 \tag{2}$$

Apart from this, other serviceability checks performed on the STG foundation are as follows:

(a) Relative radial displacement between adjacent bearings.
(b) Differential settlement at the foundation base mat.
(c) Top surface rotation of specific piers.
(d) Differential displacement of any three adjacent piers.
(e) Crack width of the deck elements.
(f) Precise location of all embeds on the deck.

6 Dynamic Analysis

Dynamic analysis of the turbine generator foundations is performed in two steps:

(a) Modal analysis—It is performed to determine the governing modes of the foundation where more than 95% of the mass participation takes place. Also, it is used to determine whether any resonance is taking place during operating condition of the machine, i.e., whether the fundamental frequencies of vibration of the foundation in X, Y, and Z directions are coinciding with the operating frequency of the machine. Also, it gives a clear picture of the mass participation in other modes through which machine passes during startup and shutdown

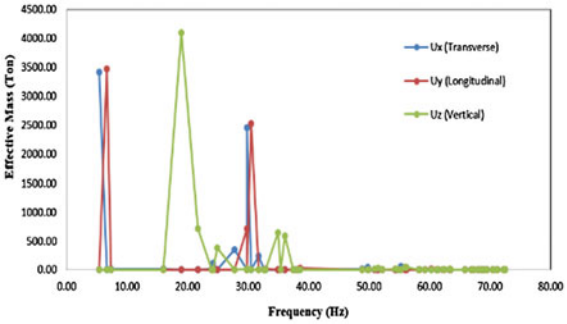

Fig. 9 Plot showing the frequencies at which maximum mass participation occurs and also indicates that no mass participation occurs within ±20% of maximum operating frequency (60 Hz)

phase. As an industry practice, the fundamental frequency of the machine foundation is kept outside the range of ±20% of the operating frequency of the machine.

The modal analysis results in Fig. 9 shows that the fundamental frequencies of the foundation are outside ±20% of the operating frequency of the machine hence the frequency analysis shows that there is no probability of occurrence of resonance under operating condition. In case the natural frequency of the foundation would have fallen within this ±20% range, then, in that case, there would have been two options that could be adopted to resolve the resonance issue. The first option is mass tuning of the foundation wherein the foundation can be either over tuned or under tuned to avoid resonance. In case mass tuning of foundation is not possible then the other option is to go for harmonic analysis in which the amplitudes are determined in the frequency range of ±20% of the operating frequency of the machine and compared with allowable amplitudes as specified by the vendor and those stipulated in the industry standards for human comfort level. Modified Reiher-Meister figure (barely perceptible, noticeable, and troublesome) is generally used to establish the limits with respect to personnel sensitivity (Figs. 10 and 11).

(b) Harmonic analysis—This is a forced vibration analysis in which the amplitudes and peak velocity of vibration of the machine are calculated at different sole plate locations and determined over a definite frequency range to assess the severity of vibration of the machine foundation. Vendor specified limits are adopted for checking the severity. For this foundation, the limiting peak velocity is adopted as 1.55 mm/sec and limiting peak amplitude is adopted as 0.004 mm.

Foundation is analyzed for unbalanced loads of the machine at the bearing locations. These loads either act in-phase or out-of-phase with each other, and effects are estimated for each of the conditions. The displacement amplitudes at the sole plate locations, as obtained from the analysis, are plotted with reference to the vendor supplied allowable limits in Figs. 12, 13, 14 and 15.

The graphs basically represent the results of sweeping frequency analysis for in-phase and out-of-phase loadings. The displacement amplitude at each of the sole

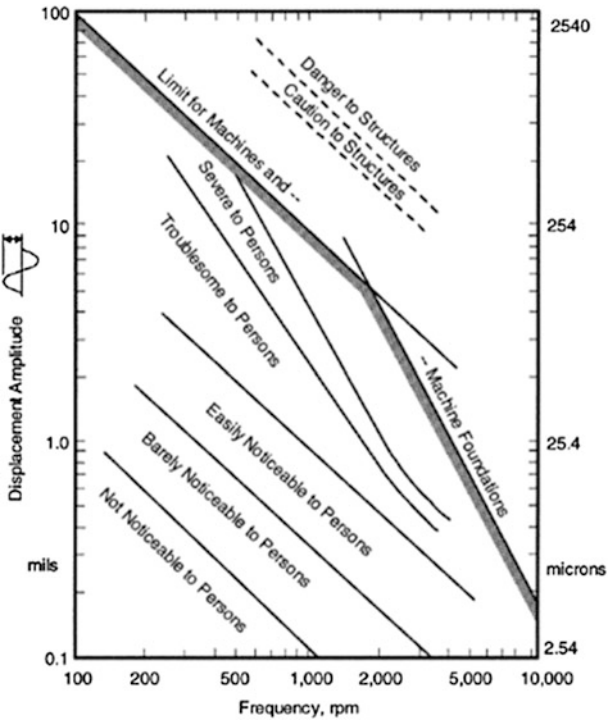

Fig. 10 Reiher-Meister chart

plate locations is found to be much below the allowable displacement amplitude limits, and hence, the foundation is considered to be safe in terms of strength and serviceability.

7 Reinforced Concrete Design

Reinforced concrete design of the components of the tabletop foundation is carried on as per the stipulated guidelines of ACI codes and ASCE task committee report on design of turbine generator foundations. Element stresses of the entire cross section of the members are taken at the support and span locations. These stresses are integrated over the cross section to calculate the axial loads, bending moments, shear forces, and torsion. All the structural components are designed as column members subjected to all the four types of design forces. In most of the cases, the sectional sizes as provided are much more than that required from design; however, these sections need to be provided to satisfy the mass criteria for the dynamic behavior of the foundation. A minimum steel of 0.5% of the cross-sectional area is

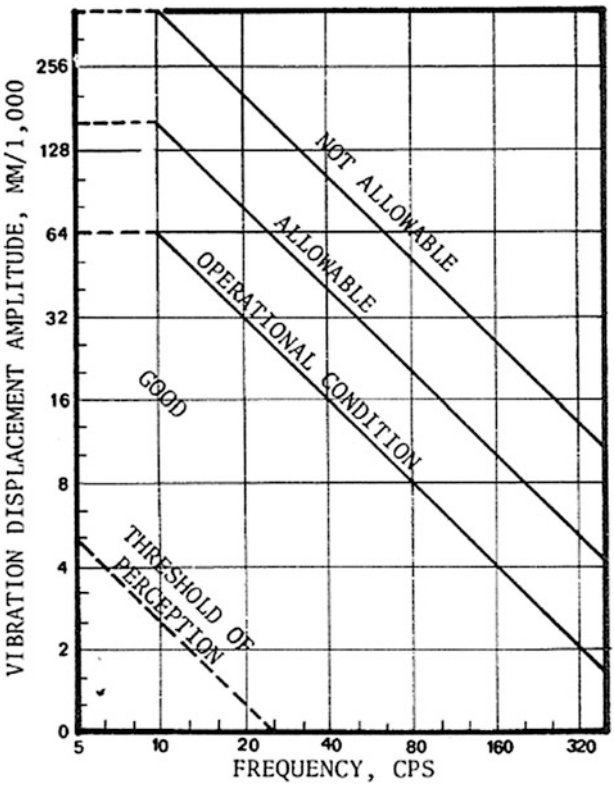

Fig. 11 Turbomachinery bearing vibration limits (Ref. [3])

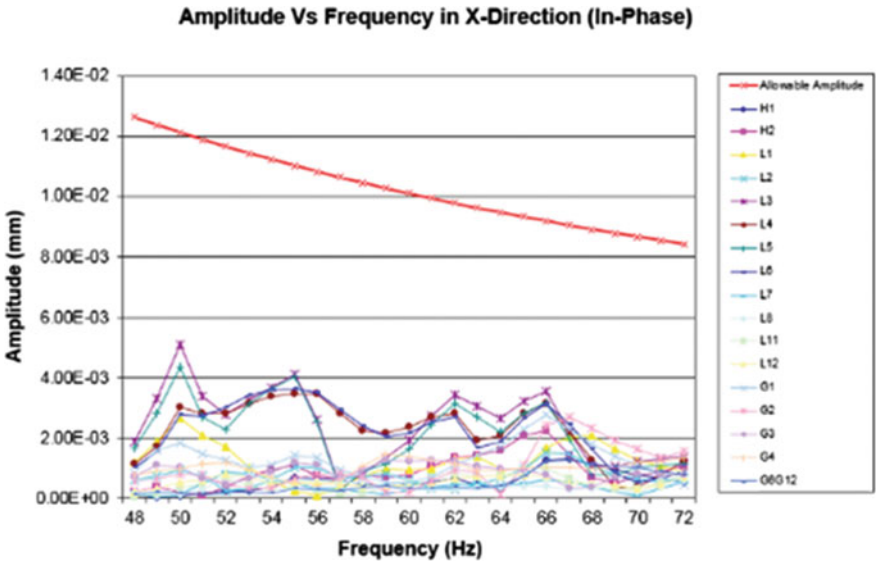

Fig. 12 Vibrations in *X*-direction (in-phase)

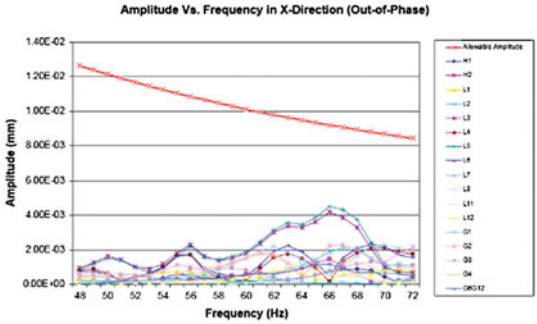

Fig. 13 Vibrations in *X*-direction (out-of-phase)

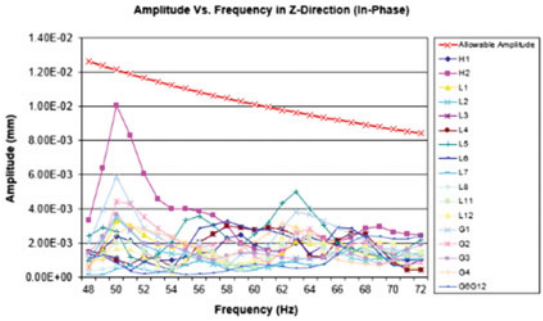

Fig. 14 Vibrations in *Z*-direction (in-phase)

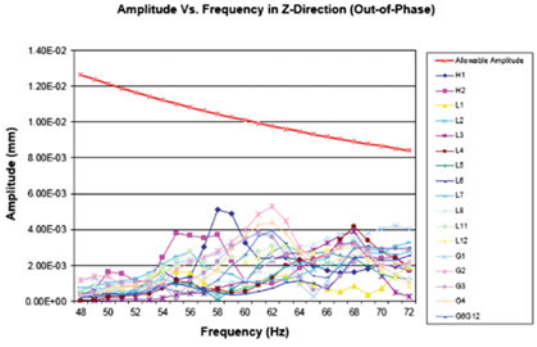

Fig. 15 Vibrations in *Z*-direction (out-of-phase)

provided as per the codal provisions. The maximum rebar spacing along any edge of concrete is limited to 250 mm. The sections are designed in two stages. In the first stage, it is checked for axial load and biaxial moment using load–moment strength interaction diagrams given in ACI SP-17 corresponding to grade of steel and concrete with reinforcement being equally distributed on all sides. A typical load–moment chart being used for the present design is shown in Fig. 16.

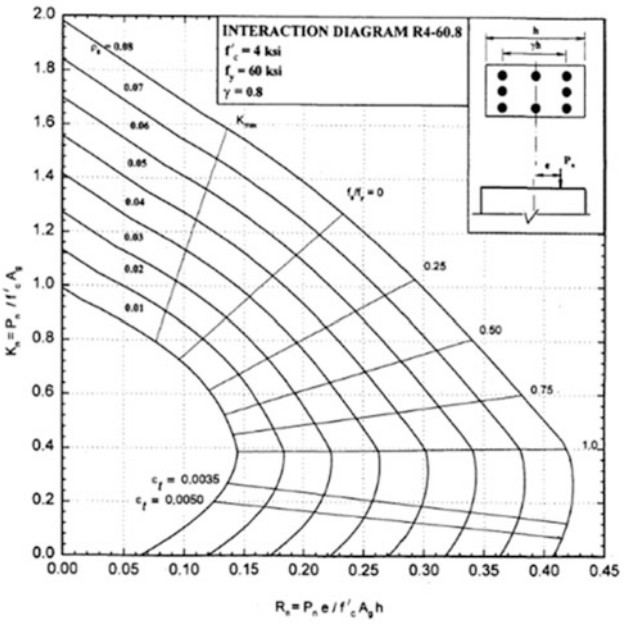

Fig. 16 Load-moment diagram, ACI Sp-17 (Ref. [4])

If the axial load on the members is more than 10% of the compression capacity of unreinforced concrete member of equivalent section, i.e., if $P_n > 0.1f_cA_g$, then Bresler reciprocal load method is used to determine the section capacity using Eq. (3).

$$P_n \leq \frac{1}{\frac{1}{P_{ox}} + \frac{1}{P_{oy}} - \frac{1}{P_o}} \tag{3}$$

where

P_n Design axial load on the member.
P_{ox} Axial capacity of the member corresponding to moment about x-axis, M_{nx}.
P_{oy} Axial capacity of the member corresponding to moment about y-axis, M_{ny}.
P_o Axial capacity of the member with zero moment.

If $P_n < 0.1f_cA_g$, then PCA load contour method needs to be used as per Eq. (4).

$$\left(\frac{M_{nx}}{M_{ox}}\right)^{\left(\frac{\log(0.5)}{\log\beta}\right)} + \left(\frac{M_{ny}}{M_{oy}}\right)^{\left(\frac{\log(0.5)}{\log\beta}\right)} \leq 1.0 \tag{4}$$

where

M_{nx}, M_{ny} Design axial load on the member about x- and y-axis.
M_{ox} Moment capacity of the member about x-axis corresponding to load $P_{o.}$
M_{oy} Moment capacity of the member about y-axis corresponding to load $P_{o.}$
β Value ranges from 0.55 to 0.7.

The second stage of design involves the checking of the section for shear and torsional capacities. Generally, such huge sections are not critical in terms of torsion. In some cases, the design of torsional reinforcement to resist local accident loads like short circuit and lost bucket can be challenging. Another important check that is performed on this structure is the ductility check where it is assured that the moment capacity of the reinforced concrete section is not less than 20% more than the cracking moment of the section. Reinforcement detailing is done as per the relevant provisions of ACI 318.

8 Conclusion

Analysis and design of the tabletop foundation is carried out to satisfy the strength and serviceability checks, and is found to be satisfactory. This analysis and design procedure is adopted to do an in-depth simulation and checking of the exact behavior of the foundation under the operating condition of the machine. This paper is mainly limited to the conventional analysis and design procedures under operating machine loads. Seismic design and detailing of these tabletop foundations is also an interesting area to deal with. IS 13920 specifies that ductile detailing needs to be done for all the reinforced concrete structures, which calls in for ductile design and detailing for these massive structures but an important thing to note here is that these structures are mostly designed as uncracked, and as such, ductile detailing need not be considered as this will unnecessarily increase the project cost. An important opportunity area that needs to be explored in the design of this kind of foundation is the simulation of the condition when seismic base excitation is applied under the operating condition of the machine. An important area which needs substantial research for these kinds of foundations is the implementation of precast technology with special emphasis on the connection design between various elements which can sustain long-term fatigue loading. This will be of tremendous impact in terms of total installation cost (TIC) of a project as cast in place foundations for these massive structures are time-consuming and labor-intensive. Also, the application of precast will help to ensure a better quality control in terms of construction for such an important structure. Since these foundations are subjected to continuous dynamic loads, posttensioning may be a good option that can be adopted in case of precast tabletop foundations.

References

1. ACI 351.3R-04. *Foundation for Dynamic Equipment.*
2. ACI 318–05. *Building Code Requirements for Structural Concrete*.
3. Arya, S., O'Neill, M., & Pincus, G. (1979). *Design of structures and foundations for vibrating machines*. Houston, Texas: Gulf Publishing Co.
4. ACI 340R-97. *ACI Design Handbook, Design of Structural Reinforced Concrete Elements in Accordance with the Strength Design Methods ACI 318-95, Publication SP-17(97).*
5. Task Committee on Turbine Foundations. (1987). *Design of Large Steam Turbine-Generator Foundations*. New York: Published by the American Society of Civil Engineers.

Effect of Infill Wall Stiffness on Seismic Analysis of High-Rise Building Resting on Sloping Ground

Kolasani Rajasekhar and Maganti Janardhana

Abstract Buildings constructed on hill slopes are highly unsymmetrical in nature. The buildings situated on hill slopes are generally irregular, torsionally coupled, and hence susceptible to severe damage when affected by earthquake ground motion. In this paper, a 21-storeyed RC framed building resting on sloping ground is studied. Seismic response of the high-rise building is carried out using linear static analysis and linear dynamic analysis (response spectrum analysis). This paper also compared the behavior of RC framed building resting on plain ground and resting on sloping ground including the effect of infill wall stiffness.

Keywords RC building · Sloping ground · Infill stiffness

1 Introduction

The Indian subcontinent has a history of earthquakes. North and northeastern parts of India have large scales of hilly region, which are categorized under seismic zones III, IV, and V. In this region, the construction of multistoried RC framed buildings on hill slopes is inevitable. Dynamic characteristics of buildings on sloping ground are significantly different from the buildings resting on flat terrain, as these are irregular and unsymmetrical in vertical directions.

K. Rajasekhar · M. Janardhana (✉)
JNTUH College of Engineering Hyderabad, Hyderabad, India
e-mail: prof.jmaganti@gmail.com

K. Rajasekhar
e-mail: kolasanirajasekhar@gmail.com

A. Rama Mohan Rao and K. Ramanjaneyulu (eds.), *Recent Advances in Structural Engineering, Volume 1*, Lecture Notes in Civil Engineering 11,
https://doi.org/10.1007/978-981-13-0362-3_2

2 Description of Building

A commercial cum residential building of G + 21 RC building having the base dimension of plan 23.62 m × 25.15 m with constant floor height of 4.0 m including the of a stilt floor is considered for the analysis.

The building has 21 storeys symmetrical in plan with five bays in *X*-direction (along the slope) and eight bays in *Y*-directions, and elevation as shown in Figs. 1 and 2, respectively. The superstructure is modeled using the commercially available software SAP2000 (v14.0.0) [3] as a space frame.

2.1 Input Data

The parameters and loads considered for the analysis are as per IS 1893 (Part1) [1] and are mentioned below.

2.1.1 Seismic Parameters

Seismic zone	III
Type of soil	Medium
Importance factor	1
Response reduction factor	3
Damping ratio	5%
Type of structure	OMRF

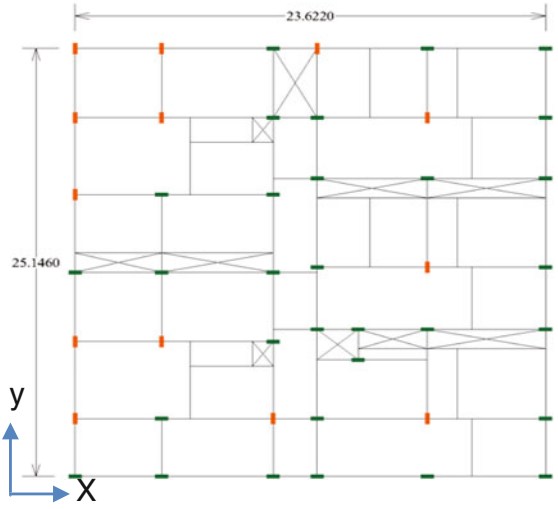

Fig. 1 Typical floor plan

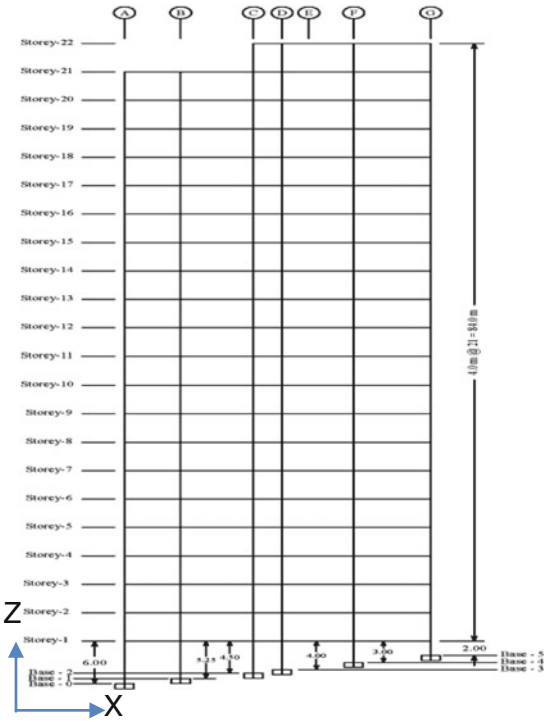

Fig. 2 Elevation

2.1.2 Seismic Parameters

Unit weight of concrete	25.0 kN/m^3
Live load (residential)	2.0 kN/m^2
Live load (cellar)	5.0 kN/m^2
Live load (roof)	1.5 kN/m^2
Staircase load—live	7.734 kN
Staircase load—dead	30.937 kN
Wall load (230 mm thick)	16.0 kN/m
Wall load (115 mm thick)	8.0 kN/m

Plinth beam size	400 × 500 mm
Roof beam size	400 × 650 mm
	400 × 750 mm
Column size	450 × 1500 mm
	1500 × 450 mm
	500 × 1500 mm
	1500 × 500 mm
Slab thickness	100 and 150 mm
Thickness of wall	230 and 115 mm

2.1.3 Material Properties

Grade of concrete M35
Grade of steel Fe500

2.1.4 Infill Walls

The infill walls are modeled as equivalent struts and shown in Fig. 3, and the strut parameters are calculated using Eq. (1) and shown in Tables 1 and 2.

The equivalent width (w) of the infill wall proposed by a scientist Hendry [2] is given by

$$w = \frac{1}{2}\sqrt{\alpha_h^2 + \alpha_L^2} \tag{1}$$

where

$$\alpha_h = \frac{\pi}{2}\left[\frac{E_f I_c h}{2E_m t \sin 2\theta}\right]^{1/4} \tag{2}$$

$$\alpha_L = \frac{\pi}{2}\left[\frac{E_f I_b L}{2E_m t \sin 2\theta}\right]^{1/4} \tag{3}$$

$$\theta = \mathrm{Tan}^{-1}\left(\frac{h}{L}\right) \tag{4}$$

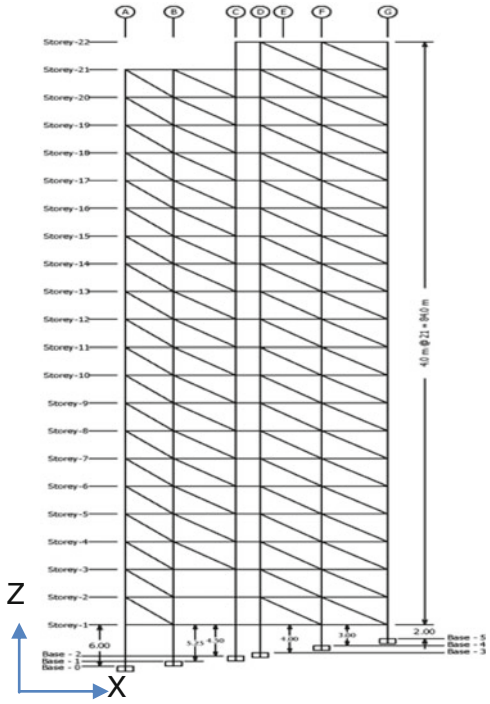

Fig. 3 Equivalent diagonal strut in *X*-direction

θ Slope of infill wall diagonal to the horizontal,
E_m Elastic modulus of masonry wall = 2720.0 N/mm^2,
E_f Elastic modulus of masonry of frame material,
t Thickness of the infill wall,
h Height of the infill wall,
L Length of the infill wall,
I_c Moment of inertia of the column of the frame,
I_b Moment of inertia of the beam of the frame, and
w Width of the equivalent strut.

Table 1 Equivalent strut parameters in *X*-direction

Strut	Wall thickness (m)	Equivalent width (m)
1	0.115	2.1
2	0.115	2.5
3	0.23	2.0
4	0.23	2.1
5	0.23	2.3
6	0.23	2.3

Table 2 Equivalent strut parameters in *Y*-direction

Strut	Wall thickness (m)	Equivalent width (m)
1	0.115	2.0
2	0.115	2.4
3	0.23	1.7
4	0.23	2.0

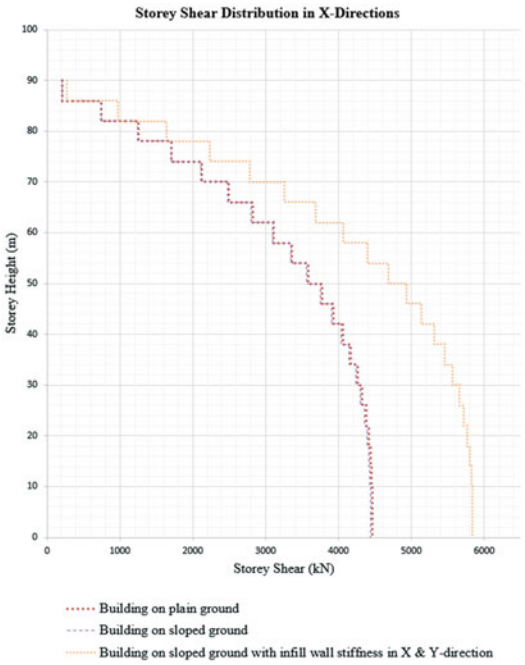

Fig. 4 Storey shear distribution for seismic load in the *X*-direction with storey height for building on plain and sloping ground

3 Results and Discussion

During vibration, reinforced concrete (RC) frame buildings having columns of different heights within one storey, the shorter columns have suffered relatively higher damage when compared to taller columns. A short column is relatively stiffer when compared with that of a tall column. Hence, it attracts relatively higher earthquake force. Structures may be irregular due to nonuniform distribution of mass, stiffness, and strength or due to their structural form. Buildings resting on sloping ground are also irregular.

A building on plain and sloping ground by considering infill wall stiffness in both *X*- and *Y*-directions was analyzed for linear static and dynamic behavior using SAP [3] (v14.0.0).

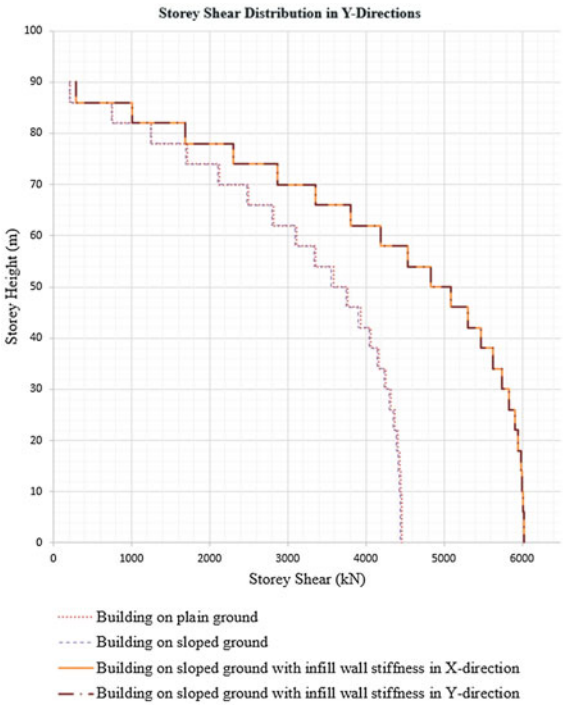

Fig. 5 Storey shear distribution for seismic load in the *Y*-direction with storey height for building on plain and sloping ground

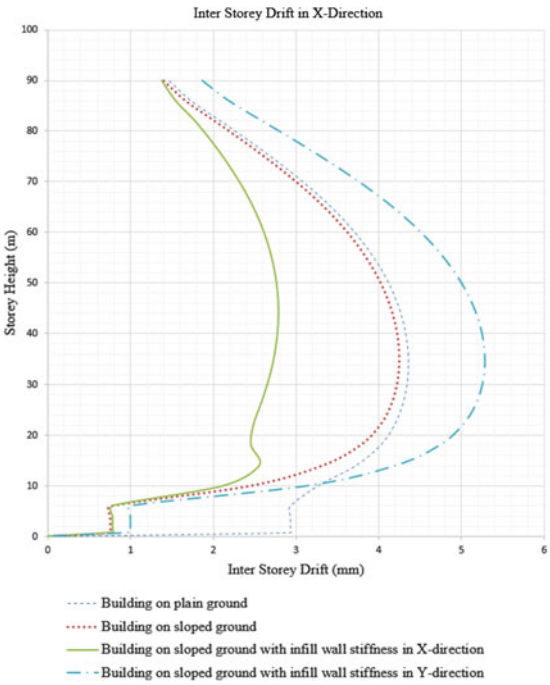

Fig. 6 Inter storey drift for seismic load in the *X*-direction with storey height for building on plain and sloping ground

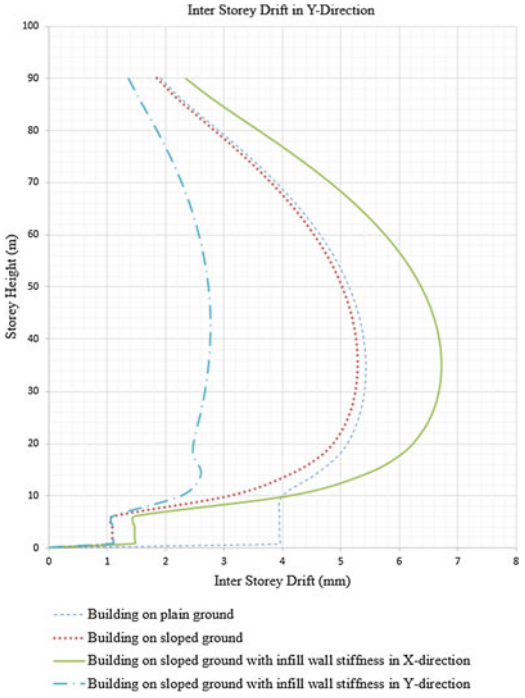

Fig. 7 Inter storey drift for load in the *Y*-direction for building on plain and sloping ground

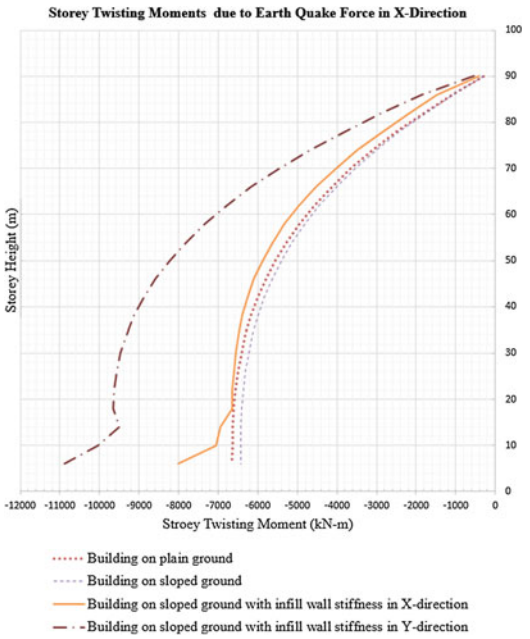

Fig. 8 Storey twisting moment in *X*-direction for building on plain and sloping ground

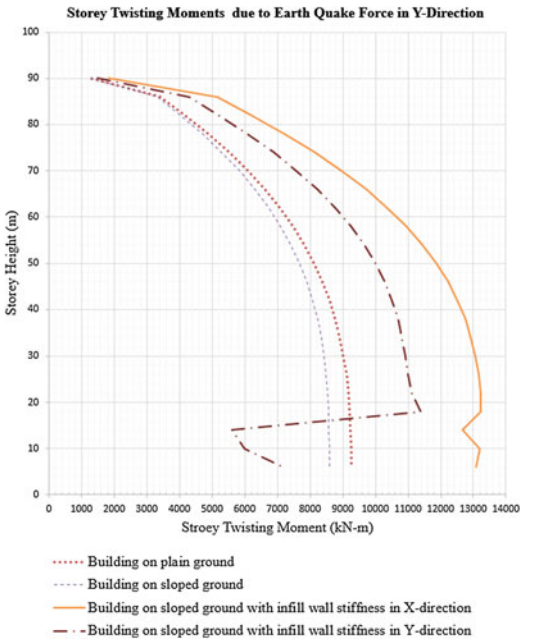

Fig. 9 Storey twisting moment in *Y*-direction with storey height for building on plain and sloping ground

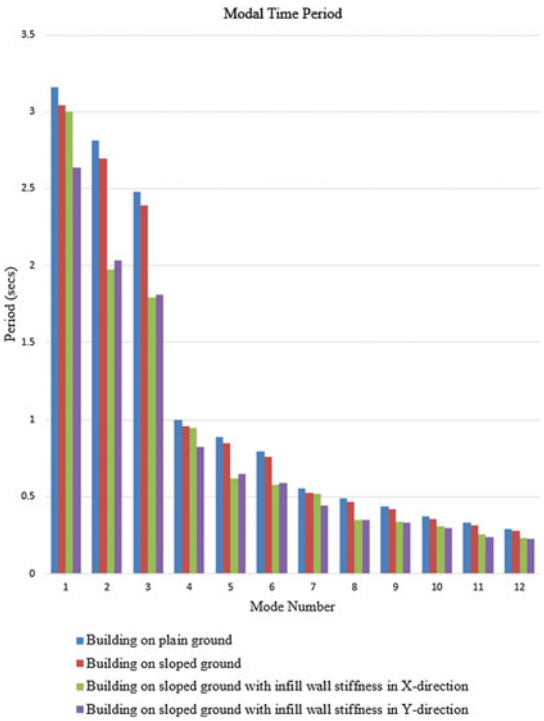

Fig. 10 Modal time period for building on plain and sloping ground

3.1 Results of Linear Static Analysis

It is observed from Figs. 4 and 5 that the base shear is relatively higher for a building if the infill wall stiffness is considered.

Inter storey drift is observed to be relatively less if the infill wall stiffness is considered as shown in Figs. 6 and 7.

When the stiffness of infill walls in the *X*-direction is considered, it is observed that there is a higher magnitude of twisting in the *Y*-direction as shown in Fig. 8. Similar behavior is observed when the infill stiffness in the *Y*-direction is considered as shown in Fig. 9.

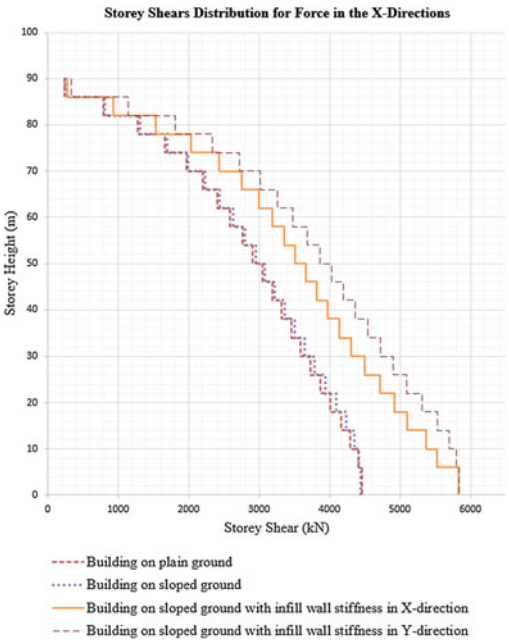

Fig. 11 Storey shear distribution for seismic load in the *X*-direction with storey height for building on plain and sloping ground

3.2 Response Spectrum Analysis Results

It is observed from Fig. 10 that there is a decrease in the time period with the increase in mode number.

There is an increase in the storey shears in the *Y*-direction when the seismic load was considered in the *X*-direction when the effect of infill wall stiffness in the *X*-direction is considered as shown in Fig. 11. Similar behavior is observed in the *X*-direction when the seismic load was considered in the *Y*-direction when the effect of infill wall stiffness in the *Y*-direction is considered as shown in Fig. 12.

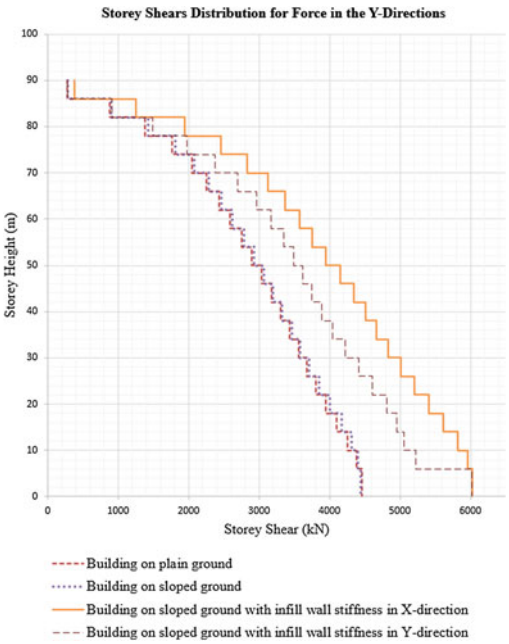

Fig. 12 Storey shear distribution for seismic load in the *Y*-direction with storey height for building on plain and sloping ground

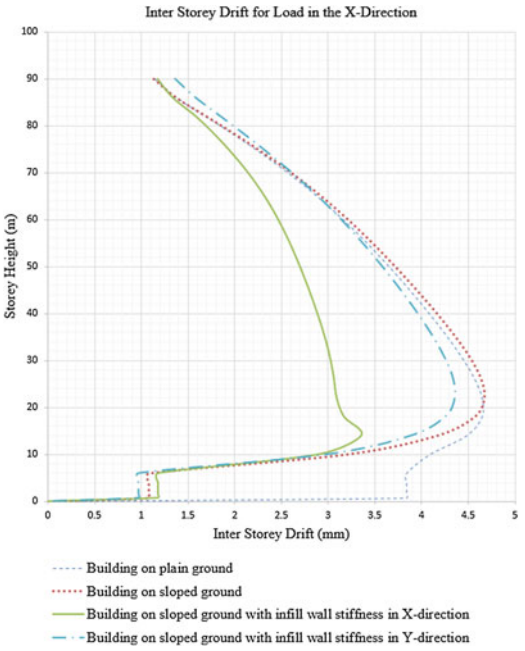

Fig. 13 Inter storey drift for seismic load in the *X*-direction for building on plain and sloping ground

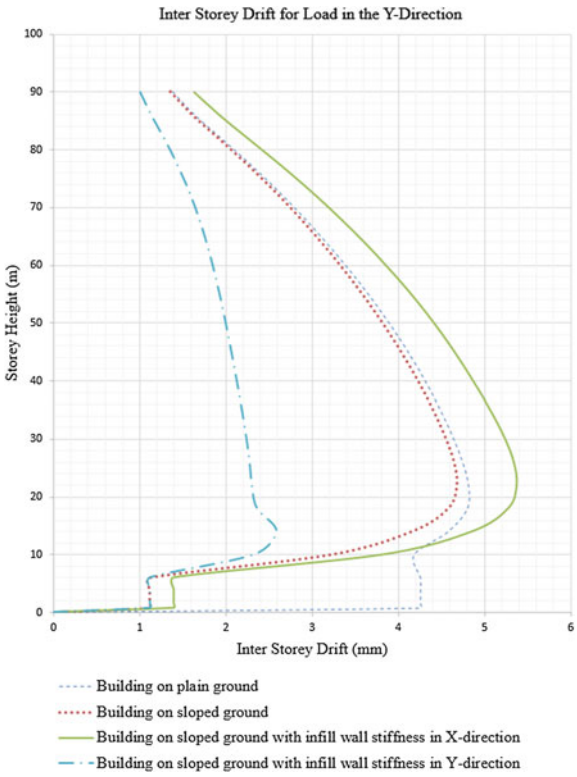

Fig. 14 Inter storey drift for seismic load in the *Y*-direction for building on plain and sloping ground

Inter storey drift is observed to be relatively less if the infill wall stiffness is considered as shown in Figs. 13 and 14 as is observed for linear static analysis case (vide: Figs. 6 and 7).

When the stiffness of infill walls in the *X*-direction is considered, it is observed that there is a higher magnitude of twisting in the *Y*-direction as shown in Fig. 15. Similar behavior is observed when the infill stiffness in the *Y*-direction is considered as shown in Fig. 16. This behavior is observed for linear static analysis (vide: Figs. 8 and 9) also.

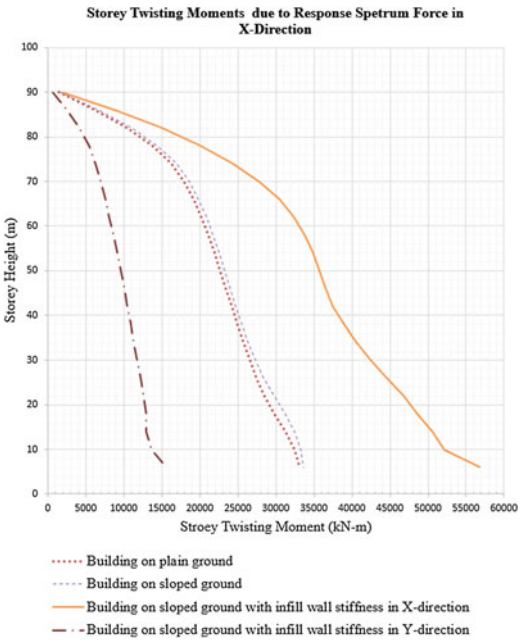

Fig. 15 Storey twisting moment in *X*-direction with storey height for building on plain and sloping ground

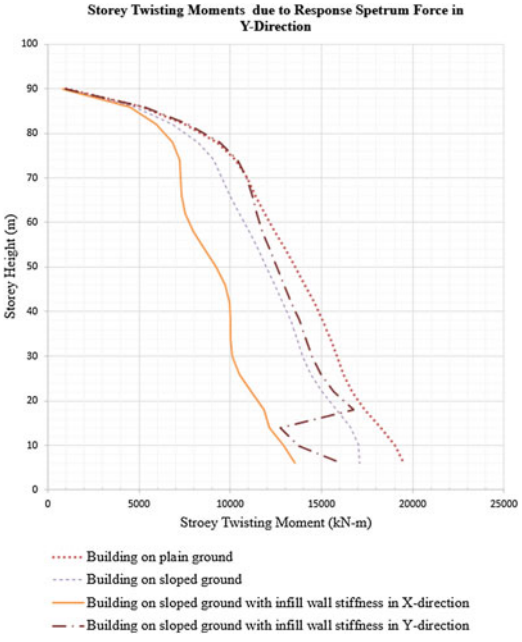

Fig. 16 Storey twisting moment in *Y*-direction for building on plain ground and sloping ground

4 Conclusions

Based on the seismic analysis of G + 21 storey building resting on sloping ground, the following conclusions are drawn:

(a) The development of torsional moments in building resting on sloping ground is higher than that in the building resting on plain ground. Hence, buildings resting plain ground are the parameters and loads considered to seismic ground motion than the building resting on sloping ground.
(b) In the building resting on a sloping ground, it is observed that extreme left columns at ground level, which are short, are the worst affected. Hence, special attention should be paid to these columns in design and detailing.
(c) From the observation of the results, it is observed that with the decrease in the time period, there will be an increase in the base shear of the building along the sloping ground.
(d) It can be concluded that drift of a storey is a not only a function of storey height but also depends on the weight of that storey. It can also be concluded that introduction of infill wall stiffness can reduce the storey drifts.
(e) Storey shear, storey drift, and storey displacements of the building are relatively lesser if response spectrum method is adopted for seismic analysis instead of equivalent static method.
(f) Time period is getting reduced with the increase in the number of modes. The time period of building with mass irregularity is comparatively lesser than that of regular building as the stiffness of the building considered is higher than that of a regular building.

References

1. IS 1893(Part 1). (2002). Criteria for earthquake resistant design of structures. Part 1 General Provisions and building, *Bureau of Indian Standards*.
2. Paulay, T., & Priestley, M. (1992). *Seismic design of reinforced concrete and masonry buildings*. New York: Wiley Inc.
3. SAP. (2000). *integrated software for structural analysis and design*. Berkeley, CA, USA: Computers and Structures Inc.

Effect of Pile Layout and Pile Cap Thickness on Load Distribution in Piles

Meenu Sharma

Abstract The paper illustrates, through practical examples, the effect of pile layout and pile cap thickness on the load distribution among different piles in a pile group. Study has been done considering square and rectangular pile cap configurations with different pile cap thickness being considered for each pile arrangement pattern. Each of these models is analyzed under axial load and biaxial moments to find out the variation in pile reactions. The baseline for comparison is considered to be the behavior of a rigid pile cap. The paper also demonstrates the effect of a pile, being directly placed under a load point, on the distribution of loads among the other piles of the group.

Keywords Pile · Pile cap · Finite element · Static analysis

1 General Introduction

Pile foundations are most preferred foundation systems adopted in major projects where loads are very high and soil condition is poor. Conventional manual methods of finding out the pile reactions are illustrated in many textbooks and literatures. However, it is important to know the limitations of these manual methods and also the effect of the pile layout and pile cap thickness on load distribution in different piles. The paper demonstrates the variation in pile reactions from the conventional rigid mat analysis results through example case studies. Often in many cases, it is observed that the practicing engineers tend to provide a pile just below a column even in a foundation system comprising more than one pile. The paper demonstrates the effects of load distribution in pile group due to the presence of a pile directly below the load bearing column. The effect of pile cap thickness and the ratio of pile spacing to cap thickness on load distribution of loads in piles are also

M. Sharma (✉)
Bechtel India Pvt. Ltd., 244-245 Udyog Vihar, Phase IV, Gurgaon 122015, Haryana, India
e-mail: msharma@bechtel.com

A. Rama Mohan Rao and K. Ramanjaneyulu (eds.), *Recent Advances in Structural Engineering, Volume 1*, Lecture Notes in Civil Engineering 11,
https://doi.org/10.1007/978-981-13-0362-3_3

studied in this paper. This study is done for square as well as rectangular geometry of the pile cap subjected to the following load conditions:

(a) Axial load
(b) Biaxial moment
(c) Axial load and biaxial moment.

2 Geometry and FEM Model

Two types of pile and pile cap configurations are adopted for conducting the study. The square pile cap is of size 19 m × 19 m and the size of the rectangular pile cap is 13 m × 19 m. Mat is modeled using plate elements, and the piles are modeled as translational springs with stiffness in three orthogonal directions *X*, *Y*, and *Z*. The intermediate distance between adjacent piles is kept as six times the pile diameter in order to avoid the group efficiency effects. In all models, the load is applied at the center of the pile cap in order to assess the behavior of the pile cap and estimate the variation in pile reactions with variation in pile cap thickness. Figures 1 and 2 show the basic geometry of the pile and pile cap arrangements adopted for this study.

Piles are considered to be H-shaped steel piles and spaced at 3.0 m center to center. Study is conducted on the pile cap thickness of magnitudes 0.3, 0.5, 1.0, 1.5, 2.0, 2.5, 3.0 and 3.5 m. Piles stiffness in horizontal directions are K_x = 3503 kN/m and K_z = 5954 kN/m and in vertical direction is K_y = 105100 kN/m. For simplicity

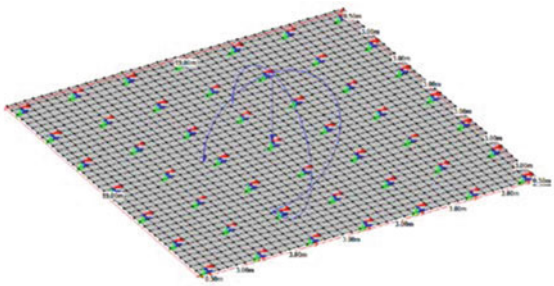

Fig. 1 Geometric details of square pile and pile cap arrangement with central pile

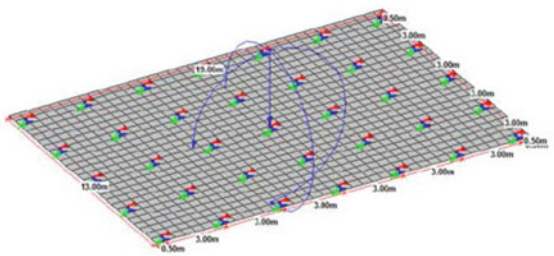

Fig. 2 Geometric details of rectangular pile and pile cap arrangement with central pile

in analysis and design in most of the cases, the rotational stiffness is avoided. From practical engineering judgement, this is fine as while estimating the lateral stiffness geotechnical group already considers the rotational factor.

3 Loads and Load Combinations

Vertical load of 10,000 kN and biaxial moment of 5000 kNm is considered for this study and is applied at the center of the mat for all the configurations of the pile and pile cap. Load combinations consider three conditions, i.e., vertical load, biaxial moment, and combinations of vertical load and biaxial moments.

4 Analysis Considering Rigid Pile Cap

With the above loading conditions, initially, a conventional analysis is done manually to assess the load distribution among piles in each of the configurations using the formula

$$F_i = \frac{P_o}{n} \pm \frac{M_x.r_{\mathrm{xi}}}{\sum_i^n r_{\mathrm{xi}}^2} \pm \frac{M_z.r_{\mathrm{zi}}}{\sum_i^n r_{\mathrm{zi}}^2} \tag{1}$$

where

F_i Reaction in the ith pile.
P_o Total vertical load on pile group.
n Total number of piles in the group.
M_x Moment about x-axis.
M_z Moment about z-axis.
r_{xi} Distance of ith pile from x-axis.
r_{zi} Distance of ith pile from z-axis.

The basic assumption for using this formula is that the pile cap is rigid in nature, i.e., the deflected shape of the pile cap under loaded condition is always a straight line. Figure 3 shows the nodes and node numbers corresponding to piles for each of the configurations.

Tables 1, 2, 3 and 4 illustrate the reactions at each pile location for rigid square and rectangular pile configurations, respectively. This data is used later for comparing the variations in pile reactions with variation in stiffness (thickness) of the pile cap under different loading conditions.

Considering these data to be the baseline values for the classical analysis of pile and pile cap arrangements, the subsequent sections will illustrate the variation in behavior of the pile and pile cap arrangements based on the adopted mathematical models.

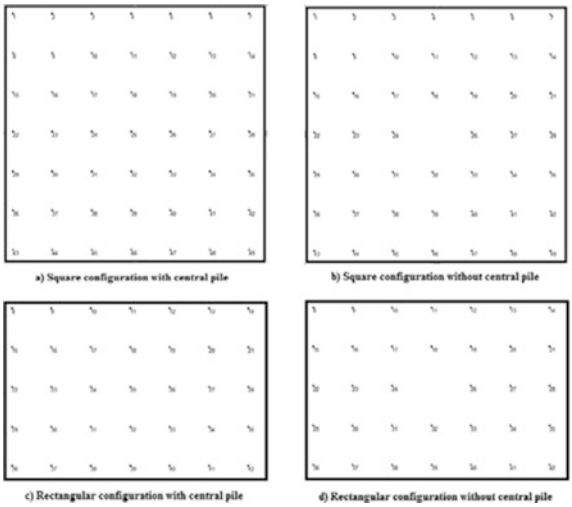

Fig. 3 Nodes and node numbers in different pile cap configurations

5 Analysis of Pile and Pile Cap Models

5.1 Square Pile Cap with Central Pile

Behavior of the pile and square pile cap arrangement is studied with respect to the distribution of loads in different piles for each of the pile cap thickness conditions when a central pile is present right below the point of application of the load. The results of the study are plotted in graphs in Figs. 4, 5 and 6. Graphs are plotted for each of the three loading conditions for piles next to central row.

Table 1 Reactions on piles for rigid square pile cap with central pile

Pile No.	F_i (kN) (vertical load)	F_i (kN) (biaxial moment)	F_i (kN) (vertical load + biaxial moment)
1	204	0.00	204.1
2	204	−8.50	195.6
3	204	−17.01	187.1
4	204	−25.51	178.6
5	204	−34.01	170.1
6	204	−42.52	161.6
7	204	−51.02	153.1
8	204	8.50	212.6
9	204	0.00	204.1
10	204	−8.50	195.6
11	204	−17.01	187.1

(continued)

Table 1 (continued)

Pile No.	F_i (kN) (vertical load)	F_i (kN) (biaxial moment)	F_i (kN) (vertical load + biaxial moment)
12	204	−25.51	178.6
13	204	−34.01	170.1
14	204	−42.52	161.6
15	204	17. 01	221.1
16	204	8.50	212.6
17	204	0.00	204.1
18	204	−8.50	195.6
19	204	−17.01	187.1
20	204	−25.51	178.6
21	204	−34.01	170.1
22	204	25.51	229.6
23	204	17.01	221.1
24	204	8.50	212.6
25	204	0.00	204.1
26	204	−8.50	195.6
27	204	−17.01	187.1
28	204	−25.51	178.6
29	204	34.01	238.1
30	204	25.51	229.6
31	204	17.01	221.1
32	204	8.50	212.6
33	204	0.00	204.1
34	204	−8.50	195.6
35	204	−17.01	187.1
36	204	42.52	246.6
37	204	34.01	238.1
38	204	25.51	229.6
39	204	17.01	221.1
40	204	8.50	212.6
41	204	0.00	204.1
42	204	−8.50	195.6
43	204	51.02	255.1
44	204	42.52	246.6
45	204	34.01	238.1
46	204	25.51	229.6
47	204	17.01	221.1
48	204	8.50	212.6
49	204	0.00	204.1

5.2 Square Pile Cap Without Central Pile

Pile and square pile cap arrangement is studied with respect to the distribution of loads in different piles for each of the pile cap thickness conditions when a central pile is absent below the point of application of the load. The results of the study are plotted in graphs in Figs. 7, 8 and 9. Graphs are plotted for each of the three loading conditions.

Table 2 Reactions on piles for rigid square pile cap without central pile

Pile No.	F_i (kN) (vertical load)	F_i (kN) (biaxial moment)	F_i (kN) (vertical load + biaxial moment)
1	208	0.00	208.3
2	208	−8.50	199.8
3	208	−17.01	191.3
4	208	−25.51	182.8
5	208	−34.01	174.3
6	208	−42.52	165.8
7	208	−51.02	157.3
8	208	8.50	216.8
9	208	0.00	208.3
10	208	−8.50	199.8
11	208	−17.01	191.3
12	208	−25.51	182.8
13	208	−34.01	174.3
14	208	−42.52	165.8
15	208	17.01	225.3
16	208	8.50	216.8
17	208	0.00	208.3
18	208	−8.50	199.8
19	208	−17.01	191.3
20	208	−25.51	182.8
21	208	−34.01	174.3
22	208	25.51	233.8
23	208	17.01	225.3
24	208	8.50	216.8
26	208	−8.50	199.8
27	208	−17.01	191.3
28	208	−25.51	182.8
29	208	34.01	242.3
30	208	25.51	233.8

(continued)

Table 2 (continued)

Pile No.	F_i (kN) (vertical load)	F_i (kN) (biaxial moment)	F_i (kN) (vertical load + biaxial moment)
31	208	17.01	225.3
32	208	8.50	216.8
33	208	0.00	208.3
34	208	−8.50	199.8
35	208	−17.01	191.3
36	208	42.52	250.9
37	208	34.01	242.3
38	208	25.51	233.8
39	208	17.01	225.3
40	208	8.50	216.8
41	208	0.00	208.3
42	208	−8.50	199.8
43	208	51.02	259.4
44	208	42.52	250.9
45	208	34.01	242.3
46	208	25.51	233.8
47	208	17.01	225.3
48	208	8.50	216.8
49	208	0.00	208.3

5.3 *Rectangular Pile Cap with Central Pile*

Pile and rectangular pile cap arrangement is studied with respect to the distribution of loads in different piles for each of the pile cap thickness conditions when a central pile is present below the point of application of the load. The results of the study are plotted in graphs in Figs. 10 and 11. Graphs are plotted for each of the three loading conditions (Fig. 12).

Table 3 Reactions on piles for rigid rectangular pile cap with central pile

Pile No.	F_i (kN) (vertical load)	F_i (kN) (biaxial moment)	F_i (kN) (vertical load + biaxial moment)
8	286	23.81	309.5
9	286	0.00	285.7
10	286	−23.81	261.9
11	286	−47.62	238.1
12	286	−71.43	214.3
13	286	−95.24	190.5
14	286	−119.05	166.7

(continued)

Table 3 (continued)

Pile No.	F_i (kN) (vertical load)	F_i (kN) (biaxial moment)	F_i (kN) (vertical load + biaxial moment)
15	286	47.62	333.3
16	286	23.81	309.5
17	286	0.00	285.7
18	286	−23.81	261.9
19	286	−47.62	238.1
20	286	−71.43	214.3
21	286	−95.24	190.5
22	286	71.43	357.1
23	286	47.62	333.3
24	286	23.81	309.5
25	286	0.00	285.7
26	286	−23.81	261.9
27	286	−47.62	238.1
28	286	−71.43	214.3
29	286	95.24	381.0
30	286	71.43	357.1
31	286	47.62	333.3
32	286	23.81	309.5
33	286	0.00	285.7
34	286	−23.81	261.9
35	286	−47.62	238.1
36	286	119.05	404.8
37	286	95.24	381.0
38	286	71.43	357.1
39	286	47.62	333.3
40	286	23.81	309.5
41	286	0.00	285.7
42	286	−23.81	261.9

5.4 Rectangular Pile Cap Without Central Pile

Pile and rectangular pile cap arrangement is studied with respect to the distribution of loads in different piles for each of the pile cap thickness conditions when a central pile is absent below the point of application of the load. The results of the study are plotted in graphs in Figs. 13, 14 and 15. Graphs are plotted for each of the three loading conditions.

Table 4 Reactions on piles for rigid rectangular pile cap without central pile

Pile No.	F_i (kN) (vertical load)	F_i (kN) (biaxial moment)	F_i (kN) (vertical load + biaxial moment)
8	294	23.81	317.9
9	294	0.00	294.1
10	294	−23.81	270.3
11	294	−47.62	246.5
12	294	−71.43	222.7
13	294	−95.24	198.9
14	294	−119.05	175.1
15	294	47.62	341.7
16	294	23.81	317.9
17	294	0.00	294.1
18	294	−23.81	270.3
19	294	−47.62	246.5
20	294	−71.43	222.7
21	294	−95.24	198.9
22	294	71.43	365.5
23	294	47.62	341.7
24	294	23.81	317.9
26	294	−23.81	270.3
27	294	−47.62	246.5
28	294	−71.43	222.7
29	294	95.24	389.4
30	294	71.43	365.5
31	294	47.62	341.7
32	294	23.81	317.9
33	294	0.00	294.1
34	294	−23.81	270.3
35	294	−47.62	246.5
36	294	119.05	413.2
37	294	95.24	389.4
38	294	71.43	365.5
39	294	47.62	341.7
40	294	23.81	317.9
41	294	0.00	294.1
42	294	−23.81	270.3

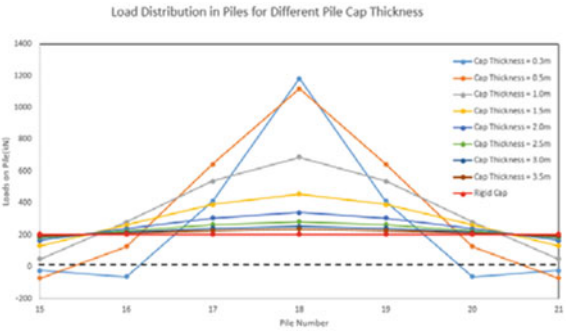

Fig. 4 Pile reactions under vertical load for square pile cap with central pile

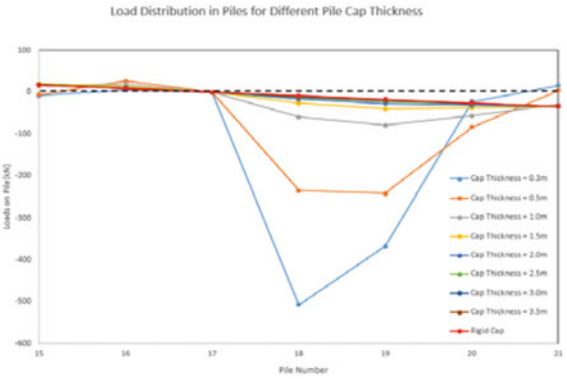

Fig. 5 Pile reactions under biaxial moments for square pile cap with central pile

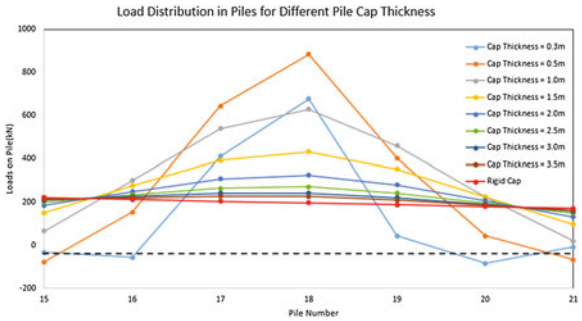

Fig. 6 Pile reactions under vertical load and biaxial moments for square pile cap with central pile

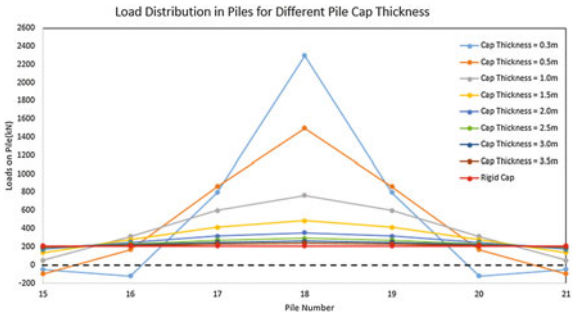

Fig. 7 Pile reactions under vertical load for square pile cap without central pile

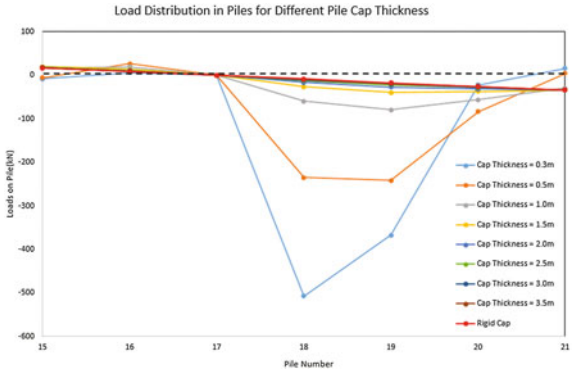

Fig. 8 Pile reactions under biaxial moments for square pile cap without central pile

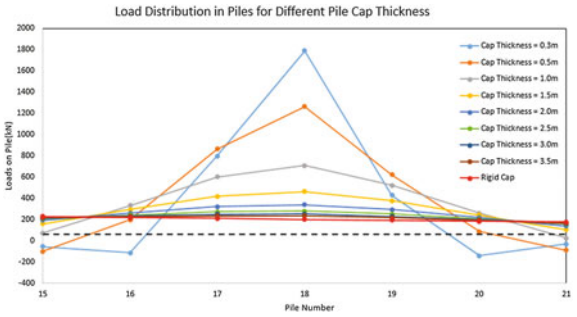

Fig. 9 Pile reactions under vertical load and biaxial moments for square pile cap without central pile

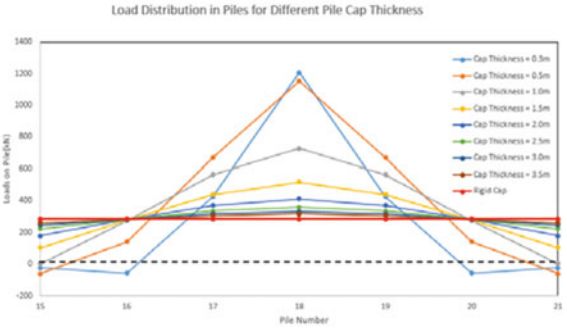

Fig. 10 Pile reactions under vertical load for rectangular pile cap with central pile

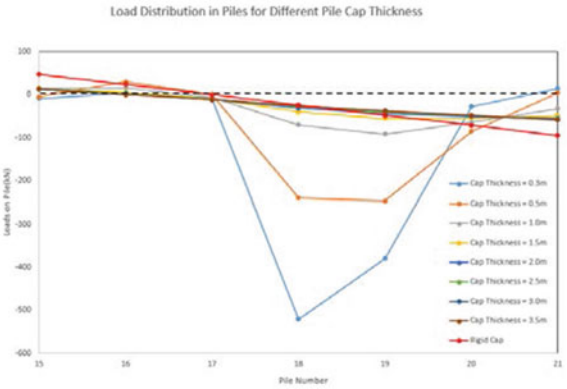

Fig. 11 Pile reactions under biaxial moments for rectangular pile cap with central pile

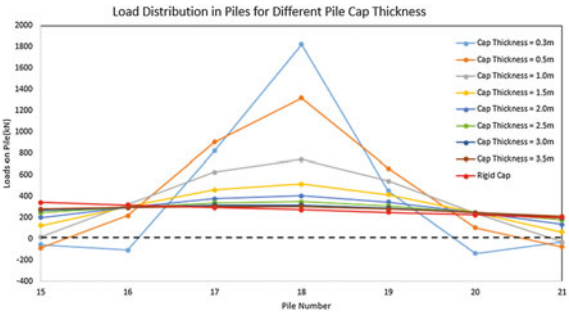

Fig. 12 Pile reactions under vertical load and biaxial moments for rectangular pile cap with central pile

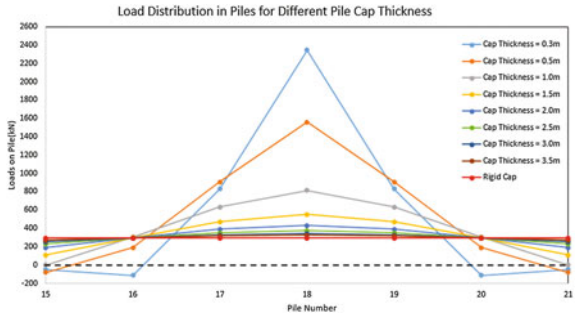

Fig. 13 Pile reactions under vertical load for rectangular pile cap without central pile

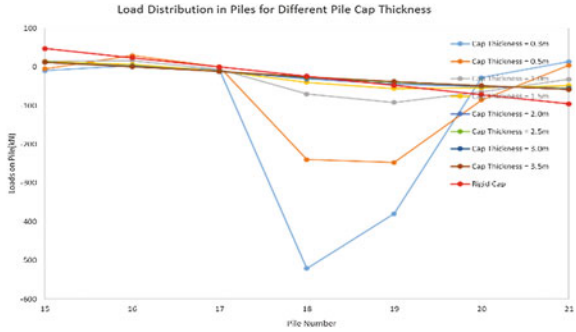

Fig. 14 Pile reactions under biaxial moments for rectangular pile cap without central pile

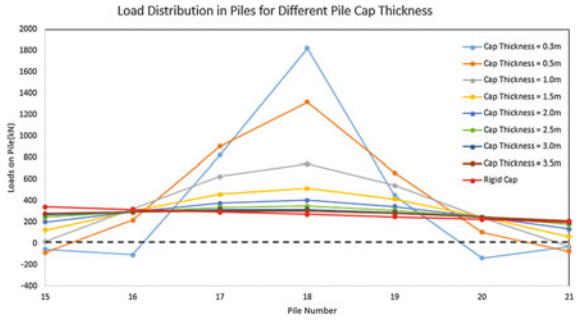

Fig. 15 Pile reactions under axial load and biaxial moments for rectangular pile cap without central pile

6 Discussion on Analysis Results

Above graphs show the analysis results for pile reactions under different loading conditions on square and rectangular piles with different pile cap thickness and pile arrangements. For a rigid pile cap, reactions at all the piles are uniform or vary linearly. However, a finite element analysis, considering the stiffness of the mat and piles, shows that the pile reactions deviate largely from the conventional rigid analysis results. The piles closest to the point of load application attract higher

amount of compressive load than the piles farther away from the center. For an extremely flexible pile cap, the farthest piles even undergo tension, and there exists a probability of a point of contraflexure being prevalent in the pile cap which needs to be properly addressed during reinforced concrete design and reinforcement detailing of the pile cap. Also, if we compare the nature of the load distribution in piles, having a central pile directly under load and that without a central pile, it is quite evident that if a pile is placed directly under the load point especially in a flexible mat, then it attracts most of the loads, and adjacent piles are under stressed. This is very important to note as overlooking this effect often increases the project cost. The pile cap when subjected to both vertical load and bending moments shows a stable result in terms of variation in pile reactions independent of whether it is a square or a rectangular pile. However, when the moments become more predominant than the vertical loads, the piles closest to the load point experience remarkably high reactions whereas the piles, farther away from load points, experience negligible reactions. Also, presence or absence of central pile and plan geometry of the mat appreciably impacts the stress concentration in and around the point of load application in a flexible pile cap. Also as the thickness increases, the difference in pile reactions start decreasing which indicates that the mat starts behaving like a rigid mat.

7 Conclusion

The point of interest for the practicing engineers is to look out for a thumb rule where a quick estimation of the probable thickness of pile cap is possible to assess whether a particular pile cap is rigid or flexible. Industry standards like ACI 351.3R-04 provide thumb rules for rigid foundation. It states that a foundation is considered to be rigid if its thickness is the greatest among 1/5 of its shorter dimension, 1/10 of its longer dimension, 0.6 m and 1/30 of the span plus 0.6 ft. However, no such thumb rule is provided by the codes especially for the mat supported on piles. Also, the application of the above thumb rule leads to a huge thickness of large pile supported mat foundations, which is very uneconomic. This paper basically aimed to provide a method to evolve a thumb rule for estimating the thickness required for a pile supported mat so that it can be considered to be behaving as a rigid mat. The basic exercise performed and the nature of the graph for pile reactions show that if the thickness of the mat is kept around 1.2–1.3 times the spacing between the piles, then the mat will demonstrate a close to perfect rigid mat behavior. This paper is just a preliminary attempt made to propose a thumb rule, and there is an ample opportunity for future research on this topic and to come up with a more refined formula considering the effect of relative location for the building columns on these pile caps.

Reaction Response of Horizontally Curved and Skewed Concrete Box-Girder Bridges

Tanmay Gupta and Manoj Kumar

Abstract Concrete box girders are widely used in horizontally curved bridges due to their high torsional rigidity. Certain geographical situation demands skew supports in addition to the curved layout of the bridge and results in complex skew-curve geometry of the deck. The present study focuses on predicting the support reaction response for each unique skew-curve combination of four-cell box-girder bridges via 3D finite element analysis. Central curvature angle for the bridges considered in this paper has been varied from 48° curving left to 48° curving right, at an interval of 12° while the skew angle is swept from 0° to 50° at an interval of 10° to generate feasible combinations possible for skew-curve case. For these unique simply supported multicell concrete box girder bridges, support reactions for dead load as well as for Class-A and Class-70R vehicular live load cases are monitored via large parametric study. Results indicate that uplifting of supports become more prominent in high skew-curve cases at acute corners, while obtuse corner reactions reach as high as 104% of total force transmitting to abutment. Reaction ratio monitored can also be used for deriving skew correction factors for skew-curved bridges.

Keywords Concrete box-girder bridges · Horizontally curved · Skew abutments 3D FEM modelling · Support reaction · Skew correction factor

T. Gupta · M. Kumar (✉)
Department of Civil Engineering, Birla Institute of Technology and Science Pilani (BITS-Pilani), Pilani 333031, Rajasthan, India
e-mail: manojkr@pilani.bits-pilani.ac.in

T. Gupta
e-mail: tanmay.gupta@pilani.bits-pilani.ac.in

A. Rama Mohan Rao and K. Ramanjaneyulu (eds.), *Recent Advances in Structural Engineering, Volume 1*, Lecture Notes in Civil Engineering 11,
https://doi.org/10.1007/978-981-13-0362-3_4

1 Introduction

Rapid urbanization and massive growth in infrastructure have created a necessity for complex transportation system for highway bridges, which often leads to unconventional, non-collinear bridge configurations. Presence of skew supports and horizontal curvature together is one such problem which significantly changes the structural response of bridges.

In such situations, concrete/prestressed concrete box-girder sections are often used, to compensate for high torsional moment and bending moment demands arriving from the virtue of geometry. Designing such girders to support a skew-curved bridge is a complex problem since the support reactions, shear and moment demands even due to gravity loads vary significantly across the girders of the bridge deck [1]. For significantly curved bridges (having central curvature angle 12° or more) with sharp skew support edges, generally there exist substantial amount of torsional deformations and potential for uplift at bearings.

Nowadays design engineers have a wide variety of approximate and sophisticated analysis and design methods at their disposal for the analysis of bridge forces. Thus, it becomes very important that the appropriate method is selected for the problem involved considering time and accuracy needed for the project. One-dimensional spine bridge modelling technique, implemented using linear line elements placed along the centre line of the bridge span, still remains the most common technique for bridge analysis in India. Sophisticated and complicated 2D grillage or full fledged 3D finite element analysis for bridges are generally not preferred, for bridges having simple geometric alignment since the spine modelling technique is accurate enough; however, it is unable to capture live load distribution effects especially when the geometry of the girder becomes horizontally curved and skewed at supports.

Capturing the complicated structural response of aforementioned bridges via simplistic spine model is thus not possible; consequently, the need for skew-curve correction factors arrives, which can attenuate the response value of spine model to actual response of the bridge [2]. The present study focuses on capturing the worst support reaction response generated for various combinations of curvature and skewness present in the bridge. As per Indian loading conditions, a case study for 12.5 m wide box-girder bridge is carried out considering unique combinations of central curvature angle (varied from 48° curving left to 48° curving right, at an interval of 12°) and the skew angle (swept from 0° to 50° at an interval of 10°). The 3D finite element models of the bridges are generated and analysed using CsiBridge, to study the effect of skewness in conjunction with curvature on the reactions at obtuse corner. Obtuse corner reactions have been plotted in the form of non-dimensional parameter normalized by total support reactions at that abutment. Results not only give a simplistic way to rectify the obtuse corner reactions obtained from spine model but also provide a deep insight for designers towards girder design for such complicated geometry bridges.

2 Skew-Curve Bridge Force Transfer Mechanism

Structural responses of skew bridges as well as curved bridges are found to differ significantly in comparison with straight/orthogonal counterpart of similar dimensions. By the virtue of geometry, force path in such bridges do not remain as simple as in case of orthogonal bridges; thus, they attract high design forces and moments, which should be aptly considered in bridge modelling.

In case of bridges having only curved geometry, the load is generally transferred along the shortest curved distance between the supports, while for only skewed bridges force tend to take shortcut route via one obtuse corner to other. For combination of skew and curved geometry, however, force path becomes tedious in nature, but in general, it remains heavily towards obtuse corner. Thus, the risk of uplifting at acute corners increases manifold in such cases, especially in case of eccentric vehicular loading, which generates high reactions at obtuse side.

Figure 1 shows the top slab geometry and force transfer mechanism in a general skew-curved bridge. In the present study, curvature towards right-hand side is considered as negative central curvature angle while bridges curving towards left-hand side are considered as positive central curvature angles. Sense of skew angle is used such that obtuse corner is created towards the outer periphery of curved geometry in the near abutment (towards approaching traffic) for bridges having negative central angle (as shown in Fig. 1), while, for positive central angle case, skew is taken in similar manner, but in this case, obtuse corner remains inward for near abutment.

In general, due to change in force transfer mechanism in skew bridges through the strip of area connecting the obtuse-angled corners, bridge deck primarily bends

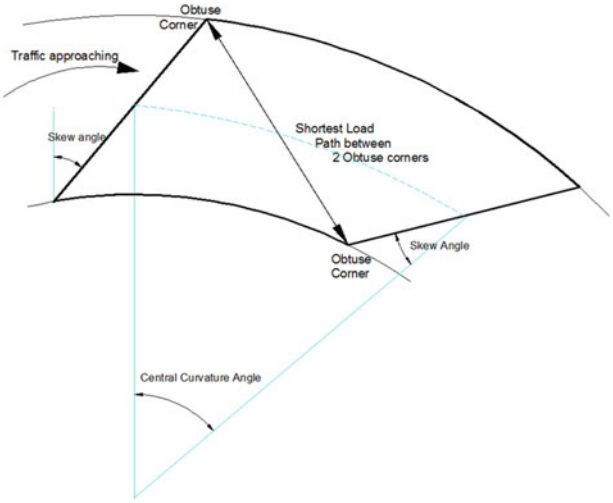

Fig. 1 Schematic diagram of skew-curved bridge showing shortest path for force transfer

along the line joining the obtuse-angled corners. The magnitude of bending moment is considered to be dependent mainly upon skew angle, ratio of the skew span and the width of the deck and the position of load on the span. However, adjacent areas of the force transfer strip in skew bridges, transfer the load only to this obtuse angle joining strip as cantilever rather than transferring the load to the supports directly. Thus, even for dead load case, skew bridges come under considerable torsional moments and unequal reaction forces at bearings. As the skew angle increases obtuse corner tend to come further near, thus generating more twisting in the section. Moreover, due to the presence of curvature in addition to skew, situations get more complicated as curve effect creates additional moments in bridge and more uneven support reaction distribution.

3 Numerical Investigation

3.1 Case Study Description

To investigate the cumulative effect of skew and curvature in concrete box-girder bridges, 54 unique skew-curve combinations are chosen in present case study. As such, box geometries attract high torsional moments; thus cross section for bridge section is chosen as box girder, which has exceptional torsional rigidity. In order to simplify the numerical investigation multi-span bridges are avoided, rather all parametric variations in geometry are applied for simply supported end conditions. The geometrical parameters for the box-girder having cross-section as shown in Fig. 2 and material properties considered in this study are as follows:

Length	25 m
Width	12.5 m
Number of cells	4
Depth	1.22 m
Top slab thickness	0.2 m
Bottom slab thickness	0.2 m
Web thickness	0.3 m
Web spacing (c/c)	2.5 m
Overhang	1.1 m

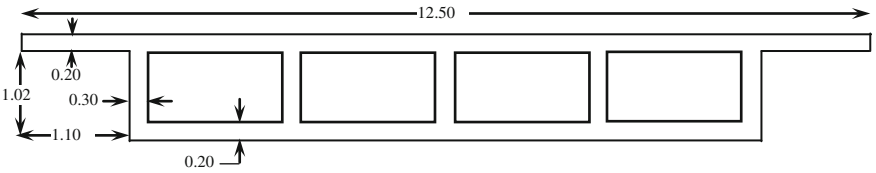

Fig. 2 Box-girder bridge cross section used in present study

Table 1 Parametric variations

Skew angle	Central curvature angle
0°–50° (at an interval of 10°)	−48° to 48° (at an interval of 12°)

Concrete grade	M35
Density	25 kN/m^3
Poisson's ratio	0.2
Elastic modulus	2.958 × 10^7 kN/m^2

For considering realistic modelling of support bearing, it is assumed to be partially rigid, having a bearing stiffness of 87.5 kN/m. The same base cross section (Fig. 4) has been used for all the skew-curve bridges considered in this study where the skewness and curvature have been varied in accordance to Table 1.

The reactions at the obtuse corner of the box girders considered in present study have been expressed as non-dimensional parameter (in %) normalized by total support reaction at that abutment, and are reported in terms of obtuse corner reaction percentage for gravity (dead) load case and for live loads specified by IRC [3].

3.2 Finite Element Modelling

For better prediction of results for such complicated geometries, full 3D modelling of bridge superstructure was implemented using well-known finite element analysis and design software CSiBridge. For simplicity, first-order linear elastic analysis is performed for all unique combinations for three different load cases, namely, dead load case, Class-A vehicle moving on three lanes and combination of Class-A loading on first lane and Class-70R vehicle moving on separate third lane. Discretization of the bridge is done using a four-noded 3D shell element having six degrees-of-freedom (three translations + three rotational) at each node. Proper connectivity of top and bottom flange elements with the webs ensures the displacement compatibility. Element size and aspect ratio of the elements have been decided via considering mesh sensitivity analysis for simplified box girder. Based on which a preferred sub-mesh area of 0.25 m^2 was chosen in order to limit the time involved in analysis. Figure 3 depicts a typical finite element model for 30° skew and −36° curved generated in CSiBridge.

3.3 Live Load Placement

The recommendations of Indian Road Congress (IRC) may be used to place the vehicular live load in transverse directions. However, it is not possible to place the

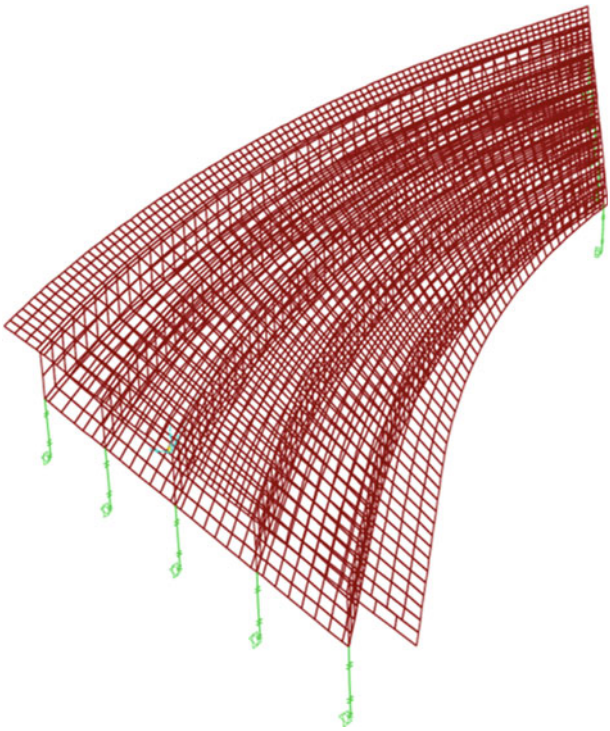

Fig. 3 3D finite element model of a typical skew-curved bridge (curving towards right) showing all discrete elements along the span length

vehicular load in longitudinal direction to develop maximum moment since the rolling load concept can be used only for normal bridges. To mitigate this problem, in the present study, vehicle load is considered to run throughout the span at an average speed of 1 m/s, for which the results of vertical support reactions are captured at an interval of one second. Thus, at every 0.1 m interval, outputs are gathered and finally, all such outputs are compared for finding out the worst condition in all cases.

Since the carriageway width of box girders considered in this study is 12.5 m, which lies in between 9.6 and 13.1 m, as per IRC-6 requirements, this bridge geometry is to be analysed as three-lane bridge. Thus, two live load combinations are implemented in this study which are

1. CASE 1: CLASS-A − 3 LANES
2. CASE 2: CLASS-A − 1 LANE + CLASS 70R (W wheeled or tracked) − 1 LANE
   (these load cases are depicted in Fig. 4)

To generate worst support reaction at obtuse corner on near abutment, heavier loads were kept as near as possible to the obtuse corner following the IRC

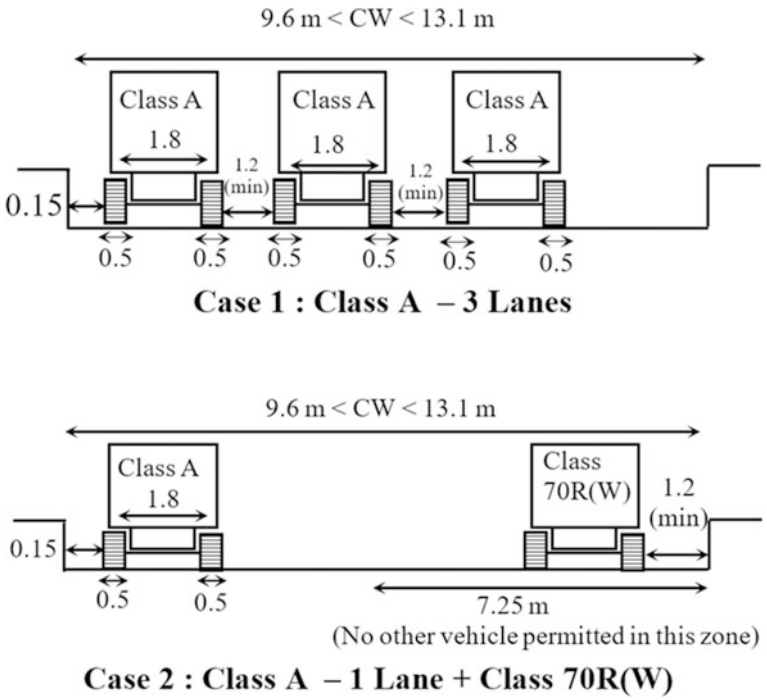

Fig. 4 Live load placement (transverse location)

recommendations. The results for IRC Class-70R tracked vehicle are not presented here since the preliminary study indicated that support reactions at obtuse corner due to tracked vehicle are less severe compared to wheeled vehicle.

For present study, it can be expected that approximately 20% of the support reaction (total five supports) will go to each support in the non-curved, non-skewed case under gravity loading, because overhang length of bridge is chosen such as to produce equal distribution of weight among the girder, but same is not true for live load cases as vehicle is kept at minimum clearance from obtuse angle side, thus generating more reaction towards obtuse side even for non-skewed, non-curved cases.

4 Results and Conclusions

4.1 Structural Response Under Dead Load Case

The results compiled in the present study specifically focus on the comparison of proportion (in %) of reaction carried by obtuse corner support bearing with respect to total abutment reaction for each unique combination of central curvature angle

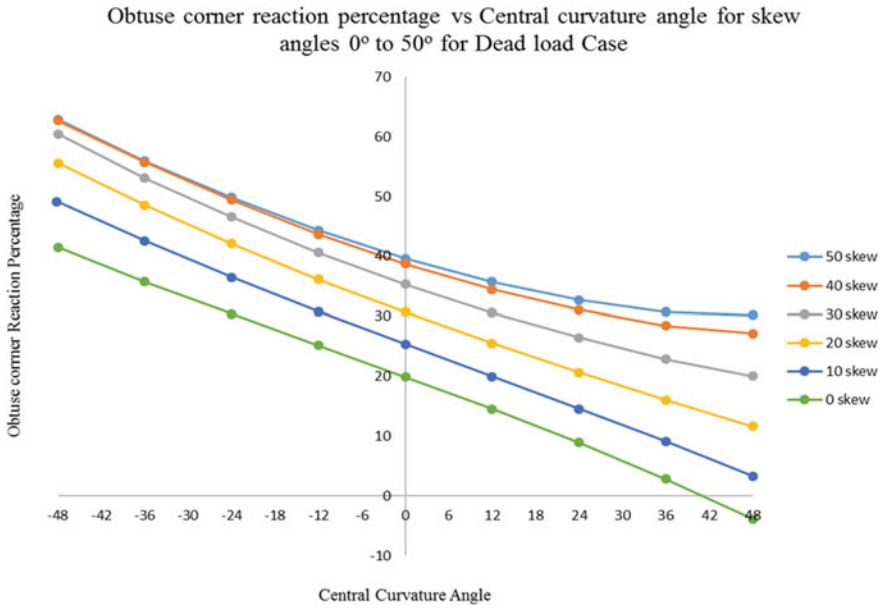

Fig. 5 Obtuse corner reaction percentage under dead load case for each unique skew-curve combination chosen

and skew angle considered. Dead load case results for each unique skew-curve combination are presented in Fig. 5 (negative curvature angle represent curving right while positive for curving left):

- From Fig. 5, it is evident that the obtuse corner reaction for the non-curved case reaches 40% at about 50° skew angle which just about doubled from non-skew non-curve bridge case.
- The curve effect greatly influences reaction response, which can be observed via uplift at corners occurring around +40° central angle case when the bridge is not skewed. It implies high central curvature itself is sufficient for uplifting even towards the obtuse side.
- For bridges curving right (+ve central angle) with high central angle and high skew, the coupled skew-curve effect is dominant, which is evident from the fact that the curve for 40° skew crosses the curves next to it (50° skew curve). Thus, it can be concluded that at higher skew angle (greater than 40°) obtuse corner tend to attract reaction at slower rate as compared with skew range of 0°–40°.

4.2 Structural Response Under Live Load Cases

The results for obtuse corner support reaction for live load case 1 (Class-A vehicle running on three lanes) and case 2 (Class70R on one first lane and Class-A on third lane) are presented in Figs. 6 and 7, respectively. As all the results are compiled for near abutment (abutment towards the incoming traffic flow) thus by changing the curvature direction from right to left, obtuse corner experiences significantly low support reactions, reason being, for right curved bridge obtuse corner remain on outer periphery while for left curved, it falls towards inside periphery of curve. Furthermore, some significant observation from Figs. 6 and 7 are as follows:

- It can be evidently seen for non-curved cases that, as the live load is eccentric, obtuse corner reaction percentage distribution in skew 0°–50° again doubles but this time from 30% to near more than 60% in both live load cases. Case 1 shows a steeper rate of increase than case 2 indicating that for higher skews as the vehicle weight gets more distributed, it tends to attract more reaction at obtuse side, while for lower skews, heavy vehicle (Class 70R in present case) running near to obtuse corner will dominate the support reaction.
- As the live load is always modelled to run near obtuse corner, no uplift occurs near obtuse side with the change in curvature from right to left for both the cases.

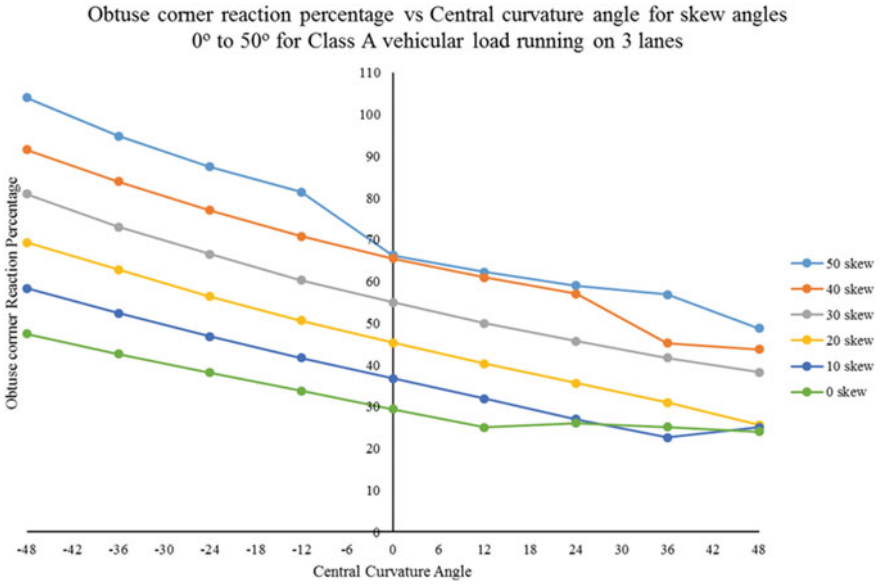

Fig. 6 Obtuse corner reaction percentage under live load case 1 for each unique skew-curve combination chosen

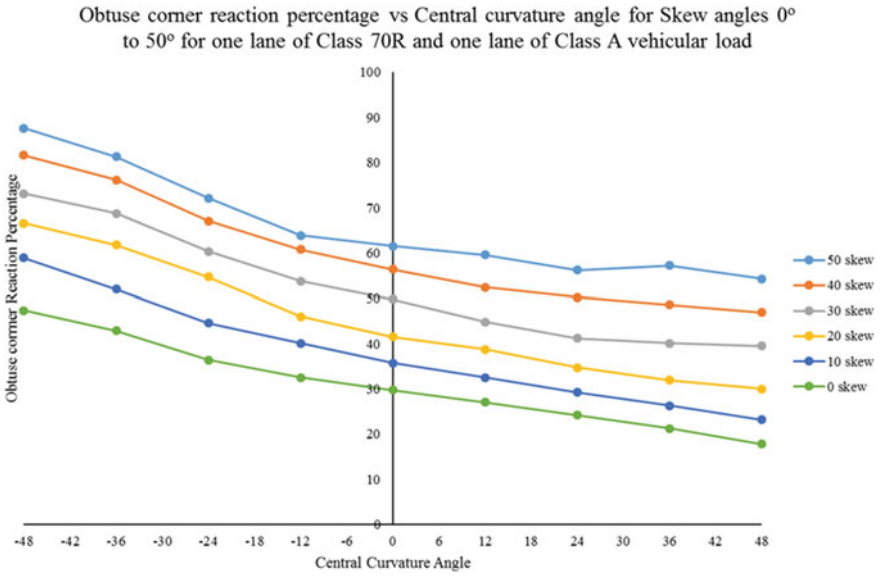

Fig. 7 Obtuse corner reaction percentage under live load case 2 for each unique skew-curve combination chosen

- Combined effect of skew and curve for case 1 generates obtuse corner reaction as high as 104% of the abutment reaction; similarly, in case 2, these values go up to 87%. These values signify that going beyond these limits of skew and curvature for single span bridges will surely create much more challenges for constructions.

4.3 Skew Correction Factors

For the simplified analysis, box-girders are modelled as spine, which comprises of only one single girder. The spine models are unable to capture the non-uniform support reactions in the skew-bridges. Skew correction factors (SCF) can be applied to the support reactions for the corresponding non-skewed bridges to account for the effect of skewness in the bridges analyzed using the simplistic spine modelling of the bridge [2]. Consequently, for superstructure shear design, the use of skew correction factors for obtuse girder regions is required. To quantify skew correction factors AASHTO LRFD [4] specifications give an empirical equation for cast-in-place concrete multicell box as $1 + (0.25 + (12L/70d))\tan\theta$, where L is bridge span in ft., d is the depth of cross section in inch and θ is skew angle. Further, as amendment to this equation in 2014, CALTRANS provided a much simpler estimation of skew correction factor as $1 + (\theta/50)$. As these equations are limited to only skew geometry, these cannot predict the behaviour of SCF for skew-curve cases.

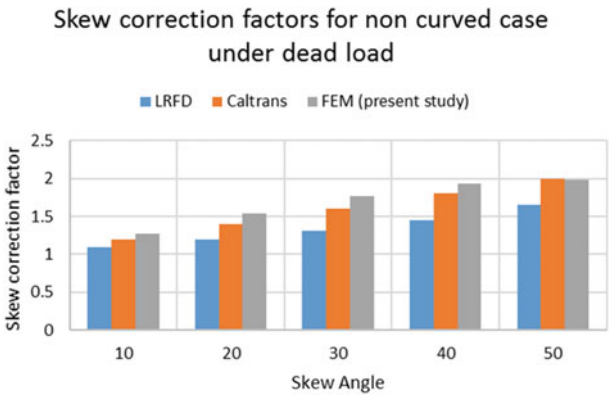

Fig. 8 SCF comparison among LRFD, CALTRANS and present study under dead load

As the nature of the curves presented obtuse corner reaction for various load cases (Figs. 5, 6 and 7) have similar trend, consequently, the nature of curves for absolute reaction (for dead plus live load case) will be almost same. Therefore, these curves may be used to determine the skew correction factors for absolute reaction at obtuse corner. Since there are no direct guidelines available on skewed bent or abutment reactions, sometimes these skew correction factors are also applied to reactions to calculate bearing forces.

Thus, SCF from the present study can be derived for obtuse corner as (obtuse corner reaction percentage/100) * no. of supports. Figure 8 shows a comparison of skew correction factors thus obtained for non-curved case under dead load from these three approaches.

Results show un-conservative values of SCF for lower skew range calculated via LRFD and CALTRANS equations. While there are no guidelines available for SCF calculations in case of IRC loading for either skew or skew-curve cases, thus, present study results can play a pivotal role in bridge design using spine models also. Similarly, for dead load cases, SCF for combined effect of skew curve are rare to find.

In conclusion, present study not only provides obtuse corner reaction response for all unique skew-curve combinations feasible but also presents simple SCF value charts for ease of designers.

References

1. Nutt, Redfield, Valentine, David Evans and Associates, (2008). *Development of design specifications and commentary for horizontally curved concrete box-girder bridges*. NCHRP report 620, Washington, DC: Transportation Research Board.
2. Zhang, Q. (2008). *Development of skew correction factors for live load shear and reaction distribution in highway bridge design*. ProQuest.
3. IRC 6:2000. *Standard specifications and code of practice for road bridges Section: II loads and stresses*. New Delhi: Indian Road Congress.
4. AASHTO. (2012). *AASHTO LRFD Bridge design specifications* (6th ed., with Interims). Washington, DC: American Association of State Highway and Transportation Officials.

Performance Estimation of Solid and Punched Shear Wall Buildings with Two Modelling Techniques

Juturu Swetha, Onkar G. Kumbhar and Ratnesh Kumar

Abstract Shear walls are generally provided in multistoried buildings to resist in-plane lateral loads by increasing strength and stiffness to control the lateral deformations. Various modelling techniques are available to model shear wall in computer models, viz. nonlinear layered shell elements, wide column, fibre elements or truss elements. The accuracy of results and time required for the analysis depends on the modelling technique adopted. In the present paper, parametric study of two modelling techniques of shear wall, i.e. wide column approach and nonlinear layered shell element, has been discussed for solid and punched shear walls. Response spectrum analysis and nonlinear static pushover analysis have been performed. In linear range, the modal analysis results, shear force and moment in the shear wall from aforementioned approaches are comparable. From nonlinear analysis, it has been observed that the wide column approach is unable to capture progressive nonlinearity in the shear wall and overestimates the stiffness of the structure.

Keywords Shear wall · Nonlinear layered shell element model
Wide column model · Nonlinear static pushover analysis

1 General

Shear walls are generally provided from the foundation in multistorey buildings to resist lateral loads. Due to cantilever behaviour of the shear wall, the lateral drift near bottom storeys is reduced. The inclusion of shear wall in frame building makes

J. Swetha · O. G. Kumbhar · R. Kumar (✉)
Department of Applied Mechanics, Visvesvaraya National Institute of Technology, South Ambazari Road, Nagpur 440010, Maharashtra, India
e-mail: ratnesh.eq@gmail.com

J. Swetha
e-mail: juturuswetha1993@gmail.com

O. G. Kumbhar
e-mail: onkar.kumbhar97@gmail.com

A. Rama Mohan Rao and K. Ramanjaneyulu (eds.), *Recent Advances in Structural Engineering, Volume 1*, Lecture Notes in Civil Engineering 11,
https://doi.org/10.1007/978-981-13-0362-3_5

it efficient by increasing strength and stiffness as well as by reducing the lateral drift. In buildings having height more than 23 m, shear walls can be curtailed at different storey levels [1]. Shear walls may fail in flexure, shear or both, depending on aspect ratio. Flexural failure occurs in high aspect ratio shear wall. When shear wall fails in the flexure, crushing of concrete compression zone and yielding of steel at tension zone take place. In mathematical modelling, shear walls can be modelled as nonlinear layered shell elements, wide column, fibre elements or truss elements. However, in the present paper, variation in the parametric results of two modelling techniques, viz. wide column approach and nonlinear layered shell element, are compared. Wide column frame analogy method was first developed by Clough et al. [2], and later it was improvised by Kwan [3]. The shear wall is treated as a structural column with the centroidal axis of shear wall coinciding with the column. The rigid beams are provided in the wide column to connect the frame members of the building with the shear wall and helps in connecting the non-coplanar shear walls at nodes along the vertical edges. The nonlinearity in the wide column can be provided as lumped plasticity over the hinge length as nonlinear flexural hinges at possible yielding locations (i.e. at maximum bending moment location). In the present research, the nonlinear hinge properties of the wide column have been calculated from the moment–curvature curve of the wide column, which is obtained from section designer in SAP2000. In nonlinear layered shell element modelling, nonlinear stress–strain curves for layers of concrete and steel in the shear wall along with the direction of nonlinearity have been defined. However, the nonlinear layered shell element modelling is computationally more time-consuming.

2 Modelling and Analysis

An eight-storey symmetrical building has been considered with storey height 3 m each. The plan of the considered building is shown in Fig. 1. The shear wall provided is 1.7% of the plan area in the longitudinal direction and 2% of the plan area in the transverse direction. The building is assumed to be situated in zone V having PGA 0.36 g, on medium soil as per Indian standard conditions. The grades of concrete and steel considered are M30 and Fe 415.

The building has been modelled in SAP2000 V 17.3 with frame elements and solid shear wall as a wide column (Fig. 2). The model has been analysed to get forces as well as moments in shear walls and designed as per Indian standard codes. The shear walls have been manually designed without openings as per IS 13920:1993 and with 1 m^2 openings in each floor as per Madheker and Jain [4] for the obtained axial, shear forces and moment. The percentages of openings provided in punched shear wall are 7 and 8% in the longitudinal and transverse directions, respectively. Four mathematical models with same building plan as well as geometry have been created using SAP2000. In one model solid shear wall has

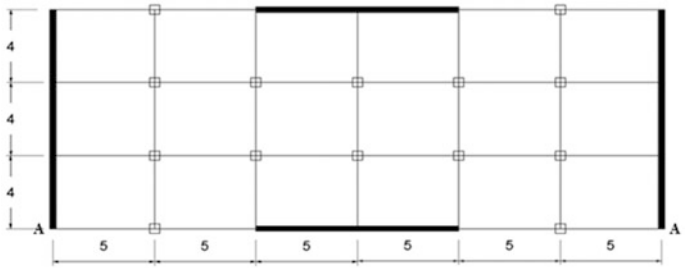

Fig. 1 Plan of considered building (all dimension are in metres)

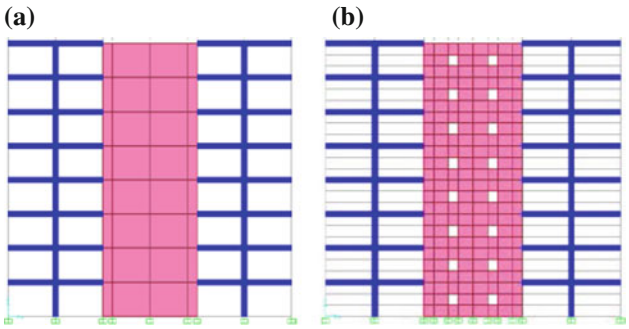

Fig. 2 Frame A–A of **a** solid shear wall building and **b** punched shear wall building

been modelled using wide column and in the second model, using nonlinear layered shell element. Another two models have been developed for punched shear wall using the same two aforementioned approaches. In all the models, the nonlinearity of frame elements (i.e. beams and columns) has been provided as lumped hinges based on FEMA 356 [5].

2.1 Solid Nonlinear Layered Shell Element Modelling

The designed solid shear walls have been modelled as nonlinear layered shell elements. The nonlinear stress–strain curves of layers of concrete and steel have been provided and direction of nonlinearity has been mentioned. The designed thickness of wall, size and spacing of reinforcement bars have been assigned in SAP2000. The nonlinearity of the layered shell element shear walls has been provided using distributed plasticity approach.

2.2 Wide Column Modelling

The designed section of shear wall has been modelled as wide column using section designer. The nonlinearity of wide column has been provided as uniaxial flexural hinges considering the in-plane behaviour of shear walls. The nonlinear flexural hinges have been provided at the ends of the wide column. The hinge properties have been calculated by converting moment–curvature curve obtained from section designer to moment–rotation curve. The formulae for conversion of curvature to rotation are given in EC8 part-3 [6] (Eqs. 1, 2 and 3).

$$\theta_y = \phi_y \frac{L_v + a_v Z}{3} + 0.0013 + \phi_y \frac{d_{bL} f_y}{8\sqrt{f_{ck}}} \tag{1}$$

The first term, second term and the third term in the above expression represent flexural contribution, shear deformation and anchorage slip of bars, respectively.

$$\theta_u = \theta_y + (\phi_u - \phi_y) L_p \left(1 - \frac{0.5 L_p}{L_v}\right) \tag{2}$$

$$L_p = 0.08\, L_v + 0.022 f_y\, d_b \tag{3}$$

where L_v is the shear length constant (1/2 of the total length of element), a_v is 1 if shear cracking is expected to precede the flexural yielding at the end section, otherwise 0, Z = length of internal lever arm, d_{bL} = mean diameter of longitudinal bars, L_p = plastic hinge length, f_{ck} = characteristic strength of concrete and f_y = yield strength of steel (Fig. 3).

The points on idealized moment–rotation curve are given in Tables 1, 2 and have been inputted in SAP2000 as hinge properties [7]. The results obtained from response spectrum analysis for solid shear wall building from two approaches are comparable.

Further nonlinear static analysis has been performed on two solid shear wall models in longitudinal and transverse directions. The capacity curves in longitudinal and transverse direction are shown in Fig. 4.

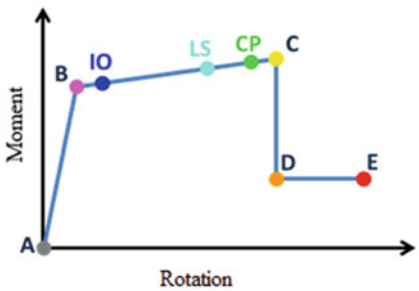

Fig. 3 Idealised moment–rotation curve

Table 1 Hinge properties of wide column

Point	Moment/SF	Rotation/SF
A	0	0
B	1	0
C	M_u/M_y	θ_p/θ_y
D	$0.2\,M_u/M_y$	θ_p/θ_y
E	$0.2\,M_u/M_y$	$1.5\,\theta_p/\theta_y$

Table 2 Acceptance criteria on moment–rotation curve

IO	$10\%\ \theta_p/\theta_y$
LS	$60\%\ \theta_p/\theta_y$
CP	$90\%\ \theta_p/\theta_y$

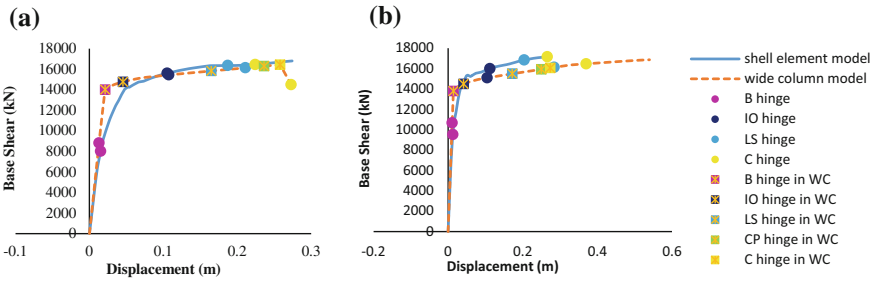

Fig. 4 Capacity curve of solid shear wall models in **a** longitudinal direction and **b** transverse direction

Various parameters have been derived and compared by idealizing the capacity curve of solid shear wall models. The derived capacity curve parameters of solid shell element model and wide column model in longitudinal and transverse direction are given in Tables 3 and 5, respectively. It can be observed that the initial stiffness of two modelling approaches is same. The capacity curve of solid shell element model deviates when nonlinearity has started in the shear wall. In wide column model, the stiffness of building is constant till *B* hinge has formed in longitudinal wide column. The stiffness in wide column abruptly reduces after nonlinearity has started in the wide column. The yield force and stiffness of wide column model are 3 and 25% greater than that of shell element model. Ductility of wide column model in the longitudinal direction is 46% more than shell element model. The ultimate base shear of solid shear wall models is nearly same. The progressive nonlinearity in the longitudinal wide column and the corresponding (at same displacement) shell stresses in concrete and steel at supports shown in Fig. 5

Table 3 Capacity curve parameters of solid shear wall models in longitudinal direction

Model	SE	WC
Yield force (kN)	14,000	14,400
Yield displacement (mm)	28	22
Effective stiffness, K_e (kN/m)	513,333	640,000
Target displacement (mm)	48	42
Ultimate displacement (mm)	225	258
Ductility capacity	8.04	11.73
Over strength ratio	2.19	2.35

SE shell element, *WC* wide column

Table 4 Hinge formation in longitudinal wide column and its corresponding nonlinear layered shell stresses (Fig. 5)

	Stress at 1		Stress at 2		Stress at 3		Stress at 4		Stress at 5	
	C	S	C	S	C	S	C	S	C	S
B	0	188.8	0	149.2	0	13.25	−10.23	−84.36	−14.69	−121.9
IO	0	421.2	−0.23	386.2	0	128.2	−14.6	−134.1	−21.96	−212.3
LP	0	415	0	415	−0.6	484.9	−11.02	−221.5	−38.09	−436.3
CP	0	427.4	0	418.3	0	437.4	−10.06	−19.8	−41.79	−449.3
C	0	433.2	0	424.1	0	426	−10.43	15.26	−42.48	−447.1

Note Negative is compression and tension is positive, considering concrete has no tensile strength, *C* concrete, *S* steel

Table 5 Capacity curve parameters of solid shear wall models in transverse direction

Model	SE	WC
Yield force (kN)	149,00	14,400
Yield displacement (mm)	19	16
Effective stiffness, K_e (kN/m)	790,000	960,000
Target displacement (mm)	36	34
Ultimate displacement (mm)	265	370
Ductility capacity	13.95	17.13
Over strength ratio	2.06	2.39

are compared in Table 4. It is to be noted that the hinge property in longitudinal direction has been modelled as shown in Fig. 6. The progression of nonlinearity in the transverse wide column and its corresponding (at same roof displacement) shell stress in concrete and steel at supports shown in Fig. 7 are given in Table 6. It is to be noted that the hinge property in longitudinal direction has been modelled as shown in Fig. 8. It is observed that the initial stiffness of nonlinear layered shell element model and wide column model in the transverse direction is same.

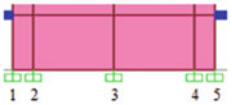

Fig. 5 Longitudinal shear wall

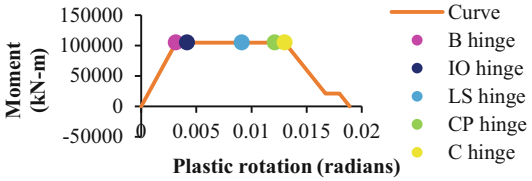

Fig. 6 Moment–rotation curve given for longitudinal wide column

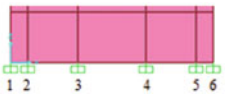

Fig. 7 Transverse shear wall

Table 6 Hinge formation in transverse wide column and its corresponding nonlinear layered shell stresses (no opening)

	Stress at 1		Stress at 2		Stress at 3		Stress at 4		Stress at 5		Stress at 6	
	C	S	C	S	C	S	C	S	C	S	C	S
B	0	143.2	0	114.2	0	32.05	−3.79	−28.28	−8.74	−72.3	−11.93	−99
IO	0	415	0	417	−0.41	382.1	0	43.28	−16.16	−140.5	−22.49	−218.7
LS	0	420.7	0	415.5	0	415	−0.31	489.9	−11.9	−234	−38.65	−439.3
CP	0	441.2	0	439.3	0	416.7	−0.27	460.3	−11.64	−142.5	−41.7	−429.2
C	0	443.6	0	442.3	0	420.6	−0.12	449.2	−11.59	−97.7	−42.27	−431.7

Note Negative is compression and tension is positive, considering concrete has no tensile strength, *C* concrete, *S* steel

The stiffness gradually decreases in shell element model due to progression of nonlinearity in the shear wall. In the wide column, the stiffness suddenly reduces after *B* hinge has formed in transverse wide column. In the transverse direction, yield force in wide column model is 3% less than that of solid shell element model, whereas stiffness is 22% higher for wide column model. Ductility of wide column model in the transverse direction is 23% more than solid shell element model. The ultimate base shear of shell element model is more than wide column model.

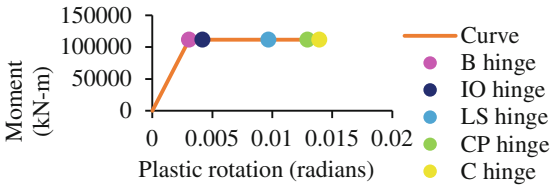

Fig. 8 Moment–rotation curve given for transverse wide column

2.3 Punched Nonlinear Layered Shell Element Modelling

The building with 1 m^2 openings in the shear wall has been manually designed for shear at two sections in a shear wall (i.e. at solid and punched sections). The reinforcement obtained near the opening was greater than at the solid section. The shear walls have been modelled as nonlinear layered shell elements similar to the solid shell element modelling.

2.4 Equivalent Wide Column Modelling

To simulate the opening in wide column, the wide column has been divided into three parts. Top, bottom parts are the solid section of shear wall, and the height of mid-part has kept equal to the height of the opening. The designed sections have been provided as wide column using section designer. The hinge properties have been calculated separately at solid and punched sections as explained for wide column modelling. The moment of inertia and shear area at the opening section have been modified according to the size of the opening in the shear wall. The property modifiers have been entered in SAP2000. Neuenhofer [8] proposed some methods to estimate lateral stiffness of shear walls with openings, and a similar approach has been used to calculate modification factors to modify moment of inertia and shear area of shear wall section used in software model (Eqs. 4 and 5).

$$\text{Moment of inertia modifier} = \frac{K_{\text{punched section}}}{K_{\text{solid section}}} = \frac{I_{\text{punched section}}}{I_{\text{solid section}}} \tag{4}$$

$$\text{Shear area modifier} = \frac{\text{Area of punched section}}{\text{Area of solid section}} \tag{5}$$

The yield force and stiffness of equivalent wide column model 7 and 24% more than punched shell element model, respectively. Ductility of punched shell element model is 12% more than wide column model (Fig. 9; Table 7).

The nonlinear hinge formation in the longitudinal equivalent wide column and corresponding punched shell stresses of concrete and steel for Fig. 10 are given in Table 8. Hinge property of punched shear wall modelled as equivalent wide column is shown in Fig. 11. The yield force of punched shear wall models in the transverse

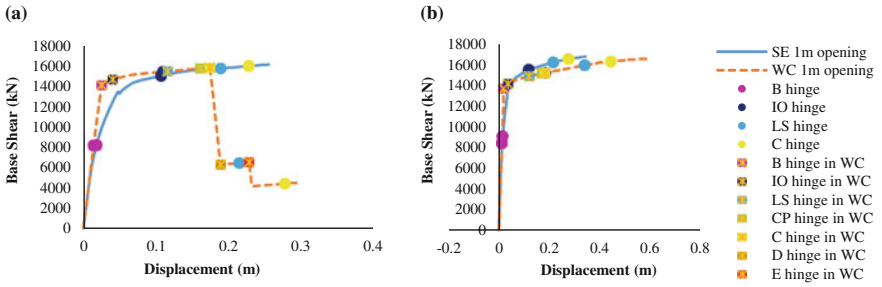

Fig. 9 Capacity curve of punched shear wall models in **a** longitudinal direction and **b** transverse direction

Table 7 Capacity curve parameters of punched shear wall with 1 m^2 openings in longitudinal direction

Model	SE 1 m opening	WC 1 m opening
Yield force	13,800 kN	14,700 kN
Yield displacement	30 mm	26 mm
Effective stiffness, K_e	453,333 kN/m	560,000 kN/m
Target displacement	54 mm	47 mm
Ultimate displacement	228 mm	174 mm
Ductility capacity	7.6	6.69
Over strength ratio	2.29	2.35

Fig. 10 Longitudinal punched shear wall

direction from the two approaches is nearly same. The stiffness of equivalent wide column model is 6% more than punched shell element model. Ductility of punched shell element model is 27% more than punched shell element model in the transverse direction.

The ultimate base shear of punched shell element model is more than equivalent wide column model (Table 9). The nonlinear hinge formation in the transverse equivalent wide column and corresponding punched shell stresses of concrete and steel for Fig. 12 are given in Table 10.

It was observed that first IO, LS, C hinges are formed in longitudinal beams connected to the longitudinal shear wall for pushover analysis in the longitudinal direction and in beams connected to transverse punched shear wall for pushover analysis in the transverse direction. The corresponding hinge property of punched shear wall as equivalent wide column is shown in Fig. 13. From inelastic stresses, it is observed that steel has started yielding just before the IO hinge formation in the transverse equivalent wide column.

Table 8 Hinge formation in longitudinal equivalent wide column and its corresponding layered punched shell stresses

	Stress at 1		Stress at corners of opening A				Stress at 3		Stress at corners of opening B				Stress at 5	
	C	S	C		S		C	S	C		S		C	S
B	−0.34	299	0	0	134	89	0	29	−1.8	−6.3	−14	−52	−17.2	−155
			0	0	123	97			−3.5	−4.6	−26	−36		
IO	0	429	0	0	304	157	0	23.5	0	−6.6	7	−52	−22.2	−215
			0	0	158	171			0	−4.5	−7	−34		
LS	0	426	−0.36	0	417	135	0	415	0	0	110	18	−38.3	−470
			−0.06	0	399	416			0	0	374	336		
CP	0	440	−0.23	0	449	149	0	415	0	0	157	72	−42.1	−452
			0	0	419	414.7			0	0	415	393		
C	0	441	−0.23	0	449	150	0	415	−0.2	0	159	104	−42.6	−453
			0	0	421	415.5			0	0	415	422		

Note Negative is compression and tension is positive, considering concrete has no tensile strength, C concrete, S steel

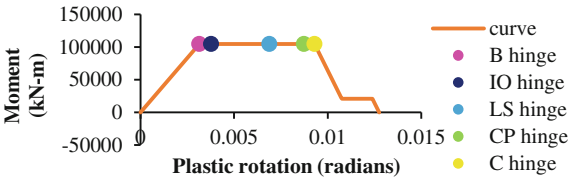

Fig. 11 Moment–rotation curve given for longitudinal equivalent wide column

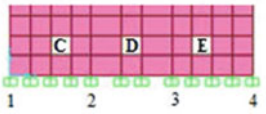

Fig. 12 Transverse punched shear wall

Table 9 Capacity curve parameters of punched shear wall models with 1 m^2 openings in transverse direction

Model	SE 1 m opening	WC 1 m opening
Yield force (kN)	14,200	14,150
Yield displacement (mm)	22	20
Effective stiffness, K_e (kN/m)	660,000	700,000
Target displacement (mm)	37	42
Ultimate displacement (mm)	274	183
Ductility capacity	12.45	9.15
Over strength ratio	2.13	2.44

Table 10 Hinge formation in transverse equivalent wide column and its corresponding layered punched shell stresses

	Stress at 1		Stress at 2		Stress at corners of opening D				Stress at 4		Stress at 5	
	C	S	C	S	C		S		C	S	C	S
B	−0.4	303	0	20	0	0	49	12	−2.8	−22	−16	−139
					0	0	41	25				
IO	0	427	0	26	0	0	151	80	0	7.7	−22	−213
					0	0	137	93				
LS	0	434	0	414.8	0	0	155	143	0	415	−39.2	−468
					0	0	415	415				
CP	0	444	0	424	0	0	157	142	0	415	−42.3	−448
					0	0	415	415				
C	0	447	0	431	0	0	158	142	0	415	−42.7	−442
					0	0	415	415				

Note Negative is compression and tension is positive, considering concrete has no tensile strength, *C* concrete, *S* steel

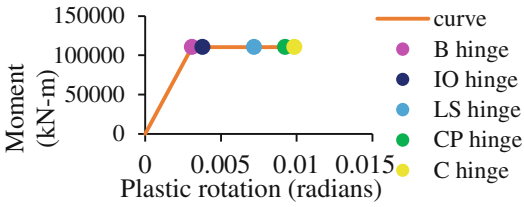

Fig. 13 Moment–rotation curve given for transverse equivalent wide column

3 Conclusions

The linear analysis results (i.e. modal analysis results, shear force and moments) of layered shell element model and their respective wide column models are comparable. The initial stiffness of the layered shell element model and wide column model is alike in both directions, which indicates that observed behaviour of shear wall building from two approaches is same within the linear range. From the nonlinear analysis, it is observed that the yield force by wide column model is 3% higher than layered shell element, whereas the bilinearized stiffness of wide column models is 25% higher than that of layered shell element model. Similarly, in case of punched shear wall, the yield force and stiffness of equivalent wide column models are 7 and 24% higher than punched layer shell element model. As in wide column model, bilinear lumped plasticity has been assigned; hence, this modelling approach is unable to capture progressive nonlinearity in the shear wall and overestimates the capacity of the building. In case of punched shear wall, the stress concentration has been observed around the shear wall opening in layered shell element model, which

plays an important role in nonlinear deformation. Overall, the layered shell element model is more effective in predicting the nonlinear response of the shear wall building than wide column model; however, it is computationally more time-consuming.

References

1. IBC. (2009). *International building code*. USA: International Code Council Inc.
2. Clough, R. W., King, I. P., & Wilson, E. L. (1964). Structural analysis of multistory buildings. *Journal of the Structural Division ASCE, 90*(3), 19–34.
3. Kwan, A. K. H. (1993). Improved wide-column-frame analogy for shear/core wall analysis. *Journal of Structural Engineering, 119*(2), 420–437.
4. Medhekar, M. S., & Jain, S. K. (1993). Seismic behaviour, design and detailing of RC shear walls, Part II: Design and detailing. *Indian Concrete Journal, 67,* 451.
5. FEMA 356. (2000). *Pre-standard and commentary for the seismic rehabilitation of buildings*. Washington, DC: Federal Emergency Management Agency.
6. EN 1998-8-3. *Design of Structures for earthquake resistance—Part 3*. London (Britain): Eurocode 8, 2005.
7. Meslem, A., & Lang, D. H. (2015). Nonlinear analysis and performance based design of multistorey buildings. New Delhi: Indo-Norwegian Training Programme Course Material.
8. Neuenhofer, A. (2006). Lateral stiffness of shear walls with openings. *Journal of Structural Engineering, 132*(11), 1846–1851.

Effect of Modeling Assumptions on Seismic Performance of RC Building

Onkar G. Kumbhar and Ratnesh Kumar

Abstract Present paper highlights the effect of some modeling assumptions on the seismic performance of reinforced concrete (RC) structure. Nonlinear seismic behavior of RC buildings for different modeling assumptions, viz., support condition, nonrigid beam-column joint, and lintel integrated with the columns, has been studied. Seismic performance has been checked by using nonlinear static analysis procedure (NSP). It has been observed that change in modeling assumption significantly affects the nonlinear performance of the building. From the study, it has been concluded that the modeling assumptions should match the realistic condition and should not be same irrespective of actual circumstances. Due to lack of specific structural modeling guidelines, the designers do not give due importance to appropriate modeling assumptions which can lead to unsafe design of buildings.

Keywords RC frame building · Modeling assumptions · Support condition
Beam-column joint · Lintel · Nonlinear static analysis

1 Introduction

The deficiency in building crops up at different stages of planning, design, and construction, and these deficiencies impart drastic reduction in seismic behavior of structure. As per Singh and Kumar [1], these deficiencies can be classified in three categories, viz., configurational deficiencies, design and detailing deficiency, and constructional deficiencies. Modeling deficiencies are also a part of design and detailing deficiency. Objective of present study is to examine the seismic performance of buildings having different types of modeling deficiencies using linear and

O. G. Kumbhar · R. Kumar (✉)
Department of Applied Mechanics, Visvesvaraya National Institute of Technology, Nagpur 440010, Maharashtra, India
e-mail: ratnesh.eq@gmail.com

O. G. Kumbhar
e-mail: onkar.kumbhar97@gmail.com

A. Rama Mohan Rao and K. Ramanjaneyulu (eds.), *Recent Advances in Structural Engineering, Volume 1*, Lecture Notes in Civil Engineering 11,
https://doi.org/10.1007/978-981-13-0362-3_6

nonlinear analysis procedure. Some modeling assumptions like joint rigidity, support condition, and lintel beams integrated in the column have been discussed. Along with some general modeling assumptions, few extreme cases of modeling assumptions (like foundation will allow 100% rotation, no damage will observe in lintel beam, etc.) are considered to observe the variation in seismic performance of structure.

In monolithic RC constructions, beam-column joints are relatively rigid; however, the effect of joint rigidity is generally ignored in the conventional structural analysis. Khan and Badre [2] carried out finite element analysis of RC beam-column connection and clearly indicated that results of the conventional frame analysis method do not reflect actual behavior of an RC frame structure. EC8 provides modeling guideline to incorporate the contribution of joint to the deformability of building. FEMA 356 [3] also recommends that the beam-column joint in monolithic construction shall be represented as stiff or rigid zone having a horizontal dimension equal to the column cross-sectional dimension and vertical dimension equal to the beam depth, except that a wider joint. ASCE/SEI 41-06 [4] also gives recommendation identical to FEMA 356 [3]. However, in update of ASCE/SEI 41 concrete provisions [5] concluded that FEMA356 overestimates the stiffness of reinforced concrete moment frames by recommending that beam-column joints to be represented as a stiff or rigid zone. Effective joint stiffness can be modeled by assigning different rigid zone factors in a centerline model based on ratio of nominal moment capacity of beam and columns. To improve the accuracy of the linear frame modeling approach, Birely et al. [6] proposed β factor on the basis of optimal offset length ratios calibrated using the available experimental data.

Inappropriate boundary condition of column foundation can affect the building performance. Lamp et al. [7] concluded that incorporating foundation stiffness in design of bridges leads to an improved solution of the overall seismic load level. FEMA 356 [3], recommends some mathematical model for considering the effect of soil stiffness for foundation. However, IS 1893(2) 2002 suggests that soil–structure interaction may be neglected in the seismic analysis for structures supported on rock or rock-like material. Fixed end condition of column foundation is the prevailing modeling assumption in the contemporary design industry in India. In present study, different fixity conditions for foundation have been dealt.

The lintel beams (i.e., is a small beam) are provided to bridge the door and window opening over masonry wall; however, the same practice is still being continued with RC frame structures in which lintel spans between columns. If the cross-sectional size of lintel is small, it does not significantly affect the behavior of building. However, it is observed that many times designer provides large lintel sizes but neglects in modeling. Due to lintel integrated into the column the behavior of structure under lateral loading changes. Such integrated lintel beam provides additional restrain to the column results in change in performance of building. Murty et al. [8] performed linear dynamic analysis of building with three different lintel sizes (100, 200, and 300 mm) and was observed that the shear demand imposed on columns increases with increase in size of lintel. The short column

effect will be predominantly seen due to lintel level beam. In present study, the effect of three lintel cross sections on seismic performance of the building has been studied.

2 Modeling and Analysis

To carryout a comparative study of proposed modeling deficiencies, a G + 5 storey building with regular plan is selected, which is very similar to the plan of office and public building, having rooms on the both side of passage way (Fig. 1). The plan is simple and symmetric in both longitudinal and transverse directions. Structural modeling, analysis, and design have been performed using SAP 2000.

The detailed mathematical model has been prepared to represent the distribution of structural stiffness and loading in plan as well as in elevation. The details of the model can be found in the paper of [9].

2.1 Effect of Monolithic Rigid Joints

Many researchers [5, 6, 10] suggested different methods for modeling of RC beam-column joint, in the present study joint has been modeled as End-length-offset by modifying centerline model having different rigidity factors. In present work, joint rigidity factor (i.e., β) has been considered, viz., $\beta = 0$, $\beta = 1$, $\beta = 0.8$, and $\beta = 0.6$ to analyze the performance of building which is designed as nonrigid joint (i.e., $\beta = 0$) frame. As per modal analysis results 15% reduction in fundamental time period has been observed as joint becomes rigid and no much change has been observed in model mass participation ratio. Details of modal analysis are not given due to page restrictions.

The capacity curves of the building models designed as general practice no joint rigidity model and analyzed by considering aforementioned joint rigidity factors are as shown in Figs. 2 and 3. Comparison of capacity curve results shows that initial stiffness of structure along longitudinal and transverse directions has been increased approximately by 23% after application of joint rigidity factor. Ultimate displacement of models with joint rigidity is reduced approximately by 32% than no offset

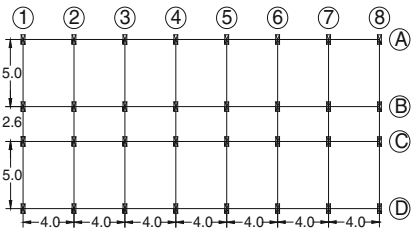

Fig. 1 Plan of a six-storey building (Model S)

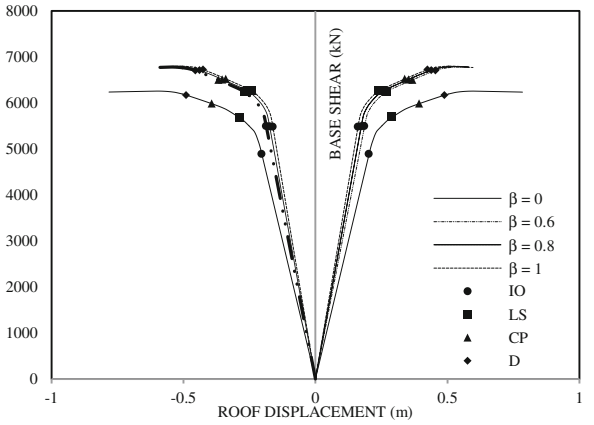

Fig. 2 Comparison of capacity curves of structures designed excluding joint rigidity factor (β) and analyzed for $\beta = 0$, $\beta = 1$, $\beta = 0.8$, and $\beta = 0.6$ in longitudinal direction

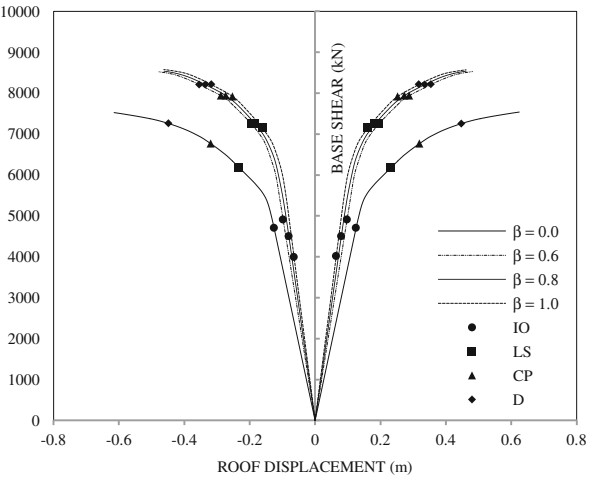

Fig. 3 Comparison of capacity curves of structures designed excluding joint rigidity factor (β) and analyzed for $\beta = 0$, $\beta = 1$, $\beta = 0.8$, and $\beta = 0.6$ in transverse direction

frame model. However, the joint rigidity factor (β) changed from 0.6 to 1, not much change has been observed in initial stiffness, yield base shear, and yield displacement of the structure. This indicates that buildings designed excluding joint rigidity behave similar irrespective of degree of joint rigidity.

Now to understand the alteration in nonlinear performance of buildings designed for 0.6, 0.8, and 1 joint rigidity value, nonlinear pushover analysis has been performed. Capacity curve obtained from NSP are shown in Figs. 4 and 5. After design, few members were failed because of additional demand of shear and

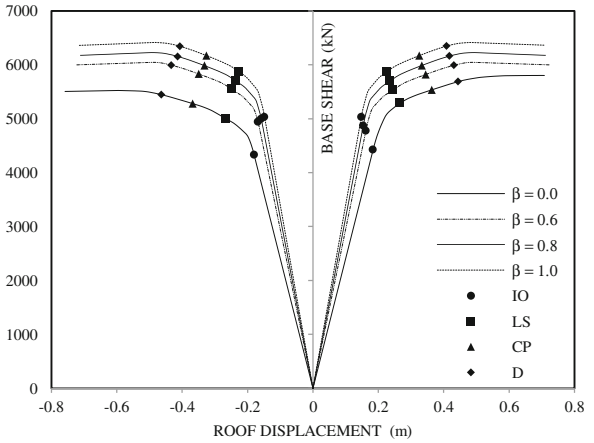

Fig. 4 Comparison of capacity curves of structures designed and analyzed for various joint rigidity factors (β) (i.e., $\beta = 0$, $\beta = 1$, $\beta = 0.8$, and $\beta = 0.6$) in longitudinal direction

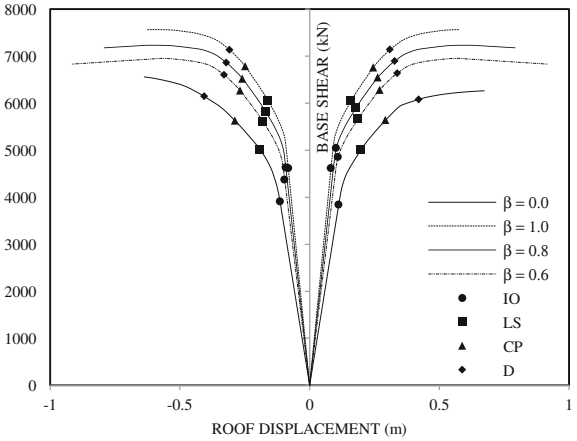

Fig. 5 Comparison of capacity curves of structures designed and analyzed for various joint rigidity factors (β) (i.e., $\beta = 0$, $\beta = 1$, $\beta = 0.8$, and $\beta = 0.6$) in transverse direction

flexure, due to which few sections has been altered. Failure in different elements of building when same considered model is designed for different joint rigidity implies that no offset frame sections are unable to fulfill the additional demand imposed by joint rigidity.

All results computed from capacity curves are given in Tables 1 and 2. From results, it is observed that target displacement of building designed as well as analyzed for same joint rigidity factor shows approximately 70–90% improvement in ductility along transverse direction and approximately 2–20% improvement in ductility along longitudinal direction compare to no offset frame. Building designed

Table 1 Comparison of capacity curve results for different joint rigidity factors in longitudinal direction

	Models designed as nonrigid joint and performance analyzed for different joint rigidity				Models designed and performance analyzed for same joint rigidity		
Joint rigidity	$\beta = 0.0$	$\beta = 0.6$	$\beta = 0.8$	$\beta = 1.0$	$\beta = 0.6$	$\beta = 0.8$	$\beta = 1.0$
Ductility	3.201	3.333	3.000	2.727	3.611	3.656	3.333
Yield force (kN)	5900	6300	6350	6400	6100	5900	5700
Yield displacement (m)	0.25	0.18	0.20	0.22	0.18	0.18	0.20
Target displacement (m)	0.213	0.132	0.127	0.123	0.220	0.227	0.235
Over strength ratio	2.14	2.280	2.298	2.316	2.20	2.135	2.063

Table 2 Comparison of capacity curve results for different joint rigidity factors in transverse direction

	Models designed as nonrigid joint and performance analyzed for different joint rigidity				Models designed and performance analyzed for same joint rigidity		
Joint rigidity	$\beta = 0.0$	$\beta = 0.6$	$\beta = 0.8$	$\beta = 1.0$	$\beta = 0.6$	$\beta = 0.8$	$\beta = 1.0$
Ductility	3.647	3.833	3.067	3.067	4.670	6.417	7.070
Yield force (kN)	6300	7205	7350	7350	6550	6500	6400
Yield displacement (m)	0.17	0.12	0.15	0.15	0.12	0.12	0.13
Target displacement (m)	0.259	0.168	0.163	0.155	0.172	0.177	0.187
Over strength ratio	1.380	2.608	2.660	2.660	2.334	2.353	2.316

as nonrigid joint frame shows increment in over strength ratio as rigidity of joint increases. On the other hand, reduction in over strength ratio can be seen in structure designed for modified joint rigidity. But overall performance of structure improves if they are designed as rigid joint frame.

2.2 Effect of Support Condition

Moment frames consist of a grid of vertical (i.e., column) and horizontal (i.e., beam) members. They resist lateral load through axial force, bending moment, and shear force generated in the structural elements (i.e., beams and columns). Member forces distribution depends upon the relative stiffness and support condition of element. In general practice, while analysis and design of structure, it is common to assume support condition as fixed, which means soil-foundation system restricts translation and rotation in all three directions, i.e., *X*, *Y*, and *Z*. However, it is not true for all practical cases [11]. In reality, soil below the foundation acts as spring. To properly

Table 3 Support conditions considered in the study

Building model nomenclatures	Support conditions
Model 1	All support as PIN support
Model 2	Peripheral support as PIN support and inner support as FIX support
Model 3	Peripheral support as FIX support and inner support as PIN support
Model 4	All support as FIX support

model the structural behavior, accurate soil spring property based on soil flexibility, amplification, and soil–structure interaction has to be determined. To roughly indicate the effect of modeling assumption regarding fixity of foundation, analysis of few cases including the two extreme cases, i.e., fixed (restrained in all six degrees of freedom) and pinned (only translational degrees of freedoms restrained) conditions of foundation, could provide some insight into structural behavior under severe ground shaking. To verify the performance of building designed for different end conditions, four different support conditions as indicated in Table 3 have been considered. To assess the seismic performance of building due to change in support condition, initially, the building is designed for fixed support condition, and the capacity curve has been developed based on nonlinear hinge properties assigned as per design, and named as Model 4. This model indicates the prevailing designer's assumption of boundary condition in field.

In reality, the support condition could be different than assumed; therefore, three separate support conditions were assigned (i.e., all support pinned, exterior support pinned, and interior fixed and exterior support fixed and interior pinned) to Model

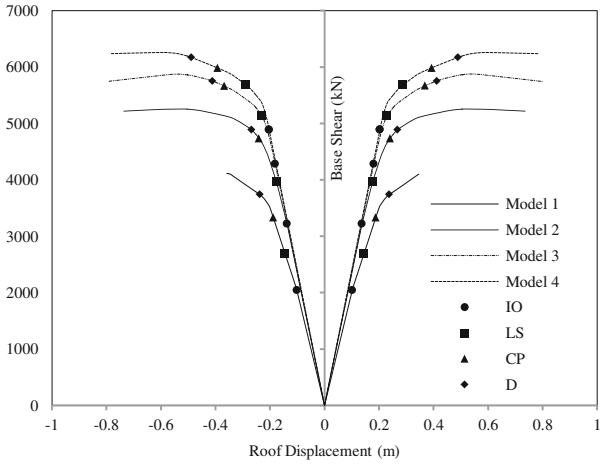

Fig. 6 Comparison of capacity curves of various support conditions in longitudinal direction

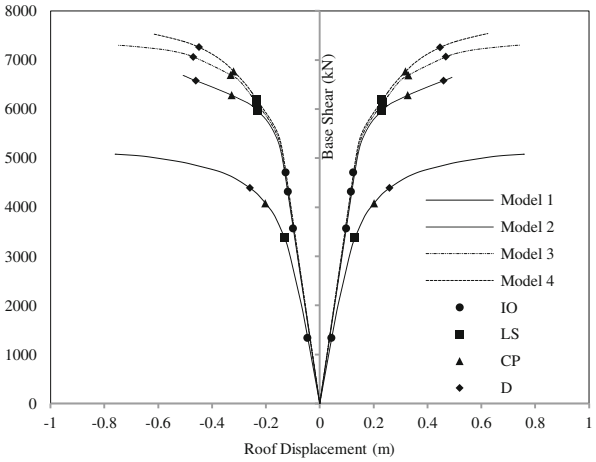

Fig. 7 Comparison of capacity curves of various support conditions in transverse direction

Table 4 Comparison of capacity curve results for different support conditions

	Pushover along longitudinal direction				Pushover along transverse direction			
Curve	I	II	III	IV	I	II	III	IV
Ductility	1.8	3.217	3.333	3.160	5.067	3.063	4.625	3.706
Yield force (kN)	3600	5100	5650	5950	5250	6650	7300	7550
Yield displacement (m)	0.2	0.23	0.24	0.25	0.15	0.16	0.16	0.17
Target displacement (m)	0.853	0.840	0.827	0.814	0.836	0.661	0.650	0.671
Over strength ratio	1.303	1.846	2.045	2.153	1.900	2.407	2.642	2.733

4. Without changing the preassigned hinge properties of frame members, and using NSP capacity, curves have been developed.

Capacity curve obtained from nonlinear analysis of aforementioned building models are shown in Figs. 6 and 7. Other results obtained from capacity curves are given in Table 4. The capacity curve results show very small change in initial stiffness of structure with change in support condition along both longitudinal and transverse directions. In comparison to Model 4, the bilinearized capacity curve of Model 1 shows that the yield point occurs at 20% less displacement and 39% less base force along longitudinal direction. Similarly, same structure yields at 6% less displacement and 70% less base force along transverse direction. In this case, the over strength ratio is reduced by 60% along longitudinal and 30% along transverse direction.

General sequence of hinge formation in considered Model is first “IO” and “C” level hinge formed in plinth beam. Further, it has been observed that in longitudinal and transverse directions, the hinges formed in lower four storeys only. In case of

Model 2, the structure yields at 8% less displacement and 14% less base force along longitudinal direction; similarly, same structure yields at 6% less displacement and 12% less base force along transverse direction than Model 4. Change in support condition shows 14 and 12% reduction in over strength ratio along longitudinal and transverse directions, respectively. In this case, no hinge has been formed in upper two storeys during pushover analysis along longitudinal direction, and hinges are formed throughout structure in pushover analysis along transverse direction. In comparison to Model 4 the yield force and displacement of Model 3 slightly decreases (i. e., less than 6%) in both longitudinal and transverse directions. Change in support condition shows 14 and 12% reduction in over strength ratio along longitudinal and transverse directions, respectively. In this case first hinge (IO) as well as collapse level hinge (C) has been formed in peripheral short column below plinth level (i.e., with restrained support condition) along longitudinal direction pushover. But along transverse direction, first hinge has been formed in short span internal plinth level beam; however, collapse hinge has been formed in short span beam but in middle storey level. Pattern of hinge formation shows that load distribution mechanism is greatly affected by end restrain of structure and which alters seismic performance of structure.

2.3 Effect of Lintel Beam

The function of a lintel is to carry the weight or load of the masonry wall constructed above it. It transmits that load to the supporting walls/columns on its either side. But lintel integrated into the column change the performance of the same structure under lateral loading. Such integrated lintel beam provides additional restrain to the column results in change in behavior of building. Generally, such lintel beams are not considered at analysis and design stage of building. To study the effect of lintel beam on seismic behavior of structure, three different sizes of lintel beams (100, 200, and 300 mm) are modeled in building, which is not designed for lintel bands, by means of two different cases, viz., (i) no hinges will form in lintel beam of size 100 mm (i.e., Model 1), 200 mm (i.e., Model 2), and 300 mm (i.e., Model 3). (ii) Minimum steel is available in lintel beam and hinges will form in lintel beam of size 100 mm (i.e., Model 4), 200 mm (i.e., Model 5), and 300 mm (i.e., Model 6). The capacity curve results are shown in Figs. 8 and 9.

In Model 4, 5 and 6 minimum steel has been provided in lintel beam which results in hinge formation in lintel at very small displacement. Therefore, the capacity curve of Model 2 and 3 shows higher stiffness than Model 5 and 6. Model 2 shows 10 and 20% more stiffness than Model 5 along transverse and longitudinal direction respectively. Similarly Model 3 shows 1.5 and 2 times more stiffness than Model 6 along transverse and longitudinal direction respectively. However insignificant change has been observed in stiffness values of Model 1 and 4, and the capacity curve is similar to Model S (i.e., without lintel model). Model 1, 2 and 3 shows 1, 35 and 50% reduction in ductility of structure as compared to Model S in

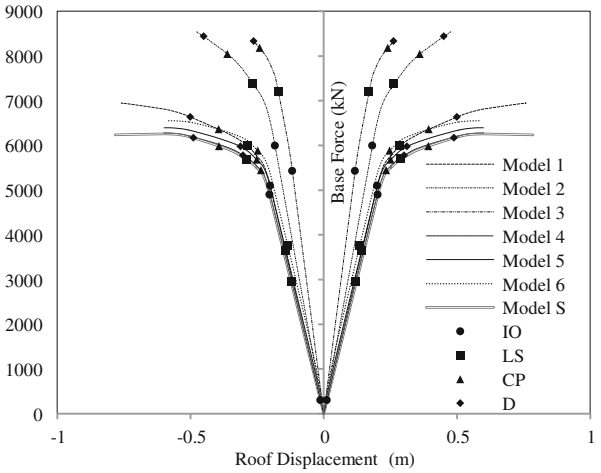

Fig. 8 Capacity curves of structure for lintel beam integrated inside column along longitudinal direction

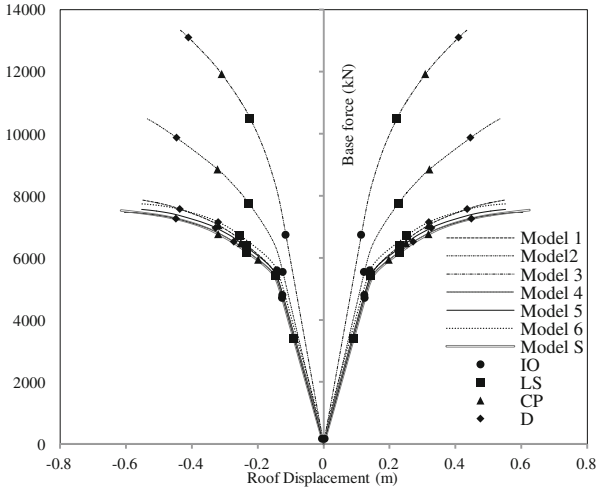

Fig. 9 Capacity curves of structure for lintel beam integrated inside column along transverse direction

longitudinal direction, also 1.5, 6 and 30% reduction along transverse direction. Results obtained from capacity curves are given in Table 5.

In every model with lintel first hinge and collapse level hinge has been formed in lintel beam but at different levels of base forces. Building model with 100 mm size lintel beam (without hinges) shows 5% higher ultimate base force and approximately equal displacement compared to no lintel model.

Table 5 Comparison of capacity curve results for different support conditions

Curve	S	I	II	III	VI	V	VI	V
Pushover along longitudinal direction								
Ductility	3.33	3.312	2.176	1.679	3.461	3.573	3.430	5.935
Yield force (kN)	5760	6200	7250	7400	5760	6100	6000	6200
Yield displacement (m)	0.235	0.23	0.22	0.16	0.22	0.22	0.23	0.10
Target displacement (m)	0.270	0.231	0.225	0.167	0.226	0.222	0.231	0.231
Over strength ratio	2.084	2.208	2.6239	2.6782	2.084	2.207	2.172	2.244
Pushover along longitudinal direction								
Ductility	3.25	3.205	3.066	2.556	3.555	3.458	3.35	4.619
Yield force (kN)	5831	6400	7300	9900	6300	6200	6400	6800
Yield displacement (m)	0.192	0.16	0.171	0.169	0.175	0.162	0.165	0.121
Target displacement (m)	0.201	0.165	0.174	0.172	0.178	0.163	0.168	0.168
Over strength ratio	2.110	2.485	2.642	2.826	2.28	2.439	2.316	2.461

In comparison to Model S the Model 2 has approximately 1.4 times larger ultimate base shear capacity in both directions. However, there is significant reduction in ductility i.e. 0.6 times in longitudinal direction and 0.9 times in transverse direction. Likewise, Model 3 also shows 34 and 78% larger ultimate base shear capacity but 66 and 27% less ultimate displacement than Model S in longitudinal and traverse directions, respectively. The capacity curve results of Model 4, 5 and 6 are similar to Model S in both the directions. It is to note that if appropriate hinges are assigned to lintels then early formation of plastic hinges are observed in lintel and columns with only minor increase in the ultimate base shear. Moreover, the ultimate displacement remains same.

3 Conclusion

In the present study, effect of some modeling assumptions, viz., nonrigid joints, support conditions and lintel integrated with column on seismic performance of the structure, has been studied. To assess the influence of joint rigidity on seismic performance of the monolithic RC structure, a comparative study of performance has been done by considering different values of joint rigidity (i.e., $\beta = 0$, $\beta = 1$, $\beta = 0.8$, and $\beta = 0.6$) at analysis and design stage of structure. If a structure designed as a fully rigid joint frame (i.e., $\beta = 1$), the ductility capacity of the structure increases by 90% in comparison to structure with full flexible joint (i.e., $\beta = 0$). In contrary, the over strength ratio reduced by 2–6%. Condition of foundation fixity depends on the soil type and foundation dimension soil below the foundation has specific stiffness and allows a certain degree of translation and rotations. To assess the effect of support condition on behavior of structure, the building is designed for all support fixed condition. Further, the same building has

been assessed for all support fixed, all support pinned, and combination of fixed-pin support conditions. If for a structure all fix support condition changes to all pin support conditions, structure yields at 6% less displacement and 70% lesser base force. In addition to this, the over strength ratio also decreases by 30–60%. In case of a combination of fixed-pin support condition, structure with peripheral supports fixed and internal supports hinged yields at 10% higher base force than the structure with peripheral support as hinged and inner support as fixed. Consideration of large size lintel integrated with columns can significantly alter the performance of building. Therefore, to study the influence of ignoring lintel beams in mathematical modeling of structure on seismic performance, three different sizes of lintels are considered (viz., 100, 200, and 300 mm). The overall performance of the building designed without considering lintel and other by considering 100 mm size lintel is similar. However, when the size of lintel beam increased to 200 and 300 mm ductility capacity of structure reduces up to 35 and 50%, respectively. From the present study, it can be concluded that, for the considered building model, the contribution of various modeling irregularities at the design and the analysis stage results in seismically deficit structure and may lead to excessive damage or complete failure during the anticipated seismic event.

References

1. Singh, Y., & Kumar, R. (2008). Performance of structures during past earthquakes: Lessons for construction industry. In *International Conference on Construction Managing Earthquake Risk* (pp. 367–377). India: India Habitat Centre.
2. Khan, M. A., & Badre, E. (1999). Study of semi-rigid properties of reinforced concrete beam column joint. *Journal of Civil Engineering and Institute of Engineering, 27*(1), 50–69.
3. FEMA 356. (2000). *Pre-standard and commentary for the seismic rehabilitation of buildings*. Washington, DC: Federal Emergency Management Agency.
4. ASCE 41. (2007). *Seismic rehabilitation of existing buildings (ASCE)*. Reston, VA: American society of Civil Engineers.
5. Elwood, K. J., Matamoros, A. B., Wallace, J. W., Lehman, D. E., Heintz, J. A., Mitchell, A. D., et al. (2007). Update of ASCE/SEI 41 concrete provisions. *Earthquake Spectra, 23*(3), 493–523.
6. Birely, A. C., Lowes, L. N., & Lehman, D. E. (2012). Linear analysis of concrete considering joint flexibility. *ACI Structural Journal, 109*(3), 381–391.
7. Lamp, I. P., Martin, G. R., & Imbsen, R. (1991). Modeling bridge foundations for seismic design and retrofitting. *Transportation Research Record No. 1290* (pp. 113–126). Washington, D.C.: Transportation Research Board—National Research Council.
8. Murty, C. V. R., Goswami, R., Vijayanarayanan, A. R. & Mehta, V. (2012). *Earthquake behavior of buildings*. Gujarat State Disaster Management Authority, Gandhinagar.
9. Kumbhar, O. G., Kumar, Ratnesh, & Adhikary, Shrabony. (2015). Effect of staircase on seismic performance of RC frame building. *Earthquakes and Structures V, 9*(2), 375–390.
10. Laura, N. L., & Arash, A. (2003). Modeling reinforced concrete beam column joint subjected to cyclic loading. *Journal of Structural Engineering, 129*(12), 1686–1697.
11. Shiuly, A. (2013). Effect of embedment of foundation in seismic analysis of RC building. *International Journal of Latest Trends in Engineering and Technology, 3*(2).

Robust Optimal Design of Buried Reinforced Concrete Pipe in Trenchless Construction Under Bounded Type Uncertainty Considering Seismic Load

S. Mukherjee, P. K. Shaw, G. Datta, S. Bhattacharjya and S. Ghosh

Abstract The adaptability of micro-tunneling of underground pipeline is getting importance day by day because of minimum disturbance requirement to the busy city life. In the present paper, a Robust Design Optimization (RDO) approach under uncertainty of such buried concrete pipeline is presented incorporating seismic effect. Often sufficient reliable data is unavailable for such problems to treat the involved parameters probabilistically. Hence, these parameters have been treated as Uncertain but Bounded (UBB) type. The limit state functions considered are the bending moment, torsional moment, crack control, shear, and minimum and maximum steel requirements as per ASCE and BS guideline. The results depict that the RDO yields solutions which are insensitive to the variation of input uncertainty. The parametric study shows that by accommodating a small increment in the optimal cost of the pipe, a more robust and reliable design solution can be achieved by the RDO approach in comparison to the deterministic design.

Keywords Robust Design Optimization · Uncertain but Bounded parameters
Buried reinforced concrete pipeline · Trenchless construction · Seismic load

S. Mukherjee · P. K. Shaw · G. Datta · S. Bhattacharjya · S. Ghosh (✉)
Department of Civil Engineering, Indian Institute of Engineering Science and Technology, Shibpur, Howrah 711103, India
e-mail: ghoshsaibal@hotmail.com

S. Mukherjee
e-mail: shanbittu04@gmail.com

P. K. Shaw
e-mail: prakashshaw27@gmail.com

G. Datta
e-mail: gaurav.rs2015@civil.iiests.ac.in

S. Bhattacharjya
e-mail: soumya@civil.iiests.ac.in

A. Rama Mohan Rao and K. Ramanjaneyulu (eds.), *Recent Advances in Structural Engineering, Volume 1*, Lecture Notes in Civil Engineering 11,
https://doi.org/10.1007/978-981-13-0362-3_7

1 Introduction

The adaptability of micro-tunneling or trenchless construction of underground pipeline is getting importance day by day because of minimum disturbance requirement to the busy city life. However, Indian design code for such an important practice has yet not come up. The most designers apply British standard [1], ASCE guidelines [2] for the design of such pipe. In the present work, an optimal design is presented for buried reinforced concrete pipeline following [1, 2]. Effect of seismic load has also been considered following IITK-GSDMA guideline [3]. The constraint functions are the bending moment, torsional moment, crack control, shear, and minimum and maximum steel requirements as per [1, 2]. The design variables are reinforcement area of inner and outer cages.

The presence of uncertainty in the trenchless construction and design method is quite natural. Thus, an attempt has been made to optimize the weight of the pipe cross section incorporating uncertainty. The most conventional approach of optimization under uncertainty is the Reliability-based Design Optimization (RBDO), where specific target reliability is sought for the critical limit states [4]. The RBDO brings specified target reliability of a design, but it focuses only on the expectation of the objective function, disregarding the variance of the objective function. As a result of which, the variance of the output design may be at quite high levels, causing undesirable deviations from the expected performance. Moreover, when the uncertainty information about the input parameters is insufficient to model them probabilistically, the RBDO cannot be applied. Because, in such cases, the probability density function is not available or cannot be constructed reliably. One such type of uncertainty is "Uncertain but Bounded (UBB)" type, which is considered in the present paper. In this case, the lower and upper bounds of the uncertain parameters are only available. With such limited information about the uncertainty, the reliability index cannot be calculated, and hence, the RBDO cannot be executed. Thus, an alternate option was in search, which is efficiently met by a comparatively newer approach called "Robust Design Optimization" (RDO). The RDO [5] becomes an attractive alternative to the RBDO approach in UBB type uncertainty cases. The RDO is fundamentally concerned with minimizing the effect of uncertainty on the output response (i.e., dispersion of the output response). The definition of the RDO may be described as, "A product or process is said to be robust when it is insensitive to the effects of sources of variability, even though sources themselves have not been eliminated" [6]. Moreover, for life cycle cost analysis, the deviation of the structural performance should be designed to a minimum to avoid maintenance and repair cost. As the RDO minimizes both the nominal value and the dispersion (or deviation) of output response simultaneously, the design solutions by the RDO will have much lesser value of dispersion than by the conventional RBDO approach. Even, with the probabilistic cases, the RDO yields more robust solution (lesser the variance of the output, more robust the solution) in comparison to the RBDO [7]. However, it has been observed that literature on RDO of buried reinforced concrete pipe is not yet available. It has been further observed that sufficient

reliable data is often unavailable for such problems to treat involved parameters probabilistically. Hence, the parameters are considered to be of UBB type in this study. The RDO essentially becomes two criteria optimization problem. The nominal value of the objective function and the associated dispersion are simultaneously optimized. The robustness in constraint function is imposed by adding suitable penalty term. A Penalty factor is further multiplied to the penalty term to enhance constraint feasibility. Once the RDO problem is formulated, the solution is done by Sequential Quadratic Programming (SQP) in MATLAB. The constraint function is approximated by a Moving Least Squares Method (MLSM) based metamodeling technique.

The development of the RDO approach with UBB parameters is presented in Sect. 2, followed by numerical study in Sect. 3. Section 4 summarizes the conclusions.

2 Development of the RDO Approach with UBB Parameters

The most common approach to deal with uncertainty is to model the structural geometric and material parameters, loads, etc., as random variables. Under these circumstances, the information about uncertainties can be modeled in the probabilistic format by using the pdf and the joint pdf. But, in many cases, for example, in preliminary design phases, even though some experimental data are available, it is not enough to construct the pdf reliably. Unfortunately, the probabilistic theory attains its limitation when insufficient reliable data are only available to describe the real-life systems with the aid of pdf. The available data can be used, particularly in combination with the engineering experience, to set some tolerances or bounds on the uncertain parameters. In the present study, owing to the essence of the problem, the involved uncertain parameters are modeled as UBB type.

Let us consider a system with N numbers of UBB parameters. The lower and upper bounds of the ith UBB parameter, u_i^{I} are denoted by u_i^{l} and u_i^{u}, respectively. With the help of interval mathematics, u_i^{I} can be expressed as [6]

$$\begin{aligned} u_i^{\mathrm{I}} &= \left[u_i^{\mathrm{l}} \quad u_i^{\mathrm{u}} \right] = \left[\bar{u}_i - \Delta u_i \quad \bar{u}_i + \Delta u_i \right] \\ &= \left[\bar{u}_i \quad \bar{u}_i \right] + \left[-\Delta u_i \quad \Delta u_i \right] = \bar{\mathbf{u}} + \Delta \mathbf{u} \end{aligned} \tag{1}$$

In the above equation, $\bar{u}_i$ is the nominal value of u_i^{I} and Δu_i denotes the maximum variation of u_i^I from its nominal value, termed as dispersion. If a practical estimation of a nominal value is available, it can be directly assigned to $\bar{u}_i$; otherwise, it is usually considered as $\bar{u}_i = \left(u_i^{\mathrm{l}} + u_i^{\mathrm{u}}\right)/2$. The standard deviation of the probabilistic variable is equivalent to dispersion in case of UBB type uncertainty. The objective function is $f(\mathbf{u})$. The deviation of the objective function (Δf) from its nominal value, $\bar{f}$ is a measure of robustness of objective function. The $\bar{f}$ and

the robustness of objective function Δf can be obtained by the first-order Taylor series expansion of $f(\mathbf{u})$ about $\bar{\mathbf{u}}$ as [8]

$$\bar{f} = f(\bar{\mathbf{u}}) \quad \Delta f = \sum_{i=1}^{N} |\partial f / \partial u_i| \Delta u_i \tag{2}$$

In the above, Δf can be visualized as gradient index, which is a function of the gradients of the performance function with respect to uncertain parameters. Using weighted sum approach, Eq. (2) can be modified as [8]:

$$\text{Minimize: } (1-\alpha)(\bar{f}/\bar{f}^*) + \alpha(\Delta f/\Delta f^*) \quad 0 \le \alpha \le 1 \tag{3}$$

where $\bar{f}^*$ and Δf^* are the optimal solutions at two ideal situations obtained for α = 0 and 1.0, respectively. The robustness of the constraint is the feasibility of the constraint needs to be guaranteed for the considered uncertainty ranges of the DVs and DPs. The nominal value ($\bar{g}_j$) and the maximum dispersion (Δg_j) of the jth constraint (g_j) with respect to its nominal value can be obtained through the first-order Taylor series expansion about $\bar{\mathbf{u}}$ as [8]:

$$\bar{g}_j = g_j(\bar{\mathbf{u}}) \quad \Delta g_j = \sum_{i=1}^{N} \left|\partial g_j / \partial u_i\right| \Delta u_i \tag{4}$$

A penalty factor, k_j is multiplied to Δg_j to further enhance the feasibility of the associated constraint. The jth constraint function is thus expressed as [8]

$$g_j(\mathbf{u}) = \bar{g}_j + k_j \Delta g_j \le 0. \tag{5}$$

Finally, the RDO problem under UBB type uncertainty can be poised by combining Eqs. (3) and (5) as

$$\begin{aligned} &\text{minimize: } (1-\alpha)\frac{\bar{f}}{\bar{f}^*} + \alpha\frac{\Delta f}{\Delta f^*} \quad 0 \le \alpha \le 1 \\ &\text{subjected to: } \bar{g}_j + k_j \Delta g_j \le 0 \quad j = 1, 2, \ldots, J \end{aligned} \tag{6}$$

The RDO is solved by SQP routine available in MATLAB.

3 Numerical Study

In this section, the RDO of a buried pipeline (Fig. 1) is presented. The Deterministic Design Optimization (DDO) is formulated first following [1] and second by [2]. The design is done under dead load, earth load, water load, and seismic load. The seismic load has been estimated following [3]. The earth load is

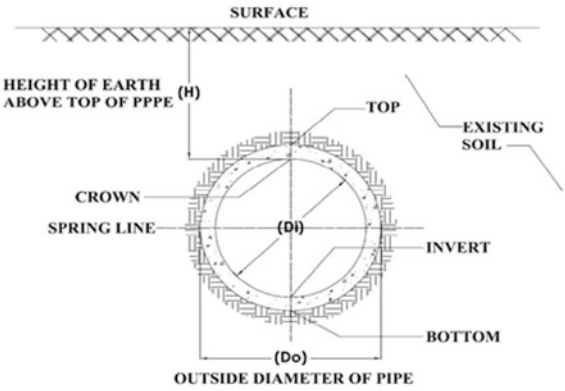

Fig. 1 The buried concrete pipe section

estimated by Marston's approach [1]. The depth of the pipe from ground is considered more than 7 m, and hence, live load is neglected. The Design Variables (DVs) for optimization are the reinforcement area requirements in the inner and outer cages. The thickness of the pipe is taken as 125 mm. The maximum reinforcement area requirement at the inner or outer cage is considered to be the objective function. The constraint functions are as follows: (i) limiting combined stress ratio for moment and axial thrust [1, 2], and (ii) crack control [2]. As per ASCE standard flexural, steel area (A_s) of the pipe is given by the following equation:

$$A_s = \frac{\left(g\emptyset_f d - N_u - \sqrt{g\left[g(\emptyset_f d)^2 - N_u(2\emptyset_f d - h) - 2M_u\right]}\right)}{f_y} \tag{7}$$

where $g = 0.85bf'_c$ and f_c is the design compressive strength of concrete, ϕ_f is a combined flexure and thrust coefficient which is equal to 0.95, d is the effective depth of pipe, h is the overall depth of pipe, N_u is the thrust, M_u is the moment, f_y is the yield strength of steel, and b is the diameter of the pipe.

The area of steel as per British standard is

$$A_s = \frac{P_u}{f_y} + \frac{\left(0.85f'_c a' b\right)}{f_y} \tag{8}$$

where P_u is the factored thrust,

$$a = \frac{2 * M_{ult}}{0.85 * f'_c * b * d_i^2} \tag{9}$$

$$a' = 14(1 - \sqrt{(1 - a)}) \tag{10}$$

The crack control factor F_{cr} as per ASCE standard is

$$F_{cr} = (B_1/5250\varphi f d A_s) * [\{(M_s + N_s(d - h/2))/ij\} - (0.083 C t b h^2 \sqrt{fc})] \tag{11}$$

where B_1 is the crack control coefficient given by

$$B_1 = \sqrt[3]{\frac{25.4 x t_b x s_1}{2xn}} \tag{12}$$

$$i = \frac{1}{1 - \frac{jxd}{e}} \tag{13}$$

$$j = \left(0.74 + \frac{2.54xe}{d}\right) \tag{14}$$

$$e = \frac{M_s}{N_s} + d - \frac{h}{2} \tag{15}$$

M_s, N_s, A_s, t_b, and s_1 are the total moment, total thrust, provided area of steel, clear cover, and spacing of circumferential reinforcement, respectively. n = 2, when tension reinforcement is made of multiple layer, and C_t = 1.00 for smooth wire plain bars.

Thus, the Deterministic Design Optimization (DDO) problem is posed as

$$\begin{aligned} &\text{Find } x_1, x_2 \\ &\text{So as to minimize:} \\ &f(\mathbf{u}) = \rho_s(x_1 + x_2) \\ &\text{subjected to:} \\ &g_1(\mathbf{u}) : (A_s)_{\text{inner cage}} - x_1 \le 0 \\ &g_2(\mathbf{u}) : (A_s)_{\text{outer cage}} - x_2 \le 0 \\ &g_3(\mathbf{u}) : F_{cr} - 1.0 \le 0 \\ &x^l \le x_1, x_2 \le x^u \end{aligned} \tag{16}$$

In the above equation, x_1, x_2 are the areas of reinforcements in the inner and outer cages, respectively. ρ_s is the density of steel, and x^l and x^u are the minimum and maximum areas of reinforcement, respectively. The Design Parameters (DPs) are shown in Table 1. The DPs are considered as UBB type. The nominal values and the associated dispersion of the DPs are also indicated in Table 1.

The soil–structure interaction is modeled by equivalent springs in axial, lateral, and vertical directions, the stiffness (k) of which is estimated following [3]. The soil is considered as saturated clay. It may be noted here that the k values depends on the UBB type DVs α, c, w, H and deterministic N_c (= 5.14), N_q (= 1), and diameter of the pipe (D). However, for the sake of simplicity, the nominal values of k are estimated substituting nominal values of the associated DPs. Then, an ad hoc

Table 1 Details of the uncertain DPs

DPs	Nominal values	Dispersion (%)
Height of earth above the top of pipe (H)	7.5 m	20
Unit weight of soil (w)	18 kN/m^3	20
Design characteristic strength of concrete (f_{ck})	50 MPa	10
Design yield strength of steel (f_y)	480 MPa	10
Coefficient of cohesion (c)	1900 N/m^2	20
Saturated top soil coefficient (K'_u)	0.15	10
Seismic time-history load (T_L)	0.3 g	20
Adhesion factor, α	1.0	10
Density of steel, ρ_s	77 kN/m^3	5

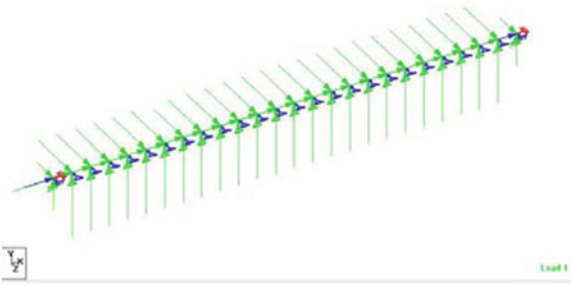

Fig. 2 The STAAD model representing pipe–soil interactions along with forces

dispersion level of 20% due to uncertainty is imposed on k. Thus, k is also considered as UBB type. The seismic effect is estimated by a time-history analysis with El-Centro NS earthquake history in STAAD.Pro software. The spring model with time-load is shown in Fig. 2.

It may be noted here that the constraint functions of Eq. (16) are implicit with the involved DVs and DPs. Hence, the Response Surface Method (RSM) is applied here to judiciously evaluate the constraints and the gradients. Conventionally, Least Squares Method (LSM) based RSM is applied for dealing optimization problems including implicit constraint functions. However, the accuracy with the LSM-based RSM, which is based on global approximation, is often challenged [9]. The authors feel that the MLSM-based RSM, a local approximating technique, will be more elegant for such problems [9]. Thus, in the present study, the MLSM-based RSM strategy has been adopted. The constraint functions are approximated by the MLSM-based RSM in terms of the DVs and DPs. The design of experiment has been performed by the redundant design scheme with axial points extending up to $\bar{\mathbf{u}} \pm 6\Delta\mathbf{u}$. Once the RSM approximation is obtained and validated by "goodness of fit" tests, the gradient evaluation becomes extremely simplified to cast the RDO problem following Eq. (6). Then, the resulting RDO problem is solved by the SQP routine available in MATLAB.

The RDO is executed first by the limit state functions of the British standard [1], referred here by RDO_BS. As a second module, the RDO is executed with ASCE standard, which will be referred as RDO_ASCE. The RDO_BS results are shown in Figs. 3 and 4 for different D and k_j values. Similarly, the RDO_ASCE results are presented in Figs. 5 and 6. The value of α is considered to be 0.5 for developing these figures. Figures 3 and 5 depict the variation of the optimal reinforcement area in the cage per meter length of pipe. It may be observed from these figures that the steel requirement is more for higher values of the penalty factor. The steel requirement by the RDO_BS is observed to be more than that of RDO_ASCE. Thus, the RDO_BS approach yields more conservative design that by the RDO_ASCE approach. Figures 4 and 6 represent the dispersion (%) of the optimal reinforcement weight requirement. Lesser the dispersion, more robust will be the design. It may be observed from Figs. 4 and 6 that even in presence of the uncertainty level as in Table 1, as high as 20%, the optimal weight has a dispersion of maximum 3.4%. This indicates that the RDO design is really insensitive to the input parameter variation due to uncertainty. The increment of the optimal weight

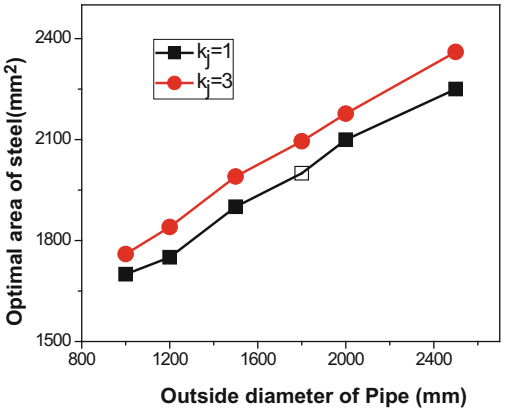

Fig. 3 Variation of the optimal area of reinforcement for different penalty factors and diameter of pipe by the RDO_BS approach

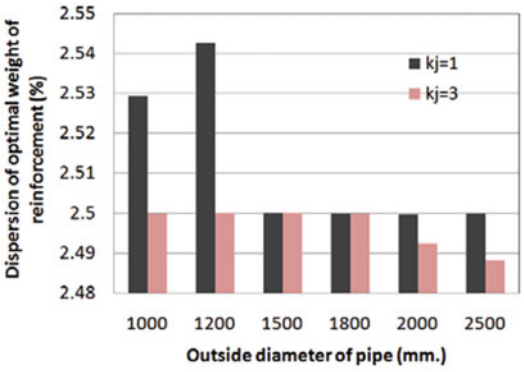

Fig. 4 Variation of the dispersion of the optimal weight of reinforcement for varying diameter and penalty factors by the RDO_BS approach

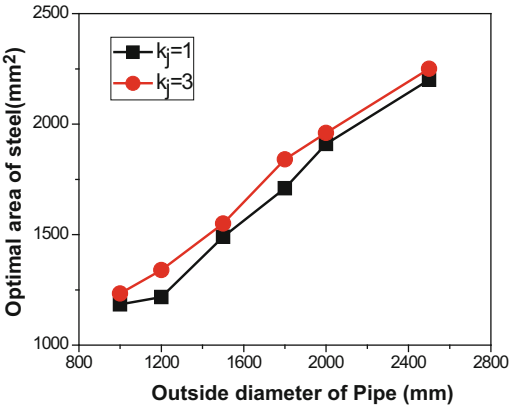

Fig. 5 Variation of the optimal area of reinforcement for different penalty factors and diameter of pipe by the RDO_ASCE approach

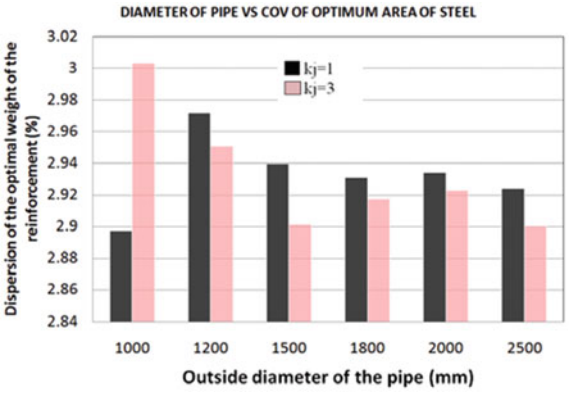

Fig. 6 Variation of the dispersion of the optimal weight of reinforcement for varying diameter and penalty factors by the RDO_ASCE approach

of steel by the RDO in comparison to the conventional DDO is on an average 5% to 11%. Thus, by sacrificing a marginal amount of cost, one can have robust and reliable design solutions by the RDO approach. The computational cost to implement the proposed RDO approach is also nominal.

It is generally observed that there is a trade-off between the objective values of a design and its robustness. If one desires more robustness, the design will be further away from its ideal optimal value. The situation can be studied further in terms of Pareto front [10]. The Pareto front is one where any improvement in one objective can only occur through worsening of at least one other objective. If one chooses a design that is not Pareto-optimal, one essentially forfeits improvements that would otherwise entail no compromise. Thus, one of the important tasks in the RDO is to obtain the Pareto front. The Pareto fronts as obtained by RDO_BS and RDO_ASCE approaches by varying the values of "α" are presented in Figs. 7 and 8, respectively. The diameter of the pipe is considered to be 1500 mm for developing these figures. k_j is considered to be 3.0.

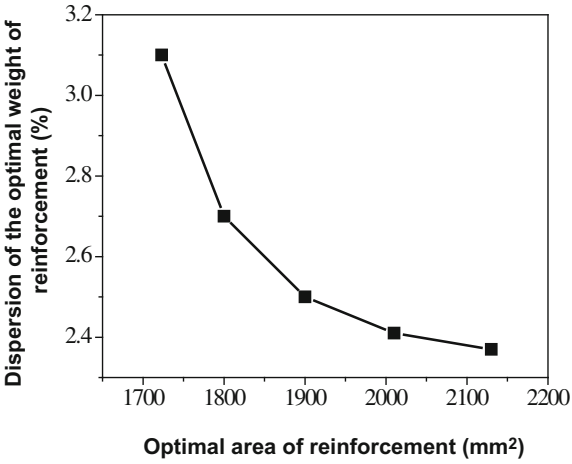

Fig. 7 The Pareto front by the RDO_BS approach

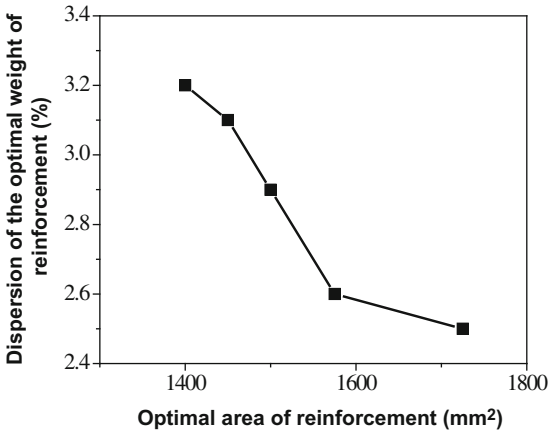

Fig. 8 The Pareto front by the RDO_ASCE approach

So far, the RDO deals with the inner and outer cages of circumferential reinforcement. The requirement of the longitudinal reinforcement is largely dictated by the jacking force during micro-tunneling operation and the effect of seismic force. The jacking force has been estimated by the approach laid in [11]. The involved parameters are assumed as UBB type with uniform probability density function. Then, the jacking force F_j is estimated by a direct Monte Carlo Simulation (MCS). The result is validated with filed data during a practical micro-tunneling project. The comparison is presented in Fig. 9. It can be observed that the experimental results are quite close to the theoretically predicted values of the jacking force.

It has been observed that on an average 1.2% steel is sufficient to cater the jacking force, when the jacking pit and receiving pits are located at a distance of 150 m. The seismic effect is calculated according to [3]. However, the maximum strain in concrete pipe is observed to be exceeded invariably under the considered

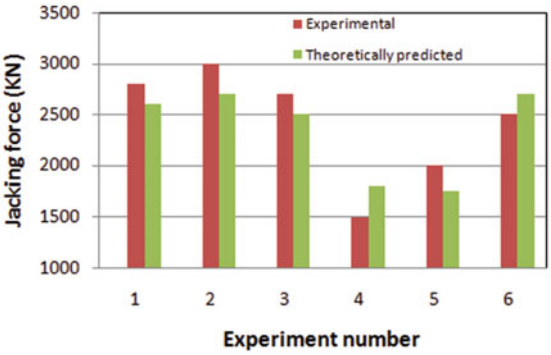

Fig. 9 Comparison between the experimental and theoretically predicted jacking force

time-history seismic load in the present study. Hence, an inside steel casing of 16 mm thickness is calculated to be essential in this regard to cater the seismic effect.

4 Conclusions

A novel RDO approach of buried concrete jacking pipe is presented in an MLSM-based RSM framework. The constraints are the limiting stress and crack control criteria under earth, water, and dead load as per British standard and ASCE standard. The seismic effect is also considered by IITK-GSDMA guideline. The jacking force has been estimated and validated with the field results. The theoretical prediction of the jacking force is in close conformity with the field test data. Since uncertainty information about the parameters is often limited in such cases, the parameters are modeled as UBB type. The parametric study shows that the British standard yields more conservative results than the ASCE standard. The results depict that the RDO yields solutions which are insensitive to the variation of input parameters due to uncertainty. By accommodating a small increment in the optimal weight (or the optimal cost) of the pipe, a more robust and reliable design solution can be achieved by the RDO approach in comparison to the deterministic design. The proposed RDO approach is computationally viable, as well.

Acknowledgements The authors acknowledge M/s Simplex Infrastructure Limited and M/s Atoz for supplying the field data during micro-tunneling operation.

References

1. BS 5911: Part 120:1989, *Precast concrete pipes, fittings and ancillary products*, England.
2. ASCE 27-00, *Standard practice for direct design of precast concrete pipe for jacking in trenchless construction*, ASCE, Virginia.

3. IITK-GSDMA, *Guidelines for seismic design of buried pipeline*, IIT Kanpur, NICEE, 2007.
4. Hu, D., Yang, J., Fei, C., Wang, R., & Choy, Y. (2016). Reliability-based design optimization method of turbine disk with transformed deterministic constraints. *Journal of Aerospace Engineering*, 04016070-1.
5. Beyer, H., & Sendhoff, B. (2007). Robust optimization—A comprehensive survey. *Computer Methods in Applied Mechanics and Engineering, 196,* 3190–3218.
6. Fowlkes, W. Y., & Creveling, C. M. (1995). *Engineering methods for robust product design—Using Taguchi methods in technology and product development*. Addison Wesley.
7. Venanzi, I., Materazzi, A. L., & Ierimonti, L. (2015). Robust and reliable optimization of wind-excited cable-stayed masts. *Journal of Wind Engineering and Industrial Aerodynamics, 147,* 368–379.
8. Lee, K., & Park, G. (2001). Robust optimization considering tolerances of design variable. *Computers & Structures, 79*(1), 77–86.
9. Chakraborty, S., & Bhattacharjya, S. (2012). Efficient robust optimization of structures subjected to earthquake load and characterized by uncertain bounded system parameters. *Structural Seismic Design Optimization and Earthquake Engineering: Formulations and Applications*.
10. Rohner, R., & Hoch, A. (2010). Calculation of jacking force by new ATV A-161. *Tunnelling and Underground Space Technology, 25*(6), 731–735.
11. Deb, K. (2011). Multi-objective optimization using evolutionary algorithms: An introduction. *KanGAL Report Number 2011003*. Department of Mechanical Engineering Indian Institute of Technology Kanpur.

Numerical Study on Flexural Capacity of Biaxial Hollow Slab

R. Sagadevan and B. Nageswara Rao

Abstract Biaxial hollow slab is a type of slab in which concrete from the middle of the slab (floor) has been eliminated by means of voids. This type of slab system is mainly used as reinforced concrete flat slab. Its main advantage is reduction in self-weight (about 30–50%). However, the presence of voids reduces the area of slab concrete, which leads to reduction in the flexural stiffness and shear resistance. In this study, simulations were carried out by using finite element software DIANA (Displacement Analyzer) to investigate the flexural capacity of the biaxial hollow slab. Parametric studies were carried out to compare the effect of different types of voids on the behaviour of the slab.

Keywords Biaxial hollow slab · Flexural capacity · Voided slab

1 Introduction

Biaxial hollow slab is reinforced concrete slabs with top and bottom reinforcing mesh and hollow plastic bubbles as voids as shown in Fig. 1. From the slab, concrete is eliminated by voids (bubbles made of recycled plastic materials); this leads to a reduction in self-weight about 30–50% compared to the conventional flat slab. It reduces the requirement of reinforcement and concrete in other structural parts of construction and gives economy and efficient floor system in construction. It is an eco-friendly system, because of the use of recycled plastic and reduction in material consumption.

Bubbles can be placed by various methods, but using the reinforcement meshes reduces material consumption and gives an optimal geometrical proportion between

R. Sagadevan (✉) · B. Nageswara Rao
Department of Civil Engineering, Indian Institute of Technology Madras, Chennai 600036, Tamil Nadu, India
e-mail: sagadevan.ceg@gmail.com

B. Nageswara Rao
e-mail: bnrao@iitm.ac.in

A. Rama Mohan Rao and K. Ramanjaneyulu (eds.), *Recent Advances in Structural Engineering, Volume 1*, Lecture Notes in Civil Engineering 11,
https://doi.org/10.1007/978-981-13-0362-3_8

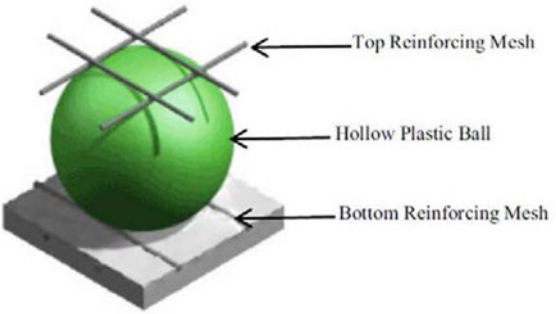

Fig. 1 Components of bubble deck

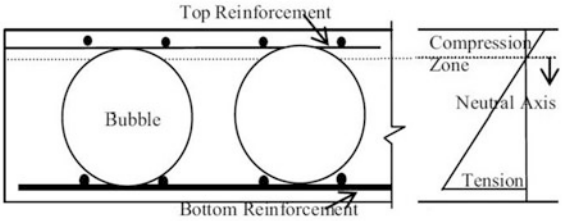

Fig. 2 Cross section of void slab and stress diagram

concrete, reinforcement and voids. The voids are positioned in the middle of the cross section, where concrete has limited effect and thus maintaining solid sections on top and bottom where high stresses can exist. Hence, the slab is fully functional with regard to both positive and negative bending. The cross section of the bubble deck slab and its stress variation at a section are shown in Fig. 2.

For the design of flat slab, flexural capacity [1] and shear resistance [2] are to be considered. These parameters are mainly influenced by voids (size and shape of the plastic bubble). In this article to investigate the flexural capacity of the voided slab, numerical simulations have been carried out by using finite element software DIANA (Displacement Analyzer) [3]. A parametric study was carried out to understand the behaviour of the biaxial hollow slab with different types of voids such us sphere, cuboid, donut and ellipsoid. These voids are selected based on experimental work carried out by various authors [4–11].

2 Simulation of Biaxial Hollow Slab

Adopting a three-dimensional model with four-noded isoparametric solid pyramid elements numerical simulation was carried out to simulate the structural behaviour of the biaxial hollow slab. Finite element model of simply supported biaxial hollow slab with plan dimension of size 5 m $\times$ 5 m subjected to uniformly distributed load (UDL) is modelled and analysed with smeared crack model [12].

Table 1 Material properties

Parameter	Value
Tensile strength of concrete (f_t)	2.5 N/mm^2
Compressive strength of concrete (f_{ck})	50.8 N/mm^2
Fracture energy (G_f)	0.09 N-mm/mm^2
Shear retention factor (β)	0.18
Cohesion (c)	14.66 N/mm^2
Friction angle (φ)	30°
Yield strength of reinforcement (f_y)	415 N/mm^2

Finite element model is analysed with smeared crack model, and it has been frequently used in finite element simulation of fracture and crack propagation problems. This crack model simulates the mechanical effects of concrete in terms of stiffness or strength reduction [13]. In this model, cracking is specified as a combination of tension cut-off, tension softening and shear retention. The material properties used for the simulation of behaviour of slab specimen are summarized in Table 1.

2.1 Parameters of Smeared Crack Model

2.1.1 Tension Cut-Off

Tensile and compressive strength of concrete are the parameters needed to define the tension cut-off in two-dimensional principal stress spaces. In this model, linear tensile stress cut-off was used, and it is shown in Fig. 3.

Fig. 3 Linear tension cut-off

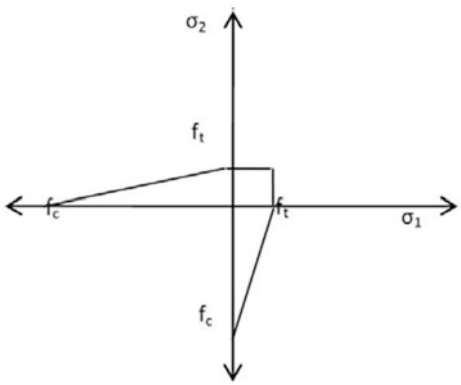

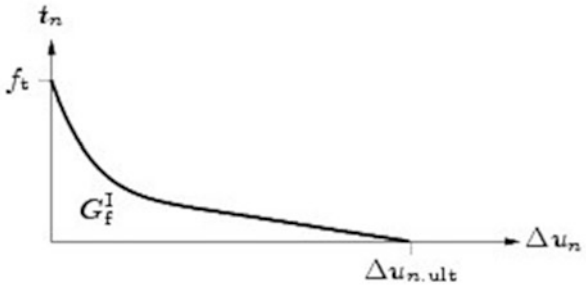

Fig. 4 Non-linear tension softening (Hordijk et al. [16])

2.1.2 Tension Softening

In order to define the softening branch of the tensile stress–strain relation of concrete by fracture mechanics, three important parameters need to be defined [14, 15]:

1. The tensile strength of concrete at which a fracture zone initiates.
2. The area under the stress–strain curve.
3. The shape of the descending branch.

Among these parameters, the first two can be considered as material constants, while the shape of the descending branch varies. Tension softening curve proposed by Hordijk et al. [16] was used in this analysis, and it is shown in Fig. 4.

2.1.3 Shear Retention Factor

The shear stiffness of concrete reduces due to the cracking. The reduced shear stiffness is quantified as shear retention [17]. The shear retention factor 'β' is less than one, but greater than zero. The cracked shear stiffness is then given by the general relation

$$D_{\text{secant}}^{\text{II}} = \frac{\beta}{1-\beta} G \tag{1}$$

From the earlier work done by the researchers in the field of non-linear finite element analysis of RC structures, it was understood that the shear retention factor is very important for simulating the experiments. Therefore, this value was varied from 0 to 0.99 to reproduce the load versus deflection curve obtained from the results.

2.1.4 Mohr–Coulomb Plasticity Model

The non-linear properties required for defining the compressive regime of concrete are cohesion (c) and friction angle (φ). Cohesion (c) can be found by knowing the compressive strength (f_{ck}) and friction angle (φ) with help of the following relationship:

$$c = \frac{f_{ck}(1 - \sin\varphi)}{2\cos\varphi} \tag{2}$$

2.2 *Finite Element Model of Slab in DIANA*

The finite element model of the slab is created in DIANA software by adopting a three-dimensional model with four-noded isoparametric solid pyramid elements. The model of slab with boundary conditions is shown in Fig. 5. Meshing of reinforcements was done by using an element called 'reinforcements embedded in concrete' with the assumption of full bonding between concrete and reinforcement. The slab (sphere shape void) model after meshing is shown in Fig. 6. Non-linear analysis was performed by adopting the material properties given in Table 1.

The slab is modelled and analysed with various types of void shapes, such as sphere, cuboid, donut and ellipsoid. The size of voids was arrived such that it eliminates 30% of the concrete.

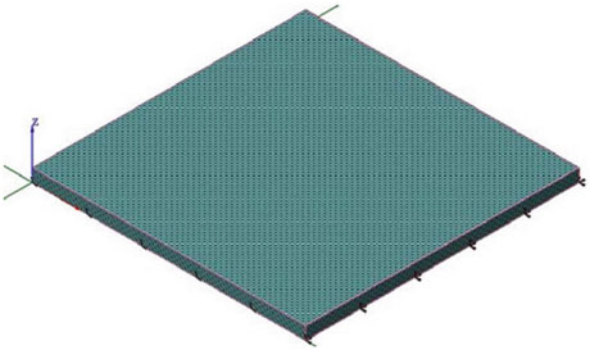

Fig. 5 Slab model with boundary conditions

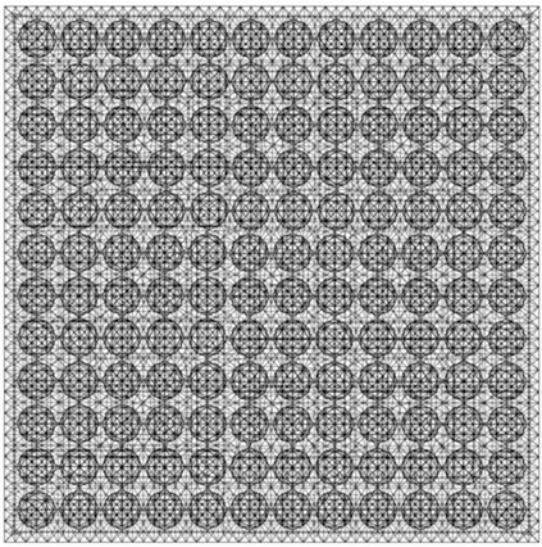

Fig. 6 Slab (sphere void) model after meshing

3 Results and Discussions

The finite element analysis results were divided into strength and serviceability criteria. For strength and serviceability criteria, the load carrying capacity and deflection were considered, respectively. The deflection contour is shown in Fig. 7.

The plot of load versus mid-span deflection for various types of void shapes is shown in Fig. 8. The behaviour of two-way hollow slab with various voids can be

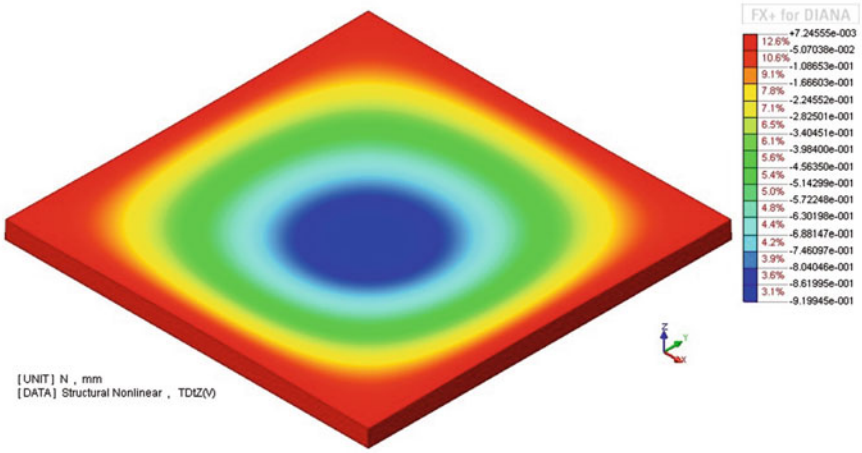

Fig. 7 Deflection contour

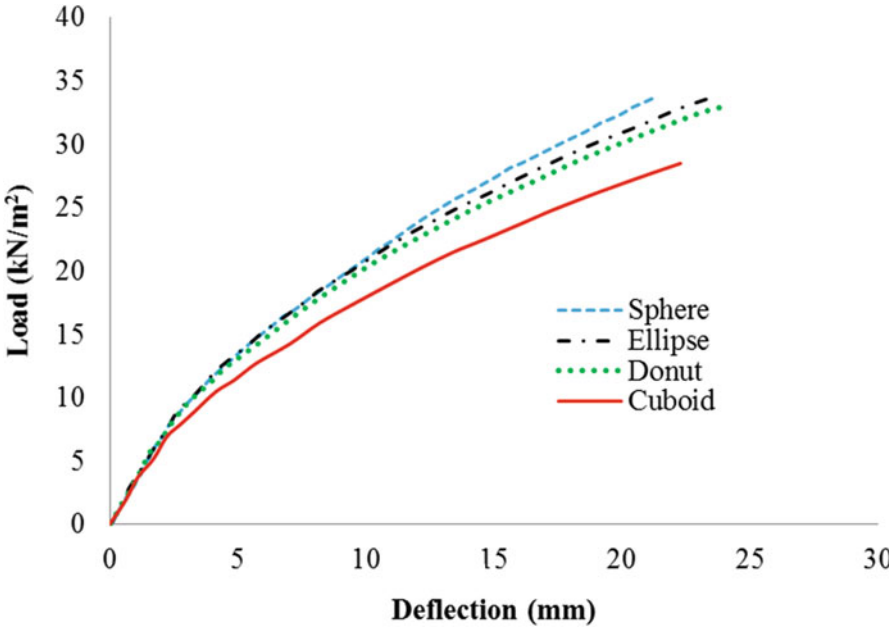

Fig. 8 Load versus mid-span deflection

Fig. 9 Load corresponding to deflection of 18.4 mm

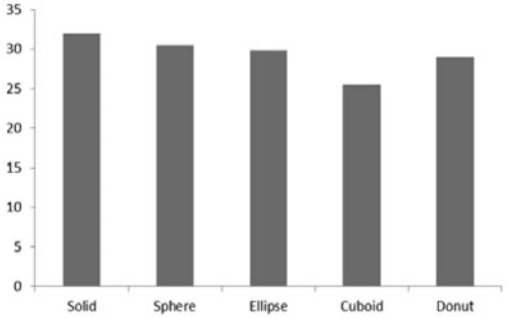

observed from the plot. From the plot, it is observed that the cuboid shape of void takes less load compared to other shapes of voids.

Figure 9 shows the load (i.e. load corresponding to the allowable deflection $l_e/250$, 18.4 mm) [18] with respect to the different void shapes; this plot clearly shows that sphere shape void has more load carrying capacity than other types of shapes.

Figure 10 shows the deflection (i.e. deflection corresponding to load of 32 kN/m^2—capacity of solid slab) with respect to the different void shapes, and it is observed that the cuboid shows maximum deflection than other shapes of voided slabs for same loading.

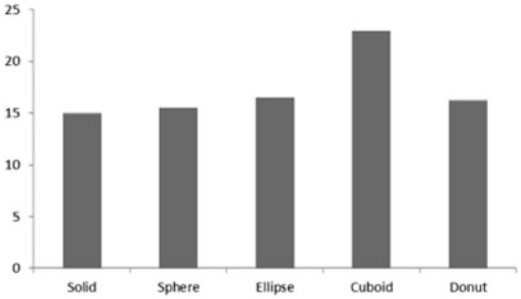

Fig. 10 Mid-span deflection corresponding to load of 32 kN/m^2

4 Conclusion

The results of non-linear finite element analysis show that the void slab also can withstand the load that is carried by solid slab. However, reduction in stiffness of void slab leads to increase in deflection. The optimum void ratio can be arrived such that the void slab satisfies both strength and serviceability requirement.

Slab with cuboid shape void carries less load than slab with other void shapes. It is because stress concentration is taking place at the corner of cuboid.

Slab with sphere shape void shows better results in terms of load carrying capacity as well as serviceability criteria.

References

1. Chung, L., Lee, S. H., Cho, S. H., Woo, S. S., & Choi, K. K. (2010). Investigations on flexural strength and stiffness of hollow slabs. *Advances in Structural Engineering, 13*(4), 591–602.
2. Aldejohann, M., & Schnellenbach-Held, M. (2003). Investigations on the shear capacity of biaxial hollow slabs—Test results and evaluation. *Darmstadt Concrete, 18,* 1–11.
3. DIANA. (2008). "User's Manual", Release 9.3, (a) Material Library, (b) FX + (for pre- and post-processors for DIANA), (c) Element Library, TNO DIANA BV, The Netherlands.
4. Kim, S., Kang, I., & Lee, H. (2007). Experimental study on the flexural behavior of I-Slab. *Proceeding of Korea Concrete Institute, 19*(2), 5–8.
5. Lee, W., Cho, S., Lee, S., Lan, C., & Cho, S. (2007). Flexural performance of hollow slab with elliptical balls. *Proceeding of Korea Concrete Institute, 19*(2), 33–36.
6. Hwang, H., Kim, S., Hwang, H., Lee, K., & Lee, J. (2008). Structural performance evaluation of hollow reinforced concrete half slabs. *Proceeding of Korea Concrete Institute, 20*(1), 45–48.
7. Chung, J. H., Ahn, N. K., Choi, H. K., & Chang, C. S. (2009). An analytical study of optimal hollow sphere shapes in hollow slab. *Journal of the Korea Institute for Structural Maintenance*, 159–162.
8. Chung, J. H., Choi, H. K., Lee, S. C., Oh, J. K., & Choi, C. S. (2009). An analytical study of the impact of hollow sphere on biaxial hollow slab. In *Proceeding of Annual Conference of the Architectural Institute of Korea* (pp. 475−478).

9. Chung, L., Lee, S. H., Cho, S. H., Woo, S. S., & Choi, K. K. (2010). Investigations on flexural strength and stiffness of hollow slabs. *Advances in Structural Engineering, 13*(4), 591–602.
10. Kim, S. H. (2010). Flexural behavior of void RC and PC slab with polystyrene forms. *Key Engineering Materials, 452,* 61–64.
11. Kim, B. H., Chung, J. H., Choi, H. K., Lee, S. C., & Choi, C. K. (2011). Flexural capacities of one way hollow slab with donut type hollow sphere. *Key Engineering Materials, 452,* 773–776.
12. Borst, R. D. (1987). Smeared cracking, plasticity, creep, and thermal loading—A unified approach. *Computer Methods in Applied Mechanics and Engineering, 62*(1), 89–110.
13. Mohammadi, S. (2008). *Extended finite element method for fracture analysis of structures. Blackwell Publishing Ltd.*
14. Cornelissen, H. A. W., Hordijk, D. A., & Reinhardt, H. W. (1986). Experimental determination of crack softening characteristics of normal weight and lightweight concrete. *Heron, 31*(2).
15. Roesler, J. (2007). Concrete fracture prediction using bilinear softening. *Cement & Concrete Composites, 29*(13), 300–312. (Elsevier Science B.V).
16. Hordijk, D. A., Reinhardt, H. W., & Cornelissen, H. A. W. (1987). Fracture mechanics parameter of concrete from uniaxial tensile test as influenced by specimen length. In *Pre-printed of SEM/RILEM International Conference on Fracture of Concrete and Rock, Houston, Tex. S. P. Shah and S. Swartz, eds., SES (Society of Experimental Mechanics)*, 138–149.
17. Scotta, R., Vitaliani Saetta, A., Nate, E. O., & Hanganu, A. (2001). A scalar damage model with a shear retention factor for the analysis of reinforced concrete structures: Theory and validation. *Computers & Structures, 99*(7), 737–755. (Elsevier Science B.V).
18. IS 456: 2000. Indian Standard Code of Practice for Plain and Reinforced Concrete. *Bureau of Indian Standards*, New Delhi.

Issues on Design Shear Strength of RC Deep Beams

J. Leon Raj and G. Appa Rao

Abstract In this paper, a simple analytical expression is proposed for limiting the design shear strength of RC deep beams, by considering following facts. The maximum shear strength equation of ACI code is same for both concentrated and uniformly distributed loading cases. The effect of $\frac{a}{d}$ needs to be accounted for properly. Second, the effect of size, tension reinforcement and limitations on compressive strength of concrete result in either overestimation or high underestimation of shear strength of beams with *a/d* ratio ranging between 1.0 and 2.0. The proposed equation is validated with the test data of 413 deep beams segregated from literature and design provisions of various codes. The proposed model overestimates only, a meagre fraction, 5% of the collected data, whereas the ACI 318-14 code equation overestimates 18.4% of collected data.

Keywords Deep beams · Shear strength limit · Shear span-to-depth ratio Size-effect

1 Introduction

Deep beams are characterized by small shear span-to-depth ratio, whose ratio, as per *ACI 318*, is restricted to 2.0, exhibiting significant shear capacity at failure with complex failure mechanisms. In view of ample shear capacity, deep beams are primarily recommended as transfer girders. These members transfer loads from loading face to supports in the transverse direction as shown in Fig. 1. The deep horizontal members predominantly fail in shear. Pile caps, corbel, brackets, foundation walls and offshore structures are few examples of RC deep beams.

J. L. Raj · G. A. Rao (✉)
Structural Engineering Division, Civil Engineering Department,
Indian Institute of Technology Madras, Chennai 600036, India
e-mail: garao@iitm.ac.in

J. L. Raj
e-mail: leonraj.civil@gmail.com

A. Rama Mohan Rao and K. Ramanjaneyulu (eds.), *Recent Advances in Structural Engineering, Volume 1*, Lecture Notes in Civil Engineering 11,
https://doi.org/10.1007/978-981-13-0362-3_9

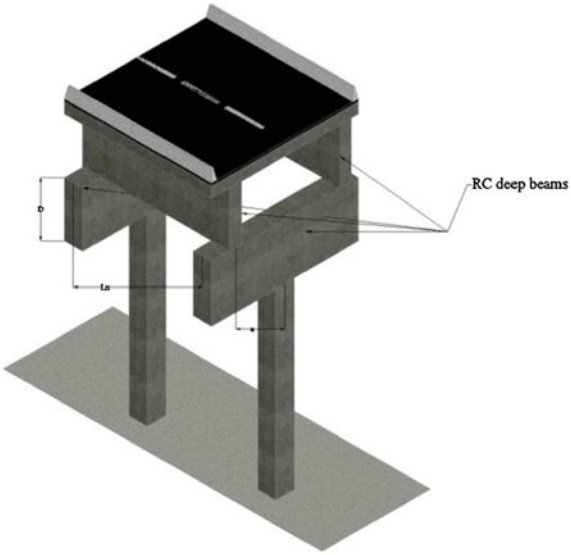

Fig. 1 Examples of deep beams in bridges

Issues on designing deep beams are different from that of normal or slender beams. First, Kani [1] reported that shear strength seems to increase with breadth of the beam, and decrease with depth of beam. Second, the variation of ultimate shear strength, V_u/bd versus compressive strength does not reveal any improvement in shear strength using high compressive strength of concrete proportionately. Third, the ACI maximum shear strength equation is common for both concentrated and uniformly distributed loading, thus, the effect of $\frac{a}{d}$ is not properly reflected for different cases of loading. Consequently, for deep beams with *a*/*d* ratio greater than 1.0, the shear strength is overestimated. Accounting for all the above-mentioned factors influencing the shear strength in the maximum shear strength equation is the main objective of this paper.

2 Review of Definition of Deep Beams

Beams are classified according to the shear span-to-depth ratio. Different codes specify different values of clear span-to-depth ratios for classifying the beams as deep beams. According to ACI 318-95 [2], a beam is defined as a deep beam when $\frac{l}{D} \leq 5.0$. Later, in 2002, ACI code modified the ratio as $\frac{l}{D} \leq 4.0$ [3, 4]. As per the Indian standard [5], a beam shall be deemed to be a deep beam when $\frac{l}{D} \leq 2.0$. Though deep beams are described by different $\frac{l}{D}$ ratios, generally, they are recognized by small span-to-depth ratio.

Figure 2 illustrates the geometric and loading discontinuity of beams. In the same figure, 'B' and 'D' regions are also explained, where B-region obeys classical

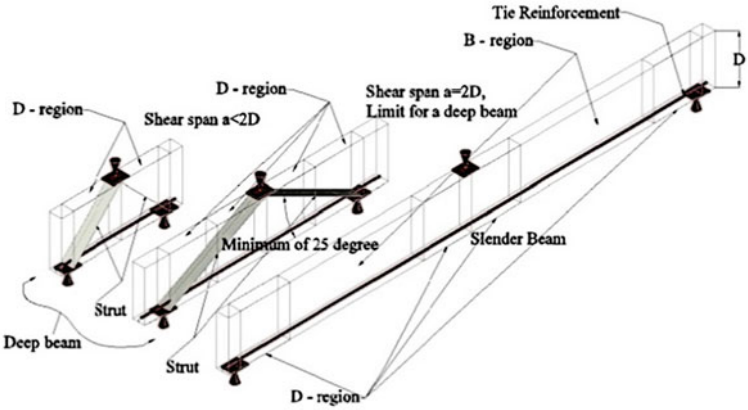

Fig. 2 ACI code definition for deep and slender beams

Bernoulli's theory, and D-region is the disturbed region. According to ACI 318, D-region is the shear span. Either strut-and-tie model or analytical approach is preferred to design the D-region.

3 Research Significance

The expression for estimating the maximum shear strength is found unconservative for deep beams with *a/d* ratio ranging between 1.0 and 2.0. The maximum shear strength equation is modified by considering the effect of size, shear span-to-depth ratio and limitations on shear resistance of high strength concrete. The proposed model has been validated with 413 test data points collected from the literature.

4 Existing Equations for Maximum Design Shear Strength

4.1 ACI 318(1995)

As per *ACI 318-95, clause 11.8.4* [2], $V_n^{\mathrm{ACI318-95}}$ in Eq. (1) is the limit on shear strength of deep beams.

$$V_n^{\mathrm{ACI318-95}} = 0.70\sqrt{f'_c}bd \ (\mathrm{SI\,Units}); \quad \frac{l_n}{d} \leq 2.0 \tag{1}$$

4.2 ACI 318(2008)

The expressions for the maximum shear strength by ACI 318 codes released before 1999 are re-examined with the test data. The support crushing is considered as the limiting criteria. *ACI 318-08 clause 11.7.3* [3], *restricts* that shear force should not exceed Eq. (2).

$$V_n^{\text{ACI318}-08} = 0.83\sqrt{f_c'}bd \ (SI\ units) \tag{2}$$

4.3 ACI 318 (2011, 2014)

ACI 318-11 clause11.7.3 [6] and *ACI 318-14* [4] *Clause 9.9.2.1* proposed same Eq. (3) for maximum design shear strength of deep beams. To make the actual equation conservative, '∅' the reduction factor is multiplied by the previous code design equation. Maximum design shear strength depends on the cylinder compressive strength of concrete and the cross-sectional area of beam. To arrest the cracking within service loads and to safeguard the deep beam against diagonal compression failure, the limit is imposed.

$$V_n^{\text{ACI318}-14} = \varnothing 0.83\sqrt{f_c'}bd; \quad \varnothing = 0.75 \tag{3}$$

4.4 BS8110

As per British code BS8110 [7], the shear strength and its limit on deep beams is given by

$$\begin{gathered}\gamma_n^{\text{BS8110}} = \frac{0.79}{\gamma_m}\left(\frac{100A_{sv}}{bd}\right)\left(\frac{400}{d}\right)^{1/4}\left(\frac{f_{ck}}{25}\right)^{1/3}2\left(\frac{d}{a}\right) \\ \gamma_n^{\text{BS8110}} \le \text{lesser of}\begin{cases} 0.8\sqrt{f_{ck}} \\ 5\ \text{MPa} \end{cases},\end{gathered} \tag{4}$$

where $\left(\frac{400}{d}\right) \le 1.0$, $f_{ck} \le 40$ MPa, and $\frac{100A_{sv}}{bd} \le 3.0$.

4.5 BD 2013

Similar to BS8110 code, the shear strength of BD 2013 [8] for deep beams is given below:

$$\begin{gathered}\gamma_n^{\text{BS8110}} = \frac{0.79}{\gamma_m}\left(\frac{100A_{sv}}{bd}\right)\left(\frac{400}{d}\right)^{1/4}\left(\frac{f_{ck}}{25}\right)^{1/3}2\left(\frac{d}{a}\right) \\ \gamma_n^{\text{BS8110}} \le \text{lesser of}\begin{cases} 0.8\sqrt{f_{ck}} \\ 7\ \text{MPa} \end{cases}.\end{gathered} \tag{5}$$

Note that, except the shear strength limit, the equations by BD 2013 and BS8110 are the same.

5 Modified Maximum Shear Strength Equation

To maintain simplicity in the proposed equation for maximum shear strength, the generic form of *ACI 318-14* equation is retained. In addition, to account for the influence of shear span-to-depth ratio and percentage tension reinforcement, the generic equation is formulated as below

$$V_n^{\mathrm{PRO}} = \frac{f_{\mathrm{c}}'^{a1}\rho_m^{a2}bd^{a3}}{\left(\frac{a}{d}\right)^{a4}}, \tag{6}$$

where $\left(\frac{a}{d}\right) \leq 2.0$.

In order to find the coefficients, namely, $a1$, $a2$, $a3$ and $a4$, $\left(\frac{V_n}{bdf_{\mathrm{c}}'}\right)$ is plotted with $\left(\frac{a}{d}\right)$ ratio, f_{c}', b and d. From the literature [9–34, 35], geometry details and strength results of 413 tests were collected. In the collected data, the beam breadth ranges from 50 to 900 mm, and the depth ranges from 100 and 2000 mm. Also, the data collection was focused on *a/d* ratio ranging from 0.50 to 2.0. The cylinder compressive strength of concrete used in the beams is varied between 10 and 100 MPa.

The best-fit curve of $\left(\frac{V_n}{bdf_{\mathrm{c}}'}\right)$ versus $\left(\frac{a}{d}\right)$ is $\left(\frac{a}{d}\right)^{-1.0}$, and the trend is exponentially decaying. First, it is challenging to account for the shear span-to-depth ratio in the proposed equation. Thus, $\left(\frac{a}{d}\right)^{a4}$ is replaced by a more consistent term $\left(\log_{10}\left(A + \frac{a}{d}\right)\right)^B$, where A and B are the empirical constants. Next, to consider the size-effect, $\frac{V_n}{bdf_{\mathrm{c}}'}$ is plotted with depth, and the best-fit curve is identified as $d^{-0.25}$. Similarly, other coefficients such as $a1$ and $a2$ are obtained by trial-and-error method. By substituting all the constants in Eq. (6), the following equation is developed:

$$V_n^{\mathrm{PRO}} = \frac{f_{\mathrm{c}}'^{1/3}\rho_m^{1/3}bd^{3/4}}{\left(\log_{10}\left(1.25 + \frac{a}{d}\right)\right)^{3/2}}, \tag{7}$$

where $\left(\frac{a}{d}\right) \leq 2.0$.

6 Influence of Parameters

Figure 3 shows the ratio of measured shear strength-to-predicted strength versus influencing parameters. Usually, the maximum shear strength equations limit the design strength. In the case of unconservative prediction, the strength factors need to be increased or influencing parameters shall be incorporated.

Irrespective of the mode of failure or size of the beam, the limiting shear strength should fall within the experimentally measured shear strength. However, ACI code overestimates 18.4% of the collected data as shown in Fig. 3. Especially, when the depth of the beam is greater than 1000 mm and *a/d* ratio ranges between 1.0 and 2.0, the maximum shear strength equation of ACI code seems to be overestimated. Similar to Kani's investigations [1], the trend of shear strength of 413 beams increases with the width of the beams.

6.1 Effect of a/d Ratio

In the proposed model, the well-established fact is that as the shear span-to-depth ratio decreases, the shear strength increases. The proposed maximum shear strength equation for deep beams with the highest and the lowest limits of *a/d* ratios are 0.50 and 2.0, respectively. Even though the *ACI 318-14* maximum shear strength equation is economic, the safety of beams shall be important. The proposed

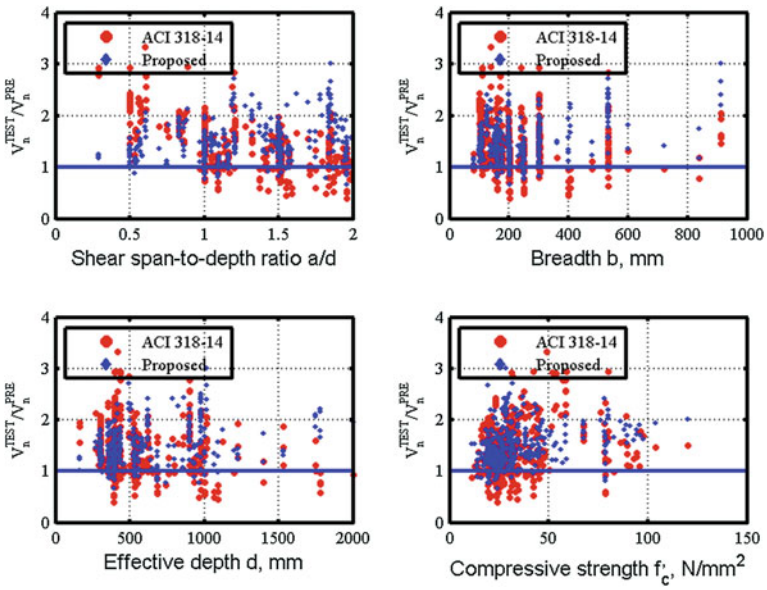

Fig. 3 Effect of influencing parameters

equation effectively accounted for the influence of shear span-to-depth ratio, and it predicts uniformly. Importantly, proposed model underestimates all the beams with *a/d* ratio 1.0 and 2.0.

In practice, maintaining $\frac{a}{d} \leq 2.0$, for girders is difficult. Thus, transfer girders of bridges, residential and commercial buildings, the shear span-to-depth ratio ranges between $0.5 \leq \frac{a}{d} \leq 3.0$. If the *a/d* ratio is greater 2.0, then maximum shear strength equation of either ACI code or the proposed model is strictly not applicable.

6.2 *Effect of Compressive Strength of Concrete*

Most of the data predicted range between 50 and 110% of the experimentally measured shear strength. Either for high strength or normal strength deep beams, the proposed model predicts uniformly for the collected data points. The normal strength concrete beams scatter more when compared to the data on high strength concrete beams.

6.3 *Effect of Depth*

As the depth of the beam increases, the shear strength decreases. It is a well-established phenomenon, known as the size-effect. Either small or large size beams, the proposed model predicts the shear strength uniformly. Since the power coefficient of '*d*' is reduced by 0.75, the proposed model underestimates all the large size beams.

7 Comparison of Proposed Model with Existing Models

The proposed equation is relatively safe when compared to the maximum shear strength equation of *ACI 318-08* and *ACI 318-14* codes. The proposed equation has the least coefficient of variation of 0.25 and fits well with the experimental data, whereas for *ACI318-14* and BS8110 equations, *COVs* are 0.34 and 0.35, respectively.

In Figs. 4 and 5, the test results are plotted versus predicted values by the maximum shear strength by ACI 318-08 and BS8110. Since a number of beams are overestimated by the ACI 318-08 code equation as shown in Fig. 4, the strength factor is introduced in the ACI 318-14 code. Moreover, the British code overestimates 30% of the collected data, and the ACI 318-08 code overestimates 44% of data.

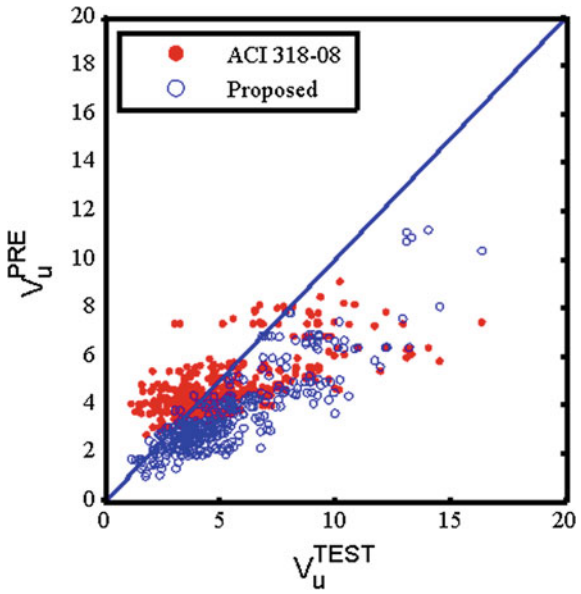

Fig. 4 V_n^{TEST} versus V_n^{PRE} (ACI 318-08)

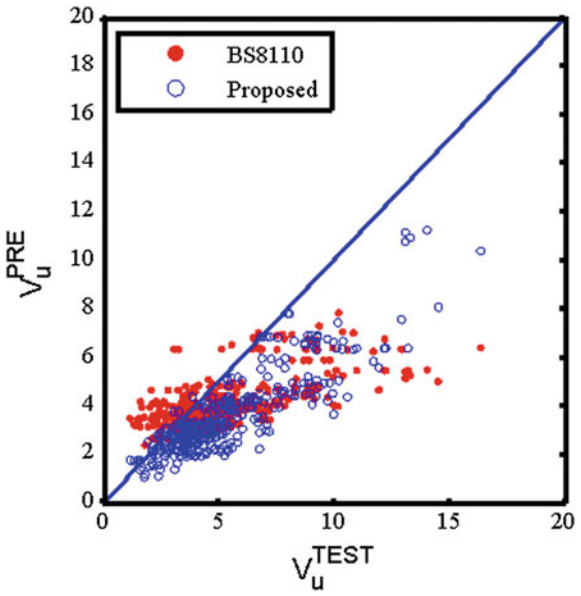

Fig. 5 V_n^{TEST} versus V_n^{PRE}

As compared to a prediction of ACI 318-08 code with ACI 318-14 and BS8110, mean of strength ratios are 11 and 32% higher. Prediction of ACI 318-08 deviates from the 45° line when the depth of the beam is greater than 1200 mm.

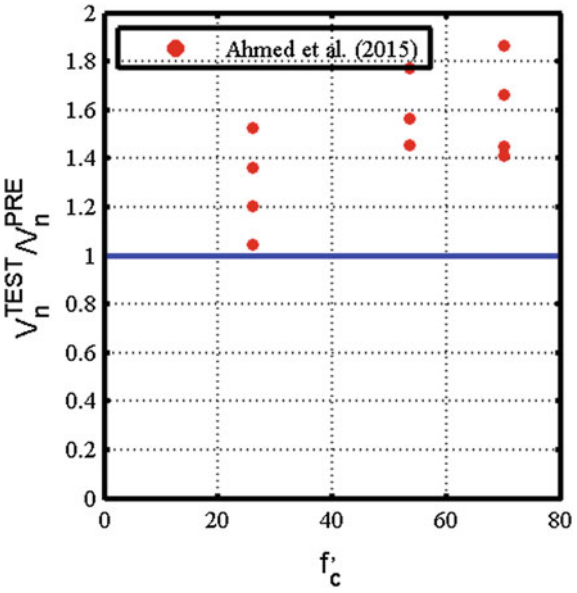

Fig. 6 Strength ratio versus compressive strength [35]

8 Case Study

Test results of Ref. [35] are used as a case study. All the 12 beams are provided without web reinforcement. The depth of the beam and the compressive strength of concrete are the variables. In Fig. 6, strength ratio versus compressive strength plot shows that the proposed model is valid even for the high strength concrete beams. The prediction for high strength concrete beams is more conservative than normal strength concrete beams.

9 Conclusion

From the analysis, the following conclusions have been drawn:

1. The proposed equation is more conservative than those models by codes of practice, such as ACI318-14, ACI 318-08, BD 2013 and BS 8110.
2. By incorporating the effect of size, tension reinforcement and limitations of high strength concrete, the proposed model shows good agreement with the test results.
3. The proposed equation has the least coefficient of variation of 0.25.

References

1. Kani, G. N. J. (1967). How safe are our large reinforced concrete beams? *ACI Journal Procedings, 64*(6), 128–141.
2. ACI Committee 318-95. (1995). *Building code requirement of reinforced concrete*. Farmington Hill, MI: American concrete Institute.
3. ACI Committee 318-08. (2008). *Building code requirements for structural concrete*. Farmington Hill, MI: American concrete Institute.
4. ACI Committee 318-14. (2014). *Building code requirements for structural concrete*. Farmington Hill, MI: American concrete Institute.
5. IS 456:2000. (2000). Indian standard plain and reinforced concrete code of practice, Fourth Revision. New Delhi: Bureau of Indian Standards.
6. ACI Committee 318–11. (2011). *Building code requirements for structural concrete*. Farmington Hill, MI: American Concrete Institute.
7. British Standards Institution (BSI) BS 8110-1. (1997). Structural use of concrete—Part 1: Code of practice for design and construction. London, UK: BSI 1997.
8. Hong Kong Buildings Department (HKBD). (2013). Code of practice for structural use of concrete 2013.
9. Clark, A. P. (1951). Diagonal tension in reinforced concrete beams. *ACI Journal Proceedings, 48*(10), 145–156.
10. Moody, K. G., Viest, I. M., Elstner, R. C., & Hognestad, E. (1954). Shear strength of reinforced concrete beams part 1—Tests of simple beams. *ACI Journal Proceedings, 51*(12), 317–332.
11. Morrow, J., & Viest, I. M. (1957). Shear strength of reinforced concrete frame members without web reinforcement. *ACI Journal Proceedings, 53*(3), 833–869.
12. Leonhardt, F., & Walther, R. (1964). "The Stuttgart Shear Tests 1961," A translation of the articles that appeared in Beton und Stahlbetonbau, Vol. 56(12), 1961 and Vol. 57 2,3,6,7 and 8, 1962. Wexham Springs, United Kingdom: Cement and Concrete Association Library Translation No. 111, 134 pp.
13. Mathey, R. G., & Watstein, D. (1963). Shear strength of beams without web reinforcement containing deformed bars of different yield strengths. *ACI Journal Proceedings, 60*(2), 183–208.
14. Kani, M. W., Huggins, M. W., & Wittkopp, R. R. (1979). *Kani on shear in reinforced concrete* (p. 225). Toronto, Canada: University of Toronto Press.
15. Lee, D. (1982). *An experimental investigation in the effects of detailing on the shear behaviour of deep beams*. (Master thesis), Department of Civil Engineering, University of Toronto, 138 pp.
16. Smith, K. N., & Vantsiotis, A. S. (1982). Shear strength of deep beams. *ACI Journal Proceedings, 79*(3), 201–213.
17. Rogowsky, D. M., & MacGregor, J. G. (1986). Tests of reinforced concrete deep beams. *ACI Journal Proceedings, 83*(4), 614–623.
18. Walraven, J., & Lehwalter, N. (1994). Size effects in short beams loaded in shear. *ACI Structural Journal, 91*(5), 585–593.
19. Tan, K. H., Kong, F. K., Teng, S., & Guan, L. W. (1995). High-strength concrete deep beams with effective span and shear span variations. *ACI Structural Journal, 92*(4), 1–11.
20. Foster, S. J., & Gilbert, R. I. (1998). Experimental studies on high-strength concrete deep beams. *ACI Structural Journal, 95*(4), 382–390.
21. Tan, K. H., & Lu, H. Y. (1999). Shear behavior of large reinforced concrete deep beams and code comparisons. *ACI Structural Journal, 96*(5), 836–846.
22. Yang, K.-H., Chung, H.-S., Lee, E.-T., & Eun, H.-C. (2003). Shear characteristics of high-strength concrete deep beams without shear reinforcements. *Engineering Structures, 25* (10), 1343–1352.

23. Tanimura, Y., & Sato, T. (2005). Evaluation of shear strength of deep beams with stirrups. *Quarterly Report of RTRI, 46*(1), 53–58.
24. Salamy, M. R., Kobayashi, H., & Unjoh, S. (2005). Experimental and analytical study on RC deep beams. *Asian Journal of Civil Engineering (AJCE), 6*(5), 409–422.
25. Zhang, N., & Tan, K.-H. (2007). Size effect in RC deep beams: Experimental investigation and STM verification. *Engineering Structures, 29*(12), 3241–3254.
26. Garay, J.D., & Lubell, A.S. (2008). *Behavior of concrete deep beams with high strength reinforcement. 2008 Structures Congress—Crossing Borders*, Vancouver, Canada, 10 p.
27. Zhang, N., Tan, K.-H., & Leong, C.-L. (2009). Single-span deep beams subjected to unsymmetrical loads. *ASCE Journal of Structural Engineering, 135*(3), 239–252.
28. Breña, S. F., & Roy, N. C. (2009). Evaluation of load transfer and strut strength of deep beams with short longitudinal bar anchorages. *ACI Structural Journal, 106*(5), 678–689.
29. Birrcher, D., Tuchscherer, R., Huizinga, M., Bayrak, O., Wood, S., & Jirsa, J. (2009). *Strength and serviceability design of reinforced concrete deep beams*, Report no. FHWA/TX-09/0-5253-1. Center for Transportation Research, The University of Texas at Austin.
30. Sahoo, D. K., Sagi, M. S. V., Singh, B., & Bhargava, B. (2010). Effect of detailing of web reinforcement on the behaviour of bottle-shaped struts. *Journal of Advanced Concrete Technology, 8*(3), 303–314.
31. Senturk, A. E., & Higgins, C. (2010). Evaluation of reinforced concrete deck girder bridge bent caps with 1950s vintage details: Laboratory tests. *ACI Structural Journal, 107,* 534–543.
32. Zhang, N., & Tan, K. H. (2010). Effects of support settlement on continuous deep beams and STM modelling. *Engineering Structures, 32*(2), 361–372.
33. Mihaylov, B. I., Bentz, E. C., & Collins, M. P. (2010). Behavior of large deep beam subjected to monotonic and reversed cyclic shear. *ACI Structural Journal, 107*(6), 726–734.
34. Lu, W. Y., Lin, I. J., & Yu, H. W. (2013). Shear strength of reinforced concrete deep beams. *ACI Structural Journal, 110*(4), 671–680.
35. El-Sayed, A. K., & Shuraim, A. B. (2015). Size effect on shear resistance of high strength concrete deep beams. *Materials and Structures, 49*(5), 1871–1882.

Detailing of Stirrup Reinforcement Along the Span and Across the Width of Reinforced Concrete Beams

D. S. R. Murty and G. Papa Rao

Abstract The extensive study of flexural behaviour of R.C beams has clarified mechanisms to such an extent that its verified outcome is already incorporated in many codes. Progress in the understanding of the behaviour of beams also subjected to shear has not been quite as spectacular. Notwithstanding many decades of experimental and theoretical research, shear failure is not yet fully understood. No rational theory exists for shear strengths, but continuing research is refining proportioning and detailing of structural concrete members for shear. Though design codes specify the maximum permissible spacing limits of stirrups legs span-wise, they are silent on the beneficial refining of stirrup spacing along the span, resulting in marginal strength increase and significant reduction in deformations. Codes are also silent on the location of stirrup legs width-wise in wide beams. The current research focuses on detailing stirrup reinforcement along the span as well as width of an R.C beam. The requirement and refinement of stirrup spacing in beams is interpreted by truss model.

Keywords Wide beams · Shear resistance · Stirrups along width and span
Crack width · Deflection

D. S. R. Murty
Department of Civil Engineering, Andhra University College of Engineering, Visakhapatnam, India
e-mail: dsrmurty14@gmail.com

G. Papa Rao (✉)
Department of Civil Engineering, Gayatri Vidya Parishad College of Engineering, Visakhapatnam, India
e-mail: gprao_74@yahoo.co.in

A. Rama Mohan Rao and K. Ramanjaneyulu (eds.), *Recent Advances in Structural Engineering, Volume 1*, Lecture Notes in Civil Engineering 11,
https://doi.org/10.1007/978-981-13-0362-3_10

1 Research Significance

Truss models are very useful for detailing. They represent the distribution of internal forces in the member of failure. Once this distribution is known, structural systems (truss models) comprised of concrete and steel can be furnished to satisfy equilibrium between applied loads and supports. Truss models are very useful for detailing of stirrup reinforcement for shear as per Anderson and Ramirez [1]. The concept of truss models in R.C members was first introduced at the turn of the nineteenth century by Ritter [2] and Morsch [3]. This pioneering work was later refined by several renowned researchers: Rausch [4], Kupfer [5] and Leonhardt [6]. Lampert and Thurliman [7] and several others have provided a foundation for truss models by means of the theory of plasticity. The truss model approach was extended to overall structures in the form of strut-and-tie systems by Schlaich et al. [8]. The truss model of R.C beam under bending and shear illustrates the function of vertical stirrups. The stirrups form the vertical tension ties of a truss, and the bottom flexural reinforcement constitutes the bottom tension chord of the truss. The concrete in the diagonal constitutes a diagonal. Under the assumption that forces can be equilibrated at the joints, stirrups must be capable of developing the required force over the entire height. Hooks are preferred for stirrup anchorage. Anchorage of stirrup hooks in the flexural tension zone is questionable because of the reduced confinement provided by the cracked concrete. Continuation of stirrup leg would seem to be only feasible alternative for stirrup anchorage in the flexural tension region. Adequate stirrup spacing is also critical span-wise as well as width-wise; large spacing in the longitudinal direction of the beam creates a concentration of diagonal compression stresses at the truss joints. This practice results in overloading of the nodal zones or the diagonal struts themselves, leading to premature failure due to concrete crushing. It is evident that longitudinal stirrup spacing has to be under control. The spacing of stirrup legs in the transverse direction (width of beam) can also be a critical factor in wide beams, when the legs are concentrated around the outer longitudinal bars. A wide beam must have a width to height ratio exceeding two, while slabs will typically have much larger ratios as per Sherwood et al. [9]. Anderson and Ramirez [1] tested $16'' \times 16''$ beam specimens referring them as wide beams. The diagonal truss members are equilibrated at the truss joint, formed by the stirrup and the longitudinal reinforcement. The vertical force component is equilibrated by the stirrup reinforcement. In wide beams with several longitudinal bars in a layer, the lack of well-distributed stirrup legs across the web of the member could lead to a concentration of diagonal compression stresses at the joint of the stirrup leg outside longitudinal bar. This situation could result in premature failure due to concrete crushing in these nodal zones and inefficient use of interior longitudinal reinforcement. To correct this situation interior stirrup legs can be placed using multi-legged stirrups to furnish the necessary vertical equilibrium resultants, thus creating additional interior truss joints. Detailing of stirrup spacing along the span is dealt with first. To eliminate shear failure, before the attainment of full moment capacity, web reinforcement is provided in the form of small-sized

bars, vertical stirrups, various national codes specify placement limits for web reinforcement as vertical stirrups placed perpendicular to the axis of the member. Although maximum permissible spacing limit is specified in the codes, they are silent regarding the influence of placement of stirrups at a lesser spacing than their maximum permitted limits. For example, shear occurring in a beam of 410 mm effective depth as per IS 456-2000, design allows placement of 12 mm dia stirrups at 300 mm (less than 0.75 d) or 10 mm dia at 200 mm intervals, or 8 mm dia at 130 mm centre to centre. In all cases, tensile force in the stirrups in beam length/one mm remains same or nearly the same. In the absence of code guidance and work done on this aspect, a designer will fail to comprehend which of these stirrup spacing is the most desirable; in all these alternative options, the amount of web reinforcement per unit length of beam remains the same. The present study undertaken fills the gap and shows the forward method to follow. Although the use of stirrups of smaller diameter at smaller spacing involves marginally higher labour, time and cost of steel cage fabrication, the disadvantage is more than offset by the resulting benefits. Stirrups intended to resist shear force directly in a beam, contribute additional shear resistance in no less way from the presence of concrete, even in cracked state. Concrete in the compression owing to confining effects of the stirrups that prevent diagonal crack propagation, provides the beam extra shear capacity. Another source of additional shear strength mobilisation is the support given to the flexural reinforcement by the stirrups, and also the prevention of longitudinal splitting by the stirrups; this strength enhancement is likely to be proportional to the decrease in stirrup spacing.

Shear reinforcement legs for one way shear must be appropriately spaced along the member length as well as across the member width. While spacing limits of stirrups are provided in design codes for the longitudinal direction, little guidance is available for spacing of them across the width; studies on this aspect also are scarce. A few studies available to date on the influence of stirrups across the width are briefly mentioned here. Well detailed web reinforcement will provide confinement to the compression block, control crack widths (and thereby enhance aggregate interlock on the crack surfaces), and control splitting action along longitudinal bars from dowel action. Thus, it is reasonable to assume that the magnitude of concrete contribution to shear resistance would be sensitive to the web reinforcement arrangement. From ACI-318 shear provisions, a wide beam has a width to overall height ratio of at least two. Without specific experimental validation presented, Leonhardt and Walther [10] suggested a shear reinforcement spacing limit in the width direction, of effective depth for low shear stresses, but noted the spacing limit should decrease as a function of the shear stress. For members with high shear stresses, a transverse spacing of 200 mm was proposed. Eurocode-2 [11] suggests spacing limits of 0.75 d or 600 mm in the width direction. ACI318-08 [12], CSA23.3-04 [13], AASHTO LFRD [14] and IS 456-2000 do not provide spacing limits across the width of sections. Vaguely engineers provide stirrup legs more than two in wide beams without any guidance from anywhere. Anderson and Ramirez [1] tested two series of beams. The second series contained four 16 × 16 in. (400 × 400 mm) wide beams; the width/depth ratio was one.

The number of vertical legs was four and three in two beams and two in the balance two beams. The adopted stirrups leg spacing related to the beams tested by them was 200 mm, subjected to shear stresses exceeding $6\sqrt{f'_c}$, where f'_c is the cylinder compressive strength in Psi. The maximum transverse leg spacing 200 mm used by them was same as the value suggested by Leonhardt and Walther [10] for beams under high shear stresses. The decrease in stirrup spacing resulted in nearly 20% increase in ultimate strength. The increase in vertical stirrup legs did not result in higher ductility in these beams. Lubell et al. [15] tested two series of wide beams to provide guidelines for maximum transverse spacing of shear reinforcement to ensure adequate safety of wide members. Beams were 1170 mm wide and 593 mm deep in one series with width/depth ratio about 2. In the second series, beams were 700 mm wide and 335 mm deep. The shear stresses in these beams at ultimate were 1.4 and 1.9 MPa less than those specified as high values of shear stress. In the first series, stirrup leg spacing varied from 235 to 625 mm; these spacing values were more than 200 mm and 50% of effective depth, in the beams having nearly high shear values. Without specific test validation, Lubell et al. [15] recommended stirrup spacing of $d/2$ and 300 mm under high shear stresses exceeding $5\sqrt{f'_c}$, where f'_c is the cylinder compressive strength in Psi.

2 Test Programme

The test programme comprised of two series of beams: first one related to stirrup spacing along beam span designated as 'A' series with shear critical beams PC21 and PC22, and the second one related to stirrup spacing across the beam width, designated as 'B' series with beams PC1, PC2 and PC3. The configuration of test specimens of both series is illustrated in Fig. 1, and the properties are detailed in Table 1. Table 2 contains the properties of steel reinforcement used in the beams tested. The beams PC21 and PC22 were identical in all respects including flexural reinforcing, except they differed in size of stirrups and their spacing, but the two-legged stirrup force was held constant per 1 mm length of beam; this was possible by using smaller diameter stirrups at smaller spacing. The objective of this part of investigation was to determine the benefits accruing to the beam by using closer stirrup spacing, but holding the amount stirrup force per mm length of beam constant. The wide beams PC1, PC2 and PC3 were identical in all respects including flexural reinforcement. The aspect ratio, width/depth of all the wide three beams was 3.64. PC1 did not have any web reinforcement. PC2 contained 12 mm two-legged stirrups at 120 mm c/c. PC3 had 8 mm four-legged stirrups at 115 mm c/c. Beam with four-legged stirrups (closer spacing of stirrup legs across the width) had about 8% less stirrup steel in comparison with two-legged stirrups. The objective of this part of study was to examine the beneficial effects of closer spacing of stirrup legs across the member width.

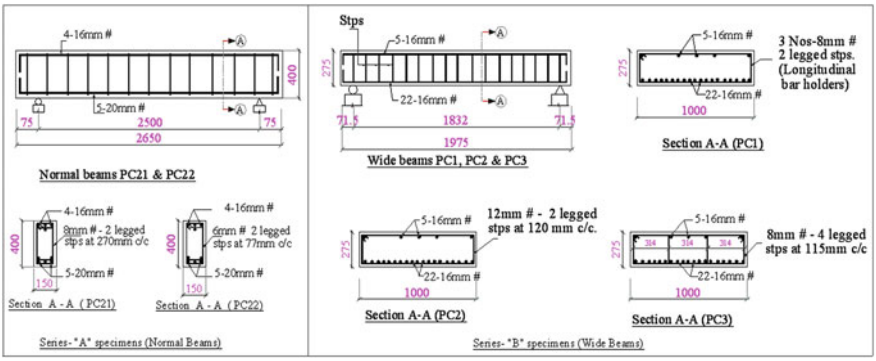

Fig. 1 Configurations of test specimens

Beam moulds for both series for casting were made of brick masonry; they were plastered and then oiled before pouring concrete. Each beam and the control specimens were poured in one batch of mix. The concrete in beams was compacted with a needle vibrator, and the controlled specimens were compacted in the standard way. After 24 h of casting, the specimens were demoulded and cured till testing, which happened after 28 days of casting. The beams were tested in bending in load frame with a concentrated load at mid-span. The test setup is shown in Fig. 2. Instrumentation included a hydraulic jack of 1000 kN capacity and a proving ring of 1000 kN capacity for the load application and load measurement, respectively.

A dial gauge is positioned at the centre of the span for measurement of transverse deflection. A handheld microscope, capable of measuring a minimum value of 0.05 mm, was used to note the crack width. Loading was done in a series of increment. The transverse load, deflection and maximum crack width were measured and noted. Cracks were noted on the test specimen. About 20 load stages were needed to bring a beam to ultimate load stage. The principal test results of both the series are noted in Table 3. Tested specimens were photographed to preserve the crack pattern and mode of failure. The tested specimens are shown in Fig. 4.

3 Presentation of Test Results

Series-I: In beam PC 21, the initial crack originated was flexural at the bottom of side face at 76.62 kN which was 36% of ultimate moment. With load increases, several diagonal cracks formed in the shear span on either side of load, on the side faces, and further increased in load, and extended the diagonal cracks to the top face. The shear failure occurred at 171.2 kNm with slight shear compression distress on the top face. The initial flexural crack in beam PC22 appeared at bottom of

Table 1 Properties of test specimens

Specimen label	Series	Cross section details		Effective span (mm)	Shear span to effective depth ratio	Flexural reinforcement		Water to cement ratio by weight	Cube compressive strength (MPa)	Split tensile strength (MPa)	Shear reinforcement
		Width (mm)	Depth (mm)			Bottom (mm)	Top (mm)				
PC21	Series-A (normal beams)	150	400	2500	3.42	5–#20	4–#16	0.56	34.20	2.68	8 mm #, two-legged stirrups @ 270 mm c/c
PC22		150	400	2500	3.42	5–#20	4–#16	0.56	32.89	2.47	6 mm #, two-legged stirrups @ 77 mm c/c
PC1	Series-B (wide beams)	1000	275	1832	3.64	22–#16	5–#16	0.535	36.14	2.64	No shear reinforcement
PC2		1000	275	1832	3.64	22–#16	5–#16	0.535	35.75	2.47	12 mm #, two-legged stirrups @ 120 mm c/c
PC3		1000	275	1832	3.64	22–#16	5–#16	0.535	35.75	2.47	8 mm #, four-legged stirrups @ 115 mm c/c

Table 2 Properties of steel reinforcement

Diameter of steel bar (mm)	Cross-sectional area (mm^2)	Yield stress (MPa)	Ultimate stress (MPa)
6	28.27	283	353
8	50.26	539	659
12	113.09	461	588
16	201.06	541	626
20	314.16	500	582

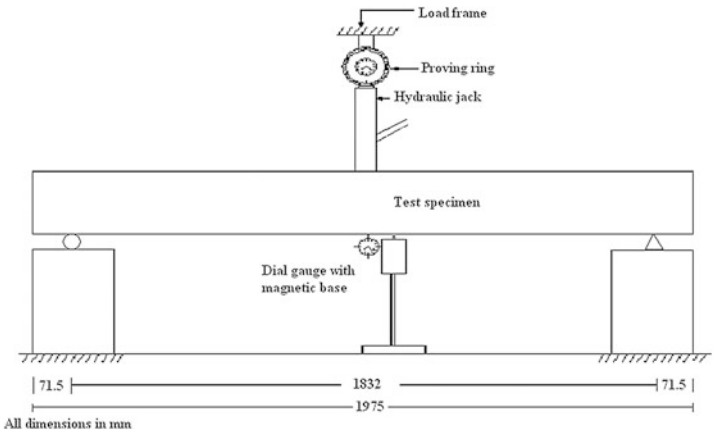

Fig. 2 Load test setup

side face at 86.12 kNm which was 38% of ultimate moment. As the load increased additional diagonal cracks formed and already formed ones extended towards top face; the crack widths widened. The shear failure occurred suddenly at moment 180 kNm.

Series-II: Beam PC1 without web reinforcement developed the first crack as flexural crack at the bottom of side face at 286.25 kNm. As the loading progressed several other flexural cracks developed and already formed ones widened. Two inclined cracks from both supports from tension zone rapidly extended to the top of the beam. One diagonal crack was wider than the other. As failure approached, the two diagonal cracks were bridged by a horizontal crack parallel and close to the top face. The failure occurred suddenly at moment 320.6 kNm which was about 11% higher than the initial crack moment. The shear stress at initial cracking and ultimate were, respectively, 1.291 and 1.446 N/mm^2. For the beam PC2, with two-legged stirrups, initial flexural crack formed at the bottom of vertical face at 206.1 kN. As loading progressed, further several cracks appeared and already formed ones extended in length to the top face and widened in width. The failure resulted in bending at 385.86 kNm moment. In beam PC3, with four legs in each stirrup, initial flexural crack appeared at 148.45 kNm at 36% of its ultimate

Table 3 Principal test results

Specimen label	Series	Moment at first crack (kNm)	Moment at 0.3 mm crack width (kNm)	At service load					At ultimate load					Type of failure
				Moment (kNm)	Shear force (kN)	Shear stress (MPa)	Deflection (mm)	Crack width (mm)	Moment (kNm)	Shear force (kN)	Shear stress (MPa)	Deflection (mm)	Crack width (mm)	
PC21	Series-A	76.62	114.62	142.67	114.13	2.08	8.33	0.59	214	171.2	3.13	13.42	1.80	Shear
PC22		86.12	152.62	142.67	120.0	2.19	7.55	0.30	225	180.0	3.29	12.58	1.20	Shear
PC1	Series-B	286.25	297.7	213.73	233.33	0.96	5.79	–	320.60	350.0	1.45	9.22	9.4	Shear
PC2		206.1	240.45	257.24	280.93	1.16	6.11	0.3	385.86	421.24	1.74	10.97	1.3	Flexure
PC3		148.85	276.17	257.24	300.00	1.24	5.87	0.2	412.20	450.0	1.86	11.75	2.0	Flexure

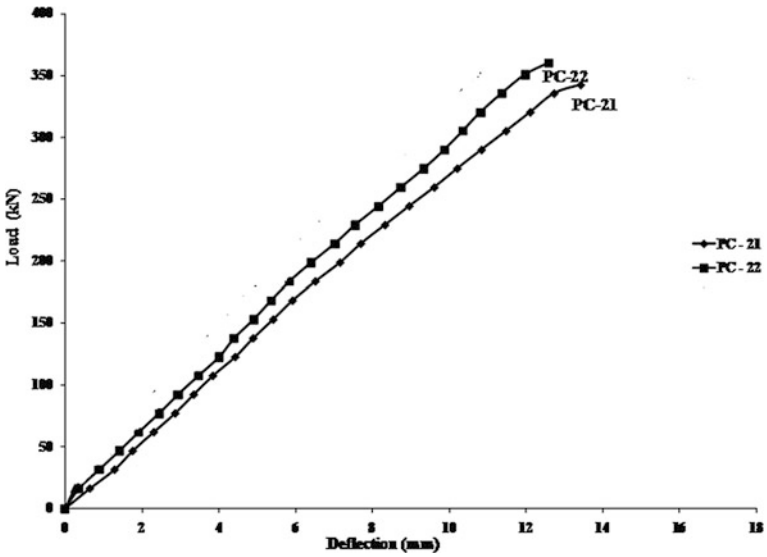

Fig. 3 Load–deflection curves of PC21 and PC22

moment. As the load increased, more number of cracks formed, cracks widened and increased in length. The beam failed in bending, with major flexural cracks widening and crushing of compression zone. Beam PC3 with four-legged stirrups failed at 7% higher load then the companion beam PC2 with two-legged stirrups. For all the beams, the measured transverse mid-span deflections were graphed versus the applied load and shown in Figs. 3 and 4. Figures 5 and 6 illustrate the moment–crack width relationships for the tested specimens. The photographs of the tested beams with crack patterns after failure are presented in Figs. 7 and 8.

4 Discussion of Test Results

In a larger study in series-A, only two specimens would be investigated by the authors, but the trend on the influence of closer spacing of the stirrup legs along the span, keeping the force of stirrup legs per mm length of the beam unaltered could be established. Beams PC21 and PC22, identical in all respects but differed only in stirrup leg spacing. Beam, PC22 with lesser stirrup spacing resulted in higher cracking strength, ultimate strength and lesser deformations than the companion beam PC21 with larger stirrup spacing. PC22 developed initial crack at 12% higher moment than PC21. At service load, closer stirrup spacing in PC22 than in PC21 facilitated the occurrence of smaller transverse deflections and crack width in PC22. PC22 and PC21 had defections 7.55 and 8.30 mm, respectively. Similarly, PC22 and PC21 had crack widths 0.3 and 0.59 mm, respectively.

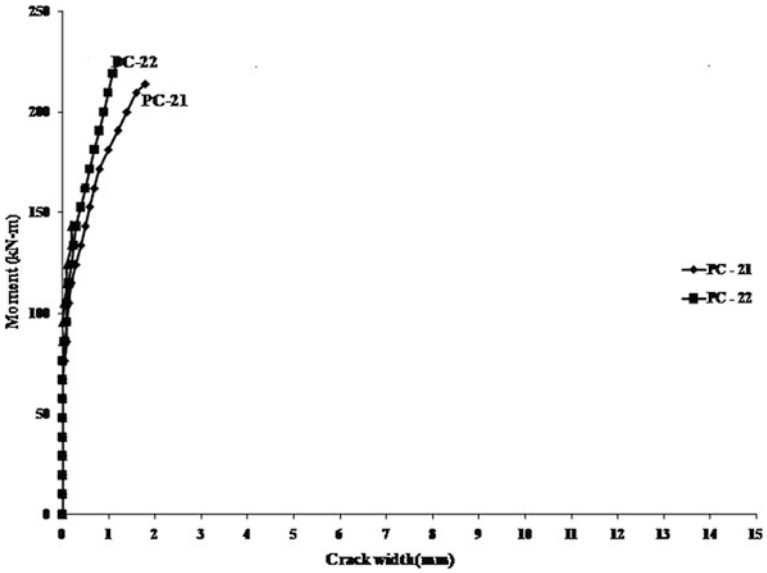

Fig. 4 Moment–crack width curve of PC21 and PC22

Fig. 5 Load–deflection curves of PC1, PC2 and PC3

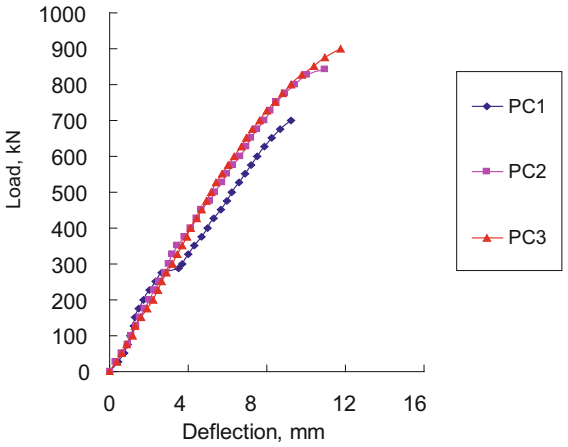

Beams PC1, PC2 and PC3 were identical in all respects including flexural reinforcing except stirrup orientation. PC1 did not have web reinforcement. Influence of providing more stirrup legs across the beam width can be studied by comparing the performance of beam PC2 and PC3. Beam PC3 with four stirrup legs recorded 7% higher ultimate strength than the companion beam PC2 with two stirrup legs. The beneficial effects in the beam with lesser stirrup legs are reflected in deformations also. Beam PC3 with four legs recorded lesser deflections and crack

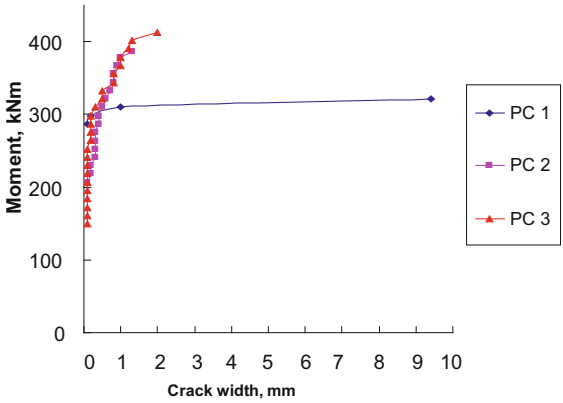

Fig. 6 Moment–crack width curve of PC1, PC2 and PC3

Fig. 7 Photographs of the tested specimens PC21 and PC22 (series-A)

Fig. 8 Photographs of the tested specimens PC1, PC2 and PC3 (series-B)

width than the beam PC2 with two legs. At service load, PC3 had a crack width 0.2 mm while PC2 had 0.3 mm and PC3 recorded deflections of 5.87 mm while PC2 recorded 6.11 mm. It is established that more number of stirrup legs across the width is needed. In this investigation, the minimum leg spacing adopted was 314 mm, and the effective depth was 242 mm, which was closer to the values recommended by earlier investigators.

5 Conclusions

Useful ideas gleaned from the study undertaken are summed up in the conclusions listed below.

1. Closer stirrup spacing resulted in marginally enhanced shear carrying capacity of beams at ultimate. Beam PC22 with smaller stirrup spacing recorded 5% higher ultimate load than the companion beam PC21 which had stirrup spacing larger than that of PC22.
2. As the stirrup spacing decreased, cracking strength of beams increased. Cracking moments of PC21 and PC22 were 36 and 38% of their ultimate moment capacities, respectively. In the post-cracking stage, the integrity of cracked concrete was more effective as the stirrup spacing decreased.
3. Deformations of the beam usefully improved at serviceability level as stirrup spacing decreased. The deterioration of cracked concrete was more restrained with the presence of closer stirrup spacing. At service load level, transverse deflections were 8.33 and 7.55 mm, and crack widths were 0.59 and 0.3 mm for beams PC21 and PC22, respectively, showing decreased deformations as stirrup spacing decreased.
4. In proportioning RC beams for shear, use of small-sized bars as stirrups at closer spacing is recommended in an empirical way, based on the findings of the current study. Such guidance is not available in any current national code.
5. Despite the slightly higher labour involved in steel cage fabrication, lower stirrup spacing imparts to the beams the beneficial effects of marginally improved ultimate strength and useful deformational behaviour.
6. Beam PC1 without shear reinforcement and with shear span/depth ratio of 3.33 failed in shear. The ultimate moment was 11% in excess of cracking moment.
7. Beams with four-legged vertical stirrups, developed 7% higher ultimate strength than the companion beam with two-legged stirrups.
8. The occurrence of lesser deformations at service load is demonstrated by the behaviour of PC2 and PC3. At service load, PC3 had a crack width of 0.2 mm, while PC2 had 0.3 mm.
9. This limited study confirms the generally held view that use of multiple legs in stirrups in width in place of conventional two legs is highly a desirable practice.

References

1. Anderson, N. S., & Ramiirez, J. A. (1989). Detailing of stirrup reinforcement. *ACI Structural Journal*, 507–515.
2. Ritter, W. (1899). Die bauweise hennebique. *Schweizerische Bauzeitung, 33*(7), 59–61.
3. Morsch, E. (1922). Der Eisenbetonbau - Science Theorie und Anwendung. 5th Edition, Wittwev, Stuttgart, V.1, Part 1, 1920, and Part 2, pp 112.
4. Rausch, E. (1953). *Drillung, Schub und Scheren im Stahlbetonbau*. Deutscher Ingenieur - Verlag, Berlin, pp. 168.
5. Kupfer, H. (1964). Erweiterung der Morsch 'schen Fachwerrkanalogie mit Hilfedes Prinzips vom Minimum der Formaderungsarbeit. Bulletin d' Information No. 40, Comite Europeen Betton, Paris, 44–57.
6. Leonhardt, F. (1965). Die Verminderte Schudeckungbei Stahlbetontragwerken. Der Baungenieur (Heidelberg), 40(1), pp. 1–15.
7. Lampert, P., & Thurliman, B. (1971). Ultimate strength and design of reinforced concrete beams in torsion and bending. IABSE, (pp. 107–131). Publication No. 31–I, Zurich.
8. Schlaich, J., Schafer, K., & Jennewein, M. (1987). Toward a consistent design of structural concrete. *Journal of Prestressed Concrete Institute, 32*(3), 74–150.
9. Edward Sherwood, G., Adam Lubell, S., Evan Bentz, C., & Micheal Collins, P. (2006). One way shear stresses of thick slabs and wide beams. *ACI Structural Journal, 103*(6), 794–802.
10. Leonhardt, F., & Walther, R. (1964). *The Stuttgart Shear Tests 1961*. London, UK: Cement and Concrete Association.
11. Eurocode 2. (2004). *Design of Concrete Structures—Part 1–1: General Rules and Rules for Buildings (EN1992-1-1).* Brussels, Belgium: European Committee for Standardization, 2004.
12. American Concrete Institute (ACI) Committee 318. (2008). *Building code requirements for structural concrete (ACI 318-08) and commentary*. Faminton Hills, MI, USA: American Concrete Institute, 2008.
13. Canadian Standards Association(CSA). (2004). *Design of concrete structures (CAN/CSA A23.3-04).* Mississauga, ON, Canada: Canadian Standards Association, 2004.
14. American Association of State Highway Transportation Officials(AASHTO). (2004). *AASHTO LRFD bridge design specifications and commentary*. Washington DC, USA: AASHTO, 2004.
15. Lubell, A. S, E. Bentz, & Collins, M. P. (2009). Shear reinforcement spacing in wide members. *ACI Structural Journal*, 205–214.
16. *Indian standard code of practice for plain and reinforced concrete for general building construction,* IS 456: 2000. New Delhi: Bureau of Indian Standards.

Pylon Shape Analysis of Cable-Stayed Bridges

R. Sharath and R. K. Ingle

Abstract Behavior of cable-stayed bridge is of great importance as the influence of moving loads, seismic, and wind forces on the cable-stayed bridge mainly depends on its characteristic behavior. The structure is of nonlinear nature and highly indeterminate. The analysis demands various elements of cable-stayed bridge to be modeled properly so as to represent the actual behavior of structures as close as possible. In the present work, various aspects of cable-stayed bridge are modeled using SAP-2000 software. The work is started with the basic model of two spanned symmetrical cable-stayed bridge. The analysis was done by taking six different pylon shapes for dead load and live load conditions as per IRC-6 2010. Then, the pylon shape which is having better responses is suggested. After this, a parametric study was conducted. The basic factors which affect the design of cable-stayed bridges are shape and stiffness of towers, areas of cables. In this study, it is intended to study the effect of shape of pylons, cable areas with different cable layouts on the response of cable-stayed bridges. Further modal analysis is carried out to determine the fundamental natural frequencies of bridges with different pylon shapes. The study is then extended for unsymmetrical cable-stayed bridges also, and appropriate pylon shape is suggested.

Keywords Pylon · Deck · Cable · Moment · Shear

1 Modeling of Cable-Stayed Bridges

The deck of the cable-stayed bridge is modeled as concrete box girders which are idealized as beam elements, connected laterally by rigid links at the points where cables need to be attached. Cables are idealized using cable elements and the tower/

R. Sharath
Senior Design Engineer, L&T Construction, Chennai 600089, India

R. K. Ingle (✉)
VNIT Nagpur, Nagpur 440010, India
e-mail: rkingle@rediffmail.com

A. Rama Mohan Rao and K. Ramanjaneyulu (eds.), *Recent Advances in Structural Engineering, Volume 1*, Lecture Notes in Civil Engineering 11,
https://doi.org/10.1007/978-981-13-0362-3_11

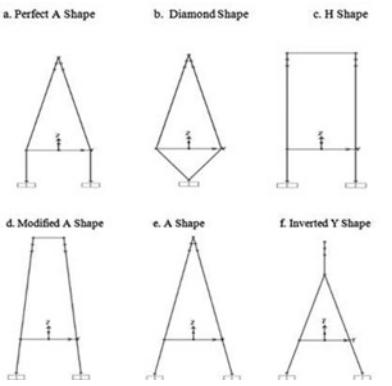

Fig. 1 Different pylon shapes considered for the analysis

pylon; top and bottom cross members are modelled using beam elements. The connection between deck slab and bottom cross beams is also provided by a rigid link, to have a compatibility between deck slab and bottom cross beam. In the present study, the nonlinear static analysis of cable-stayed bridges has been performed using SAP2000 for the analysis of dead loads. Various pylon shapes considered for the analysis are shown in Fig. 1.

2 Analysis of Symmetrical Cable-Stayed Bridges

Following data was considered, for the mathematical modeling of symmetrical cable-stayed bridges. Figure 2 shows various elements of cable-stayed bridge. Side spans: 50 m, height below deck: 10 m, height above deck: 30 m, pylon cross section = 1 m × 1 m, deck having concrete box girder of dimension: width: 9 m, depth: 2 m, thickness of flange and web = 0.5 m (cross section as shown in Fig. 3), grade of concrete: M 45, top cross beam of pylon: 1 m × 1.5 m (c/s), bottom cross beam of pylon: 1 m × 2 m (c/s), cable properties: modulus of elasticity 210 GPa, cable areas 1 and cable 2: 40,000 mm^2, cable areas 3 and cable 4: 30,000 mm^2, cable areas 5 and cable 6: 20,000 mm^2, pylon material: concrete, and deck material: concrete (Fig. 4).

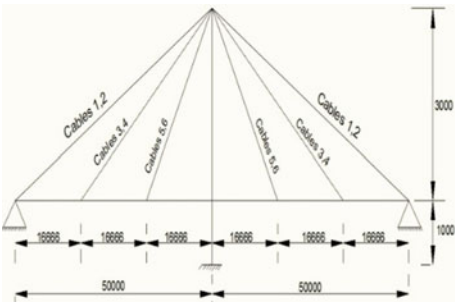

Fig. 2 Symmetrical cable-stayed bridge considered for the analysis

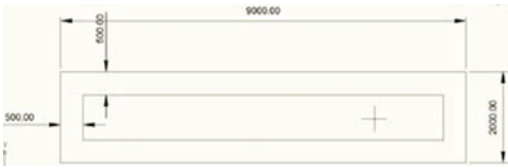

Fig. 3 Cross section of deck considered for analysis

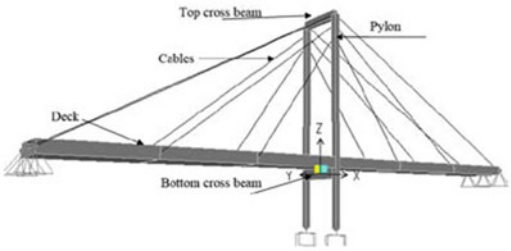

Fig. 4 Various elements of cable-stayed bridge modeled in SAP

The deck is having two lanes of 3.5 m wide; the lanes were defined in SAP. After the lane definitions, "IRC Class 70 R" and "IRC Class A" loading are defined. "Class 70 R" loading was applied to lane 1, whereas "Class A" was applied to both the lanes 1 and 2. After this, the analysis is performed for load combinations of "DL + 70R Lane 1" and "DL + 2 Class A". After the analysis is performed, the maximum responses out of these two load cases were taken, and the results are mentioned here along with their interpretation.

2.1 Comparison of Axial Forces in the Cables

The cable forces are compared by taking three cable planes as shown in Fig. 5. The variation of cable forces with reference to cable planes is as shown in Fig. 6. From the graph, it can be concluded that the axial forces in the cables are less in the case of "inverted Y shape" and more in the case of perfect A shape.

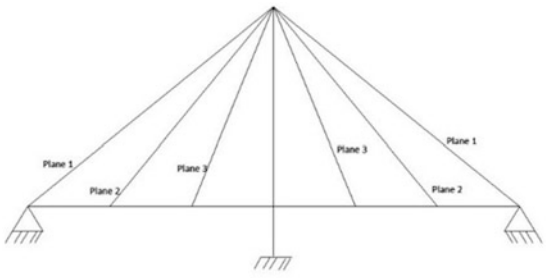

Fig. 5 Cable planes considered for reference

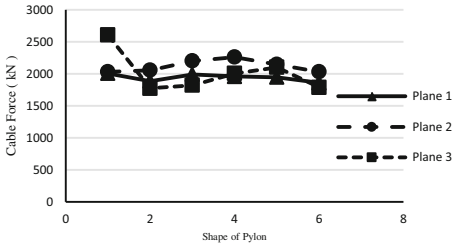

Fig. 6 Variation of cable forces in different planes

2.2 Maximum Deck Deflection Comparisons

As shown in Fig. 7, it can be seen that the maximum and minimum girder deflections are occurring in "inverted Y shape" and "H shape" pylon, respectively.

2.3 Comparisons of Deck Forces

In the following section, various responses of the deck obtained during the analysis are listed, and the change in the behavior of the deck with change in pylon shape is observed. It can be seen from Fig. 8 that axial force in deck is more in the case of "modified A shape" and lesser in the case of "perfect A shape".

From Fig. 9, it can be seen that moment M-3 in deck is more in the case of "modified A shape" and lesser in the case of "perfect A shape".

2.4 Pylon Forces Comparison

In this section, the maximum pylon responses were taken and then plotted in Figs. 10 and 11. This helps us to determine the pylon shapes by comparing maximum and minimum responses. From Fig. 10, it can be seen that axial force in the pylon is more in the case of "inverted Y shape" and lesser in the case of "modified A shape".

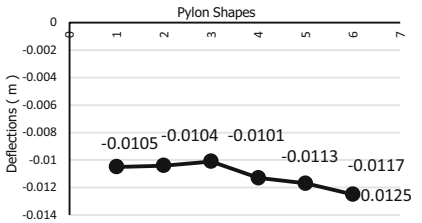

Fig. 7 Deflection variation in different pylon shapes

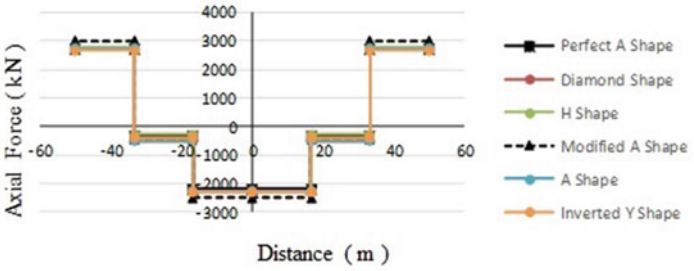

Fig. 8 Axial force variation in the deck

Fig. 9 Variation of moment M-3 along the deck

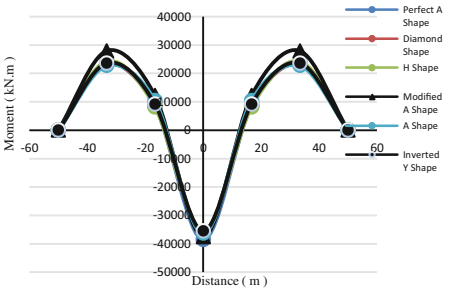

Fig. 10 Axial force variation along the pylon

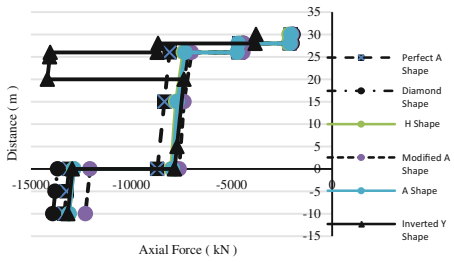

Fig. 11 Variation of moment M-3 along the pylon

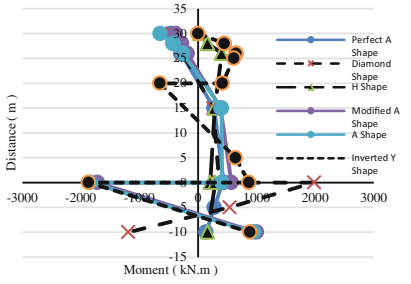

From Fig. 11, it can be seen that moment M-3 in the pylon is more in the case of "inverted Y shape" and lesser in the case of "H shape".

From the above observations, it can be concluded that

i. Considering girder deflection, deck moments, pylon moments and pylon torsion criterion, it is best to choose "H shape".
ii. Considering cable force, deck moments, pylon moments, and deck torsion criterion, it is best to choose "inverted Y shape".

2.5 *Parametric Studies of Symmetrical Cable-Stayed Bridges*

From the above conclusions, now "H shape" is taken for the following parametric studies.

i. Variation in cable areas.
ii. Variation in boundary conditions.

2.5.1 Variation in Cable Areas

In this section, it is intended to study the effect of use of uniform cable diameter and various diameter cables on the behavior of cable-stayed bridge. The various cable planes used for reference are shown in Fig. 12.

Comparison is done between constant cable area and varying cable areas. Constant cable area used is 30,000 mm^2 for all three cable planes, whereas variable cable sections used in Plane 1 is of area 40,000 mm^2, Plane 2 is of area 30,000 mm^2, and Plane 3 is having area of 20,000 mm^2.

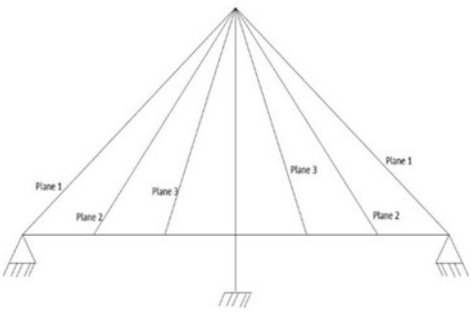

Fig. 12 Cable planes considered for reference

H Shape Pylon

Now, the variation of other responses is also plotted from Figs. 13, 14 and 15, to study the effect of variation in cable areas.

From Fig. 14, it can be seen that the axial compressive stress in the deck has been reduced, and the axial tensile stress has been increased with the use of variable cable areas in different planes, which is advantageous as the nonlinear behavior of deck will be reduced. Also since there is an increase in the cable forces, which ensures effective utilization of cable strength, it is advantageous to use different cable areas in different cable planes. Similar kind of behavior is observed in "inverted Y shape" also.

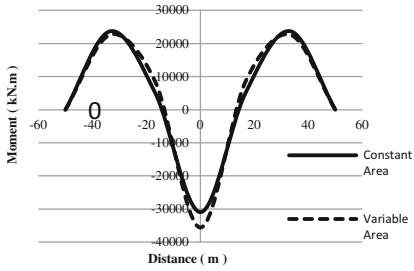

Fig. 13 Moment variation in the deck with change in cable areas

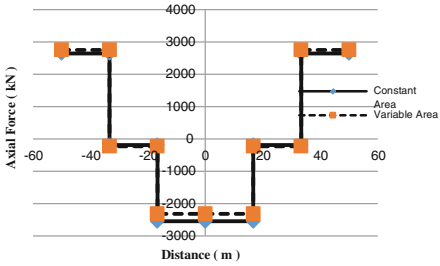

Fig. 14 Axial force variation in deck with change in cable areas

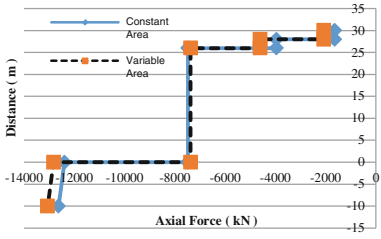

Fig. 15 Axial force variation in the pylon with change in cable areas

2.5.2 Effect Due to Various Boundary Conditions

In this section, different deck end support conditions as shown in figures below are used, and comparisons are made for "H shape" and "inverted Y shape". The results are presented below along with their observations.

H Shape

Case 1: Both ends of longitudinal girder are hinged

Table 1 shows the values of different responses for both ends hinged condition (Fig. 16).

Case 2: One end of longitudinal girder is hinged and other roller

The values of different responses are tabulated in Table 2 for one roller and one hinge condition (Fig. 17).

Case 3: Rollers at both ends of longitudinal girder

The values of different responses are tabulated in Table 3 for two rollers condition (Fig. 18).

The conclusions from the above parametric study of changing the support conditions are, the cable tension was more in case 1, i.e., both hinge condition and the cable tension decreased as the support condition was changed to roller. This is not desirable as the more cable force ensures effective utilization of the cable strength. Also in both hinged condition, the deck was in tension, which is desirable,

Table 1 Comparison of results for various deck pylon connections when both girder ends are hinged

S. No.	Element	Responses	
1	Cable	Axial (kN)	2071
2	Longitudinal deck element	Axial (kN)	2759
		Shear (kN)	−5035
		Moment (kN-m)	−35,595
3	Pylon	Axial (kN)	−13,062
		Moment (kN-m)	−445
		Shear (kN)	278

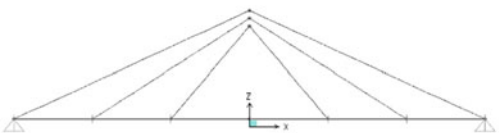

Fig. 16 Both ends of longitudinal girder are hinged

Table 2 Comparison of results for various deck pylon connections when one end is roller and another hinge

S. No.	Element	Responses	
1	Cable	Axial (kN)	2042
2	Longitudinal deck element	Axial (kN)	7968
		Shear (kN)	5047
		Moment (kN-m)	35,717
3	Pylon	Axial (kN)	13,033
		Moment (kN-m)	439
		Shear (kN)	276

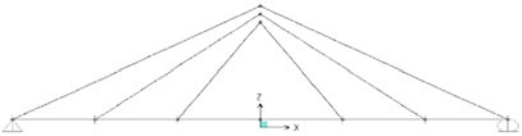

Fig. 17 One end of longitudinal girder is hinged and another roller

Table 3 Comparison of results for various deck pylon connections when both the ends are rollers

S. No.	Element	Responses	
1	Cable	Axial (kN)	2042
2	Longitudinal deck element	Axial (kN)	7918
		Shear (kN)	5047
		Moment (kN-m)	35,600
3	Pylon	Axial (kN)	13,037
		Moment (kN-m)	451
		Shear (kN)	274

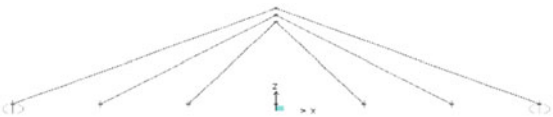

Fig. 18 Both the ends of longitudinal girder are rollers

as the nonlinear behavior of the deck will be reduced. Hence, from the above observations, it can be concluded that case 1 (i.e., both hinged condition) is most desirable support condition for both H shape and inverted Y shapes.

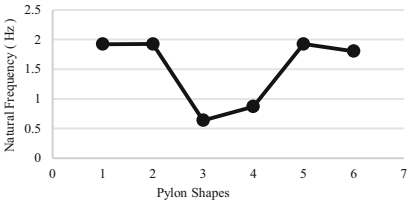

Fig. 19 Variation of natural frequency of cable-stayed bridge with pylon shapes

2.6 Fundamental Natural Frequency

In this section, the fundamental natural frequency of Symmetrical cable-Stayed Bridge is obtained by conducting the modal analysis and is presented in Fig. 19.

From the above study, it can be seen that the fundamental frequency is lesser in the case of cable-stayed bridge with pylon "H shape", which shows that cable-stayed bridge with H shape pylon is more flexible in nature, whereas the fundamental frequency is more in the case of cable-stayed bridge with pylon "inverted Y shape and A shape", which shows that they are rigid in nature.

3 Unsymmetrical Cable-Stayed Bridges

In the case of unsymmetrical cable-stayed bridges, all the material and sectional data taken for the analysis were same as symmetrical study, except one of the span, i.e., left span was taken one-third of the total span, i.e., 25 m and right span was taken as two-thirds of the total span, i.e., 75 m (refer Fig. 20), and the analysis was done to determine the best possible pylon shapes in the case of unsymmetrical cable-stayed bridges.

The study which is conducted for symmetrical cable-stayed bridges is also repeated for unsymmetrical cable-stayed bridges and it was found that "H shape" and "perfect A shape" are most suitable for unsymmetrical kind of cable-stayed bridges. Bridges with these shapes of pylons also showed lesser fundamental frequency indicating flexible behavior.

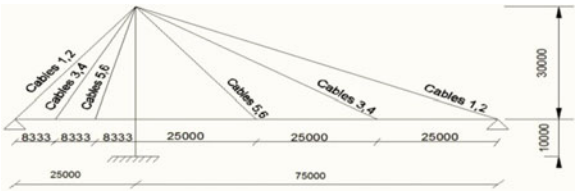

Fig. 20 Unsymmetrical cable-stayed bridges taken for modeling

4 Conclusions

In this study, the symmetrical cable-stayed bridge is analyzed for six different shapes of pylons on SAP 2000 software for dead and moving live loads. It can be concluded from the above study that "H shape" is the best possible pylon shapes for symmetrical cable-stayed bridges. The bridges with this shape showed flexible characteristic having a lesser fundamental frequency which is advantageous. Also, it has been found from the analysis that having varying cable areas in different planes is advantageous as it reduces the nonlinear behavior of the deck, also increasing the cable tensile force ensuring efficient utilization of cable strength. In the boundary conditions, it was concluded that having both hinged conditions is the more suitable one, as it reduces compression in deck thereby reducing nonlinear behavior of the deck. In the unsymmetrical cable-stayed bridges, it can be concluded that "H shape" and "inverted Y shape" are more suitable.

References

1. Agrawal, T. P. (1997). Cable-Stayed Bridges-parametric study. *Journal of Bridge Engineering, 2*(2), 61–67.
2. Au, F. T. K., Cheng, Y. S., Cheung, Y. K., & Zheng, D. Y. (2000). On the determination of natural frequencies and mode shapes of cable stayed bridges. *Applied Mathematical Modeling, 25*(12), 1099–1115.
3. Chang, C. C., Chang, T. Y. P., & Zhang, Q. W. (2001). Ambient vibration of long-span Cable-Stayed Bridges. *Journal of Bridge Engineering, 25*(6), 46–53.
4. Reddy, P., Ghaboussi, J., & Hawkins, N. M. (1999). Simulation of construction of Cable-Stayed Bridges. *Journal of Bridge Engineering*, 63–68.
5. Shu, H.-S., & Wang, Y.-C. (2001). Stability analysis of box girder Cable-Stayed Bridges. *Journal of Bridge Engineering*, 63–68.
6. IRC. (2010). Standard *specifications and code of practice for road bridges*, *IRC: 6 section II —loads and stresses*. New Delhi: Indian Road Congress.
7. Janjic, D., Pircher, M., & Pircher, H. (2003). Optimisation of cable tensioning in Cable-Stayed Bridges. *Journal of Bridge Engineering, 8*(2), 131–137.
8. John Wilson, C., & Keith, H. (2007). Seismic vulnerability and mitigation during construction of Cable-Stayed Bridges. *Journal of Bridge Engineering, 12*(1), 364–372.
9. Ren, W.-X. (1999). Ultimate behaviour of long-span Cable-Stayed Bridges. *Journal of Bridge Engineering*, 30–37.
10. Wang, Y.-C. (1999). Number of cable effects on buckling analysis of Cable-Stayed bridges. *Journal of Bridge Engineering, 22*(4), 242–248.
11. Gimsing, H. J. (1997). *Cable supported bridges: Concept and design*. New York, USA: Wiley.
12. Wang, P.-H., Tang, T.-Y., & Zheng, H.-N. (2003). Analysis of cable-stayed bridges during construction by cantilever methods. *Computer and Structures, 82*(5), 329–346.
13. Ramteke, R. R. (2002), Analysis and design of Cable Stayed Bridge (M. Tech thesis). V.N.I. T, Nagpur.

14. Shilpa, S. K. (2006). Mathematical modeling of Cable Stayed Bridge (M. Tech thesis). V.N.I. T, Nagpur.
15. Troitsky, M. S. (1988). *Cable Stayed Bridge: An approach to modern bridge design*. Oxford, England: BSP Professional Books.
16. Walther, P., & Scalzi John, B. (1976). *Construction and design of Cable Stayed Bridge*. New York, USA: A Wiley Interscience Publication.

Evaluation of Minimum Flexural Reinforcement in Design of Reinforced Concrete Beams

H. E. Nagesh and G. Appa Rao

Abstract Reinforced concrete (RC) beams are generally designed with different percentages of flexural tension reinforcement depending on the capacity requirements. The amount of reinforcement provided affects the crack propagation and failure mechanism in RC beams. This paper presents discussion on the minimum tension reinforcement requirement in code provisions for RC beams. Models based on fracture mechanics to evaluate minimum flexural reinforcement are also reviewed. Experimental study has been undertaken to understand the effect of size on the behaviour of lightly RC beams. This paper outlines how the present code provisions can be improved by applying fracture mechanics principles for the design of RC beams. Fracture mechanics approach for design of RC structures considers the energy requirements for crack growth and size effect. It also enables rational procedure to evaluate the optimum amount of steel reinforcement, which ensures safe designs by taking the effect of size and other influencing parameters.

Keywords Fracture mechanics · Minimum reinforcement · Lightly reinforced

Abbreviations

$A_{s,min}$ (ρ_{min})	Minimum area of steel
A_s	Area of steel
b	Breadth of beam
d or h	Effective depth of beam
d'	Clear cover
D	Overall depth of beam
E_c	Modulus of elasticity of concrete
E_s	Modulus of elasticity of steel

H. E. Nagesh · G. Appa Rao (✉)
Department of Civil Engineering, Indian Institute of Technology Madras, Chennai 600036, India
e-mail: garao@iitm.ac.in

H. E. Nagesh
e-mail: nageshhe@gmail.com

A. Rama Mohan Rao and K. Ramanjaneyulu (eds.), *Recent Advances in Structural Engineering, Volume 1*, Lecture Notes in Civil Engineering 11,
https://doi.org/10.1007/978-981-13-0362-3_12

f_{ck}	Characteristic cube compressive strength of concrete
f'_c	Cylinder compressive strength of concrete
f_t	Tensile strength of concrete
f_r	Modulus of rupture
f_y	Yield strength of steel
K_{Ic}	Critical stress intensity factor in mode I
M_{CR}	Moment of crack propagation
M_y	Moment at steel yielding
Np	Brittleness number
FPZ	Fracture process zone
FCM	Fictitious crack model
LEFM	Linear elastic fracture mechanics
NLFM	Non-linear fracture mechanics

1 Introduction

Concrete beams are reinforced with steel in tension zone to bear tensile stresses. The amount of reinforcement provided governs the behaviour and failure mechanism in reinforced concrete (RC) beams. The failure may be of steel yielding followed by concrete crushing in case of under-reinforced and crushing of concrete in over-reinforced beams. While designing of RC beams, minimum ductility must be ensured to perform satisfactorily. This can be achieved by providing an adequate amount of tensile reinforcement. If the beam is provided with an insufficient quantity of steel than required, the failure tends to change to brittle. Minimum reinforcement in RC beams should avoid brittle failure and must ensure adequate warning before failure.

2 Behaviour of Lightly Reinforced Concrete Beams

For an RC beam to exhibit stable response, the beam must be provided with adequate amount of tension reinforcement. Suppose if the beam is provided with less area of steel than required, then it leads to brittle failure. This leads to instability in the overall response. Before concrete cracking, the load deflection response of plain concrete beam and an RC beam is same as shown in Fig. 1. If the ultimate strength developed with the provided reinforcement is less than the flexural cracking strength, then the later determines the hyper-strength $(\rho < \rho_{min})$. This creates instantaneous crack growth and in turn causes brittle failure when tested

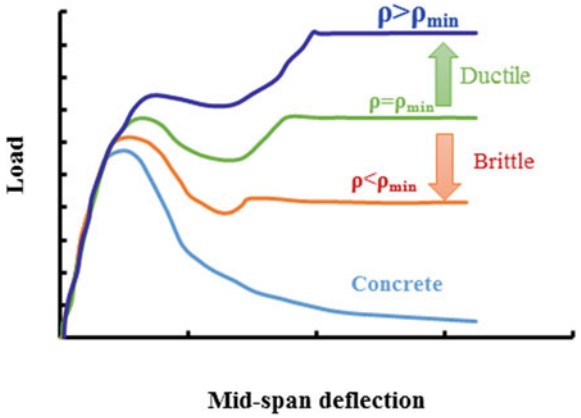

Fig. 1 Behaviour of lightly reinforced concrete beam

under load control. Hence, a certain amount of minimum tension reinforcement is required for ductile behaviour ($\rho > \rho_{min}$). Figure 1 also shows the transition from brittle to ductile with increase in tension reinforcement.

3 Code Provisions

The provisions in the present codes of practice are mainly based on serviceability and strength aspects. Many codes of practice specify empirical formulae, without theoretical background, for estimating minimum reinforcement. Such code provisions mostly incorporate compressive strength of concrete and yield strength of steel reinforcement as parameters. They neglect the non-linear behaviour of concrete in tension, toughness of concrete, and bond strength, which provides the conservative design. Moreover, mechanical behaviour of RC beams not only depends on material properties but also on the size as well. The condition for evaluation of minimum reinforcement is that the beam should not fail immediately upon concrete cracking. To achieve this condition, the ultimate capacity (M_u) of an RC beam should be greater than its cracking moment (M_{cr}).

$$M_u \geq M_{cr} \tag{1}$$

Evaluation of flexural cracking strength of concrete beams in flexure is vital because many code provisions provide tension reinforcement relatively more than what is required for cracking strength. Code provisions use modulus of rupture to evaluate the cracking stress in beams. But full-scale specimens have lower cracking flexural strength than that of modulus of rupture [1]. The code provisions for providing minimum tension reinforcement in RC beams are given in Table 3. The equation for evaluating minimum and maximum tension reinforcement, and commentary or remarks for codes are also given in Table 3.

4 Need for Fracture Mechanics-Based Design

Direct tension testing of concrete involves complex procedures. So split cylinder tests are used to get tensile strength of concrete. The uniaxial tensile strength of concrete is always much less than the flexural cracking strength of concrete. Suppose if concrete is considered as brittle material, soon after the extreme tension fibres reaches uniaxial tensile strength, it should fail instantaneously. But concrete is a quasi-brittle material due to its tension softening property. It can transfer stress across crack faces. This property can be modelled using non-linear fracture mechanics models (NLFM). Fictitious crack and cohesive crack models are able to include this quasi-brittle nature of concrete.

In the conventional design methodology, tests on cylinder compression, modulus of rupture and split tensile tests are used to characterize concrete properties.

These properties of concrete alone cannot characterize its complete behaviour. Hence, the post-cracking behaviour of concrete such as fracture softening has to be well understood. The formation of fracture process zone (FPZ) ahead of crack tip affects the crack initiation and propagation in concrete beams. The application of fracture mechanics principles is necessary to study the crack growth and fracture behaviour in concrete. Fracture mechanics principles are applied to study the behaviour of lightly RC beams because of its sensitivity to the fracture of tension reinforcement. The models based on fracture mechanics principles are given in Table 4. It can be noticed that the minimum reinforcement is found to be a function of depth of beam.

5 Experimental Programme

An experimental programme was undertaken to study size effect on the behaviour of lightly RC beams in flexure. The beams are provided with 0.25% tension reinforcement. The material properties are given in Table 1. Three geometrically similar specimens were cast with depth ranging from 150 to 600 mm. The span of the beams is six times the depth. The width of the beam was maintained constant 150 mm. Specimen designations and dimensions are given in Table 2. All three specimens were cast with the same concrete mix. Potable water was used for mixing of concrete. All specimens were cured for 28 days before testing. Mix design for concrete includes 400 kg/m^3 of 53 grade ordinary Portland cement (OPC) with water–cement ratio of 0.39. Fine aggregate with a content 736 kg/m^3 and coarse aggregate 10 mm graded with 1100 kg/m^3. The fracture energy (G_f) was obtained according to the test procedure given in the RILEM standard.

Linearly variable differential transformer (LVDT) was placed to record mid-span deflections and crack mouth opening displacements (CMOD).

Table 1 Material properties

Material property	Results
Compressive strength of concrete cube	60.7 MPa
Specific gravity of cement	3.14
Grade of cement	53 OPC
Fracture energy of concrete	97.2 N/m
Specific gravity of fine aggregate	2.78
Specific gravity of coarse aggregate	2.70
Yield strength of reinforcing steel	547 MPa
Ultimate strength of reinforcing steel	634 MPa

Table 2 Beam dimensions

Beam designation	Depth (mm)	Span (mm)
SB	150	900
MB	300	1800
LB	600	3600

6 Monotonic Testing

All beams were tested under three-point bending and actual set-up is shown in Fig. 2. Testing was carried out using actuator of 1000 kN capacity at Indian Institute of Technology Madras. The beams were loaded with displacement control up to failure. All beams failed by fracture of reinforcing steel bars. The load–deflection response is discussed in the results and discussions.

Fig. 2 Monotonic test set-up

Table 3 Code provisions for minimum and maximum tension reinforcement in beams

Codes	Minimum reinforcement	Maximum reinforcement	Remarks/provisions	Equation number
ACI 318-14 [2]	$A_{s,min} = \frac{0.25\sqrt{f'_c}}{f_y} b_w d$	Net tensile strain in extreme tensile steel $\geq$ 0.005	To prevent sudden failure moment of reinforced cracked section > moment of unreinforced concrete section	(2)
IS 456-2000 [3]	$\frac{A_s}{bd} = \frac{0.85}{f_y}$	0.04 bD	Strength of concrete was not considered	(3)
AASHTO LRFD-07 [4]	$M_r = 1.2M_{cr}$ for RC structures $M_r = 1.33M_{cr}$ for prestressed concrete	–	To avoid brittle failure, the amount of reinforcement is enough to develop a factored flexural resistance, M_r, equal to the lesser of at least 1.2 times the cracking moment	(4)
EUROCODE-2 [5]	$A_s = \frac{0.26 \times f_{ctm} b \times d}{f_y}$	0.04 A_c	Considers mean tensile strength (f_{ctm}) of concrete as governing parameter	(5)
Canada code [6] (CSA A23.3-04)	$A_s = \left(\frac{0.2 \times \sqrt{f'_c}}{f_y}\right) \times b_w h$ For T- sections $As = 0.004 \times (b - b_w) d_s$	$\frac{c}{d} < \frac{700}{700 + f_y}$	Grade of concrete as well as grade of steel is accounted	(6)
New Zealand [7] (NZS 3101-06)	$A_s = \frac{\sqrt{f'_c}}{4f_y} \times b_w d$	$\frac{f'_c + 10}{6f_y} < 0.025$	Both grade of concrete and grade of steel are considered	(7)
Australia code (AS 3600-01) [8]	$A_s = 0.22\left(\frac{D}{d}\right)^2 \frac{f_t}{f_y} \times b_w d$	–	Tensile strength of concrete and yield strength of steel are considered as governing parameters	(8)
British Standards [9] BS 8110 (1997)	0.24 = $100A_s/b_w$ h for f_y = 250 N/mm^2 0.13 = $100A_s/b_w$ h for f_y = 460 N/mm^2	0.04 bD	Based on the grade of steel only, concrete strength not been taken in to account	(9)

Table 4 Models based on fracture mechanics principles to evaluate minimum reinforcement in beams

Authors	Equation	Remarks	Equation number
Bosco et al. [10]	$N_{\mathrm{p}} = \frac{f_{\mathrm{y}}\sqrt{D}}{K_{\mathrm{IC}}}\frac{A_{\mathrm{st}}}{A}$	Used brittleness number	(10)
Bosco et al. [11]	$\rho_{\min} = \frac{K_{\mathrm{IC}}}{f_{\mathrm{y}}\sqrt{D}}(0.1 + 0.0023 f_{\mathrm{c}})$	Based on bridged crack model (LEFM)	(11)
Baluch et al. [12]	$\rho_{\min} = \frac{1.9134 K_{\mathrm{IC}}^{0.82}}{f_{\mathrm{y}}^{0.9922}\left(1.7 - 2.6\frac{C_{\mathrm{s}}}{D}\right)}$	Model based on LEFM	(12)
Gerstle et al. [13]	$\rho_{\min} = \frac{E_{\mathrm{C}}}{E_{\mathrm{s}}}\left(\sqrt{0.0081 + 0.0148\frac{f_{\mathrm{t}}' D}{E_{\mathrm{c}} w_{\mathrm{c}}}} - 0.09\right)^{1/2}$	Used fictitious crack model Unstable crack propagation Increases with depth	(13)
Hawkins Hjorselet [14]	$\rho_{\min} = 0.18305\left(1 + \frac{1}{0.85 + \frac{4.6 D f_{\mathrm{t}}'}{E_{\mathrm{c}} w_1}}\right)\frac{f_{\mathrm{t}}' D}{f_{\mathrm{y}}(D - C_{\mathrm{s}})}$	Based on cohesive crack model	(14)
Ruiz et al. [15]	$\rho_{\min} = \frac{\frac{\xi}{6(1 - C_{\mathrm{s}}/D)}\frac{1 + \left(0.85 + \frac{2.3D}{l_1}\right)^{-1}}{\frac{f_{\mathrm{y}}}{f_{\mathrm{t}}'} - \mu\left[(D/l_1)^{1/4} - 3.61 C_{\mathrm{s}}/l_1\right]}}{}$	Effective slip model	(15)
Shehata et al. [16]	$\rho_{\min} = 0.05\frac{f_{\mathrm{ck}}^{0.67}}{f_{\mathrm{y}}}\frac{\left(1 + 1.5\left(\frac{h}{100}\right)\right)^{0.7}}{\left(\frac{h}{100}\right)^{0.7}}$	$\rho_{\min} > \left(M/bd(d - 0.5\beta x) f_{\mathrm{y}}\right) < \rho_{\mathrm{bal}}$	(16)
Appa Rao et al. [17]	$\rho_{\min} = \left(\frac{4000 - D}{100D}\right)\left(\frac{f_{\mathrm{c}}^{1.14}}{f_{\mathrm{y}}^{0.57}}\right)$	Equation based on limiting crack width $\mathrm{COD}_{\mathrm{cr}}$ Increases with depth	(17)
Carpinteri [18]	$A_{\mathrm{s,min}} = 0.267\frac{\sigma_{\mathrm{u}}^{0.70} K_{\mathrm{IC}}^{0.3}}{\sigma_{\mathrm{y}}} b h^{0.85}$	$N_{\mathrm{p,L}} = 0.267 s^{-0.7}$ Derived equation of lower limit for ductile response from numerical simulations	(18)

7 Results and Discussions

7.1 Load–Deflection Response

The load versus mid-span deflection response of the small, medium and beams are shown in Fig. 4. LVDT was used to get mid-span deflection. In the initial stage up to concrete cracking, the deflection was observed to be small with high stiffness. At peak loading, the crack starts to propagate from cover towards tension reinforcement. Once the crack begins to propagate, the reduction in stiffness can be noticed with increase in deflections. As the crack crosses the tension steel reinforcement, steel being in elastic state arrests crack growth, thus demanding an extra force for crack propagation across reinforcement. This causes steel pull-out and slip simultaneously. Hence, the peak and near post peak P-δ response controlled by steel ratio, bond-slip properties and the cover. All the three beams failed due to rupture of tension reinforcement. Figure 3 shows ductile response with excessive deformations before final failure for all beams. In case of large beam (LB), the spalling of concrete cover at ultimate loading caused excessive deflection of beams; this behaviour is reflected in Fig. 4. This behaviour can also be noticed in Fig. 3.

7.2 Strain Localization

All beams tested predominantly failed due to single crack originating from the centre of beam. As the tensile stress in the concrete exceeds the tensile strength of concrete, the gradual reduction in the tension stress (tension softening) takes place. Due to single crack formation, the strain gets localized causing increased crack widths until rupture of tensile reinforcement. The horizontal strain in percentage measured using digital image correlation (DIC) for large beam is shown in Fig. 3.

7.3 Size Effect on Flexural Cracking Strength

It has been observed that as the depth of the beam increases, the flexural cracking strength decreases. This behaviour is expected because the volume of concrete in tension is relatively more, and the probability of increase in the volume of voids and imperfections is also more. Figure 5 shows that flexural cracking strength is inversely proportional to size.

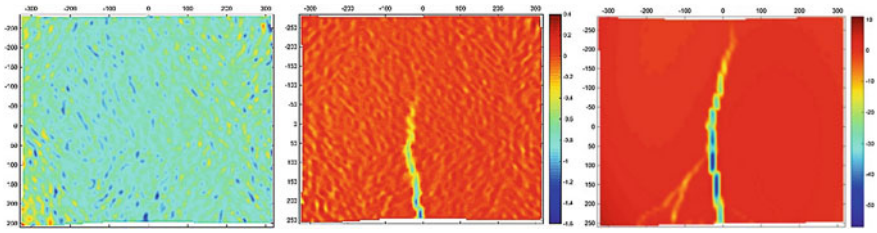

Fig. 3 Horizontal strain (%) showing strain localization

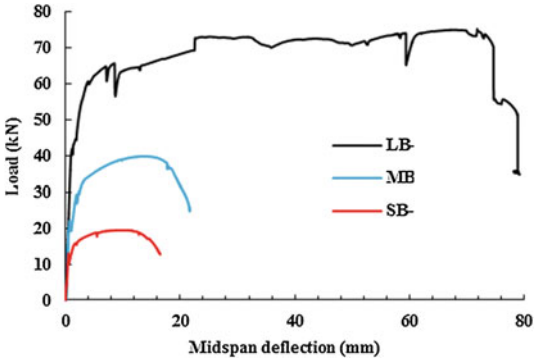

Fig. 4 Load versus deflection

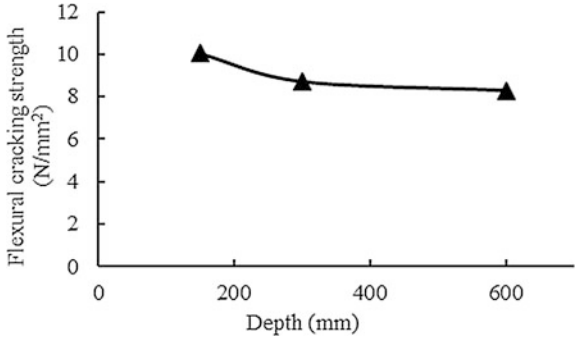

Fig. 5 Flexural cracking strength

7.4 Comparison of Equations

The comparison of equations existing in code provisions (Table 3) and equations proposed by researchers (Table 4) for evaluating minimum tension reinforcement in RC beams is shown in Fig. 6. It is observed that the codes provision equation is independent of beam depth. Whereas few models proposed by Hawkins et al., Baluch et al. and Shehata et al. clearly show the size-dependent variation in the minimum reinforcement. But the present experimental studies and the literature suggest that the lightly RC beams responses are size-dependent.

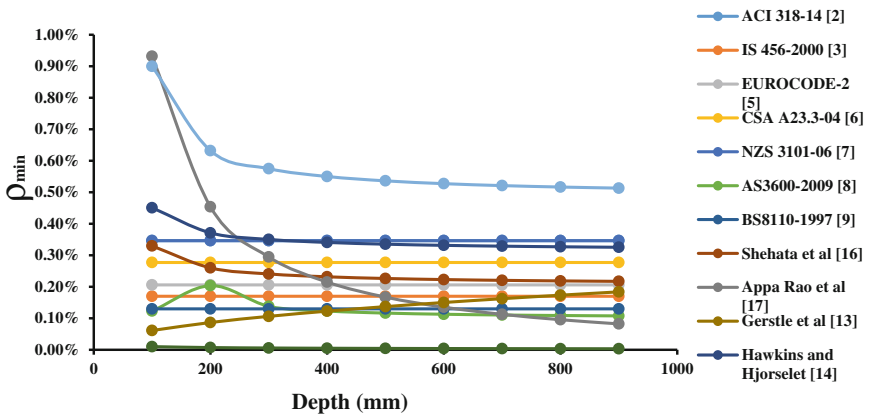

Fig. 6 Comparison of equations

8 Conclusions

It can be concluded that the code provisions for minimum tension reinforcement are based on material properties such as concrete compressive strength, yield strength of steel and cracking stress. However, it has been observed from the present experimental studies that flexural cracking strength is size-dependent. Flexural cracking strength is inversely proportional to depth of beam. Many researchers also proposed equations which recommend that minimum reinforcement should be size-dependent. The response of the beams changes with size; hence, it should be incorporated properly. The behaviour of concrete in tension, crack initiation and crack propagation, and FPZ, size-dependent response of concrete are well understood using fracture mechanics studies. Hence, fracture mechanics-based design enables rational approach ensuring safe design with the optimum amount of reinforcement.

References

1. Shioya, T., Iguro, M., Nojiri, Y., Akiyama, H., & Okada, T. (1989). Shear strength of large reinforced concrete beams. In *Fracture Mechanics: Application to Concrete, SP118* (p. 309). Detroit: American Concrete Institute.
2. ACI-318-14. (2014). *Building code requirements for structural concrete and commentary*.
3. IS 456:2000. (2000). *Plain and reinforced concrete—Codes of practice*.
4. AASHTO. (2007). *AASHTO LRFD bridge design specifications*. American Association of State Highway and Transportation Officials.
5. Eurocode 2: 1992. (2002). *Design of concrete structures—Part 1: General rules and rules for buildings*.
6. CAN/CSA-A23.3-04. (2004). *Design of concrete structures*.
7. NZS 3101: Part 1: 2006. (2006). *Concrete structures standard*.

8. AS3600. (2009). *Concrete structures*.
9. BS 8110-97. (1997). *Structural use of concrete Part 1: Code of practice for design and construction*.
10. Bosco, C., Carpinteri, A., & Debernardi, P. G. (1990). Minimum reinforcement in high-strength concrete. *Journal of Structural Engineering, ASCE, 116*(2), 427–437.
11. Bosco, C., & Carpinteri, A. (1992). Fracture mechanics evaluation on minimum reinforcement in concrete. In A. Carpinteri (Ed.), *Application of fracture mechanics to reinforced concrete* (pp. 347–377). Italy: Elsevier App Head Science.
12. Baluch, M., Azad, A., & Ashmawi, W. (1992). Fracture mechanics application to reinforced concrete members in flexure. In A. Carpinteri (Ed.), *Applications of fracture mechanics to reinforced concrete* (pp. 413–436). London: Elsevier Applied Science.
13. Gerstle, W. H., Partha, P. D., Prasad, N. N. V., Rahulkumar, P., & Xie, M. (1992). Crack growth in flexural members a fracture mechanics approach. *ACI Structural Journal, 89*(6), 617–625.
14. Hawkins, N., & Hjorsetet, K. (1992). Minimum reinforcement requirement for concrete flexural members. In A. Carpinteri (Ed.), *Applications of fracture mechanics to reinforced concrete* (pp. 37–412). London: Elsevier.
15. Ruiz, G., Elices, M., & Planas, J. (1997). Size effect and bond-slip dependence of lightly reinforced concrete beams. In A. Carpinteri (Ed.), *Minimum reinforcement in concrete members* (24). ESIS Publication.
16. Shehata, I. A. E. M., Shehata, L. C. D., & Gracia, S. L. G. (2003, Jan–Feb). Minimum steel ratios in reinforced concrete beams made of concrete with different strengths—Theoretical approach. *Materials and Structures, 36*, 3–11.
17. Rao, G. A., Aravind, J., & Eligehausen, R. (2007). Evaluation of minimum flexural reinforcement in RC beams using fictitious crack approach. *JoSE, 34*(4), 277–283.
18. Carpinteri, A., Corrado, M., & Ventura, G. (2013). Failure mode scaling transitions in RC beams in flexure: Tensile, shearing, and crushing. In *FraMCoS-8*, Spain.

Various Aspects of Detailing of Reinforcement in Two-Pile Cap Concrete

Murty Sree Rama Chandra Devalraju and Dinakar Pedapenki

Abstract Of the many types of pile caps, two-pile cap (TPC) born by two piles is extensively used. Notwithstanding being a very extensively used structural member, there is no generally accepted procedure for design of pile caps. Of the very few available methods of design, sectional force method, endorsed by IS 456:2000 (Indian Standard code of practice for plain and reinforced concrete. Bureau of Indian Standards, New Delhi [1]), and IRC 21:2000 ('Standard Specifications and Code of Practice for Road bridges' section: III Cement concrete (Plain and Reinforced). The Indian Road Congress [2]), is generally in use in India. In this method, design for flexure, two-way shear and bearing is done by standard methods. The aforementioned codes provide specifications for identification of one-way shear on pile caps, but little experimental research is reported to date, on the validity of the specifications contained in the codes. The research presented in this paper fills the void. The seven TPCs tested to failure have shown that the specifications of the code are valid. The concurrence of specifications of the codes since their inception and test results have been established for the first time by the current tests.

Keywords Pile cap · Shear · Service load · Ultimate load · Validity

1 Research Significance

Most frequently used deep foundation for various kinds of large structures is piles. The inevitable structural element, incorporated between the column in the superstructure and a group of piles, for transfer of loads from the former to the

M. S. R. C. Devalraju (✉)
Department of Civil Engineering, College of Engineering, Andhra University, Visakhapatnam 530003, India
e-mail: dsrmurty14@gmail.com

D. Pedapenki
Department of Civil Engineering, G.I.A.C.R Engineering College, Rayagada 765002, India
e-mail: p_dinakar2004@yahoo.com

A. Rama Mohan Rao and K. Ramanjaneyulu (eds.), *Recent Advances in Structural Engineering, Volume 1*, Lecture Notes in Civil Engineering 11,
https://doi.org/10.1007/978-981-13-0362-3_13

latter is pile cap. The piles are tied at their tops or capped by a spread footing or cap that distributes the column loads to all the piles in the pile group. Pile caps are labelled as single pile cap, two-pile cap (TPC), three-pile cap, four-pile cap or multiple pile cap. In spite of being a very important structural member and most extensively used item in large constructions such as bridges, industries, oil drilling platforms and high-rise structures, there is no generally accepted procedure for proportioning pile caps. Many empirical detailing rules or rules of thumb are followed in practice, but these approaches vary significantly with considerable disparity. There has been no consensus on which method provides the best approach for a working designer. There are some design approaches followed by codes and designers which include (1) truss analogy, (2) ACI method (traditional sectional design method), (3) AASHTO LFRD STANDARD and (4) strut-and-tie method. Traditional sectional force approach and strut-and-tie model approach constitute principal design approaches, used today. Sectional force design attends to bending and one-way shear separately, while catering also to two-way shear and bearing; this method is extensively used in India, supported by code IS 456:2000 [1]. Strut-and-tie model does not separate bending (tie tensile force) and one-way shear (automatically resisted by developed arch action). In sectional force method, the pile caps have traditionally been designed as beams spanning between piles with the depth selected to avoid shear fractures and the amount of longitudinal reinforcement selected to provide sufficient flexural capacity by the engineering beam theory. Design is made for two-way shear and bearing, by the standard code methods. In the current research work, sectional force method is made use of. Depending on the geometry of pile cap and orientation of column and piles, IS 456:2000 [1] specifies in Cl 34.2.4.1 and Cl 34.2.4.2 whether shear force occurs on pile cap due to pile reactions. A critical section is assumed as a vertical section through pile cap, located from the face of column at distance equal to effective depth of pile cap. The entire reaction from any pile of diameter D_p whose centre is located $D_p/2$ or more outside the critical section shall be assumed as producing shear on the section (on pile cap); the reaction from any pile whose centre is $D_p/2$ or more inside the critical section shall be assumed as producing no shear on the section (on pile cap). This IS code provision guides the designers whether to design a pile cap for shear or not. Little or no test data are available in the literature to date, on the verification of code provisions on the occurrence of one-way shear on pile caps. The principal objective of the research reported herein is to experimentally establish the validity of provision of IS 456:2000 [1] code, on the occurrence of one-way shear on TPCs. Proper substantiation is needed by the tests to evolve one-way shear design, in the sectional design method of TPCs.

2 Experimental Research

Seven numbers of TPCs were proportioned for one-way shear; the column working load for the design of all TPCs was 150 kN and tested to investigate provisions of IS 456:2000 [1] relative to occurrence of one-way shear. For the TPCs that failed in shear, identical companion TPCs were designed for shear to precipitate bending failure. In TPC, PC3, the column and the piles were oriented relative to pile cap in such a way that as per code provisions, no shear occurs on pile cap. The effective depth of TPC was 181 mm, and the distance between face of the column and outer face of pile was 180 mm which was less than 181 mm; as per the code, no shear force occurs on the TPC. Test has to verify the specification of the code (mode of failure, shear failure or bending failure). TPC, PC4 was oriented such that the effective depth was 180 mm and the distance between the face of the column and inner face of pile was 180 mm which was equal to effective depth of pile cap; as per code, total pile reaction appears as shear on TPC and shear failure is predicted. Test has to establish the mode of failure (shear or bending failure). In TPCs PC5, the distance between the face of column and outer face of pile (440 mm) is more than the effective depth of TPC (230 mm); hence, shear force occurs on the TPC leading to shear failure, which has to be proved by the test. Similarly in TPC, PC6, the distance between the column face and outer face of pile (530 mm) was more than the effective depth (229 mm) of the TPC; hence, shear force occurs on TPC leading to shear failure. Again test has to establish mode of failure. TPCs PC4, PC5 and PC6 failed in shear. TPCs PC7, PC8 and PC9 were identical and companion TPCs to PC4, PC5 and PC6 TPCs, respectively; the former three TPCs were designed for shear to eliminate shear failure and to obtain flexural failure. The details of test specimens are summarised in Table 1 and shown in Figs. 1, 2, 3, 4, 5, 6 and 7. The steel details as manufactured are shown in Tables 2 and 3.

3 Materials Properties of Test Specimens

In the concrete, made for production of test specimens, the cement used was 43 grade ordinary Portland cement, and the fine aggregate was river sand conforming to zone-II as per IS 383:1970 [3]. The coarse aggregate was locally available crushed granite stone sieved to 20 mm maximum size and satisfied the requirement of IS 383:1970 [3]. The mix proportion of concrete by weight of cement, sand and coarse aggregate was, respectively, 1:1.76:3.79 with water–cement ratio, 0.56 by weight. The concrete compressive strengths were 38.6 MPa for the first four TPCs and 39.2 MPa for the latter three TPCs.

Table 1 Properties of two-pile cap (TPC) test specimens

Specimen label	Pile cap				Span between two piles (mm)	Shear span/ effective depth (*a*/*d*)	Longitudinal reinforcement	Transverse reinforcement	Cube compressive strength at 28 days (MPa)	Split tensile strength at 28 days (MPa)
	Length (mm)	Width (mm)	Depth (mm)	Effective depth (mm)						
PC 3	610	250	210	181	360	0.58	4–8 mm dia	Not needed as per code IS 456:2000 [1]	38.6	2.8
PC 4	910	250	210	180	660	1.42	7–10 mm dia	Not provided	38.6	2.8
PC 5	1130	250	260	230	880	1.59	8–10 mm dia	Not provided	38.6	2.8
PC 6	1310	280	260	229	1060	1.99	7–12 mm dia	Not provided	38.6	2.8
PC 7	910	250	210	180	660	1.42	6–10 mm dia	2 L 10 mm stps @ 120 mm c/c	39.2	2.9
PC 8	1130	250	260	230	880	1.59	6–10 mm dia	2 L 8 mm stps @ 100 mm c/c	39.2	2.9
PC 9	1310	280	260	229	1060	1.99	6–12 mm dia	2 L 8 mm stps @ 110 mm c/c	39.2	2.9

Note PC4 and PC7, PC5 and PC8, and PC6 and PC9, respectively, were identical pile caps, with nearly same amount of flexural reinforcement was provided. As yield stresses differed, tensile force was made equal adjusting steel areas

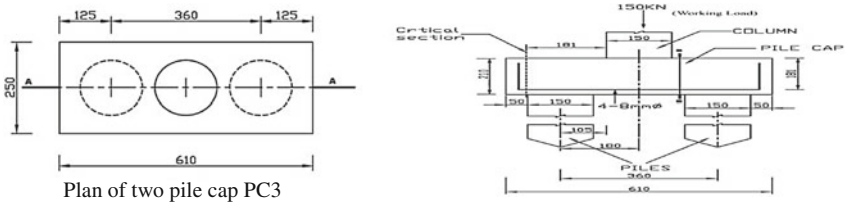

Plan of two pile cap PC3

All dimensions in mm

Section A-A

Fig. 1 Two-pile cap PC3

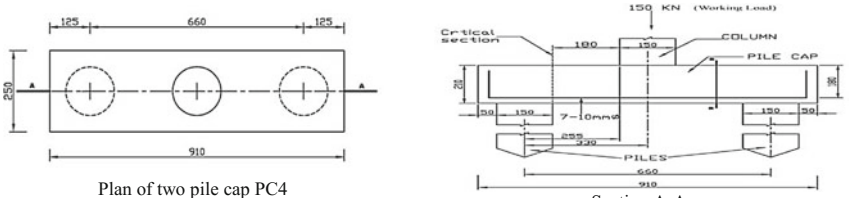

Plan of two pile cap PC4

All dimensions in mm

Section A-A

Fig. 2 Two-pile cap PC4

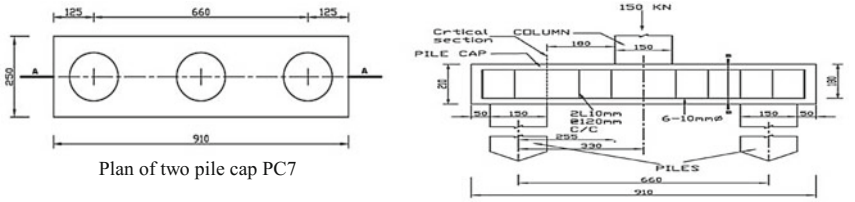

Plan of two pile cap PC7

All dimensions are in mm

Section A-A

Fig. 3 Two-pile cap PC7

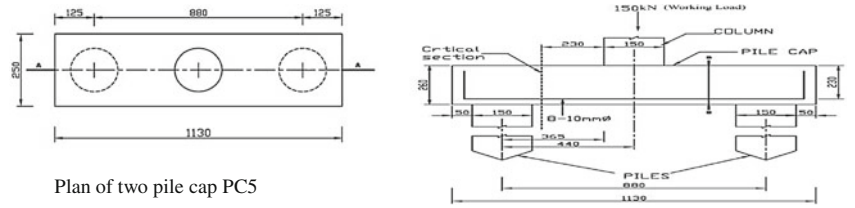

Plan of two pile cap PC5

All dimensions in mm

Section A-A

Fig. 4 Two-pile cap PC5

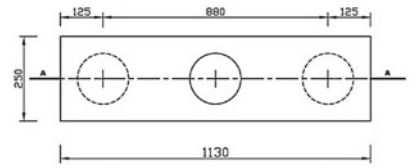

Plan of two pile cap PC8

All dimensions are in mm

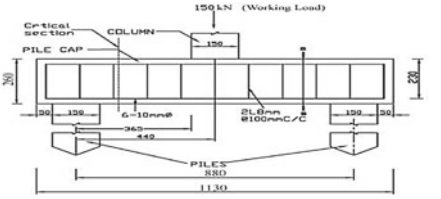

Section A-A

Fig. 5 Two-pile cap PC8

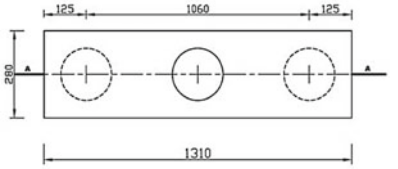

Plan of two pile cap PC6

All dimensions in mm

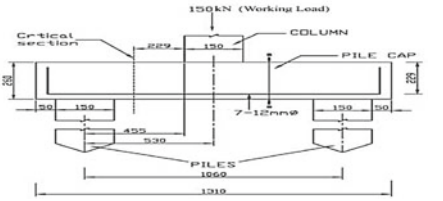

Section A-A

Fig. 6 Two-pile cap of PC6

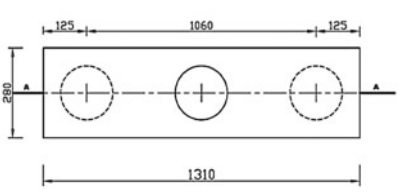

Plan of two pile cap PC9

All dimensions are in mm

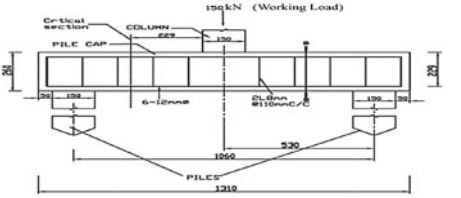

Section A-A

Fig. 7 Two-pile cap PC9

Table 2 Properties of steel reinforcement of PC3, PC4, PC5 and PC6

Nominal diameter (mm)	Area (mm^2)	Yield stress (MPa)	Ultimate tensile stress (MPa)	Percentage elongation
12	113.10	423.1	572.9	18
10	78.50	445	572.1	19
8	50.29	436.8	575.8	20

Table 3 Properties of steel reinforcement of TPCs PC7, PC8 and PC9

Nominal diameter (mm)	Area (mm^2)	Yield stress (MPa)	Ultimate tensile stress (MPa)	Percentage elongation
12	113.10	551.2	637.3	17
10	78.50	515	602.9	18
8	50.29	529.4	627.5	20

4 Fabrication and Testing of Test Specimens

The pile cap moulds for casting were made of brick masonry on the laboratory floor, plastered smooth and oiled before concrete was poured. The concrete in the pile cap was compacted with a needle vibrator, and the control specimens, cubes and cylinders were compacted in a standard way. Curing of specimens started after 24 h of casting. The pile caps were shifted from the moulds to curing tanks after 5 days of casting, on wooden planks; for these 5 days, curing was done with wet gunny bags in the laboratory. Curing was done till starting of testing at 28 days; testing of pile caps was carried out in a test load frame shown in Fig. 8. The pile caps were tested on span equal to spacing of piles which varied depending upon the type of pile cap; the spans varied from 360 to 1060 mm. Columns were simulated using 150 mm diameter and 30 mm thick steel cylindrical plate on the pile cap, over which hydraulic jack was located for load application. Piles were simulated using 150 mm concrete cubes. A hydraulic jack of 1000 kN and a proving ring of 500 kN capacity were utilised for load application and load measurement, respectively. The applied force was controlled through manual operation. Instrumentation for the test specimens was designed to obtain the measurement of transverse load and to capture the load–deflection response and crack development. Strength and serviceability data were collected for each test. A dial gauge was employed for recording deflection under the column load. A handheld microscope, capable of measuring a minimum value of 0.05 mm, was used to note crack width. Each specimen was loaded in 12–15 load increments to failure. At each load stage,

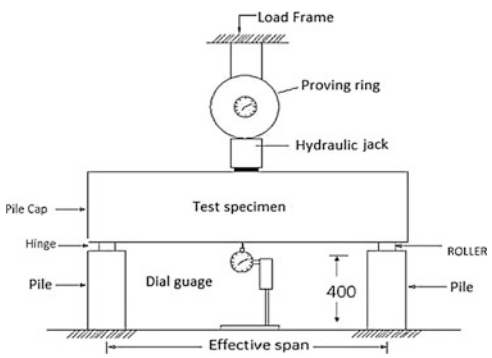

Fig. 8 Details of test setup

Plate 1 Photos of PC3, PC4 and PC 5

magnitude of the load on the test specimen and central transverse deflection of the pile cap under the column load and maximum crack width were recorded. The cracks were marked on the pile cap surfaces, and the tested specimens were photographed and shown in Plates 1 and 2. The details of seven test pile caps are shown in Figs. 1, 2, 3, 4, 5, 6 and 7 and Table 1. The properties of steel reinforcement used in the pile caps are tabulated in Tables 2 and 3.

5 Presentation of Test Results

In TPC, PC3, the initial flexural crack occurred at column load, 127.20 kN. As the load increased, two flexural cracks extended to the top face. No shear cracks appeared. As the ultimate load neared, the TPC failed in bending at column load 283.5 kN, the bending failure was correctly predicted by the code. Post ultimate load, ductility was exhibited by pile cap as shown in Fig. 9. In TPC, PC4, the first flexural crack occurred under the load at a column load of 135.15 kN. With further load increase, diagonal cracks formed joining the supports and concentrated load; with further load increase, the diagonal cracks widened and sudden shear failure occurred at column load, 309.7 kN; the shear failure was predicted as per the specifications of the code. The abrupt shear failure can be observed in Fig. 9. TPC, PC5 developed two initial flexural cracks at column load 158kN at the bottom side face under the column load. As the load increased, the flexural cracks extended to top face and additional diagonal cracks formed. At ultimate, the diagonal cracks

Plate 2 Photos of PC6, PC7, PC8 and PC 9

Fig. 9 Load–deflection curves of two-pile caps PC3 and PC4

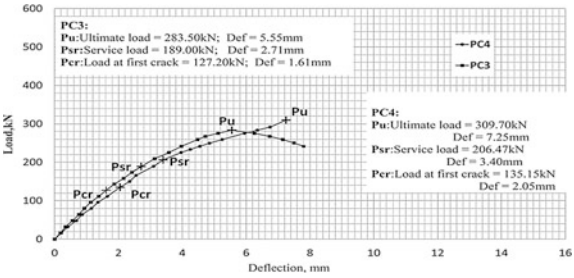

widened joining the two supports and the column load on the top face and shear failure occurred at an ultimate load 377.20 kN. From the load–deflection curve in Fig. 11, sudden shear failure can be noticed. TPC, PC6 developed initial two flexural cracks at column load 173.80 kN at the bottom of side face under the column load. Increase in column load caused the appearance of several diagonal cracks. As the failure neared, the pile cap collapsed in shear at column load of 420.75 kN. The TPCs PC7, PC8 and PC9 were, respectively, identical to the TPCs

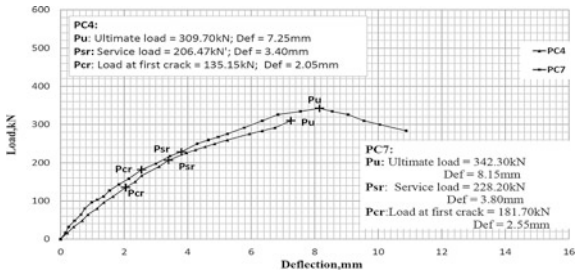

Fig. 10 Load–deflection curves of two-pile caps PC4 and PC7

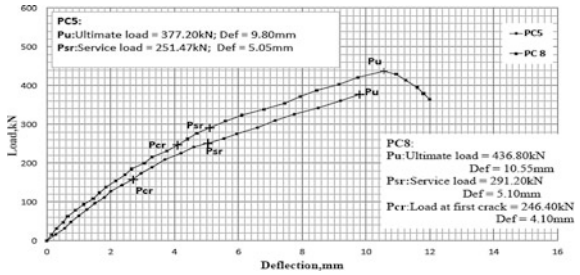

Fig. 11 Load–deflection curves of two-pile caps PC5 and PC8

PC4, PC5 and PC6 that failed in shear as per IS 456:2000 [1]. The TPCs PC7, PC8 and PC9 were proportioned for shear to transform shear failure into the desired flexural failure. Pile cap PC7 developed initial flexural crack under the load at the bottom of the side face, at 181.70 kN, column load. As the load increased, the flexural cracks extended to the top face. Finally, the failure occurred in flexure at an ultimate load, 342.30 kN. Load–deflection curve of PC7 in Fig. 10 shows the ductility characteristic of flexural failure. Pile cap PC 8 was identical to pile cap PC5 which failed in shear when designed as per IS 456:2000 [1]. Pile cap PC8 was designed for shear to allow, flexural failure to occur. The initial flexural crack occurred under the concentrated load at column load, 246.40 kN. Subsequent increases in column load forced the flexural cracks to extend to the top face with their widening. The flexural failure occurred at column load of 436.80 kN. Figure 11 shows the ductility experienced by the TPC, PC8. To see the change of shear failure of the pile cap PC6, a companion pile cap identical in all the respects to PC6, PC9 was fabricated with web reinforcement. The initial flexural crack originated at the bottom of the side face, under the column load at 292.60 kN. As the loading progressed, additional cracks formed and already formed cracks extended to the top face, widening in width. As the collapse neared, compression distress was formed in the top face at ultimate column load of 488.25 kN. Flexural failure occurred. Figure 12 shows the ductility experienced by the pile cap, PC9. No uplift of support was noticed in tests (Figs. 13, 14, 15, and 16; Table 4).

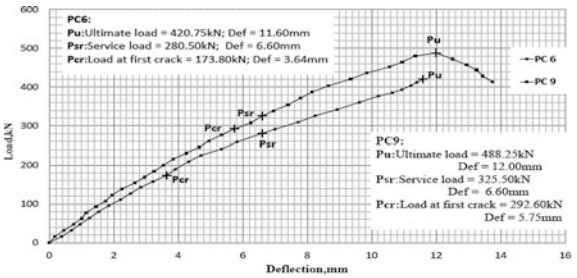

Fig. 12 Load–deflection curves of two-pile caps PC6 and PC9

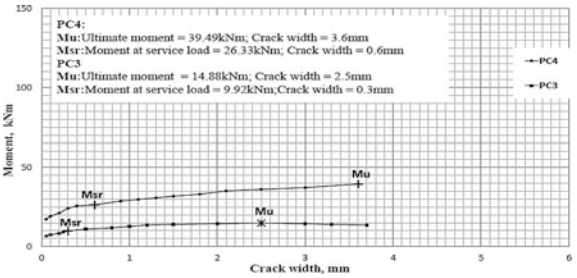

Fig. 13 Moment–crack width curves of two-pile caps PC3 and PC4

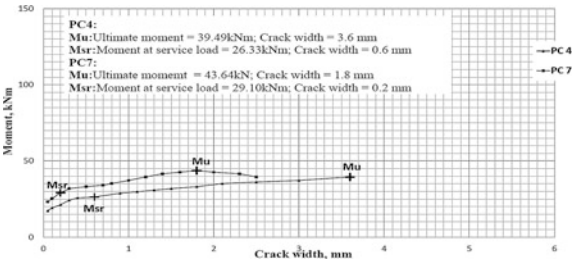

Fig. 14 Moment–crack width curves of two-pile caps PC4 and PC7

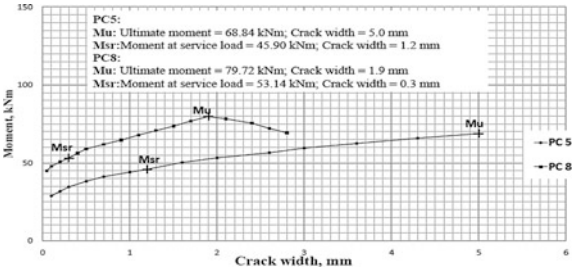

Fig. 15 Moment–crack width curves of two-pile caps PC5 and PC8

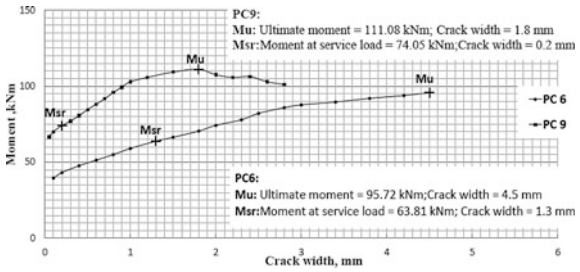

Fig. 16 Moment–crack width curves of two-pile caps PC6 and PC9

6 Discussion of Test Results

TPC, PC3 with shear span/effective depth ratio (*a*/*d*), 0.58 develops very high shear resistance by arch action. It is well known that at *a*/*d* equal to 1 shear resistance boosts to 8–10 times the normal bending shear resistance. PC3 with *a*/*d* = 0.58 develops much more shear resistance than a member with *a*/*d* equal to 1. PC3 though has high ultimate shear stress, 3.13 MPa, it is nullified by high arch action. Failure occurred in bending as predicted by the code. PC4 with *a*/*d* equal to 1.42 develops far less arch action and consequent shear resistance. Its high ultimate shear stress 3.44 MPa is not nullified completely due to less arch action, and shear failure has occurred as per code. TPCs, PC5 and PC6 have high *a*/*d* ratios 1.59 and 1.99, respectively, with less arch action and less development of shear resistance. The ultimate shear stress for both was at 3.28 MPa; consequently, both have failed in shear as per code. The three companion and identical TPCs, PC7, PC8 and PC9 to PC4, PC5 and PC6, respectively, were designed for shear to make them fail in bending.

7 Conclusions

Useful ideas gleaned from the experimental investigation undertaken are summed up in the conclusions listed below.

1. The long-awaited substantiation of specifications incorporated in IS456:2000 [1], relative to the occurrence of one-way shear on TPCs, has been established by the current tests on seven TPCs.
2. Four TPCs designed in accordance with Cl 34.2.4.1 and Cl 34.2.4.2 of IS 456:2000 [1] failed as prescribed by the code; TPC, PC3 failed in bending and TPCs PC4, PC5 and PC6 in shear. A designer of TPCs can follow the specifications of IS 456:2000 [1] to determine the mode of failure; if shear failure is predicted by the code, the TPC can be designed for shear reinforcement to force the failure in the desired flexure, as is done in the case of TPCs PC7, PC8 and PC9 in current investigation.

Table 4 Principal test results of two-pile caps

Specimen label	At initial crack					At service load					
	Column load (kN)	Moment at column face (kNm)	Shear force/ pile load (kN)	Shear stress (MPa)	Deflection (mm)	Column load (kN)	Moment at column face (kNm)	Shear force/ pile load (kN)	Shear stress (MPa)	Deflection (mm)	Rack width (mm)
PC 3	127.20	6.68	63.60	1.41	1.61	189.00	9.92	94.50	2.09	2.71	0.3
PC 4	135.15	17.23	67.58	1.50	2.05	206.47	26.33	103.24	2.29	3.40	0.6
PC 5	158.00	28.84	79.00	1.37	2.70	251.47	45.90	125.74	2.19	5.05	1.2
PC 6	173.80	39.54	86.90	1.36	3.64	280.50	63.81	140.25	2.19	6.60	1.3
PC 7	181.70	23.17	90.85	2.02	2.55	228.20	29.10	114.10	2.54	3.80	0.2
PC 8	246.40	44.97	123.20	2.14	4.10	291.20	53.14	145.60	2.53	5.10	0.3
PC 9	292.60	66.57	146.30	2.28	5.75	325.5	74.05	162.75	2.54	6.60	0.2

Specimen label	At ultimate load						Type of failure
	Column load (kN)	Moment at column face (kNm)	Shear force/ pile load (kN)	Shear stress (MPa)	Deflection (mm)	Crack width (mm)	
PC 3	283.50	14.88	141.75	3.13	5.55	2.5	Flexure
PC 4	309.70	39.49	154.85	3.44	7.25	3.6	Shear
PC 5	377.20	68.84	188.60	3.28	9.80	5.0	Shear
PC 6	420.75	95.72	210.38	3.28	11.60	4.5	Shear
PC 7	342.30	43.64	171.15	3.80	8.15	1.8	Flexure
PC 8	436.80	79.72	218.40	3.80	10.55	1.9	Flexure
PC 9	488.25	111.08	244.13	3.81	12.00	1.8	Flexure

References

1. IS 456:2000. *Indian Standard code of practice for plain and reinforced concrete*. New Delhi: Bureau of Indian Standards.
2. IRC: 21-2000. (2000). "*Standard Specifications and Code of Practice for Road bridges" section: III Cement concrete (Plain and Reinforced).* The Indian Road Congress.
3. IS 383:1970. (reaffirmed 1997). *Specifications for coarse and fine aggregates from natural sources for concrete*. New Delhi: Bureau of Indian Standards.

Comparative Study of Flat Slab-Column Connection Techniques for Seismic Loading

Aastha Mahajan, Ratnesh Kumar and Onkar G. Kumbhar

Abstract In the present paper, comparative study of flat slab-column connection techniques for lateral loading has been made for a symmetrical plan of a ten-storey building. The modelling has been done for a flat plate directly resting on columns. Since there are issues in modelling of flat slab, out of which, one of the most important issues taken in this paper is the effect of torsion transfer in the slab-column connections. The study has been done using three different torsional stiffnesses of slab-column connection, and their performance assessment has been done for a moderate seismic zone. From linear analysis, change in fundamental period of vibration has been studied. Further, the performance of these building models has been assessed using non-linear static analysis. The present study finds the results of 'Unified Equivalent Frame Model' (UEFM) to be the most reliable because of the inclusion of the effect of both gravity and lateral loads in the calculation of torsional stiffness of the slab-column connections.

Keywords Flat slab · Torsion · Pushover analysis · Lateral load
Gravity load

1 Introduction

Flat slab buildings are widely used form of RCC structures due to their efficiency in terms of easier formwork, increased storey height and better architectural appearance. Many times designers consider only gravity loads for designing flat slab buildings. Flat slab structures designed without considering seismic load may not have enough lateral strength and ductility to resist earthquake ground motions. In beams, local hinge failure is possible, but in the case when beams are not there, hinges will be formed directly in slab and in columns, which might subsequently

A. Mahajan · R. Kumar (✉) · O. G. Kumbhar
Department of Applied Mechanics, Visvesvaraya National Institute of Technology, South Ambazari Road, Nagpur 440010, Maharashtra, India
e-mail: ratneshkumars@apm.vnit.ac.in

A. Rama Mohan Rao and K. Ramanjaneyulu (eds.), *Recent Advances in Structural Engineering, Volume 1*, Lecture Notes in Civil Engineering 11,
https://doi.org/10.1007/978-981-13-0362-3_14

lead to a global structural failure quickly and catastrophically. Since the column connection is only over part of slab, hence, the rotation of slab along a transverse section at the column support will vary and will be equal to the column rotation only in the immediate vicinity of the column, resulting in torsion. Therefore, the study of behaviour of flat slab for seismic forces and the effect of torsion in slab-column connections need to be understood.

For modelling the flat slab, Allen and Darvall [1] provided tables of effective width coefficients for different combinations of plate aspect ratios (l_1/l_2) and column width-to-slab span ratios (c_1/l_1 or c_2/l_1). Hwang and Moehle [2] provided equations for effective width that indicate that the relationship between exterior and interior bays is about one-half. The following equations can be used in lieu of tables from Allen and Darvall [1]:

$$\text{For interior bays: } b = 2c_1 + \frac{l_1}{3}, \tag{1}$$

$$\text{For exterior bays: } b = c_1 + \frac{l_1}{6}, \tag{2}$$

where b is defined as the effective slab width, c_1 is defined as the column dimension parallel to span and l_1 is defined as the centre to centre span length in the direction under consideration (Fig. 1).

To take the effect of transfer of torsion, the flat slab has been modelled using the model proposed by Benavent-Climent [3], for wide beams, according to which the wide beam can be divided into three fictitious parts, and is interconnected to the columns with the help of torsional springs (as shown in Fig. 2). ACI 318 [4] provides the following equations for calculating the torsional stiffness which was derived under the basis of flat slab subjected to the gravity loads:

$$K = \sum \frac{9E_{\mathrm{CS}}C}{l_2\left(1 - \frac{c_2}{l_2}\right)^3}, \tag{3}$$

$$C = \sum \left(1 - \frac{0.63x}{y}\right)\left(\frac{x^3 y}{3}\right), \tag{4}$$

where c_2 is defined as width of column, x is defined as the shorter overall dimension of rectangular part of cross section, y = longer overall dimension of rectangular part of cross section and E_{cs} = modulus of elasticity of slab concrete.

To take the effect of lateral loads in the performance of flat slab, Park et al. [5] had proposed a different equation for the calculation of torsional stiffness, i.e. modified effective beam model. The equations for torsional stiffness as derived by Park et al. are Eqs. (5) and (6)

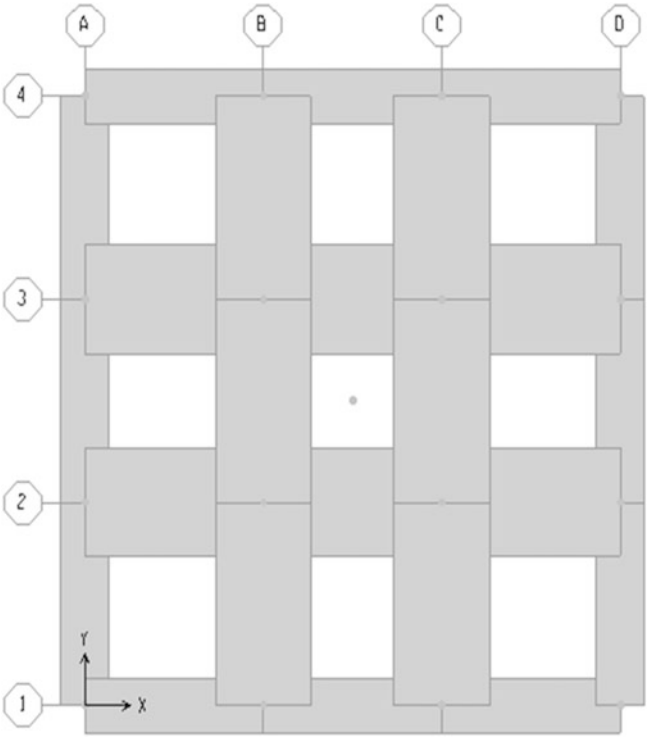

Fig. 1 Equivalent beam width model

$$K = \sum \frac{6E_{\mathrm{CS}}C}{l_2\left(1-\frac{c_2}{l_2}\right)^3}, \tag{5}$$

$$C = \sum \left(1 - \frac{0.63x}{y}\right)\left(\frac{x^3 y}{3}\right). \tag{6}$$

The equation for flexural stiffness of the slab is as given in Eq. (7).

$$K_S = \frac{4E_c I_S}{l_1}. \tag{7}$$

To take the effect of both lateral and gravity loads, Shin et al. [6, 7] proposed a different model called unified equivalent frame method to take the effect of both lateral and gravity loads in the calculation of torsional stiffness at slab-column connections as given in Eqs. (11) and (12). A new parameter called load ratio factor (λ_c) has been introduced in this model which is the relative ratio of the torsional

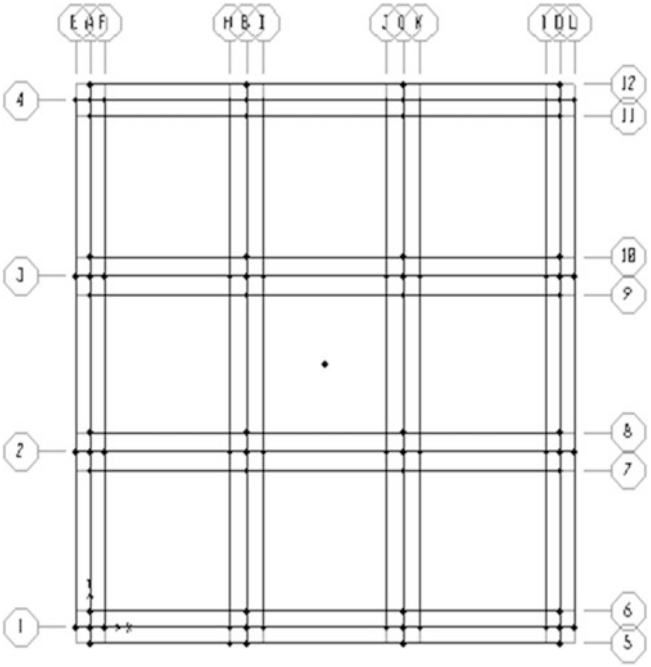

Fig. 2 Equivalent frame model with torsional springs used in the slab-column connections

moment due to lateral loads (T_l) to the torsional moment due to gravity loads (T_g) as given in Eq. (8)

$$\lambda_c = \frac{T_l}{T_g}. \tag{8}$$

For determining the load ratio factor, torsional moments due to lateral and gravity load can be found out using Eqs. (9) and (10)

$$T_g = M_S\left(\frac{K_{tg}}{K_{tg} + \sum K_{ci}}\right), \tag{9}$$

$$T_l = M_{ub}\left(\frac{K_{tg}}{K_{tl} + \sum K_{si}}\right), \tag{10}$$

$$K_{t,\lambda c} = \frac{18\,\mathrm{CE}_C(1+\lambda_c)}{l_2\alpha^2(2\alpha+3\lambda_c)}, \tag{11}$$

$$C = \sum\left(1 - \frac{0.63x}{y}\right)\left(\frac{x^3 y}{3}\right), \tag{12}$$

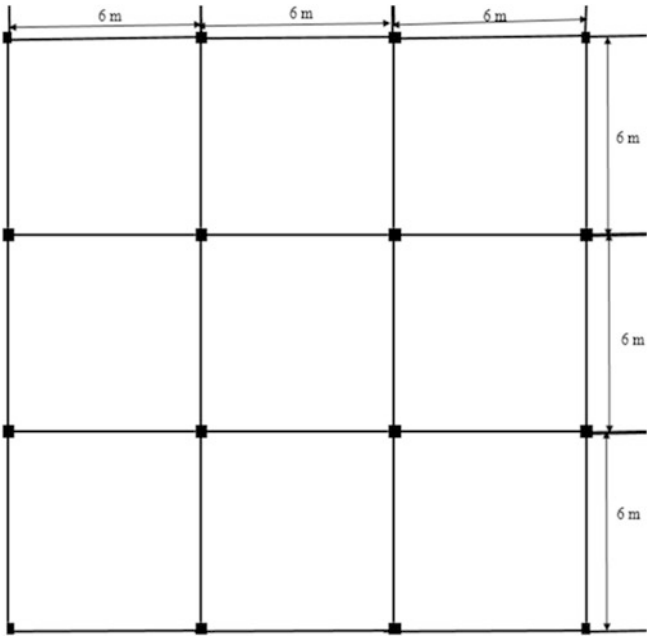

Fig. 3 Plan of the building to be analysed and designed

where α is $\left(1 - \frac{c_2}{l_2}\right)$.

Therefore, this study is limited to the analytical investigation of the seismic behaviour of the RC Flat slab buildings and the effect of modelling techniques of flat slab has been studied by performing linear and non-linear static pushover analysis on the buildings using SAP 2000. The cracking effect is not considered in this study. To avoid the effect of other geometrical deficiencies on structural behaviour, a regular and symmetrical building plan has been selected (Fig. 3). Four different building models have been developed with a same basic plan.

2 Specification of Building

Selected regular ten-storey building with symmetric plan (Fig. 3) is very much similar to the plan of an office, hotel, school or a public building. The plan is symmetric in both longitudinal and transverse directions with constant storey height of 3 m above plinth level.

Seismic force has been calculated as per Indian Standard IS 1893-Part I [8] considering a minimum base shear correction. The building is situated on medium soil in seismic zone III and designed to meet the requirements of IS 456 [9]. Effect

of cracking stiffness is ignored. Concrete with nominal characteristic compressive strength of 25 MPa and steel with 415 MPa yield strength has been used in the design.

3 Modelling and Analysis

To check the changes in performance of flat slab with different modelling approaches such as effective beam width model which is modelled without considering torsional stiffness, and the remaining three models ACI equivalent frame model [2], modified effective beam model [3] and unified effective beam model [4] are modelled using the Benavent-Climent model [1] with the equations for torsional stiffness differing from each other. Nomenclatures of all the building models and their brief description have been presented in Table 1. The sectional properties of equivalent beams used for modelling flat slabs are taken as 600 × 125 mm for central beams, 500 × 125 mm for exterior beams and 1300 × 125 mm for interior beams. Sectional properties for corner columns are 300 × 450 mm and for the other columns 600 × 600 mm.

Structural modelling, analysis and design have been performed in SAP 2000 (V-14.2.4) [10]. Effective beams and columns have been modelled using 3D frame elements. The foundation has been considered as rigid and all the six degrees of freedom at the base of the ground storey columns have been restrained. The in-plane rigidity of the slab has been modelled using diaphragm constraint. Response spectrum analysis is performed on the building to compute seismic force. Lumped plastic hinge model [FEMA 356/ASCE 41-06] [11, 12] has been used to simulate the non-linear behaviour of members. In the flat slab models, the columns have been assigned the coupled axial moment (P-M_2-M_3) auto hinges (which are inbuilt in SAP 2000), and the cracking effect in the stiffness of all the members has been ignored.

In beams, the hinges are generated using the moment curvature obtained from the section designer, the yield moment and yield rotation. These parameters are given as input in the hinge properties where the curvature is converted into rotation using Eqs. (13) and (14) from Eurocode 8—Part 3 (CEN 2005) [13]:

Table 1 Details of different models of flat slab buildings

Model	Description
ACI-EFM	Flat slab modelled as ACI-based equivalent frame model
MEFM	Flat slab modelled as modified equivalent frame model
UEFM	Flat slab modelled as unified equivalent frame model

$$\theta_y = \phi_y \frac{(L_v + a_V z)}{3} + 0.00135\left\{1 + \frac{1.5H}{L_v}\right\} + \frac{0.13\phi_y d_b f_y}{0.5 f_c}, \tag{13}$$

$$\theta_u = \theta_y + (\theta_u - \theta_y) L_p \left(1 - \frac{0.5 L_p}{L_v}\right). \tag{14}$$

Non-linear Static Procedure (NSP) has been used to study the non-linear behaviour of the buildings and to estimate the seismic performance. Lateral load deformation pattern based on storey mass as per FEMA 356 for obtaining capacity curve has been used.

3.1 Modal Analysis Results

To recognize the difference in modelling approaches on the modal parameters of flat slab structure, modal analysis has been performed on all four building models. The natural time period of ACI-EFM is 8.88% less than UEFM and that of MEFM is 2.96% more in first two modes. And in the third mode, the natural time period of ACI-EFM is 6.3% less than UEFM and that of MEFM is 2.27% more than UEFM. Thus, the time period for ACI-EFM is the least making it the stiffest structure since more stiffness leads to a reduction in natural time period of the building. It is observed that MEFM is the most flexible structure having the maximum natural time period. In terms of the models with torsional stiffness, we can conclude that the stiffness of ACI-EFM is the most, followed by UEFM and MEFM. First three natural periods of all the four models are presented in Table 2.

3.2 Non-linear Analysis Results

The different pushover curves in terms of base shear and roof displacement in longitudinal for different models are compared as shown in Fig. 4.

All curves are approximated by means of bi-linearization as stated in FEMA 356 to calculate the yield force, yield displacement and stiffness. The displacement corresponding to the ultimate base shear is calculated as ultimate displacement. Ductility and collapse margin ratio have also been calculated and shown in Table 4. Performance is assessed at three levels of drift 1, 2 and 4% as stated in FEMA 356 of the total building height since the target displacements found conventionally were misguiding.

The hinge formation pattern has been given in Table 3. From Tables 3 and 4, the following observations were made. The yield strength of UEFM is least and that of ACI-EFM is most which is correlated with the base force of the respective models. The yield strength (with respect to yield base force) of ACI-EFM is 1.06 times more

Table 2 Modal information of different models of flat slab building

Models	Vibration mode 1			Vibration mode 2			Vibration mode 3		
	Displacement direction	Time period (s)	Modal mass participating ratio (%)	Displacement direction	Time period (s)	Modal mass participating ratio (%)	Displacement direction	Time period (s)	Modal mass participating ratio (%)
ACI-EFM	T_y	2.46	75	T_x	2.44	75	T_o	2.07	22.6
MEFM	T_y	2.78	73.5	T_x	2.76	73.3	T_o	2.25	22.1
UEFM	T_y	2.7	74	T_x	2.67	74	T_o	2.2	22.3

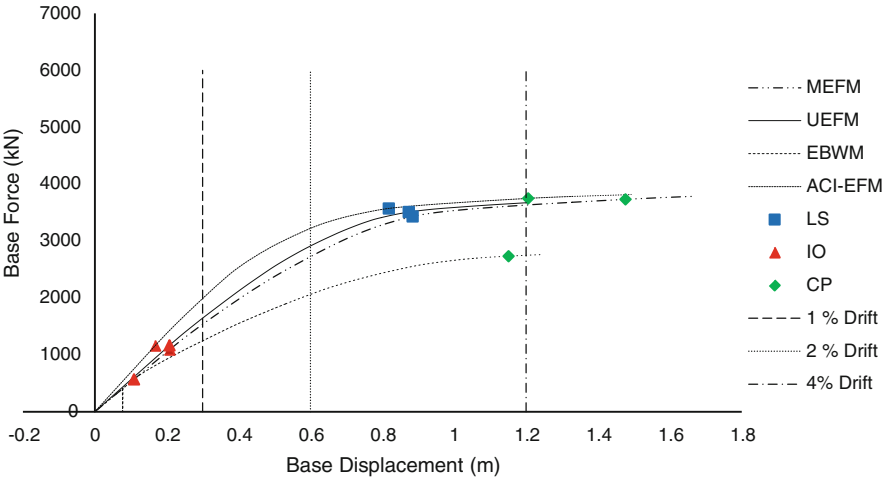

Fig. 4 Pushover analysis curves of different models of flat slab in *X* direction

than UEFM, and the yield strength of MEFM is 1.03 times that of UEFM. The base force carried at 1% drift of the total height, EBWM is carrying 0.75 times UEFM, MEFM is carrying 0.93 times UEFM and ACI-EFM is carrying 1.2 times base force. At 2% drift of the total height, ACI-EFM is carrying 1.1 times, EBWM is carrying 0.7 times and MEFM is carrying the same base force as that of UEFM.

The maximum initial stiffness is for ACI-EFM followed by UEFM and MEFM. The difference in stiffness of the various models of flat slab is directly proportional to the respective torsional stiffness of the slab-column connections. It is also found that the ductility of UEFM is the least. Ductility of ACI-EFM is 1.76 times more and that of MEFM 1.25 times more than UEFM. The yield force for ACI-EFM is 1.06 times more than UEFM. The yield displacement of ACI-EFM 0.68 times less and for MEFM 1.1 times more than UEFM. The CR at DBE level and MCE level for ACI-EFM is 1.27 times more and for MEFM, it is 1.02 times more than UEFM. The IO level hinges are first formed in MEFM, UEFM and ACI-EFM, which means that at IO level, MEFM is giving the worst performance and ACI-EFM is giving the best performance. There is no formation of CP level hinges for UEFM; therefore, the CR has been found at LS level hinge.

Inter-storey drift is found at 2% drift of the total height as shown in Fig. 5. The peak inter-storey drift % for Push *X* load case for EBWM is 0.98 times UEFM, for ACI-EFM it is 1.07 times UEFM and for MEFM it is 0.98 times UEFM.

Table 3 Hinge pattern for different models of flat slab buildings

	EBWM			ACI-EFM			MEFM			UEFM		
	1% DRIFT	2% DRIFT	4% DRIFT	1% DRIFT	2% DRIFT	4% DRIFT	1% DRIFT	2% DRIFT	4% DRIFT	1% DRIFT	2% DRIFT	4% DRIFT
IO	60	114	288	70	330	288	50	173	481	56	217	497
LS	–	–	0	–	–	0	–	–	57	–	–	–
CP	–	–	2	–	–	2	–	–	–	–	–	–

Table 4 Pushover analysis results of different models of flat slab buildings

Model	ACI-EFM	MEFM	UEFM
Yield force (KN)	3300	3200	3100
Yield displacement (mm)	400	640	580
Ultimate displacement (mm)	1480	1680	1200
Ductility	3.7	2.62	2.1
(CR) Collapse ratio at LS level			
DBE	30	24	23.6
MCE	15	12	11.8

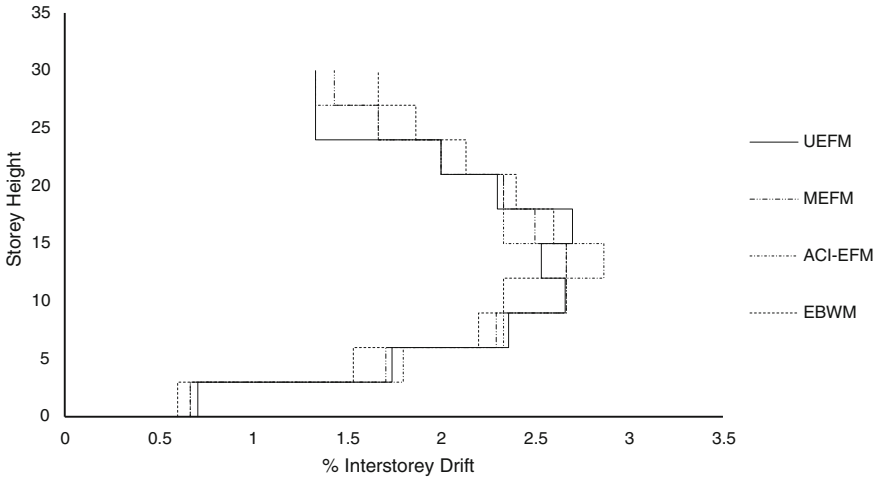

Fig. 5 Inter-storey drift (%) for different models of flat slab at 2% drift of the total height of the building

4 Conclusion

It has been observed that many times in the seismic design practice, the designers ignore the effect of torsion on slab-column connections during the modelling of flat slab. In reality, the torsion will get transferred because the width of the column supporting the flat slab will be relatively very small; therefore, the rotation of the column will be equal to the rotation of slab only in the immediate vicinity of column and will vary with the distance, and therefore, it will result in torsion. To take care of this, the present study deals with the effect of transfer of torsion in the slab-column connection by providing torsional spring of different proposed stiffnesses. From the modal analysis, it has been observed that the MEFM is the most flexible structure having the maximum natural time period. It is observed that the stiffness of ACI-EFM is the highest, followed by UEFM and MEFM. Evaluation of

Inter-storey drift also shows that the value of torsional stiffness influences the stiffness of flat slab. The peak inter-storey drift is the least for ACI-EFM and maximum for MEFM. The formation of hinges is first in MEFM and lastly in ACI-EFM. Collapse ratio values are also most conservative for ACI-EFM. The present study finds the results of UEFM most reliable, because of the inclusion of the effect of both gravity and lateral loads in the calculation of torsional stiffness of the slab-column connections.

References

1. Allen, F., & Darvall, P. (1977). *Lateral Load Equivalent Frame*. American Concrete Institute, Detroit, Michigan, *74(7)*, 294–299.
2. Hwang, S. -J., & Moehle, J. P. (2000). *Models for Laterally Load Slab–Column Frames*. American Concrete Institute, Detroit, Michigan, *97(2)*, 345–353.
3. Benavent-Climent, A. (2007). Seismic behaviour of RC wide beam-column connections under dynamic loading. *Journal of Earthquake Engineering, 11*(4), 493–511.
4. ACI 318. (2008). *Building Code Requirements for Structural Concrete*. American Concrete Institute, Michigan, United States.
5. Park, Y. M., Han, S. W., & Kee, S. H. (2009). A modified equivalent frame method for lateral load analysis. *Magazine of Concrete Research, 61*(5), 359.
6. Shin, M., Choi, S. H., Lee, D. H., Oh, J. Y., Kim, K. S., & Lee, J. Y. (2014a). Unified equivalent frame method for flat plate slab structures under combined gravity and lateral loads —Part 2: Verification.
7. Shin, M., Kim, K., Choi, S. H., Ju, H., Lee, D. H., & Lee, J. Y. (2014b). Unified equivalent frame method for flat plate slab structures under combined gravity and lateral loads—Part 1: Derivation.
8. IS 1893 (Part 1). (2002). *Criteria for Earthquake Resistant Design of Structures: Part 1 General Provision and Buildings (fifth revision)*. BIS, New Delhi, India.
9. IS 456. (2000). *Plain and Reinforced Concrete-Code of Practice*. Indian Standard, New Delhi, India.
10. SAP2000 Tutorial Manual, SAP2000 Integrated Finite Elements Analysis and Design of Structures tutorial Manual, Computers and Structures, Inc., Berkeley, California, USA.
11. FEMA 356. (2000). *Pre-standard and commentary for the seismic rehabilitation of buildings*. Federal Emergency Management Agency, Washington, DC.
12. ASCE 41. (2007). *Seismic Rehabilitation of Existing Buildings (ASCE)*. American society of Civil Engineers, Reston, VA.
13. EN 1998-3. (2005). *Design of structures for earthquake resistance—Part 3*. Eurocode 8, London, Britain.

Comparative Study of 1D and 2D Simulation Models of Hollow RC Bridge Columns Under Reversed Cyclic Loads

Vijay Kumar Polimeru, Abhideep Sahu and Arghadeep Laskar

Abstract Reinforced concrete (RC) bridge columns can be subjected to large dynamic loads during earthquakes. In order to design these structures, a thorough understanding of their nonlinear behavior is essential. 1D and 2D numerical simulation models are generally used for the analysis of these structures under axial loads and uniaxial bending. The iterative process used in the numerical simulation is cost-sensitive and time-consuming because of the complex constitute relationships of the materials. In this study, two hollow RC bridge columns tested under reversed cyclic loads at the National Centre for Research on Earthquake Engineering (NCREE) Taiwan have been analyzed using both 1D and 2D numerical simulation models. Analysis results from both simulation models such as primary backbone curves, hysteretic loops including pinching effects, and the strength degradation in the post-peak region have been compared and verified with the experimental data.

Keywords RC bridge column · Reversed cyclic load · Nonlinear analysis
Hysteretic loops

1 Introduction

Reinforced concrete (RC) bridge columns can be subjected to large dynamic loads during earthquakes. In order to design these structures, a thorough understanding of their nonlinear behavior is essential. Macro-models and micro-models are the two types of analytical models commonly used for the analysis of these structures.

V. K. Polimeru · A. Sahu · A. Laskar (✉)
Department of Civil Engineering, IIT Bombay, Mumbai 400076, India
e-mail: laskar@civil.iitb.ac.in

V. K. Polimeru
e-mail: vijaykumarpolimeru@iitb.ac.in

A. Sahu
e-mail: abhideep.sahu@gmail.com

A. Rama Mohan Rao and K. Ramanjaneyulu (eds.), *Recent Advances in Structural Engineering, Volume 1*, Lecture Notes in Civil Engineering 11,
https://doi.org/10.1007/978-981-13-0362-3_15

Macro-models analyze the bridge column by treating it as a cantilever and are essentially one-dimensional (1D) models, whereas micro-models analyze the bridge columns by treating it as a combination of plane-stress elements and beam-column elements. Hence, these models are two-dimensional (2D) models. Examples of 1D simulation models are equivalent beam model (EBM) [1], multiple vertical line element model (MVLEM) [1], and modified multiple vertical line element model [2]. These models are very good in predicting the macro-level properties such as load deformation relationships but are not useful for micro-level analysis or for doing a complete stress analysis. On the other hand, researchers have developed various rational analytical micro-models for more than three decades to study the nonlinear behavior of RC structures by predicting both the macro-level load deformation parameters and micro-level stress–strain properties. These models include equilibrium plasticity truss model [3], Mohr compatibility truss model (MCTM) [4], compression field theory (CFT) [5], modified compression field theory (MCFT) [6], rotating angle softened truss model (RA-STM) [7], fixed angle softened truss model (FA-STM) [8], softened membrane model (SMM) [9], and cyclic softened membrane model (CSMM) [10]. However, the validity of these analytical models in predicting the shear behavior of RC structures is not certain. Out of all the micro-models, cyclic softened membrane model (which is based on smeared crack concept and satisfies Navier's principles of mechanics) is able to predict the shear behavior of RC structures with reasonable accuracy [11]. The 1D and 2D simulation models can be improved by implementing the damage parameters [12, 13] in the constitutive relationships of concrete and steel. In the past, the cyclic and dynamic response of RC shear walls has been predicted using CSMM-based 2D plane-stress elements [14]. 1D models using nonlinear beam-column elements have been used to predict the seismic behavior of hollow rectangular RC bridge columns [15] and cyclic behavior of GFRP-strengthened hollow rectangular RC bridge columns [16]. Recently, a combination of nonlinear beam-column elements and CSMM-based 2D plane-stress elements has been used to predict the cyclic response of post-tensioned hollow rectangular bridge columns tested at SUNY Buffalo [17]. However, no literature on comparative study of 1D and 2D models for bridge columns is reported till date. In this study, two rectangular hollow RC bridge columns, PI1 and PI2, tested under reversed cyclic loads at the National Centre for Research on Earthquake Engineering (NCREE) Taiwan [18] have been analyzed using both 1D and 2D numerical simulation models. Plane-stress elements developed using cyclic softened membrane model (CSMM) have been used for the 2D analysis. The results obtained from the 1D and 2D models have been compared with the experimental results. The efficiency of 1D and 2D models in predicting the load deformation relationships has been studied by comparing the results. The effectiveness of implementing the damage parameters into the constitutive laws has been demonstrated by comparing the analytical results obtained from the present study with the analytical results obtained from previous simulations of the bridge columns available in the literature.

2 Methodology

Nonlinear finite element models in 1D and 2D have been developed and analyzed using OpenSees finite element software. The uniaxial material model of concrete developed by Chang and Mander [12] has been used along with a uniaxial trilinear hysteretic steel material model [13] for longitudinal reinforcement. Chang and Mander's concrete model [11] is a generalized constitutive model which defines the damage properties of concrete. In this study, the damage parameters for concrete consisting of the shape parameters in Tsai's equation [19] defined for compression (r_c) and tension (r_t), nondimensional critical strain on compression envelope (x_{cr}^{-ve}) and tension envelope (x_{cr}^{+ve}) have been calibrated with respect to aspect ratio. A detailed explanation of these parameters is given in [12]. On the other hand, the hysteretic steel model is a generalized trilinear model which also defines the damage properties of steel. In this study, the damage properties for steel consisting of thee pinching factors during reloading for strain (P_x) and stress (P_y), damage due to ductility (D_1) and energy (D_2), and power used to determine the degraded unloading stiffness based on ductility (β) have been calibrated with respect to aspect ratio. A detailed explanation of these parameters is given in [13]. The calibrated values are tabulated in Tables 1 and 2. The constitutive relationships are shown in Fig. 1. Confined concrete (concrete within the stirrups) properties have been calculated using a model developed by Mander et al. [20]. The material and geometric properties of the specimens are listed in Table 3 along with their reinforcement details. The aspect ratio (height-to-width ratio) of the specimens PI1 and PI2 is 2.7 and 2.0, respectively. The bridge columns have been modeled as a cantilever fixed at the bottom in the 1D model. 11 nonlinear beam-column elements are used for the analysis. In each element, the entire cross section of the bridge columns has been divided into 8 fibers of unconfined concrete, 4 fibers of confined concrete, and 64 fibers of steel. In the 2D model, two of the bridge column walls have been modeled with ten RC plane-stress elements, and each of the other two walls has been modeled with five nonlinear beam-column elements consisting of 4

Table 1 Properties of confined and unconfined concrete with respect to aspect ratio

Concrete type	Aspect ratio (L/d)	r_c	x_{cr}^{-}	r_t	x_{cr}^{+}
Confined	>2	7	1.035	6	10,000
Unconfined	>2	7	1.035	6	10,000
Confined	≤ 2	7	1.035	3	1.5
Unconfined	≤ 2	7	1.035	3	1.5

Table 2 Damage properties of steel with respect to aspect ratio

Aspect ratio (L/d)	P_x	P_y	D_1	D_2	β
>2	0.6	1.0	0.011	0.2	0.5
≤ 2	0.3	0.1	0.040	0.8	0.3

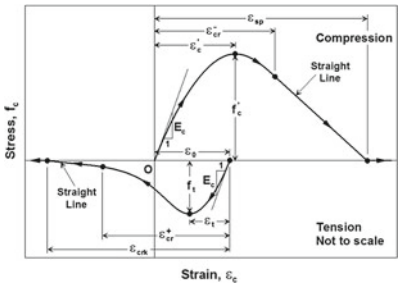

(a.) Constitutive relationship of concrete [12]

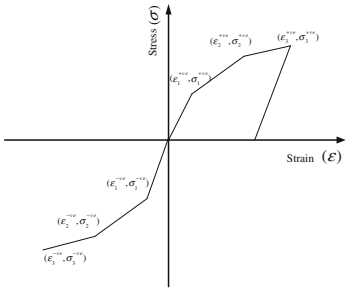

(b.) Constitutive relationship of steel [13]

Fig. 1 Constitutive relationships of steel and concrete

Table 3 Geometry and material properties of bridge columns

Specimen No.	f'_c (N/mm^2)	N (kN)	L (mm)	Longitudinal reinforcement			Transverse reinforcement		
				Dia. (mm)	f_y (N/mm^2)	f_{su} (N/mm^2)	Dia. (mm)	f_y (N/mm^2)	f_{su} (N/mm^2)
PI1	34	4000	4500	22	460.0	647.0	10	510.0	120
PI2	32	3600	3500	22	418.2	626.5	10	420.0	200

fibers of unconfined concrete, 2 fibers of confined concrete, and 32 fibers of steel. Both the columns have been subjected to a static axial load (N) and reversed cyclic load (P). The cross section and elevation of 1D and 2D models are shown in Fig. 2. Multipoint constraint has been applied at the nodes common to plane-stress and nonlinear beam-column elements. Modified Newton–Raphson method with Krylov subspace acceleration has been used for the analysis.

3 Results and Discussion

Hysteretic loops obtained from 1D to 2D models have been compared with the experimental results for both flexure dominant column PI1 and shear dominant column PI2. Comparing the results obtained from 1D to 2D simulation models developed in this study, it can be observed from Figs. 3 and 4 that the peak loads predicted from 1D to 2D analysis for specimen PI1 are 12 and 11% lower than the experimental peak loads, respectively. For specimen PI2, the predicted peak loads from 1D to 2D analyses are 1% lower and 5% higher than the test result, respectively. The run times for both 1D and 2D models were similar. Even though the absolute peaks are better predicted using 1D analysis, the slopes of loading and unloading curves and the pinching effects (pinched shape near origin) in the pre-

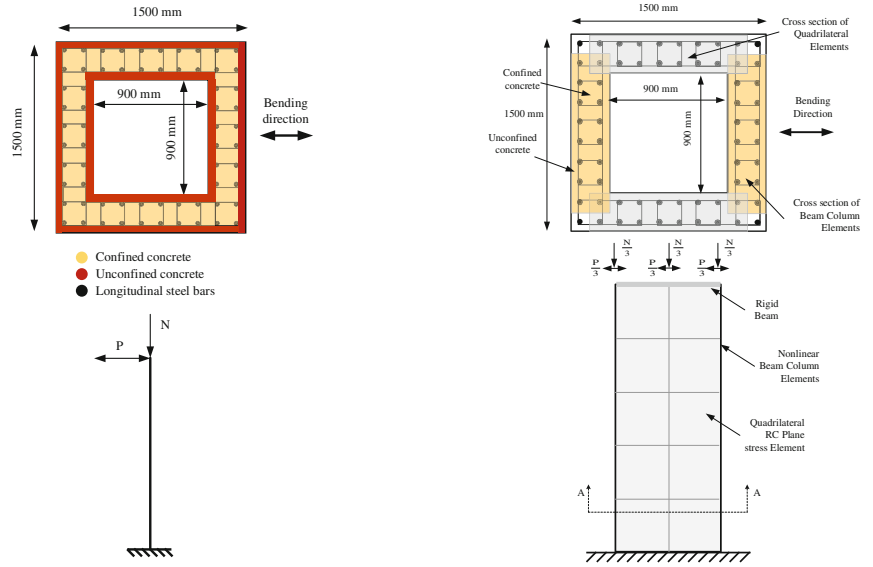

(a.) Cross section and elevation of 1D model (b.) Cross section and elevation of 2D model

Fig. 2 Cross section and elevation of 1D and 2D models

and post-peak regions of all cycles are better predicted using 2D model. It can thus be concluded that with some minor improvements in the prediction of the peak loads, CSMM-based plane-stress elements can be effectively used to predict the seismic performance of shear critical components of RC structures in place of the nonlinear beam-column element. The results obtained from the present study have also been compared with the analytical results available in the literature on these bridge columns, which were obtained using a 1D model developed by Mullapudi [21]. The constitutive relationships used were based on Kent and Park model [22] of concrete modified by adding constitutive relationship of concrete in tension, and Menegotto and Pinto model [23] was modified by Filippou et al. through addition of isotropic strain hardening effects for steel [24]. It can be observed from Figs. 5 and 6 that the present 1D model was able to better predict the peak loads, post-peak strength degradation, and pinching behavior of columns PI1 and PI2 compared to the 1D analysis results obtained by Mullapudi [21]. The better predictions obtained from the present study are due to the implementation of damage properties in the constitutive relationships of concrete and steel.

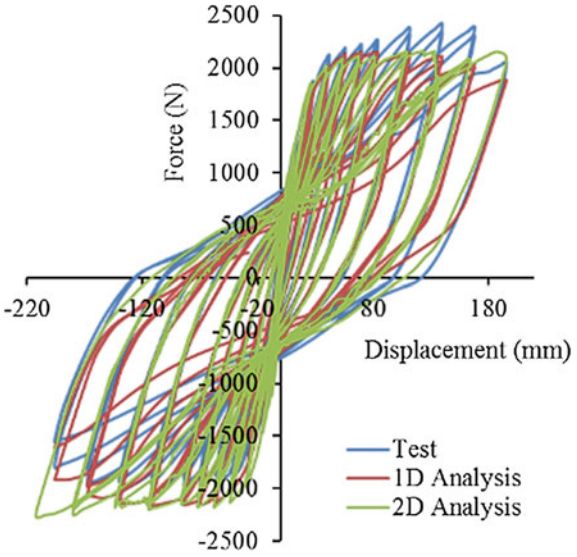

Fig. 3 Comparison of 1D and 2D analysis results of column PI1 with experimental results

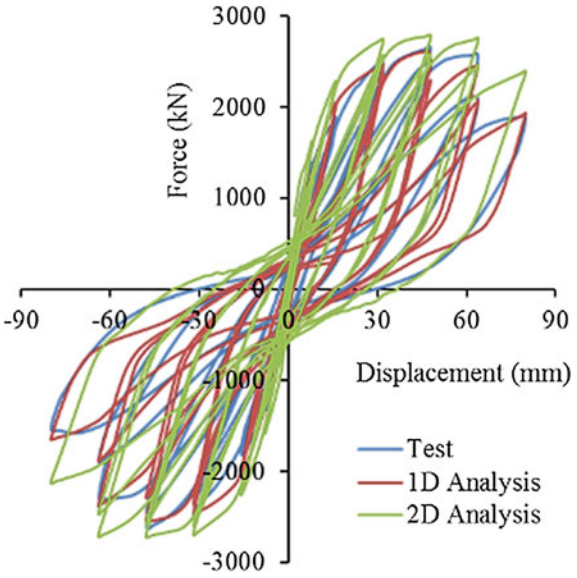

Fig. 4 Comparison of 1D and 2D analysis results of column PI2 with experimental results

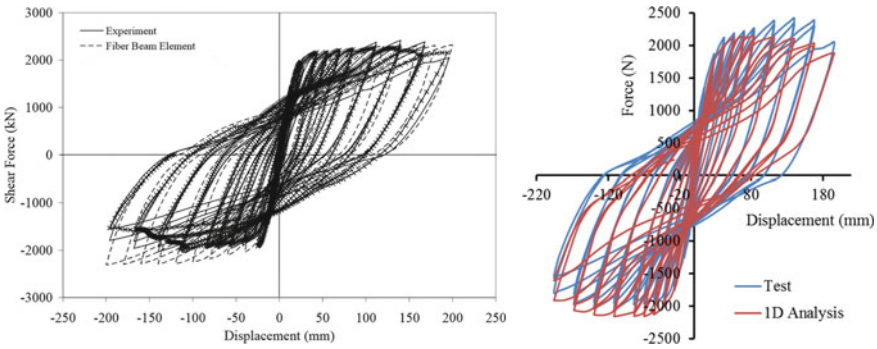

(a) Without Damage Properties (b) With Damage Properties

Fig. 5 Comparison of 1D analysis results of PI1 with experimental and Ref. [21]

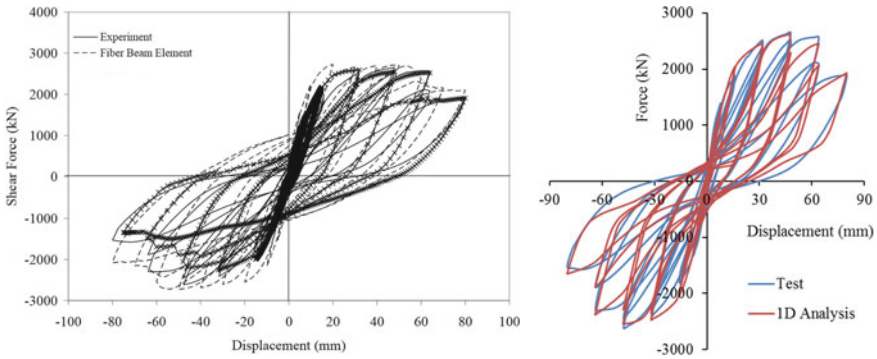

(a) Without Damage Properties (b) With Damage Properties

Fig. 6 Comparison of 1D analysis results of PI2 with experimental and Ref. [21]

4 Conclusions

The analytical results showed that the 1D model predicted the overall cyclic behavior more accurately compared to the 2D model developed in the present study. Hence, 1D model with damage parameters is effective for predicting the macro-level behavior of the bridge columns such as load deformation relationships. However, the certain characteristics of the column behavior such as the slopes of loading and unloading curves and the pinching effects in the pre- and post-peak regions of all cycles are better predicted by the 2D model. For solid columns, the results obtained from 1D to 2D analysis match for columns with higher aspect ratio (width to height greater than 0.2). At lower values of aspect ratio, the predictions from 2D analysis are higher than 1D analysis results. The implementation of the damage parameters in the constitutive relationships has improved the prediction of the shear behavior of the bridge columns compared to results available in literature

from models without damage parameters. However, the quantification of the damage properties with change of aspect ratio of the bridge column that has been implemented in the current simulation models needs to be verified with additional simulations of tested specimens.

References

1. Vulcano, A., Bertero, V. V., & Colotti, V. (1988). Analytical modeling of R/C structural walls. In *Proceedings of the 9th World Conference on Earthquake Engineering* (Vol. 6, pp. 41–46).
2. Orakcal, K., Wallace, J. W., & Conte, J. P. (2004). Flexural modeling of reinforced concrete walls-model attributes. *Structural Journal of the American Concrete Institute, 101*(5), 688–698.
3. Nielsen, M. P. (1967). Om forskydningsarmering af jernbetonbjælker (On shear reinforcement in reinforced concrete beams). Bygningsstatiske Meddeleser, *38*(2), 33–58 (Cophenhagan, Denmark).
4. Collins, M. P. (1978). Towards a rational theory for RC members in shear. *Journal of the Structural Division, ASCE, 104*(4), 649–666.
5. Mitchell, D., & Collins, M. P. (1974). Diagonal compression field theory-a rational model for structural concrete in pure torsion. *Journal Proceedings of the American Concrete Institute, 71*(8), 396–408.
6. Vecchio, F. J., & Collins, M. P. (1986). The modified compression-field theory for reinforced concrete elements subjected to shear. *Journal Proceedings of the American Concrete Institute, 83*(2), 219–231.
7. Hsu, T. T. C. (1988). Softened truss model theory for shear and torsion. *Structural Journal of the American Concrete Institute, 85*(6), 624–635.
8. Pang, X. B. D., & Hsu, T. T. C. (1996). Fixed angle softened truss model for reinforced concrete. *Structural Journal of the American Concrete Institute, 93*(2), 196–208.
9. Zhu, R. R. H. (2000). *Softened membrane model of cracked reinforced concrete considering the Poisson effect* (Ph.D. Dissertation). Department of Civil and Environmental Engineering, University of Houston, Houston, TX.
10. Mansour, M. (2001). *Behaviour of reinforced concrete membrane elements under cyclic shear: Experiments to theory* (Ph.D. Dissertation). Department of Civil and Environmental Engineering, University of Houston, Houston, TX.
11. So, M. G. (2008). *Total strain based bond/slip and shear/friction membrane model for finite element analysis of reinforced concrete* (Ph.D. Dissertation). Department of Mechanical, Aerospace and Structural Engineering, Washington University, Saint Louis, Missouri.
12. Chang, G. A., & Mander, J. B. (1994). *Seismic energy based fatigue damage analysis of bridge columns: Part I-Evaluation of seismic capacity*. Buffalo, NY: National Center for Earthquake Engineering Research.
13. Chang, Y. Y., Deng, H. Z., Lau, D. T., Ostovari, S., Tsai, K. C., & Khoo, H. A. (2004). A simplified method for nonlinear cyclic analysis of reinforced concrete structures: Direct and energy based formulations. In *Proceedings of the 13th World Conference on Earthquake Engineering*.
14. Mo, Y. L., Zhong, J., & Hsu, T. T. C. (2008). Seismic simulation of RC wall-type structures. *Engineering Structures, 30*(11), 3167–3175.
15. Zhao, Y., Jiang, H. Y., Gu, J., & Wang, R. Q. (2014). Seismic performance of reinforced concrete rectangular hollow bridge piers. *Advanced Materials Research, 859*, 95–99 (Trans Tech Publications).

16. Jia, J., Han, Q., Xu, Z., & Zhang, D. (2014). Cyclic load responses of GFRP-strengthened hollow rectangular bridge piers. *Advances in Materials Science and Engineering*.
17. Laskar, A., Mo, Y. L., & Hsu, T. T. C. (2016). Simulation of post-tensioned bridge columns under reversed-cyclic loads. *Materials and Structures*, 1–20.
18. Yeh, Y. K., Mo, Y. L., & Yang, C. Y. (2002). Full-scale tests on rectangular hollow bridge piers. *Materials and Structures, 35*(2), 117–125.
19. Tsai, W. T. (1988). Uniaxial compressional stress-strain relation of concrete. *Journal of Structural Engineering, 114*(9), 2133–2136.
20. Mander, J. B., Priestley, M. J., & Park, R. (1988). Theoretical stress-strain model for confined concrete. *Journal of structural engineering, ASCE, 114*(8), 1804–1826.
21. Mullapudi, T. R. S. (2010). *Seismic analysis of reinforced concrete structures subjected to combined axial, flexure, shear and torsional loads* (Ph.D. Dissertation). Department of Civil and Environmental Engineering, University of Houston, Houston, TX.
22. Kent, D. C., & Park, R. (1971). Flexural members with confined concrete. *Journal of the Structural Division.*
23. Menegotto, M., & Pinto, P. E. (1973). Method of analysis for cyclically loaded RC frames including changes in geometry and non-elastic behaviour of elements under combined normal force and bending. In *IABSE Congress Reports of the Working Commission* (Vol. 13, Issue 1).
24. Filippou, F. C., Popov, E. P., & Bertero, V. V. (1983). Effects of bond deterioration on hysteretic behaviour of reinforced concrete joints.

Comparative Study of Different Foundation and Sidewall Systems for Large Storage Tanks

T. Pavan Kumar, G. Papa Rao and P. Veerabhadra Rao

Abstract R.C.C tanks are widely used to store large quantities of water, and ground resting tanks without top slab are being used worldwide in sewage treatment plants (STPs). The type of foundation system and sidewall system for tanks depends on the type of soil and height of the tank. The authors tried two types of foundation systems and three types of sidewall systems keeping the capacity of tank being constant. Comparisons were made to evaluate the best structural system in terms of load dispersion and economy. To understand the behavior of large storage tanks, an open tank of size 30 m × 15 m × 5.5 m (0.5 m freeboard) is considered. The analysis is carried out in STAAD-Pro and designs were done by manually and the comparisons made between each system, and the most economic combination of sidewall and foundation system was arrived.

Keywords Water tanks · STAAD-Pro · Foundation systems

1 Introduction

R.C.C tanks are widely used to store large quantities of water and ground resting tanks without top slab are being used worldwide in sewage treatment plants (STPs). The type of foundation system and sidewall system for tanks depends on the type of soil and height of the tank. The authors tried two types of foundation systems and three types of sidewall systems keeping the capacity of tank being constant. Comparisons were made to evaluate the best structural system in terms of load

T. Pavan Kumar · G. Papa Rao (✉) · P. Veerabhadra Rao
Department of Civil Engineering, Gayatri Vidya Parishad College of Engg. (A), Visakhapatnam 530048, Andhra Pradesh, India
e-mail: gprao_74@gvpce.ac.in

T. Pavan Kumar
e-mail: pavan0971@gmail.com

P. Veerabhadra Rao
e-mail: pvr2889@gmail.com

A. Rama Mohan Rao and K. Ramanjaneyulu (eds.), *Recent Advances in Structural Engineering, Volume 1*, Lecture Notes in Civil Engineering 11,
https://doi.org/10.1007/978-981-13-0362-3_16

dispersion and economy. To understand the behavior of large storage tanks, an open tank of size 30 m × 15 m × 5.5 m (0.5 m freeboard) is considered. The analysis is carried out in STAAD-Pro and designs were done by manually and the comparisons made between each system and the most economic combination of sidewall and foundation system was arrived.

2 Modeling and Methodology

As per Indian Standard IS-3370 (PART-4), the moment coefficients for tanks with walls fixed and hinged at bottom are given for the values up to b/a = 0.5–3.0, where b = width of the wall and a = height of the wall, for ratios b/a > 3.0, the IS-3370 (PART-4) code is silent and the authors tried for b/a > 3.0. In the present study, a rectangular tank is considered of size 30 m × 15 m × 5.5 m of capacity 2250 kL, and the b/a ratio in the present study is 5.45. The main aim of this study is to understand the behavior of large storage tanks for which three sidewall systems and two foundation systems are considered. The study is carried for equal capacity of tanks with different sidewall systems such as free cantilever, framed type system, and twin wall system to resist water pressures and two foundation systems such as solid raft foundation system and cellular raft foundation system to resist uplift of the tank due to the water table effect. The tanks are analyzed and designed for hydrostatic and hydrodynamic pressures. Analysis has been carried out using STAAD-Pro software and designs were done by manually and the tanks are assumed to be fixed at the bottom and free and the top and the comparisons were made between each system. The best sidewall system and foundation system are selected based on load dispersion, and also the economy is taken into consideration and the most economic combination of sidewall and foundation system was arrived.

2.1 Preliminary Data for the Problem Taken

The dimensions of the tank considered in the analysis are of size 30 m × 15 m × 5.5 m, and the materials used are M30 grade concrete and Fe415 grade steel. Type of soil is hard rocky, and the tanks are considered to be in seismic zone-II. The capacity of the tank in all cases is taken to be 2250 m^3. The types of sidewall systems considered are shown in Figs. 1, 2 and 3, and the types of foundation systems considered are shown in Figs. 4 and 5.

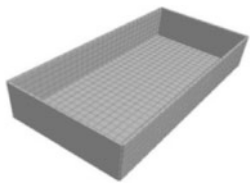

Fig. 1 Free cantilever type system

Fig. 2 Framed type system

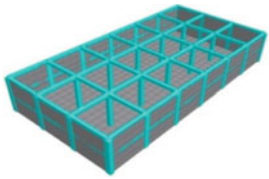

Fig. 3 Twin wall system

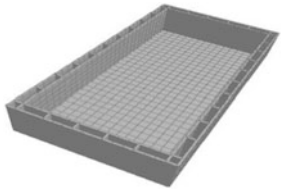

Fig. 4 Solid raft foundation system

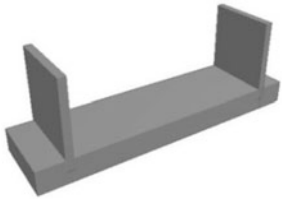

Fig. 5 Cellular raft foundation system

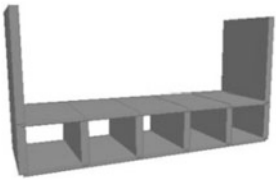

2.2 Modeling of Sidewall Systems

See Tables 1, 2 and 3.

2.3 Modeling of Foundation Systems

See Tables 4 and 5.

Table 1 Free cantilever type system

Size of tank	30 m × 15 m × 5.5 m
Wall thickness	0.3 m

Table 2 Framed type system

Size of the tank	30 m × 15 m × 5.5 m
Wall thickness	0.3 m
Distance between columns	3 m
Size of beams	0.3 × 0.45 m
Size of internal columns	0.45 m × 0.45 m
Size of external columns	0.45 m × 0.6 m

Table 3 Twin wall system

Size of the tank	30 m × 15 m × 5.5 m
Distance between transfer walls	3 m
Wall thickness	0.3 m
Width of transfer wall	1 m

Table 4 Solid raft foundation system

Size of foundation	30 m × 15 m
Water table effect from N.G.L	2 m
Slab projections of the tank base slab	2 m
Thickness of base slab	0.5 m

Table 5 Cellular raft foundation system

Size of foundation	30 m × 15 m
Center to center distance between deep beams	3 m
Thickness of top and base slabs	0.25 m
Size of deep beams	0.3 × 2.5 m

2.4 Tank Conditions

Tank condition-I: On ground resting tank with no soil pressure from outside and no water table effect on bottom surface of the tank as shown in Fig. 6.

Tank condition-II: On ground resting tank with soil pressure outside and no water table effect on bottom surface of the tank as shown in Fig. 7.

Tank condition-III: On ground resting tank with soil pressure outside and considering Water table effect on bottom surface of the tank as shown in Fig. 8.

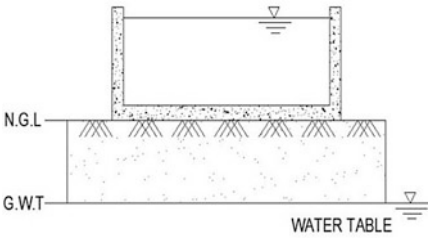

Fig. 6 Tank condition-I

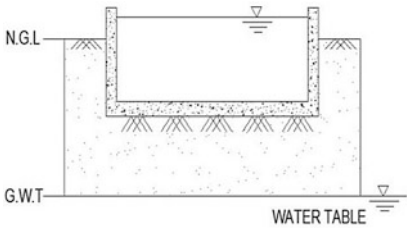

Fig. 7 Tank condition-II

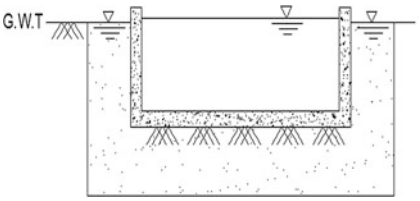

Fig. 8 Tank condition-III

2.5 Loadings Considered for the Analysis

1. Self-weight,
2. Uplift pressure,
3. Soil pressure,
4. Wind pressure,
5. Hydrostatic pressure, and
6. Hydrodynamic pressure.

2.5.1 Self-Weight

Self-weight of all the structural members such as walls, base slabs, beams, and columns are considered in the analysis. Unit weight of R.C.C is considered to be $\rho = 25$ kN/m^3.

2.5.2 Uplift Pressure

Uplift pressure of the tank is a major criterion when the water table is present above the base slab of the tank. As per IS:3370-(PART-1), the factor of safety against the uplift pressure of the tank is 1.2. The depth of water table considered in the analysis is 2 m from the ground level.

2.5.3 Soil Pressure

Soil pressure acts on the sidewalls of the tanks in both tank conditions-II and III, and soil pressure acts on sidewalls varying linearly from minimum at top and maximum at the bottom.

$$\text{Soil pressure acting on the wall} = (\text{coefficient of earth pressure}) \times (\gamma) \times (\text{height of wall}) = k_a \times \gamma \times H$$

2.5.4 Wind Pressure

Wind pressure acts on the sidewalls of the tanks in tank condition-I, and wind pressure acts on the tank sidewalls varying linearly from maximum at top and minimum at the bottom.

2.5.5 Hydrostatic Pressure

Hydrostatic pressure is the pressure exerted by water at rest condition, and hydrostatic pressure acts on sidewalls varying linearly from minimum at top and maximum at the bottom. Unit weight of water is taken to be γ_w = 9.8 kN/m^3.

$$\text{Hydrostatic pressure on the tank side wall} = (\text{unit weight of water}) \times (\text{height of wall}) = (\gamma_w) \times (H)$$

2.5.6 Hydrodynamic Pressure

Hydrodynamic pressure is the pressure exerted by water on tank sidewalls when the water is in motion. Hydrodynamic pressure depends on seismic zone and size of tank. Hydrodynamic pressure varies linearly from minimum at top and maximum at the bottom, the hydrodynamic pressure is expressed in terms of the hydrostatic pressure. Hydrodynamic pressure is calculated as per GSDMA guidelines for tank size of 30 m $\times$ 15 m $\times$ 5.5 m in zone-II.

$$\begin{pmatrix}\text{Hydrodynamic}\\ \text{pressure}\end{pmatrix} = 11.5\%\begin{pmatrix}\text{Hydrostatic}\\ \text{pressure}\end{pmatrix}$$

3 Presentation of Analysis Results

M_Y (kNm/m) = Bending moment about local Y-axis.
M_X (kNm/m) = Bending moment about local X-axis.
S_X (N/mm^2) = Axial stress along X-axis.
S_Y (N/mm^2) = Axial stress along Y-axis (Figs. 9, 10, 11 and 12).

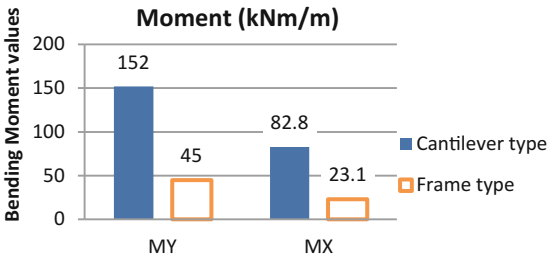

Fig. 9 Bending moments in cantilever and framed type tanks

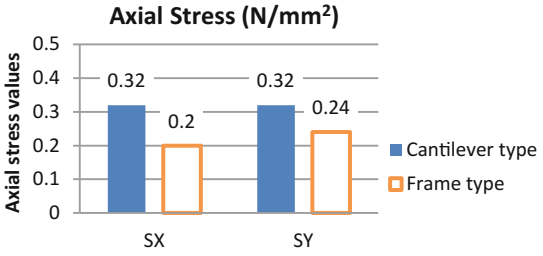

Fig. 10 Shear stresses in cantilever and framed type tanks

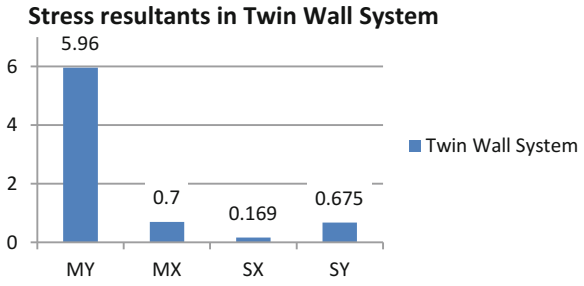

Fig. 11 Stress resultants in twin wall system

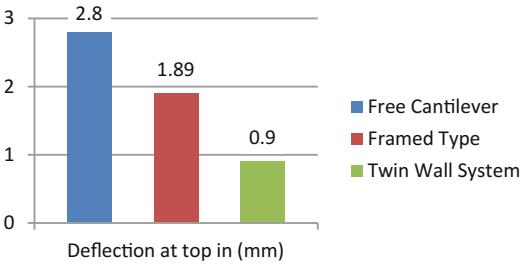

Fig. 12 Deflection in different systems

3.1 Design and Detailing of Sidewall Systems

See Figs. 13, 14, 15, 16, 17 and 18.

3.2 Design and Detailing of Foundation Systems

See Figs. 19 and 20.

4 Results and Discussions

When compared with framed type tank, the bending moment in free cantilever type tank is 83.57% higher and 92.8% lesser in twin wall system. The axial stress in free cantilever type tank is 16.67% lesser and 181.25% higher in twin wall system when

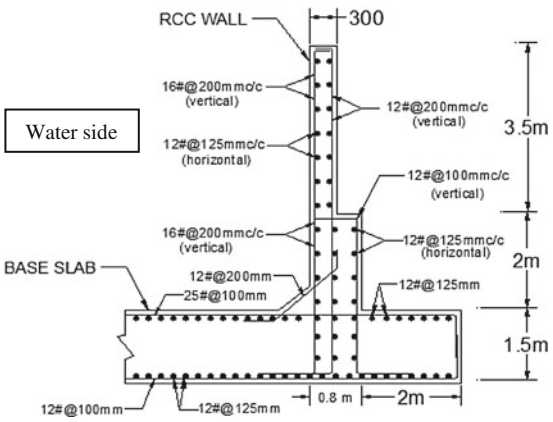

Fig. 13 Free cantilever type system

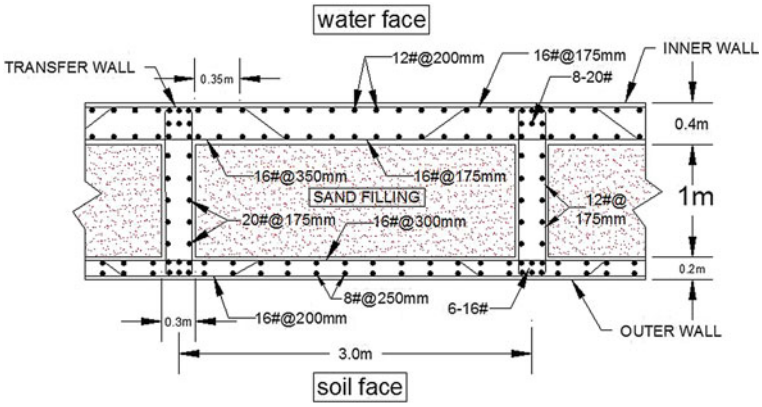

Fig. 14 Twin wall system

Fig. 15 Wall panels in framed type system

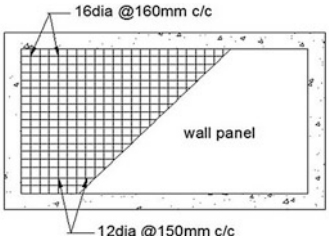

Fig. 16 C/S of beams concealed in walls in framed type tank system

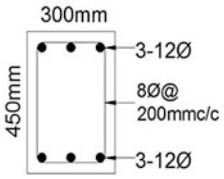

Fig. 17 C/S of beams connecting walls at top of framed type tank

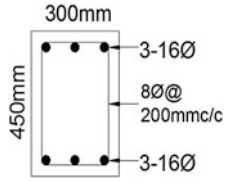

compared to framed type tank and the deflection in free cantilever type tank is 48.15% higher and 52.38% lesser in twin wall system. The cost estimation of the foundation and sidewall systems are carried out the rates per quantities as shown in Figs. 21, 22, 23 and 24; Table 6.

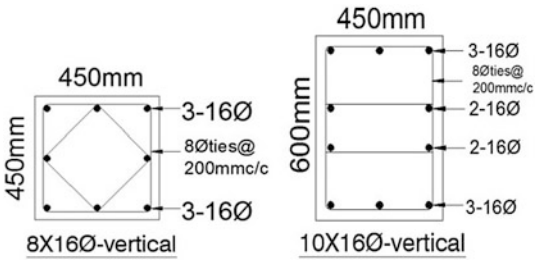

Fig. 18 Columns in framed type system

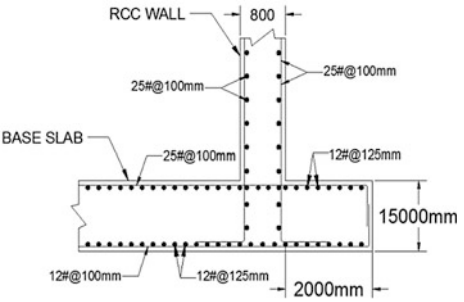

Fig. 19 Solid raft foundation system

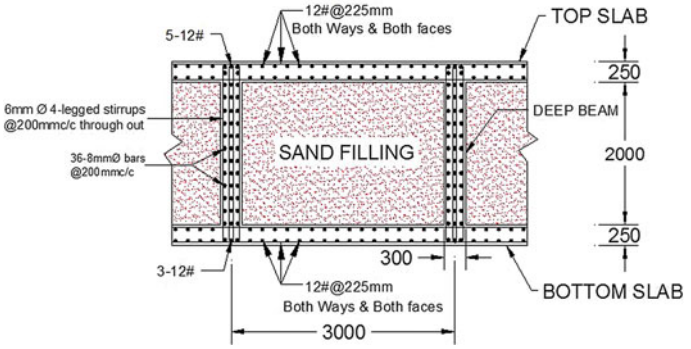

Fig. 20 Cellular raft foundation system

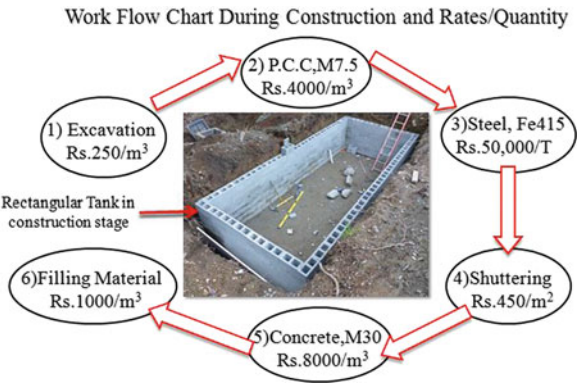

Fig. 21 Material costs per quantity

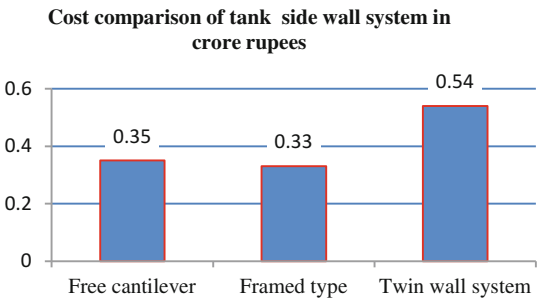

Fig. 22 Cost comparison of tank sidewall system

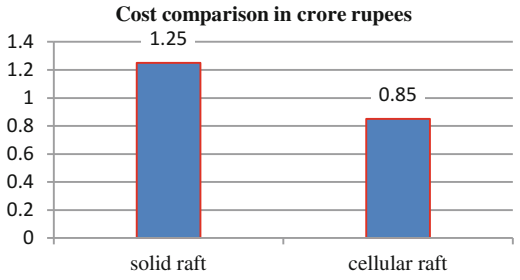

Fig. 23 Cost comparison of foundation systems

5 Conclusions

The following conclusions were drawn from the analysis.

1. Framed type sidewall system is cheaper than Free cantilever type system by 5.71% and Twin wall system by 38.88%.
2. Hydrodynamic pressure is about 11.5% of hydrostatic pressure in seismic zone-II.

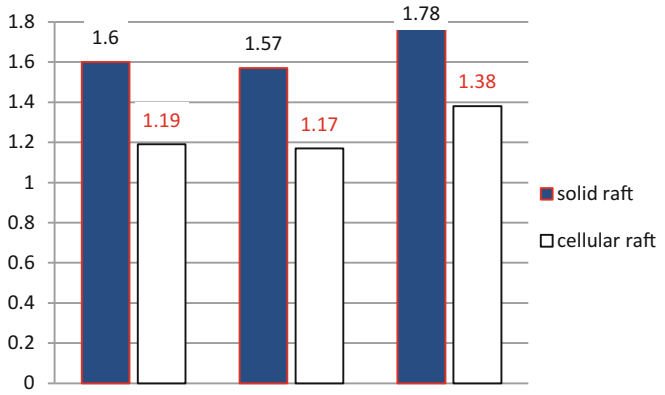

Fig. 24 Total cost comparison of sidewall systems with solid and cellular raft in crore rupees

Table 6 Cost comparison of different sidewall and foundation systems in water tanks

S. No	Type of tank sidewall system	Type of tank foundation system	Total cost in crore rupees
1.	Free cantilever	Solid raft	Rs. 15,903,310 ≅ 1.60 crores
2.	Free cantilever	Cellular raft	**Rs. 11,891,760 ≅ 1.19 crores**
3.	Frame type	Solid raft	Rs. 15,663,260 ≅ 1.57 crores
4.	Frame type	Cellular raft	**Rs. 11,651,710 ≅ 1.17 crores**
5.	Twin wall system	Solid raft	Rs. 17,757,270 ≅ 1.78 crores
6.	Twin wall system	Cellular raft	**Rs. 13,745,720 ≅ 1.38 crores**

Bold indicates to show the cost reduction by using cellular raft foundation compared with solid raft

3. Twin wall sidewall system is costlier than free cantilever and framed system due to increased concrete volume and shuttering area.
4. Framed type tank with cellular raft is cheaper than free cantilever type tank with cellular raft by 1.71% and twin wall system with cellular raft by 15.22%.
5. Cellular raft foundation system is cheaper than solid raft foundation system by 32%.
6. Framed type sidewall system with cellular raft foundation is the most economical system for large storage tanks.

References

1. IS 3370-2. (2009). Code of Practice Concrete structures for the storage of liquids, Part 2: Reinforced concrete of structures the storage of liquids.
2. IITK-GSDMA Guidelines for Seismic Design of Liquid Storage Tanks Provisions with commentary and explanatory examples.
3. IS 1893:1984 (Part I). *Criteria for earthquake resistant design of structures*. Bureau of Indian Standards, New Delhi, 1984.

Influence of Shear Core Curtailment on the Structural Response of Core-Wall Structures

Nishant Rathi, G. Muthukumar and Manoj Kumar

Abstract Shear walls and shear cores are the major lateral load resisting elements in multi-storeyed framed structures because of their proven track record in mitigating the damage under severe earthquake ground motions including the recent ones. The contrasting deflected profiles of shear core and frame actually help in reducing the drift of the structure. The reduction is primarily attributed to the level of horizontal interaction between cores and frames. The present study aims to simulate the horizontal interaction between core wall and frames using the dimensionless parameter (αH) capable of characterizing the individual behaviors of the components of the dual system using the finite element analysis with different levels of curtailment of shear core. The triangular loading has been considered, and the computations have been made considering the site located in zone 4 with medium soil characteristics. To this end, in order to identify the optimum level of curtailment, an analytical study has been done on some shear core buildings with different levels of curtailment of shear core. The structural performance of the buildings with different levels of curtailment has been assessed for different parameters, namely, storey drift, deflection, bending moment, and shear forces using finite element modeling and analysis.

Keywords Frame · Shear core · Curtailment

N. Rathi · G. Muthukumar · Manoj Kumar (✉)
Civil Engineering Department, BITS Pilani, Pilani 333031, India
e-mail: manojkr@pilani.bits-pilani.ac.in

N. Rathi
e-mail: h2014057@pilani.bits-pilani.ac.in

G. Muthukumar
e-mail: muthug@pilani.bits-pilani.ac.in

A. Rama Mohan Rao and K. Ramanjaneyulu (eds.), *Recent Advances in Structural Engineering, Volume 1*, Lecture Notes in Civil Engineering 11,
https://doi.org/10.1007/978-981-13-0362-3_17

1 Background and Introduction

Tall buildings are inevitable in urban areas because of paucity of land. Taller buildings are more susceptible to damage due to wind forces and seismic forces. Not so often that the buildings are subjected to heavy earthquake. Nevertheless, the amount of damage that the severe earthquake can cause is immeasurable. Hence, it is essential to protect the building from such severe damages. Shear walls and shear cores are the major lateral load resisting elements in multi-storeyed framed structures because of their proven track record in mitigating the damage under severe earthquake ground motions including the recent ones. The contrasting deflected profiles of shear core and frame actually help in reducing the drift of the structure. The reduction is primarily attributed to the level of horizontal interaction between cores and frames. The present study aims to simulate the horizontal interaction between core wall and frames using the dimensionless parameter (αH) capable of characterizing the individual behaviors of the components of the dual system using the finite element analysis. The triangular loading has been considered and the computations have been made considering the site located in zone 4 with medium soil characteristics.

There are ten different horizontal interactions considered with the increasing size of the frame components, characterized by an increase in the parameter αH (Table 1). On the other hand, the shear cores are conventionally provided throughout the height of the building. Nevertheless, on the basis of their incompatible behaviors, it was observed that there is a need to curtail the shear wall to minimize the force demand on the frame [1, 2]. To this end, in order to identify the optimum level of curtailment, an analytical study has been done on some shear core buildings with different levels of curtailment of shear core.

Table 1 Different horizontal interactions considered

S. No.	αH	Beam size (mm)	Column size (mm)	Shear core thickness (mm)
1.	0.5	200 × 300	450 × 450	600
2.	0.75	200 × 375	500 × 500	565
3.	1	225 × 425	525 × 525	500
4.	1.5	230 × 500	750 × 750	400
5.	2	250 × 570	800 × 800	350
6.	3	275 × 700	900 × 900	325
7.	4	300 × 820	1000 × 1000	300
8.	6	300 × 950	1200 × 1200	250
9.	8	400 × 975	1300 × 1300	175
10.	10	425 × 1050	1400 × 1400	150

2 Characteristics of Shear Core-Frame System

The shear core-frame building, when loaded laterally, deflects in a flexural configuration at the lower part of the structure and shear configuration at the upper part of the structure. The level of point of transition from the flexural configuration to the shear configuration depends on the shear stiffness of the frame and flexural stiffness of shear core. The nondimensional parameter characterizing the behavior of the frame and shear core is given by

$$\alpha H = H\left(\frac{\mathrm{GA}}{\mathrm{EI}}\right)^{1/2} \tag{1}$$

In the above equation, H = the height of the structure, EI = the total flexural rigidity of the set of shear cores, and GA = the total shear rigidity of the set of the frames.

The shear rigidity of a single uniform frame "i" is given by the expression

$$(\mathrm{GA})_i = \frac{12\,E}{h\left(\frac{1}{\sum \frac{I_c}{h}} + \frac{1}{\sum \frac{I_b}{l}}\right)_i} \tag{2}$$

In the above equation, E = the modulus of elasticity of the material of columns and beams; h = the storey height; and $\sum I_c$ = the sum of the inertias of the columns in a storey of frame i. $\sum I_b$ = the sum of the inertias of the beams at a particular level.

The lateral loading on the core-frame structures results in the lateral deflection of the structure, and subsequently, the horizontal interaction forces occur between the shear core and the frames. The approximate continuum approach of modeling and analysis of shear core-frame structure is based on the uniform properties of frame and shear core throughout the height of the structure [3]. The irregularities in the vertical plane in terms of abrupt change in the stiffness of frame and core wall cannot be dealt with the continuum approach, and the use of transfer matrix method [4] may be sought. However, the present study employs the continuum approach for the assessing the behavior of the core-frame structure and is widely used for the preliminary analysis and design of tall buildings.

2.1 Shear Core-Frame for Different Levels of Curtailment—Problem Statement and Methodology

The shear core can be curtailed in a core-wall system depending on the horizontal interaction between the two systems of the structure, i.e., core wall and the frame. The transition zone between the flexural configuration and shear configuration

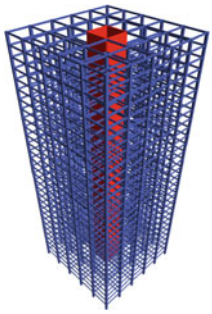

Fig. 1 3-D core-wall frame structure

needs to be identified. The height at which the transition zone occurs depends on the relative stiffness of frame and shear wall. If the shear wall is quite dominant, the transition zone shifts upward.

In order to identify the optimum height of shear core in terms of its beneficial effect of reducing the internal force demand on the frame, the shear core-frame has been analyzed for the different levels of curtailment of core wall for different systems characterized by the nondimensional parameter (αH) as defined in the earlier sections.

In the present study, a 30-storeyed shear core-framed building with aspect ratio of 2.63 with shear core located in the center of the plan has been considered (Fig. 1), as shown respective plan (Fig. 2) and elevation (Fig. 3). The plan dimensions are kept at 40 m × 40 m, and the storey height is kept at 3.5 m. The structural performance of the buildings with different levels of curtailment has been assessed for different parameters, namely, storey drift, deflection, bending moment, and shear forces using finite element modeling and analysis. The shell elements have been used to model the shear core and membrane elements are used to model the rigid slab (Figs. 2 and 3). For all the structural components such as beam, column, shear core, and slab, the grade of concrete is kept at M25 (Fig. 3).

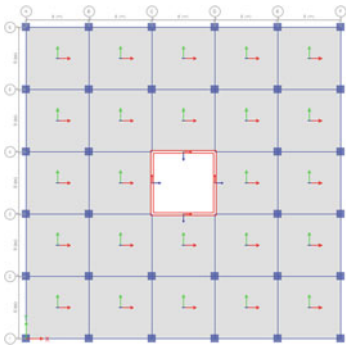

Fig. 2 Plan of shear core-framed building

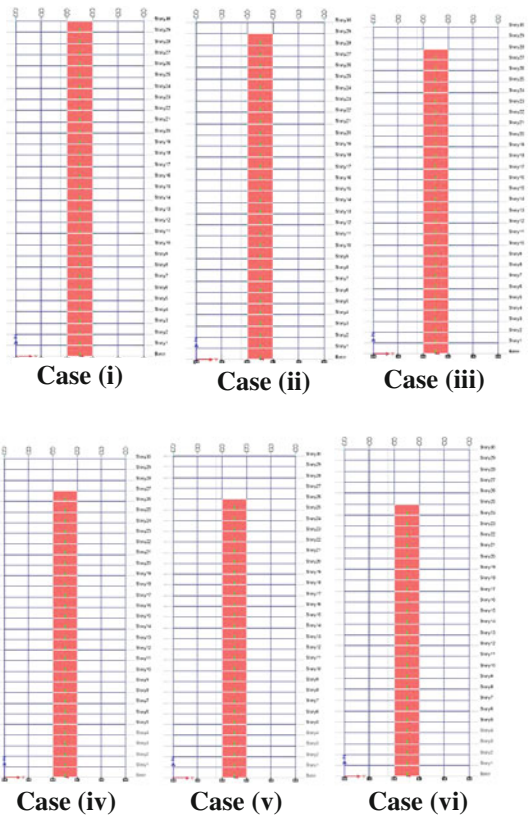

Fig. 3 Different curtailment levels of shear core

2.1.1 Response Parameters of Core-Wall Frame Structure

The following four structural response parameters are normally considered for the response analysis and are presented in Table 2.

In the above expression, the values of $k1$, $k2$, $k3$, and $k4$ represent the various coefficient factors indicating the contribution of stiffening effect of frame on the response of the shear wall or shear core. The maximum values of $k1$, $k2$, $k3$, and $k4$ are unity. For example, if the value of αH is close to zero (due to high value of EI and low value of GA), then the value of $k1$ tends to be unity, characterizing the negligible effect of the frame action in resisting the deformability of the structure. The variation of the $k1$, $k2$, $k3$, and $k4$ for the different values of αH along the height of the structure (z/H) is presented in the form of graph in the literature [5]. For the convenience, the variation of the $k1$ through $k4$ is plotted here corresponding to different levels of z/H, where z represents the elevation at which the structural response parameter is desired to be estimated (Fig. 4).

Table 2 Structural parameters considered for the present study

S. No.	Response parameter	Expression for triangular load pattern
1.	Displacement of shear wall	$y(z) = \frac{11wH^4}{120\text{EI}}\ k1$
2.	Storey drift of shear wall	$\frac{\mathrm{d}y}{\mathrm{d}z}(z) = \frac{wH^3}{8\text{EI}}\ k2$
3.	Bending moment of shear wall	$M_\mathrm{b}(z) = \frac{wH^2}{3}\ k3$
4.	Shear force of shear wall	$M_\mathrm{b}(z) = \frac{wH}{2}\ k4$

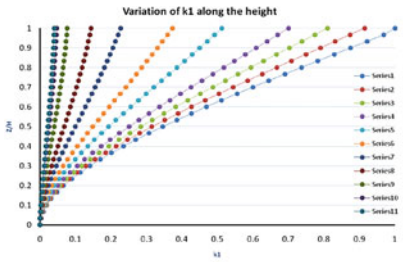

(a) Variation of k1

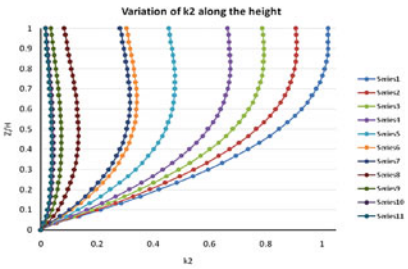

(b) Variation of k2

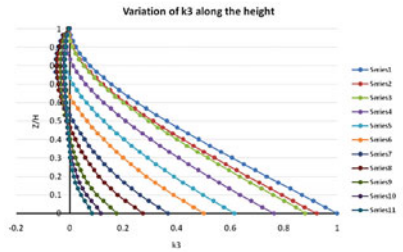

(c) Variation of k3

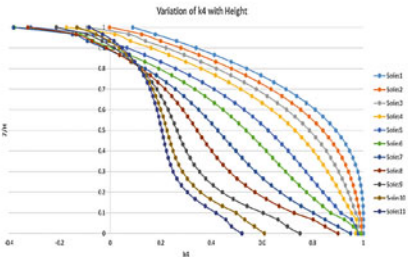

(d) Variation of k4

Fig. 4 Variation of response factors (K) for different values of z/H and αH

3 Response Analysis of Shear Core-Frame for Different Levels of Curtailment

The response analysis of the shear core-frame has been compared for different values of αH and different levels of curtailment. The current section highlights the various responses in terms of relative deflection, relative base shear, relative base moment, and relative shear (top).

The relative deflection, defined as the ratio of deflection at the top of the structure to the max deflection of the wall (with no frame included) has been shown in Fig. 5. For lower values of αH, it has been observed that the deflection pattern

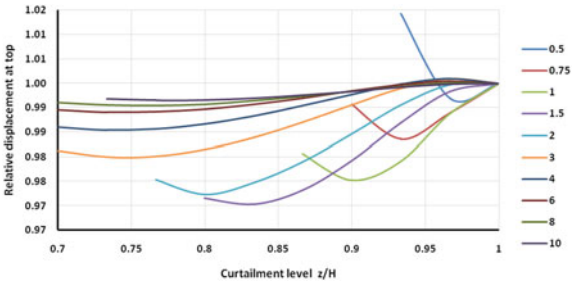

Fig. 5 Variation of relative deflection (top) for different levels of curtailment (for different αH)

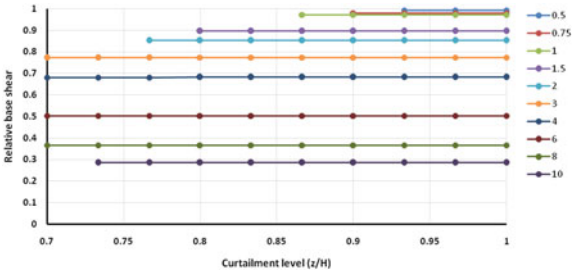

Fig. 6 Variation of relative base shear for different levels of curtailment (for different αH)

follows more of the flexural wall, whereas for higher values of αH, it follows more of a shear behavior signifying the predominant frame action.

The relative base shear, defined as the ratio of total shear carried by the shear wall to the shear applied, has been shown in Fig. 6 for different values of αH and for different levels of curtailment. The shear carried by the core wall gets affected as the value of αH increases, signifying the greater contribution by the frame. On the other hand, it has been observed that shear carried by the core wall has not been affected by the curtailment of core wall. Hence, the curtailment does not necessarily result in the reduction in the load carrying capacity of the wall.

The variation of relative base moment for different levels of curtailment and for different values of αH is shown in Fig. 7. For lower values of αH, the relative base moment, defined as the ratio of moment of the shear core at the base of the structure to the maximum moment of the structure, is contributed more by the shear core than

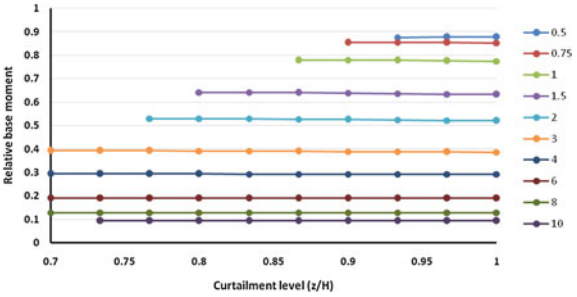

Fig. 7 Variation of relative base moment for different levels of curtailment (for different αH)

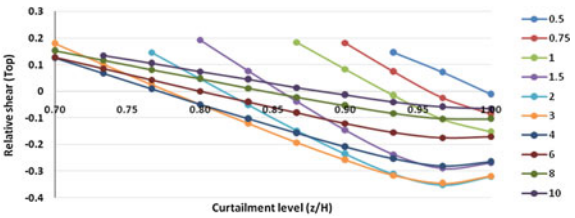

Fig. 8 Variation of relative shear (top) for different levels of curtailment (for different αH)

the frame. As the value of αH is increased, the relative base moment is contributed more by the frame rather than by the shear wall, signifying the predominant frame action. Moreover, for all values of αH, the curtailment of shear core does not seem to affect the structural response of shear core-frame structure. Hence, with respect to relative base moment, it can be concluded that the curtailment of the shear core is neither sensitive nor detrimental to the structural response.

The variation of relative shear (top) for different levels of curtailment and for different values of αH is shown in Fig. 8. The relative shear at the top of the structure is defined as the ratio of the shear at the top of the structure to the shear applied at the top of the structure. When the shear core is provided till the top of the structure, the relative shear has been on the negative side and hence creating the additional force demand on the frame of the structure especially for the higher values of αH.

The curtailment of shear core has resulted in the change in the relative shear from negative to positive, and subsequently, the position of point of contra-shear changes depending on the values of αH. It has been observed from the graph that for higher values of αH, the point of contra-shear occurs more toward the bottom of the structure, and hence, the curtailment of shear core has more pronounced effect on the structural performance by avoiding the large negative shear at the top region. The optimum level of curtailment has been found to in the range between 80 and 90% of the height of the structure. It is also to be noted that shear walls of height about 85% of the total height of building are considered advantageous [6].

4 Conclusions

On the basis of the above results, the following conclusions have been drawn on the structural performance of shear core-frame.

- The level of horizontal interaction strongly influences the structural behavior of the dual system (frame and shear core) as much as the intensity of loading.
- For lower values of αH, the behavior of the structure is dominated by the flexural action due to the influencing presence of shear core.
- The shear core carries most of the base shear and base moment for lower values of αH and the frame carries the forces for higher values of αH.

- The curtailment of the shear core at the top region has not been found detrimental with respect to base shear and base moment.
- The curtailment of the top region has actually been beneficial with respect to the reduction in the negative shear at the top of the structure, which in turn reduces the force demand on the frame.

References

1. Atik, M., Badawi, M. M., Shahrour, I., & Sadek, M. (2014). Optimum level of shear wall curtailment in wall-frame buildings: The continuum model revisited. *ASCE Journal of Structural Engineering, 140*(1), 4 pp.
2. Nollet, M. J., & Smith, B. S. (1993). Behaviour of curtailed wall-frame structures. *ASCE Journal of Structural Engineering, 119*(10), 2835–2854.
3. Heidebrecht, A. C., & Smith, B. S. (1973). Approximate analysis of tall wall-frame structures. *ASCE Journal of the Structural Division, 99*(ST2), 199–221.
4. Wang, Q., Wang, L., & Liu, Q. (2001). Effect of shear wall height on earthquake response. *Engineering Structures, 23,* 376–384.
5. Smith, B. S., & Coull, A. (1991). *Tall building structures: Analysis and design*. University of Texas Press.
6. IS 4326. (1993). *Earthquake resistant design and construction of buildings*. New Delhi, India: Bureau of Indian Standards.

Location of Balance Points on Design and Actual *P–M* Interaction Curve for RC Sections

Piyush Mehta, Sumit Kumar, Vikash Kumar, Sunil Bandawala and Kaustubh Dasgupta

Abstract The axial force–bending moment (*P–M*) interaction curve is a graphical representation of sectional capacity of a uniaxial eccentrically loaded reinforced concrete (RC) member. On the *P–M* curve, balance point represents simultaneous achievement of limit states of both concrete and reinforcing steel. Although locations of balance points are commonly used for demarcating under-reinforced and over-reinforced regimes of behavior of RC columns, these are not studied from the point of view of actual behavior. In the present study, first *P–M* curves are generated as per the actual stress–strain curves of concrete (considering the confinement action) and reinforcing steel for different sizes of column section. The balance points are located on the actual *P–M* curves based on the definition of limit states of concrete and reinforcement. The locations of balance points on the actual *P–M* curves are reviewed to determine whether the design balance points give an upper bound or lower bound of the under-reinforced range of behavior.

Keywords *P–M* interaction · Balance point · RC column · Under-reinforced behavior

P. Mehta · S. Kumar · V. Kumar · S. Bandawala · K. Dasgupta (✉)
Department of Civil Engineering, Indian Institute of Technology Guwahati, Guwahati 781039, India
e-mail: kd@iitg.ac.in

P. Mehta
e-mail: p.mehta@iitg.ac.in

S. Kumar
e-mail: sumit2013@iitg.ac.in

V. Kumar
e-mail: vikashkumar@iitg.ac.in

S. Bandawala
e-mail: s.bandawala@iitg.ac.in

A. Rama Mohan Rao and K. Ramanjaneyulu (eds.), *Recent Advances in Structural Engineering, Volume 1*, Lecture Notes in Civil Engineering 11,
https://doi.org/10.1007/978-981-13-0362-3_18

1 Introduction

The axial force–bending moment (*P–M*) interaction curve is based on the estimation of combined capacity of an RC section. Each point on the curve corresponds to a particular set of axial capacity and flexural capacity values. The points also represent primarily four failure modes of an RC section, namely, (a) tensile cracking of concrete, (b) compression failure of concrete, (c) tensile yielding of steel reinforcement, and (d) tensile rupture of steel reinforcement. Based on the different failure modes, the identified balance point demarcates (a) under-reinforced and (b) over-reinforced behavior regions along the entire *P–M* curve.

P–M interaction curve can be drawn for the design level material properties prescribed by the respective code provisions, as well as for the actual material properties obtained from the experimental tests. One of the major issues in the *P–M* interaction curve with actual material properties is the confinement effect of concrete under axial compression. Previous studies have not focused on the comparison of *P–M* interaction curves with design and actual material properties (Ref. [1, 2]). The Indian Standard for the design of RC structures, IS:456-2000 (Ref. [3]), also does not prescribe any confinement effect of concrete and failure strain for steel reinforcement.

In the current study, *P–M* interaction curve is first developed using the design stress–strain curves of concrete and reinforcement as per IS:456-2000. Then, using actual stress–strain curves of concrete and reinforcement, the *P–M* curve is redrawn. The balance points are located on both the *P–M* curves, and the locations are reviewed for sets of curves corresponding to different section sizes. The actual balance point locations represent the expected range of under-reinforced behavior during actual conditions.

2 Material Properties

The constitutive characteristics of concrete and reinforcement, under actual conditions, are discussed in the following sections.

2.1 Concrete

The presence of axial compression in an RC section mobilizes the confinement effect in the core concrete and enhances its compressive strength. In the present study, the analytical stress–strain curves proposed for unconfined and confined concrete, considering different cross-sectional shapes and levels of confinement reinforcement, have been used (Ref. [4]). The stress and strain parameters of confined concrete are established by considering equivalent uniform confinement

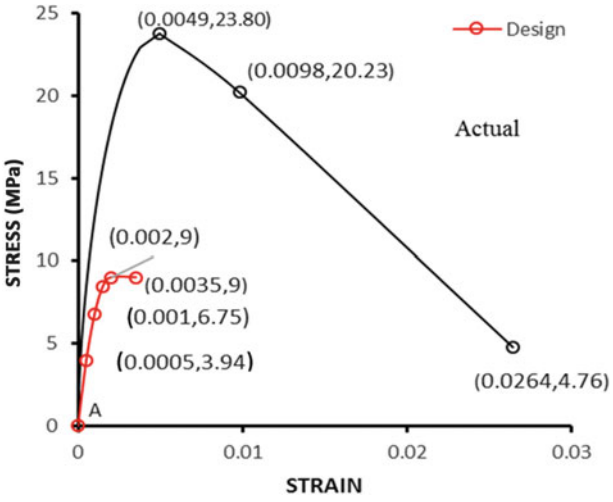

Fig. 1 Stress–strain curves of concrete under design level and confinement effects

pressure applied by the confining reinforcement. The proposed curve consists of a parabolic ascending portion and a linear descending portion. The obtained curves for unconfined and confined concrete, for M20 grade, are shown in Fig. 1.

2.2 Reinforcement

For the Fe415 grade of reinforcement considered in the present study, the design stress–strain curve is considered in two parts, namely, (a) a linear ascending part (till a strength of $0.87f_y$, where f_y is the yield strength of steel), and (b) a constant horizontal line till the final strain of 14%. Although IS:456-2000 does not prescribe any final strain value for the reinforcement, limit of 14% has been considered based on the experiments carried out with Fe415 grade of steel (Ref. [5]). The actual stress–strain curve is based on curve fitting of the tensile test results of Fe415 steel specimens with various cross-sectional sizes (Ref. [5]). The trilinear curve characterizes a linear elastic part and a strain hardening part beyond yield point along with an intermediate ascending linear part (Fig. 2).

3 Fixing the Section Variables

For drawing both the design level and the actual *P*–*M* curves, nominal cover (N_c) is considered as the minimum value of 40 mm (Ref. [3]). Diameter of the tie (d_t) is taken as 10 mm for all the cases. The distance (d') between the edge of the section

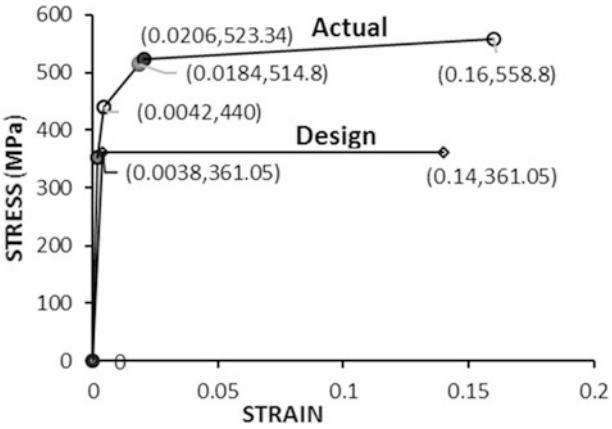

Fig. 2 Design level and actual stress–strain curves for reinforcement

and nearest centerline of longitudinal reinforcement (with diameter d) is expressed as

$$d' = N_c + d_t + \frac{d}{2}. \tag{1}$$

The d'/D ratio is assumed to be constant and taken as 0.05, 0.10, 0.15, and 0.20 for all the cases (where D is the overall depth of the section). Although d is obtained from structural design, the values are assumed according to section dimensions. For d'/D = 0.05 and 0.10, d is taken as 28 mm and for d'/D = 0.15 and 0.20, d is taken as 20 mm. For d'/D = 0.05, 0.10, 0.15, and 0.20, the depth D is obtained as 1280 mm, 640 mm, 400 mm, and 300 mm, respectively. With the assumed width of section b, the number of steel bars n is determined as per the minimum spacing along the width and depth of the section. Two cases of reinforcement distribution are considered, namely, (a) bars distributed equally on two sides, and (b) bars distributed equally on all the four sides.

4 Methodology for *P–M* Curve

For obtaining the strains and stresses across the section, the section is divided into rectangular strips of thickness t as 10 mm and length same as the width of the section (Fig. 3). For obtaining the *P–M* interaction curve, the neutral axis location is varied, with respect to the section, so that the obtained stresses are summed up to determine the P and M values. Thus, the depth of neutral axis (x_u) is varied from 10 × D to 10 mm.

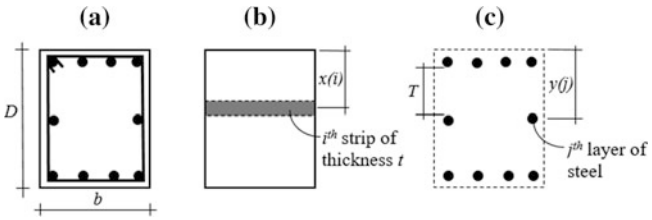

Fig. 3 Design level sectional parameters: **a** cross section with reinforcement details, **b** typical strip for concrete, and **c** reinforcement layers

4.1 Design P–M *Curve*

For each x_u, the strain distribution is obtained for the maximum compressive strain as 0.0035 for the design level response. The distance of rotation point of strain from the top edge of the section is determined by

$$u\_\text{str} = \boldsymbol{D} * \frac{(\mathbf{0.0035} - \mathbf{0.002})}{\mathbf{0.0035}}. \tag{2}$$

The strip's distance for the *i*th strip from the top of the section was calculated by (Fig. 3),

$$x(i) = \{(i-1)t + t/2\}. \tag{3}$$

The clear distance between the steel layers will be equal to,

$$T = \frac{D - 2N_\text{c} - 2d_\text{t} - d_j}{J - 1}. \tag{4}$$

The distance of the *j*th steel layer from the top edge of the section is calculated by

$$y(j) = \left\{ N_\text{c} + d_\text{t} + \left(\frac{d}{2}\right) + ((T+d) * (j-1)) \right\}. \tag{5}$$

The strain at the middle point of the strips for a given x_u was calculated using the formula,

$$\varepsilon = \begin{cases} 0.002 * \frac{x_u - x(i)}{x_u - u}, & \text{if } x_u > D \\ 0.0035 * \frac{x_u - x(i)}{x_u}, & \text{if } 0 < x_u \le D \cdot \\ 0.0035 * (x_u + x(i)), & \text{if } x_u \le 0 \end{cases} \tag{6}$$

These above mentioned strain equations will remain same for steel layers by replacing $x(i)$ with $y(j)$. The stress corresponding to the strain calculated from

Eq. (6) was obtained from the stress–strain curve developed earlier by using the following formula, where σ_{uc} is the stress in unconfined concrete:

$$\sigma_{uc} = \begin{cases} \text{interpolate values}, & \text{if } 0 < \varepsilon < 0.002 \\ 0.45 * f_{ck}, & \text{if } 0.002 \leq \varepsilon \leq 0.0035 \\ 0, & \text{if } \varepsilon > 0.0035 \text{ or } \varepsilon < 0 \end{cases}. \tag{7}$$

Design stress value for steel is obtained as

$$\sigma_s = \begin{cases} \text{interpolate values}, & 0 < \varepsilon < 0.0038 \\ 0.87 f_y, & 0.0038 \leq \varepsilon \leq 0.14 \\ 0, & \text{if } \varepsilon > 0.14 \end{cases}. \tag{8}$$

The force developed in the strips is calculated as

$$c = \sigma_{uc} * A_c, \tag{9}$$

$$A_c = \begin{cases} bt, & \text{if } 0 < x(i) < (N_c + d_t + d) \\ bt, & \text{if } (D - (N_c + d_t + d)) < x(i) < D \\ 2t(N_c + d_t + d) \text{ or } 2t(N_c + d_t), & \text{otherwise} \end{cases}, \tag{10}$$

where c is the force in strip of unconfined concrete, and A_c is the area of strip of unconfined concrete.

The force developed in a steel layer (s) is given by

$$s = \sigma_s * A_s. \tag{11}$$

Two cases of longitudinal reinforcement arrangements are considered, namely, (i) steel equally distributed on four sides, and (ii) steel equally distributed on two sides. For reinforcement equally distributed on four sides,

$$\text{No. of steel layers, } J = \frac{n}{4} + 1, \tag{12}$$

where n is the total number of longitudinal steel bars.

Area in each steel layer can be calculated using the conditional equation given below

$$A_s = \begin{cases} \left(\frac{n}{4} + 1\right)\left(\pi * \frac{d^2}{4}\right), & \text{if } j = 1 \text{ or } J \\ 2\left(\pi * \frac{d^2}{4}\right), & \text{for all other layers} \end{cases}. \tag{13}$$

For reinforcement equally distributed on two sides, the number of steel layers is 2. Then,

$$A_s = \left\{ \left(\frac{n}{2}\right)\left(\pi * \frac{d^2}{4}\right) \right\}, \tag{14}$$

where n is the total number of longitudinal steel bars.

The corresponding moments are obtained from the equations,

$$m_c = c * \left(\frac{D}{2} - x(i)\right), \tag{15}$$

$$m_s = s * \left(\frac{D}{2} - y(j)\right), \tag{16}$$

where m_c is the moment in a strip of unconfined concrete, and m_s is the moment in steel layer.

The individual forces and moments in the strips are summed to obtain the force P_c (i.e., the total force in unconfined concrete), P_s (i.e., the total force in steel layers), the moments M_c (i.e., the total moment in unconfined concrete), and M_s (i.e., the total moment in steel) capacity of the section

$$P_c = \sum c, \tag{17}$$

$$P_s = \sum s, \tag{18}$$

$$M_c = \sum m_c, \tag{19}$$

$$M_s = \sum m_s. \tag{20}$$

4.2 *Actual* P–M *Curve*

For each x_u, the strain distribution is obtained for the maximum compressive strain as 0.0264 for the actual behavior of concrete. The distance of rotation point of strain from the top edge of the section is determined by

$$u = D * \frac{(0.0264 - 0.002)}{0.0264}. \tag{21}$$

The strain at the middle point of the strips (Fig. 4) for a given x_u is calculated as

$$\varepsilon = \begin{cases} 0.002 * \frac{x_u - x(i)}{x_u - u}, & \text{if } x_u > D \\ 0.0264 * \frac{x_u - x(i)}{x_u}, & \text{if } 0 < x_u \leq D \cdot \\ 0.0264 * (x_u + x(i)), & \text{if } x_u \leq 0 \end{cases} \tag{22}$$

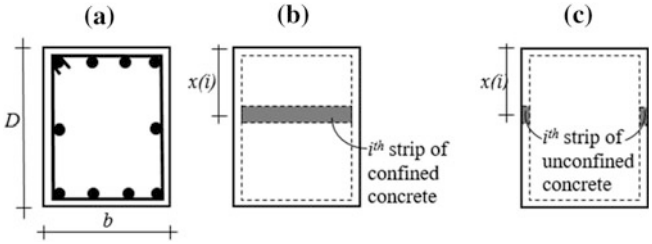

Fig. 4 Sectional parameters for actual behavior: **a** cross section with reinforcement details, **b** typical strip for confined concrete, and **c** typical strip for unconfined concrete

The stress corresponding to the strain calculated from Eq. (22) is obtained from the stress–strain curve. The stress in confined concrete (σ_{co}) is

$$\sigma_{co} = \begin{cases} \text{interpolate values}, & \text{if } 0 \le \varepsilon \le 0.0264 \\ 0, & \text{if } \varepsilon > 0.0264 \text{ or } \varepsilon < 0 \end{cases}. \tag{23}$$

Actual stress value (σ_s) in steel is obtained as

$$\sigma_s = \begin{cases} \text{interpolate values}, & \text{if } 0 \le \varepsilon \le 0.16 \\ 0, & \varepsilon > 0.16 \end{cases}. \tag{24}$$

The force developed in the strips was calculated using

$$\text{cc} = s_{co} * A_{cc}, \tag{25}$$

$$A_{cc} = \begin{cases} 0, & \text{if } 0 < x(i) < (N_c + d_t + d) \\ & bt - 2t(N_c + d_t + d) \\ & \text{or } bt - 2t(N_c + d_t), \text{ otherwise} \\ 0, & \text{if } D - (N_c + d_t + d) < x(i) < D \end{cases}, \tag{26}$$

where cc is the force in a strip of confined concrete, and A_{cc} is the area of the strip.

The force developed in a steel layer is given by

$$s = \sigma_s * A_s. \tag{27}$$

The moment in a strip of confined concrete (m_{cc}) is given by

$$m_{cc} = \text{cc} * \left(\frac{D}{2} - x(i)\right). \tag{28}$$

The individual forces and moments in the strips are summed to obtain P_{cc} (i.e., the total force in confined concrete) and M_{cc} (i.e., the total moment in confined concrete) as

$$P_{cc} = \sum cc, \tag{29}$$

$$M_{cc} = \sum m_{cc}, \tag{30}$$

$$P = (P_c + P_{cc} + P_s), \tag{31}$$

$$M = (M_c + M_{cc} + M_s). \tag{32}$$

In order to compare with the design charts of SP:16 (Ref. [6]), the axial force and moment values are converted into nondimensional parameters.

5 Results

5.1 Steel Equally Distributed on Four Sides

The percentage of steel (p) in the chosen column section is determined using

$$p = \left(\frac{\text{Ast}}{bD}\right) * 100. \tag{33}$$

For comparing the balance point values, P_a and M_a are the axial force and bending moment considering the actual stress–strain curves of steel and confined concrete, respectively. P_d and M_d are the axial force and bending moment obtained considering the design stress–strain curves of steel and concrete. With increasing percentage of longitudinal reinforcement, the normalized bending moment values for balance point locations show increasing trend for both actual and design material stress–strain curves (Tables 1 and 2). However, the normalized axial capacity values ($P_a/f_{ck}bD$) obtained with actual stress–strain curves do not show monotonic trends for d'/D values of 0.1, 0.15, and 0.2 (Table 1). For d'/D as 0.2, the balance point occurs with net axial tensile force on the section. However, for design level response, the $P_d/f_{ck}bD$ values reduce with increasing p/f_{ck} values.

For lower percentages of steel and d'/D ratios, the balance points obtained using design and actual material properties tend to lie close to each other (Fig. 5a, b). However, due to increase in $M_a/f_{ck}bD^2$ values as compared to $M_d/f_{ck}bD^2$ for the same axial force level on the column section, the deviation between the balance points increases with higher percentages of reinforcement. For d'/D as 0.2, the locus of the balance points, across the different values of p/f_{ck}, tends to be a straight line with positive slope (Fig. 5b). Similar points do not lie on a straight line for lower values of d'/D (Fig. 5a). For the design level material properties, all the balance points tend to lie on straight lines.

Table 1 Balance point values with actual material stress–strain curves

d'/D	D (mm)	b (mm)	n	p/f_{ck}	$P_a/f_{ck}bD$	$M_a/f_{ck}bD^2$
0.05	1280	300	4	0.032	0.201	0.108
	1280	400	12	0.072	0.252	0.171
	1280	500	24	0.115	0.316	0.247
	1280	650	36	0.133	0.334	0.282
	1280	800	48	0.144	0.352	0.304
0.1	640	280	4	0.069	0.166	0.169
	640	380	8	0.101	0.254	0.193
	640	440	12	0.131	0.234	0.246
	640	540	20	0.178	0.261	0.318
	640	640	28	0.210	0.276	0.368
0.15	400	200	4	0.078	0.101	0.158
	400	250	8	0.126	0.048	0.193
	400	300	12	0.157	0.155	0.244
	400	350	16	0.179	0.109	0.270
	400	400	20	0.196	0.171	0.297
0.2	300	220	4	0.095	0.091	0.159
	300	180	4	0.116	0.060	0.186
	300	250	8	0.167	−0.05	0.208
	300	280	12	0.224	0.101	0.279
	300	300	16	0.279	−0.01	0.334

5.2 *Steel Equally Distributed on Two Sides*

For reinforcement distributed equally on both sides, the same trends are observed regarding the locations of the balance points (Fig. 6a, b) as for reinforcement distributed equally on four sides (Tables 3 and 4). However, the available range for under-reinforced behavior with actual material properties reduces with increasing d'/D values. For low values of d'/D, the range for under-reinforced behavior also increases with percentage of steel. For reinforcement distributed equally on all four sides, reverse trend is observed with the mentioned range increasing with d'/D values (Fig. 5b).

The balanced axial compression values are almost the same using both design stress–strain curve and actual stress–strain curve for low d'/D values and large d'/D values for steel equally on four sides and steel equally on two sides, respectively. For steel distributed equally on all the four sides, the locus of balance points for the actual behavior does not follow a straight line with low d'/D values (Fig. 5a).

Table 2 Balance points with design material stress–strain curves

d'/D	D (mm)	b (mm)	n	p/f_{ck}	$P_d/f_{ck}bD$	$M_d/f_{ck}bD^2$
0.05	1280	300	4	0.032	0.160	0.103
	1280	400	12	0.072	0.143	0.137
	1280	500	24	0.115	0.136	0.186
	1280	650	36	0.133	0.134	0.206
	1280	800	48	0.144	0.132	0.218
0.1	640	280	4	0.069	0.152	0.148
	640	380	8	0.101	0.126	0.158
	640	440	12	0.131	0.110	0.187
	640	540	20	0.178	0.104	0.233
	640	640	28	0.210	0.092	0.264
0.15	400	200	4	0.078	0.143	0.145
	400	250	8	0.126	0.102	0.164
	400	300	12	0.157	0.079	0.188
	400	350	16	0.179	0.074	0.206
	400	400	20	0.196	0.067	0.219
0.2	300	220	4	0.095	0.121	0.144
	300	180	4	0.116	0.116	0.165
	300	250	8	0.167	0.040	0.175
	300	280	12	0.224	−0.009	0.211
	300	300	16	0.279	−0.045	0.246

However, for steel distributed equally on two sides, the locus becomes a straight line for the entire range of d'/D values (Fig. 6a, b). This is due to the contribution of the intermediate bars along the lateral edges for the first case. For grades of reinforcement Fe415 onward, a definite yield point is never observed during laboratory testing of reinforcement specimens. In absence of definite yield point and any horizontal portion of stress–strain curve, the balance point is obtained by considering the achievement of limiting strain in concrete and beginning of second linear part in the stress–strain curve of steel. Thus, for low values of d'/D in case of steel equally on four sides, the locations of balance points do not lie strictly on a linear locus (Fig. 5a). However, the trend changes with higher values of d'/D. The exact locations of balance points are expected to undergo some change for other stress–strain curves of concrete and reinforcement; however, the overall trend would remain the same.

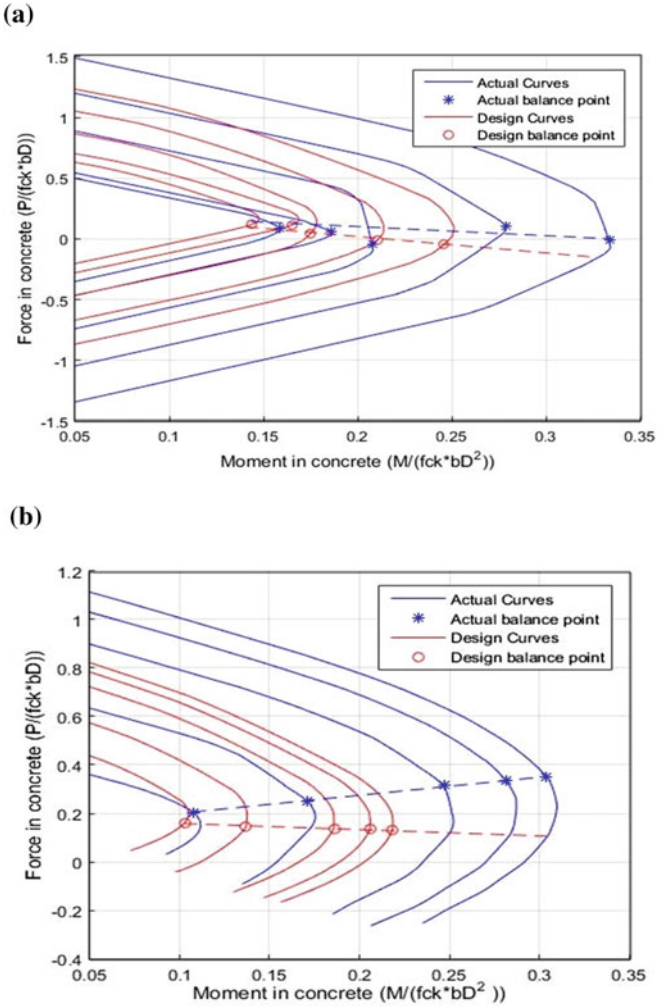

Fig. 5 Normalized *P–M* interaction curves for steel distributed equally on four sides with **a** $d'/D = 0.05$ and **b** $d'/D = 0.20$

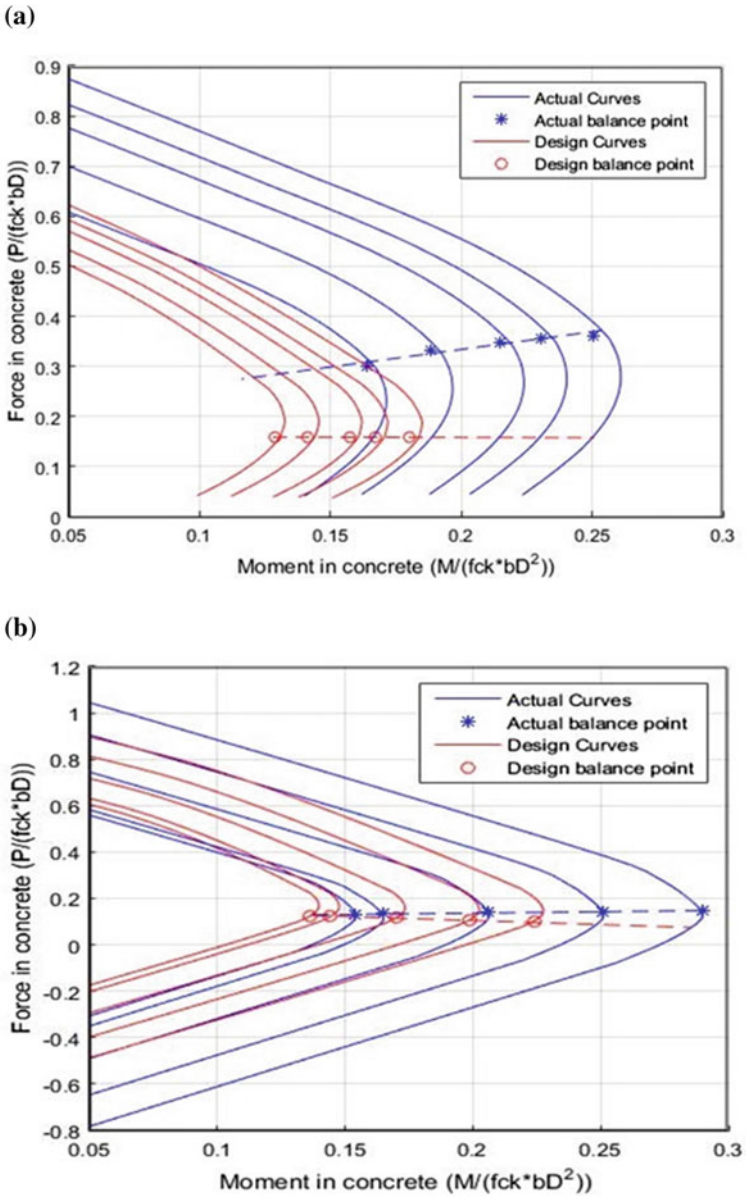

Fig. 6 Normalized *P–M* interaction curves for steel distributed equally on two sides with **a** $d'/D = 0.05$ and **b** $d'/D = 0.20$

Table 3 Balance point values with actual material stress–strain curves

d'/D	D (mm)	b (mm)	n	p/f_{ck}	$P_a/f_{ck}bD$	$M_a/f_{ck}bD^2$
0.05	1280	400	8	0.048	0.301	0.164
	1280	600	14	0.056	0.332	0.188
	1280	800	22	0.066	0.347	0.215
	1280	1000	30	0.072	0.356	0.230
	1280	1200	40	0.080	0.362	0.251
0.1	640	300	4	0.064	0.238	0.173
	640	350	6	0.082	0.254	0.213
	640	400	8	0.096	0.266	0.244
	640	500	12	0.115	0.282	0.287
	640	600	18	0.144	0.294	0.349
0.15	400	320	4	0.049	0.205	0.123
	400	340	6	0.069	0.204	0.161
	400	360	8	0.087	0.207	0.194
	400	380	10	0.103	0.210	0.224
	400	400	14	0.137	0.212	0.286
0.2	300	240	4	0.087	0.137	0.165
	300	220	4	0.095	0.128	0.154
	300	260	6	0.120	0.140	0.206
	300	280	8	0.149	0.143	0.251
	300	300	10	0.174	0.145	0.290

Table 4 Balance points with design material stress–strain curves

d'/D	D (mm)	b (mm)	n	p/f_{ck}	$P_d/f_{ck}bD$	$M_d/f_{ck}bD^2$
0.05	1280	300	4	0.032	0.159	0.129
	1280	400	12	0.072	0.159	0.141
	1280	500	24	0.115	0.159	0.158
	1280	650	36	0.133	0.159	0.167
	1280	800	48	0.144	0.158	0.180
0.1	640	280	4	0.069	0.153	0.141
	640	380	8	0.101	0.151	0.167
	640	440	12	0.131	0.150	0.187
	640	540	20	0.178	0.150	0.214
	640	640	28	0.210	0.148	0.255
0.15	400	320	4	0.049	0.146	0.109
	400	340	6	0.069	0.144	0.134
	400	360	8	0.087	0.142	0.156
	400	380	10	0.103	0.140	0.175
	400	400	14	0.137	0.137	0.217
0.2	300	240	4	0.087	0.122	0.136
	300	220	4	0.095	0.121	0.144
	300	260	6	0.120	0.115	0.170
	300	280	8	0.149	0.109	0.199
	300	300	10	0.174	0.103	0.224

6 Conclusion

The following salient conclusions are drawn from the present study:

(a) The range of under-reinforced behavior of an RC section from the actual *P–M* interaction curve may be significantly more than that estimated using design level material properties. Thus, the design level response provides a conservative estimate for reinforcement calculations during design of RC columns.
(b) The difference between the moment capacities obtained from *P–M* interaction curves using design level and actual material stress–strain curves increases for steel distributed equally on two sides as compared to steel equally on all four sides.
(c) For RC sections with steel distributed equally on all four sides, the locations of balance points give very small range of axial compression for under-reinforced behavior as compared to steel distributed equally on two sides.

Acknowledgements The authors are grateful to the Department of Civil Engineering, Indian Institute of Technology Guwahati, for providing the resources and facilities to carry out the work.

References

1. Payala, N., & Dasgupta, K. (2011). Axial force-bending moment interaction of earthquake-resistant reinforced concrete flanged structural walls. In *International Conference on Advances in Civil Engineering (ACE—2011)*, Vijayawada, Paper No. 396.
2. Majeed, A. Z., Goswami, R., & Murty, C. V. R. (2015). Mechanics-driven hand calculation approach for obtaining design P-M interaction curves of RC sections. *Indian Concrete Journal, 89*(9), 59–68.
3. BIS. (2000). Plain and reinforced concrete—Code of practice IS 456:2000. *Bureau of Indian Standards*, New Delhi.
4. Saatcioglu, M., & Razvi, S. R. (1992). Strength and ductility of confined concrete. *Journal of Structural Engineering, ASCE, 118*(6), 1590–1607.
5. Dasgupta, P. (2000). *Effect of confinement on strength and ductility of large RC hollow sections* (*Master of Technology Thesis*). Dept. of Civil Engg., Indian Institute of Technology Kanpur, India.
6. BIS. (1980). Design aids for reinforced concrete to IS: 456-1978 SP 16:1980. *Bureau of Indian Standards*, New Delhi.

Effect of Skewness on Shear Lag Effect in RC Box-Girder Bridges

Manoj Kumar, Nitin Gulhane and Tanmay Gupta

Abstract This paper deals with 3-D linear elastic finite element analysis of box-girder bridges to study the influence of skewness on the longitudinal stresses and shear lag effect in simply supported box-girder bridges. In the present study, a 20 m span simply supported box-girder bridge with different degrees of skewness varying from 10 to 60° has been considered to investigate the effect of skew angle on transverse distribution of longitudinal stresses and coefficient of shear lag (CSL). The shear lag response of the skew box-girder bridges due to dead load has been compared with the right box-girder bridge, and it has been observed that up to 20° skewness, the CSL is not much affected by the skew angle; however, for the skew angles more than 20°, shear lag effect in the box girders decreases with increase in skew angle, and it becomes remarkably low compared to right box-girder bridges. Moreover, the study shows that for the highly skew bridges, the nature of longitudinal stresses alters.

Keywords Skew box-girder bridge · Finite element · Shear lag
Longitudinal stress

1 Introduction

Construction of box-girder bridges is gaining popularity in bridge engineering fraternity because of its better stability, serviceability, economy, aesthetic appearance, and structural efficiency. In concrete bridges, most of the loads are due to

M. Kumar (✉) · N. Gulhane · T. Gupta
Civil Engineering Department, BITS, Pilani, Rajasthan, India
e-mail: manojkr@pilani.bits-pilani.ac.in

N. Gulhane
e-mail: nitindgulhane82@gmail.com

T. Gupta
e-mail: tanmay.gupta@pilani.bits-pilani.ac.in

A. Rama Mohan Rao and K. Ramanjaneyulu (eds.), *Recent Advances in Structural Engineering, Volume 1*, Lecture Notes in Civil Engineering 11,
https://doi.org/10.1007/978-981-13-0362-3_19

self-weight of bridge superstructure and in order to reduce it, box sections are constructed with thin webs and flanges and referred as thin-walled sections.

Sometimes, due to geometric and space constraints, the bridges are supported on skewed supports and these bridges are referred as sked box girders. The skew angle is defined as the angle between the normal to the centerline of the bridge and the centerline of the abutment or pier cap.

According to the simple theory, in a box girder subjected to transverse load, the longitudinal stresses induced in the flanges are assumed to be uniformly distributed across the flange width. However, in the thin-walled box sections, longitudinal stresses are found nonuniformly distributed due to the shear deformations of the flanges, consequently, the longitudinal stress near the web-flange junction becomes much larger than that far from the web. This phenomenon is known as shear lag.

In order to investigate the effect of skewness on the longitudinal stresses and shear lag, a 20 m span box-girder bridge with different degrees of skewness varying from 10 to 60° and subjected to dead load has been considered in this study.

2 Shear Lag

In the thin-walled box sections, the longitudinal stresses in top/bottom slabs are found nonuniform and the stresses in the regions close to the webs are found higher compared other locations in the respective slabs and the phenomenon associated with this nonuniform longitudinal stress distribution is known as shear lag effect (Fig. 1). Numerous studies have been made in past to understand the shear lag effect in box-girder phenomenon in the orthogonal (right) RC box-girder bridges and shear lag factors have been proposed to incorporate the shear lag effect designed by simple bending theory (SBT). The shear lag factors derived for orthogonal box sections cannot be applied to incorporate the shear lag effect in skewed box-girder bridges.

The phenomenon of shear lag was first addressed by Reissner in 1946 [1]. Using the principle of minimum potential energy, Reissner demonstrated that due to the shear lag effect, stresses at the web-flange junction may enhance up to 30% compared to simple bending theory (Fig. 1).

The simple bending theory is unable to reflect the shear lag effect. However, to determine the peak stresses at the junctions of top/bottom slabs and webs, the stresses calculated from SBT may be enhanced by multiplying these stresses by an appropriate factor known as shear lag factor. SBT is used to calculate the coefficient

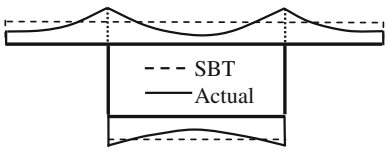

Fig. 1 Typical variation of longitudinal stresses

of shear lag (CSL) in the box girder which is defined as the ratio of longitudinal bending stress at the junction of top/bottom slab as obtained from finite element analysis to that as calculated from SBT. The CSL is calculated as

$$\text{CSL} = \frac{\bar{\sigma}}{\sigma}$$

where

$\bar{\sigma}$ = Actual longitudinal stress obtained by FEM.
σ = Longitudinal stress calculated by SBT.

The shear lag has been studied for many years. Nevertheless, most of the studies are related to orthogonal and curved box-girder bridges. Reissner [1] was the first researcher to use the variational principle of energy method to analyze the shear lag effect in box girders. Luo and Li performed experimental study [2] on box girder models made of perspex glass and used potential variational method to analyze the curved box-girder bridges [3]. Further, Luo et al. used the variational approach to investigate the effect of shear lag in simply supported, cantilever and continuous box-girders [4]. The studies made by Luo and his associates [3, 4] showed that the variational method proposed by Reissner [1] is reliable for straight as well as curved box girders. Yang et al. [5] developed the stochastic finite segment method and applied it to the analysis of shear lag effect on box girder. Lertsima et al. [6] investigated the effect of shear lag on stress concentration in the flange of box-girder bridges by the three-dimensional finite element method using shell elements. Based on the numerical results obtained, they proposed an empirical formula to compute stress concentration factors due to shear lag. Luo et al. [7] proposed a new method for the calculation of membrane forces in thin-walled box girder considering shear lag effect is proposed in this paper. The method is simple in concept and easy to implement and it can be used for design purposes. It was concluded in [7] that the shear lag not only affects the longitudinal membrane force but also the transverse membrane forces as well as the membrane shear force are influenced by shear lag effect. Chang and Yun [8] performed the analysis of right concrete box-girder bridges with varying depth. Chang [9] performed analysis of simply supported right prestressed concrete girder to investigate the influence of prestressing on shear lag effect. The abovementioned studies pertain to the shear lag effect in orthogonal box-girder bridges. Bakht [10] performed the analysis of skew bridges as right bridges for skew angles up to 20°. Mohseni and Rashid [11] performed the grillage analysis multicell skew box-girder bridges to predict the maximum moments in girders (webs) more reliably and proposed modification factors to enhance the accuracy of moment distribution among webs calculated using the AASHTO LRFD specifications. Yang et al. [12] studied the effect of shear lag in curved box-girder bridges and concluded that with the decrease of the radius of curvature, the shear lag effect of box girder becomes more serious. Song and Scordelis [13] presented a harmonic shear lag analysis using plane stress elasticity for stresses in flanges of box sections.

3 Description of Bridge

A 20 span simply supported box girder has been taken for the modeling in the Ansys, having top flange width 11 m, bottom flange width 5.9 m, both top and bottom flange thickness 0.25 m, overall depth 3.0 m, and the web thickness 0.4 m. The end diaphragms of thickness 0.3 m have been assumed at both the ends. The modulus of elasticity of concrete is taken as 3.61×10^{10} N/m^2, and the Poisson's ratio is taken as 0.15 in the analysis. The details of the cross section are shown in Fig. 2.

To this end, a 20 m span box-girder bridge with different degrees of skew varying from 0 to 60° at the interval of 10° is analyzed to investigate the effect of skew angle on the longitudinal stress and shear lag effect in the box-girder bridges subjected to dead loads.

4 Longitudinal Bending Stresses According to Simple Bending Theory

The determination of longitudinal bending stresses according to SBT needs the properties of section, namely, position of neutral axis, moment of inertia, and self-weight of girder.

4.1 Position of Neutral Axis

In order to determine the moment of inertia, there is a need to find the position of neutral axis which h may be determined as

$$\bar{y} = \frac{A_1 y_1 + A_2 y_2 + A_3 y_3 + A_4 y_4}{A_1 + A_2 + A_3 + A_4}$$

$$\bar{y} = \frac{\left[\begin{array}{r}(0.25 \times 5.9) \times (0.25/2) + 2 \times (2.5 \times 0.4) \times (0.25/2 + 0.25) \\ + (11.0 \times 0.25)(3.0 - 0.25/2)\end{array}\right]}{[(0.25 \times 5.9) + 2 \times (2.5 \times 0.4) + (11.0 \times 0.25)]}$$

$$= 1.79 \text{ m (measured from extreme top fiber)}$$

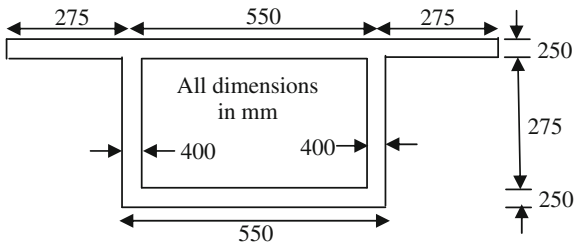

Fig. 2 Geometrical details of box-section

4.2 Moment of Inertia

$$I = \sum_{i=1}^{4} \left[(I_{\text{self}})_{A_i} + A_i y_i^2 \right]$$

$$I = \left[\frac{11.0 \times 0.25^3}{12} + (11 \times 0.25) \times \left(3 - 1.79 - \frac{0.25}{2} \right)^2 \right] + 2 \times \left[\frac{0.4 \times 2.5^3}{12} + (0.4 \times 2.5) \times \left(\frac{2.5}{2} + 0.25 - 1.79 \right)^2 \right] + \left[\frac{5.9 \times 0.25^3}{12} + (5.9 \times 0.25) \times \left(1.79 - \frac{0.25}{2} \right)^2 \right]$$

$$I = 8.558\,\text{m}^4$$

4.3 Self-weight of the Bridge

$$W_{\text{self}} = \text{Total Cross Sectional Area} \times \text{Density of Concrete}$$

$$W_{\text{self}} = [(0.25 \times 5.9) + 2 \times (2.5 \times 0.4) + (11.0 \times 0.25)] \times 25 \times 10^3$$

$$W_{\text{self}} = 154.6875 \times 10^3\,\text{N/m}$$

For 20 m span right bridge considered in this study, the bending moment at mid-span due to its self-weight may be calculated as

$$M_c = \frac{(154.6875 \times 10^3) \times (20)^2}{8}$$

$$M_c = 7.7343 \times 10^6\,\text{Nm}$$

Therefore, the bending stresses at the top fiber of the girder will be

$$\sigma_t = \frac{7.7343 \times 10^6}{8.558} \times (3 - 1.7916 - 0.25)$$

$$\sigma_t = 0.86616 \times 10^6\,\text{N/m}^2$$

and the stress at bottom fiber of the girder will be

$$\sigma_t = \frac{7.7343 \times 10^6}{8.558} \times (1.7916 - 0.25)$$

$$\sigma_t = 0.13932 \times 10^7\,\text{N/m}^2$$

For the determination of longitudinal stresses in skew bridge, an approximate method developed for skew plates has been used [14]. In this method, the skew

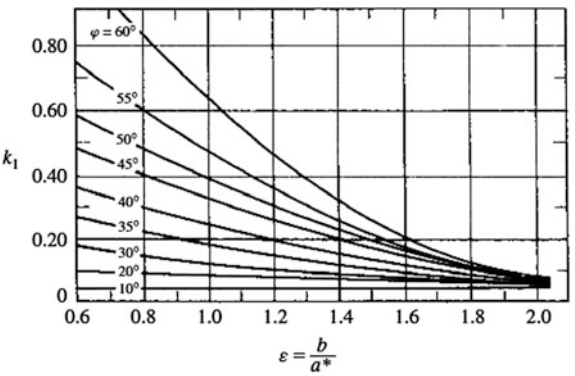

Fig. 3 Coefficient k_1 for moment in skew plate

plate under consideration is replaced by an orthogonal plate. If the maximum longitudinal moment in the equivalent orthogonal plate is $M_{x,\max}$, the longitudinal bending moment in the skew plate $\bar{M}_{x,\max}$ is approximated as

$$\overline{M}_{x,\max} = \frac{M_{x,\max}}{c_x}$$

where $c_x = (1 + k_1)$ is the correction factor to incorporate effect of skewness on longitudinal moments. The value of the coefficient k_1 is read from the graph shown in Fig. 3 corresponding to ε and angle of skewness φ. If a^* is the shortest width of skew plate and b is the simply supported span, the parameter ε is calculated as $\varepsilon = (b/a^*)$.

The longitudinal stresses at extreme top and bottom fibers of all the box-girder sections considered in this study according to SBT including the correction for skewness are shown in Table 1.

Table 1 Longitudinal stresses at top and bottom fibers by simple bending theory (kN/m^2)

φ	0°	10°	20°	30°	40°	50°	60°
At mid-span section							
$\sigma_{x,\ top}$	866	829	787	735	639	549	456
$\sigma_{x,\ bott}$	1393	1330	1270	1180	1030	883	733
At a section located 8 m from support							
$\sigma_{x,\ top}$	832	796	756	706	613	527	438
$\sigma_{x,\ bott}$	1330	1270	1210	1130	980	840	700

5 Finite Element Modeling

In this study, three-dimensional finite element analysis of box-girder bridge has been carried out using the Ansys to investigate the effect of skewness on longitudinal stresses and shear lag in simply supported box-girder bridges. The box girders considered in this study have been modeled using the 8-noded Shell91 element having six degrees of freedom per node. In order to validate the effectiveness of the analytical model, the finite element results obtained from Ansys were compared with the experimental data and found satisfactory. The finite element discretization of the bridge is shown in Fig. 4. Along the width the top slab and bottom slab have been divided into eight and four elements, respectively. The longitudinal stresses as well as the shear lag factor have been plotted at the corner nodes of the top and bottom slab elements and the numbering scheme for these nodes has been shown in Fig. 5.

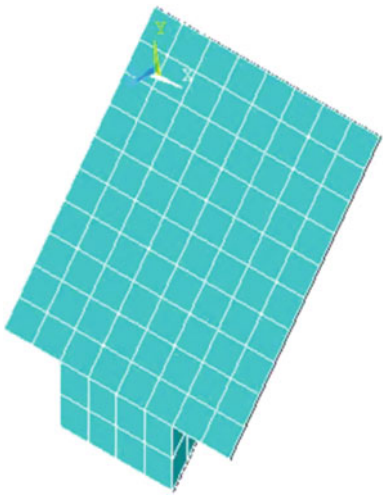

Fig. 4 Finite element discretization of 0° skew bridge

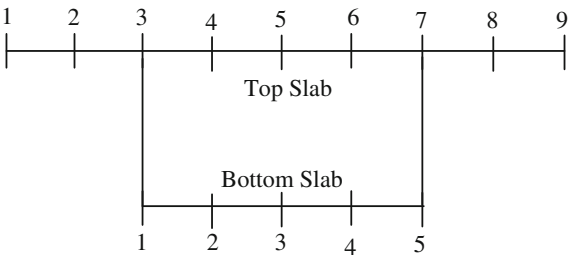

Fig. 5 Location of nodes for plotting longitudinal stress and CSL in top and bottom slabs

6 Results and Discussions

In order to investigate the influence of skewness on the longitudinal stresses and shear lag effect a 20 m span simply supported box-girder bridge with 300 mm diaphragms at both the ends, two sections have been considered in the present study, one at mid-span and other at distance 8 m from the support or at distance 2 m from the mid-span. The longitudinal stresses and the CSL have been plotted at these two sections at top and bottom slab levels. The angle of skew has been varied from 0 to 60° at the interval of 10°. All the bridges considered in this study are subjected to dead loads only due to the self-weight of bridge. The effect of skewness on longitudinal stresses and the coefficient shear lag at mid-span and at an intermediate section located at 2 m from the mid-span is discussed below.

6.1 Longitudinal Stresses at Mid-span Section

Figure 6 shows the effect of skewness on the longitudinal stress distribution along the transverse direction (breadth) in top and bottom slabs of the 20 m span simply supported RC box-girder bridges at mid-span. It may be observed from Fig. 6 that at mid-span, the stresses in the top as well as in bottom slab decreases throughout the breadth of the slabs with increase in skew angle. As the skew angle is varied from 0 to 60° the longitudinal stress at the junctions of the top and bottom slabs with webs are found to decrease by approximately 70 and 83%, respectively. Moreover, the nonuniformity of longitudinal stresses in transverse direction in top as well as in bottom slab decreases with increase in skew angle. In case of top slab, the ratio of the stress at web-slab junction and the stress at mid of the slab for the right bridge case is found 1.83 and this ratio decreases to 1.74 for 60° skew bridge. For the bottom slab case, the ratio of maximum and minimum stress for right bridge is found 1.56, and this ratio has been observed to decrease to 1.13 for the 60° skew bridge. It shows that the longitudinal stresses in bottom slab are more significantly affected by skew angle as compared to top slab.

6.2 Longitudinal Stresses at Section 2 m from Mid-span

Figure 7 shows the effect of skewness on the longitudinal stress distribution along the transverse direction of top and bottom slabs of the 20 m span simply supported RC box-girder bridge at a section located at distance 8 m from the support or 2 m from the mid-span due to dead load only. It may be observed from Fig. 7 that at the section located 2 m away from the mid-span, the stresses in the top as well as in bottom slab decreases throughout the breadth of the slabs with increase in skew angle. As the skew angle is increased from 0 to 60° the longitudinal stress at the

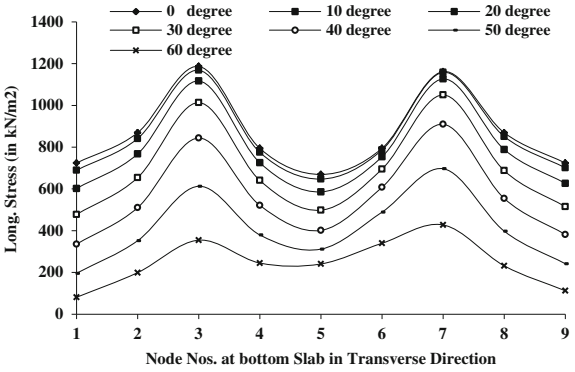

(a) Longitudinal Stresses in top slab

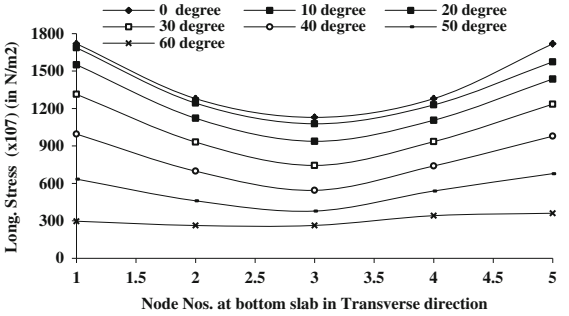

(b) Longitudinal Stresses in bottom slab

Fig. 6 Effect of skewness on longitudinal stresses at mid-span section

junctions of the top and bottom slabs with webs are found to decrease by approximately 46 and 48%, respectively. Moreover, the plots show that longitudinal stresses become un-symmetric along transverse direction in top as well as in bottom slabs due to skewness. It is interesting to note that for highly skewed bridges, the nature of stress in bottom slab changes the sign, and it becomes compressive rather than tensile which is contrary to conventional nature of stresses in bottom slab.

6.3 Shear Lag at Mid-span Section

To examine the influence the effect of skewness on shear lag effect at mid-span of the simple supported box-girder bridge, the variation of CSL in top and bottom slabs along the transverse direction is shown in Fig. 8. It may be observed from the plots for coefficient for shear lag that up to 30° skewness, the CSL is not much affected by the skew angle; however, the CSL at web-slab junction significantly decreases with increase in skew angle beyond 30°. Moreover, for the highly skewed

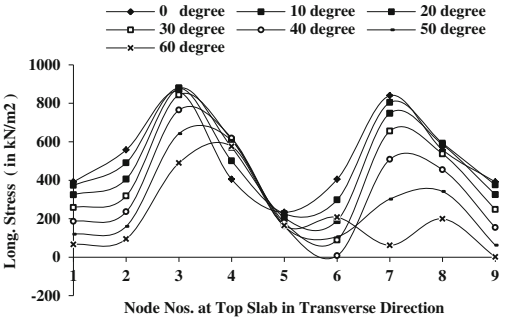

(a) Longitudinal Stresses in top slab

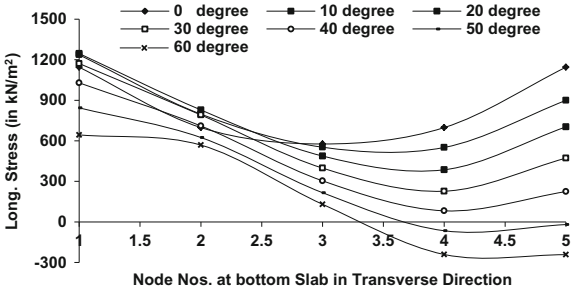

(b) Longitudinal Stresses in bottom slab

Fig. 7 Effect of skewness on longitudinal stresses at distance 2 m from mid-span

bridges with skew angle 60°, CSL becomes less than unity which indicates that the shear lag effect disappears and the longitudinal stresses throughout the top slab become less than those calculated from SBT. And the similar trend was observed in bottom slab for skew angle 40° and higher.

6.4 Shear Lag at Section 2 m from Mid-span

The variation of CSL in top and bottom slabs along the transverse direction at the section located at 8 m from the left support or say 2 m away from the mid-span are shown in Fig. 9. It may be observed from the plots for CSL that at section 2 m away from mid-span the CSL becomes highly un-symmetric, wherein the CSL for the left web-slab junction always remains more than unity, however, for the right-hand side web-slab junction, CSL always remains below unity irrespective of skew angle. Moreover, it is important to note that at the right web-slab junction, the shear lag decreases with increase in skew angle, and it becomes approximately zero for skew angle 40° and then increases with increase in skew angle beyond 40°.

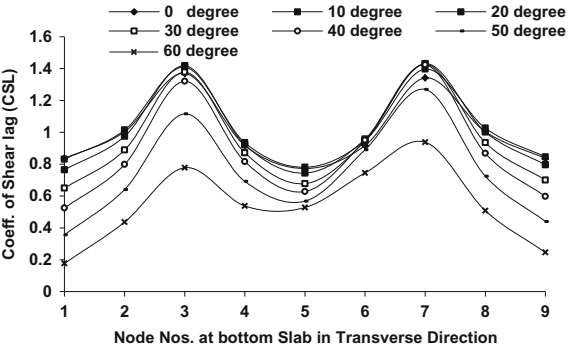

Fig. 8 Effect of skewness on coefficient of shear lag (CSL) at mid-span

(a) Coefficient of Shear Lag (CSL) in top slab

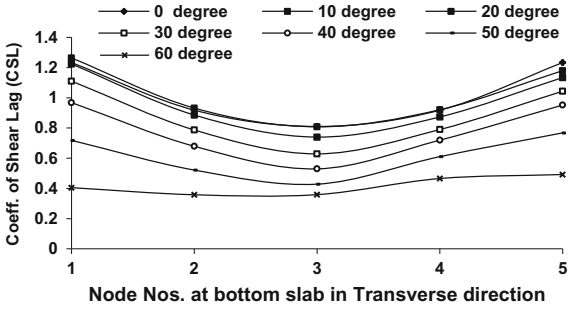

(b) Coefficient of Shear Lag (CSL) in bottom slab

7 Conclusions

In this paper, the linear elastic finite element analysis of a 20 m span simply supported single cell box-girder bridge was carried out to study the effect of skew angle on the longitudinal stresses and shear lag in top and bottom slabs at mid-span section as well as at an intermediate section located at 2 m from the mid-span. To this end, the skew angle was varied from 0 to 60° at an interval of 10°. Based on the study carried out following conclusions are drawn:

- In general, with increase in skew angle, the longitudinal stresses in top and bottom slabs at mid-span as well as at section located 2 m distance from the mid-span decrease; however, at the section 2 m away from the mid-span, the stresses at right web-slab junction decrease more rapidly compared to left web-slab junction.

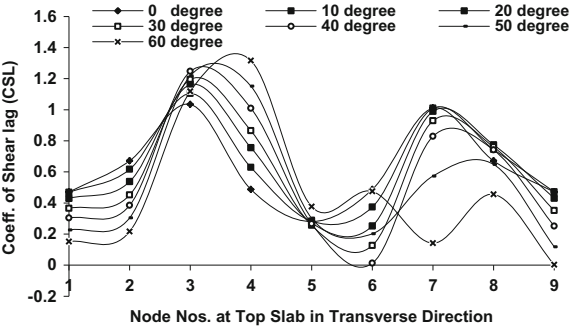

(a) Coefficient of Shear Lag (CSL) in top slab

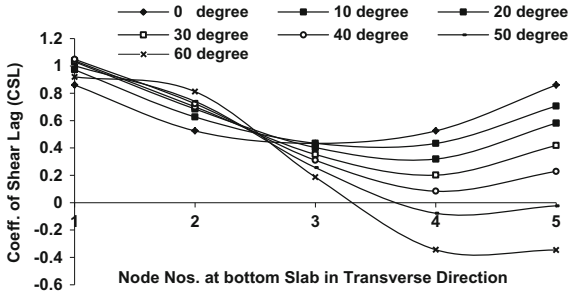

(b) Coefficient of Shear Lag (CSL) in bottom slab

Fig. 9 Effect of skewness on coefficient of shear lag (CSL) at section 2 m from mid-span

- At the mid-span section, the nonuniformity of longitudinal stresses in top and bottom slabs decreases with increase in skew angle.
- Up to 20° skewness, the CSL is not much affected by the skew angle; however, the CSL decreases with increase in skew angle beyond 20°.

References

1. Reissner, E. (1946). Analysis of shear lag in box beams by the principle of minimum potential energy. *Quarterly of Applied Mathematics, IV*(3), 268–278.
2. Luo, Q. Z., Tang, J., & Li, Q. S. (2002). Experimental studies on shear lag of box girders. *Engineering Structures, 24,* 469–477.
3. Luo, Q. Z., & Li, Q. S. (2000). Shear lag of thin-walled curved box girder bridges. *Journal of Engineering Mechanics, ASCE, 126*(10), 1111–1114.
4. Luo, Q. Z., Li, Q. S., & Tang, J. (2002). Shear lag in box girder bridges. *Journal of Bridge Engineering, ASCE, 7*(5), 308–313.
5. Yang, L. F., Leung, A. Y. T., & Li, Q. S. (2001). The stochastic finite segment in the analysis of the shear-lag effect on box-girders. *Engineering Structures, 23,* 1461–1468.
6. Lertsima, C., Chaisomphob, T., & Yamaguchi, E. (2004). Stress concentration due to shear lag in simply supported box girders. *Engineering Structures, 26,* 1093–1101.

7. Luo, Q. Z., Tang, J., Li, Q. S., Liu, G. D., & Wu, J. R. (2004). Membrane forces acting on thin-walled box girders considering shear lag effect. *Thin-walled Structures, Science Direct, 42,* 741–757.
8. Chang, S. T., & Yun, D. (1988). shear lag effect in box girder with varying depth. *Journal of Structural Engineering, ASCE, 114*(10), 2280–2292.
9. Chang, S. T. (2004). Shear lag effect in simply supported prestressed concrete box girder. *Journal of Bridge Engineering, ASCE, 9*(2), 178–184.
10. Bakht, B. (1988). Analysis of some skew bridges as right bridge. *The Journal Structural Engineering, ASCE, 114*(10), 2307–2322.
11. Mohseni, I., & Rashid, A. R. K. (2012). *Development of simplified skew correction factor equations for distribution of live load in highway multi-cell box-girder bridge*. In International Conference on Transport, Environment and Civil Engineering (ICTECE) August 25–26, 2012, Kuala Lumpur (Malaysia).
12. Yang, H., Li, R., & Chen, Z. (2015). *Curve analysis of shear lag effect of box girder bridge*. In International Conference on Materials, Environmental and Biological Engineering (MEBE) (pp. 795–798).
13. Song, Q., & Scordelis, A. (1990). Shear-lag analysis of T-, I-, and box beams. *Journal of Structural Engineering, 116*(5), 1290–1305.
14. Szilard, R. (2004). *Theory and analysis of plates, classical and numerical method*. New Delhi: Wiley.

Stress in Unbonded Tendons for Post-tensioned Concrete Members—Assessment of Prediction Equations and Experimental Investigation

R. Manisekar and K. Saravana Kumar

Abstract Post-tensioning is being widely used in bridges, namely, highway bridges, railway bridges, segmental box girder bridges, METRO bridges, and sea links. Generally, the ultimate flexural behavior of concrete members with unbonded tendons is evaluated by the stress in unbonded tendons at ultimate state. Researchers have developed the equations using various analytical concepts, namely, moment–curvature relationship, empirical methods, strain reduction coefficient method, equivalent plastic hinge length method, and finite element method. The paper intends to present the performance of the prediction equations and suitable analytical concept for calculating the stress in tendons. Performance of prediction equations for calculating the stress at ultimate in unbonded tendons f_{ps} has been evaluated using experimental data published in the literature. In the next stage, an experimental investigation on the flexural behavior of post-tensioned concrete beam is done by authors, and the results have been used for evaluation. Also, the FEM analysis using ANSYS package is also performed and compared with test results. It is concluded that the prediction equations developed using equivalent plastic hinge length concept have performed well.

Keywords Post-tensioning · Unbonded tendons · Stress increase

Notations

A_{ps} Area of prestressing steel
A_s Area of nonprestressed tensile steel
A'_s Area of nonprestressed compressive steel
b Width of the section

R. Manisekar (✉) · K. Saravana Kumar
ACTEL Division, CSIR-Structural Engineering Research Centre, Chennai 600113, India
e-mail: mani@serc.res.in

K. Saravana Kumar
e-mail: saravana@serc.res.in

A. Rama Mohan Rao and K. Ramanjaneyulu (eds.), *Recent Advances in Structural Engineering, Volume 1*, Lecture Notes in Civil Engineering 11,
https://doi.org/10.1007/978-981-13-0362-3_20

c Depth from concrete extreme compressive fiber to neutral axis
c_y Depth from concrete extreme compressive fiber to neutral axis calculated using f_{py}
d_p Depth from concrete extreme fiber to centroid of the prestressing steel
d_s Depth from concrete extreme compressive fiber to centroid of the non prestressed tensile steel
d'_s Depth from concrete extreme compressive fiber to centroid of the nonprestressed compressive steel
E_{ps} Modulus of elasticity of the prestressing steel
f_{pe} Effective stress in the prestressing steel
f_{ps} Ultimate stress in the prestressing steel
f_{pu} Ultimate strength of the prestressing steel
f_{py} Yield strength of the prestressing steel
f'_c Concrete compressive strength
f_{cu} Concrete compressive strength taken from cube test
f_y Yield strength of nonprestressed tensile steel
f'_y Yield strength of nonprestressed compressive steel
h Height of the section
h_f Thickness of the flange
L Span length between end anchorages
L_e Span length between end anchorages divided by the number of plastic hinges
L_p Width of the plastic zone
L_0 Equivalent plastic hinge length
β_1 ACI concrete compression block reduction factor
ρ_p Prestressing steel ratio
ρ_s Reinforcing steel ratio
ε_{cu} Strain in the concrete at the compressive fiber at ultimate

1 Prediction Equations Used for Evaluation

The flexural behavior of concrete members with unbonded tendons is evaluated by the stress in unbonded tendons at ultimate state. The common approach for evaluating the stress in unbonded tendons at ultimate state, f_{ps} is as follows:

$$f_{ps} = f_{pe} + \Delta f_{ps} \tag{1}$$

f_{ps} ultimate stress in unbonded tendons,
f_{pe} effective prestress, and
Δf_{ps} stress increase in tendon beyond the effective prestress, up to ultimate behavior.

Thirteen equations are taken for evaluation, which are given below:

ACI Equation [1]

$$f_{ps} = f_{pe} + 10,000 + \frac{f'_c}{100\rho_p} \quad \text{for } L/d \leq 35 \text{ Psi} \tag{2}$$

$$f_{ps} = f_{pe} + 10,000 + \frac{f'_c}{300\rho_p} \quad \text{for } L/d \geq 35 \text{ Psi} \tag{3}$$

Pannell [2]

$$f_{ps} = \frac{q_u}{\rho_p} f'_c \text{ MPa} \tag{4}$$

$$q_u = \frac{q_e + \lambda}{1 + 2\lambda} \quad q_e = \frac{A_{ps} f_{pe}}{b d_p f'_c} \quad \lambda = \frac{\psi \rho_p \varepsilon_{cu} E_{ps} d_{ps}}{L f'_c}$$

$$\psi = 10 \quad L_p = L_o = 10c$$

where $\Delta\varepsilon_{cps}$ is change in strain in the concrete at the level of the prestressing steel, L_p is length of the plastic zone occur at ultimate, Δ_l is concrete elongation at the level of the prestressing steel that measured within the length of the plastic zone, c is depth of the neutral axis at ultimate, and ε_{cu} is strain in the concrete top fiber at ultimate.

Tam and Pannell [3]

$$f_{ps} = \frac{f'_c \left[\frac{q_e + \lambda}{1 + \frac{\lambda}{\alpha}} - \frac{q_s \lambda}{\alpha + \lambda} \right]}{\rho_p} \text{ MPa} \tag{5}$$

where

$$q_e = \frac{A_{ps} f_{pe}}{b d_p f'_c} \tag{6}$$

$$q_s = \frac{A_s f_y}{b d_p f'_c} \tag{6a}$$

$$\lambda = \psi r \varepsilon_u E_s d / L f_{cu} \quad L_p = L_o = 10.5c$$

where $\alpha = 0.85\ \beta_1$ (based on cylinder compressive strength) or $\alpha = 0.68\ \beta_1$ (based on cube compressive strength), β_1 is the stress block reduction factor defined in the ACI Building Code.

Du and Tao [4]

$$f_{ps} = f_{pe} + (786 - 1920q_o)\ \text{MPa} \tag{7}$$
$$f_{ps} \leq f_{py}$$

$q_o \leq 0.3$; $0.55f_{py} \leq f_{pe} \leq 0.65f_{py}$, where f_{py} is the yield stress of the prestressing steel.

Harajli [5]

$$f_{ps} = f_{pe} + \left(10,000 + \frac{f'_c}{100\rho_p}\right)\left(0.4 + \frac{8}{S/d_p}\right) \leq f_{py}\ \text{psi} \tag{8}$$
$$f_{ps} \leq f_{pe} + 60,000\ \text{psi}$$

Harajli and Hijazi [6]

$$f_{ps} = f_{pe} + \gamma_s f_{pu}\left(1 - \beta_0 \frac{c}{d_p}\right) \leq f_{py}\ \text{Psi} \tag{9}$$

where

$\gamma_s = \frac{n_0}{n}\left(0.1 + \frac{2}{S/d_p}\right)$ for single point load; $\gamma_s = \frac{n_0}{n}\left(0.25 + \frac{1.2}{S/d_p}\right)$ for uniformly distributed load.

$\gamma_s = \frac{n_0}{n}\left(0.4 + \frac{1.1}{S/d_p}\right)$ for third point load; $\beta_0 = 1.8$ for single point load; and $\beta_0 = 1.75$ for uniform and third point loads.

Naaman and Alkhairi [7]

$$f_{ps} = f_{pe} + \Delta f_{ps} = f_{pe} + \Omega_u E_{ps}\varepsilon_{cu}\left(\frac{d_{ps}}{c} - 1\right)\frac{L_1}{L_2}\ \text{Psi} \tag{10}$$
$$f_{ps} \leq 0.94f_{py}$$

in which $\Omega_u = \frac{1.5}{\left(\frac{L}{d_{ps}}\right)}$ for one point loading. $\Omega_u = \frac{3.0}{\left(\frac{L}{d_{ps}}\right)}$ for third point or uniform loading.

L_1 length of loaded span or sum of lengths of loaded spans, influenced by the same tendon, and
L_2 length of tendon between end anchorages.

Harajli and Kanj [8]

$$f_{ps} = f_{pe} + \gamma_0 f_{pu}\left(1.0 - 3.0\frac{A_{ps}f_{pe} + A_s f_y}{bd_p f'_c}\right) \text{ Psi} \tag{11}$$

where $\gamma_0 = \frac{n_0}{n}\left(0.12 + \frac{2.5}{S/d_p}\right)$.

Chakrabarti [9]

$$f_{ps} = \frac{f_{pe} + 10,000 + A}{(1 - B)} \text{ psi} \tag{12}$$

where

$$A = \frac{f'_c}{100\rho_s}\frac{d_p}{d_s}\frac{60,000}{f_y}(1 + \rho_s/0.025) \leq 20,000 \text{ psi} \tag{12a}$$

$$B = \frac{rf'_c}{100\rho_p f_{pe}} \leq 0.25 \tag{12b}$$

$r = 1.0$ for $S/d \leq 33$,

$r = 0.8$ for $S/d > 33$.
However, when $\rho_s = 0$ and $S/d > 33$, the f_{ps} shall be reduced as follows:

$$f_{ps} = f_{pe} + \left[\frac{f_{pe} + 10,000 + A}{1 - B} - f_{pe}\right].0.65 \tag{12c}$$

With following limits:

$f_{ps} = f_{pe} + 60,000$ where $S/d \leq 33$,

$f_{ps} = f_{pe} + 40,000$ where $S/d > 33$.

Expressions of the parameters used in this equation are as follows:

Reinforcing index $\omega_{pp} = \frac{\rho_p f_{ps}}{f'_c} + \frac{\rho_s f_y}{f'_c}$;
Partial prestressing ratio PPR $= \frac{A_{ps} f_{ps}}{A_{ps} f_{ps} + A_s f_y}$;
Ratio of prestressing steel $\rho_p = \frac{A_{ps}}{bd_p}$; and
Ratio of reinforcing steel $\rho_s = \frac{A_s}{bd_s}$.

Lee et al. [10]

$$f_{ps} = 10,000 + 0.8 f_{se} + \frac{1}{15}\frac{(A'_s - A_s) f_y}{A_{ps}} + 80\sqrt{\frac{d_s}{d_p}\frac{f'_c}{\rho_p}\left[\frac{1}{f} + \frac{1}{L/d_p}\right]} \text{ psi} \tag{13}$$

in the limit of $f_{se} + 10,000 \leq f_{ps} \leq f_{py}$.

Au and Du [11]

$$f_{ps} = f_{pe} + \frac{0.0279 E_{ps}(d_p - c_{pe})}{l_e} \leq f_{py} \text{ MPa} \tag{14}$$

where $c_{pe} = \frac{A_{ps} f_{pe} + A_s f_y}{0.85 \beta_1 f'_c b} \leq f_{py}$.

Harajli [12]

$$f_{ps} = \frac{f_{pe} + K_o E_{ps} \varepsilon_{cu}\left[d_p - \frac{\rho_s d_s f_y}{0.85\beta_1 f'_c}\right]}{1 + \frac{K_o E_{ps} \varepsilon_{cu} \rho_p d_p}{0.85 \beta_1 f'_c}} \tag{15}$$

where $K_o = \varphi_{ps}\left(\frac{20.7}{f} + 10.5\right)\frac{n_p}{L_a}$.

Qi-He and Liu [13]

$$f_{ps,u} = f_{pe} + \Delta f_{ps,u} \leq 0.8 f_{pu} \tag{16}$$

$$\Delta f_{ps,u} = \kappa E_{ps} \frac{e_m}{c} R_s \cdot \frac{L_1}{L_2}$$

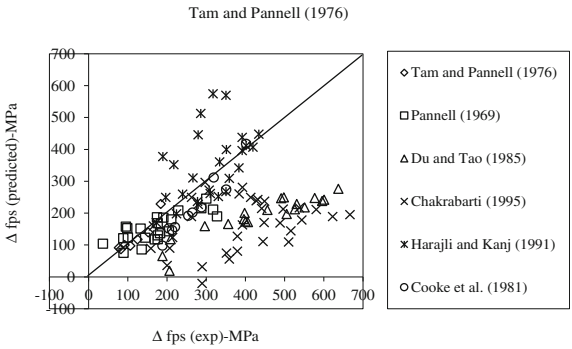

Fig. 1 Prediction of Δf_{ps} by Tam and Pannel

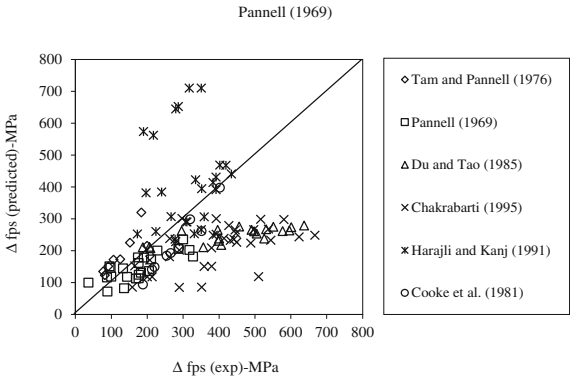

Fig. 2 Prediction of Δf_{ps} by Pannel

2 Discussion

2.1 Evaluation of Equations Using Test Results Published in the Literature

Prediction equations of Tam and Pannell [3], Pannell [2], Du and Tao [4], Chakrabarti [9], Harajli and Kanj [8], Harajli [5], Harajli and Hijazi [6], ACI 318-83, Naaman and Alkhairi [7], Lee et al. [10], Au and Du [11], Harajli [12], and Qi-He and Liu [13] were taken for evaluation. Test results of Tam and Pannell [3], Pannell [2], Du and Tao [4], Chakrabarti [9], Harajli and Kanj [8], and Cooke et al. [14] were used for evaluation.

The performance of equation of Tam and Pannell [3] is shown in Fig. 1, in which the data of Du and Tao and Chakrabarti are scattered, and it has a negative value. Figure 2 shows the evaluation of Pannell's [2] equation, which is well

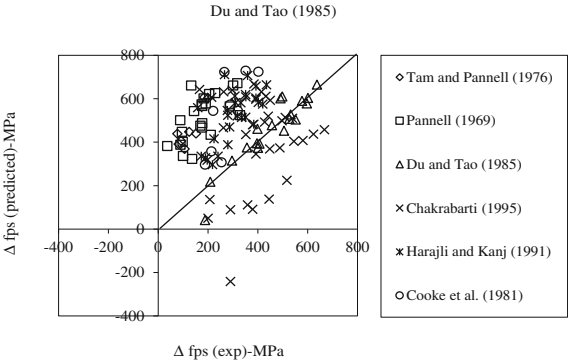

Fig. 3 Prediction of Δf_{ps} by Du and Tao

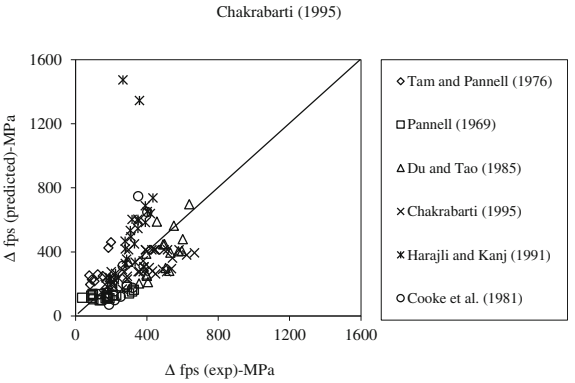

Fig. 4 Prediction of Δf_{ps} by Chakrabarti

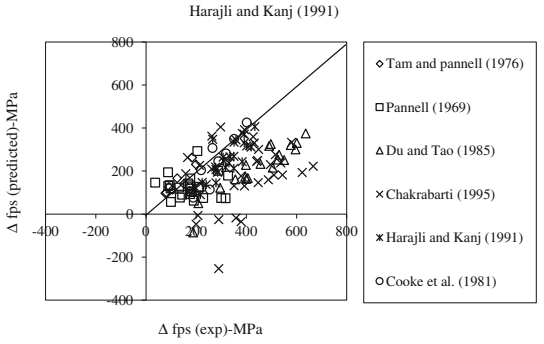

Fig. 5 Prediction of Δf_{ps} by Harajli and Kanj

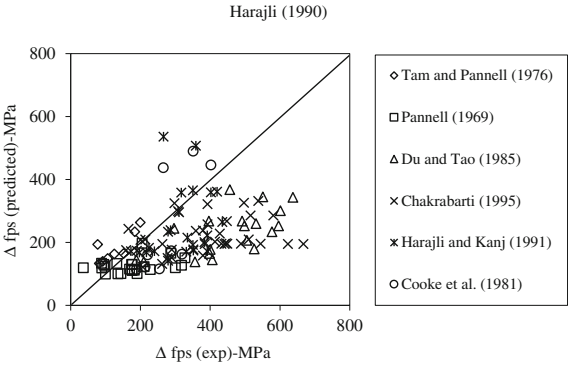

Fig. 6 Prediction of Δf_{ps} by Harajli [5]

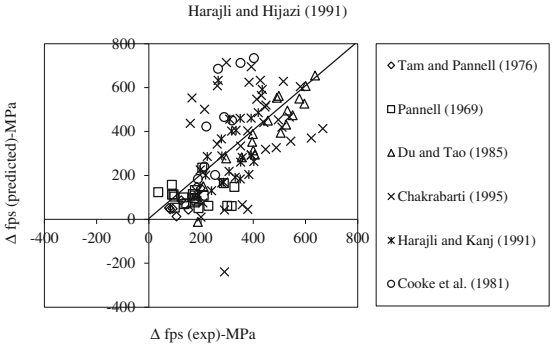

Fig. 7 Prediction of Δf_{ps} by Harajli and Hijazi

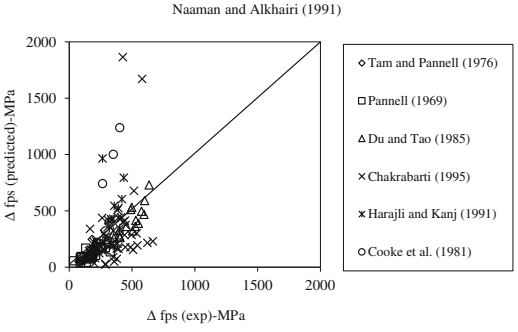

Fig. 8 Prediction of Δf_{ps} by Naaman and Alkhairi

correlated with dataset However, it does not contain the parameters associated with nonprestressing steel. The equation of Du and Tao [4] is away from four data, shown in Fig. 3. It has a negative value since the combined reinforcement index, q_o, is not within or equal to 0.30, which is a limit of the equation (i.e., $q_o \leq 0.30$). The equation of Chakrabarti [9] is correlated with dataset, as shown in Fig. 4. However, the equation is proposed on the basis of only test results and does not have any analytical ground.

The equation of Harajli and Kanj [8] predicts negative values (Fig. 5). It is due to the term $\frac{A_{ps}f_{pe}+A_sf_y}{bd_pf'_c}$ is not within or equal to 0.23 for these specimens, which is a limit of the equation: $\frac{A_{ps}f_{pe}+A_sf_y}{bd_pf'_c}$ need not be taken more than 0.23. The equations of Harajli [5], and Harajli and Hijazi [6] are shown in Figs. 6 and 7, respectively. Both the equations predict in a similar way, but little improvement in the Harajli's [5]

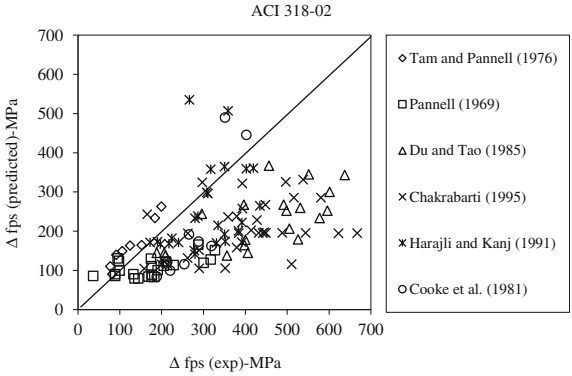

Fig. 9 Prediction of Δf_{ps} by ACI 318-02

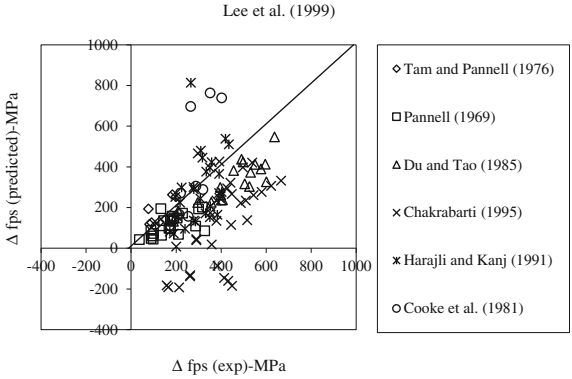

Fig. 10 Prediction of Δf_{ps} by Lee et al.

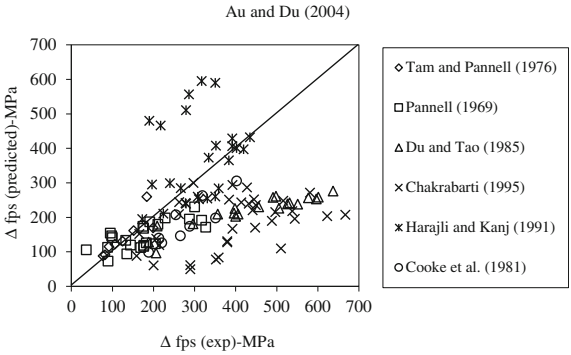

Fig. 11 Prediction of Δf_{ps} by Au and Du

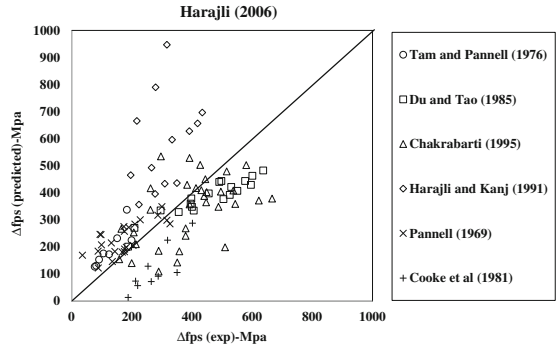

Fig. 12 Prediction of Δf_{ps} by Harajli [12]

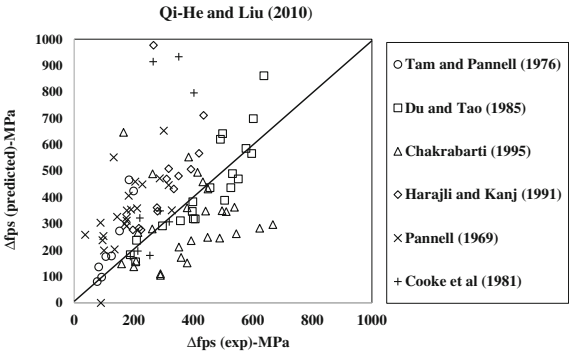

Fig. 13 Prediction of Δf_{ps} by Qi-He and Liu

equation. Harajli and Hijazi's equation shows a negative value since the c value of the equation for the particular specimen becomes high. In Fig. 8, the equation of Naaman and Alkhari [7] predicts very high Δf_{ps} values. Prediction of ACI equation [1] (Fig. 9) does not show negative values, but the graph is scattered. Moreover, the equation is limited for span to depth ratio. The equation of Lee et al. [10] is shown in Fig. 10. Here, all the data are closer to the correlation line except showing some negative values, associated with Chakrabarti's data. The negative values are predicted for the specimens, which do not contain nonprestressing steel. Although the prediction has negative values, it contains loading type and span to depth ratio in the plastic hinge length, L_o. The equation of Au and Du [11] is shown in Fig. 11, in which two datasets are away from correlation line. Figure 12 shows the prediction of Harajli [12], which perform well with all the data except some data. Also, it is comparatively better than others. Figure 13 shows the performance of equation of Qi-He and Liu [13], which is nearer to the correlation line, and exhibit some scattering in the data of Cooke et al. [14] and Harajli and Kanj [8].

From the evaluation, it is observed that the prediction of Δf_{ps} by equation of Harajli [12] and equation Lee et al. [10] found satisfactory. Others have shown unsatisfactory performance. It seems that the unsatisfactory performance of equations may be due to the inefficiency of the equations in predicting the plastic hinge formation. Manisekar and Senthil [15] and Harajli [12] have suggested that the plastic hinge formation is directly related to the stress increase in unbonded tendons, Δf_{ps}. Conventionally, the equivalent plastic hinge length is expressed as $1.5d$. Authors have used different values and expressions for equivalent plastic hinge length. Harajli [12] and Lee et al. [10] have used $L_p = \left(\frac{20.7}{f} + 105\right) \cdot c$ and $L_o = \left(\frac{1}{f} + \frac{1}{L/d_p}\right)L$, respectively, where f, c, and L/d_p are loading type, neutral axis depth, and span to depth ratio, respectively. Therefore, it is possible to believe that the Δf_{ps} could be predicted accurately if the plastic hinge formation and its length of extension in the flexural region are predicted accurately.

A second stage of evaluation on the prediction equations, an experimental investigation was done by the authors, and the test results are used for evaluating.

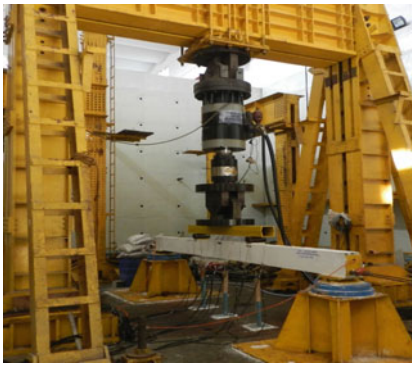

Fig. 14 Test setup of the specimen

Fig. 15 Failure of post-tensioned concrete beam

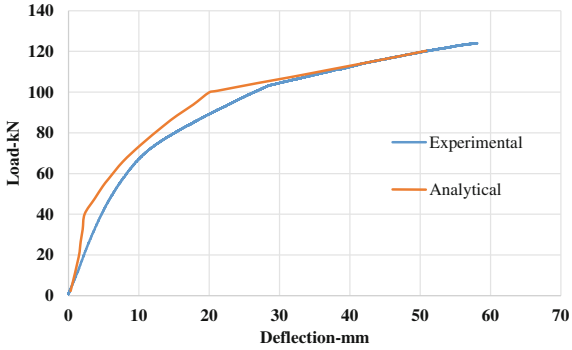

Fig. 16 Load–deflection curve

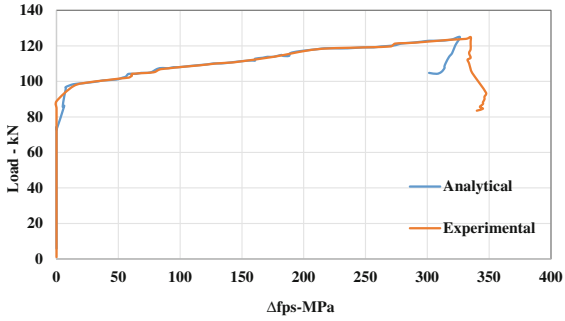

Fig. 17 Load–Δf_{ps} relation

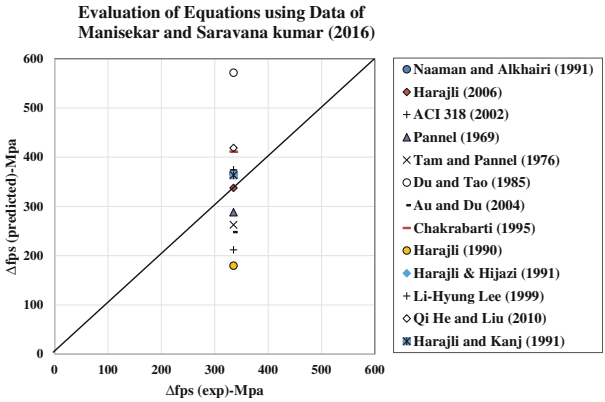

Fig. 18 Evaluation of equations using test results of authors

3 Experimental Investigation

Experimental investigation on the flexural behavior of post-tensioned concrete rectangular beam of section 150 mm × 270 mm subjected to two-point load was performed. The rectangular beam specimen consists of two numbers of 12.7 mm dia 7-ply strand with eccentricity of 75 mm, was used (Fig. 14). M45 concrete and straight tendon profile were provided. The specimen failed with concrete crushing in the extreme compressive fiber at the load of 124.05 kN with the maximum deflection of 58 mm, shown in Fig. 15. The stress at ultimate in unbounded tendons, f_{ps} was 1490 MPa and the stress increase in unbonded tendons Δf_{ps} was 335 MPa.

The comparison of FE analysis using ANSYS package with test results of authors is shown in Figs. 16 and 17.

4 Evaluation of Equations Using the Test Results of Authors (Manisekar and Saravana Kumar)

In Fig. 18, the prediction equations are compared with the test results of authors by perfect correlation line. In the evaluation, the equation of Harajli [12] is well correlated with the perfect correlation line. Equations of Lee et al. [10], Harajli and Kanj [8], and Naaman and Alkhairi [7] are nearer to the perfect correlation line. It is to mention that the equations of Harajli [12], Lee et al. [10], and Harajli and Kanj [8] have been developed based on the plastic hinge length concept.

Comparison of Δf_{ps} (exp) and Δf_{ps} (predicted) was used for evaluation, since the post-tensioned concrete members undergo deformation when stress increase in tendons occurs. In view of the evaluation of the prediction equations with published test data and the authors' experimental data, it could be concluded that the

equations developed based on the equivalent plastic hinge length concept have well correlated with the test data. It is due to the reason that the equivalent plastic hinge length is directly related to the stress increase in unbonded tendons, Δf_{ps}.

5 Conclusions

1. Prediction equations developed by the researchers have been evaluated using published test data and the authors' experimental data. It is concluded that the equations developed based on the equivalent plastic hinge length concept have well correlated with the test data rather than that of other concepts.
2. This conclusion is establishing the fact that the equivalent plastic hinge length is directly related to the stress increase in unbonded tendons, Δf_{ps}, of a post-tensioned concrete member.

Acknowledgements This paper is being published with the kind permission of the Director, CSIR-Structural Engineering Research Centre, Chennai.

References

1. ACI Committee 318 (2002). *Building code requirements for reinforced concrete*.
2. Pannell, F. N. (1969). The ultimate moment of resistance of unbonded prestressed concrete beams. *Magazine of Concrete Research, 21*(66), 43–54.
3. Tam, A., & Pannell, F. N. (1976). The ultimate moment of resistance of unbonded partially prestressed reinforced concrete beams. *Magazine of Concrete Research, 28*(97), 203–208.
4. Du, G., & Tao, X. (1985). Ultimate stress of unbonded tendons in partially prestressed concrete beams. *PCI Journal, 30*(6), 72–91.
5. Harajli, M. H. (1990). Effect of span-depth ratio on the ultimate steel stress in unbonded prestressed concrete members. *ACI Structural Journal, 87*(3), 305–312.
6. Harajli, M. H., & Hijazi, S. A. (1991). Evaluation of the ultimate steel stress in partially prestressed concrete members. *PCI Journal, 36*(1), 62–82.
7. Naaman, A. E., & Alkhairi, F. M. (1991). Stress at ultimate in unbonded post-tensioning tendons: Part 2—proposed methodology. *ACI Structural Journal, 88*(5), 683–692.
8. Harajli, M. H., & Kanj, M. Y. (1991). Ultimate flexural strength of concrete members prestressed with unbonded tendons. *ACI Structural Journal, 88*(6), 663–673.
9. Chakrabarti, P. R. (1995). Ultimate stress for unbonded post-tensioning tendons in partially prestressed beams. *ACI Structural Journal, 92*(6), 689–697.
10. Lee, L. H., Moon, J. H., & Lim, J. H. (1999). Proposed methodology for computing of unbonded tendon stress at flexural failure. *ACI Structural Journal, 96*(6), 1040–1048.
11. Au, F. T. K., & Du, J. S. (2004). Prediction of ultimate stress in unbonded prestressed tendons. *Magazine of Concrete Research, 56*(1), 1–11.
12. Harajli, M. H. (2006). On the stress in unbonded tendons at ultimate: Critical assessment and proposed changes. *ACI Structural Journal, 103*(6), 803–812.
13. Qi-He, Z., & Liu, Z. (2010). Stress in external and internal unbonded tendons: Unified methodology and design equations. *Journal of Structural Engineering (ASCE), 136*(9), 1055–1065.

14. Cooke, N., Park, R., & Yong, P. (1981). Flexural strength of prestressed concrete members with unbonded tendons. *PCI Journal, 26*(6), 52–80.
15. Manisekar, R., & Senthil, R. (2006). Stress at ultimate in unbonded post-tensioning tendons for simply supported beams: A state-of-the-art review. *Advances in Structural Engineering, 9*(3), 321–335.

Biaxial Effects in Unreinforced Masonry (URM) Load-Bearing Walls

Jacob Alex Kollerathu and Arun Menon

Abstract Under seismic loading, a structure may be subject to simultaneous in-plane and out-of-plane actions. Existing simplified methods like the storey-shear mechanism to determine the shear capacity of masonry structures neglect the out-of-plane effects leading to a non-conservative seismic assessment. In this paper, an analytical model is developed to evaluate the in-plane shear capacities of unreinforced masonry (URM) walls, in the presence of additional out-of-plane displacement. Results from this paper demonstrate that the additional out of displacements alter both the in-plane shear capacity and failure mechanism of the wall. The sensitivity of the interaction to the axial load on the wall is also studied. The proposed model is validated with non-linear finite element analysis. The developed model can be used to determine the reduced shear capacity of URM walls if the mid-height out-of-plane displacement is known. The biaxial interaction of URM walls is also studied dynamically. The model is extended to the framework of the storey-shear mechanism to study the effect of out-of-plane displacements at the global level.

Keywords Unreinforced masonry walls · Out-of-plane displacements
In-plane shear capacity · Interaction

1 Introduction

Post-earthquake studies have identified out-of-plane collapse of unreinforced masonry (URM) walls as one of the predominant modes of failure. The random nature of the ground shaking and the possible eccentricity between centres of mass

J. A. Kollerathu (✉) · A. Menon
Department of Civil Engineering, Indian Institute of Technology Madras, Chennai 600036, India
e-mail: jacobalexcivil@gmail.com

A. Menon
e-mail: arunmenon@iitm.ac.in

A. Rama Mohan Rao and K. Ramanjaneyulu (eds.), *Recent Advances in Structural Engineering, Volume 1*, Lecture Notes in Civil Engineering 11,
https://doi.org/10.1007/978-981-13-0362-3_21

and stiffness may lead to additional out-of-plane effects in masonry walls and combined in-plane and out-of-plane (biaxial) actions in a wall that can affect its in-plane shear capacity. While the seismic demand on the wall can be obtained by considering global load combinations, a method that describes the out-of-plane effects on the in-plane shear capacity of a member under seismic response does not exist. During an earthquake, the response of the wall depends on the presence of RC tie beams and type of diaphragm action (rigid/flexible). Depending on the magnitude of loading and the aforementioned factors, the wall may be subject to in-plane and out-of-plane loading. The negligible OOP resistance of URM walls prevents the exploitation of the global capacity of masonry walls associated with their in-plane capacity leading to non-conservative seismic assessment.

URM walls are significantly used as load-bearing walls, and their behaviour under combined in-plane and out-of-plane loading is important to understand the seismic assessment of masonry structures completely. Past experimental and numerical studies [1–7] indicate that there is interaction between the in-plane and out-of-plane forces. While the force-based interaction models are useful, possibly up to peak force capacity, they become limited at ultimate conditions. The current research addresses this gap area in the way biaxial effects are studied without considering the effects of out-of-plane (OOP) displacements on in-plane shear capacity in the following manner:

- Generating biaxial interaction curves for load-bearing URM walls to evaluate their shear capacity for increasing out-of-plane displacements.
- Validating the proposed analytical model by non-linear finite element analysis, under both static and dynamic effects.
- Proposed analytical model is utilized for determining the in-plane global capacity of a multi-storied URM structure, in the presence of additional out-of-plane displacements.

2 Review of Research on Biaxial Interactions

2.1 Experimental Studies

Shapiro et al. [1] experimentally studied the in-plane and out-of-plane interaction of infill walls in concrete frames, and a complete loss of out-of-plane capacity was observed in the presence of in-plane shear forces. Flanagan and Bennett [2] performed several bidirectional tests on structural clay tile infill panels in steel frames. Significant out-of-plane stability under combined loading was noticed due to arching mechanism. Al-Chaar [3] experimentally studied how large out-of-plane forces lead to a drop in the in-plane capacity URM infill walls. In this test, the in-plane capacity of the infill walls was determined at varying percentages of its out-of-plane capacity.

Recent experimental work by Najafgholipour et al. [4] developed a circular interaction surface between the in-plane and out-of-plane capacities of masonry walls using both force-based experimental and theoretical studies.

2.2 Analytical and Theoretical Studies

Hashemi and Mosalam [5] and Kadysiewski and Mosalam [6] used a simple element hysteretic model to investigate the interaction of in-plane and out-of-plane action of an infill URM wall. This study considered an infill wall with two degrees-of-freedom (DOF): one assigned to the in-plane displacement of the top plane of the wall and one for out-of-plane displacement at its mid-height.

Non-linear FE analyses by Bakshi et al. [7] have described the biaxial behaviour of URM walls and developed relations between the in-plane and out-of-plane shear forces of the wall. Masonry walls were modelled in a more rigorous manner (micromodelling) compared to the macroelement modelling approach. It is also concluded from the results that the presence of out-of-plane forces resulted in the reduction of the in-plane deformation capacity.

Results from Agnihotri et al. [8] modelled unreinforced masonry walls with 3D deformable shell elements to study the effect of in-plane deformations on OOP damage. Numerical results showed that the effect of in-plane deformations resulted in a drop in the out-of-plane capacity of the wall by nearly a third of its un-cracked capacity.

2.3 Gap Areas

The storey-shear-mechanism ignores the interactions of the out-of-plane actions on the in-plane shear capacity. Results from all the aforementioned works demonstrate that there is considerable interaction between the in-plane and out-of-plane effects, which may result in a non-conservative seismic assessment if one were to use the storey-shear mechanism. However, published literature has limited the study of biaxial behaviour of load-bearing masonry walls in terms of its force capacities with no reference to the effects of out-of-plane displacements on in-plane behaviour. Only Agnihotri et al. [8] have studied the biaxial behaviour of masonry walls in terms of its displacement. However, the authors have studied the effects of the in-plane displacement on the OOP capacity and damage. A drawback of looking at the effects of out-of-plane forces is that the biaxial interaction cannot be studied close to ultimate conditions.

3 Biaxial Effects in Masonry Walls

3.1 *Effect of Out-of-Plane Displacement on In-Plane Shear Strength*

None of the published literature has studied the effects of out-of-plane displacements on the in-plane behaviour of load-bearing walls. The effect of out-of-plane displacement demand on the in-plane shear capacity of a wall should be explored under both static and dynamic analysis to understand the interaction at out-of-plane displacements on the in-plane capacity of URM walls. In the ensuing section, the effect of the out-of-plane displacement on the in-plane shear capacity is determined under static loading conditions. An unreinforced masonry wall pinned at the top and bottom, when subjected to out-of-plane displacements, undergoes vertical bending and cracks horizontally across its thickness when its tensile strength is exceeded. The effective thickness is used to estimate the in-plane shear capacity in the presence of out-of-plane displacements that is expressed as a scaled pure in-plane shear capacity in Eq. (1):

$$V = V_c\left(1 - \sqrt{\frac{\Delta}{\Delta_{u1}}}\right) \tag{1}$$

where the pure in-plane shear capacity V_c is estimated as the shear capacity as per Magenes and Calvi [9]. Δ_{u1} corresponds to out-of-plane displacement at loss of in-plane shear strength; Δ is the out-of-plane displacement demand on the wall estimated as per Priestley [10]. Figure 1 shows the drop in shear capacity as per Eq. (1) of an unreinforced masonry wall (2000 × 2000 × 250 mm) with a compressive strength of 10 MPa wall when subjected to an axial stress of 0.1 MPa and increasing mid-height out-of-plane displacement.

3.2 *Behaviour of URM Walls Under In-Plane, Out-of-Plane and Axial Loads*

When subjected to in-plane shear forces, out-of-plane mid-height displacements and axial forces, a URM wall may fail due to loss of in-plane strength, second-order effects or due to flexural crushing at extreme fibre about the thickness. The different out-of-plane displacements at which the wall may fail in any of the above-mentioned scenarios have to be determined. The value of Δ_u in Eq. (1) is limited to the minimum of the out-of-plane displacements at which one of the failure mechanisms occurs.

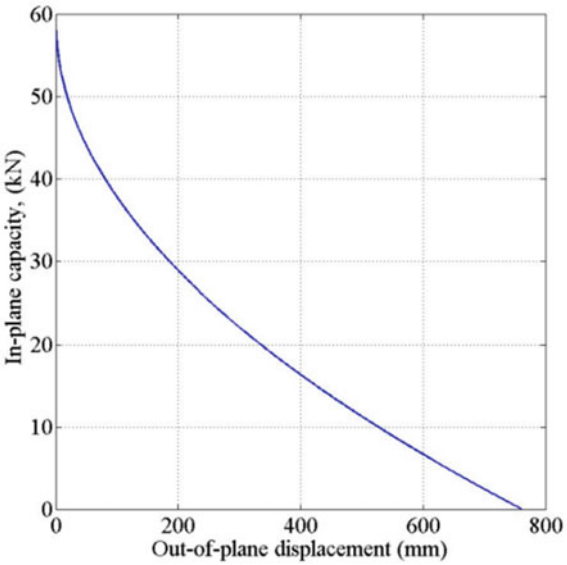

Fig. 1 Drop in in-plane capacity due to out-of-plane deformations, as per formula (1)

$$\Delta = \min(\Delta_{u1}, \Delta_{u2}, \Delta_{u3}) \tag{2}$$

Due to out-of-plane displacements, the wall is subject a strain gradient along its thickness. When the tensile strength is lost, the wall cracks across its thickness leading to a loss in its in-plane strength. The out-of-plane displacement at which the in-plane shear capacity drops to zero (Δ_{u1}) is determined as the displacement at which the in-plane strength is lost due to decreasing cross section of the wall (see Fig. 2). The out-of-plane displacement at which the wall fails due to loss in out-of-plane capacity (Δ_{u2}) is for load-bearing masonry walls (pinned at top and bottom) close to 0.5 t and for parapet walls (free at the top) close to 0.67 t [11]. The out-of-plane displacement at which the wall fails due to flexural crushing (Δ_{u3}) is the displacement at which the edge compressive stress about the thickness exceeds the strength of the masonry in flexural compression, in the presence of out-of-plane bending and axial stress (see Fig. 2).

The sensitivity of the interaction on the axial load is studied and from Fig. 3, one can establish that in walls under simultaneous in-plane and out-of-plane displacements and subject to very low axial loads ($0.01f'_m$), wall failure is due to loss in out-of-plane capacity, whereas for higher loads, it is due to flexural crushing.

3.3 Validation of Proposed Model

The model proposed in Eq. (1) has been validated using a non-linear finite element tool, TNO-Diana 9.5.5 [12] (DIANA.9.5 documentation, 2014). The wall is

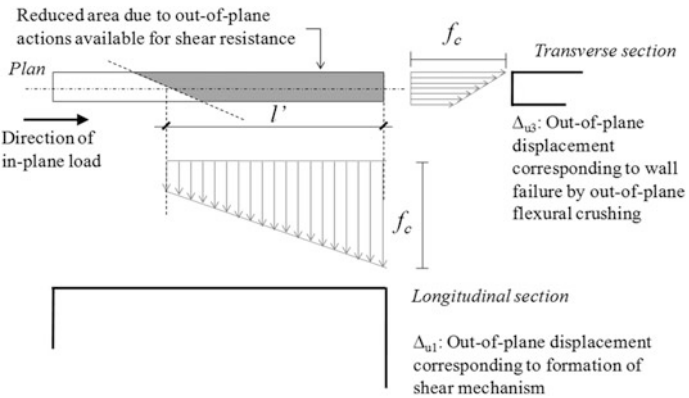

Fig. 2 Definitions of Δ_{u1} and Δ_{u3}

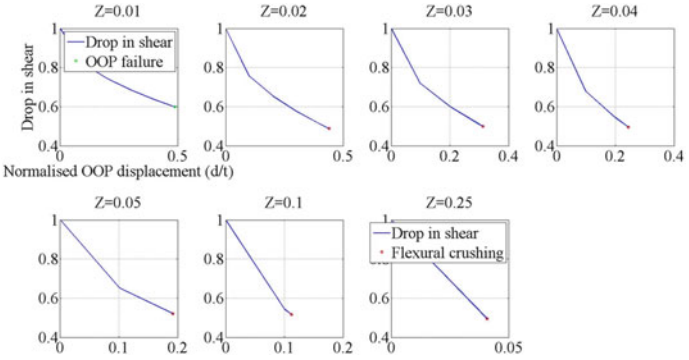

Fig. 3 Sensitivity of failure on axial load (*Z*: ratio of axial load to compressive strength)

modelled using the simplified micromodel or the meso-model approach. The brick units were modelled using eight-noded iso-parametric quadrilateral curved shell elements (CQ48S). The unit has been modelled to behave as an elastic element with a constant thickness. The unit-mortar interface has been modelled as a non-linear interface using the combined cracking–shearing–crushing model [13]. The crack in the unit is modelled in a manner that the wall has a strong unit–weak joint behaviour. The number of material properties required in both the approaches is different; however, material properties such as E, G, compressive strength and tensile strength are kept the same in both the models. The rest of the material properties have been derived from closed-form solutions and tables prescribed in Lourenço [13]. The walls are free to rotate in the out-of-plane direction at their base and at the top of the wall, they are restrained against rotations along the vertical direction and translations in the out-of-plane direction. The non-linear finite element model is pre-validated against experimental work [14] for in-plane behaviour (Table 1).

Table 1 Material properties for NLFEM modelling as per Lourenço [13]

Brick	Young's modulus (MPa)	5500
	Poisson's ratio	0.15
Brick–mortar interface	Shear stiffness (N/mm^3)	86
	Cohesion (MPa)	0.2
	Fracture energy in shear (N/mm)	0.02
	Internal friction angle	32°
	Shear stiffness (N/mm^3)	87
	Normal stiffness (N/mm^3)	38
	Tensile strength (MPa)	0.15
	Fracture energy in tension (N/mm)	0.012
	Compressive strength (MPa)	10
Vertical cracks in bricks	Normal stiffness (N/mm^3)	357
	Shear stiffness (N/mm^3)	890
	Tensile strength (MPa)	1.0

The effects of out-of-plane displacement are examined under different conditions: varying pier aspect ratios and low to high axial loads. In the ensuing section, the height and thickness of the piers studied are kept constant at 2.0 and 0.25 m, while the length of the pier is varied to account for varying piers in a wall with openings. Walls have been designated on the basis of their aspect ratios (height to length ratios) as: A (0.5), B (1.0), C (1.5) and D (2.0). For validating the proposed model in Eq. (1), the analysis procedure is carried out in two steps. In the first step, the wall is analysed under an axial load and the out-of-plane displacement represented as a uniformly distributed displacement at mid-height. In the second step, incremental in-plane displacement is applied at the top of the wall. Figure 4 (A–D) shows a comparison of the model with non-linear finite element analysis results. From Fig. 4, one can conclude that the proposed model compares well with NLFEM results in capturing the drop in shear capacity in the presence of an out-of-plane displacement. In addition, as the mode provides a lower bound of the shear capacities, it leads to a conservative seismic assessment.

4 Interaction Under Dynamic Response

In Sect. 3, the interaction of the out-of-plane displacements on the in-plane behaviour is examined under static loading. However, in an earthquake, a structure may be subject to accelerations in both the in-plane and out-of-plane accelerations. During earthquakes, large floor horizontal accelerations have been recorded in buildings that are responsible for inertial forces causing out-of-plane damage of walls leading to structural damage and even building collapse. To study this phenomenon, one has to evaluate the out-of-plane seismic demand on walls

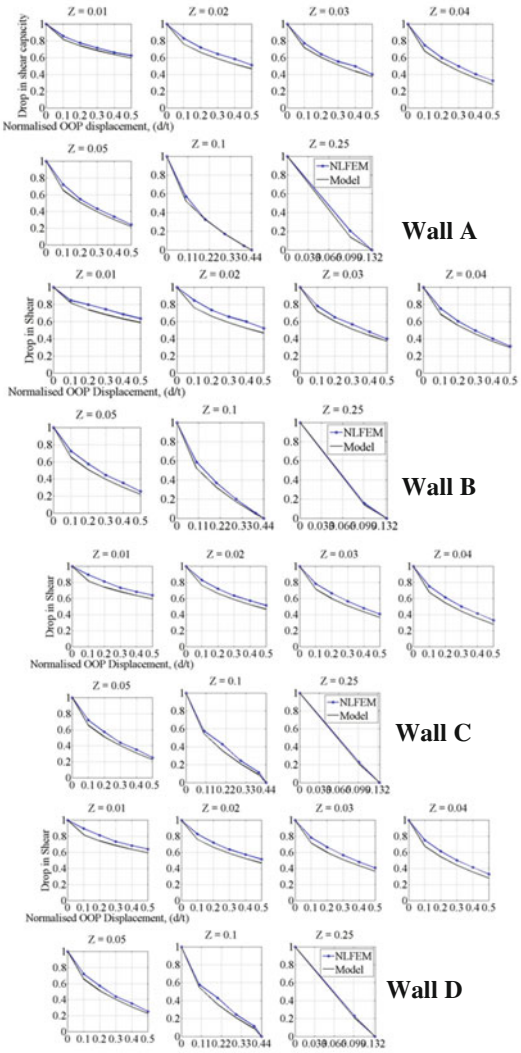

Fig. 4 Validation of Eq. (1) with NLFEM analysis

considering the dynamic filtering effect of the building and diaphragms and the dynamic response of the walls [15]. The behaviour of walls A and C subjected to axial stresses of 0.2 and 1 MPa when subjected to in-plane base excitations and out-of-plane floor accelerations is studied. The biaxial response of the wall to dynamic loading is studied by incremental dynamic analysis (IDA). An ensemble of 10 natural strong motion records from published literature [16] was used here.

Figure 5 shows the in-plane shear capacity versus in-plane displacement of walls A and C from IDA subject to biaxial accelerations and in the presence of an additional out-of-plane displacement. One observes that the shear capacity of all the

walls from IDA is a lower bound when compared to static analysis. The disparity in the capacities can be attributed to decoupling of the in-plane and out-of-plane displacements in the non-linear static analysis while in the dynamic analysis the effects are considered simultaneously, which is a more realistic representation of the behaviour during an earthquake.

In Table 2, the peak shear capacities from Fig. 5 are compared with shear capacities obtained with the analytical model. One observes that the shear capacity from IDA is a lower bound when compared to shear capacities from the model developed. However, the shear capacity obtained from the proposed analytical model is intermediate between the capacities obtained from NLSA and IDA. It is also observed that the effect of biaxial loads in terms of reducing the shear capacity is slightly more significant in a slender wall (wall A) while compared to a squat wall. This is an observation consistent with previously published work [17], which concludes that effect of out-of-plane actions is more in slender walls than squat walls.

5 Application of Analytical Model to Determine the Biaxial Effects at Global Level

The proposed analytical model is used to determine the effect of the out-of-plane displacements at the global level by introducing it within the scope of an existing method such as storey-shear mechanism (SSM). As mentioned, the storey-shear mechanism (SSM) only determines the global in-plane shear capacity of piers and ignores the out-of-plane effects which may lead to an overestimate of the shear capacity. Even when a structure is subject to pure in-plane displacement, depending on the structure's inherent eccentricity due to plan and vertical irregularities it will be subjected to an additional OOP displacement. The effects of the out-of-plane displacements determined are examined on two three-storied structures (plan in Fig. 6). Structure A is regular in plan and has an eccentricity of 0.8 m in the *X* direction and 0.67 m in the *Y* direction between the centres of mass and stiffness. Structure B has an eccentricity of 2.02 and 0.8 m. A comparison of the global

Table 2 Comparison of drop in shear capacity from NLSA, IDA and developed model

Wall	Pure in-plane shear capacity (kN)	Drop in-plane shear capacity (%)		
		Non-linear static analysis	IDA	Analytical model
A ($Z = 0.02$)	24	75	61	72
A ($Z = 0.1$)	110	52	42	51
C ($Z = 0.02$)	159	78	63	72
C ($Z = 0.1$)	490	54	45	51

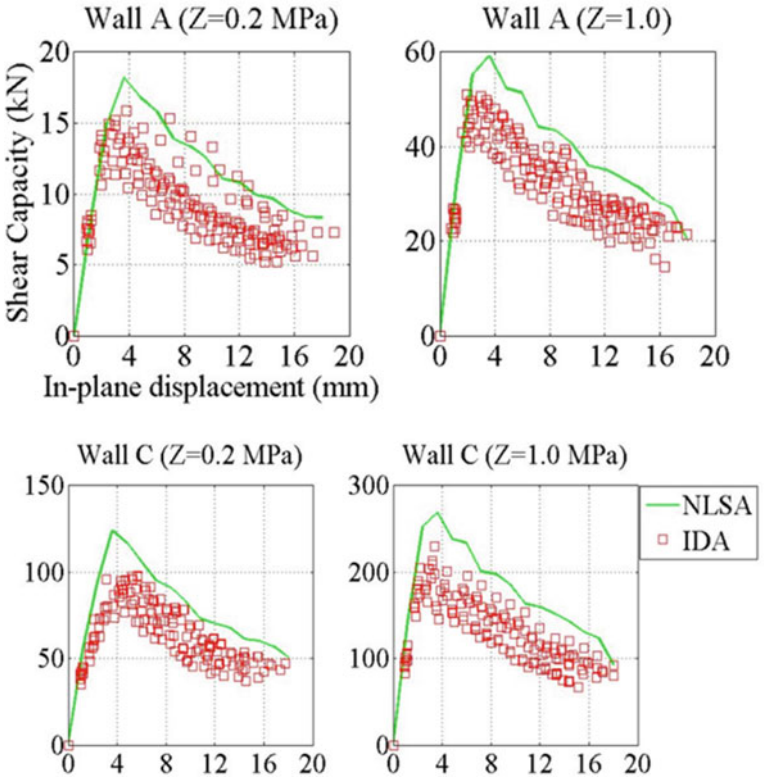

Fig. 5 Comparison of force–displacement biaxial effects (static vs. dynamic)

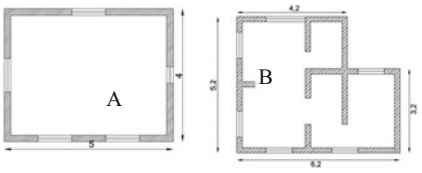

Fig. 6 Ground floor plans of **a** regular structure and **b** irregular structure

capacity neglecting and considering biaxial interactions are determined in both directions and are reported in Fig. 7a, b and Tables 3 and 4.

One observes that the SSM provides an upper bound of the shear capacities when compared to results from NLFEM analysis. However, the shear capacity obtained while considering the out-of-plane effects is a lower bound of the capacities from non-linear analysis. The underlying assumption is that NLFEM results are closer to the reality. In this context, the fact that the proposed analytical model to describe the biaxial effects gives a lower bound when compared to

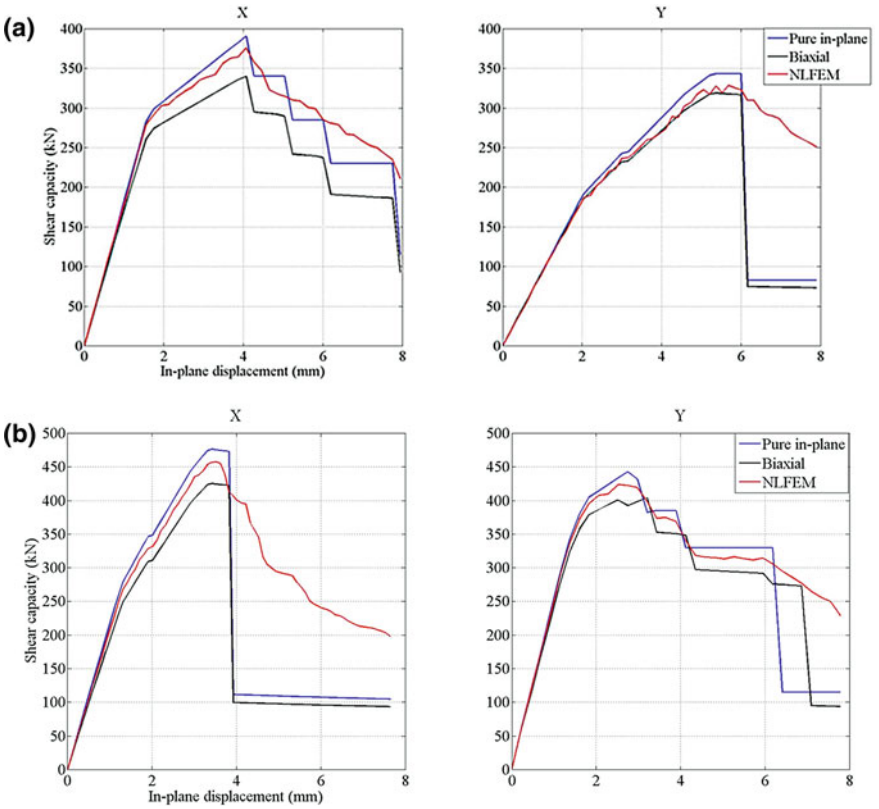

Fig. 7 **a** In-plane shear capacity of structure A under pure in-plane displacement and considering biaxial effects. **b** In-plane shear capacity of structure B under pure in-plane displacement and considering biaxial effects

Table 3 Comparison with NLFEM analysis for structure A

Structure	Capacity in *X* direction (kN)		
	Capacity neglecting interaction	Global capacity considering interaction	NLFEM (numerical model)
A	388	347	368
B	476	425	452

NLFEM results leads to conservative seismic assessment. This goes to show that the model could be a useful and simple to use tool that to describe the biaxial effects at both elemental and global level.

Table 4 Comparison with NLFEM analysis for structure B

Structure	Capacity in *Y* direction (kN)		
	Global capacity neglecting interaction	Global capacity considering interaction	NLFEM (numerical model)
A	388	347	368
B	476	425	452

6 Conclusions

An analytical model to evaluate the effect of out-of-plane mid-height displacement on the in-plane shear capacity of URM walls is proposed. The model is founded on the assumption that when a URM wall is subject to OOP displacements cracks along the thickness leading to a drop in shear capacity.

Non-linear finite element analyses under static and dynamic confirm the theoretical basis of the model. A preliminary application of the model to determine the effects of out-of-plane displacements at the global level highlights significant repercussions on the global behaviour especially in the post-peak region.

The force–displacement pushover curves obtained from the proposed method provide a lower bound solution compared to non-linear finite element analysis. In the absence of experimental results for the phenomenon addressed in the paper, the fact that the shear capacity considering the biaxial interaction is a lower bound compared to NLFEM results points to a conservative seismic assessment.

As a closing comment, the authors would like to state that the effects of elemental out-of-plane displacements have to be considered in unreinforced masonry structures especially in the ones where features to prevent the effect of out-of-plane displacements are ineffective.

References

1. Shapiro, D., Uzarski, J., Webster, M., Angel, R., & Abrams, D. (1994). *Estimating out-of-plane strength of cracked masonry infills* (Civil Engineering Studies, Structural Research Series No. 588). University of Illinois at Urbana-Champaign.
2. Flanagan, R. D., & Bennett, R. M. (1999). Bidirectional behaviour of structural clay tile infilled frames. *Journal of Structural Engineering, 125*(3), 236–244.
3. Al-Chaar, G. (2002). *Evaluating strength and stiffness of unreinforced masonry infill structures* (ERDC/CERL TR-02-1). US Army Corps of Engineers.
4. Najafgholipour, M. A., Maheri, M. R., & Lourenço, P. B. (2013). Capacity interaction in brick masonry under simultaneous in-plane and out-of-plane loads. *Construction Building Materials, 38,* 619–626.
5. Hashemi, A., & Mosalam, K. M. (2007). *Seismic evaluation of reinforced concrete buildings including effects of masonry infill walls* (PEER, Report 7100). Berkeley: Pacific Earthquake Engineering Research Center, University of California.

6. Kadysiewski, S., & Mosalam, K. M. (2009). *Modelling of unreinforced masonry infill walls considering in-plane and out-of-plane interaction* (PEER, Report 8102). Pacific Earthquake Engineering Research Center, University of California.
7. Bakshi, A., Soleimanzadeh, A., & Yekranhia, M. (2014). Interaction of in-plane–out-plane masonry walls (Paper-ID 1599). In *Proceedings of the 9th International Masonry Conference*, Guimaraes, Portugal.
8. Agnihotri, P., Singhal, V., & Rai, D. C. (2013). Effect of in-plane damage on out-of-plane strength of unreinforced masonry walls. *Engineering Structures, 57,* 1–11.
9. Magenes, G., & Calvi, G. M. (1997). In-plane seismic response of brick masonry walls. *Earthquake Engineering and Structural Dynamics, 26,* 1091–1112.
10. Priestley, M. J. N. (1985). Seismic behaviour of unreinforced masonry walls. *New Zealand National Society for Earthquake Engineering, 18*(2), 65–75.
11. Doherty, K., Griffith, M. C., Lam, N., & Wilson, J. (2002). Displacement-based seismic analysis for out-of-plane bending of unreinforced masonry walls. *Earthquake Engineering and Structural Dynamics, 31*(4), 833–850.
12. *Diana users manual* (2014). TNO DIANA BV, Delft, The Netherlands.
13. Lourenço, P. B. (1996). *A user/programmer guide for the micro-modelling of masonry structures* (Research Report, Report No. 03.21.1.31.35). Delft: Delft University of Technology.
14. Gandhi, R., & Menon, A. (2014). Seismic performance of bed-joint reinforced solid brick masonry walls. In *Proceedings of the 9th International Masonry Conference*, Guimaraes, Portugal.
15. Magenes, G. (2006). Masonry building design in seismic areas: Recent experiences and prospects from a European stand-point, Keynote lecture 9. In *Proceedings of the1st European Conference on Earthquake Engineering and Seismology*, Geneva, Switzerland.
16. Menon, A., & Magenes, G. (2011). Definition of seismic input for out-of-plane response of masonry walls: I. parametric study. *Journal of Earthquake Engineering, 15*(2), 165–194.
17. Penna, A., Magenes, G., Tomasetti, U., & Graziotti, F (2016). Out-of-plane shaking table tests on URM cavity walls (pp. 1939–1947). In *Proceeding of 16th International Brick and Block Masonry Conference*, Modena.

Bond Performance of Pretensioned Concrete Systems

Prabha Mohandoss, Sriram K. Kompella and Radhakrishna G. Pillai

Abstract Prestressed concrete technology has revolutionized the infrastructure growth in many countries, especially that of the bridge sector. The bond between prestressed strand and concrete is very important for achieving good structural performance. However, some of the codal provisions have not given enough consideration to the bond strength of pretensioned concrete system in design. This paper presents the results from a preliminary experimental program on the bond strength of 7-wire strands embedded in M35 and M55 concretes. A pull-out test method was developed, and the same was used to determine the bond strength. The bond behavior and the mechanisms at the strand–concrete interface are also discussed. Bond strength of 7-wire strand in M55 concrete is found to be about two times more than that in M35 concrete.

Keywords Pretensioned concrete · Pull-out test · Bond strength
Bond-slip · Strand–concrete interface

1 Introduction

In India, for the past five decades, the applications of prestressed concrete have been predominant in the field of bridge constructions, overpasses/flyovers, metro rail projects, commercial buildings, nuclear containment vessels, pavements, railroad sleepers, poles, piles marine structures liquefied gas, and oil storing vessels.

P. Mohandoss · S. K. Kompella · R. G. Pillai (✉)
Department of Civil Engineering, Indian Institute of Technology Madras, Chennai 600036, India
e-mail: pillai@iitm.ac.in

P. Mohandoss
e-mail: prabhamohandoss@gmail.com

S. K. Kompella
e-mail: sriram.kasyap7997@gmail.com

A. Rama Mohan Rao and K. Ramanjaneyulu (eds.), *Recent Advances in Structural Engineering, Volume 1*, Lecture Notes in Civil Engineering 11,
https://doi.org/10.1007/978-981-13-0362-3_22

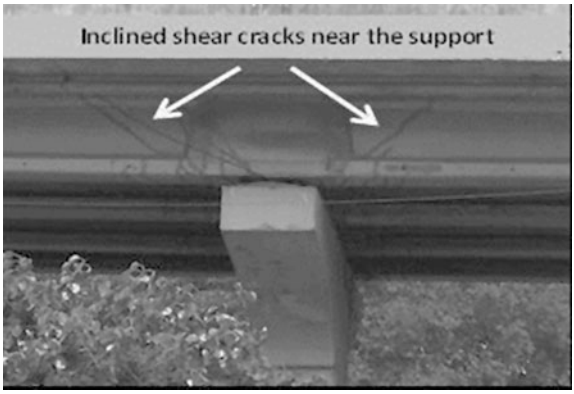

Fig. 1 Shear cracks in bridge girders due to poor bond

Moreover, bridges and railway sleepers have the most widespread application of the pretensioned concrete among all the fields.

In a pretensioned concrete (PTC) systems, prestress is transferred through a bond from the strand to the surrounding concrete. Hence, the bond between the prestressed strand and concrete is more important for its structural performance. If the bond of PTC member is not good or inadequate, then it can lead to poor structural performance leading to shear failure at the ends and cracks in the member. In India, similar types of issues have been observed in a highway bridge girder as shown in Fig. 1. One of the main reasons for this poor bond performance is the presence of the residue of the colorless, shiny, and dry lubricant on the strands. Calcium stearate (CaSt) and sodium stearate are the most commonly used dry lubricants to ease the process of cold drawing of wires during the strand manufacturing and to meet the site inspectors' demand of corrosion free strands. However, there is no test method to quantify the quality of the bond between the strand and concrete to produce the better quality product. Therefore, this study attempts to study the bond strength and bond behavior between the strand and concrete.

1.1 Bond Mechanisms

Bond mechanism of PTC systems is mainly contributed by three factors: adhesion, mechanical interlock, and friction [1]. Adhesion plays a minimal role in PTC system. Mechanical interlock and friction play a significant role in the PTC systems [2]. Mechanical interlock occurs due to the spiral twisting of the outer wires that form the strand. This helical shape of the strand results in bearing stress between the strand and concrete. Friction is attributed to concrete confinement and Hoyer effect. Hoyer effect is the expansion of strand in the transfer zone after releasing the prestress due to Poisson's effect. The bond between the strand and concrete can also be influenced by many factors such as compressive strength of concrete, type/diameter/surface condition of the strand, amount of prestress applied, etc. [3].

1.2 Bond Test Methods

Typically, the bond strength between strand and concrete is determined by using pull-out test. Many pull-out tests have been developed to determine the bond strength of strand. The Moustafa pull-out test [4] was one of the earliest test methods. It was developed to quantify the bond capacity of strands for lifting loops. In this test method, strands were pulled out from the large concrete block using a jack. Another test method is the North American Strand Producers (NASP) bond test [5], in which the strand is pulled out from the mortar. The contemporary version of the NASP bond test is adopted by American Society for Testing and Materials (*ASTM A1081 Standard test method for evaluating the bond of seven wire prestressing strand*) [6, 7]. However, none of these test methods represent the actual behavior of PTC (the bond behavior between the stressed strand and concrete), where the strands are pretensioned to certain stress level (say, 0.75 f_{pu}). Moreover, these test methods use only the unstressed strand, which may lead to wobbling issue during specimen preparation since the strands are not perfectly straight and stressed as in the field structures.

Performing pull-out test for a fully pretensioned strand member is not easy due to the requirement of long specimen length to transfer the applied pretension from the strand to concrete and the machinery required. Later, ECADA test method was developed by Marti-Vargas et al. (2006) [8] to determine the bond performance between the prestressed strand and concrete by representing the actual behavior of PTC.

This study focuses on the pull-out testing, bond strength, and bond behavior of taut strands embedded in concrete. The taut specimen is the specimen with minimal prestress—applied to keep the strands straight and avoid the wobbling effect.

2 Experimental Program

Figure 2 provides a schematic of the pull-out test specimen with a taut 7-wire strand embedded in concrete prism (500 × 100 × 100 mm in size). High strength, low-relaxation 7-wire strand of 12.7 mm diameter was used. The modulus of elasticity of the 7-wire strand was 196 MPa. The ultimate tensile strength (f_{pu}) of the 7-wire strand was 1770 MPa. Four specimens each with M35 and M55 grade

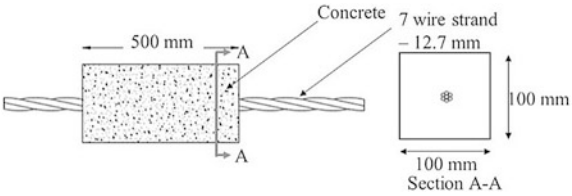

Fig. 2 Schematic of the pull-out test specimen with taut strand embedded in concrete prism

concrete with 40–50 mm slump were cast and tested. The average 28-day compressive strength of M35 and M45 concretes were 41 and 58 MPa, respectively. As shown in Fig. 2, the length of the concrete prism was 500 mm. The length of bond breaker placed inside the specimen was 50 mm. Therefore, the actual embedment length (l_e) of the strand is 450 mm.

2.1 Specimen Preparation

2.1.1 Initial Stressing

The length of the strand to be used for stressing is decided based on the length of the strand embedded in the specimen, the length of strand inside the hydraulic jack, load cell, and the thickness of the endplate including the screws. Based on this, 6 m long, 7-wire strands (12.7 mm dia.) were kept straight in the prestressing bed. Then, a hydraulic jack was used to apply a minimum load just to keep the strand straight and to avoid the wobbling effect. Before placing the wedges and tensioning the strand, a 5 cm long PVC pipe was kept around the strand (as bond breaker) near the pulling end. This was done to avoid the stress concentration in this region during the pull-out test. The wedge and barrel were placed outside the two end brackets of the prestressing bed—to maintain the stress. Also, a stress releasing system with a nut-bolt system was placed at the releasing end—to facilitate gradual release of the prestress.

2.1.2 Casting of Concrete

Fresh concrete was prepared using laboratory scale pan mixer and placed inside the specimen molds, which are placed on the prestressing bed. Concrete was hand-compacted using a standard procedure—to ensure uniformity in the concrete properties. Along with the pull-out specimens, three companion cube specimens were also cast to determine the compressive strength of concrete at the time of pull-out testing. After 24 h, the specimens were demolded, and the stress in the specimen was released. The strand was cut at both ends of the specimen—leaving 350 mm length of the strand at one end and 150 mm long at another end of the specimen. This was done to facilitate the placement of LVDTs and grip the strand at pulling end during the pull-out testing. Then, the specimens were cured for 28 days to achieve the desired concrete properties, prior to the pull-out test.

2.2 Pull-Out Test Procedure

2.2.1 Pull-Out Test Setup

Figure 3 shows the schematic of the pull-out test setup. In this, a 40 mm thick top and bottom steel plates of the frame are connected using four tension members (1.4 m long and 36 mm diameter steel rods). The center of the bottom steel plate of the frame has a 16 mm diameter hole to place the strand through and grip it using the hydraulic V-grips of the universal testing machine. One end of the hanging rod is gripped inside the upper wedge of the machine. Another end of the hanging rod has hemispherical shape to lock with the top plate of the frame to provide a swivel arrangement, which allows the free rotation of the frame while testing and avoids any torsion.

After fixing the pull-out frame on the machine, the pull-out specimen is placed in the pull-out frame. The bottom end of the strand is gripped in the MTS machine and that end is called as the live end where the load is applied. The top portion of the strand is free and known as a free end.

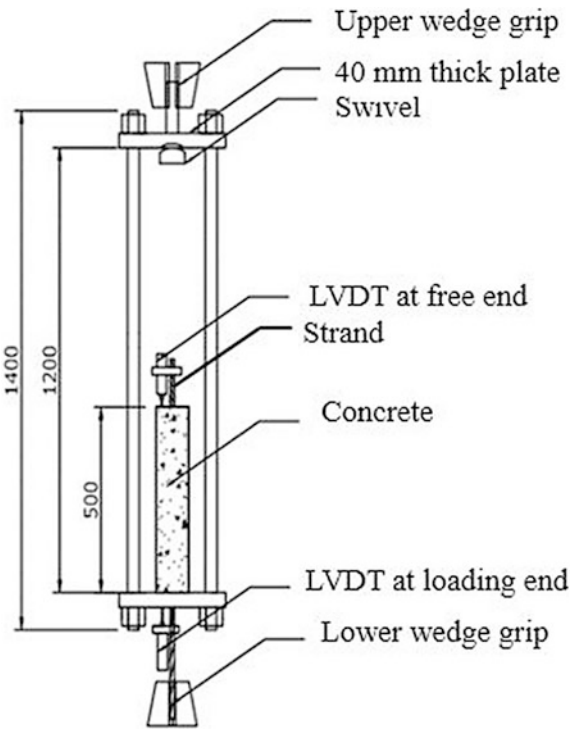

Fig. 3 Schematic of the pull-out test setup

2.2.2 Instrumentations

Two LVDTs were used. One LVDT was placed at the live end and another LVDT was placed at the free end of the strand, as shown in Fig. 3—to measure the slip of the strand with respect to the concrete during testing. An L-shaped plate of a smooth surface is placed on the surface of concrete at the free end of the specimen to place the LVDT in a position to get a uniform reading. Load was applied at the rate of 2 mm/min. Two LVDTs and the load cell of the machine were connected to a data acquisition system, and the time elapsed, load, and displacement data were recorded.

3 Results and Discussions

The bond stress-slip behavior (τ–s curve) of 12.7 mm strand embedded in M35 and M55 grade concretes is shown in Fig. 5a, b. The bond surface area is calculated as the circumference of the strand (p) multiplied by the actual embedment length (l_e). The bond strength (τ_b) is calculated as follows:

$$\tau_b = \frac{P_u}{pl_e} \tag{1}$$

where P_u is the ultimate load (or peak load).

As discussed in Sect. 1.1, the bond mechanism in PTC is governed by three factors: (i) adhesion, (ii) mechanical interlock, and (iii) friction. Hence, the bond-slip curve can be divided into three regions as follows.

- Region 1: Linear region, which is governed by the adhesion mechanism. Once adhesion is lost, then the mechanical interlock and friction are mobilized.
- Region 2: Mainly governed by mechanical interlock, which gives resistance to slip.
- Region 3: Mainly governed by friction between the strand and concrete, after the peak load.

Two types of behaviors or bond-slip patterns are observed: (i) smooth pattern and (ii) stick-slip pattern. The specimens with smooth pattern exhibited splitting and cracking of concrete, as seen in Fig. 4. The specimens with stick-slip pattern exhibited pulling-out of the strand (without the splitting and cracking of concrete).

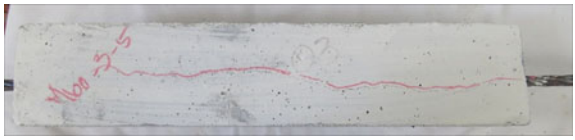

Fig. 4 Longitudinal cracks along the 7-wire strand in M55 grade in concrete

3.1 Bond Strength and Slip

Figure 5a, b shows the τ–s curves of taut strands in M35 and M55 concretes, respectively. As shown in Fig. 5, two specimens with M35 concrete and all the specimens with M55 concrete are exhibiting the smooth pattern. This happens when the concrete confinement is good. In such case, the concrete will resist the movement of the strand, resulting in an increase in the stress developed, which in turn results in longitudinal cracks in concrete (Fig. 2).

Specimens A2 and A3 in Fig. 4a exhibited the stick-slip pattern. It seems that this pattern is more predominant in the case of low strength concrete (say, below M35 concrete). When the concrete strength is low, the grooves may fail in shear and allow the strand to slide from one groove to the next one (in the longitudinal direction)—resulting in the stick-slip pattern. Also, 25°–40° rotation of strands (as they are pulled out) was observed at the peak of the τ–s curve.

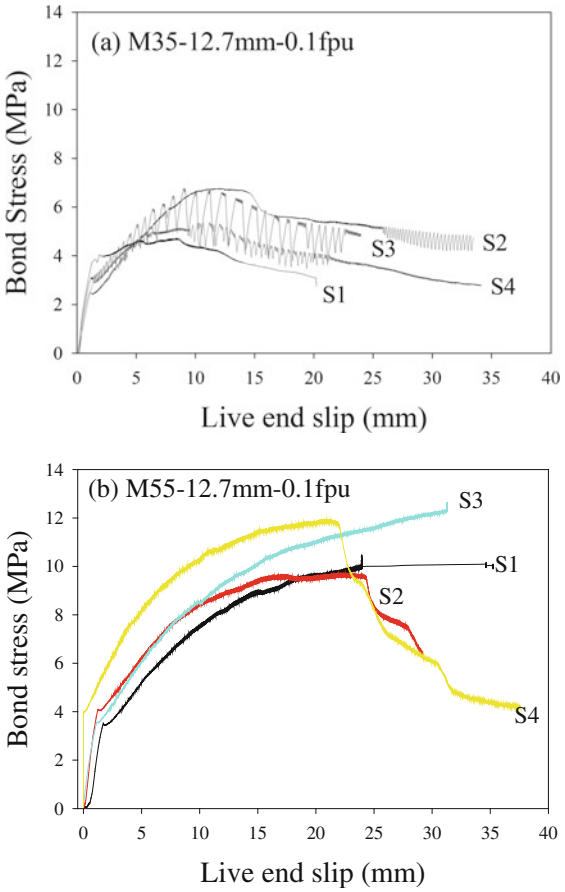

Fig. 5 Bond behavior in **a** M35 grade and **b** M55 grade concretes

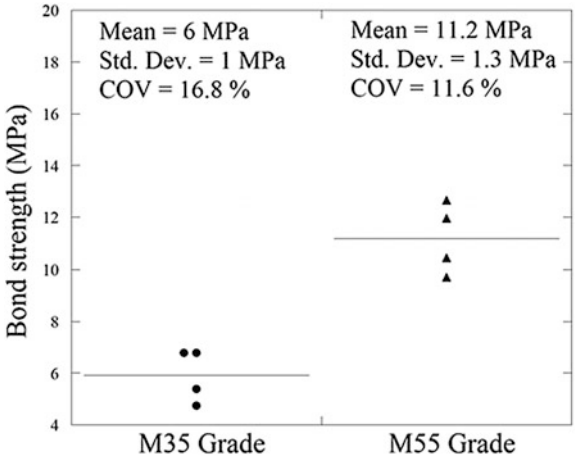

Fig. 6 Bond strength of PTC specimens as a function of compressive strength of concrete

Table 1 Bond stress values of 12.7 strands

Specimen no.	Grade of concrete	f'_c (MPa)	$\tau_{2.5}$ (MPa)	τ_{max} (MPa)	Slip at τ_{max} (MPa)
A1	M35	44.1	4.03	4.74	8.4
A2		43.8	3.04	6.77	11.9
A3		43.7	3.74	6.77	9.10
A4		42.9	3.36	5.40	11.2
B1	M55	63.1	3.65	10.50	24.0
B2		61.8	4.65	9.72	22.0
B3		60.2	4.30	12.66	31.2
B4		60.2	6.26	11.80	20.7

The measured bond strength τ_{max} of pull-out specimens is shown in Fig. 6. The term τ_{max} is defined as the maximum bond stress observed in the τ–s curves, as shown in Fig. 6. For the eight specimens tested here, the τ_{max} occurred at a slip ranging from 8 to 30 mm. However, in ASTM 1018, bond strength is calculated as the bond stress corresponding to 2.5 mm. Hence, the maximum bond stress (τ_{max}) and bond stress at 2.5 mm ($\tau_{2.5}$) are calculated and shown in Table 1. Also, the slip corresponding to τ_{max} is shown in the last column of Table 1. It can be seen that these values are in the range of 8–30 mm (i.e., greater than the design slip value of 2.5 mm).

It is observed that average $\tau_{2.5}$ is approximately half the value of τ_{max}. Also, when the grade of concrete increased from M35 to M55, the τ_{avg} increased from 6 to 11 MPa—about twofold increase.

4 Preliminary Findings

- As the characteristic compressive strength of concrete increases from 35 to 55 MPa, the average bond strength increase by about two times.
- A stick-slip τ–s behavior is observed when the strand is pulled out of the concrete with relatively low strength (say, M35).
- A smooth τ–s behavior is observed when the bond failure is due to concrete cracking or splitting.

5 Notations

d_b Nominal diameter of strand (mm)
l_e Embedded length of the strand in the concrete (mm)
p Circumference of the strand in the concrete (mm)
A_b Bonded area of the embedded length of the strand (mm^2)
P_u Ultimate load (kN)
f'_c Compressive strength of the concrete at the time of testing (MPa)
τ_{max} Measured bond strength of the strand (MPa)
τ_{avg} Average measured bond strength (MPa)
$\tau_{2.5}$ Measured bond stress at 2.5 slip (MPa)
S Slip of the strand (mm)

Acknowledgements The authors thank Prof. Ravindra Gettu and Prof. Amlan K. Sengupta for their valuable suggestions. The authors thank the faculty and staff of the BTCM division, Department of Civil Engineering, IIT Madras, Chennai, India. The authors acknowledge the financial support through the "Fund for Improvement of Science & Technology Infrastructure (FIST)", Department of Science and Technology (DST), and the Ministry of Human Resources Development (MHRD), Govt. of India.

References

1. Janney, J. R. (1954). Nature of bond in pretensioned prestressed concrete. *ACI Journal, 5*(8), 17–736.
2. Vázquez-Herrero, C., Martínez-Lage, I., & Martínez-Abella, F. (2013). Transfer length in pretensioned prestressed concrete structures composed of high performance lightweight and normal-weight concrete. *Engineering Structures, 56,* 983–992.
3. Rose, D. R. & Russell, B. W. (1997). Investigation of standardized tests to measure the bond performance of prestressing strand. *PCI Journal*, 56–80.
4. Moustafa, S. (1974). *Pull-out strength of strand and lifting loops, Technical bulletin 74–B5* (p. 34). Tacoma, WA: Concrete Technology Associates.

5. Russell, B. W., & Paulsgrove, G. A. (1999). Assessing repeatability and reproducibility of the moustafa test, the PTI bond test and the NASP bond test, Final Report 99-04. Norman, Ok: University of Oklahoma, Fears Structural Engineering Laboratory.
6. ASTM A1081/A1081M. (2012). Standard test method for evaluating bond of seven-wire steel prestressing strand. ASTM International, West Conshohocken.
7. Deng, Y., & Morcous, G. (2015). Strand bond stress—slip relationship for prestressed concrete members at prestress release. http://doi.org/10.1617/s11527-015-0546-1.
8. Marti-Vargas, J. R., Serna-Ros, P., Fernandez-Prada, M.A., Miguel-Sosa, P.F., & Arbelaez, C. A. (2006). Test method for determination of the transmission and anchorage lengths in prestressed reinforcement. *Magazine of concrete research, 58*(1), 21–29.

Part II
Analysis and Design of Steel Structures

Comparative Study of Fire-Resistant Design of Steel Structures as per IS800:2007, AS4100:1998, AISC360:2010 and EN1993-1-2

Dhara Shah and Janak Shah

Abstract Construction of any structure consists of various stages and layers, one of which is fire protection. Fire leads to temperature rise in structural members, which in turn reduces their strength. Current fire protection strategy integrates a combination of active and passive fire protection measures but very less focus is given to the fire-resistant design approach. This study focuses on comparison of fire-resistant design method for steel structures as per Indian standard (IS800), Australian standard (AS4100), Eurocode (EN1993-1-2) and American standard (AISC360). The study includes design of simply supported steel beam, laterally supported as well as unsupported, with span varying from 3 to 7 m, using IS800:2007. The fire-resistant design of the beam is done for protected and unprotected case, and is compared as per different standards. It is concluded that AISC code gives conservative value, due to the consideration of higher safety factor in the code. Further, Indian code gives economical value but restricts temperature value by 750 °C and in most cases of laterally supported beam, the value of critical temperature is higher than 750 °C, and hence, we cannot use the result of Indian code. Further, Indian code fails to provide clear representation of fire-resistant design for protected steel members.

Keywords Fire-resistant design · Steel structures · IS800:2007 AS4100:1998 · AISC360:2010 · EN1993-1-2

D. Shah (✉) · J. Shah
Faculty of Technology, CEPT University, Ahmedabad 380009, Gujarat, India
e-mail: dharashah@cept.ac.in

A. Rama Mohan Rao and K. Ramanjaneyulu (eds.), *Recent Advances in Structural Engineering, Volume 1*, Lecture Notes in Civil Engineering 11,
https://doi.org/10.1007/978-981-13-0362-3_23

1 Introduction

Fire protection is a key element in all structures. Current fire protection strategy integrates a combination of active and passive fire protection measures. Active fire protection measures consider the use of fire alarms, fire extinguishers, sprinklers, smoke detection devices, emergency exits, etc., which might be manually or automatically operated, based on the principle of early fire detection and reduced risk of large fire. It is installed mainly for the escape of people from buildings in case of fire and hence will not protect the structure. Passive fire measures are actually structural fire protection systems within the structural system of a structure with the use of certain materials such as spray protection, board protection, intumescent coatings, etc. Passive system also incorporates layout of escape routes, fire brigade access routes along with control of combustible materials of construction [1]. In past, many failures have occurred due to fire including:

- The World Trade Center (WTC), New York, 9 September 2001.
- The Mumbai High North Platform, Indian Ocean, 27 July 2005.
- Interstate 580, Oakland, 29 April 2007.
- Faculty of Architecture Building, the Netherlands, 13 May 2008.

Fire leads to temperature rise in structural members, which in turn reduces their strength. Thus, it is necessary that structural members remain intact during the evacuation of personnel and even after collapse, it will not trigger the collapse of structure. Different countries have already done sufficient work to find the temperature rise in structural member or structure as a whole during fire. They also found reduction in strength of a member with increase in steel temperature.

A general approach to fire safety of structure is to provide active fire safety measures. Very less focus is given to fire-resistant design approach. Mostly designers provide protection directly to structural members. Looking to IS800:2007 [2], code provides equations to calculate the temperature rise for unprotected steel members on the basis of standard fire test data. However, for protected members, code has provided table for structural steel beam (406 mm $\times$ 176 mm) and steel column (203 mm $\times$ 203 mm), with no information regarding protection of other sections in beams and columns. The code has more emphasis on testing of members, which is not possible all time. On the other hand, Eurocode and American code give equations for temperature rise in the steel on the basis of heat transfer theory. Thus, it is vital to compare results of Indian standards with other standards.

This study focuses on the comparison of fire-resistant design method for steel structures as per Indian standard IS800, Australian standard—AS4100 [3], Eurocode—EN1993-1-2 [4] and American standard—AISC360 [5]. The study includes the design of simply supported steel beam, laterally supported as well as unsupported at room temperature (20 °C), with span varying from 3 to 7 m, using IS800-2007. For calculation of temperature rise in steel members, ISO 834 [6] standard fire is used. The fire-resistant design of the beam is done for protected and unprotected case, and is compared as per different standards listed above.

2 Structural Steel and Its Properties

The time for which the structural member will support the applied loads when subjected to a standard fire ISO 834 is known as period of structural adequacy (PSA) of a member. Vital material properties of steel structures related to heating and load-bearing capacity of steel structures are the thermal properties of steel as a function of temperature and mechanical properties of steel at elevated temperature. Thermal properties of steel do change with varying temperature including thermal elongation, specific heat and thermal conductivity. These properties are more or less uniform throughout different standards. The difference lies in the mechanical properties of the steel across the standards which are explained below.

2.1 Yield Stress

Yield stress decreases with increase in temperature and is independent of steel grade [7]. Indian code and Australian code provide equations for variation in yield stress of steel at elevated temperature based on the regression analysis of data from elevated temperature tensile tests conducted in Australia and Britain. The equation is

$$\frac{f_y(T)}{f_y(20)} = 1.0 \text{ when } 0\ ^\circ\text{C} < T < 215\ ^\circ\text{C} \tag{1}$$

$$\frac{f_y(T)}{f_y(20)} = \frac{905 - T}{690} \text{ when } 215\ ^\circ\text{C} < T < 905\ ^\circ\text{C} \tag{2}$$

where

$f_y(T)$ Yield stress of steel at T °C.
$f_y(20)$ Yield stress of steel at 20 °C (room temperature).
T Temperature of steel in °C.

On the other hand, American standard and Eurocode provide reduction factors for stress–strain relationship of steel at elevated temperature. Figure 1 shows the comparative chart of yield stress ratio of steel versus temperature as per selected standards.

3 Modulus of Elasticity

Like yield stress, modulus of elasticity decreases with increase in temperature [7]. Indian code and Australian code provide equations for variation in modulus of elasticity of steel at elevated temperature, as recommended by the French Technical Centre for steel construction—CTICM. The equation is

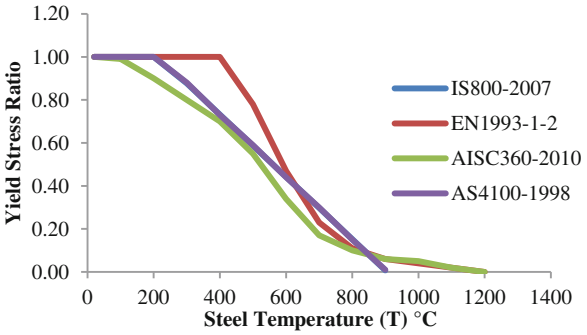

Fig. 1 Variation in yield stress of steel with temperature

$$\frac{E(T)}{E(20)} = 1.0 + \left[\frac{T}{2000\left\{\ln\left(\frac{T}{1100}\right)\right\}}\right] \quad \text{when } 0\ ^\circ\text{C} < T < 600\ ^\circ\text{C} \tag{3}$$

$$\frac{E(T)}{E(20)} = \frac{690\left(1 - \frac{T}{1000}\right)}{T - 53.5} \quad \text{when } 600\ ^\circ\text{C} < T < 1000\ ^\circ\text{C} \tag{4}$$

where

$E(T)$ Modulus of elasticity of steel at T °C.
$E(20)$ Modulus of elasticity of steel at 20 °C (room temperature).
T Temperature of steel in °C.

American standard and Eurocode provide reduction factors for variation in modulus of elasticity of steel at elevated temperature. Figure 2 shows the comparative chart of modulus of elasticity ratio of steel versus temperature as per selected standards.

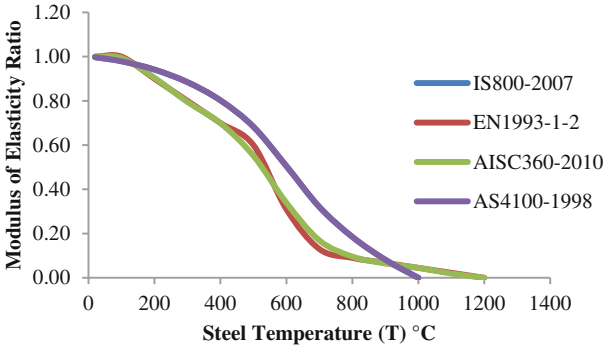

Fig. 2 Variation in modulus of elasticity of steel with temperature

From the comparison, it is observed that Eurocode provides higher values of yield stress at elevated temperature whereas Australian code and Indian code provide higher values for modulus of elasticity at elevated temperature.

4 Fire-Resistant Design

4.1 Load Combinations

The most likely loads at the time of a fire are much lower than the maximum design loads specified for normal temperature conditions. It is generally assumed that there is no explosion or other structural damage associated with the fire. Table 1 lists partial safety factors for dead load and imposed load as per different standards [8, 9], to be considered for fire-resistant design of steel members.

4.2 Shape Factor (A_m/V or H_p/a)

It is defined as the ratio of heated perimeter (H_p) to that of the cross-sectional area of the steel member (A). It is an important parameter in determining the rise of temperature of steel section. Higher the value of H_p/A, higher the rate of heating. The value of H_p depends on the type of protection (sprayed insulation, intumescent paint or board insulation which boxes the section) and whether the member is heated on four sides or three sides. Eurocode uses section factor—A_m/V instead of shape factor, where A_m is the surface area of the member per unit length (m^2/m), and V is the volume of the member per unit length (m^3/m). The unit of H_p/A (A_m/V) is m^{-1}. Indian code does not provide considerable information for shape factor. American standard uses W/D ratio where W is the weight per unit length and D is the heat perimeter. When we consider the whole equation of heat transfer for Eurocode and American code, this factor is similar because in Eurocode density and shape factor have been used separately while in American standard, both have been combined and given as one factor, i.e. W/D ratio.

Table 1 Partial load safety factors as per different standards

Standard	Partial load factors	
	Dead load (DL)	Live load (LL)
IS 800	1	0.35
AS 4100	1	0.4
EN 1991	1	0.3
ASCE	1.2	0.5

4.3 Limiting Steel Temperature/Critical Temperature

It is the temperature above which the residual strength of member is not useful. Indian code and Australian code provide equation for critical temperature based on the yield stress of steel. Eurocode gives formula based on the degree of utilization factor which is same as the load factor, given by the Indian code. American code is silent about the value of critical temperature. The equation for critical steel temperature as per IS800 and AS4100 is given as

$$T_l = 905 - 690 r_f \tag{5}$$

where

r_f Ratio of the design action on the member under the design load for fire to the design capacity (R_d) of the member at room temperature.
R_d Design strength of member at room temperature = R_u/γ_m.
R_u Ultimate strength of member at room temperature.
γ_m Partial safety factor for strength.

The equation for critical steel temperature as per EN1993-1-2 is given as

$$\theta_{cr} = 39.19 \ln \left[\frac{1}{0.9674 \mu_0 3.833} - 1\right] + 482 \tag{6}$$

where

θ_{cr} Critical temperature in steel.
μ_0 Degree of utilization.

4.4 Temperature Rise in Unprotected Steel Member

As per IS800 and AS4100, time (t) to reach critical temperature (T_l) is given by the equations obtained from regression analysis of British temperature data for unprotected steel. The equations are

(a) Four-sided exposure conditions

$$t = -4.7 + 0.0263 T_l + \frac{0.213 T_l}{K_{sm}} \tag{7}$$

(b) Three-sided exposure conditions

$$t = -5.2 + 0.0221T_l + \frac{0.433T_l}{K_{sm}} \tag{8}$$

where

t Time from the start of the test, in min.
T_l Limiting steel temperature in °C; 500 °C <= T <= 750 °C.
K_{sm} Exposed surface area to mass ratio in 10^3 mm^2/kg; 2×10^3 mm^2/kg <= K_{sm} <= 35×10^3 mm^2/kg = $(H_p/A) \times 10^6/7.85$ mm^2/kg.

For T_l < 500 °C, code suggests linear interpolation based on the time at 500 °C and an initial temperature of 20 °C at t = 0. Design temperatures for different fire resistance time for beams and columns are found in the British standard BS5950 Part-8 [10], which were used as the basis of the regression analysis. In New Zealand standard, upper temperature limit has been increased to 850 °C from its original value owing to the research performed in recent years [7]. The Indian code and Australian code have not revised the upper temperature limit, and it remains at 750 °C. As per EN1993-1-2, the equation is given as

$$\Delta\theta_{a,t} = K_{sh}\frac{A_m/V}{C_a\rho_a}h_{net,d}\Delta t \tag{9}$$

where

K_{sh} Correction factor for the shadow effect.
A_m/V Section factor for the unprotected member (1/m).
A_m Surface area of member per unit length (m^2/m).
V Volume of member per unit length (m^3/m).
C_a Specific heat of steel (J/kg k).
$h_{net,d}$ Design value of net heat transfer per unit area (W/m^2).
Δt Time interval (seconds).
ρ_a Unit mass of steel, 7850 kg/m^3.

As per AISC 360, the equation is given as

$$\Delta T_s = \frac{\alpha}{C_s(W/D)}(T_F - T_s)\Delta t \tag{10}$$

where

ΔT_s Temperature rise in steel (°C).
T_F Fire temperature (K).
T_s Steel temperature (K).
Δt Time interval (s).
W Steel section weight per unit length (kg/m).
D Heat perimeter (m).

A Heat transfer coefficient (W/m^2 °C).
C_s Specific heat of steel (J/kg °C).

4.5 Temperature Rise in Protected Steel Member

As per IS800 and AS4100, time to reach critical temperature shall be determined by a suitable series of fire test or from result of a single test. Thus, these codes provide the value for critical temperature on the basis of test with appropriate protection.

As per EN1993-1-2, time to reach critical temperature is given by equation as

$$\Delta\theta_{a,t} = \frac{\lambda_p \left(\frac{A_p}{V}\right)\left(\theta_{g,t} - \theta_{a,t}\right)}{d_p C_a \rho_a \left(1 + \frac{f}{3}\right)}\Delta t - (e^{\frac{f}{10}} - 1)\Delta\theta_{g,t} \tag{11}$$

$$\phi = \frac{C_p \rho_p}{C_a \rho_a} d_p \left(\frac{A_p}{V}\right) \tag{12}$$

where

$\frac{A_p}{V}$ Section factor for the fire protected section (1/m).
C_p Specific heat of protection material form (J/kg k).
ρ_p Unit mass of fire protection material (Kg/m^3).
Δt Time interval (seconds).
$\theta_{g,t}$ Ambient gas temperature at time t (°C).
$\theta_{a,t}$ Steel temperature at time t (°C).
d_p Thickness of protection material (m).
λ_p Thermal conductivity of fire protection system (W/mK).

As per AISC360, time to reach critical temperature is given by equation as

$$\Delta T_s = \frac{k_p}{d_p}\left[\frac{(T_F - T_s)}{C_s\left(\frac{W}{D}\right) + \frac{C_p \rho_p d_p}{2}}\right]\Delta t \tag{13}$$

where

ΔT_s Temperature rise in steel (°C).
C_p Specific heat of steel (J/kg °C).
ρ_p Unit mass of fire protection material (Kg/m^3).
d_p Thickness of protection material (m).
k_p Thermal conductivity of fire protection system (W/m °C).
Δt Time interval (seconds).

5 Problem Formulation

For calculation of temperature rise in steel, excel spreadsheet has been used. The basic data that have been taken into consideration are as follows:

Steel Grade Fe 410,
DL 20 kN/m,
LL 10 kN/, and
Type of beam Simply supported.

Member spanning from 3 to 7 m have been taken for calculation. Analysis of all beams for laterally supported and laterally unsupported has been carried out using IS 800:2007. The sections obtained for different spans as per design are given in Table 2.

For fire-resistant design of protected members, gypsum board has been used. Typical properties of gypsum board are shown in Table 3.

6 Analysis and Results

Results obtained from fire-resistant design as per different standards are shown below for unprotected and protected steel beams with laterally supported and unsupported, from span 3 to 7 m, showing critical values in terms of critical temperature, time to reach critical temperature and design moment (Tables 4, 5, 6, 7, 8, 9, 10, 11, 12 and 13).

Table 2 Steel sections obtained for different spans

Span (m)	Section
3	ISMB 350
4	ISMB 400
5	ISMB 500
6	ISMB 550
7	ISMB 600

Table 3 Properties of gypsum board

Material	Gypsum board
ρ_p	800 kg/m^3
c_p	1700 J/kg/K
λ_p	0.2 W/mK
d_p	20 mm

Table 4 Comparison of critical values for unprotected 3 m beam

Standards	Laterally supported			Laterally unsupported		
	Critical temp.	Time	Design moment	Critical temp.	Time	Design moment
	(°C)	min.	kNm	(°C)	min.	kNm
IS800:2007	839.09	29.46	27.02	775.42	22.65	27.02
AS4100-1998	838.67	29.38	27.58	772.72	22.55	27.58
AISC360-2010	708.16	23.08	32.63	648.04	19.15	32.63
EN1993-1-2	785.01	29.97	25.88	741.78	24.54	25.88

Table 5 Comparison of critical values for unprotected 4 m beam

Standards	Laterally supported			Laterally unsupported		
	Critical temp.	Time	Design moment	Critical temp.	Time	Design moment
	(°C)	min.	kNm	(°C)	min.	kNm
IS800:2007	780.56	29.37	48.21	677.4	19.74	48.21
AS4100-1998	777.98	29.25	49.21	672.67	19.57	49.21
AISC360-2010	656.01	21.56	58	576.29	17.48	58
EN1993-1-2	705.02	19.76	46	664.69	17.4	46

Table 6 Comparison of critical values for unprotected 5 m beam

Standards	Laterally supported			Laterally unsupported		
	Critical temp.	Time	Design moment	Critical temp.	Time	Design moment
	(°C)	min.	kNm	(°C)	min.	kNm
IS800:2007	839.09	29.46	27.02	775.42	22.65	27.02
AS4100-1998	838.67	29.38	27.58	772.72	22.55	27.58
AISC360-2010	708.16	23.08	32.63	648.04	19.15	32.63
EN1993-1-2	785.01	29.97	25.88	741.78	24.54	25.88

Table 7 Comparison of critical values for unprotected 6 m beam

Standards	Laterally supported			Laterally unsupported		
	Critical temp.	Time	Design moment	Critical temp.	Time	Design moment
	(°C)	min.	kNm	(°C)	min.	kNm
IS800:2007	781.49	33.37	110.33	630.62	19.47	110.33
AS4100-1998	778.97	33.25	112.58	625.02	19.25	112.58
AISC360-2010	657.35	24.28	130.5	544.64	18.58	130.5
EN1993-1-2	751.73	30.12	103.5	640.4	18.02	103.5

Table 8 Comparison of critical values for unprotected 7 m beam

Standards	Laterally supported			Laterally unsupported		
	Critical temp.	Time	Design moment	Critical temp.	Time	Design moment
	(°C)	min.	kNm	(°C)	min.	kNm
IS800:2007	774.15	34.67	151.3	592.7	18.57	151.3
AS4100-1998	771.5	34.53	154.37	586.38	18.32	154.37
AISC360-2010	648.36	24.94	177.63	512.5	18.31	177.63
EN1993-1-2	744.53	30.25	140.88	620.25	17.83	140.88

Table 9 Comparison of critical values for protected 3 m beam

Standards	Laterally supported			Laterally unsupported		
	Critical temp.	Time	Design moment	Critical temp.	Time	Design moment
	(°C)	min.	kNm	(°C)	min.	kNm
AISC360-2010	708.16	121.82	32.63	646.21	96.64	32.63
EN1993-1-2	718.55	123.75	25.88	648.37	97.42	25.88

Table 10 Comparison of critical values for protected 4 m beam

Standards	Laterally supported			Laterally unsupported		
	Critical temp.	Time	Design moment	Critical temp.	Time	Design moment
	(°C)	min.	kNm	(°C)	min.	kNm
AISC360-2010	652.05	110.07	58	576.29	84.85	58
EN1993-1-2	760.73	140.04	46	676.09	109.16	46

Table 11 Comparison of critical values for protected 5 m beam

Standards	Laterally supported			Laterally unsupported		
	Critical temp.	Time	Design moment	Critical temp.	Time	Design moment
	(°C)	min.	kNm	(°C)	min.	kNm
AISC360-2010	632.54	108.41	90.63	490.38	70.74	90.63
EN1993-1-2	788.84	151.41	71.88	686.3	113.98	71.88

7 Conclusions

- For unprotected members, Indian standard proposes higher PSA along with critical temperature among all codes. Australian standard provides almost

Table 12 Comparison of critical values for protected 6 m beam

Standards	Laterally supported			Laterally unsupported		
	Critical temp.	Time	Design moment	Critical temp.	Time	Design moment
	(°C)	min.	kNm	(°C)	min.	kNm
AISC360-2010	657.35	126.1	130.5	546.07	89.06	130.5
EN1993-1-2	834.88	181.15	103.5	731.26	135.5	103.5

Table 13 Comparison of critical values for protected 7 m beam

Standards	Laterally supported			Laterally unsupported		
	Critical temp.	Time	Design moment	Critical temp.	Time	Design moment
	(°C)	min.	kNm	(°C)	min.	kNm
AISC360-2010	647.97	129.66	177.63	512.5	18.31	177.63
EN1993-1-2	847.8	193.7	140.88	742.24	143.78	140.88

similar values as Indian standard; the minor difference in values is due to the partial load safety factor as per the standards.

- For unprotected members, AISC code provides less value of PSA. Main reason for this is the higher partial load safety factors in the standard.
- For protected members, Eurocode gives more PSA before failure when compared to American code.
- With increase in span of the member, load ratio increases thereby reducing the limiting temperature. Thus, it can be explained for T_n by

$$(T_3 > T_4 > T_5 > T_6 > T_7)$$

where T_n = critical temperature for 'n' m span, n = 3–7 m.

- Critical temperature in a member reduces with reduction in section factor (H_p/A), i.e. steel member with low section factor will take more time to reach critical temperature.
- For fire-resistant design of steel structures, AISC code gives conservative value, due to the consideration of higher safety factor in the code.
- Indian code offers economical value for fire-resistant design, but restricts temperature value by 750 °C and in most cases of laterally supported beam, the value of critical temperature is higher than 750 °C. Hence, we cannot refer the result of Indian code.

References

1. Gohil, A. (2015). *Fire resistance of steel structures*, (M.Sc. Thesis). London, UK: Brunel University.
2. IS800. (2007). *General construction in steel-code of practice*. New Delhi: Bureau of Indian Standard.
3. AS4100. (1998). *Steel structures*. NSW, Australia: Standards Association of Australia.
4. EN1993-1-2. (2005). *Eurocode 3: Design of steel structures—Part 1–2: General rules—Structural fire design*. Brussels: European Committee for Standardization.
5. ANSI/AISC360. (2010). *Specification for Structural Steel Buildings*. Chicago, Illinois, US: American Institute of Steel Construction.
6. ISO834-1. (1999). *Fire resistant tests—Elements of building construction Part-1, General requirements*. London: Indian Standard Organization.
7. Lewis, K. (2000). *Fire design of steel members—Fire engineering research report*. Christchurch, New Zealand: University of Canterbury.
8. EN1991-1-1. (2002). *Eurocode 1: Actions on structures—Part 1–1: General actions—Densities, self-weight, imposed loads for buildings*. Brussels: European Committee for Standardization.
9. NIST Technical Note. (1842). *Structural design for fire: A survey of building codes and standards* (p. 2014). US: National Institute of Standards and Technology.
10. BS5950-8. (2003). *Structural use of steelwork in building-Part 8: Code of Practice for fire resistant design*. UK: British Standards Institution.

Effects of Column-to-Beam Strength Ratio on Behaviour of Beam-to-Column Moment Joints

Arnav Anuj Kasar, S. D. Bharti, M. K. Shrimali and Rupen Goswami

Abstract Steel Moment Resisting Frames (MRFs) are believed to be very ductile structures and are highly regarded structural systems, even in areas of high seismicity. The overall ductility of a steel MRF depends on many factors, such as connection configuration, column-to-beam strength ratio, effect of joint panel zone, material and cross-sectional properties, rate of loading, etc. Seismic performance of a steel MRF depends, primarily, on the performance of beam-to-column joints in the frame. The capacity of a joint to undergo inelastic deformation determines the ductility of an MRF. In a beam-to-column moment joint, the desirable behaviour is to limit inelastic actions at beam end regions, thereby preventing irreparable damage to structures. In a simple unreinforced moment connection, this is achieved by varying the Column-to-Beam Strength Ratio (CBSR). In this paper, a minimum value of CBSR, which ensures the formation of plastic hinge at beam end region, for a simple unreinforced joint, is determined. A parametric study, using Nonlinear Finite Element Analysis (NFEA), is carried out to determine the force–deformation behaviour of ten beams to column joint subassemblages. The CBSRs are varied from 1.2 to 11 to determine the value at which inelastic actions can be limited to the beam ends. The selection of CBSRs is based on the strength of AISC standard sections and their compatibility along with the various prevalent codal provisions. Results of NFEA show that the minimum CBSR required to prevent inelastic actions in columns is close to 7.5.

A. A. Kasar · S. D. Bharti · M. K. Shrimali (✉)
Department of Civil Engineering, Malaviya National Institute of Technology Jaipur, Jaipur 302017, India
e-mail: mkshrimali@mnit.ac.in

A. A. Kasar
e-mail: arnav.kasar@gmail.com

S. D. Bharti
e-mail: sdbharti@mnit.ac.in

R. Goswami
Department of Civil Engineering, Indian Institute of Technology Madras, Chennai 600036, India
e-mail: rg@iitm.ac.in

A. Rama Mohan Rao and K. Ramanjaneyulu (eds.), *Recent Advances in Structural Engineering, Volume 1*, Lecture Notes in Civil Engineering 11,
https://doi.org/10.1007/978-981-13-0362-3_24

Keywords Steel moment resisting frames · Column-to-beam strength ratio
Capacity design · Strong axis moment joints · Force–deformation behaviour
Strong column weak beam

1 Introduction

Since their inception, steel Moment-Resistant Frames (MRFs) are considered to be the most effective structural systems. This belief is based, partially, on the inherent ductility of steel as a construction material, and partially on their ease of construction and architectural suitability. During mid-twentieth century, steel MRFs were the most preferred structural systems, especially in areas of high seismicity. It was because of their 'assumed' good ductile behaviour that these structural systems were assigned the most optimistic design parameters.

The damages sustained by steel MRFs during and in the aftermath of 1994 Northridge and 1995 Kobe earthquakes were phenomenal, and led to substantial research on the behaviour of such frames, under seismic excitations [1]. The Northridge earthquake led to the damage of nearly 200 steel MRF buildings, most of which were located in the connection region. The damage to welded beam-to-column connections can be attributed to two broad reasons: (i) improper design, leading to insufficient strength of connections; and (ii) excessive rotation, due to inelastic yielding of Joint Panel Zone (JPZ) region. As MRFs are more flexible than other common earthquake-resistant structural systems, such as braced frames and steel plate shear wall systems, they require to be designed on the basis of drift limits. When subjected to lateral forces, the lateral deformation of steel moment frames is supposed to be accommodated through inelastic flexing of beams, while the columns are supposed to remain in elastic range.

The concept of capacity design recommends that, in a frame structural members, should be proportioned to yield at predetermined sequence and locations. Thus, better control on the inelastic behaviour of structures is achieved, by accommodating the imposed ductility demand in a few predetermined locations, while rest of the structures remains in elastic range. A typical strong axis, interior beam-to-column joint subassemblage, of an MRF, is shown in Fig. 1, depicting different regions of the subassemblage. The concept of capacity design suggests that both the columns and the beam-to-column joints have to be stronger than the beams [2].

In the past, numerous researches have been carried to determine the factors on which the ductility of steel beam-to-column moment joint depends. One of the most critical factors is design of Joint Panel Zone (JPZ) region, which may be based on one of the three design philosophies: (i) Strong JPZ, wherein the JPZ remains elastic [3], forcing all inelastic actions to the beam ends; (ii) Weak JPZ, all inelastic deformations are limited to the JPZ [4] region, thereby preventing the formation of plastic hinges at beam ends; and (iii) Balanced JPZ, allows controlled inelastic yielding of JPZ [5–7] region, leading to sharing of inelasticity between beams and

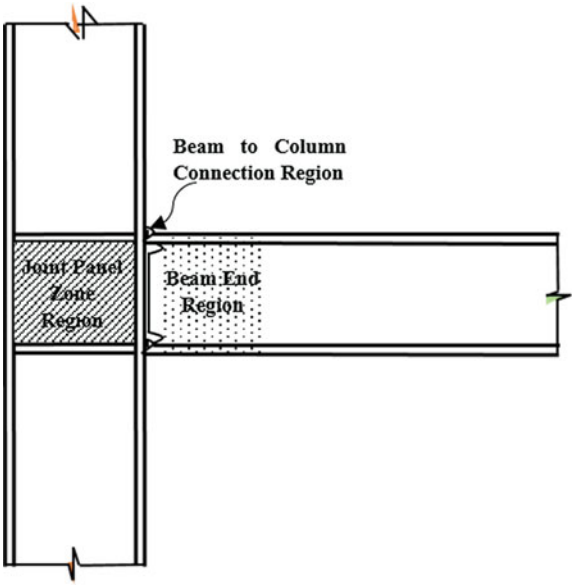

Fig. 1 A typical exterior beam-to-column moment joint subassemblage showing different regions of the joint

JPZ region. Most of the prevalent design codes recommend that the JPZ region shall be designed on the basis of the third approach, i.e., sharing of inelastic actions between beams and JPZ region.

When subjected to lateral force, JPZ region undergoes very stable shear yielding and is capable of undergoing large inelastic deformations [5]. To utilize this reserve strength, designers configured the joints such that the JPZ region is allowed to participate, along with the beams, in dissipating the input seismic energy through inelastic action. Much research has been carried out to determine the effects of behaviour of JPZ region on the overall performance of MRFs [8–12].

The objectives of code-based design are to assure life safety (strength and ductility) and, to some extent, prevent damage (limiting the drifts). The first objective may be achieved by allowing yielding of JPZ region; nevertheless, the shear yielding of JPZ region leads to uncontrolled overall deformation of the structure. Also, as the JPZ is an integral part of column, shear yielding of JPZ necessarily means yielding of column web and is irreparable in nature, and thus shall not be permitted. In the prevalent state of steel design, the JPZs are designed to undergo yielding simultaneously with the beams. This design philosophy needs to be revisited and suitable amendments need to be brought in, so that the shear yielding of JPZ can be postponed up to the formation of beam plastic hinge.

2 Modelling and Analysis

To determine the effects of CBSR on the behaviour of strong axis interior beam-to-column joint subassemblages, a range combination of columns and beams is selected. Two important deciding parameters for selecting a section as column or beam are (a) plastic section moduli and (b) width of flange. Beam sections are such selected, in which the width of beam flanges remains lesser than width of corresponding column flanges for a particular CBSR. A fair representation of a wide range of column-to-beam strength ratios is achieved through section selection. Ten beam-to-column joint subassemblages are modelled having different CBSRs, ranging from 1.2 to 11. A list of different beam and column sections, used to obtain beam-to-column joint subassemblages with different CBSRs, is presented in Table 1. The class of selected section is determined using tables B4.1a and B4.1b of AISC 361-10, and most of the sections selected are compact, while only a few are classified as non-compact.

For the purpose of analysis, both exterior and interior beam-to-column joint subassemblages are modelled starting from CBSR of 1.2, based on IS 800:2007. The subassemblages consist of column with height equal to sum of the distance of point of contraflexure, above and below the joint. Beam length for subassemblage is also taken to be equal to distance between two points of contraflexures, on either side of the column for an interior joint. The points of contraflexures are assumed at the mid-heights of members, and centerline dimensions are considered at this stage (Fig. 2).

The subassemblages are simply supported at column ends, and displacement loading is applied at beam ends. A displacement-based nonlinear finite element analysis of all the subassemblages is performed using ABAQUS software package [13]. The members are assumed to be of ASTM A36 grade steel with isotropic hardening model, the stress–strain behaviour of which is shown in Fig. 3 (yield stress of 250 MPa and ultimate stress of 415 MPa).

Table 1 Standard AISC sections used for beam-to-column joint subassemblages

S.N.	Beam sections		Column sections		CBSR M_{pC}/M_{pB}
	Section	M_{pB} (kNm)	Section	M_{pC} (kNm)	
1.	W27×84	1,000	W18×130	1,188	1.19
2.	W18×97	864	W24×176	2,093	2.42
3.	W18×71	598	W24×176	2,093	3.50
4.	W24×103	1,147	W33×318	5,203	4.54
5.	W30×124	1,671	W36×529	9,545	5.71
6.	W27×102	1,250	W36×487	8,726	6.98
7.	W21×101	1,036	W27×539	7,743	7.47
8.	W30×90	1,159	W40×503	9,504	8.20
9.	W27×84	1,000	W36×529	9,545	9.55
10.	W24×94	1,041	W40×593	11,307	10.86

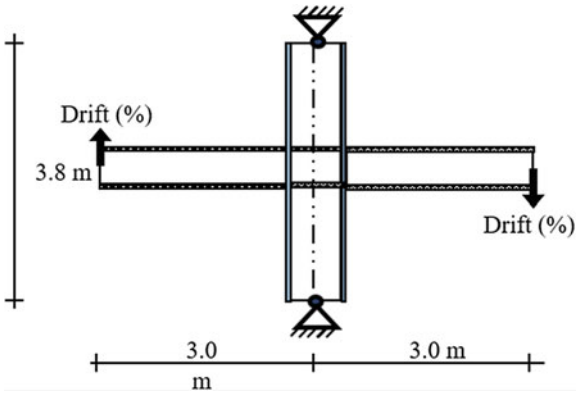

Fig. 2 Strong axis interior beam-to-column joint subassemblage modelled for analyses

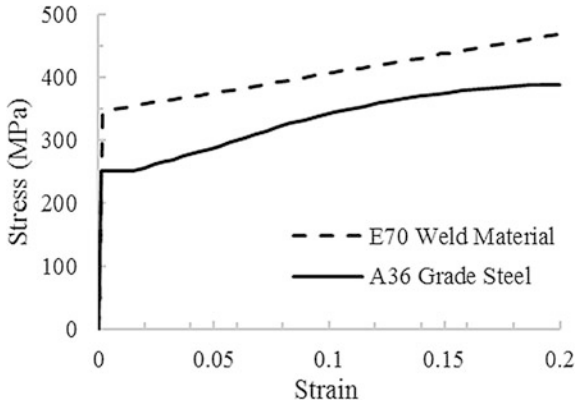

Fig. 3 Stress–strain relationship of materials used

Stress–strain relationships for A36 grade steel and E70 electrodes used for analysis are shown in Fig. 3. The modulus of elasticity and Poisson's ratio of both the materials are 200 GPa and 0.260, respectively. The height of columns in the subassemblages is 3.8 m, which, in most cases, is the average storey height (Fig. 2). The distance considered between column centerline and the point of application of load on beams is 3.0 m, representing span of beam. Nonlinear analyses are carried out on three-dimensional solid models. A uniform mesh is developed for the subassemblage models using eight-noded linear brick element (C3D8R). Single-step monotonic drift loading up to a drift level of 4% is used for analyses to obtain the differences in responses of these beam–column joints. Axial compressive load is not considered on the columns, to reduce the number of parameters on which the behaviour of subassemblage depends.

3 Results and Discussion

Displacement-based nonlinear finite element analyses are carried out for ten beam-to-column joint subassemblages. The results obtained from ABAQUS are presented in Figs. 4 and 5. Figure 4 shows the level of inelasticity induced in a beam-to-column joint, at a drift level of 4% through von-Mises stress contours. For combinations having a CBSR less than 7, inelastic yielding of JPZ is observed. The extent of inelasticity in JPZ region reduces, with an increase in CBSR. This is primarily due to increase in strength of beams, which in turn increases their participation in the dissipation of induced energy, through inelastic excursions.

Figure 5 depicts shear–stress contours for the analyzed beam-to-column joint subassemblages, at the initiation of yield. The state of inelastic shear action indicates

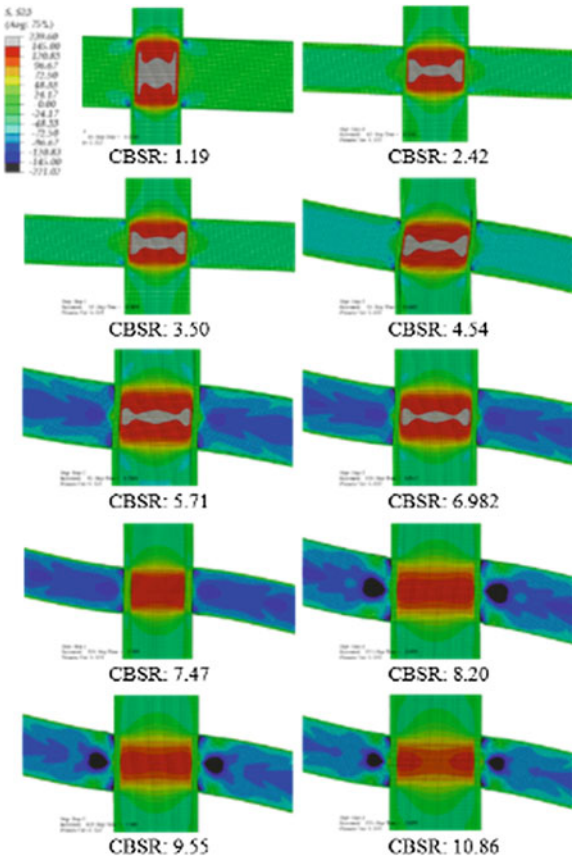

Fig. 4 Shear–stress contours of beam-to-column joint subassemblages at initiation of yield

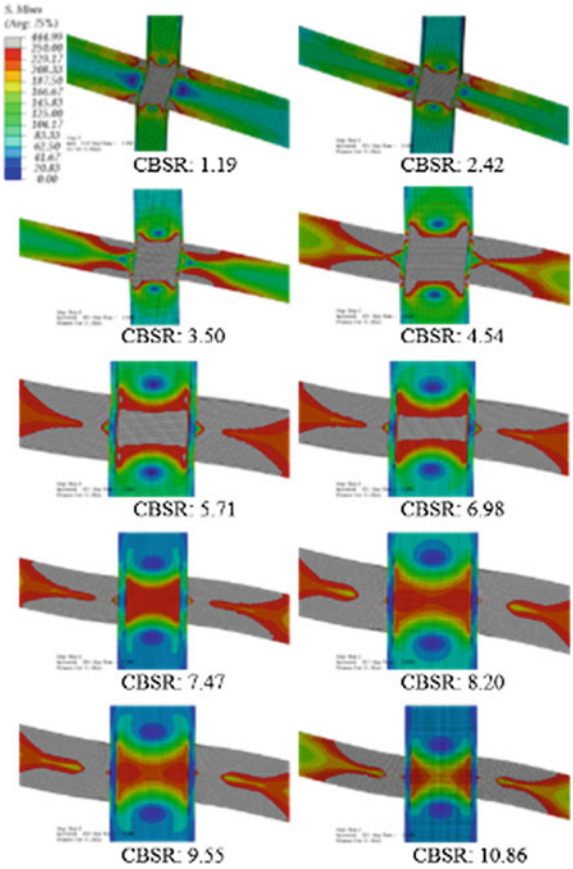

Fig. 5 von Mises stress contours of beam-to-column joint subassemblages at 4% drift

that, for joints having CBSR lesser than seven, yielding of JPZ initiates at a very small drift level. Inelastic actions in a structure at a drift level of 0.0067 rad are in-acceptable, especially in areas prone to seismic excitations. Table 2 gives the NFEA-based estimates of drifts and beam forces corresponding to those drift levels, at which yielding of three components of a beam-to-column joint occurs. From the table, it can be noted that, up to a CBSR of 4.52, there is no contribution of beams in the inelastic energy dissipation mechanism, and all the inelasticity remains limited to the JPZ region.

Figure 6 shows the force–deformation behaviour of beam-to-column joint sub-assemblages analyzed for this study. The extent of energy dissipation depends on the sections selected for designing the joint, along with the CBSR.

Table 2 Yield sequence of components of a beam-to-column moment joint

S.N.	CBSR	Panel zone yielding		Beam flange yielding		Beam plastic hinging	
		%Drift	Force (kN)	% Drift	Force (kN)	% Drift	Force (kN)
1.	1.19	**0.644**	**340.97**	1.099	453.62	–	–
2.	2.42	**0.643**	**154.60**	0.972	180.57	–	–
3.	3.43	**0.753**	**139.95**	1.065	177.05	–	–
4.	4.52	0.840	419.93	**0.699**	**394.39**	–	–
5.	5.66	2.554	976.84	**0.753**	**678.56**	2.954	1014.28
6.	7.02	3.087	773.11	**0.647**	**484.27**	2.767	751.85
7.	7.57	–	–	**0.768**	**399.93**	2.568	566.81
8.	8.43	–	–	**0.574**	**456.79**	2.434	706.58
9.	9.62	–	–	**0.613**	**401.35**	2.749	623.73
10.	10.99	–	–	**0.614**	**418.92**	2.954	660.30

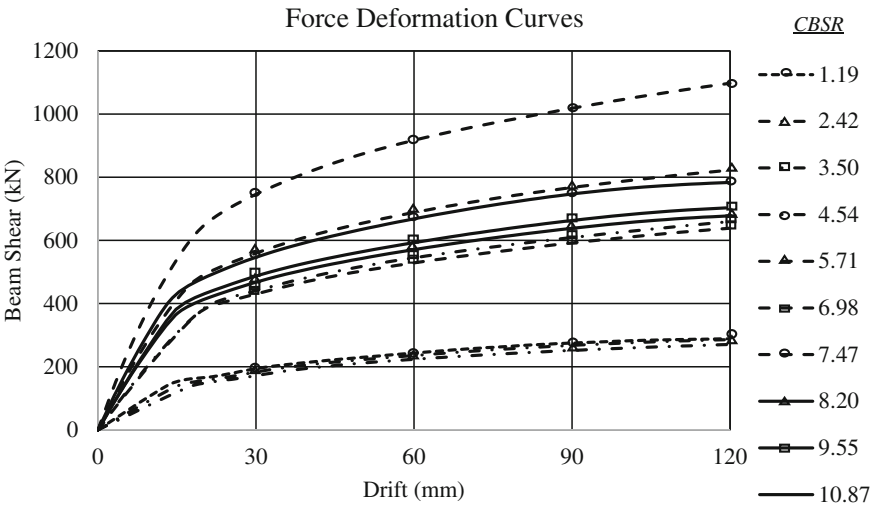

Fig. 6 Force deformation behaviour of beam-to-column joint subassemblages up to 4% drift

4 Conclusions

The seismic behaviour of steel MRFs depends primarily on the CBSR of the beam-to-column joints. The concept of capacity design recommends that the columns of a frame remain undamaged in a moderate level shaking. As joint panel zones are integral part of the columns, inelastic activities in JPZ region shall not be allowed for a moderate level shaking. Following conclusions can be drawn from the study carried out in this paper:

1. The JPZ region in a simple unreinforced beam-to-column moment joint is susceptible to inelastic actions at a drift level of 0.64%. This yield drift is much less than that expected during a moderate level of shaking.
2. The beam end regions of a beam-to-column joint subassemblage shall be allowed form plastic hinges, before shear yielding of JPZ region initiates.
3. In a beam-to-column joint subassemblage, a strong JPZ can be obtained by use of column web stiffeners of sufficient thickness. This thickness of column web region (JPZ) needs to be arrived at, on the basis of strength requirements. Further research is required to determine the column web stiffening strategy.
4. The minimum value of CBSR to prevent inelastic shear yielding of JPZ before the formation of plastic hinges in the beams is about 8.0.

It is recommended that the suitability of steel MRFs in areas of high seismicity is re-evaluated in the light of present conclusions.

References

1. Nakashima, M., Roeder, C. W., & Maruoka, Y. (2000). Steel moment frames for earthquakes in United States and Japan. *Journal of Structural Engineering, 126*(8).
2. Penelis, G. G., & Kappos, A. J. (1997). *Earthquake resistant concrete structures.* Great Britain: E & FN Spon.
3. AISC. (1980). *Specifications for the design, fabrication, and erection of structural steel for buildings, with commentary manual of steel construction* (8th ed.). American Institute of Steel Construction.
4. Kawano, A. (1984). Inelastic behavior of low-rise steel frame based on a weak beam-to-column connection philosophy to earthquake motion. In *Proceeding of 8th World Conference on Earthquake Engineering* (Vol. IV, pp. 519–526). Englewood Cliffs N.J: Prentice-Hall.
5. Krawinkler, H. (1978). Shear in beam-column joints in seismic design of steel frames. *Engineering Journal AISC, 3,* 82–91.
6. FEMA-267A. (1997). Interim guideline: Advisory no. 1, supplement to FEMA-267 SAC Joint Venture SAC-96-03 Sacramento, California.
7. Mazzolani, F. M., & Piluso, V. (1996). *Theory and design of seismic resistant steel frames*. Great Britain: E & FN Spon.
8. Bertero, V. V., Popov, E. P., & Krawinkler, H. (1973). *Further studies on seismic behaviour of steel beam-column subassemblages earthquake engineering Research Center UCB/ EERC-73/27*. Berkeley: University of California.
9. Bertero, V. V., Popov, E. P., & Krawinkler, H. (1972). Beam-column subassemblages under repeated loading. *Journal of Structural Engineering ASCE, 98*(ST5), 1137–1159.
10. Englekirk, R. E. (1999). Extant panel zone design procedures for steel frames are questioned. *Earthquake Spectra EERI, 15*(2), 361–369.
11. FEMA 355D. (2000). *State of the Art Report on Connection Performance.* Federal Emergency Management Agency.
12. FEMA 350. (2000). *Recommended Seismic Design Criteria for new Steel Moment-Frame Buildings.* Federal Emergency Management Agency.
13. Hibbitt, Karlsson & Sorensen. (2013). *HKS ABAQUS/Standard User's Manual*. RI, USA: ABAQUS Inc.

14. AISC 341-10. (2010). *Seismic Provisions for Structural Steel Buildings American Institute of Steel Construction*. Chicago, Ill.
15. IS 800:2007. (2007). *General Construction in Steel: Code of Practice*. Bureau of Indian Standards.

Moment–Rotation Response for Semi-rigid Connections

Venkatesh Patnana, A. Y. Vyavahare and Laxmikant M. Gupta

Abstract In this paper, mathematical models available for eight commonly used beam-to-column connections like single-web angle, double-web angle, top and seat angle with and without web angles, extended end-plate, flushed end-plate, and header plate connections are studied from literature. Connection analysis program is developed to obtain moment–rotation response of each type of connection using empirical data available models in the literature. Bjorhovde's classification system is used for the classification of the connections. Each type of connection as listed are analyzed; moment–rotation response of each connection is obtained using available models in literature; and results are compared.

Keywords Semi-rigid · Moment–rotation · Beam-to-column connection Classification

1 General Introduction

In general, much importance was given to the design of structural elements like bending members, compression members, and tension members. There should be a proper connection arrangement in the structure to transfer the loading from one member to another. Connection should not fail before the member failure, and importance shall be given to design the connection as that of connecting members.

Traditionally, connection is assumed as either pinned or fixed to reduce the complexity of the analysis and design. From the past research of experimental,

V. Patnana · A. Y. Vyavahare · L. M. Gupta (✉)
Department of Applied Mechanics, Visvesvaraya National Institute of Technology, Nagpur 440010, India
e-mail: lmgupta@apm.vnit.ac.in

V. Patnana
e-mail: jesvenkatesh137@gmail.com

A. Y. Vyavahare
e-mail: ayv@apm.vnit.ac.in

A. Rama Mohan Rao and K. Ramanjaneyulu (eds.), *Recent Advances in Structural Engineering, Volume 1*, Lecture Notes in Civil Engineering 11,
https://doi.org/10.1007/978-981-13-0362-3_25

analytical, mechanical, empirical, numerical, and informational models, it is evident that the connection is neither pinned nor fixed. The behavior of connection falls in between pinned and rigid, known as semi-rigid type.

Magnitude and effect of semi-rigidity in the structure will be known by observing the moment–rotation response of connection at the joint. Experimental observations show that different types of connections possess stiffness between ideally pinned and rigid. Semi-rigid connection not only changes the moment distribution but also makes the frame to drift, accordingly increase the $P-\Delta$ effect in the analysis.

The magnitude of the maximum bending moment in the beam changes due to semi-rigidity of beam-to-column connection. The behavior of frame depends upon the semi-rigid connection characteristics. The reduced bending moment will result in the reduction in the size of the member, thereby reducing the weight of structure.

2 Mathematical Moment–Rotation Models

Moment–rotation models express the relation between moment and rotation through curve fitting constants and standardization parameters. The following are the moment–rotation relationships proposed by researchers.

2.1 Frye–Morris, 1975

Frye and Morris [1] proposed a polynomial form of moment–rotation model for single-web (SWA), double-web (DWA), top and seat angle without web angle (TS), end-plate with (EEC) and without column (EEP) stiffeners, header plate (HP), and T-stub (*T*s) connection.

$$\phi = C_1(\mathrm{KM})^1 + \mathrm{C}_2(\mathrm{KM})^3 + \mathrm{C}_3(\mathrm{KM})^5 \tag{1}$$

M	Moment available at the connection,
ϕ	Relative rotation between beam and column,
C_1, C_2, and C_3	Curve fitting constants, and
K	Standardization parameter.

2.2 Prabha et al., 2015

In Ref. [2], a polynomial form of moment–rotation model for double-web angle connection is proposed. By considering the air gap between column flange and

beam web as 10 and 7 mm, Frye–Morris polynomial model is modified by Prabha et al. in [2].

$$\phi = 75.043\,(\mathrm{KM}) - 1.583 \times 10^3(\mathrm{KM})^3 + 9.816 \times 10^4(\mathrm{KM})^5 \tag{2}$$

2.3 Ang–Morris, 1984

Ramberg–Osgood power model [3] describes the stress–strain modified in Ref. [4], accompanying standardization functions for single-web angle, double-web angle, top and seat angle, header plate, and strap angle connection.

$$\frac{\phi}{\phi_0} = \frac{\mathrm{KM}}{[\mathrm{KM}]_0}\left[1 + \left(\frac{\mathrm{KM}}{[\mathrm{KM}]_0}\right)^{n-1}\right] \tag{3}$$

ϕ_0, $[\mathrm{KM}]_0$, and n—are constants that define the shape of the standardization function,

K—Standardization parameter.

2.4 Richard–Abbott, 1975

Four-parameter power model by Richard and Abbott [5] is the commonly used function as in Eq. (4).

$$M = \frac{(k_\mathrm{i} - k_\mathrm{p})|\phi|}{\left[1 + \left|\frac{(k_\mathrm{i} - k_\mathrm{p})|\phi|}{M_0}\right|^n\right]^{1/n}} + k_\mathrm{p}|\phi| \tag{4}$$

k_i, k_p, M_0 & n are initial stiffness, plastic stiffness, reference moment, and shape parameter.

2.5 Chisala, 1999

Three-parameter power model given by Chisala in [6] used to represent the non-linear moment–rotation relation for single-web angle, double-web angle, and top and seat angle with and without web angle connection.

$$M = [M_0 + K_p\phi][1 - e^{\frac{-K_i f}{M_0}}] \tag{5}$$

M_0, K_i, K_p—Interception constant, initial stiffness, and strain hardening stiffness, respectively.

2.6 Attiogbe–Morris, 1991

Attiogbe and Morris [7] derived the functions for parameters involved in Richard–Abbott model [5] for double-web angle connection as given in Eq. (6).

$$\frac{M}{M_0} = \frac{\phi}{\phi_0}\left[\frac{\left(1 - k_p\frac{\phi_0}{M_0}\right)}{\left[1 + \left|\left(\frac{1}{\phi_0} - \frac{k_p}{M_0}\right)\phi\right|^n\right]^{1/n}} + k_p\frac{\phi_0}{M_0}\right] \tag{6}$$

M_0, ϕ_0, k_p, and n are the reference moment, reference rotation, slope of the curve for large value of rotation, and sharpness parameter, respectively.

2.7 Calado et al., 2000

Calado et al. [8] conducted experiments on top and seat angle connection using neural networks and proposed a power model as given in Eq. (7).

$$\phi = \frac{M}{k_0}\left[1 + \left(\frac{M}{M_y}\right)^{r-1}\right] \tag{7}$$

M_y, k_0, and r are the yielding strength, initial stiffness, and the shape parameter, respectively.

2.8 Krishnamurthy et al., 1979

Krishnamurthy et al. [9] conducted numerical analysis using FEM and developed a simple power model (Eq. 8) for extended end-plate connection with four bolts on tension side.

$$\phi = CM^{\alpha} \tag{8}$$

α, C are curve fitting constants.

2.9 Kukreti, 1987

Kukreti et al. [10] extended the concept of FEM to know the influence of parameters on the flushed end-plate connection. Krishnamurthy power model [9] is modified by changing the geometrical parameter.

$$\phi = CM^{\alpha} \tag{9}$$

α, C are curve fitting constants.

2.10 Yee and Melchers, 1986

Four-parameter power models in Ref. [11] obtained by considering the equilibrium, material relationships, compatibility, and moment of resistance of a joint and rotational stiffness. Possible yielding and failures of connection components for bolted extended end-plate eave connection is considered.

$$M = M_{\mathrm{p}}\left[1 - \exp\left(\frac{-(k_{\mathrm{i}} - k_{\mathrm{p}} + Cf)f}{M_{\mathrm{p}}}\right)\right] + k_{\mathrm{p}}f \tag{10}$$

M_{p}, k_{i}, k_{p}, and C are plastic moment capacity of weaker section, initial stiffness, plastic stiffness, and a constant that controlling the slope of the curve, respectively.

2.11 Lui–Chen, 1986

Lui and Chen [12] proposed exponential model used to analyze single-web angle, top and seat angle, flushed end-plate, and extended end-plate connection. This model needs more curve fitting constants to get proper shape of response.

$$M = M_0 + \sum_{j=1}^{n} C_j\left[1 - \exp\left(\frac{-|\phi|}{2j\alpha}\right)\right] + k_{\mathrm{p}}|\phi| \tag{11}$$

M, M_0, C_j, ϕ, α, n, and k_p are moment in the connection, initial moment, curve fitting coefficients, absolute value of the rotation, scaling factor, and number of terms considered.

2.12 Kishi–Chen, 1986

Proposed exponential model in Ref. [12] is modified in by Kish and Chen [13] to accommodate linear components to analyze single-web angle, top and seat angle, flushed end-plate and extended end-plate connection.

$$M = M_0 + \sum_{j=1}^{m} C_j \left[1 - \exp\left(\frac{-|\phi|}{2j\alpha}\right)\right] + \sum_{k=1}^{n} D_k(\phi - \phi_k)H(\phi - \phi_k) \tag{12}$$

ϕ_k, C_j, D_k, and $H[\phi]$ are the starting rotation of linear components, curve fitting constants, and heavy side function.

3 Connection Analysis Program (CAP)

In this connection analysis program (CAP), moment–rotation responses available for experimental and empirical models are incorporated along with curve fitting constants and shape parameters.

3.1 Main Routines of CAP

a. Input for the connection analysis program is in CGS units, and the program changes the units of the data relevant to the moment–rotation models. Output is in MKS units.
b. Output of the program contains moment–rotation responses, classification of connection according to IS: 800 [14], and stiffness at 0.01 rad.
c. Visualization can be in the image or pdf format.
d. Seven types of connections and seven moment–rotation responses are included in the program.

4 Analysis of Connections Using CAP

Connection data available from the literature is collected to analyze the connections using connection analysis program (CAP). The following connections are analyzed using appropriate models reported in literature, and moment–rotation response and classification of connections are shown in Figs. 1, 2, 3, 4, 5, 6, 7, 8, 9, 10, 11, 12, 13, and 14.

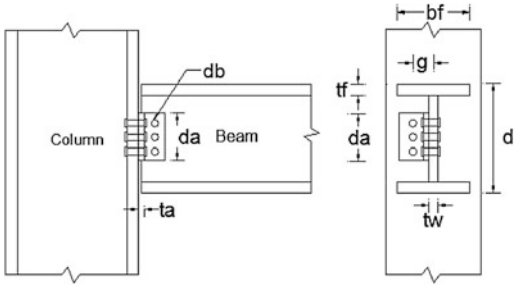

Fig. 1 Geometric parameters of SWA

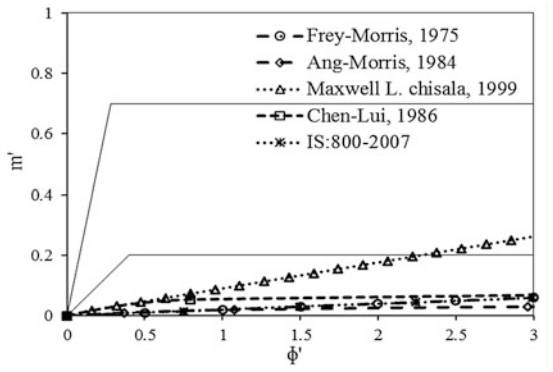

Fig. 2 Classification of SWA connection

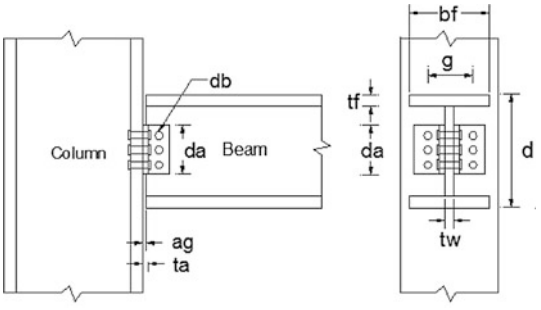

Fig. 3 Geometric parameters of DWA

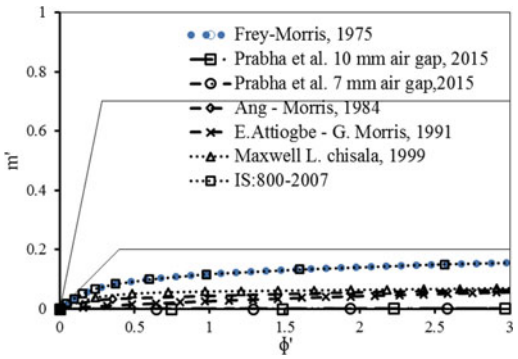

Fig. 4 Classification of DWA connection

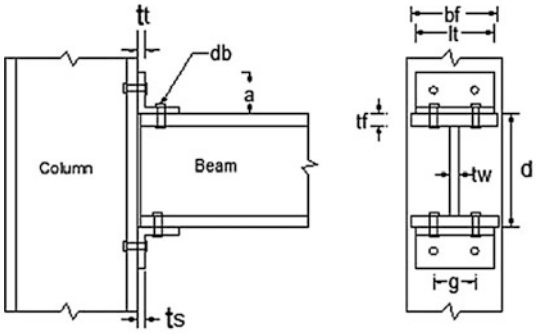

Fig. 5 Geometric parameters of TS

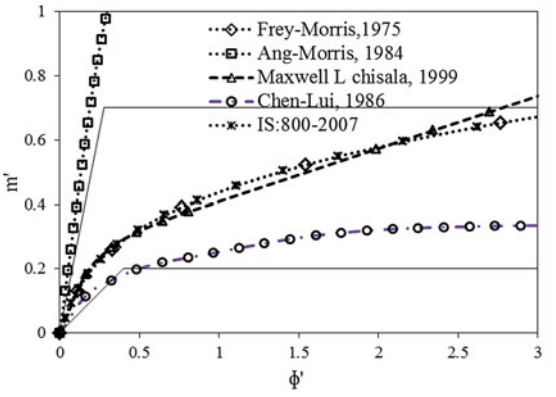

Fig. 6 Classification of TS connection

4.1 Single-Web Angle (SWA) Connection

Geometric parameters of SWA are shown in Fig. 1. Beam and column of ISMB 300 are connected by angle of 101.6 × 88.9 × 6.35 × 215.9 with gauge of 65 mm connected by 3 bolts of 19.05 mm (Table 1).

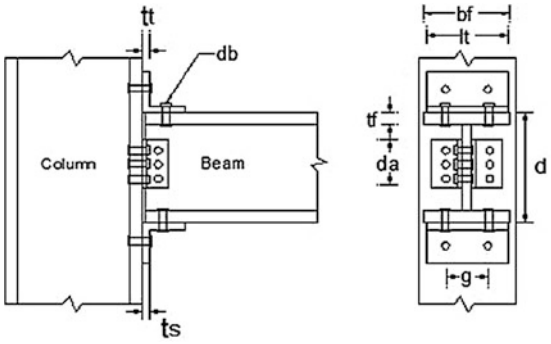

Fig. 7 Geometric parameters of TSW

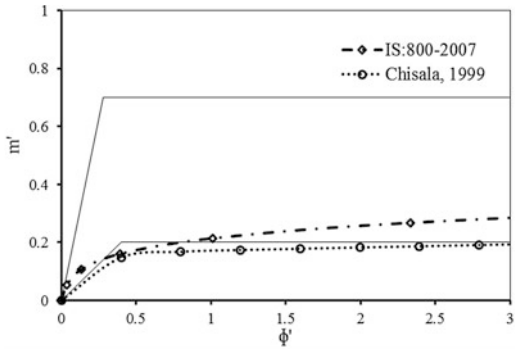

Fig. 8 Classification of TSW connection

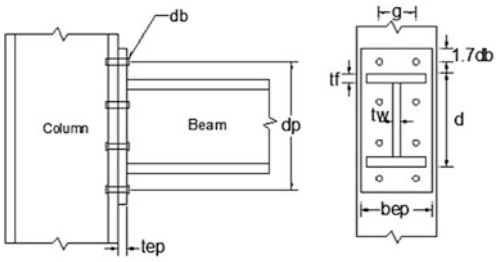

Fig. 9 Geometric parameters of EEP

4.2 Double-Web Angle (DWA) Connection

Geometric parameters of DWA are shown in Fig. 3.

Beam and column of 306.6 × 165.7 × 11.8 × 6.7 are connected by angle of ISA 65 × 65 × 6 × 180 with gauge of 72.7 mm connected by 3 bolts of 16 mm (Table 2).

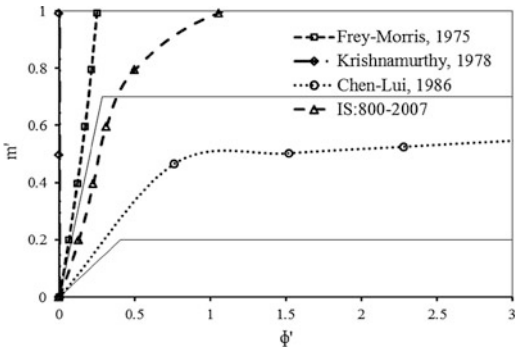

Fig. 10 Classification of EEP connection

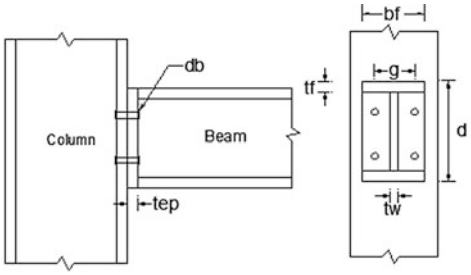

Fig. 11 Geometric parameters of FEP

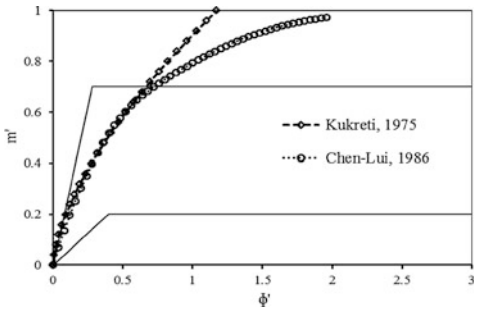

Fig. 12 Classification of FEP connection

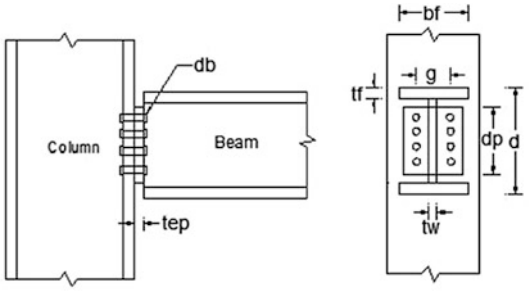

Fig. 13 Geometric parameters of HP

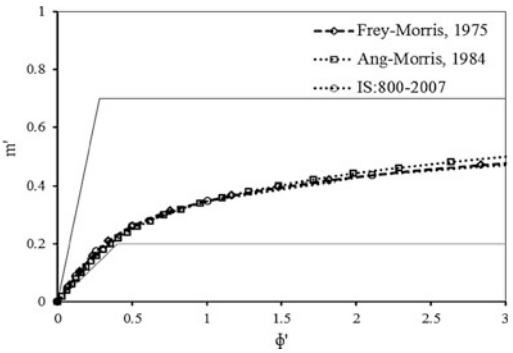

Fig. 14 Classification of HP connection

Table 1 Initial stiffness from M–ϕ response for SWA

Model	Stiffness at 0.01 rad (kN-m/rad)
Frye–Morris, 1975	316.13 (F–F)
Ang–Morris, 1984	333.33 (F–F)
Chisala, 1999	981.6 (F–SR)
Lui–Chen, 1986	1074.33 (F–F)
IS:800	318.75 (F–F)

Table 2 Initial stiffness from M–ϕ response for DWA

Model	Stiffness at 0.01 rad (kN-m/rad)
Frye–Morris, 1975	792.86 (F–F)
Prabha et al., 2015 (10 mm)	4 (F–F)
Prabha et al., 2015 (7 mm)	4.78 (F–F)
Ang–Morris, 1984	825 (F–F)
Attiogbe–Morris, 1991	970 (F–F)
Chisala, 1999	2016 (F–F)
IS:800	792.86 (F–F)

4.3 Top and Seat Angle (TS) Connection

Geometric parameters of TS are shown in Fig. 5.

Beam and column of W12×31.8 are connected by angle of 152.4 × 152.4 9.525 × 152.4 with gauge of 88.9 mm connected by 2 bolts of 36.39 mm (Table 3).

4.4 Top and Seat Angle with Web Angle (TSW) Connection

Geometric parameters of TSW are shown in Fig. 7.

Table 3 Initial stiffness from M–ϕ response for TS

Model	Stiffness at 0.01 rad (kN-m/rad)
Frye–Morris, 1975	6116.3 (SR–SR)
Ang–Morris, 1984	3740.3 (SR–R)
Chisala, 1999	3659 (SR–SR)
Lui–Chen, 1986	3593 (SR–SR)
IS:800	6116.3 (SR–SR)

Table 4 Initial stiffness from M–ϕ response for TSW

Model	Stiffness at 0.01 rad (kN-m/rad)
Chisala, 1999	1494.23 (F–SR)
IS:800	2491 (SR–SR)

Table 5 Initial stiffness from M–ϕ response for EEP

Model	Stiffness at 0.01 rad (kN-m/rad)
Frye–Morris, 1975	100,000 (R–R)
Lui–Chen, 1986	23,110.45 (SR–SR)
Krishnamurthy et al., 1979	15,800 (R–R)
IS:800	44,657.5 (SR–R)

Beam W12×31.8 and column of W12×58 are connected by a flange angle 152.4 × 152.4 × 9.525 × 152.4 and web angle 101.6 × 88.9 × 6.35 × 139.7 (Table 4).

4.5 Extended End-Plate (EEP) Connection

Geometric parameters of EEP are shown in Fig. 9.

Beam and column of W24×55 and W14×48 are connected by an end plate of 22.225 mm thick. Gauge of 139.7 mm is maintained with 25.4 mm bolt dia. at an outer distance of 692.15 mm (Table 5).

4.6 Flushed End-Plate (FEP) Connection

Geometric parameters of FEP are shown in Fig. 11.

Beam and column of W10×21 and W8×28 are connected by an end plate of 12.7 mm thick. Gauge of 88.9 mm is maintained with 19.05 mm bolt diameter, at an outer distance of 279.4 mm (Table 6).

Table 6 Initial stiffness from M–ϕ response for FEP

Model	Stiffness at 0.01 rad (kN-m/rad)
Lui–Chen, 1986	6855 (SR–R)
Kukreti, 1987	7043.5 (SR–R)

Table 7 Initial stiffness from M–ϕ response for HP

Model	Stiffness at 0.01 rad (kN-m/rad)
Frye–Morris, 1975	1800 (SR–SR)
Ang–Morris, 1984	1750 (SR–SR)
IS:800	1800 (SR–SR)

4.7 Header Plate (HP) Connection

Geometric parameters of HP are shown in Fig. 13.

Beam and column of W10×21 and W8×28 are connected by an end plate of 12.7 mm thick. Gauge of 88.9 mm is maintained with 19.05 mm bolt diameter at an outer distance of 279.4 mm (Table 7).

5 Conclusion

Analysis of all connections is carried out using the CAP program. Following observations are listed upon comparison of moment–rotation response.

a. Single-web angle connection demonstrates the flexible connection with very small initial stiffness.
b. Moment–rotation response of double-web angle connection shows large deviation among the models and fall in flexible type.
c. Moment–rotation response of top and seat angle connection shows deviation among the models other than Frye–Morris model, IS:800-2007 model, and Maxwell L Chisala model. Classification shows that it falls in semi-rigid type except for Ang–Morris model. Chen–Lui model demonstrates it as close to the boundary of flexible connection.
d. Moment–rotation response of top and seat angle with web angle connection falls on the boundary of flexible connection.
e. Moment–rotation response of extended end-plate connection shows large deviation among all models. Classification demonstrates it as rigid type connection, except Chen–Lui model which shows it as semi-rigid connection.
f. Moment–rotation response of flush end-plate connection demonstrates it as semi-rigid connection based on its initial stiffness and based on its capacity, it falls into rigid type of connection.
g. Moment–rotation response of header plate connection demonstrates semi-rigid type by all available models.

The moment–rotation response of any connection depends on its geometry and material properties. Available models to obtain moment–rotation response show large deviation among all. The observation from the analysis connection highlights the urgent need of experimental research and development of rational models to predict the moment–rotation response of beam-to-column connections so that it can be confidently included in the analysis of steel structure by the structural designer.

Acknowledgements The authors are thankful to the Director, VNIT, Nagpur, and Head of Applied Mechanics Department for their constant encouragement and support.

References

1. Frye, M. J., & Morris, G. A. (1975). Analysis of flexibly connected steel frames. *Canadian Journal of Civil Engineering, 2*(3), 280–291.
2. Prabha, P., Marimuthu, V., Saravanan, M., Palani, G. S., & Surendran, M. (2015). Modified Frye–Morris polynomial model for double web angle connections. *Journal of Advanced Structural Engineering, 7,* 295–306.
3. Ramberg, W., & Osgood, W. R. (1943). *Description of stress-strain curves by three parameters, Technical Report No. 902*. Washington, D.C.: National Advisory Committee for aeronautics.
4. Ang, K. M., & Morris, G. A. (1984). Analysis of three-dimensional frames with flexible beam-column connections. *Canadian Journal of Civil Engineering, 11,* 245–254.
5. Richard, R. M., & Abbott, B. J. (1975). Versatile elastic-plastic stress-strain formula. *Journal of the Engineering Mechanics Division, ASCE, 101*(4), 511–515.
6. Chisala, M. L. (1999). Modelling M-ϕ curves for standard beam to column connections. *Engineering Structures, 21*(11), 1066–1075.
7. Attiogbe, E., & Morris, G. (1991). Moment-rotation functions for steel connections. *Journal of the Engineering Mechanics Division, ASCE, 117*(6), 1703–1718.
8. Calado, L., De Matteis, G., & Landolfo, R. (2000). Experimental response of top and seat angle semi-rigid steel frame connections. *Material and structures, 33,* 499–510.
9. Krishnamurthy, N., Huang, H., Jeffrey, P. K., & Avery, L. K. (1979). Analytical M–ϕ curves for end-plate connections. *Journal of Structures Engineering, 105,* 133–145.
10. Kukreti, A. R., Murray, T. M., & Abolmaali, A. (1987). End plate connection moment-rotation relationship. *Journal of Constructional Steel Research, 8,* 137–157.
11. Yee, Y. L., & Melchers, R. E. (1986). Moment–rotation curves for bolted connections. *Journal of Structures Engineering, ASCE, 112*, 615–635.
12. Lui, E. M., & Chen, W. F. (1986). Analysis and behaviour of flexibly jointed frames. *Engineering Structures, 8,* 107–115.
13. Kishi, N., & Chen, W. P. (1986). *Data base of steel beam to column connections*. Lafayette: Structural Engineering Area, School of Civil Engineering, Purdue University.
14. IS 800: 2007. *Indian Standard General Construction in steel code of practice*. New Delhi: BIS.

Semi-elliptical LDSS Hollow Stub Columns Under Axial Compression

Tekcham Gishan Singh and Konjengbam Darunkumar Singh

Abstract In this paper, effect of thickness on the structural performance of concentrically loaded semi-elliptical lean duplex stainless steel (LDSS) hollow stub columns is presented via nonlinear finite element (FE) analysis by using ABAQUS. The modeling procedure has been validated against the LDSS stub column experimental results available in literature. The cross-sectional dimensions considered in this analysis conform to the commercially available semi-elliptical hollow sections from Ancofer Stahlhandel GMBH. Extensive parametric study was carried out to study the structural performance by varying the thickness from t = 5 to 14 mm. Based on the FE analyses, it has been found that, for the sections considered, a near linear increase ($\sim$+300%) in column resistance (P_u) is seen with increase ($\sim$+180%) in thickness from t = 5 to 14 mm. Further, an enhanced strain hardening effect on the load capacity can be observed for the thicker sections, i.e., $t \geq \sim$12.5 mm.

Keywords Finite element analysis · Lean duplex stainless steel
Semi-elliptical · Thickness · Strain hardening

1 Introduction

Stainless steel sections are known to provide enhanced properties over traditional carbon steel sections in terms of mechanical strength, sustainability, durability, etc., such as higher strength, high corrosion resistance, 100% recyclability, negligible maintenance required, better fire performance, good aesthetic appearance, smooth and uniform surface, high ductility, etc. Despite these enhanced properties,

T. G. Singh · K. D. Singh (✉)
Department of Civil Engineering, Indian Institute of Technology Guwahati, Guwahati, India
e-mail: darun@iitg.ernet.in

T. G. Singh
e-mail: tekcham@iitg.ernet.in

A. Rama Mohan Rao and K. Ramanjaneyulu (eds.), *Recent Advances in Structural Engineering, Volume 1*, Lecture Notes in Civil Engineering 11,
https://doi.org/10.1007/978-981-13-0362-3_26

high initial material cost and price fluctuation of important alloying element like nickel in particular hampers widespread use of stainless steel sections over the most widely used traditional carbon steel sections. Among the different types of stainless steel, austenitic steel grade which has nickel content of ~8–11% is commonly used, but due to the recent increase in the price of nickel, it becomes a difficult choice to use stainless steel in the construction industry. Lean duplex stainless steel (EN 1.4162) is a relatively new stainless steel grade with nickel content of ~1.5% and improved strength, i.e., twice the mechanical strength of austenitic steel. Hence, LDSS is an alternative choice for use of stainless steel in construction sector [1–5].

Tubular hollow stainless steel sections have been increasingly used in exposed structures where aesthetic appearance is of primary importance. In addition, tubular sections are known to provide improved torsional resistance, as compared to open sections. In the recent years, new sections such as elliptical, semi-elliptical, etc. with continuously varying curvature (with or without flat elements) have been introduced, as structural members. Semi-elliptical hollow sections (SEHS) are commercially available and manufactured by some of the prominent structural steel manufacturers, such as Ancofer Stahlhandel GMBH [6]. A typical SEHS is shown in Fig. 1.

In the literature, limited work has been reported on LDSS. Theofanous and Gardner [1, 2] studied the structural performance of square and rectangular LDSS hollow sections through experimental and numerical process and then compared the structural performance with sections made of other commonly used stainless steel grades such as austenitic steel grades. Huang and Young [7–11] also performed experimental and numerical investigations on the structural behavior of LDSS

Fig. 1 Semi-elliptical hollow section (Silvestre et al. [13])

square and rectangular sections under concentric, bending, and eccentric loading conditions. Sachidananda and Singh [3] carried out numerical investigations to study the effects of cross-sectional thickness, flat length, and curvature of end parts, on the load capacity of fixed-ended LDSS flat oval stub columns. However, for such sections especially semi-elliptical section, very limited information on their structural behavior is available in the literature. Nowzartash and Mohareb [12] studied the plastic interactions relations for semi-elliptical hollow sections (SEHS) subjected to general loading combinations involving axial force, biaxial bending, and twisting moments. Silvestre et al. [13] studied the buckling behavior, ultimate strength, and failure of SEHS columns using finite-strip analyses and finite element analyses. Both the studies are based on an idealized bilinear elastic-perfectly plastic stress–strain curve. Therefore, the additional capacity of the steel material due to strain hardening is neglected. In this present work, a parametric study on the structural performance of LDSS semi-elliptical hollow stub columns subjected to concentric compressive load is attempted, using the general-purpose, commercial FE software, ABAQUS [14].

2 Numerical Modeling

2.1 General

The effect of thickness on the structural performance of concentrically loaded semi-elliptical LDSS hollow stub columns was carried out using the commercial nonlinear FE program ABAQUS, 2009 [14]. Geometry of the semi-elliptical hollow sections considered in this study has been adapted from the commercially marketed sections from Ancofer [6]. Typical section nomenclature is followed, e.g., *h252b276L828t5,* where h = flat length, b = semi-elliptical arm length, L = length of the column, and t = thickness (as shown in Fig. 2). The flat material properties obtained from Huang and Young [7] were assigned to both flat and corner parts of the sections considered. The effect of residual stress was not considered.

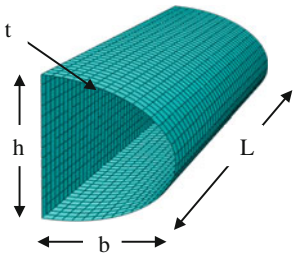

Fig. 2 Nomenclature of semi-elliptical hollow section

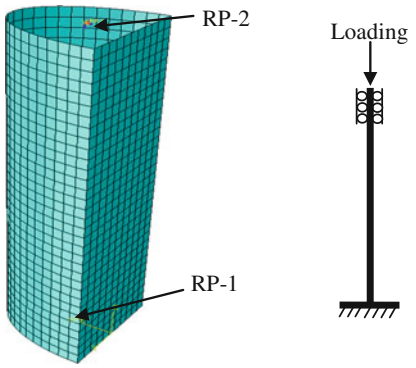

Fig. 3 Typical boundary and loading condition

2.2 Boundary and Loading Condition

In the present study, all the models were fixed at both ends by restraining all degrees of freedom except the degree of freedom in the loading direction which is allowed to translate. The ends were coupled with reference points (RP-1 and RP-2) available in ABAQUS [14] library, and load was applied through RP-2. Typical boundary and loading condition are shown in Fig. 3.

2.3 Element Type and Meshing

Due to the thin-walled nature and the SEHS under study, four-noded doubly curved shell element with reduced integration (S4R) having six degrees of freedom per node was utilized available in ABAQUS [14]. Convergence studies were carried out to find the appropriate mess size which will require optimal computational time without compromising accuracy. An approximate global mess size of 15–20 mm was found to be appropriate for this analysis and thus used to discretize the whole geometry. The number of S4R shell elements generated in various models ranges from $\sim$1,000 to 4,000. A typical FE meshing is shown in Figs. 2 and 3.

2.4 Material Modeling

The material properties obtained from the test results of Huang and Young [7] were used to derive the stress–strain model, and it is shown in Table 1. The stress–strain model up to 0.2% proof stress ($\sigma_{0.2}$) was derived using Ramberg-Osgood model [15] as given in Eq. (1) and from $\sigma_{0.2}$ to $\sigma_{1.0}$, by Gardner and Ashraf model [16], as given in Eq. (2) were employed.

$$\varepsilon = \frac{\sigma}{E_0} + 0.002\left(\frac{\sigma}{\sigma_{0.2}}\right)^2; \quad \text{For } \sigma \le \sigma_{0.2} \tag{1}$$

$$\varepsilon = \frac{\sigma - \sigma_{0.2}}{E_{0.2}} + \left(\varepsilon_{t1.0} - \varepsilon_{t0.2} - \frac{\sigma_{1.0} - \sigma_{0.2}}{E_{0.2}}\right)\left(\frac{\sigma - \sigma_{0.2}}{\sigma_{1.0} - \sigma_{0.2}}\right)^{n'_{0.2,1.0}} + \varepsilon_{t0.2}; \quad \text{For } \sigma_{0.2} \le \sigma \le \sigma_{1.0} \tag{2}$$

where σ and ε are the engineering stress and strain, respectively, E_0 is the initial young modulus, $\sigma_{0.2}$ is the 0.2% proof stress, n is the strain hardening exponent, $\sigma_{1.0}$ is the 1% proof stress, $\varepsilon_{t1.0}$ and $\varepsilon_{t0.2}$ are the total strain corresponding to $\sigma_{1.0}$ and $\sigma_{0.2}$, respectively. $n'_{0.2,1.0}$ = strain hardening exponent representing a curve that passes through $\sigma_{0.2}$ and $\sigma_{1.0}$, and its value was determined using Eq. (3) proposed by Quach et al. [17]. The engineering stress–strain has been converted into true stress (σ_{true}) and strain ($\varepsilon^{pl}_{\text{true}}$) using Eq. (4) to input in ABAQUS [14].

$$n'_{0.2,1.0} = 6.399\left(\frac{E_{0.2}}{E_0}\right)\left(\frac{\sigma_{1.0}}{\sigma_{0.2}}\right) + 1.145 \tag{3}$$

where

$$E_{0.2} = \frac{E_0\sigma_{0.2}}{\sigma_{0.2} + 0.002nE_0} \text{ and } \frac{\sigma_{1.0}}{\sigma_{0.2}} = 0.662\frac{1}{n} + 1.085$$

$$\begin{aligned} \sigma_{\text{true}} &= \sigma(1+\varepsilon) \\ \varepsilon^{pl}_{\text{true}} &= \ln(1+\varepsilon) - \frac{\sigma_{\text{true}}}{E_0} \end{aligned} \tag{4}$$

2.5 Local Geometric Imperfection

The lowest buckling mode shape was captured using linear elastic buckling analysis through Lanczos method and utilized to simulate the local geometric imperfection of the stub column. The imperfection amplitude proposed by Theofanous and Gardner [1] was used in all the models and is given in Eq. (5).

Table 1 Flat and curve coupon material properties [7]

Cross section	E (MPa)	$\sigma_{0.2}$ (MPa)	$\sigma_{1.0}$ (MPa)	n
150 × 50 × 2.5–Flat	202,000	664	766	4
150 × 50 × 2.5–Corner	967,000	831	953	6

Table 2 Cross-sectional dimension of SC6L450 [7]

Specimen	Depth (mm)	Width (mm)	Thickness (mm)	Outer radius (mm)	Length (mm)
SC6L450	150.0	50.2	2.463	4.3	450

$$w_0 = 0.023\left(\frac{\sigma_{0.2}}{\sigma_{cr}}\right)t \tag{5}$$

where

$$\sigma_{\text{cr}} = E_0\lambda\left(\frac{\Delta L}{L}\right)$$

Here, σ_{cr} is the elastic critical buckling stress, λ is the eigenvalue obtained from the buckling analysis, ΔL is the initial displacement given at the movable end, and L is the length of the column. Modified Riks method was employed to capture the complete load–displacement characteristics.

2.6 Validation of Finite Element Model

The stub column experimental results by Huang and Young [7] on LDSS rectangular hollow specimen—SC6L450—were utilized to assess the accuracy of the FE modeling approach and verify the compatibility of parametric study. The cross-sectional dimensions of the column are shown in Table 2. Similar modeling approached published in [3–5, 18] was followed in the present FE modeling. The flat and corner material properties are, respectively, assigned to the flat and corner part of the section. The load versus end-shortening comparison curve and deformation pattern between experimental and FE approach are shown in Figs. 4 and 5,

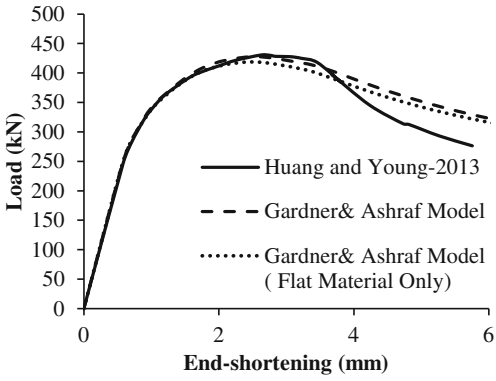

Fig. 4 Comparison of load–end-shortening curves of section 150 × 50 × 2.5

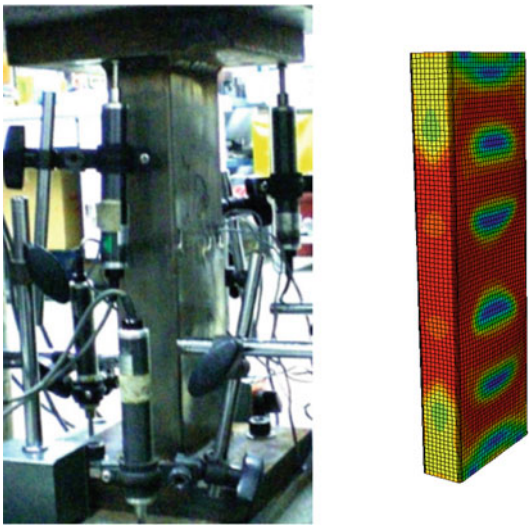

Fig. 5 Comparison of test and FE deformation mode for SC6L450

respectively. From Figs. 4 and 5, good agreement between the present FE modeling approach and experimental result from Huang and Young [7] can be seen.

3 Parametric Study

The motivation of this present study is to investigate the structural behavior of semi-elliptical hollow stub columns by varying the thickness. Finite element study on 21 stub columns was carried out using the validated FE procedure described in previous sections. Three commercially marketed cross sections from Ancofer were considered in the present study, which includes *h203b223L669*, *h225b259L777,* and *h252b276L828*. The thickness of the sections was varied from 5 −14.2 mm. The column length was taken as three times the larger dimension to capture the behavior of stub column. The flat material property from Huang and Young [7] has been utilized for all the models for both the flat and corner sections. The effect of residual stress was not considered in the present study, as their effect on the column was relatively small [19]. The initial geometric imperfection was introduced with imperfection magnitude as given in Eq. (5).

4 Result and Discussions

Nonlinear FE buckling analysis was conducted using ABAQUS [14]. The results of the FE analysis are shown in the form of table and curves. The ultimate load capacity and corresponding end-shortening magnitudes for different models are shown in Table 3. The load versus end-shortening curves, load–thickness curves, and von Mises contours are analyzed in subsequent paragraphs.

Typical load versus end-shortening behavior for *h252b276L828*, *h225b259L777,* and *h203b223L669* sections are shown in Figs. 6, 7, and 8, respectively. An enhanced strain hardening effect on the load capacity for the thicker section can be observed, i.e., $t \geq \sim 12.5$ mm. The behavior of load with the increase in thickness is shown in Fig. 9. It can be seen that there is a near linear increase ($\sim$+300%) in column resistance capacity with increase ($\sim$+180) in thickness from $t = 5$ mm.

The von Mises stress distribution contours coupled with deformed shaped corresponding to δ_u, where δ_u is the end-shortening deformation with respect to ultimate load, P_u for section corresponding to *h203b223L669t5.0* is shown in Fig. 10. From the figure, the onset of local buckling at the ultimate load can be observed.

Table 3 Key results from FE analysis

Sections	Ultimate load (kN)	δ_u (mm)
h203b223L669t05.0	2187.88	4.22
h203b223L669t06.0	2770.09	4.21
h203b223L669t06.3	2971.09	4.14
h203b223L669t08.0	4139.89	4.35
h203b223L669t10.0	5574.80	7.35
h203b223L669t12.5	7122.85	10.88
h203b223L669t14.2	8130.65	11.13
h225b259L777t05.0	2368.81	3.99
h225b259L777t06.0	2976.97	5.07
h225b259L777t06.3	3194.22	4.70
h225b259L777t08.0	4472.55	4.40
h225b259L777t10.0	6083.83	6.06
h225b259L777t12.5	8036.21	10.48
h225b259L777t14.2	9168.67	11.38
h252b276L828T05.0	2380.45	3.33
h252b276L828T06.0	3230.91	4.77
h252b276L828T06.3	3438.83	4.63
h252b276L828T08.0	4723.76	4.64
h252b276L828T10.0	6407.10	5.74
h252b276L828T12.5	8697.95	6.03
h252b276L828T14.2	9999.10	12.21

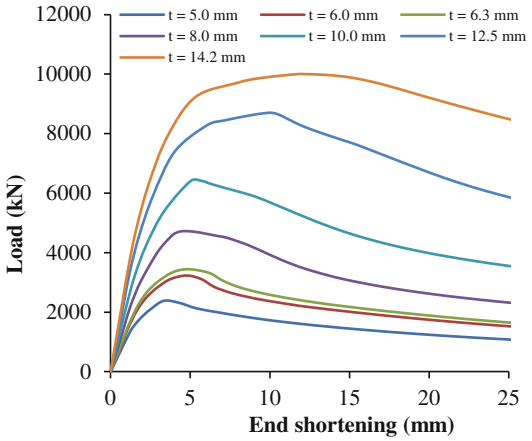

Fig. 6 Load versus end-shortening behavior for *h252b276L828*

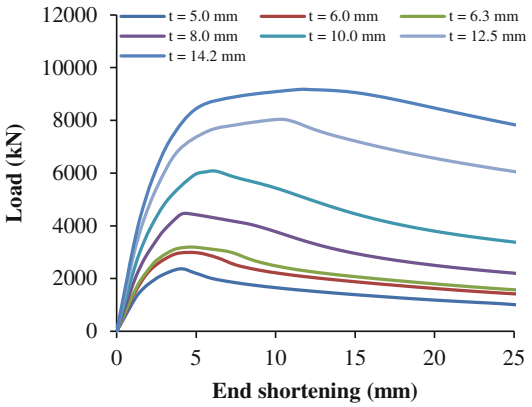

Fig. 7 Load versus end-shortening behavior for *h225b259L777*

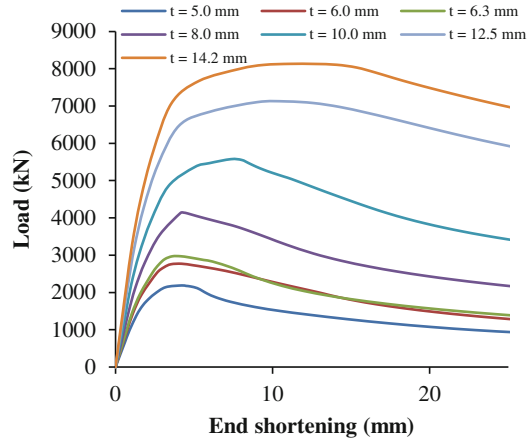

Fig. 8 Load versus end-shortening behavior for *h203b223L669*

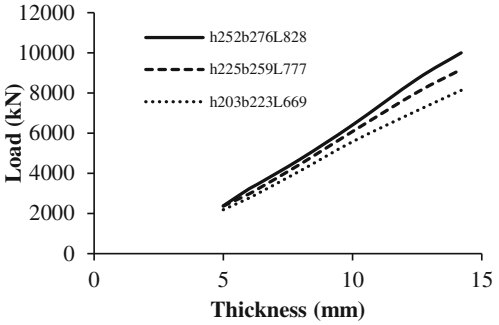

Fig. 9 Load versus thickness behavior for three sections

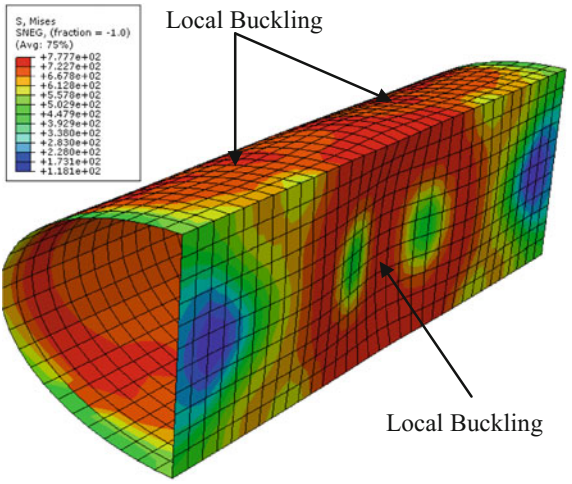

Fig. 10 Deformed shaped along with von Mises stress distribution for *h203b223L669t5.0* at P_u

5 Conclusions

(a) The column load (P_u) capacity increases in a linear fashion with increase in thickness.
(b) An enhanced strain hardening effect on the load capacity can be observed for the thicker sections.

References

1. Theofanous, M., & Gardner, L. (2009). Testing and numerical modelling of lean duplex stainless steel hollow section columns. *Engineering Structures, 31*(12), 3047–3058.
2. Theofanous, M., & Gardner, L. (2010). Experimental and numerical studies of lean duplex stainless steel beams. *Journal of Constructional Steel Research, 66*(6), 816–825.

3. Sachidananda, K., & Singh, K. D. (2015). Numerical study of fixed ended lean duplex stainless steel (LDSS) flat oval hollow stub column under pure axial compression. *Thin-Walled Structures, 30*(96), 105–119.
4. Patton, M. L., & Singh, K. D. (2012). Numerical modeling of lean duplex stainless steel hollow columns of square, L-, T-, and + -shaped cross sections under pure axial compression. *Thin-Walled Structures, 30*(53), 1–8.
5. Patton, M. L., & Singh, K. D. (2013). Buckling of fixed-ended lean duplex stainless steel hollow columns of square, L-, T-, and + -shaped sections under pure axial compression—a finite element study. *Thin-Walled Structures, 28*(63), 106–116.
6. Ancofer. (2008). *Structural hollow section catalogue*. Rheinstraße 163, 45478 Mülheim an der Ruhr, Germany: Ancofer Stahlhandel GmbH.
7. Huang, Y., & Young, B. (2012). Material properties of cold-formed lean duplex stainless steel sections. *Thin-Walled Structures, 31*(54), 72–81.
8. Huang, Y., & Young, B. (2013). Experimental and numerical investigation of cold-formed lean duplex stainless steel flexural members. *Thin-Walled Structures, 31*(73), 216–228.
9. Huang, Y., & Young, B. (2014). Experimental investigation of cold-formed lean duplex stainless steel beam-columns. *Thin-Walled Structures, 31*(76), 105–117.
10. Huang, Y., & Young, B. (2014). Structural performance of cold-formed lean duplex stainless steel columns. *Thin-Walled Structures, 31*(83), 59–69.
11. Huang, Y., & Young, B. (2014). Design of cold-formed lean duplex stainless steel members in combined compression and bending. *Journal of Structural Engineering, 141*(5), 04014138.
12. Nowzartash, F., & Mohareb, M. (2010). Plastic interaction relations for semi-elliptical hollow sections. *Thin-Walled Structures, 48*(1), 42–54.
13. Silvestre, N., Pires, T., & Duarte, A. P. (2013). Numerical analysis of semi-elliptical hollow section columns. *Proceedings of the Institution of Civil Engineers-Structures and Buildings, 166*(8), 424–433.
14. Abaqus. (2009). *Abaqus/standard user's manual (vols. I–III) and ABAQUS CAE manual*. Version 6.9-EF1. Providence, USA: Dassault Systemes Corp.
15. Ramberg, W., & Osgood, W. R. (1943). *Description of stress–strain curves by three parameters*. Technical Note No. 902, Washington, DC: National Advisory Committee for Aeronautics.
16. Gardner, L., & Ashraf, M. (2006). Structural design for non-linear metallic materials. *Engineering Structures, 28,* 925–936.
17. Quach, W. M., Gallknkkd Teng, J., & Chung, K. F. (2008). Three-stage full-range stress-strain model for stainless steels. *Journal of Structural Engineering, 134*(9), 1518–1527.
18. Anbarasu, M., & Ashraf, M. (2016). Behaviour and design of cold-formed lean duplex stainless steel lipped channel columns. *Thin-Walled Structures, 31*(104), 106–115.
19. Ellobody, E., & Young, B. (2005). Structural performance of cold-formed high strength stainless steel columns. *Journal of Constructional Steel Research, 61*(12), 1631–1649.

Assessment of Load Carrying Capacity of Thin-Webbed Castellated Beam

A. Cyril Thomas and K. Baskar

Abstract Castellated beam (CB) is a type of expanded beam with hexagonal, circular and octagonal openings. This paper reports the nonlinear behaviour of thin-webbed castellated steel beams under different lengths (high, moderate and low shear) and the effect of cut-out geometry. The sectional property of the beam is considered as semi-compact by using the ratio of depth of the web (d_w) to thickness of the web (t_w). The main objective of this study is to understand the prominent failure modes and to propose an equation to find the load carrying capacity of thin-webbed CBs. For obtaining the failure modes and load carrying capacity, finite element models were developed with initial imperfections and material nonlinearities. The parametric study was carried out to propose an empirical equation to find the load carrying capacity of the thin-webbed CBs, and simultaneously the failure modes of CBs were observed and discussed.

Keywords Castellated beam · Nonlinear finite element model
Web-post buckling · Load carrying capacity

1 Introduction

Beams are the structural members which are capable of transferring loads to the columns and withstanding load mainly by resisting against the bending. The utilization of steel structures in the construction industry increased in a drastic manner. Castellated beam is one of the most efficient structural steel members in steel structure construction.

A. Cyril Thomas · K. Baskar (✉)
Department of Civil Engineering, National Institute of Technology,
Trichy 620015, India
e-mail: kbaskar@nitt.edu

A. Cyril Thomas
e-mail: cyrilstrer@gmail.com

A. Rama Mohan Rao and K. Ramanjaneyulu (eds.), *Recent Advances in Structural Engineering, Volume 1*, Lecture Notes in Civil Engineering 11,
https://doi.org/10.1007/978-981-13-0362-3_27

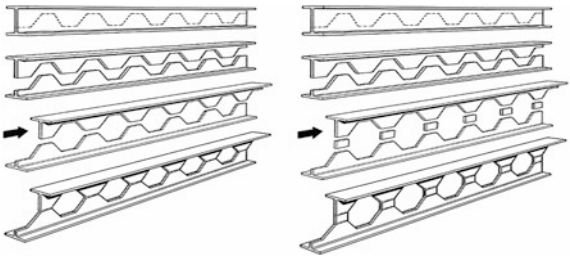

Fig. 1 Fabrication process of castellated beams

Castellated beam (CB) is a type of expanded beam with hexagonal, circular and octagonal openings. These beams are generally fabricated by cutting the web of an I-section in a zig-zag pattern where the cut portion was reassembled to the other end and welded along its length, to increase depth of the original beam. The improved depth increases its section modulus and moment of inertia, and results in greater strength and rigidity. This increment was done without adding any additional weight in the existing member.

The web opening is frequently used for ductwork, piping, etc., which conventionally suspends below the beam. Providing the holes in the web decreases the building height and the structure is in safer side from wind and seismic effects. The typical castellated beam is mentioned in Fig. 1.

2 Background

In past two decades, many research works were carried out to understand the various structural behaviours of castellated beams.

Boyer discussed the development, application and its advantages [1]. From the consideration of all failure-inducing terms, the design concepts are proposed by Blodgett and Knowles [2, 3].

The existence of opening the web in CBs leads to different failure modes [4]. The major failure modes of castellated beams are mentioned below:

(a) Lateral–torsional buckling of one or several web posts which is due to horizontal shear in the web post.
(b) Formation of Vierendeel mechanism which is due to vertical shear transfer due to the presence of hole.
(c) Rupture of welded joint in a web post which is due to horizontal shear force in the web.
(d) Web-post buckling due to vertical shear force.
(e) Lateral–torsional buckling of entire span.
(f) Formation of a flexure mechanism.

These failure modes are obtained from the experimental investigation. The experimental investigation is carried out for understanding the buckling behaviour

of CBs web post between the openings, and it was concluded that the web-post buckling is the leading failure mode in the thin-webbed (Banthan beam series) CBs [5, 6]. The same work was numerically investigated, and it was compared with euro code. The effect of imperfection in the numerical model also is studied by finite element analysis [7]. Due to the economical and lightweight usages, the thickness of the members (t_w and t_f) considered in this study is lesser than the minimum value as specified in the code and earlier studies [5–7].

In CBs, web-post buckling is one of the most important failure modes. This mode of failure occurs due to the horizontal shear force in the web post which is connected with double curvature bending over the height of the post. Hence, there are no standard accepted design concepts that are available for designing CB connected with all of its failure modes [7]. But some research works are carried out for assessing the load carrying capacity of the CBs using optimization tools like artificial neural network (ANN), gene expression programming (GEP), etc. [8, 9]. On the other hand, empirical equations are also proposed for evaluating the load carrying capacity of the CBs [10].

From the earlier studies, the load carrying capacity of the CBs depends on the weld length (e) and size of the opening (d). In this study, the empirical equations are to be proposed by using the parameters (Moment to shear ratio, weld length and size of opening).

3 Finite Element Study

3.1 General and Meshing

The main objective of this study is to analyse the leading failure modes and to assess the load carrying capacity of the thin-webbed CBs. The finite element models were developed with the initial imperfections and material nonlinearities in ABAQUS/CAE 6.10. The beam was modelled with four-node shell element (S4R) which is frequently used in previous studies [7].

The geometrical parameters of the CBs considered for this study are as follows:

1.	Width of flange (b_f)	100 mm
2.	Thickness of flange (t_f)	4 mm
3.	Depth of web (d_w)	292 mm
4.	Thickness of web (t_w)	2.5 mm
5.	Overall depth (h)	300 mm

Figure 2 shows the important terms used for modelling of CB. Mild steel material is considered for this analysis. The average value of yield stress (σ_y) of the steel is 233.3 MPa, the Young's modulus (E) is 210 GPa and Poison's ratio (v) is 0.3. A trilinear stress–strain curve of mild steel is used for calculating the true stress

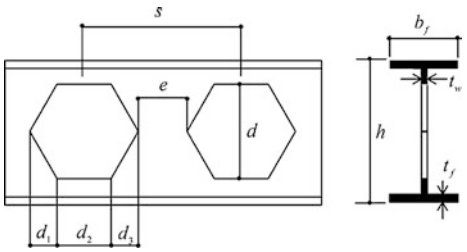

Fig. 2 Terminology of castellated beam

and plastic strain values [11]. The sectional property of the beam is considered as semi-compact as per IS 800-2007.

In ABAQUS/CAE, the developed model should complete two analyses. Buckling analysis was performed in the first step for incorporating the imperfections in the model. In general, the lowest buckling mode was considered for the nonlinear analysis [12]. The imperfection factor of $d_w/100$ was considered for this study, which is preferred from the earlier studies [7]. The second step is nonlinear analysis. This analysis was performed by using Riks analysis with geometrical and material nonlinearities.

3.2 Validation of FE Model

In general, validation is one of the most important terms. In this study, the FE model of CB was developed and it was validated with the earlier established experimental work [5]. The computed results are mentioned in Table 1.

The load computed from the FE study is 7.15% higher than the experimental work. Hence, the same steps have been initialized for this study.

3.3 Parametric Study

The validated FE model was utilized for the assessing the load carrying capacity of CB with different parameters. Totally, 27 CBs are modelled with various lengths and cross-sectional geometries. These parameters are selected based on the length and castellation geometries. The beams are analysed as 'laterally restrained simply supported condition'. In this study, all beams are analysed as single-point loading condition. The ratio between maximum bending moment to maximum shear force

Table 1 Validation of FE model

Beam name	Previous study [5] P_{EXP} (kN)	Present study P_{FEM} (kN)	Error (%)
10–3	73.84	79.12	+7.15

is known as moment–shear (M/V) ratio. In general, shear in the beam will affect the moment carrying capacity of the beam. In a simply supported beam, shear is maximum when the M/V ratio is 0.5. On the other hand, the shear is moderate when the M/V ratio is 1.0 and also the shear is low in the M/V ratio 1.5. Based on this condition, the lengths of the beams are chosen as high shear (HS), moderate shear (MS) and low shear (LS) by its moment–shear (M/V) ratio. The details of the parameters are as follows:

(a) Length—According to the moment (M) to shear (V) ratio, lengths of the CBs are considered as high shear (HS with M/V ratio 0.5), moderate shear (MS with M/V ratio 1.0) and low shear (LS with M/V ratio 1.5).
(b) Castellation geometries—The castellation geometries are considered as per the ratio of depth of the castellation (d) to depth of the web (d_w) and weld length (e) to depth of the castellation (d).

The cutting angle of castellated beams ranges from 45° to 70°. The considered cutting angle (ϕ) in this study is 60°. The dimensional terms of CB were finalized using Blodgett's approach [2].

$$\tan\phi = \frac{(d/2)}{d_1} \text{ or } \tan\phi = \frac{(d/2)}{d_3} \tag{1}$$

$$S = 2(d_1 + e) \text{ or } S = 2(d_3 + e) \tag{2}$$

Castellation geometries act as an important role in the load carrying capacity of CB. From the earlier research works, indicate the increase of the castellation depth which leads to web-post buckling. In the same manner, the increment and decrement of weld length affect the stability of web post. The complete parametric information is mentioned in Table 2. The developed FE model of CB is indicated in Fig. 3.

All the CBs are modelled with even number of holes, because in this study single-point load was applied in the centre span. To avoid local bucking, stiffeners are provided in the loading point and end points of the CB. The effect of residual stresses due to welding is very small. So this effect of residual stress is neglected in the model [7, 12].

Table 2 Parametric information

Section	M/V ratio	d/d_w ratio	e/d ratio
Semi-compact	0.5	0.55 0.65 0.75	0.2 0.3 0.4
	1.0	0.55 0.65 0.75	0.2 0.3 0.4
	1.5	0.55 0.65 0.75	0.2 0.3 0.4

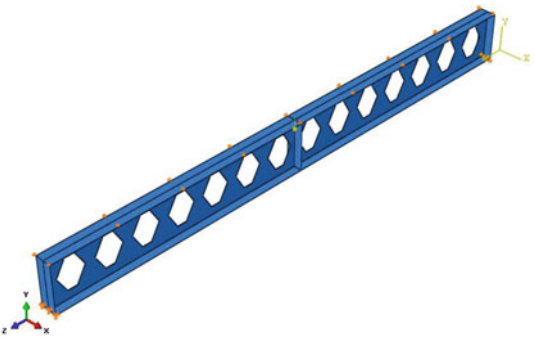

Fig. 3 Finite element model of castellated beam

4 Results and Discussions

The assessment of load carrying capacity and the leading failure modes of CB are numerically investigated. For all cut-out geometries, a constant length was not fixed; rather, the lengths of the beam for all cut-out geometries are specified by its M/V ratio. All the CBs are failed by web instability due to the formation of Vierendeel mechanism and web-post buckling. The following discussions explain the behaviour of CBs in detail.

4.1 High Shear (HS) Sections

The CB sections with the moment–shear (M/V) ratio of 0.5 are termed as HS sections. The maximum load carrying capacity was noted in the beam MV05SC554, and the minimum load carrying capacity was witnessed in the CB section MV05SC754. The computed values are mentioned in Table 3. According to the geometrical parameters of CB, it was observed that the variation in the load

Table 3 Load carrying capacity of CB in HS

Name	e (mm)	d (mm)	n	d/d_w ratio	e/d ratio	Load (kN)
MV05SC552	32	160	6	0.55	0.2	54.24
MV05SC553	48	160	6		0.3	58.13
MV05SC554	64	160	4		0.4	63.42
MV05SC652	38	190	6	0.65	0.2	44.54
MV05SC653	57	190	4		0.3	51.75
MV05SC654	76	190	4		0.4	47.42
MV05SC752	44	220	4	0.75	0.2	44.32
MV05SC753	66	220	4		0.3	41.07
MV05SC754	88	220	4		0.4	33.97

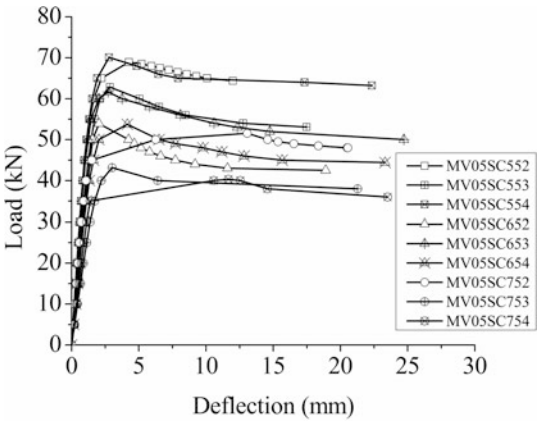

Fig. 4 Load versus deflection of HS sections

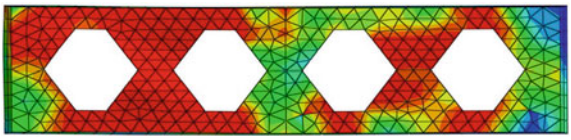

Fig. 5 Typical failure mode of HS section

carrying capacity is continuously differing in load. From the analysis, the deflection values vary from 2 to 4 mm.

From the nonlinear FE analysis, it was noted that the load–deflection behaviour of HS CBs is similar. Figure 4 clearly indicates the same.

In HS sections, shear is the most important dominant factor for failure. The typical failure mode of HS section is shown in Fig. 5. The openings in the web portions develop the double curvature bending in the web post. This leads to progress the formation of Vierendeel mechanism.

4.2 Moderate Shear (MS) Sections

To obtain the load carrying capacity, the same measure has been initialised for MS sections. The CB section with M/V ratio of 1.0 is named as MS sections. In this study, the maximum and minimum load carrying capacities were achieved by MV10SC552 and MV10SC753. The obtained values are shown in Table 4.

The length of the MS sections is higher than the HS section because of the *M*/*V* ratio. The deflection values are from 4.5 to 5.5 mm. Similarly, there are some notable changes which are found in the load carrying capacities. The load carrying capacity values are gradually increased from MV10SC552 to MV10SC554. Similarly, the same kind of variation is noticed from MV10SC752 to MV10SC754.

Table 4 Load carrying capacity of CB in MS

Name	e (mm)	d (mm)	n	d/d_w ratio	e/d ratio	Load (kN)
MV10SC552	32	160	12	0.55	0.2	54.39
MV10SC553	48	160	10		0.3	54.56
MV10SC554	64	160	8		0.4	55.76
MV10SC652	38	190	10	0.65	0.2	44.31
MV10SC653	57	190	8		0.3	48.56
MV10SC654	76	190	8		0.4	45.97
MV10SC752	44	220	10	0.75	0.2	36.00
MV10SC753	66	220	8		0.3	38.60
MV10SC754	88	220	6		0.4	39.44

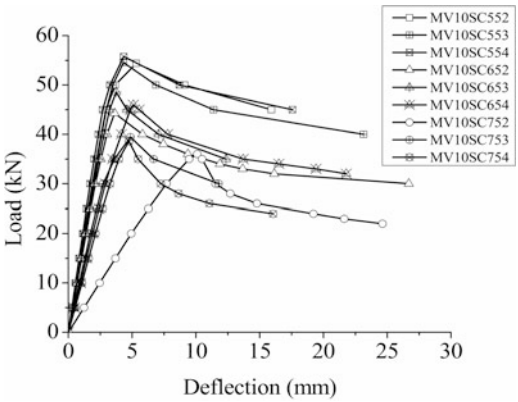

Fig. 6 Load versus deflection of MS sections

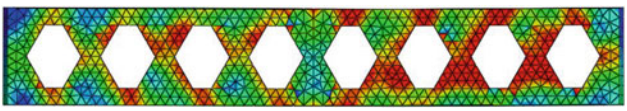

Fig. 7 Typical failure mode of MS section

But in the CB section, MV10SC653 has the maximum load carrying capacity compare to the other sections MV10SC652 and MV10SC654.

The load–deflection behaviour of MS sections is mentioned in Fig. 6. In MS sections, all the beam sections are failed due to the formation of flexural mechanism and the formation of Vierendeel mechanism. The typical failure mode of MS section is mentioned in Fig. 7.

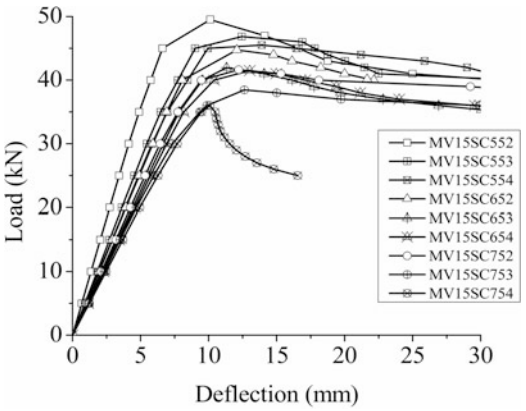

Fig. 8 Load versus deflection of LS sections

Table 5 Load carrying capacity of CB in LS

Name	e (mm)	d (mm)	n	d/d_w ratio	e/d ratio	Load (kN)
MV15SC552	32	160	20	0.55	0.2	49.51
MV15SC553	48	160	16		0.3	46.85
MV15SC554	64	160	14		0.4	45.52
MV15SC652	38	190	16	0.65	0.2	44.75
MV15SC653	57	190	14		0.3	41.97
MV15SC654	76	190	12		0.4	41.50
MV15SC752	44	220	14	0.75	0.2	41.64
MV15SC753	66	220	12		0.3	38.47
MV15SC754	88	220	10		0.4	36.00

4.3 Low Shear (LS) Sections

The CB sections with M/V ratio of 1.5 are termed as low shear (LS) sections. The similar method has been applied for assessing the load carrying capacity of the LS CB sections. The maximum load carrying capacity was attained by MV15SC552 section. The changes in the load carrying capacities are gradually decreased according to the cut-out geometries of the CB.

The load–deflection behaviour of LS sections of CB is mentioned in Fig. 8. From the results, it was observed that the deflection values of LS sections are varied from 10 to 12 mm. Similarly, the load carrying capacities of LS sections are shown in Table 5.

In LS sections, the formation of flexural mechanism is the most important failure mode. The typical flexural mechanism formation in LS sections is shown in Fig. 9.

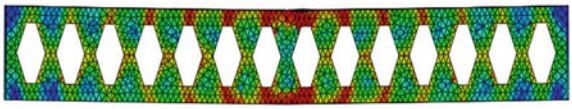

Fig. 9 Typical failure mode of LS section

5 Conclusions

The intention of this nonlinear FE study is to understand the behaviour of thin-webbed CB sections. The earlier study was carried out in the thin-webbed sections. But in this study, thickness of the web and thickness of the flange were considered 33.33 and 10.65% lesser than the previous study.

From the obtained results, the following three empirical equations are proposed to find the load carrying capacity of CBs with different M/V ratios and cut-out geometries.

$$P^{0.5} = 128.8x^2 - 233.2y^2 - 488.2xy - 115.1x + 460.1y + 47.97 \quad (3)$$

$$P^{1.0} = 17.83x^2 - 126.2y^2 + 51.75xy - 123.2x + 52.85y + 105 \quad (4)$$

$$P^{1.5} = 72.33y^2 - 41.25xy - 30.58x - 38.05y + 75.25 \quad (5)$$

where x—(d/d_w), y—(e/d) and P—Load (kN).

These equations are derived from the multilinear regression analysis. In all the equations, the coefficients have 95% confidence bounds. Also, the root mean square (RMS) values vary from 0.97 to 0.99. These equations accomplished based on the assumed parameters of this particular study which cannot be compared or elaborated with the other empirical equations.

The combination of these three proposed equations is not possible because there is no fixed beam length considered in this study. All the beam lengths are finalized based on the M/V ratio. The failure modes also vary according to the beam length. The Vierendeel mechanism is the dominant failure mode in the HS sections. In the same time, the beams fail by both Vierendeel mechanism and formation of flexural mechanism in the MS sections. In LS sections, beams failed due to the formation of flexural mechanism. Because of these various reasons, the combination of equations is not possible.

The conclusion based on the FE study is that the maximum load carrying capacity was noted in the CB sections with the geometrical properties of d/h ratio 0.55 and e/h ratio 0.2. In all M/V ratios (M/V—0.5, 1.0 and 1.5), the same results were observed. The load carrying capacity of CB sections with d/d_w ratio of 0.55 is around 10–25% higher than the CB section with d/d_w ratios of 0.65 and 0.75. Hence, it is concluded that the height of castellation is inversely proportional to the load carrying capacity.

It is also noted that the CB with M/V ratio of 1.5 is performed well when compared with other CB sections with M/V ratios of 0.5 and 1.0. Meanwhile, the

Table 6 Failure modes of CB according to *M*/*V* ratio

S. No.	*M*/*V* ratio	Failure mode
1	0.5	Vierendeel mechanism
2	1.0	Vierendeel mechanism and formation of flexural mechanism
3	1.5	Formation of flexural mechanism

CB sections with the *M*/*V* ratio 0.5 and 1.0 are failed due to shear. Table 6 indicates the different failure modes of CBs according to its *M*/*V* ratios.

Hence, it is suggested that the utilization of these types of thin-webbed CBs can be used in the lightweight structures because of its less weight, economical factor, easy handling and durability also for its aesthetic appearance. On the other hand, providing CB sections should not be used for smaller lengths due to the domination of shear in the castellation portions.

Notations

b_f	Width of the flange (mm)
d	Depth of castellation (mm)
d_1 or d_3	Inclined cutting length (mm)
d_2 or e	Weld length (mm)
E	Young's modulus (GPa)
h	Overall height of the beam (mm)
S	Distance between holes (mm)
M	Bending moment (kN m)
t_f	Thickness of the flange (mm)
t_w	Thickness of the web (mm)
V	Shear force (kN)
ϕ	Cutting angle
σ_y	Yield stress (MPa)
v	Poisson's ratio
M/V	Moment–Shear ratio
$P^{0.5}$	Load carrying capacity of HS sections (kN)
$P^{1.0}$	Load carrying capacity of MS sections (kN)
$P^{1.5}$	Load carrying capacity of LS sections (kN)
ANN	Artificial neural network
CB	Castellated beam
GEP	Gene expression programming
RMS	Root mean square
LS	Low shear section
MS	Moderate shear section
HS	High shear section

Acknowledgements The authors gratefully acknowledge the financial support provided by National Institute of Technology, Tiruchirappalli and Technical Education Quality Improvement Program (TEQIP) Phase II.

References

1. Boyer, J. P. (1964). Castellated beam-new developments. *AISC National Engineering Conference*, Omaha, Nebraska in May.
2. Blodgett, O. W. (1976). *Design of welded structures 7th printing*. USA: The James F. Lincoln Arc Welding Foundation.
3. Knowles, P. R. (1991). Castellated beams. *Proceedings of Institution of Civil Engineers, Part 1, 90,* 521–536.
4. Kerdal, D., & Nethercott, D. A. (1984). Failure modes for castellated beams. *Journal of Constructional Steel Research, 4,* 295–315.
5. Zaarour, W., & Redwood, R. (1996). Web buckling in thin webbed castellated beams. *Journal of Structural Engineering, 122,* 860–866.
6. Redwood, R., & Demirdjian, S. (1998). Castellated beam web buckling in shear. *Journal of Structural Engineering (ASCE), 124,* 1202–1207.
7. Soltani, M. R., Bouchair, A., & Mimoune, M. (2012). Non-linear FE analysis of the ultimate behavior of steel castellated beams. *Journal of Constructional Steel Research, 70*, 101–114.
8. Gholizadeh, S., Pirmoz, A., & Attarnejad, R. (2011). Assessment of load carrying capacity of castellated steel beams by neural networks. *Journal of Constructional Steel Research, 67,* 770–779.
9. Gandomi, A. H., Tabatabaei, S. M., Moradian, M. H., Radfar, A., & Alavi, A. H. (2017). A new prediction model for the load carrying capacity of castellated steel beams. *Journal of Constructional Steel Research, 67*, 1096–1105.
10. Pourbehi, P., & Pirmoz, A. (2015). Shear response of castellated beams. *International Journal of Steel Structures, 15*(2), 389–399.
11. Mohebkah, A. (2004). The moment-gradient factor in lateral-torsional buckling on in-elastic castellated beams. *Journal of Constructional Steel Research, 60,* 1481–1494.
12. Shanmugam, N. E., & Baskar, K. (2003). Steel-concrete composite plate girders subjected to shear loading. *Journal of Structural Engineering (ASCE), 129,* 1230–1242.
13. BIS 800. (2007). General construction in steel-code of practice. *Bureau of Indian standards*, New Delhi.
14. ABAQUS/CAE 6.10. *User's manual*.
15. Knowles, P. R. (1985). *Design of castellated beams: For use with BS 5950 and BS 449*. Great Britain: Steel Construction Institute.
16. Subramanian, N. (2008). *Design of steel structures, 14th impression*. New Delhi: Oxford University Press.

Evaluation of Seismic Performance of Steel Plate Shear Walls Arranged in Staggered Configuration

Abhishek Verma and Dipti Ranjan Sahoo

Abstract Steel plate shear walls (SPSWs) are used as lateral load resisting systems in building structures, which consist of thin steel plates surrounded by boundary elements. It is most often provided in the same bay along the entire height of the buildings. This results in high demands on columns and foundation. Instead of providing the plates in a single bay, it can be arranged in such a way that the column forces are reduced inherently. The current study focuses on one such possible staggered arrangement. Nonlinear dynamic and static analyses are conducted to evaluate the seismic performance of such system. The staggered steel plate shear wall shows an excellent reduction in inter-storey drifts. It proves to be economical in terms of steel usage, in case of narrow steel plate shear walls. Reduction in foundation forces is observed, which further improves the economy.

Keywords Steel plate shear wall · Staggered arrangement

1 Introduction

Steel plate shear wall (SPSW) is used as a lateral load resisting system. It consists of a thin steel plate surrounded by boundary elements. Its ductility, energy dissipation capacity and ease of construction and repair have attracted a lot of engineers and researchers over the past few years [1–5]. SPSWs are most often provided in the same bay along the complete height of the buildings. The boundary elements of this system are designed as per the capacity design approach. This results in high axial forces in columns and on foundations.

A. Verma · D. R. Sahoo (✉)
Department of Civil Engineering, Indian Institute of Technology Delhi, 110016 New Delhi, India
e-mail: drsahoo@iitd.ac.in

A. Verma
e-mail: abhiverma.civil@gmail.com

A. Rama Mohan Rao and K. Ramanjaneyulu (eds.), *Recent Advances in Structural Engineering, Volume 1*, Lecture Notes in Civil Engineering 11,
https://doi.org/10.1007/978-981-13-0362-3_28

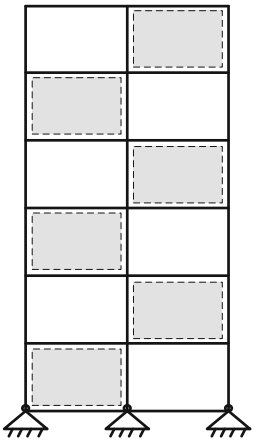

Fig. 1 SPSW with staggered arrangement of plates

A couple of techniques to reduce the column forces have been suggested by various researchers [6, 7]. Instead of providing the plates in a single bay, it can be arranged in such a way that the column forces are reduced inherently. The current study focuses on one such possible arrangement. The arrangement is shown in Fig. 1 and is referred to as staggered arrangement.

In this arrangement, unlike conventional SPSW which has two, there are three columns which need to be designed to resist lateral load. Horizontal boundary elements (HBEs) need to be designed to resist more load than a conventional SPSW, as they are pulled by the plate tension field either from top or bottom. Increased number of rigid beam–column joints and heavier HBEs result in high overstrength of such arrangements.

In this study, the overstrength of SPSW due to staggered arrangement is investigated, and an equation to predict this overstrength is proposed. Then, a design procedure for staggered SPSW, by reduction of the design base shear, is suggested. Lastly, 6- and 9-storey conventional and staggered SPSWs are modelled in OPENSEES, [8]. Nonlinear static and dynamic analyses are conducted and the results are presented.

2 Overstrength of Staggered SPSW

According to the current design practice [9], when designing an SPSW, the entire lateral load is assumed to be resisted by the plates only. Then, the boundary elements are designed as per the capacity design approach. While this approach is satisfactory for a conventional SPSW, this results in a considerably high overstrength for a staggered SPSW. The overstrength is primarily due to two reasons: (i) The number of moment resisting beam-to-column joints is twice when compared to conventional SPSW and (ii) as HBEs in such a system have plates connected to

them either at the top or the bottom flange, they must be designed to resist higher forces. This results in further overstrengthening of the system. To address the aforementioned problems, an analytical method is proposed.

The aim of the method is to design a staggered SPSW with static pushover strength similar to a conventional SPSW. It is done by analytically predicting the overstrength due to staggering, based on which the base shear reduction factor is calculated. Finally, the staggered SPSW is designed for a reduced base shear using the conventional method.

The lateral resistance of SPSW is a combination of the lateral strength provided by the plate and the frame, see Fig. 2a. The expected base shear strength of a conventional SPSW, V_{CS} can be expressed as

$$V_{CS} = \beta V_d + V_M \tag{1}$$

where V_d is the design base shear, V_M is the shear resisted by the moment frame action and β is the overstrength factor for the plate strength incorporated during the design procedure. If the thickness of plates is chosen using the equation given in the code [9], β can be expressed as

$$\beta = \frac{0.5}{0.42} \times \frac{R_y}{\phi_p} \tag{2}$$

where R_y is the ratio of the expected yield strength to the nominal yield strength of steel and ϕ_p is the resistance factor used for the design of plates. V_M can be expressed in terms of plastic moment capacities of HBEs at each floor.

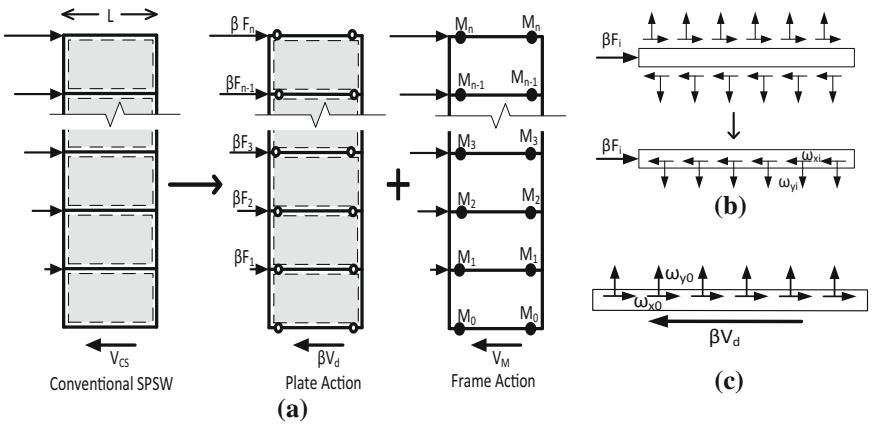

Fig. 2 Conventional SPSW **a** plate and frame action, **b** forces on intermediate HBE, **c** forces on anchor beam

$$V_{\mathrm{M}} = \frac{2\sum_{i=0}^{n} M_i}{\sum_{i=1}^{n} C_{vi} H_i} \tag{3}$$

Using Eqs. (1) and (3),

$$V_{\mathrm{CS}} = \beta V_{\mathrm{d}} + \frac{2\sum_{i=0}^{n} M_i}{\sum_{i=1}^{n} C_{vi} H_i} \tag{4}$$

It is to be noted that the plastic moment at both the ends of any HBE is assumed to be equal. This might not be true in the presence of different axial forces at the two ends, but it is expected to have a minor effect, as far as the objective of the study is concerned. Also, the effect of gravity loads is neglected for the same reason to make the expressions simpler.

Consider an intermediate HBE at any level i, as in Fig. 2b. Tension field is inclined at an angle α to the vertical. Using the equilibrium equation for horizontal and vertical directions, we obtain the following.

$$\beta F_i = w_{xi} L \tag{5}$$

$$w_{xi} = w_{yi} \tan \alpha_i \tag{6}$$

$$w_{yi} = \frac{\beta F_i}{L \tan \alpha_i} \tag{7}$$

w_{xi} and w_{yi} are the net horizontal and vertical uniformly distributed forces applied by both the plates on the HBE at any level i. Equation (8) is then used to calculate the design bending moments for HBEs [10].

$$\varphi_b M_i = \frac{w_{yi} L^2}{4} \tag{8}$$

where φ_b is the resistance factor for HBEs and M_i is the plastic moment capacity of the HBE at ith floor. Putting the value of w_{yi} in Eq. (8) from Eq. (7):

$$M_i = \frac{\beta F_i L}{4\varphi_b \tan \alpha_i} \tag{9}$$

Similarly, the moment capacity of the anchor beam at the floor level can be given by

$$M_0 = \frac{\beta V_{\mathrm{d}} L}{4\varphi_b \tan \alpha_i} \tag{10}$$

Putting the value of M_i and M_0 in Eq. (4) and assuming a constant value of α for all the stories, we obtain

$$V_{CS} = \beta V_d + \frac{2\beta L \sum_{i=0}^{n} F_i + 2\beta V_d L}{4\varphi_b \tan\alpha_i \sum_{i=1}^{n} C_{vi} H_i} \tag{11}$$

using $V_d = \sum_{i=0}^{n} F_i$

$$V_{CS} = \beta V_d \left[1 + \frac{1}{\varphi_b \tan\alpha_i} \times \frac{L}{\sum_{i=1}^{n} C_{vi} H_i}\right] \tag{12}$$

Here, for simplicity, α may be assumed to be 45°. Also, $\sum_{i=1}^{n} C_{vi} H_i$ is replaced by $\sum CH$.

$$V_{CS} = \frac{\beta V_d}{\sum CH}\left[\sum CH + \frac{L}{\varphi_b}\right] \tag{13}$$

In case of staggered SPSW, as shown in Fig. 3, moment capacity of any HBE may be given by

$$M_i = \frac{\beta V_i L}{4\varphi_b \tan\alpha_i} \tag{14}$$

where $V_i = \sum_{i}^{n} F_j$

So the equation for V_{SS} may be expressed as

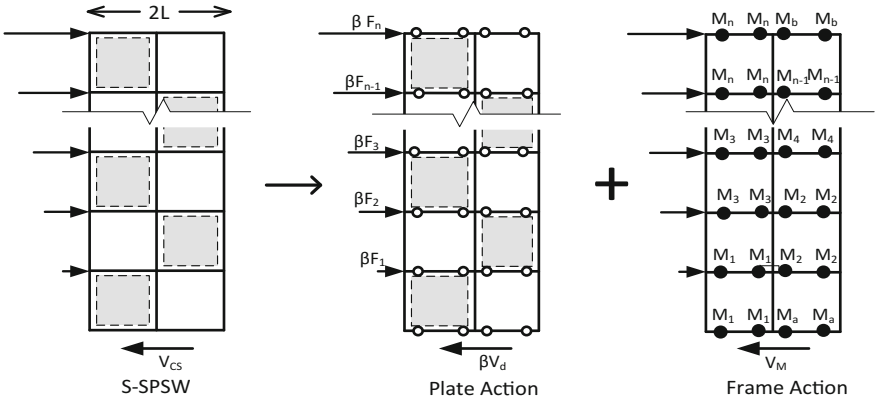

Fig. 3 Plate and frame action of staggered SPSW

$$V_{SS} = \beta V_d + \frac{\beta L \sum V}{\varphi_b \sum CH} + \frac{2(M_a + M_b)}{\sum CH} \tag{15}$$

$$V_{SS} = \frac{\beta V_d}{\sum CH}\left[\sum CH + \frac{L}{\varphi_b} \times \frac{\sum V}{V_d} + \frac{2(M_a + M_b)}{\beta V_d}\right] \tag{16}$$

where $\sum V = \sum_{i}^{n} V_i$

$$\gamma = \frac{V_{CS}}{V_{SS}} \tag{17}$$

$$\gamma = \frac{\sum CH + \frac{L}{\varphi_b}}{\sum CH + \frac{L}{\varphi_b} \times \frac{\sum V}{V_d} + \frac{2(M_a + M_b)}{\beta V_d}} \tag{18}$$

For $M_a = M_1$ and $M_b = M_n$, the equation becomes

$$\gamma = \frac{\sum CH + \frac{L}{\varphi_b}}{\sum CH + \frac{L}{\varphi_b}\left[0.5 + \frac{\sum V}{V_d} + \frac{F_n}{2V_d}\right]} \tag{19}$$

Equation (19) can used to calculate the value of γ.

γ can then be applied to the design base shear for staggered SPSWs to conservatively reduce the overstrength to be similar to that of conventional SPSWs. The adequacy of the proposed approach is validated in Sect. 4.

3 Design and Modelling

To study the static and dynamic behaviour of staggered SPSW and to validate the proposed design approach for staggered SPSW, eight specimens were designed and modelled in OPENSEES. Details of these specimens are given in Table 1. Plan of the buildings is same for all the specimen and is shown in Fig. 4a. The dead and live loads are taken to be same as the 9-storey state-of-the-art building [11]. Height of all the stories is taken as 3.96 m. The seismic parameters are same as considered in [12]. The staggered specimen is designed by applying a factor γ to the design base shear of their conventional counterpart. The values of γ obtained for the four staggered specimen, calculated using Eq. (19), are given in Table 1.

Nonlinear strip models are developed in OPENSEES using centre line approach. Offsets are taken to account for the rigid panel effect at beam–column joints. HBEs and VBEs are modelled using force based beam–column element with fibre section

Table 1 Specimen details

Model name	SPSW type	No. of stories	Aspect ratio	No. in each direction	γ
6M	Conv[a]	6	1.15	4	–
9N	Conv[a]	9	0.77	8	–
9M	Conv[a]	9	1.15	6	–
9W	Conv[a]	9	1.54	4	–
6M-S	Stag[b]	6	1.15	4	0.52
9N-S	Stag[b]	9	0.77	8	0.58
9M-S	Stag[b]	9	1.15	6	0.50
9W-S	Stag[b]	9	1.54	4	0.44

[a]Conventional SPSW
[b]Staggered SPSW

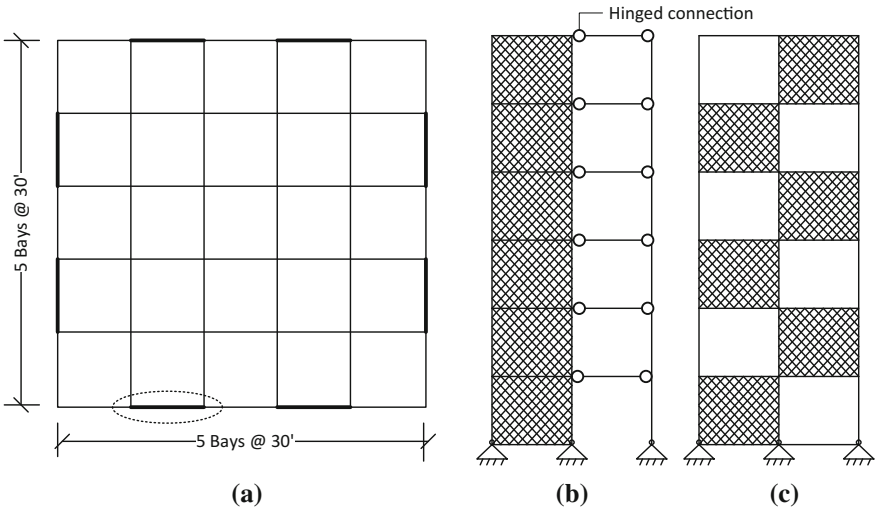

Fig. 4 **a** Plan of 6- and 9-storey specimen; strip model representation of **b** 6M **c** 6M-S

to account for P–M interaction. The fibers are assigned Steel02 material of OPENSEES library module. Diagonal strips are modelled as tension only truss members using hysteretic material. Gravity columns are modelled to account for the P-Delta effect of the gravity loads. Figure 4b shows the strip model for 6M and 6M-S.

In order to validate the analytical models, a four-storey SPSW test specimen [13] is modelled to compare its hysteretic response with the test results. The load–displacement curve obtained from the experiment and the analysis is compared in Fig. 5.

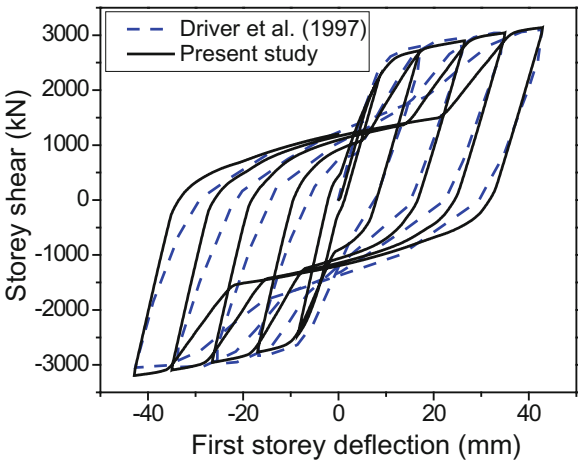

Fig. 5 Validation of the modelling technique

4 Analysis and Results

Static pushover analysis is performed to investigate the overstrength obtained for the conventional and staggered specimen, when designed by the proposed methodology. Figure 6a shows the pushover behaviour of specimen in terms of base shear, normalized by the design base shear, versus roof drift. It is evident from the figure that the overstrength of staggered SPSWs is conservatively reduced to match those of the conventional SPSWs.

Further, dynamic analysis using 20 DBE level ground motions is done for each specimen. For all the considered models, plastic hinge formations were restricted to the HBE end only. Staggered systems show excellent reduction in the inter-storey drift for 9-storey specimen. Drift distribution is also improved. For 6-storey specimen, the improvement was marginal. Figure 6b shows the median inter-storey drift ratio (MISDR) for the specimen. 9W outperformed 9N and 9M with a maximum MISDR of 1.62%. Maximum MISDR among all the staggered specimen was 1.32 for 9N-S. The reduction of drift from 6M to 6M-S was only observed in the top storey. From these results, it can be inferred that staggering of plates is ineffective in reducing the drifts in low-rise buildings, whereas it is very effective for medium-rise buildings. The study will be extended to high-rise buildings in future to investigate its effectiveness for the same.

Unlike conventional SPSW, staggered SPSW requires three supports instead of two. This might result in increased cost of foundation. But Fig. 6c shows that the maximum vertical reaction (normalized by design base shear) on the supports is highly reduced in the case of staggered specimen. Also, the reaction in the middle support is very less. This reduces the overall design force on the foundation and thus becomes more economical.

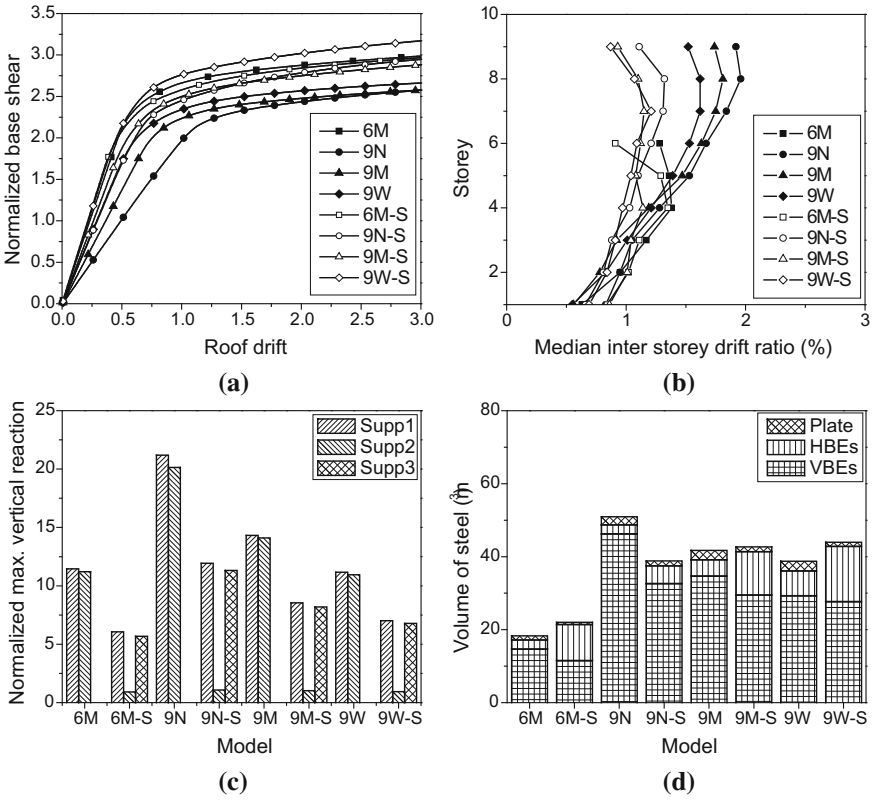

Fig. 6 **a** Normalized base shear versus roof drift, **b** median inter-storey drift, **c** normalized maximum vertical support reactions, **d** volume of steel

Volume of steel used for each configuration is compared in Fig. 6d. It should be noted that beams and columns in the gravity frame have not been included. It can be observed that staggering reduces the tonnage by about 25% in case of 9N to 9N-S. Steel tonnage tends to decrease with increase in aspect ratio of the plate for conventional SPSWs, whereas it increases in case of staggered SPSWs. 9M and 9M-S use approximately the same amount of steel, whereas, in case of wide SPSWs, 9W-S uses slightly more steel than 9W. Staggering of SPSW results in increase in the weight of HBEs but decrease in the weight of VBEs and plates. Heavier beams may result in strong beam weak column, so it is important to check against the same. For the models in the study, no correction was required as the check for weak beam strong column was satisfied for all.

5 Conclusion

The current study investigates the behaviour of a staggered arrangement of plates in a steel plate shear wall. Following conclusions can be drawn from the study.

- Staggered steel plate shear walls demand heavier horizontal boundary elements and more beam–column rigid connections than conventional SPSWs. This results in considerable increase in the overstrength of the system. An equation is proposed to estimate this overstrength due to staggering. It is proposed, for design of staggered SPSW, to reduce the design base shear by a factor γ, which can be calculated using the proposed equation. Staggered SPSWs conservatively perform similarly to their conventional counterparts.
- When subjected to DBE level ground motions, reduction in inter-storey drift and a better drift distribution is observed in staggered SPSWs for 9-storey SPSWs. The improvement is not equally remarkable in 6-storey SPSW.
- Support reactions are reduced to about half on staggering of the plates. This reduces the design force on the foundation and thus can reduce the cost incurred in the substructure.
- When the proposed design procedure is used for design of staggered SPSW, with respect to conventional SPSWs, steel tonnage is reduced for narrow medium-rise buildings. When compared to their conventional counterpart, weight of plates and columns is reduced, whereas weight of beams is increased.

References

1. Vian, D., & Bruneau, M. (2005). *Steel plate shear walls for seismic design and retrofit of building structures*. Buffalo, New York: Multidisciplinary Center for Earthquake Engineering Research.
2. Berman, J. W., Celik, O. C., & Bruneau, M. (2005). Comparing hysteretic behavior of light-gauge steel plate shear walls and braced frames. *Engineering Structures, 27*(3), 475–485.
3. Qu, B., & Bruneau, M. (2011). Plastic moment of intermediate horizontal boundary elements of steel plate shear walls. *Engineering Journal, 48*(1), 49–64.
4. Sahoo, D. R., Sidhu, B. S., & Kumar, A. (2015). Behavior of unstiffened steel plate shear wall with simple beam-to-column connections and flexible boundary elements. *International Journal of Steel Structures, 15*(1), 75–87.
5. Wang, M., Shi, Y., Xu, J., Yang, W., & Li, Y. (2015). Experimental and numerical study of unstiffened steel plate shear wall structures. *Journal of Constructional Steel Research, 112*(1), 373–386.
6. Sabelli, R., & Bruneau, M. (2006). *AISC design guide 20 : Steel plate shear walls*.
7. Hitaka, T., & Matsui, C. (2003). Experimental study on steel shear wall with slits. *Journal of Structural Engineering, 129*(5), 586–595.
8. Mazzoni, S., McKenna, F., Scott, M. H., & Fenves, G. L. (2006). *Open system for earthquake engineering simulation user command-language manual—Version 1.7.3*. Berkeley, CA: Pacific Earthquake Engineering Research Center.

9. AISC (American Institute of Steel Construction). *Seismic provisions for structural steel buildings*. Chicago: ANSI/AISC 341-10.
10. Qu, B., & Bruneau, M. (2010). Capacity design of intermediate horizontal boundary elements of steel plate shear walls. *Journal of Structural Engineering, 136*(6), 665–675.
11. Gupta, A., Krawinkler, H. (1999). *Seismic demands for performance evaluation of steel moment resisting frame structures*. John A. Blume Earthquake Engineering Center, Stanford University.
12. Berman, J. W. (2011). Seismic behavior of code designed steel plate shear walls. *Engineering Structures, 33*(1), 230–244.
13. Driver, R. G., Kulak, G. L., Kennedy, D. J. L., & Elwi, A. E. (1998). Cyclic test of four-story steel plate shear wall. *Journal of Structural Engineering, 124*(2), 112–120.

Identification of Semi-rigid Joints in Steel Frame Structures Using Vibration-Based Technique

Joy Pal and Sauvik Banerjee

Abstract The connections are the critical locations where damage commonly occurs. However, very limited vibration-based studies using the artificial neural network (ANN) are found to identify the damaged connections. Again, the ANN-based technique requires retraining of network for little variation in geometry of the structure. Moreover, those studies were limited to damage at the beam end connection. In this present study, health monitoring of steel plane frame structures having semi-rigid connections either at the beam side or at the column side using a limited number of sensors is addressed. With that purpose, a single-storey and a two-storey frame are considered. The frames are modeled using plane frame elements, in which two rotational springs are placed at the ends to affect the stiffness of the rotational springs only. The frames are excited using an impact at the right top corner, and strain time responses are collected from the connections only. The strain data are then transformed into frequency spectra. Using the frequency spectra, an objective function is developed and minimized using particle swarm optimization (PSO) to get the updated fixity factors for all the springs. In order to get more accurate values of fixity factors of the two-storey frame, it is divided into sub-structures, and it is found that the technique estimates fixity factors with an acceptable error.

Keywords Planar frame structure · Semi-rigid joint · Rotational spring
Particle swarm optimization · Substructure

S. Banerjee (✉)
Department of Civil Engineering, Indian Institute of Technology Bombay,
Mumbai 400076, India
e-mail: sauvik@civil.iitb.ac.in

J. Pal
Department of Civil Engineering, Bennett University, Tech Zone II,
Greater Noida 201310, UP, India
e-mail: j.palcob@gmail.com

A. Rama Mohan Rao and K. Ramanjaneyulu (eds.), *Recent Advances in Structural Engineering, Volume 1*, Lecture Notes in Civil Engineering 11,
https://doi.org/10.1007/978-981-13-0362-3_29

1 Introduction

Vibration-based structural health monitoring is a popular approach among the scientists and researchers due to its simplicity. Changes in mass or stiffness alter modal properties, which contain localize effect of damage. A vast amount of literature is reviewed by Fan and Qiao in Ref. [1] on various types of structures like a beam, plate, frame, etc. In these types of structures, the damage is simulated by reducing the elemental properties, added mass, and saw-cut damage. Surprisingly, very limited studies are found on joint damage identification. Loosening of bolts, defects in welding, and environmental variability are the reasons for damage at joints.

Due to joint damage, fixity level reduces which makes it semi-rigid. The elemental stiffness matrices for semi-rigid boundary conditions are developed in Ref. [2]. The study has been found on semi-rigid joint identification using the ANN-based approach in Ref. [3]. However, ANN is not a generalized technique; it requires a large amount of input–output data for training the network. Moreover, small variations in the model require retraining the network. Again, both the beam- and column-side damages were represented using a spring at beam end. Therefore, an effective theoretical model is required to represent both the beam- and column-side damages.

Since last 10 years, finite element model updating technique has received considerable attention among researchers. In this technique, a numerical model is developed as a reference structure, and updated to detect the damage-sensitive parameters. The updating operation is carried out using different optimization techniques like Nelder–Mead algorithm, GA, etc. in Refs. [4–6].

Newly developed optimization techniques, such as particle swarm optimization (PSO) proposed by Kennedy and Eberhart in Ref. [7], require lesser numbers of iterations than conventional optimization techniques, which ultimately reduces the computational costs. Moreover, it provides more accurate results than the above-mentioned algorithms. PSO was applied to complex engineering field due to its convergence speed and simplicity in Refs. [8, 9].

In the present study, an effective theoretical model is considered to represent both the beam- and column-side damages. In order to overcome the limitations of ANN-based techniques, PSO-based finite element model updating technique is utilized to identify joint damage.

2 Numerical Modeling

In order to identify the location and severity of a semi-rigid joint, a single- and a two-storey plane frame as shown in Fig. 1 are considered. The value of fixity factors of the rotational springs in the reference state of the structure is considered as 0.891 in Ref. [10]. The frame is modeled using beam–column elements.

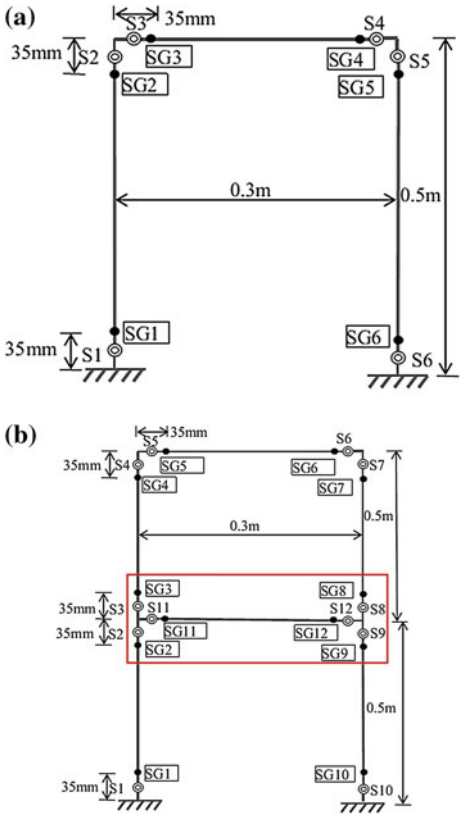

Fig. 1 Location of springs and data acquisition points of **a** a single-storey frame, **b** a two-storey frame structure

The displacement-based structural analysis assumes fixed–fixed boundary condition for stiffness and mass matrices derivation. Therefore, to introduce the effect of semi-rigidity, a rotational spring is considered at each end of an element. The elemental matrices are then derived for this type of element following the below-mentioned procedure.

2.1 Formulation of Elemental Matrices

In order to simulate the loosening of joints, the elemental matrices are formulated based on semi-rigid boundary conditions (BC). The deflected shape of an element is shown in Fig. 2. The element consists of two springs at the ends to introduce the semi-rigidity of the joints. The degrees of freedom at each node of the element are translations along x- and y-axis and rotation about the z-axis. A relative rotation will take place in the inner and the outer sides of the spring. In inner side, the rotations

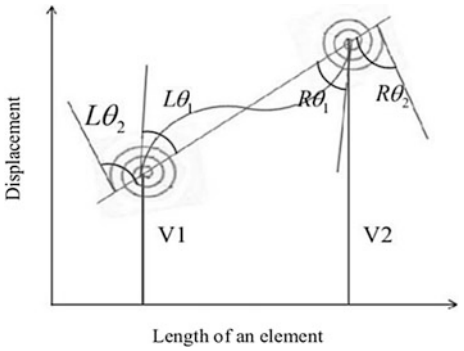

Fig. 2 Displacement profile over an element

are $L\theta_1$ and $R\theta_1$ and in outer side, these are $L\theta_2$ and $R\theta_2$, respectively. According to Monforton and Wu in Ref. [11]

$$\frac{RM}{Rr_c} = R\theta_2 - R\theta_1 \text{ and } \frac{LM}{Lr_c} = L\theta_2 - L\theta_1 \tag{1}$$

In the above equation, LM, RM, Lr_c, and Rr_c are the applied moment and rotational spring constants at left and right sides of the element, respectively. The displacement over an element is calculated by the following expression as given in Ref. [2]:

$$\begin{aligned} y = & \begin{bmatrix} P_1^2 P_2 L & P_1 P_2^2 L \end{bmatrix} \\ & \left(- \begin{bmatrix} \frac{4EI}{L} + Lr_c & \frac{2EI}{L} \\ \frac{2EI}{L} & \frac{4EI}{L} + Rr_c \end{bmatrix}^{-1} \right. \\ & \left. \begin{bmatrix} -Lr_c & 0 \\ 0 & -Rr_c \end{bmatrix} \begin{bmatrix} \frac{1}{L} & 1 & -\frac{1}{L} & 0 \\ \frac{1}{L} & 0 & -\frac{1}{L} & 1 \end{bmatrix} \begin{Bmatrix} V_1 \\ \theta_1 \\ V_2 \\ \theta_2 \end{Bmatrix} \right) \\ & + V_1 P_1 + V_2 P_2 \end{aligned} \tag{2}$$

The elemental stiffness and mass matrices are formulated considering the flexible boundary conditions in Ref. [2].

$$[k] = \int_0^L EI[N''(x)]^{\mathrm{T}}[N''(x)]\mathrm{d}x \tag{3}$$

$$[m] = \int_0^L \bar{m}[N(x)]^{\mathrm{T}}[N(x)]\mathrm{d}x \tag{4}$$

Once the elemental stiffness and mass matrices are formulated, the health monitoring of the frames is carried out using finite element model updating technique based on particle swarm optimization.

2.2 Model Updating Using Particle Swarm Optimization

In model updating, developments of an objective function and parameter selection are the two most important tasks. The function is required to be selected in such a way that it is sufficiently sensitive to the updating parameter. The requirement of a large amount of damage for the prominent identification of damage location indicates insensitivity of mode shape to the damage. Moreover, a large number of data point are required. Therefore, in the present study, a limited number of data point are used to identify the damage location and severity. For that purpose, data are collected only from the nearest nodes of the joints. Using those data, objective function is developed. The procedure of developing the objective function is given below.

2.2.1 Objective Function and Parameter Selection

In the present study, frequency shape correlation and frequency amplitude spectra are considered for the development of objective function. Shape correlation is defined as follows.

The numerical model is excited by an impulse at the top right corner. The forced vibration equation of the system can be written as

$$[M]\{\ddot{x}(t)\} + [C]\{\dot{x}(t)\} + [K]\{x(t)\} = \{f(t)\} \tag{5}$$

In the above equation, $[M]$, $[C]$, $[K]$, $\{f(t)\}$, and $\{x(t)\}$ represent the mass matrix, damping matrix, stiffness matrix, the force vector, and the displacement vector, respectively. Overdot indicates derivative of the displacement component with respect to time.

The displacement responses at *SG1* to *SG6* (for single-storey frame) and *SG1* to *SG12* (for two-storey frame) as shown in Fig. 2 are evaluated using numerical integration scheme *Newmark-Beta* in Ref. [12]. The displacement time histories are converted to strain time histories using strain–displacement relationship.

$$\varepsilon_n(t) = z x_n''(t) \tag{6}$$

where z is the distance of extreme fiber of a section from the neutral axis and double dash over x represents the curvature at that section. n stands for the numerical model.

$$\varepsilon_n(\omega) = \frac{1}{2\pi} \int_{-\infty}^{\infty} \varepsilon_n(t) \mathrm{e}^{-i\omega t} \mathrm{d}t \tag{7}$$

where ω represents frequency and $\varepsilon_n(\omega)$ represents corresponding amplitude. In the case of an experiment, the strain data are directly collected and converted into the frequency domain using Fourier transform as shown below.

$$\varepsilon_{\mathrm{exp}}(\omega) = \frac{1}{2\pi} \int_{-\infty}^{\infty} \varepsilon_{\mathrm{exp}}(t) \mathrm{e}^{-i\omega t} \mathrm{d}t \tag{8}$$

In the above expression, exp indicates experimental model. The frequency shape correlation for *i*th sensor using numerical and experimental data is defined as follows:

$$\psi_i = \frac{\sum \varepsilon_{n,i}(\omega) \varepsilon_{\mathrm{exp},i}(\omega)}{\left[\varepsilon_{n,i}^2(\omega)\right]^{1/2} \left[\varepsilon_{\mathrm{exp},i}^2(\omega)\right]^{1/2}} \tag{9}$$

where n and exp represent the undamaged and damaged structures, respectively. It is clear that if both the structures are in the same state, then the correlation value is nearer to 1 and if not then the value is away from 1. The objective function is defined as follows:

$$\begin{aligned} \mathrm{OF}\left(\gamma_{Lr_c}, \gamma_{Rr_c}\right) = \sum_{i=1}^{NS} W_i \Big[\varepsilon(\omega)_{\mathrm{ud},i} - \varepsilon(\omega)_{\mathrm{d},i}\Big]^2 \\ \Big[\omega(\mathrm{AMP}_{\max})_{\mathrm{ud},i} - \omega(\mathrm{AMP}_{\max})_{\mathrm{d},i}\Big]^2 \end{aligned} \tag{10}$$

In the above expression, γ_{Lr_c} and γ_{Rr_c} are left and right fixity factors of each member. NS indicates the number of sensors used to collect data. $\omega(\mathrm{AMP}_{\max})$ represents frequency corresponding to the maximum amplitude, and subscripts ud and d stand for undamaged and damaged data, respectively. The relationship between natural frequency and fixity factor is shown in Fig. 3a. It is found that fixity factor is having sufficient sensitivity to the natural frequency. Therefore, frequencies are utilized to form the objective function. W_i, the weight factor for each sensor, is defined as follows:

$$W_i = \frac{\psi_i^2}{\sum \psi_i^2} \tag{11}$$

Weighted sum method is used to formulate the objected function. It is presumed that the sensors near to the loosely bolted connection are affected more than the

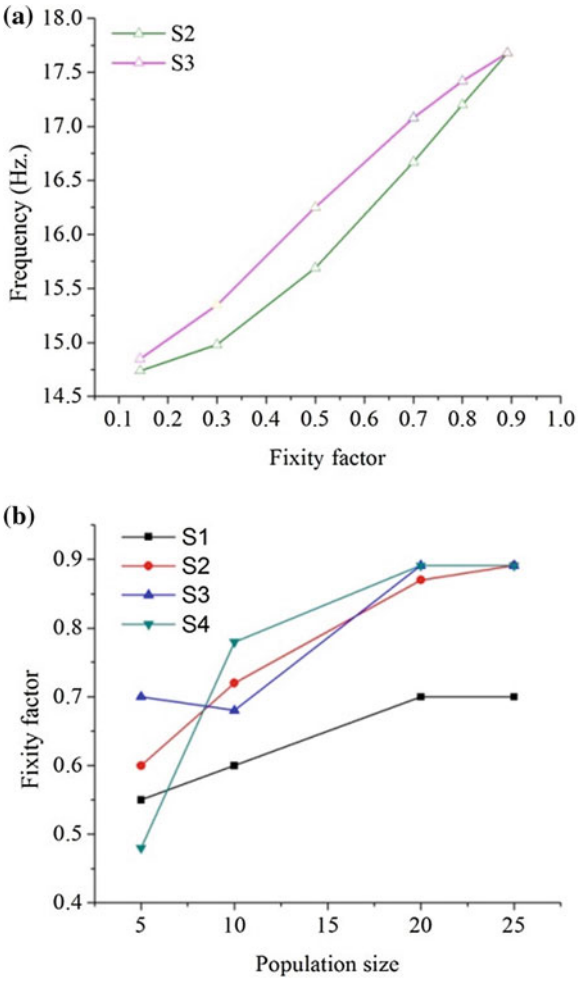

Fig. 3 **a** Fixity factor at different springs versus frequency and **b** population versus fixity factor for SD1

other sensors. Therefore, higher weight is provided to those sensors to achieve more reliable results. This will also ensure that no other set of γ_{Lr_c} and γ_{Rr_c} can give a better estimate.

Selection of parameters as an updating variable is a significant measure of optimization. The parameters, which are sensitive to the objective function, are needed to be considered as updating parameters. The relationship between fixity factor and frequency, shown in Fig. 3, indicates that with the change of fixity factor, modal frequency changes. Therefore, fixity factor can be considered as the updating variable where the objective function is needed to be developed using frequency and frequency amplitudes of the strain data. The strain responses are utilized to captures more local features of the structures.

2.2.2 Particle Swarm Optimization

Particle swarm optimization (PSO) proposed by Kennedy and Eberhart in Ref. [7] is a stochastic evolutionary computation technique, grounded on the motion and intelligence of swarms. The detail of the particle swarm optimization technique is given in Pal and Banerjee in Ref. [13]; therefore, it is not presented here for brevity. Figure 3b shows the population size versus fixity factor relationship. It is found that 20–25 population size is sufficient for the convergence of the function.

3 Numerical Results and Discussions

Various damage cases are studied in order to validate the health monitoring technique. Tables 1 and 2 listed the fixity levels at different springs in different cases of damages for single- and two-storey frame structures. The undamaged strain response and its frequency spectra are shown in Fig. 4. Using the strain frequency spectra from all the sensors, objective function is developed as mentioned earlier.

Average of 10 run results is considered as the estimated fixity factor in Ref. [13]. Table 3 depicts the estimated results for different damage cases for single-storey structure. The mean values of fixity factors at different locations are plotted and found that the technique successfully identified the damaged locations and fixity factors. The study is carried out for 80 and 70 dB levels of noise, and the efficacy of the technique by estimating the fixity factors is determined. Different types of damage cases, which include single and multiple locations, along with different levels of fixity factor at the same location are studied and in each case, the technique perfectly estimates the fixity factors.

With the increase in number of storeys, the number of variables increases thereby increasing the problem complexity. This complexity reduces the accuracy of the results. In some literature in Ref. [5], the sub-structuring method is followed by dividing the frame into some small parts and carrying out the model updating considering that part only.

In order to do so, the two-storey frame is divided into two parts, and the part inside the red box is considered. In this context, the data are collected only from that region only. The robustness of the technique is again observed in the estimation of

Table 1 Damage cases of the single-storey plane frame structure having semi-rigid connections

Structure	Spring number	Fixity level at different springs				
		SD1	SD2	SD3	SD4	SD5
Single storied	S2	0.700	0.600	0.600	0.500	0.400
	S3	0.891	0.891	0.600	0.500	0.500
	S4	0.891	0.600	0.700	0.600	0.600
	S5	0.891	0.891	0.891	0.600	0.700

Table 2 Damage cases of the single-storey plane frame structure having semi-rigid connections

Structure	Spring number	Fixity level at different springs				
		TD1	TD2	TD3	TD4	TD5
Two storied	S2	0.600	0.650	0.891	0.450	0.450
	S3	0.600	0.500	0.891	0.891	0.450
	S8	0.891	0.891	0.500	0.550	0.650
	S9	0.891	0.891	0.400	0.450	0.550
	S11	0.891	0.600	0.600	0.550	0.650
	S12	0.600	0.500	0.550	0.450	0.550

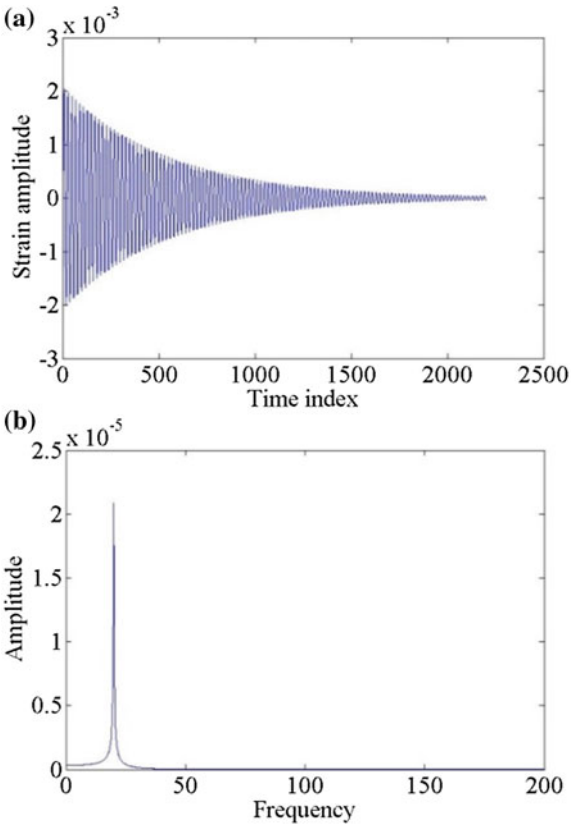

Fig. 4 **a** Strain response and **b** frequency spectra of the response obtained at node 26 of the single-storey frame

fixity levels at different springs. All the damage cases tabulated in Table 2 are studied, and the results are shown in Table 4. It is found that the sub-structuring and a limited number of data points do not affect the accuracy of results. Even the noise-based studies show perfection in estimating the fixity factors. Observing all

Table 3 Estimated fixity factor at different springs for the single-storey numerical model

Damage case	Noise	Spring			
		S2	S3	S4	S5
SD1	WN	0.7	0.891	0.891	0.891
	80 db	0.7	0.891	0.891	0.891
	70 db	0.719	0.87	0.845	0.874
SD2	WN	0.61	0.889	0.597	0.891
	80 db	0.6	0.891	0.6	0.891
	70 db	0.6	0.891	0.6	0.891
SD3	WN	0.592	0.591	0.695	0.884
	80 db	0.592	0.577	0.693	0.881
	70 db	0.598	0.596	0.694	0.884
SD4	WN	0.56	0.509	0.604	0.605
	80 db	0.511	0.538	0.605	0.607
	70 db	0.499	0.502	0.597	0.598
SD5	WN	0.398	0.496	0.596	0.696
	80 db	0.398	0.493	0.597	0.698
	70 db	0.392	0.457	0.607	0.704

Table 4 Estimated fixity factor at different springs for the two-storey numerical model

Damage case	Noise	Spring					
		S2	S3	S8	S9	S11	S12
TD1	WN	0.593	0.590	0.864	0.888	0.844	0.594
	80 db	0.600	0.600	0.891	0.891	0.891	0.600
	70 db	0.592	0.592	0.864	0.872	0.852	0.591
TD2	WN	0.633	0.487	0.855	0.846	0.560	0.485
	80 db	0.640	0.495	0.826	0.889	0.582	0.491
	70 db	0.639	0.497	0.823	0.841	0.593	0.482
TD3	WN	0.891	0.891	0.499	0.399	0.596	0.550
	80 db	0.891	0.891	0.509	0.418	0.634	0.560
	70 db	0.891	0.891	0.500	0.400	0.600	0.550
TD4	WN	0.449	0.890	0.565	0.448	0.551	0.450
	80 db	0.442	0.873	0.534	0.439	0.517	0.441
	70 db	0.451	0.888	0.556	0.451	0.554	0.450
TD5	WN	0.432	0.428	0.668	0.525	0.500	0.545
	80 db	0.466	0.470	0.685	0.566	0.522	0.559
	70 db	0.457	0.456	0.663	0.556	0.532	0.553

the results, it can be said that the technique is able to find out the fixity levels at different joints. It also indicates the effectiveness of the objective function for the estimation of fixity levels. Moreover, the technique has the capability to carry out the identification with a limited number of sensors.

4 Conclusions

In the present study, an effective theoretical model is considered to estimate joint damage either at the beam side or at the column side. In order to overcome the shortcomings of ANN-based technique, PSO-based finite element model updating technique using a limited number of data is applied. First, the effectiveness of the theoretical model is observed in the identification of joint damage either at the beam side or at the column side. Second, the ability to detect 15% change in fixity level with and without the presence of noise proves the robustness of the technique. Third, a limited number of sensors used for analysis represent its efficacy to apply in large and real-life structures. After the successful identification of semi-rigid connections, an experimental validation is needed to examine the effectiveness of the theoretical model and the health monitoring technique on a full-scale model. However, in the absence of a baseline structure, numerical model updating technique can be applied if knowledge of structural topology and some basic id are available.

Acknowledgements Authors are thankful to the MHRD for providing the scholarship to carry out the research work.

References

1. Fan, W., & Qiao, P. (2011). Vibration-based damage identification methods: A review and comparative study. *Structural Health Monitoring, 10*(1), 83–111.
2. Chan, S. L., & Goman, H. M. W. (1994). Nonlinear vibration analysis of steel frames with semi rigid connections. *ASCE Journal of structural Engineering, 120*(4), 1075–1087.
3. Yun, C. B., Yi, J. H., & Bahng, E. Y. (2001). Joint damage assessment of framed structures using a neural networks technique. *Engineering Structures, 23*(5), 425–435.
4. Zapico, L. J., Gonzalez, M. P., Friswell, M. I., Taylor, C. A., & Crewe, A. J. (2003). Finite element model updating of a small scale bridge. *Journal of Sound and Vibration, 268*(5), 993–1012.
5. Perry, M. J., Koh, C. G., & Choo, Y. S. (2006). Modified genetic algorithm strategy for structural identification. *Computers & Structures, 84*(8), 529–540.
6. Perera, R., EnFang, S., & Huerta, C. (2009). Structural crack detection without updated base line model by single and multi-objective optimization. *Mechanical Systems and Signal Processing, 23*(3), 752–768.
7. Kennedy, J., & Eberhart, R. (1995). Particle swarm optimization. In *Proceedings of IEEE International Conference*, Perth.
8. Perez, R. E. I., & Behdinan, K. (2007). Particle swarm approach for structural design optimization. *Computers & Structures, 85*(19), 1579–1588.
9. Begambre, O., & Laier, J. E. (2009). A hybrid particle swarm optimization-simplex algorithm (PSOS) for structural damage identification. *Advances in Engineering Software, 40* (9), 883–891.
10. Eurocode 3. (2003). *Design of steel structures, part 18: Design of joints*, BS EN 1993-I-8.
11. Monforton, G. R., & Wu, T. S. (1963). Matrix analysis of semi-rigidly connected frames. In *Proceedings of the American Society of Civil Engineers* (Vol. 89 (STC 6), pp. 13–42).

12. Choapra, A. K. (2009). *Dynamics of structures: Theory and applications to earthquake engineering*. New Delhi: Pearson.
13. Pal, J., & Banerjee, S. (2015). A combined modal strain energy and particle swarm optimization for health monitoring of structures. *Journal of Civil Structural Health Monitoring, 5*(4), 353–363.

Identification of Parameter of Truss Structure by Limited Static Strain Measurement

Debasish Bandyopadhyay, Sumit Saha and Tanvir Sohail

Abstract Structural health monitoring has become significantly important in recent times. Dynamic inverse technique is widely accepted but seems to be complex in case of real-life application. Whereas, the static approach is simple in nature. The proposed paper discusses parameter identification of truss structure adopting static inverse technique in a finite element framework using limited strain measurement. In addition, noise in the measured data, which is quite inevitable in real situations, is also considered to validate its applicability of the proposed model in practical situation. This study further extends in identifying the exact location of the damage in the damaged truss element. The predicated parameters seem to be accurate for various combinations of damage even with noise consideration. The exact damage location in the damaged element is also able to be identified by the proposed method.

Keywords Structural health monitoring · Strain · Parameter estimation

1 Introduction

The need of health monitoring of structures has increased manifold in recent years due to the defects occurring in the structural members. These defects can be due to various reasons, such as corrosive environment, aging, fatigue, or result of collision with foreign particles. Structural health monitoring of these structures can be performed by parameter estimation, which is a mathematical approach using the major differences between the estimated and the experimental values termed as errors.

D. Bandyopadhyay (✉) · S. Saha · T. Sohail
Department of Construction Engineering, Jadavpur University, Kolkata 700098, India
e-mail: dban65@yahoo.com

S. Saha
e-mail: sumitsaha263@gmail.com

T. Sohail
e-mail: tanvirsohail20@gmail.com

A. Rama Mohan Rao and K. Ramanjaneyulu (eds.), *Recent Advances in Structural Engineering, Volume 1*, Lecture Notes in Civil Engineering 11,
https://doi.org/10.1007/978-981-13-0362-3_30

Parameter estimation attempts to correlate changes in test data to the changes in structural elemental properties. Damages to sensitive objects like aircraft, oilrigs can be successfully identified through this technique.

Parameter estimation utilizes an art of reconciling on prior finite element model (FEM) of the structure with the nondestructive (NDT) test data. This technique updates the parameters of an analytical model of a structure such as FEM to match its response with the NDT data obtained from experiment. The estimated parameters represent the current condition of the structure. These parameters are usually stiffness, mass, and damping properties of the structural elements. Parameter estimation can be done using both static and dynamic methods. The static method is cost-effective and less complicated than the dynamic method.

In this paper, static method is utilized to detect damage of the members of truss bridges. The first truss has 21 members. The other truss has 65 members. At first, the sensitive nodes of the structure are identified using forward approach. After successfully identifying the sensitive nodes in the structure, the loads are applied at one set of DOFs and strains are measured at another subset of DOFs, which may or may not overlap. The error between the analytical values and experimental values are calculated. By minimizing square of error equation the damage parameters are identified using inverse technique. Thereafter, the model parameters are updated after each iteration. After successfully detecting the damaged member, the member is further discretized and parameter estimation is performed on the damaged member. Isoparametric element is assumed to get the exact location of the damage in the damaged element of the truss. This is performed in the same manner as for the whole trusses as proposed by Sanayei and Saletnik [1]. However, they detected the damaged element only. This method provides a good tool for damage detection for the linear truss structure. The results obtained are quite accurate. Further, the use of noise or random data enhances the accuracy of the result obtained. The result is able to pinpoint the exact location of the damages in the truss as precise as the discretization of the member.

1.1 Theoretical Formulation

The static equation of truss structure is

$$[\mathbf{F}] = [\mathbf{k}]\,[\mathbf{U}] \tag{1.1}$$

where [**F**] is the force matrix containing different set of forces, and [**U**] is the displacement matrix containing different set of displacements for each set of force. Hence,

$$[\mathbf{U}] = [\mathbf{k}]^{-1}[\mathbf{F}] \tag{1.2}$$

Displacement of each degree of freedom (DDOF) is measured for each set of force for incremental damage of each parameter. Now, this DDOF is classified on the basis of sensitivity. Then, the set of DDOF which is sensitive for all parameters of the structural model is selected as a set of MDOF.

1.1.1 Strain–Displacement Relationship

We know through the stiffness method that force is related to displacement. Therefore, we have to drive a mapping between strain and displacement, to use the measured strain data.

$$\{\boldsymbol{\epsilon}\} = [\mathbf{B}]\{\mathbf{U}\} \tag{1.3}$$

where $\{\epsilon\}$ is the elemental strain vector of the order of NEL $\times$ 1 and $\{\mathbf{U}\}$ global displacement vector, multiplication results in $\{\mathbf{B}\}$ is the elemental mapping vector of the order of NEL $\times$ NDOF.

By substituting (1.3) in (1.2), we get the strain equation

$$[\boldsymbol{\epsilon}] = [\mathbf{B}][K(p)]^{-1}[\mathbf{F}] \tag{1.4}$$

Now, the [**B**] matrix is portioned based on measured strain **a** and unmeasured strain **b**

$$\begin{bmatrix} \boldsymbol{\epsilon}_\mathbf{a} \\ \boldsymbol{\epsilon}_\mathbf{b} \end{bmatrix} = \begin{bmatrix} \mathbf{B}_\mathbf{a} \\ \mathbf{B}_\mathbf{b} \end{bmatrix} [\boldsymbol{K}(\boldsymbol{p})]^{-1} [\mathbf{F}] \tag{1.5}$$

The unmeasured strain is eliminated and we work with only the measured strain

$$[\boldsymbol{\epsilon}_\mathbf{a}] = [\mathbf{B}_\mathbf{a}][\mathbf{F}] \tag{1.6}$$

$[\epsilon_\mathbf{a}] =$ NMS $\times$ NSF, $[\mathbf{B}_\mathbf{a}] =$ NMS $\times$ NDOF, where NMS = number of measured strains. Equation (1.6) gives the relationship between force strain and parameters. It is hereby solved for the parameters $\{\mathbf{p}\}$ of size NUP $\times$ 1.

1.1.2 Output Strain Error

$$[\mathbf{E}(\mathbf{p})] = [\epsilon_\mathbf{a}(\mathbf{p})]^\mathbf{a} - [\epsilon_\mathbf{a}]^\mathbf{m} \tag{1.7}$$

The superscript refers to analytical values, and m superscript refers to measured values.

On substituting (1.6) and (1.7), we get

$$[\mathbf{E}(\mathbf{p})] = [\mathbf{B_a}][\boldsymbol{K}(\boldsymbol{p})]^{-1}[\mathbf{F}] - [\epsilon_{\mathbf{a}}]^{\mathbf{m}} \tag{1.8}$$

1.1.3 Evaluation of Parameter Vector

Now, the size of the error matrix [**E**(**p**)] is no. of measured degrees of freedom (NMD) by no of set of force (NSF). Now, the error matrix is transformed into an error vector of size NM (NMD × NSF) by 1. {**p**} is the vector containing unknown parameter. So size of {**p**} is NUP by 1. Now, the error vector is liberalized by first-order Taylor series as shown below.

$$\{E(p+\Delta p)\} = \{E(p)\} + \frac{\delta\{E(p)\}}{\delta p}\{\Delta p\} \tag{1.9}$$

where $[\mathbf{S}(\mathbf{p})] = \frac{\delta\{E(p)\}}{\delta p}\{\Delta p\}$

Now, the sensitivity matrix [**S**(**p**)] is formed by differentiating [**E**(**p**)] with respect to p_j to form $[\bar{\mathbf{S}}(\mathbf{p})]$ of the size NM × NUP.

$$[\bar{\boldsymbol{S}}(\mathbf{p})] = -[\mathbf{B_a}]\,[\boldsymbol{K}(\boldsymbol{p})]^{-\mathbf{1}}\frac{\partial}{\partial \boldsymbol{pi}}[\boldsymbol{K}(\boldsymbol{p})][\boldsymbol{K}(\boldsymbol{p})]^{-\mathbf{1}}[\boldsymbol{F}] \tag{1.10}$$

These vectors are concatenated column wise to form sensitivity matrix [**S**(**P**)].

1.1.4 Scalar Performance Error Function Minimization

The scalar performance error function can be written as

$$J(p+\Delta p) = [E(p+\Delta p)]^{\mathrm{T}}[E(p+\Delta p)] \tag{1.11}$$

Least square method is applied for minimization of error matrix.

$$\frac{\partial}{\partial\{p\}}J(p+\Delta p) = \{0\} \tag{1.12}$$

Now from the above equation, it can be developed that

$$\{\Delta p\} = -\left[[S(p)]^{\mathrm{T}}[S(p)]\right]^{-1}[S(p)]^{\mathrm{T}}\{E(p)\} \tag{1.13}$$

where $\{\Delta p\}$ is the change in size of the parameters and is of the size NUP × 1.

The size of sensitivity matrix [**S**(**p**)] is NM by NUP. So inverse of sensitivity matrix is only possible when it is a square matrix, i.e., NM = NUP. Now, the evaluated vector {Δ**p**} is added to the vector {**p**}. An iterative process is done till

error matrix becomes null matrix. Once $\{\Delta \mathbf{p}\}$ is established, an iterative process is used for solving where for each iteration k

$$\{\mathbf{p_{k+1}}\} = \{\mathbf{p_k}\} + \{\Delta \mathbf{p}\} \tag{1.14}$$

Thus, the parameter is updated after each iteration.

1.2 Isoparametric Formulation

The term isoparametric is derived from the use of the same shape functions (or interpolation functions) [N] to define the element's geometric shape as are used to define the displacements within the element. Thus, when the shape function is $u = a_1 + a_2 s$ for the displacement, we use $x = a_1 + a_2 s$ for the description of the nodal coordinate of a point on the bar element and, hence, the physical shape of the element. We will now develop the isoparametric formulation of the stiffness matrix of a simple linear bar element with two nodes as shown in Fig. 1.

Select element type first, the natural coordinate s is attached to the element, with the origin located at the center of the element, as shown in Fig. 1b. The s-axis need not be parallel to the x-axis—this is only for convenience. Consider the bar element to have two degrees of freedom—axial displacements u_1 and u_2 at each node associated with the global x-axis.

For the special case when the s and x axes are parallel to each other, the s and x coordinates can be related by

$$\mathbf{x} = \mathbf{x_c} + \frac{\boldsymbol{L}}{\mathbf{2}}\mathbf{s} \tag{2.1}$$

where x_c is the global coordinate of the element centroid. Using the global coordinates x_1 and x_2 in Eq. (2.1) with $x_c = (x_1 + x_2)/2$, we can express the natural coordinate s in terms of the global coordinates as

$$\mathbf{s} = [\mathbf{x} - (\mathbf{x_1} + \mathbf{x_2})/\mathbf{2}] \times \mathbf{2}(\mathbf{x_1} - \mathbf{x_2}) \tag{2.2}$$

We now relate global-coordinate system to its natural one through the formula

$$\mathbf{x} = \mathbf{a_1} + \mathbf{a_2}\mathbf{s} \tag{2.3}$$

On solving for a_i's terms, we get

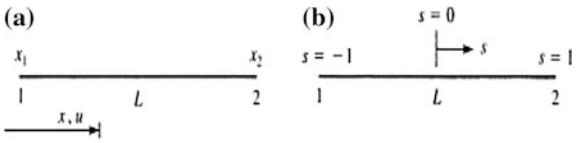

Fig. 1 Coordinate system **a** global, **b** natural

$$\mathbf{x} = \frac{1}{2}[(\mathbf{1} - \mathbf{s})\mathbf{x_1} + (\mathbf{1} + \mathbf{s})\mathbf{x_2}] \tag{2.4}$$

The matrix form can be written as

$$\{\mathbf{u}\} = [\mathbf{N_1}\mathbf{N_2}]\begin{bmatrix}\mathbf{u}_1\\ \mathbf{u}_2\end{bmatrix} \tag{2.5}$$

The final strain equation can be written as

$$\{\epsilon_{\mathbf{x}}\} = \begin{bmatrix}-\frac{1}{\boldsymbol{L}} & \frac{1}{\boldsymbol{L}}\end{bmatrix}\begin{bmatrix}\mathbf{u}_1\\ \mathbf{u}_2\end{bmatrix} \tag{2.6}$$

Since $\{\epsilon_{\mathbf{x}}\} = [\mathrm{B}]\{\mathrm{d}\}$

$$[\mathbf{B}] = \begin{bmatrix}-\frac{1}{L} & \frac{1}{L}\end{bmatrix} \tag{2.7}$$

The stiffness matrix can be represented as

$$[\mathbf{k}] = \int_0^{\boldsymbol{L}} \boldsymbol{t}[\boldsymbol{B}]^T[\boldsymbol{D}]\boldsymbol{A}\,\mathbf{d}\boldsymbol{x} \tag{2.8}$$

The jacobian is represented by in case of simple bar as

$$|\mathbf{J}| = \frac{\mathrm{d}x}{\mathrm{d}s} = \frac{L}{2} \tag{2.9}$$

The Jacobian relates an element length in the global-coordinate system to an element length in the natural-coordinate system. In general, $|\mathbf{J}|$ is a function of s and depends on the numerical values of the nodal coordinates.

After integration, the **k** matrix can be represented as

$$[\mathbf{k}] = \frac{\mathrm{AE}}{\mathrm{L}}\begin{bmatrix}1 & -1\\ -1 & 1\end{bmatrix} \tag{2.10}$$

After this isometric forward formulation, the inversion approach is same as the previous one to identify the damaged portion of the truss member.

2 Results and Discussion

The inversion approach integrates state-of-the-art in experimental and analytical approaches to parameter estimation. This simulation-based estimation is carried out with some truss examples. Both the examples are two-dimensional trusses as seen in

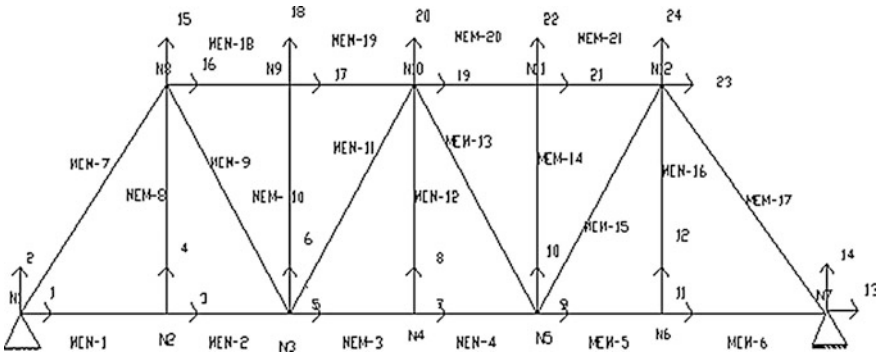

Fig. 2 Pratt truss of example 1

Figs. 2 and 10. This simulated truss structures are modeled as designed trusses. This simulation-based model algorithm helps to estimate the parameters of these truss structures. The estimation of the parameters of finite element-based truss structure is carried out with the help of measured strain data. Using simulation technique strain data with measurement noise or without measurement noise has been extracted and the algorithm must identify the true values of the parameters, respectively.

This algorithm consists of iteration processes, where the first iteration value has been taken as initial value of parameters $\{p_i\}$. The limited measured data are obtained by simulation technique using the true value of parameters $\{p_t\}$. We have to identify the sensitive degrees of freedom followed by the estimation of parameter with the simulated noise or noise-free data and then identify the portion of damaged member.

For each example, several arbitrary combination force sets are used. Using these force sets, the sensitive degrees of freedom (DOFs) can be identified. After that, the above mentioned parameter estimation process is carried out with this simulation technique.

2.1 Truss Example 1

The two-dimensional truss structure as shown in the figure is modeled as an example.

It carries only axial loads, i.e., tension and compression and pinned at both ends. In this paper, the only applicable parameter is the area of the member of truss structure. The physical properties and geometric properties of the truss structure are as follows:

Table 1 Different cases of elemental damage

Case no.	Damaged element	% of damage
1.	6	6%
2.	18	5%
3.	18	5%
	4	2%
	10	3%
	6	6%
4.	2	2–10% @ 2% increment

- Total member 21 and total nodes 12.
- 1–6, 18–21 no. member's area 25.06 cm^2; 7, 9, 11, 13, 15, 17 no. member's area 19.03 cm^2; 8, 10, 12, 14, 16 no. member's area 13.79 cm^2.
- Modulus of elasticity of all members is 2×10^5 N/mm^2.

Several experiments are carried out with the simulation data. The forward approach is used to study the sensitivity of the nodes with the help of every set of force degree of freedom (FDOF) for incremental damage of each element of the truss structure. The selection of sensitive nodes with the help of forward problem with incremental damage is able to avoid the requirement of large number of strain measurements (Table 1).

In this truss structure, node numbers 2, 6, 9, 11 are sensitive. Strain measurement of the member is easy and each element will have one strain. Now, it will be a challenge to estimate all the parameters of truss structure using inversion technique with the help of limited static strain measurements. Error in prediction can be defined by

$$\textbf{Error in prediction} = \frac{(\text{predicted value} - \text{true value})}{(\text{true value})]} \times 100$$

Few cases are discussed in this paper and 1KN is applied at four degrees of freedom (FDOFs) and corresponding result has been interpreted through the corresponding graphs (Fig. 3).

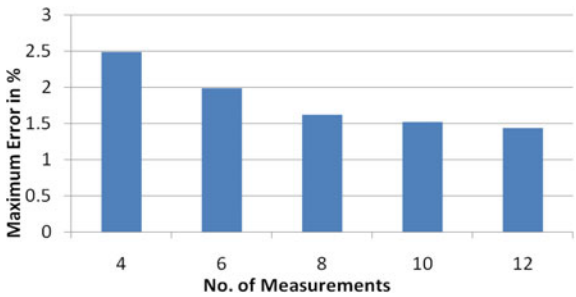

Fig. 3 Maximum error (%) versus no. of measurement

The maximum error in prediction for each type of member, i.e., top chords, bottom chords, diagonal chords, and vertical chords, is seemed to be low to the extent of 2.5% (Fig. 4).

It is noted that the error of prediction decreases with the number of measurements (Fig. 5).

The maximum error in prediction of both damaged and undamaged condition error is very less and correctly implemented with respect to the conceptual model (Fig. 6).

It is noted that the maximum error of different members' parameter prediction is very low for multiple damage scenarios (Fig. 7).

The proposed model is able to identify damages accurately for different degrees of damages.

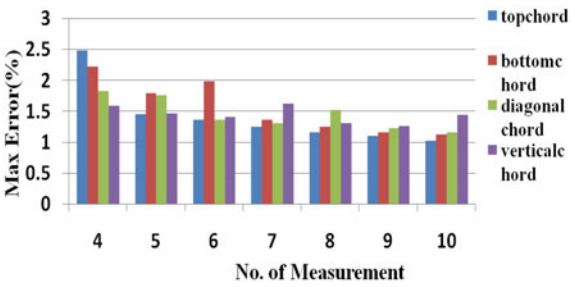

Fig. 4 Maximum error (%) versus no. of measurement

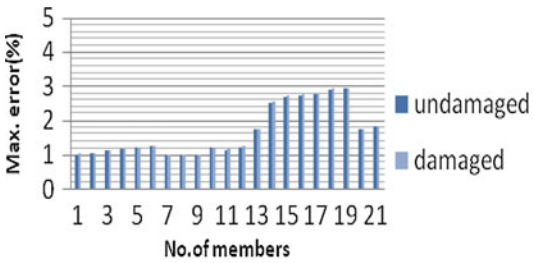

Fig. 5 Error for undamaged and damaged condition

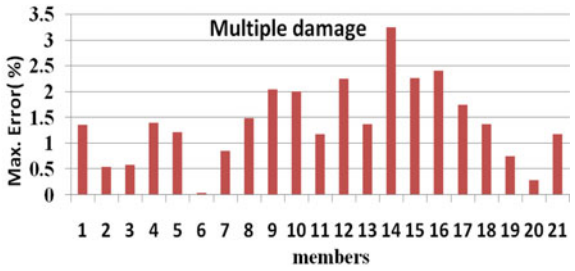

Fig. 6 Maximum error (%) for multiple damaged cases

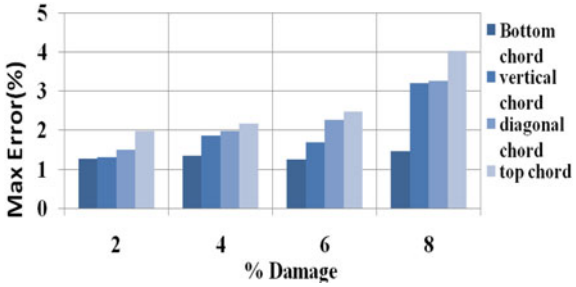

Fig. 7 Maximum error (%) for incremental damage

2.2 *Prediction of Exact Damage Location*

In the above discussion, we have talked about the prediction error of the truss member. In this article segment, we will discuss about the damaged portion of the truss member with the help of isoparametric formulation. The term isoparametric is derived from the use of the same shape function [*N*] to define the element's geometric shape as are used to define the displacements within the element. In this formulation, truss member is considered as a bar whose both ends are fixed and member is discretized into five elements.

- Area of the five segments (2 no. member) 25.06 cm^2.
- Modulus of elasticity (2 no. member): 2×10^5 N/mm^2.
- Connecting nodes: 1–2; 2–3; 3–4; 4–5; 5–6.
- Degrees of freedom: 1–2; 2–3; 3–4; 4–5; 5–6 (Table 2).

Figures 8 and 9 shows the variation of maximum error in prediction of segmental damage with respect to member segment number. The error evaluated in this case is quite small. So the model is correctly able to identify the degree and exact location of damage.

Table 2 Different cases of elemental damage

Case no.	Portion of element damage	Percent to damage (%)
1.	Third portion of fourth member	5
2.	Third portion of sixth member	5
	Fourth portion of the eighth member	8

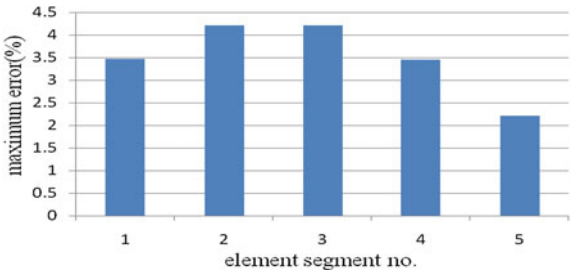

Fig. 8 Maximum error (%) for single element damage

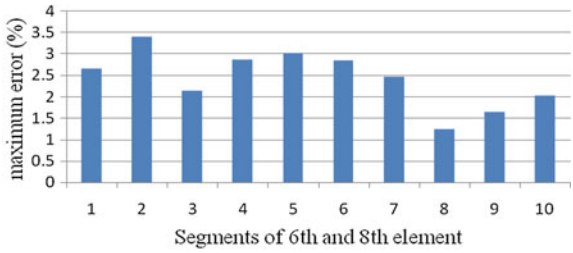

Fig. 9 Maximum error (%) for multiple element damage

2.3 Truss Example 2

A real-life pipeline bridge at Kolkata as shown in Fig. 10 is modeled as an example.

It carries only axial loads, i.e., tension and compression and pinned at both ends. In this paper, the damaged parameter is considered as the reduction of cross section area of the member of truss structure.

The physical properties and geometric properties of the truss structure are as follows:

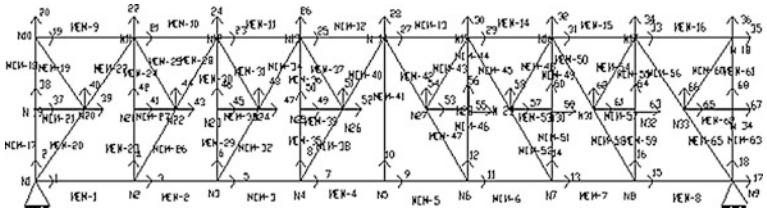

Fig. 10 Pipeline truss structure of example 2

- Total member 65 and total nodes 34
  1, 8 no. member's area 25.06 cm^2; 26, 28, 32, 34, 38, 40, 44, 46, 50, 52 no. member's area 19.03 cm^2; 23, 24, 29, 30, 35, 36, 41, 42, 47, 48 no. member's area 13.79 cm^2; 27, 33, 39, 45, 51 no. member's area 11.38 cm^2; 2–7, 15, 20, 22, 54, 56, 58, 60 no. member's area 34.59 cm^2;
  9, 16 no. member's area 21.06 cm^2; 17, 18, 61–65 no. member's area 10.74 cm^2; 19, 21, 25, 31, 37, 43, 49, 55, 57, 59 no. member's area 8.66 cm^2;
- Modulus of elasticity of all members is 2×10^5 N/mm^2
  The forward approach is first used to identify the parameter. In this truss structure, 6, 8, 12, 14, 15, 18 no. nodes are sensitive nodes. Strain measurement of the members is not as intricate as displacement measurement. The measurement is restricted to one per element. A load of 1KN is applied at 12 degrees of freedom (FDOFs) and corresponding result has been interpreted in this graph 1 for both noisy and noise-free data. Few cases have been outlined in this section (Table 3; Figs. 11 and 12).

Table 3 Different cases of elemental damage

Case no.	Damaged element	% of damage
1.	10	10
2.	1	2
	2	3
	5	5
	18	6
3.	18	2, 4

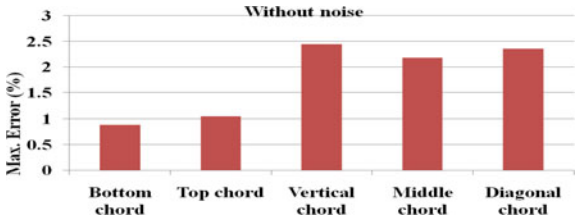

Fig. 11 Maximum error (without noise) multiple damage

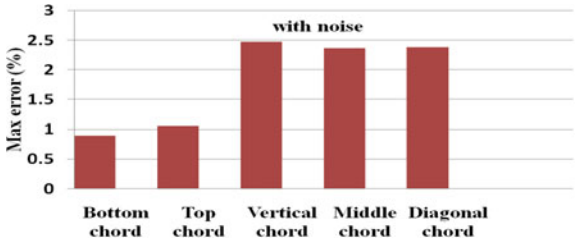

Fig. 12 Maximum error % (with noise) multiple damage

The error evaluated in both the cases considering both with and without noise is small. Thus, the validation of the proposed models for the identification of the damaged truss systems is established. However, the error seems to be more in case of noisy data.

Similarly, the change of maximum error in prediction with respect to each member of this truss example in case of multiple damage to the members has been shown in Fig. 13. It represents the contrast between maximum error in prediction with respect to vertical, diagonal middle, top, and bottom chords with the help of noise-free and noisy data.

To study the versatile applicability of the proposed method, variable damage states are considered to study the effect of multiple damages on different members. The graphical representation of considered damaged cases in terms of maximum error in prediction of structural parameters is shown in Figs. 14 and 15. It is noted that the proposed model is able to predict the maximum error for each element.

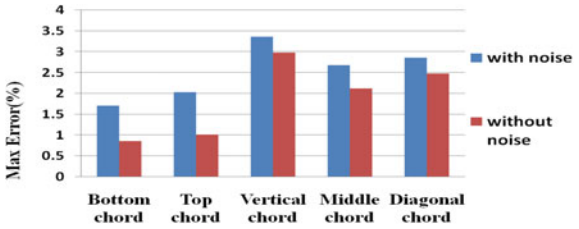

Fig. 13 Comparison of maximum error in prediction

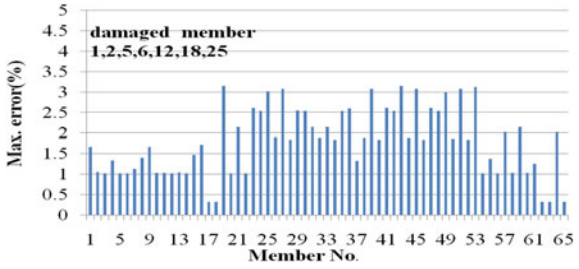

Fig. 14 Maximum error (noise) multiple damage

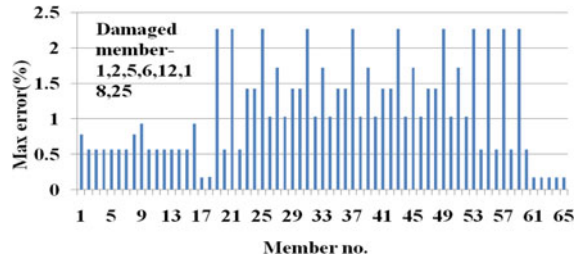

Fig. 15 Maximum error (without noise) multiple damage

3 Conclusions

Based on the numerical studies, the following conclusions maybe drawn.

- Static parameter identification is simple and experimental data can be collected easily in real-life situation in most of the cases. Structural damage mainly refers the reduction of stiffness, which is duly considered. The static displacements are the primary responses and which maybe used as the input to identify the damage state of structure.
- The selection of FDOF also plays an important role to predict the structural parameters with appreciable accuracy. The rank of the sensitivity matrices is important and responsible for the accuracy of the stiffness parameter identification.
- Noise is inevitable and may occur during experiment. The noise is assumed as zero mean unbiased random variables. It is observed that accuracy of prediction is slightly affected due to incorporation of noise. In these cases, both noisy and noise-free data are used.
- The model is able to identify the location and degree of damage with great accuracy with minimum required strain data.
- Accuracy of the predicted structural properties significantly depends on the proper selection of MDOF.
- The selection of sensitive MDOF seems to have contributed accurate prediction even with noisy data using limited strain measurement.
- The isoparametric formulation further points out the exact location of the damage in the particular element.

References

1. Banan, Mo. R., Banan, Ma. R., & Hjelmstad, K. D. (1994). Parameter estimation of structures from static response. I: Computational aspects. Measured information. *Journal of Structural Engineering, 120*(11), 3243–3258.
2. Fritzen, C. P., & Zhu, S. (1991). Updating the finite element models by means of measured information. *Computers & Structures, 40*(2), 475–486.
3. Saletnik, M. J. (1993). *Parameter identification using static strain measurements*. MS thesis, Tufts University, Medford, MA.
4. Sanayei, M., Saletnik, M. J. (1996). Parameter estimation of structures from static strain measurements. *Journal of Structural Engineering, 122*(5).

TWLIGHT-IITM—A Computational Utility for Elastic Buckling Stress Predictions of Cold-Formed Steel Elements

S. S. Ajeesh and S. Arul Jayachandran

Abstract A new design method, Direct Strength Method (DSM), has been introduced by researchers in recent years for calculating the ultimate design strength of cold-formed steel sections. DSM is basically a stress-based approach, wherein the strength of the section is reduced to take care of buckling effects. The ultimate strengths corresponding to three buckling modes, local, distortional, and global modes are distinguished in DSM, in which the elastic buckling stresses are determined using analytical expressions or by using numerical methods like finite element, finite strip, or spline finite strip method. A finite strip computational procedure for evaluating the critical elastic buckling stresses has been proposed in the present study. Also, decomposition of buckling modes into pure modes can be performed using the formulation. This formulation has been validated for a range of cross-sectional dimensions under uniaxial compression and flexure and can be used as a design utility for IS 801 based on DSM.

Keywords Finite strip method · Buckling · Direct strength method

1 Introduction

Cold-formed steel construction is becoming popular nowadays in housing and industrial sector. Cold-formed steel sections manufactured using rolling, folding, or press braking operation offer enough freedom for the designer to make a variety of cross sections. The main advantages of cold-formed sections include high strength-to-weight ratio, versatility of profile shape, variety of connections and materials which can be formed, and increase in yield strength due to cold forming.

S. S. Ajeesh · S. Arul Jayachandran (✉)
Department of Civil Engineering, Indian Institute of Technology Madras, Chennai 600036, India
e-mail: arulsteel@gmail.com

S. S. Ajeesh
e-mail: ss_ajeesh@yahoo.co.in

A. Rama Mohan Rao and K. Ramanjaneyulu (eds.), *Recent Advances in Structural Engineering, Volume 1*, Lecture Notes in Civil Engineering 11,
https://doi.org/10.1007/978-981-13-0362-3_31

The important structural applications of cold-formed steel sections include purlins, wind bracings, roof trusses, storage racks, columns, beams, and rigid frames. The slender cold-formed steel members are prone to instabilities in the form of local, distortional, and global buckling which poses the main challenge for design engineer. Traditionally, effective width method has been used for the design of cold-formed steel which involves lengthy calculations in the determination of ultimate strength of complex cross sections.

To overcome these difficulties, a new design method, Direct Strength Method (DSM), has been introduced by researchers in recent years. DSM is basically a stress-based approach, wherein the strength of the section is reduced to take care of buckling effects. Basically, the ultimate strengths corresponding to three buckling modes, local, distortional, and global modes are distinguished in DSM. This method can be easily employed in the strength determination of complex section geometries considering the interaction of individual elements. The method has been incorporated in the Australian/New Zealand standards, AS/NZS 4600:2005 [1] and North American specification, AISI S100-2007 [2] for the design of cold-formed steel structural members. The DSM requires the determination of elastic local, distortional, and global buckling stress. Elastic analysis can be done using finite element or finite strip method for the determination of buckling stress. In addition to finite element and finite strip method, analytical and semi-analytical expressions are available for the determination of elastic buckling stresses. This paper presents a finite strip code (TWLIGHT-IITM) programmed in Fortran for the evaluation of elastic buckling stresses of cold-formed steel open cross sections. This free program serves as a design utility for Indian designers in cold-formed steel member design for revised Indian code, IS 801 based on DSM.

The semi-analytical finite strip method was developed by Cheung [3, 4] for the stress analysis of isotropic and orthotropic plates with constant and variable thickness under bending. Przmieniecki [5] presented finite element analysis of plates, stiffened panels, and thin-walled columns made up of plates to predict local buckling under biaxial state of stress. Both elastic and geometric stiffness matrixes were formulated to solve the eigenvalue problem in buckling analysis. Finite strip method for the buckling analysis of thin flat isotropic plates subjected to longitudinal and transverse compression, longitudinal in-plane bending, and shear was developed in Ref. [6]. The variation of buckling mode was assumed as sinusoidal function in longitudinal direction. The method can be used to calculate natural frequencies of prismatic structures. Hancock [7] developed local, distortional, and lateral torsional buckling curves of cold-formed steel beams using finite strip method. The paper identified the signature curve of a beam cross section being plotted with buckling stress versus half buckling wavelength. Adany and Schafer [8] developed constrained finite strip method in which the buckling mode is decomposed into pure local, distortional, and global modes. Key and Hancock [9] developed finite strip method for the large displacement elastoplastic analysis to determine the nonlinear local buckling behavior of cold-formed steel sections in compression. The analysis includes geometric imperfection, variation in yield stress, and complex pattern of residual stress during the cold forming process.

Buckling of plates and channel sections subjected to localize loading using semi-analytical finite strip method by including multiple series terms in the longitudinal direction is assessed in Ref. [10].

In this paper, the finite strip formulation used in TWLIGHT-IITM is briefly presented. In order to validate the program, analysis has been done on lipped channel section under simply supported boundary condition for the determination of signature curve. The results of the proposed program are compared with CUFSM software. Also, results are presented for the decomposition of buckling modes into pure local, distortional, and global buckling modes using the proposed finite strip program.

2 Finite Strip Method

In finite strip method, the thin-walled prismatic member is discretized into strips by nodal lines in transverse direction (x-axis). Each nodal line has four degrees of freedom, two out-of-plane (flexural) displacements (w, θ_{xz}), and two in-plane (membrane) displacements (u, v) as shown in Fig. 1. In transverse direction, Lagrangian and Hermitian interpolation functions are used for membrane and flexural displacements, respectively, whereas in the longitudinal direction continuously differentiable smooth series satisfying the boundary condition has been implemented. The general displacements, u, v, and w of the plate strip, are expressed as the product of displacements of nodes and shape functions as shown in Eqs. (1–3).

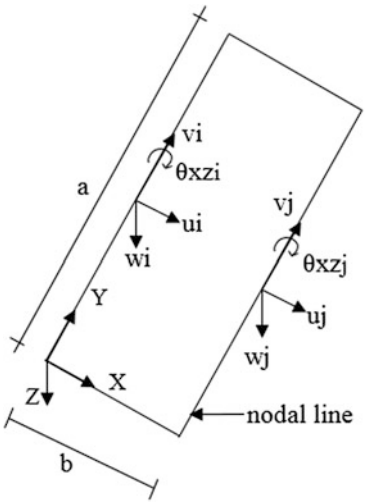

Fig. 1 Plate strip with degree of freedom

$$u = \left[\left(1 - \tfrac{x}{b}\right) \quad \tfrac{x}{b} \right] \begin{Bmatrix} u_i \\ u_j \end{Bmatrix} Y_m \tag{1}$$

$$v = \left[\left(1 - \tfrac{x}{b}\right) \quad \tfrac{x}{b} \right] \begin{Bmatrix} v_i \\ v_j \end{Bmatrix} Y_m \frac{a}{\mu_m} \tag{2}$$

$$w = \left[1 - \frac{3x^2}{b^2} + \frac{2x^3}{b^3} x \left(1 - \frac{2x}{b} + \frac{x^2}{b^2} \right) \frac{3x^2}{b^2} - \frac{2x^3}{b^3} x \left(\frac{x^2}{b^2} - \frac{x}{b} \right) \right] \begin{Bmatrix} w_i \\ \theta_i \\ w_j \\ \theta_j \end{Bmatrix} Y_m \tag{3}$$

where $\mu_m = m\pi$ and m is the number of half-waves in the longitudinal direction. Here, Y_m is the shape function in the longitudinal direction. Usually, trigonometric functions satisfying various boundary conditions are used as interpolating function in the y-direction.

The strain–displacement relation and stress–strain relation are established based on displacement function as shown in Eqs. (4, 5). The matrix B represents the strain–displacement relation and D represents the stress–strain relation based on orthotropic plate theory.

$$\{\varepsilon\} = [B]\{\delta\} \tag{4}$$

$$\{\sigma\} = [D]\{\varepsilon\} \tag{5}$$

The stiffness equation (Eq. 6) has been formulated from equilibrium equation based on variational principles. The expression of stiffness matrix is shown in Eq. (7). The loads acting on a plate strip can be in the form of pressure loads, line loads, and concentrated loads and are imposed on to the load vector appropriately.

$$[K]\{\delta\} = \{F\} \tag{6}$$

$$[K] = \int_v [B]^{\mathrm{T}} [D][B] \mathrm{d}v \tag{7}$$

The membrane and flexural stiffness matrices of the plate strip have to be developed separately. Based on linear theory, there is no interaction between in-plane membrane and out-of-plane bending characteristics of a flat plate strip. In the case of folded plate structures like thin-walled open sections, the membrane action of a flat strip will affect the bending action of the neighboring strip and vice versa. Hence, to fulfill the minimum compatibility requirement and convergence of results, the membrane and bending characteristics have to be combined and the resulting formulation has four degrees of freedom (u, v, w, and θ).

Membrane characteristics are given by

$$\begin{bmatrix} k_{ii}^m & k_{ij}^m \\ k_{ji}^m & k_{jj}^m \end{bmatrix} \begin{Bmatrix} \delta_i^m \\ \delta_j^m \end{Bmatrix} = \begin{Bmatrix} F_i^m \\ F_j^m \end{Bmatrix} \tag{8}$$

Bending characteristics are given by

$$\begin{bmatrix} k_{ii}^b & k_{ij}^b \\ k_{ji}^b & k_{jj}^b \end{bmatrix} \begin{Bmatrix} \delta_i^b \\ \delta_j^b \end{Bmatrix} = \begin{Bmatrix} F_i^b \\ F_j^b \end{Bmatrix} \tag{9}$$

Flat strip characteristics inclusive of membrane and bending characteristics is given by

$$\begin{bmatrix} k_{ii}^m & 0 & k_{ij}^m & 0 \\ 0 & k_{ii}^b & 0 & k_{ij}^b \\ k_{ji}^m & 0 & k_{jj}^m & 0 \\ 0 & k_{ji}^b & 0 & k_{jj}^b \end{bmatrix} \begin{Bmatrix} \delta_i^m \\ \delta_i^b \\ \delta_j^m \\ \delta_j^b \end{Bmatrix} = \begin{Bmatrix} F_i^m \\ F_i^b \\ F_j^m \\ F_j^b \end{Bmatrix} \tag{10}$$

The stiffness matrix and load vector of a plate strip whose local axes inclined at an angle α to the global axis are to be transformed into global system using transformation matrix. A plate strip inclined at an angle α with global axis is shown in Fig. 2, and the relationship between local and global system is given in Eq. (11).

For nodal line "*i*"

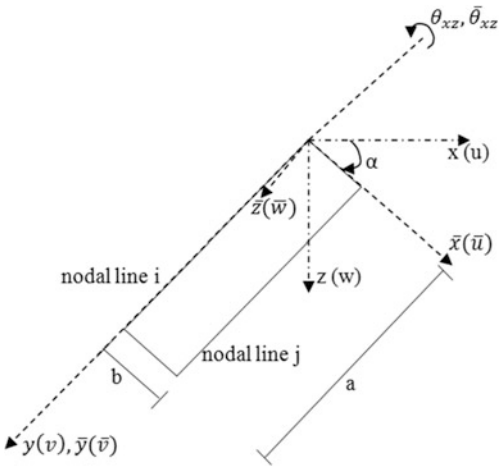

Fig. 2 Finite strip inclined to global coordinate axis

$$\begin{Bmatrix} \overline{u}_i \\ \overline{v}_i \\ \overline{w}_i \\ \overline{\theta}_{xz_i} \end{Bmatrix} = \begin{bmatrix} \cos\alpha & 0 & -\sin\alpha & 0 \\ 0 & 1 & 0 & 0 \\ \sin\alpha & 0 & \cos\alpha & 0 \\ 0 & 0 & 0 & 1 \end{bmatrix} \begin{Bmatrix} u_i \\ v_i \\ w_i \\ \theta_{xz_i} \end{Bmatrix} \tag{11}$$

In short form

$$\{\overline{\delta}_i\} = [T(\alpha)]\{\delta_i\} \tag{12}$$

The stiffness and load matrices in local coordinate system can be transformed into global system as shown in Eqs. (13, 14).

$$[K] = \begin{bmatrix} T^{\mathrm{T}}(\alpha) & 0 \\ 0 & T^{\mathrm{T}}(\alpha) \end{bmatrix} \begin{bmatrix} k_{ii} & k_{ij} \\ k_{ji} & k_{jj} \end{bmatrix} \begin{bmatrix} T(\alpha) & 0 \\ 0 & T(\alpha) \end{bmatrix} \tag{13}$$

$$\{F\} = \begin{bmatrix} T^{\mathrm{T}}(\alpha) & 0 \\ 0 & T^{\mathrm{T}}(\alpha) \end{bmatrix} \begin{Bmatrix} F_i \\ F_j \end{Bmatrix} \tag{14}$$

The element stiffness matrices are assembled to form the global stiffness matrix after transforming to global coordinate system and application of boundary conditions.

The geometric stiffness matrix for plates subjected to edge stresses has been formulated for both flexural and membrane characteristics. The increase in potential energy due to membrane deformation and flexural deformation has been formulated. The state of stress acting on a plate strip consists of longitudinal compressive stress σ_l varying linearly across the width of the strip, uniform transverse compressive stress σ_t, and uniform shear stress τ. The increase in potential energy of the membrane forces resulting from flexural and in-plane buckling deformations developed by Plank and Wittrick [6] is implemented in the present study as shown in Eqs. (15, 16):

$$W_b = -\frac{1}{2}\int_0^a \int_0^b \left\{ \sigma_l \left(\frac{\partial w}{\partial y}\right)^2 + \sigma_t \left(\frac{\partial w}{\partial x}\right)^2 + 2\tau \frac{\partial w}{\partial x}\frac{\partial w}{\partial y} \right\} t\mathrm{d}x\mathrm{d}y \tag{15}$$

$$W_m = -\frac{1}{2}\int_0^a \int_0^b \sigma_l \left\{ \left(\frac{\partial u}{\partial y}\right)^2 + \left(\frac{\partial v}{\partial x}\right)^2 \right\} t\mathrm{d}x\mathrm{d}y \tag{16}$$

Applying the principle of minimum total potential energy for infinitesimal buckling deformations, the eigen buckling equation is formulated as shown in Eq. (17), where $[K]$ and $[G]$ are the elastic stiffness and stability matrices, λ is the buckling load factor, and $\{\phi\}$ is the eigenvector.

$$([K] - \lambda[G])\{\phi\} = 0 \tag{17}$$

For certain thin-walled cross-sectional dimensions, the signature curve obtained during finite strip analysis is not able to produce distinct minima for buckling stresses. Hence, the decomposition of buckling modes into pure local, distortional, and global buckling stresses has to be performed based on the principles of generalized beam theory (GBT).

For decomposition of buckling modes, the principles of GBT are used to develop the restraint matrices corresponding to various buckling modes. For global and distortional subspace, Vlazov's hypothesis has to be satisfied, i.e., the in-plane shear strain and transverse strain has to be zero. The cross section is in transverse equilibrium. Also, the longitudinal warping is constantly not equal to zero. In the case of local buckling mode, all the warping displacements are zero and also the transverse equilibrium is violated. Other assumptions are same as the global–distortional subspace. The restraint matrices are applied on to the finite strip stiffness matrices using transformation technique. The pure buckling modes are obtained from the constrained eigenvalue analysis. For more details on the development of restraint matrices and decomposition of buckling modes, one can refer to Ref. [8].

3 Analysis of Cold-Formed Steel Sections Using TWLIGHT-IITM

The finite strip program (TWLIGHT-IITM) developed in FORTRAN has to be validated for the evaluation of elastic buckling stresses. The elastic buckling stresses are compared with finite strip software, CUFSM developed by John Hopkins University. A lipped channel cross section subjected to uniform compression and flexure with simply supported boundary condition has been analyzed using the proposed program and the buckling stress corresponding to various half buckling wavelengths (signature curve) has been compared with CUFSM as shown in Figs. 3 and 4. It has to be noted that the longitudinal term "m" is taken as one, and the lipped channel is allowed to buckle in a single half-wave in the longitudinal direction.

The signature curve evaluated in the present study matches exactly with the CUFSM software for all the half buckling wavelength compared to the present study for both uniaxial compression and flexure with simply supported ends. The minimum local, distortional, and global buckling stresses are to be applied in the DSM equations to evaluate the ultimate strength of the lipped channel cross section analyzed.

The deformation of the lipped channel section under uniaxial compression at salient points is shown in Figs. 5, 6, and 7. In Fig. 5, local buckling mode of the cross section is observed with the longitudinal edges of the member rotate without any translation. For half buckling wavelength of 1000 mm, the cross-sectional

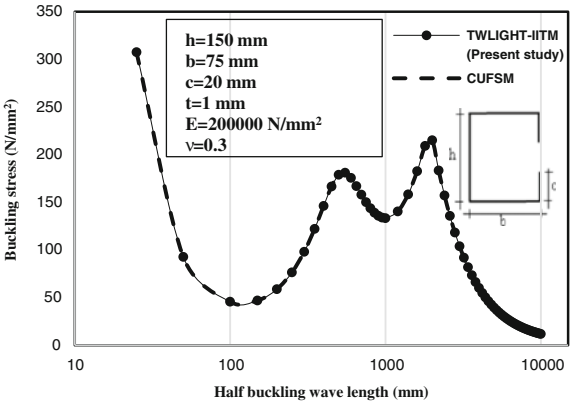

Fig. 3 Comparison of finite strip result of lipped channel in compression

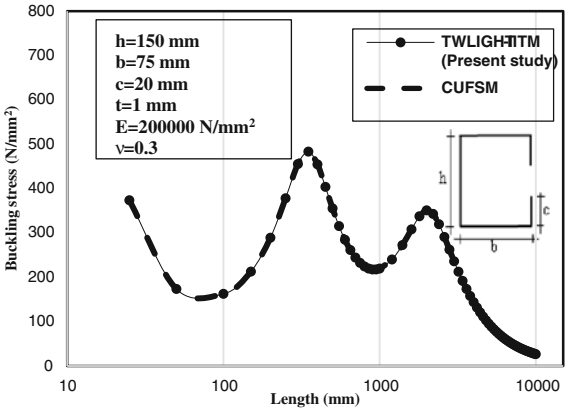

Fig. 4 Comparison of finite strip result of lipped channel in flexure

deformation mode is in the form of flange–lip combination rotating about flange–web junction (Fig. 6). This form of buckling is called distortional buckling. In Fig. 7, for a half wavelength of 10,000 mm, the member buckles in flexural torsional mode, i.e., a combination of torsional and major axis buckling mode. The local and distortional modes involve distortion of the cross section, whereas in the global buckling mode the cross section as a whole moves laterally and rotates without any distortion. In all the three modes, the member is allowed to buckle in a single half wavelength in the longitudinal direction.

The lipped channel cross section used in Figs. 3 and 4 for calculating signature curve has been used for decomposing the buckling modes into pure local, distortional, and global buckling modes. The buckling curves evaluated by constraining the finite strip model to buckle in a particular mode for both uniaxial compression and bending are shown in Figs. 8 and 9. The buckling curves match very well with

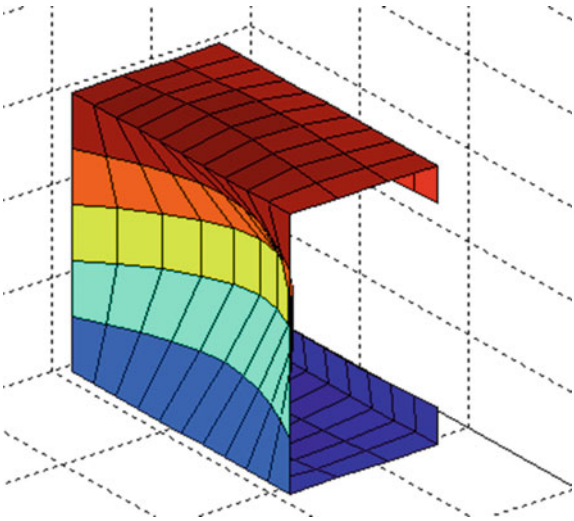

Fig. 5 Local buckling of the lipped channel (L = 100 mm)

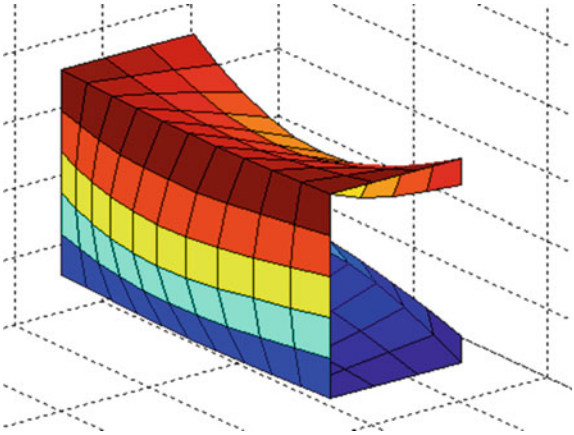

Fig. 6 Distortional buckling of the lipped channel (L = 1000 mm)

the constrained finite strip method using the software CUFSM expect for the distortional buckling in cases where the length of the member is less than 100 mm. This type of mode decomposition is useful in cases where the minima for buckling modes cannot be distinguished from the signature curves.

The study has been extended to lipped channels with various cross-sectional dimensions under uniaxial compression by varying the width (b) and thickness (t) of the cross section. The depth of the section and lip size has been maintained constant (h = 200 mm, c = 30 mm). The modulus of elasticity and Poisson's ratio has been maintained as 200,000 N/mm^2 and 0.3, respectively. The length of the member has been taken as 6000 mm for evaluating the critical global buckling stresses. The critical stresses calculated using the present study have been compared with CUFSM as shown in Table 1.

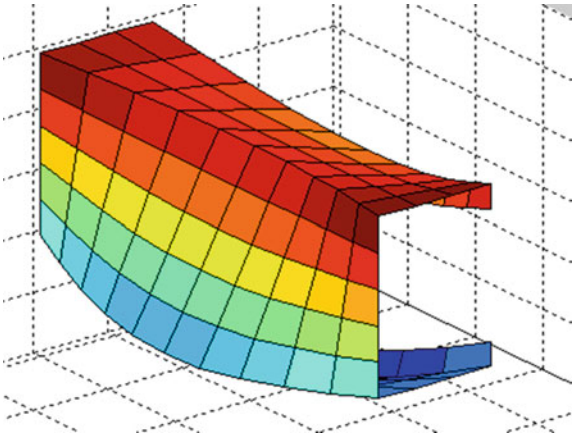

Fig. 7 Global buckling of the lipped channel (L = 10,000 mm)

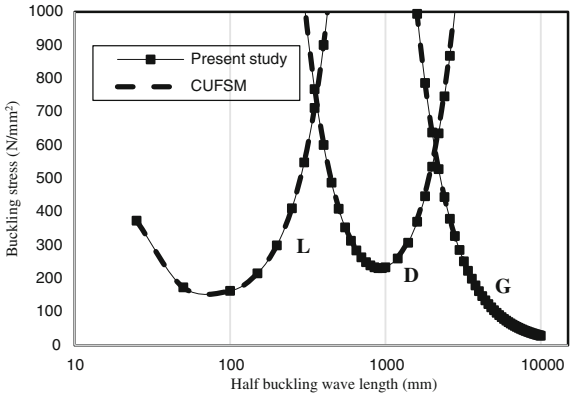

Fig. 8 Decomposition of buckling modes for lipped channel under uniaxial compression

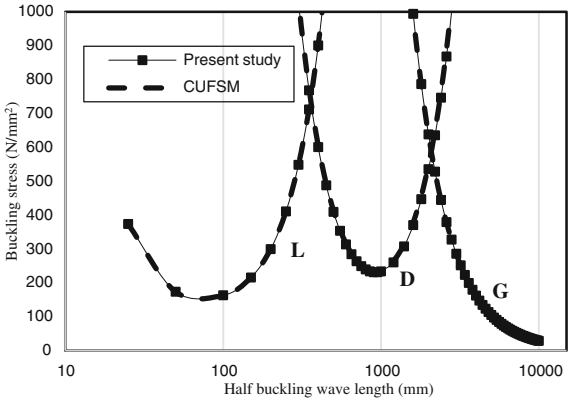

Fig. 9 Decomposition of buckling modes for lipped channel under flexure

Table 1 Comparison of critical buckling stresses for lipped channel under compression

No.	*b* (mm)	*t* (mm)	Local buckling stress (N/mm^2)		Distortional buckling stress (N/mm^2)		Global buckling stress (N/mm^2)	
			TWLIGHT-IITM	CUFSM	TWLIGHT-IITM	CUFSM	TWLIGHT-IITM	CUFSM
1	200	1	19	19	47	48	60	60
2	150	1	24	24	72	73	59	59
3	100	1	25	27	114	120	53	53
4	75	1	26	28	135	168	46	46
5	50	1	27	30	133	141	25	25
6	200	1.5	43	43	71	72	61	61
7	150	1.5	53	53	110	112	60	60
8	100	1.5	56	60	175	217	55	55
9	75	1.5	58	63	208	224	48	48
10	50	1.5	60	67	206	214	25	25
11	200	2	76	76	97	97	62	62
12	150	2	94	95	149	165	61	61
13	100	2	100	106	238	259	57	57
14	75	2	103	112	285	293	52	52
15	50	2	107	120	284	296	25	25

The critical global buckling stress predicted by both the programs is identical for all the cross-sectional dimensions compared. The critical local and distortional buckling predictions by the present study are lower bound to CUFSM for majority of the cross-sectional dimensions compared. The maximum variation in distortional buckling prediction is less than 20%, whereas in the case of local buckling the maximum variation is less than 10%.

The newly developed program (TWLIGHT-IITM) validated for lipped channel cross section is applicable for buckling stress prediction of any thin-walled open section. Currently, the program is having features similar to finite strip software, CUFSM. But new methods like GBT and spline finite strip method will be added to the formulation in future. The proposed finite strip program is a utility for Indian designers for evaluating elastic buckling stresses applicable to DSM as per IS 801 revised code (to be released).

4 Conclusion

A finite strip formulation for the buckling analysis of cold-formed steel sections has been developed in the present study. The formulation incorporated in a software is capable of effectively capturing the signature curve of cold-formed steel section under uniaxial compression and flexure, and the results compare well with the existing finite strip software, CUFSM. Also, the decomposition of general buckling modes into pure local, distortional, and global buckling is performed by the present software. The pure buckling modes calculated for a range of cross-sectional dimensions are comparable with the existing finite strip software. This finite strip software is proposed to be used for the DSM design of cold-formed steel members using the new IS 801 code.

References

1. Australian/New Zealand Standard (AS/NZS). (2005). *Cold-formed steel structures*. AS/NZS 4600:2005, Australia/New Zealand.
2. American Iron and Steel Institute (AISI). (2007). *North American specification for the design of cold-formed steel structural members*. AISI S100-2007, Washington, DC.
3. Cheung, Y. K. (1968). Finite strip method analysis of elastic slabs. *Journal of the Engineering Mechanics Division ASCE, 94*(EM6), 1365–1378.
4. Cheung, Y. K. (1976). *Finite strip method in structural analysis*. New York: Pergamon.
5. Przmieniecki, J. S. (1973). Finite element structural analysis of local instability. *Journal of the American Institute of Aeronautics and Astronautics, 11*(1), 33–39.
6. Plank, R. J., & Wittrick, W. H. (1974). Buckling under combined loading of thin, flat-walled structures by a complex finite strip method. *International Journal of Numerical Methods in Engineering, 8*(2), 323–339.
7. Hancock, G. J. (1978). Local, distortional and lateral buckling of I- beams. *Journal of the Structural Division ASCE, 104*(ST11), 1787–1798.

8. Adany, S., & Schafer, B. W. (2006). Buckling mode decomposition of thin walled, single branched open cross-section members via a constrained finite strip method. *Thin-Walled Structures, 64*(1), 12–29.
9. Key, P. W., & Hancock, G. J. (1993). A finite strip method for the elastic-plastic large displacement analysis of thin walled and cold-formed steel sections. *Thin-Walled Structures, 16*(1–4), 3–29.
10. Hancock, G. J., & Pham, C. H. (2015). Buckling analysis of thin-walled sections under localised loading using the semi-analytical finite strip method. *Thin-Walled Structures, 86*(1), 3–29.

Part III
Computational Structural Mechanics

Improved Sparse High-Dimensional Model Representation Based on Least Absolute Shrinkage and Selection Operator

Tanmoy Chatterjee and Rajib Chowdhury

Abstract The increasing complexity of real-time problems has posed a perpetual challenge to existing simulation models. In particular, such models governing any physical system usually entail long hours of simulation, making them computationally intensive for large-scale problems. In order to mitigate this issue, a novel computational tool has been developed for efficient stochastic computations. The proposed model has been developed by two-tier improvement of the existing approximation techniques. As the first improvement, Kriging (Dubourg et al., in Probab Eng Mech 33: 47–57, 2013, [1]) has been incorporated within high-dimensional model representation (HDMR) (Li et al., in J Phys Chem A 110:2474–2485, 2006, [2]) model so as to enhance approximation capabilities in terms of accuracy. Second, least absolute shrinkage and selection operator (LASSO) (Tibshirani, in 1996, J. R. Stat. Soc. B 58:267–288, [3]) has been utilized and integrated with the refined model so as to construct a sparse HDMR approximation, eventually leading to reduced computational complexity. Implementation of the proposed approach has been demonstrated with two analytical benchmark examples and a 25-element space truss problem.

Keywords Kriging · HDMR · LASSO · Sparse · Stochastic

1 Introduction

The computational effort associated with uncertainty quantification of engineering systems has been one of the prime concerns over the years. In order to mitigate the problem of computational intensiveness, the concept of surrogate modelling has been originated [4]. Surrogate modelling is a technique of approximating the

T. Chatterjee · R. Chowdhury (✉)
Department of Civil Engineering, IIT Roorkee, Roorkee 247667, India
e-mail: rajibfce@iitr.ac.in

T. Chatterjee
e-mail: tanmoydce88@gmail.com

A. Rama Mohan Rao and K. Ramanjaneyulu (eds.), *Recent Advances in Structural Engineering, Volume 1*, Lecture Notes in Civil Engineering 11,
https://doi.org/10.1007/978-981-13-0362-3_32

underlying computational model in a sample space, thereby reducing the simulation time significantly.

Among these techniques, high-dimensional model representation (HDMR) is one of the most promising dimension reduction approaches [5]. HDMR has evolved as a general set of quantitative assessment and analysis tools for capturing the high-dimensional relationship between the model input and its output. However, many of the existing forms of HDMR suffer from several drawbacks [6]. In high-dimensional complex systems, the standard HDMR models, i.e. cut-HDMR and random sampling HDMR (RS-HDMR), constructed over the whole functional space has been observed to be deficient in accurately capturing the input–output relationship [7].

Therefore, the primary objective of this work has been towards the formulation of a refined HDMR model operable in high-dimensional functional space. The following improvements have been performed on existing HDMR model: First, Kriging [8] has been incorporated with the HDMR model so as to achieve local refinements and improve its approximation capabilities. Second, least absolute shrinkage and selection operator (LASSO) [3] has been integrated within the refined model so as to construct sparse HDMR approximation at a much reduced computational cost.

The rest of the paper has been organized in the following sequence. Section 2 describes the formulation of the proposed methodology. In Sect. 3, numerical investigation has been carried out. Two analytical benchmark examples have been solved by utilizing the proposed approach in Sect. 3.1. In Sect. 3.2, a 25-element space truss has been investigated. Finally, some conclusions have been drawn in Sect. 4 based on the present study carried out.

2 Methodology

2.1 High-Dimensional Model Representation

HDMR approximates multivariate functions in such a way that the component functions of the approximation are ordered starting from a constant and gradually approaching towards multivariance as we proceed along the terms like first order, second order and so on. Let $\mathbf{i} = (i_1, i_2, \ldots, i_N) \in \mathbb{N}_0^N$ be a multi-index with $|\mathbf{i}| = i_1 + i_2 + \cdots + i_N$, and let $N \geq 0$ be an integer. Considering $\mathbf{x} = (x_1, x_2, \ldots, x_N)$ be a N-dimensional vector, representing the input variables of a structural system, HDMR expresses the response function $g(\mathbf{x})$ [9] as

$$g(\mathbf{x}) = \sum_{|\mathbf{i}|=0}^{N} g_{\mathbf{i}}(\mathbf{x}_{\mathbf{i}}) \tag{1}$$

Definition 1 Two subspace A and H in Hilbert space are spanned by basis $\{a_1, a_2, \ldots, a_l\}$ and $\{h_1, h_2, \ldots, h_m\}$, respectively. If (i) $H \supset A$ and (ii) $H = A \oplus A^{\perp}$ where $A^{\perp}$ is the orthogonal complement subspace of A in H, H is termed as extended basis and A as non-extended basis. Considering ψ is to be a suitable basis of $\mathbf{x}$, Eq. (1) can be expressed in terms of extended bases as

$$g(\mathbf{x}) = g_0 + \sum_{k=1}^{N} \left\{ \sum_{i_1=1}^{N-k+1} \cdots \sum_{i_k=i_{k-1}}^{N} \sum_{r=1}^{k} \left[\sum_{m_1=1}^{\infty} \sum_{m_2=1}^{\infty} \cdots \sum_{m_r=1}^{\infty} \alpha_{m_1 m_2 \ldots m_r}^{(i_1 i_2 \ldots i_k) i_r} \psi_{m_1}^{i_1} \ldots \psi_{m_r}^{i_r} \right] \right\} \tag{2}$$

where g_0 is a constant term representing the zeroth-order component function or the mean response of any response function $g(\mathbf{x})$. It has been observed that most real-life problems exhibit only the lower order cooperative effect and therefore, the higher order components in Eq. (2) can be ignored. Considering up to Mth order component function and sth order basis, Eq. (2) can be rewritten as

$$\hat{g}(\mathbf{x}) = g_0 + \sum_{k=1}^{M} \left\{ \sum_{i_1=1}^{N-k+1} \cdots \sum_{i_k=i_{k-1}}^{N} \sum_{r=1}^{k} \left[\sum_{m_1=1}^{s} \sum_{m_2=1}^{s} \cdots \sum_{m_r=1}^{s} \alpha_{m_1 m_2 \ldots m_r}^{(i_1 i_2 \ldots i_k) i_r} \psi_{m_1}^{i_1} \ldots \psi_{m_r}^{i_r} \right] \right\} \tag{3}$$

Once the unknown coefficients associated with the bases are determined, Eq. (3) represents the basic functional form of HDMR.

2.2 Kriging

Kriging is a surrogate modelling technique in which the interpolated values are modelled by Gaussian process governed by prior covariance [10]. Suppose $\mathbf{x} = (x_1, x_2, \ldots, x_N)$ are the input variables, where $\mathbf{x} \in D \subset \mathbb{R}^N$. Now assuming the model output $\mathbf{M_K}(\mathbf{x})$ to be a realization of a Gaussian process, one obtains

$$\mathbf{M_K}(\mathbf{x}) = \boldsymbol{\beta}^{\mathrm{T}} \mathbf{f}(\mathbf{x}) + \sigma^2 \mathbf{Z}(\mathbf{x}, \boldsymbol{\omega}) \tag{4}$$

where $\boldsymbol{\beta}^{\mathrm{T}} \mathbf{f}(\mathbf{x}) = \sum_{j=1}^{P} \beta_j f_j(\mathbf{x})$ is the mean value of the Gaussian process and $\mathbf{Z}(\mathbf{x}, \boldsymbol{\omega})$ is a zero mean, unit variance Gaussian process. σ^2 denotes the process variance. The solution of Eq. (4) with respect to β, σ^2 may be obtained as [11]

$$\boldsymbol{\beta}(\boldsymbol{\theta}) = \left(\mathbf{F}^{\mathrm{T}}\mathbf{R}^{-1}\mathbf{F}\right)^{-1}\mathbf{F}\mathbf{R}^{-1}\mathbf{y} \tag{5}$$

$$\sigma_y^2(\boldsymbol{\theta}) = \frac{1}{N}(\mathbf{y} - \mathbf{F}\,\boldsymbol{\beta})^{\mathrm{T}}\mathbf{R}^{-1}(\mathbf{y} - \mathbf{F}\,\boldsymbol{\beta}) \tag{6}$$

where $R_{ij} = R\left(\chi^{(i)}, \chi^{(j)}; \boldsymbol{\theta}\right)$ is the correlation matrix of the points in the experimental design, $F_{ij} = f_j\left(\chi^{(i)}\right)$ is the Vandermonde matrix and $\mathbf{y} = y^{(i)},\ i = 1, \ldots, M$ are the model responses at the training/sample points $\chi^{(i)},\ i = 1, \ldots, M$. The set of hyperparameters $\boldsymbol{\theta}$ defines the autocorrelation $R(\mathbf{x}, \mathbf{x}'; \boldsymbol{\theta})$ between two points $\mathbf{x}$ and $\mathbf{x}'$. The prediction of the Kriging model at a new sample $\mathbf{x_S}$, denoted by $\hat{Y}(\mathbf{x_S})$, is a Gaussian variable defined by a mean value $\mu_{\hat{Y}}$ and a variance $\sigma_{\hat{Y}}^2$ [4] as shown in Eqs. (7) and (8), respectively.

$$\mu_{\hat{Y}} = \mathbf{f}(\mathbf{x})^T\boldsymbol{\beta} + \mathbf{r}(\mathbf{x})^T\mathbf{R}^{-1}(\mathbf{y} - \mathbf{F}\,\boldsymbol{\beta}) \tag{7}$$

$$\sigma_{\hat{Y}}^2 = \sigma_y^2\left(1 - \left\langle \mathbf{f}(\mathbf{x})^T\mathbf{r}(\mathbf{x})^T \right\rangle \begin{bmatrix} 0 & \mathbf{F}^T \\ \mathbf{F} & \mathbf{R} \end{bmatrix}^{-1} \begin{Bmatrix} \mathbf{f}(\mathbf{x}) \\ \mathbf{r}(\mathbf{x}) \end{Bmatrix}\right) \tag{8}$$

where $r_i(\mathbf{x}) = R\left(\mathbf{x}, \chi^{(i)}; \boldsymbol{\theta}\right)$ is the correlation between the new sample $\mathbf{x_S}$ and the sample points in the experimental design. The Kriging model prediction is stochastic, i.e. the mean and variance of the prediction are obtained at any prediction point. It is to be noted that the prediction variance obtained using Eq. (8) is a local error measure and is useful for searching the regions of input with low prediction accuracy.

2.3 Least Absolute Shrinkage and Selection Operator

LASSO represents the most fundamental augmentation of the ordinary least squares solution which implements coefficient shrinkage and selection [3]. The sum of squared residual loss function $L\left(\hat{\beta}(\lambda)\right)$ is combined with a penalty function $J\left(\hat{\beta}(\lambda)\right)$ based on the l_1 norm as

$$\begin{aligned} \hat{\beta}(\lambda) &= \arg\min_{\beta} L\left(\hat{\beta}(\lambda)\right) + \lambda J\left(\hat{\beta}(\lambda)\right) \\ &= \arg\min_{\beta} \|\mathbf{y} - \mathbf{X}\beta\|^2 + \lambda\|\beta\|_1 \end{aligned} \tag{9}$$

The l_1 penalty promotes sparse solutions. This also means as λ increases, elements of $\hat{\beta}(\lambda)$ become zero. Due to the non-differentiability of the penalty function,

there are no closed-form solutions to Eq. (9). Further details of the computations related to LASSO have been provided in Sect. 2.4.

2.4 Proposed Approach

The proposed approach serves as a two-tier approximation tool. To be specific, HDMR ensures the approximation on a global scale and Kriging accounts for the fine deviations in the functional space. Further, in order to identify the most relevant bases required in order to construct the surrogate model, LASSO has been integrated within the above-defined model, which results in a sparse and efficient model.

Suppose $\mathbf{x} = (x_1, x_2, \ldots, x_N)$ are the input variables, where $\mathbf{x} \in D \subset \mathbb{R}^N$. Now substituting Eq. (3) in Eq. (4), the output $\mathbf{M}$ can be represented as

$$\begin{aligned}\mathbf{M} = & \left(g_0 + \sum_{k=1}^{M} \left\{ \sum_{i_1=1}^{N-k+1} \cdots \sum_{i_k=i_{k-1}}^{N} \sum_{r=1}^{k} \right.\right. \\ & \left.\left. \left[\sum_{m_1=1}^{s} \sum_{m_2=1}^{s} \cdots \sum_{m_r=1}^{s} \alpha_{m_1 m_2 \ldots m_r}^{(i_1 i_2 \ldots i_k) i_r} \psi_{m_1}^{i_1} \ldots \psi_{m_r}^{i_r} \right] \right\} \right) \\ & + \sigma^2 \mathbf{Z}(\mathbf{x}, \boldsymbol{\omega})\end{aligned} \tag{10}$$

Alternatively, Eq. (10) can be represented as

$$\mathbf{d} = \boldsymbol{\psi}\,\boldsymbol{\alpha} + \mathbf{e} \tag{11}$$

where $\mathbf{d}$ is the difference between response at the sample point and the mean response and $\boldsymbol{\psi} \in \mathbb{R}^{mxp}$. It is also assumed that

$$E[e_i] = 0, \quad E\left[e_i e_j\right] = \sigma^2 R_{ij} \tag{12}$$

where R_{ij} is the (i, j)th element in the covariance matrix $\mathbf{R}$. E(•), used in Eq. (12), denotes expectation operator. Equation (12) can be expressed in matrix form as

$$E[\mathbf{e}] = 0, \; E\left[\mathbf{e}\mathbf{e}^{\mathrm{T}}\right] = \sigma^2 \mathbf{R} \tag{13}$$

Primarily, the errors are assumed to be uncorrelated and have the same variance such that $\mathbf{R} = \mathbf{I}$, and maximum likelihood estimate of the parameter is the least square solution $\boldsymbol{\alpha}^*$, obtained as

$$\boldsymbol{\alpha}^* = \left(\boldsymbol{\psi}^{\mathbf{T}} \boldsymbol{\psi}\right)^{-1} \boldsymbol{\psi}^{\mathbf{T}} \mathbf{d} \tag{14}$$

The maximum likelihood estimate of the variance is obtained as

$$\sigma^2 = \frac{1}{m}(\mathbf{d}-\boldsymbol{\psi}\boldsymbol{\alpha}^*)^{\mathbf{T}}(\mathbf{d}-\boldsymbol{\psi}\boldsymbol{\alpha}^*) \tag{15}$$

Now, the errors are assumed to be uncorrelated and have different variance such that $E[e_i e_i] = \sigma_i^2$ and $E\left[e_i e_j\right] = 0$ for $i \neq j$. In this case, the covariance matrix and the weight matrix $\mathbf{W_K}$ are defined as

$$\mathbf{R} = \text{diag}\left(\frac{\sigma_1^2}{\sigma^2}, \ldots, \frac{\sigma_m^2}{\sigma^2}\right) \tag{16}$$

$$\mathbf{W_K} = \text{diag}\left(\frac{\sigma}{\sigma_1}, \ldots, \frac{\sigma}{\sigma_m}\right) \tag{17}$$

Comparing Eqs. (16) and (17), it is implied that $\mathbf{W_K^2} = \mathbf{R^{-1}}$. The weighted observations $\tilde{\mathbf{d}} = \mathbf{W_K d} = \mathbf{W_K d}\,\boldsymbol{\alpha} + \tilde{\mathbf{e}}$ have been observed to satisfy the relations in Eq. (18) [12].

$$E[\tilde{\mathbf{e}}] = 0,\ E\left[\tilde{\mathbf{e}}\tilde{\mathbf{e}}^{\mathbf{T}}\right] = \mathbf{W_K} E\left[ee^T\right]\mathbf{W_K^T} = \sigma^2\mathbf{I} \tag{18}$$

From Eq. (18), the transformed set of observations is observed to satisfy the assumptions depicted in Eq. (13) and it follows that $\boldsymbol{\alpha}^*$ and $\boldsymbol{\sigma}$ can be found by replacing $\boldsymbol{\psi}$, $\mathbf{d}$ in Eqs. (14) and (15) by $\mathbf{W_K}\boldsymbol{\psi}$, $\mathbf{W_K d}$, respectively. Hereafter, one can very easily obtain the weighted normal equations as shown in Eqs. (19) and (20)

$$\left(\boldsymbol{\psi}^{\mathbf{T}}\mathbf{R^{-1}}\boldsymbol{\psi}\right)\boldsymbol{\alpha}^* = \boldsymbol{\psi}^{\mathbf{T}}\mathbf{R^{-1}}\mathbf{d} \tag{19}$$

$$\sigma^2 = \frac{\mathbf{1}}{\mathbf{m}}(\mathbf{d} - \boldsymbol{\psi}\boldsymbol{\alpha}^*)^{\mathbf{T}}\mathbf{R^{-1}}(\mathbf{d} - \boldsymbol{\psi}\boldsymbol{\alpha}^*) \tag{20}$$

In general, the correlation parameters $\boldsymbol{\theta}$ are a priori unknown. The optimal parameters have been obtained by maximum likelihood estimate [13]. The objective function to be minimized is shown in Eq. (21).

$$f_{ML}(\boldsymbol{\theta}) = \frac{1}{N}\log|\mathbf{R}(\boldsymbol{\theta})| + \log\left(\mathbf{d}^{\mathbf{T}}\mathbf{R}(\boldsymbol{\theta})^{-\mathbf{1}}\mathbf{d}\right) \tag{21}$$

Alternatively, Eq. (19) can be represented as shown in Eq. (22)

$$\begin{gathered}\mathbf{B}\,\boldsymbol{\alpha} = \mathbf{C} \\ \text{where, } \mathbf{B} = \boldsymbol{\psi}^{\mathbf{T}}\mathbf{R^{-1}}\boldsymbol{\psi},\ \mathbf{C} = \boldsymbol{\psi}^{\mathbf{T}}\mathbf{R^{-1}}\mathbf{d},\ \boldsymbol{\alpha} = \boldsymbol{\alpha}^*\end{gathered} \tag{22}$$

On obtaining the form as defined by Eq. (22), the unknown coefficients have been determined. The estimate $\hat{\alpha}$ as illustrated in Eq. (23) is equivalent to the LASSO estimate

$$\hat{\alpha} = \arg\min \sum_{i=1}^{l} \left(\sum_{j=1}^{d} \alpha_j B_{ij} - C_i \right)^2 + \frac{\lambda}{d} \left(\sum_{j=1}^{d} |\alpha_j| \right)^2 \tag{23}$$

where λ is the Lagrange multiplier and Eq. (23) imposes the constraint $\left(\sum_{j=1}^{d} |\alpha_j|\right)^2 / d \leq K_1$. The expectation–maximization (EM) algorithm utilized to determine the unknown coefficients has been demonstrated below.

At each step s, the EM algorithm estimates the optimal parameters $\lambda_j^{(s)}$ of the Bayes prior based on the estimate $\alpha_j^{(s-1)}$, and then maximizes the posterior to evaluate the current estimate $\alpha_j^{(s)}$. (α, λ) have been parameterized to (γ, δ) in order to avoid divergent solutions, which yields

$$\begin{aligned} \delta_j^{(s+1)^2} &= \frac{d\gamma_j^{(s)^2}}{\sum_{k=1}^{d} \gamma_k^{(s)^2}} \\ \gamma^{(s+1)} &= \left(\mathrm{diag}\left(\delta^{(s+1)}\right) \mathbf{B}^{\mathbf{T}} \mathbf{B}\, \mathrm{diag}\left(\delta^{(s+1)}\right) + \lambda \mathbf{I} \right)^{-1} \\ &\quad \times \mathrm{diag}\left(\delta^{(s+1)}\right) \mathbf{B}^{\mathbf{T}} \mathbf{C} \end{aligned} \tag{24}$$

where $\gamma_j = \sqrt{\frac{\lambda_j}{\lambda}} \alpha_j$ and $\delta_j = \sqrt{\frac{\lambda}{\lambda_j}}$, $j = 1, \ldots, d$. Thus, the unknown coefficients can be evaluated iteratively by utilizing Eq. (24). For easy understanding of the readers, the proposed approach has been briefly summarized in algorithm 1.

Algorithm 1: Pseudocode for the proposed approach

1: Input the variable bounds and distributional parameters. Generate sample points within the outer limits and evaluate actual response
2: Normalize the variables
3: $g_0 \leftarrow \frac{1}{n} \sum_{n} g(x_s)$
4: **for** $i = 1 : n$
$d_i \leftarrow g(x_i) - g_0$
end for
5: $\boldsymbol{\psi} \leftarrow \left[\psi(\mathbf{x}^1) \quad \psi(\mathbf{x}^2) \quad \cdots \quad \psi(\mathbf{x}^N) \right]^{\mathrm{T}}$
6: $\mathbf{d} \leftarrow \left[d_1 \quad d_2 \quad \cdots \quad d_n \right]^{\mathrm{T}}$
7: $\mathbf{R} \leftarrow \mathrm{diag}\left(\frac{\sigma_1^2}{\sigma^2}, \ \ldots, \ \frac{\sigma_m^2}{\sigma^2} \right)$
8: $\mathbf{W_K} \leftarrow \mathrm{diag}\left(\frac{\sigma}{\sigma_1}, \ \ldots, \ \frac{\sigma}{\sigma_m} \right)$
9: Minimize objective function Eq. (21) to determine the correlation parameter
10: $\mathbf{B} \leftarrow \boldsymbol{\psi}^T \mathbf{R}^{-1} \boldsymbol{\psi}, \ \mathbf{C} \leftarrow \boldsymbol{\psi}^T \mathbf{R}^{-1} \mathbf{d}$

(continued)

(continued)

11: $\gamma^{(s+1)} \leftarrow \left(\text{diag}\left(\delta^{(s+1)}\right)\mathbf{B}^{\mathbf{T}}\mathbf{B}\,\text{diag}\left(\delta^{(s+1)}\right) + \lambda\mathbf{I}\right)^{-1} \times \text{diag}\left(\delta^{(s+1)}\right)\mathbf{B}^{\mathbf{T}}\mathbf{C}$

12: Construct $\hat{g}(\mathbf{x})$ using γ (the parameterized unknown coefficients)

13: Evaluate response using $\hat{g}(\mathbf{x})$

3 Numerical Examples

This section has been bifurcated into two portions, the first containing two analytical examples and the second containing a finite element (FE) model of a 25-element space truss. The performance of the proposed approach has been represented in the form of probability density function (PDF) plot of responses. Results obtained using the proposed approach have been validated with that of full-scale Monte Carlo simulation (MCS). Comparison of the proposed approach has also been carried out w.r.t HDMR and Kriging in case of the analytical examples.

Out of the various available uniform and non-uniform sampling techniques, Latin hypercube sampling [14] has been utilized. Gaussian correlation function has been utilized in Kriging [15]. For all of the examples investigated, various error metrics have been evaluated, in order to access the performance of the proposed approach. The use of such statistical metrics is quite recurrent in the literature in order to access the performance of computational models in terms of their prediction accuracy.

3.1 Analytical Examples

Two nonlinear test functions have been selected in order to investigate the performance of the proposed approach. The description of the problems and random variables have been provided in Tables 1 and 2, respectively. The number of sample points utilized has been reported in Table 3.

Table 1 Description of the analytical test problems

Name	Function
Ishigami function [17]	$f(\mathbf{x}) = \sin(x_1) + a\sin^2(x_2) + bx_3^4\sin(x_1)\,;$ $a = 7, b = 0.1,\ -\pi \le \mathbf{x} \le \pi$
30-D function [18]	$f(\mathbf{x}) = \sum_{i=1}^{n} x_i^2 + \left(\sum_{i=1}^{n}(1/2)ix_i\right)^2 + \left(\sum_{i=1}^{n}(1/2)ix_i\right)^4,$ $i = 1, 2, \ldots, n,\ n = 30$

Table 2 Description of the random variables

Function	Distribution	Parameters
Ishigami function	Uniform	$[-\pi, \pi]$
30-D function	Uniform	$[1, 5]$

Table 3 Number of sample points utilized

Function	No. of samples
Ishigami function	256
30-D function	3000

The results of the two problems obtained have been represented in Figs. 1, 2 and Tables 4, 5. Good agreement with that of MCS reveals accurate performance of the proposed approach. On comparing the performance of PA, w.r.t Kriging and HDMR, it has been observed that PA performs well, especially in Ishigami function (refer Table 4), where both Kriging and HDMR fail to accurately the capture the nonlinearity in the functional space. In case of the 30-D function, it can be observed from Table 5 that HDMR performs the best; however, the performance of PA is worth mentioning as the difference in error metrics obtained seems to be quite less. The performance of PA in approximating a highly nonlinear function and a high-dimensional problem is observed to be good in terms of accuracy. Further, in order to illustrate the computational efficiency of PA, an FE model of a 25-element space truss is solved in the next section.

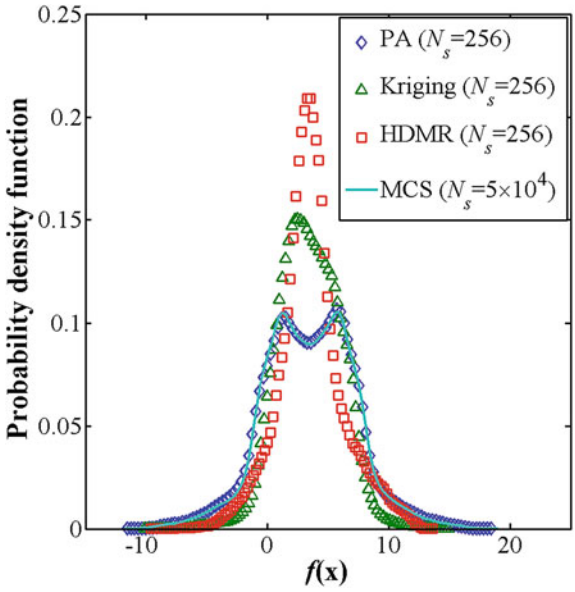

Fig. 1 Response PDF for Ishigami function

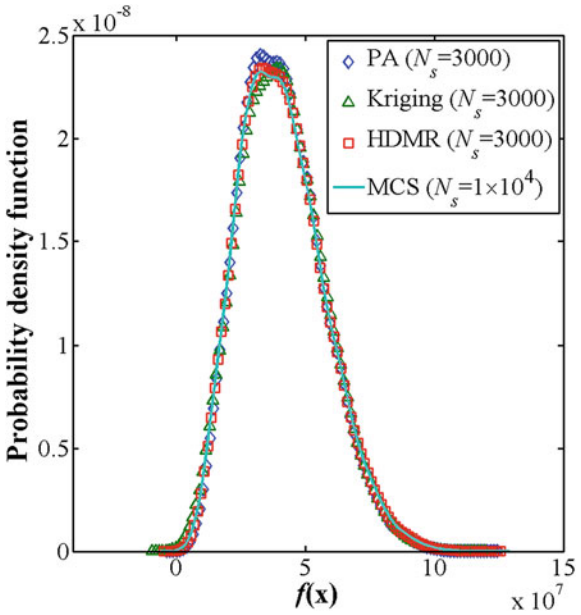

Fig. 2 Response PDF for 30-D function

Table 4 Comparison of the error metrics for Ishigami function

Approach	R^2	RMSE	E (%) [19]
PA	0.992	0.331	6.496
Kriging	0.651	2.199	43.118
HDMR	0.505	2.620	51.356

Table 5 Comparison of the error metrics for 30-D function

Approach	R^2	RMSE	E (%) [19]
PA	0.996	9.843×10^5	2.222
Kriging	0.975	2.603×10^6	5.878
HDMR	0.998	7.429×10^5	1.677

3.2 FE Model of a 25-Element Space Truss

A 25-element space truss [16] as shown in Fig. 3 has been considered in this section. The truss structure consisting of 10 nodes and 25 elements is subjected to seven loads (for details refer [16]). All the loads acting on the truss structure have been considered to be random. Furthermore, the cross-sectional area of all 25 members A_i, i = 1–25 and Young's modulus (E) have been considered to be random. As a result, there are 35 random variables in this problem. The description of the random variables has been provided in Table 6. Stochastic response analysis has been carried out in terms of maximum nodal displacement of the truss.

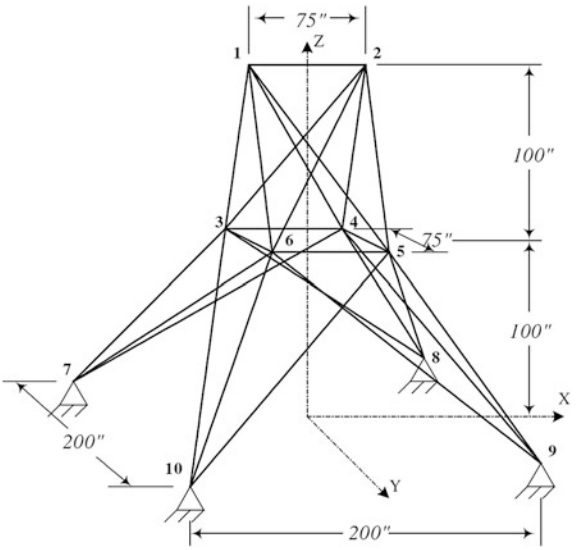

Fig. 3 Twenty-five element space truss

Table 6 Description of the random variables

Variable	Unit	Distribution	Parameters
P_1	lb	Gumbel	Mean = 1000 cov = 0.1
P_2–P_5	lb	Gumbel	Mean = 10,000 cov = 0.1
P_6	lb	Gumbel	Mean = 500 cov = 0.1
P_7	lb	Gumbel	Mean = 600 cov = 0.1
E	ksi	Beta	Mean = 10,000 cov = 0.1
A_1–A_{25}	sq.in	Uniform	[0.5, 2.0]

Good agreement with MCS illustrates robust performance of PA in terms of accuracy (refer Fig. 4 and Table 7). The number of sample points utilized for PA is 3000, which is significantly less than that of MCS ($N_s = 3 \times 10^4$). This illustrates the computational efficiency of PA with excellent accuracy achieved.

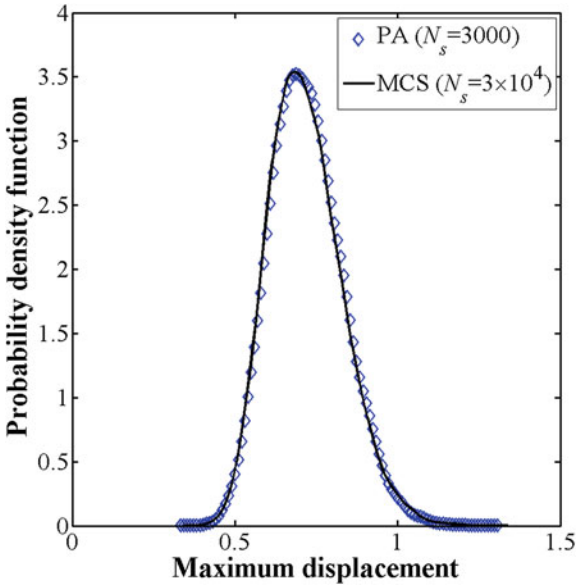

Fig. 4 Comparison of response (maximum displacement in inches) PDF obtained by PA ($N_s = 3000$) w.r.t MCS ($N_s = 3 \times 10^4$)

Table 7 Error metrics obtained by PA ($N_s = 3000$)

R^2	RMSE	E (%) [19]
0.9637	0.0216	2.9746

4 Conclusion

In this work, a novel computational model for stochastic computations has been proposed. The potential of the proposed model both in terms of approximation accuracy and computational effort has been well illustrated through the numerical study carried out. Some of the highlights of the proposed method have been summarized below:

- The proposed model is non-intrusive in nature, which allows a broad class of problems to be addressed.
- PA is flexible to be utilized with any sampling strategies.
- The two-tier approximation framework of the proposed model enhances the ability to capture nonlinear functional space adequately.
- LASSO enables the proposed approach to construct a sparse model, which results in lesser computational complexity w.r.t respective full model.

References

1. Dubourg, V., Sudret, B., & Deheeger, F. (2013). Metamodel-based importance sampling for structural reliability analysis. *Probabilistic Engineering Mechanics, 33,* 47–57.
2. Li, G., Hu, J., Wang, S. W., Georgopoulos, P. G., Schoendorf, J., & Rabitz, H. (2006). Random Sampling-High Dimensional Model Representation (RS-HDMR) and orthogonality of its different order component functions. *Journal of Physical Chemistry A, 110*(7), 2474–2485.
3. Tibshirani, R. (1996). Regression shrinkage and selection via the lasso. *Journal of the Royal Statistical Society. Series B, 58*(1), 267–288.
4. Sudret, B. (2012). Meta-models for structural reliability and uncertainty quantification. In *Proceedings of 5th Asian-Pacific Symposium on Structural Reliability and its Applications (APSSRA, 2012)*, Singapore (pp. 53–76).
5. Chastaing, G., Gamboa, F., & Prieur, C. (2011). *Generalized Hoeffding-Sobol decomposition for dependent variables—Application to sensitivity analysis*. Stat: Electron. J.
6. Jiang, L., & Li, X. (2015). Multi-element least square HDMR methods and their applications for stochastic multiscale model reduction. *Journal of Computational Physics, 294,* 439–461.
7. Yuan, Q., & Liang, D. (2011). A new multiple sub-domain RS-HDMR method and its application to tropospheric alkane photochemistry model. *Numerical Analysis And Modeling, Series B, 2*(1), 73–90.
8. Dubourg, V., Sudret, B., & Bourinet, M. (2011). Reliability-based design optimization using kriging surrogates and subset simulation. *Structural and Multidisciplinary Optimization, 44* (5), 673–690.
9. Li, G., Rosenthal, C., & Rabitz, H. (2001). High dimensional model representation. *Journal of Physical Chemistry A, 105,* 7765–7777.
10. Sacks, J., Welch, W., Mitchell, T., & Wynn, H. (1989). Design and analysis of computer experiments. *Statistical Science, 4*(4), 409–423.
11. Kaymaz, I. (2005). Application of kriging method to structural reliability problems. *Structural Safety, 27*(2), 133–151.
12. Dubourg, V. (2011). *Adaptive surrogate models for reliability analysis and reliability-based design optimization* (Ph.D. thesis). Universite Blaise Pascal, Clermont-Ferrand, France.
13. Marrel, A., Iooss, B., Van Dorpe, F., & Volkova, E. (2008). An efficient methodology for modelling complex computer codes with Gaussian processes. *Computational Statistics & Data Analysis, 52,* 4731–4744.
14. McKay, M. D., Beckman, R. J., & Conover, W. J. (1979). A comparison of three methods for selecting values of input variables in the analysis of output from a computer code. *Technometrics, 2,* 239–245.
15. Lophaven, S., Nielson, H., & Sondergaard, J. (2002). DACE A MATLAB Kriging Toolbox, IMM-TR-2002-12. Technical University of Denmark.
16. Chakraborty, S., & Chowdhury, R. (2015). A semi-analytical framework for structural reliability analysis. *Computer Methods in Applied Mechanics and Engineering, 289,* 475–497.
17. Sobol, I., & Levitan, Y. (1999). On the use of variance reducing multipliers in Monte Carlo computations of a global sensitivity index. *Computer Physics Communications, 117,* 52–61.
18. Tavassoli, A., Haji Hajikolaei, K., Sadeqi, S., Wang, G. G., & Kjeang, E. (2014). Modification of DIRECT for high-dimensional design problems. *Engineering Optimization, 46*(6), 810–823.
19. Chakraborty, S., & Chowdhury, R. (2015). Multivariate function approximations using the D-MORPH algorithm. *Applied Mathematical Modelling, 39*(23–24), 7155–7180.

Reliability-Based Design Optimization—A Hybrid PCFE-Based Approach

Souvik Chakraborty and Rajib Chowdhury

Abstract This paper presents a novel approach for reliability-based design optimization. The proposed approach facilitates a novel surrogate modelling technique, referred to as hybrid polynomial correlated function expansion (H-PCFE), for reliability analysis and a particle swarm optimization for solving the optimization. H-PCFE performs a bi-level approximation: first on a global scale by using polynomial correlated function expansion and second on a local scale by using Kriging. Application of the proposed approach has been illustrated with three numerical examples. For all the problems, the proposed approach is found to yield excellent results, outperforming popular approaches available in literature. Moreover, the computational effort associated with the proposed approach, as indicated by the number of actual function evaluations, is significantly low which indicates the possible application of the proposed approach for large-scale problems.

Keywords RBDO · H-PCFE · PCFE · Kriging

1 Introduction

Reliability-based design optimization (RBDO) is an important prototype for performing optimization in the presence of uncertainties. The basic goal of RBDO is to ensure that the configuration obtained at the end of the optimization loop is reliable. To this end, an additional constraint, describing the reliability of the system, is introduced into the optimization framework. An RBDO problem reads [1]

S. Chakraborty · R. Chowdhury (✉)
Department of Civil Engineering, Indian Institute of Technology Roorkee, Roorkee 247667, India
e-mail: rajibfce@iitr.ac.in

S. Chakraborty
e-mail: csouvik41@gmail.com

A. Rama Mohan Rao and K. Ramanjaneyulu (eds.), *Recent Advances in Structural Engineering, Volume 1*, Lecture Notes in Civil Engineering 11,
https://doi.org/10.1007/978-981-13-0362-3_33

$$\begin{aligned} \arg\min_{\mathbf{x}\in\mathbb{R}} \quad & f(\mathbf{x}) \\ & g_i(\mathbf{x}) \leq 0, \quad i = 1, 2, \ldots, n_{\text{ie}} \\ \text{s.t.} \quad & g_i^p(\mathbf{x}) \geq g_{\text{threshold}}, \quad i = 1, 2, \ldots, n_{\text{p}} \\ & h_j(\mathbf{x}) = 0, \quad j = 1, 2, \ldots, n_{\text{e}} \end{aligned} \tag{1}$$

where $f(\mathbf{x})$ represents the objective function, $g_i(\mathbf{x})$ represents the equality constraints, $g_i^{\text{p}}(\mathbf{x})$ represents the probabilistic constraints and $h_{\text{j}}(\mathbf{x})$ represents the equality constraints. n_{ie}, n_{p} and n_{e}, respectively, denote the number of inequality constraints, number of probabilistic constraints and number of equality constraints.

Solving Eq. (1) described above entails solving a reliability analysis problem. It is well established that solution of an RBDO problem is heavily dependent on the methods used for reliability analysis. The methods for RBDO, available in literature, can be broadly classified into two groups: (A) first-order reliability method (FORM)-based RBDO techniques [2, 3] and (B) surrogate-based RBDO techniques [4]. The FORM-based RBDO techniques are again categorised into three categories, namely (a) double-loop approach [2], (b) single-loop approach [3] and (c) decoupled approach [5]. As the name suggests, double-loop approach uses two loops coupled with each other for solving the RBDO problem. Two parallel approaches namely reliability index-based approach and probability measure-based approach are available for double-loop approach [2]. Nonetheless, the double-loop approach is computationally inefficient. In order to address this issue, the other two variants have emerged. However, all the three approaches rely on the FORM for performing reliability analysis and hence, results obtained for high-dimensional and highly nonlinear problems are often erroneous. Due to this reason, the other possible alternative that is the surrogate-based RBDO technique has emerged. The basic idea of this approach is to utilise surrogate models for the reliability analysis. Naturally, choice of surrogate model becomes extremely important for this approach. Surrogate models that have been used for RBDO are Kriging [4] and least square based response surface method [6]. However, as already demonstrated, Kriging-based approach requires significantly more sample points [7] making the procedure inefficient. On the other hand, the least square based response surface approach yields satisfactory results only for linear and weakly nonlinear systems.

In order to address the above-mentioned issues, a hybrid polynomial correlated function expansion (H-PCFE)-based RBDO approach has been proposed in this paper. H-PCFE [8, 9] is a novel surrogate model recently proposed by the authors. Unlike conventional surrogates, H-PCFE performs a bi-level approximation: first on a global scale by using the PCFE [10–14] and second on a local scale by using Kriging [15]. As a consequence, accuracy is significantly enhanced. In this paper, the H-PCFE has been coupled into a conventional particle swarm optimization (PSO) tool. While H-PCFE is used for performing the reliability analysis, optimization is performed by using the PSO. As a consequence, the computational effort associated with the RBDO problem is significantly reduced.

The rest of the paper is organised as follows. In Sect. 2, the basic formulation of H-PCFE has been provided. In Sect. 3, the proposed approach for RBDO has been

presented. Section 4 presents three numerical examples to illustrate the performance of the proposed approach. Comparison with other state-of-the-art techniques has also been presented. Finally, Sect. 5 presents the concluding remarks.

2 H-PCFE

Suppose, $\mathbf{x} = (x_1, x_2, \ldots, x_N)$ are the input variables, where $\mathbf{x} \in D \subset \mathbb{R}^N$. In H-PCFE, the output $\mathbf{M}^{(\mathbf{H-PCFE})}$ can be represented as

$$\begin{aligned}\mathbf{M}^{(\mathbf{H-PCFE})} = \Bigg(g_0 + \sum_{k=1}^{M} \Bigg\{ \sum_{i_1=1}^{N-k+1} \cdots \\ \sum_{i_k=i_{k-1}}^{N} \sum_{r=1}^{k} \Bigg[\sum_{m_1=1}^{s} \sum_{m_2=1}^{s} \cdots \\ \sum_{m_r=1}^{s} \alpha_{m_1 m_2 \ldots m_r}^{(i_1 i_2 \ldots i_k) i_r} \psi_{m_1}^{i_1} \ldots \psi_{m_r}^{i_r} \Bigg\} \Bigg) + \sigma^2 \mathbf{Z}(\mathbf{x}, \boldsymbol{\omega})\end{aligned} \tag{2}$$

where g_0 is a constant and referred to as zeroth-order component function. M denotes the maximum order of component function and ψ denotes some suitable basis. Writing Eq. (2) in matrix form

$$\mathbf{d} = \boldsymbol{\psi}\,\boldsymbol{\alpha} + \mathbf{e} \tag{3}$$

where $\mathbf{d}$ is the difference between response at the sample point and the mean response and $\boldsymbol{\psi} \in \mathbb{R}^{mxp}$. If the errors are assumed to be uncorrelated and have the same variance such that $\mathbf{R} = \mathbf{I}$, and maximum likelihood estimate of the parameter is the least square solution $\boldsymbol{\alpha}^*$, obtained as

$$\boldsymbol{\alpha}^* = \left(\boldsymbol{\psi}^{\mathbf{T}}\boldsymbol{\psi}\right)^{-\mathbf{1}} \boldsymbol{\psi}^{\mathbf{T}}\mathbf{d}, \tag{4}$$

the maximum likelihood estimate of the variance is obtained as

$$\sigma^2 = \frac{1}{m}(\mathbf{d} - \boldsymbol{\psi}\,\boldsymbol{\alpha}^*)^{\mathbf{T}}(\mathbf{d} - \boldsymbol{\psi}\,\boldsymbol{\alpha}^*) \tag{5}$$

Now extending the above concept for uncorrelated errors having different variances such that $E(e_i e_i) = \sigma_i^2$ and $E(e_i e_j) = 0$ for $i \neq j$

$$\left(\boldsymbol{\psi}^{\mathbf{T}}\mathbf{R}^{-\mathbf{1}}\boldsymbol{\psi}\right)\boldsymbol{\alpha}^* = \boldsymbol{\psi}^{\mathbf{T}}\mathbf{R}^{-\mathbf{1}}\mathbf{d} \tag{6}$$

$$\sigma^2 = \frac{1}{\mathbf{m}}(\mathbf{d} - \boldsymbol{\psi}\boldsymbol{\alpha}^*)^{\mathbf{T}}\mathbf{R}^{-1}(\mathbf{d} - \boldsymbol{\psi}\boldsymbol{\alpha}^*) \tag{7}$$

where $\mathbf{W_K} = \text{diag}\left(\frac{\sigma}{\sigma_1}, \ldots, \frac{\sigma}{\sigma_m}\right)$.

Equation (6) can be written in a matrix form as

$$\mathbf{B}\,\boldsymbol{\alpha} = \mathbf{C} \tag{8}$$

where $\mathbf{B} = \boldsymbol{\psi}^{\mathbf{T}}\mathbf{R}^{-1}\boldsymbol{\psi}$, $\mathbf{C} = \boldsymbol{\psi}^{\mathbf{T}}\mathbf{R}^{-1}\mathbf{d}$, $\boldsymbol{\alpha}\,\boldsymbol{\alpha}^*$. Since H-PCFE employs extended bases [9] as already shown in Eq. (2), matrix $\mathbf{B}$ has identical rows. These are redundants and can be removed. Removing the redundants, one obtains

$$\mathbf{B}'\boldsymbol{\alpha} = \mathbf{C}' \tag{9}$$

where $\mathbf{B}'$ and $\mathbf{C}'$ correspond to $\mathbf{B}$ and $\mathbf{C}$, respectively, after removing the redundant equations. Equation (9) represents a set of underdetermined equations, and naturally there exists an infinite solution given as

$$\boldsymbol{\alpha} = (\mathbf{B}')^{-1}\mathbf{C}' + \left(\mathbf{I} - (\mathbf{B}')^{-1}\mathbf{B}'\right)\mathbf{v}(s) \tag{10}$$

where $(\mathbf{B}')^{-1}$ denotes the generalised inverse of $\mathbf{B}'$ that satisfies partially or completely all four Penrose conditions [16]. $\mathbf{I}$ represents an identity matrix of dimensions $q \times q$.

Out of all the possible solutions for Eq. (10), the solution that minimises the least squared error and satisfies the hierarchical orthogonality of the component functions [10] is termed as the 'best' solution.

In H-PCFE, homotopy algorithm [17–20] is employed to determine the 'best' solution. Employing homotopy algorithm, the 'best' solution is obtained as

$$\boldsymbol{\alpha}^*_{\text{HA}} = \left[\mathbf{V}_{\text{q-r}}\left(\mathbf{U}^T_{\text{q-r}}\mathbf{V}_{\text{q-r}}\right)^{-1}\mathbf{U}^T_{\text{q-r}}\right](\mathbf{B}')^{\dagger}\mathbf{C}' \tag{11}$$

where

$$\mathbf{PW_{HA}} = \mathbf{U}\begin{bmatrix}\mathbf{A}_r & 0\\ 0 & 0\end{bmatrix}\mathbf{V}^T \tag{12}$$

and

$$\mathbf{P} = \mathbf{I} - (\mathbf{B}')^{\dagger}\mathbf{B}' \tag{13}$$

$(\mathbf{B}')^{\dagger}$ in Eq. (13) is the generalised inverse of $\mathbf{B}'$ satisfying all four Penrose conditions. $\mathbf{W}_{\mathrm{HA}}$ in Eq. (12) is the weight matrix utilised for formulating the objective function in homotopy algorithm. For details regarding the formulation of weight matrix, interested readers may refer [10, 21]. For details regarding homotopy algorithm, interested readers may refer [17–20].

Once the unknown coefficient vector $\boldsymbol{\alpha}^{*}_{\mathrm{HA}}$ is determined, the prediction mean and prediction variance are given as

$$\mu(x) = g_0 + M\boldsymbol{\alpha}^{*}_{\mathrm{HA}} + r(x)\mathbf{R}^{-1}\left(\mathbf{d} - \Psi\boldsymbol{\alpha}^{*}_{\mathrm{HA}}\right) \tag{14}$$

and

$$s^2(x) = \sigma^2\left(1 - r(x)\mathbf{R}^{-1}r(x)^T + \frac{\left(1 - \Psi^T\mathbf{R}^{-1}r(x)^T\right)}{\Psi^T\mathbf{R}^{-1}\Psi}\right) \tag{15}$$

where

$$M = \left(\psi_1\left(x_{\mathrm{p}}\right), \psi_2\left(x_{\mathrm{p}}\right), \ldots\right) \tag{16}$$

at the prediction point x_{p} and

$$r(x) = \left(R\left(x_{\mathrm{p}}, x_1\right), R\left(x_{\mathrm{p}}, x_2\right), \ldots\right) \tag{17}$$

3 H-PCFE-Based RBDO Framework

H-PCFE described in the previous section provides an efficient means to represent the constraint functions in a RBDO problem and perform reliability analysis. As for the objective function(s), it is generally not necessary to employ H-PCFE since the objective functions are more or less simple. However, as a special case, if the objective function of a RBDO problem involves stochastic computations, it is possible to employ H-PCFE by using the same procedure. One such problem is presented in example 3 of this paper.

There exist multiple alternatives for formulating an RBDO framework by using the H-PCFE. The obvious option is to represent the constraint by using H-PCFE at each optimization step. However, such an approach is computationally inefficient. In this work, an alternative approach has been adopted. The basic idea of the proposed approach is to first generate a single H-PCFE-based surrogate and subsequently update it based on local refinement. The different steps involved in the proposed approach are as follows:

Step 1: Input the statistical properties of the input parameters. Also provide number of particles, number of iteration count and technology parameter.

Step 2: Using the H-PCFE, generate approximate functions for the probabilistic constraint(s).
Step 3: Randomly initialize the position and velocity of the particles.
Step 4: For each particle, perform the followings steps (for the probabilistic constraints):

(a) Generate random numbers corresponding to each input variable.
(b) Predict response using the H-PCFE model. Also, predict error in prediction (Eq. 15).
(c) Identify the sample points corresponding to which prediction error is significant. Place additional points in the vicinity of those points. Update the H-PCFE model.
(d) Compute the probability of failure and hence, the probabilistic constraints.
(e) Compute other deterministic constraints as well.

Step 5: If for each particle, all the constraints are satisfied, proceed. Else, **go to** step 3.
Step 6: For each particle, calculate fitness value. If fitness value is better than the best fitness value in history, repeat Step 4 to check whether the constraints are satisfied. If constraints are satisfied, set the current value as the best value (*pbest*).
Step 7: For each particle, choose the particle with the best *pbest* as the *gbest*.
Step 8: Calculate particle velocity and particle position.
Step 9: Increment iteration count by 1.
Step 10: iteration > maximum iterations, **go to step 5**.

4 Numerical Examples

In this section, three numerical examples are presented to illustrate the performance of the proposed approach. For all the examples, only a second-order H-PCFE model and a third-order basis have been used. As for the stochastic part of H-PCFE, Gaussian covariance function has been used due to its superior performance [22]. The sample points required for H-PCFE have been generated by using the sequential experimental design scheme based on optimal Latin hypercube sampling. Further details of this scheme can be found in [1].

Results obtained using the proposed approach have been validated against brute force optimization performed by using Monte Carlo simulation (MCS) with PSO. Additionally, comparison with results obtained using other state-of-the-art techniques has been presented to illustrate the superior performance of the proposed approach.

4.1 A Highly Nonlinear Test Function

In this example, a two-dimensional mathematical problem first proposed by Lee and Jung [23] has been considered. The typicality resides in the probabilistic counterpart of this problem. The two performance functions involved are

$$g_1(\mathbf{x}) = -x_1 \sin(4x_1) - 1.1x_2 \sin(2x_2) \tag{18}$$

$$g_2(\mathbf{x}) = x_1 + x_2 - 3 \tag{19}$$

where $\mathbf{x}$ represents the realisation of the random vector $\mathbf{X}$ composed of two independent Gaussian random variables with standard deviation $\sigma = 0.1$. For solving the RBDO problem, the mean of the random variables is considered to be the design variables. The objective function for this problem reads

$$c(\mathbf{d}) = (\mu_1 - 3.7)^2 + (\mu_2 - 4)^2 \tag{20}$$

The problem domain is restrained to the following hyper-rectangular design space:

$$\mathbb{D} = [0; 3.7] \times [0; 4] \tag{21}$$

The probabilistic constraints associated with this problem are

$$\mathbb{P}[g_1(\mathbf{X}(\mathbf{d})) \leq 0] \leq \Phi(-\beta) \tag{22}$$

$$\mathbb{P}[g_2(\mathbf{X}(\mathbf{d})) \leq 0] \leq \Phi(-\beta) \tag{23}$$

where β represents the generalised reliability index. For both the probabilistic constraints,

$$\beta = 2 \tag{24}$$

has been considered.

Results obtained using the proposed approach have been presented in Table 1. It is observed that the results obtained using the proposed approach are almost identical to the benchmark solution. Additionally, the number of sample points required using the proposed approach is significantly less as compared to other state-of-the-art methods.

Table 1 Comparative results for the nonlinear function

Method	μ_1	μ_2	Cost	β_1^a	β_2^a	g_1/g_2 - call
Brute Force	2.79	3.28	1.34	2	∞	10^7
PMA	2.82	3.30	1.26	1.67	>8	296
PMA-Kriging	2.82	3.30	1.26	1.67	>8	90
Meta-RBDO	2.81	3.25	1.35	2	>8	80/10
H-PCFE RBDO	2.8	3.27	1.34	2	∞	32/12

4.2 Euler Buckling of Straight Column

In this example, the well-known Euler buckling of straight column [1] problem has been considered. The underlying problem involves three random variables and two design variables. The objective is to minimise the overall cross-sectional area, i.e.

$$f(\mathbf{x}) = \mu_b \mu_h \tag{25}$$

The problem is subjected to a probabilistic constraint defined in terms of the buckling load. Hence, the performance function of the system is

$$g_1(\mathbf{x}) = \frac{\pi^2 E b h^3}{12L^2} - \frac{\pi^2 \mu_E \mu_b^{(0)} \mu_h^{(0)3}}{12L^2} \tag{26}$$

where E, b and h are the random variables with mean μ_E, μ_b and μ_h. The details regarding the random variables are provided in Table 2. The probabilistic constraint reads

$$\mathbb{P}(g_1(\mathbf{x})) \leq \Phi(-\beta) \tag{27}$$

where β denotes the generalised reliability index. For this problem,

$$\beta = 3 \tag{28}$$

has been considered. Additionally, one deterministic constraint, as shown in Eq. (29), is also involved with this problem

$$g_2(\mathbf{x}) = \mu_h - \mu_b \leq 0 \tag{29}$$

Proposed approach has been employed for RBDO of the above-mentioned problem. Results obtained have been shown in Table 3. In the absence of result obtained using the other state-of-the-art RBDO techniques, only the results obtained using the proposed approach and brute force approach (benchmark solution) have been shown. It is observed that the results obtained using the proposed approach are almost identical to the benchmark solution. Additionally, number of sample points required using the proposed approach is significantly less as compared to the benchmark solution.

Table 2 Statistical parameters for Euler buckling problem

Variable	Distribution	Mean	COV
E (MPa)	Lognormal	10,000	15%
b (mm)	Lognormal	μ_b	5%
h (mm)	Lognormal	μ_h	5%
L (mm)	Deterministic	3,000	–

Table 3 RBDO results for Euler buckling of column problem

Method	μ_1	μ_2	g_1 - call
Brute force	231	231	10^7
H-PCFE RBDO	230.8	231.1	64

4.3 A Short Column Under Oblique Bending

The last example considered involves a short column under oblique bending. This is a well-known example that has been widely used for RBDO problems. It is inspired by the article by Royset et al. [5].

The structure under consideration is a short column with rectangular cross section $b \times h$. It is subjected to two moments M_1 and M_2 and an axial force P. The system described above is referred to as *oblique bending* because of the rotation of the neutral axis, as illustrated in Fig. 1. According to the actual reference, the performance function describing the ultimate serviceability of the column is given as

$$g(\mathbf{x}) = 1 - \frac{4M_1}{bh^2\sigma_y} - \frac{4M_2}{b^2h\sigma_y} - \left(\frac{P}{bh\sigma_y}\right)^2 \tag{30}$$

Equation (30) is obtained by assuming the constitutive material to be having an elastic-perfectly plastic behaviour. The stochastic model considered involves six independent random variables. Statistical properties of the random variables are given in Table 4. Similar to the previous example, μ_b and μ_h are considered to be the design variables.

The objective function of this problem is given as

$$\begin{aligned} c(\mathbf{d}) &= c_0(\mathbf{d}) + p_f(\mathbf{d})c_f(\mathbf{d}) \\ &= c_0(\mathbf{d})(1 + 100p_f(\mathbf{d})) \\ &= \mu_b\mu_h(1 + 100p_f(\mathbf{d})) \end{aligned} \tag{31}$$

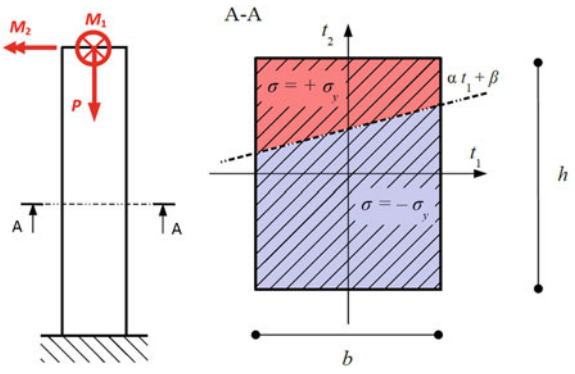

Fig. 1 Short column under oblique bending

Table 4 Probabilistic model for short column subjected to oblique bending

Variable	Distribution	Mean	COV
M_1 (N.mm)	Lognormal	250×10^6	0.3
M_2 (N.mm)	Lognormal	125×10^6	0.3
P (N)	Lognormal	2.5×10^6	0.2
σ_y (MPa)	Lognormal	40	0.1
b (mm)	Normal	μ_b	0.01
h (mm)	Normal	μ_h	0.01

Table 5 Comparative results for the beam subjected to oblique bending

Method	μ_b	μ_h	Cost	β_1^a	g_1 - call
Brute Force	359	556	2.15×10^5	3.1	19×10^6
DSA	372	449	2.15×10^5	3.38	4×10^6
Nested FORM	399	513	2.12×10^5	3.38	9472
Meta-RBDO	358	560	2.15×10^5	3.32	70
H-PCFE RBDO	360	557	2.15×10^5	3.16	48

where $p_f c_f$ is the expected failure cost which, in this case, is considered to be proportional to the construction cost c_0. The search for the optimal designs is subjected to the following geometric constraints:

$$\frac{1}{2} \leq \frac{\mu_b}{\mu_h} \leq 2 \tag{32}$$

and

$$100 \leq \mu_b, \mu_h \leq 1000 \tag{33}$$

The minimum reliability index is considered to be 3.

Proposed approach has been employed for RBDO of the above-mentioned problem. Results obtained have been tabulated in Table 5. Similar to the first example, results obtained have been compared with that obtained using other state-of-the-art techniques. It is observed that the proposed framework yields excellent results outperforming other methods in both accuracy and efficiency.

5 Conclusions

In this paper, a novel approach for reliability-based design optimization (RBDO) has been presented. The proposed approach facilitates a novel surrogate model, referred to as hybrid polynomial correlated function expansion (H-PCFE) for

reliability analysis and particle swarm optimization for solving the optimization. It is argued that coupling H-PCFE into the optimization framework significantly reduces the computational cost without affecting the accuracy. Additionally, a scheme to update the generated H-PCFE model has also been proposed in this work.

Performance of the proposed approach for RBDO has been illustrated with three numerical examples. For all the examples, the proposed approach yields highly accurate results. Additionally, the computational effort as indicated by the number of actual function evaluations has also been reduced significantly.

Acknowledgements SC acknowledges the support of MHRD, Govt. of India. RC acknowledges the support of CSIR via grant no. 22(0712)/16/EMR-II.

References

1. Dubourg, V. (2011). *Adaptive surrogate models for reliability analysis and reliability-based design optimization*. Clermont-Ferrand, France: Universite Blaise Pascal.
2. Tu, J., Choi, K. K., & Park, Y. H. (1999). A new study on reliability-based design optimization. *Journal of Mechanical Design, 121*(4), 557.
3. Kuschel, N., & Rackwitz, R. (1997). Two basic problems in reliability-based structural optimization. *Mathematical Methods of Operational Research, 46*(3), 309–333.
4. Dubourg, V., Sudret, B., & Bourinet, M. (2011). Reliability-based design optimization using kriging surrogates and subset simulation. *Structural and Multidisciplinary Optimization, 44* (5), 673–690.
5. Royset, J. O., Der Kiureghian, A., & Polak, E. (2001). Reliability-based optimal structural design by the decoupling approach. *Reliability Engineering & System Safety, 73*(3), 213–221.
6. Gu, L., Yang, R. J., Tho, C. H., Makowskit, M., Faruquet, O., & Li, Y. L. (2004). Optimisation and robustness for crashworthiness of side impact. *International Journal of Vehicle Design*.
7. Chakraborty, S., & Chowdhury, R. (2015). A semi-analytical framework for structural reliability analysis. *Computer Methods in Applied Mechanics and Engineering, 289*(1), 475–497.
8. Chakraborty, S., & Chowdhury, R. (2016). Moment independent sensitivity analysis: H-PCFE–based approach. *Journal of Computing in Civil Engineering*. (Accepted), 06016001:1–06016001:11.
9. Chatterjee, T., Chakraborty, S., & Chowdhury, R. (2016). A bi-level approximation tool for the computation of FRFs in stochastic dynamic systems. *Mechanical Systems and Signal Processing, 70–71,* 484–505.
10. Chakraborty, S., & Chowdhury, R. (2014). Polynomial correlated function expansion for nonlinear stochastic dynamic analysis. *Journal of Engineering Mechancs, 141*(3), 04014132:1–04014132:11.
11. Chakraborty, S., & Chowdhury, R. (2016). Modelling uncertainty in incompressible flow simulation using Galerkin based generalised ANOVA. Computer Physics Communication (Accepted).
12. Chakraborty, S., & Chowdhury, R. (2016). Sequential experimental design based generalised ANOVA. *Journal of Computational Physics, 317,* 15–32.
13. Chakraborty, S., & Chowdhury, R. (2016). Assessment of polynomial correlated function expansion for high-fidelity structural reliability analysis. *Structural Safety, 59,* 9–19.

14. Chakraborty, S., Mandal, B., Chowdhury, R., & Chakrabarti, A. (2016). Stochastic free vibration analysis of laminated composite plates using polynomial correlated function expansion. *Composite Structures, 135,* 236–249.
15. Mukhopadhyay, T., Chakraborty, S., Dey, S., Adhikari, S., & Chowdhury, R. (2016). A critical assessment of Kriging model variants for high-fidelity uncertainty quantification in dynamics of composite shells. *Archives of Computational Methods in Engineering* (Accepted).
16. Rao, C. R., & Mitra, S. K. (1971). Generalized inverse of a matrix and its applications. In *Proceedings of the Sixth Berkeley Symposium on Mathematical Statistics and Probability*.
17. Li, G., & Rabitz, H. (2010). D-MORPH regression: Application to modeling with unknown parameters more than observation data. *Journal of Mathematical Chemistry, 48*(4), 1010–1035.
18. Li, G., Rey-de-Castro, R., & Rabitz, H. (2012). D-MORPH regression for modeling with fewer unknown parameters than observation data. *Journal of Mathematical Chemistry, 50*(7), 1747–1764.
19. Chakraborty, S., & Chowdhury, R. (2015). Multivariate function approximations using D-MORPH algorithm. *Applied Mathematical Modelling, 39*(23–24), 7155–7180.
20. Chakraborty, S., & Chowdhury, R. (2015). Nonlinear stochastic dynamic analysis—A meta modelling based approach. In *1st International Conference on Uncertainty Quantification in Computational Sciences and Engineering*. Greece: Crete Island.
21. Li, G., & Rabitz, H. (2012). General formulation of HDMR component functions with independent and correlated variables. *Journal of Mathematical Chemistry, 50*(1), 99–130.
22. Kaymaz, I. (2005). Application of Kriging method to structural reliability problems. *Structural Safety, 27*(2), 133–151.
23. Lee, T. H., & Jung, J. J. (2008). A sampling technique enhancing accuracy and efficiency of metamodel-based RBDO: Constraint boundary sampling. *Computers and Structures, 86*(13–14), 1463–1476.

Numerical Modeling of Spalling in High Strength Concrete at High Temperature

Patnayakuni Ravi Prakash and Gaurav Srivastava

Abstract High strength concrete (HSC) is predominantly used in high-rise reinforced concrete buildings. While excellent from strength point of view at room temperature, HSC is known to be prone to spalling, when exposed to high temperatures (e.g., in case of a fire). Fire resistance evaluated from building codes (CEN in Design of concrete structures. Part 1–2: general rules—structural fire design, Eurocode-2, Brussels, 2004; Bureau of Indian Standards in Indian code of practice for fire safety of buildings (General): details of construction code of practice. IS-1641, New Delhi, 1989) [1, 2] and simulation-based studies typically does not consider the effects of spalling. To alleviate these difficulties, a 2-D hydrothermal model has been developed for predicting the extent of spalling in HSC. The numerical model evaluates pore pressure inside the concrete as a function of time using the laws of thermodynamics. Spalling is said to occur when the pore pressure built-up within concrete exceeds its tensile strength. The model depends on several parameters such as permeability, initial moisture content, and thermomechanical properties of concrete. All of these parameters are considered by the model through a two-way coupling between the pore pressure analysis and thermal analysis, both implemented using the finite element method. Validity of the numerical example is established by comparing the spalling predictions obtained from the numerical model against standard experiments available in the literature. Parametric studies have also been performed using the numerical model to quantify the effects of model parameters such as permeability, grade of concrete, and type of fire scenario on the prediction of spalling.

Keywords NSC · HSC · Spalling · Permeability · Fire response

P. R. Prakash · G. Srivastava (✉)
Department of Civil Engineering, IIT Gandhinagar, Gandhinagar, India
e-mail: gauravs@iitgn.ac.in

P. R. Prakash
e-mail: patnayakuni.prakash@iitgn.ac.in

A. Rama Mohan Rao and K. Ramanjaneyulu (eds.), *Recent Advances in Structural Engineering, Volume 1*, Lecture Notes in Civil Engineering 11,
https://doi.org/10.1007/978-981-13-0362-3_34

1 Introduction

Reinforced concrete structures are extensively utilized as load-bearing mechanisms in residential, office, and industrial buildings. In addition to the usual service loads, these buildings carry the risk of being exposed to fire during their design life. Hence, quantification of their response against fire is vital. In recent years, use of high strength concrete in structural engineering applications like high-rise buildings, bridges, etc. has increased significantly. This is mainly due to economic and architectural advantages associated with HSC compared to conventional normal strength concrete (NSC). For performance-based design of these HSC structures, understanding the behavior of HSC at elevated temperatures is vital. Concrete structures, in general, exhibit good fire resistance compared to steel and timber structures. However, they are prone to explosive spalling which enhances the risk of structural collapse during fire. Previous studies on spalling in concrete structures [3, 4] revealed that HSC structures are more prone to spalling compared to NSC when subjected to rapid heating. HSC is characterized by high density, high strength, and low permeability and hence, it is more susceptible to spalling at elevated temperatures. Spalling occurs due to the accumulation of built-up pore pressure inside concrete. Low permeability and high density of HSC can cause internal pore pressures of as high as 6 MPa. Such internal vapor pressures can be critical for materials like concrete which possess low tensile strength and eventually result in explosive spalling at elevated temperatures.

Fire-induced spalling is a key physical behavior which needs to be incorporated in coupled thermomechanical analysis of concrete structures, especially for HSC, primarily because spalling can cause significant reduction in the cross section/thickness of the structural member which, in turn, accelerates the heat transfer to the embedded steel rebars and eventually affects the load carrying capacity of the structure. Experimental investigations as reported in the literature [3, 4] infer contradictory picture of spalling mechanism as well as spalling occurrences. Many research investigations reported explosive spalling during laboratory fire tests as well as full-scale tests on HSC structures [5]. At the same time, there were tests on HSC where almost no spalling has been reported [5]. The main reason for this phenomenon is that spalling is dependent on several interdependent physical parameters. In terms of spalling mechanisms, in-built pore pressure based and thermal dilatation based spalling mechanisms are most widely accepted. Present study focuses mainly on in-built pore pressure based spalling mechanism.

A very limited number of numerical models [6, 7] are available to quantify the pore pressure across a concrete section at elevated temperatures. Aforementioned numerical models perform combined 3-D heat and mass transfer analysis in concrete structures and are computationally intensive. Also, to accurately capture the spalling phenomenon using the aforementioned numerical models, input parameters like mass of liquid, mass of vapor, and material permeability tensor coupled with material stiffness tensor should be known at elevated temperatures. However, some of these parameters are not accurately defined even at room temperatures.

To alleviate these difficulties, few researchers suggested simplified analytical methods to predict spalling in concrete structures. Kodur et al. [8] proposed temperature-based spalling criteria. Their spalling criteria had been developed from the experimental observations of full-scale fire tests on HSC structures. However, these simplified analytical methods cannot be relied upon due to the uncertainties pertaining in spalling monitoring system. Also, the effects of parameters like grade of concrete, permeability, porosity, etc. are not accounted for in the aforementioned analytical method. In terms of codal provisions, very few guidelines are available regarding spalling in concrete structures without actually integrating it into the design philosophy. Eurocode-2 [1] provides simplified guidelines to prevent spalling in concrete structures. It suggests that concrete structures with moisture content less than 3% are not prone to spalling. However, it ignores the effects of permeability and strength of concrete which can accelerate spalling phenomenon even at low moisture contents. ACI 216.1 [9] suggests that spalling can be avoided with the aid of polypropylene fibers in the design mix. Abovementioned guidelines are developed on the basis of laboratory tests on small samples without accounting for built-up pore pressure due to moisture migration. Also, abovementioned laboratory test uses standard fire curves and does not account for design fire curves. The lack of reasonably accurate spalling prediction framework is the principle reason for ignoring spalling effects in building codes as well as in typical thermomechanical analysis frameworks. Hence, a reasonably accurate, computationally efficient framework is required for spalling prediction in concrete structures.

Pore pressure inside concrete sections can be computed in a computationally efficient manner using a pore pressure analysis coupled to a heat transfer analysis. The hydrothermal model is essentially derived from the laws of thermodynamics and structural mechanics. Dwaikat and Kodur [10] developed a 1-D hydrothermal model for pore pressure computations inside concrete structures utilizing laws of thermodynamics and validated against standard experiments. However, parameters like critical state of water and permeability of concrete were not addressed properly. In the present study, utilizing the laws of thermodynamics, a-2D coupled heat transfer pore pressure analysis framework is developed for spalling prediction in concrete structures. Due consideration is given to critical state of water while computing the Bazant's isotherms [11], which are required for pore pressure analysis. In case of permeability, a non-uniform permeability suggested by Gawin et al. [6] is followed for realistic structures utilizing a thermomechanical solver developed by Prakash and Gaurav [12]. Utilizing the developed framework, validation studies are performed for standard experiments available in the literature. Also, parametric studies are demonstrated to quantify the effect of permeability and grade of concrete on the extent of explosive spalling in HSC structures.

2 Thermal Analysis

Thermal analysis is performed for concrete cross sections by solving the transient heat conduction equation in 2D given by

$$k\nabla^2 T + Q = \rho c \frac{\partial T}{\partial t}, \tag{1}$$

where k is the coefficient of thermal conductivity, c is the specific heat, and ρ is the mass density of the material; Q is the heat source, t represents time, and T represents temperature. The effects of convection and radiation have been considered through boundary conditions given by

$$k\nabla T \cdot \mathbf{n} = h(T - T_\infty), \tag{2}$$

where T_∞ is the ambient temperature, h is the temperature-dependent combined convective–radiative heat transfer coefficient, and $\mathbf{n}$ is the vector normal to the boundary. The fire exposure of concrete structures is considered by linking T_∞ with the fire temperature. For instance, to subject a structural member to the standard fire ASTME119 [13], T_∞ is prescribed as

$$T_\infty = T_0 + 750(1 - \exp(-3.9953\sqrt{t_h})) + 170.41\sqrt{t_h}, \tag{3}$$

where T_0 is the initial ambient temperature and t_h is time in hours. Equation (2) is discretized in space using four-noded bilinear quad elements and is solved using the Galerkin method [14]. Upon spatial discretization of Eq. (2), a first-order nonlinear ordinary differential equation in time is obtained as

$$\mathbf{M}_\mathrm{T}\dot{\mathbf{T}} + \mathbf{K}_\mathrm{T}\mathbf{T} = \mathbf{F}, \tag{4}$$

where $\mathbf{M}_\mathrm{T}$ is the heat capacity matrix, $\mathbf{K}_\mathrm{T}$ is the conductivity matrix, and $\mathbf{F}$ is the heat flux vector. The generalized trapezoidal scheme in time domain is applied to Eq. (4) which yields a system of nonlinear algebraic equations given by

$$\begin{aligned}(\mathbf{M}_\mathrm{T} + \tau\beta\mathbf{K}_\mathrm{T})\mathbf{T}_{\mathrm{n}+1} = {} & (\mathbf{M}_\mathrm{T} - \tau(1-\beta)\mathbf{K}_\mathrm{T})\mathbf{T}_\mathrm{n} \\ & + \tau(\beta\mathbf{F}_{\mathrm{n}+1} - (1-\beta)\mathbf{F}_\mathrm{n}),\end{aligned} \tag{5}$$

where τ is the time step, β is a constant between 0 and 1 ($\beta \geq 0.5$ for unconditional stability), and the subscripts n or $n + 1$ represent functions being evaluated at times t_n or t_{n+1}, respectively. Equation (5) is highly nonlinear due to temperature-dependent material properties as well as the convective–radiative boundary conditions and is solved iteratively using the Newton–Raphson (NR) method. The NR residual Rs_{n+1} at a given time t_{n+1} is defined from Eq. (5) and the iterations are continued until the residual reaches a specified relative tolerance of 10^{-4}.

3 Pore Pressure Analysis

To quantify the extent of spalling in concrete structures, a 2-D two-way coupled pore pressure and heat transfer analysis needs to be performed. Two-way coupling between thermal and pore pressure analysis is required to cater for cross-sectional reduction due to spalling and is accounted for in the subsequent heat transfer analysis. In the present study, the following assumptions are considered while performing the pore pressure analysis.

- Concrete is assumed to be an isotropic continuum medium.
- Water vapor is treated as an ideal gas with due consideration to the critical state of water in the numerical model.
- Mass transport of liquid water is ignored as permeability of liquid water in concrete is much smaller compared to that of water vapor.
- Mass transport of water vapor through concrete is modeled using Darcy's law.
- Spalling is assumed to occur when the built-up pore pressure exceeds the temperature-dependent tensile strength of concrete.

Based on the abovementioned assumptions, 2-D pore pressure inside concrete is modeled by

$$k_{\mathrm{p}}\nabla^2 P_{\mathrm{v}} + Q_{\mathrm{p}} = A\frac{\partial P_{\mathrm{v}}}{\partial t}, \tag{6}$$

where $k_{\mathrm{p}} = m_{\mathrm{v}}\frac{\kappa_{\mathrm{t}}}{\mu}$, $A = \left[\left(1 - \frac{m_{\mathrm{v}}}{V_{\mathrm{v}}\rho_{\mathrm{l}}}\right)\frac{dm_{\mathrm{l}}}{dP_{\mathrm{v}}} + \frac{V_{\mathrm{v}}\zeta}{RT}\right]$, P_{v} is the pore pressure, μ is the coefficient of dynamic viscosity, m_{v} is the mass of water vapor, V_{v} is the volume of water vapor, ρ_{l} is the density of liquid water, ζ is the molar mass of water, R is the ideal gas constant, κ_{t} is the coefficient of intrinsic permeability, and Q_{p} is the mass flow rate of water vapor computed using Bazant's isotherms and can be found in [10, 11]. The initial condition for above vapor diffusion model is given by

$$P_{\mathrm{vo}} = R_{\mathrm{ho}}P_{\mathrm{so}} \tag{7}$$

where P_{vo} is the initial pore pressure in concrete, R_{ho} is the initial relative humidity in concrete, and P_{so} is the initial saturation pressure. Equation (6) is discretized in spatial domain using four-noded bilinear quad elements and is solved using the Galerkin method [14]. Upon spatial discretization, a first-order nonlinear ordinary differential equation in time is obtained as

$$\mathbf{A}_{\mathrm{P}}\dot{\mathbf{P}}_{\mathrm{V}} + \mathbf{K}_{\mathrm{P}}\mathbf{P}_{\mathrm{V}} = \mathbf{F}_{\mathrm{P}}. \tag{8}$$

Furthermore, a generalized trapezoidal scheme is applied to Eq. (8) and series of nonlinear algebraic equations are obtained and are solved iteratively using NR method as discussed in the thermal analysis. Spalling is said to occur in an element when the built-up pore pressure exceeds temperature-dependent tensile strength of

concrete ($\eta.P_v \geq f_T^{'}$), where η is the porosity of concrete and $f_T^{'}$ is the temperature-dependent tensile strength of concrete and is taken from constitutive relationship proposed by Rots et al. [15].

4 Numerical Examples

This section illustrates validation studies on spalling in HSC structures. For validation studies, the following examples are considered.

- HSC block exposed to fire and
- HSC concrete beam exposed to fire.

4.1 HSC Block Subjected to Fire

An HSC block shown in Fig. 1 with specifications in Table 1 is subjected to ASTM-E1529 fire exposure. Bilodeu et al. [16] investigated the experimental spalling response of aforementioned HSC block (Fig. 2) exposed to a 2 h ASTM-E1529 [6] fire. Reduced block thickness due to spalling had been measured only at the end of experiment. 2-D hydrothermal analysis is performed for this HSC

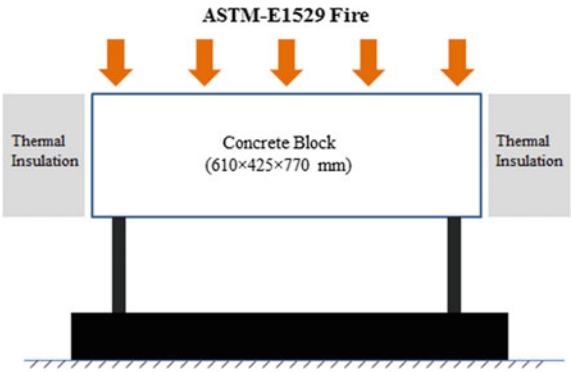

Fig. 1 HSC block subjected to ASTM-E1529 fire

Table 1 Specifications of HSC block [16]

Physical property	Value
κ_t (m^2)	1×10^{-18}
ρ_c (kg/m^3)	461
V_{so} (m^3)	0.96
f_{ck} (MPa)	65
R_h (%)	86

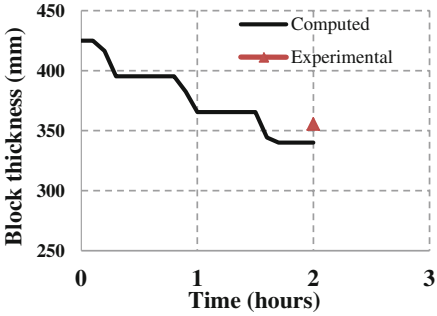

Fig. 2 Reduction in block thickness due to spalling

block and temperature-dependent spalling prediction is obtained and compared against experimental counterpart as shown in Fig. 2. The developed numerical model is able to predict the reduction in the thickness of the block due to spalling with reasonable accuracy.

4.2 HSC Beam Exposed to Fire

An HSC beam with specifications in Table 2 is considered. Dwaikat and Kodur [17] experimentally characterized the spalling response history of this beam which is subjected to a long-term design fire as shown in Fig. 3.

In case of HSC structures subjected to flexure, initial intrinsic permeability is non-uniform depending upon the extent of mechanical damage in compression and tension regimes. Gawin et al. [6] addressed this issue by proposing a modification factor which is a function of damage in concrete. In the present study, mechanical damage in concrete is quantified from the thermomechanical analysis framework developed by Prakash and Srivastava [12] and is utilized in permeability computations. Also, spalling is assumed to occur outside of the confinement as observed from many full-scale fire tests. Incorporating abovementioned phenomena, 2-D hydrothermal analysis is performed for the HSC beam under consideration. Volume of concrete spalled is compared against experimental observations as shown in Fig. 4. The spalling response history computed by the model shows good

Table 2 Specifications of concrete beam [17]

Physical property	Value
Dimensions (mm)	254 × 406
κ_t (m^2)	1×10^{-18}
ρ_c (kg/m^3)	513
V_{so} (m^3)	0.929
f_{ck} (MPa)	93.3
R_h (%)	86
Clear cover (mm)	38

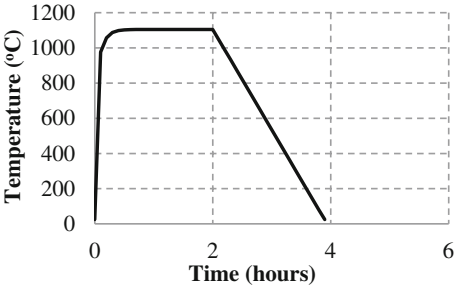

Fig. 3 Long-term design fire for HSC beam

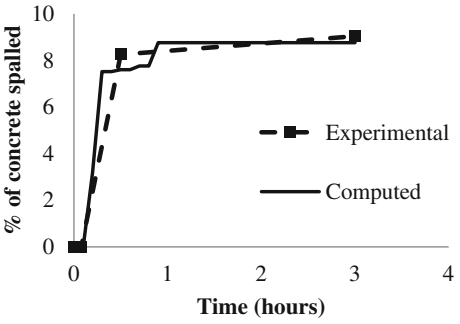

Fig. 4 Comparison of experimental and computed spalling response

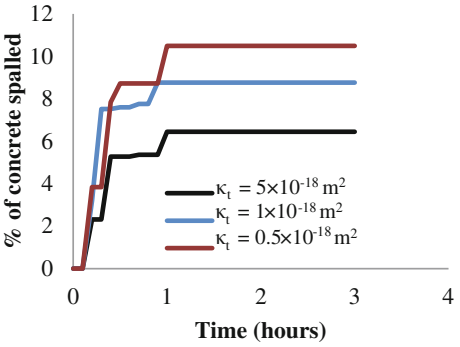

Fig. 5 Effect of intrinsic permeability on spalling response

agreement with the experimental observations. Further, parametric studies are performed to study the effects of intrinsic permeability and grade of concrete on the response of this beam, as shown in Figs. 5 and 6. Parametric studies indicate that intrinsic permeability and grade of concrete have a significant effect on spalling response of concrete structures under fire.

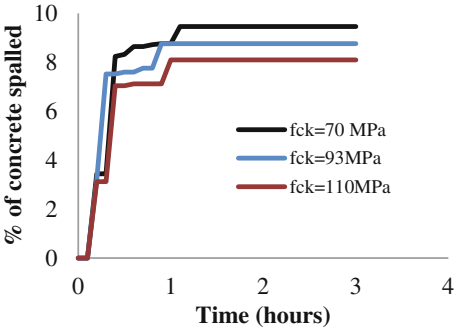

Fig. 6 Effect of grade of concrete on spalling response

5 Conclusions

A simplified framework for the prediction of the spalling response of HSC structures at elevated temperatures has been developed. The developed framework considered two-way coupling between thermal and pore pressure analysis with temperature-dependent thermal and mechanical properties. The accuracy of the developed framework was demonstrated through two numerical examples. The numerical examples indicate that developed framework is reasonably accurate for spalling prediction in HSC structures. Furthermore, parametric studies were performed to study the effect of permeability and grade of concrete on spalling in HSC structures. Parametric studies showed that permeability of concrete has significant effect on the extent of concrete spalling. Higher permeability leads to lower spalling and vice versa. Also, higher tensile strength of concrete leads to lower spalling and vice versa.

References

1. CEN (European committee for Standardization). (2004). *Design of concrete structures. Part 1–2: General rules—Structural fire design.* Brussels: Eurocode-2.
2. Bureau of Indian Standards. (1989). *Indian code of practice for fire safety of buildings (General): Details of construction-code of practice.* New Delhi: IS-1641.
3. Phan, L. T. (1996). *Fire performance of high-strength concrete: A report of the state-of-the art*. US Department of Commerce, Technology Administration, National Institute of Standards and Technology, Office of Applied Economics, Building and Fire Research Laboratory.
4. Diederichs, U., Jumppanen, U. M., & Schneider, U. (1995). High temperature properties and spalling behaviour of high strength concrete. In *Proceedings of Fourth Weimar Workshop on High Performance Concrete* (pp. 219–235). Germany: HAB Weimar.
5. Kodur, V. K. R. (2000). Spalling in high strength concrete exposed to fire—Concerns, causes, critical parameters and cures. In *Proceedings, ASCE Structures Congress* (pp. 1–8), Philadelphia, PA, USA.

6. Gawin, D., Majorana, C. E., & Schrefler, B. A. (1999). Numerical analysis of hygro-thermal behaviour and damage of concrete at high temperature. *Mechanics of Cohesive-fictional Materials, 4*(1), 37–74.
7. Gawin, D., Pesavento, F., & Schrefler, B. A. (2006). Towards prediction of the thermal spalling risk through a multi-phase porous media model of concrete. *Computer Methods in Applied Mechanics and Engineering, 195*(41), 5707–5729.
8. Kodur, V. K. R., Wang, T. C., & Cheng, F. P. (2004). Predicting the fire resistance behaviour of high strength concrete columns. *Cement and Concrete Composites, 26*(2), 141–153.
9. ACI 216.1 M-07. (2007). *Standard method for determining fire resistance of concrete and masonry construction assemblies*. Detroit, USA: American Concrete Institute.
10. Dwaikat, M. B., & Kodur, V. K. R. (2009). Hydrothermal model for predicting fire-induced spalling in concrete structural systems. *Fire Safety Journal, 44*(3), 425–434.
11. Bazant, Z. P., & Thonguthai, W. (1978). Pore pressure and drying of concrete at high temperature. *Journal of Engineering Mechanics, 104*(5), 1059–1079.
12. Prakash, P. R., & Srivastava, G. (2015). Development of a matrix method based framework for the thermo-mechanical analysis of RCC frames. In *Response of Structures Under Extreme Loading: Proceedings of PROTECT-2015*, pp. 972–980.
13. ASTM. (2001). *Standard methods of fire test of building construction and materials, Test Method.* West Conshohocken: American Society for Testing and Materials.
14. Cook, R. D., Malkus, D. S., Plesha, M. E., & Witt, R. J. (2007). *Concepts and applications of finite element analysis*. Berlin: Wiley.
15. Rots J. G., Kusters, G. M. A., & Blaauwendraad, J. (1984). The need for fracture mechanics options in finite element models for concrete structures. In *International Conference on Computer Aided Analysis and Design of Concrete Structures*, pp. 19–32.
16. Bilodeau, A., Kodur, V. K. R., & Hoff, G. C. (2004). Optimization of the type and amount of polypropylene fibres for preventing the spalling of lightweight concrete subjected to hydrocarbon fire. *Cement and Concrete Composites, 26*(2), 163–174.
17. Dwaikat, M. B., & Kodur, V. K. R. (2010). Fire induced spalling in high strength concrete beams. *Fire Technology, 46*(1), 251–274.

A Study on Finite Element Modelling of Acoustic Emission Waveforms in Composite and Sandwich Plates

Sanjay Sengupta, Pijush Topdar and Aloke Kumar Datta

Abstract Acoustic Emission (AE) technique is non-destructive Structural Health Monitoring (SHM) technique which has the potential to detect internal damages in real time. Literature reveals that researchers have used three-dimensional (3d) Finite Element Method (FEM) to predict AE waveforms in isotropic and single-layer anisotropic plates. However, the study to predict acoustic emission waveforms using FEM in layered composites and sandwich plates is limited in literature. Modelling of such layered plates is challenging as material properties may vary from one layer to another across the plate thickness. In this study, an effort has been made for two-dimensional finite element modelling for predicting AE waveforms in layered composites and sandwich plates using a generalised refined plate theory modelling. Numerical examples are first solved for isotropic and anisotropic plates and validated with the results obtained from 3d FEM. New results are presented for multilayered composites and sandwich plates.

Keywords Acoustic emission · Finite element method · Structural health monitoring · Layered composites · Sandwich plates

1 Introduction

Acoustic Emission (AE) technique is non-destructive Structural Health Monitoring (SHM) technique which has the potential to detect internal damages in real time. Study on AE waveforms using Finite Element Method (FEM) for structural

S. Sengupta
Dr. B.C Roy Engineering College, Durgapur 713206, India
e-mail: sanswati2004@gmail.com

P. Topdar · A. K. Datta (✉)
National Institute of Technology, Durgapur 713209, India
e-mail: dattarec@yahoo.com

P. Topdar
e-mail: topdar72@yahoo.co.uk

A. Rama Mohan Rao and K. Ramanjaneyulu (eds.), *Recent Advances in Structural Engineering, Volume 1*, Lecture Notes in Civil Engineering 11,
https://doi.org/10.1007/978-981-13-0362-3_35

investigations is considered to be an important area of research [1]. Researchers have used three-dimensional (3d) Dynamic Finite Element Method (DFEM) to predict acoustic emission waveforms in isotropic and anisotropic plates [2, 3]. In carbon fibre-reinforced plastic undamaged and damaged specimens, the simulation of acoustic emission was studied through FEM by researchers [4, 5]. Literature reveals that FEM is used by the researchers to study the acoustic waveforms generated by glass capillary fracture for calibration of sensors [6, 7]. To model AE signal propagation in an isotropic plate with an attached waveguide, FEM is used recently [8]. In most of these studies using FEM, researchers have used either isotropic plates or single-layer anisotropic plates. However, the study to predict acoustic emission waveforms using FEM in layered composites and sandwich plates is limited in literature. Modelling of such layered plates is challenging as material properties may vary from one layer to another across the plate thickness. Moreover, most studies focus on circular plates or plates with infinite geometry, which are not supported at the extreme outer boundary and primarily the displacements in the in-plane direction, i.e. extensional/compressional modes are considered using some wave propagation-based approach. However, the geometries for the practical structure of interests for AE monitoring are not necessarily infinite in lateral extent; instead, they are often supported at their ends. Very often structures like plates are supported in such a way that they are more sensitive in the transverse/out-of-plane direction and such out-of-plane displacement is actually equivalent to the flexural response. Thus, flexural mode is predominant in those cases and can be better predicted using vibration-based approach than the wave propagation-based approach. Therefore, in detecting, damage in layered composite/laminate prediction of flexural behaviour of any given structure can be useful. In this study, an effort has been made for two-dimensional finite element modelling for predicting AE waveforms in layered composites and sandwich plates using a generalised refined plate theory modelling. More emphasis is given to predicting the flexural waveforms. Numerical examples are first solved for isotropic and anisotropic plates. Results obtained for such plates using present study are compared with three-dimensional DFEM. In general, agreement between the two theoretical approaches is good. Moreover, the present two-dimensional approach is computationally more efficient than that of the three-dimensional approach. New results are presented for layered composites and sandwich plates using the present formulation.

2 Mathematical Formulation

In this study, a generalised Refined Plate Theory (RPT) as proposed by Cho and Parmerter [9] is used for modelling so that the transverse shear stress continuity at the interface of two consecutive layers is satisfied, which is very critical for laminated composite and sandwich plates. The 3d view of the plate is shown in Fig. 1. Displacements at the reference plane (midplane of the plate) along x-axis, y-axis and

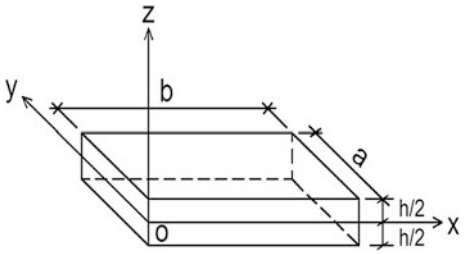

Fig. 1 3d view of plate along with axis system

z-axis are represented as u, v and w, respectively. The variation of in-plane displacements across the plate thickness is expressed as a combination of linearly varying zigzag component and a cubically varying continuous component. The transverse displacement is taken to be constant over the plate thickness. A rectangular higher order C^1 continuous element having four nodes at its four corners is used considering eight degrees of freedom $u, v, w, w_{,x}, w_{,y}, w_{,xy}, \gamma_x, \gamma_y$ at each node [10]. The field variables u, v, γ_x and γ_y are approximated by bi-linear interpolation functions, whereas the transverse displacement w is approximated by bi-cubic interpolation function.

The Hamilton's variation principle of dynamics is applied to get the equation of motion of the system. For an element, if $\{\delta\}$ is the nodal displacement vector, considering the effect of damping, the equation of motion for an element may be expressed as

$$[M_e]\left\{\ddot{\delta}\right\} + [C_e]\left\{\dot{\delta}\right\} + [K_e]\{\delta\} = \{R\} \tag{1}$$

The element level mass matrix $[M_e]$, damping matrix $[C_e]$ and stiffness matrix $[K_e]$ and load vector $\{R\}$ for all the elements can be computed and assembled together to form the system level mass matrix $[M]$, damping matrix $[C]$, stiffness matrix $[K]$ and load vector $\{F\}$ for the entire structure. The equation of motion for the system may be expressed as

$$[M]\left\{\ddot{\Delta}\right\} + [C]\left\{\dot{\Delta}\right\} + [K]\{\Delta\} = \{F\} \tag{2}$$

where $\{\Delta\}$ is the global displacement vector for the entire plate. The governing equation of dynamic response, i.e. Eq. (2), can be solved by direct time integration scheme following Newmark's β method, which is an explicit time integration technique [11].

3 Numerical Examples and Discussion

3.1 Preliminary Remarks

The implementation of the mathematical formulation as described above is done by solving numerical problems. In AE technique, structural damage is studied in real time. Signal generated due to damage developed is considered in the present modelling. However, signal corresponding to a particular damage and its identification is a grey area of research. Due to non-availability of exact signal corresponding to a particular type of damage in a structure, researcher normally adapts the signal generated by pencil lead break widely available in literature. Authors have tried to check the efficacy of the mathematical model in simulated environment. Thus, the damage/crack is simulated by a forcing function corresponding to a pencil lead break which can be considered to be an equivalent AE source [3]. The forcing function is considered to be a unit step function of duration 150 μs following Prosser et al. [3] for each problem. To obtain the flexural AE waveforms, the forcing function is applied out of the plane, i.e. in transverse direction of the plate in all cases. Rectangular plate geometry is used for all the problems with simple supported boundary condition along all the edges. This condition is implemented by making $u = w = w_{,x} = w_{,xy} = \gamma_x = 0$ along the boundary line parallel to x-axis and $u = w = w_{,y} = w_{,xy} = \gamma_y = 0$ along the boundary line parallel to y-axis. Displacement, velocity and acceleration at initial time were considered as zero. Damping is not considered. The time step used for solution using Newmark's β method is taken as 0.164 μs and the values of α and ψ are taken as 0.25 and 0.50, respectively.

3.2 Example 1

The present formulation is used to study an isotropic plate, made of aluminium, as studied by Prosser et al. [3] for validation purpose, before studying layered composites and sandwich plates. The dimensions of the plate along x- and y-direction are 0.508 and 0.381 m, respectively. The plate is 0.003175 m thick. The material properties are as follows:

Density	2770 kg/m^3
Young's Modulus	73×10^9 N/m^2
Poisson's Ratio	0.3

The plate is analysed in the present study (RPT). The x- and y-coordinates for the AE source are 0.254 and 0.127 m, respectively. The flexural waveform responses are obtained along y-direction at a distance of 0.0762 and 0.127 m from the source. Based on convergence study, the mesh size used is 40×30. The displacement responses at a distance 0.0762 m from source in the z-direction, i.e. the flexural

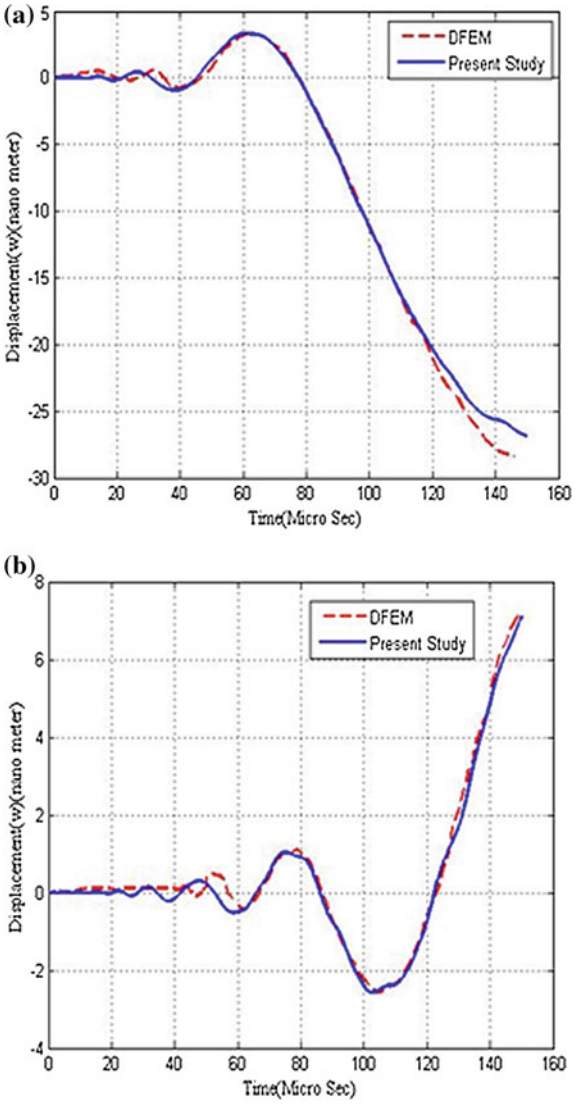

Fig. 2 Comparison of flexural waveform response for isotropic (aluminium) plate at propagation distance **a** 0.0762 m, **b** 0.127 m

mode is plotted for the present study, and obtained by Prosser et al. [3] from 3d FEM in Fig. 2a. The flexural waveform responses at a distance 0.127 m from source are presented in Fig. 2b. It is observed from Fig. 2a, b that the responses obtained by Prosser et al. [3] using 3d FEM and the present study (i.e. RPT) agree well. From the comparison, it can be inferred that for isotropic plates for predicting flexural AE waveforms, 2d FEM using RPT may be used effectively instead of 3d FEM. The computational efficiency for 2d FEM will be much higher than that of 3d FEM.

3.3 Example 2

In this example, the applicability of the present model for single-layered anisotropic plates is studied and validated with the available results of 3d FEM [10]. The plate is made of anisotropic material AS4/3502 graphite/epoxy. The dimensions of the plate along x- and y-direction are 0.254 and 0.1524 m, respectively. The plate is 0.00254 m thick. The x-axis is along the fibres and the y-axis is perpendicular to the fibres in the plane of the plate. The material is unidirectional and transversely isotropic.

The material properties are chosen as reported by Prosser et al. [3]:

Density : 1550 $\mathrm{kg/m^3}$
$C_{11} : 147.1 \times 10^9\ \mathrm{N/m^2}$ $C_{12} : 4.11 \times 10^9\ \mathrm{N/m^2}$
$C_{13} = C_{12}$
$C_{22} : 10.59 \times 10^9\ \mathrm{N/m^2}$ $C_{23} : 3.09 \times 10^9\ \mathrm{N/m^2}$
$C_{33} = C_{22}$
$C_{44} : 3.75 \times 10^9\ \mathrm{N/m^2}$ $C_{55} : 5.97 \times 10^9\ \mathrm{N/m^2}$
$C_{66} = C_{55}$.

The source is positioned at $x = 0.0508$ m and $y = 0.0762$ m. Based on convergence study, the mesh size used is 40×24. The responses are recorded along the fibre direction, i.e. along the x-direction at a distance of 0.0762 and 0.127 m from the source and are presented in Fig. 3a, b. It is observed that the AE flexural wave responses obtained using the present study and the study by Prosser et al. [3] using 3d FEM for the single-layer anisotropic material are in good agreement.

Some discrepancies observed at long times in the waveforms may be due to the differences in the contribution from reflections at the plate edges which has been taken care in the DFEM modelling. However, with the present model (RPT), the results obtained are found to be matching well with 3d FEM in the near field and shorter times, where the plate edge reflections do not have a major impact in the response.

3.4 Example 3

In the previous two examples, the present model is validated for isotropic and single-layered anisotropic material. In this example, the present model is used to further study the four-layer orthotropic plate [0/90/90/0] of graphite/epoxy. The plate dimension and material properties are same as in Example 2. The source is positioned at $x = 0.0508$ m and $y = 0.0762$ m. The flexural waveforms, i.e. out-of-plane displacement time history, are obtained using the present study at a distance of 0.0762 and 0.127 m from the source along the direction of the longer side of the plate, i.e. along the x-direction. The responses are presented in Fig. 4a, b, respectively. In this context, it can be mentioned that, in the present model (RPT),

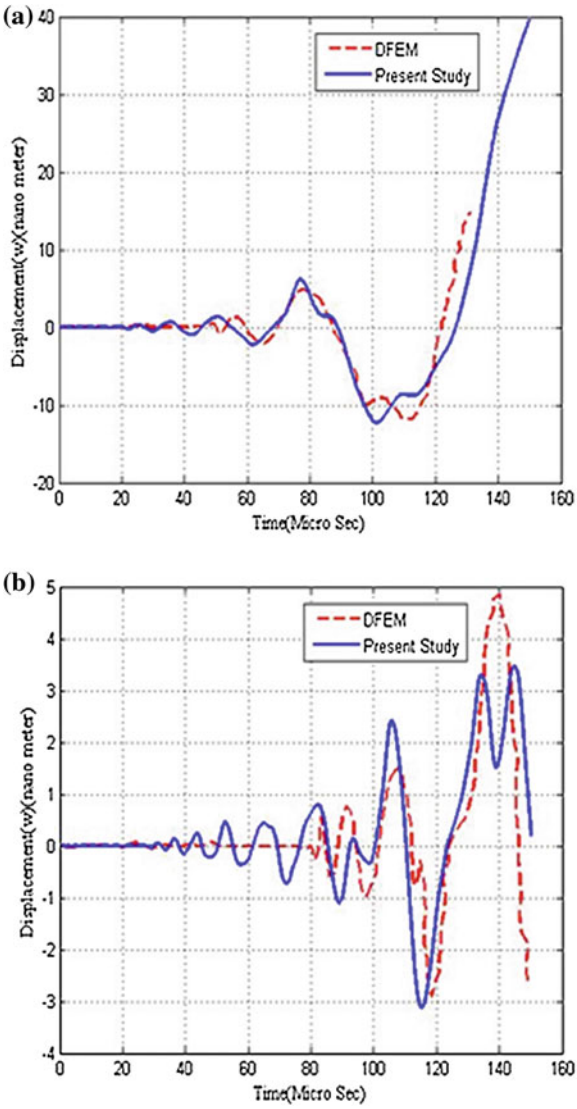

Fig. 3 Comparison of flexural waveform response for anisotropic (graphite/epoxy) material perpendicular to the fibre direction at propagation distance **a** 0.0762 m, **b** 0.127 m

the transverse shear stress continuity at the interface of two consecutive layers is considered, which is a very important consideration while modelling the composite plates for predicting flexural AE response which is not taken care of while modelling using 3d FEM [10]. Hence, it is expected that 2d model using RPT will predict the flexural AE responses in a better way for multilayered composites than that of the 3d FEM.

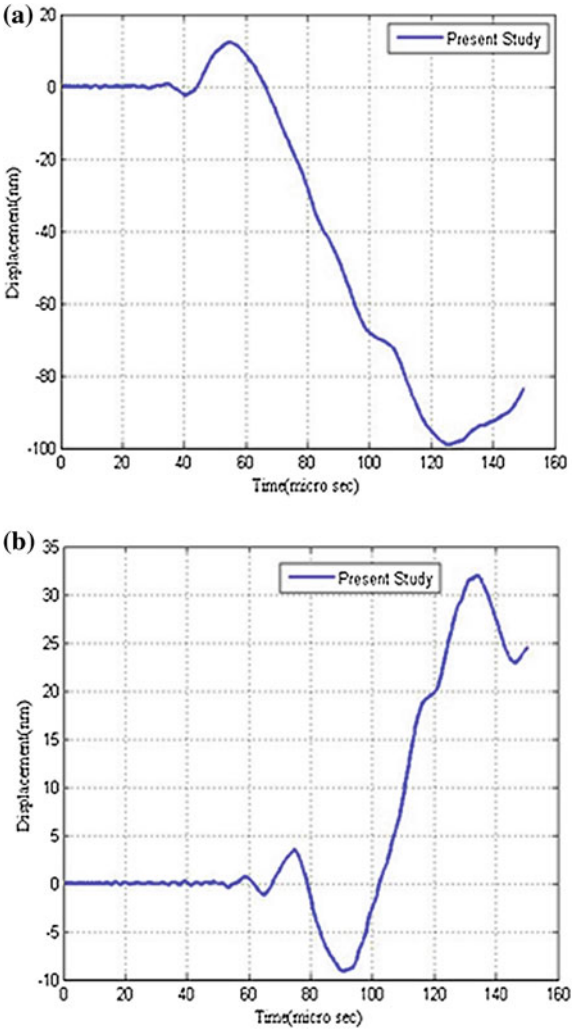

Fig. 4 Flexural waveform response for four-layer [0/90/90/0] (graphite/epoxy) material along the *x*-direction at propagation distance **a** 0.0762 m, **b** 0.127 m

3.5 Example 4

In this example, the present model is used to the flexural response of a sandwich plate due to out-of-plane AE source. For this, a rectangular sandwich composite plate [f(0/90)/c/f(90/0)] having core-to-face thickness ratio of 3 is considered. Each face is 0/90 Fibre-Reinforced Laminated Composite (FRLC). The dimension of the plate is considered to be same as in Example 2. The material properties used are after Kant et al. [12]:

For Face:
Density = 1580 kg/m^3
Young's modulus:
$E_1 = 1308 \times 1008$ N/m^2 $E_2 = 106.0 \times 10^{08}$ N/m^2 $E_3 = 106.0 \times 10^{08}$ N/m^2
Poisson's Ratio:
$v_{12} = 0.28$ $v_{13} = 0.28$ $v_{23} = 0.34$
Shear modulus:
$G_{23} = 39.0 \times 10^{08}$N/m^2 $G_{13} = 60.0 \times 10^{08}$ N/m^2
$G_{12} = 60.0 \times 10^{08}$ N/m^2
For Core:
Density = 100.9 kg/m^3
Young's Modulus:
$E_1 = 1.0 \times 10^{06}$ N/m^2 $E_2 = 1.0 \times 10^{06}$ N/m^2
$E_3 = 1.0 \times 10^{15}$ N/m^2
Poisson's Ratio:
$v_{12} = 0$ $v_{13} = 0$ $v_{23} = 0$
Shear modulus:
$G_{23} = 1.772 \times 10^{08}$ N/m^2 $G_{13} = 5.206 \times 10^{08}$ N/m^2
$G_{12} = 0.5 \times 10^{06}$ N/m^2

The source is positioned at x = 0.0508 m and y = 0.0762 m. The responses for different *a/h* ratios of 60, 30 and 15 are studied in this case at a distance of 0.0762 m from the source along the longer direction of the plate using the present study and are presented in Fig. 5a. Similar responses at a distance 0.127 m from the source are presented in Fig. 5b. Reason behind taking different thickness ratios is to check the effect of shear deformation in case of composite plates on total structural behaviour in flexural mode. Here, an attempt is made to develop a purely mathematical model which can later be verified with experimental observations. The basis of the mathematical model and mechanism of the plate consider the linear flexural behaviour as well as continuity of shear stress at the laminar interfaces. The results indicate that with the decrease in *a/h* ratio, i.e. with the increase in thickness of the plate, the flexural AE responses are reducing. Thus, using the present model, the responses for thin to moderately thick sandwich plates can be predicted well. However, deviations are observed in the flexural response obtained after some time step for different *a/h* ratios. This may be linked to the typical mechanism of the structure under consideration. Further investigation in this regard is under way for establishment of the same in the proposed mathematical model.

In this context, it can be mentioned that as sandwich plates are made of low strength core and high strength laminated stiff face sheets; the material properties of the plate under consideration are varying widely between consecutive layers. In such cases, modelling of transverse shear stress continuity at the layer interfaces becomes very critical for realistically predicting the flexural AE response.

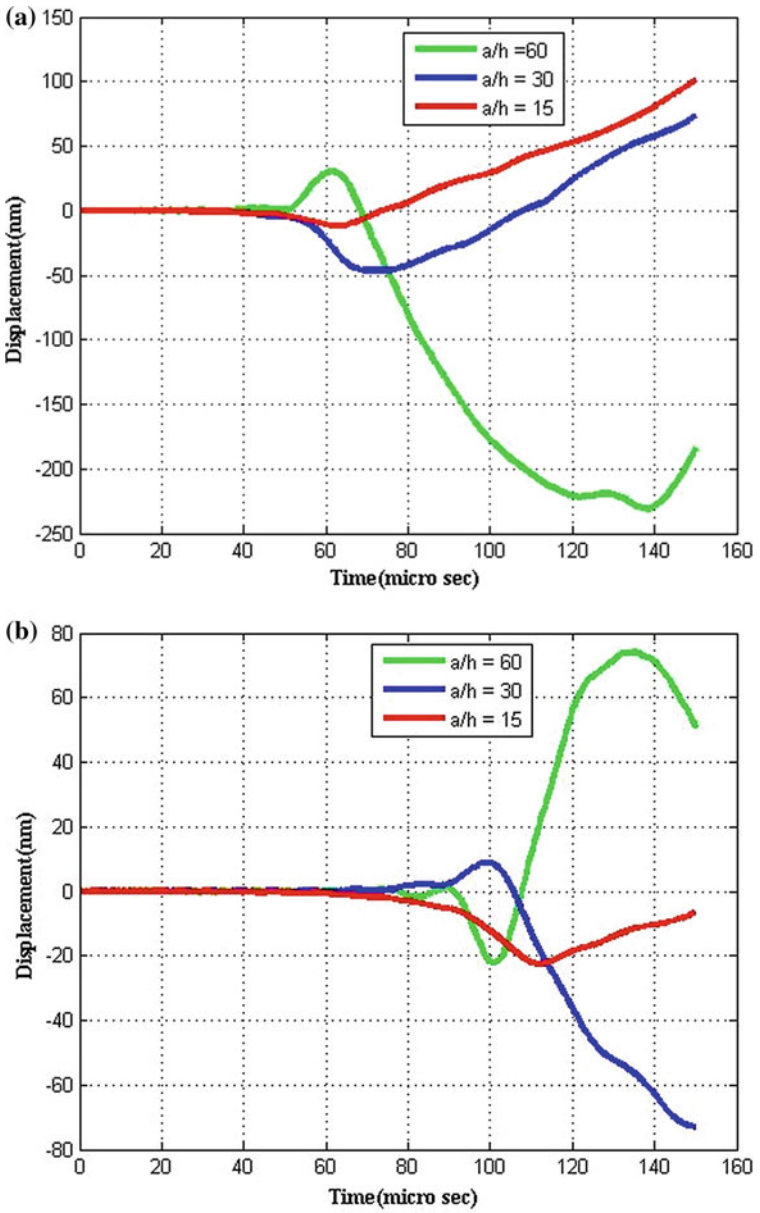

Fig. 5 Comparison of flexural waveform response for sandwich plate [f(0/90)/c/f(90/0)] for different *a*/*h* ratios along the *x*-direction at propagation distance **a** 0.0762 m, **b** 0.127 m

The present model (RPT) takes care of this requirement. However, the results predicted by the present study, for sandwich plates, may be used for validation with experimental results.

4 Concluding Remarks

In this paper, multilayered composite and sandwich plates under simulated out-of-plane AE source are studied for predicting flexural waveforms. An RPT is used for modelling. The model is highly computationally efficient and comparable with the 3d FEM as proposed by the researchers earlier. Moreover, it is very general in nature and captures the variation in material properties of multilayered plates. A C^1 continuous four-node rectangular element is used for FE modelling and implementations of RPT. Numerical examples are solved by this finite element model for different types of plate. It is observed that the present model can predict flexural wave modes due to AE source for thin to moderately thick isotropic, anisotropic, layered orthotropic, FRLC and sandwich plates realistically. The results from the present study may be used as standard solutions for future research in the absence of experimental results of FRLC and sandwich plates for predicting flexural AE waveforms. The in-plane (i.e. non-flexural) responses due to out-of-plane excitations are found to be very feeble and hence are not included in the results. Using the proposed model, the effect of extensional mode is yet to be studied.

References

1. Sengupta, S., Datta, A. K., & Topdar, P. (2015). Structural damage localisation by acoustic emission technique: A state of the art review. *Latin American Journal of Solids and Structures, 12,* 1565–1582.
2. Hamstad, M. A., Gary, J., & O'Gallagher, A. (1996). Far-field acoustic emission waves by three-dimensional finite element modeling of pencil breaks on a thick plate. *Journal of Acoustic Emission, 14*(2), 103–114.
3. Prosser, W. H., Hamstad, M. A., Gary, J., & O'Gallagher, A. (1999). Finite element and plate theory modeling of acoustic emission waveforms. *Journal of Nondestructive Evaluation, 18* (3), 83–90.
4. Sause, M. G. R., & Horn, S. (2010). Simulation of acoustic emission in planar carbon fiber reinforced plastic specimens. *Journal of Nondestructive Evaluation, 29,* 123–142.
5. Sause, M. G. R. (2013). Acoustic emission signal propagation in damaged composite structures. *Journal of Acoustic Emission, 31,* 1–18.
6. Burks, B. (2011). Re-examination of NIST acoustic emission sensor calibration: Part I—Modeling the loading from glass capillary fracture. *Journal of Acoustic Emission, 29,* 167–174.
7. Hamstad, M. A. (2011). Re-examination of NIST acoustic emission absolute sensor calibration: Part II—Finite element modeling of acoustic emission signal from glass capillary fracture. *Journal of Acoustic Emission, 29,* 175–185.

8. Zelenyak, A. M., Hamstad, M. A., & Sause, M. G. R. (2015). Modeling of acoustic emission signal propagation in waveguides. *Sensors, 15,* 11805–11822.
9. Cho, M., & Parmerter, R. R. (1993). Efficient higher order plate theory for general lamination configuration. *AIAA Journal, 31*(7), 1299–1308.
10. Topdar, P., Sheikh, A. H., & Dhang, N. (2007). Vibration characteristics of composites/ sandwich laminates with piezoelectric layers using a refined hybrid plate model. *International Journal of Mechanical Sciences, 49,* 1193–1203.
11. Bathe, K. J. (1996). *Finite Element Procedures*. Prentice Hall.
12. Kant, T., Varaiya, J. H., & Arora, C. P. (1990). Finite element transient analysis of composite and sandwich plates based on a refined theory and implicit time integration schemes. *Computers & Structures, 36*(3), 401–420.

HDMR-Based Bayesian Structural System Identification

O. A. Shereena and B. Nageswara Rao

Abstract This paper presents a method for faster identification of structural systems within a Bayesian framework with the use of High-Dimensional Model Representations (HDMR). For system identification problems solved within Bayesian framework, the intractable multidimensional integrals involved always pose a problem. To address this issue, the multidimensional integrands are expanded approximately by HDMR, an exact hierarchical representation for the multivariable functions, thereby significantly reducing the computational expenditure and ensuring the applicability of the procedure to systems of infinite dimensionality. The proposed method combines HDMR with Bayesian inference and follows an iterative procedure for convergence. In the present study, a stochastic plane strain field and a single degree of freedom system are analyzed. The results obtained are compared with the estimates from Extended Kalman Filter. In future, the proposed method will be tested on structural identification problems involving nonlinearity, non-Gaussianity, and high dimensionality.

Keywords High-Dimensional Model Representation · Structural identification Bayesian inference

1 Introduction

Structural system identification techniques are of particular interest because of its potential use in structural health monitoring, damage detection, etc. [1–3]. This requires the structural parameters, such as vibration frequencies, damping ratios, and stiffness to be identified in real time. Starting from the method of least squares,

O. A. Shereena · B. Nageswara Rao (✉)
Structural Engineering Division, Department of Civil Engineering,
Indian Institute of Technology Madras, Chennai 600036, Tamil Nadu, India
e-mail: bnrao@iitm.ac.in

O. A. Shereena
e-mail: ce14d020@smail.iitm.ac.in

A. Rama Mohan Rao and K. Ramanjaneyulu (eds.), *Recent Advances in Structural Engineering, Volume 1*, Lecture Notes in Civil Engineering 11,
https://doi.org/10.1007/978-981-13-0362-3_36

Kalman Filter (KF) and its variants, sampling-based techniques, such as Monte Carlo methods and particle filters have been adopted for the same from time to time for different types of challenges with consistent improvements on a variety of aspects, say nonlinear, non-Gaussian, and high-dimensional systems.

Extended Kalman Filter (EKF) is a modification over KF to accommodate nonlinearity of systems. EKF linearizes the nonlinear relations by Taylor series expansions and proceeds in a similar manner as does KF. Linearization leads to significant bias and convergence issues as the number of variables increases. Further demand of avoiding the calculation of Jacobian matrices, all these together led to the development of Unscented Kalman Filter (UKF). This technique employs a set of sigma points and performs an unscented transformation to estimate the mean and variance of the state variables and system parameters. Additionally, there are various Gaussian filters too.

The basic idea behind these approaches is Bayes' theorem. Mathematical representation of the theorem contains multidimensional integrals. Computation of these integrals is quite difficult. Hence, the above-cited methods are developed, avoiding the need for computation of these multifold integrals, and are in wide and efficient use for the appropriate applications. Here, we attempt to evaluate the high-dimensional integrals with the help of High-Dimensional Model Representations (HDMR) [4–7] to proceed through the Bayes' theorem combined with the basic concepts of probability and estimation. This attempt is done with an intention of employing this method for high-dimensional nonlinear dynamic systems in future.

2 Bayesian Inference with HDMR

Bayes' theorem helps to predict the posterior distribution, combining the available observation data and the prior distribution. This relation contains a multidimensional integral in the denominator as shown in Eq. (1), which forms the normalizing constant. The computation of this term is almost practically impossible. The normalizing constant is evaluated by expanding the integrand with HDMR. To do this, we incorporate prior information on each of the state variables in the form of lower and upper bounds. The numerator term, i.e., the product of likelihood and prior density—which is the same as integrand in the denominator integral is also expressed in the HDMR expanded form. This is required in order to evaluate the conditional means and variances from the multidimensional marginal densities obtained.

Brief descriptions on Bayesian inference and HDMR are followed. Thereafter, the proposed method is explained.

2.1 Bayesian Inference

By Bayes' theorem, for continuous X, the observations and Θ, the parameters

$$f_{\underline{\Theta}|X}(\underline{\theta}|x) = \frac{f_{\underline{\Theta}}(\underline{\theta}) \cdot f_{X|\Theta}(x|\underline{\theta})}{\int_{\Theta} f_{\underline{\Theta}}(\underline{\theta}) \cdot f_{X|\underline{\Theta}}(x|\underline{\theta}) d\underline{\theta}} \tag{1}$$

Integral in denominator of the expression for posterior density function and thereby, the normalization constant are quite difficult to compute, particularly if Θ is multidimensional. Hence, common practice is to adopt the techniques such as KF and its extensions. Here, we are attempting to evaluate the multidimensional integral with HDMR technique, for the estimation of Θ in a more direct manner. The subsequent computation of marginal distributions of each parameter and conditional mean and mean square errors are also carried out, employing HDMR.

Let the set of state variables and parameters we wish to estimate be

$$\underline{\Theta} = [\Theta_1, \Theta_2, \ldots, \Theta_n] \tag{2}$$

Marginal density function of Θ_1 is given by

$$f_{\Theta_1}(\theta_1) = \int \ldots \int f_{\underline{\Theta}|X}(\underline{\theta}|x) \mathrm{d}\theta_2 \ldots \mathrm{d}\theta_n \tag{3}$$

Similarly marginal density functions for each parameter should be derived to be used to calculate the conditional estimates of each.

Conditional mean is calculated by

$$\widehat{\theta}_1 = \int \theta_1 \cdot f_{\Theta_1}(\theta_1) \mathrm{d}\theta_1 \tag{4}$$

Mean squared error is estimated as

$$\mathrm{MSE}_{\widehat{\theta_1}} = \int (\theta_1 - \widehat{\theta}_1)^2 \cdot f_{\Theta_1}(\theta_1) \mathrm{d}\theta_1 \tag{5}$$

In the same manner, each of the state variables and system parameters in the state vector will be analyzed for their respective mean values and standard deviations.

2.2 High-Dimensional Model Representation (HDMR)

A multidimensional nonlinear function $g(x)$, where x is a vector of "N" variables/parameters, is expanded by HDMR technique, taking into account the cooperative

effects between the variables to the most extent. The hierarchical expansion representation of $g(x)$ is given as follows:

$$\begin{aligned} g(x) = g_0 + \sum_{i=1}^{n} g_i(x_i) + \sum_{1 \le i_1 \le i_2 \le N} g_{i_1 i_2}(x_{i_1}, x_{i_2}) + \cdots \\ + \sum_{1 \le i_1 < \cdots < i_l \le N} g_{i_1 \ldots i_l}(x_{i_1}, x_{i_2}, \ldots, x_{i_l}) \\ + \cdots + g_{12\ldots N}(x_1, x_2, \ldots, x_n) \end{aligned} \tag{6}$$

g_0 is a constant term obtained by evaluating the function $g(x)$ at a reference point. It represents the mean response of the function $g(x)$. This term can also been seen as the zeroth order component in the HDMR expansion approximation of the function $g(x)$. $g_i(x_i)$'s are the first-order components expressing the effect of any variable *xi* acting alone towards the representation of the function $g(x)$. Succeeding higher order terms represent the joint interaction contributions of the respective number of variables. Inclusion of the final term is to ensure an exact approximation. Typically, the expansion up to the second order will serve the purpose of approximate expansion by the assumption that contribution of higher order terms to the overall performance is negligible.

Consider the functional

$$\begin{aligned} \int_{\Gamma} \Bigg[& g(x) - g_0 + \sum_{i=1}^{n} g_i(x_i) \\ & + \sum_{1 \le i_1 \le i_2 \le N} g_{i_1 i_2}(x_{i_1}, x_{i_2}) + \cdots + \sum_{1 \le i_1 < \cdots < i_l \le N} g_{i_1 \ldots i_l}(x_{i_1}, x_{i_2}, \ldots, x_{i_l}) \\ & + \cdots + g_{12\ldots N}(x_1, x_2, \ldots, x_n) \Big]^2 \mathrm{d}\mu(x) \end{aligned}$$

Subjected to the constraint

$$\int_{[0,1]} g_{i_1 \ldots i_l}(x_{i_1}, x_{i_2}, \ldots, x_{i_l}) \mathrm{d}x_{i_k} = 0$$

This functional is minimized to obtain the terms $g_{i_1 i_2}(x_{i_1}, x_{i_2}, \ldots, x_{i_l})$ uniquely.

Major and popular HDMR techniques are Analysis of Variance (ANOVA) HDMR, Random Sampling (RS) -HDMR, Cut-HDMR, and ANOVA-HDMR based on Cut-HDMR expansions. In this paper, we are using Cut-HDMR technique for approximating the nonlinear relations.

Cut-HDMR expands the multidimensional function $g(x)$ with respect to a reference point "*c*," chosen within the neighborhood of interest of the input variables and the final outcome is independent of "*c*" at the convergence limit.

Cut-HDMR yields

$$g_0 = g(c) \tag{7a}$$

$$g_i(x_i) = g\left(x_i, c^i\right) - g_0 \tag{7b}$$

$$g_{i_1 i_2} = g\left(x_{i_1}, x_{i_2}, c^{i_1 i_2}\right) - g_{i_1}(x_{i_1}) - g_{i_2}(x_{i_2}) - g_0 \tag{7c}$$

and so on.

g_0 is evaluated at the reference point "c." $g(x_i, c^i) = g(c_1, c_2, \ldots, c_{i-1}, x_i, c_{i+1}, \ldots, c_N)$ denotes the function in terms of the input variable x_i alone, i.e., univariate and at all the other variables at their reference point value. The second-order bivariate term $g_{i_1 i_2}(x_{i_1}, x_{i_2})$ takes into account the cooperative effects of binary sets of input variables. Subtracting off the lower order terms from higher order terms is to ensure the unique contribution from each term.

First- and second-order approximations of $g(x)$, excluding the higher order residual terms and with reference to the reference point, are as follows:

$$\tilde{g}(x) = g(x_1, x_2, \ldots, x_N) = \sum_{i=1}^{N} g(c_1, c_2, \ldots, c_{i-1}, x_i, c_{i+1}, \ldots, c_N) - (N-1)g(c) \tag{8}$$

and

$$\begin{aligned} \tilde{g}(x) &= S_2 - (N-2) \times S_1 + \frac{(N-1)(N-2)}{2} g(c) \\ S_2 &= \sum_{i_1=1, i_2=1 i_1 < i_2}^{N} g(c_1, c_2, \ldots, c_{i_1 - 1}, x_{i_1}, c_{i_1+1}, \ldots, c_{i_2-1}, x_{i_2}, c_{i_2+1}, \ldots, c_N) \\ S_1 &= \sum_{i=1}^{N} g(c_1, c_2, \ldots, c_{i-1}, x_i, c_{i+1}, \ldots, c_N) \end{aligned} \tag{9}$$

Along the cut points, this approximation gives exact values. For any arbitrary point in the domain, response surface models are required.

The first-order interaction term for an arbitrary point x_i^{new} is

$$g_i\left(x_i^{\text{new}}\right) = \sum_{j=1}^{n} \Phi_j\left(x_i^{\text{new}}\right) g\left(c_1, \ldots, c_{i-1}, x_i^j, c_{i+1}, \ldots, c_n\right) \tag{10}$$

where $\Phi_j\left(x_i^{\text{new}}\right)$ is one-dimensional Lagrange interpolation polynomial.

In a similar fashion, the second-order interaction term for any two arbitrary points is as follows:

$$g_{ij}\left(x_{i_1}^{\text{new}}, x_{i_2}^{\text{new}}\right) = \sum_{j=1}^{n} \Phi_{j_1 j_2}\left(x_{i_1}^{\text{new}}, x_{i_2}^{\text{new}}\right) * g\left(c_1, \ldots, c_{i_1-1}, x_{i_1}^{j_1}, c_{i_1+1}, \ldots, c_{i_2-1}, x_{i_2}^{j_2}, c_{i_2+1}, \ldots, c_n\right) \tag{11}$$

where $\Phi_{j_1 j_2}\left(x_{i_1}^{\text{new}}, x_{i_2}^{\text{new}}\right)$ is the tensor product of $\Phi_{j_1}\left(x_{i_1}^{\text{new}}\right)$ and $\Phi_{j_2}\left(x_{i_2}^{\text{new}}\right)$.

In the proposed method, all the multidimensional integrals involved in Bayesian inference problems are computed with the help of HDMR. For the same, the bounds of the parameters or variables of interest need to be specified. Thereof, the integrands are approximated by HDMR expansions and then the integrals are evaluated.

3 Numerical Example 1

Consider a single degree of freedom system governed by the equation

$$\ddot{x} + 2\varsigma\omega_0\dot{x} + \omega_0^2 x = f(t) \tag{12}$$

The excitation force is taken to be harmonic with a known deterministic frequency ω_1 (= 1.5 Hz). The parameters ς and ω_0 need to be identified. The analysis is carried out in time domain. Prior knowledge of the bounds of the parameter values is used in constructing the prior density function.

Assumed bounds

$$\begin{array}{ll} \text{For } \omega_0, & 4 - 12 \text{ Hz} \\ \text{For } \varsigma, & 5 - 15\% \end{array}$$

Statistics of the displacement response is evaluated using the tools of stochastic dynamics.

Impulse response function for the system is given by

$$h(t) = \frac{1}{m\omega_d}\exp(-\varsigma\omega_0 t) \cdot \sin(\omega_d t) \tag{13}$$

where $\omega_d = \omega_0\sqrt{1-\varsigma^2}$.

Let $f(t) = A\cos(\omega_1 t)$; $A \sim N(1,1)$.

The mean excitation is

$$\mu_f(t) = \mu_A \cdot \cos(\omega_1 t). \tag{14}$$

Autocovariance of the forcing function is

$$K_{\mathrm{FF}}(t,s) = \sigma_A^2 \cdot \cos(\omega_1 t) \cdot \cos(\omega_1 s) \tag{15}$$

Mean response is

$$\mu_x(t) = \int_0^t \mu_f(t) \cdot h(t-r) \cdot \mathrm{d}r \tag{16}$$

Autocovariance of the response is

$$K_{\mathrm{xx}}(t,s) = \int_0^s \int_0^t K_{\mathrm{FF}}(t,s) \cdot h(t-r_1) \cdot h(s-r_2) \cdot \mathrm{d}r_1 \cdot \mathrm{d}r_2 \tag{17}$$

The likelihood function, i.e., conditional density function for the response over a specified time span is obtained thereof. The normalization constant is calculated by integrating the complicated integrand which is the product of the prior density and likelihood, on first-order HDMR expansion approximation of the integrand. Posterior distribution thus arrived is utilized to compute the marginal densities of each of the unknown parameters. The conditional expectation or mean and variance of each parameter are computed from the marginal densities as usual. With the updated variance and mean value, an iterative procedure is followed for convergence.

The observations were generated as such there is coefficient of variation of 0.1% around the mean, and with $\omega_0 = 6.28$ Hz and $\varsigma = 9\%$. Initial conditions were assumed to be at rest. i.e. Initial displacement u(0)=0 and initial velocity u′(0)=0. Initial values for calculation $\omega_0 = 6.0$ Hz and $\varsigma = 8\%$.

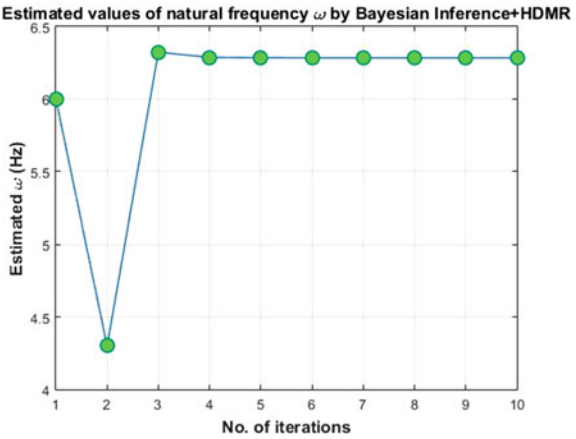

Fig. 1 Natural frequency as identified using HDMR combined Bayesian inference

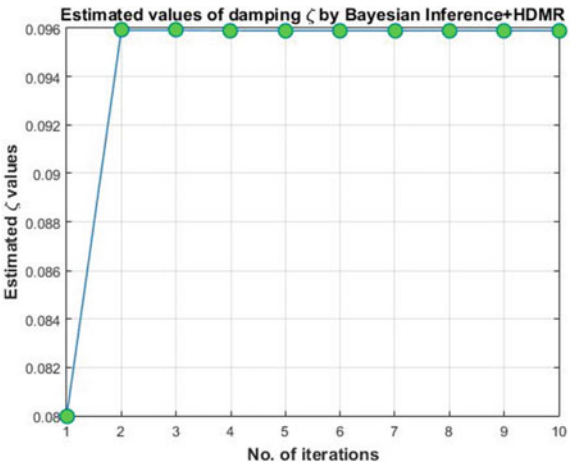

Fig. 2 Damping ratio as identified by HDMR combined Bayesian inference

The results are represented graphically as shown in Figs. 1 and 1. Natural frequency is converging to the original value, as shown in Fig. 1. From Fig. 2, it can be observed that damping ratio is converging to a value of 9.6%, i.e., with a slight deviation. These estimates may be used to identify the stiffness "K" and damping 'c' of the system.

4 Numerical Example 2

A stochastic plane strain elastic field [8] with specified nodal loads is analyzed to identify the equivalent moduli of elasticity over three different sets of layers of similar characteristics.

Top two layers of the field

$$E_1 = 1000 \text{ tonf}/\text{m}^2$$

Middle three layers of the field

$$E_2 = 2000 \text{ tonf}/\text{m}^2$$

Bottom three layers of the field

$$E_3 = 3000 \text{ tonf}/\text{m}^2$$

Measurement model for the problem is

$$d = K^{-1}F$$

where d is the displacement vector, K is the stiffness matrix, and F the external force vector (Fig. 3).

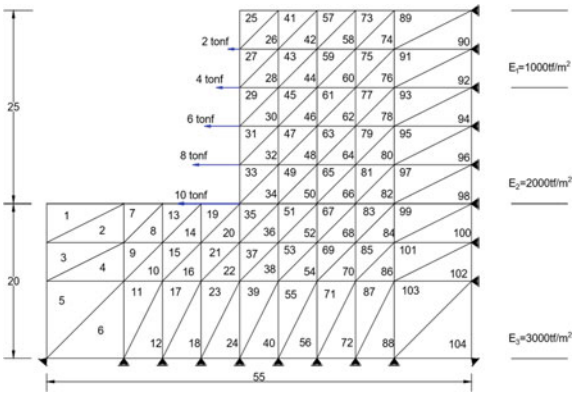

Fig. 3 Plane strain field as considered in the problem

Lateral displacements at given nodes are taken as observations. They are assumed to be with a known coefficient of variation and uncorrelated.

The estimation is carried out by Bayesian inference approximated by first-order HDMR and second-order HDMR as well. Six sets of measurements of displacements are used in the identification process. With each set of measurement, a suitable number of local iterations are performed. Then iterations are started afresh with a new set of measurements. As the procedure shows good convergence at the end of iterations with the third set of measurements, it can be concluded that six sets of measurements are good enough to prove the stability of the algorithm.

The HDMR Bayesian identification procedure is carried out for two sets of initial values to test the robustness, along with the application of first and second order HDMR. The same field is analyzed using Extended Kalman Filter and results are shown graphically for comparison. Figure 4 shows the application of HDMR-Bayesian procedure with first-order HDMR, using a set of initial values [1500, 2500, 3500] tonf/m^2 as mean, to identify the moduli of elasticity of each of the three layers.

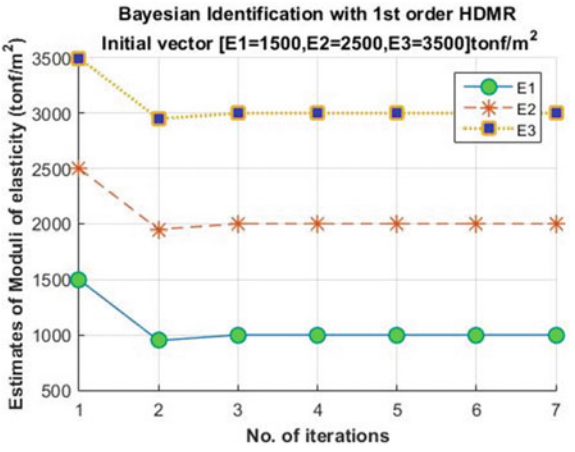

Fig. 4 Estimation using HDMR combined Bayesian inference with **first**-order HDMR and set of mean initial values [1500, 2500, 3500] tonf/m^2

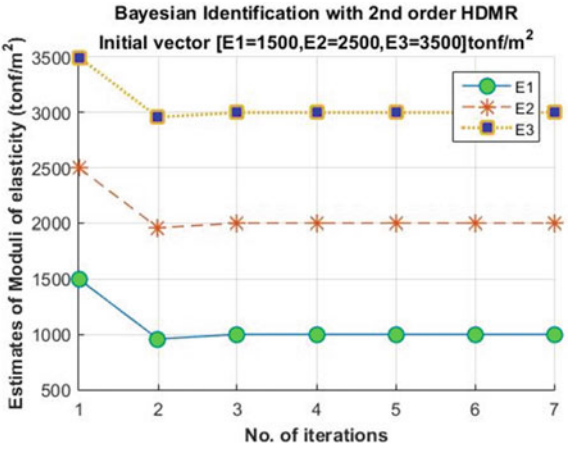

Fig. 5 Estimation using HDMR combined Bayesian inference with **second-**order HDMR and set of mean initial values [1500, 2500, 3500] tonf/m^2

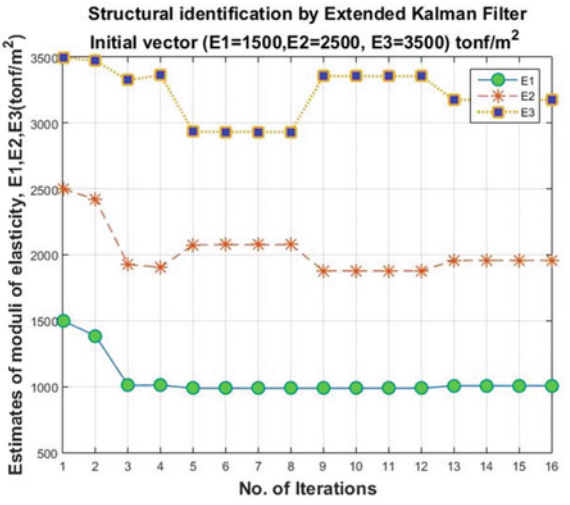

Fig. 6 Estimation using EKF for mean initial values [1500, 2500, 3500] tonf/m^2

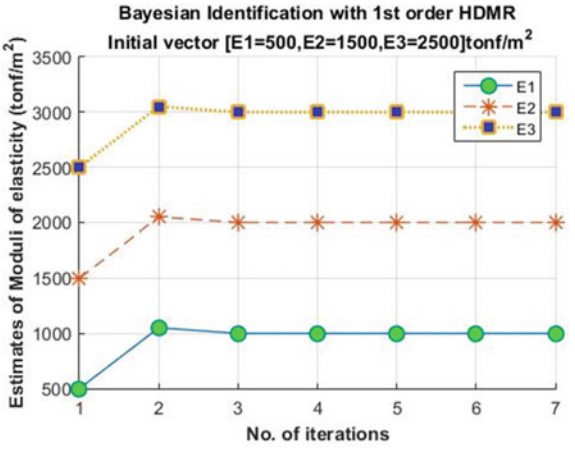

Fig. 7 Estimation using HDMR combined Bayesian inference with first-order HDMR and set of mean initial values [500, 1500, 2500] tonf/m^2

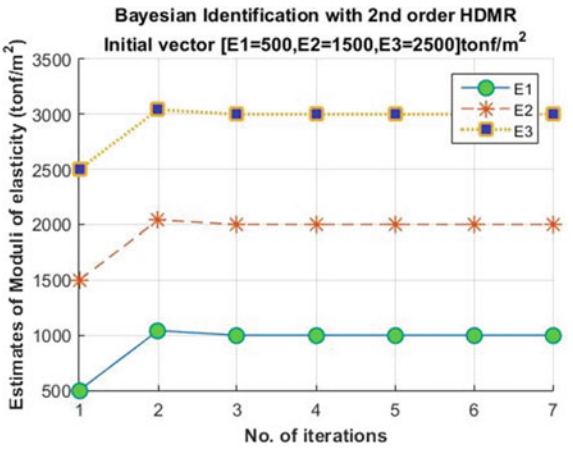

Fig. 8 Estimation using HDMR combined Bayesian inference with second-order HDMR and set of mean initial values [500, 1500, 2500] tonf/m^2

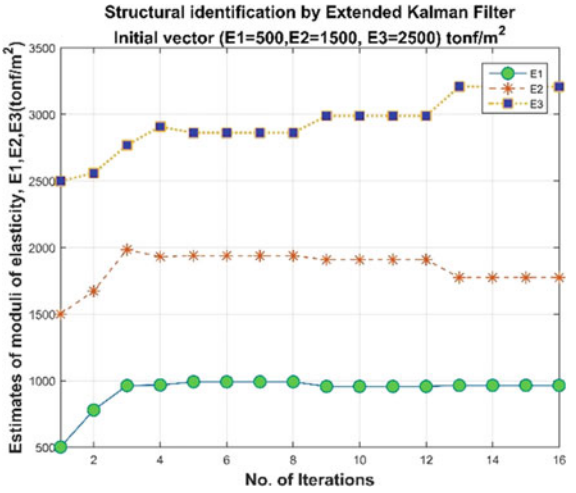

Fig. 9 Estimation using EKF for mean initial values [500, 1500, 2500] tonf/m^2

Figure 5 shows the results when second order HDMR is used for the same set of initial values. Figure 6 shows the estimated values by Extended Kalman Filter for the same set of initial values. Then, choosing a different set of initial values [500, 1500, 2500] tonf/m^2, HDMR Bayesian procedure is applied with first order HDMR (Fig. 7) and with 2nd order HDMR (Fig. 8). Results from EKF for the same set of initial values is shown in Fig. 9. It can be observed that EKF requires more number of iterations for convergence.

5 Conclusions

In this paper, we attempted to identify the moduli of elasticity of a stochastic plane strain field, with the displacement measurements available at specified nodes. This problem has a nonlinear measurement model. EKF may be used for the state estimation in such a case. It has certain convergence issues. Here, we attempt to carry out the identification by HDMR-based Bayesian inference. This method provides results with better convergence. This may be compared against sampling-based approaches/filters for efficacy, accuracy, and faster convergence. In this problem, the state variables/system parameters are not changing with time. We have also considered an SDOF system with a known harmonic excitation input. In this problem, the damping and stiffness are identified with the proposed method. Identification of a SDOF system by the proposed method yields faster convergence as compared to that obtained by EKF. The identification of material or structural parameters of various structures such as multistory buildings, bridges, etc., under different types of dynamic loadings, will be found useful in damage detection, health monitoring, etc. These problems involve nonlinear high-dimensional relations which are not easy to be handled with the conventional methods in terms of the computational issues. The proposed method will be applied to check the same in future.

References

1. Jones, N. P., Shi, T., Ellis, J. H., & Scanlan, R. H. (1995). System-identification procedure for system and input parameters in ambient vibration surveys. *Journal of Wind Engineering and Industrial Aerodynamics, 54,* 91–99.
2. Koh, C. G., & See, L. M. (1994). Identification and uncertainty estimation of structural parameters. *Journal of Engineering Mechanics, 120*(6), 1219–1236.
3. Sirca, G. F., & Adeli, H. (2012). System identification in structural engineering. *Scientia Iranica, 19*(6), 1355–1364.
4. Chowdhury, R., Rao, B. N., & Prasad, A. M. (2009). High-dimensional model representation for structural reliability analysis. *Communications in Numerical Methods in Engineering, 25*(4), 301–337.
5. Rabitz, H., & Alis, O. F. (1999). General foundations of high-dimensional model representations. *Journal of Mathematical Chemistry, 25,* 197–233.
6. Smith, R. C. (2014). Uncertainty quantification: Theory, implementation, and applications. *SIAM Computational Science and Engineering*.
7. Sobol, I. M. (2003). Theorems and examples on high dimensional model representation. *Reliability Engineering & System Safety, 79*(2), 187–193.
8. Hoshiya, M., & Sutoh, A. (1993). Kalman filter—Finite element method in identification. *Journal of Engineering Mechanics, 119,* 197–210.

Adaptive Metamodel-Based Efficient Robust Design Optimization of Offshore Structure Under Wave Loading

Gaurav Datta, Soumya Bhattacharjya and Subrata Chakraborty

Abstract The present paper deals with the Robust Design Optimization (RDO) of an offshore steel structure under wave loading considering parameter uncertainty. A novel Moving Least Squares Method (MLSM)-based metamodelling strategy has been adopted in the framework of MCS to evade extensive computational time requirement. The optimization problem is posed as weight minimization problem under displacement constraint. The proposed MLSM-based RDO strategy yields more accurate solutions than the conventional Least Squares Method (LSM)-based metamodelling when compared with the direct MCS results as benchmark. The proposed approach requires less computational time than the direct MCS. The results show that by compromising a small increment in structural weight, one can achieve robust and reliable design solution within affordable computational time by the proposed RDO approach.

Keywords Robust design optimization · Offshore structure · Parameter uncertainty · Wave load · Moving least squares method

1 Introduction

The studies on deterministic design concepts, methods and cost-effectiveness of offshore structure in last decade are exhaustive [1]. Among different elements of marine structure, the support structure has the highest cost share [2]. Currently, the most widely used support structure is steel tubular tower that is connected through a

G. Datta · S. Bhattacharjya · S. Chakraborty (✉)
Department of Civil Engineering, Indian Institute of Engineering Science and Technology, Shibpur, Howrah 711103, India
e-mail: schak@civil.iiests.ac.in

G. Datta
e-mail: gaurav.rs2015@civil.iiests.ac.in

S. Bhattacharjya
e-mail: soumya@civil.iiests.ac.in

A. Rama Mohan Rao and K. Ramanjaneyulu (eds.), *Recent Advances in Structural Engineering, Volume 1*, Lecture Notes in Civil Engineering 11,
https://doi.org/10.1007/978-981-13-0362-3_37

transition piece to a mono pile which is a suitable concept for water depths of up to 40 m [3]. It has been now well established that disregarding uncertainty in the Deterministic Design Optimization (DDO) process will invite catastrophic consequences [4]. Hence, there is a growing trend to incorporate uncertainty directly in the optimization process. In recent years, efforts have been observed to explore probabilistic optimization and design under wave load. Critical parameters for designing such an elevated structure are the wave height crest and its probability distribution. The most conventional approach of optimization under uncertainty is the Reliability-Based Design Optimization (RBDO), where specific target reliability is sought for the critical limit states [5]. However, the RBDO yields design which may be sensitive to input parameter variation due to uncertainty. A Robust Design Optimization (RDO) becomes an attractive alternative to the RBDO approach in such cases to make a design least sensitive to input parameter uncertainty. Moreover, for life cycle cost analysis, the deviation of the structural performance should be designed to a minimum to avoid maintenance and repair cost. It has been observed that the RDO study on offshore structure is scarce. Application of RDO in designing offshore structure is felt to be more prudent under such extreme loadings, largely uncertain in nature. The present study focuses on the RDO of a steel offshore structure under wave loading considering parameter uncertainty.

In [6], RDO of offshore turbine supporting structure is presented considering normally distributed dimension and material properties. However, uncertainty in load and robustness of constraints are not considered in their study. The direct Monte Carlo Simulation (MCS) have been applied to offshore structure optimization that makes the implementation procedure extensively time-consuming [6–8]. It is of worth mentioning that solution of RDO of such structure would involve complex computer codes and numerical analyses by the direct MCS approach. Also, several repetitive analyses of finite element model would be involved to yield a single solution of RDO. Moreover, the gradients of the constraint functions are required to be evaluated many times during the execution of the RDO process. Therefore, in the present study, metamodelling technique based on Response Surface Method (RSM) has been adopted to evade complex interlinked repetitive evaluation of structural response and their gradients. Once the RSM approximation is obtained and validated by 'goodness of fit' tests, the gradient evaluation becomes extremely simplified to cast the RDO problem. Conventionally, Least Squares Method (LSM)-based RSM is applied for dealing optimization problems including implicit constraint functions. However, the accuracy with the LSM-based RSM is often challenged. On the other hand, the Moving Least Squares Method (MLSM) is found to be more efficient in this regard [9]. Thus, in the present study, a novel MLSM-based adaptive metamodelling strategy has been adopted in place of the direct MCS to avoid extensive computational time requirement. The proposed RDO approach is elucidated by a numerical study on a steel jack-up platform.

2 Development of the Proposed RDO Approach

The performance of an optimal design depends on the Design Variables (DVs) and the Design Parameters (DPs). The DVs are the variables that the designer wants to optimally evaluate. The DPs are the other involved system parameters used for design which cannot be controlled by the designer. The objective of a typical design optimization is to determine the DVs to meet the desired design performance. Design objectives are normally specified by a performance function associated with a set of constraints. The Deterministic Design Optimization (DDO) can be mathematically expressed as

$$\begin{aligned} &\text{minimize} && f(u) \\ &\text{subjected to} && g_j(u) \le 0 \qquad j = 1, 2, \ldots, J \\ & && x_i^{\mathrm{L}} \le x_i \le x_i^{\mathrm{U}}, \quad i = 1, 2, \ldots, K \end{aligned} \tag{1}$$

In above, $f(u)$ is the performance function; $g_j(u)$ denotes the jth constraint; $u = x \cup z$ is a n-dimensional vector composed of both the DVs and DPs denoted by

$$\mathbf{x} = [x_1, x_2, \ldots, x_K]^{\mathrm{T}} \quad \text{and} \quad \mathbf{z} = [z_1, z_2, \ldots, z_L]^{\mathrm{T}},$$

respectively; x_i^{L} and x_i^{U} are the lower and the upper bounds of the ith DV, respectively. J, K and L are the total number of constraints, DVs and DPs, respectively. It can be noted here that the DDO problem as described by Eq. (1) does not consider the effect of randomness in x and z. But the performance function and the constraints are the function of x and z. Thus, the randomness in x and/or z are expected to propagate at the system level, influencing the performance function and the constraints of the related optimization problem. The development of the RDO methodology is described next in the Sect. 2.1. Then, in Sect. 2.2, the MLSM strategy is briefly discussed.

2.1 The RDO Methodology

The presence of uncertainty in structural parameters causes significant deviation of performance of a structural system from its desired behaviour. Such undesirable deviation of system performance indicates a poor quality and added life cycle cost of the structure, including inspection, repair and other maintenance costs in the perspective of the entire design life of the structure. To decrease such deviation, one possible way is to reduce or even to eliminate the source of uncertainty in the structural parameters by prudent design and construction practice [10], which may either be practically impossible or adds much to the total cost of the structure. Another way is to find a design, in which the structural performance is less sensitive to the variations of the parameters without eliminating the cause of parameter

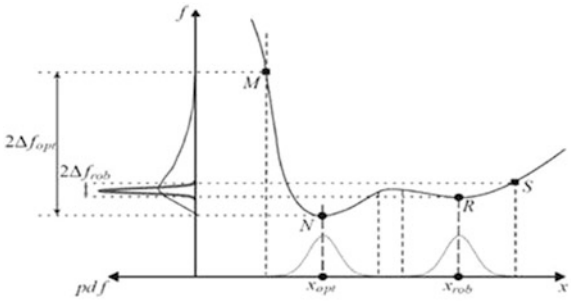

Fig. 1 A robust solution versus an optimal solution [11]

variations. This latter one is the task of the RDO. The RDO is fundamentally concerned with minimizing the effect of uncertain DVs and DPs to the output response. The concept of RDO is presented in Fig. 1. Two designs, conventional optimal design under uncertainty (x_{opt}) and RDO (x_{rob}), are shown in the same figure. Both design inputs (x) are deviated with same amount due to uncertainty. However, probability density function of the output response is considerably less deviated by the RDO (Δf_{rob}) than the other case (f_{opt}). Also, it can be readily observed from Fig. 1 that the RDO captures comparatively a flatter insensitive region of the performance function. The RDO is formulated by simultaneously optimizing the expected value and the variation of the performance function. The robustness in constraint is ensured by adding suitable penalty term and ensuring a target reliability index.

The RDO problem is formulated in the following [12] and [13]:

$$\begin{array}{lll} \text{minimize:} & \phi(\mathbf{u}) = (1-\alpha)\frac{\mu_{\text{f}}}{\mu_{\text{f}}^*} + \alpha\frac{\sigma_{\text{f}}}{\sigma_{\text{f}}^*}, & 0 \le \alpha \le 1 \\ \text{subjected to:} & \mu_{g_j} + k_j\sigma_{g_j} \le 0 & j = 1, 2, \ldots, J \\ & x_i^{\text{L}} \le x_i \le x_i^{\text{U}}, & i = 1, 2, \ldots, K \end{array} \tag{2}$$

where k is a designer specified penalty factor to enhance the feasibility of the jth constraint and can be obtained as $\Phi^{-1}\{1 - \Phi(-\beta^{\text{T}})\}$ and β^{T} is the target reliability index and Φ is the cumulative density function of a standard normal distribution. $\phi(u)$ is a new objective function, called desirability function, and the parameter α serves as a weighting factor; μ_{f} and σ_{f} are the mean and the standard deviation of the performance function, respectively; μ_{f}^* and σ_{f}^* are the optimal values of the mean and the standard deviation obtained for α equals to 0.0 and 1.0, respectively; μ_{g_j} and σ_{g_j} are the mean and the standard deviation of the jth constraint g_j, respectively.

2.2 The MLSM-Based RSM Strategy

The MLSM-based RSM is a weighted LSM that has varying weight functions with respect to the position of approximation [14]. The weight associated with a particular sampling point x_i decays as the prediction point x moves away from x_i. The weight function is defined around the prediction point x and its magnitude changes with x. The modified error norm $L_y(x)$ can be defined as the sum of the weighted errors [14]

$$L_y(x) = \varepsilon^{\mathrm{T}} W(x)\varepsilon = (Y - Q\beta)^{\mathrm{T}} W(x)(Y - Q\beta) \tag{3}$$

where ε is the lack of fit error term; Y represents the response of the structure; and Q is the design matrix and β is the unknown coefficient vector. The coefficient $\beta(x)$ can be obtained by the matrix operation as below [14]:

$$\beta(x) = [Q^{\mathrm{T}} W(x)Q]^{-1} Q^{\mathrm{T}} W(x)Y \tag{4}$$

In the above equation, $W(x)$ is the diagonal matrix of the weight function and it depends on the location of the associated approximation point of interest (x); $W(x)$ may be obtained by utilizing the weighting function as an exponential function [14]:

$$w(x - x_{\mathrm{I}}) = w(d) = \exp(-d/R_{\mathrm{I}}) \tag{5}$$

where R_{I} is the approximate radius of sphere of influence, chosen as twice the distance between the most extreme points from the centre point considered in the Design of Experiment (DOE). The exponential form of the weight function is used in the present numerical study. The weight matrix $W(x)$ can be constructed using the weighting function in diagonal terms as below:

$$W(x) = \begin{bmatrix} w(x - x_1) & 0 & \dots & 0 \\ 0 & w(x - x_2) & \dots & 0 \\ \dots & \dots & \dots & \dots \\ 0 & 0 & \dots & w(x - x_n) \end{bmatrix}$$

3 Estimation of Extreme Wave Loading

Offshore structures are subjected to temporally and spatially varying random loads due to wind, wave, earthquake, ice and thermal gradient. The complexity of wind and earthquake load is compounded by the wave environment. The long-term behaviour of loads is nonstationary and due to nonlinear functional dependence, it is non-Gaussian as well [15]. The wave forces on the offshore structures depend on the characteristic of the wave environment and the geometric and dynamic

properties of the structure. Morison et al. [16] proposed an empirical formula or the in-line force per unit length as

$$\begin{aligned} &F(s,t) = F_{\mathrm{I}} + F_{\mathrm{D}} = M_{\mathrm{I}}\,\ddot{U} + C_{\mathrm{H}}\,\dot{U}\left|\dot{U}\right| \\ &\text{where, } M_{\mathrm{I}} = C_{\mathrm{M}}\rho\frac{\pi D^2}{4} = (C_{\mathrm{m}}+1)\rho\frac{\pi D^2}{4} \\ &\text{and } C_{\mathrm{H}} = C_{\mathrm{D}}\frac{\rho D}{2} \end{aligned} \tag{6}$$

where F_{I} and F_{D} are the inertia and drag force, respectively; D is the diameter of a single column; ρ is the density of the seawater; $\dot{U}$ is the fluid particle velocity; $\ddot{U}$ is the fluid particle acceleration; C_{M} is the inertia coefficient; C_{m} is the hydrodynamic mass and C_{D} is the drag coefficient. The wave force can be rewritten as

$$\begin{aligned} &F_{\mathrm{h}} = \pi\rho D\frac{H^2 L}{T^2}\left[\begin{array}{l}\frac{\pi D}{4H}C_{\mathrm{m}}K_2\sin 2\pi\left(\frac{x}{L}-\frac{t}{T}\right) \\ +C_{\mathrm{d}}K_1\left|\cos 2\pi\left(\frac{x}{L}-\frac{t}{T}\right)\right|\cos 2\pi\left(\frac{x}{L}-\frac{t}{T}\right)\end{array}\right] \\ &\text{where,} \\ &K_1 = \frac{\frac{4\pi S_2}{L}-\frac{4\pi S_1}{L}+\sin\mathrm{h}\left(\frac{4\pi S_2}{L}\right)-\sin\mathrm{h}\left(\frac{4\pi S_1}{L}\right)}{16\left[\sin\mathrm{h}\left(\frac{2\pi d}{L}\right)\right]^2} \\ &\text{and } K_2 = \frac{\sin\mathrm{h}\left(\frac{2\pi S_2}{L}\right)-\sin\mathrm{h}\left(\frac{2\pi S_1}{L}\right)}{\sin\mathrm{h}\left(\frac{2\pi d}{L}\right)} \end{aligned} \tag{7}$$

where S_1 is the level of equivalent force from the bottom of sea and S_2 refers to the depth of the sea; L is the length of wave; D is the diameter of a single column; T is the time period of wave; t is the time step interval; and H is the maximum wave height.

3.1 Morison Equation for Flexible Members

The original Morison equation of Eq. (6) is modified for flexible or moving members, by replacing the absolute velocity by relative velocity and including an added mass term associated with the acceleration of the structure [17]. The modified equation is represented as

$$\begin{aligned} F(s,t) &= (C_{\mathrm{M}}-1)\frac{\rho\pi D^2}{4}\ddot{Y} + \frac{\rho\pi D^2}{4}\ddot{U} + \frac{1}{2}\rho C_{\mathrm{D}}D\dot{Y}\left|\dot{Y}\right| \\ &= M_{\mathrm{a}}\ddot{Y} + M_{\mathrm{w}}\ddot{U} + C_{\mathrm{H}}\dot{Y}\left|\dot{Y}\right| \end{aligned} \tag{8}$$

where $\dot{Y} = \dot{U} - \dot{X}$ is the relative velocity and $X(t)$ is the displacement in the direction of the wave propagation. The modified hydrodynamic load vector $\bar{F}(t)$

may be obtained by aggregating the hydrodynamic load on each member. It includes the effect of inertia, drag and fluid–structure interaction.

$$\begin{aligned} &\bar{F}(t) = M_1\ddot{U} - M_a\ddot{\bar{X}} + C_H\left|\dot{U} - \dot{\bar{X}}\right|\left(\dot{U} - \dot{\bar{X}}\right) \\ &\text{where, } M_I = \rho C_M V, \quad M_a = \rho(C_M - 1)V, \quad C_H = \frac{1}{2}\rho C_D A \end{aligned} \tag{9}$$

$\dot{U}$, $\ddot{U}$ are the fluid particle velocity and fluid particle acceleration, respectively; $A = \frac{\pi}{4}D^2$ and $V = \frac{\pi}{4}D^2 l$, where l is the length of a column.

4 Numerical Study

A single storied jack-up platform made up of steel plates is taken up to study the proposed RDO procedure. The structure is considered to be subjected to wave load with a maximum wave height of 3 m, and the corresponding wave period is taken as 8.25 s. The values of C_M and C_D are taken as 2 and 1, respectively, [18]. In this particular problem, DVs are taken as column diameter (d_c) and bracing diameter (d_b). The sections are tubular with uniform thickness of 25 mm. The uncertain DPs are maximum height of wave (H_{max}), time period of wave (T), modulus of elasticity of steel (E_s), unit weight of steel (γ_s), unit weight of seawater and weight of deck. The DVs and DPs are tabulated in Table 1. The mean values of the DPs are taken from Ref. [15]. Time period 'T' is assumed to be log-normally distributed [15], whereas all other parameters are assumed as random normal. The structure and the sea level are shown in Fig. 2. $S_2 = d = 25$ m. SWL refers to the mean seawater level. The DDO is then formulated as

$$\begin{aligned} &\text{Find} \quad x_1, x_2 \\ &\text{To minimize} \quad f(u) = \text{Weight of frame} \\ &\text{subjected to:} \quad g(u) = \delta \le \delta_{al}, \quad \mathbf{x}^L \le \mathbf{x} \le \mathbf{x}^U \end{aligned} \tag{10}$$

Table 1 Details of the uncertain DVs and DPs

Variable		Notation	Mean	CoV (%)
DPs	H_{max} (m)	z_1	4.34	20
	T (s)	z_2	8.51	10
	E_s (t/m^2)	z_3	2.1×10^7	10
	γ_s (t/m^3)	z_4	7.83	10
	γ_w (t/m^3)	z_5	1.03	10
	W (t)	z_6	3000	10
DVs	Dia. of col (d_c) (m)	x_1	3	5
	Dia. of bracing (d_b) (m)	x_2	1	5

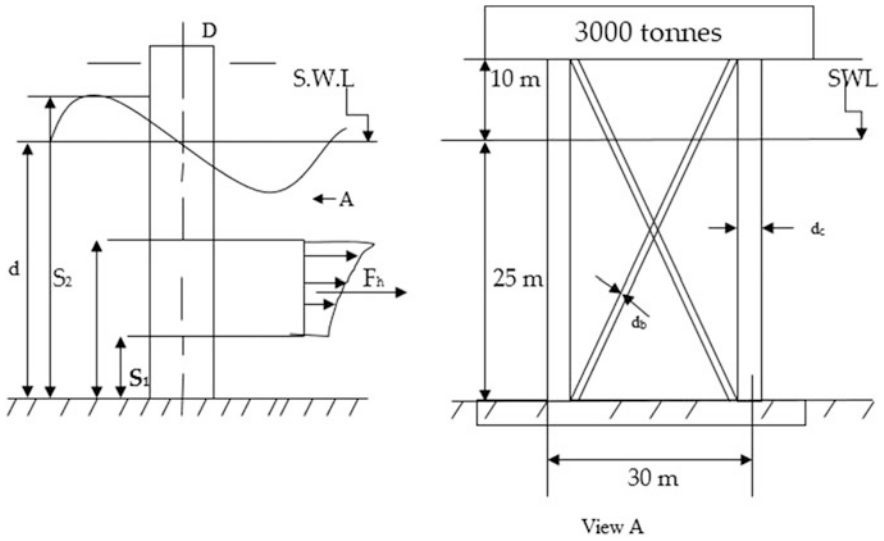

Fig. 2 The jack-up platform

where δ and δ_{al} are the maximum top displacement and allowable displacement, respectively. δ_{al} is taken as (H_s/500), where H_s refers to the height of the structure.

The RDO has been performed by (i) the direct MCS framework, (ii) the MLSM-based RSM framework and (iii) the LSM-based RSM framework.

The DoE for generating the RSM approximation is performed by randomly generating 20 sampling points as per Latin hypercube sampling method. The RDO is executed by sequential quadratic programming routine available in MATLAB. The results are presented for varying reliability index in Figs. 3, 4, 5 and 6. The results obtained from the direct MCS, the conventional LSM-based RSM and the proposed MLSM-based RSM are shown in the same figure. The direct MCS result

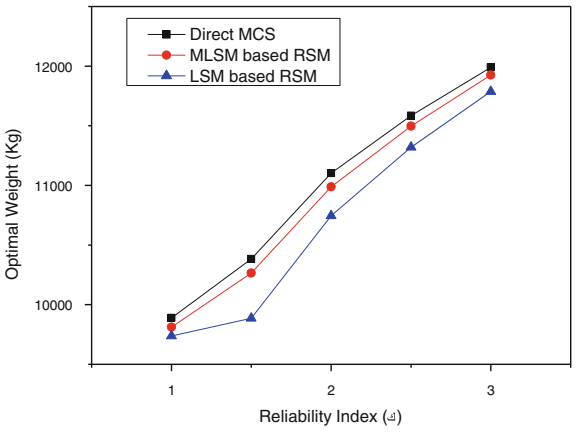

Fig. 3 Optimal weight versus reliability index

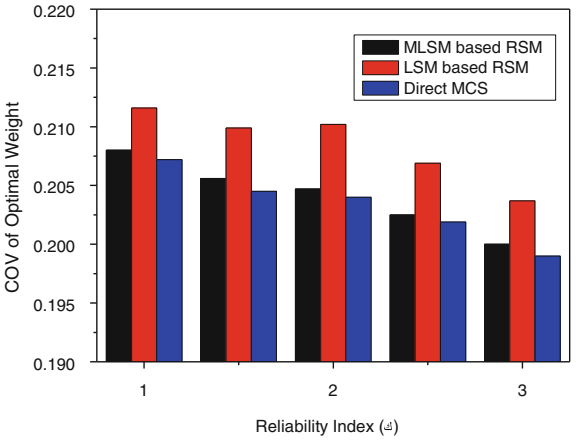

Fig. 4 CoV of optimal weight versus reliability index

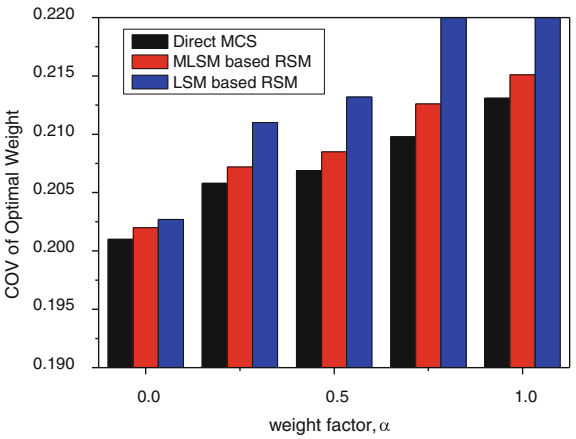

Fig. 5 CoV of optimal weight versus weight factor

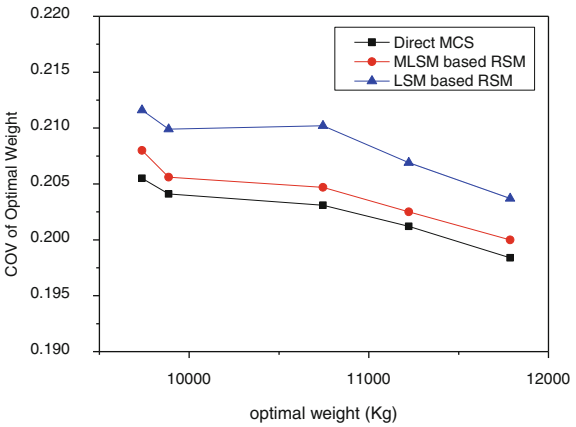

Fig. 6 The Pareto-optimal curve

serves here as the benchmark for the comparison. In Fig. 3, optimal weight is plotted. The Coefficient of Variation (CoV) of optimal weight is presented in Fig. 4. It can be observed from these figures that the optimal weight and its CoV increase with increase in target reliability index. The trend is similar by all the three approaches. From Figs. 3 to 4, it can be observed that the optimal weight and the CoV of optimal weight by the MLSM-based RSM approach is in close conformity with the direct MCS-based approach. From Fig. 3, it can be observed that the results by the conventional LSM-based RSM approach are significantly deviated from the direct MCS results. Hence, the results by the LSM-based RSM seem to yield inaccurate design solutions, which may be even to the unsafe side inviting catastrophic failure consequences. This warrants the application of the LSM-based RSM in the RDO. The marginal deviation of the results by the MCS and the MLSM predictions is expected to be further reduced by taking more sample points, iterative improvement of the DoE which is under study at this stage. The CoV of the optimal weight (Fig. 4) obtained by the conventional LSM-based RSM approach is not only more (i.e. less robust) than the MLSM-based RSM results, but also not in agreement with the benchmark direct MCS results. The RDO results for different values of the parameter 'α' are presented in Fig. 5 showing the variation of the CoV of optimal weight with the weight factor. The inaccuracy with the conventional LSM-based RSM approach is pertinent here also. On the other hand, the MLSM-based RSM approach is in close agreement with the benchmark MCS solutions and more robust than the LSM-based RSM, as well. It can be further observed that the robustness (i.e. less CoV of the optimal weight) achievement is more for decrease in the value of 'α' from 1.0 to 0.0.

It is generally observed that there is a trade-off between the objective values of a design and its robustness. If one desires more robustness, the design will be further away from its ideal optimal value. The situation can be studied further in terms of Pareto front [19]. The function space representation of the Pareto-optimal set is the Pareto-optimal front. When there are two objectives, the Pareto-optimal front is a curve, when there are three objectives, the Pareto-optimal front is represented by a surface and if there are more than three objectives, it is represented by a hypersurface. The Pareto-optimal front in multi-objective optimization problems is useful to visualize and assess trade-offs among different design objectives. In addition to identify compromise solutions, this also helps the designer to set realistic design goals. The Pareto front is one where any improvement in one objective can only occur through worsening of at least one other objective. If one chooses a design that is not Pareto-optimal, one essentially forfeits improvements that would otherwise entail no compromise. Thus, one of the important tasks in the RDO is to obtain the Pareto front. The Pareto fronts as obtained by the proposed and the conventional RDO approaches are plotted in Fig. 6. It can be readily observed from this figure that to achieve a specific level of variation in the desired objective (CoV of the weight here), the required weight by the proposed MLSM-based RSM approach is lesser than that by the conventional LSM-based RSM approach. On the other hand, for a prescribed weight of the structure, the CoV of optimal weight as obtained by the proposed MLSM-based RSM approach is lesser than that obtained by the conventional LSM-based RSM approach.

Hence, more robust (i.e. lesser CoV) solutions are achieved by the proposed MLSM-based RSM approach, which is also more economic (i.e. lesser structural weight yielded by the proposed approach), as well. Moreover, the MLSM-based RSM results are in close conformity with the benchmark direct MCS solutions in comparison to the conventional LSM-based RSM results. Thus, more efficient Pareto front is obtained by the proposed MLSM-based RSM approach as compared to the conventional LSM-based RSM approach.

It has been observed that the direct MCS approach requires on an average 9 minutes, whereas the proposed MLSM-based RDO approach takes 15 seconds for producing a single solution of the RDO. The LSM-based RSM yields result in approximately 5 seconds. This endorses the computational efficiency of the proposed approach. The MLSM-based RSM approach takes more time than the LSM-based RSM since the former fits a new RSM curve for each of the iterations of the RDO.

5 Conclusions

An efficient RDO of offshore structure is presented under wave loading. The MLSM-based RSM approach is used in the present study to reduce the high computational time requirement by the direct MCS. It has been observed that with respect to the conventional deterministic design, the RDO yields 18% higher optimal weight considering uncertainty in load and other system parameters. The proposed MLSM-based RDO approach is not only computationally efficient but also acceptably accurate as evinced from the numerical study. The proposed MLSM-based RSM approach yields more efficient Pareto front than the conventional LSM-based RSM approach. The results indicate that by sacrificing a small increment in the structural weight designer can achieve robust and reliable design solution within affordable computational time by the proposed RDO approach. The proposed RDO method is valid and general approach for extending to other types of large offshore structures considering uncertainty. The RDO can reduce the sensitivity of several other responses of the supporting structure, such as stress. Thus, future research studies can be focused on vibration control and fatigue design using the RDO method.

References

1. Ashuri, T., & Zaaijer, M. B. (2007). Review of design concepts, methods and considerations of offshore wind turbines. In *European Offshore Wind Conference and Exhibition*, Berlin, Germany.
2. Blanco, M. I. (2009). The economics of wind energy. *Renewable and Sustainable Energy Reviews, 13*(6), 1372–1382.

3. Hezarjaribi, M., Bahaari, M. R., Bagheri, V., & Ebrahimian, H. (2013). Sensitivity analysis of jacket-type offshore platforms under extreme waves. *Journal of Constructional Steel Research, 83,* 147–155.
4. Wang, X. M., Koh, C. G., & Zhang, J. (2014). Substructural identification of jack-up platform in time and frequency domains. *Applied Ocean Research, 44,* 53–62.
5. Zhang, Y., & Lam, J. S. L. (2015). Reliability analysis of offshore structures within a time varying environment. *Stochastic Environmental Research and Risk Assessment, 29,* 1615–1636.
6. Yang, H., & Zhu, Y. (2015). Robust design optimization of supporting structure of offshore wind turbine. *Journal of Marine Science and Technology, 20,* 689–702.
7. Ziegler, L., Voormeeren, S., Schafhirt, S., & Muskulus, M. (2016). Design clustering of offshore wind turbines using probabilistic fatigue load estimation. *Renewable Energy, 91,* 425–433.
8. Haghi, R., Ashuri, T., van der Valk, P. L. C., & Molenaar, D. P. (2014). Integrated multidisciplinary constrained optimization of offshore support structures. *Journal of Physics: Conference Series*.
9. Chakraborty, S., & Bhattacharjya, S. (2012). Efficient robust optimization of structures subjected to earthquake load and characterized by uncertain bounded system parameters. *Structural Seismic Design Optimization and Earthquake Engineering: Formulations and Applications*.
10. Knoll, F., & Vogel, Th. (2009). *Steel construction* (Vol. 2, Issue 2, p. 147).
11. Augusto, O. B., Fouad Bennis, F., & Stephane Caro, S. (2012). Multiobjective engineering design optimization problems: A sensitivity analysis approach. *Pesquisa Operacional, 32*(3), 575–596.
12. Doltsinis, I., Kang, Z., & Cheng, G. (2005). Robust design of non-linear structures using optimization methods. *Computer Methods in Applied Mechanics and Engineering, 194,* 1779–1795.
13. Beyer, H. G., & Sendhoff, B. (2007). Robust optimization—A comprehensive survey. *Computer Methods in Applied Mechanics and Engineering, 196*(33–34), 3190–3218.
14. Taflanidis, A. A. (2012). Stochastic subset optimization incorporating moving least squares response surface methodologies for stochastic sampling. *Advances in Engineering Software, 44,* 3–14.
15. Nigam, N. C., & Narayanan, S. (1994). *Applications of random vibrations.* Berlin: Springer; New Delhi: Narosa Publishing House.
16. Morison, J. R., O'Brien, M. P., Johnson, J. W., & Schaaf, S. A. (1950). The forces exerted by surface waves on piles. *Journal of Petroleum Technology, 189*, 149–154 (The American Institute of Mining, Metallurgical, and Petroleum Engineers).
17. Berge, B., & Penzien, J. (1974). Three dimensional stochastic response of offshore towers to wave forces. In *Proceedings Offshore technology Conference*, Paper No. OTC 2050.
18. Agerschou, H., & Edens, J. (1965). Fifth and first order wave-force coefficients for cylindrical piles. In *Proceeding of ASCE Coastal Engineering Specialty Conference* (pp. 219–248), Santa Barbara, USA.
19. Deb, K. (2011). Multi-objective optimization using evolutionary algorithms: An introduction. *KanGAL Report Number 2011003*, Department of Mechanical Engineering Indian Institute of Technology Kanpur.

Shear Strength of Semi-corrugated Webbed Beam

Anjaly J. Pillai and Laxmikant M. Gupta

Abstract The main purpose of using corrugation is to increase the shear strength of the web, hence no stiffeners are required for the same. This helps in reducing the material and fabrication cost. For a simply supported beam, the shear force is less in the middle portion of the span. Therefore, the web is kept plain in the middle portion and corrugations are provided for the remaining portion. Hence, it is called as semi-corrugated web. In this paper, various models of the web are analysed in ABAQUS. The shear stress of the plain-webbed beam and that of semi-corrugated webbed beam is compared for the same loading. The behaviour of the semi-corrugated web is then observed by changing the height of the web. The optimum depth of corrugation is found out by changing the flange width and the depth of corrugation.

Keywords Corrugation · Shear strength · Web

1 Introduction

Plate girder structure, fabricated from welded steel plate, is well recognized. Economical design of girders and beams normally requires thin webs. But if the web is extremely thin, the problem of plate buckling may arise. Possible ways to reduce this risk consist of using thicker plates, web stiffeners or strengthening the web by making it corrugation. The conventional provision of stiffeners to allow the use of thin webs has two disadvantages, i.e. high fabrication cost and a possible reduced life due to fatigue cracking that may initiate at the stiffener weld. The use of corrugated plates is used to replace the flat stiffened plates as the web can eliminate

A. J. Pillai · L. M. Gupta (✉)
Department of Applied Mechanics, Visvesvaraya National Institute of Technology, Nagpur 440010, India
e-mail: lmgupta@apm.vnit.ac.in

A. J. Pillai
e-mail: anjalypillai92@gmail.com

A. Rama Mohan Rao and K. Ramanjaneyulu (eds.), *Recent Advances in Structural Engineering, Volume 1*, Lecture Notes in Civil Engineering 11,
https://doi.org/10.1007/978-981-13-0362-3_38

both disadvantages. It is assumed that the web carries only shear forces due to the accordion effect in a corrugated web. Due to this, the corrugated steel webs fail due to shear buckling or yielding. Three different shear buckling modes (local, global and interactive) are possible, depending on the geometric characteristics of corrugated steel webs.

Extensive experimental and numerical investigations were found in the literature highlighting the behaviour and ultimate strength of girders with corrugated webs when subjected to compressive patch loads applied at the top flange explained in Elgaaly et al. [1]. The test results provided by Elgaaly et al. [1] have given information regarding failure of corrugated web under compressive patch loading. The behaviour of corrugated webs under fatigue loads has been carried out by Elgaaly et al. [2]. In this, six trapezoidally corrugated web plate girders are tested under monotonic and repeated loading under different stress ranges. Relationship between stress range (F_r) and the number of cycles (N) is developed for trapezoidally corrugated web plate girders. The shear strength and failure modes of corrugated webs are given by Driver et al. [3]. The effect of web initial geometric imperfections is assessed through measurements of out-of-plane displacements of the web. A lower bound equation is proposed considering web imperfections due to fabrication process and material nonlinearities. This equation takes into account both local and global bucklings of the web in elastic and inelastic domain. The shear strength and design criteria of trapezoidal corrugated webs, based on the first-order interactive equation, are given by Moon et al. [4]. The shear buckling parameter of corrugated webs, λ_s, is then proposed. The shear buckling strength, considering material inelasticity, residual stresses and initial imperfections, is determined from the buckling curves using the proposed λ_s. A series of tests were performed with large corrugated webs in order to verify the proposed shear strength. The shear buckling strength and design of curved corrugated steel webs for bridges considering material inelasticity are studied by Eldib [5]. The inelastic buckling strength is determined from the buckling curves based on the proposed shear buckling parameter λ_s. Shear buckling formula is proposed which depends on the geometric properties of the curved corrugated web profile. The parameters considered are web thickness to web height t_w/h_w, the radius R of the curved web and the corrugation angle θ.

In this paper, using a general-purpose finite element (FE) programme (ABAQUS), a numerical parametric study was carried out for a simply supported semi-corrugated web plate girders of length 5 m. The parameters considered to observe the effect on shear stress are height of web, flange width and depth of corrugation. Also, the optimum depth of corrugation was found out by varying the parameters mentioned.

2 Numerical Parametric Study

A numerical parametric study was carried out on simply supported plate girders with semi-corrugated web in ABAQUS [6], a general-purpose finite element programme. Parametric study was performed on number of models with varying the web height, flange width and depth of corrugation. The modelling including the loading, material and boundary conditions is described in the next section.

2.1 Verification of Finite Element Model

To verify the result of the finite element model, an eigenvalue analysis (with elastic properties of steel, i.e. modulus of elasticity E = 200,000 MPa and Poisson's ratio 0.3) of various plate girders is carried out to find their critical moment value that corresponds to lateral torsional buckling mode of failure. Critical moment of simply supported plate girder with plain web is evaluated, considering depth 100 and 300 mm. The end of the simply supported plate girder subjected to uniform end moment is shown in Fig. 1. The critical moment given by Timoshenko [7] is given by Eq. (1):

$$M_{\mathrm{cr}} = \sqrt{\frac{\Pi^2 EI_{\mathrm{y}}}{L^2}\left[GI_{\mathrm{t}} + \frac{\Pi^2 EI_{\mathrm{w}}}{L^2}\right]}. \tag{1}$$

where L is the unbraced length, I_{y} is the minor moment of inertia of the cross section, GI_{t} and I_{w} are the torsional and warping constants of the beam, respectively. The results of the comparison of manual calculation as per Eq. (1) and that from ABAQUS are summarized in Table 1. The deformed shape of the plate girder when undergoing lateral torsional buckling in mode 1 is shown in Fig. 2. It is

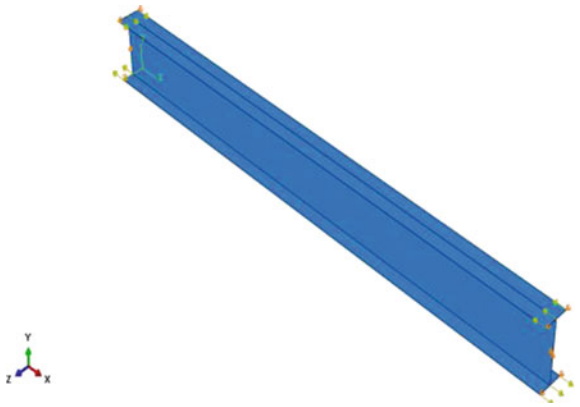

Fig. 1 Plain web with end moments and boundary conditions

Table 1 Comparison of critical moment (M_{cr})

Plate girders of depth (mm)	M_{cr} (manual calculation) (kNm)	M_{cr} (ABAQUS) (kNm)	% Error
100	14.6	16	9.5
300	241.7	249.1	3

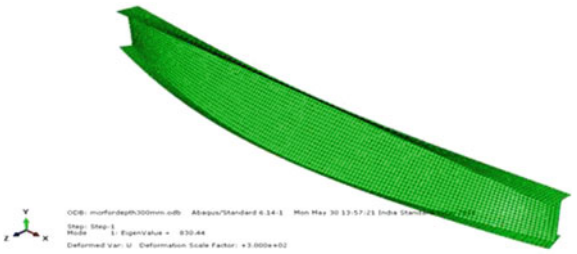

Fig. 2 Deformed shape of plate girder in buckling mode 1

understood from the figure that the beam deflects in the direction of load and then rotates about its longitudinal axis.

2.2 *Description of the FE Models for Semi-corrugated*

In this study, various models were prepared by changing the depth of corrugation, web height and flange width. The modelling of semi-corrugated webbed beam is explained below.

The element used in the models was four-node doubly curved shell element (S4R) available in ABAQUS [6]. The dimension of the upper and lower flange is 200 mm × 12 mm. The web thickness is 8 mm. The span of the plate girder is 5 m. Area load applied on the upper flange was of magnitude 0.0075 N/mm^2. The dimensions of the plain-webbed beam are shown in Fig. 3. The geometric notations

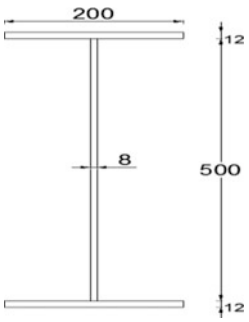

Fig. 3 Dimensions of the plain-webbed beam

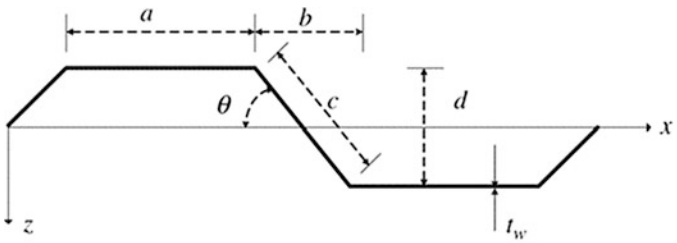

Fig. 4 Geometric notations of the semi-corrugated web (Shear strength and design of trapezoidally corrugated steel webs by Moon et al. [4])

Table 2 Comparison of shear stress values obtained for area load of 0.0075 N/mm^2

Shear stress at section	Manually (N/mm^2)	ABAQUS (N/mm^2)
At support	0.77	0.76
At 500 mm from support	0.61	0.61

of the semi-corrugated webbed beam shown in Fig. 4 and the dimensions used for modelling are given below.

Depth of corrugation, $d = 120$ mm
Flat panel width, $a = 200$ mm
Horizontal projection of the inclined panel width, $b = 200$ mm
Inclined panel width, $c = 233.24$ mm
Thickness of the web, $t_w = 8$ mm

Boundary conditions were applied to either end of the model to simulate the simply supported boundary condition by restraining appropriate degrees of freedom.

An elastic material was modelled with modulus of elasticity E = 200,000 MPa and Poisson's ratio 0.3.

The shear stress distribution along the cross section of the beam is calculated by the formula given in Eq. (2). For area load of 0.0075 N/mm^2, the shear stress for a plain-webbed beam at support and at 500 mm from the support is calculated using the shear stress equation and from ABAQUS. The values obtained are compared as shown in Table 2.

Also, the shear stress of a plain-webbed beam and that of semi-corrugated webbed beam caused due to area load of 0.0075 N/mm^2 is compared in Table 3. The semi-corrugated webbed beam modelled in ABAQUS [6] is shown in Fig. 5.

$$\tau = \frac{VA\bar{y}}{Ib_1}, \tag{2}$$

Table 3 Comparison of shear stress of plane web from that of semi-corrugated web for area load of 0.0075 N/mm^2

Shear stress at section	Plane web	Semi-corrugated web
	Analytically (N/mm^2)	Analytically (N/mm^2)
At support	0.68	0.54
At 500 mm from support	0.61	0.48

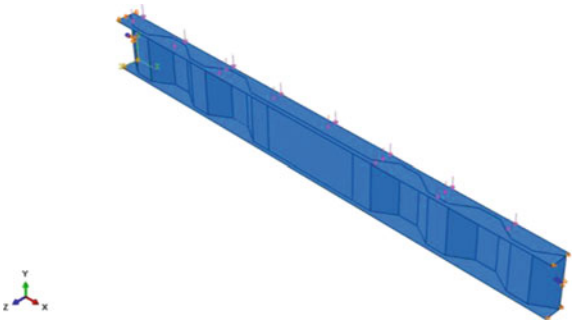

Fig. 5 Semi-corrugated web modelled in ABAQUS with loading and boundary conditions

Table 4 Comparison of maximum deflection

	Plain web	Semi-corrugated web
Maximum deflection (mm)	0.16	0.08

where $A\overline{y} = \int_{y_1}^{y_{max}} ydA$.

Since the cross section is same for both plain-webbed and semi-corrugated webbed beams, the shear stress variation is also the same. The maximum deflection in the direction of loading is compared as shown in Table 4.

The shear stress was compared by changing the following parameters tabulated in Table 5. These variations are explained below.

2.2.1 Depth of Corrugation

The depth of corrugation was changed from 80 to 120 mm with an increment of 10 mm for a web height of 500 mm and flange width of 200 mm.

Table 5 Parametric variations

Parameter varied	Parameter kept constant	Dimensions
Depth of corrugation (d)	Height of web (h_w) is 500 mm, flange width (b_f) is 200 mm	80–120 mm with an increment of 10 mm
Height of web (h_w)	Depth of corrugation (d) is 120 mm, flange width (b_f) is 200 mm	400–600 mm with an increment of 100 mm
Flange width (b_f)	Depth of corrugation (d) is 120 mm, height of web (h_w) is 500 mm	200–250 mm with an increment of 50 mm

2.2.2 Height of Web

The height of the web was changed from 400 to 600 mm with an increment of 100 mm for a depth of corrugation 120 mm and flange width 200 mm.

2.2.3 Flange Width

The flange width was changed from 200 to 250 mm. The depth of corrugation was also changed from 80 to 120 mm with an increment of 10 mm for 250 mm flange width.

3 Results of the Parametric Study

Figure 6 and Table 6 show the variation of shear stress by varying the depth of corrugation from 80 to 120 mm with an increment of 10 mm for 200 mm flange width.

From Fig. 6 and Table 6, it was observed that the shear stress was found to decrease from 80 to 100 mm and then increase from 110 and 120 mm. Therefore, the optimum depth of corrugation is 100 mm giving the least shear stress.

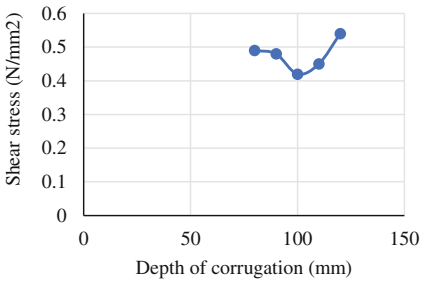

Fig. 6 Plot of shear stress and depth of corrugation

Table 6 Shear stress at the support on changing the depth of corrugation for the area load of 0.0075 N/mm^2

Models	Depth of corrugation, d (mm)	Shear stress at support (N/mm^2)
1	80	0.49
2	90	0.48
3	100	0.42
4	110	0.45
5	120	0.54

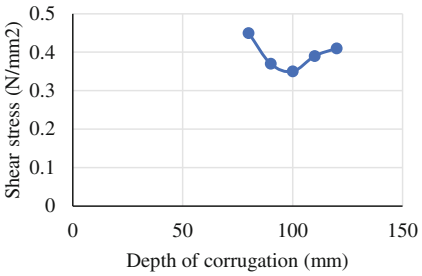

Fig. 7 Plot of shear stress and depth of corrugation for flange width of 250 mm

Table 7 Shear stress at the support on changing the flange width to 250 mm and increasing the depth of corrugation for the area load of 0.0075 N/mm^2

Models	Depth of corrugation, d (mm)	Shear stress at support (N/mm^2)
1	80	0.45
2	90	0.37
3	100	0.35
4	110	0.39
5	120	0.41

Figure 7 and Table 7 show the variation of shear stress for 250 mm flange width. Depth of corrugation was changed from 80 to 120 mm with an increment of 10 mm. There is no change in shear stress variation when the flange width is increased to 250 mm.

Figure 8 and Table 8 show the variation of shear stress for an increase in web height from 400 to 600 mm with an increment of 100 mm. The depth of corrugation was kept as 120 mm and flange width 200 mm.

The behaviour of semi-corrugated web on increasing the height of web was same as that of the plain web.

Reduction in shear stress with an increase in height of web is observed. The shear stress is reduced due to an increase in web area.

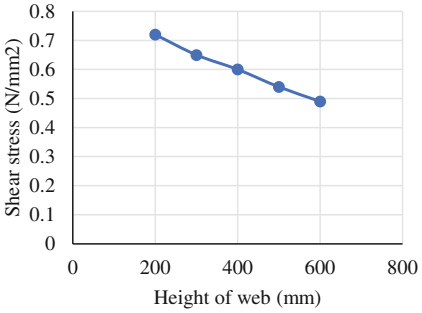

Fig. 8 Plot of shear stress and height of web

Table 8 Shear stress at support and at 500 mm from support on changing the height of web for the area load of 0.0075 N/mm^2

Models	Height of web, h_w (mm)	Shear stress at support (N/mm^2)
1	200	0.72
2	300	0.65
3	400	0.6
4	500	0.54
5	600	0.49

4 Conclusions

The aim of this study was to observe the variation in shear stress of semi-corrugated web by changing various parameters. Based on the results obtained, the following conclusions are made:

1. The shear stress distribution is same for a plate girder with plain web and that of corrugated web.
   The cross section is an I-section for both the cases. The only difference in semi-corrugated web is that the moment of inertia about *y*-axis increases due to shift of web from the centroid plane either to the left or right. Hence, the shear stress values are zero at top and bottom and maximum at the neutral axis.
2. The maximum deflection in the direction of loading was compared for a plain-webbed beam and that of semi-corrugated webbed beam. The maximum deflection obtained for semi-corrugated webbed beam was found to be less than that of plain-webbed beam. Hence, stiffness provided by the semi-corrugated webbed beam is more than that of plain-webbed beam.
3. Shear stress was found to decrease and then increase when the depth of corrugation was increased. Therefore, the depth of corrugation giving least shear stress termed as optimum depth of corrugation was found out for the loading considered.

4. The shear stress was found to decrease as the height of web increases due to increase in web area.
5. No change in shear stress variation was observed when the flange width was increased from 200 to 250 mm.

Acknowledgements The authors are thankful to the Director, Visvesvaraya National Institute of Technology, Nagpur.

References

1. Elgaaly, M., & Seshadri, A. (1997). Girders with corrugated webs under partial compressive edge loading. *Journal of Structural Engineering, 123*(6), 783–791.
2. Ibrahim, S. A., El-Dakhakhni, W. W., & Elgaaly, M. (2006). Behavior of bridge girders with corrugated webs under monotonic and cyclic loading. *Engineering Structures, 28*(14), 1941–1955.
3. Driver, R. G., Abbas, H. H., & Sause, R. (2006). Shear behavior of corrugated web bridge girders. *Journal of Structural Engineering, 132*(2), 195–203.
4. Moon, J., Yi, J. W., Choi, B. H., & Lee, H. E. (2009). Lateral–torsional buckling of I-girder with corrugated webs under uniform bending. *Thin-Walled Structures, 47*(1), 21–30.
5. Eldib, M. H. (2009). Shear buckling strength and design of curved corrugated steel webs for bridges. *Journal of Constructional Steel Research, 65*(12), 2129–2139.
6. ABAQUS. (2007). Version, ABAQUS 6.7 *User's manual. Inc. and Dassault systems.*
7. Timoshenko, S. P., & Gere, J. M. (1961). *Theory of elastic stability*. McGraw Hill.
8. EN 1993-1-5. *Eurocode 3: Design of steel structures-Part 1–5: Plated Structural Elements*.
9. Elgaaly, M., Hamilton, R. W., & Seshadri, A. (1996). Shear strength of beams with corrugated webs. *Journal of Structural Engineering, 122*(4), 390–398.
10. Elgaaly, M. (1999). *Plate and box girders. Structural engineering handbook*. US, Boca Raton: CRC Press LLC.
11. Duggal, S. K. (2000). *Design of steel structures*. Tata McGraw-Hill Education.
12. Abbas, H. H., Sause, R., & Driver, R. G. (2007). Behavior of corrugated web I-girders under in-plane loads. *Journal of Engineering Mechanics, 132*(8), 806–814.
13. Subramanian, N. (2008). *Design of steel structures* (pp. 980–983). Oxford University Press.
14. Moon, J., Yi, J., Choi, B. H., & Lee, H. E. (2009). Shear strength and design of trapezoidally corrugated steel webs. *Journal of Constructional Steel Research, 65*(5), 1198–1205.
15. Romeijn, A., Sarkhosh, R., & Hoop, H. (2009). Basic parametric study on corrugated web girders with cut outs. *Journal of Constructional Steel Research, 65*(2), 395–407.
16. Pasternak, H., & Kubieniec, G. (2010). Plate girders with corrugated webs. *Journal of civil engineering and management, 16*(2), 166–171.
17. Kiymaz, G., Coskun, E., Cosgun, C., & Seckin, E. (2010). Transverse load carrying capacity of sinusoidally corrugated steel web beams with web openings. *Steel and Composite Structures, 10*(1), 69–85.
18. Davison, B., & Owens, G. W. (Eds.). (2011). *Steel designers' manual.* Wiley.
19. Sause, R., & Braxtan, T. N. (2011). Shear strength of trapezoidal corrugated steel webs. *Journal of Constructional Steel Research, 67*(2), 223–236.
20. Divahar, R., & Joanna, P. S. (2014). The effect of web corrugation in cold-formed steel beam with trapezoidal corrugated web. *American Journal of Engineering Research, 3*(6), 137–142.

Failure Analysis of Composite Cylindrical Shells Using Continuum Damage Mechanics

Maharshi Kintada and Arbind Kumar Singh

Abstract Progressive failure analysis of laminated composite cylindrical shells subjected to internal pressure is carried out based on continuum damage mechanics. The state of distributed microscopic damage is modeled as the damage variable in the irreversible thermodynamic formulation. The damage tensor for composite material accounts for the breakage of fibers, matrix cracking in perpendicular to the fiber direction. The damaged constitutive modeling is formulated by the assumption of strain energy equivalence. The damage analysis of composite shells is carried out using C^0 continuous degenerated shell element which uses 3D continuum properties to reduce thickness degrees of freedom onto the surface in terms of rotations. Selective reduced integration is employed. In the present paper, brittle damage analysis of composite shell is investigated by implementing plane stress conditions into the damage evolution functions and assuming the damage distribution to be linear across the thickness of the shells. The nonlinear governing equations are solved using Newton–Raphson iterative technique to trace the equilibrium path. Examples have been presented to apply the employed model for composite shell problems.

Keywords Failure analysis · Continuum damage mechanics · Degenerated shell element

M. Kintada · A. K. Singh (✉)
Department of Civil Engineering, Indian Institute of Technology Guwahati, Guwahati 781039, India
e-mail: arvind@iitg.ac.in

M. Kintada
e-mail: maharshi.kintada@gmail.com

A. Rama Mohan Rao and K. Ramanjaneyulu (eds.), *Recent Advances in Structural Engineering, Volume 1*, Lecture Notes in Civil Engineering 11,
https://doi.org/10.1007/978-981-13-0362-3_39

1 Introduction

Laminated composite cylindrical shells have their wide range of applicability in aerospace engineering, turbine industry, and automobile industry. Progressive failure analysis of such shells is required to understand the structural integrity during their life cycle. Continuum Damage Mechanics (CDM) has developed as a tool to predict the progressive failure of laminated composites [1, 2]. A realistic analysis based on CDM is relied on the proper selection of damage variable and its evolution. Analytical solution of shells using CDM based constitutive relations is almost impossible to obtain. Finite element method is popularly used to analyze shell structures. A continuum-based shell element often called as degenerated shell element is employed in the present study. In the following paragraph, various damage models for composites and its implementation for shells are briefly reviewed.

Continuum damage mechanics has been used to understand the crack initiation, fracture and failure of metals and alloys, concrete, ceramics, and composites. Details of the formulation are available in many textbooks and monographs [1–4]. Application of CDM to composites started in 80s of last century [5, 7]. The breakage of fiber, cracking of matrix, debonding of fiber–matrix interface, and also delamination have been modeled in CDM using scalar [5, 6], vector [7], second-order tensor [8], and fourth-order tensor [9, 10] for damage variables.

Ladeveze and Le Dantec [6] proposed a ductile damage model for composites. The matrix cracking and the interface debonding were represented by individual scalar damage variable. The unilateral effect of matrix cracks along with only matrix plastic deformations was modeled. The elastic but nonlinear nature of composites in longitudinal (fiber) direction is observed by Allix et al. [11]. A modification of material characteristic parameter for the fiber direction modulus nonlinearity was presented. Matzenmiller et al. [9] proposed a damage model based on the failure criterion by Tsai–Wu. The effective stress is formulated by the strain equivalence concept. A fourth-order damage tensor was utilized to model the effective stresses in in-plane principal directions and also a separate variable for shear stress reduction. The damage evolution in accordance with strain rate effects was also presented. The failure mode of fiber in compression is introduced to be fiber kinking termed as fiber buckling modes, kink band models [12]. Barbero and DeVivo [10], Barbero and Lonetti [13] introduced a generalized damage evolution model based on Tsai–Wu failure criterion for in-plane loading and bending of composite plates. A fourth-order damage tensor was used which considers the damage as fiber breakage (longitudinal tension), fiber kinking (longitudinal compression), and matrix cracking in only tension. This model only needs the experimental shear stress–strain curve for its model parameters and critical damage parameters identification. In Lonetti et al. [14], composites with ductile polymer resins are modeled for unrecoverable plastic strains in matrix directions. The inter-laminar delamination is also accommodated with the damage variable in thickness direction. The unilateral effect is considered in Chapter Issues on Design

Shear Strength of RC 2 Deep Beams by Mayugo and Barbero in Barbero's book [12] for the deducing the effective stiffness in compression and tension for fiber damage. Kennedy and Nahan [15] utilized the eigenvalues of second-order damage tensor at lamina level for formulating the effective stress resultant and effective moment resultant at the laminate level. The extension-bending coupling matrix is assumed to be zero, i.e., the model is applicable only for symmetric laminates. It was assumed that the only membrane tension was dominant and flexure does not induce any compressive damage. A nonlocal damage model was also implemented to avoid mesh sensitivity problems in strain softening region. Shell buckling and post-buckling response effects on intra-laminar and inter-laminar progressive failure of composite panels with circular cutouts are carried out by Goyal et al. [16]. A second-order damage tensor is presented relating the damaged and undamaged material modulus. The Hashin failure criterion is used for constructing the damage evolution in fiber, matrix, and fiber-matrix shear damages.

Robbinson et al. [17] implemented the Barbero and DeVivo damage model to shear deformable laminated composite plates. A 3D element with quadratic damage distribution among the element area as well as thickness is considered. The failure load sensitivities for different element types, mesh densities, element distortion levels, and element integration schemes are compared. Gupta et al. [18, 19] analyzed shallow cylindrical shells using modified Love–Sanders shell theory based element with and without damage. Geometric nonlinearity is also implemented along with exact shear correction scheme. Problems with different radii of curvature, thickness, and lamina schemes are analyzed.

In the present paper, the continuum damage mechanics based progressive failure analysis of shells using degenerated shell element is carried out. Degenerated shell element is a general continuum shell element of which applicability is not limited to certain geometry. The advantages of degenerated shell element are its general applicability and easy implementation of large deformation formulation.

2 Continuum Damage Mechanics Model

The constitutive relations for damaged composites are obtained using strain energy equivalence principle [4] which can be stated as

$$\{\bar{\sigma}\} = [M]\{\sigma\};\ \{\bar{\varepsilon}\} = \left[M^{-1}\right]\{\varepsilon\} \tag{1a}$$

$$\{\sigma\} = [\bar{C}^{e}]\{\varepsilon\};\ \{\bar{\sigma}\} = [C^{e}]\{\bar{\varepsilon}\} \tag{1b}$$

where terms with overbar are effective quantities and $[M]$ is the fourth-order damage effect tensor which is related to the integrity tensor as [12]

$$M_{\mathrm{ijkl}} = \frac{1}{2}\left(\Omega_{\mathrm{ik}}\Omega_{\mathrm{jl}} + \Omega_{\mathrm{il}}\Omega_{\mathrm{jk}}\right) \tag{2}$$

The dual variable of the damage tensor is the integrity tensor, $\boldsymbol{\Omega} = \sqrt{\boldsymbol{I} - \boldsymbol{D}}$ and

$$D_{\mathrm{ij}} = d_i\delta_{\mathrm{ij}};\ i = 1,\ 2,\ 3.\ (\mathrm{no} - \mathrm{sum\ on\ i}) \tag{3}$$

where D_{ij} are the components of the second-order damage tensor $\boldsymbol{D}$. The coordinate system coinciding with the principal directions of $\boldsymbol{D}$ coincides with the fiber, transverse, and thickness directions and d_i are the eigenvalues of the damage tensor, which represents the damage ratio along these directions.

The damaged stiffness tensor $\bar{\boldsymbol{C}}^{\mathrm{e}}$ is derived from the concept of strain energy equivalence with the help of fourth-order damage effect tensor $\boldsymbol{M}$ and virgin constitutive matrix $\boldsymbol{C}^{e}$ as Barbero [12]

$$\bar{\mathbf{C}}^{\mathrm{e}} = \boldsymbol{M}^{\mathrm{T}}\boldsymbol{C}^{\mathrm{e}}\boldsymbol{M} \tag{4}$$

The Helmholtz-free energy density Φ for damaged composite considering the damage hardening can be written as

$$\Phi = \Phi(\boldsymbol{\varepsilon}, \boldsymbol{D}, \delta) = \left(\frac{1}{\rho}\right)\varnothing(\boldsymbol{\varepsilon}, \boldsymbol{D}) + \pi(\delta) \tag{5}$$

The internal variable δ in the above equation is a nondimensional damage hardening parameter that symbolizes the overall state of damage. The Clausis–Duhem inequality is given as [2],

$$\left(\{\sigma\} - \rho\frac{\partial\Phi}{\partial\{\varepsilon\}}\right)\{\dot{\varepsilon}\} - \left(\rho\frac{\partial\Phi}{\partial\{D\}}\right)\{\dot{D}\} - \left(\rho\frac{\partial\Phi}{\partial\delta}\right)\dot{\delta} \geq 0 \tag{6}$$

where ρ is the material density and $\{\dot{\square}\}$ indicates the time derivative of the quantity. The thermodynamic damage driving force Y and damage hardening variable γ are defined as [4]

$$\{Y\} = -\rho\frac{\partial\Phi}{\partial\{D\}} = -\frac{\partial\left(\frac{1}{2}\{\varepsilon\}^{\mathrm{T}}[\bar{C}^{\mathrm{e}}]\{\varepsilon\}\right)}{\partial\{D\}} = -\frac{1}{2}\{\varepsilon\}^{\mathrm{T}}\frac{\partial[\bar{C}^{\mathrm{e}}]}{\partial\{D\}}\{\varepsilon\} \tag{7a}$$

$$\gamma = -\rho\frac{\partial\Phi}{\partial\delta} \tag{7b}$$

A generalized damage loading surface proposed by Barbero and Lonetti [13] which uses thermodynamic force and hardening parameters is employed in the present study. The damaged surface defined as a convex surface is given as

$$g(Y,\gamma) = \sqrt{J_{11}Y_1^2 + J_{22}Y_2^2 + J_{33}Y_3^2} - (\gamma_0 + \gamma(\delta)) \tag{8}$$

where J_{11}, J_{22}, and J_{33} represent experimentally obtained material constants that define the damage tolerance of the material. Y_1, Y_2, and Y_3 are thermodynamic forces in principal directions. The hardening function $\gamma(\delta)$ denotes the damage surface expansion threshold and γ_0 is the initial damage surface threshold. These material constants are taken from experimental results as in Barbero and DeVivo [10]. Extremization of the dissipative inequality $\{Y\}\{\dot{d}\} - \gamma\dot{\delta} \geq 0$ subjected to the constraint $g(Y,\gamma) = 0$ yields damage evolution equations

$$\dot{D}_{ii} = \dot{\lambda}\frac{\partial g}{\partial Y_{ii}},\ \dot{\gamma} = \dot{\lambda}\frac{\partial g}{\partial \delta} \tag{9}$$

where $\dot{\lambda}$ is the Lagrange multiplier. The implementation of the above constitutive equations is employed in the nonlinear finite element formulation discussed in next section.

3 Finite Element Formulation

In this paper, an eight-noded degenerated shell element formulation for laminated composite shells is employed with Gauss integration along the thickness direction.

Geometric definition of the element:

In the present formulation, four types of coordinate systems are employed: shell coordinate system (x', y', z'), global coordinate system (x, y, z), parent element coordinate system (ξ, η, ς), and material coordinate system (1, 2, 3). The coordinate of any point is a transformation of element coordinate system using [20]

$$\begin{Bmatrix} x \\ y \\ z \end{Bmatrix} = \sum N_i \begin{Bmatrix} x_i \\ y_i \\ z_i \end{Bmatrix} + \sum N_i \varsigma \frac{t_i}{2} \begin{Bmatrix} l_{3i} \\ m_{3i} \\ n_{3i} \end{Bmatrix} \tag{10}$$

in which N_i is the shape function of ith node of the eight-node quadratic plane elements (x_i, y_i, and z_i) that are the mid-surface global coordinates of the ith nodal point and l_{3i},m_{3i}, and n_{3i} represent the directional cosines of the mid-surface unit normal. At any typical node i, one can write a thickness direction vector V_{3i} as

$$V_{3i} = t_i \begin{Bmatrix} l_{3i} \\ m_{3i} \\ n_{3i} \end{Bmatrix}; \text{ where } \begin{Bmatrix} l_{3i} \\ m_{3i} \\ n_{3i} \end{Bmatrix} = \frac{1}{t_i} \begin{Bmatrix} x_m - x_n \\ y_m - y_n \\ z_m - z_n \end{Bmatrix} \tag{11}$$

Displacement field definition of the element:

The displacement of point P on the vector V_{3i} is formed by displacement of node "i" plus the displacement relative to node "i" created by rotation of V_{3i} with respect to V_{1i} and V_{2i}. The relative displacement components must be resolved into (x, y, z) components before being added to the displacements of node "i". Thus, the total displacement at the node "i" is [20]

$$u_i^{\mathrm{P}} = u_i - \alpha_i \left(\varsigma \frac{t_i}{2}\right) l_{2i} + \beta_i \left(\varsigma \frac{t_i}{2}\right) l_{1i} \tag{12}$$

Displacement of an arbitrary point in the element is

$$\begin{Bmatrix} u \\ v \\ w \end{Bmatrix} = \sum N_i \begin{Bmatrix} u_i \\ v_i \\ w_i \end{Bmatrix} + \sum N_i \varsigma [\mu] \begin{Bmatrix} \alpha_i \\ \beta_i \end{Bmatrix} \tag{13}$$

The strains are expressed as

$$\begin{Bmatrix} \varepsilon_{\mathrm{xx}} \\ \varepsilon_{\mathrm{yy}} \\ \varepsilon_{\mathrm{zz}} \\ \gamma_{\mathrm{xy}} \\ \gamma_{\mathrm{yx}} \\ \gamma_{\mathrm{zx}} \end{Bmatrix} = \left\{ \frac{\partial u}{\partial x} \quad \frac{\partial v}{\partial y} \quad \frac{\partial w}{\partial z} \quad \frac{\partial u}{\partial y} + \frac{\partial v}{\partial x} \quad \frac{\partial v}{\partial w} + \frac{\partial w}{\partial y} \quad \frac{\partial u}{\partial z} + \frac{\partial w}{\partial x} \right\}^T = [H][J]^{-1}[G]\{\mathrm{u}\}$$

$$= [B]\{\mathrm{u}\} \tag{14}$$

Here, $[G]$ matrix is displacement derivative matrix with respect to (ξ, η, ς), $[H]$ is relating matrix from strains to displacement derivatives, and $[J]^{-1}$ is the inverse of the 9×9 Jacobian matrix $[J]$. All six strains are included in the above equation because the shell mid-surface has no particular orientation with respect to Cartesian coordinates (x, y, z) and left if any stiffness arises after converting the constitutive matrix to the shell coordinate system. Plane stress condition $\sigma_3 = 0$ is implemented through the stress–strain relation shown in next paragraph. As the displacement and strains are defined in (x, y, z) space only, it cannot be applied directly to a problem in shell coordinate system. With the assumption of no thickness stress, i.e., $\sigma_3 = 0$ is in global axis, and applying this formulation to a shell coordinate system requires a transformation of the current (x, y, z) system to the shell coordinate system (x', y', z'):

$$\{\varepsilon'\} = [\mathrm{T}_\varepsilon]\{\varepsilon\} \tag{15}$$

The above discussed is a way of orienting element properties to element face using element Jacobian [21]. The constitutive relation for an orthotropic material is given as

$$\begin{Bmatrix} \sigma_{11} \\ \sigma_{22} \\ \sigma_{33} \\ \tau_{12} \\ \tau_{23} \\ \tau_{31} \end{Bmatrix} = \begin{bmatrix} \frac{E_{11}}{(1-\upsilon_{12}\upsilon_{21})} & \frac{\upsilon_{21}E_{11}}{(1-\upsilon_{12}\upsilon_{21})} & 0 & 0 & 0 & 0 \\ \frac{\upsilon_{12}E_{22}}{(1-\upsilon_{12}\upsilon_{21})} & \frac{E_{22}}{(1-\upsilon_{12}\upsilon_{21})} & 0 & 0 & 0 & 0 \\ 0 & 0 & 0 & 0 & 0 & 0 \\ 0 & 0 & 0 & G_{12} & 0 & 0 \\ 0 & 0 & 0 & 0 & G_{23} & 0 \\ 0 & 0 & 0 & 0 & 0 & G_{31} \end{bmatrix} \begin{Bmatrix} \varepsilon_{11} \\ \varepsilon_{22} \\ \varepsilon_{33} \\ \gamma_{12} \\ \gamma_{23} \\ \gamma_{31} \end{Bmatrix} \tag{16}$$

$$\{\sigma\} = [C^{\mathrm{e}}]\{\varepsilon\}$$

where these directions (1, 2, 3) are presumed to be in the principal material directions of the material, i.e., as orthotropic configuration.

The governing equations are solved using Newton–Raphson method given as

$$[K_{\mathrm{T}}]\{\Delta u^i\} = \{f\} - \int_V [B]^T\{\sigma^i\}dV \tag{17}$$

where $[K_{\mathrm{T}}]$ is the tangential stiffness at the ith iteration.

$$[K_{\mathrm{T}}]^e = \iint \int_{-1}^{1} [B]^T[C_T][B]|J|d\xi\,\mathrm{d}\eta\,\mathrm{d}\zeta \tag{18}$$

where $[C_{\mathrm{T}}]$ is the tangential constitutive relation obtained from Newton–Raphson solution of nonlinear constitutive relations in Sect. 2. As the composite consists of lamina which is having different material configurations, a layer-wise thickness integration scheme is recommended by Panda and Natarajan [21]. Using incremental finite element formulation as in Eq. (17), the incremental displacements are found out upon a proportional load increment, and the strains at each Gauss point are calculated. The incremental damage variable values are calculated and the damage variables are updated. This iterative procedure is repeated till the norm of the incremental displacement vector between two consecutive iterations is less than the specified convergence tolerance (0.001%). The loading increments are continued till the maximum value of the damage variables reaches unity or convergence failure.

Layer-wise integration

In the present work, 3 x 3 x 2 for bending and 2 x 2 x 2 for shear terms (selective reduced integration) is used for thick and thin shells respectively. For layer-wise integration scheme, the integration limits are not from −1 to 1 in any layer. To overcome this, the variable in any *k*th layer is changed to ζ_k such that ζ_k varies from −1 to 1 in the *k*th layer. Thus, the stiffness integration becomes

$$\varsigma = -1 + \frac{1}{t}\left[-h_k(1-\varsigma_k) + 2\sum_{j=1}^{k} h_j\right] \tag{19a}$$

$$[K_T]^e = \sum_{k=1}^{n} \iint \int_{-1}^{1} [B]^T [C_{Tk}][B]|J| \frac{h_k}{t} d\xi \, d\eta \, d\zeta_k \tag{19b}$$

The internal force vector is evaluated by integrating the stresses at the Gauss points (ξ, η, ζ),

$$\{r^e\} = \int_V [B]^T \{\sigma\} dV = \sum_{k=1}^{n} \iint \int_{-1}^{1} [B]^T \{\sigma\} |J| \frac{h_k}{t} d\xi \, d\eta \, d\zeta_k \tag{20}$$

4 Results

The developed finite element formulation is applied to a composite cylindrical shell with lamina configurations of $[0/90]_{ns}$ (where n is any number) to carry out damage analysis. Problems involving shallow and deep shells are chosen to check the performance of the present degenerated shell element in combination with progressive failure analysis for membrane and bending failure loads. The results are plotted in contour levels by linear extrapolation of the results from Gauss points to the nodes. The evolution of damage of a laminated composite shell subjected to uniformly distributed transverse loading is analyzed. The shear correction factor for the first-order shear deformation theory to account for through the thickness variation of transverse shear stresses is taken as $k = 1.2$. The boundary conditions considered unless otherwise specified are as follows:

Immovable simply supported or hinged (S):

$$u_0 = v_0 = w_0 = \theta_x = 0 \, \textit{along curved edges}$$

$$u_0 = v_0 = w_0 = \theta_y = 0 \, \textit{along straight edges}$$

Clamped (C):

$$u_0 = v_0 = w_0 = \theta_x = \theta_y = 0 \, \textit{along all edges}$$

The combinations of support conditions considered are

SSSS: All edges simply supported;
CCCC: All edges clamped;
SSFF: Simply supported along straight edges and free along curved edges;
CCFF: Clamped along straight edges and free along curved edges.

Unless specified, material properties considered are [10] as follows:

E_{11} = 167 GPa, E_{22} = 8.13 GPa, $G_{12} = G_{23} = G_{31}$ = 8.8252 GPa, υ_{12} = 0.27; F_{1t} = 3060 MPa, F_{1c} = 1255 MPa, F_{2t} = 35.8 MPa, F_6 = 75 MPa; J_{11} = 0.9524 10^{-15}, $J_{22} = J_{33}$ = 0.4381 $\times$ 10^{-12}, and k = 7.595 $\times$ 10^{-07} where E, G, and υ are Young's modulus, shear modulus, and Poisson's ratio, respectively. The subscripts 1, 2, and 3 represent the principal material directions (Figure 1).

The present degenerated shell element formulation along with evolving damage is validated with four-layered cross-ply $[0/90]_S$ laminated SSFF cylindrical panel. The geometrical properties of the problem are

a = 2 m, a/h = 100, r_1/a = 2.0, and ϕ = 0.4 rad.

Laminated cylindrical shell: $[0/90]_2$.

Boundary Conditions: SSFF.

The values in the brackets are the results from Gupta et al. [18]. The values of maximum damage eigenvalues column are obtained from the maximum of all the eigenvalues for the specific principal direction only at failure load.

It has been observed that the present elastic damage analysis results are in close with the solutions given by Gupta et al. [18]. The present FEM analysis stopped at 9.2 MPa due to convergence failure. The transverse loading effects on the evolution of damage variable in thickness direction are observed to very low than damage variables in other principal directions. The composite laminate is failed in matrix

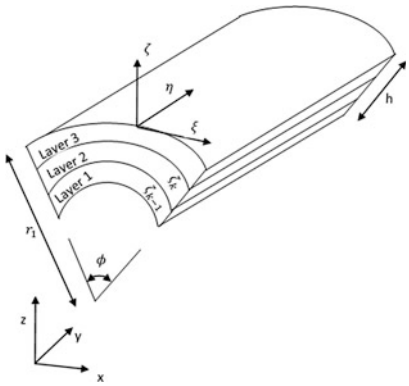

Fig. 1 Typical laminated cylindrical shell with global and local coordinate system

Table 1 Mesh convergence study and validation with results of damage analysis of laminated cylindrical shell

Mesh	Failure load (MPa)	$w_{0\ center}/h$	Max-D_1	Max-D_2	Max-D_3
5 × 5	9.2 (9.2)	9.7867 (10.622)	0.2411 (0.2313)	0.8445 (0.8881)	4.113×10^{-03} (1.407×10^{-04})
10 × 10	9.2 (9.2)	9.7867 (10.622)	0.2411 (0.2313)	0.8445 (0.8881)	4.118×10^{-03} (1.323×10^{-04})
20 × 20	9.2 (9.2)	9.7867 (10.622)	0.2411 (0.2312)	0.8445 (0.8880)	4.118×10^{-03} (1.284×10^{-04})

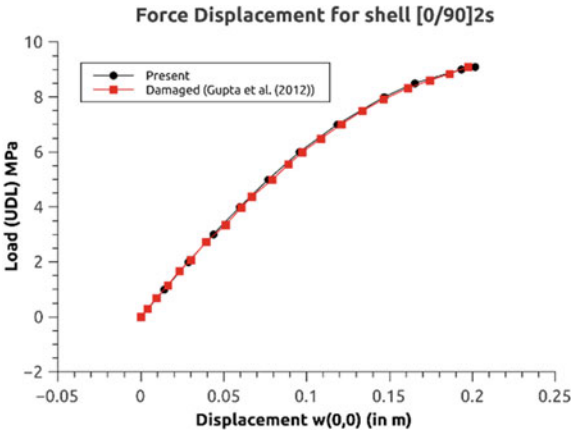

Fig. 2 Force–displacement curve of a shell with $[0/90]_{2s}$ configuration

cracking in the upper middle layer (top Gauss points) which yielded the maximum damage variable of 0.8445 at (x/a = 0.511, y/b = 0.511, and z/h = 0.65). There is no much mesh sensitivity observed in the results after 5by5 mesh (Table 1).

The present shell element is based on degenerated shell element, whereas Gupta et al. [18] is based on Love–Sanders shell theory. The present element can also be used for doubly curved shells. Force–displacement curves using degenerated shell element with plane stress constitutive model and linear distribution of damage along thickness are plotted in Fig. 2 which is exactly matching with equilibrium path given in Gupta et al. [18]. Hence, a linear distribution of damage across thickness with plane stress constitutive model can also be sufficient for thin shells.

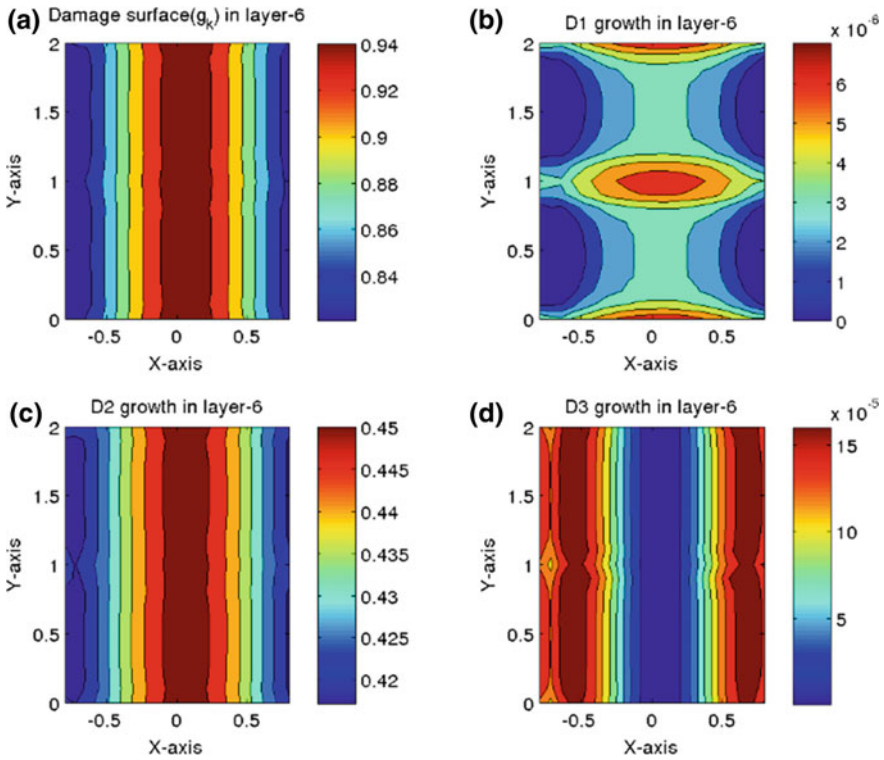

Fig. 3 Damaged surface and all damage eigenvalues plotted at sixth layer of Gauss points at a load of 5 MPa

The damage contours were plotted using MATLAB as shown in Figs. 3, 4, 5, and 6 to understand the progression of damage across the whole shell. *Y*-axis shows the length and *X*-axis shows the angular direction of the cylindrical shell (here, *X* and *Y* are used for legibility rather than *x* and *y* used before). The layer (Here, layer means layer of Gauss points starts from bottom along the whole laminate—2 Gauss points layer along thickness per lamina) is chosen where maximum transverse matrix cracking is occurring (Figs. 3, 4, and 5). The D_2 contours for different load steps are plotted at 5, 8.2, and 9.2 MPa as shown in Figs. 3, 4, and 5. A contour plot at layer of maximum D_1 is also plotted in Fig. 6b. It was observed

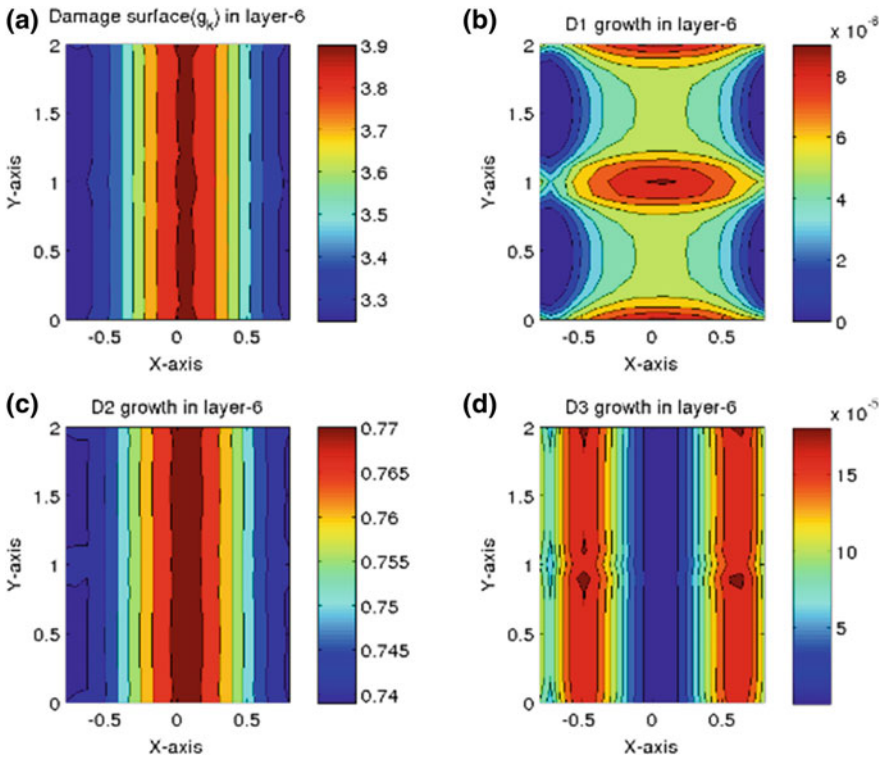

Fig. 4 Damaged surface and damage eigenvalues plotted at sixth layer of Gauss points at a load of 8.2 MPa

from the Figs. 3, 4, and 5 that the matrix cracking was initiated near the $X = 0$, and it can be interpreted as the matrix damage, i.e., debonding occurred at the fiber–matrix interfaces.

The critical eigenvalues D_2 were initiating at $X = 0$ and spreading across the Y-axis in either direction. At the failure load (final stage), the fibers act as a loose bundle of fibers. The contour showing maximum damage eigenvalue D_1 plotted at eighth layer of laminate is shown in Fig. 6b. It can be interpreted from Fig. 6b that the multiple brittle fractures of fibers have occurred (same location near $X = 0$).

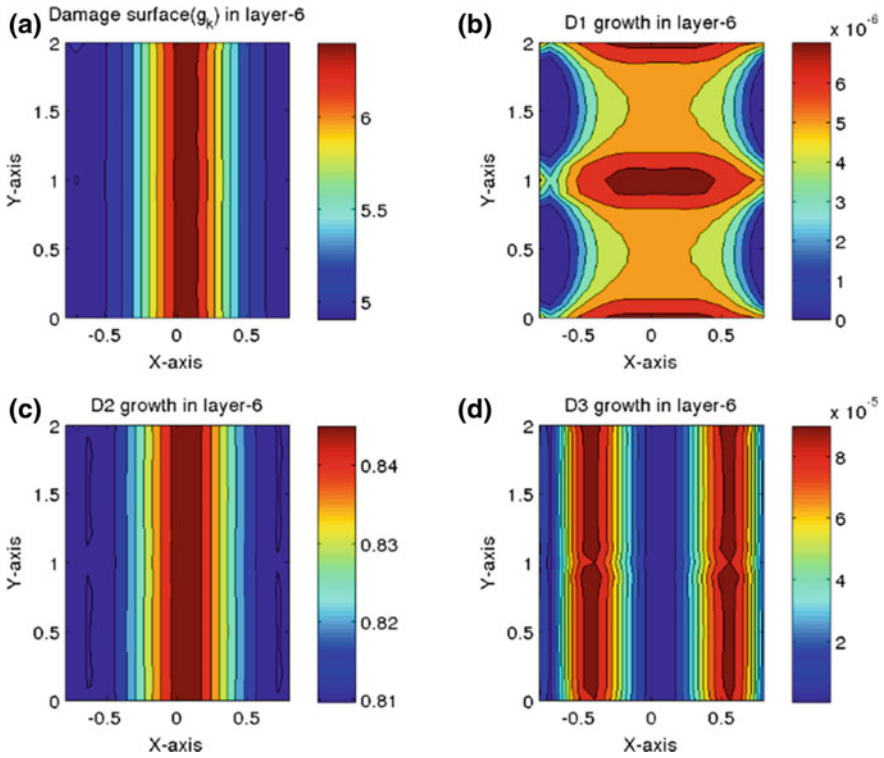

Fig. 5 Damaged surface and eigenvalues plotted at sixth layer of Gauss points at a load of 9.2 MPa

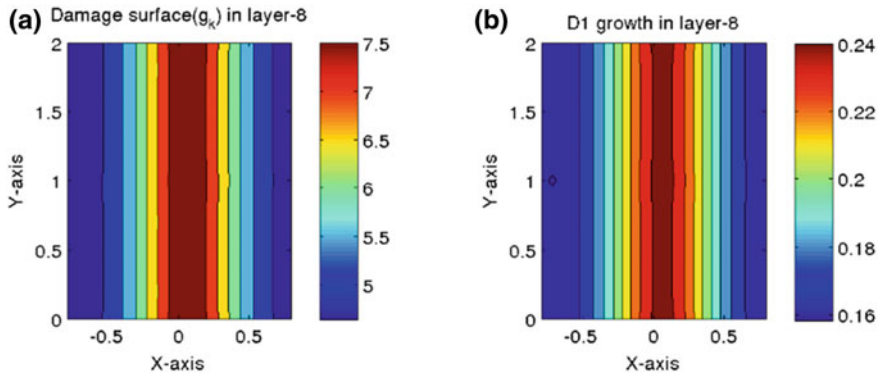

Fig. 6 Damaged surface and damage eigenvalue D_1 plotted at eighth layer of Gauss points at a load of 9.2 MPa

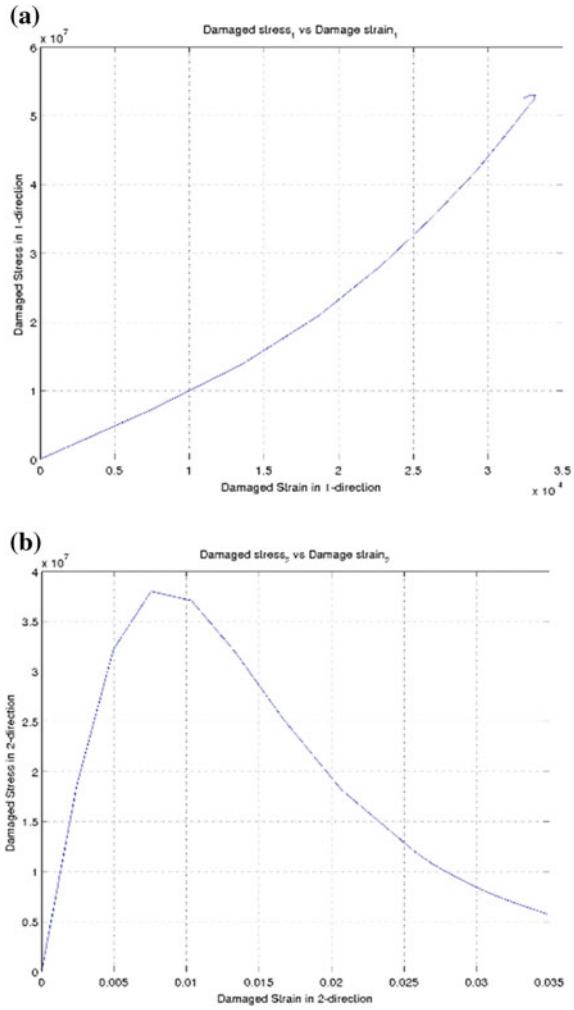

Fig. 7 Damaged stress–strain curves at the critical gauss point at the failure load (9.2 MPa)

The degraded stress–strain curve in Fig. 7 shows the stiffness degradation at the D_2 maximum critical Gauss point. As the damaged surface (Figs. 3a, 4a, 5a and 6a) is obtained from Tsai–Wu failure criterion, the damaged surface here serves as indicative measure of the damage level at that corresponding load.

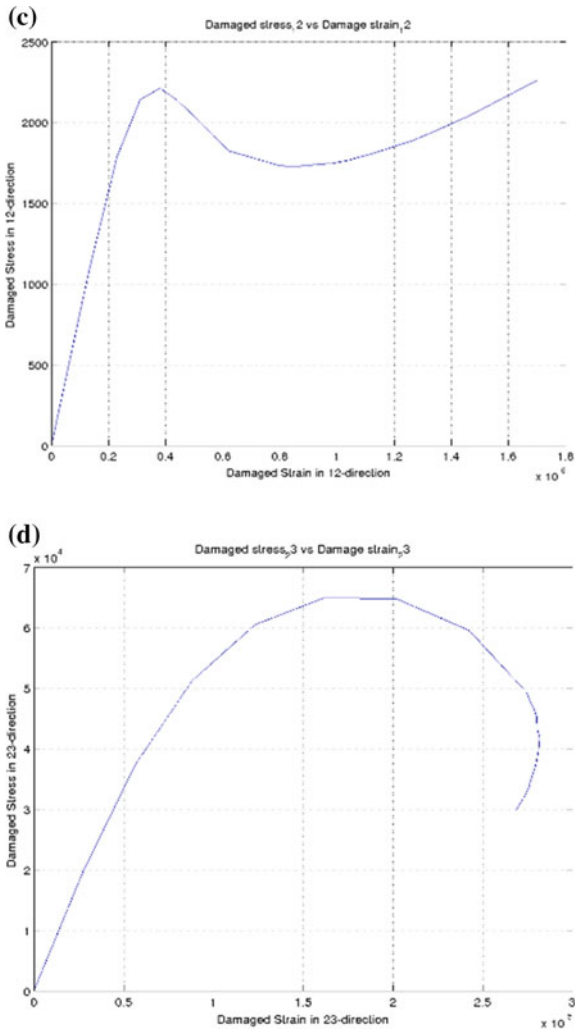

Fig. 7 (continued)

5 Conclusions

Failure analysis of composite laminated shell with $[0/90]_{2S}$ configuration is carried out using degenerated shell element based on continuum damage mechanics. It was observed that assumption of plane stress condition and linear distribution of damage across thickness is sufficient for thin shells. It was also shown that the damage initiation is possible at $X = 0$ and spread of damage will occur across the y-axis. Maximum damage of fibers occurred in topmost layer, while matrix damage is in

middle layer. The failure of composite cylindrical shells is possible by damage in longitudinal bending than cylindrical bending.

References

1. Krajcinovic, D. (1996). *Damage mechanics* (Vol. 41). Elsevier.
2. Lemaitre, J., & Desmorat, R. (2005). Engineering damage mechanics: Ductile, creep, fatigue and brittle failures. Springer Science & Business Media.
3. Voyiadjis, G. Z., & Kattan, P. I. (2005). *Damage mechanics*. CRC Press.
4. Zhang, W., & Cai, Y. (2010) Continuum damage mechanics and numerical applications. Springer Science & Business Media.
5. Dumont, J. P., Ladeveze, P., Poss, M., & Remond, Y. (1987). Damage mechanics for 3-D composites. *Composite Structures, 8*(2), 119–141.
6. Ladeveze, P., & Le Dantec, E. (1992). Damage modelling of the elementary ply for laminated composites. *Composite Science and Technology, 43,* 257–267.
7. Talreja, R. (1985). A continuum mechanics characterization of damage in composite materials. In *Proceedings of the Royal Society of London A: Mathematical, Physical and Engineering Sciences* (Vol. 399, No. 1817, pp. 195–216). The Royal Society.
8. Voyiadjis, G Z., Venson, A. R., Abu-Alrub, R. K. (2012). *Advances in damage mechanics: Metals and metal matrix composites*. Elsevier.
9. Matzenmiller, A., Lubliner, J., & Taylor, R. L. (1995). A constitutive model for anisotropic damage in fiber-composites. *Mechanics of Materials, 20,* 125–152.
10. Barbero, E. J., & De Vivo, L. (2001). A constitutive model for elastic damage in fiber-reinforced PMC laminae. *International Journal of Damage Mechanics, 10*(1), 73–93.
11. Allix, O., Ladeveze, P., & Vittecoq, E. (1994). Modelling and identification of the mechanical behavior of composite laminates in compression. *Composites Science and Technology, 51,* 35–42.
12. Barbero, E. J. (2011). *Finite element analysis of composite materials*. CRC Press.
13. Barbero, E. J., & Lonetti, P. (2001). Damage model for composites defined in terms of available data. *Journal of Composite Materials, 4*(8), 299–315.
14. Lonetti, P., Zinno, R., Greco, F., & Barbero, E. J. (2003). Interlaminar damage model for polymer matrix composites. *Journal of Composite Materials, 37*(16), 1485–1504.
15. Kennedy, T. C., & Nahan, M. F. (1996). A simple nonlocal damage model for predicting failure of notched laminates. *Composite Structures, 35*(2), 229–236.
16. Goyal, V. K., Jaunky, N. R., Johnson, E. R., & Ambur, D. R. (2004). Intralaminar and interlaminar progressive failure analyses of composite panels with circular cutouts. *Composite Structures, 64*(1), 91–105.
17. Robbins, D. H., Jr., Reddy, J. N., & Rostam-Abadi, F. (2005). An efficient continuum damage model and its application to shear deformable laminated plates. *Mechanics of Advanced Materials and Structures, 12*(6), 391–412.
18. Gupta, A. K., Patel, B. P., & Nath, Y. (2012). Continuum damage mechanics approach to composite laminated shallow cylindrical/conical panels under static loading. *Composite Structures, 94*(5), 1703–1713.
19. Gupta, A. K., Patel, B. P., & Nath, Y. (2013). Continuum damage modeling of composite laminated plates using higher order theory. *Composite Structures, 99,* 141–151.
20. Krishnamoorty, C. S. (1994). *Finite element analysis: Theory and programming*. Mc Graw Hill.
21. Panda, S., & Natarajan, R. (1981). Analysis of laminated composite shell structures by finite element method. *Computers & Structures, 14*(3–4), 225–230.

Prediction of Compressive Strength of Concrete: Machine Learning Approaches

Dipro Dutta and Sudhirkumar V. Barai

Abstract Abrams' law is commonly used to predict the compressive strength of concrete with respect to the water content of the mix, but it is largely inaccurate. High-performance concrete, with its complex additional ingredients, makes the prediction more difficult. The goal of the paper is to find the most accurate model for prediction of the compressive strength of a given concrete mix using machine learning (ML). First, the various ML models are explained along with their working principles. Second, the evaluation methods used for the error analysis in the study are discussed. Third, the findings of the study are displayed and inferences are drawn from them. It is found that the 2-nearest-neighbour performs the best with an error of 8.5% and a standard deviation of 1.55.

Keywords Machine learning · Prediction · Strength of concrete

1 Introduction

The compressive strength is the most important property of a concrete mix. Abrams' law of 1919 gives an inverse proportionality between the compressive strength of hardened concrete and the water-to-cement ratio (*w*/*c*) used in the concrete mix measured by volume [1]. It, hence, implies that the strengths of distinct but comparable concrete are identical as long as their *w*/*c* ratios remain the same, regardless of the details of their composition. The law is acceptable within wide limits but is not completely accurate [2]. Abrams assumed that the concrete is completely compacted. For this, the air gaps present between the cement and the

D. Dutta
Civil Engineering, Manipal Institute of Technology, Manipal 576104, India
e-mail: diprodutta96@gmail.com

S. V. Barai (✉)
Department of Civil Engineering, Indian Institute of Technology Kharagpur, Kharagpur 721302, West Bengal, India
e-mail: skbarai@civil.iitkgp.ernet.in

A. Rama Mohan Rao and K. Ramanjaneyulu (eds.), *Recent Advances in Structural Engineering, Volume 1*, Lecture Notes in Civil Engineering 11,
https://doi.org/10.1007/978-981-13-0362-3_40

dry particles of the aggregates need to be removed completely after the addition of water-to-concrete mix. However, in practice, fully compacted concrete still contains 1% of air gaps [3].

Along with the basic components of conventional concrete (Portland cement, fine and coarse aggregates and water), HPC incorporates supplementary cementitious ingredients like fly ash, silica fume, blast furnace slag and usually a chemical admixture, such as superplasticizer. These additional ingredients make HPC a complex conglomerate, and predicting its strength becomes difficult.

Compressive strength can also be predicted using regression analyses and several methods which can be collectively classified as machine learning (ML). One of the popular machine learning approaches is Artificial Neural Networks (ANN). The ANN model is inspired by the biological neural network. It utilises several computing elements to parallel process the input data. These elements, called artificial neurons, are arranged in layers and interact with each other via weighted connections. Backpropagation algorithms are popularly used to solve problems of ANN. Backpropagation minimises the error using a gradient descent method. Yeh [5] compared regression and ANN for predicting compressive strength of the concrete. He found that the ANN model performs better than regression.

There is a need to search and develop better machine learning models apart from well-reported ANN models. This study explores ANN further, along with another model of ML called the Instance-Based Learning (IBL) or *k*-Nearest Neighbours (k-NN).

In the present study, the main objective is to compare the machine learning models—ANN and IBL—for predicting compressive strength of the concrete. This study presents—ANN based two back propagation algorithms and the IBL model for integral values of k ranging from 1 to 6.

2 Background of Tools Used

Machine learning (ML), a subset of artificial intelligence, has evolved from the study of pattern recognition. Two ML subfields have been studied. Yeh [5] compared regression and ANN for predicting compressive strength of the concrete. He found that the ANN model performs better than regression.

Instance-based learning (IBL) is a learning method which compares new problem instances with the instances that the programme has been trained. Its *k*-nearest training examples (*k*-nearest neighbours or k-NN) are utilised to deliver the output, and the value is determined as the mean of the output values of its *k*-nearest neighbours.

The contribution of the neighbours has weights assigned to them. This allows the output to be more similar to the nearer neighbours than the distant ones.

Artificial neural networks (ANN) is learning method used to solve problems requiring nonlinear and parallel processing through a mesh of simple computing elements called artificial neurons. Each neuron can have R inputs (x) and each input is

weighted (w). There is a bias with a constant input of 1. The sum of the weighted inputs and the bias passes through the transfer function (f) and generates an output (a).

$$a = f\left(b + \sum_{1}^{R} w_i x_i\right)$$

Backpropagation algorithm, commonly used in ANN, minimises the error by the gradient descent method. The neurons are arranged in two or more layers and interact with each other via weighted connections. The first layer is an input layer where the data is fed into the network, and the last layer is an output layer which contains the response of the network to the given input. The intermediate layers (hidden layers) facilitate the interactions between the elements of the network. The learning process goes through several iterations (epochs) where the weights are modified till the network can properly associate between the inputs and their respective outputs. Once trained, the network can rapidly simulate the desired output to a given input of similar nature.

Backpropagation further involves several algorithms such as the Levenberg–Marquardt algorithm (LM) and a variable-learning-rate-with-momentum gradient descent algorithm (GDX).

LM is an iterative technique that locates the minimum of a function as the sum of squares of nonlinear functions. It is used to solve nonlinear least-squares problems [4].

In the standard steepest descent algorithm, the training rate is a constant value. An optimum learning rate is important for the algorithm's performance. A high rate makes the algorithm oscillate unstably, whereas a low rate makes the algorithm take too long to converge. In fact, the ideal rate keeps changing during the training of the network. The algorithm performs better if the learning rate is allowed to change during training. GDX implements a momentum factor to determine the varying rate.

3 Data Collection and Analysis

The data was collected from the machine learning repository of the University of California, Irvine [5]. It provided 1030 samples. The output variable is the compressive concrete strength (MPa) which depends on eight input variables:

1. Cement (kg/m^3),
2. Fly ash (kg/m^3),
3. Blast furnace slag (kg/m^3),
4. Water (kg/m^3),
5. Superplasticizer (kg/m^3),
6. Coarse aggregate (kg/m^3),
7. Fine aggregate (kg/m^3)
8. Age at the time of testing (days).

Table 1 Feature summary of the data set

	Min	1st Quartile	Median	Mean	3rd Quartile	Max
Cement	102	160.1	260.5	265.4	322.2	540
Slag	0	0	94.3	86.3	160.1	359.4
Ash	0	0	59.5	62.8	120.0	200.1
Water	121.7	171	185	183.1	193.2	247
S.P.	0	0	7.8	7.0	10.3	32.2
C.A.	801	882.2	953	956.1	1012.4	1145
F.A.	594	712	769.2	764.4	810.9	992.6

The set includes data from several sources. This verifies the reliability of the data [2]. Only, the 28-day samples have been taken for the study. The summary of the 425 samples is shown in Table 1.

The data set was randomised before each iteration. 43 samples ($\approx$ 10%) were kept aside for testing, while the remaining was used for training the algorithm. The same sets of randomised data were utilised to conduct the experiment across the three algorithms to ensure a perfect comparison between the three.

4 Model Development

4.1 Instance-Based Learning

The weighting scheme used in the analysis gave each neighbour a weight, which was the inverse of the Euclidean distance between the simulation point and the neighbour. The analysis was run for 1-NN through 6-NN models. The average of the absolute error in the prediction of the output had been calculated and a graph of predicted versus expected values of the output was generated.

4.2 Artificial Neural Network

The feedforward neural network is trained using seven inputs in the input layer and one output in the output layer. Training is the process of presenting testing data to the network and has it to modify its weights to accurately produce the strength when presented with the mix proportions. The performance function in the networks is mean squared normalised error (MSE). The parameters for the training of the network are as follows:

For LM,

- No. of hidden layers = 1,
- No. of hidden units = 7,
- Initial momentum (mu) = 0.001,

- mu increase factor = 0.1,
- mu decrease factor = 10,
- Max. validation failures = 6,
- Max. epochs to train = 1000.

For GDX,

- No. of hidden layers = 1,
- No. of hidden units = 7,
- Learning rate (lr) = 0.01,
- Ratio to increase lr = 1.05,
- Ratio to decrease lr = 0.7,
- Momentum constant (mc) = 0.9,
- mu increase factor = 0.1,
- mu decrease factor = 10,
- Max. validation failures = 6
- Max. epochs to train = 1000.

5 Model Performance

The absolute error percentage (AEP) was calculated for each testing data point and subsequently, the mean of that was calculated (MAEP). The MAEP thus produced by each algorithm (IBL, LM and GDX) was statistically analysed using hold-out and cross-validation. These give an estimate of the accuracy of the performance of the models in a practical setting [6].

In hold-out (HO), the data was divided randomly into training and testing sets consisting of 90% and 10% of the entire data. The errors in the output of the testing set were used for the analysis. Ten iterations of each k-NN, LM and GDX were evaluated using HO.

Cross-validation (CV) is preferred for prediction models [6]. In *k*-fold cross-validation, the data set is equally split into *k* subsets, each of which is used as the test set while the others (*k-1*) are used together as the training set. The average error of the *k* trials is calculated. A 10-fold cross-validation has been used for the analysis.

6 Results

6.1 Instance-Based Learning

1-NN through 6-NN models were run and the experiment was iterated 10 times and analysed. Table 2 shows the results of the hold-out experiments. The 2-NN model has shown the best performance and its summary is as follows:

Table 2 Arithmetic mean and standard deviation for the absolute error percentage in the hold-out analysis of the k-NN model

	MAEP	SD
NN 1	9.24	2.56
NN 2	8.50	1.55
NN 3	9.00	1.72
NN 4	8.99	1.78
NN 5	8.77	1.82
NN 6	8.71	1.79

$$\begin{aligned}
&\text{Mean} && = 8.5\% \\
&\text{S.D.} && = 1.55 \\
&\text{Minimum} && = 5.81\% \\
&\text{Maximum} && = 10.87\% \\
&\text{1st Quartile} && = 7.60\% \\
&\text{Median} && = 8.25\% \\
&\text{3rd Quartile} && = 10.08\%
\end{aligned}$$

The 10-fold cross-validation analysis on the k-NN model too shows that the 2-NN algorithm performs the best. Table 3 shows evaluation of the analysis, and its summary is presented as follows:

$$\begin{aligned}
&\text{Mean} && = 9.32\% \\
&\text{S.D.} && = 0.78 \\
&\text{Minimum} && = 8.52\% \\
&\text{Maximum} && = 11.49\% \\
&\text{1st Quartile} && = 8.99\% \\
&\text{Median} && = 9.17\% \\
&\text{3rd Quartile} && = 9.33\%
\end{aligned}$$

A scatter plotted graph of the expected values versus the predicted values of the fifth experiment of 2-NN using hold-out is shown in Fig. 1.

Table 3 Arithmetic mean and standard deviation for the absolute error percentage in the cross-validation of the 2-NN model

	MAEP	SD
E 1	9.26	1.53
E 2	9.02	2.15
E 3	8.98	2.17
E 4	8.52	1.39
E 5	9.35	1.76
E 6	8.65	1.68
E 7	9.25	3.00
E 8	9.08	1.56
E 9	9.62	1.54
E 10	11.49	3.03

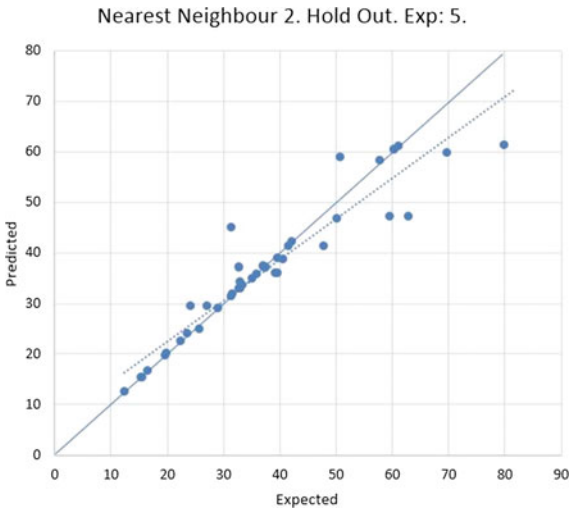

Fig. 1 Scatter plot of expected versus predicted values for Exp. 5 of hold-out for 2-NN

Table 4 Arithmetic mean and standard deviation of ANN models using hold-out

	LM	GDX
MAEP	15.18	20.18
SD	2.36	6.93

6.2 Artificial Neural Networks

A hold-out analysis was performed on the artificial neural network models. Table 4 shows the AEPs and MAEP as calculated from the LM and GDX algorithms. The summary of the findings are as follows:

For LM,

$$\begin{aligned}
\text{Mean} &= 15.18\% \\
\text{S.D.} &= 2.36 \\
\text{Minimum} &= 11.39\% \\
\text{Maximum} &= 18.67\% \\
\text{1st Quartile} &= 13.80\% \\
\text{Median} &= 15.54\% \\
\text{3rd Quartile} &= 16.78\%
\end{aligned}$$

Table 5 Arithmetic mean and standard deviation for the absolute error percentage in the cross-validation of the LM algorithm

	MAEP	SD
E 1	9.26	1.53
E 2	9.02	2.15
E 3	8.98	2.17
E 4	8.52	1.39
E 5	9.35	1.76
E 6	8.65	1.68
E 7	9.25	3
E 8	9.08	1.56
E 9	9.62	1.54
E 10	11.49	3.03

Table 6 Arithmetic mean and standard deviation for the absolute error percentage in the cross-validation of the GDX algorithm

	MAEP	SD
E 1	29.86	13.02
E 2	27.82	14.00
E 3	21.43	7.37
E 4	23.04	11.29
E 5	25.49	11.82
E 6	21.61	7.17
E 7	19.77	5.63
E 8	23.66	8.00
E 9	24.71	6.75
E 10	19.85	4.71

For GDX,

$$\begin{aligned}
\text{Mean} &= 20.18\% \\
\text{S.D.} &= 6.93 \\
\text{Minimum} &= 12.89\% \\
\text{Maximum} &= 38.39\% \\
\text{1st Quartile} &= 16.84\% \\
\text{Median} &= 18.62\% \\
\text{3rd Quartile} &= 20.49\%
\end{aligned}$$

Tables 5 and 6 show the evaluation of the 10-fold analysis of the fifth experiment of neural network method using LM and GDX, respectively. Their summaries are as follows:

For LM,

Mean	= 14.2%
S.D.	= 1.2
Minimum	= 12.83%
Maximum	= 16.33%
1st Quartile	= 13.1%
Median	= 14.08%
3rd Quartile	= 14.75%

For GDX,

Mean	= 19.45%
S.D.	= 4.19
Minimum	= 14.52%
Maximum	= 30.29%
1st Quartile	= 17.42%
Median	= 18.62%
3rd Quartile	= 20.56%

Scatter plotted graphs of the expected values versus the predicted values of the seventh experiment of LM and GDX using hold-out are shown in Figs. 2 and 3, respectively.

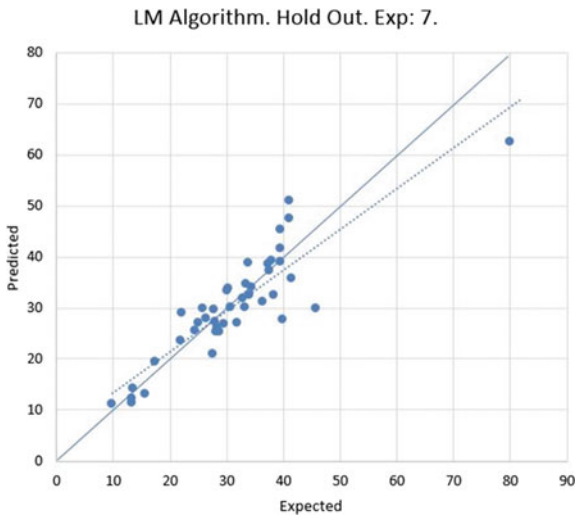

Fig. 2 Scatter plot of expected versus predicted values for Exp. 7 of hold-out for LM

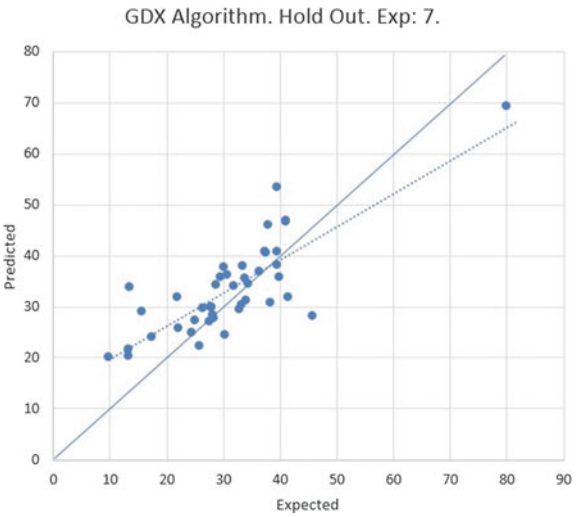

Fig. 3 Scatter plot of expected versus predicted values for Exp. 7 of hold-out for GDX

7 Comparative Study

The analysis shows that the ML algorithms can predict the compressive strength of 28-day hardened concrete with varying accuracy. A comparison of the data in Tables 2 and 4 is shown in Fig. 4.

Figure 4 shows that IBL performs considerably better than either of the neural network algorithms. It follows that the 2-NN model performs slightly better than the other k-NN models with an MAEP of 8.50%. The 2-NN model also has the lowest SD at 1.55.

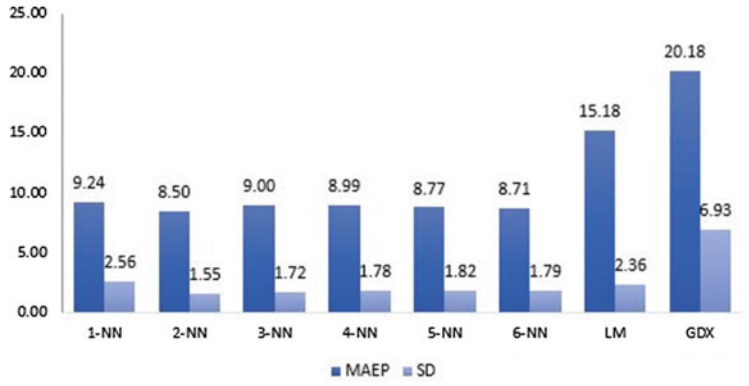

Fig. 4 Comparison of the MAEPs and SDs of the three algorithms

The variable-learning-rate-with-momentum gradient descent algorithm (GDX) has a very high-performance error at 20.18%. The standard deviation of 6.93 indicates that it may not be dependable to produce consistent results.

The Levenberg–Marquardt algorithm (LM) performs better than GDX and other gradient descent algorithms. It has an error of 15.18% and a standard deviation of 2.36.

8 Conclusions

HPC is a complex material and that makes the modelling and predicting its behaviour difficult. The study was an attempt to demonstrate the possibilities of using machine learning to predict the compressive strength of concrete. The initialisation values were not optimised, and hence there is a scope for further study of the ANN models. Optimising the initial weights and constants may give better results.

It must be noted that none of the explored methods is applicable to extrapolation. Hence, the minimum and maximum of the training set must be selected carefully. Also, more training instances will produce more accurate predictions. Hence, larger training data sets should be utilised for modelling.

Based on the comparison of the models, the following can be concluded:

- Instance-Based Learning (IBL) is a preferred choice for the prediction of the compressive strength with the seven parameters.
- The neural network models are comparatively easier to train and hence easier to simulate the predictions, but their performance is relatively poor.
- The Levenberg–Marquardt (LM) algorithm can be used for approximations where the tolerance for error is high (preferably above 15%).
- It is advisable to not use the variable-learning-rate-with-momentum gradient descent algorithm (GDX) for the prediction.

References

1. Kleiger, P. (1994). *Significance of tests and properties of concrete and concrete-making materials* (Issue 169, Part 3). ASTM.
2. Yeh, I.-C. (1998). Modeling of strength of high performance concrete using artificial neural networks. *Cement and Concrete Research, 28*(12), 1797–1808.
3. Gani, M. S. J. (1997). *Cement and concrete*. Chapman & Hall.
4. Lourakis, M. I. A. (2005). A brief description of the Levenberg-Marquardt algorithm implemented by levmar. *Foundation of Research and Technology, 4*, 1–6.
5. Yeh, I. C. (2007, August 03). *UCI machine learning repository: Data set*. Irvine: University of California.
6. Reich, Y., & Barai, S. V. (1999). Evaluating machine learning models for engineering problems. *Artificial Intelligence Engineering, 13*.

Numerical Study of the Effect of Boundary Conditions on Buckling Behaviour of Flat Oval LDSS Stub Column Under Axial Compression

Khwairakpam Sachidananda and Konjengbam Darunkumar Singh

Abstract This paper presents the effects of two support boundary conditions, viz. simply mounted and fixed on the buckling capacity of flat oval Lean Duplex Stainless Steel (LDSS) stub columns of two thicknesses (t = 20 mm and 5 mm, corresponding to Class 3 and 4 sections, respectively) under pure axial compression, analysed using Abaqus. It is observed that the ultimate load (P_u) capacity of both the boundary conditions (BCs) is similar for the Class 3 section, whereas simply mounted specimen showed lower value of P_u as compared to the fixed support boundary condition, for the Class 4 section considered. Further, in contrast to the Class 3 section, the Class 4 section with fixed BCs showed the formation of elephant foot near the end of column with denting located at the quarter height of column, while the simply mounted column showed mid-height denting only.

Keywords Stub · Flat oval · LDSS · Simply mounted · Fixed

1 Introduction

Tubular steel sections are popular choices in the construction industry as they provide relatively higher moment of inertia and torsion capacity than those of open sections. In the recent years, several new sections such as elliptical, oval, flat oval, etc. have become available (or proposed) in the steel market, due to their enhanced aesthetics. As they are relatively new, many researchers, e.g. [1–3], have devoted their attention to study their structural performances. In the experimental studies

K. Sachidananda (✉)
Department of Civil Engineering, National Institute of Technology Manipur, Imphal, India
e-mail: khwairakpam@iitg.ernet.in

K. D. Singh
Department of Civil Engineering, Indian Institute of Technology Guwahati, Guwahati, India
e-mail: darun@iitg.ernet.in

A. Rama Mohan Rao and K. Ramanjaneyulu (eds.), *Recent Advances in Structural Engineering, Volume 1*, Lecture Notes in Civil Engineering 11,
https://doi.org/10.1007/978-981-13-0362-3_41

reported, three types of support boundary conditions (BCs), viz. fixed, hinged or simply mounted (the specimen being simply placed between steel plates), were used while assessing the tubular column strength. The importance of end boundary conditions on cylindrical panels, ellipse/oval section under axial load, has been studied by different researchers [2, 4]. Theofanous et al. [2] showed the inaccuracy of the FE models with fixed end columns for the experiments conducted on oval section with both of its ends simply mounted on flat plate compression testing machine. Shariati et al. [4] reported the increased load carrying capacity for clamped/fixed section as compared to the section under simply supported. Simply mounted or fixed BCs are generally adopted for stub column tests, due to their easier support preparation. In the literature, for the case of square sections, experimental geometrical dimensions considered are L = 332.2 mm, B = 80 mm, r_i = 3.6 mm, H = 80 mm, t = 3.81 mm, respectively, as shown in Table 1, where L, B, r_i, H, t represent length, breadth, corner radius, height and thickness, and numerical studies are reported by Park and Yu [6], Zhu and Young [3, 7] and Sachidananda and Singh [8], considering mainly fixed-ended stub columns. Liang [9] describe the importance of boundary conditions (i.e. simply supported steel plates and free plates) in determining the strength of steel plate columns. From the literature review, it is found that the effects of such support boundary effects on the behaviour of stub flat oval columns have not been reported. Hence, an attempt has been made in this study, to assess the effects of both simply mounted and fixed boundary conditions on the buckling capacity of flat oval Lean Duplex Stainless Steel (LDSS) stub columns under pure axial compression. LDSS such as grade EN 1.4162 belongs to the family duplex stainless steel and provides attractive benefits, e.g. lower initial cost (due to lower nickel content $\sim$1.5% as compared to austenitic stainless steel), enhanced strength, high-temperature performance, weldability and fracture toughness properties, etc. (e.g. Theofanous and Gardner [10]). In this work, two thicknesses, viz. t = 20 and 5 mm, are considered to represent Class 3 and Class 4 sections, as per EN 1993-1-4 [11] for the analysis of flat oval column.

2 Finite Element Modelling

FE modelling of the flat oval stub column has been conducted with the FE software, Abaqus [12]. Typical geometrical dimensions considered are l = 300 mm, w = 300 mm, r = 150 mm, h = 900 mm, t = 5 (class 4) and 20 mm (class 3) respectively, where l, w, r, t, h represent flat length of cross-section, width between flat plates,

Table 1 Stub column dimensions [5]

Specimen	L (mm)	B (mm)	H (mm)	t (mm)	r_i (mm)
80 × 80 × 4-SC2	332.2	80	80	3.81	3.6

L = Length, B = width, H = depth, t = thickness, r_i = internal corner radius

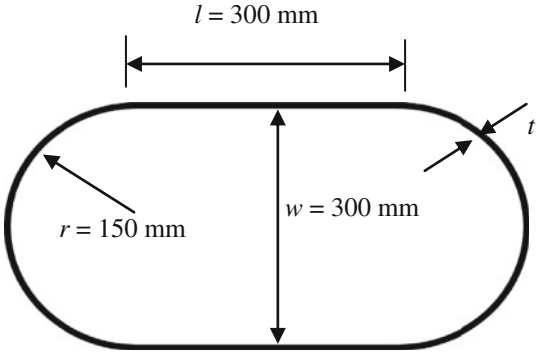

Fig. 1 Flat oval hollow section

curvature radius of curve portion, thickness and height of column. Schematic diagram of the flat oval section is presented in Fig. 1. The stub column has been meshed using four-noded element, S4R element with six degrees of freedom per node (available in Abaqus [12]) as reported in the literature for such work, e.g. [3]. The boundary conditions of the columns were applied through reference points (RP-1 and RP-2) by constraining the end nodes of the column through kinematic coupling [12] as shown in Fig. 2.

In the FE model, simply mounted and fixed BCs are accomplished by constraining the rotation and axial displacement degree of freedom for the simply mounted support (i.e. U1 $\neq$ 0, U2 $\neq$ 0, U3 = 0; UR1 = UR2 = UR3 = 0) and constraining both rotation and vertical displacements (U1 = U2 = U3 = 0; UR1 = UR2 = UR3 = 0) at the fixed support, respectively, e.g. [2] as shown in Fig. 3. At the loaded end also, corresponding similar boundary conditions have been applied, except that vertical translation is allowed (i.e. U3 $\neq$ 0). Typical mesh size of 10 mm $\times$ 10 mm with the aspect ratio of 1 was taken for the analysis, based on mesh convergence study. Following previous work, e.g. [5], nonlinear buckling analyses have been performed, considering a local imperfection magnitude of $t/100$. The material properties for the LDSS are taken as Young's modulus (E) = 197,200 MPa, yield stress ($\sigma_{0.2}$ = 657 MPa) from the experimental study of Theofanous and Gardner [5] as shown in Table 2. Before proceeding with the FE study, the FE modelling procedure was validated by comparing the present FE result with that of an experimental result from Theofanous and Gardner [5] in the form of load (P) versus axial displacement (δ), as shown in Fig. 4. From Fig. 4, it can be seen that the FE analysis is able to predict the experimental result with reasonable accuracy, and hence the FE procedure followed herein can be considered as acceptable. The von Mises stress superimposed on deformed shape for the experimental and FE results in Fig. 5 shows the accuracy of the FE modelling as it shows similar stressing and deformation.

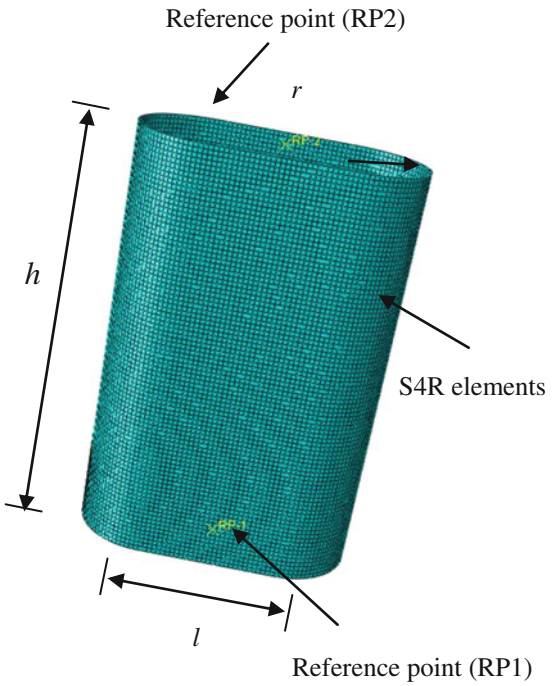

Fig. 2 Typical FE meshing with boundary condition

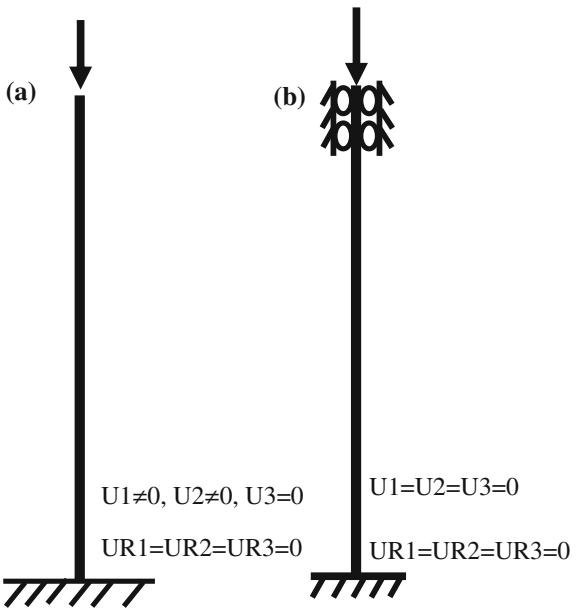

Fig. 3 Typical FE **a** Simply mounted support, **b** fixed support

Table 2 Compressive flat material properties [5]

Cross section	E (MPa)	$\sigma_{0.2}$ (MPa)	$\sigma_{1.0}$ (MPa)	R-O coefficients	
				n	$n'_{0.2,\ 1.0}$
80 × 80 × 4-SC2	197,200	657	770	4.7	2.6

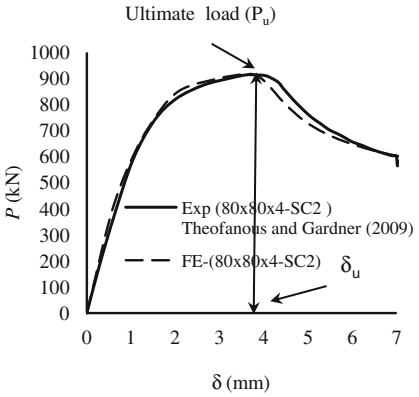

Fig. 4 SHC 80 × 80 × 4-SC2

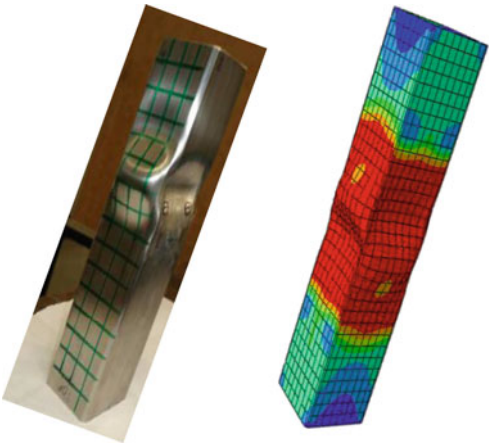

Fig. 5 Von Mises stress superimposed on deformed shape for stub LDSS column [5]

3 Results and Discussion

The performances of flat oval column under different boundary conditions of fixed-ended and simply mounted have been presented in the form of load (P) versus displacement (δ) in Figs. 6a and 7a for different thicknesses of t = 5 (Class 4) and t = 20 mm (Class 3) sections. For different boundary conditions of column,

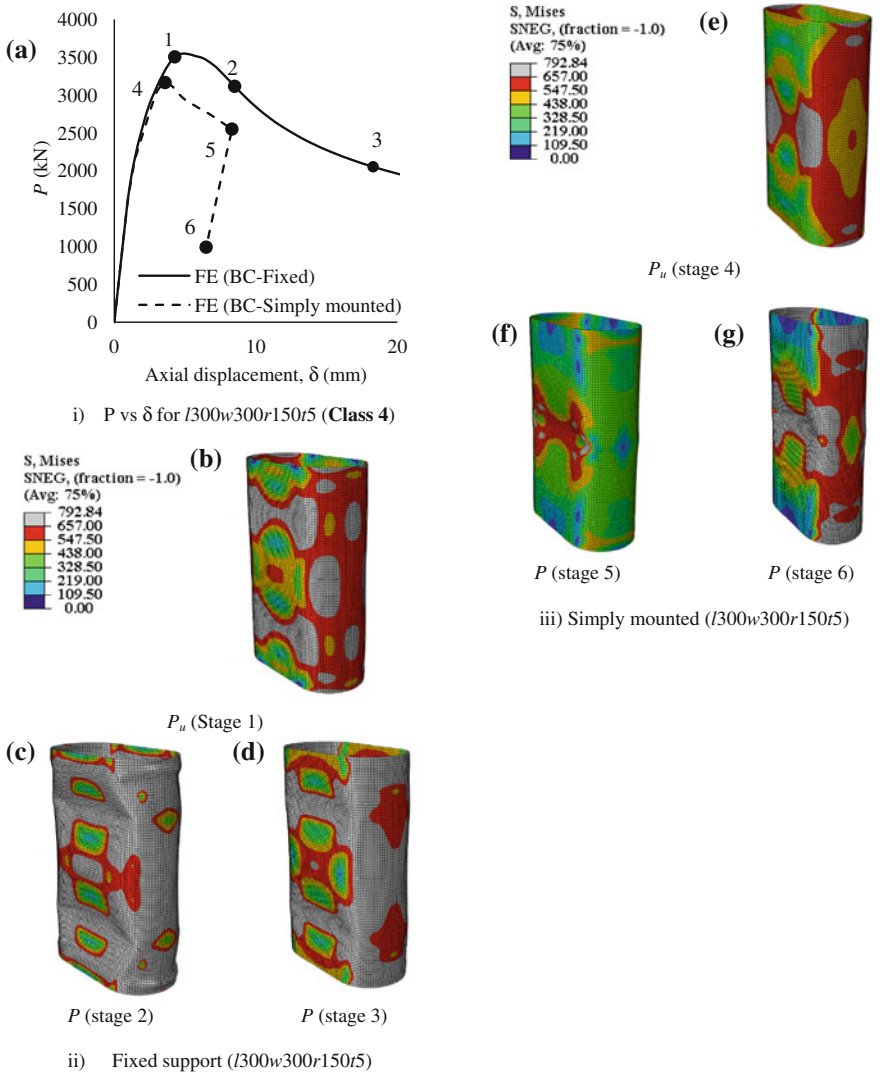

Fig. 6 (i) *l*300*w*300*r*150*t*5 (Class 4) (**a**) *P* versus *δ*; von Mises superimposed on deformed shape for (ii) fixed support (**b**, **c**, **d**) and (iii) simply mounted (**e**, **f**, **g**)

von Mises stress contour superimposed on different stages of deformed shapes are also shown in Figs. 6 and 7 (Note that the contour intervals are kept same so that comparison can be made easily; also the grey colours indicate the region that has crossed the yield stress). It can be seen from Figs. 6 and 7 that the load carrying capacity of column increases up to $P_{u,}$ after which the load capacity decreases in post-$P_{u,}$ irrespective of the boundary condition (BC) of column. Further, a sudden drop in the post-P_u profile is seen after a short post-P_u axial displacement, for the

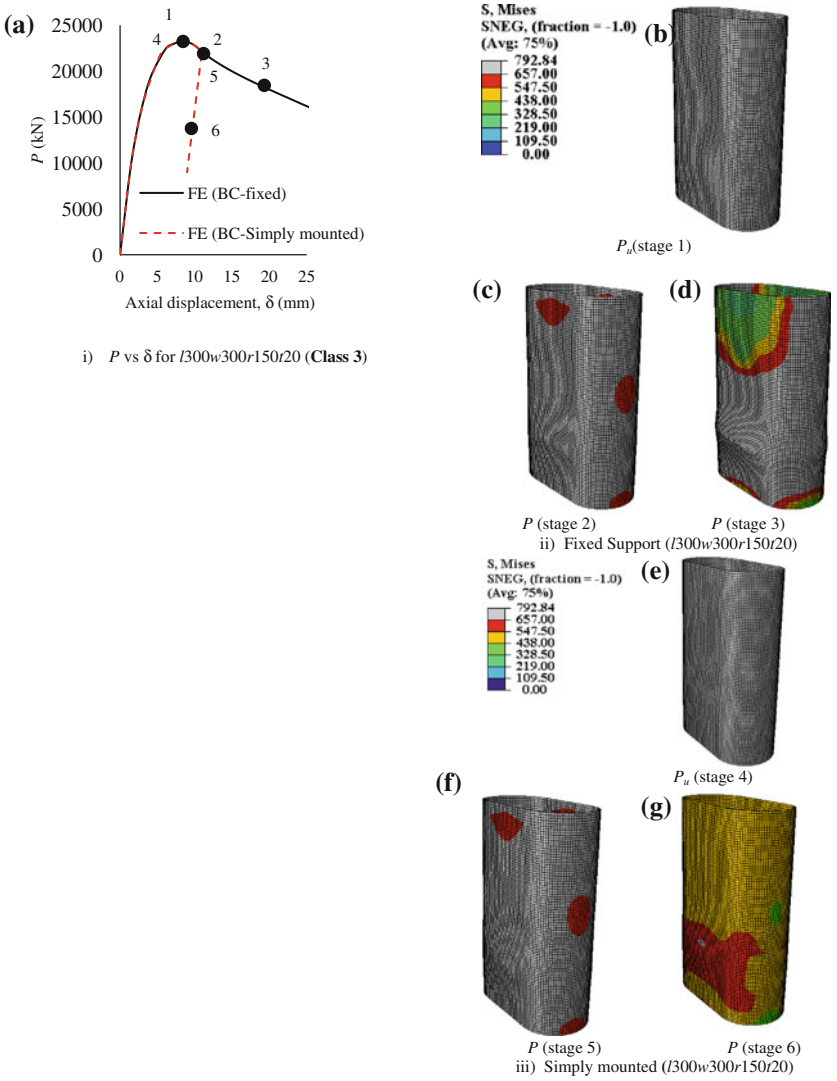

Fig. 7 (i) *l*300*w*300*r*150*t*20 (Class 3) (**a**) *P* versus δ; von Mises superimposed on deformed shape for (ii) fixed support (**b**, **c**, **d**) and (iii) simply mounted (**e**, **f**, **g**)

simply mounted boundary condition. For the Class 4 section, a distinct drop in P_u can be observed for the simply mounted BC (Fig. 6). A comparison of the von Mises stress contour plot shows that local buckling is seen at two locations on the flat element, with the formation of elephant foot at the ends (or near the support and loading BCs), when the supports are fixed (see inset figure c of Fig. 6); however, when the supports are simply mounted, local buckling at the mid-height of the

column is seen, with no significant formation of elephant foot (see inset figure f of Fig. 6). On the other hand, for the Class 3 section, up to a small axial deformation beyond post-P_u (up to inset stage 2 or 5 in Fig. 7), both the BCs produced similar load–deformation profile (see also similar von Mises stress contour in Fig. 7). Although initiation of outward local buckling can be seen for both types of BCs (see stages 2 and 5 in Fig. 7), in the case of fixed BC, at Stages 3, it is seen that most region of the column is yielded, whereas at Stage 6, corresponding to simply mounted BC, the column has started significant distressing. In general, the post-P_u with sudden drop in load for the simply mounted cases may be related to the relatively unstable boundary condition imposed as compared to that of fixed BC. Further, it is also observed that elephant foot type of local buckling is not seen for the thicker Class 3 section, using fixed BC.

4 Conclusions

Based on the study of flat oval column for different boundary conditions (Simply mounted and fixed), the following conclusions have been concluded.

(1) The load carrying capacity of fixed-ended flat oval column is relatively higher than simply mounted in case of Class 4 section (t = 5 mm) but for Class 3 section (t = 20 mm), there is negligible effect.
(2) Elephant foot formation can be seen in the case of fixed-ended column while it is absent in case of simply mounted column for t = 5 mm (Class 4 section).
(3) The load carrying capacity of post-P_u is more in case of fixed condition as compared to simply supported boundary condition, where the column failed suddenly once it reached the P_u.
(4) The columns buckle in mid-height for the case of simply supported column, while the fixed-ended column shows the local buckling in quarter height of column at t = 5 mm (Class 4 section).
(5) For thicker section (t = 20 mm, Class 3 section), there is no formation of elephant footing on the column.

References

1. Chan, T. M., & Gardner, L. (2008). Compressive resistance of hot-rolled elliptical hollow sections. *Engineering Structures, 30,* 522–532.
2. Theofanous, M., Chan, T. M., & Gardner, L. (2009). Structural response of stainless steel oval hollow section compression members. *Engineering Structures, 31*(4), 922–934.
3. Zhu, J., & Young, B. (2012). Design of cold-formed steel oval hollow section columns. *Journal of Constructional Steel Research, 71,* 26–37.

4. Shariati, M., Saemi, J., Sedighi, M., & Eipakchi, H. R. (2011). Experimental and numerical studies on buckling and post-buckling behaviour of cylindrical panels subjected to compressive axial load. *Strength of Materials, 43*(2), 190–200.
5. Theofanous, M., & Gardner, L. (2009). Testing and numerical modelling of lean duplex stainless steel hollow section columns. *Engineering Structures, 31*(12), 3047–3058.
6. Parks, M. B., & Yu, W. W. (1989). Local buckling behaviour of stiffened curved elements. *Thin-Walled Structures, 7,* 1–22.
7. Zhu, J., & Young, B. (2011). Cold-formed-steel oval hollow sections under axial compression. *Journal of Structural Engineering, 137*(7), 719–727.
8. Sachidananda, K., & Singh, K. D. (2015). Numerical study of fixed ended lean duplex stainless steel (LDSS) flat oval hollow stub column under pure axial compression. *Thin Walled Structures, 96,* 105–119.
9. Liang, Q. Q. (2015). *Analysis and design of steel and composite structures*. New York: CRC Press, Taylor and Francis Group.
10. Theofanous, M., & Gardner, L. (2010). Experimental and numerical studies of lean duplex stainless steel beams. *Journal of Constructional Steel Research, 66,* 816–825.
11. EN 1993-1-4. (2006). Design of steel structures. General rules, Supplementary rules for stainless steel.
12. ABAQUS. (2009). Version 6.9-EF1 HibbittKarlsson and Sorensen Inc USA.

Two-Dimensional Mesoscale Compressive Damage Analysis of CT Images of a Concrete Cube

S. Vinay Kumar and Nirjhar Dhang

Abstract This paper evaluates the two-dimensional (2D) compressive response of a computed tomography (CT) scan image. The image of size 150 × 150 mm has been used in numerical simulation. The CT image consists of realistic structures of the aggregates, mortar, and voids inside the concrete. The effect of the shapes and the distribution of the aggregates and the voids on load carrying capacity have been studied. The numerical results indicate that the concrete modeled as mortar and aggregate has a high nucleation of micro-cracks near the vicinity of aggregates and also high load carrying capacity compared to concrete modeled with voids. Aggregates modeled as a regular shape with the same area and centroid show comparable load carrying capacity with real aggregate shape.

Keywords CT scan · Mesoscale · Aggregate shape and voids

1 Introduction

Concrete is a heterogeneous material consists of cement, sand and coarse aggregates. Inclusion of these embedded constituents in a numerical model would result in better understanding of failure of concrete. The mesoscale ranges from 10^{-1} to 10^{-3} mm. Reduction of scale of study from the macro- to meso-level exhibits distribution of aggregates and voids. The numerical analysis of mesoscale consists of two steps. The first step generates mesoscale geometry consisting of aggregate and voids. The second step applies individual material properties, and responses are simulated using numerical methods Ref. [1].

The aggregates occupy 60–70% of the volume of concrete. These aggregates are the skeleton of concrete and carry the bulk of the load Ref. [2]. The shape, size,

S. V. Kumar · N. Dhang (✉)
Departement of Civil Engineering, Indian Institute of Technology, Kharagpur, India
e-mail: nirjhar@civil.iitkgp.ernet.in

S. V. Kumar
e-mail: 2007.bitmtech@gmail.com

A. Rama Mohan Rao and K. Ramanjaneyulu (eds.), *Recent Advances in Structural Engineering, Volume 1*, Lecture Notes in Civil Engineering 11,
https://doi.org/10.1007/978-981-13-0362-3_42

distribution, and volume fraction of these aggregates play an important role in the fresh and hardened states of concrete Refs. [3, 4]. The aggregate properties, such as shape, size, volume fraction, and distributions, are included in the mesoscale model of concrete. Regular shapes of aggregates such as circles, ellipses, squares, rectangles, pentagons, and hexagons, are used in the numerical analysis Refs. [1, 5, 6, 7]. The circular shape of aggregates is commonly used due to the ease of application in the packing algorithm.

Mortar is a designed mix proportion of cement and sand. Mortar is simulated using damage plasticity model. Abaqus finite element software adopts the coupled plasticity model to simulate separate strain softening in tension and compression. These equations capture the stress hardening and softening behaviors of concrete Refs. [8, 9]. Hsu and Hsu [8] developed an empirical stress–strain model for high-strength concrete; this model consists of separate equations for the hardening part and the softening part of the curve. Naraine and Sinha [9] developed an exponential stress–strain relationship consisting of a single equation for the hardening and softening part of the curve, with only three simple parameters required to develop the curve.

The mesoscale geometry is developed using two methods namely ordered and random packing. Ordered packing arranges aggregates into a predefined pattern Ref. [10]. Random packing adopts statistical distributions and Monte Carlo simulation for particle generation Refs. [11–13]. This paper emphasizes the use of CT scan images to capture the realistic geometrical shapes and the spatial distribution of aggregates with voids embedded inside the concrete. CT scan is very versatile technique, where series of 2D images are produced from three-dimensional (3D) objects Ref. [14]. CT scan in concrete technology is mainly used to develop the numerical and statistical models from the real geometrical shape, spatial distribution of aggregates, and voids Refs. [15, 16]. CT images are also used for better understanding of the microstructural characterization, heat generation during hydration, curing, permeability, and damage evolution Refs. [16–20].

This paper focuses on finite element simulation of the CT-scanned image model under the influence of compressive displacements. Models of regularly shaped aggregates are prepared based on the areas and centroids of actual aggregates extracted from CT images. The mesoscale analysis of concrete is performed using the following steps. The first step consists of the preparation of concrete with a specified proportion and curing for 28 days. Next, CT scan imaging was performed on the cube to non-destructively determine the actual shape of the aggregates and the voids from the images. In the second step, a critical image was selected from the series of captured images. The threshold segmentation technique was performed on the CT image to separate mortar, aggregate, and voids. A computer-aided drawing (CAD) was prepared from the image model. In the third step, finite element simulation was performed on the CAD model by using the commercially available finite element analysis software, Abaqus 6.11. The mesoscale simulations evaluate the effects of the shape, size, and volume fraction of the aggregates and the voids on micro-crack localization and the load carrying capacity of concrete.

2 2D CT Image Model

CT scanning is a nondestructive technique which is used for visualizing the embedded features within solids. It provides 3D image model from the series of 2D images Ref. [14]. The 2D image contains exact shape, position, distributions of aggregates, and voids. The development of irregular shape of aggregates model from the CT image has been explained in this section.

2.1 Specimen Preparation

Nominal mix design for M20 grade of concrete consists of 1(Cement):1.5(Sand):3 (Coarse aggregates) proportion with water–cement ratio of 0.45 was used for making cubes of dimension 150 mm. After casting process, the concrete was allowed to air cure for 24 h and then water cured for 28 days. After completion of curing period, concrete cubes were oven dried and packed for CT scanning.

2.2 Working Principle of CT Scanning

The CT scan machine consists of X-ray emitter, detector, and centrally placed concrete specimen. The process of CT scan starts with placing the concrete specimen at the center of donut-shaped gantry which consists of 360° of X-ray emitters and detectors. The X-ray emitters emit beam of X-rays which passed through concrete specimen are captured by detectors. The CT scan performs 360° of X-ray emission and detection on the specimen. These data are stored in computers, where it uses advanced algorithms to form the 2D image. The CT scan detects the embedded materials inside the concrete based on the density variation as shown in Fig. 1a. The CT image contains exact shape, position, surface roughness, distributions of aggregates, and voids.

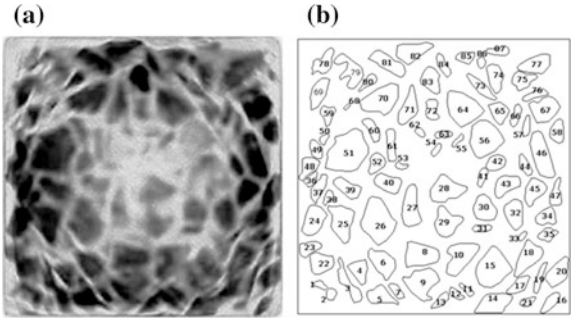

Fig. 1 CT model of aggregates. **a** CT image of concrete. **b** Edge model of concrete consisting of coarse aggregate and each aggregate had been marked with the number

2.3 *Mesoscale Model of Concrete*

The CT image exhibits mortar, aggregates, and voids inside the concrete as shown in Fig. 1a. This image is converted into computer model of lines, which separates aggregates and mortar. The computer model consists of total of 87 coarse aggregates as shown in Fig. 1b. The aggregates are randomly distributed over the mortar domain, consisting of different shapes, sizes, and aggregates surface possess numerous sharp corners. The air pockets get trapped between the aggregates. For simulation, air voids are introduced into the model.

3 Regular Geometric Shape of the Aggregates

The regular geometric-shaped aggregate was created from the area and centroid from the CT image as shown in Fig. 2a. The different regular geometric shapes considered are circular, elliptical, triangle, square, pentagon, and hexagon as shown in Fig. 4. The areas of all the aggregates are calculated by dividing the shapes into rectangles, triangles, and trapezoidal shapes, and the centroid of each aggregate is evaluated from the left corner. The modeled regular geometric shape of aggregates also account for the orientation of the real model. In some cases, the area and the centroids of aggregates collide with each other. In that case, the aggregates are randomly searched from space until there is no overlapping of the area of the aggregates.

4 Finite Element Analysis

Mesoscale compressive behaviors are simulated using the commercially available Abaqus 6.11 finite element software. The mesoscale finite element simulations were performed in four steps. The first step involves importing the CAD drawings to Abaqus and the creation of the geometrical models of each phase separately. The second step consists of the application of the mechanical properties to each phase. Aggregates are modeled as linear elastic and stress-softening models for mortar. The interaction between aggregates and mortar is modeled as being perfectly bonded with no gap. The third step is meshing, performed by using triangular plane stress elements with unit thickness. In the fourth step, a vertical compressive displacement of 200 μm is applied on the top surface, and the fixed boundary condition is applied to the bottom edge of the surface. The Abaqus explicit technique is used to analyze the displacement controlled simulation of the models. Stress, strain, force, displacement, and compressive damage are evaluated. The finite element simulations are also used to evaluate the effects of the shape and distribution of the aggregates and voids.

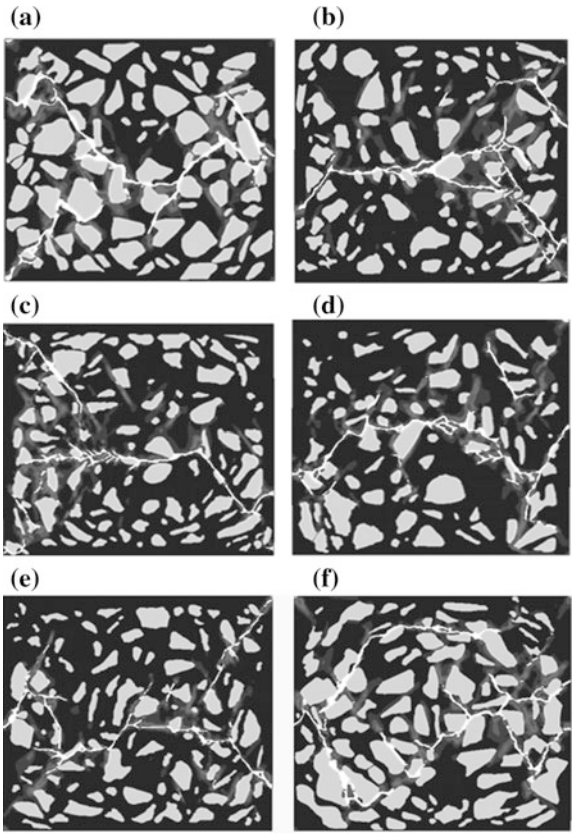

Fig. 2 Micro-crack localization of CT-scanned slices at different positions of the cube

4.1 Material Properties Aggregates and Mortar

The aggregates are comprised of higher strength and stiffness material compared to the mortar. Igneous dolerite crushed aggregates are used in this study. Young's modulus and the Poisson ratio of the aggregates are 70 GPa and 0.2, respectively.

The compressive stress–strain model proposed by Naraine and Sinha [9] was used to model the compressive and tensile stress–strain response of the mortar. This stress–strain model consists of a single equation for the strain hardening and softening parts of the curve. Three parameters, namely, maximum strength, strain at maximum strength, and ultimate strain, are required to capture the strain softening characteristics in the mortar. The tensile stress–strain responses are modeled considering the reduced strength and stiffness of the compression curve. Equation (1) shows the empirical stress–strain model [9].

$$\sigma = \sigma_u \left(\frac{\varepsilon}{\varepsilon_u}\right) \exp\left(1 - \frac{\varepsilon}{\varepsilon_u}\right) \quad (1)$$

in which σ_u, ε_u, and ε_f represent the ultimate strength, the strain at the ultimate strength, and the failure strain, respectively. In the compressive and tensile stress–strain curve for mortar phase using Eq. (1), the parameters for compression are taken as $\varepsilon_u = 0.0015$ and $\varepsilon_f = 0.007$; and the parameters for tension are taken as $\varepsilon_u = 0.00015$ and $\varepsilon_f = 0.0007$. σ_u for the compression and tension strength of the mortar 56 and 6 MPa are used in simulation.

5 Results and Discussion

In this section, results of compressive response of mesoscale model to aggregates shapes, distribution, and fractions and voids have been discussed.

5.1 Effect of the Distribution of Aggregates and the Volume Fraction

CT image slices provide insight into the distribution and volume fraction of the aggregates inside the concrete. The effects of CT image slices with different volume fraction and distribution of aggregates on compressive displacement are investigated. For simulation, six slices at different locations of the cube are selected, as shown in Fig. 2. These slices vary in the distribution and volume fraction of the aggregates. The result shows that the localization of micro-cracks, and the load carrying capacity is different for all the slices, as represented in Figs. 2 and 3, which suggest that the volume fraction of the aggregates and the distribution of the aggregates affect the compressive response of the concrete. Therefore, it can be concluded from this study that the initiation of micro-cracks is affected by the volume fraction of the aggregates. The distribution of the aggregates influences the propagation and localization of the micro-cracks.

5.2 Effect of Aggregate Shape and Position

This section presents the effects of the shapes of the aggregates on the compressive behavior of concrete. The models of circular, elliptical, square, hexagonal, and pentagonal aggregates are presented in Fig. 4.

The result reveals that localization of micro-cracks is different for each of the aggregate shape models, as visualized from Fig. 4. The ultimate loads carried by the

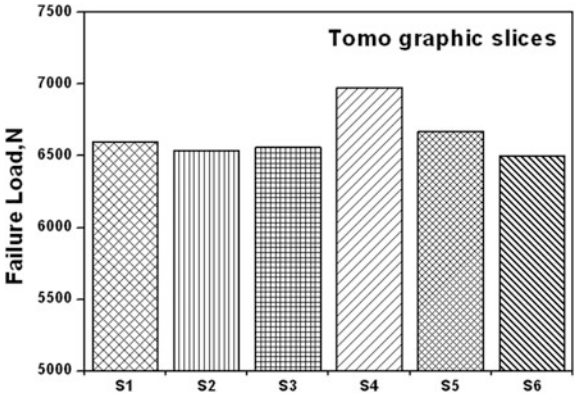

Fig. 3 Load carrying capacity of CT slices at different positions of the cube

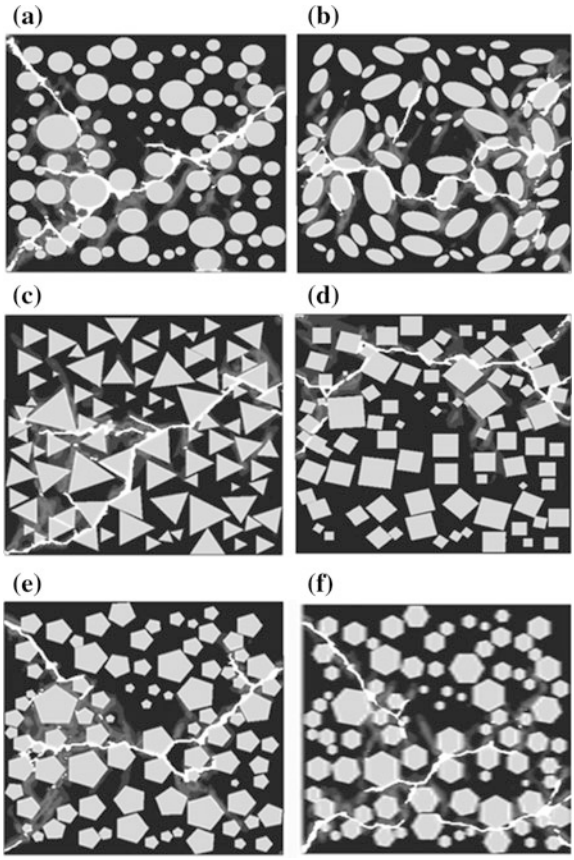

Fig. 4 Micro-crack localization of regular aggregates shape in concrete. **a** Circle. **b** Ellipse. **c** Triangle. **d** Square. **e** Pentagon. **f** Hexagon

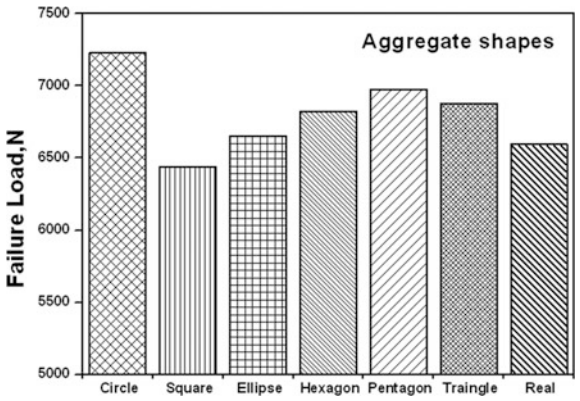

Fig. 5 Load carrying capacity of different aggregate shapes

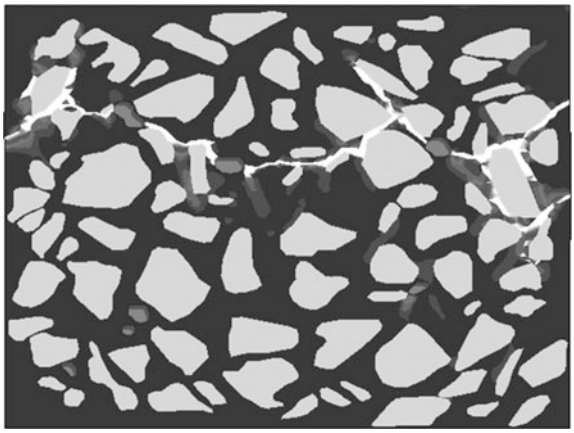

Fig. 6 Micro-crack localization around aggregates and voids region

models of different shapes of aggregates are shown in Fig. 5. The circular aggregates carried the maximum failure load, with 10.35% variation from the actual shape of aggregates. The elliptical aggregates carried the nearly same load as the model of irregular shapes of aggregates, that is, the actual shapes of the aggregates. In the hexagonal, pentagonal, and square models, the failure loads vary from 3.44 to 5.80%. Therefore, it can be concluded from this study that the shape and position of the aggregates have less influence on the load carrying capacity and failure pattern of concrete under compressive load.

5.3 Effect of the Voids

The voids are empty spaces created by entrapped air pockets due to an excessive water–cement ratio, insufficient compaction, surface roughness of the aggregates,

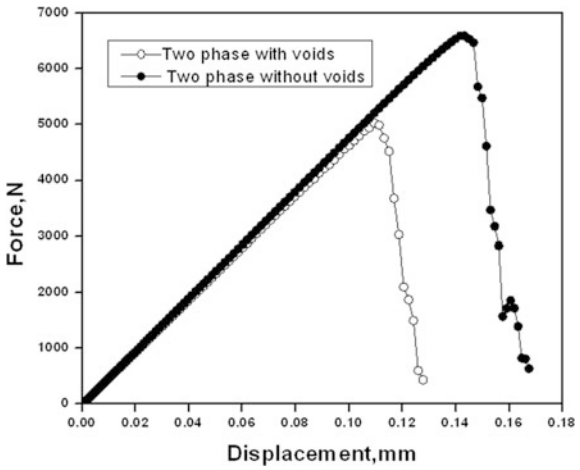

Fig. 7 Load carrying capacity of models with and without voids

and the materials and shape of the molds used for the concrete specimen. The voids are included into the mortar phase to evaluate the compression response of the mesoscale model. The void shapes collected from CT images are placed between aggregates. The CAD software employs pick-and-place methods for placing voids (0.65% of the area of the model). Figure 6 illustrates that the introduction of voids increases the localization of micro-cracks and reduces the load carrying capacity. The load–displacement curves for mesoscale models with and without voids are shown in Fig. 7. The inclusion of voids into the concrete model reduced the load carrying capacity to 23.72%. The result shows that for voids with 0.65% area occupation, the micro-cracks are diverted to the region of the voids. From this study, it can be concluded that voids significantly control the ability of the concrete load carrying capacity.

6 Conclusion

An X-ray CT scan technique was used to capture the realistic mesostructure of a concrete cube. The numerical simulation was performed using Abaqus 6.11 finite element software. In the simulation, the material behavior of the aggregates is considered to be linear elastic, and damage plasticity models are used for mortar. The effect of the shape and distribution of aggregates and the inclusion of voids were studied in relation to the load carrying capacity, the stress–strain response, and the strain localizations of concrete. Based on the numerical results, the following conclusions can be drawn.

- The two-phase model that considers only mortar and aggregates carries the bulk of the load compared to air-void model. CT slices at different locations attract different paths of strain localizations due to the random distribution of coarse

aggregates. The positions of the aggregates inside the concrete play a dominant role in the load carrying capacity of concrete.

- Models of regular-shaped aggregates developed based on the area and centroid of the actual shape of the aggregates show a variation in the load carrying capacity of up to 10%. The model of the circular aggregates carried more load compared to the model using irregularly shaped aggregates. Each aggregate shape has different strain localizations, which proves that the aggregate shape has an effect on the load carrying capacity of the concrete model.
- The inclusion of voids in mortar results in micro-cracks localized near the empty space. Due to the voids inside the model, the concrete load carrying capacity is reduced by 23.72%, which proves that voids play an important role in the mesoscale model. Porous structure (voids) should be considered while modeling, analyzing, and designing concrete.

In summary, CT scan is an effective technique for capturing the real shape of aggregates and voids inside concrete. Finite element simulations of the realistic mesoscale models can be effectively performed using Abaqus 6.11 software. The effects of the size, shape, and distribution of the aggregates were elucidated. The influences of voids in the mesoscale models were evaluated. These realistic mesoscale models facilitate a better understanding of the failure process of concrete.

References

1. Kim, S. M., & Abu Al-Rub, R. K. (2011). Meso-scale computational modeling of the plastic-damage response of cementitious composites. *Cement and Concrete Research, 41*(3), 339–358.
2. Chen, B., & Liu, J. (2004). Effect of aggregate on the fracture behavior of high strength concrete. *Construction and Building Materials, 18*(8), 585–590.
3. Elices, M., & Rocco, C. G. (2008). Effect of aggregate size on the fracture and mechanical properties of a simple concrete. *Engineering Fracture Mechanics, 75*(13), 3839–3851.
4. Rocco, C. G., & Elices, M. (2009). Effect of aggregate shape on the mechanical properties of a simple concrete. *Engineering Fracture Mechanics, 76*(2), 286–298.
5. Du, X., Jin, L., & Ma, G. (2014). Numerical simulation of dynamic tensile-failure of concrete at meso-scale. *International Journal of Impact Engineering, 66,* 5–17.
6. Skarżyński, Ł., & Tejchman, J. (2010). Calculations of fracture process zones on meso-scale in notched concrete beams subjected to three-point bending. *European Journal of Mechanics-A/Solids, 29*(4), 746–760.
7. Unger, J. F., Eckardt, S., & Konke, C. (2011). A mesoscale model for concrete to simulate mechanical failure. *Computers and Concrete*, *8*(4), 401–423.
8. Hsu, L. S., & Hsu, C. T. T. (1994). Stress-strain behavior of steel-fibre high-strength concrete under compression. *ACI Structural Journal, 91*(4), 448–457.
9. Naraine, K., & Sinha, S. (1989). Behavior of brick masonary under cyclic compressive loading. *Journal of Construction Engineering and Management, 115*(2), 1432–1445.
10. Mostofinejad, D., & Reisi, M. (2012). A new DEM-based method to predict packing density of coarse aggregates considering their grading and shapes. *Construction and Building Materials, 35,* 414–420.

11. Hafner, S., Eckardt, S., Luther, T., & Konke, C. (2006). Mesoscale modeling of concrete: Geometry and numerics. *Computers & Structures, 84,* 450–461.
12. Wang, Z. M., Kwan, A. K. H., & Chan, H. C. (1999). Mesoscopic study of concrete I: Generation of random aggregate structure and finite element mesh. *Computers & Structures, 70,* 533–544.
13. Wriggers, P., & Moftah, S. O. (2006). Mesoscale models for concrete: Homogenisation and damage behaviour. *Finite Elements in Analysis and Design, 42*(7), 623–636.
14. Henry, M., Darma, I. S., & Sugiyama, T. (2014). Analysis of the effect of heating and re-curing on the microstructure of high-strength concrete using X-ray CT. *Construction and Building Materials, 67,* 37–46. (Part-A).
15. Dai, Q. (2011). Two and three-dimensional micromechanical viscoelastic finite element modeling of stone-based materials with X-ray computed tomography images. *Construction and Building Materials, 25*(2), 1102–1114.
16. Ren, W., Yang, Z., Sharma, R., Zhang, C., & Withers, P. J. (2015). Two-dimensional X-ray CT image based meso-scale fracture modelling of concrete. *Engineering Fracture Mechanics, 133,* 24–39.
17. Fukuda, D., Nara, Y., Kobayashi, Y., Maruyama, M., Koketsu, M., Hayashi, D., et al. (2012). Investigation of self-sealing in high-strength and ultra-low-permeability concrete in water using micro-focus X-ray CT. *Cement and Concrete Research, 42*(11), 1494–1500.
18. Kogbara, R. B., Iyengar, S. R., Grasley, Z. C., Rahman, S., Masad, E. A., & Zollinger, D. G. (2014). Relating damage evolution of concrete cooled to cryogenic temperatures to permeability. *Cryogenics, 64,* 21–28.
19. Wang, L. B., Frost, J. D., Voyiadjis, G., & Harman, T. P. (2003). Quantification of damage parameters using X-ray tomography images. *Mechanics of Materials, 35*(8), 777–790.
20. Wong, R. C. K., & Chau, K. T. (2005). Estimation of air void and aggregate spatial distributions in concrete under uniaxial compression using computer tomography scanning. *Cement and Concrete Research, 35,* 1566–1576.

Flutter Reliability Studies of a Swept Back Plate

G. Shanthini, A. C. Pankaj and M. Manjuprasad

Abstract In the present paper, an attempt has been made to calculate the flutter reliability of a swept back plate taking uncertainties in material and aero properties into consideration. As flutter analysis for computing flutter speed involves finite element analysis followed by an extensive interpolation process, a regular Monte Carlo Simulation (MCS) is infeasible. Hence, in the present work, a novel approach involving Response Surface Method (RSM) of simulation followed by MCS has been used for the study. The variation in flutter speeds due to uncertainties in the material properties such as Young's modulus and mass density and aero parameters such as air density and Mach number are studied and the reliability has been computed for different failure conditions.

Keywords Flutter · Reliability · Response Surface Method · Monte Carlo Simulations

1 Introduction

Aeroelastic analysis is very important in the aircraft design. Flutter analysis, a typical aeroelastic problem in aircraft design, is carried out as a deterministic analysis assuming complete determinacy of structural parameters. However, there are uncertainties of geometric properties, material properties, load distributions, working environment, etc. So the deterministic analysis cannot provide complete information about the flutter boundaries required for defining the flight envelope.

G. Shanthini (✉) · A. C. Pankaj · M. Manjuprasad
Structural Technologies Division, CSIR-National Aerospace Laboratories, Bangalore 560017, India
e-mail: shanthini@nal.res.in

A. C. Pankaj
e-mail: acpankaj@nal.res.in

M. Manjuprasad
e-mail: manjuprasad@nal.res.in

A. Rama Mohan Rao and K. Ramanjaneyulu (eds.), *Recent Advances in Structural Engineering, Volume 1*, Lecture Notes in Civil Engineering 11,
https://doi.org/10.1007/978-981-13-0362-3_43

A robust solution for any analysis should take into account all the model uncertainties possible. In the present work, probabilistic methods are used to compute the flutter reliability [1–5] of a swept back plate considering uncertainties in material and aero properties. An RSM [6, 7] combined with MCS method has been used for the study reported in this paper.

2 Methodology

Flutter analysis of aircraft structures is a complex problem involving finite element analysis followed by extensive interpolation process. A closed-form solution of flutter response is not available due to its complexity. Therefore, first-order reliability method and its corresponding improved methods for the explicit limit state function will be impracticable due to the inaccuracy and excessive computational cost.

Response Surface Method (RSM) is one such method which can be used for reliability analysis of structures with implicit limit state functions.

A major advantage of this method is that the implicit limit state function is represented by the explicit form, and the existing reliability analysis methods can be readily implemented. So the RSM has been widely applied to the reliability analysis of structures. However, the selection of experimental points and the form of response surface function are two unsolved problems for the reliability analysis of complex structure with highly nonlinear limit state function, and sometimes the RSM may be not converged.

Monte Carlo Simulation (MCS) is a traditional method for the probabilistic analysis. The main advantage of this method is that engineers with only a basic knowledge of probability and statistics will be able to use it and it always provides correct results when very large times of simulations are performed. However, its computational cost is very high. A direct Monte Carlo simulation for flutter reliability studies is infeasible as human intervention and logical reasoning is needed in certain conditions of interpolation process.

Because of the abovementioned drawbacks, a hybrid method has been adopted for flutter reliability studies. Response surface method has been used to establish explicit limit state function based on the basic variables considered, and a Monte Carlo simulation is run on the explicit limit state function to obtain flutter reliability.

3 Structural Model

A swept back aluminum cantilever plate is considered as test specimen to represent the wing-like structure (Fig. 1). The plate has a thickness of 3 mm, length of 300 mm, and chord varying from 130 to 70 mm and has a sweep angle of 23.80 at the leading edge. The candidate structure has Young's modulus of 71 GPa,

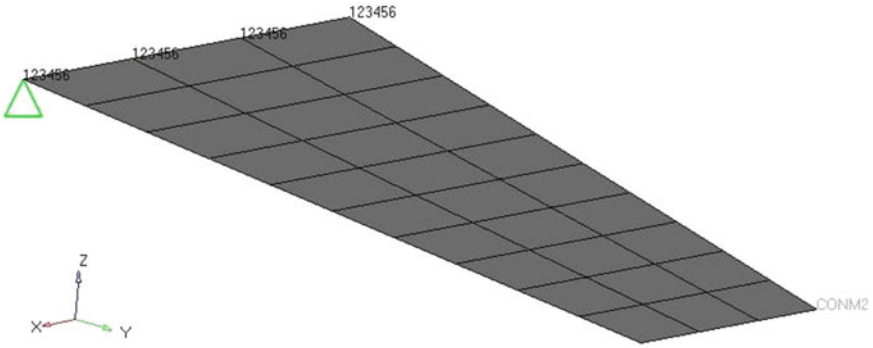

Fig. 1 FE model of the swept back plate

Table 1 Natural frequencies of the plate FE model

S. No.	Mode description	Frequency (Hz)
1.	First bending	30.395
2.	Coupled bending torsion	161.899
3.	Torsion	205.118
4.	Third bending	427.332

Poisson's ratio of 0.3, and density of 2722.77 kg/m^3. The natural frequencies of the plate are tabulated in Table 1. The first three mode shapes of the plate are shown in Figs. 2, 3, and 4.

4 Aerodynamic Model

The aerodynamic model for the plate is a mesh consisting of flat panels based on doublet lattice method for the lifting surface of the plate model, idealized by means of trapezoidal boxes lying parallel to the flow direction. Surface spline functions are used to generate the necessary interpolation matrix to estimate the displacement of aerodynamic grids based on the displacement of structural grids.

5 Analysis

For the probabilistic flutter studies, three cases were considered. (1) Structural parameters considered as random variables; (2) Structural and aero parameters considered as random variables; and (3) Critical parameters as random variables. Flutter analysis has been carried out using Doublet lattice aerodynamics and PK

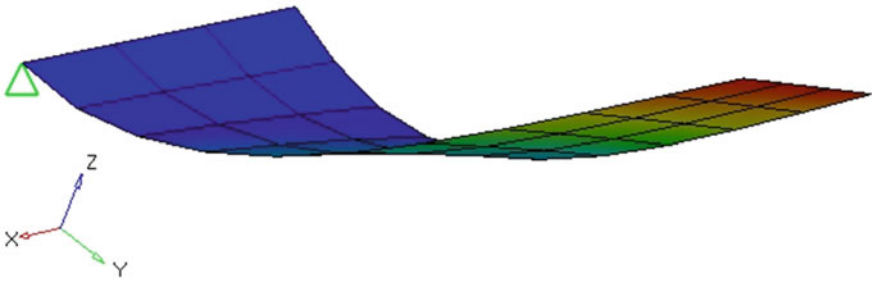

Fig. 2 First bending mode of the swept back plate

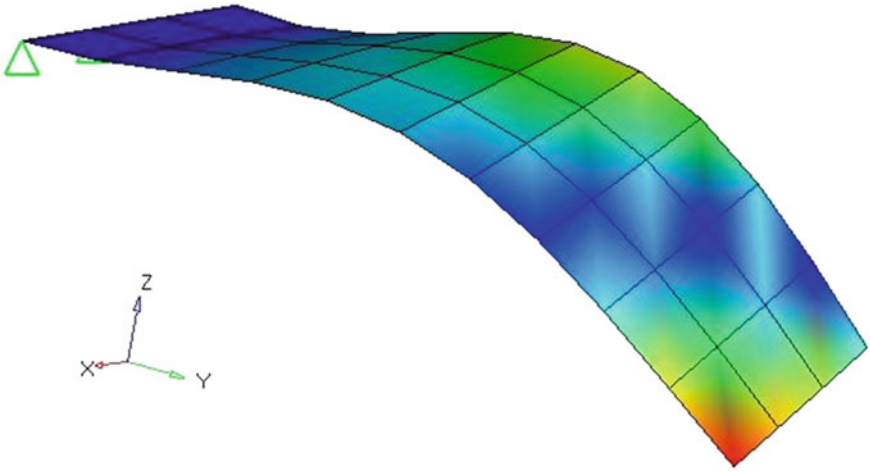

Fig. 3 Coupled bending torsion mode of the swept back plate

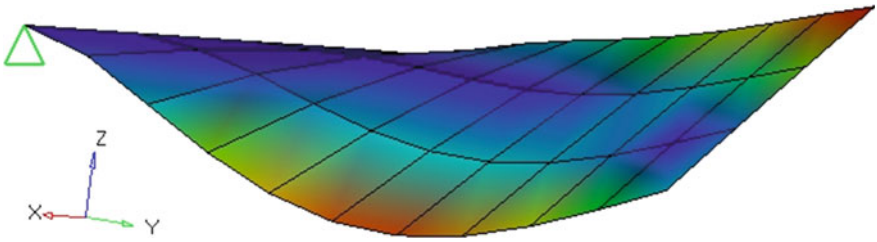

Fig. 4 Torsional mode of the swept back plate

method of NASTRAN [8] for the limited samples considered. Typical V–g V–f plots for the plate are shown in Fig. 5.

Based on the concept of Design of Experiments (DoE), in order to minimize the number of simulation runs, the upper and lower bounds of flutter are computed

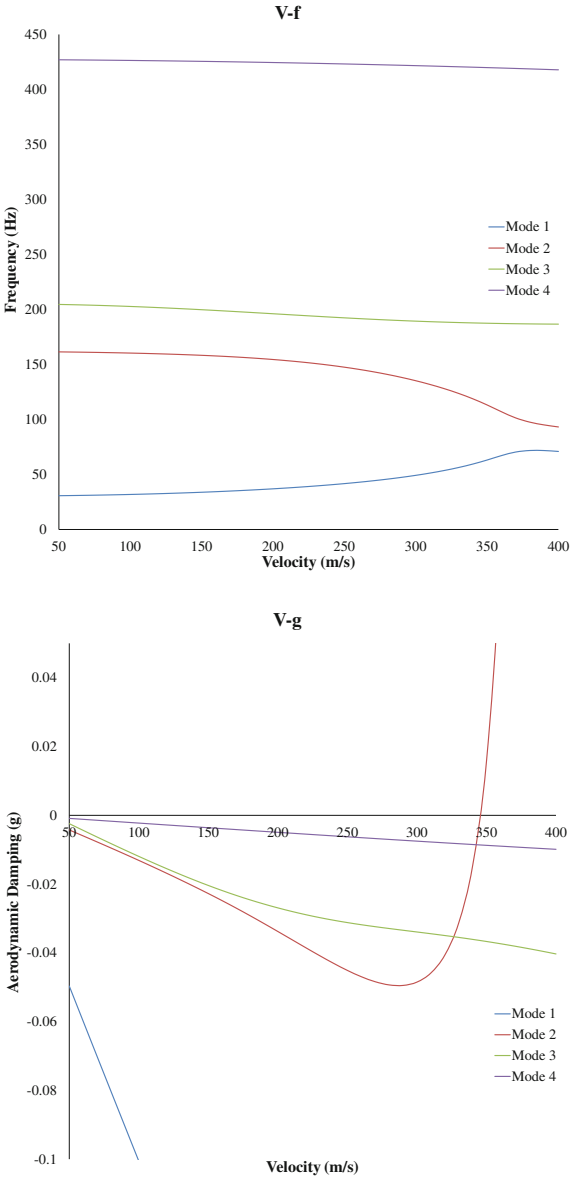

Fig. 5 Flutter plots of the swept back plate

considering the possible combinations of extreme and mean values of the design variables. A response surface is fitted based on the DoE results. A response surface fit is obtained using different methods like least square regression model, moving least squares regression model, hyper-Kriging regression model, and radial basis function. As the radial basis function response surface fit resulted in minimum error, stochastic studies were carried out using this model. MCS was run using the radial

basis function response fit assuming uniform distribution of the design variables. Failure probability is defined as the probability of the flutter velocity being lesser than the limiting flutter velocity. Therefore, reliability represents the probability of the flutter velocity being greater than the limiting flutter velocity. Reliability has been computed as a complement of the failure probability for different limiting flutter velocities for all the cases.

5.1 Structural Parameters as Random Variables

For the flutter reliability studies, two parameters namely Young's modulus and mass density are considered as design variables with a variation of 10%. The Young's modulus varies between 63.9 and 78.1 Gpa, and density of the material varies between 2450.49 and 2995.05 kg/m^3. Density of air is considered as 1.0 kg/m^3, and flutter analysis is carried out at Mach 0.5. Based on the concept of Design of Experiments (DoE), the possible combinations of extreme and mean values of the two design variables and the flutter response results are tabulated in Table 2.

MCS was run using the radial basis function response fit assuming uniform distribution of both the design variables. Reliability has been computed for different flutter margins and is presented in Table 3.

Table 2 Design of experiments results

S. No.	*E* (GPa) (DV1)	DEN_MAT (kg/m^3) (DV2)	Flutter speed (m/s) (response)
1.	78.1	2995.05	361.588
2.	78.1	2722.77	361.956
3.	78.1	2450.49	362.431
4.	71.0	2995.05	344.416
5.	71.0	2722.77	344.847
6.	71.0	2450.49	345.395
7.	63.9	2995.05	326.847
8.	63.9	2722.77	327.316
9.	63.9	2450.49	327.91

Table 3 Flutter reliability analysis results

S. No.	Flutter limit (m/s)	Probability of failure	Reliability
1.	330	0.11	0.89
2.	335	0.27	0.73
3.	340	0.38	0.62
4.	345	0.53	0.47
5.	350	0.61	0.39
6.	355	0.76	0.24

5.2 *Structural and Aero Parameters as Random Variables*

In order to study the effect of variations in aero parameters on flutter boundaries, two parameters in addition to the abovementioned structural parameters namely Mach number and density of air were considered as design variables, with a variation of 40 and 22%, respectively. The Mach number varies from 0.3 to 0.7, and density of air varies between 0.774 and 1.226 kg/m^3. Based on the concept of Design of Experiments (DoE), the possible combinations of extreme and mean values of all the design variables and the results are tabulated in Table 4.

MCS was run using the radial basis function response fit assuming uniform distribution of all the design variables and the reliability values are tabulated in Table 5. The effect of variation in Young's modulus, density of material, density of air, and Mach number on flutter speeds is shown in Figs. 6, 7, 8, and 9. It has been seen that Young's modulus and density of air have major influence on flutter speeds, whereas density of material and Mach number have little influence.

5.3 *Critical Parameters as Random Variables*

From the above studies, it has been observed that Young's modulus and density of air have maximum effect on flutter boundaries, whereas density of material and Mach number have least effect. So a flutter reliability analysis has been carried out considering the two critical parameters, namely Young's modulus and density of air as design variables with a variation of 10 and 22%, respectively. Density of material is considered as 2722.77 kg/m^3 and flutter analysis is carried out at Mach 0.5. Based on the concept of Design of Experiments (DoE), in order to minimize the number of simulation runs, the upper and lower bounds of flutter are computed considering the possible combinations of extreme and mean values of the two design variables and the results are tabulated in Table 6.

MCS was run using the radial basis function response fit assuming uniform distribution of both the design variables. Reliability has been computed for different flutter margins and is presented in Table 7.

6 Summary and Conclusions

The flutter reliability results of all the cases are summarized in Table 8. The maximum and minimum flutter speeds for the three cases are given in Table 9. The variation of reliability with respect to flutter limits is shown in Fig. 10.

It can be seen that in all the cases reliability comes down as the flutter limit increases. When compared to the case with structural parameters as design variables (Case 1), the case with structural and aero parameters as design variables (Case 2),

Table 4 Design of experiments results

S. No.	*E* (GPa) (DV1)	DEN_MAT (kg/m^3) (DV2)	DEN_AIR (kg/m^3) (DV3)	Mach No. (DV4)	Flutter speed (m/s)
1.	78.1	2995.05	1.226	0.7	326.463
2.	78.1	2995.05	1.226	0.5	326.655
3.	78.1	2995.05	1.226	0.3	324.263
4.	78.1	2995.05	1	0.7	361.326
5.	78.1	2995.05	1	0.5	361.588
6.	78.1	2995.05	1	0.3	359.485
7.	78.1	2995.05	0.774	0.7	410.446
8.	78.1	2995.05	0.774	0.5	410.952
9.	78.1	2995.05	0.774	0.3	408.38
10.	78.1	2722.77	1.226	0.7	327.061
11.	78.1	2722.77	1.226	0.5	327.099
12.	78.1	2722.77	1.226	0.3	324.6
13.	78.1	2722.77	1	0.7	361.742
14.	78.1	2722.77	1	0.5	361.956
15.	78.1	2722.77	1	0.3	359.968
16.	78.1	2722.77	0.774	0.7	410.815
17.	78.1	2722.77	0.774	0.5	411.323
18.	78.1	2722.77	0.774	0.3	408.879
19.	78.1	2450.49	1.226	0.7	327.889
20.	78.1	2450.49	1.226	0.5	327.74
21.	78.1	2450.49	1.226	0.3	325.1
22.	78.1	2450.49	1	0.7	362.279
23.	78.1	2450.49	1	0.5	362.431
24.	78.1	2450.49	1	0.3	360.364
25.	78.1	2450.49	0.774	0.7	411.297
26.	78.1	2450.49	0.774	0.5	411.79
27.	78.1	2450.49	0.774	0.3	409.491
28.	71.0	2995.05	1.226	0.7	311.555
29.	71.0	2995.05	1.226	0.5	311.552
30.	71.0	2995.05	1.226	0.3	309.735
31.	71.0	2995.05	1	0.7	343.895
32.	71.0	2995.05	1	0.5	344.416
33.	71.0	2995.05	1	0.3	342.344
34.	71.0	2995.05	0.774	0.7	391.048
35.	71.0	2995.05	0.774	0.5	391.632
36.	71.0	2995.05	0.774	0.3	389.543
37.	71.0	2722.77	1.226	0.7	311.928
38.	71.0	2722.77	1.226	0.5	311.855
39.	71.0	2722.77	1.226	0.3	310.081

(continued)

Table 4 (continued)

S. No.	*E* (GPa) (DV1)	DEN_MAT (kg/m^3) (DV2)	DEN_AIR (kg/m^3) (DV3)	Mach No. (DV4)	Flutter speed (m/s)
40.	71.0	2722.77	1	0.7	344.417
41.	71.0	2722.77	1	0.5	344.847
42.	71.0	2722.77	1	0.3	342.683
43.	71.0	2722.77	0.774	0.7	391.426
44.	71.0	2722.77	0.774	0.5	391.994
45.	71.0	2722.77	0.774	0.3	390.011
46.	71.0	2450.49	1.226	0.7	312.456
47.	71.0	2450.49	1.226	0.5	312.299
48.	71.0	2450.49	1.226	0.3	310.433
49.	71.0	2450.49	1	0.7	345.079
50.	71.0	2450.49	1	0.5	345.395
51.	71.0	2450.49	1	0.3	343.119
52.	71.0	2450.49	0.774	0.7	391.191
53.	71.0	2450.49	0.774	0.5	392.46
54.	71.0	2450.49	0.774	0.3	390.396
55.	63.9	2995.05	1.226	0.7	294.958
56.	63.9	2995.05	1.226	0.5	295.198
57.	63.9	2995.05	1.226	0.3	293.22
58.	63.9	2995.05	1	0.7	326.269
59.	63.9	2995.05	1	0.5	326.847
60.	63.9	2995.05	1	0.3	324.586
61.	63.9	2995.05	0.774	0.7	370.966
62.	63.9	2995.05	0.774	0.5	371.508
63.	63.9	2995.05	0.774	0.3	369.545
64.	63.9	2722.77	1.226	0.7	295.46
65.	63.9	2722.77	1.226	0.5	295.578
66.	63.9	2722.77	1.226	0.3	293.509
67.	63.9	2722.77	1	0.7	326.875
68.	63.9	2722.77	1	0.5	327.316
69.	63.9	2722.77	1	0.3	324.951
70.	63.9	2722.77	0.774	0.7	371.317
71.	63.9	2722.77	0.774	0.5	371.846
72.	63.9	2722.77	0.774	0.3	370
73.	63.9	2450.49	1.226	0.7	296.154
74.	63.9	2450.49	1.226	0.5	296.126
75.	63.9	2450.49	1.226	0.3	293.938
76.	63.9	2450.49	1	0.7	327.635
77.	63.9	2450.49	1	0.5	327.91
78.	63.9	2450.49	1	0.3	325.419

(continued)

Table 4 (continued)

S. No.	*E* (GPa) (DV1)	DEN_MAT (kg/m^3) (DV2)	DEN_AIR (kg/m^3) (DV3)	Mach No. (DV4)	Flutter speed (m/s)
79.	63.9	2450.49	0.774	0.7	371.774
80.	63.9	2450.49	0.774	0.5	372.28
81.	63.9	2450.49	0.774	0.3	370.36

Table 5 Flutter reliability analysis results

S. No.	Flutter limit (m/s)	Probability of failure	Reliability
1.	330	0.27	0.73
2.	335	0.33	0.67
3.	340	0.40	0.60
4.	345	0.47	0.53
5.	350	0.53	0.47
6.	355	0.59	0.41

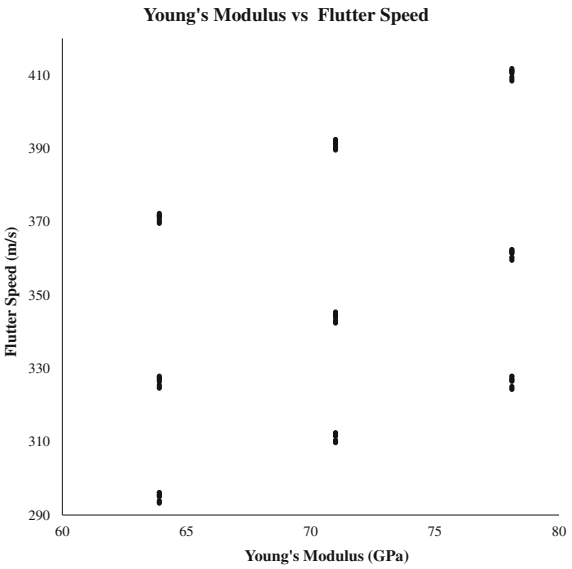

Fig. 6 Effect of Young's modulus on flutter speed

and case with critical parameters as design variables (Case 3) have lower reliability. But as the flutter limit reaches 345 m/s, the Case 2 and Case 3 have higher reliability when compared to Case 1. This is because Case 2 and Case 3 have higher flutter range when compared to Case 1 and so number of flutter points above the flutter limit for these cases are high resulting in higher reliability. When compared to Case 2, Case 3 has slightly lower reliability as the flutter range is slightly low for Case 3. The more the number of design variables, the greater is the accuracy of

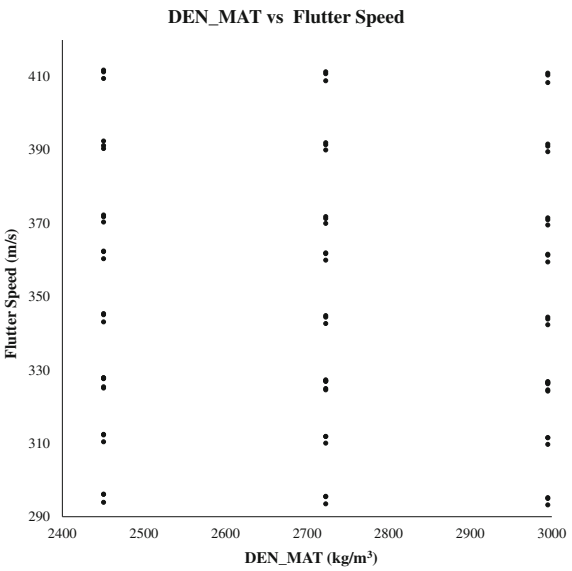

Fig. 7 Effect of density of material on flutter speed

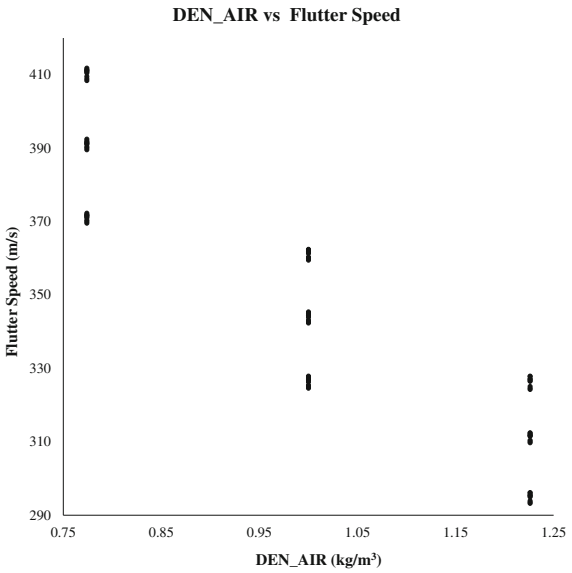

Fig. 8 Effect of density of air on flutter speed

reliability. Case 2 here is more reliable when compared to other two cases as it considers all the possible uncertainties. When there is a constraint on time and cost, it is necessary to select critical parameters affecting the phenomenon to get reasonably accurate results which in here happens to be Case 3. Case 3 considers critical parameters affecting flutter as design variables and so the reliability results

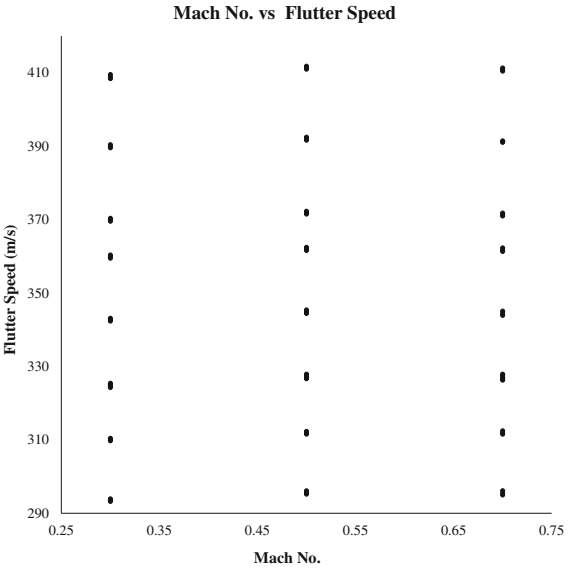

Fig. 9 Effect of Mach number on flutter speed

Table 6 Design of experimental results

S. No.	*E* (GPa) (DV1)	DEN_AIR (kg/m^3) (DV2)	Flutter speed (m/s) (response)
1.	78.1	1.226	327.099
2.	78.1	1.0	361.956
3.	78.1	0.774	411.323
4.	71.0	1.226	311.855
5.	71.0	1.0	344.847
6.	71.0	0.774	391.994
7.	63.9	1.226	295.578
8.	63.9	1.0	327.316
9.	63.9	0.774	371.846

Table 7 Flutter reliability analysis results

S. No.	Flutter limit (m/s)	Probability of failure	Reliability
1.	330	0.29	0.71
2.	335	0.36	0.64
3.	340	0.43	0.57
4.	345	0.48	0.52
5.	350	0.56	0.45
6.	355	0.60	0.40

Table 8 Flutter reliability analysis results

S. No.	Flutter limit	Case 1	Case 2	Case 3
		2DV (structural)	4DV (structural and aero)	2DV (critical)
1.	330	0.89	0.73	0.71
2.	335	0.73	0.67	0.64
3.	340	0.62	0.60	0.57
4.	345	0.47	0.53	0.52
5.	350	0.39	0.47	0.45
6.	355	0.24	0.41	0.40

Table 9 Statistics of flutter speeds

S. No.	Max flutter speed (m/s)	Min flutter speed (m/s)	Mean	Range
Case 1	362.43	326.85	344.64	35.58
Case 2	411.79	293.22	352.51	118.57
Case 3	411.32	295.58	353.45	115.74

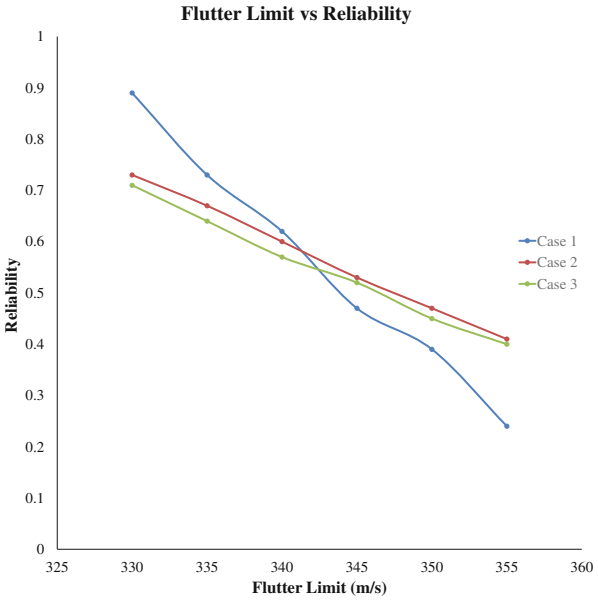

Fig. 10 Effect of flutter limit on reliability

are comparable to that of Case 2. Though Case 2 has four design variables, it predicts higher reliability values when compared to Case 3 which may be because remaining parameters ignored in Case 3 might have a positive effect on flutter speeds.

Acknowledgements The authors would like to thank the Head, Structural Technologies Division, NAL and the Director, NAL for their constant encouragement and support given to carry out the work reported in this paper.

References

1. Ueda, T. (2005). Aeroelastic analysis considering structural uncertainty. *Aviation, 9*(1), 3–7.
2. Song, S., Lu, Z., Zhang, W., & Ye, Z. (2009). Reliability and sensitivity analysis of transonic flutter using improved line sampling technique. *Chinese Journal of Aeronautics, 22*(5), 513–519.
3. Cheng, J., Cai, C. S., Xiao, R. C., et al. (2005). Flutter reliability analysis of suspension bridges. *Journal of Wind Engineering and Industrial Aerodynamics, 93*(10), 757–775.
4. Missoum, S., & Dribusch, C. (2010). Reliability-based design optimization of nonlinear aeroelasticity problems. *Journal of Aircraft, 47*(3), 992–998.
5. Wang, X., & Qiu, Z. (2009). Nonprobabilistic interval reliability analysis of wing flutter. *AIAA Journal, 47*(3), 743–748.
6. Gavin, H. P., & Yau, S. C. (2008). High order limit state functions in the response surface method for structural reliability analyis. *Structural Safety, 30*(2), 162–179.
7. Deng, J. (2006). Structural reliability analysis for implicit performance function using radial basis function network. *International Journal of Solids and Structures, 43*(11–12), 3255–3291.
8. MSC NASTRAN documentation. (2008). USA: MSC Software Corporation.

Nonlinear Static Analysis of Offshore J-Lay Risers Using Finite Element Method

S. Madhuri, B. Narendra Kumar and K. Venkateswara Rao

Abstract Risers are used for carrying crude oil/gas from seabed to supporting platform. These risers experience various environmental loads while carrying the fluids. Generally, the length of the riser depends on water depth, type of the platform that is attached to, sea state and environmental conditions. The deformation characteristics of the risers shall be analyzed in order to assess the design parameters and safety operation. A nonlinear finite element analysis of the riser at 300 and 2000 m water depth has been performed under wave, current and wave + current loading in the present study. The riser is modeled as a two-dimensional beam element considering six degree of freedom which is suspended in the floating drilling platform and subjected to both axial and lateral forces. A straight riser at 300 m water depth is considered for the present study. As the J-Lay technique of the riser is easy and mostly used in the industry, a J-Lay at 2000 m is also analyzed. A MATLAB code 'Riser Stat' is developed to analyze the riser. The axial extensions of all the elements are estimated considering top tension, weight of the riser, internal liquid weight and buoyancy. Morison equation is used to estimate the wave force on the riser. The axial and horizontal displacements are at each node of the finite element model of the riser and are estimated due to the effect of top tension and wave force in a wave cycle. Series of analyses are performed on the J-Lay riser under wave height of 2.0 m and wave period of 5–15 s at and increment in wave period of 1 s. Linearly varying current velocity of 1.4 and 1.0 m/s at sea surface to 0 m/s at a depth of 200 m is considered to estimate the current loading. The effective tension along the length of the riser at 2000 m water depth is compared

S. Madhuri (✉)
Department of Civil Engineering, University College of Engineering Kakinada, JNTU, Kakinada, India
e-mail: madhuri.seeram@gmail.com

B. N. Kumar · K. V. Rao
Department of Petroleum Engineering and Petrochemical Engineering, University College of Engineering Kakinada, JNTU, Kakinada, India
e-mail: narendrakumar.bezawada@gmail.com

K. V. Rao
e-mail: profkvrao@gmail.com

A. Rama Mohan Rao and K. Ramanjaneyulu (eds.), *Recent Advances in Structural Engineering, Volume 1*, Lecture Notes in Civil Engineering 11,
https://doi.org/10.1007/978-981-13-0362-3_44

with the Lenci and Callegari (Acta Mech 178:23–39, 2005) [1]. The results are compared well. The response of the riser under the combination of wave and current showed more when compared with the response of the riser under only wave loading.

Keywords Riser stat · Axial displacement · Lateral displacements
Effective tension

Nomenclature

A	Cross-sectional area of the riser (m^2)
a	Wave amplitude (m)
C_d	Drag coefficient
C_m	Inertia coefficient
d	Water depth (m)
d_f	Wave loading per unit length (kN/m)
D	Outer diameter of the riser
E	Modulus of elasticity of the riser material (N/m^2)
f	Force vector
g	Acceleration due to gravity (m/s^2)
I	Area moment of inertia (m^4)
k	Wave number (m^{-1})
K_E	Elastic stiffness matrix
K_G	Global elemental stiffness matrix
K_l	Local elemental stiffness matrix
L	Length of the element
l_i	Length of the riser element
S_i	Curved length of the riser
S_E	Geometric stiffness matrix
t	Time step (s)
T	Transformation matrix
T_{i-1}	Effective tension of the previous element (kN)
T_{Eff}	Effective tension in the element (kN)
u	Water particle velocity (m/s)
u_c	Current velocity (m/s)
$\dot{u}$	Water particle acceleration (m/s^2)
w_r	Weight of the riser element (kg)
w_i	Weight of the internal fluid (kg)
w_B	Buoyancy of the riser element (kg)
x	Spatial location of the node in the direction of the wave
x_i	Spatial location of the riser in the direction of the wave
y_i	Spatial location of the riser in the direction of water depth
z	Elemental water depth (m)
ρ	Density of sea water (kg/m^3)

Δ Displacement vector
θ_i Angle of the riser with vertical axis
σ Wave angular frequency (Hz)

1 Introduction and Literature Review

In offshore industries, risers play a key role in bringing the hydrocarbons from the seabed to the offloading vessel (ship) in deep/ultra-deepwater. In deepwater, installation of risers is most efficient and economical for transportation of crude oil and natural gas. The subsea risers are subjected to environmental loading such as wind, wave and current motions in different directions, vessel motion, pipeline seabed interaction, etc. Various studies on risers are discussed below. Bernitsas et al. [2] presented the three-dimensional, nonlinear and large deformation of marine riser analysis using small strain theory for three numerical applications. It was concluded that the stiffening effects of nonlinearity were important in the analysis of the risers. Lenci and Callegari [1] proposed an approach to boundary layer phenomenon by considering the stiffness of the soil of a J-Lay riser and concluded that the boundary layer effect of the soil shall be given importance on predicting the accurate results. Jinlong and Menglan [3] performed finite difference method analysis of a steel lazy wave riser (SLWR) considering small deflection and large deflection beam theories including soil–pile interaction, internal flow of the riser under ocean wave and current loading. Based on the analysis, it was observed that the increase in current velocity increased the axial tension at touchdown point but decrease in equivalent stress. The deformation [4] of riser and stress analyses [5] of riser were carried out under wave and wave + current including vessel motions using OrcaFlex. Lucile et al. [6] presented variations of the maximum stress at TDZ for SCRs of riser using FRONTIER and OrcaFlex softwares. Yang et al. [7] examined riser stability and the bottom over pull margins using a mechanical analysis approach and verified the results with common methods. The effects of true axial force and effective axial forces were examined and concluded that the stability of the riser depends on effective tension. Based on the brief literature review, it is observed that the nonlinear response studies of J-Lay riser under wave, wave + current loading are minimal. The variation of effective tension, axial and horizontal displacement along the length of the riser during its operation is minimal. Hence, a MATLAB [8] code, 'RiserStat', is developed to analyze the riser at any water depth using finite element method. The internal fluid velocity and the motions of the vessel are ignored in the present analysis.

2 Finite Element Modeling

The riser is descritized into finite elements. The coordinates of the riser elements, connectivity of the elements, dimensions, material properties and boundaries are given as input. The elements are modeled as two-dimensional beam elements by considering three degrees of freedom (axial, lateral and rotational) at each node. The elemental stiffness matrices (K_l) were developed based on elastic stiffness (Eq. 1) and geometric stiffness (Eq. 2). Elastic stiffness matrix is developed based on material properties, cross-sectional area and length of the riser element. Geometric stiffness matrix is developed based on effective tension in each element of the riser. Top tension at the vessel connecting point is applied. The effective tension of each element is estimated considering top tension, weight of the riser element, weight of internal fluid and buoyancy of the riser element (Eq. 4). Global stiffness matrices (Eq. 3) were generated using transformation technique. All the elemental stiffness matrices are assembled based on their elemental connectivity. The translational degrees of freedom are arrested (hinge) at vessel connection point and at touchdown point.

$$K_{\mathrm{E}} = \begin{bmatrix} \frac{AE}{L} & 0 & 0 & -\frac{AE}{L} & 0 & 0 \\ 0 & \frac{12EI}{L^3} & \frac{6EI}{L^2} & 0 & -\frac{12EI}{L^3} & \frac{6EI}{L^2} \\ 0 & \frac{6EI}{L^2} & \frac{4EI}{L} & 0 & -\frac{6EI}{L^2} & \frac{2EI}{L} \\ -\frac{AE}{L} & 0 & 0 & \frac{AE}{L} & 0 & 0 \\ 0 & -\frac{12EI}{L^3} & -\frac{6EI}{L^2} & 0 & \frac{12EI}{L^3} & -\frac{6EI}{L^2} \\ 0 & \frac{6EI}{L^2} & \frac{2EI}{L} & 0 & -\frac{6EI}{L^2} & -\frac{4EI}{L} \end{bmatrix} \tag{1}$$

$$S_{\mathrm{E}} = \frac{T_{\mathrm{eff}}}{L} \begin{bmatrix} 0 & 0 & 0 & 0 & 0 & 0 \\ 0 & \frac{6}{5} & \frac{L}{10} & 0 & \frac{-6}{5} & \frac{L}{10} \\ 0 & \frac{L}{10} & \frac{2L^2}{15} & 0 & \frac{-L}{10} & \frac{-L^2}{30} \\ 0 & 0 & 0 & 0 & 0 & 0 \\ 0 & \frac{-6}{5} & \frac{-L}{10} & 0 & \frac{6}{5} & \frac{-L}{10} \\ 0 & \frac{L}{10} & \frac{-L^2}{30} & 0 & \frac{-L}{10} & \frac{2L^2}{15} \end{bmatrix} \tag{2}$$

$$K_{\mathrm{l}} = K_{\mathrm{E}} + S_{\mathrm{E}}$$

$$K_G = \left[T^T\right][K_l][T] \tag{3}$$

$$T_{\mathrm{eff}} = T_{i-1} - 0.5(w_{\mathrm{r}} + w_{\mathrm{i}} - w_{\mathrm{B}}) \tag{4}$$

The wave force is estimated using Morison equation [9] as the D/L ratio of the riser is less than 0.2. The wave force is estimated for one cycle of wave by incremental time step method. The wave force is taken as combination of inertia

and drag forces (Eq. 5). The water particle kinematics (velocity and acceleration, Eqs. 6a, 6b) at each time step are estimated using linear Airy's wave theory. As the wave height-to-wavelength ratio is less than one in the present case, linear Airy's wave theory is considered.

$$df = C_{\mathrm{m}}\,\rho\frac{\pi}{4}D^2\dot{u} + \frac{1}{2}C_{\mathrm{d}}\,\rho D(u+u_{\mathrm{c}})|u+u_{\mathrm{c}}| \tag{5}$$

$$u = \frac{agk}{\sigma}\frac{\cosh(d+z)}{\cosh kd}\cos(kx-\sigma t) \tag{6a}$$

$$\dot{u} = agk\frac{\cosh(d+z)}{\cosh kd}\sin(kx-\sigma t) \tag{6b}$$

$$\Delta = [K_{\mathrm{G}}]^{-1}\{f\} \tag{7}$$

The global stiffness matrix and load vectors are generated based on geometry and boundary conditions of the riser. The displacement vector (Eq. 7) is estimated using stiffness method. The axial forces obtained due to the effective top tension in each riser element are considered for the first time step. The coordinates of the nodes are updated based on the global displacement, and the variation in top tension is also estimated. The obtained displacements are used to estimate the displaced coordinates of the nodes. The displaced coordinates and estimated top tension are given as input for the analysis in the next time step. The stiffness matrix and load vector are estimated for the updated coordinates. The wave force is estimated in addition to top tension. The displacement and top tension are estimated and are used for the next time step, and this process is continued for one cycle of the wave. The axial and lateral deformations at each time step are obtained as output in the MATLAB code. The flowchart [10] of the present analysis is shown in Fig. 1.

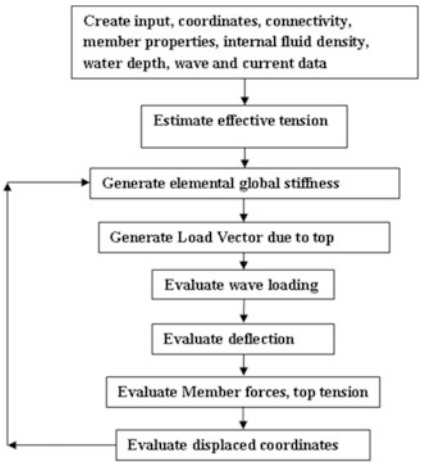

Fig. 1 Scheme of nonlinear static analysis of riser

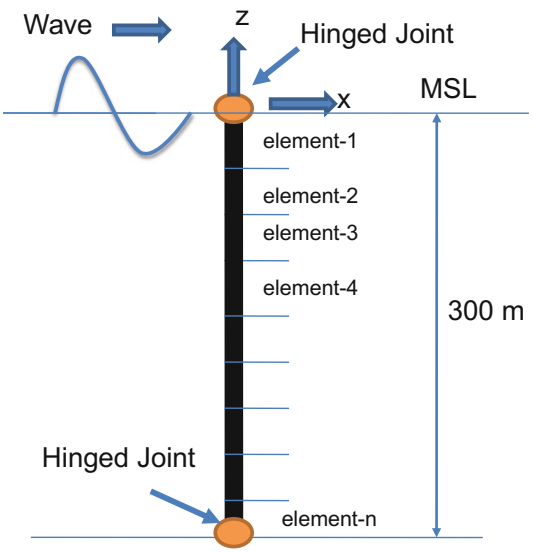

Fig. 2 Schematic diagram of riser at 300 m water depth

3 Analysis of Straight Riser at 300 m Water Depth

A straight steel riser of 0.6 m outer diameter and 0.05 m wall thickness is analyzed under the combination of top tension and wave loading. The schematic diagram of straight riser is shown in Fig. 2. The details of the riser are given in Table 1. Wave height of 2 m and wave period of 10 s are assumed for the analysis. Uniform current velocity of 1 m/s is considered for current load estimation. The axial and lateral deformations at different time steps under wave loading are presented (Fig. 3a, b). The variation of top tension in one wave cycle with and without current is shown in Fig. 4.

Table 1 Details of straight riser

Description	Quantity	Units
Outer diameter	0.6	m
Inner diameter	0.55	m
Water depth	300	m
Top tension	2700	kN
young's modulus	2.1×10^5	N/m^2
Density of sea water	1030	kg/m^3
Density of steel	7850	kg/m^3
Density of crude oil	800	kg/m^3
Wave height	2	m
Wave period	10	s
Current velocity	1.0	m/s

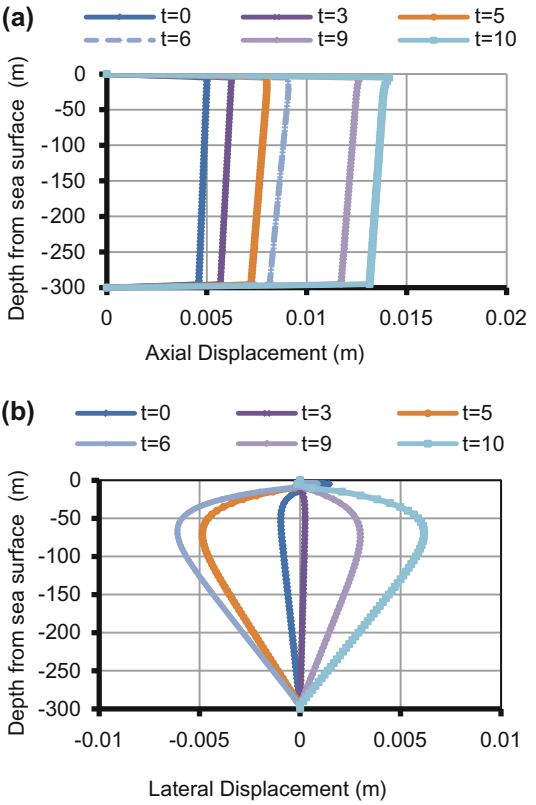

Fig. 3 **a** Axial displacement of straight riser. **b** Lateral displacement of straight riser

Fig. 4 Variation of top tension in one wave cycle of straight riser

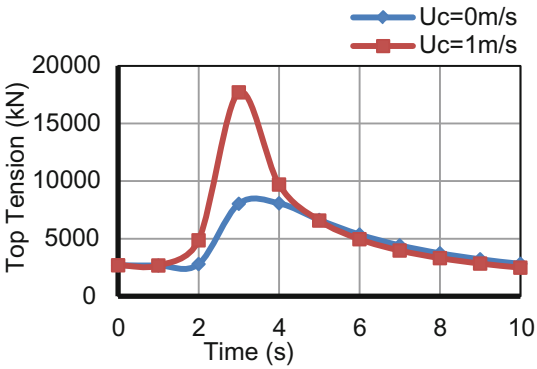

4 Analysis of Catenary Riser at 2000 m Water Depth

As the oil exploration is going towards deeper and ultra-deepwater depths, installation of straight risers is not feasible. Flexible risers are being used at deeper and ultra-deepwater depths. J-Lay risers are common and easy to install. Hence, a J-Lay catenary riser at 2000 m water depth is analyzed using the developed MATLAB code RiserStat. The schematic diagram of catenary riser is shown in Fig. 5. The length of the riser is considered from free hang point to touchdown point in catenary shape. The origin of global coordinates system is taken at free hang point. The free hang point of the riser is assumed at sea surface. The pipeline welding ramp angle of 80° with the vertical axis at free hanging point is considered. The horizontal distance between touchdown point and free hanging point is assumed about 1200 m. Top tension of 7×10^6 N is applied. The riser details are given in Table 2.

The coordinates of the elements of the catenary riser are estimated using the following equations:

$$x_i = a_i \left[\sinh^{-1}\left(\frac{l_i}{a_i} + \tan\theta_i \right) - \sinh^{-1}(\tan\theta_i) \right] \tag{8}$$

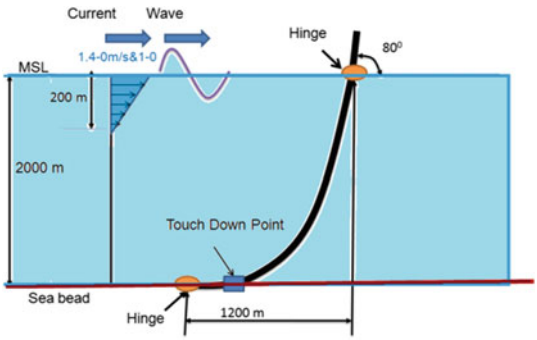

Fig. 5 Layout of catenary riser

Table 2 Details of catenary riser (Lenci and Callagari [1])

Description	Quantity	Units
Outer diameter of pipeline	0.6	m
Inner diameter of pipeline	0.55	m
Water depth	2000	m
Elastic modulus of riser	2.1×10^5	N/mm^2
Density of sea water	1030	kg/m^3
Density of steel material	7850	kg/m^3
Density of crude oil	800	kg/m^3
Top tension	7×10^6	N
wave height	2	m
Wave period range	5–15	s

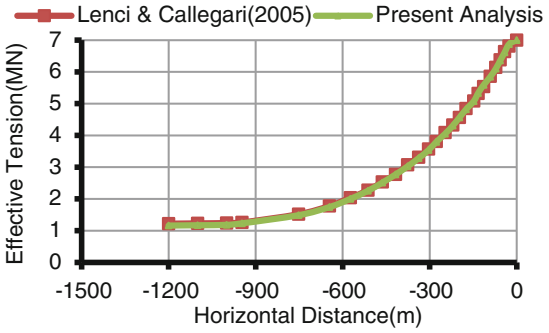

Fig. 6 Effective tension variation of catenary riser

$$y_i = a_{\mathrm{i}}\left[\cosh\left(\frac{x_i}{i} + \sinh^{-1}(\tan\theta_i)\right) - \cosh\left(\sinh^{-1}(\tan\theta_i)\right)\right] \tag{9}$$

$$S_{\mathrm{i}} = a_{\mathrm{i}}\left(\sinh\left(\frac{x_i}{a_i} + \sinh^{-1}(\tan\theta_i)\right) - \tan\theta_i\right) \tag{10}$$

$$\tan(\theta_{i+1}) = \tan\left(\theta_i + \frac{S_{\mathrm{i}}}{a_{\mathrm{i}}}\right) \tag{11}$$

The catenary riser is analyzed using RiserStat, and the effective tension variation along the length of the riser is compared with Lenci and Callagari [1]. The comparison is shown in Fig. 6. Results show that the effective tension is compared well along the length of the riser. A nonlinear finite analysis of riser is performed under wave loading, and the maximum axial and lateral deformations in a wave cycle are recorded. The nonlinear analysis is performed by varying wave period from 5 to 15 s with an increment of 1 s. Linearly varying current velocity for a depth of 200 m from mean sea level (MSL) is applied as current loading. The current velocity is considered in two cases. In case I, current velocity of 1.0 m/s at MSL and 0 m/s at a depth of 200 m from MSL is considered. In case II, current velocity of 1.4 m/s is considered at MSL. The combined effect of wave and current loading is estimated. The maximum axial and lateral deformations of the riser in the considered wave and current load combinations are obtained and amplification factor (Ratio of maximum deflection and wave height) of the riser for each case is plotted against wave periods. The maximum axial and lateral amplification factors of the riser in the considered cases are shown in Figs. 7 and 8, respectively.

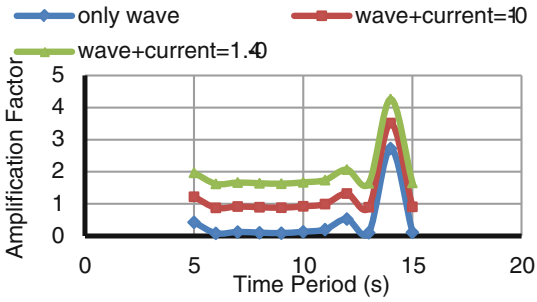

Fig. 7 Maximum axial deformation of catenary riser

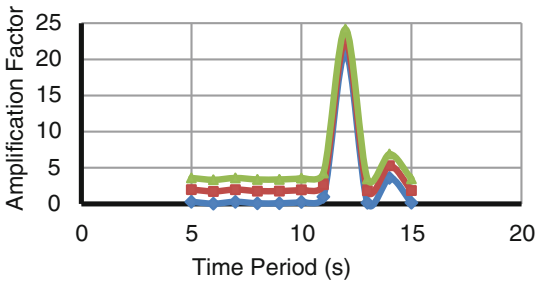

Fig. 8 Maximum lateral deformation of catenary riser

5 Results and Discussions

A MATLAB code RiserStat is developed to perform nonlinear static analysis of the riser. Analysis is performed for in two different risers at 300 and 2000 m water depth. The variation of effective top tension one wave cycle (10 s wave period) of straight riser is plotted against time step. The results indicate that the maximum effective tension is obtained at 3 s time step which is indicating that the riser crests at 3 s time step. This behavior is observed due to increase in water particle velocity and acceleration at 3 s time step. The maximum effective top tension under wave loading is about 2.97 times of initial top tension. The maximum effective top tension under wave and uniform current loading are about 6.55 times of initial top tension. The maximum axial and lateral displacements in straight riser are observed about 50 m below the MSL.

A catenary riser at 2000 m water depth is also analyzed, and effective tension variation along the length of the riser is compared well with Lenci and Callegari [1]. Nonlinear static analysis is performed for catenary riser, and amplification factors are plotted against wave period. The comparison of lateral and axial amplification under wave loading indicates that the maximum lateral amplification factor is about 10 times the maximum axial amplification factor which is indicating that the riser is flexible in nature. The comparison of amplification factors under wave and wave + current loadings cases indicates that the increase in current velocity increased the response of the riser. The maximum axial amplification under

wave + current (case I) loading is observed 29% higher than the axial amplification factor under wave loading. 57% higher axial amplification is observed when case II current velocity is compared with maximum axial amplification under wave loading. No major significant effect is observed in the lateral deformation even current velocity is applied in addition to wave loading.

6 Conclusions

The present MATLAB code 'RiserStat' is developed using finite element method by neglecting internal fluid velocity and vessel motions. A straight riser at 300 m water depth and a catenary riser at 2000 m water depth are analyzed using the developed code. The variation of the top tension in one wave cycle under wave loading of 2 m wave height and 10 s wave period is studied, and maximum effective top tension is obtained at wave crest location. The maximum axial and lateral displacements are observed at 50 m below the MSL. The present effective tension variation of catenary riser is compared well with Lenci and Callegari [1]. The increase in current velocity indicated the increase in amplification factor of the riser. The present analytical results show that the lateral deformations of the catenary raiser are about 10 times the axial deformations indicating that the riser is flexible in nature.

References

1. Lenci, S., & Callegari, M. (2005). Simple analytical models for the J-lay problem. *Acta Mechanica, 178,* 23–39.
2. Bernitsas, M. M., Kokarakis, J. E., & Imron, A. (1985). Large Deformation three dimensional static analysis of deep water marine riser. *Applied Ocean Research*, *7*(4), 178–187.
3. Wang, J., & Duan, M. (2015). A nonlinear model for deepwater steel lazy-wave riser configuration with ocean current and internal flow. *Ocean Engineering, 94,* 155–162.
4. Wang, Y., Gao, D., & Fang, J. (2014). Static analysis of deep-water marine riser subjected to both axial and lateral forces in its installation. *Journal of Natural Gas Science and Engineering, 19,* 84–90.
5. Senthil, B., & Selvam, R. P. (2015). Dynamic analysis of a J-lay pipeline. *Procedia Engineering*, *116* (730–737). In *8th International Conference on Asian and Pacific Coasts*.
6. Queau, L. M., Kimiaei. M., & Randolph, M. F. (2015). Approximation of the maximum dynamic stress range in steel catenary risers using artificial neural networks, *Engineering Structures*, *92*, 172–185.
7. Yang, J., Meng, W., Yao, M., Gao, D., Zhou, B., & Xu, Y. (2015). Calculation method of riser top tension in riser deep water drilling. *Petroleum -Exploration and Development, 42*(1), 119–122.
8. MATLAB 7.10.0. *User guide*.
9. Morison, J. R., O'Brien, M. P., Johnso, J. W., & Schaaf, S. A. (1950). The force exerted by surface waves on piles. *Petroleum Transactions, 189,* 149–154. (AIME).
10. Bathe, K. J. *Finite element procedures*. New Jersey: Prentice Hall.

Estimation of Modal Characteristics of a Reduced-Order Fluid–Structure Interaction System

Hridya P. Lal, W. Dheelibun Remigius, Sayan Gupta and Sunetra Sarkar

Abstract Understanding of modal characteristics of fluid–structure interaction (FSI) systems plays a vital role in avoiding large oscillations and instabilities. Further, with parametric uncertainties, the onset of the instabilities may change and hence it is important to know the statistics of the modal characteristics of the coupled system to avoid system failures. The primary objective of the study is to estimate the statistics of modal characteristics of the stochastic FSI system which demands intensive computation resources especially for large ordered FSI systems. The present study also focusses on developing and implementing a stochastic reduced-order model to resolve pressure-induced oscillations of a disc-like structure as a generic fluid–structure interaction system. The stochastic reduced-order model uses a modal reduction approach together with spectral projection-based polynomial chaos expansion (PCE) to truncate both the system degrees of freedom (dofs) and the random modes. Interfacing algorithms have also been developed that enable finite element (FE) modelling of the FSI system using commercial software and in-house developed codes.

Keywords Modal characteristics · SEREP · FSI · PCE · Reduced-order model

H. P. Lal · S. Gupta (✉)
Department of Applied Mechanics, Indian Institute of Technology Madras, Chennai 600036, India
e-mail: gupta.sayan@gmail.com

H. P. Lal
e-mail: hridyaplal@gmail.com

W. Dheelibun Remigius · S. Sarkar
Department of Aerospace Engineering, Indian Institute of Technology Madras, Chennai 600036, India
e-mail: remigius.dheelibun@gmail.com

S. Sarkar
e-mail: sunetra.sarkar@gmail.com

A. Rama Mohan Rao and K. Ramanjaneyulu (eds.), *Recent Advances in Structural Engineering, Volume 1*, Lecture Notes in Civil Engineering 11,
https://doi.org/10.1007/978-981-13-0362-3_45

1 Introduction

This study focuses on estimating the modal characteristics of a stochastic fluid–structure interaction (FSI) system. The system being studied consists of a thin annular disc immersed in a compressible fluid-filled cylindrical enclosure. The interaction between the disc and the acoustic system arises either from the flow-induced vibrations of the disc or from the structure-induced acoustic oscillations [1]. Additionally, it is assumed that there exist uncertainties in the mathematical modelling of the system properties, which are treated as random variables. A first step in understanding the dynamical behaviour of the FSI system involves characterizing the modal properties such as the coupled natural frequencies, mode shapes and the frequency response functions of the coupled system. Deterministic eigenvalue analysis reveals the dependence of the system parameters on the disc and acoustic-dominated coupled mode shapes. Due to uncertainties in system parameters and depending on the coupling, an eigenvalue veering phenomenon may occur. As a result, a structure-dominated coupled mode may become an acoustic-dominated mode and vice versa. Hence, this kind of FSI systems requires the development of high fidelity finite element (FE) models for both the disc and the fluid. This result in system matrices of high dimensions and the computational cost associated with estimating the modal characteristics can be significant. The problem is compounded by the presence of stochasticity in the model. There is thus a need to investigate methodologies for reducing computational cost.

Reduced-order models for the stochastic FSI system which can reduce the computational costs without compromising the accuracy of the solution are developed in this study. A scheme based on polynomial chaos expansion (PCE) [2] and system equivalent reduction expansion process (SEREP) [3] has been developed that enables formulation of reduced-order models for the FSI system. Reduction in the globally coupled system matrices is obtained through SEREP by retaining the active dofs along with the dominant dynamic modes and in uncertainty quantification through PCE by retaining only the first few dominant stochastic modes. Interfacing algorithms have been developed that enable finite element (FE) modelling of complex systems using commercial FE software and the developed codes.

2 Problem Formulation

This section explains the evaluation of the coupled frequencies using FE approach for the full FSI model shown in Fig. 1. Further, the development and the implementation of the PCE-based SEREP formulation is also explained in this section.

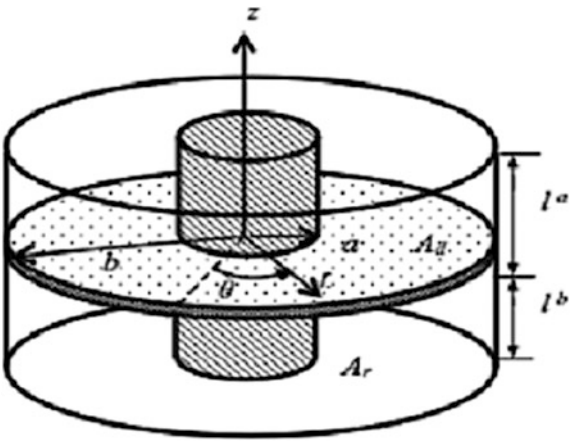

Fig. 1 A schematic of the considered FSI model (Ref. [4])

2.1 Full FSI Model

Consider a thin annular disc backed by an annular cavity as shown in Fig. 1. The system shown in Fig. 1 can effectively model the fluid–structure interaction behaviour of the various engineering systems such as compact disc drives, saw blades and impeller discs of the centrifugal compressors, etc. The FSI behaviour of the considered system involves the interaction of the elastic field of the disc with the acoustic field of the surrounding fluid.

Based on the discretization technique given by Ref. [1], the field equations governing the pressure oscillations in the upper and lower cavities coupled with disc oscillations are rewritten as (Ref. [5]),

$$[G]^a\{\ddot{p}(t)\}^a + [H]^a\{p(t)\}^a = (\rho c)^2[A^T]^a\{\ddot{u}(t)\}, \tag{1}$$

$$[G]^b\{\ddot{p}(t)\}^b + [H]^b\{p(t)\}^b = -(\rho c)^2[A^T]^b\{\ddot{u}(t)\}, \tag{2}$$

where the column matrix $\{p\} \in \Re^{N\times 1}$ gives the pressure at the grid points of the finite element mesh, $\{\ddot{u}\} \in \Re^{Q\times 1}$ is the structural acceleration vector and $[A^T] \in \Re^{N\times Q}$ is the transposed structural-acoustic coupling matrix of the boundary surface areas. $[G], [H] \in \Re^{N\times N}$ represent acoustic mass and stiffness matrices, respectively. Here, the superscripts *a and b* denote the upper and lower cavities, respectively, and ρ, c are the fluid density and wave propagation speed in the fluid medium, respectively.

Similarly, the finite element field equation governing the disc displacement u coupled with the fluid oscillations p is discretized and rewritten as (Refs. [1, 5])

$$[M]\{\ddot{u}(t)\} + [D]\{\dot{u}(t)\} + [K]\{u(t)\} = \{[A]^b\{\ddot{p}(t)\}^b - [A]^a\{\ddot{p}(t)\}^a\} + \{F(t)\}, \tag{3}$$

where $\{u\} \in \Re^{Q\times 1}$ designates the structural displacement vector; $[M], [D], [K] \in \Re^{Q\times Q}$ represent structural mass, damping and stiffness matrices, respectively; $\{F\} \in \Re^{Q\times 1}$ is the vector of external forces applied to the structure; and $[A] \in \Re^{Q\times N}$ is the structural-acoustic coupling matrix of the boundary surface areas (Ref. [5]).

The field Eqs. (1, 2, 3) are rewritten in matrix form, with damping and forcing neglected, as

$$\begin{bmatrix} [M] & [0] & [0] \\ -(\rho c)^2[A^T]^a & [G]^a & [0] \\ (\rho c)^2[A^T]^b & [0] & [G]^b \end{bmatrix} \begin{Bmatrix} \{\ddot{u}(t)\} \\ \{\ddot{p}^a(t)\} \\ \{\ddot{p}^b(t)\} \end{Bmatrix} + \begin{bmatrix} [K] & [A]^a & -[A]^b \\ [0] & [H]^a & [0] \\ [0] & [0] & [H]^b \end{bmatrix} \begin{Bmatrix} \{u(t)\} \\ \{p^a(t)\} \\ \{p^b(t)\} \end{Bmatrix} = \begin{Bmatrix} \{0\} \\ \{0\} \\ \{0\} \end{Bmatrix} \tag{4}$$

This equation yields the eigenvalue problem of the gyroscopically coupled disc-acoustic system from which one can get the coupled mode shapes and the system frequencies in the physical coordinate system. Since the physical coordinate involves all the degrees of freedom (dof), which makes the analysis computationally intensive especially for large-order systems. In order to reduce the computational cost, as a conventional way, the field equations are converted into generalized coordinate system using the following transformation:

$$\{u(t)\} = [\tilde{\Phi}_s]\{\tilde{\eta}_s(t)\}, \quad \{p(t)\} = [\tilde{\Phi}_f]\{\tilde{\eta}_f(t)\}, \tag{5}$$

where $[\tilde{\Phi}_s] \in \Re^{Q\times k}$ and $[\tilde{\Phi}_f] \in \Re^{N\times l}$ are the uncoupled modal matrix of the disc and the acoustic cavity with k and l dominant dynamic modes, respectively.

$\{\tilde{\eta}_s(t)\} \in \Re^{l\times 1}$ and $\{\tilde{\eta}_f(t)\} \in \Re^{k\times 1}$ are the generalized coordinates of the disc and the acoustic cavity, respectively. Making use of the transformation (5), the Eq. (4) becomes

$$\begin{bmatrix} [m] & [0] & [0] \\ -(\rho c)^2[C^T]^a & [g]^a & [0] \\ (\rho c)^2[C^T]^b & [0] & [g]^b \end{bmatrix} \begin{Bmatrix} \{\ddot{\tilde{\eta}}_s(t)\} \\ \{\ddot{\tilde{\eta}}_f(t)\}^a \\ \{\ddot{\tilde{\eta}}_f(t)\}^b \end{Bmatrix} + \begin{bmatrix} [k] & [C]^a & -[C]^b \\ [0] & [h]^a & [0] \\ [0] & [0] & [h]^b \end{bmatrix} \begin{Bmatrix} \{\tilde{\eta}_s(t)\} \\ \{\tilde{\eta}_f(t)\}^a \\ \{\tilde{\eta}_f(t)\}^b \end{Bmatrix} = \begin{Bmatrix} \{0\} \\ \{0\} \\ \{0\} \end{Bmatrix} \tag{6}$$

where $[C] = [\tilde{\Phi}_s]^T[A][\tilde{\Phi}_f]$ is the modal coupling matrix, $[m] = [\tilde{\Phi}_s]^T[M][\tilde{\Phi}_s]$, etc. are diagonal matrices. The elements of $[C]$ represent the product of the structural modes with the acoustic cavity modes weighted by the bounding area attributed to each boundary point. Further, it is worth noting here that the modal coupling matrix $[C]$ describes the gyroscopic coupling between the disc and cavity mode shapes (Ref. [6]). Each coupled mode is designated either as a disc-dominated mode or as an acoustic-dominated mode depending upon its energy content (Ref. [6]). The cavity and disc mode shapes are in general expressed as (k_1, k_2, k_3) and (k_4, k_5), respectively. Here, k_1 and k_4 represent the number of nodal diameters, k_2 and k_5 represent the number of nodal circles and k_3 represents the z-directional node number. Moreover, for a large-order FSI system, the analysis in the modal domain by retaining the selected modes is still computationally intensive which encourages the use of the model reduction techniques.

2.2 Reduced FSI Model Using SEREP Technique

Among all model reduction techniques, SEREP has been found to be more reliable and accurate (Ref. [7]) which preserves the essential dynamical behavioural characteristics of the full-scale model by retaining only lesser number of dofs known as active dofs along with modal truncation. SEREP is an eigenvalue-based reduction technique, used to find a low-dimensional subspace in order to approximate the state vectors $\{u(t)\}$ and $\{p(t)\}$. Partitioning the state vectors in terms of active and deleted dofs by retaining the few important modes, one can write

$$\begin{aligned} \{p(t)\} &= \begin{Bmatrix} \{p_r(t)\} \\ \{p_e(t)\} \end{Bmatrix} = \begin{Bmatrix} [\widetilde{\Phi}_r] \\ [\widetilde{\Phi}_e] \end{Bmatrix} \{\widetilde{\eta}_f(t)\}, \\ \{u(t)\} &= \begin{Bmatrix} \{u_o(t)\} \\ \{u_d(t)\} \end{Bmatrix} = \begin{Bmatrix} [\widetilde{\Phi}_o] \\ [\widetilde{\Phi}_d] \end{Bmatrix} \{\widetilde{\eta}_s(t)\}. \end{aligned} \tag{7}$$

Here, r, o and e, d are the active and deleted dofs of the cavity and the disc, respectively. Using Eq. (5), the truncated modal vector can be expressed as

$$\{\tilde{\eta}_f(t)\} = [\widetilde{\Phi}_r^g]\{p_r(t)\}, \quad \{\tilde{\eta}_s(t)\} = [\widetilde{\Phi}_o^g]\{u_o(t)\}, \tag{8}$$

where the superscript g refers to a generalized inverse of $[\widetilde{\Phi}_r]$ and $[\widetilde{\Phi}_o]$, respectively. Substituting Eq. (8) into Eq. (5), one gets

$$\begin{aligned} \{p(t)\} &= [\widetilde{\Phi}_f][\widetilde{\Phi}_r^g]\{p_r(t)\} = [T_f]\{p_r(t)\}, \\ \{u(t)\} &= [\widetilde{\Phi}_s][\widetilde{\Phi}_o^g]\{u_o(t)\} = [T_s]\{u_o(t)\}, \end{aligned} \tag{9}$$

where $[T_f] \in \Re^{N\times r}$ and $[T_s] \in \Re^{Q\times o}$ are the transformation matrix which relates the full system and the reduced system. Using the transformation matrices, Eq. (4) is reduced as

$$\begin{bmatrix} [M_o] & [0] & [0] \\ -(\rho c)^2[A_{\text{ro}}^T]^a & [G_r]^a & [0] \\ (\rho c)^2[A_{\text{ro}}^T]^b & [0] & [G_r]^b \end{bmatrix} \begin{Bmatrix} \{\ddot{u}_o(t)\} \\ \{\ddot{p}_r(t)\}^a \\ \{\ddot{p}_r(t)\}^b \end{Bmatrix} + \begin{bmatrix} [K_o] & [A_{\text{or}}]^a & -[A_{\text{or}}]^b \\ [0] & [H_r]^a & [0] \\ [0] & [0] & [H_r]^b \end{bmatrix} \begin{Bmatrix} \{u_o(t)\} \\ \{p_r(t)\}^a \\ \{p_r(t)\}^b \end{Bmatrix} = \begin{Bmatrix} \{0\} \\ \{0\} \\ \{0\} \end{Bmatrix}. \tag{10}$$

Here, the reduced submatrices are

$$[M_o] = [T_s]^T[M][T_s], \quad [G_r] = [T_f]^T[G][T_f],$$
$$[K_o] = [T_s]^T[K][T_s], \quad [H_r] = [T_f]^T[H][T_f],$$
$$[A_{or}] = [T_s]^T[A][T_f].$$

Equation (10) yields the gyroscopic eigenvalue problem of the reduced system. In the modal domain, Eq. (10) can be rewritten as

$$\begin{bmatrix} [m_o] & [0] & [0] \\ -(\rho c)^2[C_{\text{ro}}^T]^a & [g_r]^a & [0] \\ (\rho c)^2[C_{\text{ro}}^T]^b & [0] & [g_r]^b \end{bmatrix} \begin{Bmatrix} \{\ddot{\tilde{\eta}}_s(t)\} \\ \{\ddot{\tilde{\eta}}_f(t)\}^a \\ \{\ddot{\tilde{\eta}}_f(t)\}^b \end{Bmatrix} + \begin{bmatrix} [k_o] & [C_{\text{or}}]^a & -[C_{\text{or}}]^b \\ [0] & [h_r]^a & [0] \\ [0] & [0] & [h_r]^b \end{bmatrix} \begin{Bmatrix} \{\tilde{\eta}_s(t)\} \\ \{\tilde{\eta}_f(t)\}^a \\ \{\tilde{\eta}_f(t)\}^b \end{Bmatrix} = \begin{Bmatrix} \{0\} \\ \{0\} \\ \{0\} \end{Bmatrix} \tag{11}$$

In the following subsection, the effect of system randomness is going to be incorporated into the deterministic model and uncertainty quantification (UQ) is carried out in order to obtain the statistics of the modal characteristics.

2.3 *Uncertainty Quantification*

Uncertainties can occur due to modelling limitations and these uncertainties associated with the system parameters are treated here as random variables θ. After incorporating the randomness, the deterministic model will become a stochastic model. To get the statistics of the modal characteristics, as a conventional approach, one has to solve the deterministic model corresponding to each sample realization. This statistical sampling-based approach is widely known as Monte Carlo

simulations (MCS). However, to obtain the desired level of accuracy, one needs to generate large sample sets which in turn require a large number of solutions of the problem. For large ordered system, this can be computationally prohibitively expensive.

As an alternative approach, spectral projection-based approach known as PCE has been used here. In this approach, the stochastic quantities are projected using a family of orthogonal polynomials in the random space. The polynomials are chosen from the generalized Askey scheme. A projection-based non-intrusive version of PCE has been used here. In the PCE form, stochastic state vectors can be written as follows (Ref. [2]):

$$u(t,\theta) = \sum_{i=0}^{B} \hat{u}_i(t)\psi_i(\xi(\theta)), \quad p(t,\theta) = \sum_{j=0}^{E} \hat{p}_j(t)\psi_j(\xi(\theta)), \tag{12}$$

where $\hat{u}(t), \hat{p}(t)$ are deterministic coefficients, ψ_i, ψ_j are the orthogonal polynomials of the order i, j, respectively, B, E are the highest order of the orthogonal polynomials and ξ is the basis random variables. Deterministic coefficients are evaluated as follows:

$$\begin{aligned} \hat{u}_i(t) &= \frac{\langle u(t,\varsigma), \psi_i \rangle}{\langle \psi_i, \psi_i \rangle}, \quad i = 0, 1, \ldots, B, \\ \hat{p}_j(t) &= \frac{\langle p(t,\varsigma), \psi_j \rangle}{\langle \psi_j, \psi_j \rangle}, \quad j = 0, 1, \ldots, E, \end{aligned} \tag{13}$$

The inner product in the numerator is evaluated using a tensor product quadrature as follows:

$$\begin{aligned} \langle u(t,\varsigma), \psi_i \rangle &= \sum_{i=0}^{B_1} u(t,\varsigma)\psi_i w_i, \quad \text{where } B_1 \geq B, \\ \langle p(t,\varsigma), \psi_j \rangle &= \sum_{j=0}^{E_1} p(t,\varsigma)\psi_j w_j, \quad \text{where } E_1 \geq E. \end{aligned} \tag{14}$$

Here, B_1, E_1 are the total numbers of collocation points and w_i, w_j are the weight functions corresponding to the ith, jth collocation points. The weighing function depends on the orthogonal polynomials being used; for Hermite polynomials, the associated function is the Gaussian distribution function and the orthogonality condition becomes $\langle \psi_j, \psi_j \rangle = j!$ and $\langle a, b \rangle$ represents the standard inner product. These deterministic coefficients are substituted back into Eq. (12) and subsequently MCS runs are carried out on these expressions to get the statistics of the modal characteristics. The computational time reduction in the uncertainty quantification has been achieved through PCE formulation for the full FSI model. Moreover, for the large ordered stochastic FSI model, further reduction in computational time can

be achieved by extending the SEREP technique to this PCE approach. The following subsection explains how the SEREP is applied through the PCE formulation to a large ordered stochastic FSI system.

2.4 PCE-Based SEREP Formulation

The method of stochastic collocation can be used to obtain the spectral representation of the reduced-order system as well. The SEREP formulation explained in Sect. 2.2 has been applied to the field equations in Eq. (4) at the collocation points. Retaining only a specified number of dofs by partitioning the state vectors at the collocation points into active dofs and deleted dofs, the transformation matrices at the collocation points can be obtained as

$$\begin{aligned}\{p(t,\varsigma)\} &= \left[\widetilde{\Phi}_f(\varsigma)\right]\left[\widetilde{\Phi}_r^g(\varsigma)\right]\{p_r(t,\varsigma)\} = [T_f(\varsigma)]\{p_r(t,\varsigma)\},\\ \{u(t,\varsigma)\} &= \left[\widetilde{\Phi}_s(\varsigma)\right]\left[\widetilde{\Phi}_o^g(\varsigma)\right]\{u_o(t,\varsigma)\} = [T_s(\varsigma)]\{u_o(t,\varsigma)\}.\end{aligned} \tag{15}$$

Using the transformation matrices, the reduced stochastic FSI model at the collocation points can be obtained as

$$\begin{aligned}&\begin{bmatrix} [M_o(\varsigma)] & [0] & [0] \\ -(\rho(\varsigma)c(\varsigma))^2[A_{\mathrm{ro}}(\varsigma)^T]^a & [G_r(\varsigma)]^a & [0] \\ (\rho(\varsigma)c(\varsigma))^2[A_{\mathrm{ro}}(\varsigma)^T]^b & [0] & [G_r(\varsigma)]^b \end{bmatrix}\begin{Bmatrix} \{\ddot{u}_o(t,\varsigma)\} \\ \{\ddot{p}_r(t,\varsigma)\}^a \\ \{\ddot{p}_r(t,\varsigma)\}^b \end{Bmatrix}\\ &+\begin{bmatrix} [K_o(\varsigma)] & [A_{\mathrm{or}}(\varsigma)]^a & -[A_{\mathrm{or}}(\varsigma)]^b \\ [0] & [H_r(\varsigma)]^a & [0] \\ [0] & [0] & [H_r(\varsigma)]^b \end{bmatrix}\begin{Bmatrix} \{u_o(t,\varsigma)\} \\ \{p_r(t,\varsigma)\}^a \\ \{p_r(t,\varsigma)\}^b \end{Bmatrix} = \begin{Bmatrix} \{0\} \\ \{0\} \\ \{0\} \end{Bmatrix}.\end{aligned} \tag{16}$$

Equation (16) yields the gyroscopic eigenvalue problem of the stochastic reduced system. In the modal domain, Eq. (16) can be rewritten as

$$\begin{aligned}&\begin{bmatrix} [m_o(\varsigma)] & [0] & [0] \\ -(\rho(\varsigma)c(\varsigma))^2[C_{\mathrm{ro}}(\varsigma)^T]^a & [h_r(\varsigma)]^a & [0] \\ (\rho(\varsigma)c(\varsigma))^2[C_{\mathrm{ro}}(\varsigma)^T]^b & [0] & [g_r(\varsigma)]^b \end{bmatrix}\begin{Bmatrix} \{\ddot{u}_o(t,\varsigma)\} \\ \{\ddot{p}_r(t,\varsigma)\}^a \\ \{\ddot{p}_r(t,\varsigma)\}^b \end{Bmatrix}\\ &+\begin{bmatrix} [k_o(\varsigma)] & [C_{\mathrm{or}}(\varsigma)]^a & -[C_{\mathrm{or}}(\varsigma)]^b \\ [0] & [h_r(\varsigma)]^a & [0] \\ [0] & [0] & [h_r(\varsigma)]^b \end{bmatrix}\begin{Bmatrix} \{u_o(t,\varsigma)\} \\ \{p_r(t,\varsigma)\}^a \\ \{p_r(t,\varsigma)\}^b \end{Bmatrix} = \begin{Bmatrix} \{0\} \\ \{0\} \\ \{0\} \end{Bmatrix},\end{aligned} \tag{17}$$

and has to be solved to obtain the modal characteristics at the collocation points. The corresponding spectral representation of the desired random coupled

eigenvalue output can be obtained using the procedure explained in Sect. 2.3 and the statistics of the same can be evaluated.

3 FE Modelling

To demonstrate the proposed methodology described in Sect. 2, the FSI system shown in Fig. 1 with the system parameters described in Ref. [4] has been considered here. The uncoupled disc and cavity are modelled in COMSOL with appropriate boundary conditions. The disc and the cavity are discretized using 296 edge elements, 640 hexahedral (bricks) elements, 1,424 quadrilateral elements and 16 vertex elements with total dofs of 23,616 and 7, 872, respectively. The dofs at each node for the disc correspond to the displacements along the Cartesian coordinates and denoted by *u, v and w* while for the cavity, the dof at each node represents the fluid pressure and is denoted by p. The meshed geometries of the cavity and the disc are shown in Figs. 2 and 3. The radial, the circumferential and the axial direction are consisting of 41, 64 and 3 nodes, respectively.

Interfacing algorithms have been used to extract the uncoupled deterministic system matrices $[G], [H]$ and $[M], [K]$ from both the FE models. The coupled FSI

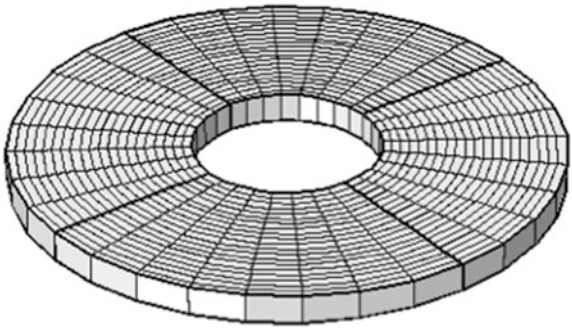

Fig. 2 Meshed geometry for the upper cavity

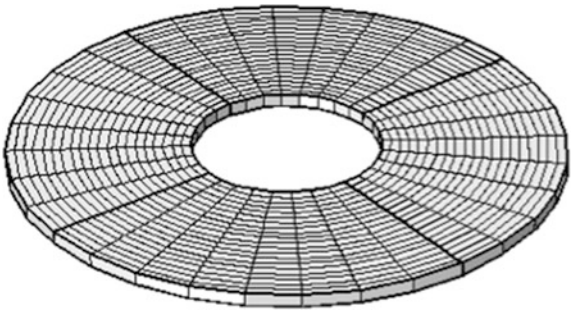

Fig. 3 Meshed geometry for the disc

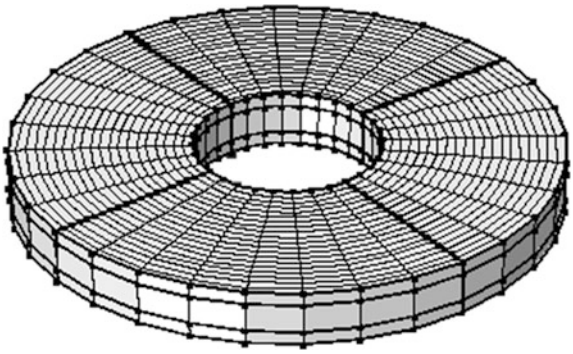

Fig. 4 Meshed geometry for the coupled FSI model

system also has been modelled to extract the structural-acoustic coupling matrix of the boundary surface areas $[A]$. The same FE discretization of the uncoupled models (see Figs. 2 and 3) is adopted for the coupled FSI model as well and is shown in Fig. 4.

4 Results and Discussions

As a first step, deterministic eigenvalue analysis has been carried out to get the in vacuo structural modes and rigid wall acoustic modes using the uncoupled system matrices. Then, the uncoupled system matrices and the coupling coefficient matrix in the modal domain have been evaluated by retaining only the dominant uncoupled modes. Further, the coupled eigenvalue analysis of the full FSI model has been carried out in the modal domain using Eq. (6).

Next, the reduced uncoupled system matrices and the coupling coefficient matrix have been obtained by retaining only the active dofs, along with the dominant modes. As in full system, the reduced uncoupled system matrices and the coupling coefficient matrix in the modal domain have been evaluated by performing the reduced uncoupled eigenvalue analysis. Further, the coupled eigenvalue analysis of the reduced FSI model has been carried out in the modal domain using Eq. (11). In order to show the computational efficiency of the SEREP model, two case studies have been performed based on the number of dominant modes.

4.1 Case 1

In this study, for the full system, first 3000 in vacuo disc modes, first 2000 rigid wall acoustic modes for each cavity have been considered for the coupled eigenvalue analysis. As a result, the system matrices in the modal domain has the size of 7000×7000. It is worth noting here that the full system has 39,360 dofs.

Table 1 Comparison of coupled frequencies of the reduced system with the full system for the case 1

Modes	Full FSI model (Hz)	SEREP model (Hz)	% of error
(1, 0, 0)	408.7221	408.7360	0.0034
(2, 0, 0)	781.2173	781.5462	0.0421
(1, 0)	916.9915	918.1361	0.1248
(0, 1)	927.2655	928.8834	0.1745
(2, 0)	1052.2	1053.6	0.1331
(3, 0, 0)	1117.5	1117.6	0.0089
(4, 0, 0)	1129.6	1129.8	0.0177
(5, 0, 0)	1421.3	1421.4	0.0070
(3, 0)	1633.6	1636.2	0.1592
(4, 0)	2633.6	2633.6	0

Next for the reduced system, the uncoupled system matrices for the disc and the cavity are obtained by arbitrarily choosing 100 dofs, first 100 in vacuo modes and 80 dofs, first 80 rigid wall modes for each cavity, respectively. Hence, the size of the system matrices is 260×260. The results for the first five acoustic-dominated modes and the disc-dominated modes of both the full and the reduced systems are given in Table 1.

As in Table 1, the agreement between the SEREP systems with the full system seems to be good. The computational time taken for the full system is around 48 min, whereas the time taken for the SEREP system is around 0.7 s. Compared to full system, the computational time has been reduced by 99.97%.

4.2 Case 2

This study has been performed by keeping first 50 in vacuo disc modes, first 50 rigid wall acoustic modes for each cavity for both the full and the reduced systems. As a result, the system matrices in the modal domain for both the systems have the size of 150×150. Here, the reduced uncoupled system matrices are obtained by considering 50 arbitrary dofs for both the disc and the cavity. The results for coupled eigenvalue analysis of both the full and the reduced systems are given in Table 2.

There is an exact match between the SEREP and the full system frequencies for most of the modes as shown in Table 2. The computational time taken for the full system is around 13 s, whereas the time taken for the SEREP system is around 0.4 s. Compared to full system, the computational time has been reduced by 96.92% with very high accuracy. It is also important to note here that the accuracy of this case study can be improved by increasing the number of active dofs.

Table 2 Comparison of coupled frequencies of the reduced system with the full system for the case 2

Modes	Full FSI model (Hz)	SEREP model (Hz)	% of error
(1, 0, 0)	408.7452	408.4248	0.0784
(2, 0, 0)	781.2618	779.8770	0.1773
(1, 0)	918.4455	918.4402	0.0006
(0, 1)	929.0226	929.0226	0
(2, 0)	1054.1	1054.2	0.0095
(3, 0, 0)	1117.6	1117.6	0
(4, 0, 0)	1129.9	1130.3	0.0354
(5, 0, 0)	1421.5	1421.5	0
(3, 0)	1634.8	1634.8	0
(4, 0)	2633.3	2633.3	0

Further owing to the system randomness, the analysis will be extended to stochastic domain and the analysis of obtaining the statistics of the modal characteristics is currently being studied.

5 Conclusions

In the present work, the PCE-based SEREP formulation has been developed for a dynamic FSI system. By means of the interfacing algorithms, the FE modelling of the uncoupled systems has been carried out using COMSOL. Subsequently, the FE system matrices of the uncoupled system have been imported from the commercial software environment and the modal characteristics are obtained by carrying out the coupled eigenvalue analysis. Two case studies have been carried out based on the number of dominant modes used for the analysis. From these two case studies, it is observed that the computational complexities associated with the full eigenvalue problem have been reduced significantly by SEREP reduction strategy. The case study with equal number of dominant modes in both full and the reduced systems seems to be more accurate than the other study in which the number of dominant modes is unequal. For the purpose of brevity, the article reports the modal characteristics of the deterministic model only. However, using the proposed PCE-based SEREP technique, the statistics of the modal characteristics can be obtained easily.

References

1. Dowell, E. H., Gorman, G. F., & Smith, D. A. (1977). Acoustoleasticty: General theory, acoustic natural modes and forced response to sinusoidal excitation including comparisons with experiment. *Journal of Sound and Vibration, 52*(4), 519–542.
2. Ghosh, D., & Ghanem, R. (2011). An iterative-subspace based approach to the random eigenvalue problem of systems with clustered spectrum. *International Journal of Numerical Methods in Engineering, 91*(4), 378–396.
3. Avitabile, P., Callahan, J., & Pan, E. R. (1989). Effects of various model reduction techniques on computed system response. In *Proceedings of the Seventh International Modal Analysis Conference* (pp. 1109–1115), Las Vegas, Nevada.
4. Remigius, W. D., Hridya, P. L., Jainendra, K. D., Siddhesh, M. G., Gupta, S., & Sarkar, S. (2016). Stochastic reduced order modelling of a fluid structure interaction system. *Procedia Engineering, 144,* 1213–1219.
5. Nefske, D. J., Wolf, J. A., & Howell, L. J. (1982). Structural-acoustic finite element analysis of the automobile passenger compartment: a review of current practice. *Journal of Sound and Vibration, 80*(2), 247–266.
6. Kang, N., & Raman, A. (2004). Aeroelastic flutter mechanisms of a flexible disk rotating in an enclosed compressible fluid. *Journal of Applied Mechanics, 71*(1), 120–130.
7. Avitabile, P. (2005). Model reduction and model expansion and their applications: Part-1, theory. In *Proceedings of the 23rd International Modal Analysis Conference*, Orlando, FL, US.

A Simple NURBS Finite Element for 2D Sloshing Analysis

Mrityunjoy Mandal and Shaikh Jahangir Hossain

Abstract A simple and accurate Non-Uniform Rational B-Spline (NURBS) based Finite Element (FE) is proposed for examining the dynamic characteristics of a partially liquid-filled rigid container. The present NURBS-FE is founded on a variational problem that arises from small amplitude sloshing of incompressible and inviscid liquid where the flow field is assumed to be irrotational. The superiority of C^k-NURBS-based FE over conventional C^0-FE in terms of accuracy and robustness is witnessed through solving a set of numerical problems.

Keywords Rigid container · Sloshing · FE analysis · Isogeometric analysis NURBS · Degree of the basis function · Frequency · Free surface

1 Introduction

Liquid sloshing in a container due to external disturbance is of major concern in many engineering fields. The motion of liquid inside a partially filled container during sloshing creates significant changes in the hydrodynamic forces. This abrupt change of hydrodynamic force often causes structural damage and may destabilize the vehicle that carries the container. Besides the safety issues, moving liquid container gets severely affected by sloshing, particularly when the liquid is of reactive in nature. Thus, it becomes important to have the comprehensive knowledge about the slosh dynamics before the design of liquid container. Significant amount of research efforts have been made over last few decades comprising of analytical [1, 2, 7, 11, 13], numerical [3–6, 8, 10], and experimental methods [1, 3, 9]. These studies reveal that the incompressibility of liquid along with the presence

M. Mandal · S. J. Hossain (✉)
Department of Civil Engineering, Indian Institute of Technology Kharagpur, Kharagpur 721302, India
e-mail: sjh@civil.iitkgp.ernet.in

M. Mandal
e-mail: mritce@iitkgp.ac.in

A. Rama Mohan Rao and K. Ramanjaneyulu (eds.), *Recent Advances in Structural Engineering, Volume 1*, Lecture Notes in Civil Engineering 11,
https://doi.org/10.1007/978-981-13-0362-3_46

of free surface place an intricate mathematical problem, because the time varying position of free surface cannot be known a priori. Analytical methods are mainly limited to the linearized dynamic boundary conditions [1, 2, 11, 13]. In few cases, the perturbation methods are applied where the weakly nonlinear dynamic boundary condition is considered [13]. However, in almost all situations, the considered container shapes are kept simple. In the numerical methods, i.e., based on Finite Difference Method (FDM) [6], Boundary Element Method (BEM) [8, 10], and Finite Element Method (FEM) [3–5], these limitations are partially removed. In FEM, it is a common practice to employ the same function space for approximating both the geometry and fields, i.e., isoparametric elements. This isoparametric FEM has become popular due to its simplicity. On the other hand, the generated mesh, in this way, only can approximate the geometry and the presence of C^0 connections introduces non-smoothness in the geometry which in turn affects the performance of the model, i.e., it delays the convergence rate. Again, it is extremely difficult to accommodate the incompressibility satisfying approximation function space in the aforementioned numerical methods. These necessitate a postprocessing step to approximately recover the dependent fields. The violation of mass conservation in velocity potential based model occurs due to such postprocess step involved in recovering the velocity components.

In recent days, the NURBS-based finite element or the *Isogeometric Analysis* (IGA) has emerged as a viable alternative to the conventional C^0-based FEM. In IGA, same function spaces are used for approximating both the geometry and the fields. However, unlike the isoparametric FEM, the IGA function space is capable of representing the exact geometry. Moreover, the enrichment of the approximation space can be made through *h*-refinement, *p*-refinement, and *k*-refinement.

In this paper, we present the IGA-based analysis method for linear slosh dynamics of a partially liquid-filled container of various shapes. The variational problem associated with the slosh dynamics is given in Sect. 2. In Sect. 3, we present numerical results highlighting various features of IGA.

2 Mathematical Formulation

The initial-boundary value problem associated with the sloshing of liquid in a partially filled container is presented in this section. First, we start with the continuous problem where we assume the Helmholtz type orthogonal split of the velocity field. Thereafter, we use the incompressibility condition along with the irrotational flow constraint which in turn yields the modified momentum balance involving *Bernoulli* pressure, velocity potential, and the potential of the existing body force. The free surface dynamic boundary condition is then identified directly from the modified momentum balance through which the velocity potential and the free surface displacement interact. On the other hand, the conservation of mass or the continuity equation defines the governing equation as the Laplacian of the velocity potential. These define the continuous problem which can be treated as a

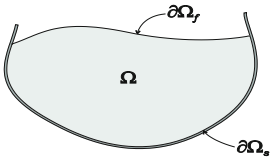

Fig. 1 Representation of fluid domain

Neumann type problem with time varying data. However, for present analysis, we use an equivalent variational problem which is presented after the continuous problem. Subsequently, we discuss the basic ingredients related to NURBS-based FEM.

We use a two-dimensional bounded domain $\Omega \subset \Re^2$ with the boundary $\partial\Omega$ for representing the fluid domain. Further we assume $\partial\Omega = \partial\Omega_{\mathrm{f}} \cup \partial\Omega_{\mathrm{s}}$ with $\partial\Omega_{\mathrm{f}} \cap \partial\Omega_{\mathrm{s}} = \emptyset$ where $\partial\Omega_{\mathrm{f}}$ represents the free surface and $\partial\Omega_{\mathrm{s}}$ is the interface between the fluid and the rigid container. This is shown in Fig. 1. The components of velocity field at a generic point $(x, y) \in \Omega$ are denoted by (u, v).

2.1 Continuous Problem

For an incompressible fluid, the continuity equation and the momentum equation in the Eulerian description are given by

$$\operatorname{div} \mathbf{v} = 0 \text{ in } \Omega \tag{1}$$

$$\mathbf{v}_t + (\operatorname{grad} \mathbf{v})\mathbf{v} + \frac{1}{\rho}\operatorname{grad} p + \frac{1}{R_{\mathrm{e}}}\operatorname{curl}(\operatorname{curl} \mathbf{v}) = f \tag{2}$$

For irrotational flow, i.e., $\operatorname{curl} \mathbf{v} = 0$ in Ω, one obtains a unique representation the velocity field $\mathbf{v} = -\operatorname{grad} \varphi$ in Ω where φ is the so-called velocity potential. In light of these, the momentum balance equation Eq. (2) takes the following form:

$$\operatorname{grad}\left(-\varphi_t + \frac{p}{\rho} + \frac{1}{2}\|\operatorname{grad} \varphi\|^2 - gZ\right) = 0 \text{ in } \Omega \tag{3}$$

The dynamic boundary condition can be identified by applying Eq. (3) at the free surface. Neglecting the nonlinear term the dynamic boundary condition can be written as

$$\partial_n \varphi = \frac{1}{g}\varphi_{\mathrm{tt}} \quad \text{on } \partial\Omega_{\mathrm{f}} \tag{4}$$

where $\partial_n \varphi$ refers the partial derivative of the potential function φ in the normal direction and this yields the normal velocity at the boundary.

Therefore, we define the continuous problem as

Problem(P) Find $\varphi \in H^2(\Omega) \times]0,T[$ that satisfies

$$\left.\begin{array}{cc} \nabla^2\varphi = 0 & \text{in}\,\Omega \\ \partial_n\varphi + v_n^s = 0 & \text{on}\,\partial\Omega_s \\ \partial_n\varphi = \frac{1}{g}\varphi_{tt} & \text{on}\,\partial\Omega_f \end{array}\right\} \tag{5}$$

The Variational Problem

Here, we start with the following variational problem that is equivalent to Eq. (5)

Problem(Q) Find $\varphi \in \mathcal{U} \times]0,T[\subset H^1(\Omega) \times]0,T[$, such that

$$a(\varphi,\delta\varphi) = l(\delta\varphi) \forall\, \delta\varphi \in \mathcal{U} \times]0,T[\subset H^1(\Omega) \times]0,T[\tag{6}$$

Here $a(\cdot,\cdot)$ and $l(\cdot)$ are the bilinear and the linear forms, which are respectively defined as

$$\left.\begin{array}{l} a(\varphi,\delta\varphi) := \int\limits_{\Omega} \nabla\delta\varphi \cdot \nabla\varphi \,\mathrm{d}\Omega \\ l(\delta\varphi) := -\frac{1}{g}\int\limits_{\Omega_f} \delta\varphi\, \varphi_{,tt}\mathrm{d}s \end{array}\right\} \tag{7}$$

It may be verified that the Euler–Lagrange's equations associated with Eq. (5) are none other than those given in Eq. (5).

In this paper, we study the modal analysis using Eq. (5) where we assume a product decomposition $\varphi(x,y,t) = \exp(i\omega t)\Phi(x,y)$. Using this, we obtain the following Eigen value problem:

Problem($\mathbf{Q^h}$) Find $\varphi^h \in \mathcal{U}^h \subset \mathcal{U}$, such that

$$[a(\varphi^h,\delta\varphi^h) = b(\varphi^h,\delta\varphi^h) \quad \forall\, \delta\varphi^h \in \mathcal{U}^h] \tag{8}$$

where the bilinear form $b(\varphi^h,\delta\varphi^h)$ is defined as

$$b(\varphi^h,\delta\varphi^h) := \frac{\omega^2}{g}\int\limits_{\Omega_f} \delta\varphi^h\, \varphi^h \,\mathrm{d}s \tag{9}$$

2.1.1 NURBS-Based Finite Element Analysis

Let $\{N_i\}_1^{n_{\text{patch}}}$ be the set of NURBS basis function defined over a patch that contain n_{patch} number of control points. These basis functions are defined in terms of spline basis. The detailed procedure for constructing the NURBS basis functions is given

in Ref. [12]. The 1D B-spline basis functions on a set of knot points $\Xi = \{\xi_1, \xi_2, \ldots, \xi_{n+p+1}\}$ are computed based on Cox-de Boor recursive formula as

$$N_{i,p}(\xi) = \frac{\xi - \xi_i}{\xi_{i+p} - \xi_i} N_{i,p-1}(\xi) + \frac{\xi_{i+p+1} - \xi}{\xi_{i+p+1} - \xi_{i+1}} N_{i+1,p-1}(\xi) \tag{10}$$

for $p > 0$ and

$$N_{i,0}(\xi) = \left\{ \begin{array}{ll} 1 & \text{if } \xi_i \leq \xi \leq \xi_{i+1} \\ 0 & \text{otherwise} \end{array} \right\} \tag{11}$$

for $p = 0$.

With the aid of the NURBS basis, the velocity potential and its variation are approximated as

$$\varphi^h = \sum_{i=1}^{N_{\text{patch}}} N_i \, \varphi^h{}_i, \quad \text{and} \quad \delta\varphi^h = \sum_{i=1}^{N_{\text{patch}}} N_i \, \delta\varphi^h{}_i \tag{12}$$

where Φ_i represents the control point velocity potential and should not be confused with the nodal velocity potential in C^0-based FE.

The discrete algebraic Eigenvalue problem is generated upon using the approximation Eq. (12) in the variational statement given in Eq. (8) and is written as

$$\mathbf{K}\Psi = \lambda \mathbf{M}\Psi \quad \text{where,} \quad \lambda = \omega^2 \tag{13}$$

where $\mathbf{K}$, $\mathbf{M}$, and ω refers to the reduced stiffness matrix, reduced mass matrix, and natural frequency, respectively.

It may be noted at this point that this stiffness matrix is rank deficient in the absence of Dirichlet data. In the present study, we use the following averaged Dirichlet condition to make Eq. (13) meaningful

$$\int_{\Omega_f} \varphi^h \, \mathrm{d}s = 0 \tag{14}$$

3 Results and Discussions

Numerical results are presented in this section to evaluate the performance of developed NURBS-based analysis procedure. First, we consider liquid in a partially filled rigid 2D rectangular container. Next, we present natural slosh frequencies for trapezoidal shaped container.

3.1 Rectangular Container

A rigid container of width 'w' and water depth 'h' is considered in this problem. The initial free surface is assumed to be horizontal. Separate codes are developed based on both the isoparametric FEM- and NURBS-based isogeometric FEM. The geometric and material data assumed in this example problem are given in Table 1.

The mesh sizes used for the convergence study are 4 × 4, 8 × 8, 16 × 16, and 32 × 32.

The computed slosh frequencies are then plotted along with the known analytical results Ref. [13]. Here, only 16 × 16 mesh size is considered for the plotting. From Figs. 2 and 3, it is found that the computed slosh frequencies are in excellent agreement with the frequencies obtained using analytical technique Ref. [13]. The figures also indicate that higher degree of the basis function produces higher convergence rate irrespective of the dimension of the container. It is also noted that the numerical results for C^0 basis converged with the analytical results for lower modes and the rate of convergence decreasing for higher modes. But for higher

Table 1 Geometric and material parameters

Geometric data	Material data
w = 2 m, 2 m	ρ = 1.00 kg/m^3
h = 2 m, 1 m	g = 9.81 kN/m^2

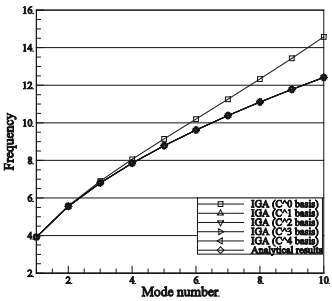

Fig. 2 Comparison of natural frequencies using a 16 × 16 mesh for 2 m × 2 m container

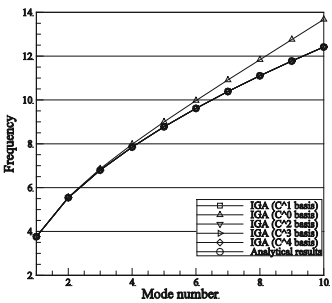

Fig. 3 Comparison of natural frequencies using a 16 × 16 mesh for 2 m × 1 m container

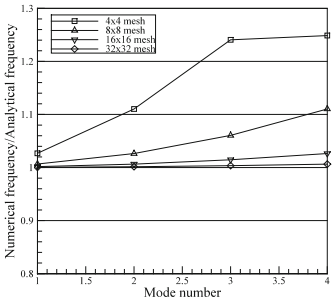

Fig. 4 Convergence study of natural frequencies for various mesh sizes for FEM (biquadratic C^0) basis

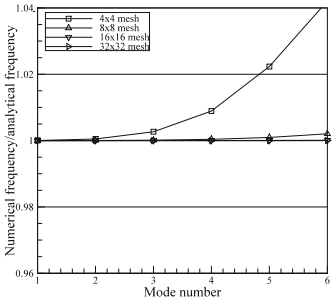

Fig. 5 Convergence study of natural frequencies for various mesh sizes for IGA (biquadratic C^1) basis

degree basis functions, the numerical results are in good agreements with the analytical results in all the modes irrespective of the container dimensions. That means higher degrees of basis function provides higher convergence rate for a given mesh.

Convergence behavior of both the FEM (biquadratic C^0) and the IGA (bi-quadratic C^1) based analysis are shown in Figs. 4 and 5. For this purpose, a 2 m $\times$ 2 m container is considered.

Further, it is observed from Figs. 4 and 5 that C^0 type FEM results converge with a slow rate when compared with those obtained from IGA. Thus, even with a coarse mesh IGA-based results become meaningful.

Higher rate of convergence of the IGA-based computed slosh natural frequencies is noted. The slosh natural frequencies obtained from bi-quadratic C^0 FEM are compared with those obtained from biquadratic C^1 IGA and are presented in Figs. 6 and 7.

It may be worthy to note from Table 2 that IGA-based computation outperforms in terms of computation time and complexity. The results reported in Table 2 are obtained from biquadratic C^0 FEM and biquadratic C^1 IGA and are denoted only by FEM and IGA. Here, we choose a 2 m $\times$ 2 m container.

It is also observed from Table 2 that for a given mesh size the Degree Of Freedom (DOF) obtained using FEM is higher than that of IGA. Hence, the CPU time required to solve a problem in FEM is higher than that of IGA. It is important

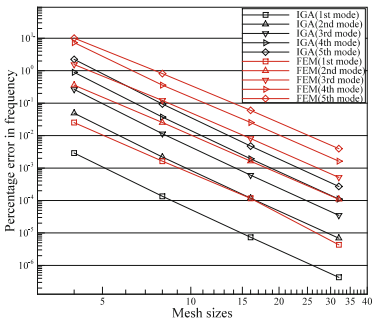

Fig. 6 Comparison of convergence rate of natural frequencies for a 2 m × 2 m container

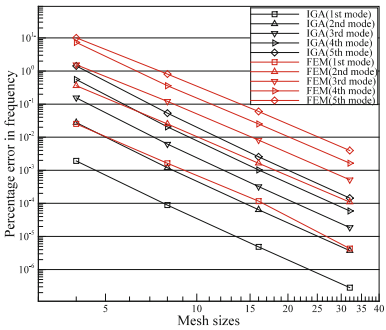

Fig. 7 Comparison of convergence rate of natural frequencies for a 2 m × 1 m container

Table 2 Comparison of computational cost

Mesh size	DOF		CPU time required (s)	
	FEM	IGA	FEM	IGA
4 × 4	81	36	0.109	0.109
8 × 8	289	100	0.172	0.125
16 × 16	1089	324	0.672	0.547
32 × 32	4225	1156	8.906	2.125
64 × 64	16,641	4356	322.797	15.266

to note that the increase of total DOF with the mesh refinement is negligible for the IGA. This makes the IGA attractive when compared with the FEM.

The convergence behavior of the slosh natural frequencies considering higher order basis functions is presented in Figs. 8, 9, 10 and 11. A 2 m × 2 m container is considered for all the cases. The optimal rate of convergence is observed for all IGA-based results.

Insignificant increase of computation time with the increase of polynomial degree may be observed from Table 3. Results presented in Table 3 are generated for a 2 m × 2 m container.

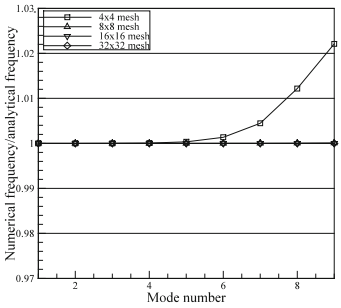

Fig. 8 Convergence study of natural frequencies for various mesh sizes for IGA (bi-cubic C^2) basis function

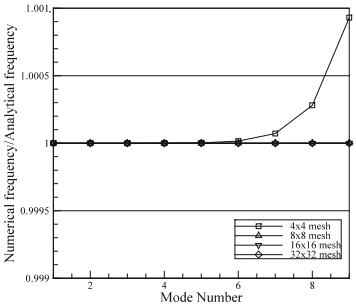

Fig. 9 Convergence study of natural frequencies for various mesh sizes for IGA (bi-quartic C^3) basis function

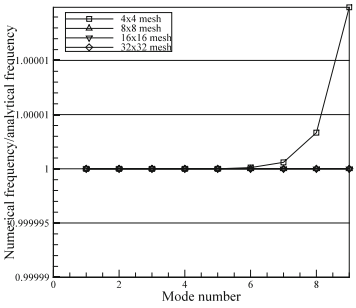

Fig. 10 Convergence study of natural frequencies for various mesh sizes for IGA (bi-quintic C^4) basis function

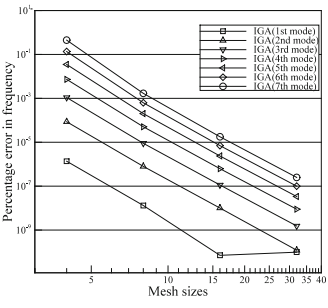

Fig. 11 Convergence rate of natural frequencies for various mesh sizes for IGA (bi-cubic C^2) basis function

Table 3 Computational cost for IGA basis functions

Mesh size	DOF			CPU time required (s)		
	$p = 3\ C^2$	$p = 4\ C^3$	$p = 5\ C^4$	$p = 3\ C^2$	$p = 4\ C^3$	$p = 5\ C^4$
4 × 4	49	64	81	0.125	0.141	0.672
8 × 8	121	144	169	0.234	0.500	2.500
16 × 16	361	400	441	0.969	0.166	10.031
32 × 32	1225	1296	1369	3.906	6.625	40.052
64 × 64	4489	4624	4761	24.484	37.375	185.109

N.B. 'p' represents polynomial degree and it is assumed that 'p' is identical in all direction

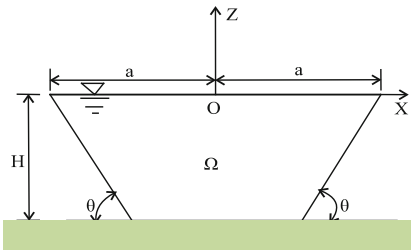

Fig. 12 Problem geometry for trapezoidal container

3.2 *Trapezoidal Container*

A trapezoidal container is considered in this example problem and a schematic diagram is shown in Fig. 12.

The used geometric data and the computed slosh natural frequencies are reported in Table 4. From Table 4, it is observed that the slosh natural frequency of trapezoidal container decreases with the increases of the water depth of the container and the span of the free surface.

Table 4 Geometric data and the corresponding slosh frequencies

Geometric data	Natural slosh frequency (Hz)				
	Mode 1	Mode 2	Mode 3	Mode 4	Mode 5
H = 0.04 m a = 0.1143 m Θ = 30°	1.191	1.933	2.583	3.182	3.681
H = 0.07 m a = 0.166 m Θ = 30°	1.019	1.611	2.174	2.658	3.085
H = 0.1 m a = 0.218 m Θ = 30°	0.895	1.406	1.903	2.317	2.676

4 Conclusions

The slosh natural frequencies of an incompressible fluid in a rigid container are presented in this paper. A NURBS-based FEM or IGA-FEM analysis procedure has been developed for this purpose. The developed NURBS-based FEM is then evaluated through solving a set of numerical example problems. Comparative study on the convergence behavior of the developed IGA elements is made. It is seen that the IGA elements outperform the conventional C^0 finite elements.

The developed IGA elements are then used to study the slosh dynamics of an incompressible liquid in rigid non-rectangular containers. The developed elements show high convergence rate in computing natural slosh frequencies when compared with the conventional C^0-based finite elements. Unlike the conventional FE, the developed IGA-FE requires insignificant increase of computer resources, i.e., memory, for *hp*-refinement.

Study on slosh dynamics in a flexible container is under progress.

References

1. Aslam, M., Godden, W. G., & Scanlinell, D. T. (1979). Earthquake sloshing in annular and cylindrical tanks. *Journal of Engineering and Mechanics Division, 105,* 371–389.
2. Bauer, H. F., & Eidel, W. (1999). Frictionless liquid sloshing in circular cylindrical container configurations. *Journal of Aerospace Science and Technology, 3,* 301–311.
3. Okamoto, T., & Kawahara, M. (1990). Two-dimensional sloshing analysis by Lagrangian finite element method. *International Journal for Numerical Methods in Fluids, 11*(5), 453–477.
4. Wu, G. X., & Taylor, R. E. (1994). Finite element analysis of two dimensional nonlinear transient water waves. *Journal of Applied Ocean Research, 16,* 363–372.
5. Tokuda, N., Sakurai, T., & Teraoku, T. (1995). Sloshing analysis method using existing FEM structural analysis code. *Journal of Pressure Vessel Technology, 117*(3), 268–272.
6. Chen, W., Haroun, M. A., & Liu, F. (1996). Large amplitude liquid sloshing in seismically excited tanks. *Journal of Scientific & Industrial Research, 25,* 653–669.
7. Solaas, F., & Faltinsen, O. M. (1997). Combined numerical and analytical solution for sloshing in two-dimensional tanks of general shape. *Journal of Ship Research, 41*(2), 118–129.
8. Gedikli, A., & Ergüven, M. E. (1999). Seismic analysis of a liquid storage tank with a baffle. *Journal of Sound and Vibration, 223*(1), 141–155.
9. Saeki, S., Madarame, H., & Okamoto, K. (1999). Growth mechanism of self-induced sloshing caused by horizontal plane jet. In *Proceedings of the 1999 3rd ASME/JSME Joint Fluids Engineering Conference, FEDSM* (pp. 18–23), Vol. 99.
10. Dutta, S., & Laha, M. K. (2000). Analysis of the small amplitude sloshing of a liquid in a rigid container of arbitrary shape using a low-order boundary element method. *International Journal for Numerical Methods in Engineering, 47,* 1633–1648.
11. Cho, J. R., Lee, H. W., & Kim, K. W. (2002). Free vibration analysis of baffled liquid-storage tanks by the structural-acoustic finite element formulation. *Journal of Sound and Vibration, 258,* 847–866.
12. Cottrell, J. A., Hughes, T. J. R., & Bazilevs, Y. (2009). *Isogeometric analysis toward integration of CAD and FEA*. United Kingdom: Wiley Publication.
13. Ibrahim, R. A. (2005). *Liquid sloshing dynamics theory and applications*. New York: Cambridge University Press.

Numerical Study on Cyclic Response of Self-centering Steel Buckling-Restrained Braces

Ahmad Fayeq Ghowsi, Amanollah Faqiri and Dipti Ranjan Sahoo

Abstract A self-centering buckling-restrained brace (SC-BRB) is capable of dissipating the seismic energy through metallic hysteresis under cyclic axial loading without any instability. The use of shape memory alloy (SMA) rods along with steel BRB core helps in controlling the residual drift response of the braced frames under seismic loading. This paper is focused on the evaluation of the optimum length of SMA rods required to achieve the desired energy dissipation with the effectively controlling the residual deformation. A numerical study has been conducted for a SC-BRB by varying the SMA length in the range of 0–125% of the BRB core lengths. The SC-BRB has been modelled and analysed using a computer software Opensees to assess the self-centering ability, hysteretic response, energy dissipation and ductility capacity. Results show that SC-BRBs with the higher SMA length ratio exhibited more stable energy dissipation.

Keywords Buckling-restrained braces · Self-centering system · Hysteretic energy Numerical modelling · Shape memory alloy

1 Introduction

Steel buckling-restrained braces (BRBs) are capable of nearly symmetric hysteretic response due to the yielding in both tension and compression without any premature instability under the cyclic axial loading [1]. A BRB consists of two basic

A. F. Ghowsi · D. R. Sahoo (✉)
Department of Civil Engineering, Indian Institute of Technology Delhi, New Delhi 110016, India
e-mail: drsahoo@civil.iitd.ac.in

A. F. Ghowsi
e-mail: faieq.ghowsi@gmail.com

A. Faqiri
Department of Civil Engineering, Herat University, Herat 3001, Afghanistan
e-mail: amanollahfaqiri@gmail.com

A. Rama Mohan Rao and K. Ramanjaneyulu (eds.), *Recent Advances in Structural Engineering, Volume 1*, Lecture Notes in Civil Engineering 11,
https://doi.org/10.1007/978-981-13-0362-3_47

components: (i) a steel core element that carries the brace axial force, and (ii) an external restraining element that prevents the core from buckling in compression. The restraining element is typically a concrete (or mortar) filled steel tube without any bonding with the steel core. The excellent energy dissipation potential of BRBs helps the buckling-restrained braced frames (BRBFs) to resist the seismic loading with limited damages in the frame members. However, BRBFs show the relatively higher post-earthquake residual drift response resulting in the costly repair and high downtime [2, 3].

A self-centering BRB (SC-BRB) has the ability to dissipate energy and also return to their original position after ground shaking [4, 5]. SC-BRBs exhibited the excellent hysteretic performance resulting in the significant reduction in residual drift response under the seismic loading. The length of SMA rods in SC-BRBs plays an important role in exhibiting the self-centering capability. One of the possible ways to enhance the high ductility and hysteretic energy dissipation of SC-BRBs with the minimum residual drift response is to optimise the length and strength ratio of the BRB cores and the SMA rods [6, 7].

The present study is focused on predicting the hysteretic response of SC-BRBs by varying the parameters of BRB core segments and SMA rods for a constant yielding cross-sectional area. The SC-BRBs are modelled and analysed under the reversed cyclic loading using computer software Opensees [8]. The main parameters investigated are the hysteretic response, backbone curves and hysteretic energy factors.

2 Numerical Modelling

A SC-BRB specimen tested by Mliller et al. [7] has been considered for the numerical investigation in this study. Figure 1 shows the longitudinal and cross-sectional views of the SC-BRB assembly. The end segments of BRB are intentionally made stronger to remain elastic under the expected range of cyclic loading. For SC-BRB, the size of BRB end segments at both ends may be different. This is because of the connection requirements of the inner and outer tubes. The arrangements of these tubes and SMA rods are made in such a way that the SMA rods are subjected to tension forces in either direction of cyclic loading. Both these tubes are attached to the BRB end segments only at one end alternatively, whereas the other ends are supported by the movable plates through bearing action. SMA rods are connected to these movable plates through bolted connections.

Figure 2 shows the numerical modelling of SC-BRB assembly in computer software Opensees [8]. Various elements of SC-BRB are modelled as link elements. The element connecting nodes 1–10 represent BRB, with a total length of 3.2 m. The element connecting nodes 1–5 and 6–10 represent the elastic portion of BRB including the transition zones with total length of 0.93 and 0.48 m, respectively. The element of 5–6 represents the BRB core with total length of 1.83 m.

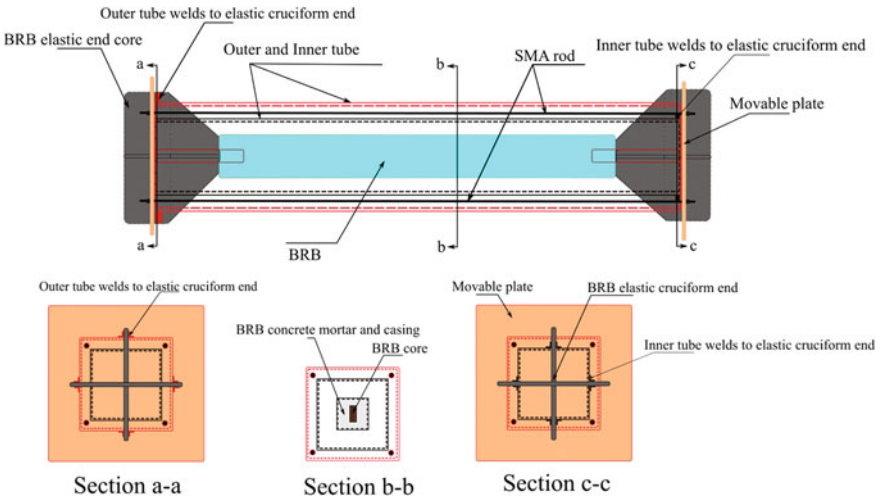

Fig. 1 Longitudinal and cross-sectional views of SC-BRB specimen

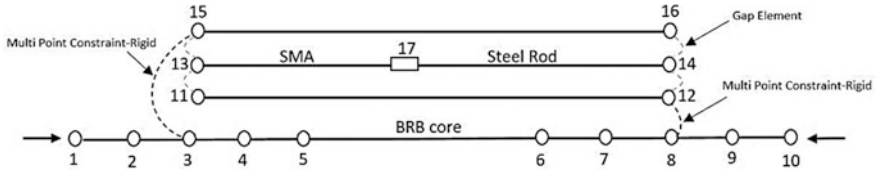

Fig. 2 Numerical modelling of SC-BRB assembly

The elements connecting 11–12 and 15–16 represent with the same total length of 2.58 m inner and outer tube, respectively. The outer and inner tubes are connected to the BRB's elastic portion using the multi-point constraint-rigid links of 8–12 and 3–15. The outer and inner tubes are connected to the elastic portion of BRB only from one end of tubes. The other ends of tubes are supported on each other.

Let SMA rod be the link 13–17 that represents the four numbers of SMA rods of 22 mm diameter and total length of 1.07 m and placed between the outer and inner tubes. These tubes are connected to two elastic movable plates over the elastic zones of BRB ends (Fig. 2). The SMA bar is under pre-tension while the SC-BRB is under zero load. The SMA wire is expected to be under tension when BRB core under some shortening or elongation. The preloading in SMA rods are carried by these tubes and hence, the load-resisting capacity of BRBs is not altered.

The link 17–14 has been provided as a rigid link to limit the length of SMA within SC-BRB. The rigid link is modelled by assuming their axial stiffness significantly higher than SMA rods. The prestress in SMA rods should also be considered in rigid links. The links 13–15, 13–11, 14–12, and 14–16 in Fig. 2 represent the gap elements to consider the translations of movable plates under axial loading.

While the SC-BRB is at zero position under no loading, the inner and outer tubes are in contact with the movable plates on both sides. Any cyclic loading on BRB cores results in a gap at one end with bearing contact at the other. The gap elements chosen in this numerical modelling are capable of resisting the compression loads without providing any resistance to tension forces.

The rigid links 8–12 and 3–15 are provided to represent the inter-dependency of inner and outer tubes in transferring the cyclic loading to the SMA rods. This means that if the inner tube is connected to the right side of elastic portion of node 8 and the other end of the tube should be free and not connected to any other elements. The outer tube has to be connected to the left end of the elastic portion of BRB at node 3 and not to be connected to the other end.

Since the elements representing the force–displacement behaviour of SMA rods do not exist in Opensees [8] library, a UMAT code has been written in C++ following the recommendations of Taftali [9] and is implemented in the numerical models in this study. The parameters of force–displacement characteristics are modified suitably to match the experiment result [7]. Two main parameters considered are the residual strength and the change in slope in the unloading segments of hysteretic response in martensitic phase of SMA. This slope changes in every cycle with the increasing strain demand on SMA rods.

Figure 3 shows the material model used by Taftali [9] with the inputs as Young's modulus (E_{SMA}), yield stress (F_S^{AS}), austenite slope (R_S), ultimate slope in austenite (R_m) and similar variables for negative loading regions. The same slope in martensitic has been considered under plastic reverse displacement. However, cyclic tests have shown that the unloading slope of SMA keeps changing with the plastic deformations [7]. As shown in Fig. 4, the force–deformation characteristics of SMA rod are modified in this study that represent the residual displacements and varying slope of martensite unloading branch. Thus, the influence of residual strain is considered in this study to compare the numerical results with the past experimental studies.

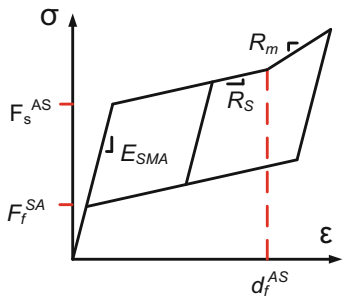

Fig. 3 Material model used by Taftali [9]

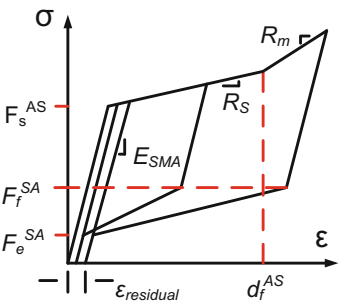

Fig. 4 Modified material model used in this study

3 Validation of Numerical Model

Figure 5a shows the comparison of predicted stress–strain and force–deformation response of SMA coupons with test results. SMA coupons are of 21.6 mm in diameter and of 122 mm in gage length. The numerical models successfully predicted the material response of SMA rods.

Figure 5b shows the comparison of force–strain response of SMA rods used in SC-BRB specimen. The outer and inner tubes have been used over the BRB to keep the SMA rod under and preventing the BRB from SMA pre-tension demand. The movable plates are kept in contact on both ends of outer and inner tubes. The SMA is connected from one to another end, in between outer and inner tubes. The material for outer and inner tubes are selected as in HSS standard section. The same properties of SMAs used in experiment [7] are also considered in this numerical

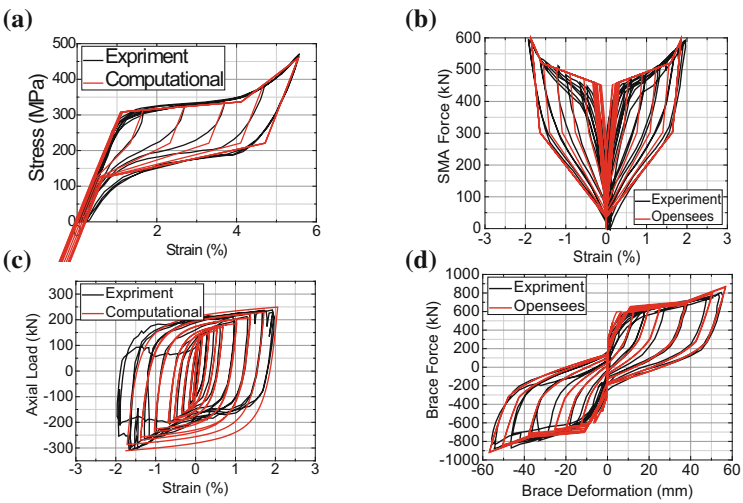

Fig. 5 Validation of numerical models with experimental results **a** SMA coupons, **b** SC-BRB specimens

study. The properties of E_{SMA}, F_s^{AS}, R_s and R_m for SMA are assumed as 28,650 MPa, 308 MPa, 3.3% $E_{SMA,}$ and 20% E_{SMA}, respectively. The results of the numerical study for SMA rods of SC-BRB specimen also matched very well with the experimental results.

The size of BRB core plate in SC-BRB specimen is 12 mm thickness and 36.6 mm width, same as used in the past experimental study [7]. The BRB core plate is modelled as fibre sections using uniaxial material Steel02 elements in Opensees [8] platform. The material yield stress and modulus of elasticity of BRB are 305 MPa and 200 GPa, respectively. To prevent the buckling of BRB core plates under the axial loading, the moment of inertia of fibre sections increased keeping the same cross-section area. A small value of eccentricity has been used in the numerical models to consider the imperfections in BRB core plates. The beam column element has been selected from Opensees library for modelling of BRB end segments. The force–displacement response of BRB of SC-BRB specimen obtained from the numerical models has been compared with the experimental results as shown in Fig. 5c. The numerical model successfully predicted the axial strengths at different plastic deformations and cyclic hardening behaviour in tension.

Since the movable plates of SC-BRB remain in the elastic range as modelled by using gap elements with compression and no tension, there compression hardening parameters of BRB of SC-BRB assembly are noted to be different from the conventional BRB as shown in Fig. 5c. Further, the friction at the interface of the movable plates and the BRB plates, which is not considered in the model, maybe another reason for discrepancy noted in the hysteretic response of BRB.

The numerically predicted hysteretic response of combined assembly of SC-BRB predicted matched very well with the test results as shown in Fig. 5d with less residual strain and good energy dissipation.

4 Preliminary Design of SC-BRB

The design procedure for SC-BRB has been carried out as per the current practice for design of BRBs [9, 10]. The design parameters, i.e. the response modification coefficient R, the deflection amplification factor C_d, and the system overstrength factor Ω_0 for BRBFs are considered from the past study [6]. Elastic properties of SC-BRBs are assumed similar to the BRBs with the corresponding material strengths. The axial strength of SC-BRB is a combination of a BRB core strength and pre-tension in SMA wire. The design axial strength of BRB can be expressed as follows:

$$p_{u-\mathrm{BRB}} = \phi p_{\mathrm{yBRB}} \tag{1}$$

where p_{yBRB} = yield strength of BRB core. The ultimate strength of SC-BRB is given by

$$p_{u-\mathrm{SC-BRB}} = \phi\, p_{\mathrm{yBRB}} + \phi\, p_{i-\mathrm{SMA}} \tag{2}$$

$$p_{u-\mathrm{SC-BRB}} = 0.9F_{\mathrm{ysc}}A_{\mathrm{core}} + 0.9F_{i-\mathrm{SMA}}A_{\mathrm{SMA}} \tag{3}$$

where F_{ysc} = yield strength of steel BRB core, $F_{i\text{-SMA}}$ = initial prestress in the SMA, A_{core} = area of BRB steel core, and A_{SMA} = area of SMA bar. The initial prestress in the SMA should be able to overcome the BRB core yield stress. The following condition has to be met for the adjacent brace strengths based on AISC seismic provision [11].

$$p_{\mathrm{adj-BRB}} = \beta\, \omega\, F_{\mathrm{ysc}}A_{\mathrm{sc}} \leq F_{i-\mathrm{SMA}}A_{\mathrm{SMA}} \tag{4}$$

where β = compression strength factor, and ω = the hardening adjustment factor. Since the material yield stress is assumed to be obtained from the coupon tests, the material overstrength factor (R_y) factor is omitted from the adjusted brace strength equations. The cross-sectional area of BRB can be calculated using the following expression:

$$A_{\mathrm{SC}} = \frac{P_u}{\phi\, F_{\mathrm{ysc}}(1+\beta\omega)} \tag{5}$$

Similarly, the area of SMA area can be found as follows:

$$A_{\mathrm{SMA}} = \frac{\beta\omega F_{\mathrm{ysc}}A_{\mathrm{sc}}}{F_{i-\mathrm{SMA}}} \tag{6}$$

The above equations can be used for the preliminary design. Hence, a detailed study is required to optimise the design procedure for SC-BRB considering the various values of design parameters and relative length/area ratio of BRB and SMA rods.

5 Results and Discussions

Numerical model is validated by comparing the brace force–deformation response and SMA force–strain response measured in the past experiment. In this study, the length of SMA rods is varied in the range of 0–125% of BRB core lengths. Figure 6 shows the comparison of hysteretic response of SC-BRB models. It can be seen that the martensitic effect of SMA is more pronounced if the length of SMA rods is 25% of BRB core length. However, this results in the less energy dissipation though the residual drift response can be controlled effectively. The energy dissipation and equivalent damping potential of all SC-BRB models are also computed for the hysteretic response. The results concluded that the SMA length ratios can significantly influence the hysteretic behaviour of SC-BRBs.

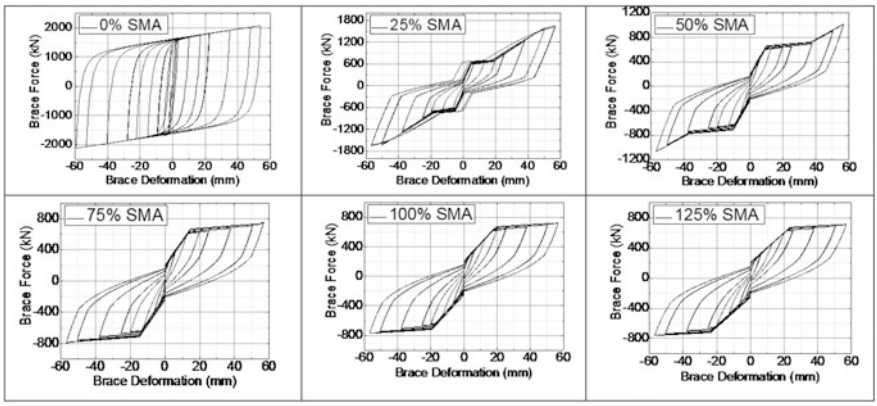

Fig. 6 Hysteretic response of SC-BRB with varying SMA length ratio

Fig. 7 Hysteretic energy dissipation

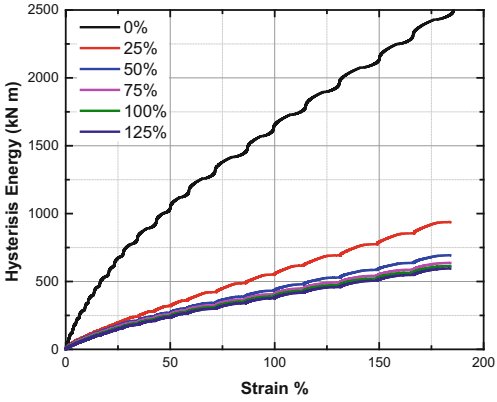

Figure 7 shows the variation of energy dissipation with different values of SMA-to-BRB core ratio. The increase in the SMA length resulted in less energy dissipation. The SC-BRB with 0% of SMA shows the higher energy dissipation because of the rigid link used along with BRB. The higher energy dissipation is noted in SC-BRB with the smaller lengths of SMA rods.

Table 1 shows the maximum ductility values of SC-BRB under varying SMA ratios. The result showed the higher ductility in SC-BRB with 0% of SMA ratio, but no changes are observed in ductility for SMA ratios varying in the range of 25–125%.

Table 1 Variation of maximum displacement ductility with SMA ratio in SC-BRBs

SMA ratio (%)	μm
0	21.32
25	20.35
50	20.35
75	20.35
100	20.35
125	20.35

6 Conclusions

Based on this numerical study, the following conclusions can be drawn from this study:

- The length of SMA rods should not exceed the 50% of BRB core length in order to control the residual drift effectively.
- The optimum range of length ratio can be considered to be in the range of 50–75% for the better energy dissipation and desired residual drift reduction.
- More detailed optimum design is required for cross-section area ratio as well as modification factor, amplification and overstrength factor to be used in the design of SC-BRBs.

References

1. Clark, P., Kasai, K., Aiken, ID., & Kimura, I. (2000). Evaluation of design methodologies for structures incorporating steel unbonded braces for energy dissipation. In *Proceedings, 12th World Conference on Earthquake Engineering*. Upper Hut, New Zealand.
2. Ghowsi, A. F., & Sahoo, D. R. (2015). Fragility assessment of buckling-restrained braced frames under near-field earthquakes. *Steel and Composite Structures, 19*(1), 173–190.
3. Chao, S. H., Karki, N. B., & Sahoo, D. R. (2013). Seismic behavior of steel buildings with hybrid braced frames. *ASCE Journal of Structural Engineering, 139*(6), 1019–1032.
4. Christopoulos, C., Tremblay, R., Kim, H.-J., & Lacerte, M. (2008). Self-centering energy dissipative bracing system for the seismic resistance of structures: Development and validation. *ASCE Journal of Structural Engineering, 134*(1), 96–107.
5. Dolce, M., & Cardone, D. (2006). Theoretical and experimental studies for the application of shape memory alloys in Civil Engineering. *ASME Journal of Engineering Materials Technology, 128*(3), 302–311.
6. Eatherton, M. R., Fahnestock, L. A., & Miller, D. J. (2014). Computational study of self-centering buckling-restrained braced frame seismic performance. *Earthquake Engineering and Structural Dynamics, 43,* 1897–1914.
7. Miller, D. J., Fahnestock, L. A., & Eatherton, M. R. (2012). Development and experimental validation of a nickel-titanium shape memory alloy self-centering buckling-restrained brace. *Engineering Structures, 40,* 288–298.
8. Mazzoni, S., McKenna, F., Scott, M. H., & Fenves, G. L. (2015). *Open system for earthquake engineering simulation user command language manual*. OpenSees Version 2.5.

9. Taftali, B. (2007). Probabilistic seismic demand assessment of steel frames with shape memory alloy connections Ph.D. dissertation. USA: Georgia Institute of Technology.
10. IBC structural seismic design manual. (2012). *Structural Engineers Association of California, and International Code Council*. Sacramento, CA: Structural Engineers Association of California.
11. American Institute of Steel Construction. (2010). *Seismic provisions for structural steel buildings*. Chicago, IL: American Institute of Steel Construction, Inc.

Computational Modelling of Cement Hydration to Evaluate the Mechanical and Transport Properties

B. S. Sindu, S. Radha Meenaloshini and Saptarshi Sasmal

Abstract Concrete is heterogeneous and is not perfectly isotropic. It has many distinct phases which are not homogenously distributed. It also contains a network of capillary pores and grains of unhydrated (crystalline and amorphous) cement. Hydration of cement-based materials is a complex phenomenon. During hydration, many physical and chemical changes take place. The present study deals with the computational modelling of cement hydration. CEMHYD3D has been employed in this study to investigate the hydration behaviour of cement paste. The influence of parameters like water–cement ratio on various transport and mechanical properties during hydration has been investigated. It is significant to mention here that the rate of change in behaviour parameters is not consistent and it greatly depends on the reaction state and activism during a particular time frame. The results obtained from the computational studies are verified with the results obtained from experimental studies. The study would greatly help not only to understand the mechanism of cement and cementitious materials at different time frame during hydration, it also signifies the reaction kinetics and possible states of hydration.

Keywords Micromechanics · Cement hydration · Reaction kinetics
Transport properties

1 Introduction

At macroscopic level, concrete is homogeneous and isotropic and consists of coarse aggregates embedded in cement matrix whereas at microscopic level, concrete is heterogeneous and is not perfectly isotropic. It has many distinct phases which are not homogenously distributed. Apart from that, cement-based materials undergo

B. S. Sindu (✉) · S. Radha Meenaloshini · S. Sasmal
CSIR-Structural Engineering Research Centre, Chennai, India
e-mail: sindu@serc.res.in

B. S. Sindu · S. Sasmal
Academy of Scientific and Innovative Research, New Delhi, India

A. Rama Mohan Rao and K. Ramanjaneyulu (eds.), *Recent Advances in Structural Engineering, Volume 1*, Lecture Notes in Civil Engineering 11,
https://doi.org/10.1007/978-981-13-0362-3_48

many interrelated phenomena, some of which are well understood and others still remain ambiguous. One such phenomenon is the hydration process. Hydration is an exothermic process and it is complex to be described by simple chemical equations.

It is extremely useful, though complicated, to understand the hydration kinetics of cement paste and the mechanism during the hydration process. This understanding would help in developing the new class of cementitious/cement-based materials with desired properties. For the structural/civil engineers, though it is most important to obtain the physical and mechanical properties of concrete after complete hydration, there is a pressing need to understand the science behind it to tailor, to the possible extent, the properties of cement/mortar/concrete at different time and geometrical scales.

The properties of the final hydrated product depend upon many influencing factors such as the degree of hydration, composition and particle size distribution of cement, curing temperature and water–cement ratio. There are innumerable experimental and numerical techniques to determine the properties and the influencing parameters of final hydrated product whereas it is very difficult to experimentally determine (trace) the evolution of mechanical properties and the influencing parameters during the course of hydration. Computer-based simulation becomes handy in such situations. It also helps in bridging the gap between theoretical predictions and engineering practice.

For a wise simplification of the real hydration process, it is necessary to deal with the complexity of simulating the hydration reaction. Hydration models simulate the development of microstructure and evolution of hydration reactants and products. The results obtained from the computer simulation can be extended to know about various parameters of cement at their microscopic level.

Jennings and Johnson [1] developed a mathematical model in which the development of microstructure of tricalcium silicate (C_3S) when reacted with water was demonstrated. In this model, cement hydration is considered as the nucleation and growth of spherical particles in space. In 1991, van Breugal [2] developed a model named HYMOSTRUC which can simulate the development of microstructure of cement particles during hydration and predict its bulk properties. According to this model, all the hydration products deposit over the cement particles and hence the hydrating cement particles are represented as growing spheres. Maekawa et al. [3] developed a model called DUrability of COncrete Model (DUCOM) which can demonstrate the microstructure formation of hardening concrete and also evaluate the durability properties of concrete. Navi and Pignat [4] developed a model to accurately represent the development of microstructure of cement called integrated particle kinetics model (IPKM). In this model, the calcium-silicate-hydrate (C-S-H) which is hydration product deposits on C_3S whereas Portlandite (CH) is assumed to form in pore space enabling the modelling of the evolution of each particle independently. Hence, this model is capable of demonstrating the evolution of individual phases and also calculating the interactions between them. But, due to the modelling of all possible interactions, this model is very slow and limits the simulation to be carried out only for small number of particles. To overcome this shortcoming, [5] developed a model called μic in which millions of particles can be

simulated within short time incorporating all the interactions. The main advantage of this model is that it enables customisation of many aspects. It can be seen that all the above models are continuum models. Bullard [6] developed a numerical model to simulate the cement hydration and microstructure development at their early and later ages called HydratiCA. HydratiCA is a stochastic reaction-transport model that simulates the complex interactions among the coupled nonlinear chemical reactions and mass transport phenomena. Bentz [7] developed a model named CEMHYD3D which uses digital image processing approach to simulate the cement hydration process. This model is capable of simulating the microstructure development of plain and blended concrete and also measures its thermo-mechanical properties. The main advantage of this model is that it allows the representation of multi-size and non-spherical particles.

In this study, CEMHYD3D has been used to model the evolution of microstructure of cement paste during hydration. This study helps in understanding the underlying mechanism of cement hydration and its influencing parameters. The spatial distribution of various reaction products and pores has also been investigated. The influence of parameters like water–cement ratio and hydration time on the transport and mechanical properties has also been investigated.

2 Modelling of Cement Hydration

The computational volume of size 100 × 100 × 100 voxels is created at first. This computational volume is distributed with digitised spheres. The number of spheres and the size of spheres placed inside depend upon the particle size distribution of the cement powder under investigation (shown in Fig. 1) and the desired water–cement ratio of the mix.

The next step is to sort these spherical particles into different phases according to the phase distribution in the SEM image of the cement matrix. Cement powder of interest is mixed with epoxy resin and made into a dry paste. The specimen is cut, polished and coated with thin film of carbon. Then the specimen is viewed through SEM and analysed for backscattered electrons and X-rays emitted due to the

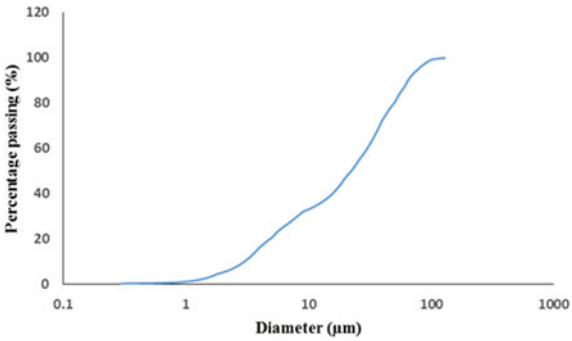

Fig. 1 Particle size distribution of the cement powder under investigation

specimen-primary electron beam interactions. These backscattered electron images and X-ray images collected for Ca, Si, S, Al and Fe are used to determine the phase distribution such as tricalcium silicate (C_3S), dicalcium silicate (C_2S), tricalcium aluminate (C_3A), tetracalcium aluminoferrite (C_4AF) and gypsum (CSH_2) in the sample. The X-ray and backscattered electron images are obtained for the same area of specimen. So, at one pixel location, six signals are available, the backscattered electron intensity and five x-ray signals. From the collective information of all these six signals, the phase separation is carried out using autocorrelation function.

For an $M \times N$ image, the autocorrelation function $S(x; y)$ takes the form

$$S(x;y) = \sum_{i=1}^{M-x} \sum_{j=1}^{N-y} \frac{I(i,j) \times I(i+x, j+Y)}{(M-x) \times (N-y)} \tag{1}$$

where $I(x,y)$ has a value of 1 if the pixel located at (x,y) meets the user criteria and 0 otherwise.

The two-point correlation function for silicates is used for separating the cement particles into silicates and aluminates. For this, each pixel in three-dimensional cement particle image is assigned a random number following a normal distribution, $N(x,y,z)$, generated using the Box-Muller method. The random number image is then filtered using the autocorrelation function, $F(x,y,z)$:

$$F(r) = F(x,y,z) = \frac{S(r = \sqrt{(x^2+y^2+z^2)} - S(0) \times S(0)}{[S(0) - S(0) \times S(0)]} \tag{2}$$

The silicates are further segmented into C_3S and C_2S and aluminates to C_3A and C_4AF. More detailed information on the image processing can be found elsewhere [8]. Figure 2 shows the obtained SEM image and the segmented image showing different phases.

Using the point counting procedure, the area and perimeter of each phase are calculated (shown in Table 1). In order to create a good representation of the cement paste, phase volume fractions, phase surface area fractions and phase autocorrelation structure should be described with extreme clarity.

Once the initial microstructure is created, a set of rules are employed to simulate the hydration behaviour. The phase of each voxel gets updated in the next time step through cellular-automata (CA) algorithm (shown in Fig. 3). Each voxel may undergo dissolution, diffusion or reaction according to the state transition rules to form solid hydrated phase.

2.1 Dissolution

In Fig. 3, the first set of pixel shows the initial states and the next three sets show possible states if the centre pixel moves in the direction mentioned in the arrows. It can be seen in the dissolution phase that if the solid pixel moves towards water,

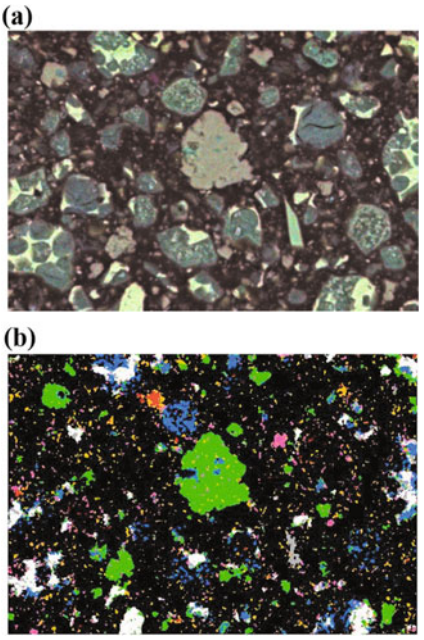

Fig. 2 SEM image **a** obtained and **b** segmented with different phases

Table 1 Calculated volume fraction and surface area

S. No	Phase	Volume fraction	Surface area
1.	C3S	0.657354787	0.708161988
2.	C2S	0.097637795	0.203423923
3.	C3A	0.076457834	0.047693546
4.	C4AF	0.168549583	0.040720544

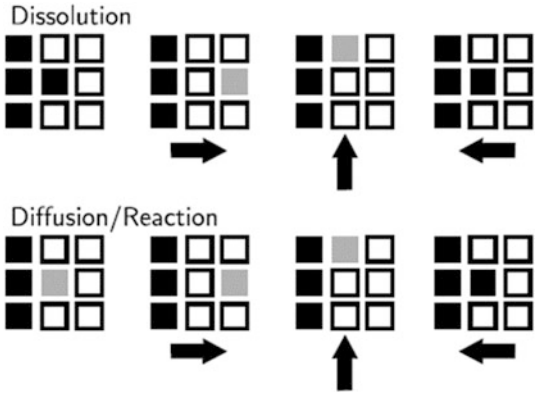

Fig. 3 Cellular automata algorithm applied in CEMHYD3D for dissolution, diffusion and reaction (black—solid phase, grey—diffusing phase and white—water phase)

it becomes a diffusing pixel and if it moves towards solid pixel, it remains as such. To shift the dissolution rate, the soluble phase is allotted possibilities of zero and unity. In this way, hydration is adjusted in such a way that C_3A react faster than C_3S followed by C_2S and C_4AF.

2.2 Diffusion

Likewise, the probable diffusing species is formed by dissolution process that comprises of diffusing CH, diffusing C-S-H, diffusing C_3A, diffusing gypsum and diffusing FH_3. It can be seen in diffusion phase that the diffusing pixel has the liberty to move towards the water but if it moves towards solid pixel, it undergoes reaction to form another solid phase otherwise it keep on as such.

2.3 Reaction

Numerous reactions are considered for modelling the cement hydration. For simulating the nucleation process, a diffusing species is allocated to certain probability of altering to its solid form. The probability (P) is made to be exponentially dependent on the number of diffusing species in solution (c):

$$P = P_0(1 - e^{-c/c_m}) \tag{3}$$

where P_0 and c_m are constants. This functional equation brings a nucleation probability that will deteriorate rapidly as c becomes less than c_m so that few new crystals will form late in the hydration. Figure 4 shows the state transition rules that are followed for modelling the cement hydration. Arrow patterns denote the dissolution, nucleation and collision of two species to form a hydration product. f[X] denotes that nucleation or dissolution probability is a function of concentration or volume fraction of phase X.

Flowchart in Fig. 5 shows the basic steps involved in modelling of cement hydration process using CEMHYD3D.

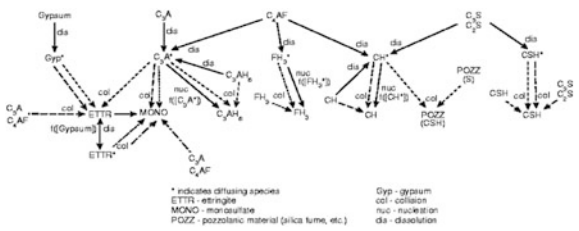

Fig. 4 State transition diagram for 3-D Cement Hydration Model

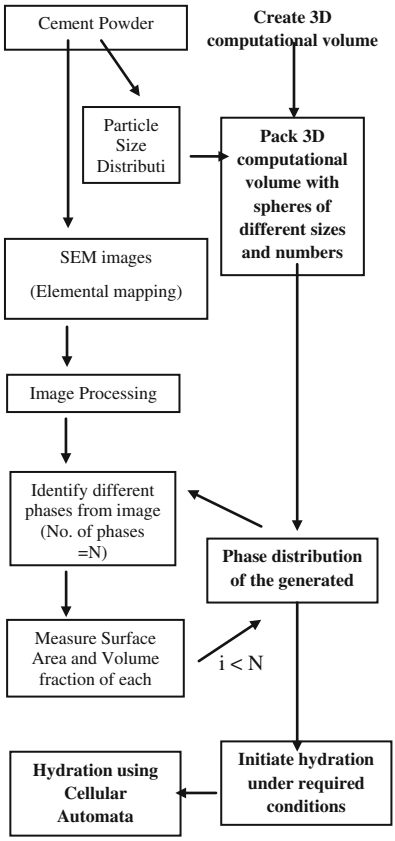

Fig. 5 Flowchart explaining modelling of cement hydration process using CEMHYD3D

3 Results and Discussion

With the above procedure, the evolved microstructure is obtained during each time step. Figure 6 shows the microstructures obtained at different times. From the microstructure, various physical and mechanical properties are determined.

3.1 Degree of Hydration

The degree of hydration denotes the quantity of cement matrix that has undergone hydration. It is calculated using the following relation:

$$\text{Degree of hydration} = (M_{\text{i}} - M_t)/M_{\text{i}} \tag{4}$$

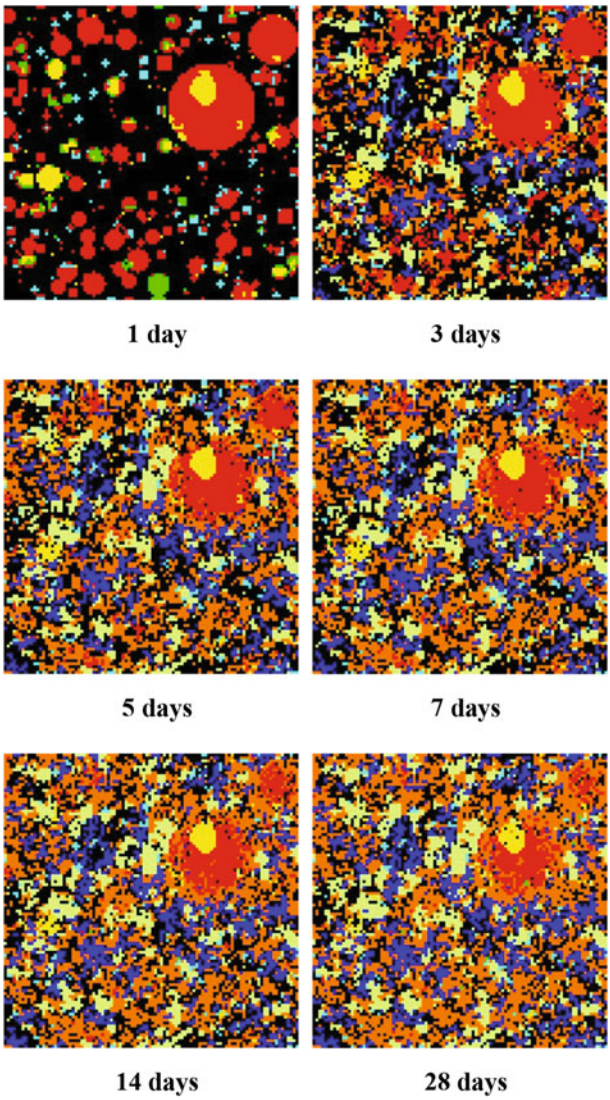

Fig. 6 Microstructures obtained at different hydration times

where

M_i Mass of initial clinker materials which is calculated by multiplying with its specific gravity. (i.e. number of pixels containing each clinker material at the initial stage is multiplied with their respective specific gravity) and

M_t Mass of clinker materials remaining unhydrated at time t.

3.2 Chemical Shrinkage

The volume stoichiometry of all ongoing chemical reactions is calculated in order to determine the chemical shrinkage. The molar volume of water left out is deducted from the molar volume of total porosity (including self-desiccation porosity) for calculating the chemical shrinkage.

$$\text{Chemical Shrinkage} = \left(mv_{\text{p}} - mv_{\text{w}}\right) * h_f \tag{5}$$

where

mv_{p} molar volume of porosity,
mv_{w} molar volume of water left out and
h_f heat conversion factor (arbitrary value to fit the numerical value with experimental results).

3.3 Compressive Strength

The compressive strength of the hardened cement paste is predicted using the gel-space ratio concept developed by Powers [9]. According to this method, the compressive strength is calculated using

$$\sigma_{\text{c}} = AX^n \tag{6}$$

where

A Intrinsic strength of the cement paste, MPa depending upon clinker composition,
n Constant which takes the value between 2.6 and 3 depending upon the cement being investigated and
X gel-space ratio which is defined as the ratio of volume of hydration product to the combined volume of the hydration product and capillary porosity which can be given as

$$X = (0.68\alpha)/(0.32\alpha + w/c) \tag{7}$$

where α is the degree of hydration on mass basis.

The values of A and n depends upon the type of cement and the Bogue composition. For the type of cement considered in this study, the value of A is 250 MPa and n is taken as 2.6.

3.4 Porosity

The microstructure is distributed with different chemical constituents. The count of number of pixels occupied by pores (pixel value = 0) gives the porosity of the matrix at any point of time.

The compressive strength and heat release of cement paste obtained using the above procedure is compared with that of the experimental results (shown in Fig. 7). It can be observed from Fig. 7 that the results obtained from numerical simulation are well corroborated with that obtained from experiments. Further, with the validated computational model, other mechanical and transport properties like the degree of hydration, porosity and chemical shrinkage are calculated. The influence of parameters like water–cement ratio and hydration time on various transport and mechanical properties has also been evaluated (shown in Fig. 8). The model can be used to evaluate the influence of addition of pozzolanic and non-pozzolanic materials on the transport and mechanical properties.

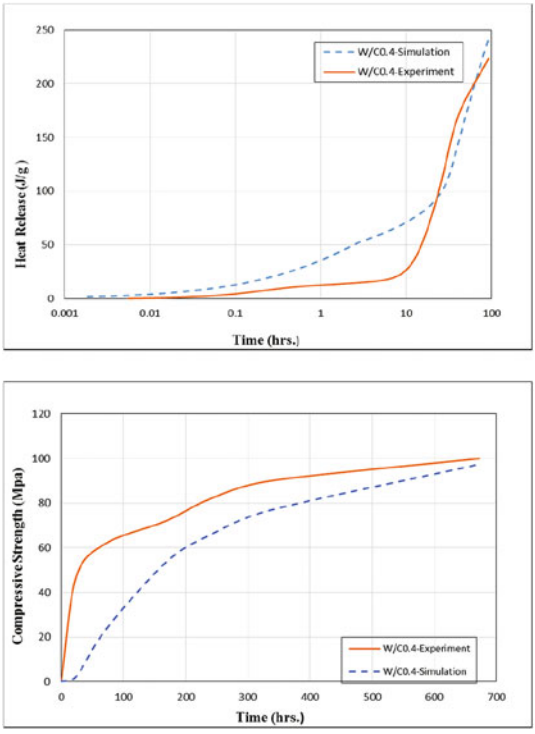

Fig. 7 Comparison of experimental and numerical results

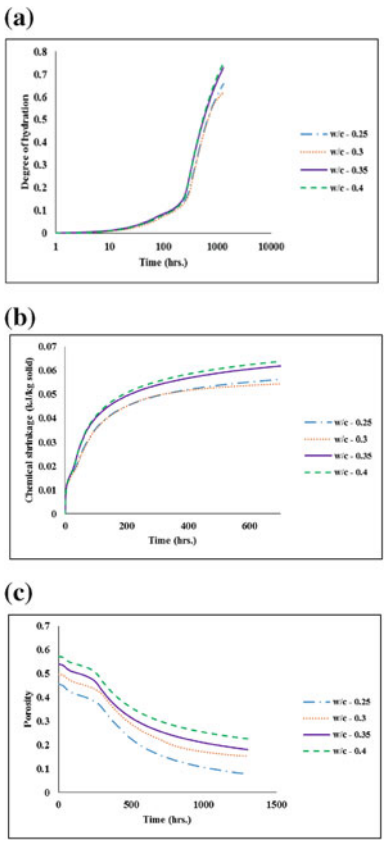

Fig. 8 **a** Degree of hydration, **b** chemical shrinkage and **c** porosity

4 Conclusion

This study deals with the computational modelling of cement hydration. CEMHYD3D has been used to investigate the hydration behaviour of cement paste and the influence of parameters like water–cement ratio and hydration time on various transport and mechanical properties. The study would greatly help not only to understand the mechanism of cement and cementitious materials at different time frame during hydration but also signifies the reaction kinetics and possible states of hydration. For any further enhancement of physical/chemical or mechanical properties of cement-based materials, this study would provide a tool to estimate the reaction kinetics and particle reactions for effective and desired performance.

References

1. Jennings, H. M., & Johnson, S. K. (1986). Simulation of microstructure development during the hydration of a cement compound. *Journal of the American Ceramic Society, 69*(11), 790–795.
2. Van Breugel, K. (1991). Simulation of hydration and formation of structure in hardening cement-based materials.
3. Maekawa, K., Chaube, R., & Kishi, T. (1999). Modelling of concrete performance.
4. Navi, P., & Pignat, C. (1996). Simulation of cement hydration and the connectivity of the capillary pore space. *Advanced Cement Based Materials, 4,* 58–67.
5. Bishnoi, S., & Scrivener, K. L. (2009). μic: A new platform for modelling the hydration of cements. *Cement and Concrete Research, 39*(4), 266–274.
6. Bullard, J. W. (2008). A determination of hydration mechanisms for tricalcium silicate using a kinetic cellular automaton model. *Journal of the American Ceramic Society, 91*(7), 2088–2097.
7. Bentz, D. P. (1997). Three-dimensional computer simulation of Portland cement hydration and microstructure development. *Journal of the American Ceramic Society, 80*(1), 3–21.
8. Stutzman, P. (2004). Scanning electron microscopy imaging of hydraulic cement microstructure. *Cement and Concrete Composites, 26*(8), 957–966.
9. Powers, T.C. (1962). Physical properties of cement paste. In *Proceedings of the 4th International Symposium on the Chemistry of Cement* (pp. 577–613), Vol. 2. Washington, D.C.

Three-Dimensional Analytical Solution for FGM Plate with Varying Material Properties in In-plane Directions Using Extended Kantorovich Method

Poonam Kumari and Agyapal Singh

Abstract A three-dimensional analytical solution for a functionally graded plate with longitudinally varying material properties is developed the first time. The plate is subjected to Levy-type boundary condition. A closed-form solution is developed using extended Kantorovich method. Deflections and stresses by taking three varying indexes (δ_1) are studied under different boundary conditions.

Keywords Functionally graded material · Kantorovich method
Analytical · Power series method

1 Introduction

Functionally graded materials (FGMs) are a new class of advanced composite materials in which material properties vary gradually with respect to the spatial coordinates. Bamboo, bones, teeth, and wood are the excellent example of natural occurring FGMs. Manmade designed\fabricated FGMs are specially used in aerospace and biomedical field. Jha et al. [1] presented the current state of research for static and dynamic analysis of thermoelastic FGM plates. Very recently, a comprehensive review of mathematical models for FGM plate under bending, buckling, and dynamic analysis is presented by Swaminathan et al. [2]. In literature, most of the research work is related to modeling and analysis of FGM plates and shells having material property variation along the thickness direction. Very limited work is reported in the literature for FMG plates with a longitudinal variation of material properties. Lu et al. [3] applied the differential quadrature method (DQM) to solve 3-D elasticity equation of Levy-type multidirectional functionally graded rectangular plates with an exponential variation of material properties along x and

P. Kumari (✉) · A. Singh
Department of Mechanical Engineering, IIT Guwahati, Guwahati 781039, Assam, India
e-mail: kpmech@iitg.ernet.in

A. Singh
e-mail: agyapal@iitg.ernet.in

A. Rama Mohan Rao and K. Ramanjaneyulu (eds.), *Recent Advances in Structural Engineering, Volume 1*, Lecture Notes in Civil Engineering 11,
https://doi.org/10.1007/978-981-13-0362-3_49

z-direction. Recently, Tahouneh and Naei [4] developed 3D dynamic solution for thick two-directional functionally graded Levy-type FGM plate using two-dimensional DQM. Liu et al. [5] analyzed a Levy-type rectangular plate considering power law variation of material properties along the longitudinal direction. Classical plate theory (CPT) is used to develop the governing equation and Runge–Kutta method is applied for a solution. Very recently, Amirpour et al. [6] developed the analytical solution using higher order shear deformation theory for all round simply supported FGM plate assuming an in-plane variation of stiffness. Mostly numerical or semi-analytical techniques were used for three-dimensional analysis of in-plane or multidirectional functionally graded structures. As per author's knowledge, there is no three-dimensional analytical solution exist for plates having in-plane stiffness variation. The powerful extended Kantrovich method (EKM) originally proposed by Kerr [7] for two-dimensional (2D) elasticity problems is generalized to the three-dimensional (3D) elasticity solution for the multilayered plate by Kapuria and Kumari [8, 9]. In this paper, EKM is applied to develop an analytical solution for rectangular functionally graded plate considering a variation of material properties along the x-direction. By employing the variational process along the in-plane (x) and thickness (z) directions, yield a system of $6n$ ODEs with variable constant and $3n$ algebraic equation in the direction of x and a similar set of equations with constant coefficient in the z-direction. In thickness direction, exact closed-form solutions are obtained using the approach given in Ref. [9] and along in-plane direction, the system of ordinary differential equation has variable coefficients, which is then solved by employing the modified power series method suggested by Kukla [10]. Numerical results are obtained for a thick FGM plate with different boundary conditions considering three value of variation index (δ_1).

2 Basic Assumption

A rectangular FG plate of uniform thickness h, span length 'a' along the x-direction and length b along y-direction as shown in Fig. 1 is considered for the present study. The plate is made of FGM material.

For the present case, material properties are assumed to vary along x-axis as

$$\bar{s}_{1j}^{m} = \bar{s}_{1j}(1 + \delta_1 \xi_1) \Rightarrow \bar{s}_{1j} + \hat{s}_{1j} \quad \text{for } j = 1, 2, 3 \tag{1}$$

where $\bar{s}$ is compliance properties, δ_i is varying constant, and $\xi_1 = x/a$, $\xi_2 = y/b$ are nondimensional quantities. The plate is subjected to simply supported boundary conditions along the y-axis and along x-axis any boundary conditions can be applied, e.g., clamped, free, soft-clamped.

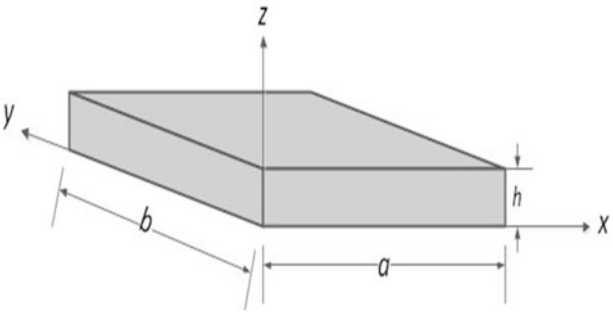

Fig. 1 Geometry of FGM plate

3 Theoretical Formulation

By using mixed Reissner-type variational principle for a linear elastic medium, the weak form of governing equation considering material variation along *x*-axis is expressed as

$$\begin{aligned}\int_V \big[&\delta u(\tau_{xz,z}+\sigma_{x,x}+\tau_{xy,y})\\ &+\delta v\big(\tau_{yz,z}+\tau_{xy,x}+\sigma_{y,y}\big)+\delta w\big(\sigma_{z,z}+\tau_{zx,x}+\tau_{yz,y}\big)\\ &+\delta\sigma_x\big\{(\bar{s}_{11}+\hat{s}_{11})\sigma_x+(\bar{s}_{12}+\hat{s}_{12})\sigma_y\\ &+(\bar{s}_{13}+\hat{s}_{13})\sigma_z-u_x\big\}+\delta\sigma_y\big\{(\bar{s}_{12}+\hat{s}_{12})\sigma_x\\ &+(\bar{s}_{22})\sigma_y+(\bar{s}_{23})\sigma_z-v_y\big\}-\delta\sigma_z\{w_z\\ &-(\bar{s}_{13}+\hat{s}_{13})\sigma_x-(\bar{s}_{23})\sigma_y-(\bar{s}_{33})\sigma_z\big\}\\ &-\delta\tau_{yz}\big\{v_z+w_y-(\bar{s}_{44})\tau_{yz}\big\}-\delta\tau_{zx}\{u_z\\ &+w_x-(\bar{s}_{55})\tau_{zx}\}+\delta\tau_{xy}\big\{(\bar{s}_{66})\tau_{xy}-v_x-u_y\big\}\big]\mathrm{d}V=0\end{aligned} \tag{2}$$

The boundary conditions at top and bottom surfaces of the plate are

$$\begin{aligned}&\text{at } z=-h/2 \quad \sigma_z=-p_1, \quad \tau_{yz}=0, \quad \tau_{zx}=0\\ &\text{at } z=-h/2 \quad \sigma_z=-p_2, \quad \tau_{yz}=0, \quad \tau_{zx}=0\end{aligned} \tag{3}$$

The boundary conditions at the edges $\xi_1 = 0$ and 1 are set according to type of support given as

$$\begin{aligned}&\text{Simply Supported}(S): \quad w=0, \sigma_x=0, v=0\\ &\text{Clamped}(C): \quad w=0, u=0, v=0\\ &\text{Free}(F): \quad \tau_{xz}=0, \sigma_x=0, \tau_{xy}=0\end{aligned} \tag{4}$$

The boundary conditions at edges $\xi_2 = 0$ and 1 are assumed to be hard simply supported (SH)

$$w = 0, \sigma_y = 0, u = 0$$

4 EKM Approach

The field variables to be solved are in column matrix form as

$$X = [u, v, w, \sigma_x, \sigma_y, \sigma_z, \tau_{xy}, \tau_{yz}, \tau_{zx}]^{\mathrm{T}}$$

The solution is assumed in separable form as

$$X_l(\xi_1, \xi_2, \zeta) = X_l^x(\xi_1) X_l^y(\xi_2) X_l^z(\zeta) \quad \text{for } l = 1, 2, \ldots, 9 \tag{5}$$

To obtain analytical solution in y-direction, the field variables X_l^y are expressed in term of Fourier series in y-direction as

$$(u, w, \sigma_x, \sigma_y, \sigma_z, \tau_{zx}) = \sum_{m=1}^{\infty} (u, w, \sigma_x, \sigma_y, \sigma_z, \tau_{zx})_m \sin m\pi\xi_2$$
$$\Rightarrow \sum_{m=1}^{\infty} X_l(\xi_1, \zeta)_m X_{lS}^y(\xi_2)$$

$$(v, \tau_{yz}, \tau_{xy}) = \sum_{m=1}^{\infty} (v, \tau_{yz}, \tau_{xy})_m \cos m\pi\xi_2$$
$$\Rightarrow \sum_{m=1}^{\infty} X_l(\xi_1, \zeta)_m X_{lC}^y(\xi_2)$$

where $(\ )_m$ denotes mth Fourier component which is a function of x and z.

The solution for the lth variable X_l is assumed in the following form:

$$X_l(\xi_1, \xi_2, \zeta) = \sum_{m=1}^{\infty} X_{lS}^y(\xi_2) \text{ or } X_{lC}^y(\xi_2) \left\{ \sum_{i=1}^{n} f_l^i(\xi_1) g_l^i(\zeta) + \delta_{l6}[p_a + z p_d] \right\} \quad \text{for} \quad l = 1, 2, \ldots, 9 \tag{6}$$

wherein $f_l^i(\xi_1)$ and $g_l^i(\zeta)$ are the univariate function of ξ_1 and ζ respectively, for the ith term of the n-term series solution. These functions are to be determined iteratively, satisfying all homogenous boundary conditions.

5 First Iteration Step

In this step, functions $f_l^i(\xi_1)$ are assumed, for which the variation δX_l is obtained as

$$\delta X_l = \sum_{m=1}^{\infty} \left[X_{lS}^v \text{ or } X_{lC}^v\right] \sum_{i=1}^{n} f_l^i(\xi_1)\delta g_l^i \quad \text{for } l = 1, 2, \ldots, 9 \tag{7}$$

Functions $g_l^i(\zeta)$ are partitioned into a column vector $\bar{G}$ of that six variables which appear in the boundary and interface conditions and a column vector $\hat{G}$ consisting of the remaining three variable

$$\bar{G} = [\, g_1 \quad g_2 \quad g_3 \quad g_6 \quad g_8 \quad g_9 \,]^{\mathrm{T}}$$
$$\hat{G} = [\, g_4 \quad g_5 \quad g_7 \,]^{\mathrm{T}}$$

Equation (7) is substituted in Eq. (2) and integration is performed over ξ_1 direction on the known function of ξ_1. Since the variation δg_l^i is arbitrary, thus coefficient of δg_l^i must be zero individually. This result in the following system of $9n$ differential algebraic equations for δg_l^i

$$M\bar{G}_{,\zeta} = \bar{A}^m\bar{G} + \hat{A}^m\hat{G} + \bar{Q} \tag{8}$$

$$K\hat{G} = \tilde{A}^m\bar{G} + \tilde{Q}^m \tag{9}$$

where

$$\bar{A}^m_{6n\times 6n} = \bar{A} + \bar{A}^v; \quad \hat{A}^m_{6n\times 3n} = \hat{A} + \hat{A}^v$$
$$\tilde{A}^m_{3n\times 6n} = \tilde{A} + \tilde{A}^v \quad \tilde{Q}^m_{6n\times 1n} = \tilde{Q}_p + \tilde{Q}^v_p$$

$()$, $()^v$ contain constant and varying components, respectively. Substituting the $\hat{G}$ from Eq. (9) into Eq. (8) gives

with

$$\begin{aligned} \bar{G}_{,\zeta} &= A\bar{G} + Q_p \\ A &= M^{-1}[\bar{A}^m + \hat{A}^m K^{m-1}\tilde{A}^m] \\ Q_p^m &= M^{-1}[\bar{Q}_p^m + \hat{A}^m K^{m-1}\tilde{Q}^m] \end{aligned} \tag{10}$$

The general solution for Eq. (10) is

$$\bar{G}(\zeta) = \sum_{i=1}^{6n} F_i(\zeta)C_i + U_0 + \zeta U_1 \tag{11}$$

This complete the first iteration step.

6 Second Iteration Step

The solution of $g_l^i(\xi_1)$ from the previous step is now taken as known a priori, where f_l^i are considered unknown. The variation δX_i for this case is obtained as

$$\delta X_l = \sum_{m=1}^{\infty} \left[X_{lS}^y \text{ or } X_{lC}^y\right] \sum_{i=1}^{n} g_l^i(\zeta)\delta f_l^i \quad \text{for } l = 1, 2, \ldots, 9 \tag{12}$$

Functions $f_l^i(\xi_1)$ are partitioned into a column vector $\bar{F}$ consisting of that six variables that appear in the boundary conditions along the x-direction given in Eq. (4) and a column vector $\hat{F}$ of the remaining three variable

$$\bar{F} = [f_1 \quad f_2 \quad f_3 \quad f_4 \quad f_7 \quad f_9]^{\mathrm{T}}$$
$$\hat{F} = [f_5 \quad f_6 \quad f_8]^{\mathrm{T}}$$

Equation (12) is substituted in Eq. (2) and integration is performed over ζ direction on the known function of ζ. Considering that variation δf_l^i are arbitrary, the coefficient of δf_l^i in the resulting left-hand side expression is equated to zero individually. This results in the following system of differential algebraic equations for f_l^i

$$N\bar{F}_{,\xi_1} = \bar{B}^f\bar{F} + \hat{B}^f\hat{F} + \bar{P}_m^f \tag{13}$$

$$L\hat{F} = \tilde{B}^f\bar{F} + \tilde{P}_m^f \tag{14}$$

where

$$\bar{B}^f = \bar{B} + \xi_1\bar{B}^v; \quad \hat{B}^f = \hat{B} + \xi_1\hat{B}^v$$
$$\bar{P}_m^f = \bar{P} + \xi_1\bar{P}^v; \quad \tilde{B}^f = \tilde{B} + \xi_1\tilde{B}^v$$
$$\tilde{P}_m^f = \tilde{P}_m + \xi_1\tilde{P}_m^v$$

and

N, $\bar{B}^f$, $\hat{B}^f$, L, $\tilde{B}^f$ are $6n \times 6n$, $6n \times 6n$, $6n \times 3n$, $3n \times 3n$, $3n \times 6n$ matrices, respectively

Substituting the $\hat{F}$ from Eq. (14) for into Eq. (13) gives

$$\bar{F}_{,\xi_1} = (B_0 + \xi_1 B_1 + \xi_1^2 B_2)\bar{F} + P_0 + \xi_1 P_1 \tag{15}$$

where

$$B_0 = N^{-1}(\bar{B} + \hat{B}L^{-1}\tilde{B});$$
$$B_1 = N^{-1}(\bar{B}^v + \hat{B}L^{-1}\tilde{B}^v + \hat{B}^v L^{-1}\tilde{B});$$
$$B_2 = N^{-1}(\hat{B}^v L^{-1}\tilde{B}^v);$$
$$P_0 = N^{-1}(\bar{P}_m + \hat{B}L^{-1}\tilde{P}_m);$$
$$P_1 = N^{-1}(\bar{P}_m^v + \hat{B}^v L^{-1}\tilde{P}_m);$$

The above Eq. (15) is set of non-homogenous ordinary differential equations with the variable coefficients. Thus, the solution for Eq. (15) is expanded in terms of a power series in the dimensionless axial coordinate $\xi_1 (0 \leq \xi_1 \leq 1)$ as

$$\bar{F}(\xi_1) = \sum_{i=1}^{n} \frac{Y_i \xi_1^i}{i!} \tag{16}$$

Further above assumed solution is modified as

$$\bar{F}^j(\xi_1) = \sum_{i=1}^{\infty} Z_i^j \xi_1^i + \left(\sum_{i=1}^{\infty} H_i^j \xi_1^i \right) C_0 \tag{17}$$

where C_0 is evaluated by applying edge conditions where $Z_i(\xi_1)$ and $H_i(\xi_1)$ are given by recursive relations which are obtained by substituting Eq. (17) into Eq. (15). The infinite power series is truncated to a finite number of terms such that the contribution of the first neglected term is less than 10^{-10}.

7 Numerical Results

A thick square metal FG plate with $S = 5$ and Young's modulus (66.2 GPa) of plate varies along the length with variation index of $\delta_1 = 0,\ 0.5,\ 1.0$ is considered for the numerical study. Poisson's ratio $(v = 0.33)$ is assumed to be constant. The plate response is obtained for following pressure load at the top of the plate.

$$p_2 = p_0 \sin(\pi y/b)$$

The results are nondimensionalized with $Y_0 = 10.3$ GPa as follows:

$$\bar{w} = 100\, wY_0/p_0 hS^4;$$
$$(\bar{\sigma}_x, \bar{\sigma}_y, \tau_{xz}, \tau_{yz}) = (\bar{\sigma}_x, \bar{\sigma}_y, S\tau_{xz}, S\tau_{yz})/p_0 S^2$$

Since there exists no analytical solution for a plate with longitudinal varying material properties. Therefore, the present method is validated with respect to 3D

FE results. For FE analysis, spatially graded property distribution (at different Gauss points) with the quadratic hexahedral solid element is implemented by employing user material subroutine (UMAT) in ABAQUS FE software.

The longitudinal variation of deflection and stresses (normal and shear) for different boundary conditions (e.g., CC, SS, SF, and FF) are presented in Figs. 2, 3, 4 and 5 for the thick plate ($S = 5$). Results are presented for different variation index $\delta_1 = 0, 0.5, 1$. Figure 2 presents the longitudinal variation of deflection ($\bar{w}$) and in-plane stress ($\bar{\sigma}_x$) for simply supported-simply supported (SS) and clamped-clamped (CC) boundary conditions. For comparison, 3D FE results are also plotted for $\delta_1 = 0.5$ and it is observed that as the variation index for material properties increases, the location of maximum deflection and in-plane stress shifts toward right for both cases (SS as well as CC boundary). It is also observed that there is significant variation in in-plane stress ($\bar{\sigma}_x$) for SS and in deflection for CC boundary conditions. Longitudinal variation of transverse shear stresses $\bar{\tau}_{zx}$, $\bar{\tau}_{yz}$ is plotted in Fig. 3 and it observed that there is noticeable variation in $\bar{\tau}_{yz}$ as compared to $\bar{\tau}_{zx}$ for both cases. It is evident from Figs. 2 and 3 that present results are in good agreement with 3D FE results. Similarly, Figs. 4 and 5 present the variation of deflection and stresses for simply supported-free (SF) and free-free (FF) boundary conditions. As variation index increases, the deflection ($\bar{w}$) for FF boundary conditions decreases. While for other support conditions it increases and the reverse trend is followed by stress ($\bar{\sigma}_x$). No significant variation is observed for transverse shear stress under SF and FF boundary conditions. These results can be taken as benchmark results for verifying 2D theories and numerical results.

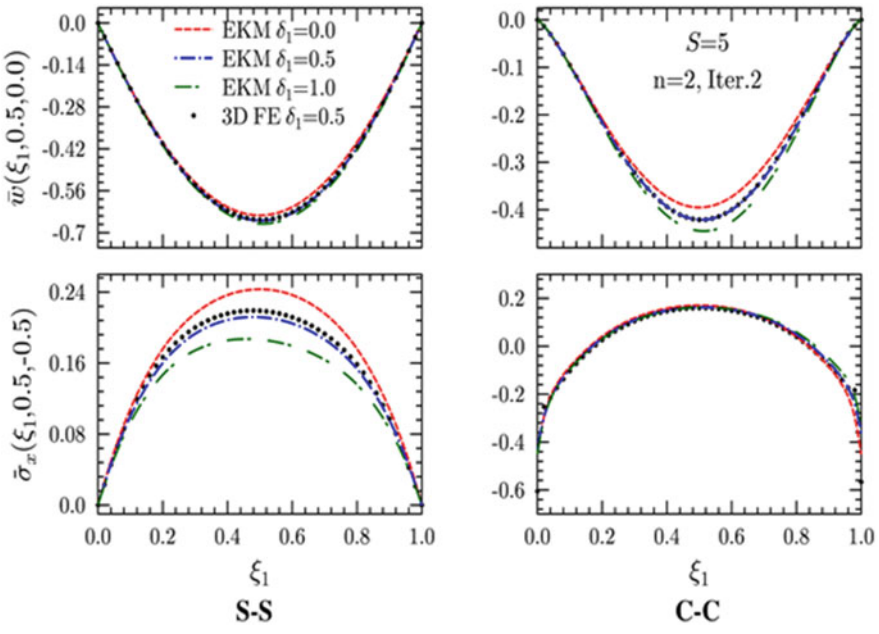

Fig. 2 Variation of deflection $\bar{\omega}$ and normal stress $\bar{\sigma}_x$ in single layer FGM plate with different δ_1

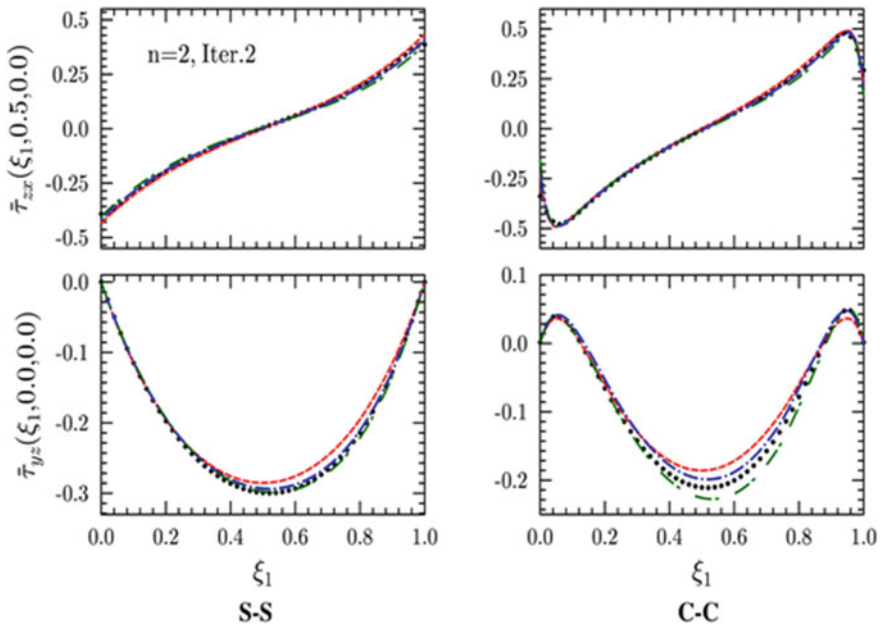

Fig. 3 Variation of transverse stresses $\bar{\tau}_{zx}, \bar{\tau}_{yz}$ in single layer FGM plate with different δ_1

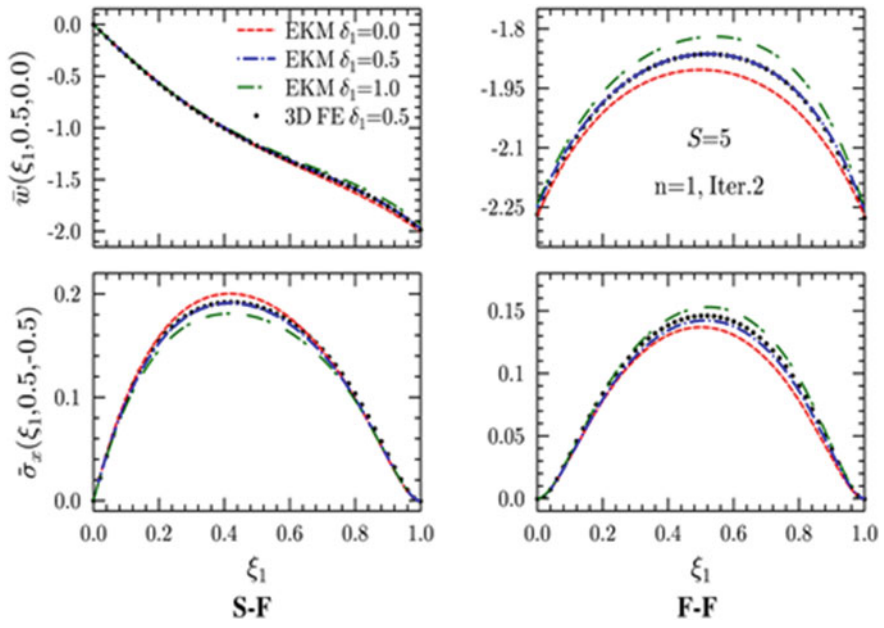

Fig. 4 Variation of deflection $\bar{\omega}$ and normal stress $\bar{\sigma}_x$ in single layer FGM plate with different δ_1

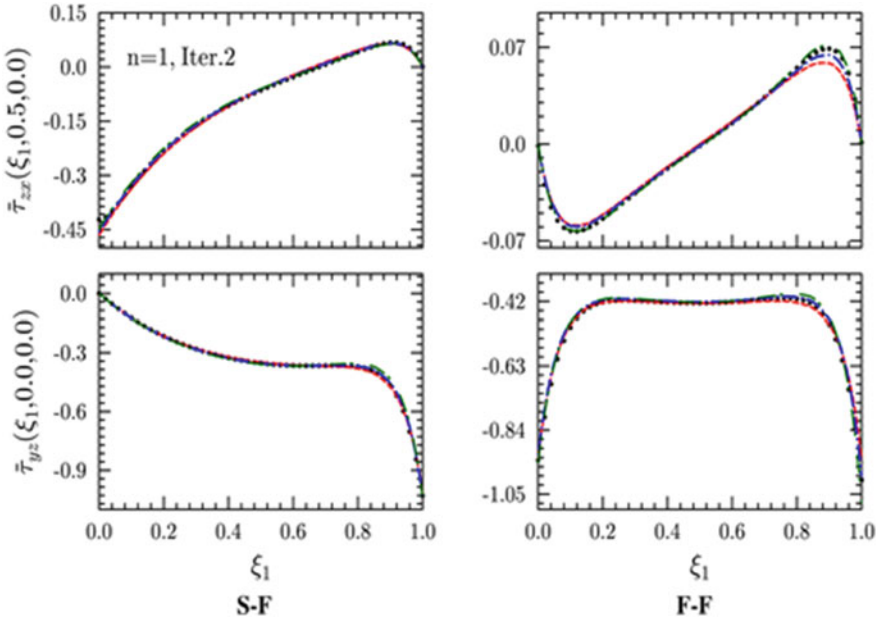

Fig. 5 Variation of transverse stresses $\bar{\tau}_{zx}, \bar{\tau}_{yz}$ in single layer FGM plate with different δ_1

8 Conclusion

The first time a closed-form 3D solution is presented for a functionally graded plate with longitudinally varying material properties. The location of maximum deflection and maximum stresses in the case of in-plane FG plate are different than the homogeneous plate. The significant effect of properties variation on a deflection and in-plane stress is observed and boundary condition plays an important role in the behavior of longitudinal varying FGM plate.

References

1. Jha, D. K., Kant, T., & Singh, R. K. (2013). A critical review of recent research on functionally graded plates. *Composite Structures, 96,* 833–849.
2. Swaminathan, K., Naveenkumar, D. T., Zenkour, A. M., & Carrera, E. (2015). Stress, vibration and buckling analyses of FGM plates—A state-of-the-art review. *Composite Structures, 120,* 10–31.
3. Lu, C., Lim, C. W., & Chen, W. (2009). Semi-analytical analysis for multi-directional functionally graded plates: 3-D elasticity solutions. *International Journal for Numerical Methods in Engineering, 79*(1), 25–44.

4. Tahouneh, V., & Naei, M. (2014). A novel 2-D six-parameter power-law distribution for three-dimensional dynamic analysis of thick multi-directional functionally graded rectangular plates resting on a two-parameter elastic foundation. *Meccanica, 49*(1), 91–109.
5. Liu, D., Wang, C., & Chen, W. (2010). Free vibration of FGM plates with in-plane material inhomogeneity. *Composite Structures, 92*(5), 1047–1051.
6. Amirpour, M., Das, R., & Saavedra Flores, E. I. (2016). Analytical solutions for elastic deformation of functionally graded thick plates with in-plane stiffness variation using higher order shear deformation theory. *Composites Part B, 94,* 109–121.
7. Kerr, A. D. (1968). An extension of the Kantorovich method. *Quarterly of Applied Mathematics, 4,* 219–229.
8. Kapuria, S., & Kumari, P. (2011). Extended Kantorovich method for three-dimensional elasticity solution of laminated composite structures in cylindrical bending. *Journal of Applied Mechanics, 78*(6), 061004.
9. Kapuria, S., & Kumari, P. (2012). Multi-term extended Kantorovich method for three dimensional elasticity solution of laminated plates. *Journal of Applied Mechanics Transactions ASME, 79*(6).
10. Kukla, S., & Zamorska, I. (2014). Power series solution of first order matrix differential equations. *Journal of Applied Mathematics and Computational Mechanics, 13*(3), 123–128.

Effect of Support Settlement on the Behaviour of Stone Masonry Arch Bridge

T. P. Vijayalekshmi and Job Thomas

Abstract In this paper, the behaviour of an existing masonry stone arch bridge when subjected to foundation settlement is evaluated. The 13 Arch Bridge, also called Kannara Bridge situated in the Kollam–Shenkottai Railway line is considered for this study. This bridge is originally designed for Metre Gauge (MG) load and is now being upgraded for Broad Gauge (BG) load. CATIA V5 is used to model the bridge in its original form and strengthened form. Transient load analysis is carried out in ANSYS V15 to study the deformation of the bridge in different situations. The cases, namely, when the supports are intact and when the central support sinks with respect to the other supports were analysed for the original bridge and for the strengthened bridge. The middle support deflection and maximum principal stresses were determined. A parametric study on the influence of thickness of the concrete jacket on the deformation properties of the bridge was carried out. Three thicknesses for the concrete jacket, namely, 200, 450 and 600 mm, were considered. It is found that the provision of concrete jacket offers high resistance against deformation of the bridge due to settlement. The concrete jacket of 450 mm is suggested as a feasible solution to mitigate the settlement problems.

Keywords Stone masonry · Arch bridge · Support settlement · Transient analysis · Middle support deflection

T. P. Vijayalekshmi · J. Thomas (✉)
School of Engineering, Cochin University of Science and Technology,
Kochi 682022, Kerala, India
e-mail: job_thomas@cusat.ac.in

T. P. Vijayalekshmi
e-mail: vlekshmi.tp@gmail.com

A. Rama Mohan Rao and K. Ramanjaneyulu (eds.), *Recent Advances in Structural Engineering, Volume 1*, Lecture Notes in Civil Engineering 11,
https://doi.org/10.1007/978-981-13-0362-3_50

1 Introduction

Masonry arch bridges are surprisingly strong structures; most of them are constructed centuries ago. These structures are still in use and have to carry increased loads than they are actually designed for. These bridges have a major role in transportation in many countries. There are about 19,600 masonry arch bridges in Indian Railways, which are originally designed for loads lower than that in the new code provisions. The present study aims to understand the behaviour of a modified stone arch bridge situated in the Kollam–Shenkottai Railway line when subjected to foundation settlement. These structures are getting worldwide attention and there are certain studies on masonry arch bridges regarding pier settlement and strengthening. Gilbert [1] modelled a twin-span bridge subjected to central support settlement in Ring software. It is found that support settlement may lead to incremental damage to the structure. Luboweicka et al. [2] indicated that due to the live load, there is local bending of the arch which causes tensile stress and foundation settlement affects the total stress state in the bridge structure. Farhad et al. [3] analysed three stone arch bridges of the Iran railway using SAP2000. It is suggested that strengthening the arches results in a considerable increase in lateral capacity of stone arch bridges. Gonen et al. [4] found that excessive stresses at critical points cause failure of stone arch bridges. Behnamfara and Afshari [5] suggested that the lateral load carrying capacity of stone arch bridges increases as a result of strengthening. Domede et al. [6] predicted the effects of existing cracks in presence of displacement of supports. It is concluded that the compressive strength of the masonry remains a decisive factor in the load-bearing capacity of the bridge. Kindij et al. [7] in a study observed that differential settlement of pier foundations cause damage to the pier itself and also cause damage of the barrel, spandrel walls, or drainage system. Reccia et al. [8] analysed an existing bridge under foundation settlements. It is found that a vertical small displacement of the pile could worsen the serviceability conditions.

2 Salient Features of the Stone Masonry Arch Bridge

The bridge under study is 143.22 m long and has 13 arches of 9.14 m span and 3 m rise. The central pier is about 19.895 m high. It is a stone masonry arch built a hundred years ago. The stone arch of the original bridge is 600 mm thick. Concrete jacketing is provided for all the 12 piers. The intrados of the arches are provided with 450 mm jacketing. The original bridge is shown in Fig. 1.

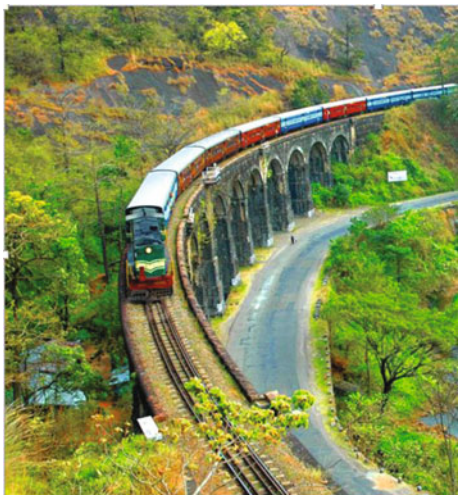

Fig. 1 Stone masonry arch bridge under study

3 Geometric Model

The software used for modelling is CATIA V5. It is a solid modelling commercial tool used for modelling of complex structures like masonry arch bridges. The central pier, two adjacent piers, two central full spans and two half spans on either side of the bridge were considered for the analysis. The drawing of the original bridge and strengthened bridge is shown in Figs. 2 and 3 respectively.

The parts of the railway masonry arch bridge namely piers, arches, spandrel walls, infill and ballast are separately modelled in the part workbench and assembled in the assembly workbench of CATIA V5.

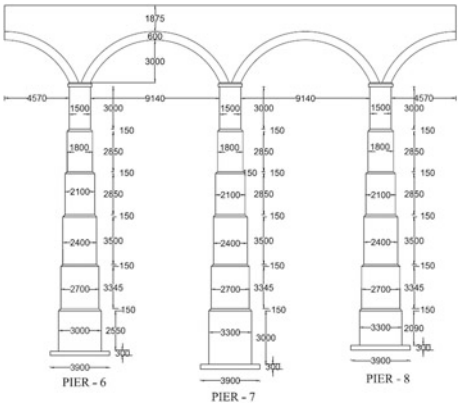

Fig. 2 Original bridge drawing

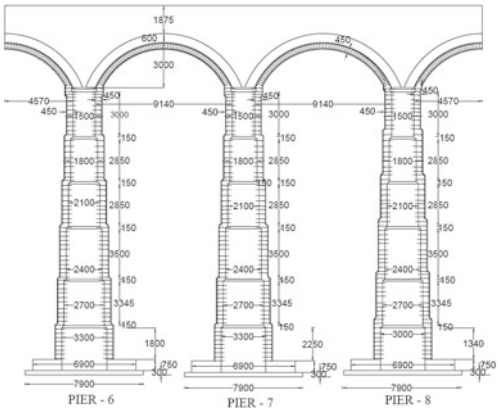

Fig. 3 Strengthened bridge drawing

4 Finite Element Model

The geometric model of the bridge is imported to the ANSYS V15 environment. The material properties are assigned to all parts of the bridge. Proper meshing is done to the geometry. Supports are introduced so that the middle support is free to sink. Loads are applied according to the Bridge Rules [9].

4.1 Material Properties

The geometric model of the bridge is imported to the ANSYS V15 environment. The material properties of stone masonry are assigned to the piers and arches. Young's modulus of masonry is taken as 10,000 MPa, Poisson's ratio as 0.2, and density as 2200 kg/m^3 [10]. The nonlinear stress–strain response of stone masonry as suggested by Grandjean and Brühwiler [11] is considered and is given in Fig. 4a. Young's modulus of fill material is taken as 5000 MPa, Poisson's ratio 0.2, density 1800 kg/m^3, cohesion 0.5 kPa and angle of internal friction 30° [12]. Drucker–Prager criterion is used to model the soil fill. The ballast properties are Young's modulus 150 MPa, Poisson's ratio 0.35 and density 2500 kg/m^3 [13]. In the case of strengthened bridge, the stress–strain response of concrete in compression as shown in Fig. 4b is considered [14].

4.2 Element and Meshing

SOLID 186 is a 3D-brick element and is used for modelling the structure. 10-noded tetrahedral elements and 20-noded hexahedral elements are used in the meshing of various parts of the structure. The element sizes used in the meshing of the original

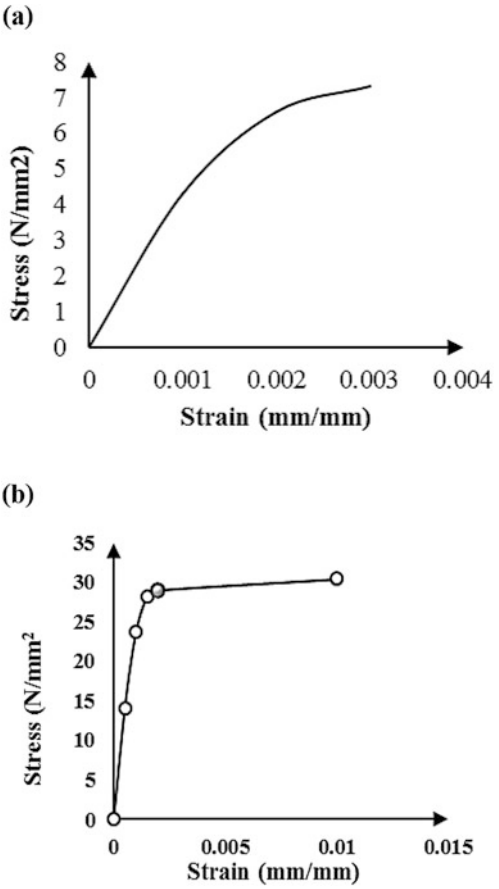

Fig. 4 Stress–strain curves. **a** Stone masonry, **b** concrete in compression

bridge model and retrofitted bridge model are 150 and 200 mm, respectively. The finite element models of the original structure and the retrofitted structure are shown in Figs. 5 and 6 respectively.

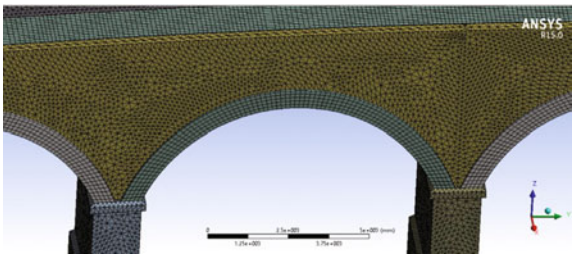

Fig. 5 Finite element model of original structure

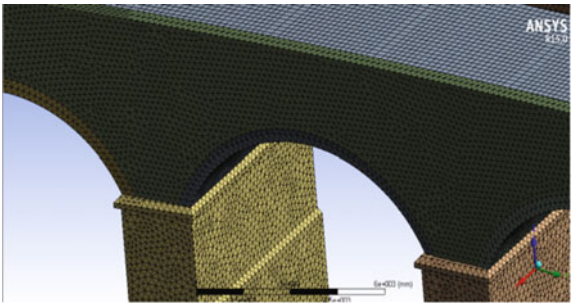

Fig. 6 Finite element model of strengthened structure

4.3 Boundary Conditions

Supports are assigned beneath the piers at the ends. The settlement of the middle pier is modelled with no supports beneath the central pier. Loads based on the Bridge Rules [9] are considered in the analysis. Dead load is the self-weight of the structure together with the permanent loads and it is applied by selecting the standard earth gravity option. Live load is the BG load plus the dynamic effects. The BG loco load is shown in Fig. 7. The axle load is 245.25 kN and there are 12 axles. The distance between the axles at the ends is 26.688 m. The dynamic effect is accounted for in the computation of load and the impact factor is 1.11.

The centrifugal effect may be negligible [15] for these types of massive structures. As recommended in the Arch Bridge Code [16], the tractive effort and breaking effect are not considered.

5 Finite Element Analysis

Transient analysis is carried out and the middle support deflection and stresses in the structural elements of the bridge are determined. In transient analysis, the position of load is varying with time. The movement of load in the structure is considered and it takes 8.3 s for the BG loco load to cross the bridge corresponding to the train speed of 31 km/h as laid down in the route specification. The middle

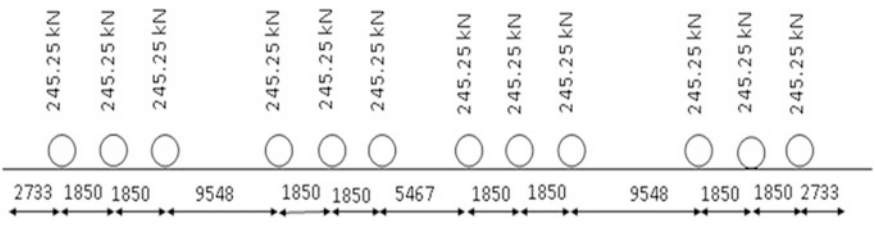

Fig. 7 Broad Gauge loco loading (all dimensions are in mm)

support deflection and maximum principal stresses at every second in the analysis of the original bridge is determined. Similar analyses were carried out for the retrofitted bridge with varying thicknesses of concrete jacket namely 200, 450 and 600 mm.

6 Results

The deflection values evaluated in the various cases, with settlement are given in Table 1.

The maximum middle support deflection was found to be 85.80 mm in the original bridge. By providing 200-mm-thick concrete jacketing, the middle support deflection is reduced to 20.39 mm. A further reduction of 5.16 mm is seen when the thickness of the jacket is increased to 450 mm. In the case of retrofitted bridge with 600 mm jacketing, the value is found to be 14.95 mm. There is only 0.28 mm reduction even if the thickness is increased from 450 to 600 mm. It is found that the 450-mm-thick concrete jacket offers high resistance against deformation of the bridge due to settlement. Hence, it can be concluded that the support settlement problems can be effectively mitigated using the jacketing. The middle support deflection plotted against time for the original bridge, 200, 450 and 600-mm-thick retrofitted bridge is given in Fig. 8.

Table 1 Predicted deflection in settlement

Particulars	Middle support deflection (mm)
Original bridge	85.80
Strengthened bridge with 200-mm-thick jacketing	20.39
Strengthened bridge with 450-mm-thick jacketing	15.23
Strengthened bridge with 600-mm-thick jacketing	14.95

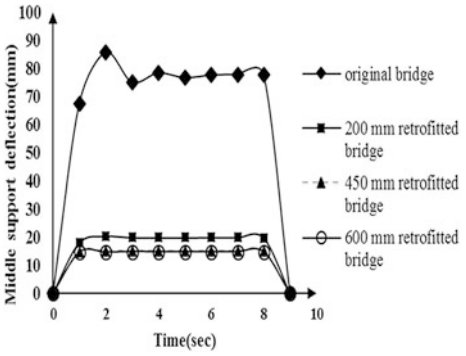

Fig. 8 Middle support deflection versus time

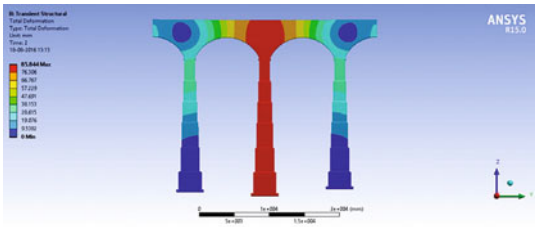

Fig. 9 Total deformation in original bridge

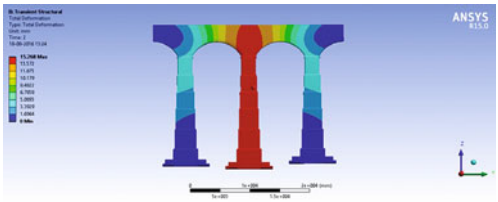

Fig. 10 Total deformation in 450-mm-thick retrofitted bridge

The deformation contour of the original bridge and 450 mm retrofitted bridges are shown in Figs. 9 and 10, respectively.

The maximum principal tensile stress due to the settlement of middle pier in the original structure was found to be 6.1248 MPa and the location is near the middle support. By introducing the concrete jacket of 450 mm, the maximum principal tensile stress was found to be 0.70446 MPa, which is significantly lower than the magnitude in the original structure. It is found that jacketing is an effective solution in reducing the stress in the structural elements of arch bridge subjected to support settlement.

7 Conclusions

In the analysis, excessive deformation is observed for original masonry arch bridge. In the case of retrofitted arch bridge, the deformation is found to be reduced to a large extent. Concrete jacketing at the intrados of the arches and around the piers is found to be effective in controlling the settlement of intermediate pier. It is found that 450 mm concrete jacket is a solution to control the excessive deformation due to middle support settlement. The principal tensile stresses in the structural elements of arch bridge subjected to support settlement are found to be considerably reduced by introducing the concrete jacket.

References

1. Gilbert, M. (2007). Limit analysis applied to masonry arch bridges: State-of-the-art and recent developments. In *ARCH'07—5th International Conference on Arch Bridges*.
2. Luboweicka, I., Arias, P., Reiveiro, B., & Solla, M. (2011). Multidisciplinary approach to the assessment of historic structures based on the case of a masonry bridge in Glacia (Spain). *Computers & Structures, 89,* 1615–1627.
3. Farhad, B., & Mahmood, A. (2011). Collapse analysis and strengthening of stone arch bridges against earthquake. *International Journal of Architectural Heritage, 7*(1).
4. Gonen, H., Dogan, M., Karacasu, M., Ozbasaran, H., & Gokdemir, H. (2013). Structural Failures in retrofit historical Murat masonry arch bridge. *Engineering Failure Analysis, 35,* 334–342.
5. Behnamfara, F., & Afshari, M. (2013). Collapse analysis and strengthening of stone arch bridges against earthquake. *International Journal of Architectural Heritage: Conservation, Analysis, and Restoration*, *7*(1).
6. Domede, N., Sellier, A., & Stablon, T. (2013). Structural analysis of a multi-span railway masonry bridge combining in situ observations, laboratory tests and damage modelling. *Engineering Structures, 56,* 837–849.
7. Kindij, A., Mandić Ivanković, A., & Vasilj, M. (2014). Adjustment of small-span masonry arch bridges to present-day demands, *Građevinar 1/2014, 66* (1), 37–49.
8. Reccia, E., Milani, G., Cecchi, A., & Trali, A. (2014). Full 3D homogenization approach to investigate the behavior of masonry arch bridges: The Venice trans-lagoon railway bridge. *Construction and Building Materials, 66,* 567–586.
9. Bridge Rules, *Research Designs and Standards Organization, Lucknow.*
10. Fanning, P. J., & Boothby, T. E. (2001). Three-dimensional modelling and full-scale testing of stone arch bridges. *Computers & Structures, 79,* 2645–2662.
11. Grandjean, A., & Brühwiler, E. (2009). Load-bearing capacity of masonry arch bridges using a plastic model. In Mazzolani (Ed.), *Protection of historical buildings, PROHITECH 09—© 2009*. London: Taylor & Francis Group. (*ISBN* 978–0-415-55803-7).
12. Raj, E. S., Srinivas, V., & Sakaria, E. P. (2014). Failure behaviour of masonry arch bridges using finite element analysis. *International Journal of Emerging Technology and Advanced Engineering, 4*(11).
13. Sowmiya, L. S., Shahu, J. T., & Gupta, K. K. (2010). Three dimensional finite element analysis of railway track. In *Indian Geotechnical Conference, GEOtrendz, IGS Mumbai Chapter & IIT Bombay*.
14. Sabale, V. D., Borgave, M. D., & Joshi, P. K. (2014). Non-linear finite element analysis of deep beam. *International Journal of Engineering Research & Technology (IJERT), 3*(5).
15. Molins, C., Casa, J., & Roca, P. (2007). Ultimate capacity of a curved multi-span arch bridge subjected to railway loads. In *Book of Congress Proceedings 5th International Conference on Arch Bridges* (pp. 593–600).
16. Arch Bridge Code; Code of Practice for the design and construction of masonry and plain concrete, Lucknow, India.

Part IV
New Building Materials for Sustainable Construction

Experimental Studies on Physical Properties and Strength Response of Construction and Demolition Wastes

Ashok Kumar Suluguru, Arkamitra Kar, Anasua GuhaRay and Naveen James

Abstract There is increasing inclination towards the reuse of construction and demolition wastes (CDWs), primarily containing building derived materials (BDM) in engineering practices such as ground improvement. Currently BDMs are used in the form of recycled aggregates that incur extra cost due to refinements. The present study, thereby, emphasizes on the use of virgin BDM. No previous studies related to its characterization and utilization in ground improvement have been reported till now. Hence, this study focuses on the characterization of BDM and its durability aspects through physical, chemical, and microscopic studies to test their compatibility when used in conjunction with local soil contaminated with aggressive chemicals. Soil composition varies based on the vicinity of a chemical plant, waste processing plant, or a coastal area. Results from this study can be used to encourage the practical use of BDM especially in chemically contaminated soil and developing relevant standard codes.

Keywords Construction and demolition wastes · Characterizations

A. K. Suluguru · A. Kar (✉) · A. GuhaRay
Department of Civil Engineering, BITS-Pilani Hyderabad Campus, Hyderabad 500078, India
e-mail: arkamitra.kar@hyderabad.bits-pilani.ac.in

A. K. Suluguru
e-mail: p2015406@hyderabad.bits-pilani.ac.in

A. GuhaRay
e-mail: guharay@hyderabad.bits-pilani.ac.in

N. James
Department of Civil Engineering, Indian Institute of Technology Ropar, Punjab 140001, India
e-mail: naveen.james@iitrpr.ac.in

A. Rama Mohan Rao and K. Ramanjaneyulu (eds.), *Recent Advances in Structural Engineering, Volume 1*, Lecture Notes in Civil Engineering 11,
https://doi.org/10.1007/978-981-13-0362-3_51

1 Introduction

Due to rapid urbanization and development of infrastructure, huge volume of construction waste is generated. Additionally, periodic renovation and modification of these structures produce large quantities of demolition waste. Further, natural calamities like earthquake may also lead to destruction of structures, creating a significant amount of solid demolition waste [1]. U.S. Environmental Protection Agency (USEPA) defines construction and demolition waste (CDW) as waste materials consisting of the debris generated during the construction, renovation, and demolition of buildings, roads, and bridges. As the construction industry greatly contributes to the present environmental unbalances, it is necessary to (i) drastically reduce the consumption of nonrenewable natural resources and (ii) limit the dumping of waste from CDW that takes up ever more limited space. Possible solutions to overcome these challenges are investigated in the present study. The primary component of CDW is building derived materials (BDM).

This paper is specifically aimed at working upon the analysis of BDM characteristics, so that they can be used for practical purposes such as ground improvement. Due to a critical shortage of natural aggregates, the availability of demolished concrete for use as BDM is rapidly increasing [2]. Presently, BDMs are used in the form of recycled concrete aggregates, but this refinement incurs extra cost due to chemical and mechanical processes associated with it [3–5]. Considering the Indian scenario, "Over the last five years, India's first and only recycling plant for CDW has saved the already-polluted Yamuna and the overflowing landfills of Delhi from 15.4 lakh tonnes of debris. A Ministry of Urban Development circular on June 28, 2012, directed States to set-up such facilities in all cities with a population of over 10 lakhs. But, till now the existing facility at Burari is the only one." [6]. Hence, the present study emphasizes on the use of virgin BDM to conserve natural aggregate, reduce the impact on landfills, and provide cost and energy benefits. If BDM are to be used for ground improvement, knowledge of its load carrying and durability characteristics are of utmost importance. The present study investigates the durability characteristics BDM on exposure to aggressive chemical environment. The results obtained from these tests are compared with the standard natural aggregate values for concrete pavement, owing to the lack of available data for BDM. The results obtained from Los Angeles abrasion test, specific gravity test, water absorption test, and aggregate impact value test comply with standard results for natural aggregates. Since the chemical composition of soil varies with location, the responses of BDM to aggressive chemicals are assessed. The BDM are immersed in separate solutions of seawater, sulfuric acid (5% v/v), nitric acid (5% v/v), and hydrochloric acid (5% v/v) for 7 days. The aforementioned aggregate tests are repeated for these BDM to identify the effect of these chemicals on BDM performance. According to ASCE, there are no global standards for recycled BDM in geotechnical applications [7, 8]. Hence, the results obtained from the proposed study can be used to establish a basis for the practical use of BDM in geotechnical

applications and provide recommendations which can be used to prepare standard codes of practice for these materials.

2 Materials

The BDM used for this study are procured from local construction sites. The Hyderabad campus of the Birla Institute of Science and Technology (BITS)-Pilani is undergoing extension, and thus producing huge amounts of construction as well as demolition wastes. The primary sources of these wastes are the demolition of some existing structural elements that are no longer serviceable, and the concrete cubes, cylinders, and prism specimens which are rejected from the concrete technology laboratory after preliminary testing for the new phase of construction.

The BDM used in the present study are thus predominantly concrete wastes. The compositions of cement, sand, and coarse aggregates used for the preparation of the relevant concrete mixes are available from the supplier. The procured concrete wastes were crushed to particles having sizes of 10 mm or less, based on suggestions from existing literature for inclusion of foreign materials in soil. The crushed BDM were then graded through sieve analysis and the results are furnished in Sect. 4. Seawater used for immersion of BDM is procured from the coastal regions in the vicinity of the Bay of Bengal. Commercially available laboratory grade sulfuric acid, hydrochloric acid, and nitric acid are procured and necessary amounts of deionized water added to prepare the respective 5%v/v solutions. The experimental techniques are detailed in the following section.

3 Experimental Methodologies

Before exposure to the aggressive chemical environmental conditions, some preliminary tests were carried out in order to identify the mineralogical composition of the available BDM. These include:

- X-ray diffraction (XRD) to identify the minerals present in the BDM. Bruker D8 Discover was the model used. The CuKα X-rays were generated at 40 mA and 40 kV. Scans were performed over 20°–80° 2θ range at 0.02° 2θ steps and integrated at the rate of 2 s step^{-1}. The results are presented in Fig. 1.
- Particle size analysis (following IS 2720 Part 4:1985 and Stereo microscopic imaging). Olympus SXZ7 stereo microscope was used to investigate the dimensions of the different particles comprising the crushed BDM having maximum size of 10 mm (Fig. 2). The minimum dimension that can be identified by this microscope is 20 μm. Stereo microscopy was also used to identify any characteristic surface features of the BDM for future comparison with BDM exposed to aggressive chemicals.

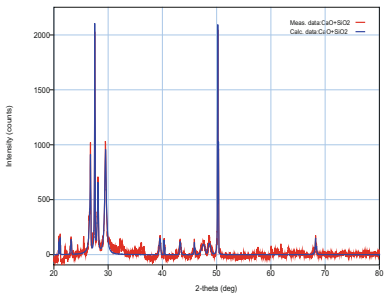

Fig. 1 X-ray diffractogram for virgin BDM powder

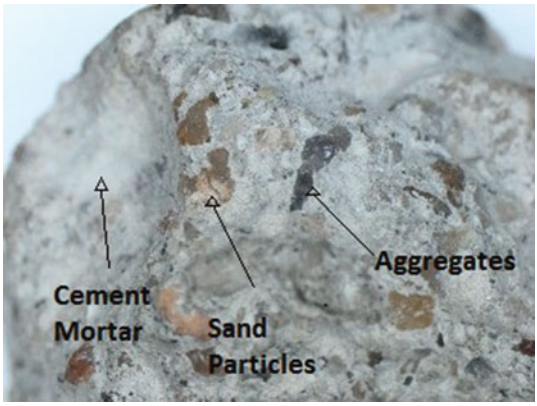

Fig. 2 Stereo microscopic image for virgin BDM particle at 2.5× magnification

Table 1 Comparison of AIV for BDM, before and after exposure to aggressive chemical attacks

Prevailing condition	AIV (%)
Before any chemical attack	35
After sea water attack	43.3
After sulfuric acid attack	36.7
After hydrochloric attack	36.7
After nitric acid attack	40

- Aggregate Impact Value Test according to IS-2386 Part 3 (1963) to identify the resistance of the BDM to degradation when subjected to impact. The values from this test were then compared with those from BDM exposed to aggressive chemical attacks (Table 1).
- Specific gravity and aggregate water absorption according to IS 2386-Part 3 (1963) were also determined for BDM to evaluate their compatibility when included in soil.

The BDM samples were then tested after exposure of 7 days to each of the following chemicals:

- *Sea water*
- *Sulfuric acid*
- *Hydrochloric acid*
- *Nitric acid*

5% v/v solutions of sulfuric acid, hydrochloric acid, and nitric acid were prepared for checking sulfate, chloride and nitrate attack, respectively. To study the extent of the attack, the samples were tested for the following after 7 days of immersion in the agents mentioned above:

- *Study of surface under stereo microscope*: After immersing the BDM in different aggressive chemicals for 7 days, they were observed under a stereo microscope to check for changes in surface characteristics (Figs. 3, 4, 5 and 6).
- *Study of loss of impact value due to attack*: An indirect idea about the bearing strength of aggregates can be measured by conducting the aggregate impact value test. After immersing the BDM in chemicals for 7 days, they were tested for impact value (as per IS: 2386 (Part IV)-1963). The difference in impact values due to these immersions is presented in Table 1.
- *Check for change of weight due to attack*: Depending on the compositions of the BDM, their immersions in different chemicals can produce different outcomes. Reactions may lead to either an increase in weight of the BDM or a decrease. This was being determined by measuring the BDM weight prior to immersion in the chemicals; and comparing these weights with those after 7 days of immersion. The differences were expressed in percentages w.r.t. the weight of BDM before immersion. The results are provided in Sect. 4.5.
- *XRD for BDM immersed in different chemicals*: To identify possible chemical changes upon comparison with the XRD patterns from virgin BDM. The results are provided in Sect. 4.6 (Figs. 7, 8, 9 and 10).

Fig. 3 Stereo microscopic image for BDM particle after 7-day immersion in seawater at 2.5× magnification

Fig. 4 Stereo microscopic image for BDM particle after 7-day immersion in sulfuric acid (5% v/v) solution at 2.5× magnification

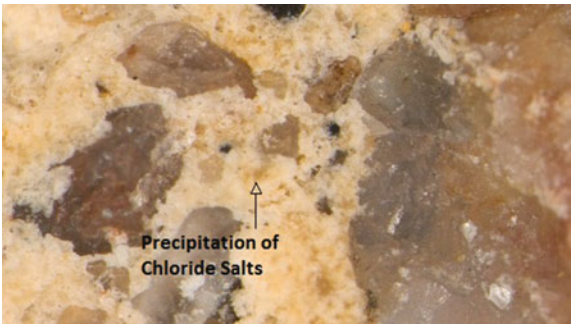

Fig. 5 Stereo microscopic image for BDM particle after 7-day immersion in hydrochloric acid (5% v/v) solution at 2.5× magnification

Fig. 6 Stereo microscopic image for BDM particle after 7-day immersion in nitric acid (5% v/v) solution at 2.5× magnification

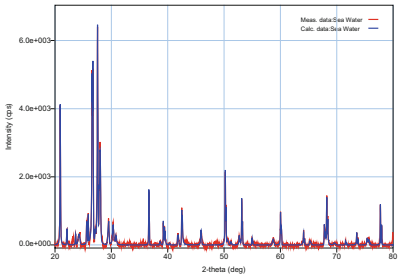

Fig. 7 X-ray diffractogram for powdered sample of BDM immersed in seawater for 7 days

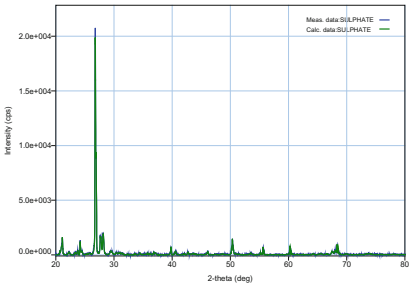

Fig. 8 X-ray diffractogram for powdered sample of BDM immersed in sulfuric acid for 7 days

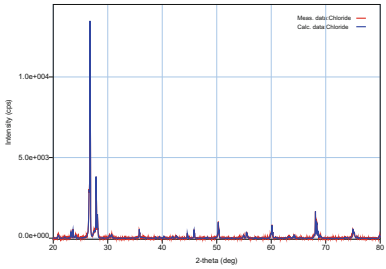

Fig. 9 X-ray diffractogram for powdered sample of BDM immersed in hydrochloric acid for 7 days

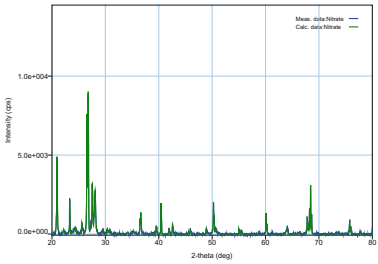

Fig. 10 X-ray diffractogram for powdered sample of BDM immersed in nitric acid for 7 days

4 Results and Discussions

4.1 X-ray Diffraction (XRD)

XRD patterns for powdered BDM showed the predominance of calcium silicates and quartz, as expected from Portland cement concrete. The sharp peaks corresponding to 2-theta values near 21°, 26°, and 51° represent crystalline quartz or silica. The smaller peaks between 2-theta values of 30° to 40° represent the tricalcium silicate and dicalcium silicate component of Portland cement, whereas the peaks near 2-theta values of 36° and 45° represent the calcium hydroxide component due to hydration of Portland cement. The flatter portions of the diffractogram containing small humps represent amorphous hydrated cementitious paste

component. These conclusions were drawn through comparisons with existing research [9–11].

4.2 Stereo Microscopy

As mentioned earlier, the virgin BDM particles having maximum size of 10 mm were investigated under the stereo microscope. The regions of interest were selected at random. The advantage of a stereo microscope over an optical microscope is the identification of surface undulations or unevenness. If two regions on the same image have difference in focus or clarity, it indicates that they are different elevations. Before exposure to aggressive chemicals, visual inspection of the images (Fig. 2) showed the BDM consisted of hardened cementitious paste, cement mortar, and aggregates. Grayish areas on the image indicate the hardened cementitious and cement mortar. The brownish regions may indicate sand particles and the blackish areas are most likely to indicate the limestone aggregate components. The images were captured at magnification of 2.5×. The dimensions of the area covered in each image for that magnification are 3.376 mm (length) by 1.894 mm (height), which is the total area visible in each image (Figs. 2, 3, 4, 5 and 6). Knowledge of these dimensions provides a perspective on the respective sizes of the particles visible in the images. Section 4.5 presents the images taken on separate BDM specimens after immersion in different chemicals for 7 days.

4.3 Aggregate Impact Value (AIV) Test

This section presents the results of the AIV test (Table 1) for BDM specimens, before and after immersion in different chemicals. The duration of immersion was 7 days. The impact value test on the virgin BDM (max. size of 10 mm) resulted in the value of 35%. This is equal to the maximum permissible AIV for natural aggregates according to IS-2386: Part 3 (1963) for cement concrete pavements. Sulfuric acid and hydrochloric acid immersions did not affect much of its AIV (36.7% compared to 35% before the immersion). But as the limiting value is 35%, the use of BDM in sulfuric acid or sulfate-prone zones and in the presence of chlorides are discouraged. In case of nitric acid attack, the impact value is found to be 40% (relatively high in comparison to the prior value) much higher than the limiting value and thus this kind of attack results in adverse effects. The impact value is very high (43.3%) in case of a seawater immersion.

4.4 Specific Gravity and Water Absorption

The average specific gravity for the BDM was determined to be 2.48 after taking means of three samples. The specific gravity of aggregates used for road construction lies in the range of 2.5–3.0 with an average value of 2.68 as a preferred value. The BDM used for the present study was thus almost complying with the lower limit of the standard coarse aggregate values.

The water absorption for the same BDM was found to be 1.182%, which is less than the maximum permissible limit of 2% for aggregates used in cement concrete pavements. These two tests serve as a metric to evaluate the quality of BDM obtained from various sources.

4.5 Stereo Microscopy on BDM in Aggressive Chemicals

4.5.1 Seawater

Figure 3 presents the stereo microscopic image for BDM particle after 7-day immersion in seawater, at 2.5× magnification. The dimensions of this image are identical to Fig. 2. Visual comparison of BDM before exposure to seawater shows whitish deposition on the surface. These deposits are the effect of dissolved salts present in seawater. The resulting change in weight of BDM was determined and found to be less than 1%, hence negligible. However, this deposition distorts the physical appearance of the BDM and also reduces its impact value, as mentioned in Table 1.

4.5.2 Sulfuric Acid

Figure 4 presents the stereo microscopic image for BDM particle after 7-day immersion in sulfuric acid, at 2.5× magnification. The dimensions of this image are identical to Fig. 2. Visual comparison of BDM before exposure to sulfuric acid solution (5% v/v) shows yellowish white deposition on the surface. These deposits could be precipitation of sulfate salts on the BDM surface. The resulting change in weight of BDM was determined and found to be 6.67%. This significant amount of deposition distorts the physical appearance of the BDM and also reduces its impact value, as mentioned in Table 1.

4.5.3 Hydrochloric Acid

Figure 5 presents the stereo microscopic image for BDM particle after 7-day immersion in hydrochloric acid, at 2.5× magnification. The dimensions of this

image are identical to Fig. 2. Visual comparison of BDM before exposure to hydrochloric acid solution (5% v/v) shows light brown to yellowish white deposition on the surface. These deposits could be precipitation of chloride salts on the BDM surface. The resulting change in weight of BDM was determined and found to be less than 1%. This deposition distorts the physical appearance of the BDM and also reduces its impact value, as mentioned in Table 1.

4.5.4 Nitric Acid

Figure 6 presents the stereo microscopic image for BDM particle after 7-day immersion in nitric acid, at 2.5× magnification. The dimensions of this image are identical to Fig. 2. Visual comparison of BDM before exposure to nitric acid solution (5% v/v) shows yellow to brown deposition on the surface. These deposits could be precipitation of nitrate salts on the BDM surface. The resulting change in weight of BDM was determined and found to be less than 1%. This deposition distorts the physical appearance of the BDM and also reduces its impact value, as mentioned in Table 1.

4.6 XRD for BDM Immersed in Chemicals

XRD patterns for powdered BDM showed the predominance of calcium silicates and quartz, as expected from Portland cement concrete.

4.6.1 BDM in Seawater

On comparison with Fig. 1, additional peaks were observed for KCl (26°, 28°, 42°, 68°, 74°), NaCl (32°, 44°, 66°, 77°), $CaCl_2$ (29°, 31°, 42°, 43°, 61°) [12, 13]. These results are consistent with the fact that seawater contains these dissolved salts. This also explains the change in appearance of the BDM when investigated through stereo microscope and the possible reason for the decrease in AIV.

4.6.2 BDM in Sulfuric Acid

On comparison with Fig. 1, additional peaks were observed for gypsum, $CaSO_4.0.5H_2O$ (21°, 23°, 29°) [14]. This is expected due to the high sulfate content in sulfuric acid. This explains the change in appearance of the BDM when investigated through stereo microscope and also the possible reason for the decrease in AIV.

4.6.3 BDM in Hydrochloric Acid

On comparison with Fig. 1, additional peaks were observed for gypsum, $CaCl_2$ (29°, 43°, 61°) [14]. This is expected due to the high chloride content in sulfuric acid. Presence of KCl was also observed (26°, 68°, 74°). This explains the change in appearance of the BDM when investigated through stereo microscope and also the possible reason for the decrease in AIV and change in weight.

4.6.4 BDM in Nitric Acid

On comparison with Fig. 1, additional peaks were observed for potassium nitrate, KNO_3 (27°, 29°, 68°) [15]. This showed presence of potassium in the BDM and the corresponding deposition on its surface. This can be the possible reason for the decrease in AIV.

It was observed that weight of the sample increased by 6.67% after sulfuric acid attack. But, there was no notable change in weight of the BDM due to any of the other attacks.

5 Conclusions

From the aggregate impact values, it is clearly visible that the BDM get strongly influenced by the presence of aggressive chemicals. The decrease in AIV results clearly suggests that durability of BDM in such chemical environment is significantly less. Change in weight of BDM due to sulfuric acid immersion indicates the possibility of expansion if they are exposed to a soil containing sulfates. Thus, further studies are required to improve the durability characteristics of BDM if it to be used as an inclusion material in soils containing such chemical contaminant. As a follow-up to the present study, soil-BDM mixtures will be tested in the future, for bearing capacity and shear strength through plate load tests and shear box tests. This will help to evaluate the utility of BDM in ground improvement.

Acknowledgements The authors would like to thank the Science and Engineering Research Board (SERB), Govt. of India for supporting the present study through the Early Career Research Award. The authors are grateful to BITS-Pilani, Hyderabad campus for providing the materials and the laboratory setup required to conduct the experiments. The authors would also like thank Ms. Stuti Mondal, Mr. P. Hemanth Kumar, and Mr. Kaushal Raut for their assistance with the experimental work.

References

1. USEPA. (2015). *Lifecycle challenge competition seeks new ideas to reduce construction and demolition debris*. http://www3.epa.gov/region9/waste/solid/construction/. Last accessed on February 11, 2016.
2. Meyer, C. (2004, August). Concrete materials and sustainable development in the United States. *Structural Engineering International*, 10 p.
3. Sustainability Victoria. (2005*). Annual survey of Victorian recycling industries 2004–2005* (1–28).
4. Arulrajah, A., Piratheepan, J., Ali, Y. M. M., & Bo, M. W. (2012). Geotechnical properties of recycled concrete aggregate in pavement sub-base applications. *Geotechnical Testing Journal, 35*(5), 1–9.
5. Poon, C. S., & Chan, D. (2006). Feasible use of recycled concrete aggregates and crushed clay brick as unbound road sub-base. *Construction and Building Materials, 20,* 578–585.
6. The Hindu. (2014). *India's first plant that recycles construction waste*. Available at: http://www.thehindu.com/news/cities/Delhi/indias-first-plant-that-recycles-construction-waste/article6362727.ece. Last accessed on February 12, 2016.
7. Melton, J. S. (2015, July 24). Recycled base aggregates in pavement applications—Part III of VI (AWI051611). *Sustainable Geotechnical Applications*: Webinar hosted by ASCE.
8. Edil, T. B. (2015, July 24). Tire derived aggregate in geotechnical and environmental applications—Part V of VI (AWI062811). *Sustainable Geotechnical Applications*: Webinar hosted by ASCE.
9. Kupwade-Patil, K., & Allouche, E. (2011). Effect of alkali silica reaction (ASR) in geopolymer concrete. In *World of Coal Ash (WOCA) Conference*, May 9–12, 2011, Devnver, CO, USA.
10. Kar, A., Ray, I., Halabe, U. B., Unnikrishnan, A., & Dawson-Andoh, B. (2014). Characterizations and estimation of alkali activated binder paste from microstructures. *International Journal of Concrete Structures and Materials, 8*(3), 213–228.
11. Mindess, S., Young, J. F., & Darwin, D. (2003). *Concrete.* New Jersey: Prentice Hall, Pearson Education, Inc.
12. Bontempi, E., Zacco, A., Borgese, L., Gianoncelli, A., Ardesi, R., & Deper, L. E. (2010). A new method for municipal solid waste incinerator (MSWI) fly ash inertization, based on colloidal silica. *Journal of Environmental Monitoring, 12,* 2093–2099.
13. Lim, M., Han, G. C., Ahn, J. W., & You, K. S. (2010). Environmental remediation and conversion of carbon dioxide (CO(2)) into useful green products by accelerated carbonation technology. *International Journal of Environmental Research and Public Health, 7*(1), 203–228.
14. U. S. Geological Survey Open-File Report 01-041. (2016). *A laboratory manual for X-ray powder diffraction*, Available at: http://pubs.usgs.gov/of/2001/of01-041/htmldocs/links.htm. Last accessed: September 7, 2016.
15. Yildirim, M., Kipcak, A. S., Senberber, F. T., Asensio, M. O., Derun, E. M., & Piskin, S. (2015). The determination of the potassium nitrate, sodium hydroxide and boric acid molar ratio in the synthesis of potassium borates via hydrothermal method. *World Academy of Science, Engineering and Technology International Journal of Chemical, Molecular, Nuclear, Materials and Metallurgical Engineering, 9*(5), 597–600.

Combined Effect of Steel Fibers with Ferrochrome Slag on Hardened Concrete

Rohit Shah and Tribikram Mohanty

Abstract Research on concrete technology is of vital importance in the present world as concrete is used in a variety of environments, many of them being aggressive in nature. As such, new explorations are being done in an everyday basis, to increase the mechanical properties of concrete, as well as making them cost-efficient. But significant research has not been done in the combined effects of steel fiber along with ferrochrome ash, and hence not much is known about the effects imposed by the combination on the properties of concrete. Ferrochrome ash is a by-product of industrial wastes, which has been seen to have considerable resistive strength. This, in combination with steel fiber, which is known for its strength-increasing property in concrete was used. The results of the experiment were found to be satisfactory, as the use of small proportions in ferrochrome ash along with steel fiber was seen to considerably improve the mechanical properties. Compressive strength was seen to develop at a great rate in the different combinations, however for the combination of 10% ferrochrome + 2% steel fiber, all the properties were seen to get the highest influence. Strength started depreciating however, on increasing the steel fiber beyond 2%, as it resulted in lower workability. Thus through this study, properties of ferrochrome ash as well as steel fiber, and their effects on concrete strengths, were presented.

Keywords Ferrochrome slag · Steel fibers · Fiber reinforced concrete

1 Introduction

As we all know concrete is weak in tension and strong in compression. Hence, ordinary concrete is used with steel reinforcement. Nowadays, concrete is reinforced with fibers which are distributed in a random way. Along with toughness and energy absorption ability, tensile strength and flexural strength are also improved

R. Shah · T. Mohanty (✉)
Department of Civil Engineering, KIIT University, Bhubaneswar 751024, Odisha, India
e-mail: tmohantyfce@kiit.ac.in

A. Rama Mohan Rao and K. Ramanjaneyulu (eds.), *Recent Advances in Structural Engineering, Volume 1*, Lecture Notes in Civil Engineering 11,
https://doi.org/10.1007/978-981-13-0362-3_52

[1]. Micro-cracks which are present in mortar aggregate interface are responsible for inborn weakness of ordinary concrete. This can be reduced by the addition of fiber in concrete mixture [2]. Toughness and resistant to crack growth can be improved by adding various type of fibers in ordinary concrete. When the load is distributed to micro-crack by the help of fibers in concrete, the concrete is known as fiber reinforced concrete [1, 3]. Fibers of different sizes and shapes are obtained from steel, glass, natural materials, and carbon. Generally, steel fibers are preferred for both nonstructural and structural purpose. At failure, mechanical properties of concrete are affected by the addition of fiber in concrete. The strong mechanism of fibers contains the distribution of stress from the matrix to fibers by the bond between the matrix and fibers [4]. Behavior of fiber reinforced concrete in strength is controlled by fiber content and its efficiency. Effectiveness of fiber is maintained by the resistance to pull out which generally depends on bond at interface of fiber matrix. Pullout resistance improves with length of the fiber which is directly proportional to inter-facial area. It has been found that with decrease in diameter of fiber, inter-facial area available is large enough for bonding. The bond is comparatively more effective for small area of a given length of a fiber. This effect is expressed by aspect ratio. Ratio of length of fiber to diameter of fiber is known as aspect ratio. Higher aspect ratio improves the efficiency of fiber. The preparations of FRC are done by using lower water/cement ration and higher cement content [5].

Ferrochrome is considered as a relatively nonhazardous industrial waste material in the form of powder is prepared from the ferrochromium industry. Nowadays, the requirement of concrete is increased rapidly with the growing population. Major component of concrete is cement. Manufacture of cement is a highly energy taking process [6]. Huge amount of CO_2 (Carbon dioxide) and other greenhouse gases are released from cement industries, causing global warming. To reduce global warming and conserve natural resources, we have to reduce the generation and utilization of cement. Thus, the replacement of cement has become necessary to reduce global warming. A number of researches have been done on how to use industrial wastes as a replacement material in concrete constitute. From the researches, the results which were obtained show that replacing substituent materials not only increases the concrete properties but also leads to development in the concrete strength economically [6].

It is well known fact that ferrochrome is produced at a quantity of 6.5–9.5 million ton worldwide. The increment in the rate of production is 2.8–3% per annum. From approximately 1.2 metric ton of solid waste, 1 metric ton of ferrochrome powder is obtained. Another application of ferrochrome powder is utilization as dumping waste in landfills [6].

Few researches have been carried out to use ferrochrome slag aggregates by partially replacing normal aggregates along with partially lime replacement by cement in concrete, without sacrificing or even improving strength and durability properties of concrete.

In this present experimental study, ferrochrome powder has been used as an alternative construction material instead of OPC along with application steel fiber by the replacement of weight of concrete.

2 Literature Review

Shende et al. [1] investigated compressive, flexural, split tensile strength of SFRC, containing 0, 1, 2 and 3% hooked end steel fiber by volume fiber for M-40 grade of concrete with water cement ratio 0.35. Steel fiber with aspect ratio of 50, 60 and 67 was used. The data obtained has been studied and compared with standard concrete sample (0% fiber). From the result data, it was observed that properties of SFRC are on higher side for 50 aspect ratio in comparison to 60 and 67 aspect ratio. With the addition fiber, it was seen that compressive, flexural and split tensile strength was increased by 10–30%. Almottiri [2] investigated that the structural behavior of steel fiber reinforced fly ash concrete under compression and flexure by conducting tests on standard control specimens. Addition of steel fiber and fly ash in concrete improves the structural properties, mainly its flexural strength. It was found that for up to 1.5% of steel fiber and up to 30% of fly ash in concrete compressive and flexural strength both gets improved. Research showed that SFRC shows better resisting ability to flexural stress whereas fly ash concrete shows better resisting ability to compressive stress. 1–1.5% of steel fibers by volume of concrete along 15–25% of fly ash which was replaced by cement and it was considered as the optimum percentage. By inclusion of fly ash, the workability of concrete was improved which was necessary for higher quantity of steel fibers. Khadake and Konapure [3] studied the properties of SFRC for M-25 grade of concrete having mix proportion 1:1:5:3.17 and water/cement ratio 0.465. They used the hooked end steel fiber of aspect ratio of 71. They used the fiber at 0.5–1.5% by volume of concrete and fly ash from 10 to 30% by weight of cement. They compared the result with standard concrete and from the results it was seen that compressive strength was more for fly ash 10 and 20% for 1 and 2% steel fiber in it. From Acharya and Patro [6] study, it was found that they replaced the ferrochrome ash with cement from 10 to 40% along with 7% of lime. They investigated the properties of concrete like compressive, flexural, and split tensile strengths along with water permeability of concrete. The results showed that there was improvement in early strength. For 40% ferrochrome ash and 7% lime replacement in concrete with cement shows nearly equal properties to that of ordinary concrete for 28 days. Durability of concrete was improved for later age in concrete. From their study, it was found that there was maximum improvement in durability properties and strengths for mix having 10% ferrochrome and 7% lime. It was also found that bonding was improved between cement paste and aggregates due to the addition of ferrochrome and lime (Fig. 1).

Fig. 1 Steel fiber

3 Materials and Its Properties

3.1 Cement

For this present study, OPC-43 grade of cement was used which was tested as per IS: 8112-1989.

3.2 Aggregates

For preparing cement mix, fine aggregate (sand) has been collected from local river bed conforming to Zone-III. The maximum size of sand particles was 4.5 mm tested as per IS: 383-1970. Fresh coarse aggregate of 10–20 mm size was taken for experimental purpose as per IS: 383-1970.

3.3 Steel Fiber

FRC is defined as a composite material mixed with ordinary Portland cement, aggregate, and adding discrete discontinuous fibers. It is well known in improving the structural durability of the concrete. In terms of shape and size, there are various steel fiber available in the market such as straight, crimped, hooked end, deformed, and irregular steel fiber. Their cross section varies from 0.25 to 0.75 mm. For this experimental study, crimped from of steel fiber was used. Its diameter was 0.6 and 30 mm long with aspect ratio (l/d) 50 (Fig. 2).

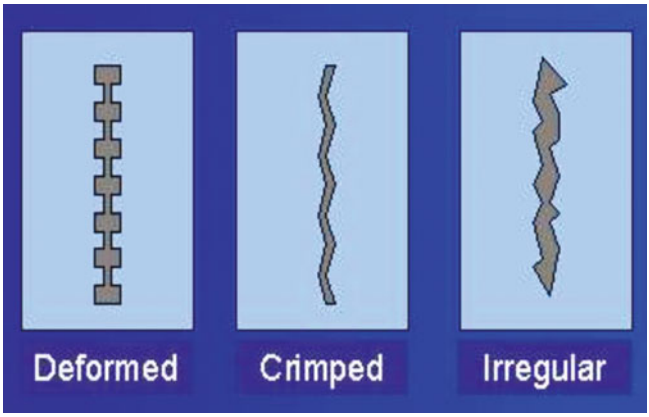

Fig. 2 Types of steel fiber

3.4 Ferrochrome Powder

Ferrochrome (FeCr) known as "Charge Chrome" is a corrosion resistant alloy of chrome and iron containing between 50 and 65% Chrome. Ferrochromium is extracted from the chromium ore to produce the final product. The metal and primary slags are tapped from the furnaces approximately at every 2 h. The chrome is tapped through a furnace tap hole into a ladle and is then cast into silica and ferrochromium fines moulds. Primary slag (also termed untreated), a semisolid waste still containing ferrochromium and 2% moisture, is tapped into a slag bell (a big round pot-like container) and processed through a metal-recovery processing (MRP) plant where the slag is crushed, screened, and separated from the residual metal through a hydro-jigging process. The metal and slag (now termed final, treated, or weathered slag) are separated during this process as a result of their differences in density and the final slag is dumped on site. So ferrochrome slag is a by-product from the production of ferrochrome, an essential component in stainless steel. Extensive tests have been carried out on the physical properties of the ferrochrome slag from different organization and it was found to be highly suitable as construction material [6].

4 Experimental Program

For concrete with steel fiber and ferrochrome powder replacement:

In this mix, steel fiber was replaced with by various (1, 2 and 3%) weights of concrete and ferrochrome powder was replaced with by weight of cement (10, 20 and 30%).

1. First, dry tray and bucket were taken.
2. Required weight of aggregate was taken in tray and put in the pan mixer.
3. Sand of required weight was taken in tray and put in the pan mixer.
4. Ferrochrome powder of required weight is taken and it was also put in the pan mixer and all the three materials were dry mixed for 1–2 min.
5. After that steel fiber of required weight was taken in tray and put in the pan mixer. Now, water of required weight was taken in bucket and mixed in dry mixture in small quantities gradually so that the mix is uniformly gauged and workability is proper. Now, run the mixer for 2–3 min and check the mix quality.

5 Results

See Figures 3, 4 and 5, Tables 1, 2 and 3.

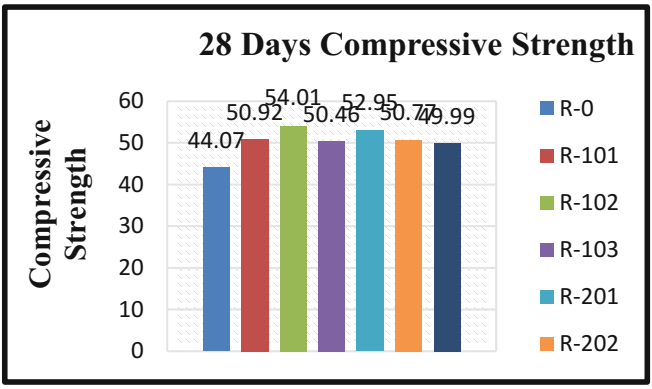

Fig. 3 28 Days compressive strength

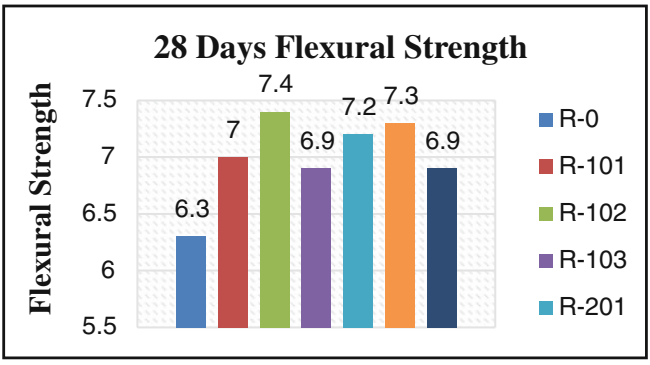

Fig. 4 28 Days flexural strength

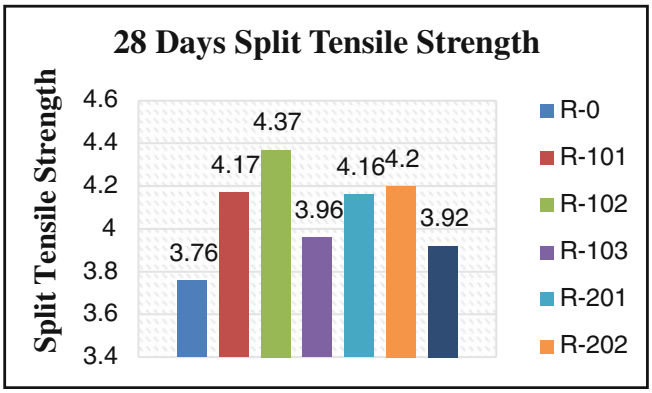

Fig. 5 28 Split tensile strength

Table 1 Compressive strength of SFFCA concrete

Mix type	Age in days	Test details	Steel fiber and FeCr ash concrete			
			C-1	C-2	C-3	Avg.
R-201	7	Wt. in Kg.	9.13	9.17	9.07	9.12
		Load in KN	697.95	707.18	692.55	699.3
		Stress in Mpa	31.02	31.43	30.78	31.08
	28	Wt. in Kg.	9.09	9.14	9.2	9.14
		Load in KN	1195.88	1206.68	1171.58	1191.3
		Stress in Mpa	53.15	53.63	52.07	52.95
R-202	7	Wt. in Kg.	9.18	9.12	9.06	9.12
		Load in KN	696.38	702.68	682.2	693.9
		Stress in Mpa	30.95	31.23	30.32	30.84
	28	Wt. in Kg.	9.03	9.12	9.09	9.08
		Load in KN	1136.7	1156.5	1133.78	1142.3
		Stress in Mpa	50.52	51.4	50.39	50.77

6 Conclusions

In this present experimental study, the combined effect of steel fiber and ferrochrome ash has been discussed in a detailed manner. Considering the behavior of additive added in concrete mixes, some of the important observation can be noted:

1. Results show that concrete mix containing steel fiber + ferrochrome ash proved to be effective in increasing the compressive strength of hardened concrete.
2. Observation from graphs reveal that approximately 10–25% increment in compressive strength can be achieved.

Table 2 Flexural strength of SFFCA concrete

Mix type	Age in days	Test details	Steel fiber and FeCr ash concrete		
			P-1	P-2	Average
R-101	7 Days	Load in KN	13	13.5	13.25
		Stress in MPa	5.2	5.4	5.3
	28 Days	Load in KN	17	18	17.5
		Stress in Ma	6.8	7.2	7.0
R-102	7 Days	Load in KN	13.8	14	13.9
		Stress in Mpa	5.5	5.6	5.55
	28 Days	Load in KN	18	19	18.5
		Stress in Mpa	7.2	7.6	7.4
R-103	7 Days	Load in KN	15.5	15.0	15.75
		Stress in Mpa	6.2	6.0	6.3
	28 Days	Load in KN	17.5	17.0	17.25
		Stress in Mpa	7.0	6.8	6.9

Table 3 Split tensile strength of SFFCA concrete

Mix type	Age in days	Test details	Steel fiber and FeCr ash concrete		
			CY-1	CY-2	Average
R-101	7 Days	Load in KN	232.0	238.0	235.0
		Stress in Mpa	3.28	3.37	3.33
	28 Days	Load in KN	293.5	296.5	294.0
		Stress in Mpa	4.15	4.19	4.17
R-102	7 Days	Load in KN	265.0	270.0	267.5
		Stress in Mpa	3.75	3.82	3.79
	28 Days	Load in KN	306.5	311.0	308.75
		Stress in Mpa	4.34	4.40	4.37
R-103	7 Days	Load in KN	236.5	240.5	238.5
		Stress in Mpa	3.35	3.40	3.38
	28 Days	Load in KN	277.0	282.0	279.5
		Stress in Mpa	3.92	3.99	3.96
R-201	7 Days	Load in KN	15.5	16.5	16.0
		Stress in Mpa	6.2	6.6	6.4
	28 Days	Load in KN	17.5	18.5	18.0
		Stress in Mpa	7.0	7.4	7.2
R-202	7 Days	Load in KN	15.5	15.0	15.25
		Stress in Mpa	6.2	6.0	6.1
	28 Days	Load in KN	18.0	18.5	18.25
		Stress in Mpa	7.2	7.4	7.3

3. Substitution of 2% steel fiber + 10% ferrochrome ash and 1% steel fiber + 20% ferrochrome ash proved to be the best combination for compressive strength.
4. It is observed from graph that there is 10–15% increment in flexural strength of concrete mix containing steel fiber + ferrochrome ash.
5. Observation from graph show that approx. 5–10% of increment in split tensile strength can be achieved.
6. Substitution of 2% steel fiber + 10% ferrochrome ash and 2% steel fiber + 20% ferrochrome ash proved to be the best combination for flexural and split tensile strength.

References

1. Shende, A. M., Pande, A. M., & Pathan, M. (2012). Gulfam, experimental study on steel fiber reinforced concrete for M-40 grade. *International Refereed Journal of Engineering and Science (IRJES), 1*(1), 043–048.
2. Almottiri, F. A. (2011). Physical properties of steel fiber reinforced cement composites made with fly ash. *Jordan Journal of Civil Engineering, 5*(2), 281–286.
3. Khadake, S. N., Konapure, C. G. (2012) An investigation of steel fiber reinforced concrete with fly ash. *IOSR Journal of Mechanical and Civil Engineering (IOSR-JMCE), 4*(5), 01–05. ISSN: 2278-1684.
4. Sakthieswaran, N., & Ganesan, K. (2014). Compressive strength of concrete containing fly ash, copper slag, silica fume and fibres–prediction. *International Journal of Engineering and Computer Science*, *3*(2), 3891–3896. ISSN:2319-7242.
5. Rai, A., & Joshi, Y. P. (2014). Applications and properties of fibre reinforced concrete. *Int. Journal of Engineering Research and Applications (IJERA), 4*(5) (version1), 123–131.
6. Acharya, P. K., & Patro, S. K. (2015). Effect of lime and ferrochrome ash (FA) as partial replacement of cement on strength, ultrasonic pulse velocity and permeability of concrete. *ScienceDirect, Construction and Building Materials, 94,* 448–457.

An Experimental Investigation to Determine the Properties of Fly Ash Based Geopolymers as per Indian Standards

Suman Saha and C. Rajasekaran

Abstract Production of ordinary Portland cement requires huge quantity of natural resources and also releases huge quantity of carbon dioxide into the atmosphere. Research efforts have been continuing to establish geopolymer as an alternative cementitious material for the replacement of ordinary Portland cement. This paper presents the study to find out the properties of fly ash based geopolymer paste and 28 days compressive strength of geopolymer mortar. Standard consistency, setting time of geopolymer paste has been determined using vicat's apparatus (according to Indian Standards), which is followed for cement paste, varying the concentration of sodium hydroxide solution from 6 to 16 M. Results indicate higher standard consistency, more time required for setting for fly ash based geopolymer than that of cement paste. Compressive strength of the geopolymer paste and mortar 17 specimens increases with the increase of the concentration of sodium hydroxide solution and decrease beyond 14 M.

Keywords Geopolymer · Standard consistency · Setting time · Compressive strength · Paste · Mortar

1 Introduction

Concrete is the most used construction material next to water. Ordinary Portland cement (OPC) is the main ingredient of the concrete. At present scenario, usage of ordinary Portland cement becomes very high due to the huge demand of concrete as construction industry is growing rapidly. The huge demand for concrete using OPC has resulted in high volume of carbon dioxide (CO_2) emission, and leads to

S. Saha · C. Rajasekaran (✉)
Department of Civil Engineering, National Institute of Technology Karnataka, Surathkal, Mangalore 575025, India
e-mail: bcrajasekaran@nitk.edu.in

S. Saha
e-mail: sumansaha.civil@gmail.com

A. Rama Mohan Rao and K. Ramanjaneyulu (eds.), *Recent Advances in Structural Engineering, Volume 1*, Lecture Notes in Civil Engineering 11,
https://doi.org/10.1007/978-981-13-0362-3_53

environmental problems continuously and also results in huge depletion of natural resources. The production process of OPC emits huge quantity of CO_2 into the atmosphere. The cement manufacturing industries release approximately 1 tonne of carbon dioxide into the atmosphere to produce 1 tonne of OPC. This is approximately 5–7% CO_2 emissions of the global CO_2 emissions [1, 2]. Research efforts are continuing throughout the world to find alternative binder materials for the production of concrete. Geopolymer is produced from the reaction between materials, which are rich in Si or Al (e.g. fly ash, slag, etc.) and alkali solutions (sodium hydroxide and sodium silicate), is trying to consider as replacement of cement in concrete. 'Geopolymer' was first introduced by Prof. Davidovits in 1978 to represent a broad range of materials characterized by chains or networks of inorganic molecules [3]. Geopolymer does not form calcium-silicate-hydrates (C–S–Hs) for matrix formation and strength, but utilize the poly-condensation of silica and alumina precursors to attain structural strength. Two main constituents of geopolymer are source materials and alkaline liquids. The source materials should be rich in silicon (Si) and aluminium (Al). They can be by-product materials such as fly ash, silica fume, slag, rice husk ash, red mud, etc. Geopolymers are also unique in comparison to other alumino-silicate materials (e.g. alumino-silicate gels, glasses, and zeolites). The mechanism of geopolymerization has been divided into three main stages: (i) Dissolution of oxide minerals from the source materials (usually silica and alumina) under highly alkaline condition; (ii) transportation/orientation of dissolved oxide minerals followed by coagulation/gelation; (iii) poly-condensation to form 3-D network of silico-aluminates structures [1]. Based on the types of resultant chemical bonding, three types of structures can be derived from the 3-D alumino-silicate network: poly (sialate) (–Si–O–Al–O–), poly (sialate-siloxo) (Si–O–Al–O–Si–O) and poly (sialate-disiloxo) (Si–O–Al–O–Si–O–Si–O) [4].

The schematic formation of geopolymer material is described as shown below [5–7].

$$(Si_2O_5.Al_2O_2)_n + H_2O + OH^- \longrightarrow Si(OH)_4 + Al(OH)^{4-}$$

$$Si(OH)_4 + Al(OH)^{4-} \longrightarrow (-\underset{\underset{O}{|}}{Si}-O-\underset{\underset{O}{|}}{Al}-O-)_n + 4H_2O$$

A brief description of conceptual model of geopolymerization was described as shown in Fig. 1 [8].

Investigation on the effect of silica and alumina contents on setting, phase development, and physical properties of high calcium fly ash (Class C) based geopolymers reveals that setting of geopolymer was accelerated with the increase of both alumina and silica [9]. Whereas setting time of fly ash based geopolymer with use of potassium hydroxide (KOH) for different fly ash to alkaline solution ratio reported that as the ratio increases, the setting time decreases [4]. Study on the mechanical and physical properties of fly ash based geopolymer by varying solid-to-liquid ratio using sodium hydroxide as the only activator was carried out and reported optimum solid/liquid ratio of 4 for getting highest compressive strength [10]. Two different temperatures (65 and 85 °C) as curing temperature and

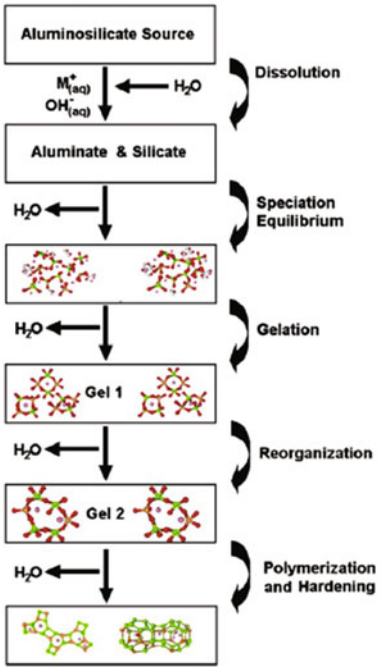

Fig. 1 Conceptual model of geopolymerization [8]

three different durations (2, 5 and 24 h) of heat curing were used to determine the properties of class F type of fly ash based geopolymer varying the concentration of sodium hydroxide solution and concluded that the optimal concentration of NaOH solution was 6 M and observed that an increase in the curing temperature increased the compressive strength [11]. Different curing conditions on the properties of high calcium fly ash based geopolymer were investigated and high early compressive strength for temperature curing was observed [12].

In this paper, an attempt has been made to study the properties of fly ash based geopolymers by varying the concentration of sodium hydroxide solution and the ratio of sodium silicate solutions to the hydroxide solutions. To determine the properties of geopolymer, casting of samples, test procedures, etc., has been done as described in Indian Standards (IS-4031), which is followed to determine the properties of ordinary Portland cement [13–17].

2 Experimental

2.1 Materials

In the present investigation, fly ash, locally available sand, alkali solutions (combination of sodium hydroxide solution and sodium silicate solution) and water were used as materials for the preparation of samples.

Table 1 Properties of fine aggregates

Characteristics	Value
Type	Sand
Specific gravity	2.67
Fineness modulus	2.78
Grading zone	II

2.1.1 Fly Ash

Fly ash (FA) is a by-product waste material of thermal power plants resulting from the combustion of pulverized coal in the coal-fired furnaces. There are two types of fly ash. For this research work, class F type of fly ash was used.

2.1.2 Sand

The aggregate material which passes through 4.75 mm IS sieve and retained on 75 micron IS sieve is termed as fine aggregate [18]. The sand used for the experimental works is locally procured and conformed to grading zone II (IS: 383-1970) [19]. Table 1 represents the properties of fine aggregates used in this study. Figure 2 shows the particle size distribution of sand used for this experimental work.

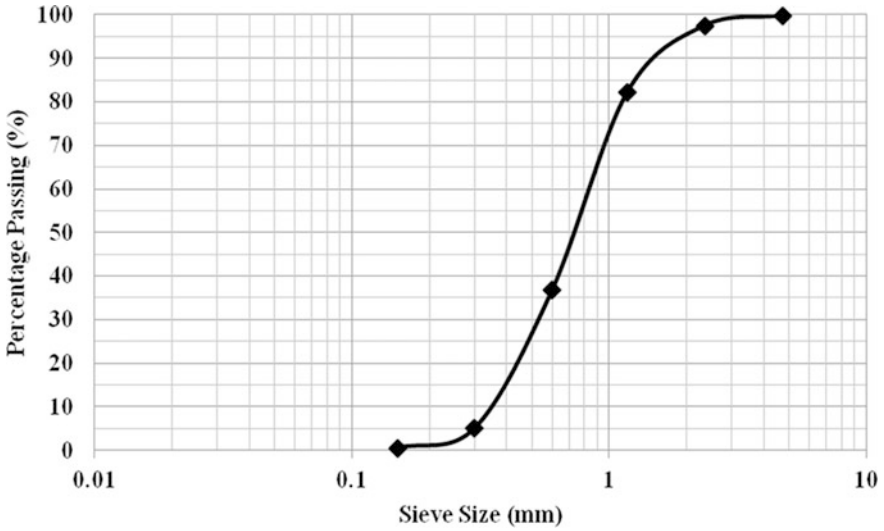

Fig. 2 Particle size distribution of sand

2.1.3 Alkali Solutions

A combination of sodium silicate solution and sodium hydroxide solution was chosen as the alkaline liquid. Sodium silicate (Na_2SiO_3) is available commercially in solution form. The chemical composition of sodium silicate is Na_2O—8.5%, SiO_2—28.0% and water—63.5% by mass. The sodium hydroxide (NaOH) is available commercially in flakes or pellets form. For the present study, NaOH flakes with 98% purity were used for the preparation of alkaline solution. In this study, ratio of sodium silicate solution to sodium hydroxide solution was also varied and taken as 1.0, 1.5 and 2.0. Alkali solution, i.e. mixture of sodium silicate and sodium hydroxide solution was prepared before 24 h prior to use in mixes.

2.1.4 Water

In the present investigation, distilled water was used for the preparation of NaOH solution.

2.1.5 Ordinary Portland Cement (OPC)

Ordinary Portland cement (OPC) was used for the purpose of comparison of the properties with geopolymer paste and mortar. Ordinary Portland cement of grade—43 (UltraTech Cement) conforming to Indian standard IS: 8112-1989 has been used [20]. The results of the various tests on cement properties are given in Table 2.

2.2 Methods

In this section, procedures to perform the test to determine the properties of geopolymer paste and mortar have been discussed.

Table 2 Properties of ordinary Portland cement

Characteristics	Value
Normal consistency	31%
Initial setting time	75 min
Final setting time	190 min
Fineness	1.43%
Compressive strength at 28 days	
Paste	51.6 MPa
Mortar	45.5 MPa

2.2.1 Standard Consistency

The standard consistency of a binder paste, i.e. cement paste is defined as that consistency which will permit the vicat plunger of having dimension of 10 mm diameter and 50 mm length to penetrate to a point 5 mm to 7 mm from the bottom of the vicat mould. Here, standard consistency of geopolymer paste was determined as the amount of alkaline solution (expressed as the percentage by mass of dry fly ash) required to get penetration 5 mm to 7 mm from the bottom of the vicat mould by the above said plunger. In this experimental investigation, the procedure to conduct the test was followed as mentioned at IS-4031 (part 4)—1988 [13].

2.2.2 Setting Time

Initial setting time of cement paste is required to delay the process of hydration or hardening. Final setting time of cement paste is the duration when the cement paste completely loses its plasticity. It is the duration taken for the cement paste to harden sufficiently and gain the shape of the mould in which it is cast. Therefore, determination of initial and final setting time of geopolymer paste is essential to use geopolymer concrete in real practices properly. Initial setting time should not be too less to allow time for mixing, transporting and placing concrete. For determining setting times, quantity of alkaline solution was taken as 0.85 times of standard consistency for the preparation of geopolymer paste sample. Vicat apparatus was used again to find out the setting time. For finding initial setting time, vicat apparatus with 1 mm diameter needle and for final setting time, vicat apparatus with a needle having circular cutting edge 5 mm in diameter and set of 0.5 mm behind the tip of the needle were used. In this study, the procedure to conduct the test was followed as mentioned at IS-4031 (part 5)—1988 [14].

2.2.3 Compressive Strength

Compressive Strength is one of the most important properties and it is determined to check whether the geopolymer mortar will be able to develop required compressive strength of concrete. To determine compressive strength of geopolymer paste, cubes having dimension of 50 mm $\times$ 50 mm $\times$ 50 mm were cast and for mortar sample, cubes having 50 cm^2 surface area were cast. Geopolymer mortar was produced by mixing fly ash and sand at ratio 1:3. After de-moulding, cubes with paste and mortar were kept at room temperature for curing. Cast samples were tested after 28 days of curing. Tests to determine compressive strength were conducted according to IS-4031 (part 6)—1988 [15].

3 Results and Discussion

The results of experimental tests, which have been mentioned in the previous sections, are discussed in the following. All the above mentioned tests to find out the properties of geopolymer paste and mortar were conducted according to the specifications given in Indian Standards, which are followed to find the properties of cement. Effects of the concentration of sodium hydroxide solution and the ratio of sodium silicate solution to sodium hydroxide solution have been discussed.

3.1 Standard Consistency

Experimental results show higher value of standard consistency of the geopolymer paste compared to that of cement paste. Figure 3 shows the values of standard consistency of geopolymer paste produced with the different concentration of sodium hydroxide solutions and different ratios of sodium silicate solution to sodium hydroxide solutions. From the experiment, it has been seen that the range of the value of standard consistency of geopolymer paste varies from 38 to 42% whereas standard consistency of cement paste is 31%. Therefore, to get geopolymer paste with normal consistence, high amount of alkaline solution is required.

3.2 Setting Time

It has been observed from this experimental investigation that initial and final setting time of geopolymer paste both were reduced with the increment of the ratio of sodium silicate solution to sodium hydroxide solution (SS/SH ratio). Figure 4 shows the variation of initial setting time (IST) and Fig. 5 represents the final setting time (FST) of the geopolymer paste for different concentration of sodium

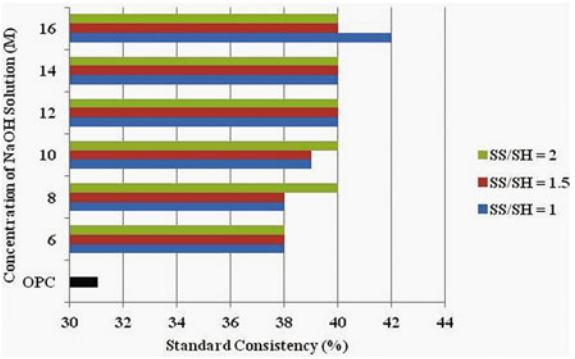

Fig. 3 Standard consistency of geopolymer paste

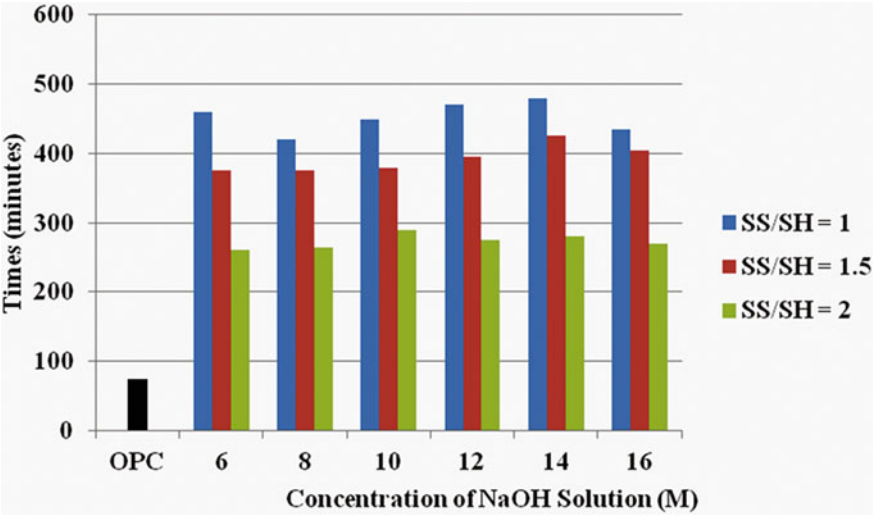

Fig. 4 Initial setting time of geopolymer paste

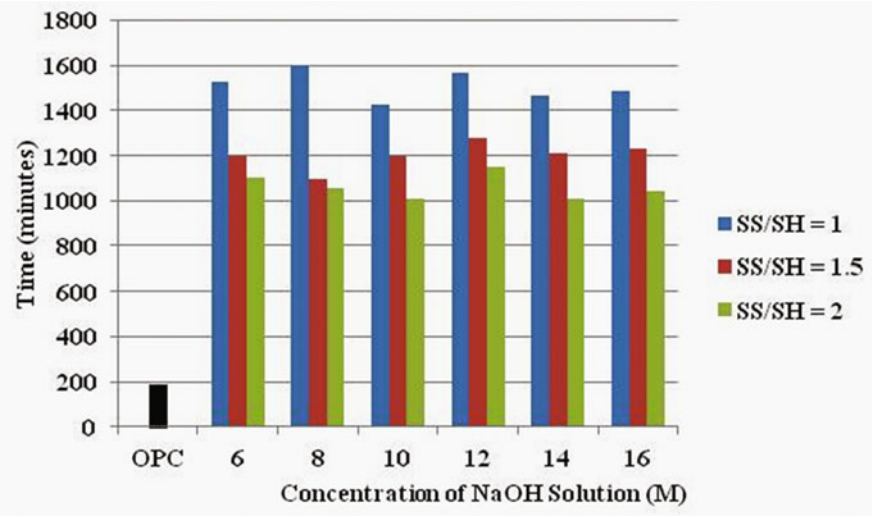

Fig. 5 Final setting time of geopolymer paste

hydroxide solution and different ratios of sodium silicate to sodium hydroxide solution. Initial setting time of geopolymer paste was found to be in the range of 260–480 min and final setting time to be in the range of 1000–1600 min in this study. Therefore, with respect to the initial and final setting time of ordinary Portland cement paste, geopolymer paste requires more time for initial set and final

set. Most of the researchers concluded that geopolymer paste will show less duration for setting and high strength with the heat curing.

Setting of ordinary Portland cement is associated with the formation of calcium-silicate-hydrate gel (C–S–H). Like that geopolymer paste is typically dependent on the formation of sodium aluminate silicate hydrate gel (N–A–S–H) [18]. From the experiments, it is clear that formation of sodium aluminate silicate hydrate gel will be formed when the quantity of sodium silicate solution in alkaline solutions is high. As a result, geopolymer paste produced with alkaline solutions having high ratio of sodium silicate solution to sodium hydroxide solution (in this study it is 2.0) shows comparatively less durations for initial setting and final setting.

3.3 Compressive Strength

Compressive strength of geopolymer paste (samples cured at ambient temperatures) was found to be increasing trend while the concentration of sodium hydroxide solution was increased up to 14 M. Geopolymer paste samples, which were prepared with 14 M sodium hydroxide solution and the ratio of sodium silicate to sodium hydroxide solution as 1.5, showed the highest compressive strength at 28 days. The variation of compressive strength at 28 days of geopolymer paste has been shown in Fig. 6.

Experimental results show increasing trend of compressive strength of geopolymer mortar (50 cm^2 cube samples cured at ambient temperatures) with the

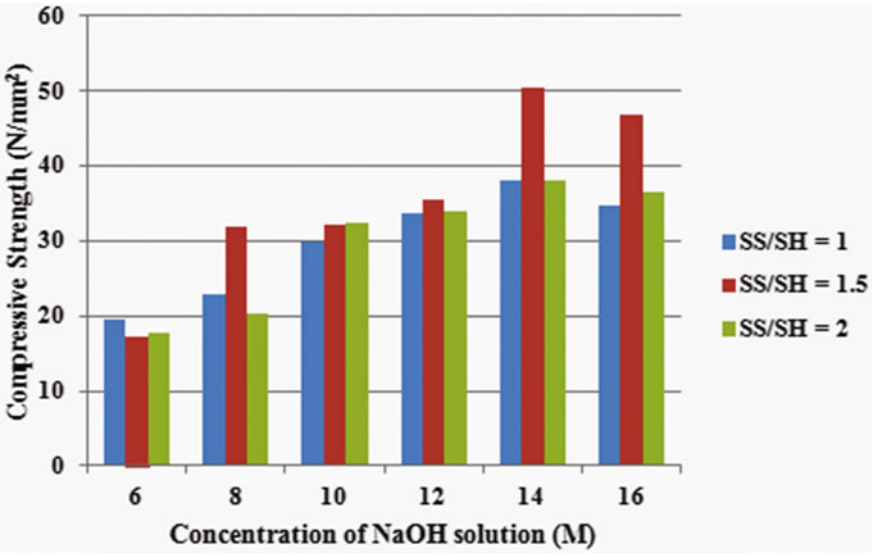

Fig. 6 Compressive Strength of geopolymer paste at 28 days

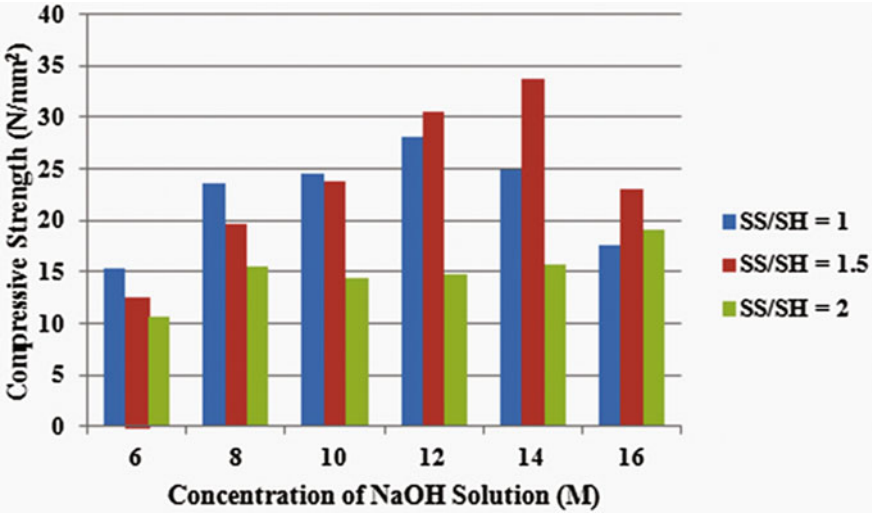

Fig. 7 Compressive strength of geopolymer mortar at 28 days

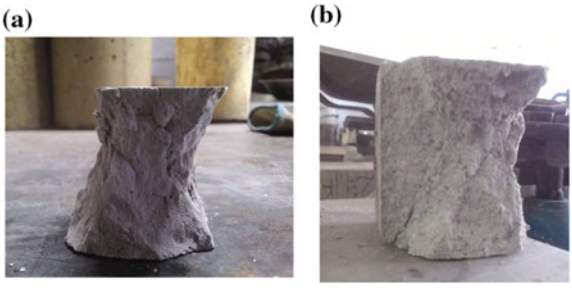

Fig. 8 **a** Paste cubes after compression test, **b** Mortar cubes after compression test

increment of the concentration of sodium hydroxide solution up to 14 M. Geopolymer mortar samples, which were prepared with 14 M sodium hydroxide solution and the ratio of sodium silicate to sodium hydroxide solution as 1.5, showed the highest compressive strength at 28 days. Figure 7 represents the compressive strength of geopolymer mortar for the different concentrations of sodium hydroxide solutions and different ratios of sodium silicate solution to sodium hydroxide solutions.

Compressive strength of geopolymer is attributed by the formation of sodium aluminate silicate hydrate gel (N–A–S–H) and poly-condensation to form 3-D network of silico-aluminates structures. Therefore, from this study it can be stated that with ambient curing, combination of 14 M sodium hydroxide solution with the ratio of sodium silicate solution to sodium hydroxide solution of value 1.5 helps to form sufficient sodium aluminate silicate hydrate gel (N–A–S–H) and leads to poly-condensation. As a result, stable 3-D network of silico-aluminates is produced

to provide high strength to the fly ash based geopolymer. Cube samples of geopolymer paste and geopolymer mortar after compression test are shown in Fig. 8a, b, respectively.

4 Conclusions

In this paper, experimental investigation to determine the properties of fly ash based geopolymers is presented and discussed. From this investigation, the following conclusions can be drawn:

- Standard consistency of geopolymer paste is higher than that of OPC paste. The range of standard consistency value of geopolymer paste was found to be 38–42%.
- Geopolymer paste requires more time to set. But geopolymer paste produced with high ratio of sodium silicate solution to sodium hydroxide solution took comparatively less time to be set. When compared to OPC paste, geopolymer paste needs more time for the final setting. In this study, initial setting time of geopolymer paste was found to be in the range of 260–480 min and final setting time to be in the range of 1000–1600 min. This time range does not satisfy the limits given in Indian Standards for OPC paste.
- Highest compressive strength of 50.4 MPa after 28 days ambient curing has been observed for geopolymer paste produced with sodium hydroxide solution having concentration 14 M and ratio of sodium silicate solution to sodium hydroxide solution as 1.5. Geopolymer mortar produced with sodium hydroxide solution having concentration 14 M and ratio of sodium silicate solution to sodium hydroxide solution as 1.5 shows highest compressive strength of 33.8 MPa after 28 days ambient curing.
- Increase in compressive strength of fly ash based geopolymer paste and mortar has been observed with the increase of the concentration of sodium hydroxide solution up to 14 M. But, compressive strength is found to be in decreasing trend while the concentration of sodium hydroxide solution is beyond 14 M.

Using fly ash (a by-product of thermal power station) to produce geopolymer will help to control the usage of OPC, solve the dumping problems of by-product materials, reduce environmental problems, etc. But, there is an immense need to study how to reduce the setting time of geopolymer with ambient curing.

Acknowledgements The authors would like to thank Department of Civil Engineering of National Institute of Technology Karnataka, Surathkal for the support to conduct this research.

References

1. De Silva, P., Sagoe-Crenstil, K., & Sirivivatnanon, V. (2007). Kinetics of geopolymerization: Role of Al_2O_3 and SiO_2. *Cement and Concrete Research, 37,* 512–518.
2. Neville, A. M. (1997). *Properties of concrete* (4th ed.). New York: WileyInc.
3. Worldwide increase in geopolymer research. http://www.geopolymer.org/. Retrieved December 05, 2015.
4. Rahmiati, T., Khairun A. A., Zakaria M., Lukman I., & Muhd F. N. (2014). Effect of solid/liquid ratio during curing time fly ash based geopolymer on mechanical property. *Materials Science Forum*, *803*.
5. Davidovits, J. (1994). *Properties of geopolymer cements alkaline cements and concretes*. Ukraine: Kiev.
6. Davidovits, J. (1991). Geopolymers: Inorganic polymeric new materials. *Journal of Thermal Analysis, 37,* 1633–1656.
7. Davidovits, J. (2002). 30 Years of successes and failures in geopolymer applications. In *Market Trends and Potential Breakthroughs. Geopolymer 2002 Conference*, October 28–29, Melbourne, Australia.
8. Duxson, P., Fernandez-Jimenez, A., Provis, J. L., Lukey, G. C., Palomo, A., & van Deventer, J. S. J. (2007). Geopolymer technology: The current state of the art. *Journal of Materials Science., 42,* 2917–2933.
9. Chindaprasirt, P., De Silva, P., Sagoe-Crentsil, K., & Hanjitsuwan, S. (2012). Effect of SiO_2 and Al_2O_3 on the setting and hardening of high calcium fly ash-based geopolymer systems. *Journal of Material Sciencs, 47,* 4876–4883.
10. Rahim, A., Rosniza, H., Khairun, A. A., Zakaria, M., Rahmiati, T., & Lukman, I. (2014). Effect of solid to liquid ratio on the mechanical and physical properties of fly ash geopolymer without sodium silicate. *Applied Mechanics and Materials, 625,* 46–49.
11. Gorhan, G., & Kurklu, G. (2014). The influence of the NaOH solution on the properties of the fly ash-based geopolymer mortar cured at different temperatures. *Composites: Part B, 58,* 371–377.
12. Pattanapong, T., Chindaprasirt, P., & Sata, V. (2015). Setting time, strength, and bond of high-calcium fly ash geopolymer concrete. *Journal of Materials in Civil Engineering, 27*(7), 04014198.
13. IS: 4031 (Part 4)—1988. *Method of physical tests for hydraulic cements (Part 1: Determination of consistency of standard cement paste).* New Delhi: Bureau of Indian Standards.
14. IS: 4031 (Part 5)—1988. *Method of physical tests for hydraulic cements (Part 1: Determination of initial and final setting times).* New Delhi: Bureau of Indian Standards.
15. IS: 4031 (Part 6)— 1988. *Method of physical tests for hydraulic cements (Part 1: Determination of compressive strength of hydraulic cement other than masonry cement).* New Delhi: Bureau of Indian Standards.
16. IS: 4031 (Part 1)—1996. *Method of physical tests for hydraulic cements (Part 1: Determination of fineness of cement by dry sieving).* New Delhi: Bureau of Indian Standards.
17. IS: 456—2000. *Code of practice for plain and reinforced concrete*. New Delhi: Bureau of Indian Standards.
18. Shetty, M. S. (2003). *Concrete technology—Theory and practice*. Ram Nagar, New Delhi, India: S. Chand & Company Ltd.
19. IS: 383-1970. *Specifications for coarse and fine aggregates from natural sources of concrete*. New Delhi: Bureau of Indian Standards.
20. IS: 8112—1989. *43 grade ordinary Portland cement—Specification*. New Delhi: Bureau of Indian Standards.

Impact Response of Paver Blocks with Waste Tyre Crumb Rubber

R. Bharathi Murugan, E. Rama Sai and C. Natarajan

Abstract Waste materials utilisation has been a very important aspect in the concrete manufacturing to develop the green construction in the last decade. The disposal of waste tyres is one of the most problematic issues in the present scenario. The use of waste tyres in the concrete production is very important to control the waste accumulation and preserve the natural resources. The aim is to investigate the effect of partial replacement of sand by waste tyre crumb rubber in the production of concrete paver blocks. The specimens were prepared for 5, 10, 15, 20 and 25% replacements by volume for sand. M40 grade concrete was designed and used in this study. The paver blocks were prepared in the industry and tested in the laboratory to determine the impact resistance. The test results revealed that the impact resistance for both first crack and ultimate failure increased with an increase in the crumb rubber content up to 25%.

Keywords Paver block · Waste tyre · Crumb rubber · Impact energy
Ductility index

1 Introduction

Recycling of waste tyres is considered as one of the major environmental challenges faced by every country. Many countries follow two easiest ways of disposing. First, burning of tyres and second, used as a landfill due to low density and poor degradation. Nowadays, some of the countries do not accept the burning

R. Bharathi Murugan · E. Rama Sai · C. Natarajan (✉)
Department of Civil Engineering, National Institute of Technology at Trichy, Trichy, Tamil Nadu, India
e-mail: nataraj@nitt.edu

R. Bharathi Murugan
e-mail: rbmmecivil@gmail.com

E. Rama Sai
e-mail: ramsai.eeda@gmail.com

A. Rama Mohan Rao and K. Ramanjaneyulu (eds.), *Recent Advances in Structural Engineering, Volume 1*, Lecture Notes in Civil Engineering 11,
https://doi.org/10.1007/978-981-13-0362-3_54

method because while burning the waste tyres, large amount of smokes is produced which will get mixed in the natural air and lead to the environmental issues. The second method of landfill techniques is also not advisable because of uneven settlement and the stagnation of storm water during rainy season as this will produce mosquitoes which spread many diseases. Hence, this becomes a more dangerous health hazard [1–3].

Several investigations were done on the effect of waste tyre crumb rubber replacement for sand (or) aggregate in the concrete mixtures and few studies were done with waste tyre powder as a replacement of cement. These studies indicate that the presence of rubber in concrete seems to reduce the compressive strength and enhance the elastic behaviour [4, 5].

The size of the crumb rubber also influences the strength of the concrete. The use of coarse crumbs gave lower compressive strength than the fine crumbs. Even though, the strength of concrete seems to reduce by the addition of crumb rubber, there are several other properties of concrete that are beneficial. For example, concrete mixed with crumb rubber is found to have lower density, higher impact and toughness resistance, enhanced durability and better sound insulation.

In this study, the performance of Precast Concrete Paver Blocks (PCPB) with waste tyre crumb rubber as a partial replacement of fine aggregate, under drop weight impact loading is examined. The drop weight impact test was conducted on PCPB added with waste tyre crumb rubber as the replacement of 5, 10, 15, 20 and 25% by volume of fine aggregate. The impact energies to induce the first visible crack and ultimate failure on each paver block were investigated.

2 Materials and Methods

2.1 Materials

Ordinary Portland cement of 53 grades was used in this study and it conforms to IS 12269:1987 [6]. The physical properties are presented in Table 1.

Table 1 Physical properties of cement

Sl. No.	Property	Results	Limits as per IS 12269:1987
1.	Fineness (m^2/kg) (Specific surface)	290	>225
2.	Initial setting time (min)	85	<30
3.	Final setting time (min)	280	<600
4.	Soundness by Le-Chatelier	1	<10
5.	Compressive strength 7 days (N/mm^2) 28 days (N/mm^2)	 38.60 56.96	 >37 >53

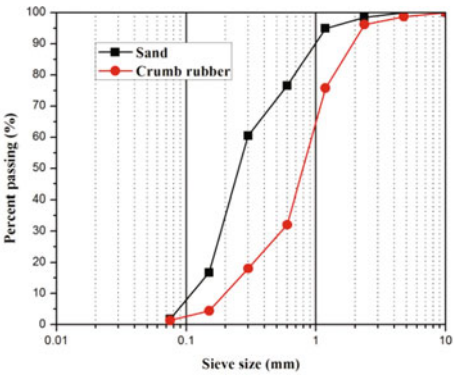

Fig. 1 Gradation of sand and crumb rubber

Fig. 2 Crumb rubber

Locally available river sand passing through 4.75 mm IS sieve conforming to grading zone III as per IS: 383-1970 [7] having a fineness modulus of 2.51 and a specific gravity of 2.65.

The coarse aggregate used in the concrete mixtures was crushed granite stone, having the maximum size of 12.5 mm, a fineness modulus of 5.94 and a specific gravity of 2.72. Sieve analysis was performed on the coarse aggregate, according to IS: 383-1970 [7].

Shredding and chipping is the mechanical process of shredding tyres into particles up to 4.75 mm. A tyre shredder is a machine with a disc of cutting edges, rotating in one direction to create a shearing motion, that effectively cuts or shreds tyres as they are fed into the machine. In the present study, a shredded rubber is used as partial fine aggregate replacement. Sieve analysis was performed as per IS: 383-1970 [7]. Crumb rubber is a fine material with gradation is close to that of river sand and the gradation curves are shown in Fig. 1. The fineness modulus is 3.72 and specific gravity is 0.84. Figure 2 shows the crumb rubber used in the current study.

Light brown colour superplasticiser (SikaViscoCrete 20HE) was used to improve the workability with the specific gravity of 1.08.

2.2 Manufacturing Concrete Paver Blocks

Paver block manufacturers followed two methods of specimen preparation which are given as follows:

(i) Wet cast method
(ii) Dry cast method

In the dry casting method, low water–cement ratio (0.30–0.36) was used. It has a zero slump and the forms can be stripped as soon as the concrete has been compacted. A dry casting method is especially followed for the mass production because it requires expensive equipments. In wet casting method, the concrete should have a minimum water cement ration of 0.4. In the wet casting method, the concrete is placed in the rubber moulds and levelled off by using a rake or similar. Table vibrator is then used to make the concrete compact, fill any small voids and force any small air pockets/bubbles to expel via the open top surface (which will become the base of the finished paved blocks). After a successive period of vibration, all the moulds are moving on to the storage area. In this method, the curing is not required because sufficient water is present in the mould in the hydration process. For that, all the moulds are covered by the plastic cover to avoid the evaporation of the water. The moulds are manually removed as soon as 24 h after casting. After demoulding, all the specimen thickness and surface were checked. In this current study, paver blocks of size 250 mm × 120 mm × 80 mm were produced by using a wet casting method. M40 grade concrete had cement, fine aggregate and coarse aggregate in the ratio of 1: 2.20: 2.66 with water–cement ratio of 0.4. The mix was designed as per IS 10262 [8] and the target strength was found to be 48.25 MPa. Fine aggregate was partially replaced with crumb rubber by volume (5, 10, 15, 20 and 25%). The identification and details of the specimens are presented in Table 2.

Table 2 Mix proportions

Mix ID	Details of mix ID	C	FA	CA	CR	W/C	SP
R0	Control mix	1	2.27	2.65	0	0.42	0.04
R5	5% FA replaced by CR	1	2.08	2.65	0.19	0.42	0.04
R10	10% FA replaced by CR	1	1.97	2.65	0.30	0.42	0.04
R15	15% FA replaced by CR	1	1.86	2.65	0.41	0.42	0.04
R20	20% FA replaced by CR	1	1.75	2.65	0.52	0.42	0.04
R25	25% FA replaced by CR	1	1.64	2.65	0.63	0.42	0.04

C cement, *FA* fine aggregate, *CA* coarse aggregate, *CR* crumb rubber, *W/C* water–cement ratio and *SP* superplasticiser

2.3 Test Setup and Procedure

A 4.54 kg weight was lifted to 0.457 m above the specimen and then released. The drop weight impact testing machine is shown in Fig. 3. The impact load was applied via the free fall of the drop weight onto a centre of the paver block by the guidelines of ACI committee 544.2R-89 [9]. The weight was dropped repetitively and the number of blows required for the first visible crack and the complete failure of the specimens was noted. The failure of the specimen during the testing was shown in Fig. 4. The impact energy was calculated for each paver block using the following equation:

$$U = \frac{nmv^2}{2} \tag{1}$$

where U = impact energy; n = number of blows; m = weight of the hammer = 4.54 kg; v = drop weight hammer velocity = $\sqrt{2(0.9g)h}$; g = gravitational acceleration; h = drop height. The factor 0.9 accounts for effect of the air resistance and friction between the lifting weight and the guide rails.

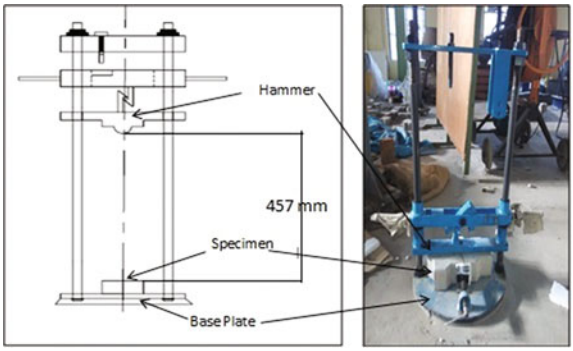

Fig. 3 Impact testing machine

Fig. 4 Failure specimens after impact testing

3 Results and Discussion

3.1 Impact Energy

The number of blows required for producing the first visible crack and the complete failure for each type of paver blocks is presented in Table 3. Based on the number blows, the first crack impact energy and failure impact energy were calculated by using Eq. (1) and plotted in Fig. 5.

As compared to conventional concrete paver blocks, the first crack impact energy was increased by 34.48, 51.23, 71.92, 91.62 and 112.31% and the failure impact energy was increased by 35.81, 53.02, 74.88, 96.27 and 118.14% to 5, 10, 15, 20 and 25% of sand replaced by crumb rubber by volume, respectively.

Hence it was observed that increasing the replacing percentage of shredded rubber increases the impact energy of paver blocks significantly, in both the first crack stage as well as failure stage [10–12]. The impact resistance of R25 is approximately twice than R0 (CPB) because crumb rubber absorbs more energy. This proves that the rubber acts as a fibre and effective crack arrestor, when an impact load is encountered. Thus, the plain concrete exhibits an early brittle failure when compared to FRC which shows better ductile properties [13]. The mode of failure of concrete depends upon the cement matrix strength, aggregate strength and bond strength of fibre with aggregate matrix.

Average, statistical value of first crack and failure impact energy and the number of test specimens for each PCPB at the level of 5, 10, 15, 20 and 25% of crumb rubber replacement by sand volume are presented in Tables 4 and 5 respectively.

In this study, paired *t*-test was mainly used to determine whether the average impact energy (first crack and failure stage) for PCPB with different percentage crumb rubber content is compared to the control concrete (without crumb rubber).

At the statistical level of 0.05 (95% level of confidence), it is required to have t_α critical value of 2.571 with the degree of freedom of 5. The *t*-statistical values were calculated and presented in Tables 4 and 5. The statistical analysis results show at a 0.05 level of significance and the calculated *t*-statistical values are greater than the critical value (t_α). Therefore, it is possible to show the significant difference in the average impact energy at first crack and failure conditions between control PCPB and 5, 10, 15, 20, 25% of crumb rubber content.

3.2 Ductility Index

Ductility index is defined as the ratio of energy absorbed at failure to energy absorbed at first crack [14]. The ductility index may quantitatively represent the ductility of the paver blocks. Figure 6 shows the variations of the ductility index of the wet cast paver blocks based on the crumb rubber replacements at various percentages. It was observed that the ductility index value increases if the

Table 3 impact test results for plain and rubber mixed concrete

Mix ID	No. of blows		Average no. of blows		Impact energy (J)		Average impact energy (J)		Ductility index	Average ductility index
	First crack	Failure	First crack	Failure	First crack	Failure	First crack	Failure	N2/N1	Average of (N2/N1)
R0	49	51	40.60	43.00	890.82	927.19	738.11	781.74	1.040	1.060
	41	43			745.38	781.74			1.048	
	36	39			654.48	709.02			1.083	
	38	41			690.84	745.38			1.078	
	39	41			709.02	745.38			1.0512	
R5	46	50	54.60	58.40	836.28	909.01	992.63	1061.72	1.08	1.069
	53	57			963.55	1036.27			1.075	
	56	58			1018.09	1054.45			1.035	
	60	66			1090.81	1199.89			1.100	
	58	61			1054.45	1108.99			1.051	
R10	65	68	61.40	65.80	1181.71	1236.25	1116.24	1196.25	1.046	1.072
	71	76			1290.79	1381.69			1.070	
	59	64			1072.63	1163.53			1.084	
	55	59			999.91	1072.63			1.072	
	57	62			1036.27	1127.17			1.087	
R15	71	78	69.80	75.20	1290.79	1418.05	1268.97	1367.15	1.098	1.079
	74	80			1345.33	1454.41			1.081	
	59	66			1072.63	1199.89			1.118	
	79	82			1436.23	1490.77			1.037	
	66	70			1199.89	1272.61			1.060	
R20	88	94	77.8	84.40	1599.88	1708.93	1414.41	1534.40	1.068	1.085
	71	77			1290.79	1399.87			1.084	

(continued)

Table 3 (continued)

Mix ID	No. of blows		Average no. of blows		Impact energy (J)		Average impact energy (J)		Ductility index	Average ductility index
	First crack	Failure	First crack	Failure	First crack	Failure	First crack	Failure	N2/N1	Average of (N2/N1)
	84	92			1527.13	1672.57			1.095	
	74	80			1345.33	1454.41			1.081	
	72	79			1308.97	1436.23			1.097	
R25	86	96	86.20	93.80	1563.49	1745.29	1567.13	1705.30	1.116	1.091
	98	104			1781.66	1890.74			1.061	
	86	89			1563.49	1618.08			1.034	
	90	98			1636.21	1781.66			1.088	
	71	82			1290.79	1490.77			1.154	

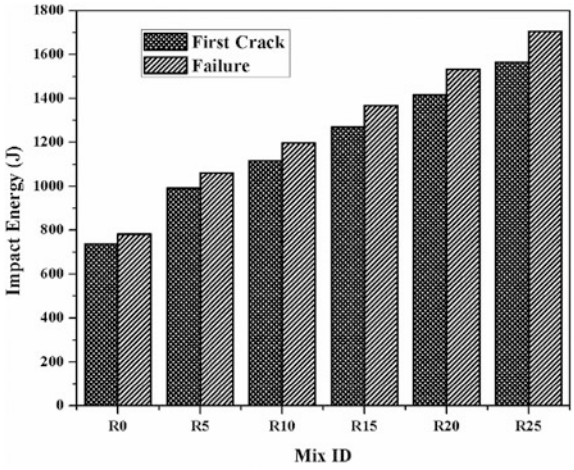

Fig. 5 Impact energy of wet casting paver blocks

Table 4 Paired *t*-tests for crumb rubber-concrete paving blocks (first crack)

Mix ID	No. of specimen	Average impact energy (first crack)	Standard deviation	*t*-value	*p*-value	Remarks
R0	5	738.11	91.44	–	–	–
R5	5	992.63	99.24	3.062	0.0376	Significant
R10	5	1116.24	118.23	8.011	0.0013	Very significant
R15	5	1268.97	139.28	6.506	0.0029	Very significant
R20	5	1414.41	139.88	12.044	0.0003	Extremely significant
R25	5	1567.13	178.31	9.621	0.0007	Extremely significant

Table 5 Paired *t*-tests for crumb rubber-concrete paving blocks (failure)

Mix ID	No. of specimen	Average impact energy (first crack)	Standard deviation	*t*-value	*p*-value	Remarks
R0	5	781.74	85.21	–	–	–
R5	5	1061.72	106.72	3.455	0.0255	Significant
R10	5	1196.25	119.49	7.853	0.0014	Very significant
R15	5	1367.15	124.90	11.217	0.0004	Extremely significant
R20	5	1534.40	144.64	12.800	0.0002	Extremely significant
R25	5	1705.30	154.47	13.754	0.0004	Extremely significant

percentage of the crumb rubber increases in the concrete mix. The sand replacement by crumb rubber (5, 10, 15, 20 and 25%) increases the ductility index by 0.93, 1.16, 1.82, 2.3 and 2.94%.

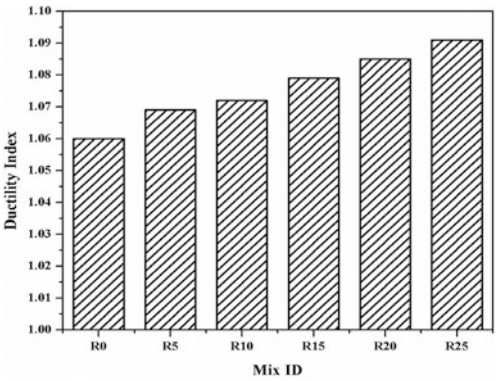

Fig. 6 Ductility index of the wet cast paver blocks

4 Conclusions

- The impact resistance of paver blocks was investigated for the paver blocks with partial replacements of 5, 10, 15, 20 and 25% volume of sand by waste tyre crumb rubber.
- The impact resistance of the paver blocks was mainly calculated in two stages; (i) First cracks impact resistance and (ii) Failure impact resistance. Both stages of impact resistance were increased by the replacement of sand with crumb rubber up to 25% by volume of sand. The ductility index also increased with the crumb rubber content increases up to 25%.
- All the test results are statistically validated by using paired *t*-test and proved that both first crack and failure impact resistance were statically significant. The results show that 25% of rubber content replacement fine aggregate considerably increase the impact energy in case of CPB with crumb rubber when compared to conventional CPB.
- The incorporation of rubber content to concrete changes the failure pattern from brittle mode to ductile, which displays the beneficial effects of CPB with crumb rubber used in absorbing vibrations.

References

1. Oikonomou, N., & Mavridou, S. (2009). Improvement of chloride ion penetration resistance in cement mortars modified with rubber from worn automobile tyres. *Cement & Concrete Composites, 31*(6), 403–407.
2. Topcu, I. B., & Avcular, N. (1997). Collision behaviours of rubberized concrete. *Cement and Concrete Research, 27*(12), 1893–1898.
3. Issa, C. A., & Salem, G. (2013). Utilization of recycled crumb rubber as fine aggregates in concrete mix design. *Construction and Building Materials, 42*(1), 48–52.

4. Al-Tayeb, M. M., Abu Bakar, B., Ismail, H., & Akil, H. M. (2012). Impact resistance of concrete with partial replacements of sand and cement by waste rubber. *Journal of Polymer-Plastic Technology and Engineering, 51*(12), 1230–1236.
5. Bharathi Murugan, R., & Natarajan, C. (2016). Investigation on precast concrete paver block with waste tyre crumb rubber. *Road Materials and Pavement Design*, *17*(3), 719–736.
6. IS: 12269-1987. *Indian standard specification for 53grade ordinary Portland cement*. New Delhi: Bureau of Indian Standards.
7. IS: 383-1970. *Indian standard specification for coarse and fine aggregates from natural sources for concrete*. New Delhi: Bureau of Indian Standards.
8. IS 10262: 2009. *Recommended guidelines for concrete mix design*. New Delhi: Bureau of Indian Standards.
9. ACI 544.2R-89. (1999). *Measurement of properties of fiber reinforced concrete*. USA, MI: American Concrete Institute (ACI), Farmington Hills.
10. Mahmoud, N., & Afroughsabet, V. (2010). Combined effect of silica fume and steel fibers on the impact resistance and mechanical properties of concrete. *International Journal of Impact Engineering, 37*(8), 879–886.
11. Yildirim, S. T., Cevdet, E. E., & Findik, F. (2010). Properties of hybrid fiber reinforced concrete under repeated impact loads. *Russian Journal of Non-destructive Testing*, *46*(7), 538–546.
12. Nia, A. A., Hedayatian, M., Mahmoud, N., & Sabet, V. A. (2012). An experimental and numerical study on how steel and polypropylene fibers affect the impact resistance in fiber-reinforced concrete. *International Journal of Impact Engineering, 46*(1), 62–73.
13. Swamy, R. N., & Jojagha, A. H. (1982). Impact resistance of steel fibre reinforced lightweight concrete. *International Journal of Cement Composites and Light Weight Concrete, 4*(4), 209–220.
14. Senthilvadivel, T., Thenmozhi, R., & Doddurani, M. (2014). Experimental behaviour of waste tyre rubber aggregate concrete under impact loading. *IJST-Transactions of Civil Engineering, 38*(1), 251–259.

AAC Block Masonry with Ready Mix Mortar—An Experimental and Numerical Analysis

Deepa Doddamani and Mangala Keshava

Abstract The evolution of masonry form of construction predates history. Although it is used from prehistoric times, it continues to be used widely currently. Bricks consume huge amount of energy during the firing stage of its manufacturing process thus leading to emission of greenhouse gases. Alternatively, there has been a development of concrete blocks and light weight concrete blocks. Autoclaved Aerated Concrete (AAC) blocks are one such light weight concrete blocks. These AAC blocks are being used with another alternative material apart from conventional mortar called Ready Mix Mortar (RMM). The present study aims to explore the suitability of AAC block masonry with ready mix mortar in load bearing masonry construction with experimental and numerical investigation using NISA. Also a comparison is attempted with masonry made with conventional blocks (Hollow concrete blocks) and conventional mortar of mix proportion 1:6.

Keywords Autoclaved aerated concrete blocks · Ready mix mortar
Hollow concrete blocks · Masonry · Experimental investigations
Numerical investigations

1 Introduction

Some of the world's most significant architecture such as the Egyptian Pyramids, the Colosseum in Rome, India's Taj Mahal, and the Great Wall of China are built with masonry [1]. Masonry construction is resistant to fire, sound and earthquake and can withstand wear and tear for centuries. Clay bricks and concrete blocks are the most frequently used masonry units for masonry construction. Development in

D. Doddamani · M. Keshava (✉)
Department of Civil Engineering, BMSCE, Bangalore 560050, India
e-mail: mk.civ@bmsce.ac.in

D. Doddamani
e-mail: deepadoddamani04@gmail.com

A. Rama Mohan Rao and K. Ramanjaneyulu (eds.), *Recent Advances in Structural Engineering, Volume 1*, Lecture Notes in Civil Engineering 11,
https://doi.org/10.1007/978-981-13-0362-3_55

masonry has led to production of hollow concrete blocks and subsequently Autoclaved Aerated Concrete (AAC) blocks.

Concrete blocks were used by Roman, Greeks, and Egyptian for building the huge monuments, however the modern-type concrete blocks were first caste in the middle of nineteenth century. Joseph Aspidin in the year 1987 developed the first basic mix of blocks. The mix consisted of powdered limestone and clay mixed with water. Block manufacturing became an established industry in the recent twentieth century. The first Hollow Concrete blocks was designed by Harman S Palmer in the year 1890 [2]. The blocks designed were of size 8 in. × 10 in. × 30 in. which was very heavy for manual handling. The blocks were carried with the help of a small crane from one place to another.

Based on the density and manufacturing process, concrete blocks can be classified as dense concrete blocks, light weight concrete blocks, and aerated concrete blocks. Dense concrete blocks are being used since 1940. These blocks are manufactured from cement, aggregates, and sand and have a thermal conductivity of 0.70–1.28 W/mK [3]. Light weight concrete blocks are less strong then dense concrete blocks. These are manufactured from cement along with man-made aggregates which includes granulated/blast furnace slag, expanded clay or shale, furnace bottom ash, pulverized fuel ash. The thermal conductivity of these blocks was typically found to be between 0.25 and 0.60 W/mK [3]. Aerated blocks are well known as cellular or gas concrete blocks. These blocks have a thermal conductivity of 0.09–0.20 W/mK [3].

1.1 Autoclaved Aerated Concrete Blocks

Autoclaved Aerated Concrete Blocks (AAC) are the extra light concrete blocks which are suitable for high rise construction as it is lighter than conventional bricks and blocks. These blocks are manufactured with the reaction of aluminum with a proportionate blend of fly ash, lime, and cement. The hydrogen gas that escapes during the reaction creates millions of tiny air cells giving it a strong cellular structure which is further strengthened by high pressure steam curing in autoclaves hence the name autoclaved aerated concrete blocks. AAC blocks are one of the most commonly used light weight concrete blocks due to its low density and unique thermal properties and high fire resistant. These blocks also provide excellent sound and fire insulation apart from being eco-friendly. AAC blocks were first commercially produced in Sweden in 1923 [1]. These autoclaved aerated concrete blocks are being used with the thin jointing material called ready mix mortar instead of conventional mortar with the mix proportion of 1:6. The present investigation aims to know the suitability of these blocks with ready mix mortar and conventional mortar. As a comparison, Hollow Concrete Blocks (HCB) with Ready Mix Mortar (RMM) and Conventional Mortar (CM) are also attempted. Several tests are carried out on both types of masonry with ready mix mortar and conventional mortar.

Hence, this paper presents the suitability of ready mix mortar on two types of concrete blocks.

2 Literature Review

Research carried out on various light weight concrete blocks such as foamed concrete blocks, aerated concrete block and autoclaved aerated concrete blocks was studied. Foamed concrete blocks are also known as "cellular light weight blocks". These are manufactured by adding aqueous foam to the mixture of slurry of cement, fly ash or sand, water and other additives in the foam mixer. Chaipanich [4], in his study, reports that foamed concrete blocks can be made by adding detergent, resin soaps, glue resin, protein such as keratin as a foaming agent. Krishna Bhavani [5], in her study, conducted experiments on foamed concrete blocks which were produced by adding a foaming agent which is diluted in 40 parts of portable water. The minimum weight of foam was 80 g/l. The nominal dimension of the blocks produced was of length 400, 500, or 600 mm, height 250 or 300 mm, width 100, 150, 200, or 250 mm. These blocks were cured for 2–3 weeks. The compressive strength of Cellular Light weight Concrete (CLC) blocks of density 800 kg/m^3 was found to be 35 kg/cm^2. Water absorption of these blocks was 12.5% as against 20% for burnt clay bricks. Thermal conductivity was found to be in the range of 0.131–0.151 W/mK showing a great thermal conductivity due to number of closed cavities.

Mirza et al. [6] tested aerated concrete blocks for compressive strength, fire resistance, and moisture penetration. Five different sands around Saudi were used to manufacture Non-autoclaved aerated concrete blocks and compressive strength of these blocks was found to be in the range of 58–120 kg/cm^2. Further sulfate attack tests on these blocks showed that non-autoclaved blocks showed reduction in strength between 20 and 40% while autoclaved blocks showed 10–20% reduction when compared to its original strength.

Densities of aerated concrete blocks range between 400 and 800 kg/m^3. These blocks consume less than 60% energy and save up to 45% construction cost. Water absorption of these blocks was found to be 2/3rd of the normal brickwork and 1/6th of autoclaved aerated concrete blocks.

Narayanan et al. [7], in his paper "structure and properties of aerated concrete blocks," found that the compressive strength for AAC block for density of 700 kg/m^3 was found to be 3.9–2.8 N/mm^2 but reduces to 1.3–2.8 N/mm^2 when the density is 400 kg/m^3. Albayrak et al. [4] showed that the compressive strength for the density range of 270–500 kg/m^3 was found to be 1.1–5 N/mm^2 showing an increase in the strength with density. Flexural strength was in the range of 0.15–0.35 N/mm^2. Newman et al. [8] in his study advanced concrete technology processes has presented the typical properties of AAC blocks for various densities which is tabulated in Table 1.

Table 1 Typical properties of aerated concrete blocks

Dry density (kg/m^3)	Compressive strength (N/mm^2)	Flexural strength (N/mm^2)	Modulus of elasticity (GPa)	Thermal conductivity (W/mK)
450	3.2	0.65	1.6	0.12
525	4.0	0.75	2.0	0.14
600	4.5	0.85	2.4	0.16
675	6.3	1.00	2.5	0.18
750	7.5	1.25	2.7	0.20

Table 2 Mechanical properties of AAC

Density (kg/m^3)	Compressive strength (N/mm^2)	Static modulus of elasticity (N/mm^2)
400	1.3–2.8	0.18–0.17
500	2.0–4.4	1.24–1.84
600	2.8–6.3	1.76–2.64
700	3.9–8.5	2.42–3.58

Andolsun [9] has studied the material properties of autoclaved aerated concrete and has reported the mechanical properties and density of AAC which is presented in Table 2.

The literature review shows that the studies are carried out on the unit properties of AAC blocks. No studies have been attempted on the properties of ready mix mortar. Also no research is available to understand the behavior of AAC along with ready mix mortar. Hence, this paper brings out the compressive strength behavior of AAC block masonry with ready mix mortar with the help of masonry prisms.

3 Properties of Masonry Blocks and Mortar

A block is a masonry unit whose one of the external dimension is greater than the corresponding dimension of the brick as specified in IS 3952:1978 [10] and of such size and mass as to be handled by one man. Furthermore to avoid confusion with slabs and panels, the height of the block shall not exceed either its length or six times its width. The present study focuses on two types of blocks namely AAC blocks which come under the light weight block category and hollow concrete blocks that come under conventional block category. Tests carried out on these blocks are as per IS 2185 (Part 2)—1983 [11]. The various tests are dimensionality test, block density test, compressive strength test, flexural strength, and modulus of elasticity.

Table 3 Unit properties of AAC blocks and hollow concrete blocks

S. No.	Tests	Results	
		AAC (IS 2185 (Part 3)—1983)	HCB (IS 2185 (Part 2)—1983)
1.	Dimensionality (mm)	600.5 × 200.2 × 149.4	390.5 × 191 × 139.5
2.	Block density (kg/m^3)	766.88	1264.90
3.	Initial Rate of absorption (kg/m^2/min)	2.44	5.42
4.	Water absorption (%)	19.75	6.12
5.	Compressive strength (MPa)	3.46	4.63
6.	Flexural strength (MPa)	1.16	1.31
7.	Modulus of elasticity (MPa)	8276	9031.5

Tests on AAC blocks and hollow concrete blocks are carried out as per IS 2185 (Part 3) and (Part 2)—1983 and the test results of these blocks obtained are tabulated in Table 3.

The block density of AAC blocks is 65% lower than the hollow concrete blocks. IRA of AAC blocks is well within the range of 0.8–3 kg/m^2/min as per ASTM standards. However, it has exhibited high water absorption when compared to hollow concrete blocks. The structural properties such as compressive strength, flexural strength of AAC blocks are slightly below than that of hollow concrete blocks.

Mortar is a homogenous mixture produced by mixing cementitious material, water, and inert material such as sand to the required consistency to bind with the masonry units. Choice of masonry mortar is governed by several conditions such as type of masonry, situation of use, degree of exposure to weather, strength requirements, besides special considerations like fire resistance, insulation, rate of setting and hardening, etc. Cementitious ingredients may be cement or lime or combinations of these and with or without additions of pozzolanas, plasticizers, etc. The proportions in which they are to be mixed depend largely on practical experience with local materials. Mud mortar was the choice several centuries ago, conventional mortar basically comprising of cement has been in use for decades. However, the modern trend is to use ready mix mortar. Ready mix mortar is applied as a thin bed of 2–5 mm. Properties of ready mix mortar are determined using IS 2250–1981 [12]. The experiments conducted are flow table test, compressive strength test, flexural strength, tensile strength, and modulus of elasticity and the results are tabulated in Table 4.

The properties of ready mix mortar are found to be better than conventional mortar. Compressive strength of ready mix mortar was found to be 30% more than conventional mortar. Also there is increase in flexural strength of ready mix mortar when compared to conventional mortar.

Table 4 Properties of ready mix mortar and conventional mortar (1:6)

S. No.	Tests	Results		Ref.
		Conventional mortar	RMM	
1.	Flow table test	1.36	22%	IS 2250: 1981
2.	Compressive strength (MPa)	6.95	9.67	
3.	Flexural strength (MPa)	1.56	2.79	
4.	MOE (MPa)	7093	38042	
5.	Tensile strength (Mpa)	0.91	1.26	ASTM C 190

The properties of AAC blocks and ready mix mortar have indicated the suitability of using these two materials in masonry. Hence, experimental and numerical investigations are taken up to understand the behavior of masonry under compression.

4 Experimental and Numerical Investigations on Masonry Prisms

Masonry is an assemblage of units and mortar which are bonded together and placed in a predetermined orientation. To determine the masonry strength three types of specimen can be considered namely, masonry prisms, masonry wallettes, and masonry walls. Failure pattern can be analyzed by three methods such as experimental investigations, analytical investigations, and numerical investigations. Experimental investigations include tests on unit and mortar and masonry specimens such as masonry prisms, masonry wallettes, and full scale wall specimens. Analytical investigations include determining compressive strength of masonry and masonry efficiency using Lenczner's theorem or Hilsdorf's equation. Numerical investigations help in determining the stress contours in masonry prisms using software tools such as NISA, ANSYS, etc. This paper involves experimental and numerical investigations on masonry prisms for four different combinations such as AAC with RMM, AAC with conventional mortar, HCB with RMM and HCB with conventional mortar. Thickness of bed for ready mix mortar is 3 mm and 10 mm for conventional mortar.

4.1 Experimental Investigations on Masonry Prisms

Masonry prisms are cast using AAC blocks and HCB with ready mix mortar and conventional mortar. Since ready mix mortar does not require curing the prisms with ready mix mortar are tested after 7 days without curing and prisms with conventional mortar are tested after 28 days of curing using wet burlaps.

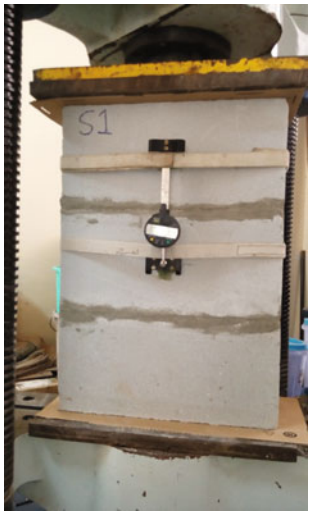

Fig. 1 Test setup of compression test

The masonry prism specimen is placed in the universal testing machine and the demec gauge is fixed as shown in Fig. 1. A constant load of 14 N/mm^2 per minute is applied and the deformation is noted from the demec gauge for every load change. Compressive strength of the prism is calculated using the formula (1) and a graph is plotted to determine the modulus of elasticity,

$$\text{Compressive strength} = \frac{\text{Failure load}}{\text{Area of specimen}} \tag{1}$$

The masonry efficiency is calculated for all the prism combination using the formula

$$\text{Masonry efficiency} = \frac{\text{Masonry strength}}{\text{Masonry unit strength}} \times 100 \tag{2}$$

Table 5 presents the compressive strength, modulus of elasticity, and masonry efficiency of the four masonry combinations selected for the present study. Figure 2 shows the typical graph (for AAC with RMM) drawn to understand the stress–strain relationship and hence to obtain the modulus of elasticity of masonry prisms.

The results show that the compressive strength of AAC with RMM is the least when compared with the results of other prism combinations. However, hollow concrete block prisms exhibited relatively higher compressive strength and masonry efficiency when compared with AAC block masonry.

Table 5 Properties of masonry prims

Prism combination	Compressive strength (N/mm^2)	Modulus of elasticity (N/mm^2)	Masonry efficiency (%)
AAC + RMM	2.02	1525.1	58.38
AAC + CM	2.82	3461.6	81.41
HCB + RMM	4.73	6364.9	102.0
HCB + CM	4.35	7903.9	93.78

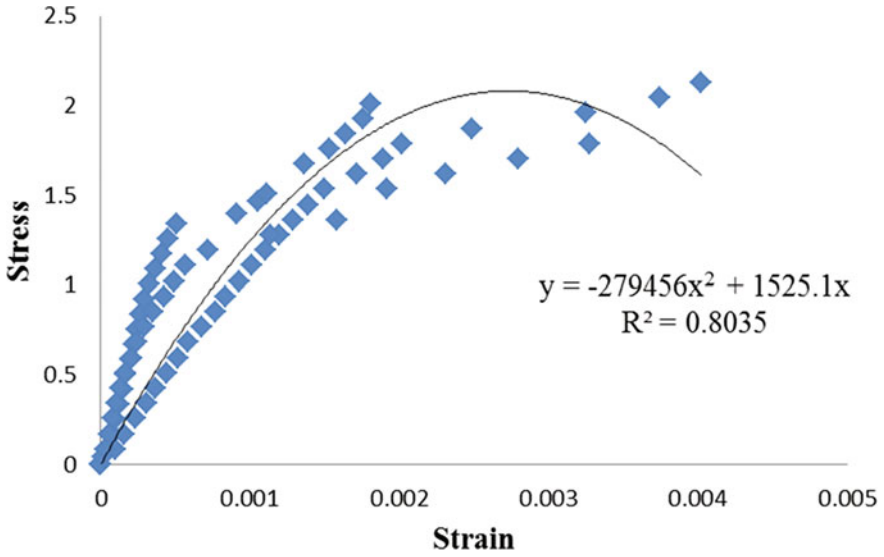

Fig. 2 Stress–strain curve of AAC with RMM

4.2 Numerical Investigations on Masonry Prisms

Numerical simulation is carried out on the same four combinations subjected for experimental investigations using Numerically Integrated Structural Analysis (NISA) tool. Masonry specimens are modeled in NISA. Figure 3 shows the physical model of a masonry prism as used for experimental investigation and the finite element model as is modeled in NISA. Numerical simulation helps to determine the various stresses acting on the specimen when the prisms are subjected to loading.

Any element subjected to loading has stresses induced in the element. The stresses induced are normal stress, tangential stress/shear stresses, and principal stresses.

These specimens are subjected to compression along the longitudinal direction (*Y*-axis). The masonry is modeled as a heterogeneous material by assigning the

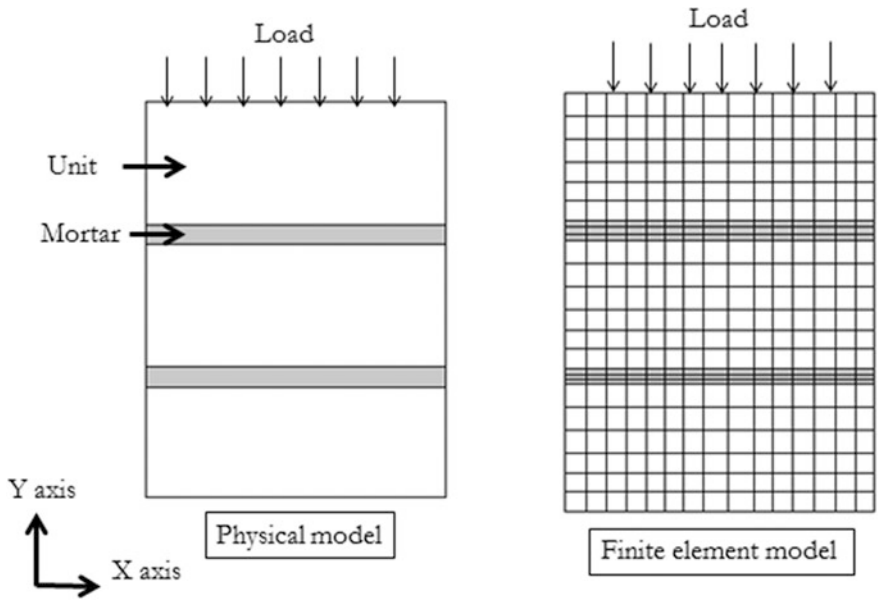

Fig. 3 Physical and finite element models

respective elastic properties to unit and mortar as obtained from experimental study. The study comprised of two parts, in the first part, the analysis is carried out with RMM of 3 mm thickness. The second part comprised of masonry specimens modeled with RMM of 10 mm thickness. Nature of stresses in mortar and unit developed along the longitudinal (along *y*-axis) and lateral stresses (along *x*-axis) are studied for the four masonry prism combinations. The stress contours hence obtained from the simulation for the prisms are shown in Figs. 4, 5, 6 and 7.

Stresses developed in lateral direction for AAC with RMM and HCB with RMM combinations are found to be compression in unit and tension in mortar. However

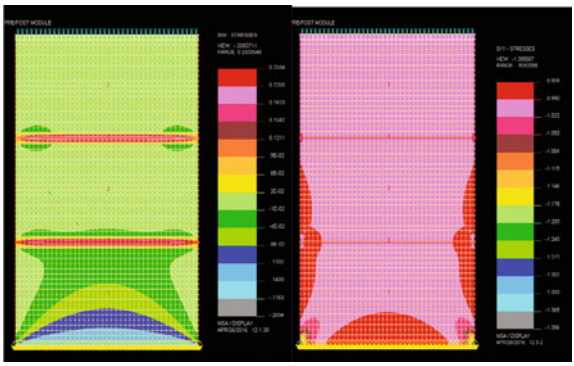

Fig. 4 Stresses in *x* and *y* direction for AAC with RMM

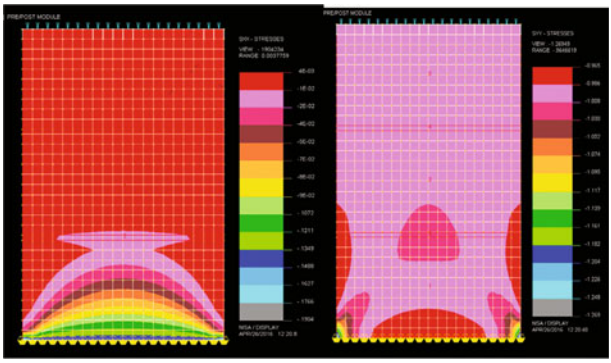

Fig. 5 Stresses in *x* and *y* direction for AAC with CM

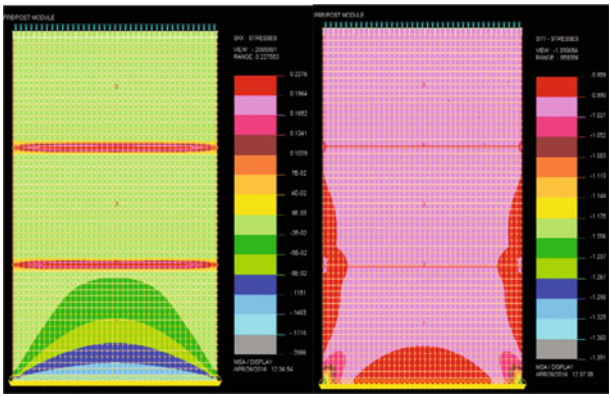

Fig. 6 Stresses in *x* and *y* direction for HCB with RMM

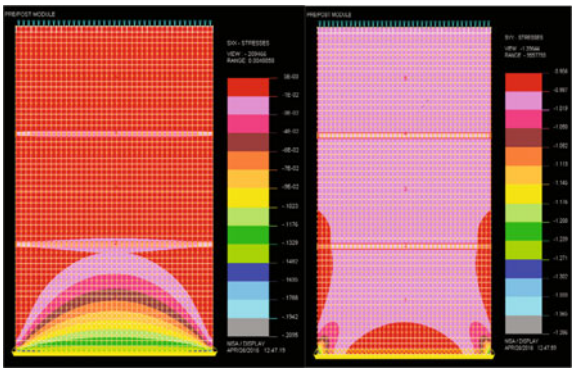

Fig. 7 Stresses in *x* and *y* direction for HCB with CM

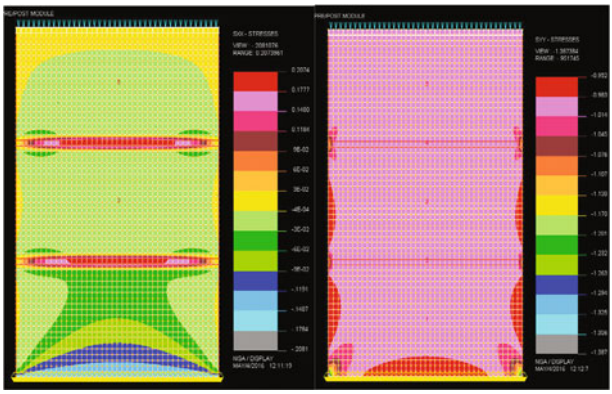

Fig. 8 Stress in *x* and *y* direction for AAC with 10 mm RMM

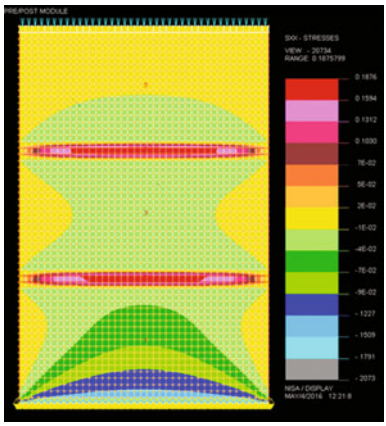

Fig. 9 Stress in *x* direction for HCB with RMM

when conventional mortar is used with HCB, it is found to be reversed. In case of AAC with CM, both the unit and mortar developed tensile stresses. Stresses developed in longitudinal direction are found to be in compression for all the prism combination.

Further, the masonry prism specimens are modeled with RMM of 10 mm thickness. The stress contours developed are as shown in Figs. 8 and 9.

Numerical simulation of the test on compressive strength of masonry prisms with increase in thickness of RMM from 3 to 10 mm has resulted in partial development of compression and tension zones in the unit and tensile stresses in mortar in the lateral direction. Thus, increase in mortar thickness did not show any prominent changes in the nature of stresses developed in masonry.

5 Conclusion

From the experimental and numerical study the following conclusion can be drawn:

1. Properties of AAC block satisfy as a masonry unit. Similarly ready mix mortar exhibited properties similar to conventional mortar.
2. Compressive strength of AAC + RMM is found to be the least among the four combinations which is 2.02 N/mm^2. The compressive strength of HCB + RMM is the highest with a value of 4.73 N/mm^2.
3. Stresses developed in lateral direction for AAC with RMM and HCB with RMM combinations are found to be compression in unit and tension in mortar. However, when conventional mortar is used with HCB, it was found to be reversed. In case of AAC with CM, both the unit and mortar developed tensile stresses. Similar pattern is observed when the thickness was increased from 3 to 10 mm.
4. In both experimental and numerical analysis, the performance of hollow concrete blocks with conventional mortar or ready mix mortar is relatively better than AAC blocks with conventional or ready mix mortar.

References

1. Doddamani, D. (2016). *Experimental and numerical analysis on AAC block masonry with ready mix mortar*. M. Tech thesis, Submitted to Visveswarayya Technological University, Belgaum.
2. Brebbia, C. A., Telles, J. C. F., & Wrobel, L. C. (1984). *Boundary element techniques*. Berlin and New York: Springer. http://www.madehow.com/Volume-3/Concrete-Block.html.
3. http://www.greenspec.co.uk/building-design/blocks/.
4. Chaipanich, A., et al. (2015). *The properties and durability of autoclaved aerated concrete masonry blocks.* Chiang Mai, Thailand: Chiang Mai University.
5. Krishna Bhavani, K. (2012). Cellular light weight concrete blocks as a replacement of burnt clay bricks. *International Journal of Engineering and Advanced Technology (IJEAT), 2*(2).
6. Mirza, W. H., et al. (1986). Utilisation of Saudi sand for aerated concrete production. *The International Journal of Cement Composites and Lightweight Concrete, 8*(2).
7. Narayanan, N., et al. (2000*). Structure and properties of aerated concrete: A review*. Chennai: Building Technology and Construction Management Division, Department of Civil Engineering, Indian Institute of Technology Madras.
8. Newman, J., Choo, B. S., & Owens, P. (2003). *Advanced concrete technology processes* (Part 2, pp. 2/7–2/9). Elsevier Ltd.
9. Andolsun, S. (2006). *A study of material properties of autoclaved aerated concrete (AAC) and its complementary wall elements*. Middle East Technical University.
10. IS 3952—1978 (Reaffirmed 1995). Indian Standard specification for burnt clay hollow bricks for walls and partitions, Bureau of Indian Standards, New Delhi, February 1989.
11. IS: 2185(Part 2)—1983 (Reaffirmed 1989). Indian standard specification for concrete masonry units, Bureau of Indian Standards, New Delhi, December 1996.
12. IS 2250—1981 (Reaffirmed 1995). Indian Standard code of practice for preparation and use of masonry mortars, Bureau of Indian Standards, New Delhi, February 1993.

Effect of Addition of Fly Ash and Superplasticizer on Ultra-fine Slag Based Geopolymer Mortar

Sulaem Musaddiq Laskar and Sudip Talukdar

Abstract Geopolymer is a promising sustainable supplementary cementitious material in construction industry. Researchers have found it to have strong potential for replacing the Portland cement in mortar and concrete. The present study reports experimental works performed on geopolymer mortar prepared from ultra-fine ground granulated blast furnace slag. Geopolymer mixes were prepared with alkali activator composed of sodium hydroxide solution and addition of certain admixtures such as fly ash and superplasticizer. The mixes were tested to study properties such as setting time, workability and strength. Addition of fly ash to slag based geopolymer was advantageous in terms of setting time and workability performance. However, very high amount of fly ash in the mix caused significant reduction in strength. Superplasticizer also modified the properties of geopolymer mixes at fresh and hardened state. High dosage of superplasticizer caused deterioration of performance of geopolymer mix.

Keywords Ultra-fine ground granulated blast furnace slag · Fly ash Superplasticizer · Setting time · Workability · Compressive strength

1 Introduction

Geopolymer is an emerging sustainable supplementary cementitious material in construction industry. Till date, numerous research works have been carried out to understand the behaviour of geopolymeric systems in terms of workability, strength, durability, etc. [1–8]. Geopolymers have capacity of sustaining strength when exposed to high temperature of order 800 °C [9]. The compressive and bond

S. M. Laskar · S. Talukdar (✉)
Department of Civil Engineering, Indian Institute of Technology Guwahati, Guwahati 781039, India
e-mail: s.taluk@iitg.ernet.in

S. M. Laskar
e-mail: sulaem@iitg.ernet.in

A. Rama Mohan Rao and K. Ramanjaneyulu (eds.), *Recent Advances in Structural Engineering, Volume 1*, Lecture Notes in Civil Engineering 11,
https://doi.org/10.1007/978-981-13-0362-3_56

strength; and abrasion resistance of geopolymeric systems are superior to Portland cement (PC) based ones [10]. While some of the geopolymers have to be cured at elevated temperature for attaining strength, slag based geopolymer can gain strength even when cured at ambient temperature [11, 12].

Ultra-fine slag has been successfully employed to produce geopolymeric systems of superior performance. Such geopolymer can gain sufficient strength at early ages [2, 13]. Ultra-fine materials also help to exhibit better durability performance [2, 14]. However, mortar or concrete prepared by ultra-fine material exhibit lower setting time and workability compared to the mortar or concrete prepared with same binder of lower fineness [15].

To modify the setting behaviour and workability of geopolymer mixes, researchers have performed series of experiments by adding various types of chemical admixtures to geopolymer mixes [16]. Douglas and Brandstetr [17] added very high amount of superplasticizer (SP) to slag based geopolymer and found that workability improved, but the strength reduced when compared to the strength of geopolymer consisting no SP. Bakharev et al. [18] found that addition of ligno-sulphonate admixture to geopolymer improved workability however, it retarded strength development.

Activators of various types have been used for geopolymerisation process in both isolated and combined form [1, 2, 4, 19–22]. Researchers found alkali metal silicates and/or hydroxides to be the most suitable. However, alkali silicates are expensive, they cause shortening of setting time and reduce workability [22]. Hence, to get rid of such disadvantages, alkali metal hydroxides can be better alternative. Sodium hydroxide (SH) activated geopolymer can attain higher strength compared to sodium silicate (SS) activated geopolymer when cured at ambient temperature [11]. Carbon footprint of alkali metal hydroxide based geopolymer is lower than alkali metal silicate based ones [23].

Till date, inadequate investigations were performed on SH activated ultra-fine ground granulated blast furnace slag (UGGBS) based geopolymer. Such geopolymeric systems have very low setting time and workability. Therefore, an attempt has been made in this study to investigate the setting time, workability and strength behaviour of UGGBS based geopolymer. Effect of addition of FA and SP on fresh and hardened state properties of geopolymer mortar have been investigated through series of laboratory experiments.

2 Materials and Method

UGGBS available indigenously was used as primary binding agent in the geopolymer mixes. Class F FA obtained from thermal power plant at Farakka, India was used as an additive. Physical and chemical properties of UGGBS and FA are given in Table 1. Physical properties such as median particle size and specific surface area have been evaluated by laser particle size analyzer and specific gravity

Table 1 Chemical and physical properties of binder

Chemical composition (% mass)	UGGBS	FA
Silicon dioxide (SiO_2)	33.6	55.47
Aluminium oxide (Al_2O_3)	22.5	25.37
Ferric oxide (Fe_2O_3)	1.3	6.2
Calcium oxide (CaO)	34.0	6.24
Magnesium oxide (MgO)	6.8	1.55
Sulphur oxide (SO_3)	0.15	0.9
Physical properties		
Specific gravity	2.84	2.42
Median particle sized d50 (μm)	3.579	26.33
Specific surface area (cm^2/g)	30,100	8940

Table 2 Mix proportion (kg)

Mix	UGGBS	FA	SP dosage (%)
M1	100	0	0
M2	80	20	0
M3	70	30	0
M4	60	40	0
M5	50	50	0
M6	70	30	0.5
M7	70	30	1.5
M8	70	30	3

by laboratory experiment as per Indian Standard (IS) [24]. Chemical property, i.e. oxide composition has been determined by X-ray fluorescence spectrometer (XRF).

In this paper, UGGBS and FA are together referred as total binding agent. Commercially available SH pellets were used to prepare the alkali activator. SH solution of required concentration was prepared by mixing SH pellets having 97–98% purity with distilled water. Alluvial sand conforming to zone III of IS [25] having specific gravity of 2.69 and water absorption of 1.7% was used as fine aggregate. Polycarboxylate ether based SP were used in the study.

Table 2 presents the mix proportion of geopolymer mortar mixes prepared as per IS [24] to study the effect of addition of FA of varying amounts of 20, 30, 40 and 50% by weight of total binding agent in the mortar; and addition of SP of varying amounts of 0.5, 1.5 and 3% by weight of total binding agent in the mortar. The ratio of total binding agent to fine aggregate was 1:3 [24]. Alkali activator to binding agent ratios (*a*/*b*) of 0.6 was selected for preparing the mixes. Concentration of SH solution was 10 molar (M). Mixes M1 to M5 were tested to observe the effect of addition of FA of varying amounts to the UGGBS based geopolymer. M3, M6, M7 and M8 were tested for finding the effect of addition of SP of varying amounts to the UGGBS based geopolymer.

Prior to casting of geopolymer mortar specimens, alkali activator was prepared. SH solution was prepared by mixing SH pellets with distilled water as per desired

molarity 24 h before the casting of specimens and then allowed to cool. Before addition of alkali activator to the mortar mixes, UGGBS, FA and fine aggregates were manually mixed dry thoroughly for 2 min. Later, to this dry mix, alkali activator was added and further mixed for 3 min. SP was added to the mix after addition of alkali activator. For geopolymer pastes preparation for conducting setting time tests, similar procedure and mix proportions were maintained as that of corresponding geopolymer mortar excluding fine aggregate addition.

Cube specimens of size 50 mm × 50 mm × 50 mm were used to perform compressive strength test of geopolymer mortar. Fresh geopolymer mortars were placed into cubes in two layers, each layer being tamped 25 times by tamping rod. Later, these were placed under ambient temperature of 20 ± 2 °C. After 24 h of casting, the cubes were demolded and completely submerged inside water tank maintaining temperature of 20 ± 2 °C and stored till the arrival of test day.

The provisions mentioned in IS [24] were adopted for performing setting time tests of geopolymer pastes using Vicat apparatus, workability test and compressive strength tests of geopolymer mortar. For assessing workability property of fresh geopolymer mortars, flow table test was conducted immediately after mixing the mortar ingredients. The results are indicated in terms of flow index as given below:

$$\mathrm{FI} = \frac{\mathrm{FD} - \mathrm{ID}}{\mathrm{ID}} \times 100 \tag{1}$$

where FI is the flow index in percent. FD is the average final base diameter of mortar mass measured on four diameters after jolting as per the codal provisions, ID is the original base diameter, which is 100 mm. Compressive strength tests were conducted on the cube specimens at 7, 28 and 91 days to assess the strength of the geopolymer mortars at both early and later ages.

Field emission scanning electron microscopic (FESEM) images of UGGBS, FA, combination of 80% UGGBS and 20% FA; and 50% UGGBS and 50% FA were obtained.

3 Results and Discussions

Addition of FA to the mixes retarded the setting time (see Table 3). Gradual increase in setting time occurred with the increase in FA content. This phenomenon is due to the fact that unlike UGGBS, FA cannot form geopolymerisation products instantly at early stages when subjected to curing at ambient temperature [12, 26], thereby delaying the setting of the mixes. Moreover, since FA particles are spherical shaped as seen in Fig. 1, its addition allowed better mobility of particles in the mixes which eventually contributed to delay of setting time. However, the increase was more pronounced in mixes with FA content of 30% and above, compared to those with FA content of 20%.

Addition of SP to the mixes at constant FA content contributed to the retardation of early setting by preventing the geopolymerisation products from formation of

Table 3 Results from setting time test (mins)

Mix	Initial setting time	Final setting time
M1	13	24
M2	20	51
M3	35	60
M4	37	69
M5	44	71
M6	37	68
M7	58	88
M8	53	80

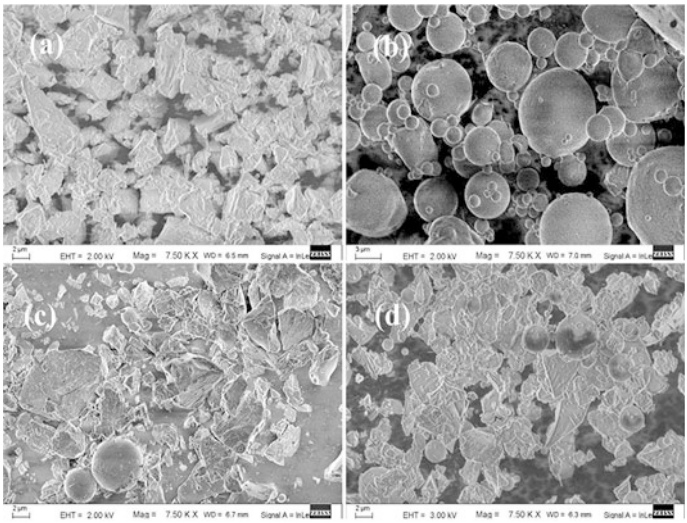

Fig. 1 FESEM images of **a** UGGBS, **b** FA, **c** 80% UGGBS and 20% FA; and **d** 50% UGGBS and 50% FA

bonds at early period. The reason for this is similar to that of addition of FA in the mixes which provide better mobility to particles by producing less viscous mixes and thus retarding the setting times. In fact, the accelerating capacity of SP which is otherwise shown in decreasing the setting times of PC based systems is not shown in these geopolymeric mixes. Retarding effect deteriorated at dosage higher than 1.5%. Figure 2 shows that by increasing the content of FA in the mixes, higher workability can be attained. The steep rise of FI curve beyond 20% FA content point indicated that increase in FI with increasing FA content was more for mixes with FA content higher than 20%. Increase in addition of FA increases the availability of smooth and spherical particles in the mixes which contribute to better sliding among the particles and reduction of friction which is otherwise caused due

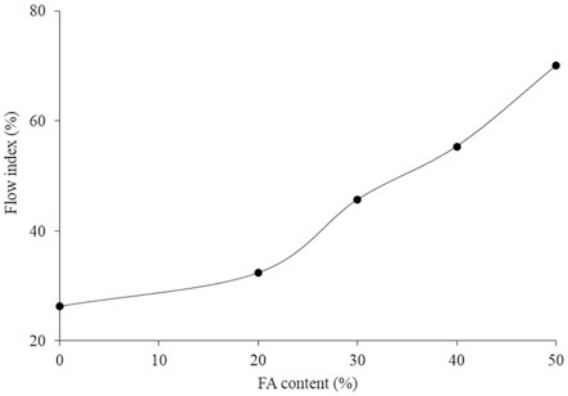

Fig. 2 Effect of FA content on workability of mixes

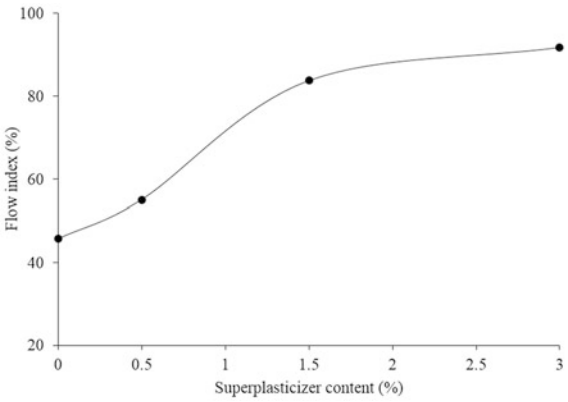

Fig. 3 Effect of SP content on workability of mixes

to presence of angular UGGBS particles. FESEM images in Fig. 1 show the particle shape and distribution in mixes. As FA content in the mixes increases, reduction of total friction among the particles occurs leading to better workability.

SP contributed towards increasing workability of the mixes with constant FA content of 30% (see Fig. 3). It helped in releasing the liquid component in the mixes trapped in flocs by dispersing the solid particles. Higher dosage of SP (>1.5%) led to segregation in the mix. At SP dosage of 3%, solid particles in the mixes got highly dispersed causing separation of semiliquid phase from the solid phase. Such behaviour of mixes with SP have also been observed by Laskar and Bhattacharjee [27] in their work on FA based geopolymeric mixes consisting of SP. Criado et al. [28] observed similar changes due to addition of SP in the geopolymeric mixes.

Though addition of FA in the mixes retarded setting time and improved workability as seen in Table 3 and Fig. 3. However, it reduced strength of mixes at early age (see Fig. 4). The reduction in the strength was more significant in mixes with FA content 40 and 50%. Strengths of these mixes at later ages, i.e. 28 days and

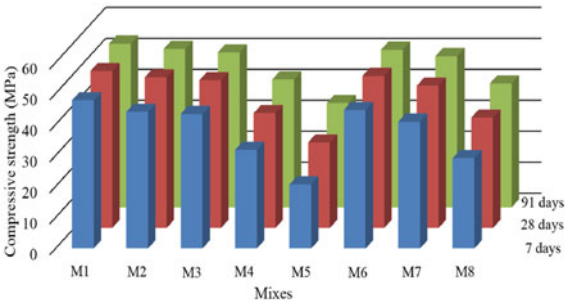

Fig. 4 Compressive strength of mixes at 7, 28 and 91 days

beyond were notably higher than those at early age indicating the contribution of FA in long term strength when cured at ambient temperature. However, such contribution could not help the mixes with FA content 40 and 50% to attain strengths similar to that of the other mixes.

The main product in UGGBS based geopolymer is calcium silicate hydrate (C–S–H) when activated with alkaline solution [29]. The formation of C–S–H takes place even at ambient temperature. FA on the other hand is rich in SiO_2 and Al_2O_3. In alkaline medium, polymerisation occurs to transform aluminosilicates minerals to three dimensional polymeric chains [30]. However, FA can contribute to the strength development in geopolymer at early days only if cured at elevated temperature [26, 31]. In this study, geopolymer mortars were cured at ambient temperature. Thus, contribution of FA in the strength development is insignificant at early age.

In the mixes, angular UGGBS particles contributed to early strength gain by enhanced rate of geopolymerisation due to availability of higher particle surface areas. But, the angular shape and higher particle surface area reduced workability and accelerated setting of the mixes rendering it unsuitable for use as building material. On the other hand, though the smooth and spherical FA particles led to lower rate of geopolymerisation, but they balanced the workability loss and retarded the setting.

The amount of SP significantly affected the strength of the mixes. Huge variation in strength at various days was observed in mixes with various amount of SP (see Fig. 4). Compared to 28 days strength, more than about 80% strength was attained at 7 days by the mixes containing SP. Mix with 0.5% SP exhibited highest strength at each selected day. Higher dosage (>0.5% SP) led to reduction of strength. Though in mixes with 1.5% SP dosage, the strength drop compared to mixes with 0.5% SP dosage was lower but pronounced strength drop was observed for mixes with 3% SP dosage. The strength drop can be attributed to the fact that at 3% SP dosage, segregation occurred in the mix which was observed while performing the workability test of fresh mortar mix. Similar strength reduction with increase of SP content was observed by Douglas and Brandstetr [17].

4 Conclusions

This paper reports the results of laboratory experiments performed on eight different UGGBS based geopolymer mixes activated by SH. Admixtures such as FA and SP were added to the mixes and their influence on setting time, workability and strength was observed. Following important observations were made from the study:

1. Addition of FA in the mixes retarded the early setting property and improved the workability of the mixes. Significant improvement of properties of mixes in fresh state was observed when FA content was 30% and higher.
2. Amount of FA higher than 30% of total binder content resulted in reduction in strength of the mixes at early age. It also causes reduction in the strength at later ages.
3. SP retarded the early setting property and improved the workability of the mixes. Change in the trend of the influence of SP was observed at higher dosage, i.e. beyond 1.5% SP dosage. SP showed better performance up to dosage 1.5%.
4. Strength of mixes improved with the addition SP. However, SP dosage higher than 0.5% of total binder content led to significant reduction strength of the mixes.

Acknowledgements The authors are grateful to Counto Microfine Products Private Limited, India and Fosroc Chemicals India Private Limited, India for providing materials required for laboratory tests in the current research at IIT Guwahati.

References

1. Morsy, M. S., Alsayed, S. H., Al-Solloum, Y., & Almusallam, T. (2014). Effect of sodium silicate to sodium hydroxide ratios on strength and microstructure of fly ash geopolymer binder. *Arabian Journal of Science and Engineering, 39,* 4333–4339.
2. Brough, A. R., & Atkinson, A. (2002). Sodium silicate-based, alkali-activated slag mortars part I. Strength, hydration and microstructure. *Cement and Concrete Research, 32,* 865–879.
3. Law, D. W., Adam, A. A., Molyneaux, T. K., & Patnaikuni, T. (2012). Durability assessment of alkali activated slag (AAS) concrete. *Materials and Structure, 45,* 1425–1437.
4. Vargas, A. S., Molin, D. C. C. D., Masuero, A. B., Vilela, A. C. F., Castro-Gomes, J., & Gutierrez, R. M. (2014). Strength development of alkali-activated fly ash produced with combined NaOH and $Ca(OH)_2$ activators. *Cement and Concrete Composite, 53,* 341–349.
5. Gorhan, G., & Kurklu, G. (2014). The influence of the NaOH solution on the properties of the fly ash-based geopolymer mortar cured at different temperatures. *Composites: Part B, 58,* 371–377.
6. Kim, Y. J., Kim, S. C., & Kim, Y. T. (2003). Corrosion resistance and hydration heat of concrete containing ground granulated blast furnace slag. *KSCE Journal of Civil Engineering, 7*(4), 399–404.

7. Pacheco-Torgal, F., Castro-Gomes, J., & Jalali, S. (2008). Alkali-activated binders: A review part 1. Historical background, terminology, reaction mechanisms and hydration products. *Construction and Building Materials, 22,* 1305–1314.
8. Singh, B., Ishwarya, G., Gupta, M., & Bhattacharyya, S. K. (2015). Geopolymer concrete: A review of some recent developments. *Construction and Building Materials, 85,* 78–90.
9. Wenzhong, Z., & Jing, Z. (2013). The effect of elevated temperature on bond performance of alkali-activated GGBFS paste. *Journal of Wuhan University of Technology Material Science Edition, 28*(4), 721–725.
10. Hu, S., Wang, H., Zhang, G., & Ding, Q. (2008). Bonding and abrasion resistance of geopolymeric repair material made with steel slag. *Cement and Concrete Composite, 30,* 239–244.
11. Altan, E., & Erdogan, S. T. (2012). Alkali activation of a slag at ambient and elevated temperatures. *Cement and Concrete Composite, 34,* 131–139.
12. Yang, K. H., Song, J. K., Ashour, A. F., & Lee, E. T. (2008). Properties of cementless mortars activated by sodium silicate. *Construction and Building Materials, 22,* 1981–1989.
13. Binici, H., Temiz, H., & Kose, M. M. (2007). The effect of fineness on the properties of the blended cements incorporating ground granulated blast furnace slag and ground basaltic pumice. *Construction and Building Materials, 21,* 1122–1128.
14. Teng, S., Lim, T. Y. D., & Divsholi, B. S. (2013). Durability and mechanical properties of high strength concrete incorporating ultra fine Ground Granulated Blast-furnace Slag. *Construction and Building Materials, 40,* 875–881.
15. Collins, F., & Sanjayan, J. G. (1999). Effects of ultra-fine materials on workability and strength of concrete containing alkali-activated slag as the binder. *Cement and Concrete Research, 29,* 459–462.
16. Rattanasak, U., Pankhet, K., & Chindaprasirt, P. (2011). Effect of chemical admixtures on properties of high-calcium fly ash geopolymer. *International Journal of Minerals, Metallurgy and Materials, 18*(3), 364–369.
17. Douglas, E., & Brandstetr, J. (1990). A preliminary study on the alkali activation of ground granulated blast-furnace slag. *Cement and Concrete Research, 20,* 746–756.
18. Bakharev, T., Sanjayan, J. G., & Cheng, Y. B. (2000). Effect of admixtures on properties of alkali-activated slag concrete. *Cement and Concrete Research, 30,* 1367–1374.
19. Somna, K., Jaturapitakkul, C., Kajitvichyanukul, P., & Chindaprasirt, P. (2011). NaOH-activated ground fly ash geopolymer cured at ambient temperature. *Fuel, 90,* 2118–2124.
20. Gu, K., Jin, F., Al-Tabbaa, A., Shi, B., & Liu, J. (2014). Mechanical and hydration properties of ground granulated blastfurnace slag pastes activated with MgO–CaO mixtures. *Construction and Building Materials, 69,* 101–108.
21. Abdalqader, A. F., Jin, F., & Al-Tabbaa, A. (2016). Development of greener alkali-activated cement: Utilisation of sodium carbonate for activating slag and fly ash mixtures. *Journal of Cleaner Production, 113*, 66–75.
22. Khan, M. I., Azizlin, K., Sufian, S., & Man, Z. (2015). Sodium silicate-free geopolymers as coating materials: Effects of Na/Al and water/solid ratios on adhesion strength. *Ceramic International, 41,* 2794–2805.
23. Phoo-ngernkham, T., Maegawa, A., Mishima, N., Hatanaka, S., & Chindaprasirt, P. (2015). Effects of sodium hydroxide and sodium silicate solutions on compressive and shear bond strengths of FA–GBFS geopolymer. *Construction and Building Materials, 91,* 1–8.
24. Bureau of Indian Standard. (2004). Methods of test for pozzolanic materials, IS: 1727-1967, New Delhi, India.
25. Bureau of Indian Standard. (2002). Specification for coarse and fine aggregates from natural sources for concrete, IS: 383-1970, New Delhi, India.
26. Nath, P., & Sarker, P. K. (2014). Effect of GGBFS on setting, workability and early strength properties of fly ash geopolymer concrete cured in ambient condition. *Construction and Building Materials, 66,* 163–171.

27. Laskar, A. I., & Bhattacharjee, R. (2013). Effect of plasticizer and superplasticizer on rheology of fly-ash-based geopolymer concrete. *ACI Materials Journal, 110*(5), 513–518.
28. Criado, M., Palomo, A., Fernendez-Jimenez, A., & Banfill, P. F. G. (2009). Alkali activated fly ash: Effect of admixtures on paste rheology. *Rheologica Acta, 48,* 447–455.
29. Song, S., Sohn, D., Jennings, H. M., & Mason, T. O. (2000). Hydration of alkali-activated ground granulated blast furnace slag. *Journal of Material Science, 35,* 249–257.
30. Duxson, P., Fernández-Jiménez, A., Provis, J. L., Lukey, G. C., Palomo, A., & Van Deventer, J. S. J. (2007). Geopolymer technology: The current state of the art. *Journal of Material Science, 42,* 2917–2933.
31. Puertas, F., Martinez-Ramirez, S., Alonso, S., & Vazquez, T. (2000). Alkali-activated fly ash/slag cement Strength behaviour and hydration products. *Cement and Concrete Research, 30,* 1625–1632.

Carbonation, Shrinkage and Long-Term Studies on Recycled Aggregate Concrete

V. Bhashya and B. H. Bharatkumar

Abstract Crushing demolition waste concrete to produce recycled aggregates for production of new concrete is one common means for achieving a more environmentally friendly concrete. In this paper, durability properties such as drying shrinkage, carbonation and long-term exposure up to one year explained in detail. Increase in compressive strength of control and recycled aggregate concrete was around 20% after a exposure period of one year whereas reduction in water absorption were 1.5 and 6%, respectively, for control and recycled aggregate concrete. The carbonation depths and drying shrinkage in the recycled aggregate concrete were higher than conventional concrete. The use of heat treated recycled aggregates and incorporating fly ash/silica fume in addition to cement reduced the carbonation depth and drying shrinkage in concrete. Reduction of carbonation depth and drying shrinkage in recycled aggregate concrete was due to the minimization of pores in recycled aggregate after heating and abrasion treatment and incorporation of fly ash or silica fume in addition to cement in recycled aggregate concrete.

Keywords Recycled aggregate concrete · Carbonation · Shrinkage
Long-term studies

1 Introduction

The construction industry is one which, to a great extend, depends on natural resources. The large scale depletion of natural resources for extraction of natural aggregates, simultaneously, huge amount of construction and demolition (C&D) waste is produced during construction (construction waste), due to demolition of aged

V. Bhashya (✉) · B. H. Bharatkumar
Academy of Scientific and Innovative Research (AcSIR),
CSIR-Structural Engineering Research Centre, Chennai 600113, India
e-mail: bhashya@serc.res.in

B. H. Bharatkumar
e-mail: bharat@serc.res.in

A. Rama Mohan Rao and K. Ramanjaneyulu (eds.), *Recent Advances in Structural Engineering, Volume 1*, Lecture Notes in Civil Engineering 11,
https://doi.org/10.1007/978-981-13-0362-3_57

concrete structures (demolition waste) and insufficient number of landfills for dumping such waste led to search for a viable option for effective utilization of C&D Waste. The separate rules 'Construction and Demolition Waste Management Rules' for management of C&D waste was published by the Ministry of Environment, Forest and Climate Change, India, wide notification no. G.S.R.317(E) dated 29th, March 2016 [1]. The rules defined thresholds (more than 20 tonnes or more in one day or 300 tonnes per project in a month) above which construction and demolition wastes have to be sorted into four streams such as concrete, soil, steel, wood and plastics, bricks and mortar in order to facilitate their subsequent recovery.

In India, the Central Pollution Control Board has estimated solid waste generation to be about 48 million tonnes per year, of which 25% is from the construction industry [2]. It is seen from the literature [3–7] that the properties such as, density, water absorption, specific gravity, crushing value have a negative influence on recycled aggregate concrete quality. Grabiec et al. [8] concluded that the method of bio-deposition of calcium carbonate improved the quality of recycled aggregate. The acid concentration of 0.1 M proposed in the acid pre-soaking method developed by Tam et al. [9] was reported to result in only 7.27–12.17% reduction in the water absorption of the RCA samples tested. The acid concentration of 2 M proposed in the method developed by Akbernezhad et al. [10] was reported to result in less than one percentage of water absorption of the recycled concrete aggregates.

Yildiram et al. [11] studied shrinkage of recycled concrete having different *w/c* ratios. Authors reported for *w/c* = 0.7, Shrinkage (after 112 days) in recycled aggregate concrete two times more when compared to control concrete. For *w/c* = 0.6, a mere 16% difference was reported between highest and lowest shrinkage values after 112 days, while the corresponding difference for *w/c* = 0.5 was 37%. After 112 days, the differences in relative shrinkage tended to decrease with time. Ismail and Ramli [12] studied the shrinkage behaviour of three different types of concrete mixes by using natural, recycled and treated recycled aggregates. In particular, RCA concrete was likely related to the poor quality and low stiffness of untreated, coarse RCA, which was reported as affected in long run. However, enhancing the quality of treated RCA after surface treatment positively affected and slowed down drying shrinkage stress.

Leemann et al. [13] studied the carbonation of concrete having lime stone powder, micro silica and GGBS. The exposure conditions were 1% CO_2 (20 °C, 57%RH) and carbonation chamber with 4% CO_2(20 °C, 57%RH) sheltered outdoor and unsheltered outdoor exposure until the age of 56 days. The cement replacement with limestone powder, micro silica and GGBS reported higher carbonation coefficient than the use of ordinary Portland cement. The carbonation coefficients in the sheltered conditions are higher than in the unsheltered conditions. Miguel bravo et al. [14] concluded that the mixes with recycled aggregate have lower carbonation resistance than the control concrete. This was predictable since, when the water absorption was analysed, a property influenced by the same factors, the same trend occurred.

Experimental studies on recycled aggregate concrete have shown use of RCA has poor mechanical and durability properties of concrete. RCA has the greatest

potential to reduce the overall durability of RCA concrete, likely due to the greater amount of fissures created by RCA, into which water can permeate and diffuse. It is important to consider that climate can affect long-term performance of recycled aggregate concrete. Therefore, it is necessary to evaluate the durability responses and performance of concrete prepared using RCA. From the detailed review of existing literatures, several investigations are found in India related to the mechanical (compressive strength, split tensile strength, flexural strength and modulus of elasticity) and durability properties (water absorption, sorptivity, chloride ion permeability) recycled aggregate concrete. However, limited studies have been carried out to evaluate the carbonation, shrinkage and long-term performance of recycled aggregate concrete. Therefore, the present research focuses on carbonation, shrinkage and long-term studies of concrete prepared using RCA and use of treated RCA, incorporation of pozzolanic materials (fly ash and silicafume) to improve its properties.

2 Experimental Programme

2.1 Materials

Recycled coarse aggregates were prepared by crushing the demolished concrete in a jaw crusher set at an opening of 20 mm with the jaws in the closed position. Crusher products from each of the demolished concretes were screened into two size ranges (25–12.5 and 12.5–4.75 mm) and recombined into a recycled coarse aggregate of approximately the same grading as the natural aggregate (*i.e.* 60% of 25–12.5 mm, and 40% of 12.5–4.75 mm material). To improve the quality of the recycled aggregates, a heating and abrasion treatment described in the next section was used. Ordinary 53-grade Portland cement conforming to IS 12269 [15] was used. Locally available river sand passing through a 4.75-mm sieve was used as fine aggregate. Blue granite crushed stone aggregate of size ranging 12.5–25 and 4.75–12.5 mm was used in a ratio of 60:40 by volume as coarse aggregate for the control concrete. Fly ash from a thermal power plant near Chennai in India and silica fume supplied by a company in Mumbai was used in this research. The chemical composition of fly ash and silica fume is presented in Table 1.

2.2 Heating and Abrasion Treatment for the Recycled Aggregates

The presence of mortar was the main reason for lower quality of the recycled aggregates compared to natural aggregates. The adhered mortar can be removed by chemical treatment, heat treatment and microwave treatment [16]. Using this

Table 1 Chemical composition of fly ash and silica fume

Chemical compound	Fly ash (% by mass)	Silica fume (% by mass)
SiO_2	62.10	94.73
Al_2O_3	27.44	–
Fe_2O_3	4.57	–
CaO	0.83	–
MgO	0.55	–
Na_2O	0.04	0.51
K_2O	1.17	–
TiO_2	1.09	–
Mn_2O_3	0.04	–
SO_3	0.4	0.2
Chlorides	–	0.07

method, the recycled concrete aggregates were heated to 250 °C for four hours, after which the heated aggregates were immediately immersed in water causing a sudden reduction in the aggregate temperature and creating internal thermal stresses. After cooling, the adhered mortar became brittle. These aggregates were dry-mixed in a pan-type mixer for 2 to 3 minutes to remove the adhered mortar. Then, the mixture of recycled aggregates and removed mortar was sieved through standard sieves for preparation of treated recycled aggregates.

2.3 Mix Proportion and Test Specimens

Experimental investigations were carried out to investigate the carbonation, shrinkage and long-term performance of concrete, produced by replacing the natural aggregates with recycled aggregates coming from construction and demolition of waste. The concrete mix proportions were designed in accordance with IS 10262 [17], with a common target slump of 70 ± 10 mm. A super plasticizer made of sulphonated naphthalene formaldehyde was used. The content was 0.5% by weight of the binder. The details of the mix are given in Table 2. Totally four mixes have

Table 2 Mix proportions per 1 m^3 of concrete

Specimen Id	Cement (kg/m^3)	Fly ash/silica fume (kg/m^3)	Sand (kg/m^3)	Coarse aggregates (kg/m^3) (RCA)
Mix 1	362	–	832	–
Mix 2	362	–	793	921
Mix 3	362	92	782	828
Mix 4	362	46	784	875

Coarse aggregate (NA) 1030 kg/m^3, water 170 kg/m^3

been cast. Mix 1 contained 100% natural aggregates. This group serves as control mix. In Mix 2, 100% of the natural aggregate was replaced with RCA. The samples in Mix 3 contained fly ash 10% of the coarse aggregate in addition to cement and Mix 4 produced with 5% of the coarse aggregate was replaced by silica fume. The natural coarse aggregates in Mix 3 and Mix 4 were replaced with 100% treated RCA. The test specimens were casted for both conventional concrete mixes and RAC with water to cement ratio of 0.5.

2.4 Long-Term Studies

Experimental studies on recycled aggregate concrete have shown use of RCA has poor mechanical and durability properties of concrete. These effects on concrete properties can affect the long-term performance of the concrete mix. RCA has the greatest potential to reduce the overall durability of RCA concrete, likely due to the greater amount of fissures created by RCA, into which water can permeate and diffuse. Also, it is important to consider that climate can affect long-term performance of recycled aggregate concrete. Therefore, it is necessary to evaluate the responses and performance of RCA concrete in the long-term through experimental studies. In the present study, performance of natural and recycled aggregate concrete exposed to open atmosphere up to a period of one year have been studied.

2.5 Carbonation

The accelerated carbonation test was carried out on recycled aggregates obtained from construction and demolition waste. The test specimens were casted for both conventional concrete mixes and RAC with water cement ratio of 0.5. Concrete cubes of size 100 mm were cast to determine the compressive strength and carbonation of recycled aggregate concrete. The specimens taken from the curing chamber were directly put into the accelerated carbonation apparatus. Exposing the concrete specimens to the accelerated carbonation process will be continued for a period of 1 and 2 months. The specimens were subjected to 2.5% carbon dioxide in a chamber with a temperature of 20 °C and 65% RH, until the time required for testing.

2.6 Drying Shrinkage

Experimental investigations were carried out to investigate the shrinkage of concrete, produced by replacing the natural aggregates with recycled aggregates coming from construction and demolition of waste. The main aim of this work was

to determine shrinkage variations experienced in recycled concrete, and comparing it to control concrete. Concrete specimens having size 100 × 100 × 500 mm were prepared to conduct shrinkage test. The change in length of the specimens was recorded when their age of curing reached 3, 7, 28, 60, 90, 120,150 and 180 days.

3 Results and Discussion

3.1 Bulk Density

Recycled aggregates have lower density when compared to natural aggregates. This was due to the presence of adhered mortar in the recycled aggregates. Bulk density of natural and recycled aggregate is presented in Table 3. Reduction in bulk density was observed by 9% and 12% for RCA sizes ranging from 4.75 to 12.5 mm and 12.5 to 25 mm, respectively, in comparison to natural aggregates. After heating and abrasion treatment bulk density of recycled aggregates increased by 8 and 10% for aggregates of sizes ranging from 4.75 to 12.5 mm and 12.5 to 25 mm, respectively.

3.2 Water Absorption

Recycled concrete aggregate sizes ranging from 12.5 to 25 mm and 4.75 to 12.5 mm had very high percentages of water absorption. Water absorption of natural aggregate of size 12.5–25 mm was found to be 0.7%, whereas for recycled aggregate it was 4.8% by weight. The water absorption of recycled concrete aggregate was 6.8 times that of natural aggregate, while many investigations found the water absorption about 6–10 times [18–20]. This was due to the porous characteristics of the mortar residue adhering to the original aggregate particles. The heating and abrasion method reduces the water absorption to 1.62% by weight. Hence, it is observed that there is a 66% reduction in water absorption of recycled aggregate after treatment. For the 4.75–12.5 mm aggregates, after treatment with the heating and abrasion method, water absorption was reduced to 1.59 from 2.67%.

Table 3 Bulk density of recycled aggregates

Aggregate type	Bulk density (Kg/m^3)	
	(4.75–12.5 mm)	(12.5–25 mm)
NA	1572	1690
RCA	1430	1483
Treated RCA	1550	1664

3.3 Results of Long Studies on RAC

Table 4 presents results of compressive strength of recycled aggregate concrete specimens exposed to open atmosphere for a period of one year. Compressive strength of control (Mix 1) and recycled aggregate concrete specimens (Mix 2) tested after one year have 20 and 18% increment in strength, respectively, this may be due to strength gained by concrete during the period of exposure. The increase in strength in the specimens with fly ash and silica fume, when 100% of the coarse aggregate was replaced by recycled aggregate was 33% (Mix 3), and 32% (Mix 4100). Fly ash or silica fume could improve the compressive strength with age because of a pozzolanic reaction.

Table 5 presents results of water absorption of recycled aggregate concrete specimens exposed to open atmosphere for a period of one year. Reductions in water absorption for control (Mix 1) and recycled aggregate concrete specimens (Mix 2) tested after one year were 1.49 and 6.14%, respectively. The water absorption of heat treated recycled aggregate concrete with addition of fly ash and silica fume was reduced by 1.78 (Mix 3) and 1.9% (Mix 4), respectively. Hence, a significant amount of reduction in water absorption was observed when the addition of mineral admixtures in concrete with heat treated recycled aggregates.

3.4 Results of Carbonation

The specimens were taken out after completion of the test and the depth of carbonation was measured by spraying the surface of a freshly broken concrete cube specimen with a 1% phenolphthalein indicator solution. Purple red colour is obtained in the non-carbonated part of the specimen where the concrete is still highly alkaline, while in the carbonated part of the specimen due to the carbonation,

Table 4 Compressive strength of RAC exposed to one year

Age of concrete	28 days	1.0 years
Mix 1	38.25	46.27
Mix 2	31.74	37.49
Mix 3	45.51	60.95
Mix 4	44.75	59.07

Table 5 Water absorption of RAC exposed to one year

Specimen designation	Water absorption (%)	
	28 days	1.0 years
Mix 1	4.22	4.15
Mix 2	6.49	6.03
Mix 3	4.92	4.83
Mix 4	4.86	4.76

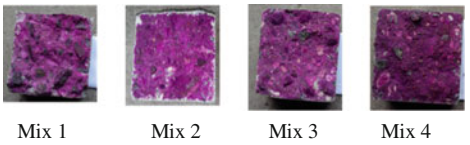

Fig. 1 Carbonation in conventional and recycled aggregate concrete

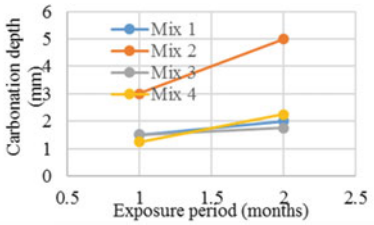

Fig. 2 Depth of carbonation of recycled aggregate concrete (*w/c* = 0.5)

the alkalinity of concrete is reduced and no colour occurs (Fig. 1). Immediately after spraying the indicator, the average depth of the colourless phenolphthalein region has been measured. In conventional concrete, the carbonation depth measured was around 2 mm, whereas in recycled aggregate concrete it was higher. Figure 2 shows the depth of carbonation recycled aggregate concrete for *w/c* 0.5. It is observed that the recycled aggregate concrete was 2.0–2.5 times greater than that of conventional concrete. This may be attributed to the recycled aggregate being more porous. The use of heat treated recycled aggregates and incorporating fly ash/silica fume in addition to cement reduced the carbonation depth in concrete. This is due to the reduction of pores in recycled aggregate after treatment and fly ash or silica fume in addition to cement reduced the porosity of recycled aggregate concrete.

3.5 Results of Shrinkage on RAC

Figures 3 and 4 show the carbonation and percentage weight loss in RAC with age. The results from the shrinkage test showed that the drying shrinkage values of all

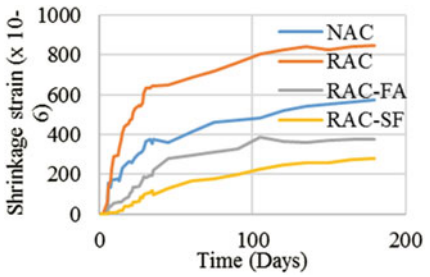

Fig. 3 Comparison of shrinkage strain in RAC with conventional concrete

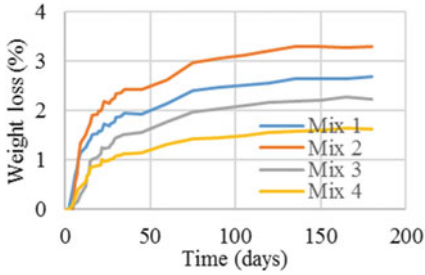

Fig. 4 Comparison of weight loss (%) with age in RAC with conventional concrete

specimens, which were measured up to 180 days, fell below 850 microstrains. From the results during the early ages up to 28 days, the drying shrinkage behaviour of all four concrete mixes was observed to similar. After 28 days, however, different drying shrinkage values became clearer. In particular, concrete having 100% RCA exhibited a high shrinkage value compared with the control concrete. Shrinkage in the recycled concrete was 79% higher than that of the control concrete after a period of 180 days. The higher shrinkage of the 100% RCA mix may be the relatively easier loss of moisture from the RCA particles because it is likely that this is free water and is not required to hydrate the cement in the residual mortar which is already hydrated. However, enhancing the quality of treated RCA after surface treatment positively affected and slowed down drying shrinkage in concrete with fly ash and silicafume. At the age of 180 days, the shrinkage strains in concrete with fly ash were 20% and with silicafume were 47% lesser than in control mix. Based on these observations, it is obvious that the RCA mixes produced by using treated RCA and mineral admixtures experience less long-term shrinkage than the concrete prepared by using untreated RCA.

4 Conclusions

Experimental investigations were carried out on concrete with coarse recycled concrete aggregates. The study presents the physical and mechanical properties of the recycled concrete aggregate (RCA) and the durability of concrete prepared with RCA. Durability properties such as drying shrinkage, carbonation and long-term exposure up to one year were presented. Increase in compressive strength of control and recycled aggregate concrete was around 20% after a exposure period of one year whereas, reduction in water absorption was 1.5 and 6%, respectively, for control and recycled aggregate concrete. The carbonation depths drying shrinkage in the recycled aggregate concrete were higher than conventional concrete. It was observed that the carbonation depth in recycled aggregate concrete was 2.0–2.5 times greater than that of conventional concrete. The use of heat treated recycled aggregates and incorporating fly ash/silica fume in addition to cement reduced the carbonation depth and drying shrinkage in concrete. This is due to the reduction of

pores in recycled aggregate after treatment and fly ash or silica fume in addition to cement reduced the porosity of recycled aggregate concrete.

Acknowledgements The authors gratefully acknowledge the support of the technical staff at the Advanced Materials Laboratory (AML), SERC, Chennai, during the experimental work.

References

1. Construction and demolition waste management rules. *Ministry of Environment, Forest and Climate Change*, India, Notification No. G.S.R.317(E), March 29, 2016.
2. Rao, M. C., Bhattacharyya, S. K., & Barai, S. V. (2011). Recycled coarse aggregate and its use in concrete. *Indian Concrete Institute Journal, 11*(4), 27–40.
3. Katz, A. (2003). Properties of concrete made with recycled aggregate from partially hydrated old concrete. *Cement and Concrete Research, 33*(5), 703–711.
4. Hansen, T. C., & Narud, H. (1983). Strength of recycled concrete made from crushed concrete coarse aggregate. *Concrete International, 5*(1), 79–83.
5. Yang, J., Du, Q., & Bao, Y. (2011). Concrete with recycled concrete aggregate and crushed clay bricks. *Construction and Building Materials, 25*(4), 1935–1945.
6. Rao, M. C., Bhattacharyya, S. K., & Barai, S. V. (2011). Behaviour of recycled aggregate concrete under drop weight impact load. *Construction and Building Materials, 25*(1), 69–80.
7. Belén, G. F., Fernando, M. A., Diego, C. L., & Sindy, S. P. (2011). Stress–strain relationship in axial compression for concrete using recycled saturated coarse aggregate. *Construction and Building Materials, 25*(5), 2335–2342.
8. Grabiec, A. M., Klama, J., Zawal, D., & Krupa, D. (2012). Modification of recycled concrete aggregate by calcium carbonate bio deposition. *Construction and Building Materials, 34,* 145–150.
9. Tam, V. W., Tam, C. M., & Le, K. N. (2007). Removal of cement mortar remains from recycled aggregate using pre-soaking approaches. *Resources, Conservation & Recycling, 50*(1), 82–101.
10. Akbarnezhad, A., Ong, K. C. G., Zhang, M. H., Tam, C. T., & Foo, T. W. J. (2011). Microwave-assisted beneficiation of recycled concrete aggregates. *Construction and Building Materials, 25*(8), 3469–3479.
11. Yildirim, S. T. (2015). Christian meyer, simon herfellner Effects of internal curing on the strength, drying shrinkage and freeze-thaw resistance of concrete containing recycled concrete aggregates. *Construction and Building Materials, 91,* 288–296.
12. Ismail, S., & Ramli, M. (2014). Mechanical strength and drying shrinkage properties of concrete containing treated coarse recycled concrete aggregates. *Construction and Building Materials, 68,* 726–739.
13. Leemann, A., Nygaard, P., Kaufmann, J., & Loser, R. (2015). Relation between carbonation resistance, mix design and exposure of mortar and concrete. *Cement and Concrete Composites, 62,* 33–43.
14. Bravo, M., de Brito, J., Pontes, J., & Evangelista, L. (2015). Durability performance of concrete with recycled aggregates from construction and demolition waste plants. *Construction and Building Materials, 77,* 357–369.
15. Bureau of Indian Standards (BIS). (1987). Specifications for 53 grade ordinary portland cement, IS 12269, BIS, New Delhi, India.
16. Juan, M. S., & Gutierrez, P. A. (2009). Study on the influence of attached mortar content on the properties of recycled concrete aggregate. *Construction and Building Materials, 23*(2), 872–877.

17. Bureau of Indian Standards (BIS). (2009). Concrete mix proportioning-guidelines, IS 10262, BIS, New Delhi, India.
18. Somna, R., Jaturapitakkul, C., Chalee, W., & Rattanachu, P. (2012). Effect of the water to binder ratio and ground fly ash on properties of recycled aggregate concrete. *Journal of Materials in Civil Engineering, 24*(1), 16–22.
19. Poon, C. S., Shui, Z. H., & Lam, L. (2004). Effect of microstructure of ITZ on compressive strength of concrete prepared with recycled aggregates. *Construction and Building Materials, 18*(6), 461–468.
20. Tangchirapat, W., Buranasing, R., Jaturapitakkul, C., & Chindaprasirt, P. (2008). Influence of rice husk-bark ash on mechanical properties of concrete containing high amount of recycled aggregates. *Construction and Building Materials, 22*(8), 1812–1819.

Mechanical Properties of PVA and Polyester Fibers Based Engineered Cementitious Composites

S. B. Singh and Pankaj Munjal

Abstract Engineered cementitious composite (ECC) is a mortar based composite reinforced with polymeric fibers and exhibits strain hardening characteristic through the process of multiple micro-cracking. In this study, two types of polymeric fibers (i.e., polyvinyl alcohol (PVA) fibers and polyester (Poly) fibers) were used for making of ECC. The uniaxial compressive, uniaxial tensile, and four point bending test were carried out to characterize the mechanical behavior of PVA-ECC and Poly-ECC with same mix proportions. The compressive, tensile and flexural stress–strain responses of ECC are plotted. The ratio of compressive strengths of cylinder (150 × 300 mm), and small cube (70.7 × 70.7 × 70.7 mm) to the compressive strength of standard cube (150 × 150 × 150 mm) is determined. The experimental results show that PVA-ECC exhibits higher compressive, tensile and flexural strength in comparison to the Poly-ECC.

Keywords Compressive strength · ECC · Polyester fiber · PVA fiber
Stress–strain response · Tensile stress

1 Introduction

Engineered cementitious composite (ECC) is cement based composite which contain discontinuous short polymeric fibers featuring high ductility and strain hardening behavior based upon micromechanics. ECC can be developed with a variety of polymeric fibers such as polyvinyl alcohol (PVA), polyethylene fiber

S. B. Singh (✉) · P. Munjal
Department of Civil Engineering, BITS Pilani, Pilani 333031, Rajasthan, India
e-mail: sbsinghbits@gmail.com

P. Munjal
e-mail: pankaj710munjal@gmail.com

A. Rama Mohan Rao and K. Ramanjaneyulu (eds.), *Recent Advances in Structural Engineering, Volume 1*, Lecture Notes in Civil Engineering 11,
https://doi.org/10.1007/978-981-13-0362-3_58

(PE), and polyester fibers [1]. Most investigations so far have been carried out on polyvinyl alcohol (PVA) and polyethylene (PE) fibers for making of ECC. There is a difference in basic micromechanics of these two fibers. The PE fibers are hydrophobic and do not make any bond with cement matrix but PVA fibers are hydrophilic and makes bond with cement matrix [2]. Li [1] initially used the high modulus PE fiber to produce the ECC, then, Kanda and Li [3] studied the behavior of PVA-ECC which has shown good agreement. Since the cost of high modulus of PE fibers is 6–7 times higher than PVA fibers, researchers started using PVA fibers instead of PE fibers to produce ECC. Most of the researchers [4–8] had used oiled PVA fiber (oil coating to the surface of fiber) because unoiled PVA fiber may be ruptured in a cementitious matrix due to the strong chemical bonding to cement hydrates [9]. The oiled PVA fiber is mainly supplied by Kuraray Co. Ltd. Japan and its cost is very high.

As a result, it is difficult to put ECC into large scale practical applications. It is worth studying on the low-cost ECC. Polyester fiber is another alternative which can be used for producing ECC and its cost is relatively lower, about 1/4th that of PVA fibers. Polyester fibers are neither completely hydrophobic nor hydrophilic in nature but it exhibits intermediate behavior. This distinctive properties of polyester fibers develop the very good bond strength between fiber and cementitious matrix [10].

Some researchers [10–13] have been conducted on the use of polyester fibers for making ECC. Rathod and Patodi [10] conducted the experimental study on interface tailoring of polyester fiber in ECC matrix against pullout and have concluded that polyester fibers do not require any extra treatment such as oiling agent or plasma treatment to enhance the performance of ECC. Ahamed et al. [11] studied the flexural behavior of ECC beam made up of polyester fibers and have investigated material properties of polyester-ECC. Singh et al. [12] studied the flexural response of masonry beams with polyester-ECC as bed joint in place of cement mortar and concluded that masonry beam with ECC as bed joint could be used as a structural beam. Singh and Munjal [13] have shown the comparative response of masonry beams with PVA-ECC and Poly-ECC as bed joints. Authors [13] concluded that masonry beams with PVA-ECC as bed joints exhibit better performance, and the load carrying capacity is found to be 1.5 times of that of masonry beam with Poly-ECC as bed joint.

Most of these past studies indicate that there are limited studies on the use of polyester fiber for making of ECC. The aim of the present paper is to determine the mechanical properties such as compressive strength, tensile strength, split tensile strength, and flexural strength of Poly-ECC. Moreover, the mechanical properties of Poly-ECC are compared with the PVA-ECC of the same mix proportion. Furthermore, compressive, tensile, and flexural stress–strain responses of ECC made up of PVA and polyester fibers are presented.

2 Experimental Details

2.1 Materials and Mix Design

ECC generally consists of mixtures of cement, silica sand, fly ash, water, super-plasticizer, and polymeric fibers to reinforce the mix. In this study, Portland pozzolana cement (PPC) as binder, microsilica sand with an average grain size of 100 µm, and class F fly ash (pozzocrete-63) was used to prepare the ECC. The material properties of Portland pozzolana cement explained by Singh et al. [14] is used and briefly presented Table 1. Glenium Sky 8777 provided by BASF India Ltd. was used as the super plasticizer. The present study used two types of polymeric fibers such as polyester fibers of triangular shape and polyvinyl alcohol (PVA) fibers. The material properties of polymeric fibers are given in Table 2. The mix proportion of ECC has been presented in Table 3.

2.2 Mixing Process and Specimen Preparations

Hobart mixer was used to prepare the ECC. The mixing process is completed in the three steps.

Table 1 Physical properties of PPC

PPC properties	Test results
Blaine fineness (m^2/kg)	375
Specific gravity	3.15
% Fly ash addition	30
Normal consistency (%)	30.8

Table 2 Materials properties of polymeric fibers

Properties	Polyester fiber	PVA fiber
Fiber diameter (mm)	0.025–0.035	0.04
Fiber length (mm)	12	8
Tensile strength (MPa)	480	1600
Elongation (%)	30	–
Rupture strain (%)	–	7
Manufacturer by	Reliance, India	Kuraray & Co., Japan

Table 3 Mix proportion of ECC in kg/m^3

Cement	Silica sand	Fly ash	Water	Super plasticizer	Fiber
620	620	620	290	8.5	26

Step 1: Water and super plasticizer are added and thoroughly mixed using Hobart mortar mixer.
Step 2: Silica sand is then added and is mixed for around 2 min. Then fly ash is added and the mixing process is continued.
Step 3: Further cement is added and mixed about 5 min. Fibers are then added slowly. The entire process takes around 20–25 min. In this mixing method, cement is added in the step 3 because entire process will take around 20–25 min, since cement would attain its initial setting time in this period.

After mixing the ECC, cubes of size 150 × 150 × 150 mm and 70.7 × 70.7 70.7 mm, cylinders of size 150 × 300 mm and 100 × 200 mm, tensile coupons of size 310 × 75 × 13 mm, and rectangular prisms of size 100 × 100 × 500 mm were cast. A thin layer of release agent was spread on the interiors of the moulds using a clean brush and then a paste of ECC was poured into the mould. Specimens were left in the mould inside the moist room (temperature 27 ± 3 °C and relative humidity 65%) for a period of 24 h. The specimens were removed from the mould and placed inside the curing tank at temperature of 27 ± 3 °C for 28 days. ECC specimens were divided into two categories, i.e., PVA-ECC and Poly-ECC as differentiated with type of the fibers inclusion.

3 Experimental Method and Test Procedure

3.1 Compressive Strength

Five cylindrical specimens (150 × 300 mm) and ten cube (150 × 150 × 150 mm and 70.7 × 70.7 × 70.7 mm) specimens were tested in Compression Testing Machine (CTM) of capacity 2000 kN after 28 days. Cylindrical and cube specimens were tested as per ASTM C39 [15] and IS 516:1959 [16], respectively. Compressive strength was measured by placing the specimens in the contact of bearing surface of the CTM and the load was applied at the rate of 2–5 N/mm^2 per minute until failure occurs. The compressive strength was calculated by dividing the maximum load applied to the specimen during the test by cross sectional area. The modulus of elasticity and Poisson's ratio of cylindrical specimens were calculated using Eqs. (1) and (2) [17], respectively. The strain was measured by the extensometer attached with the CTM as shown in Fig. 3.

$$E_c = \frac{(S_2 - S_1)}{(\varepsilon_2 - \varepsilon_1)} \tag{1}$$

$$\mu = \frac{(\varepsilon_{t2} - \varepsilon_{t1})}{(\varepsilon_2 - \varepsilon_1)} \tag{2}$$

where

E_c chord modulus of elasticity, MPa
S_2 stress corresponding to 40% of ultimate load, MPa
S_1 stress corresponding to a longitudinal strain (ε_1), MPa
ε_2 longitudinal strain produced by stress S_2, mm/mm
ε_1 3.45E−7 (longitudinal strain in mm/mm)
μ Poisson's ratio
ε_{t2} transverse strain at mid-height of the specimens produced by stress S_2, mm/mm
ε_{t1} transverse strain at mid-height of the specimens produced by stress S_1, mm/mm

3.2 Split Tensile Strength

The split tensile strength of ECC was measured through testing of five cylindrical specimens (100 × 200 mm) of each category as per IS 5816-1999 [18] and BS 1881-part 117 [19]. The split tensile strength can be calculated using Eq. (3). In this equation, f_{ct} is split tensile strength, P is the load applied to the specimen, and l, d are length and diameter of the specimen, respectively.

$$f_{ct} = \frac{2P}{\pi dl} \tag{3}$$

3.3 Tensile Strength

Five specimens of ECC coupons of each category were tested in automated deformation controlled hydraulic Universal Testing Machine (UTM) of capacity 100 kN and the load was applied at displacement control rate of 0.5 mm/min. The size of coupons was 310 × 75 × 13 mm and gauge length was maintained as 200 mm. The tensile stress–strain response of ECC coupons was measured by the UTM.

3.4 Bending Test

Four point bending tests were performed on the five rectangular prism specimens of each category on servo hydraulic actuator of capacity 200 kN as per ASTM D790 [20]. The load was applied on the prisms at the displacement control rate of 0.5 mm/min. The flexural stress, strain, and modulus were calculated using Eqs. (4)–(6), respectively.

$$\sigma_f = \frac{PL}{bd^2} \tag{4}$$

$$\varepsilon_f = \frac{6Dd}{L^2} \tag{5}$$

$$E_b = \frac{L^3 m}{4bd^3} \tag{6}$$

where

σ_f flexural stress, MPa,
P load at a given point on the load–deflection curve
L support span, mm
b width of the beam, mm
d depth of beam, mm
ε_f flexural strain in the outer surface, mm/mm
D maximum deflection of the axis of the beam, mm
E_b modulus of elasticity in bending, MPa
m slope of the tangent to the initial portion of the load–deflection curve, N/mm.

4 Experimental Results and Discussions

4.1 Compressive Strength

The results of compressive strength, strain at peak stress, failure strain, and modulus of elasticity are presented in Table 4. The failure strain is defined throughout this paper as the strain corresponding to stress equal to 80% of the peak stress in the post peak region. This definition of the failure strain is arbitrary in the sense that after reaching the peak stress, a sudden drop in stress value is observed with small increment in the strain. Thereafter, strain is increasing with higher rate due to crushing of ECC. The average compressive strength of cube (150 mm), cylinder, and small cube (70.7 mm) specimens is observed to be 54.05, 45.12, and 61.74 MPa, respectively for PVA-ECC whereas it is found to be 46.25, 38.55, 50.88 MPa, respectively for Poly-ECC. The compressive strengths of cylinder (150 × 300 mm), and small cube (70.7 × 70.7 × 70.7 mm) are observed to be 0.83 and 1.14 times of compressive strength of standard cube (150 × 150 × 150 mm), respectively for PVA-ECC whereas they are observed to be 0.83 and 1.10 times of compressive strength for Poly-ECC. The compressive strength of PVA-ECC is found 1.17 times of the compressive strength of Poly-ECC. The compressive axial stress–strain response of the cylindrical specimens of ECC (PVA-ECC and Poly-ECC) is shown in the Fig. 1. It is seen that, initially both the curves are linear up to about half of the peak stress after which it becomes nonlinear

Table 4 Experimental results of compressive strength and split tensile strength tests

ECC types	Cube[a]	Cube[b]	Cylinder, 150 × 300 mm					Cylinder, 100 × 200 mm
	Comp. strength (MPa)	Comp. strength (MPa)	Comp. strength (MPa)	Peak comp. strain (mm/mm)	Failure strain[c] (mm/mm)	Comp. modulus (GPa)	Poisson's ratio	Split tensile strength (MPa)
Poly-ECC	46.25	50.88	38.55	0.0030	0.0031	16.85	0.164	3.81
PVA-ECC	54.05	61.74	45.12	0.0032	0.0033	22.24	0.172	4.24

[a]Cube = size of cube is 150 × 150 × 150 mm

[b]Cube = size of cube is 70.7 × 70.7 × 70.7 mm

[c]Failure strain = strain corresponding to stress equal to 80% of the peak stress in the post peak region

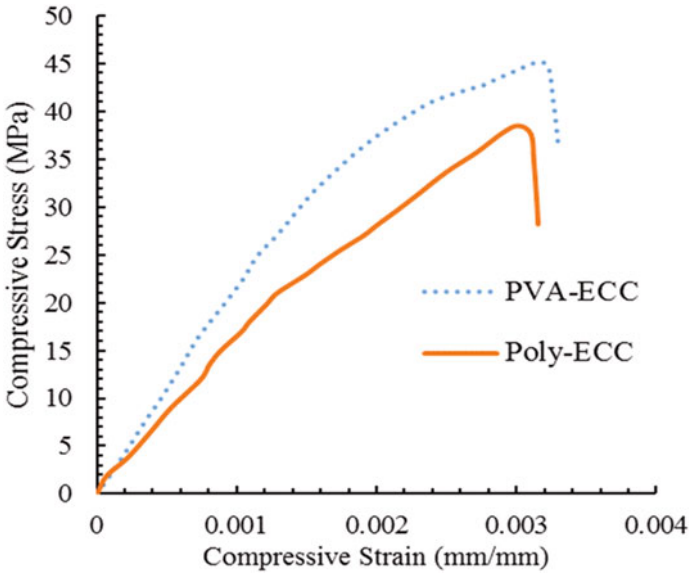

Fig. 1 Compressive stress–strain response of ECC cylinder specimens

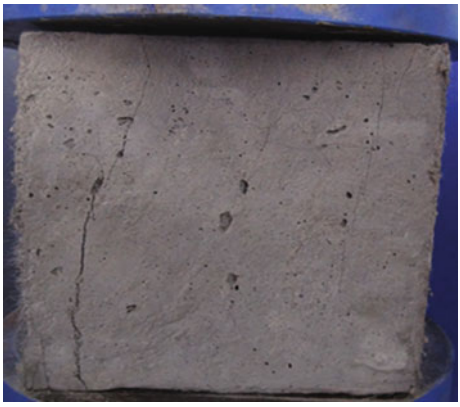

Fig. 2 Failure pattern of cube specimen

accompanied by a sudden drop in the stress is observed after peak load. The failure patterns of cubes and cylindrical specimens are shown in Figs. 2 and 3, respectively. It has been observed that vertical axial cracks develop in the most of the specimens (Fig. 2). In case of cylinder specimens under compression test, initial cracks developed at top and propagated to the bottom with increase in load and then the cracks got widened at failure along the top of the specimen as shown in Fig. 3.

Fig. 3 Failure pattern of cylindrical specimen

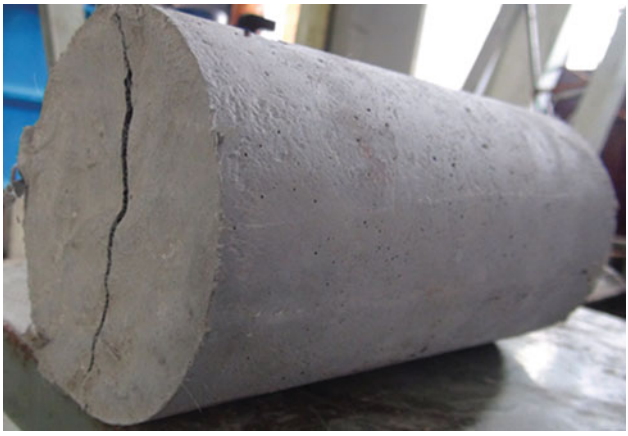

Fig. 4 Failure pattern of cylindrical specimen after split tensile strength test

4.2 Split Tensile Strength

The results of split tensile strength of ECC are presented in Table 4. Failure modes of split tensile strength test of cylindrical specimens are shown in Fig. 4. It is observed that cylinder specimens got split into two pieces as shown in Fig. 4.

4.3 Tensile Strength of ECC Coupons

The results of tensile strength of ECC coupons are presented in Table 5. The failure pattern of Poly-ECC coupon during the tensile strength test is shown in Fig. 5. All the coupons have shown multiple cracking and pseudo strain hardening behavior.

After the first crack, load is continued to rise without fracture. Subsequently, parallel cracks developed and increase the crack width with increasing stress. The average tensile stress–strain response of the ECC coupons is presented in Fig. 6.

Table 5 Experimental results of tensile strength of ECC coupons

Properties	Poly-ECC	PVA-ECC
Tensile strength (MPa)	2.42	4.78
Peak strain (%)	0.04	0.20
Rupture strain (%)	3.20	4.60
Young's modulus (GPa)	16.42	21.82

Fig. 5 Failure pattern of poly-ECC coupon during tensile strength test

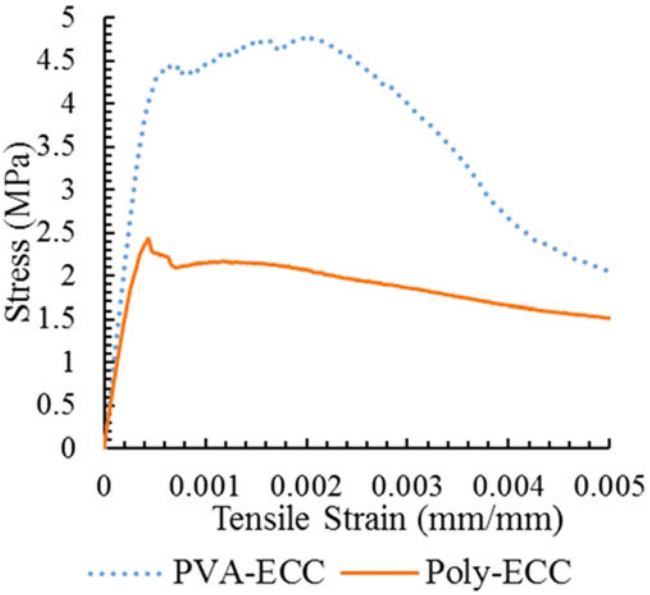

Fig. 6 Tensile stress–strain response of ECC coupon

It is seen that PVA-ECC has higher tensile strength in comparison to the Poly-ECC. The tensile strength of PVA-ECC is about two times of tensile strength of Poly-ECC. After the first crack, the tensile stress is increased in PVA-ECC due to bridging action of cement and fibers bonding whereas in Poly-ECC, small drop in stress is observed after the first crack and then, stress increases due to strain hardening. The reason behind this significant strength is PVA-ECC, i.e., PVA fiber which has higher tensile strength and stronger bonding with cement matrix in comparison to polyester fibers.

4.4 Flexural Strength

The results of the four point bending test of ECC prisms are presented in Table 6. The average flexural strength of PVA-ECC and Poly-ECC is observed to be 9.49 and 8.52 MPa, respectively. The average peak compressive strain of PVA-ECC is 0.017 whereas it is found to be 0.016 for Poly-ECC. The flexural stress–strain response of the ECC prism is presented in Fig. 7. PVA-ECC prism has shown more flexural stress in comparison to Poly-ECC. The flexural strength of PVA-ECC prism is found to be 1.11 times of the flexural strength of Poly-ECC prism. The failure pattern of ECC prism during four point bending test is shown in Fig. 8. The vertical flexural cracks developed in the tension zone and propagated towards the compression zone as shown in Fig. 8.

Table 6 Experimental results of bending test of ECC prism

Properties	Poly-ECC	PVA-ECC
Flexural strength (MPa)	8.52	9.49
Peak strain (%)	1.59	1.68
Failure strain (%)	1.60	1.73
Flexural modulus (MPa)	98.74	83.15

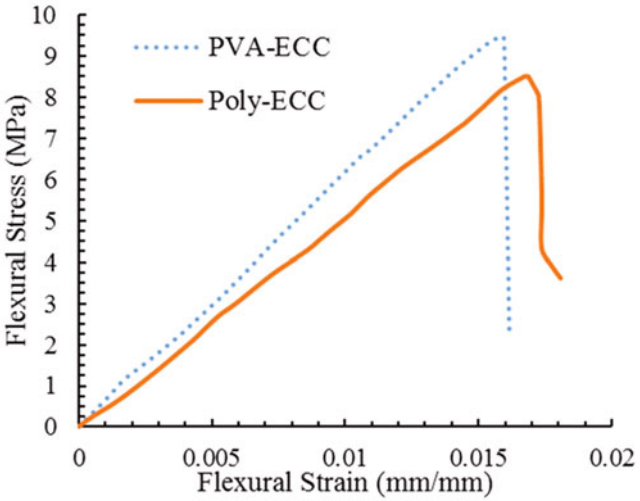

Fig. 7 Flexural stress–strain response of ECC prism

Fig. 8 Failure of ECC prism during four point bending test

5 Conclusions

The experimental study was conducted on the mechanical properties of ECC using two types of polymeric fibers. The following conclusions are drawn from this study.

- The compressive strengths of cylinder specimens and small cube specimens are found to be 0.833 and 1.20 times of the compressive strength of standard cube (150 mm size).
- The compressive, tensile, and flexural strength of PVA-ECC are respectively found to be 1.14, 2, and 1.11 times of compressive, tensile, and flexural strength of Poly-ECC.
- The compressive, tensile, and flexural modulus of PVA-ECC are found to be 22.24, 9.58, and 0.98 GPa, respectively, whereas for Poly-ECC, they are 16.85, 7.50, and 0.83 GPa, respectively.

Acknowledgements The authors would like to acknowledge the support of the Department of Science and Technology (DST), New Delhi [Grant# SR/S3/MERC/051/2012] and Aditya Birla Group.

References

1. Li, V. C. (1998). Engineered cementitious composites-tailored composites through micromechanical modeling. In N. Banthia, A. Bentur, & A. Mufti (Eds.), *Fiber reinforced concrete: Present and the future* (pp. 64–97). Montreal: Canadian Society for Civil Engineering.
2. Madappa, V. R. S. (2011). *Response and micromechanics based design of engineered cementitious composite structures*. Ph.D. thesis, BITS Pilani, Pilani, pp. 11–16.
3. Kanda, T., & Li, V. C. (1998). Interface property and apparent strength of high-strength hydrophilic fiber in cement matrix. *Journal of Material in Civil Engineering, 10*(1), 5–13.
4. Singh, S. B., & Madappa, V. R. S. (2008). A review of innovative engineered cementitious composites for construction. *Civil Computing Magazine, Asian Center for Engineering Computations and Software (ACECOMS)* (Vol. M 35-0313-0508, pp. 42–45).
5. Pan, J. L., Yuan, F., Luo, M., & Leung, C. K. Y. (2012). Effect of composition on flexural behavior of engineered cementitious composites. *Science China Technological Sciences, 55* (12), 3425–3433.
6. Huang, X., Ranade, R., Zhang, Q., Ni, W., & Li, V. C. (2013). Mechanical and thermal properties of green lightweight engineered cementitious composites. *Construction and Building Materials, 48*(11), 954–960.
7. Zhang, Z. G., Qian, S. Z., & Ma, H. (2014). Investigating mechanical properties and self-healing behavior of micro-cracked ECC with different volume of fly ash. *Construction and Building Materials, 52*(2), 17–23.
8. Zhou, J., Pan, J., & Leung, C. K. Y. (2014). Mechanical behavior of fiber-reinforced engineered cementitious composites in uniaxial compression. *Journal of Materials in Civil Engineering, 27*(1), 04014111–11.
9. Pan, Z., Wu, C., Liu, J., Wang, W., & Liu, J. (2015). Study on mechanical properties of cost-effective polyvinyl alcohol engineered cementitious composites (PVA-ECC). *Construction and Building Materials, 78,* 397–404.

10. Rathod, J. D., & Patodi, S. C. (2010). Interface tailoring of polyester-type fiber in engineered cementitious composite matrix against pullout. *ACI Materials Journal, 107*(2), 114–122.
11. Ahamed, A., Sunitha, S., Vinod, P., & Bindhu, K. R. (2012). A comparative study on the flexural behaviour of RCC and R/ECC beams. In *International conference on green technologies (ICGT), IEEE* (pp. 223–227), Trivandrum, Kerala, India.
12. Singh, S. B., Munjal, P., & Thammishetti, N. (2015). Strengthening of masonry beam with ECC as bed joint. *Journal of Engineering Science and Technology, 8,* 29–39.
13. Singh, S., & Munjal, P. (2016). Flexural behavior of reinforced masonry beams with ECC as bed joint. *In International Conference on Advances in Concrete Technology, Materials & Construction Practices* (pp. 16–21), Goa, India, June 22–24, 2016.
14. Singh, S. B., Munjal, P., & Thammishetti, N. (2015). Role of water/cement ratio on strength development of cement mortar. *Journal of Building Engineering, 4,* 94–100.
15. ASTM C39/C 39M-03. (2003). *Standard test method for compressive strength of cylindrical concrete specimens*. USA: American Society for Testing Materials.
16. IS 516-1959. (2006). *Methods of tests for strength of concrete* (18th ed.). New Delhi: Bureau of Indian Standards.
17. ASTM C469/C469M-14. (2002). *Standard test method for static modulus of elasticity and Poisson's ratio of concrete in compression*. USA: American Society for Testing Materials.
18. IS 5816-1999. (1999). *Splitting tensile strength of concrete-method of test.* New Delhi: Bureau of Indian Standards.
19. BS 1881: Part 117. (1983). *Testing concrete method for the determination of tensile splitting strength*. London: British Standard Institute.
20. ASTM D790-15e2. (2015). *Standard test methods for flexural properties of unreinforced and reinforced plastics and electrical insulating materials*. USA: American Society for Testing Materials.

A Correlation Study Between Lime Reactivity Strength Test and Calorimeter for Different SCMs

Anuj Parashar, Vineet Shah, Geetika Mishra and Shashank Bishnoi

Abstract Supplementary cementitious materials (SCMs) are added to improve various mechanical and durability properties of cement and concrete. One of the indirect benefits of binary and ternary blended cements is to reduce CO_2 emissions. As per Indian standards (IS), reactivity of pozzolanic material is observed in the presence of calcium hydroxide (CH) using lime reactivity test. A pozzolana should qualify lime reactivity test before adding it to the cement. In this study, reactivity of SCMs was observed using lime reactivity strength test and isothermal calorimeter. For this purpose, different calcined clays, fly ashes (FA), and slags were selected. Lime reactivity test was used to study the mechanical strength potential of SCMs and calorimeter was performed to measure total energy evolved during the reaction of SCMs with CH in the presence of water at 27 °C. Strength data from lime reactivity test was then finally correlated with the calorimeter heat evolved data in different conditions.

Keywords Pozzolana · Lime reactivity · Isothermal calorimeter

1 Introduction

Pozzolanic materials majorly contain reactive silica and reactive alumina. In the presence of calcium hydroxide, reactive silica reacts which forms similar hydration products as of cement. Pozzolanic materials can be classified as natural pozzolana

A. Parashar · V. Shah · G. Mishra · S. Bishnoi (✉)
Indian Institute of Technology Delhi, Hauz Khas, New Delhi 110016, India
e-mail: shashank.bishnoi@civil.iitd.ac.in

A. Parashar
e-mail: anujparashar29@gmail.com

V. Shah
e-mail: vineet.shah9@gmail.com

G. Mishra
e-mail: geetika.mishra30@gmail.com

A. Rama Mohan Rao and K. Ramanjaneyulu (eds.), *Recent Advances in Structural Engineering, Volume 1*, Lecture Notes in Civil Engineering 11,
https://doi.org/10.1007/978-981-13-0362-3_59

such as volcanic glasses, volcanic tuffs, calcined clay, etc., and industrial by-products such as fly ash, blast furnace slag, silica fume, rice husk ash, etc. [1].

In India, FA, slag and calcined clay are majorly used pozzolanic material either for making pozzolanic Portland cement or for directly adding them to the concrete. However, according to Indian Standard (IS), every pozzolanic material has to qualify the minimum required specification before adding them to cement and concrete. Currently, IS 1727-1967 "Methods of test for pozzolanic materials" provides the guideline and criteria which every material has to fulfill for qualifying as a pozzolana. This standard also contains the most important method to check the reactivity of pozzolanic material that is lime reactivity test [2].

This approach of testing pozzolanic reactivity is extensively used in many studies to check the reactivity of FA, pond ash, calcined clay, rice husk ash, etc [3–6]. This method does not include the testing of ground granulated blast furnace slag due to the fact that slag behaves as hydraulic pozzolana and does not require much CH for its pozzolanic reaction.

According to this test, mortar cubes of 5 cm prepared and conditioned according to the specification given in the standard need to be tested for compressive strength at the age of 10 days [2, 7]. This method has various advantages over the other reactivity test methods due to the fact that it is easy to perform, requires less efforts, can be applicable almost on every pozzolanic material and the result is easy to understand. However, there are some disadvantages associated with this method and one of the major disadvantages is the requirement of number of trials for workability of mortar. The test for workability requires additional amount of material and time for testing [7]. Some authors also tried to correlate an alternative of this test by finding out the soluble content in fly ash and its fineness [8].

An alternative to study the reactivity potential of pozzolanic materials can be their energy evolved during the pozzolanic reaction in the presence of calcium hydroxide using isothermal calorimeter. Some recent efforts have already proven that isothermal calorimeter can be used perfectly for predicting the strength at the age of 28 and 90 days using the energy data upto the age of 7 days [9, 10]. However, such efforts are only made for correlating cement mortar compressive strength with energy of SCM in the presence of CH.

In this study, efforts were made to provide alternative for lime reactivity tests specially in case when very less amount of material is available (50 g or so) and less period of time. For the objective, isothermal calorimeter was used for the study of energy released in the pozzolanic reaction of pozzolanic material in the presence of CH [7]. Various attempts were made to look at the effect of CH ratio on energy released. Additionally, effect of gypsum as an accelerator was also studied. Finally, the lime reactivity strength data was correlated with the energy evolved by various pozzolana.

2 Materials

Total 8 pozzolans were focused for this study. Total 4 FA were used due to the fact that FA is most widely used pozzolanic material in India. One FA was directly collected from the thermal power plant and was comparatively coarse and unprocessed. Two-processed Fine FA was collected from two different suppliers. One fly ash was processed in the lab by crushing the one FA that was directly collected from the plant. One pure metakaolin with almost 90% purity and other calcined clay having around 55–60% kaolinite was procured and two slags were selected. There is only fineness difference with in the slags. All the materials were characterized with XRF and reported in Table 1. The fineness of all the materials was obtained with the help of particle size analyser. The mean value of particle diameter for d(50) is reported in Table 1. Lab grade calcium hydroxide having more then 96% purity was used for all the testing study. Double distilled water was used for Lime reactivity as well as calorimeter study.

3 Methodology

Lime reactivity test was performed as per the Indian standard. All the raw materials were stored in the temperature-controlled room at 27 ± 2 °C for 24 h for conditioning. After casting, all the cubes were stored in the temperature and humidity controlled chamber at 27 ± 2 °C and 65%, respectively, for next 48 h. During this period, the moulds were covered with a glass plate and a wet cloth placed over and around the glass plate. After 48 h, the cubes were demoulded and then were kept in a plastic box with a moist cloth to maintain the humidity inside the box.

Table 1 Chemical and physical properties of SCMs

S No.	Constituents %		*K*1	*K*2	FA1	FA2	FA3	Slag
1.	Loss on ignition LOI		3.03	4.34	1.11	1.74	0.86	0.32
2.	Silica SiO_2		53.53	52.70	58.82	67.66	54.85	32.26
3.	Iron Fe_2O_3		1.15	4.00	6.19	5.32	32.17	1.93
4.	Aluminum Al_2O_3		40.03	38.14	30.62	22.18	4.97	23.16
5.	Calcium CaO		0.08	0.09	1.01	0.32	1.33	33.88
6.	Magnesium MgO		0.02	0.2	0.41	0.18	1.11	7.01
7.	Sulfate SO_3		0.12	0.01	0.12	0.02	0.06	Traces
8	Sodium Na_2O		0.24	0.18	0.19	0.43	0.23	0.34
9.	Potassium K_2O		0.07	0.17	1.30	1.60	1.49	0.65
12.	Manganese Mn_2O_3		–	0.01	–	0.12	0.06	0.30
13.	Specific gravity		2.64	2.61	2.26	2.28	2.36	2.87
14.	Particle size distribution	D (50)	5.86	5.39	37.3	11.9	5.01	12.2

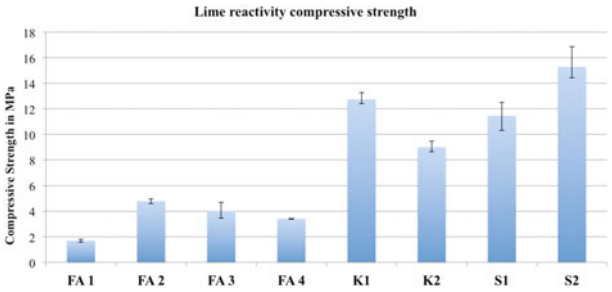

Fig. 1 Lime reactivity compressive strength

The objective of using box was to maintain the humidity same for next 8 days, continuously. Hygro meter was kept inside the chamber to monitor, humidity and temperature inside the box were monitored. Then the plastic box was kept in temperature and controlled chamber at 50 ± 3 °C and a minimum of 90% humidity. All the cubes were tested under compression using a compression testing machine having a maximum capacity of 50 kN. The reason for that is because high capacity compression testing machine will lead to indecorous strength value. Strength data for the average of min. 3 cubes is given in Fig. 1.

Isothermal calorimeter Ical 8000 supplied by Calmetrix having 8 channels was used. For this study, the amount of paste and water/binder ratio kept same for the entire test. A total of 50 g of powder with 0.6 water binder ratio was used. All the testing was done in a temperature-controlled room at 27 ± 2 °C. For the test procedure, first water was kept inside calorimeter for 2 hrs for conditioning. After that dry powders were mixed and then placed in the mould. After that, water was taken out from the calorimeter and mixed with the dry mixed powders. The mixing was done uniformly with the help of spoon and vortex mixer. The paste was kept inside the cell of calorimeter immediately just after mixing. The average time for entire mixing process was approximate 2 min.

Three different approaches were focused in this study. One approach was with high CH content and low SCM content including sulfates. Total 3% gypsum was added and rest was divided into 70% CH and 30% SCM. This approach leads to the fact that SCM is the one, which will be controlling the reactivity of CH. This is also used in different ways in different studies [9, 10]. Second approach was to provide equal amount of CH and SCM with 3% of gypsum. And in third approach CH and SCM was mixed equally without adding any sulfates. This approach is more realistic to the reaction of SCM in lime reactivity system.

4 Results and Discussion

4.1 Lime Reactivity

All the materials were tested for the compression test with minimum 3 cubes. FA1 was found to be least reactive which could be due to its coarser nature. In fact, after grinding the FA1 to the similar fineness level of FA2 (i.e., FA4), its reactivity increases almost by 1.5 times the original. The reactivity order for FA was FA2 > FA3 > FA4 > FA1.

As it is very well known that calcined clay is highly reactive than FA, the same behavior was obtained in the result and its reactivity order was $K1 > K2$. However, among all maximum strength was maximum for $S2$ that is because of its high fineness. Compressive strength of all the SCMs is shown in Fig. 1.

As this test only find out the compressive strength for checking the reactivity, but, their can be some problems during the mixing and curing. Due to this fact, the repeatability of this test was also tested. As given in Fig. 2, FA1, FA2, $K1$, $S1$, and $S2$ were repeated. A very good repeatability of this test was observed.

4.2 Calorimeter

In the first case of 3% gypsum with 70% CH and 30% pozzolan, cumulative energy is plotted in Fig. 3a. It was observed that due to the excessive CH and gypsum content, the energy evolved was higher due to acceleration of the reaction. The correlation of cumulative energy evolved at 7 days and compressive strength is plotted in Fig. 3b. It was observed that a good correlation was observed but due to addition of gypsum into the system, the energy was recorded also for aluminates and gypsum reaction that lead to the formation of ettringite. This behaviour can exist in the pozzolanic materials having highly soluble alumina content such as calcined clay and slag.

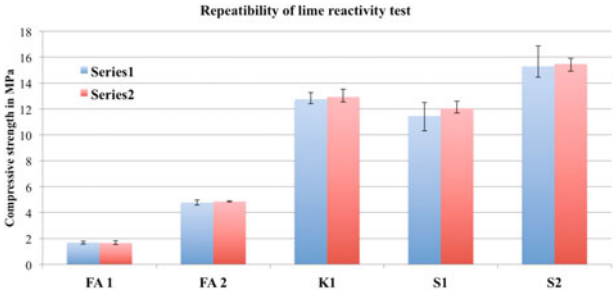

Fig. 2 Repeatability of lime reactivity test tested by repeating two series of test over same SCMs

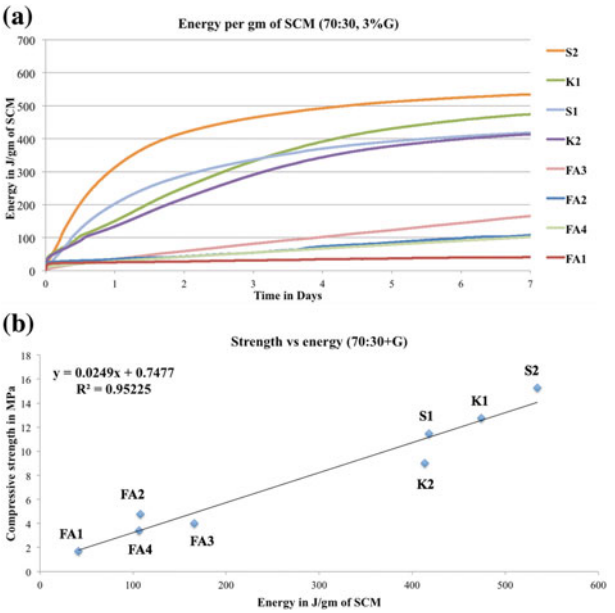

Fig. 3 **a** Energy plot for calorimeter data having 3% gypsum and rest 70% CH and 30% SCM **b** correlation between lime reactivity strength and calorimeter data having 3% gypsum and rest 70% CH and 30% SCM

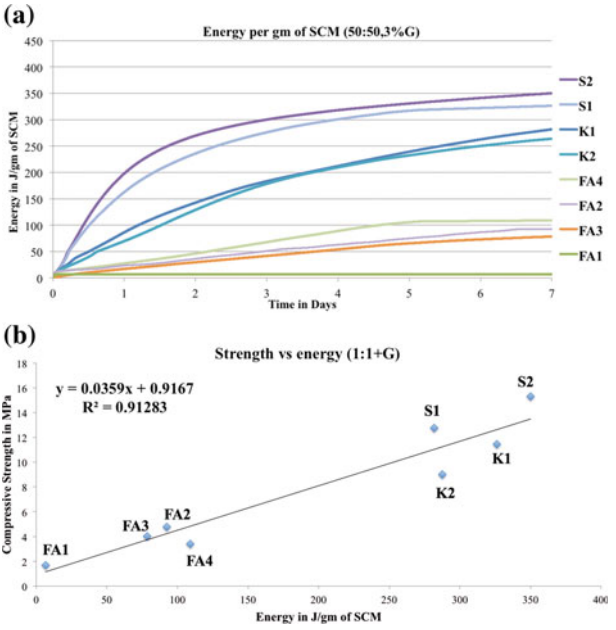

Fig. 4 **a** Energy plot for calorimeter data having 3% gypsum and rest 50% CH and 50% SCM **b** correlation between lime reactivity strength and calorimeter data having 3% gypsum and rest 50% CH and 50% SCM

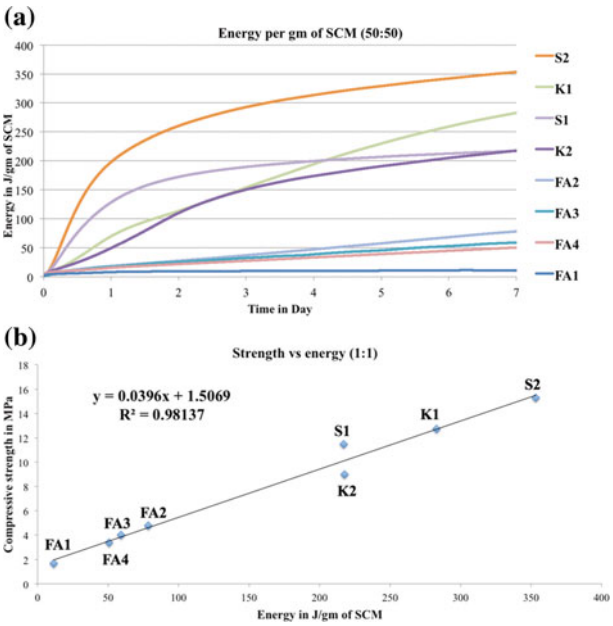

Fig. 5 **a** Energy plot for calorimeter data having 50% CH and 50% SCM **b** correlation between lime reactivity strength and calorimeter data having 50% CH and 50% SCM

For the second case having 3% gypsum and rest 50:50 was CH:SCM, lower amount of energy was recorded as shown in Fig. 4a. Correlation obtained for the same is plotted in Fig. 4b. In this case, the correlation was comparatively not good than the first one.

In the last set of experiments having 50:50 SCM and CH without any gypsum, the energy evolved was even lesser than other two cases. This condition was more close to the realistic conditions of lime reactivity test. Additionally, no accelerator such as gypsum was added which can lead for aluminate reaction. The energy data is reported in Fig. 5a. In fact, the correlation was best among the all other approaches and is reported in Fig. 5b. The only reason for that can be the close conditions to the real situation. More amount of CH in the system can also accelerate the reactivity in compare with lime reactivity test conditions.

5 Conclusion

Efforts was made to correlate lime reactivity strength data with energy evolved in reaction of SCM and CH in presence of additional accelerators. It was observed that addition of gypsum to the system can give aluminate reaction and leads to additional energy generation especially in case of slag and calcined clay. A good

correlation was found in condition that was close to the realistic conditions of lime reactivity test. This new method based on isothermal calorimeter can be very useful in the case when a limited quantity of material is available and need to be tested for lime reactivity. Another benefit was lesser time duration and less amount of work required to perform the test.

References

1. Mehta, P. M., & Monteiro, P. J. M. (2006). *Concrete microstructure, properties and materials* (3rd ed.). McGraw-Hill.
2. Bureau of Indian Standard. (2004). *Methods of test for pozzolanic materials*. IS: 1727.
3. Ranganath, R., Bhattacharjee, V., & Krishnamoorthy, S. (1998). Influence of size fraction of ponded ash on its pozzolanic activity. *Cement and Concrete Research, 28,* 749–761.
4. Bahurudeen, B., Wani, K., Basit, M. B., & Santhanam, M. (2016). Assessment of pozzolanic performance of sugarcane bagasse ash. *Journal of Materials in Civil Engineering, 28*(2).
5. Luxan, M. P., De Rojas, M. S., & Frias, M. (1989). Investigations of fly ash-calcium hydroxide reaction. *Cement and Concrete Research, 19,* 69–80.
6. Murat, M. (1983). Hydration reaction and hardening of calcined clays and related materials. I. Preliminary investigation on metakaoline. *Cement and Concrete Research, 13,* 259–266.
7. Parashar, A., Krishnan, S., & Bishnoi, S. (2015). Testing of suitability of supplementary materials mixed in ternary cements. In *Proceedings 1st International Conference on Calcined Clays for Sustainable Concrete*, 23rd–25th June.
8. Avet, F., Snellings, R., Diaz, A. A., Haha, M. B., & Scrivener, K. (2016). Development of a new rapid, relevant and reliable (R3) test method to evaluate the pozzolanic reactivity of calcined kaolinitic clays. *Cement and Concrete Research, 85,* 1–11.
9. Snellings, R., & Scrivener, K. (2015). Rapid screening tests for supplementary cementitious materials: Past and future. *Materials and Structures*.
10. Sharma, R. C., Jain, N. K., & Ghosh, S. N. (1993). Semi-theoretical method for the assessment of reactivity of fly ash. *Cement and Concrete Research, 23,* 41–45.

Effects of Steel Fibre on Self-Compacting Concrete with Fly Ash

Gaurav Udgata and Ashoke Kumar Rath

Abstract This era of constructions demands easily usable construction materials which are cost-effective and durable. Self-Compacting Concrete (SCC) is also known as Self-Consolidated Concrete and is considered as high strength modified concrete material. The objective of the present work is to study the effects of steel fibres on the strength and workability of the SCC. A rational method was used for design mix with fly ash. VMA was used to control the flow properties. The fresh properties were determined for various fractions of steel fibre by volume. It was observed that steel fibres reduced the flowability of the specimens. Hardened tests on fibre reinforced SCC were also determined and it was found that the flexural strength and the split tensile strength were directly proportional with the addition of fibres but the compressive strength reduced after reaching a peak value. Thus, this combination of steel fibres and SCC along with fly ash can become very innovative for modern constructions.

Keywords Flexural · Split tensile · Compressive · Flowability
VMA

1 Introduction

The initiation of the Self-Compacting Concrete (SCC) made a huge step towards the improvement of efficiency and working conditions on construction sites. A low degree of automation of the concrete industry, the durability problems of concrete and shortage of labourers forced Japanese researchers to think for the future; as a result, SCC was developed Okamura et al. [1]. SCC spreads homogenously, without any externally applied energy, and spreads without air getting entrapped.

G. Udgata (✉) · A. K. Rath
School of Civil Engineering, KIIT University, Bhubaneswar, Odisha, India
e-mail: gaurav.udgatafce@kiit.ac.in

A. K. Rath
e-mail: akrathfce@kiit.ac.in

A. Rama Mohan Rao and K. Ramanjaneyulu (eds.), *Recent Advances in Structural Engineering, Volume 1*, Lecture Notes in Civil Engineering 11,
https://doi.org/10.1007/978-981-13-0362-3_60

The vibration of concrete is eliminated and also other improvements are gained, e.g. shorter periods of casting, a more esthetical appearance of concrete surface and improved characteristics in the hardened state. Filling capability, resistance to segregation and ability of passing are the key characteristics of SCC. Dense reinforcement configurations, architectural concrete and remote casting are applications tailored for SCC. The concrete that is placed successfully without manual compaction or vibration and without segregation of its constituents and also has enough mobility to flow under its own weight without settlement of its constituents is known as Self-Compacting Concrete (SCC). It happens to be a high performance, more reliable and uniform quality concrete. It flows under its own weight in plastic state and homogeneity is maintained without having segregation when dropped from a certain height while filling the formwork and flowing inside the reinforcement. The following are the types of SCC mixes:

1. Powder-type SCC
2. VMA-type SCC
3. Combined type SCC (when the VMA-type SCC and powder-type SCC are combined).

Advantages of SCC are as follows:

1. Quicker Construction
2. Limiting site manpower
3. Improved surface finish
4. Comfortable and smooth placing
5. Enhanced durability
6. Better freedom in design
7. Decreased noise level.

Since many years, SCC has come to practical applications in major construction areas with different mix proportions as per the requirement. Since the SCC is not given any compaction, special admixtures are added to improve the durability and strength of SCC, which could be achieved when the mix was added with some Pozzolonas. Pozzolanic material like fly ash was used for this purpose. It was observed that compared to the normal SCC when Pozzolona like fly ash was added to it, the hardened properties of concrete were enhanced according to Mahure et al. [2].

This continued up to few years then research was done to increase the strength of concrete with the tensile and flexural properties of SCC. Thus fibres came into the action. The bridging nature of fibres helped in the improvement of tensile and flexural properties of SCC. But the problem arose when the fibres reduced the workability of concrete. Since the major characteristics of SCC are flowability. These fibres affected the flowable properties of SCC negatively. The strength was increased when the fibres were added to the SCC up to an extent and then the reduction of strength was observed. Hence an optimum quantity of fibres was found from researches which gave the maximum tensile and flexural strength and also

maintaining the compressive strengths of concrete. The steel fibre maintains the stress developed due to dry shrinkage. It restricts the cracks developed in the concrete.

Applications of Steel Fibre reinforced SCC

Structural

1. By the use of steel fibre, the dry shrinkage can be controlled which may be caused due to high cement to an aggregate fraction.
2. Repair and patch the concrete structures where tensile strength is to be enhanced.
3. The span between the columns can be increased because the buckling strength increases.
4. In concrete by use of steel fibres, the ductility ratio can be increased.

Construction

Pile foundations, concrete used for retaining wall, pump concrete, congested reinforcement member and long column.

2 Literature Review

A study done by Kamran and Mishra [3] gives an idea on the type of the cement better for casting SCC. Three mixes were made for each of Ordinary Portland Cement (OPC) and Pozzolona Portland Cement (PPC) specimens and the fly ash was varied at 15, 25 and 35% as replacement. Fresh properties were looked and the strength consideration was also observed. It was found that OPC had better strength and flow properties compared to PPC. 25% fly ash addition to OPC gave the best flowability. Compressive strength and fly ash addition were inversely proportional. 15% fly ash content for the 28 days compressive strength for OPC mix was 34.12 MPa and PPC mix was 27.7 MPa.

A research by Mahure et al. [2] showed that the SCC mix prepared with 20% replacement of fly ash using OPC grade cement confirming to IS: 8112-1989 gave an optimum strength for M30 grade concrete. The fly ash added to the concrete helped to reduce the micro-cracks formed in the structure found by Bhalchandra and Bajirao [4]. This may be the reason of enhancement of compressive strength. The rise in compressive strength at over normal SCC at 7 days is 21.35% and 28 days is 53.49%, respectively, for 3% fibre content by volume fraction. There was an increase from 3.48 to 41.76% at 7 days and from 4.91 to 34.97% at 28 days in the flexural strength of concrete.

Fibre gives high strength to the concrete but at the same time also becomes an obstacle for the SCC to achieve its flowability properties. Fibres are generally parallel to the direction of flow and only few fibres are perpendicular as suggested

by Ponikiewski and Golaszewski [5]. The aspect ratio and optimum volume fraction of fibre for giving best results in terms of strength were found to be 25 and 1% respectively by Rao and Ravindra [6].

Pozzolanic reactions were low in early ages when the fly ash volume was high in the composite, but considerable effect has been seen in strength when the specimen age became more than 56 days. Fibres like steel fibre and Pozzolonas like fly ash can improve the mechanical properties of specimens. The workability characteristics of SCC was enhanced when the volume of fly ash was increased.

Admixture is an important part for fresh and hardened properties of concrete. The viscosity properties and flowability of admixture increase the fresh properties of steel fibre reinforced SCC without much increase of w/c ratio in concrete. A gain in strength of concrete was depicted when the w/c ratio was reduced.

2.1 European Federation of National Associations Representing for Concrete (EFNARC) [7]

They define SCC and also provide information on standards related to testing and to the associated constituent materials used in the production of SCC. The admixture should bring about the required water reduction and fluidity but should also maintain its dispersing effect during the time required for transport and application. Admixtures are an essential component of SCC because they provide it with the basic nature, the flowability and the resistance to segregation when dropped from a certain height water reduction. The admixtures that are responsible for modification of the cohesion of the SCC without significantly altering its fluidity are called Viscosity Modifying (VMA). There is no standard method for SCC mix design and many academic institutions, admixture, ready-mixed, precast and contracting companies have developed their own mix proportioning methods. These mix proportion are not fixed. Some SCC mixes may also be different than this range (Table 1).

As per EFNARC, some acceptance criteria for SCC have been made with the maximum aggregate size up to 20 mm. However these values are not fixed, future developments may lead to different requirements being adopted. Some of the typical requirements are shown in the table based on current knowledge and practice (Table 2).

Table 1 EFNARC guidelines for mix proportion

Constituent	Range of mass (kg/m^3)	Range of volume (litres/m^3)
Water/powder ratio by volume	0.85–1.10	
Water	150–210	150–210
Coarse aggregate	750–1000	270–360
Powder (cement & fly ash)	380–600	
Fine aggregate (sand)	Typically 48–55% of total aggregate weight	

Table 2 Acceptance criteria for SCC [8]

	Methods	Unit	Min.	Max.
1.	Slump flow (D)	mm	650	800
2.	L-box	h2/h1	0.8	1
3.	U-box	(h2–h1) mm	0	30
4.	V-funnel	sec	6	12

A slump flow diameter of range 500–700 mm is considered as the slump required for a concrete to be accepted as SCC investigated by Fujiwara and Nagataki [9].

3 Materials Used in SCC and Their Properties

3.1 Cement

Cement used in this project was Ramco Cement. This cement is confirmed to IS8112 and 43 grade. The grade is based on the 28-day compressive strength of the cement mortar (tested as per IS 4031), which is at least more than 43 MPa.

3.2 Water

Water used in concrete is required to hydrate cement and other cementitious materials as well as to produce workability of the mixture.

3.3 Aggregates

Aggregates of size 10–20 mm are desirable for structures having congested reinforcement. The maximum size of aggregates is generally limited to 20 mm. Well-graded cubical or rounded aggregates are desirable in SCC because they increase the workability and do not provide unnecessary frictional forces to the mobility of concrete.

3.4 Admixtures

There are two types of admixtures:

(1) Mineral admixtures:

- Fly ash
- Silica fume

- Stone powder
- Ground Granulated Blast Furnace Slag (GGBFS)
- Fibres.

(2) Chemical admixture:

- Shrinkage Reducing Admixtures (SRA)
- Poly-Carboxylate Ethers (PEC)
- Air Entering Admixture (AEA)
- Viscosity Modifying Admixtures (VMA).

3.5 Admixtures Used

Sika® ViscoCrete®2004 NS is the admixture that was used in SCC to enhance the flowable properties. It imparts very high workability, improved workability retention and allows a large reduction in water content.

Dosage Optimum dosage of Sika® ViscoCrete® 2004 should be determined by lab trials for achieving the best flowability properties. Recommended dosage: 0.2–2% by weight of powder, i.e. cement and fly ash.

Dispensing Sika® ViscoCrete® 2004 NS can be added into the mixing water or directly into the concrete mixer.

4 Experimental Procedures

4.1 Mix Proportions

Rational method was used for the design mix of M30 Grade concrete. There is no codal provision of SCC for mix proportions. After performing the entire test, the following mix proportion was used for the present study (Table 3).

With different designations according to the amount of steel fibre used, the mix proportions was finalized. The mix M0 corresponds to normal SCC without any

Table 3 Mix proportions of SCC used

Materials	Proportions by weight	Weight in kg/m^3
Cement	1	450
Fine aggregates (sand)	1.15	517
Coarse aggregates (<16 mm)	2.09	940
Fly ash	0.2	90
Water/cement ratio	0.45	202

fibres added to it. Similarly, M1, M2 and M3 correspond to the mix with 1, 2 and 3% steel fibres added by volume fraction.

4.2 Fresh Tests on Concrete

The fresh concrete was prepared according to the above-designated design mix. VMA content was varied so that the mix comes in the range of acceptance criteria of SCC. Slump flow test was conducted on the mix to check its acceptance criteria for SCC. The distance between the cone and the spread concrete was measured for slump test, but in slump flow test the diameter of the spread was determined. The slump flow test was carried out for all the four mixes, i.e. M0, M1, M2 and M3 and the values were tabulated.

4.3 Hardened Tests on Concrete

The concrete was prepared according to the above-designated design mix. Dry mix should be proper to ensure homogenous distribution of steel fibres in the mix and to avoid formation of balls. The admixture should be added with water and then mixed to dry mix. It should not be vibrated or tamped while putting inside the mould.

Mixes each for M0, M1, M2 and M3 were cast in 150 × 150 × 150 mm cube, 100 × 100 × 500 mm prism and 150 mm diameter and length of 300 mm cylinders. Then these moulds were kept in curing chamber and were taken out for compressive strength, split tensile strength and flexural strength tests at 7 and 28 days (Table 4).

Table 4 7 and 28 days strength results in MPa

Mix	Compressive strength		Flexural strength		Split tensile strength	
	7 days	28 days	7 days	28 days	7 days	28 days
M0	36.8	56.44	7.15	8.25	4.1	4.26
M1	41.7	60.07	5.1	7	4.36	5.105
M2	50.2	63.61	7.6	12.05	6.39	6.53
M3	46.1	57.36	9.55	12.65	7.06	7.24

Table 5 Slump flow test results in mm

Mix	Slump flow (mm)
M0	700
M1	610
M2	540
M3	460

5 Results

5.1 Fresh SCC Test Results

The slump flow test was carried out and the test results were determined (Table 5).

5.2 Hardened SCC Test Results

Two specimens each for 7 and 28 days for all the mixes were subjected to compressive, flexural and split tensile strength test. The test results were calculated and the average value was determined.

6 Conclusions

- The slump flow test results for mixes M0, M1 and M2 can be accepted as SCC under the criteria mentioned but mix M3 may not pass the acceptance criteria successfully.
- The increase in compressive strength was 36.43% in 7 days and 12.7% in 28 days over normal SCC till 2% fibre addition by volume fraction. A compressive strength of 63.61 MPa was obtained at 28 days at this fibre content. But when fibres more than this fibre content were added, a reduction in compressive strength was observed. The self-compacting properties of concrete at 3% fibre content did not allow the concrete to get compacted under its own weight. Excess fibre addition reduced the workability of the SCC developing voids inside the specimen and hence the compressive strength was reduced.
- The flexural strength and split tensile strength increased with the additions of fibres proportionally. The increase in flexural strength was 33.5% in 7 days and 53.33% in 28 days over normal SCC. Increase in split tensile strength was 72.1% in 7 days and 70% in 28 days over normal SCC.
- Fly ash did not help much with the flowability but it helped in setting of SCC without external vibration or tamping.
- There was not much difference in peak split tensile strengths of 7 and 28 days. But the strength was increased by around 70% compared to normal SCC due to addition of fibres at 3% by volume fraction.

Fig. 1 Effects of steel fibre on flexural strength of the beam

- Addition of fibres helped to bridge the cracks in the structures preventing it from cracking. Thus when the normal SCC was given two point load of 8.25 MPa during flexural test, the prism collapsed into two parts but when it was reinforced with fibres, the prism got just deflected but did not collapse at a higher load of 12.65 MPa. Fibres helped to reduce deflections (Shown in Fig. 1).

- 3% by volume fraction of fibres firstly did not qualify the SCC acceptance criteria also it was not much good for practical applications because addition of fibres increased the dead load of the structure which was not considered safe and economical. The flexural strength 12.65 MPa (28 days) and split tensile strength 7.24 MPa (28 days) developed at this fibre content were nearly same to the strength developed at 2% fibre volume fraction, i.e. 12.05 MPa as flexural strength and 6.53 MPa as split tensile strength for 28 days. Already from the results, we found that 2% fibre content gives maximum compressive strength. It has 11% more strength than strength at 3% fibre content. Hence it can be concluded that 2% of steel fibre addition by volume is the optimum content to achieve the best mechanical properties of fibre reinforced SCC which will be safe for the structure in practical application and economical delivering a high strength.

Future Work

The properties of fibre-reinforced SCC can be studied by varying different types of fibres like propylene, glass fibre, hybrid fibre, etc.

References

1. Okamura, H. & Ouchi, M. (1998) Self compactiong high performance concrete. *Progress in structural engineering and materials*, *1*(4), 378–383.
2. Mahure, J. K., Mohitkar, V. M., & Ravi, K. (2014). Effect of fly ash on fresh and hardened properties of self compacting concrete. *I JESRT International Journal of Engineering Sciences & Research Technology, 3*(2), 944–948.
3. Kamran, M., & Mishra, M. (2014). Behaviour of SCC Using PPC and OPC with different composition of fly ash. *IJRET: International Journal of Research Engineering and Technology, 3*(9), 342–345.
4. Bhalchandra, S. A., & Bajirao, P. A. (2012). Performance of steel fiber reinforced self compacting concrete. *International Journal Of Computational Engineering Research, 2*(4), 1042–1046.
5. Ponikiewski, T., & Golaszewski, J. (2013). Steel fiber reinforced self compacting concrete for optimal rheological and mechanical properties on the precast beams. In *Concrete and Concrete Structure 2013 Conference* (pp. 290–296).
6. Rao, B. K, & Ravindra, V. (2010). Steel fiber reinforced self compacting concrete incorporating class F fly ash. *International Journal of Engineering Science and Technology 2*(9), 4936–4943.
7. EFNARC. (2002). *Specification and guidelines for self-compacting concrete, English edition*. Norfolk, UK: European Federation for Specialist Construction Chemicals and Concrete systems, February 2002.
8. The European Guidelines for Self Compacting Concrete, Specification, Production and Use. (2005 May).
9. Nagataki S, & Fujiwara, H. (1995). In V. M. Malhotra (Ed.) *Self-compacting property of highly flowable concrete*, Vol. Sp 154 (pp. 301–314). American Concrete Institute.

Investigation on Characteristics of *Spinacia oleracea* as an Innovative Internal Curing Agent in Combination with Self-compacting Admixtures

G. S. Rampradheep, M. Sivaraja, M. Geetha, R. Saranya, R. Sathish, V. Vignesh, G. Kavin, K. Gayathiri, M. Balaji and R. Divya

Abstract Exploratory study made on spinach also termed as *Spinacia oleracea*, a self-curing agent in self-compacting concrete is unveiled in this paper. Here, the study was made for natural self-curing agent in-built with water reducing and viscosity-based admixtures like super plasticizers and viscosity modifying agent in the brand name Master Glenium Sky (MGS) 8233. Fixed 2% based on cement weight was used throughout the study incorporated with self-curing admixtures. The main notion behind the usage of spinach as a self-curing agent is the presence of bond water in and its effective presence of hydroxyl and ether group in a chemical structure of spinach family. The design grade of concrete was fixed as M40 and its manufacturing procedure for such modern concrete was entirely based on trial and error and its end results were compared with the EFNARC specifications. Outcome from other commonly used curing agent such as Poly-Ethylene Glycol (PEG) (Bentz and Snyder in Cement Concr Res 29:1863–1867, 1999, [1], Dhir et al., Mater Struct 27:606–615, 1994, [2]) and conventional methods are collated with the payoff from spinach (Dhir et al., Mag Concr Res 50:85–90, 1998, [3], Dhir et al., Cem Concr Res 25:1153–1158, [4]). The sample test results have been given which splash the behaviour of internal curing agent under a designed laboratory conditions. Initially, the agent used for robotic curing purpose was studied to examine its water holding capacity analysis. Here for the special case, explanatory results were appraised using Fourier Transform Infra Red (FTIR) spectrum analyser. Different tests were conducted to determine the

G. S. Rampradheep (✉) · R. Saranya · R. Sathish · V. Vignesh · G. Kavin
K. Gayathiri · M. Balaji · R. Divya
Department of Civil Engineering, Kongu Engineering College,
Erode 638052, Tamil Nadu, India
e-mail: gsramcivil34@gmail.com

M. Sivaraja
N.S.N. College of Engineering and Technology, Karur 639063,
Tamil Nadu, India
e-mail: m.shivaraj2006@gmail.com

M. Geetha
CSI Polytechnic College, Salem 636007, Tamil Nadu, India
e-mail: geethacsi@yahoo.co.in

A. Rama Mohan Rao and K. Ramanjaneyulu (eds.), *Recent Advances in Structural Engineering, Volume 1*, Lecture Notes in Civil Engineering 11,
https://doi.org/10.1007/978-981-13-0362-3_61

workability properties, mechanical properties, microstructural properties and durability properties of the concrete. Test such as compression test, split tensile test and flexural test were conducted to determine the mechanical properties of concrete. Tests on bond of spinach with concrete matrix, Scanning Electron Microscope (SEM) Analysis, water sorptivity and shrinkage were carried out. Results show that alike PEG, spinach is also an effective curing agent and improves the cement hydration, compressive strength, diminishes shrinkage and accelerates the durability of concrete whereas the conventional methods need improvement. Their outcomes are found to be satisfactory as per IS standards, EFNARC specifications and ASTM codal provisions.

Keywords Spinach · Poly-Ethylene Glycol (PEG) · Viscosity Sorptivity · Shrinkage

1 Introduction

Over the last few decades, a great deal of interest has been shown in the study of making concrete better by the process of incorporating specifically engineered ingredients and simulating the methods of batching and mixing. Compared to traditional concrete, modern types of concrete are highly advantageous in as much as they provide good workability in the fresh state, possess high strength and low permeability. However, these types of concrete have also shown to be more sensitive to early age cracking than traditional concrete. The significant problem of self-desiccation and shrinkage was observed for the concrete with 0.4 (*w*/*c*) using the light weight aggregate by Bentz & Snyder [1]. One of the major problems with these mixtures is their tendency to undergo early age cracking. While this cracking may or may not compromise the compressive strengths of these concretes, it likely does compromise their long-term durability. The phenomenon of early age cracking is complex and depends on thermal effects, autogenous strains and stresses, drying stress relaxation. The volume change in the concrete under the different sizes of the light weight aggregate particles at an early age of specimen was investigated by Lura & Van Breugel [5].

Concrete with internal curing may also have evolved from the concept of self-curing concrete, which is based on the introduction of a chemical admixture that is able to reduce water evaporation by a retaining function. The addition of a self-cure chemical based on a water-soluble polymeric glycol leads to improved durability of concrete cured in air, which was pointed out by Dhir et al. [4]. However, the performance of such admixture does not attain the efficiency of the water film curing as discussed by Hewlett et al. [6]. The use of water retaining agents should not be seen as internal curing, since it is conceptually based on the internal sealing rather than internal curing. The latter consists of a water curing agent capable of enhancing cement hydration maintaining optimal curing

conditions. In either case, there are many examples that require other forms of curing procedures rather than the traditional or external curing methods, e.g. high strength concrete applied in submerged pipe systems within oil platform structures. In high-performance concrete, capillary discontinuity may significantly delay and even limit the water movement throughout the system as pointed by Cusson & Hoogeveen [7]. This makes the use of water ponding or other external curing methods inefficient in assuring the continuous internal moisture of the material. In this case, the use of internal curing methods may be required to counteract autogenous deformation. As there is only little experience on the practical use of internal curing methods to improve early age properties of high-performance concrete, the subject constitutes a great challenge to technicians and industrialists of the modern age.

2 Experimental Investigation

2.1 Materials Used

The concrete was cast with basic ingredients of OPC 53 grade confirms to IS: 12269-2013 [8], Class F Fly ash based on ASTM C 618 [9] and aggregates that confirm to IS: 383-1970 [10]. Potable water free from salts was adopted to mix the concrete ingredients for the design mix. Spinach was used as a natural curing agent and the outcomes were compared with Poly-Ethylene Glycol (PEG), the existing curing agent and the conventional cured concrete which involves Full/Immersion Curing (FC) and Sprinkler Curing (SPRC). Figure 1 shows the hydroxyl ion presence for PEG under Fourier Transform Infrared (FTIR).

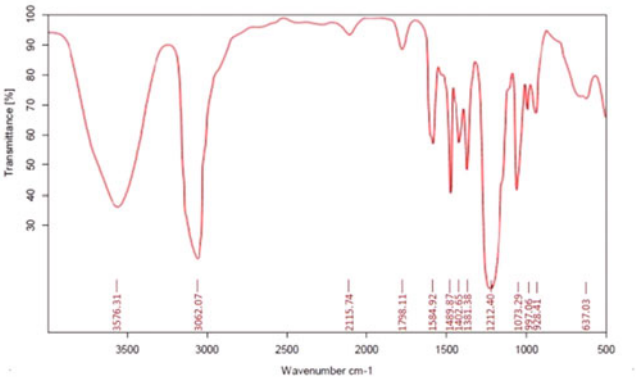

Fig. 1 OH ion presence for PEG

2.2 Spinacia oleracea

The spinach leaves were obtained naturally from the agriculture land, cleaned well using normal water and it was used as a curing agent as investigated earlier by Geetha & Malathy [11]. The chemical extract and the molecular structure of spinach were shown in Fig. 2. The presence of OH ions observed using FTIR analyser for spinach extract was shown in Fig. 3.

2.3 *Mix Proportion*

The mix constitution was designed to convince all performance norms of the concrete in both fresh and hardened stages. Here, the four trails were acquired as per EFNARC identification to gain medium strength Self-Compacting concrete of grade M40. In this work, contrary percentage of fly ash content was achieved for each trail. The divergent percentage of fine aggregate with regard to total weight of aggregate was believed for each trail mix. The percentage of Master Glenium Sky (MGS) impelled to all mix proportions was kept 2% in constant. The collation of materials used for each trail mix is designed in Table 1. Each divergent percentage of two Self-curing agents was impelled to all four trail mix to survey the best trail mix constitution. So, totally 24 trail mix constitutions were tried out in this study.

a. Chemical Extract

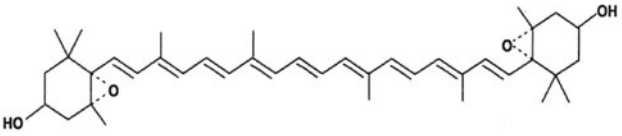

b. Molecular structure

Fig. 2 *Spinacia oleracea*

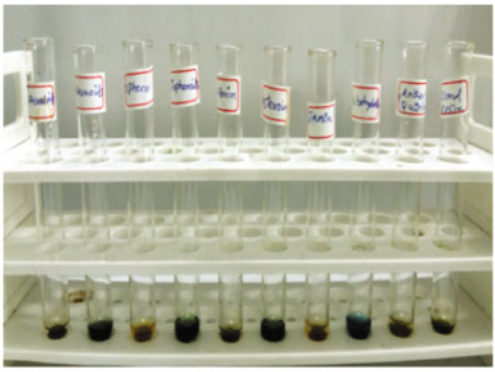

a. Extract separation

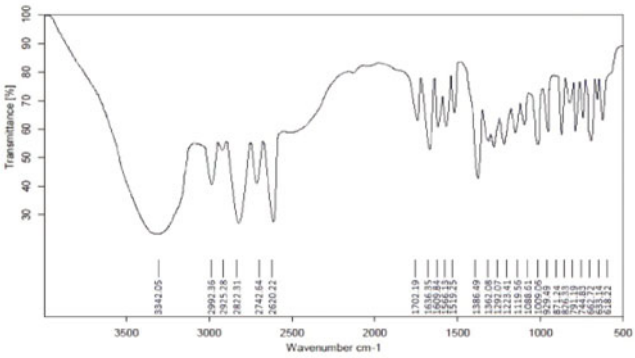

b. FTIR output

Fig. 3 Presence of OH ion for *Spinacia oleracea*

Table 1 Mix proportion

Trial mix	Cement (kg/m^3)	Fly ash (kg/m^3)	Fine aggregate (kg/m^3)	Coarse aggregate (kg/m^3)	Water (kg/m^3)
1.	435	145	720	760	180
2.	445	155	740	810	180
3.	470	130	730	760	180
4.	460	140	790	720	180

For each four trail, conventional concrete was cast without impelling self-curing agent and cured by conventional method. PEG and *Spinacia oleracea* (SO) were impelled to the concrete mix as a percentage of weight of cement. For a basic trial, the percentage of each curing agents in the order was assumed at 0.2, 0.5 and 0.7%

for PEG and SO, and its individual effects under each mix have been observed with conventional concrete under full/immersion cured and sprinkler cured concrete.

2.4 Casting, Curing and Testing of Specimens

For verifying the ability of concrete on horizontal flow, filling and to assess the extent to which concrete is subject to blocking slump flow and T_{50}, V funnel, L box and U box tests were conducted based on the guidelines for self-compacting concrete given in EFNARC specification [12]. Concrete specimens were cast to perform significant tests such as compressive strength for cube of size 150 mm, split tensile strength for cylinder of size 150 mm diameter and 300 mm height and flexural strength of prism of size 500 mm × 100 mm × 100 mm. All the specimens were tested at the age of 28 days. PEG and SO were used as internal curing agents and the specimens were left free to the atmospheric temperature after casting without curing. Full Curing (FC) or normal conventional curing and Sprinkler Curing (SPRC) were used for comparison of the results and the curing was continued for 28 days. In sprinkler curing method, the water was sprinkled on the cubes at a time interval of 3 h. Figure 4 indicates the different conditions of curing made at a constant temperature of 30 °C.

Figure 5 shows the durability tests such as water sorptivity for concrete specimen of size 50 mm diameter and 100 mm height and tested as per ASTM C 1585-O4e1 [13]. The test was made up to 3 h at a time interval of 30 min. Here, the side faces of the specimen were coated with epoxy to protect the ingress of moisture to inside and out from the specimen. Drying shrinkage was carried out based on ASTM C 596-O9e1 [14]. Figure 6 shows the shrinkage tests.

3 Results and Discussions

The optimized percentage was found from trial mix 4 and the test results for workability, mechanical, durability and microstructure properties were given in Tables 2 and 3. All the self-cured specimens were compared with conventional cured specimens.

3.1 Outcomes from Workability Test

From Table 2, it was cleared that concrete with internal curing agents behaves appreciable workability than conventional concrete. It was noticed that internal curing concrete possess 22% increase in workability behaviour than conventional concrete under full curing and 36% under sprinkler curing averagely. But all the

a. Full / Immersion curing

b. Sprinkler curing

c. Self-curing

Fig. 4 Different profiles of curing

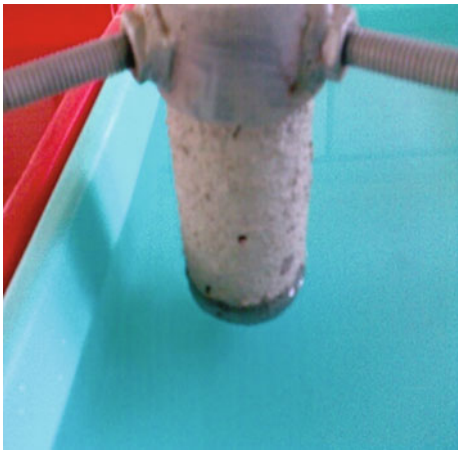

Fig. 5 Water sorptivity test

Fig. 6 Drying shrinkage test

Table 2 Workability Results

Concrete type	Slump flow (mm)	T_{50} cm slump flow (s)	V funnel (s)	L Box (H_2/H_1)	U Box ($H_2 - H_1$) mm
PEG	720	3	7.2	0.82	10
SO	710	3	8.5	0.84	9
FC	690	4	10.4	0.94	15
SPRC	700	4	10.6	0.92	17

Table 3 Mechanical and Durability Results

Concrete type	Mechanical properties at 28 days			Durability properties	
	Compression strength (N/mm^2)	Split tensile strength (N/mm^2)	Flexural strength (N/mm^2)	Water sorptivity at 180 min. (g/mm^2) × 0.0001	Drying shrinkage at 240 days(mm)
PEG	44.5	3.68	5.62	9.9	0.20
SO	43.8	3.45	5.48	10.2	0.20
FC	45.2	3.98	6.26	19.2	0.68
SPRC	39.6	3.22	3.98	22.7	1.20

values from various concrete types get satisfied as per EFNARC specifications. Even though the conventional concrete under both curing types falls within the range, the ultimate sustainability depends on the internal matrix of the ingredients as it based on the moisture holding capacity by the curing agents.

3.2 Outcomes from Mechanical and Durability Test

From Table 3, it was cleared that concrete with internal curing agents behaves superior mechanical properties than conventional concrete under sprinkler curing. It was noticed that internal curing concrete possess 10.31% increase in strength behaviour than sprinkler cured concrete and a very slight reduction in strength percentage of 2.3% was observed for self-cured concrete than full cured concrete. In concern with durability properties on water sorptivity, the self-cured concrete possesses greater reduction in bottom permeation than conventionally cured specimens. It was examined that nearly 56.38% permeability increase occurred for sprinkler cured specimen which was a major drawback in the view of concrete sustainability. The shrinkage value was 83.33% less for self-cured specimen than sprinkler cured specimen which shows the first-string performance of natural curing regime in the conventional concrete.

3.3 Micro-Structural Properties

The internal arrangement of the structure of concrete for self-cured and conventional cured specimens was shown in Fig. 7. The perfect bond between the ingredients was obtained for the concrete with self-curing agents and the weakest bond could be observed for the concrete without curing agents. Interfacial Transition Zone (ITZ) was well protected by the incorporation of automatic curing agents, and the presence of OH ions makes the concrete to prevent from self-desiccation.

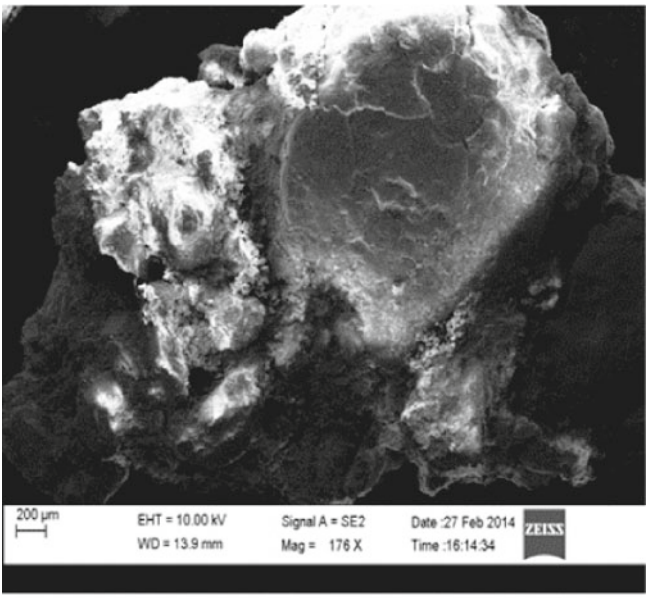

a. Self-cured concrete

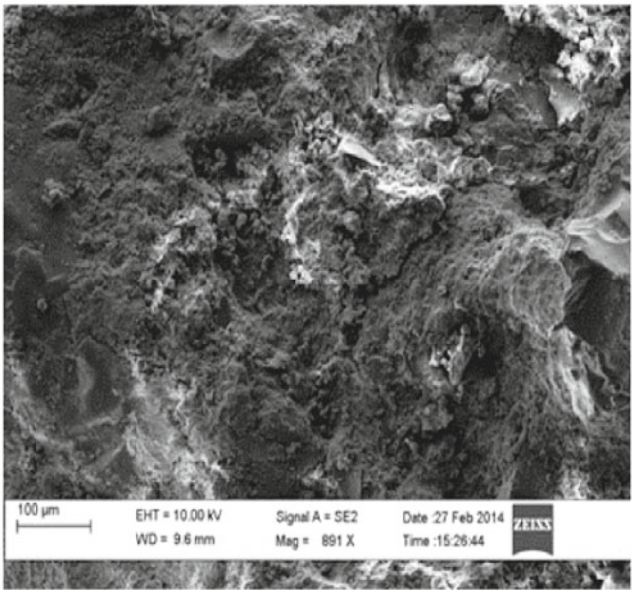

b. Conventional concrete

Fig. 7 SEM image

But the condition is reverse for the conventional concrete, as it allows self-evaporation from the inner part of the concrete.

4 Conclusion

From the various test results on concrete with and without self/internal curing agents, the following conclusions arrived.

(i) OH ions are mainly responsible for hardening of concrete during curing process. From FTIR results, it is confirmed that OH ions are present in spinach and hence it could be used as an internal curing agent, a substitute for existing curing agent and an innovative product for conventional concrete.
(ii) Workability results get satisfied for self-cured concrete using spinach as per EFNARC specifications.
(iii) Mechanical properties show superior performance for spinach cured concrete than sprinkler cured concrete.
(iv) Notable achievement was observed for self-cured concrete with spinach than conventional concrete.

References

1. Bentz, D. P., & Snyder, K. A. (1999). Protected paste volume in concrete: Extension to internal curing using saturated lightweight fine aggregate. *Cement and Concrete Research, 29* (11), 1863–1867.
2. Dhir, R. K., Hewlett, P. C., Lota, J. S., & Dyer, T. D. (1994). An investigation into the feasibility of formulating self-cure concrete. *Materials and Structures/Materiaux et Constructions, 27*(174), 606–615.
3. Dhir, P. K., Hewlett, P. C., & Dyre, T. D. (1998). Mechanism of water retention in cement pastes containing a self-curing agent. *Magazine of Concrete Research, 50*(1), 85–90.
4. Dhir, R. K., Hewlett, P. C., & Dyer, Tom. (1995). Durability of self-cure concrete. *Cement and Concrete Research, 25*(6), 1153–1158.
5. Lura, P., & Van Breugel, K. (2015). Effect of size of lightweight aggregate particles on volume changes of lightweight aggregate concrete at early ages. In *ICE Virtual Library Innovations and Developments in Concrete Materials and Construction* (pp. 651–660).
6. Hewlett, P. C., Tom, Dyer, & Dhir, R. K. (1998). Mechanisms of water retention in cement paste containing self-curing agent. *Magazine of Concrete Research, 50*(1), 85–90.
7. Cusson, D., & Hoogeveen, T. (2008). Internal curing of high-performance concrete with pre-soaked fine lightweight aggregate for prevention of autogenous shrinkage cracking. *Cement and Concrete Research, 38*(6), 757–765.
8. IS: 12269-2013. *Indian Standard for ordinary portland cement, 53 grade - specification*. Bureau of Indian Standards, New Delhi–110002.
9. ASTM C 618: 1997. *Standard specification for coal fly ash and raw or calcinated natural pozzolan for use in concrete.* Philadelphia, PA: American Society for Testing and Materials.

10. IS: 383-1970. *Indian Standard specification for coarse and fine aggregates from natural sources for concrete*. Reaffirmed 2002. Bureau of Indian Standards, New Delhi–110 002.
11. Geetha, M., & Malathy, R. (2010). "Durability properties of self curing concrete by addition of vegetative material as Admixtures" in technology today. *Quarterly Journal* 2(1), 99–104. (ISSN: 2180-0987).
12. EFNARC. (2002). *Specifications and guidelines for self-compacting concrete.* EFNARC, Association House, 99 West Street, Farnham, Surrey GU9 7EN, UK.
13. ASTM C 1585-04e1. *Standard test method for measurement of rate of absorption of water by hydraulic-cement concretes.* West Conshohocken: ASTM International.
14. ASTM C 596-09e1. Standard test method for drying shrinkage of mortar containing hydraulic cement. West Conshohocken: ASTM International.

Recycled Aggregate Concrete: Particle Packing Method (PPM) of Mix Design Approach

Subhasis Pradhan, Shailendra Kumar and Sudhirkumar V. Barai

Abstract The reuse of old concrete as a source of aggregate is a reliable alternative to Natural Aggregate (NA) in concrete construction. Because of poor quality of Recycled Aggregate (RA), the performance of Recycled Aggregate Concrete (RAC) is not up to the mark in fresh stage and hardened stage as compared to Natural Aggregate Concrete (NAC). In this work, Recycled Coarse Aggregate (RCA) is replaced 100% to produce RAC. The Particle Packing Method (PPM) is proposed for the mix proportioning of concrete. In PPM, the smaller particles are selected to fill up the voids between large particles and so on. PPM is found out to be cost-effective than IS code method of mix design because of the requirement of lesser quantity of cement. The 7 and 28 days compressive strength of conventional concrete and RAC using PPM design mix are very similar. But, the increment in compressive strength from 28 to 90 days curing is higher for NAC than RAC.

Keywords Recycled Coarse Aggregate (RCA) · Recycled Aggregate Concrete (RAC) · Natural Aggregate Concrete (NAC) · Particle Packing Method (PPM) Compressive strength

S. Pradhan · S. V. Barai
Department of Civil Engineering, Indian Institute of Technology Kharagpur, Kharagpur 721302, India
e-mail: subhasisiitg@gmail.com

S. V. Barai
e-mail: skbarai@civil.iitkgp.ernet.in

S. Kumar (✉)
Department of Civil Engineering, Guru Ghasidas Vishwavidyalaya (A Central University), Bilaspur 495009, India
e-mail: shailendrakmr@yahoo.co.in

A. Rama Mohan Rao and K. Ramanjaneyulu (eds.), *Recent Advances in Structural Engineering, Volume 1*, Lecture Notes in Civil Engineering 11,
https://doi.org/10.1007/978-981-13-0362-3_62

1 Introduction

The rapid growth in population and economy in India leads to the unavoidable process of industrialization and urbanization. It requires a huge amount of construction works and also produces large quantities of Construction and Demolition (C&D) wastes. According to Ministry of Environment and Forests (MoEF), India generates nearly 530 million tonnes of C&D waste annually. In this C&D debris waste, concrete percentage is very high. The reuse of old concrete as a source of aggregate is a reliable alternative to Natural Aggregate (NA) mined from nature in concrete construction. Demolished building, rejected precast concrete member, concrete road beds, unused concrete in ready-mix concrete plant and tested specimens from different laboratories are the sources of waste concrete.

Recycled Aggregate (RA) is yielded by crushing the waste concrete procured from C&D debris. NA and adhered hardened mortar are the constituents of RA. The concrete in which NA is replaced partially or fully by RA is known as Recycled Aggregate Concrete (RAC). The adhered mortar layer and its quantity are the main reasons for having inferior physical and mechanical properties of RA as compared to NA and also for the poor performance of RAC. Fresh RAC has the lower workability than conventional concrete as the water absorption capacity of RA is on the higher side due to its structure [1–8]. Compressive strength of RAC is primarily influenced by replacement ratio of natural aggregate and *w/c* ratio. The reduction in compressive strength of RAC is not very significant when the replacement of RCA is up to 30% [9–11]. It has been observed by many researchers that the reduction in compressive strength of RAC is up to 30% at 100% replacement of NA [5, 10, 11].

The techniques approached by different researchers to improve the performance of RAC are the incorporation of mineral admixture, using different mix design methods and modifying the mixing process. The addition of mineral admixtures to RAC improves the workability in fresh stage [12]. The use of fly ash or GGBS as partial replacement of cement reduces the compressive strength of RAC [12, 13]. However, using fly ash as the addition of cement increases the compressive strength [13].

Direct Weight Replacement (DWR) method, Equivalent Mortar Replacement (EMR) method [14] and Direct Volume Replacement (DVR) method are three different aggregate replacement methods employed by different researchers. In DWR method, the weight of coarse aggregate (natural coarse aggregate plus RCA), cement and water content are kept constant for any replacement ratio. In order to produce same volumetric yields, the fine aggregate amount is reduced. In Ref. [14], the EMR method was proposed and in this method, RCA was considered as a two-phase material rather than a single coarse aggregate. In EMR method, the total volume of mortar (residual and fresh mortar) content in RAC remains the same as the fresh mortar content of target natural aggregate concrete. The DVR method considers RCA as a single-phase coarse aggregate. In this method, the volume of replacing RCA is the same as the volume of natural aggregate. The amount of fine aggregate, cement and water are unaffected as the total volume of coarse aggregate

remains constant. In EMR method, workability reduces significantly and replacement ratio more than 20% needs changes in mix proportions and high dose of water reducing admixture. The compressive strength is not influenced significantly by any of these mix design methods at any replacement ratio [15].

Some modified mixing approaches, such as double mixing method, Two-Stage Mixing Approach (TSMA) and Triple Mixing Method (TM) have been employed by different authors to enhance the performance of RAC. Tam et al. [11] have proposed a TSMA and basically, this method divides the mixing process into two parts and water is added in two steps at different times. The TSMA helps in developing a stronger ITZ by effectively filling the voids and cracks present in RCA. The compressive strength of RAC is increased up to 21% and TSMA is also effective in enhancing durability [11]. The TM contributes significantly to improving workability, compressive strength and flexural strength in comparison to double mixing method.

2 Research Importance

Review of literature shows that the poor performance of RAC both in fresh stage and hardened stage is related to the inferior quality of RA. The DWR and DVR methods are not very useful in improving the performance of RAC, whereas the performance of RAC using EMR method of mix design is quite encouraging. But, the major drawback of EMR method is that 100% replacement of RCA is never achievable. There is no specific code or guidelines available for mix design of RAC as per BIS. So, most of the researchers follow the mix design procedure used for conventional concrete to produce RAC. Therefore, in the present study, an attempt is made to use Particle Packing Method (PPM) of design mix to improve the performance of RAC and to overcome the disadvantages of different mix design methods.

3 Proposed Mix Design Method

The basic concept of PPM of mix design is to minimize the voids content [16–18]. This is a process of optimization where the smaller particles are selected to fill up the voids between large particles and so on. In PPM, the aim is to obtain maximum possible packing density using coarse and fine aggregates. In this regard, it involves the proper determination of proportions of different sizes of coarse aggregates and fine aggregate and packing density of the mixture of coarse and fine aggregate. The increase in packing density leads to the minimization of voids and hence the requirement of binder and water will be less.

3.1 Materials

The concrete mixtures were prepared using Ordinary Portland Cement (OPC) of 53 Grade conforming to Bureau of Indian Standard Specifications (BIS) (IS: 8112-1989), Natural Coarse Aggregate (NCA), Recycled Coarse Aggregate (RCA), clean river sand conforming to grading Zone II (IS: 383-1970) and potable water. The specific gravity and 28 days compressive strength of the cement used were found out to be 3.13 and 60.59 MPa, respectively. The NCA used to produce conventional concrete was collected from locally available quarries with maximum size of 20 mm and satisfying the grading requirements of BIS (IS: 383-1970). The processed RCA was collected from the IL&FS Environmental Infrastructure and Services Ltd. Plant (New Delhi). The physical and mechanical properties of NCA, RCA and fine aggregate are shown in Tables 1 and 2 by following the procedure given in BIS (IS: 2386 (Part I)-1963, IS: 2386 (Part III)-1963 and IS: 2386 (Part IV)-1963).

3.2 Aggregate Fractions and Packing Density

In this study, 20–12.5 mm, 12.5–10 mm, 10–6.3 mm and 6.3–4.75 mm sized RCA and 20–12.5 mm, 12.5–10 mm and 10–4.75 mm sized NCA were used along with Zone II fine aggregate to optimize the packing density. Compacted bulk density and specific gravity for each size of aggregates were determined. First 20–12.5 mm and 12.5–10 mm aggregates were mixed in different proportions by mass, such as 90:10, 80:20, 70:30, etc., and the bulk density of each mixture was determined. The Packing Density (PD) and Voids Content (VC) of the aggregate mixture were determined at each proportion using Eqs. (1) and (2), respectively. As the smaller sized aggregate fraction increases, the bulk density of the mixture increases. But after a certain proportion of the mixture, the bulk density starts decreasing.

$$\mathrm{PD} = \sum \frac{\text{Bulk Density} \times \text{Weight Fraction}}{\text{Specific Gravity}} \tag{1}$$

$$\mathrm{VC} = 1 - \sum \frac{\text{Bulk Density}}{\text{Specific Gravity}} \tag{2}$$

The proportion at which maximum PD obtained was determined. This particular weight fraction of first two different sized aggregate mixture was used while preparing mixture along with 10–6.3 mm aggregate size. So, the mixture of 20–12.5 mm, 12.5–10 mm sized aggregates was blended with 10–6.3 mm sized aggregates was blended with 10–6.3 mm sized RCA to prepare mixtures of different proportions. The PD of the mixture of three different sized RCA was

Table 1 Physical properties of NCA, RCA and fine aggregate

Properties of aggregates		Coarse aggregate types and sizes								Sand
		20 mm		12.5 mm		10 mm		6.3 mm		
		NCA	RCA	NCA	RCA	NCA	RCA	NCA	RCA	
Specific gravity		2.93	2.54	2.88	2.53	2.8	2.43	–	2.29	2.66
Water absorption (%)		1.59	3.63	1.67	3.4	1.06	4.2	–	5.09	0.24
Bulk density (kg/m^3)	Loose	1447.02	1303.9	1435.8	1230.9	1414.74	1191.6	–	1146.5	1443.74
	Compacted	1647.72	1374	1598.6	1315.1	1594.4	1271.6	–	1288	1578.2

Table 2 Mechanical properties of NCA and RCA

Properties of aggregate	NCA	RCA	BIS limits (upper)
Los Angeles abrasion value (%)	14.34	34.08	50
Impact value (%)	13.87	24.23	45
Crushing value (%)	17.66	23.32	45

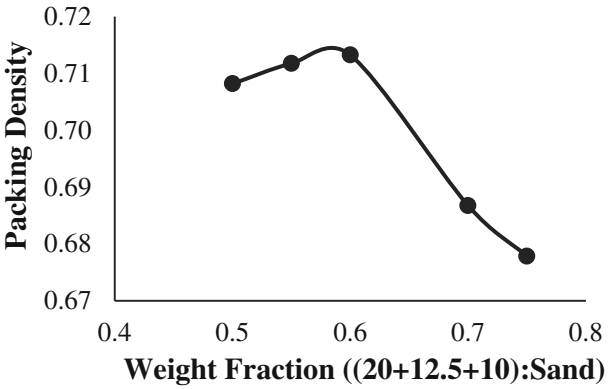

Fig. 1 Packing density of (NCA (20 mm + 12.5 mm + 10 mm):sand)

calculated for each weight fraction. The maximum PD of the mixture and its corresponding weight fraction were determined.

Then 6.3–4.75 mm RCA was added to the mixture of 20–12.5 mm, 12.5–10 mm and 10–6.3 mm sized aggregates in different proportions and the proportion at which maximum PD obtained was determined. Finally, fine aggregate was added to the mixture of four different sized RCA in different proportions by mass. For each weight fraction, PD was calculated and the maximum PD and its corresponding weight fraction were determined.

By conducting the whole exercise, maximum packing density for the RCA and fine aggregate mixture was found out to be 0.728. The corresponding proportion of 20–12.5 mm, 12.5–10 mm, 10–6.3 mm, 6.3–4.75 mm sized RCA and fine aggregate to achieve maximum packing density was 31.92:13.68:11.4:3:40. For conventional concrete production, 20–12.5, 12.5–10, 10–6.3 size of natural coarse aggregate and fine aggregate has been used. The maximum packing density was found out to be 0.713 in the aggregate proportion of 38.4:9.6:12:40 for 20–12.5, 12.5–10, 10–6.3 sized NCA and fine aggregate. In Figs. 1 and 2, the packing density at different weight fractions, for the mixture of NCA with sand and RCA with sand are shown respectively.

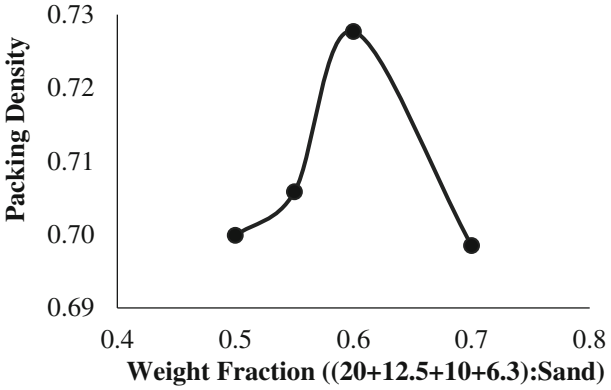

Fig. 2 Packing density of (RCA (20 mm + 12.5 mm + 10 mm + 6.3 mm):sand)

3.3 Determination of Paste Content

In PPM, the higher degree of packing density leads to minimum voids, maximum density and minimum requirement of binder. The total packing density (PD) obtained by mixing 20–12.5 mm, 12.5–10 mm, 10–6.3 mm, 6.3–4.75 mm RCA and natural fine aggregate is 0.728.

Hence, Voids Content$(\mathrm{VC}) = 1 - \mathrm{PD}$

The total paste content in this method is the sum of the voids content found in the aggregate mixture and excess quantity of paste required to coat the aggregate particle and to obtain desirable workability of the concrete. From multiple trials, it was found out that 16% excess paste content is required for M30 grade of concrete and desired workable condition (Tables 3 and 4). Hence,

$$\text{Total Voids Content} = \mathrm{VC} + \text{Excess Paste Content} \times \mathrm{VC}$$

$$\text{Now, Volume of aggregates} = 1 - \text{Total Voids Content}$$

Table 3 Mix proportions for different types of concrete

Type of concrete	Mix design method	*w/c* ratio	Water (kg/m^3)	Cement (kg/m^3)	Sand (kg/m^3)	Coarse aggregate (kg/m^3)			
						20 mm	12.5 mm	10 mm	6.3 mm
NAC	IS 10262: 2009	0.45	215.85	438.13	610.19	755.77		485.63	
NAC	PPM	0.45	203.51	410.04	762.12	666.85	247.69	228.64	
RAC	IS 10262: 2009	0.45	234.18	422.22	621.24	671.45		416.73	
RAC	PPM	0.45	225.79	410.04	702.03	560.22	240.09	200.1	52.65

Table 4 Compressive strength of different types of concrete

Type of concrete	Mix design method	*w/c* ratio	7 days strength (MPa)	28 days strength (MPa)	90 days strength (MPa)
NAC	PPM	0.40	30.87	51.27	65.49
		0.43	28.74	44.29	58.87
		0.45	25.35	42.75	56.15
		0.47	23.69	38.18	52.52
NAC	IS: 10262 (2009)	0.45	29.69	47.68	64.85
RAC	PPM	0.40	31.71	49.33	56.34
		0.43	29.48	48.09	53.72
		0.45	25.14	42.82	47.69
		0.47	24.48	42.48	47.59
RAC	IS: 10262 (2009)	0.45	35.99	45.23	54.46

$$\text{Total solid volume of aggregates} = \sum \frac{\text{Weight fraction of aggregates}}{\text{Specific Gravity}}$$

$$\text{Weight of the aggregate} = \frac{\text{Volume of aggregates}}{\text{Total solid volume of aggregates}} \times \text{Weight fraction} \times 1000$$

The water–cement ratio for M30 grade of concrete is determined by conducting the trials at *w/c* ratio 0.4, 0.43, 0.45 and 0.47 and finally, it is fixed at 0.45 to achieve the target mean strength specified for M30.

$$w/c \text{ ratio} = 0.45;\ w = 0.45c$$

$$\text{Total paste content} = c + w = \frac{c}{\text{Specific Gravity}_{\text{cement}}} + \frac{0.45c}{\text{Specific gravity}_{\text{water}}}$$

$$\text{Cement content} = \frac{\text{Total voids content}}{\text{Total paste content}} \times 1000$$

$$\text{Water content} = w/c \text{ ratio} \times \text{Cement content}$$

4 Mixing Process

The TSMA proposed by Tam et al. [11] is adopted for the current study, as the process helps in improving the performance of the concrete by improving its quality at microstructure level. This may be attributed to the effect of internal curing. In this method, water is added in two stages of mixing. The steps involved in TSMA are shown in Fig. 3.

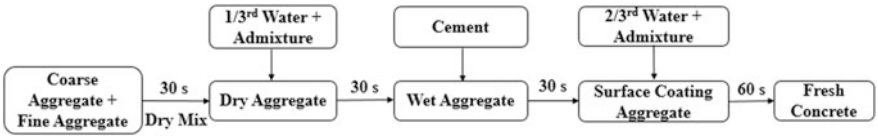

Fig. 3 Schematic diagram of Two-Stage Mixing Approach

5 Performance Evaluation of Concrete

In order to verify the performance of hardened concrete, both NAC and RAC (100% replacement) were prepared using PPM design mix, TSMA and established method as per IS: 10262–2009, normal mixing method. So, four types of concrete were produced using *w/c* ratio of 0.45.

5.1 Fresh Concrete

The property of fresh concrete was examined by its workability in terms of slump value. In this study, 75–100 mm slump was kept constant for both conventional concrete and RAC. In conventional concrete, desired workability was obtained without addition of any admixture. But for RAC, Master Glanium ACE 30 (BASF) admixture was added 0.32% by weight of cement to achieve the required slump.

5.2 Hardened Concrete

The hardened concrete performance can be studied as its short-term and long-term behaviour. The short-term properties of hardened concrete include compressive strength, tensile strength and modulus of elasticity. The compressive strength of concrete was measured using standard cubes and cylinders in accordance with BIS (IS: 516-1959).

5.2.1 Compressive Strength

The 7 days compressive strength shows negligible difference for NAC and RAC using PPM design at different *w/c* ratio. For *w/c* ratio 0.4, 0.43 and 0.47, the 7 days compressive strength of RAC is 2.57–3.3% higher than that of NAC. Whereas for *w/c* ratio 0.45 the 7 days compressive strength of NAC is 0.84% higher than RAC.

In PPM mix proportioning except *w/c* ratio 0.4, the 28 days compressive strength of RAC are 0.16–11.26% higher in comparison to NAC and the 28 days compressive strength obtained at *w/c* ratio 0.4 for NAC is 3.93% higher than that of RAC. So, the 7 and 28 days compressive strength of RAC are slightly on the higher side than NAC. But, interestingly the 90 days curing compressive strength of RAC at different *w/c* ratio are 9.58–17.74% lower than NAC. There is an increase of 27–37% observed in compressive strength at different *w/c* ratio of NAC from 28 to 90 days; whereas for RAC, only 11–14% increment is observed for the same time period (Figs. 4, 5, 6, 7 and 8).

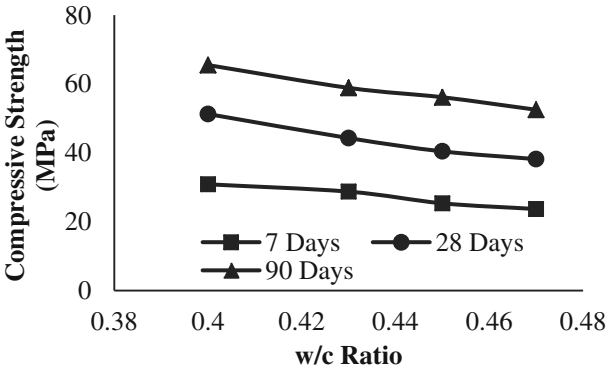

Fig. 4 Compressive strength of NAC versus *w/c* ratio at different ages

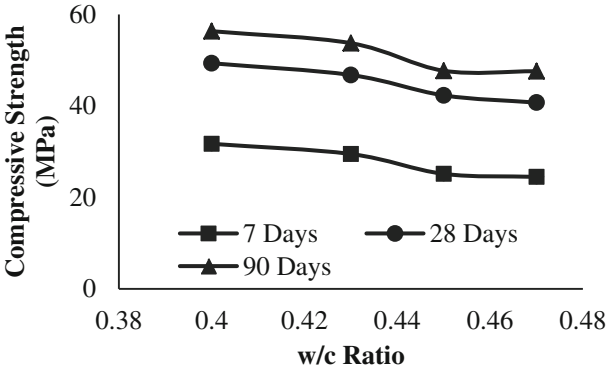

Fig. 5 Compressive strength of RAC versus *w/c* ratio at different ages

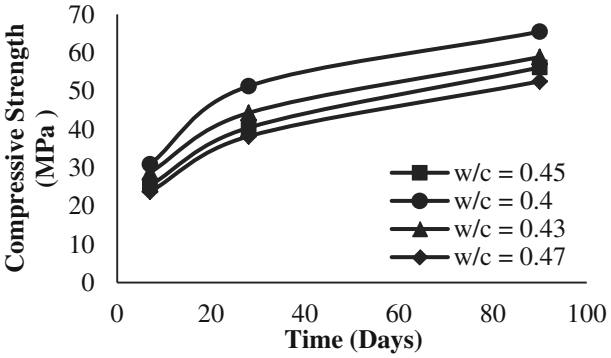

Fig. 6 Compressive strength of NAC versus curing age for different *w/c* ratio

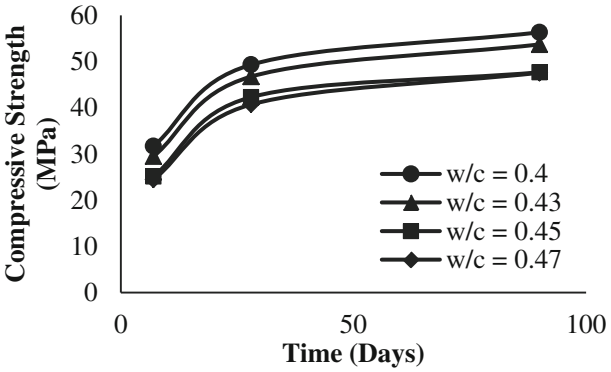

Fig. 7 Compressive strength of RAC versus curing age for different *w/c* ratio

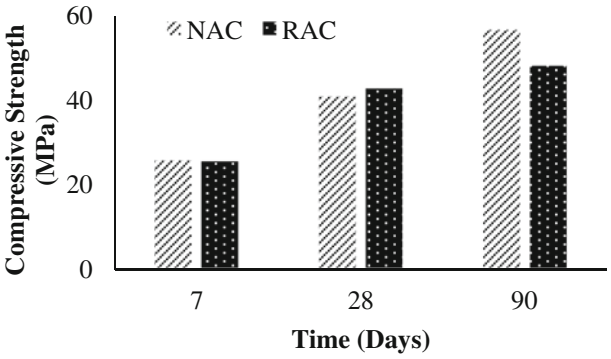

Fig. 8 Comparison of compressive strength versus curing time (days) of NAC and RAC

6 Conclusions

In this study, the physical and mechanical properties of the materials used are verified. The PPM is proposed for the mix proportioning of concrete and the compressive strength of both NAC and RAC are experimentally analysed.

- The bulk density and specific gravity are lower and water absorption is on the higher side for RCA because of the adhering mortar layer. The mechanical properties of RCA are relatively inferior to NCA, but the values are within the permissible limits of BIS.
- The proposed PPM design mix requires lesser quantity of cement, but more fine aggregate in comparison to IS: 10262 (2009) method of mix proportioning without affecting the properties of fresh and hardened concrete. The lesser demand for cement in the PPM design mix indicates the cost-effectiveness of the method.
- The RAC is having lower workability than NAC. The PPM mix proportioning has no significant effect in improving the workability of the fresh concrete for both NAC and RAC.
- The 28 days curing compressive strength of RAC is found out to be very close to that of NAC in PPM design mix at *w/c* ratio 0.45. But, the gain in strength from 28 to 90 days is less for RAC than NAC. It is very difficult to separate PPM and IS code mix proportioning on compressive strength parameter of the concrete.

Further study for other performance parameters is under investigation.

Acknowledgements First, author gratefully acknowledges the financial support provided for the project on 'Sustainable and Cost Effective Housing using Recycled Aggregate Based Concrete' under the mega project on Future of Cities by MHRD, Government of India. Authors gratefully acknowledge the support extended by IL&FS Environmental Infrastructure and Services Ltd. Plant (New Delhi) for providing recycled aggregate.

References

1. Rahal, K. (2007). Mechanical properties of concrete with recycled coarse aggregate. *Building and Environment, 42*(1), 407–415.
2. Abdulla, N. A. (2014). Effect of recycled coarse aggregate type on concrete. *Journal of Materials in Civil Engineering, 27*(10), 04014273.
3. Behera, M., Bhattacharyya, S. K., Minocha, A. K., Deoliya, R., & Maiti, S. (2014). Recycled aggregate from C&D waste & its use in concrete—A breakthrough towards sustainability in construction sector: A review. *Construction and Building Materials, 68,* 501–516.
4. Yang, K.-H., Chung, H.-S., & Ashour, A. F. (2008). Influence of type and replacement level of recycled aggregates on concrete properties. *ACI Materials Journal, 105*(3), 289–296.
5. Butler, L., West, J. S., & Tighe, S. L. (2013). Effect of recycled concrete coarse aggregate from multiple sources on the hardened properties of concrete with equivalent compressive strength. *Construction and Building Materials, 47,* 1292–1301.

6. Ho, N. Y., Lee, Y. P. K., Lim, W. F., Zayed, T., Chew, K. C., Low, G. L., et al. (2013). Efficient utilization of recycled concrete aggregate in structural concrete. *Journal of Materials in Civil Engineering, 25*(3), 318–327.
7. Manzi, S., Mazzotti, C., & Bignozzi, M. (2013). Short and long-term behavior of structural concrete with recycled concrete aggregate. *Cement & Concrete Composites, 37*(1), 312–318.
8. McNeil, K., & Kang, T. H. (2013). Recycled concrete aggregates: A review. *International Journal of Concrete Structures and Materials, 7*(1), 61–69.
9. Rao, M. C., Bhattacharyya, S., & Barai, S. (2011). Influence of field recycled coarse aggregate on properties. *Materials and Structures, 44*(1), 205–220.
10. Xiao, J., Li, J., & Zhang, C. (2005). Mechanical properties of recycled aggregate concrete under uniaxial loading. *Cement and Concrete Research, 35*(6), 1187–1194.
11. Tam, V. W., Gao, X., & Tam, C. (2005). Microstructural analysis of recycled aggregate concrete produced from two-stage mixing approach. *Cement and Concrete Research, 35*(6), 1195–1203.
12. Limbachiya, M., Meddah, M. S., & Ouchagour, Y. (2012). Use of recycled concrete aggregate in fly-ash concrete. *Construction and Building Materials, 27*(1), 439–449.
13. Kou, S. C., Poon, C. S., & Chan, D. (2008). Influence of fly ash as a cement addition on the hardened properties of recycled aggregate concrete. *Materials and Structures, 41*(7), 1191–1201.
14. Fathifazl, G., Abbas, A., Razaqpur, A. G., Isgor, O. B., Fournier, B., & Foo, S. (2009). New mixture proportioning method for concrete made with coarse recycled concrete aggregate. *Journal of Materials in Civil Engineering, 21*(10), 601–611.
15. Knaack, A. M., & Kurama, Y. C. (2013). Design of concrete mixtures with recycled concrete aggregates. *ACI Materials Journal, 110*(5), 483–492.
16. Glavind, M., Olsen, G. S., & Munch-Petersen, C. (1993). Packing calculation and concrete mix design. *The Nordic Concrete Federation, 2,* 21–34.
17. De Larrard, F., & Sedran, T. (2002). Mixture-proportioning of high-performance concrete. *Cement and Concrete Research, 32*(11), 1699–1704.
18. De Larrard, F. (1999). *Concrete mixture proportioning: A scientific approach.* Boca Raton: CRC Press.

Durability of Fly Ash Added Reinforced Concrete in Chloride and Composite Chloride–Sulfate Environment

Arya Anuj Jee and Bulu Pradhan

Abstract This work reports the corrosion performance of steel reinforcement in OPC and OPC with 20% fly ash concrete mixes exposed to chloride (5% NaCl) and composite chloride–sulfate solutions (5% NaCl + 2% $MgSO_4$ and 5% NaCl + 4% $MgSO_4$). The reinforced concrete specimens were exposed to these solutions for a period of 12 months with alternate wetting–drying cycles. Compressive strength and corrosion parameters were measured on concrete cube specimens and reinforced concrete specimens, respectively. The half-cell potential test and linear polarization resistance measurement (LPR) were performed to evaluate the corrosion parameters of steel reinforcement. From the results, it is observed that the compressive strength of the OPC concrete mix was higher as compared to OPC with 20% fly ash. From the results of corrosion parameters, it is observed that the addition of magnesium sulfate in composite solutions reduced the probability of occurrence of steel reinforcement corrosion and corrosion current density till the exposure period of 12 months. The replacement of the OPC with fly ash improved the performance of concrete mix against corrosion of steel reinforcement. Further, mostly there was less probability of occurrence of steel reinforcement corrosion and lower corrosion current density at lower *w*/*b* ratio as compared to that at higher *w*/*b* ratio.

Keywords Concrete · Fly ash · Corrosion · Chloride · Sulfate
Composite solution

A. A. Jee · B. Pradhan (✉)
Department of Civil Engineering, Indian Institute
of Technology Guwahati, Guwahati 781039, Assam, India
e-mail: bulu@iitg.ernet.in

A. A. Jee
e-mail: a.jee@iitg.ernet.in

A. Rama Mohan Rao and K. Ramanjaneyulu (eds.), *Recent Advances in Structural Engineering, Volume 1*, Lecture Notes in Civil Engineering 11,
https://doi.org/10.1007/978-981-13-0362-3_63

1 Introduction

The partial replacement of cement with supplementary cementitious materials in the preparation of concrete has become more popular nowadays. It improves the mechanical and durability performance of concrete [1, 2]. Reinforced concrete is a composite material that is composed of concrete and steel bar and it is frequently used for the construction of structures such as bridges, buildings, tunnels, etc. The service life of these structures is mainly associated with environmental exposure conditions and physical and chemical protection provided by concrete [3, 4]. The reinforced concrete structures deteriorate mainly due to corrosion of steel bar as a result of chloride attack and carbonation and due to sulfate attack [5]. These ions enter into hardened concrete from external sources through the crack of concrete and by diffusion process [6–8]. In concrete, chloride ions are present in the form of free chloride and bound (physically adsorbed by C–S–H gel and chemically bound with the hydrated C_3A) chloride. Free chloride ions are mainly accountable for corrosion of steel bar in concrete [9]. The attack of sulfate ions results in deterioration of concrete because of formation of expansive products (gypsum and ettringite) as a result of chemical reaction between sulfate ions with cement hydration products (calcium hydroxide and hydrated C_3A) [5, 7].

The presence of sulfate ions together with chloride ions in concrete may influence the corrosion of steel reinforcement. Several studies have been reported on corrosion behavior of steel reinforcement in concrete subjected to chloride exposure conditions [2, 10, 11]. However, there is limited literature on corrosion behavior of steel reinforcement in concrete subjected to composite solutions of chloride and sulfate ions [3, 12, 13].

In the present work, an experimental investigation has been carried out to evaluate the corrosion performance of steel in concrete exposed to chloride and composite chloride–sulfate environment. The corrosion performance of steel reinforcement in concrete made with ordinary Portland cement (OPC) and OPC with fly ash and exposed to chloride and composite chloride–sulfate solutions have been evaluated by conducting half-cell potential test and linear polarization resistance (LPR) measurement. The half-cell potential provides information about the probability of occurrence of steel reinforcement corrosion whereas, LPR measurement determines the corrosion current density of steel reinforcement.

2 Experimental Work

2.1 Materials and Mix Composition

In the experimental investigation, two types of binders namely ordinary Portland cement (OPC) 43 grade confirming to IS: 8112-2013 [14] and OPC with 20% fly ash (by weight of binder) were used. Coarse aggregates of size 20 mm MSA

Table 1 Concrete mix composition

Binder type	*w/b* ratio	Binder content		Proportion of binder:sand: coarse aggregate (by mass)
		Cement (kg/m^3)	Fly ash (kg/m^3)	
OPC	0.50	410.00	–	1:1.58:2.69
	0.55	372.72	–	1:1.77:3.02
OPC with 20% fly ash	0.50	328.00	82.00	1:1.58:2.69
	0.55	298.18	74.54	1:1.77:3.02

(maximum size of aggregate) and 10 mm MSA each with specific gravity of 2.65 and locally available river sand as fine aggregate with specific gravity 2.62 were used in the preparation of concrete mixes. The mix proportioning of the ingredients of concrete mix was carried out using DOE method [15] with some modifications. The *w/b* ratios used in the preparation of concrete mixes were 0.50 and 0.55. As already stated, this experimental work has been carried out to evaluate the corrosion performance of steel reinforcement in concrete exposed to chloride and composite chloride–sulfate solutions. The penetration of chloride and sulfate ions into concrete is normally affected by its porosity, which in turn depends on *w/b* ratio of the concrete mix. Keeping this in view, in the present work, the above values of *w/b* ratio were taken to study its effect (i.e., change from 0.50 to 0.55) on variation in corrosion parameters of steel reinforcement. From trial tests, a water content of 205 kg/m^3 was selected for both *w/b* ratios for slump value ranging from 30 to 60 mm. The proportion of 20 mm MSA and 10 mm MSA aggregates was fixed at 62 and 38%, respectively, of the total mass of coarse aggregate. The composition of concrete mixtures is shown in Table 1.

2.2 Specimen Preparation

Cube specimens of size 150 mm were prepared from each concrete mix for determining compressive strength. Prismatic reinforced concrete specimens of size 62 mm × 62 mm × 300 mm with a centrally embedded steel bar and 25 mm cover depth (from longitudinal face) were prepared for measurement of corrosion parameters. Tempcore TMT steel bar of diameter 12 mm was used as the steel reinforcement. The steel bars of length 380 mm were cleaned with a wire brush to remove any surface scale and insulating tape followed by epoxy coating was applied for preventing the crevice corrosion, at places where there is a discontinuity of steel bar with the surrounding concrete. After 24 h of preparation, the cubes and prismatic specimens were demoulded and subjected to water curing in a curing tank for 28 days from the day of preparation. At the end of the curing period, the compressive strength test was performed on cube specimens and the prismatic reinforced concrete specimens were kept in the laboratory drying condition for a

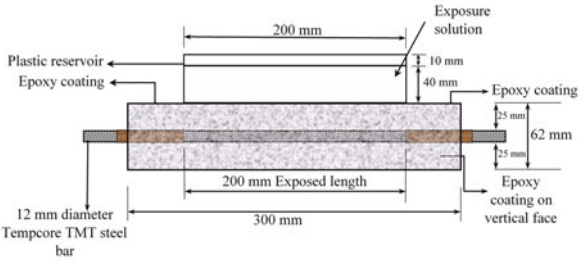

Fig. 1 Schematic diagram of prismatic reinforced concrete specimen

period of 14 days. Subsequently, a plastic reservoir of size 50 mm × 42 mm 200 mm (internal dimensions) was fixed on a longitudinal face of prismatic specimens with epoxy to store the exposure solution during the wetting period. Further, epoxy coating was also applied on four vertical faces and on the remaining portion of the top face of the prismatic specimen outside the plastic reservoir. The schematic diagram of prismatic reinforced concrete specimens is shown in Fig. 1. The exposure length of the steel bar inside the prismatic specimen is 200 mm.

2.3 Compressive Strength Test

After completion of moist curing, the 28 days compressive strength of concrete mix made with OPC and OPC with 20% fly ash at *w/b* ratios of 0.50 and 0.55 was determined in the compression testing machine. For a given mix, the average value of three replicate cube specimens was reported as the compressive strength of that mix.

2.4 Exposure to Chloride and Composite Solutions

The prismatic reinforced concrete specimens were exposed to chloride solution (5% NaCl) and composite chloride–sulfate solutions (5% NaCl + 2% $MgSO_4$ and 5% NaCl + 4% $MgSO_4$) with alternate wetting–drying cycles for a duration of 12 months. The chloride solution and composite chloride–sulfate solutions were prepared by adding these salts in water at above concentrations. The details of chloride and composite chloride–sulfate solutions are shown in Table 2.

The wetting–drying cycle consists of 5 days of wetting (filling the solution in the reservoir) followed by 10 days of laboratory drying. The corrosion parameters were measured at the start of exposure and at the end of exposure periods of 6 months and 12 months.

Table 2 Details of exposure solutions

Solution type	Exposure solutions
Chloride solution	5% NaCl
Composite chloride–sulfate solution	5% NaCl + 2% $MgSO_4$
	5% NaCl + 4% $MgSO_4$

2.5 *Corrosion Monitoring Tests*

For corrosion monitoring of steel reinforcement, half-cell potential and corrosion current density (I_{corr}) were measured using potential and linear polarization resistance (LPR) measurements, respectively. For this purpose, three-electrode system consisting of saturated calomel electrode (SCE) as reference electrode, embedded steel bar as working electrode and stainless steel plate as auxiliary electrode was used. The half-cell potential of steel bar was measured with reference to saturated calomel electrode. For measurement of corrosion current density by LPR technique, the steel bar (working electrode) was polarized to ±20 mV from the corrosion potential at scan rate of 6 mV per minute. Only top half surface area of steel bar was assumed to be polarized. The corrosion tests were conducted using corrosion monitoring instrument (make: ACM, Gill AC serial no. 1542-sequencer). The experimental setup of three-electrode system for corrosion monitoring of steel reinforcement in the prismatic reinforced concrete specimen is shown in Fig. 2.

The corrosion current density (I_{corr}) of steel reinforcement was determined using Stern–Geary equation [3, 13].

$$I_{corr} = \frac{B}{R_p}$$

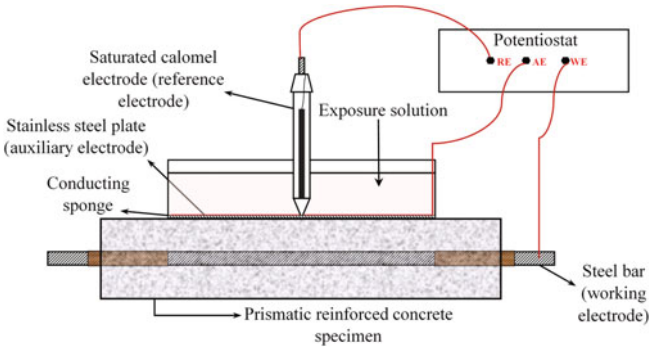

Fig. 2 Experimental setup for corrosion tests

where R_p is polarization resistance of steel reinforcement and B is Stern–Geary constant. The value of B depends on anodic and cathodic Tafel constants. In this work, the value of B was taken as 26 mV considering the reinforcing steel bar in active condition [3, 13].

3 Result and Discussion

3.1 Compressive Strength

The 28 days compressive strength values of concrete mixes made from OPC and OPC with 20% fly ash at *w/b* ratios of 0.50 and 0.55 are shown in Fig. 3. Each value shown in this figure is the average value of three replicate cube specimens of a given concrete mix. From Fig. 3, it is observed that the concrete mix made from OPC exhibited higher 28 days compressive strength as compared to that made from OPC with 20% fly ash at both *w/b* ratios. The lower 28 days compressive strength of concrete mix made from OPC with 20% fly ash indicates that the pozzolanic reaction was not effective in enhancing the compressive strength of fly ash added concrete up to the age of 28 days. Further, the compressive strength of concrete decreased with increase in *w/b* ratio for both types of binder as observed from Fig. 3.

3.2 Half-Cell Potential

The measured half-cell potential values of embedded steel bar in the prismatic specimens are shown in Fig. 4a–d for OPC and OPC with 20% fly ash respectively. As already stated, the prismatic specimens were exposed to chloride and composite chloride–sulfate solutions for a period of 12 months and corrosion tests were

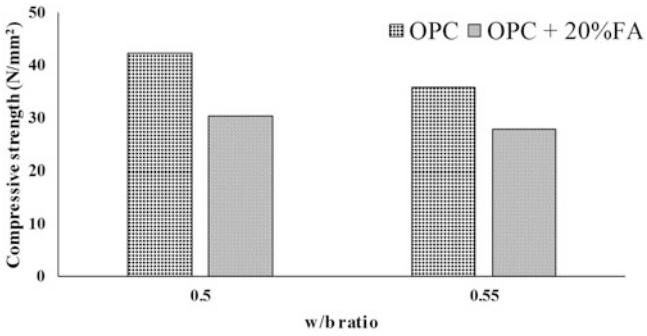

Fig. 3 Compressive strength of concrete mixes

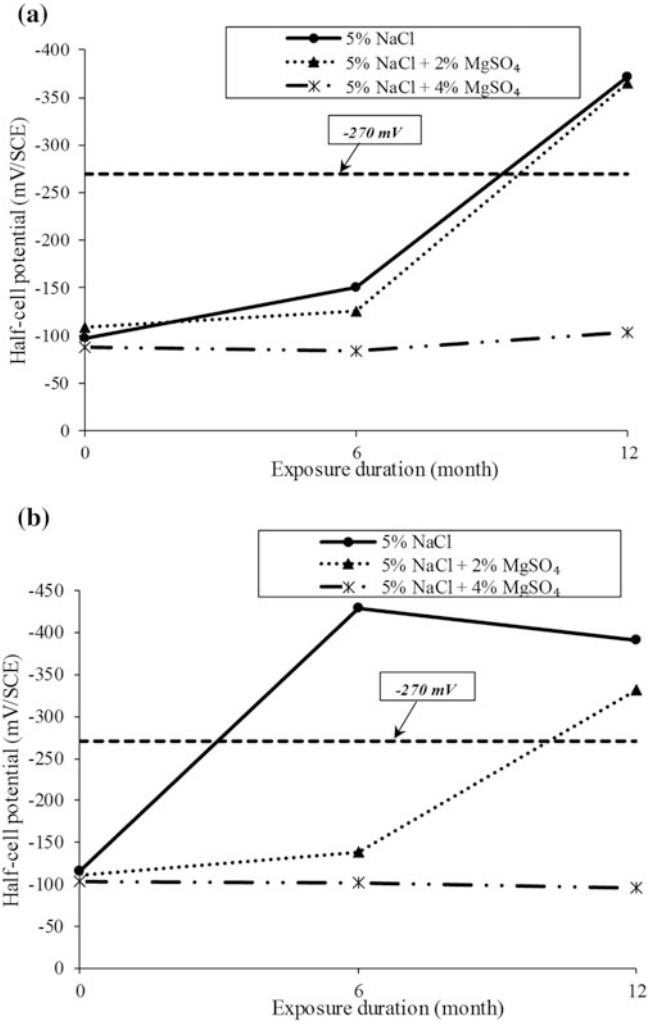

Fig. 4 **a** Half-cell potential versus exposure duration for OPC at *w/b* ratio of 0.50 and exposed to chloride and composite chloride–sulfate solutions. **b** Half-cell potential versus exposure duration for OPC at *w/b* ratio of 0.55 and exposed to chloride and composite chloride–sulfate solutions. **c** Half-cell potential versus exposure duration for OPC with 20% fly ash at *w/b* ratio of 0.50 and exposed to chloride and composite chloride–sulfate solutions. **d** Half-cell potential versus exposure duration for OPC with 20% fly ash at *w/b* ratio of 0.55 and exposed to chloride and composite chloride–sulfate solutions

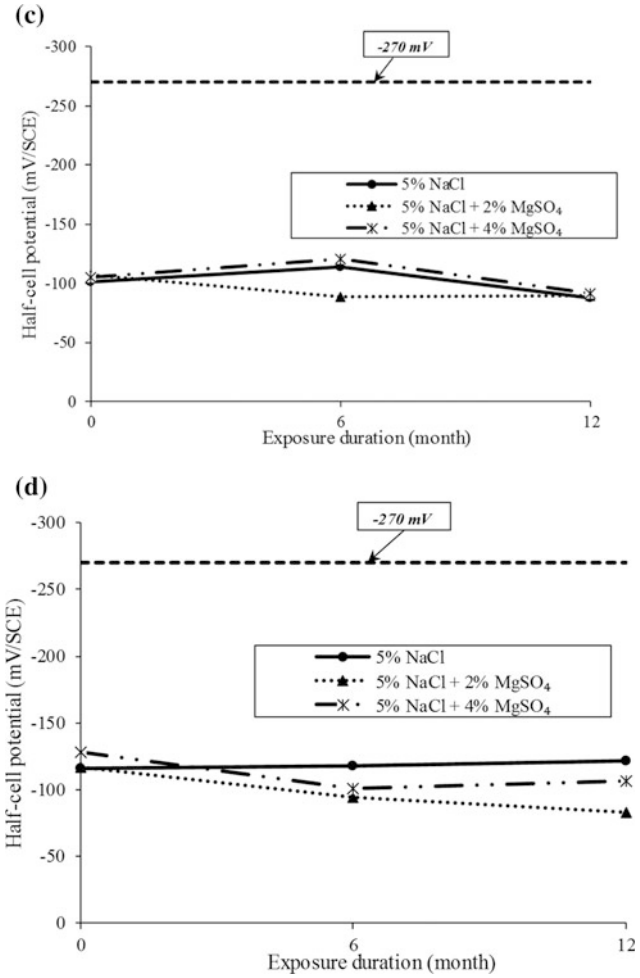

Fig. 4 (continued)

performed at the start of exposure and at the end of exposure periods of 6 months and 12 months.

From Fig. 4a, b, it is observed that the half-cell potential values of steel in OPC specimens exposed to chloride solution (5% NaCl) were more negative than those exposed to composite chloride–sulfate solutions (5% NaCl + 2% $MgSO_4$ and 5% NaCl + 4% $MgSO_4$) at both *w/b* ratios till the exposure period of 12 months. This indicates higher probability of occurrence of steel reinforcement corrosion when exposed to chloride solution as compared to composite chloride–sulfate solution. In addition, the potential values became less negative with increase in concentration of

$MgSO_4$ in the exposure solution for OPC specimens till the exposure period of 12 months. Further, it is noted that the potential values became more negative than −270 mV (SCE) mostly at the end of exposure period of 12 months in OPC specimens exposed to 5% NaCl solution and composite solution of 5% NaCl + 2% $MgSO_4$ as observed from Fig. 4a, b, which correspond to greater than 90% probability of occurrence of steel reinforcement corrosion according to ASTM C876 criteria [16].

From Fig. 4 c, d, it is observed that the steel reinforcement in concrete made from OPC with 20% fly ash showed potential values less negative than −270 mV (SCE) till the exposure period of 12 months. Further, the variations in potential values between chloride solution and composite chloride–sulfate at different exposure periods were very small. However, the specimens exposed to chloride solution (5% NaCl) mostly showed more negative potential values than those exposed to composite chloride–sulfate solutions (5% NaCl + 2% $MgSO_4$ and 5% NaCl + 4% $MgSO_4$) till the exposure period of 12 months.

On comparing the effect of *w/b* ratio on half-cell potential values, it is observed that the specimens made with *w/b* ratio of 0.50 mostly exhibited less negative potential values as compared to those made with *w/b* ratio of 0.55 for both types of binder and different exposure solutions. Further, it is observed that the specimens made from OPC with 20% fly ash mostly showed less negative potential values than those made with OPC for different exposure solutions and both *w/b* ratios as observed from Fig. 4a–d.

3.3 Corrosion Current Density

Figure 5a–d shows the variation in corrosion current density of embedded steel reinforcement in concrete for different *w/b* ratios, binders, and exposure solutions till the exposure period of 12 months. From these figures, it is observed that the corrosion current density of steel reinforcement was mostly lower in the specimens exposed to composite solutions (5% NaCl + 2% $MgSO_4$ and 5% NaCl + 4% $MgSO_4$) as compared to those exposed to chloride solution (5% NaCl) for both types of binder (OPC and OPC with 20% fly ash) and *w/b* ratios (0.50 and 0.55). This may be attributed to higher resistivity of concrete when exposed to composite sodium chloride plus magnesium sulfate solution than exposure to only sodium chloride solution. The similar observation of mostly lower corrosion current density in the specimens exposed to composite solutions of NaCl plus $MgSO_4$ as compared to those exposed to NaCl solutions for OPC has been reported in literature [13], wherein the slab specimens with a centrally embedded steel bar were exposed to sodium chloride and composite sodium chloride plus magnesium sulfate solutions with alternate wetting (7 days of immersion of slab specimens in chloride and composite chloride–sulfate solutions) and drying (7 days of laboratory drying) cycles and after exposure, the corrosion parameters were measured at the age of 300 days from the day of preparation of the specimens.

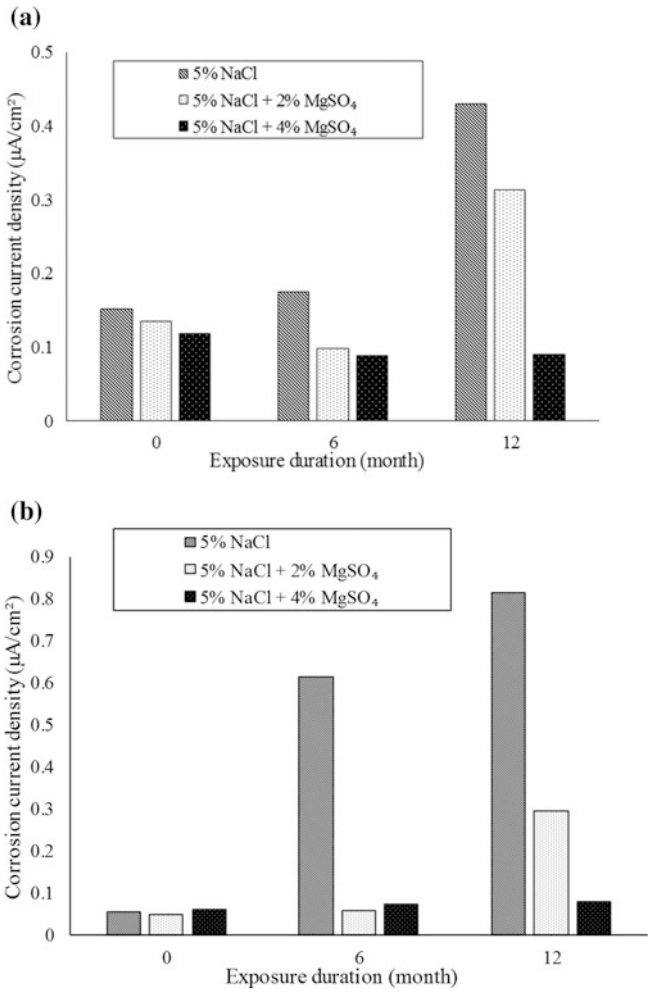

Fig. 5 **a** Corrosion current density versus exposure duration for OPC at *w*/*b* ratio of 0.50 and exposed to chloride and composite chloride–sulfate solutions. **b** Corrosion current density versus exposure duration for OPC at *w*/*b* ratio of 0.55 and exposed to chloride and composite chloride–sulfate solutions. **c** Corrosion current density versus exposure duration for OPC with 20% fly ash at *w*/*b* ratio of 0.50 and exposed to chloride and composite chloride–sulfate solutions. **d** Corrosion current density versus exposure duration for OPC with 20% fly ash at *w*/*b* ratio of 0.55 and exposed to chloride and composite chloride–sulfate solutions

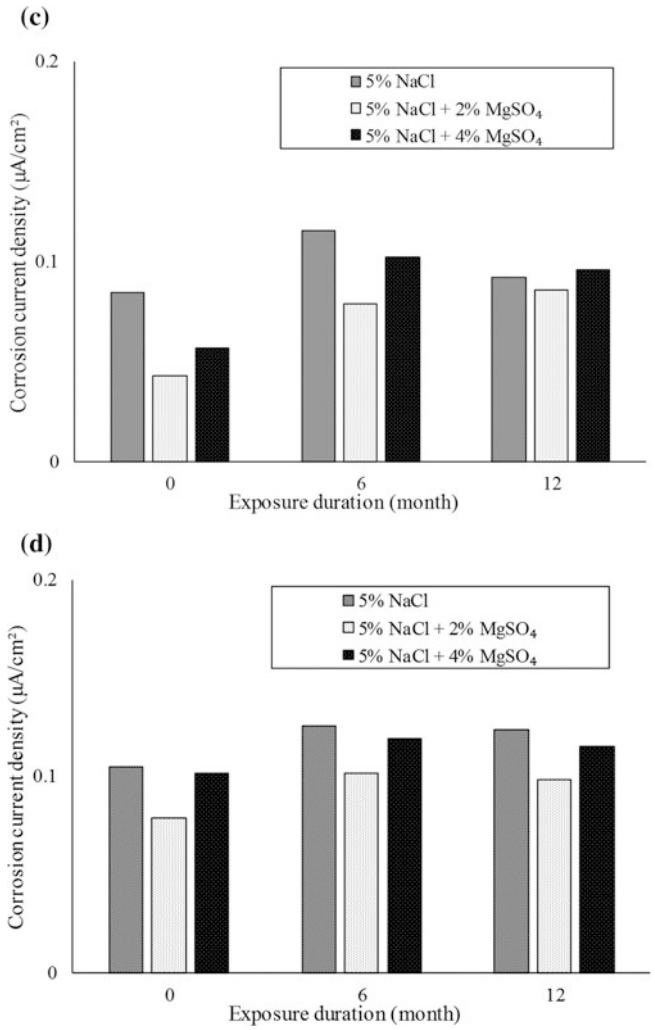

Fig. 5 (continued)

Further, from these figures, it is noted that the specimens made from OPC with 20% fly ash mostly exhibited lower corrosion current density as compared to those made from OPC for different exposure solutions and *w/b* ratios. The lower corrosion current density in concrete made from OPC with 20% fly may be attributed to retarding of the ingress of aggressive ions into concrete due to the formation of denser microstructure as a result of the formation of additional C–S–H gel in concrete due to pozzolanic reaction.

On evaluating the effect of *w/b* ratio, it is observed that the corrosion current density was mostly lower at *w/b* ratio of 0.50 as compared to that at *w/b* ratio of

0.55 for different exposure solutions and binders except in few cases for the specimens made with OPC and exposed to composite solutions. Mostly lower corrosion current density at lower *w/b* ratio is attributed to higher resistivity of concrete due to the formation of denser microstructure.

4 Conclusions

From the experimental investigation on corrosion performance of steel reinforcement in concrete exposed to chloride solution (5% NaCl) and composite chloride–sulfate solutions (5% NaCl + 2% $MgSO_4$ and 5% NaCl + 4% $MgSO_4$), the following conclusions were drawn.

The presence of magnesium sulfate in composite solutions (sodium chloride plus magnesium sulfate) resulted in less negative half-cell potential values and lower corrosion current density as compared to only chloride solution (sodium chloride) for both types of binder and *w/b* ratios up to exposure duration of 12 months.

The reinforced concrete specimens prepared from OPC with 20% fly ash showed better performance against corrosion of steel reinforcement as compared to OPC specimens in terms of less negative potential and mostly lower corrosion current density for different exposure solutions and *w/b* ratios.

The specimens made with lower *w/b* ratio mostly exhibited less negative potential values and lower corrosion current density as compared to those made with higher *w/b* ratio.

References

1. Chung, C., Shon, C., & Kim, Y. (2010). Chloride ion diffusivity of fly ash and silica fume concretes exposed to freeze–thaw cycles. *Construction and Building Materials, 24,* 1739–1745.
2. Asrar, N., Malik, A. U., Ahmad, S., & Mujahid, F. S. (1999). Corrosion protection performance of microsilica added concretes in NaCl and seawater environments. *Construction and Building Materials, 13,* 213–219.
3. Dehwah, H. A. F., Maslehuddin, M., & Austin, S. A. (2002). Long-term effect of sulfate ions and associated cation type on chloride-induced reinforcement corrosion in Portland cement concretes. *Cement & Concrete Composites, 24,* 17–25.
4. Liu, R., Jiang, L., Huang, G., Zhu, Y., Liu, X., Chu, H., et al. (2016). The effect of carbonate and sulfate ions on chloride threshold level of reinforcement corrosion in mortar with/without fly ash. *Construction and Building Materials, 113,* 90–95.
5. Neville, A. M., & Brooks, J. J. (2013). *Concrete Technology*. New Delhi: Pearson Education.
6. Neves, R., Fonseca, B. S., Branco, F., Brito, J., Castela, A., & Montemor, M. F. (2015). Assessing concrete carbonation resistance through air permeability measurements. *Construction and Building Materials, 82,* 304–309.
7. Sun, C., Chen, J., Zhu, J., Zhang, M., & Ye, J. (2013). A new diffusion model of sulfate ions in concrete. *Construction and Building Materials, 39,* 39–45.

8. Costa, A., & Appleton, J. (1999). Chloride penetration into concrete in marine environment—Part I: Main parameters affecting chloride penetration. *Materials and Structures, 32,* 252–259.
9. Cheewaket, T., Jaturapitakkul, C., & Chalee, W. (2010). Long term performance of chloride binding capacity in fly ash concrete in a marine environment. *Construction and Building Materials, 24,* 1352–1357.
10. Pradhan, B., & Bhattacharjee, B. (2009). Half-cell potential as an indicator of chloride-induced rebar corrosion initiation in RC. *Journal of Materials in Civil Engineering (ASCE), 21,* 543–552.
11. Kayali, O., & Zhu, B. (2005). Chloride induced reinforcement corrosion in lightweight aggregate high-strength fly ash concrete. *Construction and Building Materials, 19,* 327–336.
12. Al-Amoudi, O. S. B., & Maslehuddin, M. (1993). The effect of chloride and sulfate ions on reinforcement corrosion. *Cement and Concrete Research, 23,* 139–146.
13. Pradhan, B. (2014). Corrosion behavior of steel reinforcement in concrete exposed to composite chloride–sulfate environment. *Construction and Building Materials, 72,* 398–410.
14. IS 8112:2013. (2013). *Ordinary Portland cement, 43 grade—specification (Second revision)*. New Delhi: Bureau of Indian Standards.
15. SP 23: 1982. (1990). *Handbook on concrete mixes (Based on Indian standard)*. New Delhi: Bureau of Indian Standards.
16. ASTM C876-09. (2009). *Standard test method for corrosion potentials of uncoated reinforcing steel in concrete*. West Conshohocken (PA): ASTM International.

Study on Strength Reduction Factor of Blended Concrete Exposed to Seawater

T. Jena and K. C. Panda

Abstract This article reports the mechanical properties of blended concrete containing fly ash (FA) and silpozz exposed to seawater. The reduction in strength is evaluated between normal water curing (NWC) and seawater curing (SWC) samples by strength reduction factor (SRF) in percentage. The microstructural analysis is done by scanning electron microscopy (SEM). It is revealed from the test results that the SRF for compressive strength is 4% for 10% FA and 20% silpozz replaced with ordinary Portland cement (OPC) for 6 months exposure to seawater. The SRF for flexural strength and split tensile strength is 1 and 0.80% at 90 days exposure. The minimum slip is 1 mm after 28 days of testing bond strength for NWC samples. The SRF in bond strength is also evaluated and found as 10.35% for 28 days SWC samples. The dense and compact microstructure was observed in 28 days NWC samples.

Keywords Blended concrete · Bond strength · Fly ash · Seawater Silpozz

1 Introduction

Long-term durability of structures has become vital to the economics of all nations. Concrete for the twenty-first century can be much stronger, more durable and at the same time cost and energy efficient. Failure of concrete in a period less than its design life may be caused by external factors such as the environment to which it

T. Jena
Department of Civil Engineering, SOA (Deemed to be University), Bhubaneswar, Odisha 751030, India
e-mail: trilochanjena@soauniversity.ac.in

K. C. Panda (✉)
Department of Civil Engineering, Government College of Engineering, Kalahandi, Bhawanipatna, Odisha 766002, India
e-mail: kishoriit@gmail.com

A. Rama Mohan Rao and K. Ramanjaneyulu (eds.), *Recent Advances in Structural Engineering, Volume 1*, Lecture Notes in Civil Engineering 11,
https://doi.org/10.1007/978-981-13-0362-3_64

has been exposed or by a variety of internal causes. External factors may be physical or chemical in nature, such as weathering, extreme variation of temperatures, abrasion and exposure to aggressive chemicals. Internal causes may lie in the choice of materials or inappropriate combination of materials. Some of the researchers have reported the deterioration mechanism in marine exposure condition such as Kumar [1] studied the percentage decrease in compressive strength for the period of one year of exposure both in freshwater and seawater curing and the effect of marine environment on concrete is to decrease its compressive strength and this loss increases with age of exposure. Menon et al. [2] studied the effect of mineral admixtures such as fly ash (FA), silica fume (SF), and ground granulated blast furnace slag with superplasticizer on high strength concrete in development of compressive strength under severe exposure seawater tidal zone and found that the high strength concrete would withstand severe seawater exposure without serious deterioration. Wegian [3] reported all forms of deterioration can be controlled by using higher cement content in seawater. Anwar and Roushdi [4] showed the improvement of mechanical properties of concrete containing OPC, FA, and SF in artificial seawater and resist against environmental deterioration. Jena and Panda [5, 6] studied the development of mechanical properties in blended concrete made with silpozz to improve the durability of marine structures. Shen et al. [7] found that the slip corresponding to bond strength decreases with increase in compressive strength at early age. Aggrawal and Siddique [8] and Weiting et al. [9] studied the microstructural properties of concrete using waste foundry sand and bottom ash as a partial replacement of fine aggregates.

The objective of the present article is to study the strength reduction factor (SRF) of mechanical properties of blended concrete such as compressive, flexural, split, and bond strength exposed to seawater as well as microstructural analysis by scanning electron microscopy (SEM).

2 Experimental Study

2.1 Properties of Materials Used

In this study, the materials used are OPC 43 grade, course aggregates, fine aggregates, normal water, seawater, and high-end superplasticizer (SP). The tested physical properties of OPC as per IS 8112-1989 [10] are presented in Table 1. The experimental value of aggregates as per IS 383-1970 [11] is given in Table 2. FA is a fine material and possesses good pozzolanic activity. Silpozz is an effective mineral admixture and specially mixed in marine concrete to improve mechanical and durability properties. Silpozz is a commercial name for micro-silica produced from rice husk ash. FA and silpozz sample is shown in Fig. 1. Physical properties FA and silpozz are given in Table 3 and chemical composition of cementitious materials is presented in Table 4.

Table 1 Physical properties of OPC

Characteristics	Experimental value	Value specified by IS 8112:1989
Setting time, (min)		
Initial setting time	165	30 (min)
Final setting time	360	600 (max)
Standard consistency (%)	34	NA
Specific gravity	3.15	3.15
Compressive strength (MPa)		
(a) 3 days	28 MPa	23 MPa
(b) 7 days	42 MPa	33 MPa
(c) 28 days	48 MPa	43 MPa
Fineness (m^2/kg)	333	225 (min)

Table 2 Properties of aggregates

Specifications	Experimental value as per IS: 383-1970	
	Coarse aggregates	Fine aggregates
Fineness modulus	7.0	3.03 (Zone-3)
Specific gravity	2.86	2.67
Water absorption (%)	0.2	0.4
Bulk density (kg/m^3)	1424	1568
Abrasion value (%)	34.78	–
Impact value (%)	24	–
Crushing value (%)	23.3	–

Fig. 1 FA and silpozz

Table 3 Physical properties of FA and silpozz

Physical properties	FA	Silpozz
Specific gravity	2.12	2.3
Bulk density (gm/cc)	1.2	0.23
Specific surface, m^2/g	33	17
Particle size (Micron)	34	25
Color	Gray	Gray black
Physical state	–	Solid nonhazardous

Table 4 Chemical composition of cementitious materials

Oxides (%)	Cement (OPC)	Silpozz	FA
SiO_2	20.99	88.18	58.13
Al_2O_3	6.05	1.61	31.00
Fe_2O_3	6.01	0.56	4.10
Carbon	–	2.67	–
CaO	62.74	1.59	0.60
MgO	1.33	1.63	0.10
K_2O	0.40	1.67	0.90
Na_2O	0.04	–	0.05
SO_3	1.82	–	0.12
TiO_2	.025	–	1.63
Others	–	2.09	0.011
Moisture content (%)	–	0.79	3.0
Loss on ignition (%)	1.14	0.04	0.29

2.2 Mix Proportions and Identifications

The mix design is targeted for M30 as it is the marine exposure condition as per IS 10262-2009 [12]. The obtained material ratio was (1:1.44:2.91), W/B ratio 0.43. The control specimen made 0% replacement of FA and silpozz with cement and without SP. The blended concrete samples made 0% FA and 10, 20 and 30% replacement of silpozz with cement and doses of SP. Another blended cement concrete samples also made with 10% replacement of FA and 10, 20 and 30% replacement of silpozz with cement. The controlled specimen is prepared with 100% OPC without SP and there is no change of quantity of materials. As SP is used in blended concrete mixes, the amount of water was reduced by 20% based upon the several trial mixes in order to maintain the slump in between 25 and 50 mm. Two sets of samples (cube, cylinder, and prism) have been prepared. One set of sample cured normal water and the other set of samples has been cured in seawater for 7, 28, 90, and 180 days and their strength reduction factor (SRF) in percentage was studied after getting the results of compressive strength. The split tensile strength and flexural strength was studied up to 90 days and their SRF (%) evaluated. The bond strength of the seawater curing (SWC) and normal water

Table 5 Details of cementitious materials with SP

Mix Identity	OPC (%)	FA (%)	Silpozz (%)	SP (%)
MC100F0S0	100	0	0	–
M1C90F0S10	90	0	10	0.20
M1C80F0S20	80	0	20	0.29
M1C70F0S30	70	0	30	0.40
M1C80F10S10	80	10	10	0.22
M1C70F10S20	70	10	20	0.33
M1C60F10S30	60	10	30	0.47

curing (NWC) samples is tested at 28 days and the slips are observed. The mix identity MC100F0S0 means OPC 100%, FA 0% and silpozz 0% without SP. Similarly, the mix M1C90F0S10 means OPC 90%, FA 0% and silpozz 10% with SP 0.2% and so on. The details of mix identity along with their percentage of cementitious materials with SP are presented in Table 5.

2.3 Specimen Preparation and Exposure Conditions

Standard concrete cubes of size 150 × 150 × 150 mm were used for measuring the compressive strength. For the split tensile strength, the concrete cylinders of size 100 mm diameter and 200 mm height were taken and concrete beams of size 100 × 100 × 500 mm were employed for the determination of flexural strength. The specimen size for pull out test is 150 mm × 150 mm × 150 mm with a reinforcing tor bar of 12 mm diameter. Total length of the bar is 120 mm with a bond length of 60 mm. The compressive strength was determined for cube samples after 7, 28, 90 and 180 days of NWC and SWC. The flexural and split tensile strength was tested at the age of 7, 28, and 90 days of NWC and SWC for the samples of prism and cylinder, respectively. The bond strength was tested for 28 days of NWC and SWC samples. The materials were batched into the mixer according to the following sequence: coarse aggregate followed by sand, and then cementitious materials (OPC, FA, and Silpozz were well mixed outside the mixer). The total mixing time was 3 minutes which is divided into two stages, starting with 60 s dry mixing, followed by the addition of the required water within 30 s, then the mixer continued for the next 1.5 min of wet mixing and after adding SP the mixture continued for extra 1.5–2 min for wet mixing. The doses of SP were added to the silpozz based samples of 10–40% replaced with OPC. After casting, the concrete moulds were compacted by a vibrator. The samples were finished, and stripped from their moulds the day after casting. The specimens were cured in water until testing. The compressive test, flexural test, split tensile test, and bond test setup are shown in Figs. 2, 3, 4 and 5.

Fig. 2 Compressive test set up for cube

Fig. 3 Flexural test set up for prism

Fig. 4 Split tensile test set up for cylinder

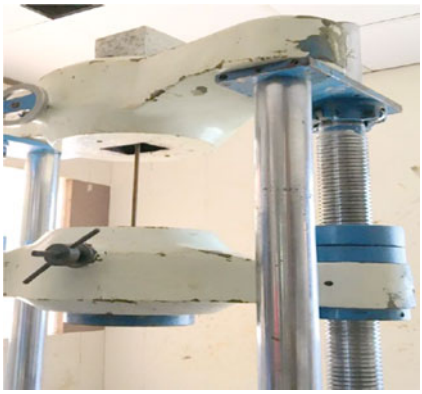

Fig. 5 Bond test set up

3 Experimental Results and Discussions

3.1 Properties of Fresh Concrete

The workability of fresh concrete was measured by slump value and compaction factor. The dose of SP was added only to maintain the slump in between 25 and 50 mm and the experimented slump ranging from 34 to 42 mm was observed. The compaction factor ranges from 86.20 to 96.20% which shows good workable concrete at all levels.

3.2 Properties of Hardened Concrete

The properties of hardened concrete are evaluated by their SRF in percentage for compressive strength up to 180 days curing period. For flexural strength and split tensile strength, the SRF (%) evaluated up to 90 days and for bond strength 28 days of NWC and SWC. The SRF is defined as $SRF = (1 - \sigma_s)/\sigma_n \times 100$, where σ_s = strength of cubes after exposed to seawater for a period of 't' days, σ_n = strength of cubes in normal water curing after 't' days, t = curing period in days.

3.3 Compressive Strength

The SRF(%) versus age in days in compressive strength is shown in Fig. 6. The SRF is limited to 7% for 6 months study but the sample having 10% FA and 20% silpozz replaced with OPC gives minimum 4% SRF than the other samples. It is observed from Fig. 6 that the normal mix shows higher SRF at all ages of curing. The sodium chloride and some amount of CO_2 present in seawater reacts with Ca

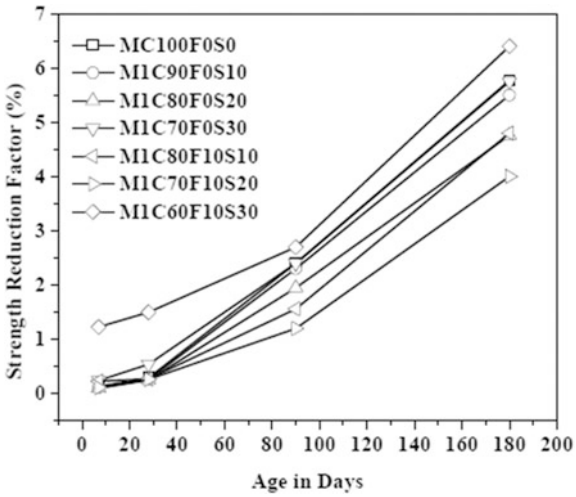

Fig. 6 SRF (%) versus age in days

Table 6 Compressive strength of NWC (MPa)

Concrete mix	Compressive strength of NWC (MPa)			
	7	28	90	180
MC100F0S0	36.95	51.15	62.50	65.80
M1C90F0S10	44.50	56.85	66.50	69.85
M1C80F0S20	47.20	58.25	67.80	71.40
M1C70F0S30	41.50	55.40	66.10	69.50
M1C80F10S10	43.00	55.00	65.00	68.50
M1C70F10S20	44.00	56.00	66.80	69.80
M1C60F10S30	41.00	54.00	64.50	67.30

Table 7 Compressive strength of SWC (MPa)

Concrete mix	Compressive strength of SWC (MPa)			
	7	28	90	180
MC100F0S0	36.9	51	61	62
M1C90F0S10	44.45	56.7	65	66
M1C80F0S20	47.15	58.1	66.5	68
M1C70F0S30	41.4	55.1	64.5	65.5
M1C80F10S10	42.9	54.85	64	65.2
M1C70F10S20	43.95	55.85	66	67
M1C60F10S30	40.5	53.2	62.8	63

$(OH)_2$ and the formation of hydrochloric acid and $CaCO_3$ may reduce the strength gain in seawater. But FA and silpozz with proper doses of SP restricted the intrusion of chloride and CO_2, thus SRF is decreasing. The compressive strength of NWC and SWC is given in Tables 6 and 7.

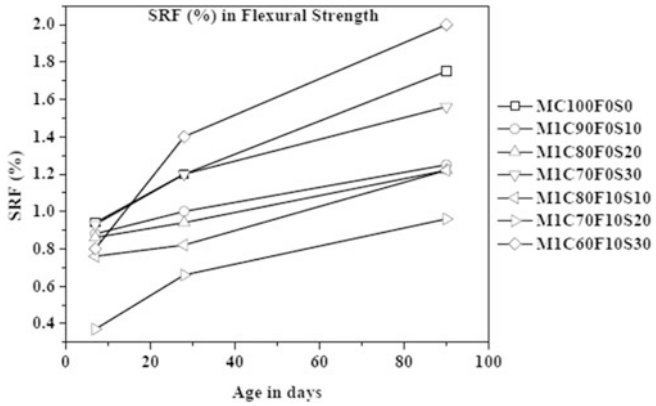

Fig. 7 SRF (%) versus age in days

3.4 Flexural Strength

The SRF (%) versus age in days in flexural strength is shown in Fig. 7. The higher value of SRF is 2% at 90 days and 0.8% at 7 days for 10% FA and 30% silpozz replaced with OPC.

The minimum value of SRF is 0.37, 0.67 and 1% at 7, 28 and 90 days age for 10% FA and 20% silpozz replaced with OPC, respectively. The SRF is limited to 1% at 7 days age for all samples and it is increased only after 28–90 days. The SRF is directly proportional to the exposure conditions. The SRF of sample containing 10% FA and 30% silpozz is 0.8% at 7 days which is almost al equal to the SRF of other samples except M1C70F10S20 but the SRF increased up to 2% at 90 days which is the highest value in this study. As silpozz was replaced by 30% with OPC as a result of which early strength gains may be the reason of reducing the SRF at 7 days age. The highest value of SRF in flexural strength is limited to 2% at 90 days.

3.5 Split Tensile Strength

The SRF (%) versus age in days for split tensile strength is shown in Fig. 8. It is observed from the Fig. 8 that some of the intermediate samples having al most al equal SRF at all ages. But the sample containing 10% FA and 20% silpozz shows 0.54, 0.64 and 0.78% SRF at 7, 28 and 90 days age which is the minimum value than the control specimen. The maximum value is 1.65% for 10% FA and 30% silpozz sample at 90 days age and it is equal to the value of control specimen for same curing periods. The SRF is same for M1C80F0S20 and M1C70F10S20

sample at 90 days curing. The combined sample with FA and silpozz performed better SRF as compared to control specimen up to 90 days.

3.6 Bond Strength

The specimen size for pull out test is 150 mm × 150 mm × 150 mm with a reinforcing tor bar of 12 mm diameter. Total length of the bar is 120 mm with a bond length of 60 mm. For all specimens, the load rate was 0.1 KN/s. The types of failure were identified for each test by recording the bond strength slip results measured at the free end with a dial micrometer an accuracy of 0.0025 mm. The ultimate bond strength was calculated from $\tau_b = F_{max}/\pi\Phi L$, where τ_b is the bond strength, F_{max} is the maximum pull out force, Φ is the diameter of the tor bar and L is the bond length. The bond strength set up is shown in Fig. 5. The SRF in bond strength versus types of mix is shown in Fig. 9. It observed from Fig. 9 that the lowest value of SRF is 10.35% for sample of 10% FA and 20% silpozz replaced with OPC. The highest value of SRF is 14.11% for control specimen at 28 days of curing. The combined samples having FA and silpozz performed better in seawater. The slip in 'mm' versus types of mix is shown in Figs. 10 and 11. It is observed from Fig. 10 that slip is limited to 1.40 mm for normal concrete and minimum slip is 1 mm for silpozz based concrete. Slip mainly depends upon the bond between cement concrete matrix and steel reinforcement. It was noted at the time of maximum applied load. When FA is added with silpozz the slip is controlled and less than the control specimen. It was observed that slip corresponding to bond strength decreases as the compressive increases. The sample 10% FA and 20% silpozz gives higher bond strength and compressive strength with minimum slip of 1 mm.

It is observed from Fig. 11 that the maximum slip is limited to 1.462 mm for control specimen and 1.12 mm for M1C80F0S20 in SWC samples at 28 days.

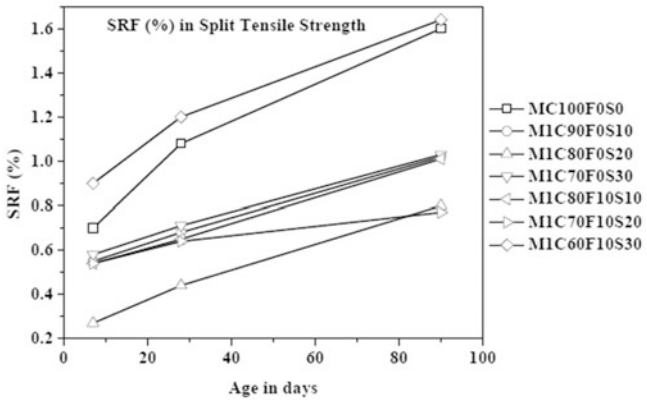

Fig. 8 SRF (%) versus age in days

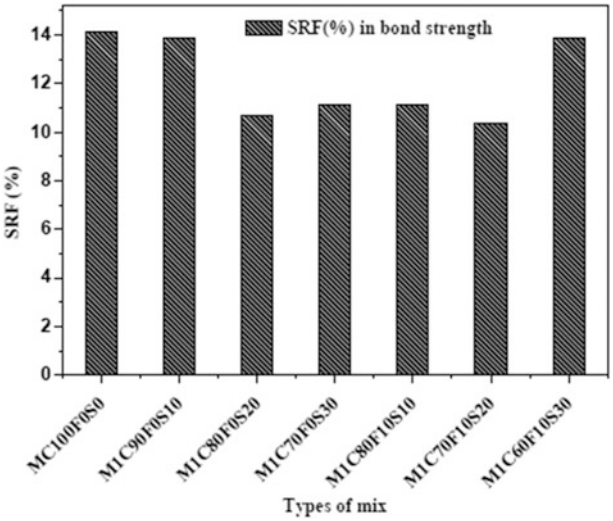

Fig. 9 SRF (%) versus types of mix

3.7 Microstructural Analysis

Internal construction of cement concretes and properties within concretes are essential elements for a structural designer who deals with concrete properties and behavior in service. SEM studies are essential for developing mathematical models and durability of concrete. SEM for the sample M1C70F10S20 is given in Figs. 12 and 13 both in NWC and SWC. The phases of different SEM images are studied as per the literature available [8, 9]. It is observed from Fig. 12 that the bright and dark matter stands for calcium–silicate–hydrate (C–S–H) gel present inner aggregates during subsequent curing process and acting as a binder in the paste thus improving mechanical properties. In some places, the voids and pores are also visible along with salt accumulation marked by white spots. In due process, C–S–H gels are formed during hardening process and voids are eliminated therefore strength gains. In SWC samples, the formation of C–S–H gels is hardly visible and salt accumulation is observed in some places by white spots along with voids thus deterioration takes place at later age which are shown in Fig. 13. Furthermore, deterioration takes place by various chemical and physical attacks in marine environment which can change their inner structures as well as their characteristics.

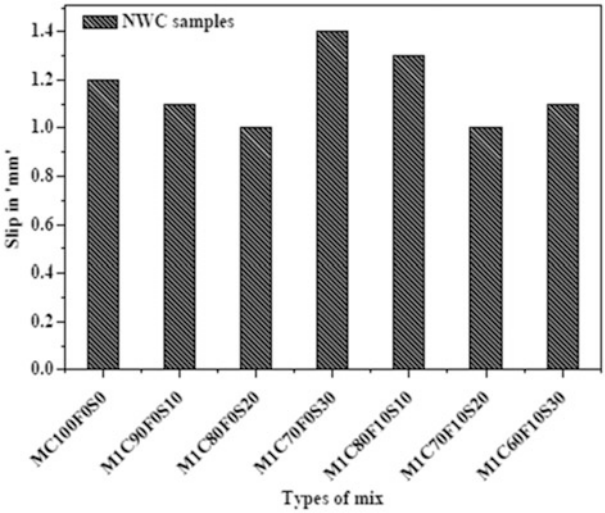

Fig. 10 Slip in 'mm' versus types of mix

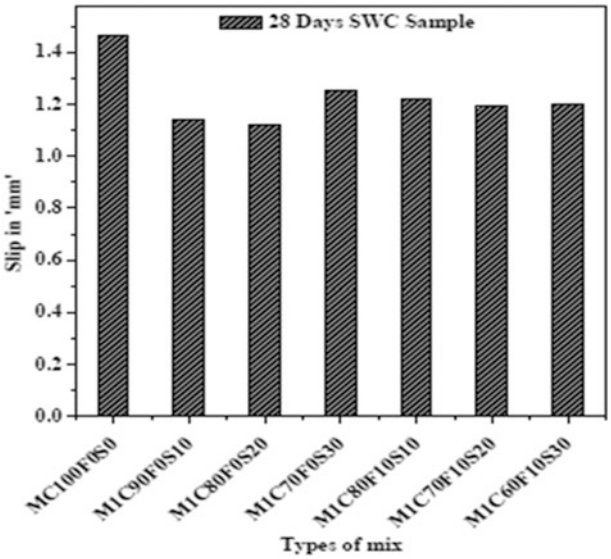

Fig. 11 Slip in 'mm' versus types of mix

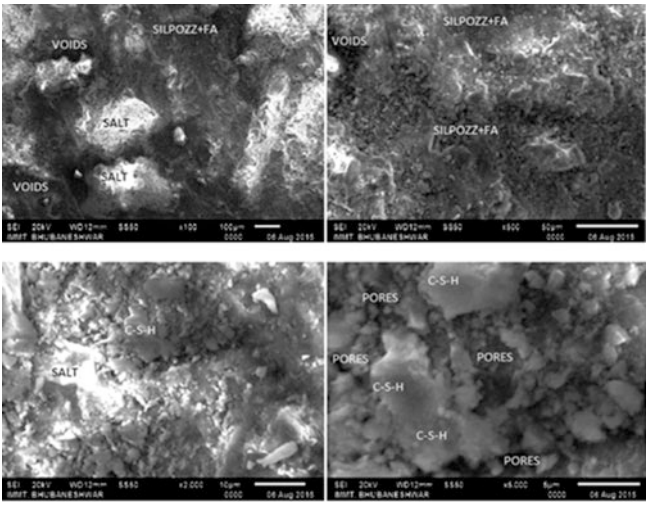

Fig. 12 SEM of NWC sample (M1C70F10S20)

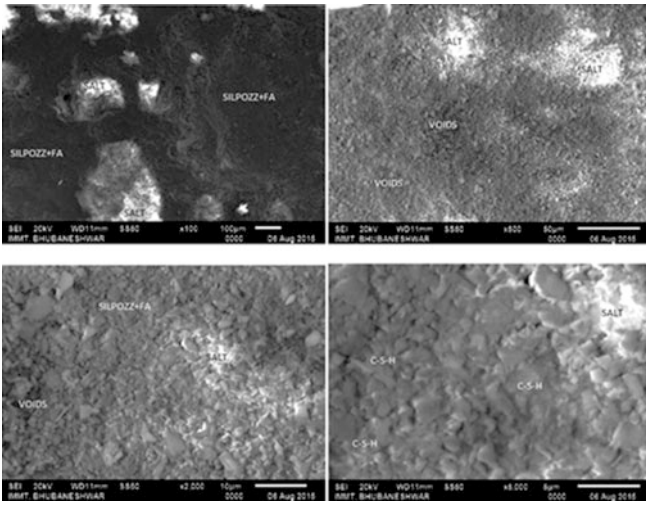

Fig. 13 SEM of SWC sample (M1C70F10S20)

4 Concluding Remarks

The following conclusions may be drawn from the present study:

It is observed that 10% replacement of FA and up to 20% silpozz with cement, the SRF in compressive strength is found to be less than 4% at 180 days of exposure.

The SRF in flexural strength for the sample 0% FA and 20% silpozz replaced with OPC was found 1.22% at 90 days and 1% for sample 10% FA and 20% silpozz replaced with OPC. It seems to be negligible but in long term, this may lead to the vulnerability of coastal structures.

The SRF in split tensile strength for sample 0% FA and 20% silpozz replaced with OPC was found as 0.3%. 0.45 and 0.8% at 7, 28 and 90 days age which is less than the SRF value for sample 10% FA and 20% silpozz.

The lowest value of SRF in bond strength is 10.35% for sample of 10% FA and 20% silpozz replaced with OPC. The highest value of SRF is 14.11% for control specimen at 28 days of curing. The maximum and minimum slips are 1.40 mm and 1 mm for control specimen and M1C70F10S20 sample, respectively, in 28 days NWC. But the slips were observed as 1.146 and 1.19 mm for control specimen and M1C70F10S20, respectively, in 28 days SWC.

In the present study of SEM, the sample M1C70F10S20 with SP showed large formation of C–S–H gel needs the development of dense microstructures.

The addition of SCM such as FA and silpozz with SP enhances the homogeneity of cement paste and densifies the microstructure of the cement considerably as well as improves the mechanical properties of marine concrete.

It is concluded that Silpozz is having average particles size of 25 microns and below, so that it fills the interstices in between the cement in the aggregate as fine filler with the help of SP which gives better strength and resistance to seawater attack.

Acknowledgements Authors would like to thank IIMT and SOA (Deemed to be University), Bhubaneswar, Odisha, to conduct experimental work.

References

1. Kumar, S. (2000). Influence of water quality on the strength of plain and blended cement concretes in marine environments. *Cement and Concrete Research, 30,* 345–350.
2. Menon, A. H., Radin, S. S., Zain, M. F. M., & Trottier, J. F. (2002). Effect of mineral and chemical admixtures on high strength concrete in sea water. *Cement and Concrete Research, 32,* 373–377.
3. Wegian, M. F. (2010). Effect of sea water for mixing and curing on structural concrete. *The IES Journal Part A, Civil and Structural Engineering, 3*(4), 235–243.
4. Anwar, M., & Roushdi, M. (2014). Improved concrete properties to resist saline water using environmental by-product. *Water Science Journal, 27,* 30–38.
5. Jena, T., & Panda, K. C. (2015). Effect of fly ash and silpozz on strength and durability properties of concrete in sea water. *Indian Journal of Science and Technology, 8*(29), 1–7.
6. Jena, T., & Panda, K. C. (2015). Influence of sea water on strength and durability properties of concrete. *Advances in Structural Engineering*, *03*, 1863–1873.
7. Shen, D., Shi, X., Zhang, H., Duan, X., & Jiang, G. (2016). Experimental study of early-age bond behavior between high strength concrete and steel bars using a pull out test. *Construction and Building Materials, 113,* 653–663.

8. Aggrawal, Y., & Siddique, R. (2014). Microstructure and properties of concrete using bottom ash and waste foundry sand as partially replacement of fine aggregates. *Construction and Building Materials, 54,* 210–223.
9. Weiting, X., Tommy, Y. L., & Shazim, A. M. (2012). Microstructure and reactivity of rice husk ash. *Construction and Building Materials, 29,* 541–547.
10. IS: 8112-1989. *43 grade OPC specifications (first revision)*. New Delhi, India: Bureau of Indian Standards.
11. IS: 383-1970. *Indian Standard Specification for course and fine aggregates from natural sources for concrete (second revision)*. New Delhi, India: Bureau of Indian Standards.
12. IS: 10262-2009. *Guide lines for concrete mix design proportioning*. New Delhi, India: Bureau of Indian Standards.

Influence of Fly Ash and Silpozz on the Concrete Containing Crusher Dust as Sand Replacement Material

S. Jena and K. C. Panda

Abstract This paper is aimed at finding out any other alternate materials to be used in concrete without compromising its desired quality and durability. The mix design is targeted for M30 grade concrete with *w/b* ratio 0.43. The investigation comprises of 12 numbers of concrete mixes. First two mixes were made by replacing 0 and 50% of natural fine aggregate (NFA) with crusher dust (CD). Then at each replacement level of NFA, cement is replaced partially with both fly ash (FA) and silpozz. The studied parameters include the workability, compressive, split tensile and flexural strength of concrete samples after 7, 14, and 28 days of curing period. Workability decreases with increase in CD and silpozz content and increases with FA. The hardened concrete test results indicate that CD-based concrete increases the compressive, split tensile and flexural strength. Use of FA and silpozz increases the strength and maximum strength is achieved at 20% replacement of cement with silpozz.

Keywords Crusher dust (CD) · Fly ash (FA) · Silpozz · Compressive strength Flexural strength · Split tensile strength

1 Introduction

In this era of rapid industrialization, there is exponential growth in infrastructure sector. To sustain this infrastructural growth, raw materials and related requisites are to be fetched in abundance. Since natural resources are depleting by the day,

S. Jena
Department of Civil Engineering, SOA (Deemed to be University), Bhubaneswar 751030, Odisha, India
e-mail: sjena4203@gmail.com

K. C. Panda (✉)
Department of Civil Engineering, Government College of Engineering, Kalahandi, Bhawanipatna 766002, Odisha, India
e-mail: kishoriit@gmail.com

A. Rama Mohan Rao and K. Ramanjaneyulu (eds.), *Recent Advances in Structural Engineering, Volume 1*, Lecture Notes in Civil Engineering 11,
https://doi.org/10.1007/978-981-13-0362-3_65

the time has come for us to look for alternative to these resources that can be used efficiently. Concrete is used extensively in developing the infrastructure of any kind. Cement and sand being its two important ingredients, scarcity of good quality natural sand is hindering the progress of many infrastructure projects. Extensive sand quarrying has also its own adverse environmental impact. Therefore, it is high time we explored the possibility for replacement of sand in concrete. There are so many materials available as industrial or agricultural by-products that can be recycled as construction material. When rocks are processed in crusher to produce aggregates of various sizes, the residue is called crusher dust (CD). Disposal of these CD is a difficult proposition as huge area of land is required for this purpose. There is always risk of pollution if these fine particles mingle with air/water. To overcome these problems and to find an economically viable alternative to river sand, we can use CD in concrete.

CD is successfully being used in road projects in place of river sand. Similarly, use of cement is increasing exponentially. Production of cement is energy consuming and expensive. Environmental pollution is its another drawback. During the production of 1 MT of Portland cement, nearly 1 MT of CO_2 is released into the atmosphere, contributing to the Global warming, which has reached a severe stage. On the other hand, disposal and stockpiling of industrial by-products such as blast furnace Slag, fly ash (FA) and Silpozz, etc., are becoming difficult day by day. The only solution to these problems is to explore ways for replacement of Portland cement with these by-products so that consumption of cement will be less at the same time these by-products will be disposed of efficiently.

FA is recognized as a cementitious material. Workability of concrete can be improved if cement is suitably substituted with FA. Water requirement of the concrete shall also be reduced. Similarly, Silica fume can efficiently be replaced with eco-friendly and low-cost Silpozz to enhance the strength and workability of concrete.

According to Pofale and Quadri [1], at all replacement levels of natural fine aggregates (NFA) with CD, there is reduction of 1–6% in workability. They further concluded that compressive strength of concrete is increased up to 5–22% when NFA is substituted with CD. They also mentioned that when percentage replacement level of NFA with CD is 40%, maximum compressive strength was achieved. With the increase in percentage of dust content, slump value decreases according to Celik and Marar [2]. According to Eren and Marar [3], water permeability is reduced with increasing content of CD.

Utmost compressive, tensile and flexural strength are achieved when NFA is replaced by 50% CD according to Balamurugan and Perumal [4]. They further concluded that CD can be put to use in place of NFA when replaced by 50%, with giving additional strength. Compressive strength of concrete is increased considerably with the addition of FA and but tensile strength is not that much affected by FA according to Sama et al. [5]. They further concluded that utilization of FA in concrete as the partial replacement of cement leads to a cost-effective and environmental friendly product. According to Pitroda et al. [6] Coal and thermal industry disposal cost can be saved with utilization of FA. It also leads to

construction with 'greener concrete'. But it is noticed that with the addition of FA, percentage change in compressive as well as tensile strength decreases. According to Jalal et al. [7], workability of concrete increases with increasing FA content. They further concluded that as compared to OPC concrete, FA concrete is more durable. Pradhan and Panda [8] concluded that addition of silpozz in concrete, as partial replacement of cement enhances the strength remarkably. At all age of curing, the strength of all concrete mixes prepared with the different combination of silpozz and RHA is higher than control mix as per Panda and Prusty [9].

Aim of this study is to investigate on the effect of FA and silpozz on the properties of concrete containing CD. To evaluate the fresh concrete properties, slump test and hardened concrete properties were known from compressive, split tensile and flexural strength tests.

2 Experimental Details

2.1 Material

In this study, ordinary Portland cement, NFA, NCA, CD, FA, Silpozz and potable water were used. OPC 43-grade is used in the present study having specific gravity 3.15. The physical properties of cement are obtained experimentally and the value specified by IS 8112:1989 [10] is presented in Table 1. Silpozz was supplied by N. K. Enterprises, Jharsuguda. Colour grey, particle size 25 μ-mean, specific gravity 2.3, surface area 17.1 m^2/gm. FA of class F was supplied from Nava Bharat Ventures Ltd., Dhenkanal, Odisha. The chemical composition of OPC, FA and average batch analysis report of silpozz is given in Table 2. Sand is used as NFA which is passing through IS 4.75 mm sieve. It is having specific gravity 2.68 and conforming to zone II, and was used in the present study. NCA was of 20 mm downgraded and its specific gravity is 2.77. CD used was from a local crusher of zone I, with specific gravity 2.80. The physical properties of NFA, NCA and CD as

Table 1 Physical properties of cement (OPC-43 grade)

Characteristics	Test value	Value as per IS: 8112-1989
Normal consistency, percent	32.5	NA
Specific gravity	3.15	3.15
Setting time, minutes		
Initial setting time	121	30 (min)
Final setting time	410	600 (max)
Compressive strength (Mpa)		
3 days	30	23 (min)
7 days	43	33 (min)
28 days	51	43 (min)

Table 2 Chemical composition of OPC, FA and Silpozz

Oxide	OPC	FA	Silpozz
SiO_2	20.50	60.69	91.86
Al_2O_3	5.05	22.55	1.98
Fe_2O_3	2.99	3.52	0.58
CaO	62.00	0.007	1.03
MgO	2.07	0.005	0.67
SO_3	2.40	0.012	–
LOI	3.10	3.27	1.99
Carbon	–	–	0.79
Na_2O	–	–	0.14
K_2O	–	–	0.87
Others	–	–	0.87
Moisture	–	–	0.74

Table 3 Physical properties of aggregates and CD

Characteristics	Test value (as Per IS: 383-1970)		
	NFA	NCA	CD
Fineness modulus	2.76 (zone II)	6.93	3.37 (zone I)
Specific gravity	2.68	2.77	2.80
Water absorption	0.80	0.22	0.80

per IS: 383-1970 [11] obtained experimentally are presented in Table 3. The residues obtained from different CD particles passing through different sieves are shown in Fig. 1. Particle size gradation curve of NFA and CD is shown in Fig. 2.

3 Mixture Proportion

To acquire target mean strength, design mix of M30 grade of concrete was done as per IS: 10262-2009 [12]. The target mean strength was found to be 38.25 MPa for a tolerance factor of 1.65. Here, the mix proportion 1:1.535:2.746 was taken in this experiment. Two different mixes of concrete mixtures were made by replacing 0 and 50% of NFA with CD. The same mixes have been tested in a constant *w/b* ratio, i.e. 0.43 for cement concrete. In this study, total 12 mixes were prepared for CD Concrete. MCD indicates concrete mix with 0 and 50% replacement of NFA with CD, with *w/b* ratio 0.43. MCD0 indicates 0% CD, 100% cement, 100% NFA, and 100% NCA, MCD50 indicates 50% CD, 100% cement, 50% NFA and 100% NCA. Designation of mix proportion for their identification is done as per the degree of replacement of different ingredients. Then total ten different mixes of concrete (5 in each percentage interval of replacement of NFA) were made. The sample MCD0F10S0 represents 0% replacement of NFA with CD, 10% replacement of

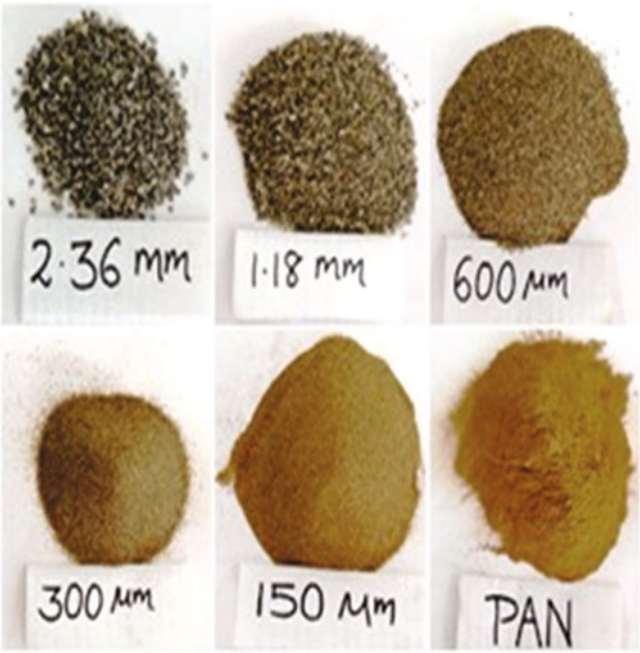

Fig. 1 Residues of crusher dust passing through different sieves

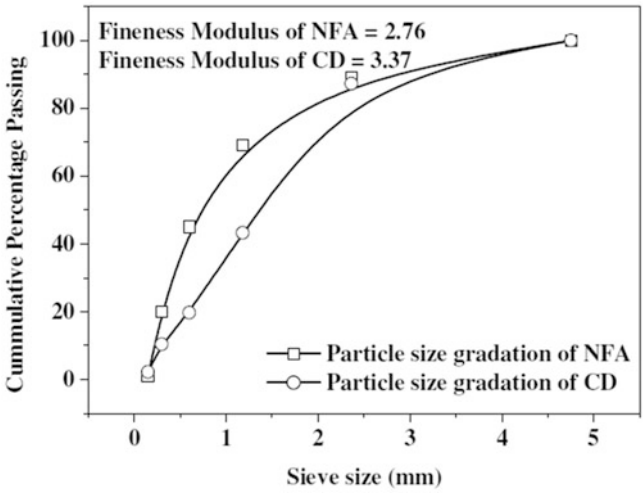

Fig. 2 Particle size gradation curve of NFA and CD

cement with FA and 0% replacement of cement with silpozzz. Similarly, MCD50F10S0 represents 50% replacement of NFA with CD, 10% replacement of cement with FA and 0% replacement of cement with silpozz.

3.1 Casting and Testing of Specimen

After the cementitious materials such as OPC, FA, silpozz along with NCA, NFA and CD were weighed in different proportions as per test sampling to homogeneous mixture by placing them in the concrete mixer, specified quantity water as per *w*/*b* respective ratio was weighed and added to this mix and further mixed in the mixer till a uniform homogeneous mix is obtained. The mixing procedure is same for all the test samples. The workability of the mixed concrete was carried out immediately by the slump test. Test specimens were placed in moulds of specified size. 40 mm size needle vibrator was used for in compacting the concrete specimens. The specimens were kept in the mould for 24 h. After removal from moulds, the specimens were placed in curing tank using potable water for 7, 14 and 28 days. The objective of the curing is to provide an appropriate environmental condition within a concrete structure (temperature and humidity) to ensure smooth progression of hydration reactions (Table 4).

In this study, cubes of size 150 mm × 150 mm × 150 mm, cylinders of size 100 mm diameter and 200 mm height and prisms of size 100 mm × 100 mm 500 mm are used. The hardened concrete properties such as compressive strength for cubes, flexural strength for prisms and split tensile strength for cylinders were tested in the laboratory.

Table 4 Details of mix quantity per m^3 of concrete

Mix Identity	Filler (%)	Cementitious materials per m^3 of concrete			NFA (kg)	NCA (kg)	CD (kg)	Water (kg)
		Cement (kg)	Fly ash (kg)	Silpozz (kg)				
MCD0	0	432.55	0	0	663.96	1187.78	0	185.99
MCD50	50	432.55	0	0	331.84	1187.78	331.84	185.99
MCD0F10S0	0	389.29	43.25	0	663.96	1187.78	0	185.99
MCD0F20S0	0	346.04	86.51	0	663.96	1187.78	0	185.99
MCD0F0S10	0	389.29	0	43.25	663.96	1187.78	0	185.99
MCD0F0S20	0	346.04	0	86.51	663.96	1187.78	0	185.99
MCD0F10S10	0	346.04	43.25	43.25	663.96	1187.78	0	185.99
MCD50F10S0	50	389.29	43.25	0	331.84	1187.78	331.84	185.99
MCD50F20S0	50	346.04	86.51	0	331.84	1187.78	331.84	185.99
MCD50F0S10	50	389.29	0	43.25	331.84	1187.78	331.84	185.99
MCD50F0S20	50	346.04	0	86.51	331.84	1187.78	331.84	185.99
MCD50F10S10	50	346.04	43.25	43.25	331.84	1187.78	331.84	185.99

Workability of fresh concrete mixture was measured by slump test. Fresh concrete mix was prepared and then slump test was conducted immediately after the mixing. The slump values of concrete mixtures were obtained experimentally where *w/b* ratio is 0.43. Characteristics of the hardened concrete specimens were obtained by testing the specimens after specified curing time, i.e. 7, 14 and 28 days. The compressive strength, split tensile strength test and flexural strength test were conducted to know hardened concrete properties of the specimens.

The compressive strength was computed by using the equation:

$$f_{ck} = P/B^2 \tag{1}$$

where

f_{ck} compressive strength, MPa
P maximum applied load in Newton
B size of the cube specimen in mm

The split tensile strength was computed by the equation:

$$f_{sp} = 2P/\pi Ld \tag{2}$$

where

f_{sp} split tensile strength, MPa
P maximum compressive load on the cylinder in Newton
L length of the cylinder in mm
d diameter of the cylinder in mm

The flexural strength was computed using the equation:

$$f_b = PL/BD^2 \tag{3}$$

where,

f_b flexural strength, MPa,
P maximum applied load in Newton,
L span length in mm,
B width of the specimen in mm
D depth of the specimen in mm

4 Results and Discussions

The test results are presented along with their graphical plots and discussions.

4.1 Fresh Concrete Test Results

The concrete mixes were prepared in different proportions and the fresh concrete test is conducted after the mixing. It is observed that in the control specimen, i.e. MCD0, the slump value was 35 mm. But when sand is replaced with 50% of CD, the slump was 15 mm. The test results indicate that as CD content increases the workability of fresh concrete decreases. In the absence of CD, when cement is replaced with 10 and 20% FA, the slump values were 38 and 39 mm, respectively. But when sand is replaced with 50% of CD and cement is replaced with 10 and 20% FA, the slump values were 19 and 21 mm, respectively. The test results indicate that workability of concrete mix with FA and CD is less as compared to concrete mix without CD. In the absence of CD, when the cement is replaced with 10 and 20% silpozz, the slump values were 12 and 6 mm, respectively. But when sand is replaced with 50% of CD and cement is replaced with 10 and 20% of silpozz, the slump values were zero. It is observed that addition of silpozz without CD decreases the workability. Further decrease in workability is observed in the presence of silpozz and CD. In the absence of CD, when cement is replaced with combination of 10% FA and 10% of silpozz, the slump value was 35 mm. But when sand is replaced with 50% of CD and cement is replaced with combination of 10% FA and 10% of silpozz, the slump value was 16 mm. It is observed that with combination of FA and silpozz, the workability is not so significant.

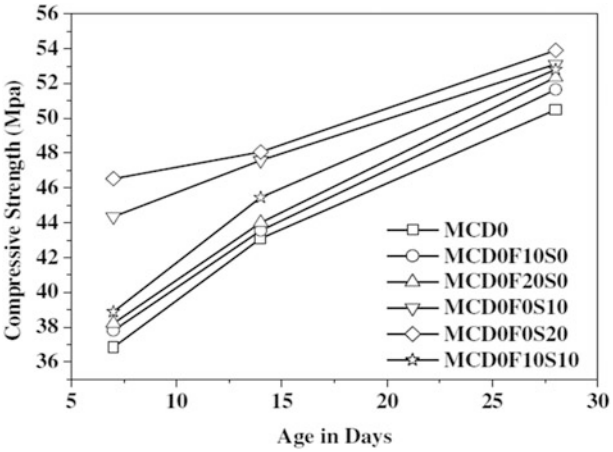

Fig. 3 Compressive strength versus age in days for concrete without CD

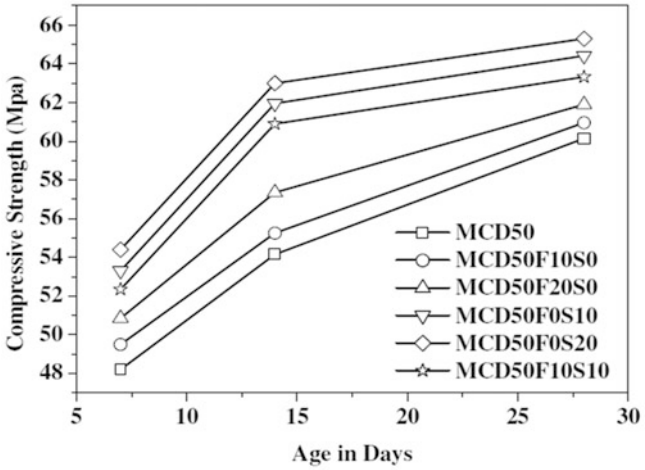

Fig. 4 Compressive strength versus age in days for concrete with 50% CD

4.2 Hardened Concrete Test Results

4.2.1 Compressive Strength

Nine numbers of cubes were cast for each mix and each of the three cubes was tested after 7, 14 and 28 days of curing. Figures 3 and 4 show the plot between the compressive strength in MPa and age in days for concrete without CD and with CD.

It is observed that the compressive strength of concrete mix with 50% replacement of NFA with CD increases up to 30.80, 25.63 and 19.13% at 7, 14 and 28 days respectively as compared to control specimen. Whereas in concrete mix with 50% CD and with 20% replacement of cement with FA, the compressive strength increases up to 34, 28.19, 20.71 at 7, 14 and 28 days, respectively. In concrete mix with 50% CD and with 20% replacement of cement with silpozz, the compressive strength increases up to 44.66, 43.73, 27.58% at 7, 14 and 28 days, respectively. In the presence of 50% CD and with 20% replacement of cement with combination of 10% FA and 10% silpozz, the compressive strength increases up to 42.06, 41.29, 25.41% at 7, 14 and 28 days, respectively, as compared to control specimen. The compressive strength of all concrete mixes with and without CD and with cementitious material is giving higher value as compared to control specimen.

4.2.2 Split Tensile Strength

Nine numbers of cylinders were cast for each mix and each of the three cylinders was tested after 7, 14 and 28 days of curing. Figures 5 and 6 show the plot between the split tensile strength in MPa and age in days for concrete without CD and with CD.

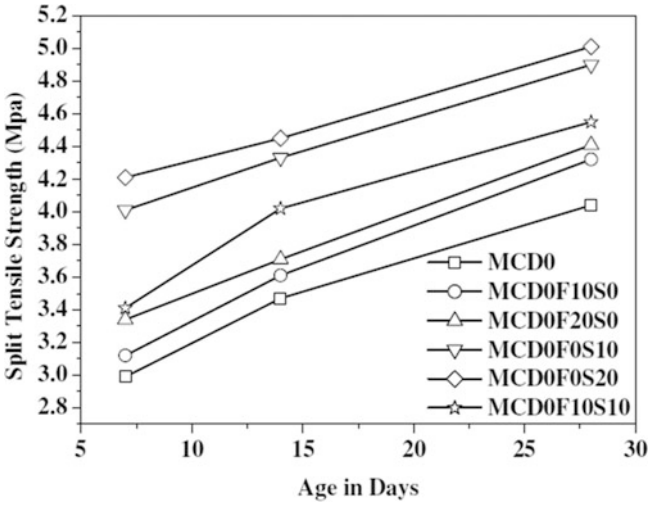

Fig. 5 Split tensile strength versus age in days for concrete without CD

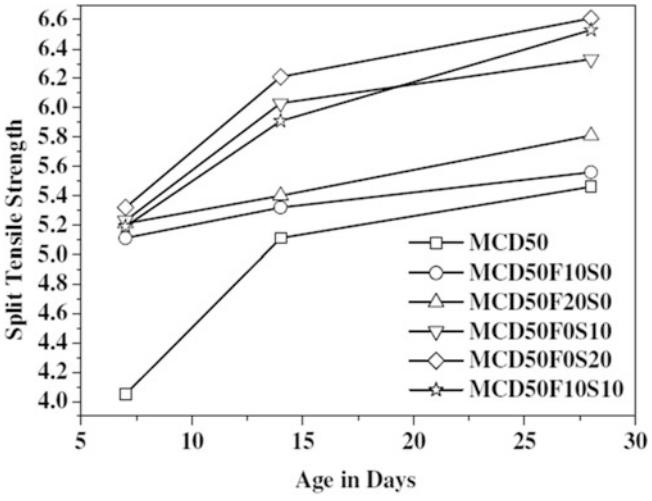

Fig. 6 Split tensile strength versus age in days for concrete with 50% CD

It is observed that the split tensile strength of concrete mix with 50% replacement of NFA with CD increases up to 35.45, 47.26 and 35.14% at 7, 14 and 28 days, respectively, as compared to control specimen. Whereas in concrete mix with 50% CD and with 20% replacement of cement with FA, the split tensile strength increases up to 74, 55.61 and 43.81% at 7, 14 and 28 days, respectively. In the presence of 50% CD with 20% replacement of cement with silpozz, the split tensile strength increases up to 77.92, 78.96 and 63.61% at 7, 14 and 28 days,

respectively. In the presence of 50% CD with 20% replacement of cement with combination of 10% FA and 10% silpozz, the split tensile strength increases up to 73.57, 70.31 and 61.63% at 7, 14 and 28 days, respectively, as compared to control specimen. The split tensile strength of all concrete mixes with and without CD and with cementitious material is giving higher value as compared to control specimen.

4.2.3 Flexural Strength

Nine numbers of prisms were cast for each mix and each of the three prisms was tested after 7, 14 and 28 days. Figures 7 and 8 show the plot between the flexural strength in MPa and age in days for concrete without CD and with CD, respectively.

It is observed that in comparison to control mix, with 50% replacement of NFA with CD, the flexural strength increases up to 28.78, 25 and 24.19% at 7, 14 and 28 days respectively. Secondly, when there is 20% replacement of cement with FA in the above mix, the flexural strength increases up to 48.48, 36.53 and 30.06% at 7, 14 and 28 days respectively. In the presence of 50% CD, with 20% replacement of cement with silpozz, the flexural strength increases up to 78.78, 59.61 and 50% at 7, 14 and 28 days, respectively. In the presence of 50% CD with 20% replacement of cement with combination of 10% FA and 10% silpozz, the flexural strength increases up to 42.06, 41.29 and 25.41% at 7, 14 and 28 days, respectively as compared to control specimen. The flexural strength of all concrete mixes with and without CD and with cementitious material is giving higher value as compared to control specimen.

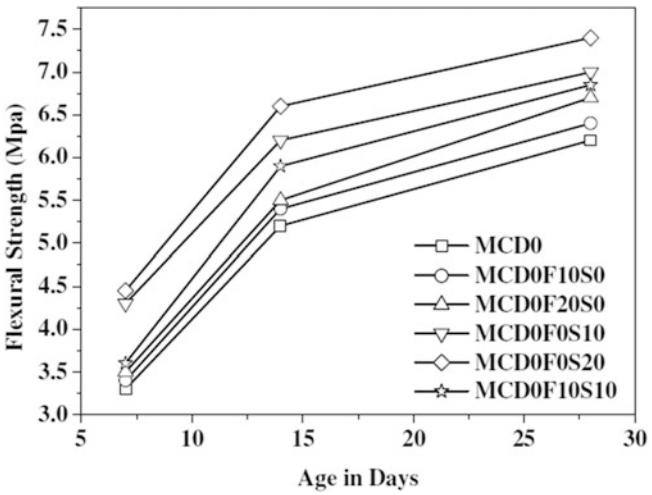

Fig. 7 Flexural strength versus age in days for concrete without CD

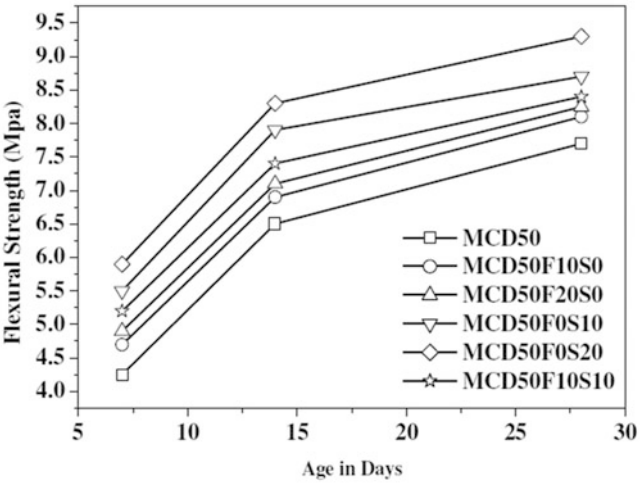

Fig. 8 Flexural strength versus age in days for concrete with 50% CD

5 Conclusions

Based on the above studies or results, the following conclusion may be drawn.

- Workability of concrete samples decreases with increase in CD content.
- With respect to control specimen, at all replacement levels of NFA (0 and 50%), when the cement is replaced with FA starting from 10 up to 20%, the workability increases.
- At all replacement levels of NFA with CD, when the cement is replaced with silpozz starting from 10 up to 20%, the workability of concrete decreases with respect to control specimen.
- With respect to control specimen, when cement is replaced with the combination of 10% of FA and 10% of silpozz, the rate of increase in workability is not so significant.
- At all replacement levels of NFA with (0 and 50%) CD, when the cement is replaced with FA starting from 10 up to 20% the compressive strength, split tensile strength and flexural strength increases with respect to control specimen.
- With respect to control specimen, at all replacement levels of sand with CD, when the cement is replaced with silpozz starting from 10 up to 20% the compressive strength, split tensile strength and flexural strength increases remarkably. With the increase in silpozz, the strength of concrete increases due to its higher pozzolanic effect.
- With respect to control specimen, when cement is replaced with the combination of 10% of FA and 10% of silpozz, the increase in compressive, split tensile and flexural strength is not so significant.

- It is noticed that at all replacement level of FA and silpozz in presence of CD, the percentage of increase in early strength, i.e. at 7 days is higher than 28 days strength. It may be due to the early hydration process of cement.
- NFA can be replaced with CD up to 50% resulting in increasing strength.

Acknowledgements The authors wish to thank SOA (Deemed to be University) for the support of conducting the experimental work. Also, thankful to the N K Enterprises, Jharsuguda and Nava Bharat Ventures Ltd., Dhenkanal for supplying the materials.

References

1. Pofale, A. D., & Quadri, S. R. (2013). Effective utilization of crusher dust in concrete using Portland Pozzolana cement. *International Journal of Scientific and Research Publications, 3,* 2250–3153.
2. Celik, T., & Marar, K. (1996). Effects of crushed stone dust on some properties of concrete. *Cement and Concrete Research, 26,* 1121–1130.
3. Eren, O., & Marar, K. (2009). Effects of limestone crusher dust and steel fibers on concrete. *Construction and Building Materials, 23,* 625–633.
4. Balamurugan, G., & Perumal, P. (2013). Behaviour of concrete on the use of Quarry dust to replace sand—an experimental study. *Engineering Science and Technology: An International Journal, 3*(6), 776–781.
5. Sama, T., Lalwani, D., Shukla, A., & Sofi, A. (2014). Effect of strength of concrete by partial replacement of cement with fly ash and addition of steel fibres. *Journal of Civil Engineering and Environmental Technology, 1,* 5–9.
6. Pitroda, J., Zala, L. B., & Umrigar, F. S. (2012). Experimental investigations on partial replacement of cement with fly ash in design mix concrete. *International Journal of Advanced Engineering Technology, 3,* 126–129.
7. Jalal, M., Pouladkhan, A., Harandi, O. F., & Jafari, D. (2015). Comparative study on effects of class F fly ash, nano silica and silica fume on properties of high performance self-compacting concrete. *Construction and Building Materials, 94,* 90–104.
8. Pradhan, S. S., & Panda, K. C. (2014). Effect of silpozz and LSP on fresh and hardened properties of SCC. *Journal of Civil Engineering and Environmental Technology, 1,* 84–90.
9. Panda, K. C., & Prusty, S. D. (2015). Influence of silpozz and rice husk ash on enhancement of concrete strength. *Advances in Concrete Construction, 3,* 203–221.
10. IS: 8112-1989. *Indian Standard, 43 Grade ordinary Portland cement specification* (first revision). New Delhi: Bureau of Indian Standards.
11. IS: 383-1970. *Indian standard specification for coarse and fine aggregates from natural sources for concrete* (second revision). New Delhi, India: Bureau of Indian Standards.
12. IS: 10262-1982. *Recommended guidelines for concrete mix design*. NewDelhi, India: Bureau of Indian Standards.

Behaviour of RC Structural Elements with Laced Reinforcement

V. Sai Venkata Ramanjaneyulu and G. Papa Rao

Abstract This study investigates the performance of RC elements, and the benefits accruing to them with Laced Reinforced Concrete (LRC). Investigations are carried out on four beams specimens. The variations in the four beam specimens were in the arrangement of shear reinforcement such as, first beam without shear reinforcement (B1), second beam (B2) is provided with conventional double-legged stirrups as shear reinforcement. Third and fourth beams B3 and B4 are fabricated with inclined continuous laced shear reinforcement, of 4 and 6 mm dia, which are inclined at an angle of 50° with longitudinal reinforcement arranged on both the faces of the beam respectively. All the four beams were designed and tested to compare the strength and performance of beams with conventional two-legged stirrups as shear reinforcement and laced reinforcement used as continuous shear reinforcement. LRC beams and slabs are widely used to resist the lateral forces and the sudden loads. Lacing is a form of continuous shear reinforcement which is placed on both the faces of the beam. With the help of transverse bars, the laced reinforcement is anchored and it is placed in the plane of principal bending [1]. The concentric load is applied at half the span of the specimen. The experimental results demonstrate that, as the LRC arrangement adapted to the specimens, achieved greater ultimate loads and decreases the deformation characteristics like deflection and crack widths. The structural integrity and ductility of the elements improve more in LRC elements. In this study, the comparison is done between the performance of the specimens with conventional and laced reinforcement as shear reinforcement under the monotonic loading. The beneficial aspect of using LRC makes the elements to resist the sudden impact and blast loads, which also reduces the spalling of the concrete.

V. Sai Venkata Ramanjaneyulu · G. Papa Rao (✉)
Department of Civil Engineering, Gayatri Vidya Parishad College of Engg. (A), Visakhapatnam 530048, Andhra Pradesh, India
e-mail: gprao_74@gvpce.ac.in

V. Sai Venkata Ramanjaneyulu
e-mail: sai.vetapalem5915@gmail.com

A. Rama Mohan Rao and K. Ramanjaneyulu (eds.), *Recent Advances in Structural Engineering, Volume 1*, Lecture Notes in Civil Engineering 11,
https://doi.org/10.1007/978-981-13-0362-3_66

Keywords Laced reinforced concrete · Monotonic loading · Ductility
Crack width · Deflection

1 Introduction

The main aim of the current investigation is to characterize the magnitude of the ductility in terms of deflections and crack widths between the beams with conventional shear reinforcement and laced reinforcement arrangement of different varieties. The structural elements without shear reinforcement lose their structural integrity at 2° support rotation due to lack of confinement of concrete. The structural members with conventional two-legged closed stirrups lose their structural integrity at 4° support rotation and the structural members arranged with laced reinforcement due to their truss action, the reinforcement in the structural member will restrain through its complete strain hardening region until the tension failure of reinforcement occurs at 12° support rotation [2]. Here, the static monotonic loading is applied on the centre of the specimens, and deflections and the crack widths are measured and the graphs are plotted between load versus deflection and moment versus crack width. Ductility is the important parameter for the structural elements and the ductility of the structural elements has shown improved by adopting LRC. LRC structures have been advocated, where high-intensity nonuniform loads like blast and earthquake loads.

2 Research Significance

Investigations carried out by Srinivasa Rao et al. [3] indicate that ductile failure of R.C beams with conventional stirrups is not possible when shear span to depth ratio is <2.5 due to the influence of severe diagonal cracking. After conducting tests on 20 LRC specimens under monotonic and cyclic loading, the test results indicated that LRC beams even with large tension steel reinforcement can effectively eliminate brittle failure thus ensuring large ductility and sustained over large yield plateau. Tegos et al. [4] have conducted experimental studies on low slender structural elements having shear span to depth ratio varying between 1.0 and 2.0. The plastic rotations obtained using rhombic reinforcements were compared to be large with conventional reinforced specimens under combined flexure and shear influence. Thus, it shows that inclined reinforcement is found to be one of the most effective ways to improve the seismic resistance of reinforced short columns and beams, specially under predominant shear influence. Akshaya et al. [5] investigate that LSCC (laced steel concrete composites) is having specified increase in load carrying capacity as well as ductile property as compared to conventional R.C due to lacing in flexural members gives confining to concrete and avoid sudden failure in the element. Experimental investigations on laced and R.C beams are carried out

under monotonic and reverse cyclic load and the ductility of LSCC beam with 60° lacing is found more than that of RC beam. Pauly [6] introduced the concept of diagonal arrangement of main reinforcements to prevent concrete spandrel beams from brittle failure under shear

3 Experimental Programme

The experimental programme involves in evaluating the ductility, flexural strength and crack widths between the specimens provided with conventional and laced reinforcement. Here, the specimens are designed for 100 kN concentrated load and tested for monotonic loading applied at the centre of the specimen. All the specimens were cast using M25 grade concrete. The lacing bars were 4 mm diameter for beam B3 and 6 mm diameter for beam B4 fabricated on both sides of beam. The angle of inclination with respect to principle reinforcement is kept 50° for beams. In beam specimens, 3 no's of 16 mm diameter bars were used as tension reinforcement and 2 no's of 12 mm diameter bars are used as holder bars. The spacing between the conventional two-legged shear reinforcement in B2 is 200 mm. In beam B3 and B4 with laced reinforcement used as shear reinforcement, the lacing nodes are kept at a distance of 200 mm. The concrete used in the study was M25 grade. The fine aggregate was river sand and coarse aggregate was locally available granite stone sieved to 20 mm maximum size. The details of the test specimens used are shown in Fig. 1. All the specimens were under curing till testing. It took 30 days before testing could be started (Fig. 2).

4 Test Procedure

All the test specimens were tested in a 100 T capacity steel load frame shown in Fig. 2. The specimens were tested on a simply supported span of 1300 mm with a concentrated load at half of the span. The load was applied by a hydraulic jack of 1000 kN capacity. The load applied on the specimen was controlled by manual operation. To measure the deflection, a dial gauge of 20 mm run was utilized at mid-span having least count of 0.01 mm. The crack widths are measured using handheld microscope with least count of 0.02 mm. After each load application, the applied load, transverse deflection and maximum crack width were recorded. The crack patterns were observed on the beam sides and noted. As initial cracking and ultimate loads were approached, load intensity was reduced. About 10–12 load increments were needed to reach ultimate loads. At the termination of the test, the beams were photographed to depict the failure and crack patterns. From the measured deflections and the crack widths, graphs are plotted between load versus deflection and moment versus crack width.

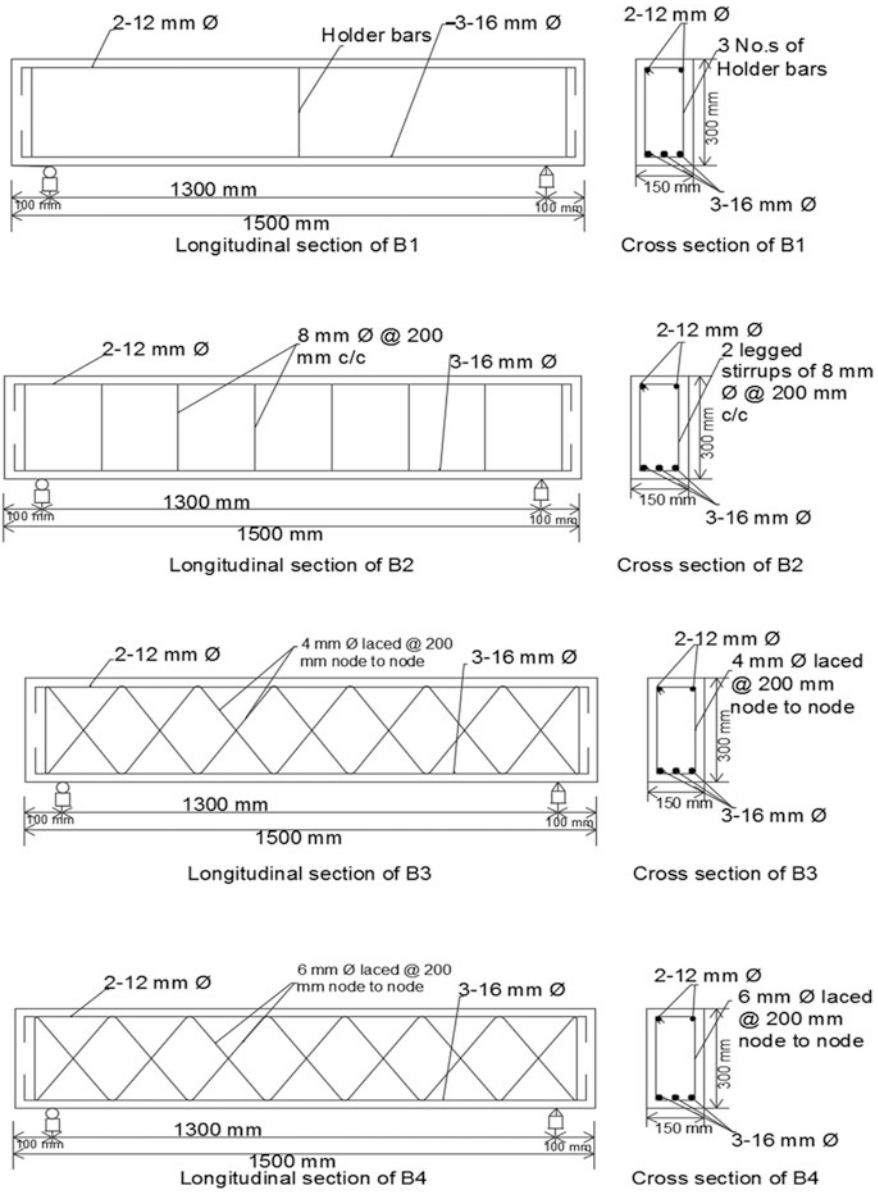

Fig. 1 Longitudinal and cross-sectional configurations of test specimens

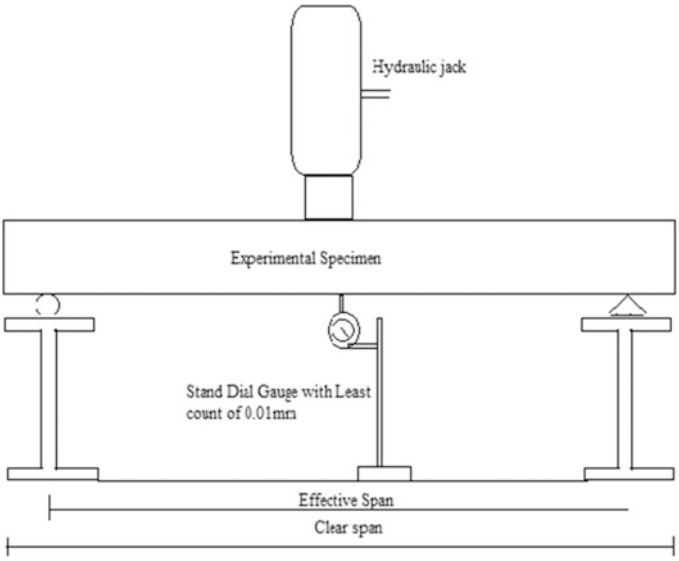

Fig. 2 Schematic diagram of the load test set-up for the test specimens

5 Test Results

All the specimens which are tested under the loading frame, the measured deflections and crack widths at the working and ultimate load are provided in Table 1. For the purpose of comparison of test specimens, deflection and crack width at service load of B2, i.e. (2/3 * (170) = 112 kN) are tabulated in Table 2. The deflections are measured using dial gauge of 20 mm run and the crack widths are measured at every load increment using handheld microscope which has a measuring capacity up to 1.8 mm. For the measurement of crack widths more than 1.8 mm, refined measuring scale was used. The failure patterns of the specimens after testing are shown in Figs. 3, 4, 5 and 6.

Failure patterns of beam specimens: See Figs. 7 and 8.

Table 1 Principal test results of beam specimens

Specimen identity	Design load (kN)	Ultimate load (kN)	Deflection in mm at		Crack width in mm at	
			Design load	Ultimate load	Design load	Ultimate load
B1	100	110	3.99	4.55	0.36	0.4
B2	100	170	2.59	5.7	0.22	0.8
B3	100	160	2.95	6.10	0.2	1.24
B4	100	200	2.19	6.10	0.06	1.12

Table 2 Deflection and crack width at service load

S. No.	Specimen	Deflection (mm)	Crack width (mm)
1.	B1	4.45	0.4
2.	B2	2.98	0.28
3.	B3	3.25	0.4
4.	B4	2.35	0.075

Service load of B2, B3 and B4 were taken as service load of B2, i.e. (2/3 * (170) = 112 kN)

Fig. 3 Failure pattern of B1

Fig. 4 Failure pattern of B2

Fig. 5 Failure pattern of B3

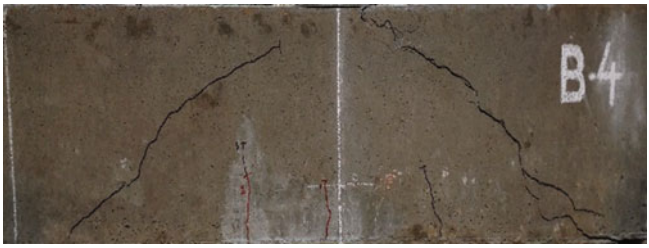

Fig. 6 Failure pattern of B4

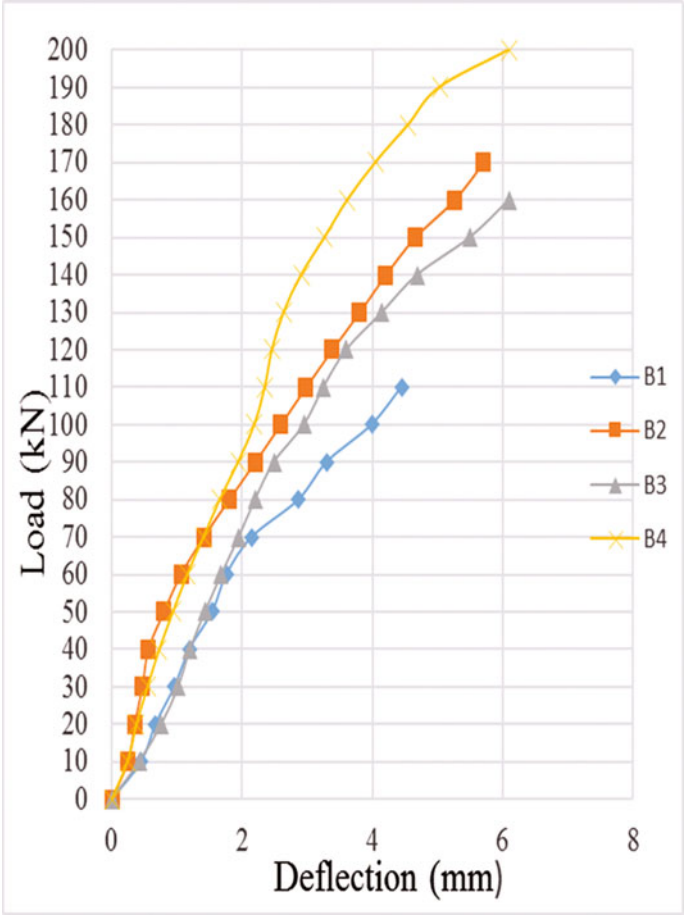

Fig. 7 Load–deflection curves of B1, B2, B3 and B4

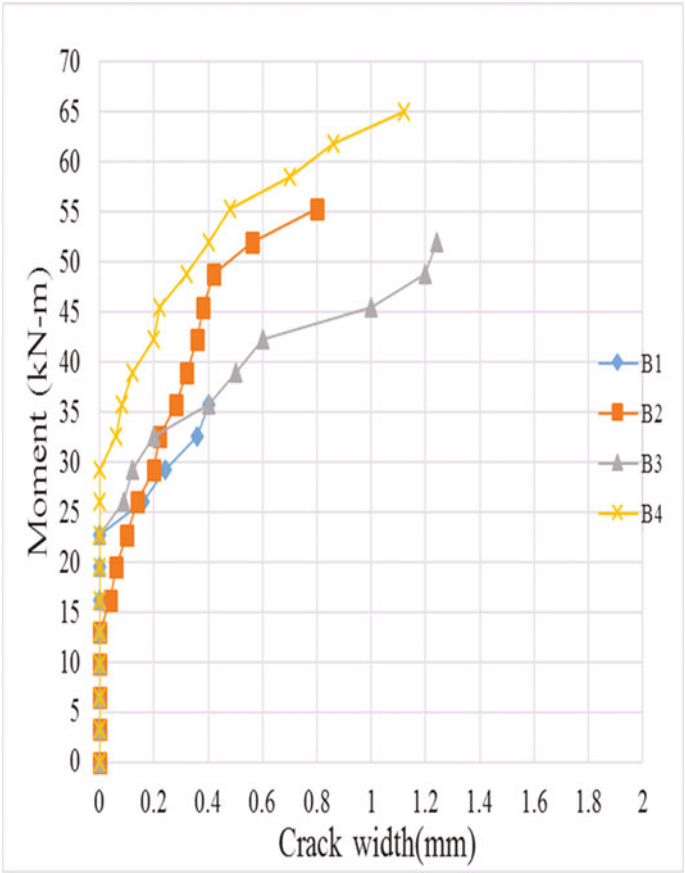

Fig. 8 Moment–crack width curves of B1, B2, B3 and B4

6 Discussion of Test Results

All the test specimens in this investigations are designed for a working load of 100 kN. The flexural reinforcement is kept same for all beams with the variation in the pattern of shear reinforcement. The beam B1 without shear reinforcement failed suddenly at an ultimate load of 110 kN. With the provision of conventional vertical two-legged 8 mm dia. stirrups as shear reinforcement, the load carrying capacity increased to an ultimate load of 170 kN. By adopting inclined continuous laced reinforcement of 4 mm dia. in B3 as shear reinforcement in lieu of conventional shear reinforcement, it failed at an ultimate load of 160 kN. The reduction of load carrying capacity in B3 is due to less percentage of shear steel which is about 58% of shear steel used in B2. By adopting inclined continuous laced reinforcement of 6 mm dia. in B4 as shear reinforcement in lieu of conventional shear reinforcement

the load carrying capacity is increased to an ultimate load of 200 kN which is 17.5% more than the companion specimen B2. In beam B4, the percentage of shear steel used in nearly equal to percentage of shear steel provided in B2.

The design load (100 kN) deflections of beams specimens, B1 without shear reinforcement is 3.99 mm, B2 with conventional two-legged shear reinforcement is 2.59 mm, B3 with 4 mm dia. inclined continuous reinforcement is 2.95 mm which has 13.9% more deflection than B2 and for B4 with 6 mm dia. inclined continuous reinforcement is 2.19 mm which is 15.5% less than B2. At service load of B2, i.e. (2/3 * (170) = 112 kN), the deflection was 2.98 mm at same load the deflection of B3 and B4 are 3.25 and 2.35 mm which is 9% more and 20.3% less than the companion specimen B2. At failure load, the deflection of B2 is 5.7 mm at that load B4 has a deflection of 4.05 mm which is 30% less compared to B2.

For B1 without shear reinforcement, the first crack of 0.16 mm started at 80 kN, at that load B2, B3 and B4 have crack widths of 0.14 mm, 0.09 mm and no crack observed, respectively. At design load, the crack widths for B1 and B2 are 0.36 and 0.22 mm and for B3 and B4 are 0.2 and 0.06 mm which is 10 and 72.7% less by the companion specimen B2, respectively. At service load of B2, i.e. (2/3 * (170) = 112 kN) the crack width was 0.28 mm at same load, the crack widths of B3 and B4 are 0.4 and 0.075 mm which is 42% more and 73.21% less than the companion specimen B2.

7 Conclusions

Following conclusions are drawn from the present study

1. The laced reinforced beams with equal percentage of shear steel used in conventional stirrups have shown greater ultimate load carrying capacity which is 17.5% more than their companion specimens.
2. At design load and ultimate loads, the deflections of laced reinforced beams reduced by 15.5% and 30% to their companion specimens, respectively.
3. At design load and ultimate loads, the crack widths of laced reinforced beams reduced by 72% to their companion specimens, respectively.
4. The specimens with laced reinforcements showed more ductility than the conventional vertical two-legged stirrups.
5. From the experimental investigation laced reinforcement with lacing angle of 50° for beams with respect to principal reinforcement achieved the improved ductility, lesser deflections and control in crack width than their companion specimens, so these are preferable lacing angles to RC elements.
6. From this investigation, we can conclude by using the same amount of reinforcement and by altering the pattern of shear reinforcement, the load carrying capacity has been increased, and deflection and crack widths have been greatly reduced which proved that laced reinforcement had achieved greater structural integrity.

References

1. Madheswaran, C. K., Gnanasundar, G., Gopala Krishnan, N. (2015). Performance of laced reinforced geopolymer concrete (LRGPC) beams under monotonic loading. *Advances in Structural Engineering*, 355–367.
2. Anandavalli, N., Lakshmanan, N., Iyer, N. R., Prakash, A., Ramanjaneyulu, K., Rajasankar, J., et al. (2012). Behavior of blast loaded laced reinforced concrete structure. *Defense Science Journal, 62*(5), 284–289.
3. Srinivasa Rao, P., Sarma, B. S., Lakshmanan, N., Stangenberg, F. (1996). Seismic behavior of laced reinforced concrete beams. In *Eleventh World Conference on Earthquake Engineering* (pp. no. 1740).
4. Tegos, I. A., Penelis, G. (1988). Seismic resistance of short columns and coupling beams reinforced with inclined bars. *ACI Structural Journal*, *85*(1), pp 82–88 January 1988.
5. Akshaya, S. G., Ananthakrishnan, R., Arunprasadh, V. B., Manikandan, G., Sanjeevi, R. (2006). Experimental studies on laced steel concrete composite elements extreme loading condition. *ISOR Journal of Mechanical and Civil Engineering*, pp. 54–61 (e-ISSN: 2278-1684, p-ISSN: 2320-334X).
6. Pauly, T. (1971). Simulated seismic loading of spandrel beams. *ASCE*, ST9–67, 2407–2419
7. SP 34: 1987. *Handbook on reinforced concrete and detailing*. Bureau of Indian Standards, March 1999.
8. IS 456: 2000. (2000). *Plain and reinforced concrete—Code of practice*. New Delhi, India: Bureau of Indian Standards.

Influence of Metakaolin and Silpozz on Development of High-Strength Concrete

P. Sarangi and K. C. Panda

Abstract Supplementary cementitious materials (SCM) have converted a fundamental part of high-strength and high-performance concrete. Using mineral admixtures as the replacement substance of cement in concrete has an affinity to increase by the future in order to provide greater sustainability in construction fields. This study investigates the coupled substitution of 20% of metakaolin (MK) and silpozz in ordinary Portland cement. This paper presents the influence of MK and silpozz on mechanical properties of concrete. Cement was partially replaced with up to 20% MK and silpozz with two types of *w/b,* i.e., 0.35 and 0.30. The test results revealed that substitution of MK and silpozz had significant effects on mechanical properties of high-strength concrete. For *w/b* 0.35, the concrete mix with 15% silpozz and 5% MK gave higher strength as compared to other mixes and exactly opposite combination gave increased strength for *w/b* 0.30. The strength of concrete appreciably increased in its early ages and also long-term strength can be achieved.

Keywords Metakaolin (MK) · Silpozz · Superplasticizer (SP)
Compressive strength · Split tensile strength · Flexural strength

1 Introduction

In recent decades, the construction sector has faced many challenges. The positive attitude of construction industry towards innovations will work as a catalyst for the development of durable, cheap, and new construction materials compared to

P. Sarangi
Department of Civil Engineering, SOA (Deemed to be University),
Bhubaneswar 751030, Odisha, India
e-mail: pratikshasarangi@gmail.com

K. C. Panda (✉)
Department of Civil Engineering, Government College of Engineering,
Kalahandi, Bhawanipatna 766002, Odisha, India
e-mail: kishoriit@gmail.com

A. Rama Mohan Rao and K. Ramanjaneyulu (eds.), *Recent Advances in Structural Engineering, Volume 1*, Lecture Notes in Civil Engineering 11,
https://doi.org/10.1007/978-981-13-0362-3_67

the conventional ones, resulting in low-cost, and energy-efficient structure. The worldwide demand for cement-based materials has increased for high-strength and high-performance concrete. Substitution of usual construction materials fully or partially with the industrial by-product (e.g., fly ash, rice husk ash, blast furnace slag, and silica fume) and natural product (limestone, calcined clay and pozzolan) improves the strength, durability, workability, toughness and makes it cost-effective. Some of the researchers have improved the strength of concrete using supplementary cementitious materials (SCM) and conducted experiment on the enhancement of strength using silpozz and rice husk ash such as Panda and Prusty [1]. The total percentage of replacement was done 20%. Three different water–binder ratios (*w/b*) were used, i.e., 0.375, 0.325, and 0.275. The study reveals that the percentage increase in strength at early age is more as compared to later ages. Kadri et al. [2] investigated the use of SCM in cement-based systems. The metakaolin (MK) and silica fume (SF) were replaced 10% with cement.

It was observed that the hydration heat of SF is greater than that of MK. The study showed that SF exhibits higher pozzolanic activities than MK [2]. The appropriate amount of superplasticizer was required to obtain the desired slump flow in MK and SF mortars.

Poon et al. [3] investigated the mechanical properties of the MK and SF concrete and demonstrated that MK concrete had relatively higher strength development than control specimen depending on the replacement level of MK and *w/b* ratio. MK and SF are the most popular mineral admixtures used in the production of high-strength concrete. However, the improvement of construction materials which provides technical and environmental reimbursement is the foremost challenge of the new millennium. Wild et al. [4] studied that the manner in which highly reactive pozzolans condensed silica fume (CSF) and MK influence the rate of strength improvement of concrete is highly complex. When MK and CSF replaced then they rapidly remove calcium hydroxide (CH) from mix and accelerate the hydration of cement.

The present study aims to reveal the comparative effectiveness of utilization of MK and silpozz on the mechanical properties of high-strength concrete using two different types of *w/b,* i.e., 0.35 and 0.30 with the required amount of superplasticizer to attain the desired workability.

2 Experimental Investigation

2.1 Materials

Ordinary Portland cement 43 grade (OPC), zone II fine aggregate, natural coarse aggregate (20 mm passing), MK, silpozz, and superplasticizer (SP)—(CONXL—PCE DM—360) in an adequate amount in the mixes to achieve desired slump value of 25–50 mm and potable water are used. The physical properties of these materials

Table 1 Physical properties of OPC, MK and silpozz

Physical properties	OPC	MK	Silpozz
Specific gravity	3.15	2 ± 0.1	2.3
Compressive strength			
3 days (MPa)	30	–	–
7 days (MPa)	43	–	–
28 days (Mpa)	51	–	–
Initial setting time (min)	121	–	–
Final setting time (min)	410	–	–

Table 2 Properties of aggregates

Properties	Value obtained experimentally as per IS:383-1970	
	Coarse aggregate	Fine aggregate
Specific gravity	2.78	2.68
Abrasion value (%)	47.46	–
Flakiness index (%)	21.18	–
Crushing value (%)	24.50	–
Impact value (%)	29.63	–
Water absorption (%)	0.22	0.80
Fineness modulus	6.93	2.76 (zone II)

are given in Table 1. The properties of aggregates obtained experimentally as per IS: 383-1970 [5] are presented in Table 2. The cementitious materials used in high-strength concrete mixes were ordinary Portland cement (OPC), MK, and silpozz. MK is highly pure kaolinitic clays which can be calcined at comparatively low temperature 600–700 °C to keep silica and alumina in amorphous state. Silpozz is an organic micro-silica, otherwise known as amorphous silica, with silica content of above 90% having particle size of 25 microns mostly.

2.2 Mix Proportions and Identification

The details of mix proportions found out according to IS: 10262-2009 [6] and mix identifications and quantities of this research were presented in Tables 3, 4, 5, and 6, respectively. Two mix proportions for two different types of *w/b* are prepared, i.e., 1:1.576:3.035 and 1:1.268:2.552 for the *w/b* 0.35 and 0.30, respectively. M40 grade concrete is designed as per standard specification IS: 10262-2009 to achieve the target mean strength 48.25 MPa for both the *w/b* (0.35 and 0.30). Total 12 mixes are prepared. Six mixes are prepared for each *w/b*.

The enhancement of concrete strength is carried out using two water–binder ratios. Both MK and silpozz are replaced combinedly by 20% and five set of concrete mixes are prepared for each *w/b* (i.e., M0S20, M5S15, M10S10, M15S5,

Table 3 Details of concrete mix (HC1) proportion along with identification

Concrete mix proportions	Mix identity
C 100% + MK 0% + S 0% + *w/b* 0.35 + SP 0.40%	HC1M0S0
C 80% + MK 20% + S 0% + *w/b* 0.35 + SP 0.44%	HC1M20S0
C 80% + MK 0% + S 20% + *w/b* 0.35 + SP 0.80%	HC1M0S20
C 80% + MK 5% + S 15% + *w/b* 0.35 + SP 0.51%	HC1M5S15
C 80% + MK 10% + S 10% + *w/b* 0.35 + SP 0.65%	HC1M10S10
C 80% + MK 15% + S 5% + *w/b* 0.35 + SP 0.50%	HC1M15S5

Table 4 Details of concrete mix (HC2) proportion along with identification

Concrete mix proportions	Mix identity
C 100% + MK 0% + S 0% + *w/b* 0.30 + SP 0.50%	HC2M0S0
C 80% + MK 20% + S 0% + *w/b* 0.30 + SP 0.51%	HC2M20S0
C 80% + MK 0% + S 20% + *w/b* 0.30 + SP 0.95%	HC2M0S20
C 80% + MK 5% + S 15% + *w/b* 0.30 + SP 0.65%	HC2M5S15
C 80% + MK 10% + S 10% + *w/b* 0.30 + SP 0.70%	HC2M10S10
C 80% + MK 15% + S 5% + *w/b* 0.30 + SP 0.55%	HC2M15S5

Table 5 Details of mix proportion (HC1) quantity per m^3 of concrete

Mix Identity	SCM replacement (%)	Cementitious materials per m^3 of concrete			NFA (kg)	NCA (kg)	SP (kg)	Water (kg)
		Cement (kg)	MK (kg)	SF (kg)				
HC1M0S0	0	425	0	0	670	1290	1.70	148.8
HC1M20S0	20	340	85	0	670	1290	1.87	148.8
HC1M0S20	20	340	0	85	670	1290	3.40	148.8
HC1M5S15	20	340	21.25	63.75	670	1290	2.17	148.8
HC1M10S10	20	340	42.5	42.5	670	1290	2.76	148.8
HC1M15S5	20	340	63.75	21.25	670	1290	2.12	148.8

and M20S0) and compared the value with control specimen (M0S0). HC1 indicates high-strength concrete for *w/b* 0.35 and HC2 indicates high-strength concrete for *w/b* 0.30. M and S are used for MK and silpozz, respectively.

2.3 Mixing, Casting, and Curing Details

The batching, mixing, and casting of concrete were accomplished properly. For curing, the specimens as shown in Fig. 1 were removed from the moulds after 24 h

Table 6 Details of mix proportion (HC2) quantity per m^3 of concrete

Mix Identity	SCM replacement (%)	Cementitious materials per m^3 of concrete			NFA (kg)	NCA (kg)	SP (kg)	Water (kg)
		Cement (kg)	MK (kg)	SF (kg)				
HC2M0S0	0	496	0	0	629	1266	2.48	148.8
HC2M20S0	20	396.8	99.20	0	629	1266	2.52	148.8
HC2M0S20	20	396.8	0	99.20	629	1266	4.72	148.8
HC2M5S15	20	396.8	24.80	74.40	629	1266	3.22	148.8
HC2M10S10	20	396.8	49.60	49.60	629	1266	3.47	148.8
HC2M15S5	20	396.8	74.40	24.80	629	1266	2.72	148.8

Fig. 1 After 24 h of casting

of casting and placed in water tank at normal temperature (27–30 °C) for 7, 28 and 90 days.

2.4 Testing

Slump cone test was performed for each mix to measure the desire slump value as Fig. 2. Compressive strength tests were performed using 150 mm cubic moulds. Three samples per batch were tested using compressive testing machine (CTM) with capacity of 3000 KN as shown in Fig. 3.

Split tensile strength tests were carried out using cylindrical mould of size 100 mm dia × 200 mm length. Three samples per mix were tested using compressive testing machine (CTM), and the average value was measured. Flexural strength tests were performed with prism mould of dimension 500 mm × 100 mm × 100 mm using flexural testing machine with capacity of 100 KN as shown in Fig. 3. The samples were tested and the average value was taken into consideration.

Fig. 2 Slump test

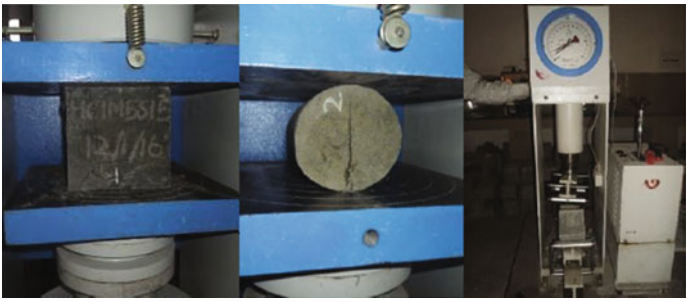

Fig. 3 Compression, split, and flexural strength test

3 Results and Discussion

3.1 Fresh Concrete Test Results

To achieve the desired workability, required amount of SP was added to the mixes. For *w/b* 0.30, the amount of SP was required slightly higher than that of *w/b* 0.35. For HC1 mixes, the slump values obtained in the range of 16–46 mm, whereas for HC2 mixes the values were 25–35 mm.

3.2 Hardened Concrete Test Results

3.2.1 Compressive Strength

The effect of MK and silpozz can be observed from the Figs. 4 and 5. The data concerning the compressive strength development with both the *w/b,* i.e., 0.35 and 0.30 and the ages of curing for the concrete incorporating MK and silpozz are presented in Fig. 6. The silpozz and MK-based concretes had consistently higher compressive strength than that of control specimen.

From Fig. 4, it may be observed that for *w/b* 0.35 the concrete mix with 15% MK and 5% silpozz gives higher compressive strength. The percentage increase in compressive strength of HC1M15S5 is 60.32% in its early stage, i.e., at 7 days, 47.56% at 28 days, and 30.29% at 90 days. The 28 days compressive strength of concrete with *w/b* 0.35 is observed as 90.60 MPa for specimen HC1M15S5.

From Fig. 5, it may be observed that, for *w/b* 0.30, the concrete mix with 5% MK and 15% silpozz combination gives higher compressive strength than all other specimens. The percentage increase in compressive strength of HC2M5S15 is 34.88% at its early stage, i.e., at 7 days, 34.49% at 28 days, and 26.07% at 90 days. The 28 days compressive strength of concrete with *w/b* 0.30 is observed as 102.15 MPa for specimen HC2M5S15.

In the figure, it may be observed that HC2 has more compressive strength than HC1 due to the addition of more amount of SP. Because of the low *w/b* of HC2 as

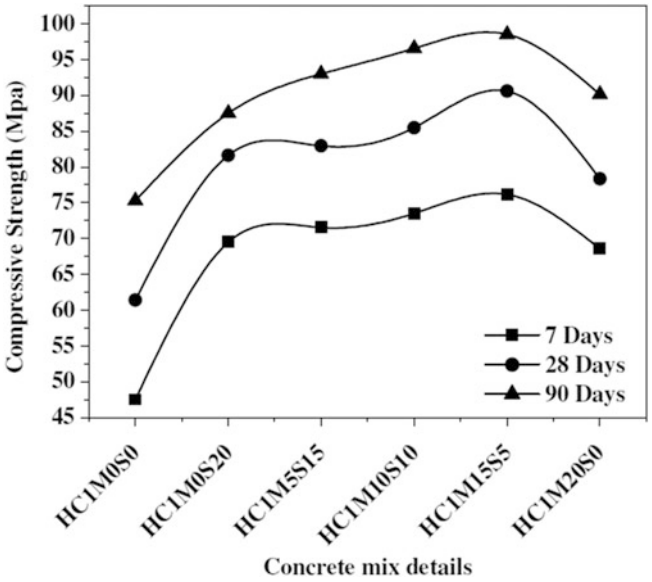

Fig. 4 Compressive strength versus HC1 concrete mix

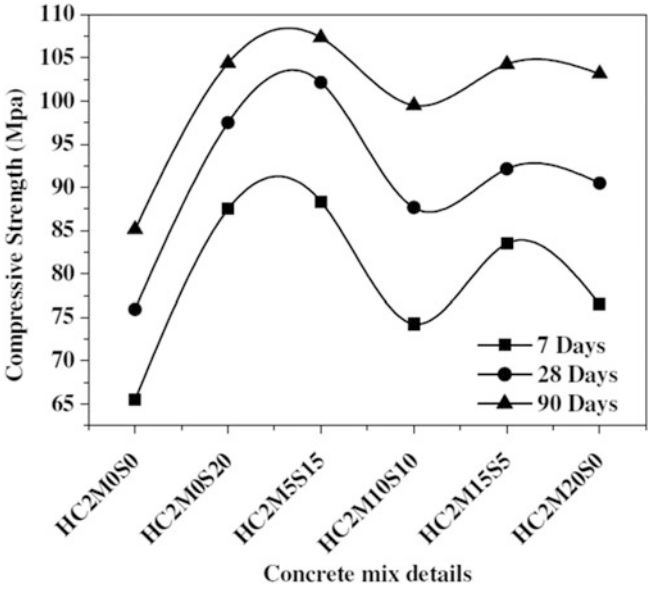

Fig. 5 Compressive strength versus HC2 concrete mix

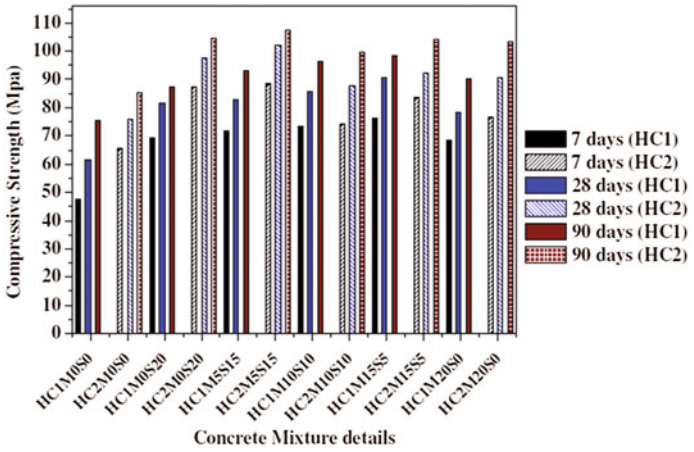

Fig. 6 Comparison of compressive strength for HC1 and HC2

compared to HC1 and the amount of SP added to the mixture is more. Addition of MK and silpozz improves the bond between the cement paste and aggregate particles which in turn significantly improves the strength of concrete.

3.2.2 Split Tensile Strength

Neville [7] reported that there is a direct proportionality between split tensile strength and compressive strength of concrete, i.e., while the compressive strength increased, the tensile strength also increased at a lower rate. From Figs. 7 and 8, it may be observed that the split tensile strength of the concrete mix with 10% of replacement of MK and silpozz is higher as compared to other specimens. The maximum strength observed in HC1M10S10 is 5.40 MPa at 28 days and the percentage increase in split tensile strength is 44.12% at 7 days, 22.73% at 28 days, and 26.32% at 90 days.

From Fig. 8, it may be observed that the maximum split tensile strength of concrete specimen HC2M10S10 is 5.85 MPa at 28 days which is 27.17% more as compared to control specimen. Due to more amount of SP addition in HC2 concrete, the strength is higher as compared to HC1 concrete.

Figure 9 illustrates the split tensile strength development pattern of HC1 and HC2 mixes. The maximum split tensile strength is observed in HC2M10S10 mix.

3.2.3 Flexural Strength

Figures 10 and 11 show the flexural strength with the different curing ages of concrete mix with combination of MK and silpozz replacement. Figure 10 illustrates that HC1M20S0 has maximum flexural strength and the increase in flexural

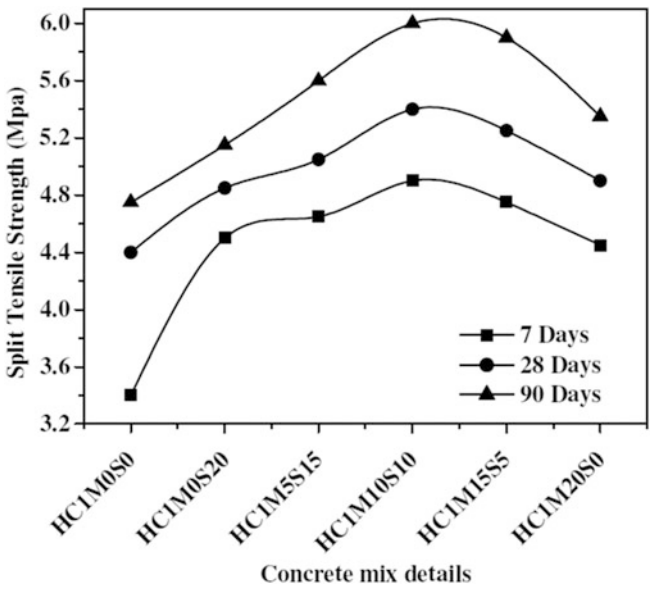

Fig. 7 Split tensile strength versus HC1 concrete mix

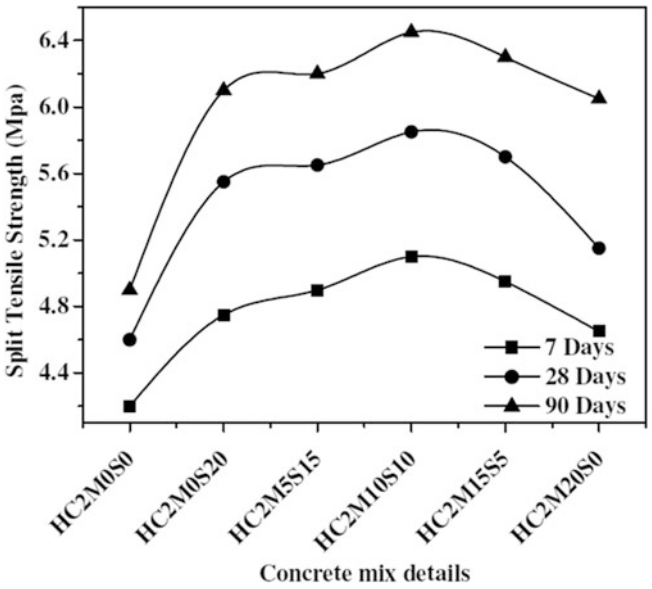

Fig. 8 Split tensile strength versus HC2 concrete mix

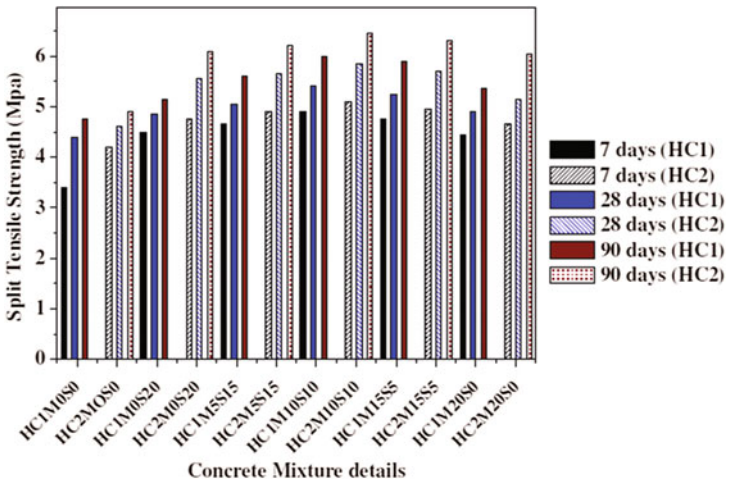

Fig. 9 Comparison of split tensile strength for HC1 and HC2

tensile strength is 33.33% at 7 days whereas in HC1M10S10, the maximum increased flexural tensile strength is 23.94 and 25% at 28 and 90 days, respectively. The rate of flexural strength development in MK is higher, as investigated by Yerramala et al. [8].

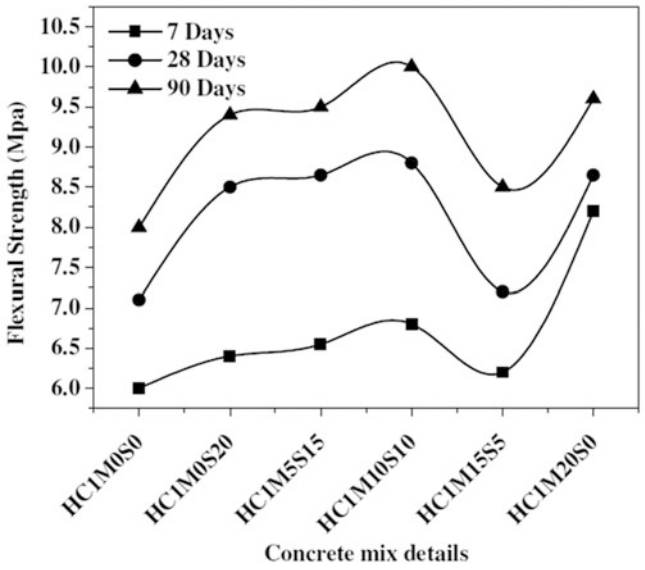

Fig. 10 Flexural strength versus HC1 concrete mix

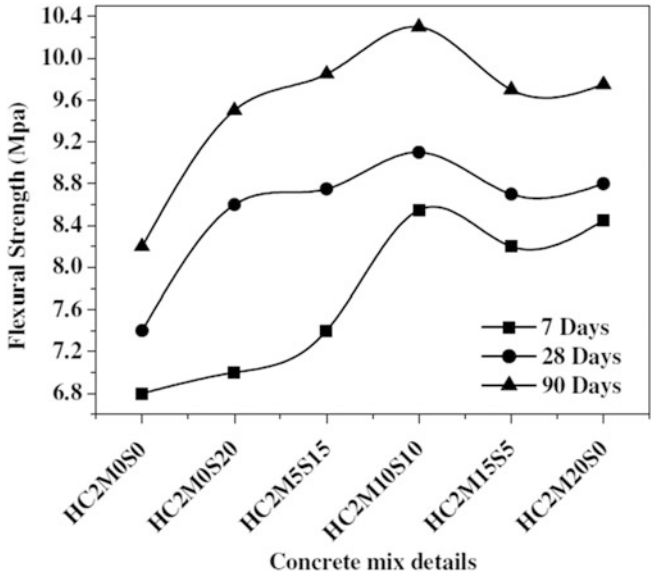

Fig. 11 Flexural strength versus HC2 concrete mix

Figure 11 represents that the percentage change in flexural strength is maximum in concrete when cement is replaced with silpozz in 10% and MK in 10%, i.e.,

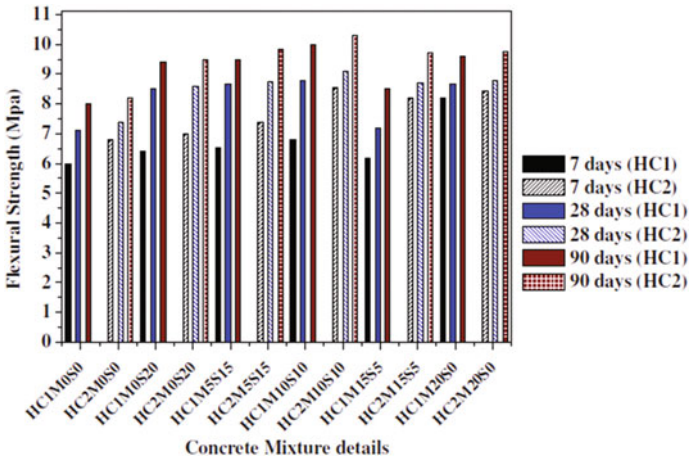

Fig. 12 Comparison of flexural strength for HC1 and HC2

HC2M10S10. The increase in flexural strength of HC2M10S10 is 25.73% at 7 days, 22.97% at 28 days, and 25.61% at 90 days as compared to control specimen.

It is seen in Fig. 12 that the relative strength of HC2M15S5 is greater than that of HC1M15S5, i.e., 23.26% at 7 days, 20.83% at 28 days, and 14.12% at 90 days. The results suggest that the replacement between 10 and 20% is advantageous for long-term rate of strength gain.

4 Conclusions

Based on the studies, the following conclusions may be drawn:

- As water–binder ratio decreases the compressive strength, split tensile strength and flexural strength of HSC increase.
- The improvement of strength in early age is higher as compared to the later age due to the presence of SP and micro-silica effect of silpozz and MK.
- Requirement of SP for MK based concrete was lesser than that of Silpozz based concrete.
- For HC1, the concrete mix with 15% silpozz and 5% MK gives higher compressive strength whereas for HC2 5% silpozz and 15% MK gives higher compressive strength as compared to other mixes.
- For flexural and split tensile strength, the concrete mix with 10% silpozz and 10% MK gives higher strength than other mixes for both HC1 and HC2.
- HC2 specimens have higher strength than that of HC1 because of the reduction of water amount in HC2 and addition of more SP than HC1.

- The bond between cement paste and aggregate particles increases due to combined effect of MK and SP.

Acknowledgements The authors would like to thank SOA (Deemed to be University) for the support of conducting the experimental work and Golden Micro Chemicals (Maharashtra), CHEMCON tecsys (Chennai) and NK enterprises (Jharsuguda), Aditya Enterprises (Bhubaneswar) for supplying the materials.

References

1. Panda, K. C., & Pusty, S. D. (2015). Influence of silpozz and rice hask ash on enhancement of concrete strength. *Advances on Concrete Construction, 3,* 203–221.
2. Kadri, E. H., Kenai, S., Ezziane, K., Siddique, R., & Schutter, G. D. (2011). Influence of metakaolin and silica fume on the heat of hydration and compressive strength development of mortar. *Applied Clay Science, 53,* 704–708.
3. Poon, C. S., Kou, S. C., & Lam, L. (2006). Compressive strength, chloride diffusivity and pore structure of high performance metakaolin and silica fume concrete. *Construction and Building Materials, 23,* 858–865.
4. Wild, S., Khatib, M. R., & Jones, A. (1996). Relative strength, pozzolanic activity and cement hydration in super plasticised metakaolin concrete. *Cement and Concrete Research, 26,* 1537–1544.
5. IS: 383-1970. *Indian standard specification for coarse and fine aggregates from natural sources for concrete* (second revision). New Delhi, India: Bureau of Indian Standards.
6. IS: 10262:2009. *Concrete mix proportioning-guidelines*. New Delhi, India: Bureau of Indian Standards.
7. Neville, A. M. (1996). *Properties of concrete* (4th and final ed.). England: Addison Wesley Logman.
8. Yerramala, A., Ramachandurdu, C., & Bhaskar Desai, V. (2013). Flexural strength of metakaolin ferrocement. *Composites: Part B, 55,* 176–183.

Influence of Particle Packing Method on Sustainable Concrete Using Fly Ash and Recycled Aggregates

Sushree Sunayana and Sudhirkumar V. Barai

Abstract The construction industry, using concrete most widely, is not sustainable as (i) it consumes large quantities of natural resources (for aggregates), (ii) The principal binder in concrete is cement whose production is a major contributor to greenhouse gas emissions (iii) Performance of concrete structures relies on rapid strength gain rather than durability and long-term effects. So, use of fly ash and recycled aggregates (RA) in concrete production may become a sustainable construction material with less environmental and economic impact if the performance of concrete structures is satisfied. Effect of RA and fly ash on compressive strength (CS) of concrete is addressed in present context by adopting particle packing method of mix design and modifying mixing techniques. Theoretical and experimental packing density is obtained and compared. A comparison of PPM and Indian standard (IS) code method of mix design is being done for the observed CS. Results concluded that PPM is suitable in terms of compressive strength for RAC with fly ash.

Keywords Recycled aggregates · Packing density · Compressive strength Particle packing method

1 Introduction

Achieving sustainability in construction practices is a major concern nowadays. Rapid industrialization and urbanization result in the generation of huge quantities of construction and demolished wastes. Concrete, the most common construction material, uses large quantities of nonrenewable resources in the form of aggregates

S. Sunayana · S. V. Barai (✉)
Department of Civil Engineering, Indian Institute of Technology Kharagpur, Kharagpur 721302, West Bengal, India
e-mail: skbarai@civil.iitkgp.ernet.in

S. Sunayana
e-mail: sushree111@gmail.com

A. Rama Mohan Rao and K. Ramanjaneyulu (eds.), *Recent Advances in Structural Engineering, Volume 1*, Lecture Notes in Civil Engineering 11,
https://doi.org/10.1007/978-981-13-0362-3_68

(75%). Concrete construction also requires large quantities of cement, the production of which results in the release of greenhouse gas emissions thereby affecting the environment adversely. So, there is an urgent need to address the issue of natural resources depletion and waste disposal problem. Use of recycled aggregates (RA) in concrete producing recycled aggregate concrete (RAC) has been evolved as one of the emerging solutions for present scenario. Fly ash has been used to replace cement partly in conventional concrete as in Ref. [1].

The use of fly ash in recycled aggregate concrete has been studied in literatures. Fly ash at 0, 25, and 35% by weight replacements of cement reduced the compressive strength (CS), tensile strength, and static modulus of elasticity values of the concrete at all ages. However, the use of fly ash as a substitute for cement improved resistance to chloride ion penetration and decreased the drying shrinkage and creep of the RAC Ref. [2].

Pulverized fly ash at 30% recovered the reduction in compressive strength of concrete containing recycled aggregate at 7, 28, 90, and 180 days observed in Ref. [3]. Use of ground fly ash up to 35% by weight of cement can increase the compressive strength for *w*/*b* of 0.45 and up to 20% part replacement can increase the CS at *w*/*b* of 0.55 and 0.65 as studied in Ref. [4]. For RAC, various mix design methods have been used such as direct weight replacement method, equivalent mortar volume method (Ref. [5]) and direct volume replacement method. Particle packing method (PPM) of mix design has been studied for natural aggregate concrete through various theoretical models such as Toufar model, Dewar model, De Larrard Linear Packing Model (LPM), De Larrard Compressible Packing Model (CPM) and Modified Compressible Packing Model Ref. [6] and also experimentally as in Refs. [7, 8]. Two-stage mixing approach (TSMA) was developed in Ref. [9] and triple mixing method were proposed in Ref. [10] for concrete with the use of mineral admixture.

2 Research Significance

The behavior of RAC with fly ash is not well understood from the limited study as mentioned in the literature. In this paper, the effect of fly ash on the behavior of concrete produced using 100% replacement of natural coarse aggregates with recycled coarse aggregates using PPM mix design is studied. Concrete with only natural aggregates without the addition of fly ash is used as control concrete.

3 Materials

The behavior of concrete primarily depends on the properties of its constituents such as aggregates, cement, the interface characteristics, etc.

3.1 Cement and Fly Ash

Ordinary Portland cement (OPC) 43 Grade cement is used and its characterization is done according to IS: 4031-1988 [11] as shown in Table 1. Fly ash characterization as per IS: 3812-2003 (part II) and chemical analysis for cement and fly ash as per IS: 4032:1985 are performed as presented in Table 2.

3.2 Aggregates

Crushed dolerite was used as the natural aggregate and recycled aggregate collected from a recycling facility in New Delhi was used. The nominal sizes of the natural and recycled coarse aggregates are 20 mm and their particle size distributions are done as per particle packing method (PPM) The physical and mechanical properties

Table 1 Properties of cement and fly ash

Property		Values
Consistency (%)		29
Fineness modulus		2.65
Specific gravity(cement)		3.13
Specific gravity(fly ash)		2.29
Specific surface area		306
Setting time(min)	Initial	75
	Final	295
Compressive strength	3 days	30.46
	7 days	44.4
	28 days	55.06

Table 2 Chemical composition of cement and fly ash

Compounds	Cement (%)	Fly ash (%)
SiO_2	22.48	55.805
Al_2O_3	7.12	35.17
Fe_2O_3	3.01	4.61
CaO	59.03	1.546
MgO	1.77	0.574
K_2O	1.33	1.821
Na_2O	0.36	0.094
TiO_2	0.37	1.907
MnO_2	0.05	0.069
SO_3	4.20	0.255
L.O.I (1,000 °C)	3.846	2.50
Moisture content	0.127	0.062

Table 3 Physical properties of coarse (NA and RA) and fine aggregates

Coarse aggregate type	Size of aggregate (mm)	Specific gravity	Water absorption
NCA	20	2.9	1.59
	12.5	2.88	1.67
	10	2.8	1.06
RCA	20	2.54	3.63
	12.5	2.53	3.4
	10	2.43	4.2
	6.3	2.29	5.09

Table 4 Mechanical properties of coarse (NA and RA) and fine aggregates

Property	NCA	RCA
Flakiness index (%)	19.14	15.17
Elongation index (%)	49.42	18.24
Los Angeles abrasion value (%)	14.4	34.08
Impact value	13.87	24.23
Crushing value	17.66	23.32

of the coarse aggregate obtained as per BIS (IS:2386(Part3)-1963) [12] are shown in Tables 3 and 4. Locally available river sand confirming to zone II specification of BIS (IS 383-1970) is used as the fine aggregate in the concrete mixtures.

3.3 Water Reducing Admixture (WRA)

To maintain a slump of 120 ± 20 mm, this chemical admixture is added. The dosage of WRA percentage is found out as per trials based on total cementitious materials content.

4 Concrete Mix Design

The mix design procedure of concrete mix using PPM and details of quantities of materials are calculated in the following section.

4.1 Calculation of Packing Density

There is no specific mix design process for RAC. Here, mix design is done using particle packing method (PPM) and the results are compared with Indian Standard

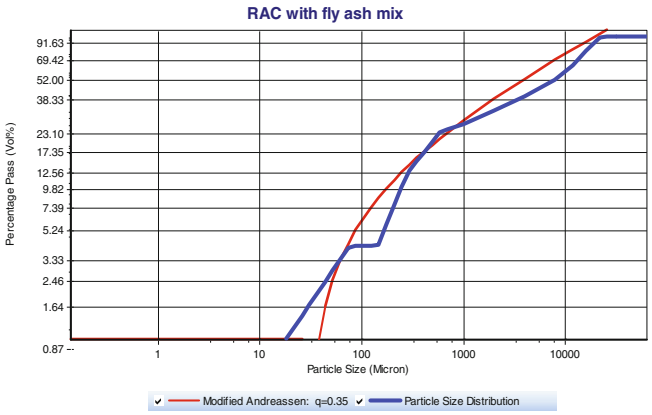

Fig. 1 Comparison between theoretical and modified Andreassen curve

(IS) method. To calculate theoretical packing density (PD), the theoretical volumetric proportion of aggregates to obtain maximum PD is obtained from EMMA mix analyzer by using modified Andreassen curve. Distribution coefficient is varied within the range to get the gradation curve that matches with Anderson curve which is as shown below in Fig. 1.

4.2 Theoretical Packing Density Using CPM

Then the theoretical PD is obtained using compressible packing model (CPM).

Virtual packing density of a mixture containing n size classes with category i being dominant is expressed as:

$$\beta_{ti} = \frac{\beta_i}{1 - \sum_{j=1}^{i-1}\left[1 - \beta_i + b_{ij}\beta_i\left(1 - 1/\beta_j\right)\right]r_j - \sum_{j=i+1}^{n}\left[1 - a_{ij}\beta_i/\beta_j\right]r_j} \tag{1}$$

For mono sized particle class β_j, experimentally calculated PD

$$\alpha_j = \beta_j / \left(1 + \frac{1}{k}\right) \tag{2}$$

Coefficient representing loosening effect

$$a_{ij} = \sqrt{1 - \left(1 - d_j/d_i\right)^{1.02}} \tag{3}$$

Coefficient representing wall effect

$$b_{ij} = 1 - \left(1 - d_i/d_j\right)^{1.5} \tag{4}$$

Compaction index

$$K = \sum k_i = \sum_{i=1}^{n} \frac{r_i/\beta_i}{(1/\alpha_t - 1/\beta_{ti})} 1 \tag{5}$$

Using the proportions of aggregates obtained from the theoretical gradation curve from EMMA, maximum theoretical packing density is obtained as 0.758 in CPM model. The virtual packing density physically represents the maximum PD achieved if the aggregates are placed one by one and packed accordingly.

4.3 Experimental Packing Density

Experimental packing density is obtained as follows which is used further for the mix design steps given in Ref. [8].

- Bulk density of coarse aggregate (20 mm and 12.5 mm) is determined for different proportions by mass (90:10, 80:20, 70:30, and so on).
- Packing density is determined for different mixture combination and the proportion at which maximum packing density achieved was found out.
- With this proportion of bigger size aggregates, smaller size of aggregate (10 mm) is added at different proportions by mass. (90:10, 80:20, 70:30 and so on).
- These processes are repeated for smaller size aggregates (6.3 mm and fine aggregate) to find out the proportions of all participating aggregates for which maximum possible packing density (PD) can be achieved.

$$\text{Packing density} = \sum \frac{\text{bulk density} \times \text{weight fraction}}{\text{specific gravity}} \tag{6}$$

$$\text{Void content}(\%) = \sum \frac{\text{specific gravity} - \text{bulk density}}{\text{specific gravity}} \times 100 \tag{7}$$

The experimental packing density obtained as per methods given above and the bulk density and corresponding PD obtained for different proportions of aggregates to select the proportions for maximum PD are shown in Fig. 2. There is a good match observed between theoretical and experimental PD. By knowing the aggregate proportions of different coarse aggregate sizes (20, 12.5, 10 and 6.3 mm)

for which maximum packing density is achieved and using the value of maximum packing density as 0.728, mix design is done as per PPM mentioned in Ref. [8].

Water-to-binder (*w/b*) ratio of 0.45 is maintained for all the mixes as obtained from trials mixes. Fly ash is used as 20 and 30% of the total cementitious content for RAC mixes. RAC mixes contain 100% replacement of natural aggregates with RA. Three types of concrete mixes are prepared for each mix design method, i.e., NAC mix with 100% natural aggregates without any addition of mineral admixture and superplasticizer (NAC), RAC mix with 100% recycled aggregates with 20% (RAC + FA20) and 30% replacement of cement by fly ash (RAC + FA30). For Indian standard (IS) method of mix, design IS 10262:2009 [13] code is followed.

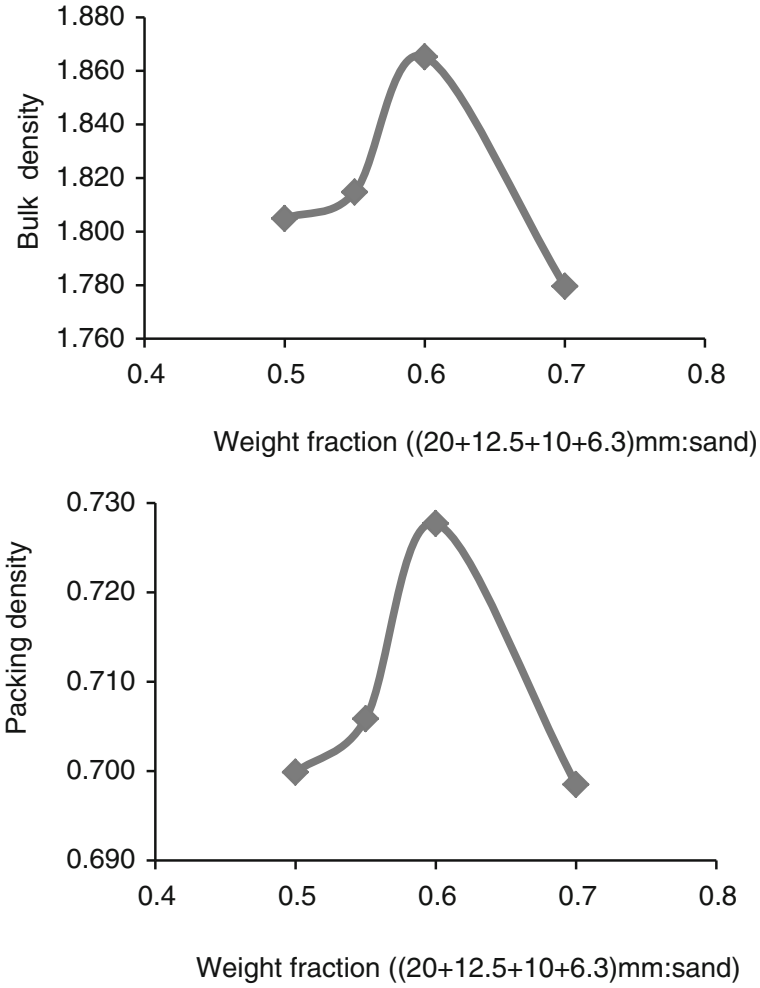

Fig. 2 Experimental bulk density and corresponding packing density curve

All mixes are designed for M30 grade of concrete. Adjustments are made in quantities of materials for water absorption and moisture content. The difference in quantity of RCA and NA is due to its density. The mix proportion of concrete used for the mixes is shown in Table 5.

5 Mixing Process and Specimen Casting

Triple mixing method [10] is used for mixing process which is proved to be an effective method in terms of compressive strength and other mechanical properties for concrete with use of mineral admixture.

For each concrete mixture, 150 mm cubes and 150 mm × 300 mm cylinders were prepared for compressive strength tests. Concrete mix for M30 grade is designed using PPM and IS code method. Specimens were tested at 7, 28, and 90 days of curing.

6 Tests and Results

Compressive strength test is done using a compression testing machine of 300 ton capacity in accordance with BIS (IS: 516-1959) [14]. The concrete mixtures are tested for Indian standard (IS) method and particle packing method of mix design. For selection of *w/b* ratio, trial mixes were prepared considering *w/b* ratio of 0.4, 0.43, 0.45, and 0.47. Variation of 28-day compressive strength (CS) with change in *w/b* ratio is shown in Table 6. Compressive strength decreases with increase in *w/b* ratio for all the mix types. The target strength is achieved for *w/b* 0.45 and the variation of CS at this *w/b* ratio for all the mixes is less compared to other *w/b* ratio. So, it is considered in the mix design for all the concrete mixes. CS variation with *w/b* ratio is plotted in Fig. 3. RAC + FA30 mix shows lower CS at 28 days in compared to RAC + FA20 mix by 3.2–5.5%. Increase in CS for RAC + FA20 mix in compared to NAC in some of the *w/b* ratio may be due to improvement in microstructure of the concrete in the latter case due to proper coating of fly ash on aggregates because of the mixing method adopted.

Effect of curing ages (7, 28, and 90 days) on compressive strength of concrete mixes is shown in Table 7. Three cubes have been used for each test and the average values of these results are reported. For NAC mixes, the CS variation with curing ages is shown in Fig. 4. It is observed that with increase in curing ages there is increase in CS of NAC mix for considered *w/b* ratio. The 7 days CS is 59.3–64.9% of the 28 days strength. There is an increase of 27.74–32.92% from 28 to 90 days compressive strength.

Figure 5 represents the variation of CS at different curing ages for RAC + FA20 mix. It is observed that 7 days strength is 52–55% of 28 days strength indicating

Table 5 Mix design proportions

Mix type	Method	*w/b*	Cement	Fly ash	NA		Sand	RCA	
					20–12.5 mm	10–6.3 mm		20–12.5 mm	10–6.3 mm
RAC + FA20	PPM	0.45	360.83	90.21	–	–	658.87	751.11	237.19
RAC + FA30	PPM	0.45	315.73	135.31	–	–	659.3	761.99	242.71
NAC	IS code	0.45	438.13	–	755.77	485.63	610.19	–	–
RAC + FA20	IS code	0.45	325.11	139.33	–	–	599.61	663.74	415.45
RAC + FA30	IS code	0.45	371.55	92.88	–	–	599.61	663.74	415.45

Table 6 Variation of 28-day compressive strength (CS) with *w/b* ratio

w/b ratio	NAC	RAC + FA20	RAC + FA30
0.4	51.27	48.52	46.25
0.43	44.29	44.58	43.09
0.45	42.75	43.21	41.82
0.47	40.51	42.57	40.2

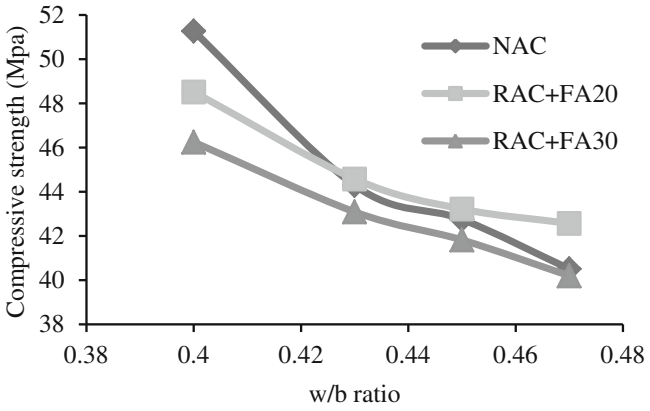

Fig. 3 Variation of CS (28-day) with *w/b* ratio

Table 7 Compressive strength variations with *w/b* ratio

Age (day)	Mix	*w/b*			
		0.4	0.43	0.45	0.47
7	NAC	30.87	28.74	25.35	23.69
28		51.27	44.29	42.75	39.51
90		65.49	58.87	55.96	55.85
7	RAC + FA20	26.6	23.49	22.59	22.05
28		48.52	44.58	43.22	42.57
90		58.4	52.58	50.64	49.3
7	RAC + FA30	22.09	21.74	17.57	17.1
28		46.25	43.09	41.82	40.2
90		52.4	48.26	46.74	44.67

slower strength gain due to fly ash replacement than NAC. There is an increase of 15.8–20.3% from 28 to 90 days strength.

Figure 6 shows the relation between CS and curing ages for RAC + FA30 mix. The development of strength at 7-day is observed to be slower than the other two mixes considered, i.e., 42–50% of 28 days strength is achieved at 7 days. At 90-day, 11–13% strength gain is achieved compared to 28-day strength. The strength gain in long term is smaller in case of recycled aggregate concrete mix with

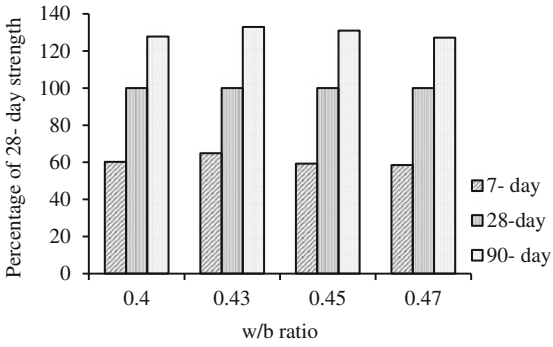

Fig. 4 Variation of compressive strength with curing ages at different *w/b* (NAC mix)

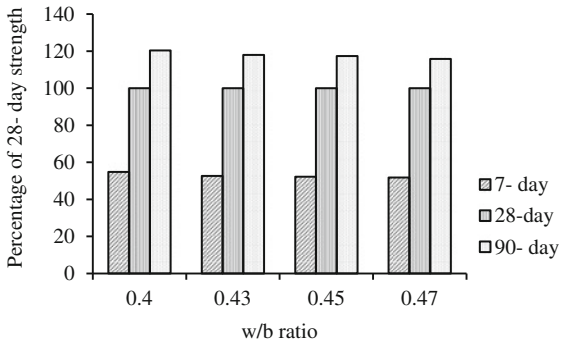

Fig. 5 Variation of compressive strength with curing ages at different *w/b* (RAC + FA20 mix)

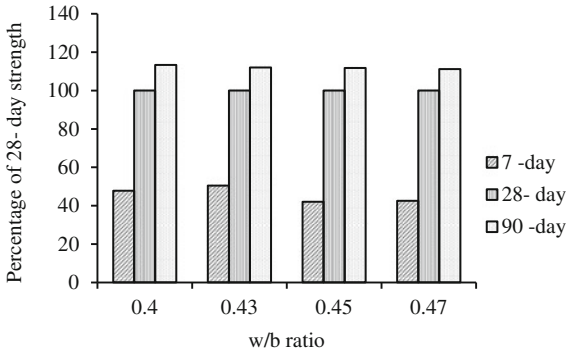

Fig. 6 Variation of compressive strength with curing ages at different *w/b* (RAC + FA30 mix)

fly ash in compared to NAC mixes may be due to adhered mortar content in recycled aggregates. The plots represent CS in percentage of 28-day strength.

A comparison of hardened concrete property, i.e., compressive strength of the considered mixes in the PPM mix design adopted in the present study and IS code method is done. CS at 28-day is observed and the values in Table 8 represents relative CS in compared to NAC in IS method of mix design for both the cubes and cylinder specimen considered in the present study. Figure 7 shows the comparison

Table 8 Comparison of CS of different concrete mix

Mix	Mix design method	Cube strength	Cylinder strength
NAC	IS	46.07	30.13
	PPM	42.75	–
RAC + FA20	IS	43.83	25.60
	PPM	43.22	26.01
RAC + FA30	IS	41.24	24.95
	PPM	41.82	25.09

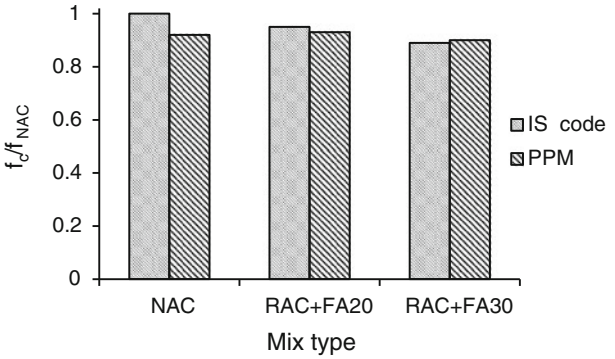

Fig. 7 Comparison of compressive strength in PPM and IS code method

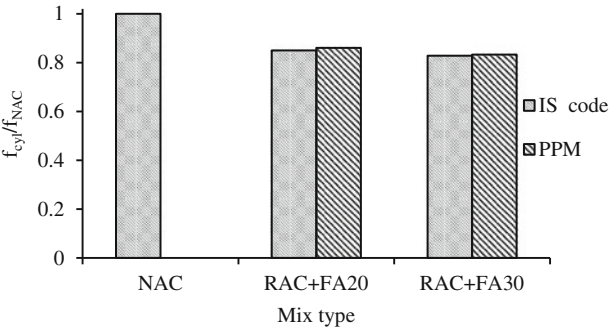

Fig. 8 Comparison of 28-day cylinder compressive strength with PPM and IS code method

which indicates that there is not much difference in the relative strength of all the mixes considered at 28-day in both the method.

Increase in compressive strength of RAC + FA20 as compared to NAC in PPM may be due to pozzolanic property of fine particles of fly ash. It may be attributed to the improvement in microstructure and filling up of micro-cracks already present in recycled aggregates due to mixing method involving coating of fly ash.

The effect of RAC with 20 and 30% replacement of fly ash is also observed in case of cylinder strength in compression as shown in Fig. 8. The strength relative to NAC designed with IS code method is plotted. The cylinder strength is observed to be approximately 60–65% of cube strength. Failure in cylinders is less affected by the restraining effect of the platens and these are cast and tested in the same position.

7 General Discussions

- Particle packing method of mix design was followed experimentally and also verified theoretically to get the proportioning of aggregates for maximum packing density.
- The fresh (slump) and hardened concrete property (compressive strength) of recycled aggregate concrete mix incorporating fly ash were studied.
- Slow rate of strength gain is observed for RAC with fly ash mixes in compared to NAC mix but the target strength was achieved at 28 days.
- Increase in long-term strength at 90 days though lower than natural aggregate concrete was significant in case of RAC with fly ash, i.e., approximately 20% for RAC + FA20 mix and 13% for RAC + FA30 mix.

8 Conclusions

In the present study, PPM mix design method is used both theoretically and experimentally for RAC with fly ash. It showed nearly equivalent or higher results in terms of compressive strength compared to Indian standard method. Hence, PPM can be used for such concrete mix as it has other advantages in terms of minimization of cement content and voids which may have other advantageous effects on performance properties of concrete.

Acknowledgements First author gratefully acknowledges the financial support provided for the project on "Sustainable and Cost Effective Housing by using Recycled Aggregate Based Concrete" under the mega project—Future of Cities by MHRD, Government of India. Authors gratefully acknowledge the support extended by IL&FS Environmental Infrastructure and Services Ltd. Plant (New Delhi) for providing recycled aggregates.

References

1. Atis, C. D. (2004). High-volume fly ash concrete with high strength and low drying shrinkage. *Materials in Civil Engineering ASCE, 15*(2), 153–156.
2. Kou, S., & Poon, C. (2008). Influence of recycled aggregates on long term mechanical properties and pore size distribution of concrete. *Cement & Concrete Composites, 33*(2), 286–291.
3. Ann, K., Moon, H., Kim, Y., & Ryou, J. (2008). "Durability of recycled aggregate concrete using pozzolanic materials. *Journal of Waste Management, 28*(6), 993–999.
4. Somna, R., Jaturapitakkul, C., Chalee, W., & Rattanachu, P. (2012). Effect of the water to binder ratio and ground fly ash on properties of recycled aggregate concrete. *Materials in Civil Engineering, 24*(1), 16–22.
5. Fathifazl, G. (2009). New mixture proportioning method for concrete made with coarse recycled concrete aggregate. *Materials in Civil Engineering, 21*(10), 601–611.
6. De Larrard, F., & Sedran, T. (1994). Optimization of ultra-high-performance concrete by the use of a packing model. *Cement and Concrete Research, 24*(6), 997–1009.
7. Jacobsen, S., & Arntsen, B. (2007). Aggregate packing and void saturation in mortar and concrete proportioning. *Materials and Structures, 41*(4), 703–716.
8. Raj, N., Patil, S. G., & Bhattacharjee, B. (2014). Concrete mix design by packing density method. *IOSR Journal of Mechanical and Civil Engineering, 11*(2), 34–46.
9. Tam, V. W., Gao, X., & Tam, C. (2005). Micro structural analysis of recycled aggregate concrete produced from two-stage mixing approach. *Cement and Concrete Research, 35*(6), 1195–1203.
10. Kong, D., Lei, T., Zheng, J., & Ma, C. (2010). Effect and mechanism of surface-coating pozzalanics materials around aggregate on properties and ITZ microstructure of recycled aggregate concrete. *Construction and Building Materials, 24*(5), 701–708.
11. IS:4031. (1988). *Methods of physical tests for hydraulic cement part II,III,IV,V and VI*. New Delhi, India: Bureau of Indian Standards (Reaffirmed 2000).
12. IS:2386. (1963). *Indian standards methods of tests for aggregates for concrete part I,III and IV*. New Delhi, India: Bureau of Indian Standards.
13. IS:10262. (2009). *Indian standards concrete mix proportioning guidelines*. New Delhi, India: Bureau of Indian Standards.
14. IS: 516. (1959). *Indian standards methods of tests for strength of concrete*. New Delhi, India: Bureau of Indian Standards (Reaffirmed 2004).

Glass Fibre Reinforced Gypsum Panels for Sustainable Construction

S. R. Gouri Krishna, Philip Cherian, Devdas Menon and A. Meher Prasad

Abstract The tremendous housing need of India is causing the depletion of virgin building materials. In an era of scarce resources, sustainable solutions are always preferable. Glass Fibre Reinforced Gypsum (GFRG) technology is one such solution where all the structural members are constructed using hollow panels infilled with reinforced concrete (RC), as per structural design. This paper discusses the sustainability of construction using GFRG panels in terms of embodied energy and indoor thermal comfort. The case study building at IIT Madras campus was found to have lesser embodied energy compared to conventional buildings. The result is significant considering the fact that the building sector consumes 40% of the total energy in world. Also, the inside temperature was found to be lesser by 2 °C which will help in reducing the air conditioning requirement of the building and thereby the operational energy.

Keywords GFRG · Embodied energy · Sustainable construction

1 Introduction

There is a great need to find innovative solutions to tackle the booming problem of housing shortage in India, distinctly for the poverty-stricken people of our society. In particular, there is a necessity to address the shelter needs of the lower income

S. R. Gouri Krishna · P. Cherian · D. Menon (✉) · A. M. Prasad
Department of Civil Engineering, Indian Institute of Technology Madras, Chennai 600036, India
e-mail: dmenon@iitm.ac.in

S. R. Gouri Krishna
e-mail: gouriksr@gmail.com

P. Cherian
e-mail: philiph.cherian@gmail.com

A. M. Prasad
e-mail: prasadam@iitm.ac.in

A. Rama Mohan Rao and K. Ramanjaneyulu (eds.), *Recent Advances in Structural Engineering, Volume 1*, Lecture Notes in Civil Engineering 11,
https://doi.org/10.1007/978-981-13-0362-3_69

groups and their aspirations. The challenge is to make these aspirations a reality, by providing an affordable solution that is also fast. Ideally, the solution should be scalable—to reach the masses—and should be quickly buildable. There would be significant demand for construction materials such as cement, steel, burnt clay bricks and water in order to fulfill this huge demand. While chasing this big target, the requirement for future generation should also be kept in mind. These requirements, rapidity, affordability and sustainability, oblige to the promotion of innovative new materials and methods of construction. Although there are a number of solutions for resolving the housing shortage problem, the scope of this paper focusses on one such solution using Glass Fibre Reinforced Gypsum (GFRG) panels. This holds the promise of providing sustainable, rapid and affordable mass housing.

GFRG is a new building panel product, known commercially as Rapidwall® in the industry. GFRG panels are lightweight load-bearing panels that are most suitable for rapid mass-scale building construction. They are manufactured out of gypsum reinforced by special glass rovings and were first introduced in Australia in 1990. Panels are manufactured to a standard size of 12 m × 3 m × 0.124 m and every 1 m of panel houses four cavities of inner dimension 230 × 94 mm as shown in Fig. 1.

The technology found its roots in India in 2003 and since then, several buildings were constructed using GFRG load-bearing panels, without any beams and columns. Studies conducted in India and elsewhere have contributed to ensure satisfactory structural performance of the individual components as well as the system as a whole. But in the present scenario of construction, sustainability also plays a key role which cannot be fulfilled by the fast depleting conventional construction materials. GFRG panels, which are manufactured in India out of the industrial fertilizer waste, are fairly competent in this aspect.

The term sustainability is applicable to materials as well as building as a whole. A material will be termed as sustainable, when it satisfies certain criteria in manufacturing, usage and disposal stages [1]. Numerically, sustainability is expressed in terms of CO_2 emission rate and embodied energy (total energy associated with the manufacturing of material, starting from the extraction of components). The green rating of a building depends on several factors such as selection of site, energy efficiency, water conservation, materials and resources used, indoor environment quality, provision for rainwater harvesting, waste management, etc. Two rating systems, namely Leadership in Energy and Environmental Design (LEED) Green

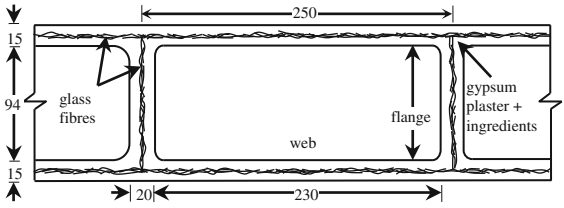

Fig. 1 Cross section of GFRG panel

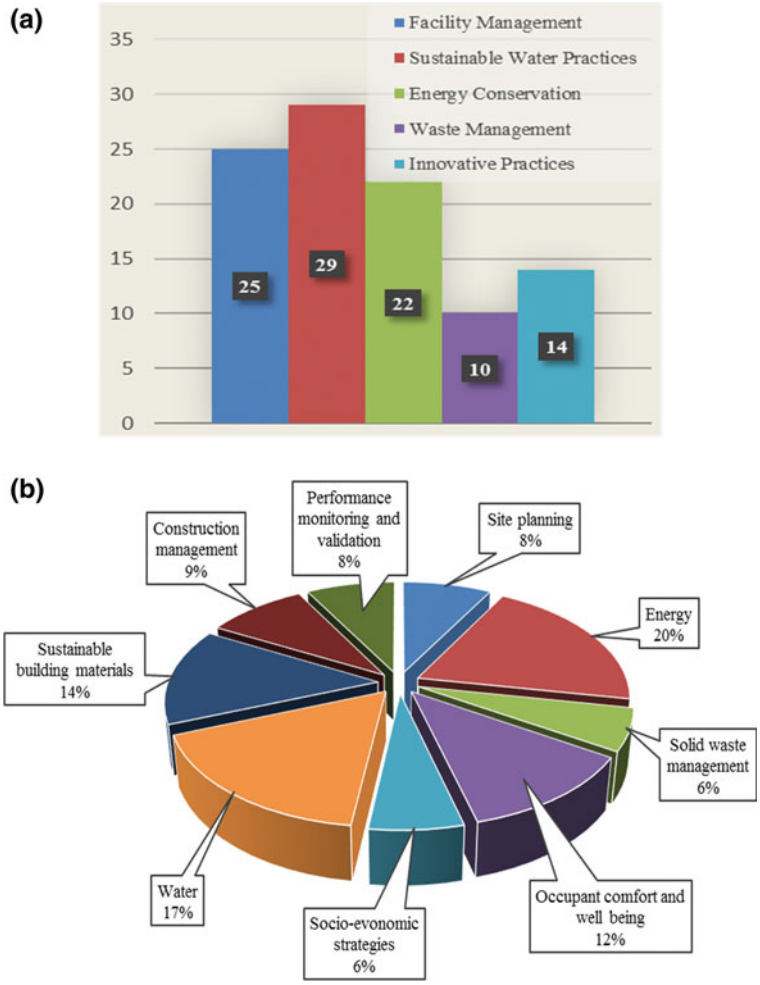

Fig. 2 **a** Weightage for various factors according to LEED [2]. **b** Weightage for various factors according to GRIHA [3]

Building Rating System (managed by Indian Green Building Council (IGBC)) and Green Rating for Integrated Habit Assessment (GRIHA) (under The Energy and Resources Institute (TERI)), are responsible for the green rating of buildings in India. Figure 2a, b shows various factors and respective weightages as per the two rating schemes.

According to the above distribution, around 50% of the rating depends on the materials used for construction. In this regard, it is necessary to ascertain the suitability of GFRG as a sustainable alternative to conventional construction materials. The embodied energy of GFRG panel as well as GFRG buildings is

Fig. 3 GFRG demonstration building at IIT Madras campus

considered for assessing sustainability. In addition, the thermal comfort is also accounted because thermally uncomfortable environment lowers the energy efficiency of the building GFRG demonstration building inside the IIT Madras campus (Fig. 3), constructed for showcasing the features of this technology such as rapidity, affordability, sustainability, etc., which was considered for the calculation of embodied energy and assessment of thermal comfort through field measurements.

2 Construction of GFRG Buildings

GFRG panels can be used as walls (both external and internal), slabs, staircases, lift-well walls, parapet walls, sunshades, etc., with Reinforced Concrete (RC) filling inside the cavities. The number, diameter and spacing of rebars are decided based on the structural design. Foundation for GFRG building is same as that of conventional buildings up to the basement/plinth level (above ground level). The type of foundation depends on the number of storeys and soil condition at the site. The connectivity between foundation and superstructure is achieved with the help of starter bars with L anchorage, provided to the network of RC plinth beams at basement footing level. Panels are cut into required sizes in the factory based on

requirement and are packed in stillages, loaded on to trucks, and then transported to the construction site. At the site, panels in stillages are unloaded using vehicle mounted cranes and are stacked at a convenient location. Panels are handled at site using special lifting jaws fitted onto cranes. For construction, the erection of walls is to be done as per the building plan (marked with notations of panels) by installing the respective panels in perfect plumb and level by specially trained installation team. Wall panels are fixed in position using specially manufactured adjustable lateral props in order to hold them in rigid position. Concrete is poured on to the cavities wherever required. The leftover cavities of the wall panel are filled with quarry dust. After infilling concrete in the wall panel, construction of staircase waist slabs is carried out. The slab panels shall be laid on suitable support system and concrete infilling can be done after cutting the flanges of specified cavities. The upper storeys can be constructed in a similar manner. After the construction of superstructure, proper waterproofing and finishing works need to be carried out (For details of construction, 'GFRG construction Manual, 2016' [4] shall be referred).

3 Embodied Energy of Building

The energy consumed by the building over its entire life cycle can be considered as a measure of sustainability. The components of Life Cycle Energy (LCE) are illustrated in Fig. 4. In this paper, only the initial embodied energy is considered for assessing sustainability.

Initial embodied energy is given by

$$E_{im} = \sum m_i M_i \tag{1}$$

where

m_i total quantity of the ith material;
M_i energy density of the ith material;

For calculating the embodied energy, the quantity of different materials needs to be evaluated.

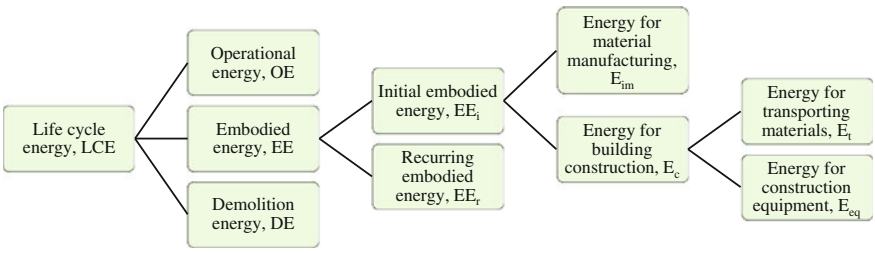

Fig. 4 Components of life cycle energy

4 Details of Case Study Building

The GFRG demonstration building, built inside IIT Madras campus, is considered for assessing sustainability. Figure 5 shows the building plan of a typical floor.

The two-storey building houses four flats with a built-up area of 184 m^2 (two for Economically Weaker Section (EWS) having carpet area of 25 m^2 each and two for Low Income Group (LIG) having carpet area of 46 m^2). The construction was completed in 40 days (11 days for foundation and 29 days for superstructure). The foundation was strip footing, constructed using fly ash blocks. Every structural member except sunshade was constructed using GFRG panels with concrete infill. The steps of staircase were constructed using concrete. The front doors are made of wood and the interior doors, and all windows are made of aluminium. Ceramic tiles were used for the floor finishing.

5 Estimation of Quantities of Various Materials Used

The total quantity of various materials used for the construction of foundation, walls, slabs, lintel cum sunshade, parapet, staircase headroom, etc. and finishing works (such as waterproofing, tiling, rendering, priming and painting) were calculated. Table 1 shows the values obtained.

As GFRG buildings are constructed using prefabricated wall and slab panels, the joints need to be waterproofed in order to prevent the ingress of water, unlike conventional buildings. The quantity of waterproofing products used is given in Table 2.

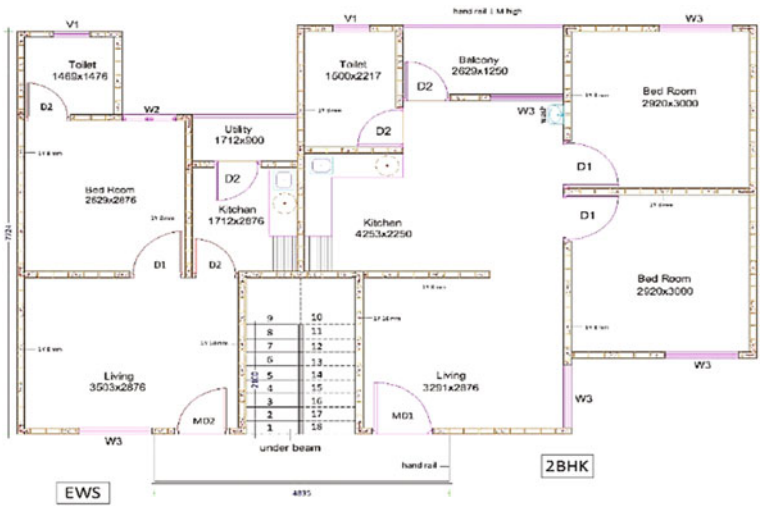

Fig. 5 Typical floor plan

Table 1 Quantity of building materials

Component of building	Constituents of component	Materials used	Quantity (kg)
Foundation	Concrete for PCC layer, floor and plinth beam	Cement	3878.6
		Coarse aggregate	26,721.0
		River sand	13,360.7
		Water	1861.4
	Block work	Fly ash blocks	85,067.5
	Mortar and plastering	Cement	4100.2
		River sand	24,318.7
		Water	1845.1
	Infill	River sand	35,660.3
		Quarry dust	22,848.0
	Reinforcement for plinth beam	Steel	361.2
Walls (including parapet)	Wall panels	GFRG panels	21,714.9
	Concrete infill (M20 grade)	Cement	4937.9
		Coarse aggregate	19,751.5
		River sand	9875.8
		Water	2222.0
	Reinforcement	Steel	509.9
	Inert infill	Quarry dust	36,901.8
Slabs	Slab panels	GFRG panels	7721.7
	Concrete (M25 grade)	Cement	7974.7
		Coarse aggregate	23,924.1
		River sand	11,962.0
		Water	3588.6
	Reinforcement (including weld mesh)	Steel	1339.3
Staircase headroom	Panels for walls, slabs and parapet	GFRG panel	2261.5
	Concrete infill in walls (M20 grade)	Cement	409.9
		Coarse aggregate	1639.8
		River sand	819.9
		Water	184.5

(continued)

Table 1 (continued)

Component of building	Constituents of component	Materials used	Quantity (kg)
	Inert infill	Quarry dust	2335.0
	Concrete for slabs (M25 grade)	Cement	328.5
		Coarse aggregate	985.6
		River sand	492.8
		Water	147.8
	Reinforcement (including weld mesh)	Steel	181.4
Finishing works	Priming	WD P30	19.3
		WD thinner	16.3
	Rendering (interior and exterior)	Wall putty	783.6
		Water	132.2
		Elastobar	41.7
	Painting	Paint	247.2
	Tiling	Tiles	4721.4
	Plastering	Cement	2033.2
		Sand	7999.2
		Water	915.0
Doors/windows/ventilators	Door/window frame	Aluminium	259.5
	Window/ventilator panes	Glass	218.7
	Doors	Wood	47.9
MEP works	Pipes	PVC	300.5
	Fittings	Ceramic	58
		Iron	93.0
		Stainless steel	270.6
Miscellaneous (Lintel cum sunshade, landing beam, beam in balcony, etc.)	Concrete (M20 grade)	Cement	2373.6
		Coarse aggregate	7502.8
		River sand	3751.4
		Water	1068.1
	Reinforcement	Steel	550.1

The total embodied energy of materials calculated using Eq. (1) is given in Table 3. The energy for transportation of materials and construction equipment are not considered in this study. It was observed that materials for envelope hold the major part of embodied energy.

Table 2 Quantity of waterproofing chemicals used

Waterproofing product	Quantity (kg)
Zycosil	7.8
Zycoprime	18.9
ZMB60	116.5
ZMB thinner	1.0
Elastobar	48.6
Stretch fab	13.6
Total	240.6

Table 3 Calculated embodied energy

Material	Total quantity, m_i (kg)	Embodied energy, M_i (MJ/kg) [5–9]	Total embodied energy (MJ)
Quarry dust	62,084.8	0.15	9312.72
Fly ash blocks	85,067.5	0.64	54,443.2
Cement	26,050.5	6.85	178,445.9
GFRG panels	31,698.1	5.44[a]	172,437.7
Steel	2941.9	35.1	103,260.7
Tiles	4721.4	3.33	15,722.3
Aluminium	259.5	155[b]	40,222.5
Paint	247.2	144	35,596.8
Coarse aggregate	80,524.8	0.4	32,209.9
PVC	300.5	106	31,853
Waterproofing	240.6	90.67	21,815.2
River sand	108,261.1	0.15	16,239.2
Stainless steel	270.6	56.7[b]	15,343.0
Primer	35.6	144	5126.4
Wall putty	783.6	5.3[b]	4153.1
Iron	93	25[b]	2325
Ceramic	58	29[b]	1682
Glass	218.7	25.8	5642.5
Wood	47.9	7.2	344.9
Total			746,176

[a]Embodied energy value from Ref. [5]
[b]Embodied energy value from Ref. [9]

Figures 6 and 7 show the distribution of weight and embodied energy of various materials used. The large quantity of usage can be misleading in terms of embodied energy. For example, river sand and coarse aggregate together constitute 46.8% of the total quantity. But in the context of embodied energy, their contribution is only 4%.

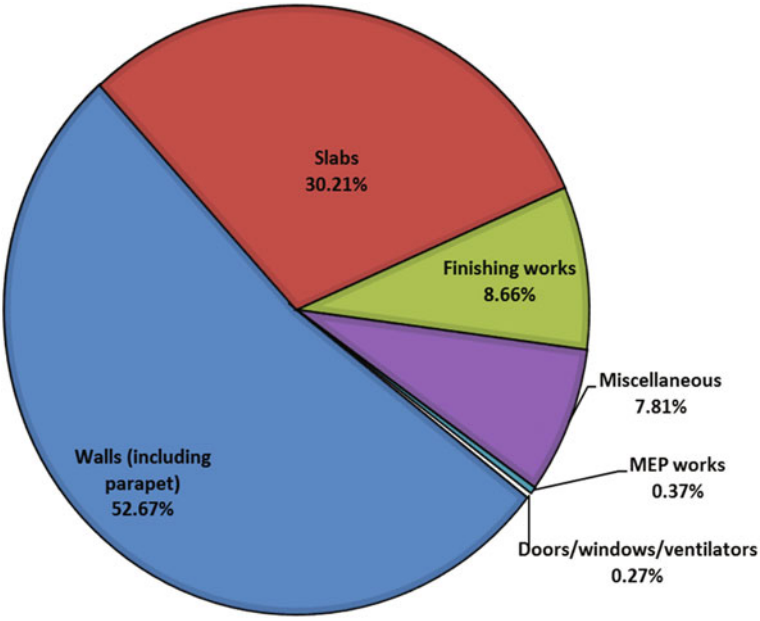

Fig. 6 Percentage distribution of weight of different structural and non-structural components of building

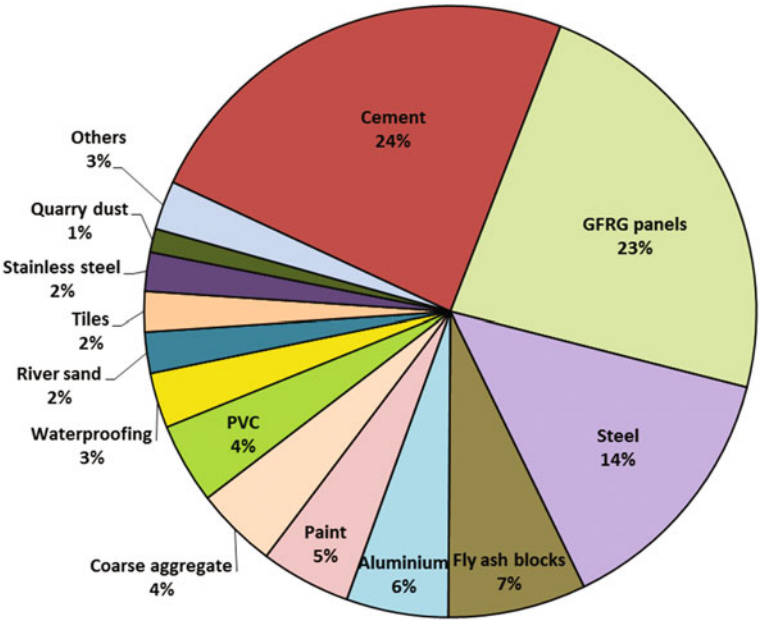

Fig. 7 Percentage distribution of embodied energy of different materials used for construction

6 Evaluation of Indoor Thermal Comfort

The thermal performance of GFRG building was analysed through real-time field measurements. The purpose of this test was to compare the thermal performance of GFRG buildings with that of the conventional reinforced concrete framed buildings. For this, the case study buildings selected were the GFRG demo building inside the IIT Madras campus and a conventional RC framed building in the same campus. The latter was located just adjacent to the demo building and was subjected to similar shading conditions as that of the former. The test was done on harsh summer days (10–13 June 2015) and was conducted by installing digital thermometers inside one of the rooms in both the buildings. Each thermometer had two thermocouples, of which one was fixed on the selected wall surface and the other on an exterior wall of the building. The thermometer was set to record temperatures at every hour, and the readings were taken continuously for 3 days. After analysis, it could be seen that the variation in the measured temperatures followed a similar pattern. The measured values for a typical day are shown in Table 4, and a plot of the same is shown in Fig. 8. The difference in the temperatures measured in the exterior thermocouples of the two case study buildings was very minimal, but those in the interior showed considerable difference.

It was observed that the temperatures inside the GFRG building were lesser than the conventional building by a maximum of 2 °C. It could also be observed that the trend was reversed during the afternoon hours, where the conventional building was up to 0.6 °C cooler. But the number of discomfort hours was considerably less.

7 Conclusion

A similar study conducted on the evaluation of embodied energy on a conventional reinforced concrete framed building shows that the embodied energy per unit area is 10.8 GJ/m^2 [10]. For the GFRG demo building, the embodied energy works out to be only 5.24 GJ/m^2, which shows that GFRG has almost 50% lesser embodied energy when compared to conventional building system. This makes GFRG a competent alternative to conventional building materials and systems. Moreover, GFRG buildings offer better interior thermal comfort even during the hottest days. This minimizes the energy requirement for air conditioning of the building and thereby results in saving of electricity. This reveals that the use of GFRG panels in building construction improves the sustainability of the building sector.

Table 4 Temperature measurements

Time	Outside temperature (°C)	Temperature inside conventional building (°C)	Temperature inside GFRG building (°C)
12:00 AM	30.9	33.5	32.2
01:00 AM	30.8	33.6	32.1
02:00 AM	30.9	33.4	32
03:00 AM	30.4	33.3	32
04:00 AM	29.9	33.5	32
05:00 AM	29.4	33.2	31.7
06:00 AM	28.8	33.2	31.3
07:00 AM	29.4	32.9	31.2
08:00 AM	30.7	33.1	31.1
09:00 AM	32.4	32.9	31.1
10:00 AM	34.8	32.2	31.4
11:00 AM	36.2	32.7	31.6
12:00 PM	36.6	32.9	31.8
01:00 PM	39.4	33	32.3
02:00 PM	40	32.5	32.7
03:00 PM	36.7	32.6	33
04:00 PM	34.9	32.9	33.5
05:00 PM	34.8	32.9	33.4
06:00 PM	33.3	33	33.2
07:00 PM	32.9	33.8	33.1
08:00 PM	32.6	33.7	33
09:00 PM	32.2	33.5	33
10:00 PM	31.5	33.7	32.8
11:00 PM	31.3	34.2	32.6

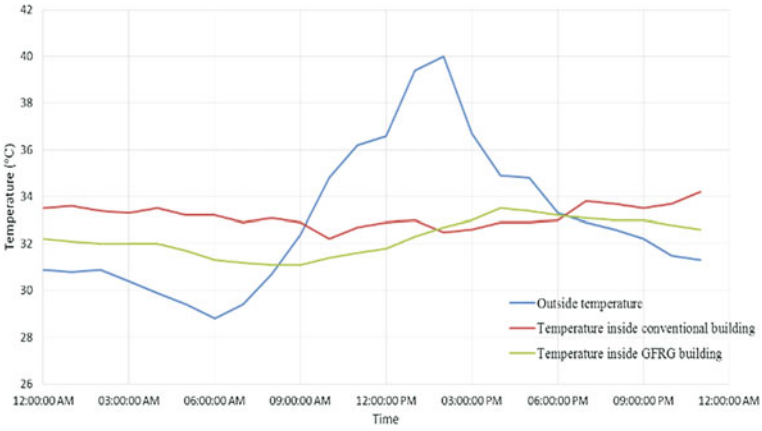

Fig. 8 Variation of temperature with time

Acknowledgements The authors are thankful to the Engineering Unit of IIT Madras for their support. The funding for the construction of the demo building by IIT Madras and Department of Science and Technology is gratefully acknowledged.

References

1. Monteiro, A. (2015) *Assessing initial embodied energy in building structures using LCA methodology* (MS thesis). New University of Lisbon, Portugal.
2. https://igbc.in/igbc/.
3. www.grihaindia.org.
4. Structural Engineering Division, IITM. (2016). *GFRG Construction manual*, BMTPC, MHUPA.
5. Omahen, R. (2002). *Ecologically sustainable development: Approaches in the construction industry* (Thesis). University of Regensburg, Germany.
6. Reddy, B. V. V., & Jagadish, K. S. (2003). Embodied energy of common and alternative building materials and technologies. *Energy and Buildings, 35,* 129–137.
7. Shukla, A., Tiwari, G. N., & Sodha, M. S. (2009). Embodied energy analysis of adobe house. *Renewable Energy, 34,* 755–761.
8. Chani, P. S., & Najamuddin, K. S. K. (2003). Comparative analysis of embodied energy rates for walling elements in India. *Institution of Engineers (India) Journal-Architecture, 84,* 47–50.
9. Hammond, G., & Jones C. (2008). *Inventory of carbon and energy (ICE), Version 1.6a*. UK: University of BATH.
10. Pinky, D. L., & Palaniappan, S. (2014). A case study on life cycle energy use of residential building in southern India. *Energy and Buildings, 80,* 247–259.

A Study on the Strength and Performance of Geopolymer Concrete Subjected to Elevated Temperatures

G. Mallikarjuna Rao, T. D. Gunneswara Rao, M. Siva Nagi Reddy and D. Rama Seshu

Abstract The present paper presents the experimental studies on the mechanical performance of Geopolymer Concrete (GPC), produced by alkali activation of fly ash and GGBS combination, at different temperatures. Being an innovative alternative material for cement concrete, GPC requires performance studies under elevated temperatures. In view of this, an experimental investigation has been carried out on GPC subjected to elevated temperatures. The parameters of the study of GPC (M20) include different levels of elevated temperatures (200, 400, 600 and 800 °C) and different durations of exposure (30, 60 and 90 min) and two different cooling regimes like air cooling and water quenching. The change in mass, compressive strength and X-ray diffraction (XRD) analysis for different GPC specimens are evaluated. The results indicate that the mass and compressive strength of concrete are decreased with increasing temperatures and air cooling resulted in higher values of residual compressive strength than water quenching. XRD analyses presented indicated the mineralogical variations in the material at higher temperatures and at longer durations as a result of which the mechanical properties of GPC are decreased.

Keywords Geopolymer concrete · Fly ash · GGBS · Elevated temperature XRD · Residual compressive strength

G. Mallikarjuna Rao
Department of Civil Engineering, Vardhaman College of Engineering, Shamshabad, Hyderabad 506004, India
e-mail: gmyadav25@gmail.com

T. D. Gunneswara Rao (✉) · M. Siva Nagi Reddy · D. Rama Seshu
Department of Civil Engineering, National Institute of Technology Warangal, Warangal 506004, India
e-mail: tdgtdg@gmail.com

M. Siva Nagi Reddy
e-mail: msnrmce@gmail.com

A. Rama Mohan Rao and K. Ramanjaneyulu (eds.), *Recent Advances in Structural Engineering, Volume 1*, Lecture Notes in Civil Engineering 11,
https://doi.org/10.1007/978-981-13-0362-3_70

1 Introduction

With the growth in infrastructure development and a boom in the housing sector, the demand for cement is bound to increase. Due to environmental concerns of the cement industry, there arises a strong need to make use of alternate sustainable technology. Geopolymer (Inorganic polymer concrete) is an emerging class of cementitious material and could be the next-generation concrete for civil infrastructure applications. The main advantage of geopolymer concrete (GPC) is environmentally friendly (reduces emission of CO_2 into the atmosphere by replacement of cement with alkali activated fly ash), which can be achieved by the effective utilization and operation of natural resources. Geopolymerization is a geosynthesis —a reaction that chemically integrates minerals [1]. Geopolymers can be formed by treating aluminosilicate materials (such as fly ash, ground-granulated blast furnace slag, etc.) with alkaline activators at high temperatures. In general, fly ashes from the combustion of coal consist of an inhomogeneous mix of aluminosilicate and silica plus small amounts of crystalline materials including mullite, quartz, hematite and magnetite [2]. The commonly used combination of the alkaline solution is NaOH and Na_2SiO_3. This solution binds the loose aggregates in the mixture to form GPC which has high strength, durability and low creep [3]. This solution activates SiO_2 and Al_2O_3 in fly ash to form N-A-S-H and C-S-H gels by reacting with calcium in ground-granulated blast furnace slag. The curing conditions especially, temperature significantly impacts the polymerization process [4]. The compressive strength and performance of GPC depends on type of alkaline activator, concentration of alkali and curing temperature. According to Hardjito et al. [5] sodium activators provide high strength as compared to that of potassium activators. Various authors studied the importance of molar of Na_2SiO_3/NaOH and suggested as 2.5 for maximum compressive strength at constant binder content [6]. Purdon [7] was probably the first researcher to investigate the alkaline activated slags. Subsequent to this, many researchers performed studies on alkali-activated slag shows a promise as an alternative binder to Ordinary Portland Cement. However, performance and behaviour of geoploymers when exposed to elevated temperatures have received less attention than it deserves. To the author's knowledge, there is no known published data available on the fire resistance of alkali-activated slag binder [8–15] was perhaps first to study the fire resistance behaviour of the alkali-activated concrete activated by sodium Hydroxide. In continuation to this, [16–19] performed studies on the thermomechanical properties of alkali-activated slag mortars (activated by NaOH, Na_2SiO_3 and a combination of these activators) and concluded that remarkable high-temperature resistance, exhibited superior mechanical properties comparable with the properties of the original material not subjected to any thermal load. Subsequent to these studies [20, 21] reported that the residual compressive strength of alkali-activated fly-ash-based GPC is constant at temperatures 800–1000 °C, whereas for the Portland cement concrete the residual compressive strength falls to zero beyond 800 °C. However, the research on the performance of fly ash and GGBS-based GPC at elevated temperatures at different heat exposure

periods is still lacking. Thus, the present investigation focuses on the study of strength, performance and mineralogical behaviour of GPC subjected to elevated temperatures following a cooling regime with different heat exposure periods. Such a study is very much necessary to establish the durability of new concrete.

2 Present Investigation

This study examines the performance of GPC as a structural grade for concrete application, aiming for the optimal percentage replacement of GGBS to meet target strength of M20. The experimental program was conducted to investigate the residual behaviour of GPC subjected to elevated temperatures. The primary aim of the experimental study is to compare the compressive strengths of GPC of M20 grade with air cooling and water quenching cooling regimes with different heat exposure periods. The program consists of cast and testing a total 150 number of cubes of 150 × 150 × 150 mm size each. Different sets of three cubes were tested for different elevated temperatures (200, 400, 600 and 800 °C) maintained for a period of 30, 60 and 90 min. After heating, the specimens were subjected to two different types of cooling regimes, one is by air cooling and another is by water quenching. A comparative study has been conducted to evaluate the residual behaviour of GPC subjected to elevated temperatures under two different cooling regimes. Test results show that cooling regime plays a critical role in the assessment of the residual behaviour of GPC subjected to elevated temperatures under different exposure periods.

3 Experimental Program

The experimental Program consisted of finding the hardened state properties of GPC by casting specimens for M20 grade. Total of 72 cubes of size 150 mm × 150 mm × 150 mm were cast and tested for determining thermal properties at different temperatures exposed for different time periods.

3.1 Materials

3.1.1 Fly Ash and GGBS

Fly ash and GGBS are used as source materials in the present study. Ground-granulated blast furnace slag is obtained from Toshali Cements Pvt. Ltd., Bayyavaram, India and fly ash is collected from National Thermal Power Plant, Ramagundam, India. The specific gravity of fly ash and GGBS are 2.17 and 2.90 respectively. Chemical composition details are shown in Table 1. The morphology

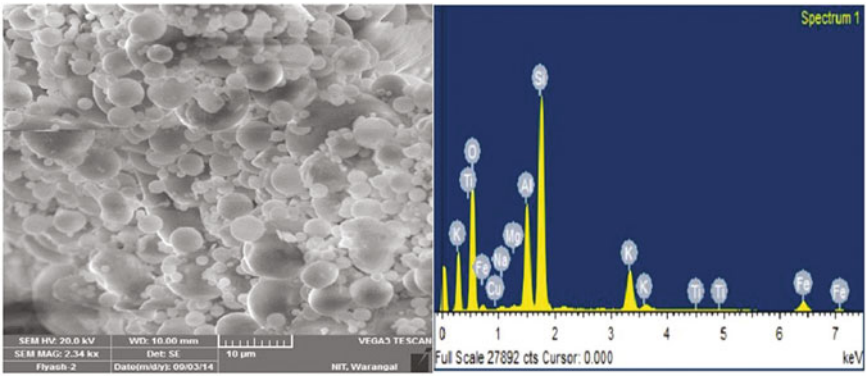

Fig. 1 SEM and EDAX of fly ash

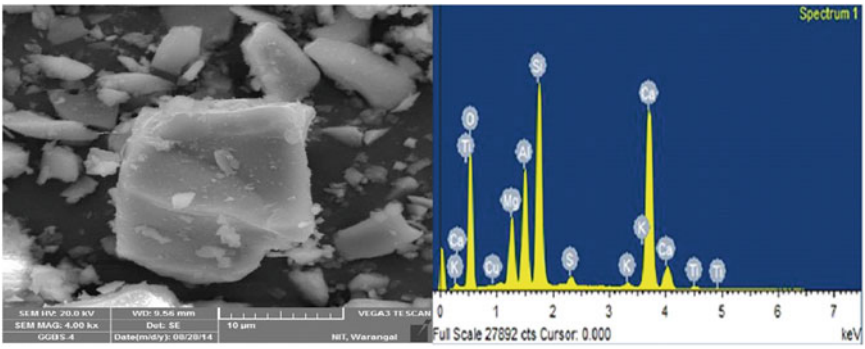

Fig. 2 SEM and EDAX of GGBS

Table 1 Chemical composition of fly ash and GGBS (% by mass)

Chemical composition	Fly ash	GGBS
SiO_2	60.11	34.06
Al_2O_3	26.53	20
Fe_2O_3	4.25	0.8
SO_3	0.35	0.9
CaO	4.00	32.6
MgO	1.25	7.89
Na_2O	0.22	NIL
LOI	0.88	NIL

of fly ash and GGBS were examined using Scanning Electron Microscope (SEM). Fly ash particles were spherical in shape. The fly ash is mainly composed of large percentages of silica and alumina. The shape of the GGBS grains is crystalline and angular form and From the EDAX, it can be observed that GGBS is

predominated with calcium and silica while compared to other elements are shown in Figs. 1 and 2. The mineralogical characterization of fly ash and GGBS sample has been carried out for the X-Ray diffraction (XRD) analysis which has been shown in Figs. 3 and 4.

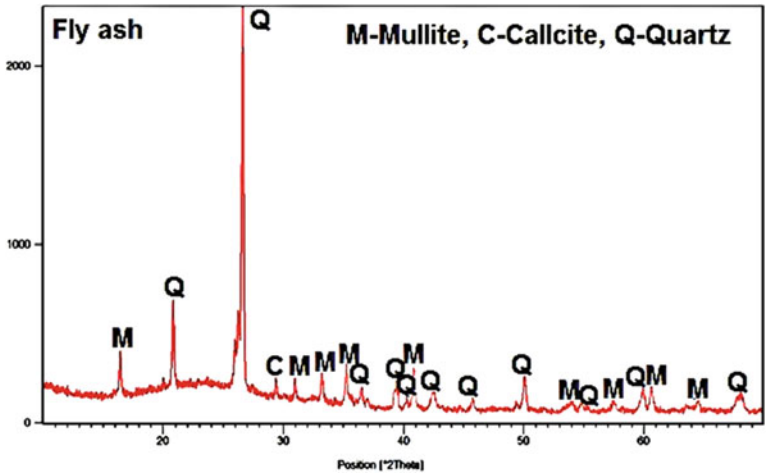

Fig. 3 XRD analysis for fly ash

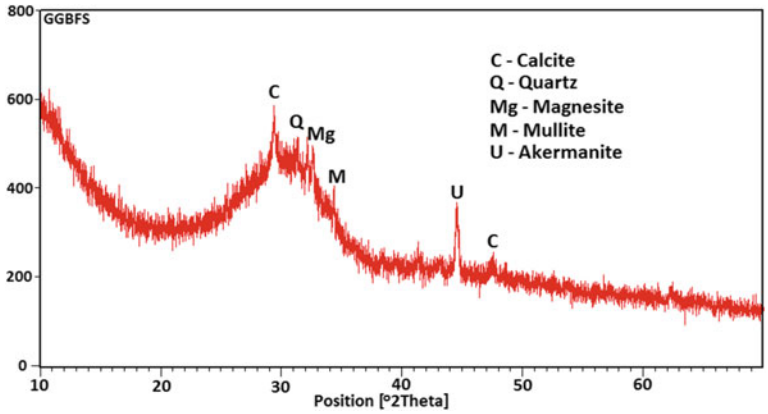

Fig. 4 XRD analysis for GGBS

3.1.2 Fine Aggregate

The nearby river sand conforming to Zone-2 according to IS 383 (BIS, 1970) [22] is preferred as fine aggregate. The specific gravity and bulk density of fine aggregate are 2.65 and 1.45 g/c.c. respectively.

3.1.3 Coarse Aggregate

Crushed granite of 20 mm nominal size obtained from a local crushing unit is taken as coarse aggregate and the aggregate is well-graded aggregate according to IS 383 (BIS, 1970) [22]. The specific gravity and bulk densities are 2.80 and 1.5 g/c.c. are shown in Table 2.

3.1.4 Water

Potable water was used in the experimental work for preparation of alkaline solution.

3.1.5 Superplasticizer

Sulphated naphthalene formaldehyde-based superplasticizer is used for the improvement of workability.

3.2 Preparation of Alkaline Solution

Molarity of NaOH solution plays a crucial role in the strength of GPC. The nominal molarity for fly ash and GGBS mixes range from 2 to 10 M, but higher strength can be obtained when the concentration approaches the maximum range [23]. From 8 to 16 M, there was a rise in the compressive strength for all mixes [24]. According to previous studies, it was found that with the higher concentration of NaOH solution, i.e. above 10 M, a lower rate of polymerization takes place and results in decreased compressive strength [25]. In the present experimental work, the properties of GPC were examined with 8 M NaOH were examined.

Table 2 Physical properties of fine and coarse aggregate

Physical properties	Fine aggregate	Coarse aggregate
Specific gravity	2.65	2.80
Bulk density	1.45	1.5
Fine modulus	2.57	7.3
Water absorption (%)	2	0.5

Table 3 Mix proportion of geopolymer concrete

Mix	Fly ash (kg/m^3)	GGBS (kg/m^3)	F.A. (kg/m^3)	C.A. (kg/m^3)	Alkaline solution (kg/m^3)
M20	252	108	770	1090.8	198

320 g of NaOH pellets were dissolved in potable water to make one litre of 8 M sodium hydroxide solution. To achieve the required strength the ratio of sodium silicate solution to sodium hydroxide solution is considered as 2.5 and the mixed solution is stored for 24 h at room temperature (25 ± 2 °C) and relative humidity of 65%, before it is used for casting. Because dissolution of NaOH in water is an exothermic reaction and a substantial amount of heat will be generated when added in concrete, hence the heat liberated is to be reduced and come down to ambient temperature.

In the present investigation, a series of laboratory experiments were performed to determine the optimum mix proportions of concrete with minimum binder content. Before carrying out actual experimentation several trials were carried out for control mixes as per IS: 10262-2009 for M20 grade of concrete. The mix design of geopolymer concrete was similar to ordinary concrete but cement was replaced by binder and water with an alkaline solution. NaOH solution and Na_2SiO_3 solution were used as alkaline activators. The alkaline activator-to-binder ratio was taken as 0.55 for M20. NaOH solution concentration was maintained as 8 M (320 g of NaOH of 98% purity were dissolved in tap water to prepare one litre NaOH solution). Preparation of alkaline solution is an exothermic reaction and hence the quantified NaOH and Na_2SiO_3 solution were mixed and stored at room temperature for 24 h prior to mix in concrete. After certain trail mixes and testing of cast specimens, a final mix proportion shown in Table 3 was adopted to carry out mechanical properties at elevated temperatures.

3.3 Casting and Curing of GPC

The individual dry materials weighed were mixed using a rotating drum pan mixer of 100 kg capacity. The alkaline liquid and superplasticizer of optimum dosage were added after uniform mixing of dry materials. Proper homogenous mixing would be ensured by continuous mixing for 5–7 min and fresh property tests were carried out to ensure workability of GPC. The fresh concrete was transferred into concrete moulds (150 mm × 150 mm × 150 mm) followed by table vibration for a period of 45 s and allowed to set for 24 h. The specimens are demoulded after 24 h of casting and cured in outdoor condition. For outdoor curing, specimens were left out at outdoor (temperature—35 ± 2 °C and relative humidity—75%) up to the specified age of testing 28 days. Temperature and humidity control were not necessary for outdoor-cured specimens.

3.4 Elevated Temperature Exposure Regime

After 28 days of curing, before going to the heating process, the original weight of all the specimens was measured. GPC specimens were subjected to sustained elevated temperatures of 200, 400, 600 and 800 °C and in each case retention periods were 30, 60 and 90 min has been adopted. For any particular temperature, after reaching the specified retention periods the exposed specimens were kept outside for air cooling and water quenching. Air cooling method was adopted in this study for bringing down the temperature of the specimens to ambient temperature. The specimens left for air cooling were allowed to cool at the room temperature for 1 day whereas for water quenching the specimens taken out from the muffle furnace after the specific temperature and exposure period is reached. The heated specimens were kept in 15 L of water and allowed to cool until the water temperature reaches the room temperature. The final weights of the cooled specimens were measured and compressive strength test was done. Fragment pieces are obtained from the tested specimens and powdered to use for XRD analysis (Figs. 5 and 6).

Fig. 5 Specimens kept in an electric furnace

Fig. 6 Specimens testing for compression

3.5 Testing Procedure for Compressive Strength

Standard cube specimens of size 150 mm × 150 mm × 150 mm are cast and tested under compression using 3000 kN compression testing machine at a standard rate of loading suggested by IS 516 (BIS, 1956) [26]. The strength values reported at 28 days outdoor curing and various temperatures and different heat exposure periods and the reported results are the averages of three cubes.

4 Results and Discussion

4.1 Change in Weight

Average percentage loss in weight of fly ash and GGBS-based GPC specimens, after exposure to various elevated temperatures with respect to the unheated specimens, are shown in Fig. 7. From Fig. 4, it can be seen that the weight loss of GPC is gradually increasing with increase in temperature up to 800 °C. The increase in loss is also observed with an increase in the exposure period irrespective of the heating temperature. The weight loss in GPC increases significantly due to the evaporation of moisture within the specimen. The average weight loss for M20 is 1.35% at 200 °C for an exposure period of 90 min, which is very less and negligible, whereas for 400, 600 and 800 °C, the average weight loss at heat exposure period of 90 min is 3.86, 4.42 and 5.05%, respectively, displaying a significant trend with the change in temperature.

The heat exposure period has a significant effect at lower temperatures and has no considerable influence at 600 °C and above. The weight loss in GPC is due to the evaporation of sodium aluminosilicate hydrate and calcium alumina-silicate gels. Based on the experimental results of GPC prepared with fly ash and GGBS for M20 grade it can be concluded that the weight loss of GPC with an increase in temperature and with longer exposure period, has increased in general. Particularly, the loss is more pronounced at 800 °C for 90 min exposure period which does not have a crucial effect on the density of GPC.

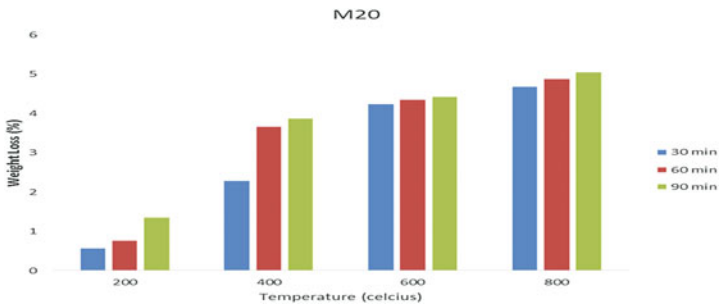

Fig. 7 Weight loss after different elevated temperatures

4.2 Water Quenching

The average percentage weight gain results of M20 and subjected to different heat exposure periods of different temperatures are presented in Fig. 8. From Fig. 8, it can be observed that, the GPC specimens exposed to high temperatures have gained weight after quenching them in water immediately after taking out from the furnace. The percentage of weight gain is increased as the temperature increases from 200 to 800 °C for M20 at all exposure periods. Exposure period also plays an important role in the weight gain of GPC Specimens. As the exposure period increases weight gain for the specimens M20 increases with a rise in temperature. In GPC the weight loss is observed when the specimens are subjected to different temperatures prior to the quenching process. The weight loss of the specimens already mentioned in the air-cooled specimens is shown in Fig. 7. From the literature it is reported, the reacted geopolymer contains free water and structurally bonded water. The structural water was bonded to reaction product namely N-A-S-H gel [27]. Thus, loss in structural water gives an indirect estimation of the reaction product. More weight loss is due to the formation of the new reaction products already reported in air cooling. Here, in this study, the different pattern was for the water cooling is quite different from the other studies, here the specimens are kept in constant volume of water for 6 h in order to measure the thermal diffusivity for the specimens subjected to the elevated temperature. In this process, the weight gain was observed for all the specimens, which are kept at different exposure periods and different temperatures. The mass gain is due to the disconnected fine pore structures in the matrix filled with the water. The water absorption of M20 increases with increase in the exposure period. The weight gain values for M20 grade GPC at 200 °C are 2.5, 3.13 and 4.05% for 30, 60 and 90 min exposure periods respectively. There is a sudden increase in weight gain at 400 °C at 30 min compared to 200 °C 30 min. This may be due to the fact that the specimens are subjected to the thermal shock.

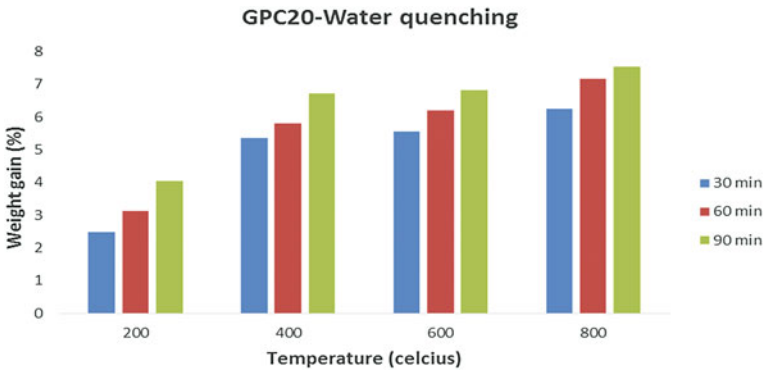

Fig. 8 Percentage weight gain for GPC20 (water quenching)

4.3 Change in Compressive Strength for Air Cooling

The variation in the compressive strength of GPC specimens subjected to elevated temperatures under different heat exposure periods is displayed in Fig. 9.

The compressive strength test results presented in Fig. 9 indicate that the strength is gained about 40% higher than that of the unheated specimen at 200 °C. It shows a significant difference in the strength with different exposure periods attaining a peak of around 44 MPa for 90-min exposure period. As the temperature increases further, the rate of gain is reversed producing the results in lower side of those at 200 °C. This decreasing trend is continued till 800 °C, but the difference is more pronounced in between 600 and 800 °C. Even though the degradation of GPC is started at 600 °C, it has retained the strength highly above the characteristic strength with a minimum of 80% of the unheated GPC strength. At 800 °C, it lost almost 65% of the strength, which is vulnerable to a structural grade concrete. Here, the duration of heat exposure also has a significant effect in gaining/ losing the compressive strength. At relatively lower temperatures, the strength of GPC has an increment, this is mainly attributed to the fact that moderate exposure to a normal temperature could make the geopolymerization process to continue forming new hard products.

The decrease in the strength of GPC at higher temperatures mainly results from the loss of cohesive bond between the matrix and aggregates, thermal incompatibility, i.e. unmatched expansion and contraction between the matrix and aggregate components, which lead to the formation of a significant amount of minor cracks within the specimen. Also, mineralogical changes by water evaporation and the crystalline phases are also factors contributing to the strength loss, which were shown in XRD analysis.

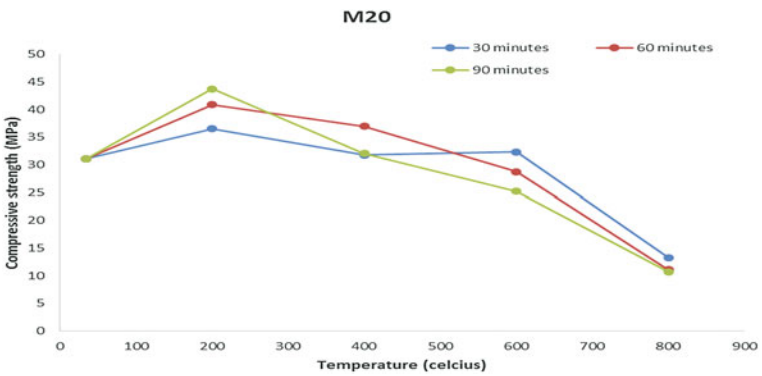

Fig. 9 Change in compressive strength at different elevated temperatures and different heat exposure periods

4.4 Change in Compressive Strength for Water Quenching

The compressive strength of the GPC specimens subjected to elevated temperature was shown in Fig. 10. The cooling regime selected here is the water quenching. The cooling regime has an influence on the properties of the GPC prepared with different percentages of fly ash and GGBS contents. The compressive strength of the water-cooled specimens is lower compared with the air-cooled specimens. This may due to the fact that the specimens are subjected to the thermal shock was also reported by [28]. By keeping the specimens in a certain volume of water after taking the specimens directly from the furnace which causes rapid cooling and it leads to a significant thermal gradient and a non-uniform stress distribution in the specimen, which makes the initiation and expansion of microcracks and causes more severe damage to GPC specimens. As shown in Fig. 10, reduction in compressive strength more was observed at 600 °C from 30 min heat exposure period in water quenching for M20. Then, the strength decreases continuously with increase in temperature at different heat exposure periods also, while the specimens have a relatively higher bearing capacity up to 600 °C in air cooling whereas for water cooling the strength degradation starts from 200 °C for an exposure period of 30 min. For temperature above 600 °C, the compressive strength decreases considerably and only roughly 35% of the original strength is retained at 800 °C for M20. Therefore, from the strength point of view, it can be concluded that the temperature of 600 °C is critical for M20 in both water cooling and air cooling.

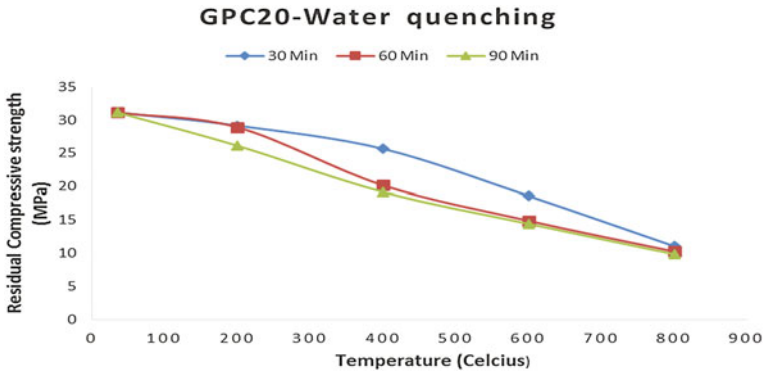

Fig. 10 Change in compressive strength at different elevated temperatures and different exposure periods of GPC20 (water quenching)

4.5 XRD Analysis

X-Ray Diffraction (XRD) Analysis

The XRD patterns of M20 grade powdered samples at different temperatures for heat exposure periods 30, 60, 90 min were presented in Figs. 11, 12, 13 and 14. From the figures, it can be seen that the samples contain quartz **(SiO_2)**, mullite **($Al_2(Al_{2.8}Si_{1.2})O_{9.6}$)** and calcite **($CaCO_3$)** and are the main minerals which are present in the source materials. The highest peak for all heat exposure periods was contributed by quartz **(SiO_2)** at different elevated temperatures. For different heat exposure periods at temperature 200 °C, quartz **(SiO_2)**, mullite **($Al_2(Al_{2.8}Si_{1.2})O_{9.6}$)**, calcite **($CaCO_3$)** and albite **($Na(AlSi_3O_8)$)**, microcline **($KAlSi_3O_8$)** peaks were detected and there is no much variation in peaks to an exposure period of 30, 60 and 90 min retention period at 200 °C. There is an increase in the strength of the GPC specimens at 200 and 400 °C for different retention periods than the initial strengths this may due to the further geopolymerization process in the concrete specimens [29]. However, for the different retention periods (30, 60 and 90 min) at 200 and 400 °C the peaks pertaining to Albite **($Na(AlSi_3O_8)$)** were found at $2\theta = 28°$ approximately. The geopolymerization of fly ash and GGBS with alkaline activators resulted in the synthesis of Albite which also resulted in transformations from amorphous to crystalline phases. The synthesis of albite a crystalline phase of the N-A-S-H (aluminosilicate gel) contributed to the maximum compressive strength and also for the sample exposed to 90 min [30].

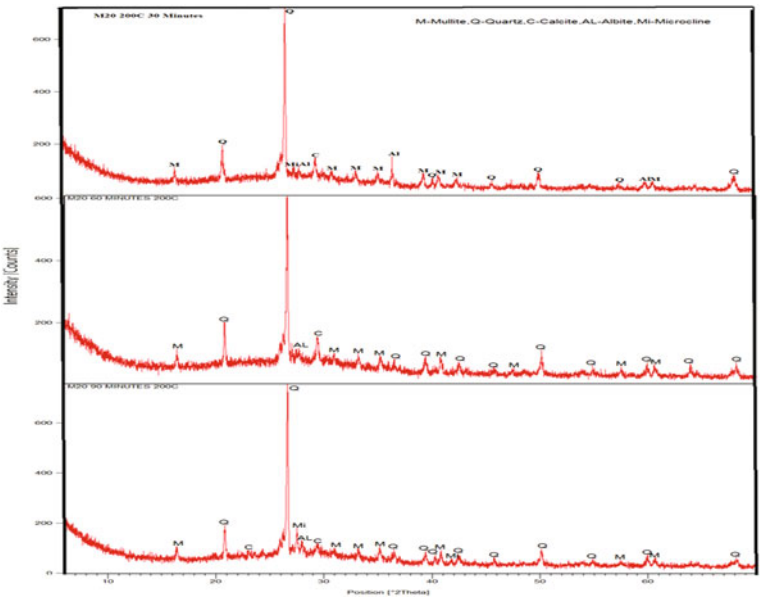

Fig. 11 XRD analysis of geopolymer concrete at 200 °C for different heat exposure periods for M20

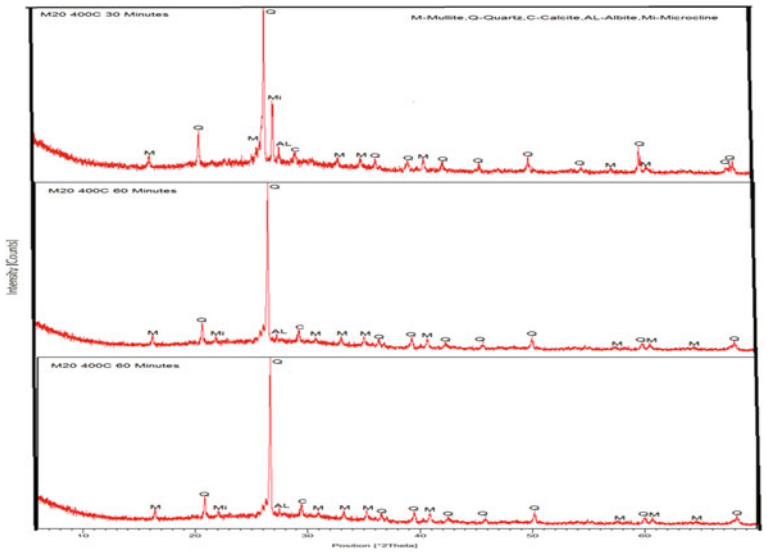

Fig. 12 XRD analysis of geopolymer concrete at 400 °C for different heat exposure periods for M20

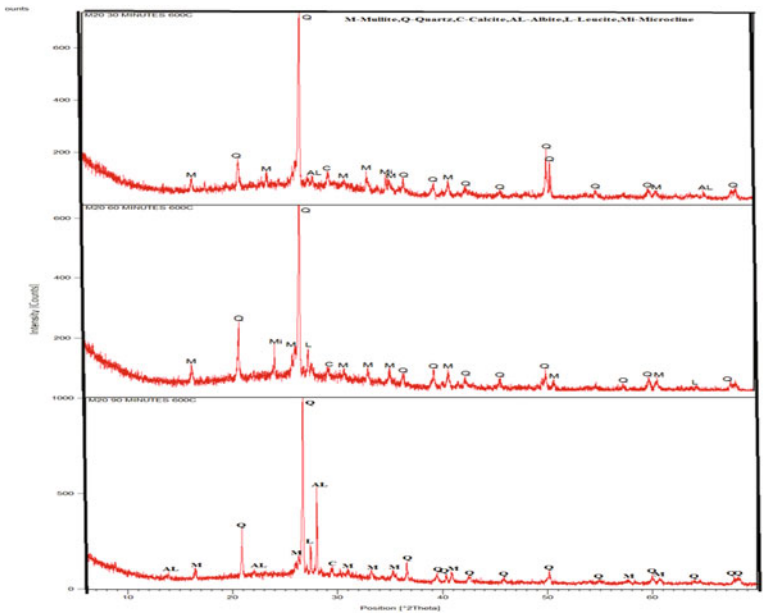

Fig. 13 XRD analysis of geopolymer concrete at 600 °C for different heat exposure periods for M20

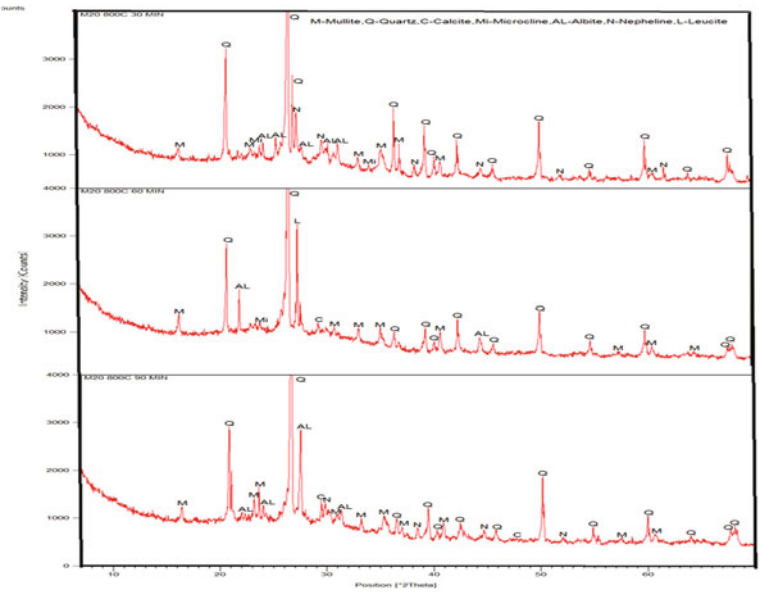

Fig. 14 XRD analysis of geopolymer concrete at 800 °C for different heat exposure periods for M20

The reason for this superior behaviour of could be attributed to the formation of crystalline phases called anhydrous alumina silicates such as albite and Microcline. These phases improve the crystallinity during heating up to 200–400 °C and then recrystallize to new phases albite and microcline. This contributes to the enhancement of mechanical strength for M20 [31]. As shown in Figs. 13 and 14, the XRD patterns for all the geopolymer samples are quite similar for the 600 and 800 °C. The samples exposed for the high temperatures showed marginal mineralogical changes. Leucite **($KAlSi_2O_6$)** and nepheline **($NaAlSiO_4$)**, microcline (**$KAlSi_3O_8$**), albite **($(Na(AlSi_3O_8))$)** were mainly formed at 600 and 800 °C of different retention periods. Leucite is not observed at a lower temperature, this crystalline phase change was observed at a high temperature other than 400 °C. The similar observations of formation of gel binder fully crystallized Leucite at high temperatures in geopolymer composites were reported by Lin et al. [32]. The increase in strength is due to the formation of new minerals like albite and leucite. Whereas the reduction in strength at high temperatures was attributed to a thermal expansion mismatch of the different compounds. At 800 °C, new phase formation nepheline (**$NaAlSiO_4$**) was identified which is in the form of amorphous aluminosilicate and the same pattern was observed in the literature [33]. Studies have shown that at a temperature below 500 °C the strength was improved for GPC specimen. The primary reaction products of amorphous aluminosilicate semi-crystalline gels such as N-A-S-H are formed along with the crystals of mullite. This formation of crystals is due to the presence of the minerals in both the fly ash and GGBS and the chemical activator used for the activation of the combination of Fly ash and GGBS.

4.6 XRD Analysis of Water Quenching

X-Ray Diffraction (XRD) Analysis for M20 Grade

The XRD patterns of M20 grade powdered samples at different temperatures for heat exposure periods 30, 60, 90 min subjected to water quenching were presented in Figs. 15, 16, 17 and 18. From the figure, it can be seen that the samples contain quartz **(SiO_2),** mullite **($Al_2(Al_{2.8}Si_{1.2})O_{9.6}$)** and calcite **($CaCO_3$)** and these minerals are already identified in fly ash. The highest peak for all heat exposure periods was contributed by quartz at different elevated temperatures. Through geopolymerisation of fly ash and GGBS with alkaline activators resulted in the synthesis of Albite which also resulted in transformations from amorphous to crystalline phases. The synthesis of albite, a crystalline phase of the N-A-S-H (**aluminosilicate gel)** contributed to maximum compressive strength. For different heat exposure periods at temperature 200 °C, quartz **(SiO_2)**, mullite **($Al_2(Al_{2.8}Si_{1.2})O_{9.6}$)**, calcite **(Calcium Carbonate)** and sandine **(Potassium Sodium Calcium Aluminium Silicate)**, microcline **(Sodium potassium Aluminium Silicate)** peaks were detected and there is no much variation in peaks to an exposure period of 30,60 and 90 min at 200 °C. However, the heat exposure period for 30 and 60 min, peaks pertaining to albite **(Sodium Calcium Aluminium Silicate)** were found at $2\theta = 28°$, approximately. The reason for this superior behaviour could be attributed to the formation of crystalline phases called anhydrous alumina silicates such as sodalite, microcline and sandine. These phases improve the crystallinity during heating up to 200–600 °C

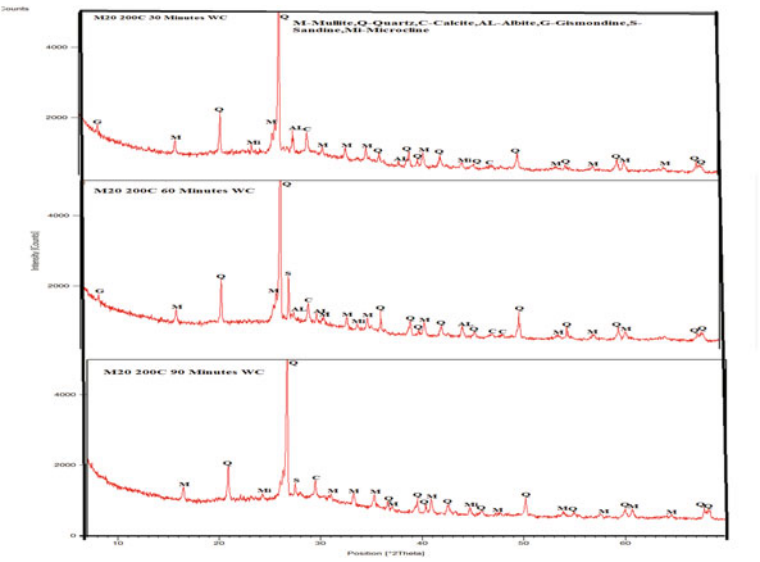

Fig. 15 XRD analysis of geopolymer concrete at 200 °C for different heat exposure periods for M20 (water quenching)

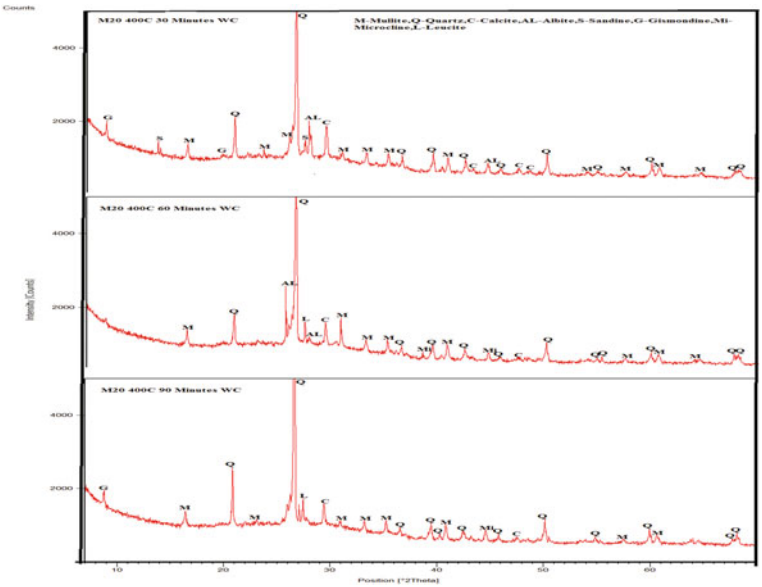

Fig. 16 XRD analysis of geopolymer concrete at 400 °C for different heat exposure periods for M20 (water quenching)

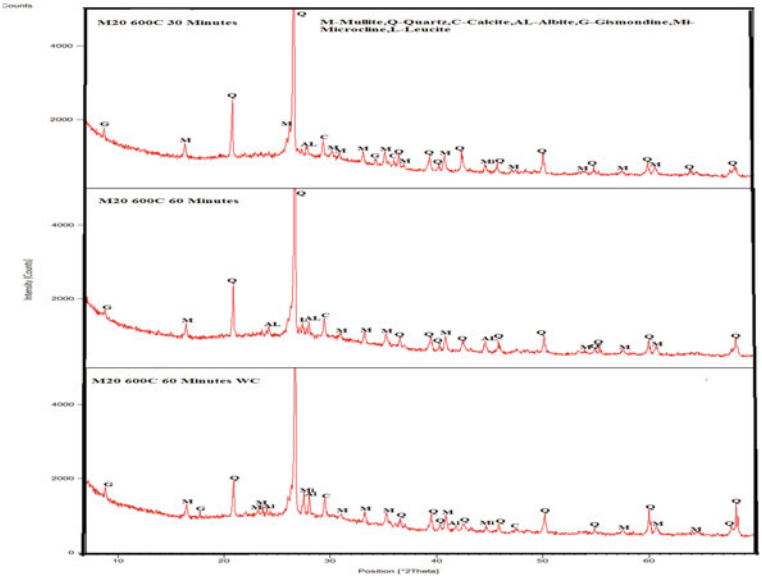

Fig. 17 XRD analysis of geopolymer concrete at 600 °C for different heat exposure periods for M20 (water quenching)

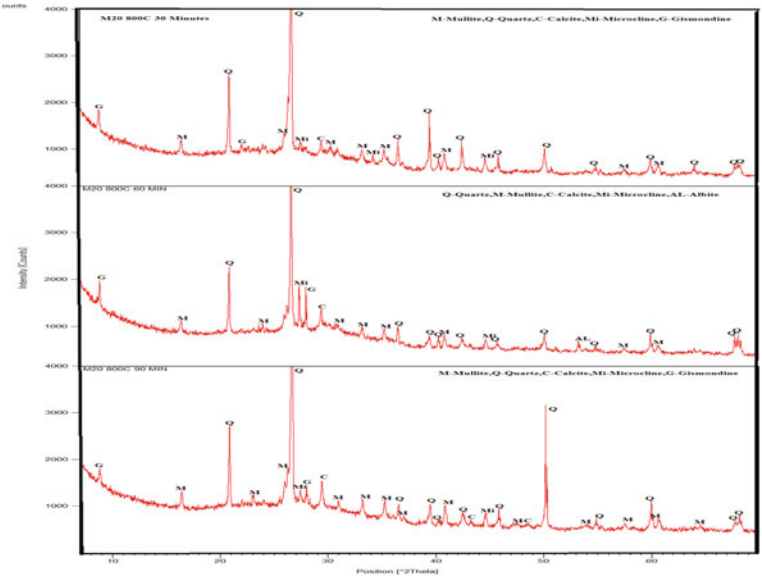

Fig. 18 XRD analysis of geopolymer concrete at 800 °C for different heat exposure periods for M20 (water quenching)

and then recrystallize to new phases albite, nepheline. This contributes to the enhancement of mechanical strength for M20 after quenching process. As shown in Figs. 15, 16, 17 and 18 the XRD patterns for all the geopolymer samples are quite similar for the 400, 600 and 800 °C after the specimens are subjected to the quenching process. The samples exposed to the high temperatures showed marginal mineralogical changes. Leucite **(Sodium Potassium Aluminium Silicon Oxide)** was mainly formed at 400, 600 and 800 °C of different exposure periods in air cooling. Leucite is not observed at any temperature in water cooling, this crystalline phase change was observed at a high temperature other than 200 °C. The similar observations of formation of gel binder fully crystallized Leucite at high temperatures in geopolymer composites were reported by Lin et al. [32]. The increase in strength is due to the formation of new minerals like albite and lucite. Whereas the reduction in strength at high temperatures was attributed to a thermal expansion mismatch of the different compounds. The primary reaction products of amorphous aluminosilicate semi-crystalline gels such as N-A-S-H are formed along with the crystals of Mullite. This formation of crystals is due to the presence of the minerals in both the fly ash and GGBS and the chemical activator used for the activation of the combination of Fly ash and GGBS.

5 Conclusions

From the experimental investigation carried out on GPC subjected to elevated temperatures, the following conclusions were arrived.

(1) The weight loss of GPC with an increase in temperature and with longer exposure periods has increased in general. Particularly the loss is more pronounced at 600 °C.
(2) The compressive strength of GPC has a gain of around 45% strength of unheated GPC after exposure to 200 °C and the rate of gain is lowered at 400 °C.
(3) Up to 600 °C, GPC retained its strength with a maximum loss of 19%, beyond this the degradation is more rapid. Hence, 600 °C can be the critical temperature for this mix proportion.
(4) At the temperature of 800 °C, the reduction in strength is more pronounced with a loss of 65% of the strength.
(5) Heat exposure period also has a significant effect at all temperatures.
(6) The XRD analysis indicated that the crystalline structure of GPC is affected by the increase in elevated temperatures and with longer exposure periods. These changes are in line with the strength and weight loss observation made on GPC.
(7) The influence of cooling regime has a significant effect in deterioration of GPC cooled by water quenching is more serious than that of specimens cooled by air cooling.
(8) The specimens for both air and water quenching the critical temperature for M20 is 600 °C. For air cooling, there is an increase in the strength up to 600 °C 30 min whereas the specimens subjected to water quenching there is a slight loss of strength at 200 °C itself.

References

1. Khale, D., & Chaudhary, R. (2007). Mechanism of geopolymerization and factors influencing its development: A review. *Journal of Materials Science, 10*, 729–746.
2. Song, S., Sohn, D., Jennings, H.M., & Mason, T. O. (2000). Hydration of alkali-activated ground granulated blast furnace slag. *Journal of Materials Science, 35*, 249–257.
3. Wang, S. D., Pu, X. C., Scrivener, K. L., & Pratt, P. L. (1995). Alkali-activated slag cement and concrete a review of properties and problems. *Advance Cement Research, 27,* 93–102.
4. Glukhovsky, V. D. (1959). *Soil silicates*. Gosstroiizdat, Kiev (in Russian).
5. Hardjito, D., Wallah, S. E., Sumajouw, D. M. J., & Rangan, B. V. (2004). On the development of fly ash-based geopolymer concrete. *ACI Materials Journal, 101*(6), 467–472.
6. Pinto, A. (2004). *Alkali-activated metakaolin based binders* (Ph.D. thesis). University of Minho.
7. Purdon, A. O. (1940). The action of alkalis on blast-furnace slag. *Journal of the Society of Chemical Industry, 59,* 191–202.
8. Talling, B., & Brandstetr, J. (1989). In *Proceedings of the 3rd International Conference on Fly Ash, Slag and Natural Pozzolans in Concrete*, Trondheim, Norway. ACI SP 114, Vol 2, 1519.

9. Bakharev, T. (2001). *Alkali activated slag concrete. Chemistry, microstructure and durability*. Ph.D., Department of Civil Engineering, Monash University, Melbourne.
10. Collins, F. G. (1999). *High early strength concrete using alkali activated slag*. Ph.D., Department of Civil Engineering, Monash University, Melbourne.
11. Collins, F. G., & Sanjayan, J. G. (1999). Workability and mechanical properties of alkali activated slag concrete. *Cement and Concrete Research, 29*(3), 455–458.
12. Bakharev, T., Sanjayan, J. G., & Cheng, Y. B. (1999). Alkali activation of Australian slag cements. *Cement and Concrete Research, 29*(1), 113–120.
13. Collins, F. G., & Sanjayan, J. G. (2001). Early age strength and workability of slag pastes activated by sodium silicates. *Magazine of Concrete Research, 53*(5), 321–326.
14. Collins, F. G., & Sanjayan, J. G. (1998). Early age strength and workability of slag pastes activated by NaOH and Na2CO3. *Cement and Concrete Research, 28*(5), 655–664.
15. Jumppanen, U.-M., Diederichs, U., Hinrichsmeyer, K. (1986). *Material properties of f-concrete at high temperatures*. Technical Research Centre of Finland, Research Report 452, Espoo, November 60.
16. Mejia de Gutiérrez, R., Maldonado, J., & Gutierrez, C. (2004). Performance of alkaline activated slag at high temperatures. *Material Construction, 54*(276), 87–94.
17. Rovnanikova, P., Bayer, P., Rovnanik, P., & Novak, J. (2005). Properties of alkali activated aluminosilicate materials with fire resistant aggregate after high temperature loading. In *Cement Combinations for Durable Concrete, Proceedings Of The International Conference*, Dundee, UK (pp. 277–286).
18. Rovnanik, P., Bayer, P., & Rovnanikova, P. (2006). New possibilities of fire protection of tunnel walls. In *Concrete Structures for Traffic Network, Proceedings of the 2nd central European Congress on Concrete Engineering*, Hradec Kralove, Czech Republic (pp. 496–501).
19. Zuda, L., Pavlik, Z., Rovnanikova, P., Bayer, P., & Cerny, R. (2006). Properties of alkali activated aluminosilicate material after thermal load. *International Journal of Thermo Physics, 27*(4), 1250–1263.
20. Kong, D. L. Y., & Sanjayan, J. G. (2008). Damage behaviour of geopolymer composites exposed to elevated temperatures. *Cement & Concrete Composites, 30*(10), 986–991.
21. Songpiriyakij, S. (2010). *Alkali-activated fly ash concrete*. Thailand: King Mongkut's Institute of Technology North Bangkok.
22. BIS (Bureau of Indian Standards). (1970). *IS 383–1970: Specification for coarse and fine aggregates from natural sources for concrete*. New Delhi, India: Bureau of Indian Standard.
23. BIS (Bureau of Indian Standards). (1956). *IS 516–1956 (Reaffirmed 1999): Indian Standard methods of tests for strength of concrete*. New Delhi, India: Bureau of Indian Standard.
24. Song, X. (2007). *Development and performance of class F fly ash based geopolymer concretes against sulphuric acid attack* (Doctoral thesis). School of Civil and Environmental Engineering, University of New South Wales, Sydney, Australia, January 2007.
25. Raijiwala, D. B., & Patil, H. S. (2011). Geopolymer concrete: A concrete of next decade. *JERS, 2*(1), 19–25.
26. Alonso, S., & Palomo, A. (2001). Alkaline activation of metakaolin and calcium hydroxide mixtures: Influence of temperature, activator concentration and solids ratio. *Materials Letter, 47*(1–2), 55–62.
27. Nath, S. K., Maitra, S., Mukherjee, S., & Sanjay Kumar, (2016). Microstructural and morphological evolution of fly ash based geopolymers. *Construction and Building Materials, 111,* 758–765.
28. Peng, G. F., Bian, S. H., Guo, Z. Q., Zhao, J., Peng, X. L., & Jiang, Y. C. (2008). Effect of thermal shock due to rapid cooling on residual mechanical properties of fiber concrete exposed to high temperatures. *Construction and Building Materials, 22*(5), 948–955.
29. Pan, Z., Sanjayan, J. G., & Rangan, B. V. (2009). *Journal Mater Science, 44,* 1873–1880.
30. Garcia-Lodeiro, I., Fernandez-Jimenez, A., Palomo, A., & Macphee, D. E. (2010). Effect of fresh C-S-H gels of the simultaneous addition of alkali and aluminium. *Cement and Concrete Research, 40*, 27–32.

31. Fernandez-Jimenez, A., Paster, J. Y., Martin. A., & Palomo, A. (2010). High temperature resistance in alkali-activated cement. *Journal of American ceramic Society, 93*, 3411–3417.
32. Lin, T. S., Jia, D. C., He, P. G., & Wang, M. R. (2009). Thermo-mechanical and microstructural characterization of geopolymers with α-Al2O3 particle filler. *International Journal Thermo Physics, 30*(5), 1568–1577.
33. Dimitrijevic, R., Dondur, V., Vulic, P., Markovic, S., & Macura, S. (2004). *Journal of Physics and Chemistry of Solids, 65,* 1623.

Degradation Kinetics of Cement-Based Materials in Citric Acid

K. P. Ramaswamy and Manu Santhanam

Abstract Cementitious materials being highly alkaline in nature are easily attacked by the acids present in industrial effluents, with implications in its mechanical and durability properties. This paper aims to evaluate the degradation kinetics of cement paste when exposed to citric acid solution by performing a static immersion-based-accelerated leaching test. Binders such as Class F fly ash (30% replacement), blast furnace slag (50% replacement), silica fume (10% replacement) are considered as mass replacements to cement in addition to the control mix containing ordinary Portland cement only. A holistic test protocol was developed with and without abrasive action and the degradation kinetics was investigated by measuring mass changes, thickness changes, changes in pH of the acid solution, strength changes and imaging using X-ray micro-tomography. The results showed that citric acid is highly aggressive to cement-based materials as it resulted in strong leaching. The performance of binders such as fly ash and slag was found to be ordinary while the mix containing silica fume showed better resistance to citric acid.

Keywords Degradation kinetics · Leaching · Citric acid · Paste
Micro-tomography

K. P. Ramaswamy · M. Santhanam (✉)
Department of Civil Engineering, Indian Institute
of Technology Madras, Chennai 600036, India
e-mail: manusanthanam@gmail.com

K. P. Ramaswamy
e-mail: ramaswamy1985@gmail.com; ramaswamykp@tkmce.ac.in

K. P. Ramaswamy
Department of Civil Engineering, TKM College
of Engineering, Kollam 691005, India

A. Rama Mohan Rao and K. Ramanjaneyulu (eds.), *Recent Advances in Structural Engineering, Volume 1*, Lecture Notes in Civil Engineering 11,
https://doi.org/10.1007/978-981-13-0362-3_71

1 Introduction

The attack by acidic waters represents a topic of growing significance due to increasing damages to concrete structures globally. Concrete structures undergo rapid deterioration when it comes into contact with acidic solutions in varied situations, and the range of aggressive species is wide. This undesirable situation is a consequence of increasing sources of acidic media due to growing urban and industrial activities, and because cementitious materials are highly vulnerable in acidic environments due to their high alkalinity [1, 2]. Industrial effluents contain a wide range of organic acids whose action may lead to severe degradation of concrete structures. A review of the literature on the acid attack on concrete reinforces the fact that even though considerable research has been done on the effect of inorganic acids on concrete, only very few studies have focused on the effect of organic acids [3].

Organic acids are either present naturally in the agricultural products themselves (i.e. plants or fruit) and/or are intermediary or final products of the metabolism of microorganisms growing in the effluents. Organic acids also arise in industrial applications, but particularly in the agro-food industry [4]. Of all the organic acids, citric acid is found to be the most aggressive and leads to rapid deterioration [3, 4]. Sugarcane vinasses produced by the sugar industry and whey water from dairy industry contain citric acid, in addition to other organic acids detailed in Table 1. Concrete structures storing these effluents are vulnerable to the acid attack. Also, citric acid is the main constituent of lime/lemon juices and the juice shop floors and drains are prone to the acid attack. Acid attack is a complex process influenced by many factors related to materials and test method, and this process of degradation is still not properly understood. Currently, there are no codes or standards available for evaluating the resistance of materials to acid attack. Hence, this study attempts

Table 1 Organic acids in some agro-food industries [4]

Industry	Wastewaters	Acids	Concentration (mmol/L)	pH
Sugar industries	Sugar cane vinasses	Lactic Glycolic Citric Trans-aconitic Cis-aconitic Oxalic Fumaric Total (max.)	18–80.4 12–25 1.7–10.4 0.2–4.8 0.1–2.8 0.08–0.8 0.1–0.4 124.2	4–7
Dairy industries	Whey	Acetic Citric Lactic Propionic Butyric Total (max.)	14.0 9.2–9.6 3.4–5.7 1.0 0.6 30.9	4–6

to investigate further, the alteration kinetics in these conditions by developing accelerated test methods and thus, to design materials that perform well in these environments.

2 Materials and Methods

Currently, there are no codes or standards available for evaluating the material resistance to acid attack. Hence, the current study attempts to come up with a test method for evaluating the resistance of cement paste against acid attack. In order to study the role of binders in influencing alteration kinetics, binders such as Class F fly ash (30% replacement, FA30), densified silica fume (10% replacement, SF10), ground granulated blast furnace slag (50% replacement, BFS50) are considered as mass replacements to cement in addition to the control mix containing Ordinary Portland 53 Grade Cement (OPC) only. Particle size distribution of binders was studied using laser diffraction technique and is shown in Fig. 1. Slag was finer compared to cement and fly ash. Table 2 gives the physical properties of the binders. All mixes were prepared with constant water to binder ratio of 0.40. Polycarboxylate ether (PCE) based admixture at suitable dosage was used for the mix containing silica fume for improving the fluidity and dispersibility.

According to De Belie et al. [5], accelerated tests are preferred, in which the degradation rate can be increased by means of higher concentrations of the acid solution, larger contact surfaces, smaller sized specimen, etc. Hence, a static immersion based, accelerated leaching test was conducted on prismatic cement paste specimens of size 10 × 10 × 60 mm. Specimens were initially cured in saturated limewater for a period of 28 days. After the initial curing, saturated

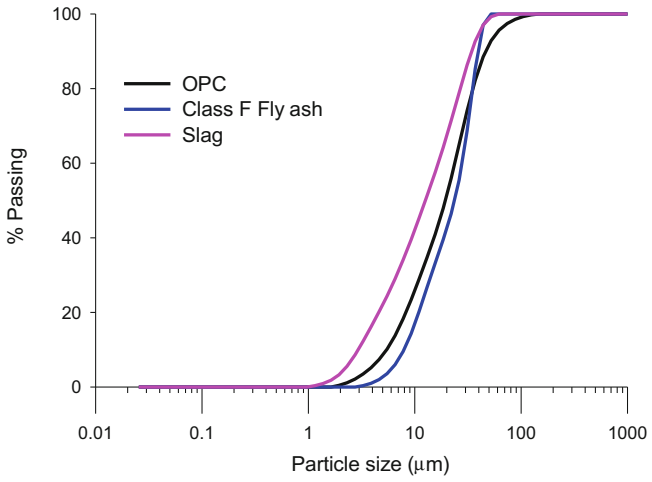

Fig. 1 Particle size distribution of binders

Table 2 Physical property of binders

Property	OPC	Class F fly ash	Slag	Silica fume
Specific gravity	3.15	2.21	2.88	2.04
Blaine's fineness (m^2/kg)	318	241	398	20000*
Loss on ignition (%)	3.43	0.08	−0.02	1.49

*BET surface area

Table 3 Test methods for evaluating the degradation kinetics

Test method	Remarks
Mass changes	In the case where brushing of specimens (with nylon brush) was done to remove the loosely held corroded particles, mass changes before and after the brushing were noted using a weighing balance having the precision of 0.1 mg. Parameters such as mass loss/gain, cumulative mass precipitated/leached and abraded were estimated based on the mass data collected, to demarcate the effect of brushing and precipitate/leaching. In the case of no brushing, mass changes were noted immediately after taking out the specimens from the acid solution.
Thickness changes	The thickness of the specimens was noted using a digital caliper having a sensitivity of 0.001 mm. When brushing is done, the thickness was measured after the brushing.
pH changes	Changes in pH of the acid solution were monitored using a digital pH meter, on a weekly basis just before the renewal of the acid.
X-ray micro-tomography (CT)	X-ray computed micro-tomography (CT) was used to get the 3-D and 2-D images of the cut specimen of size 10 × 10 × 10 mm before and after the degradation.
Compressive strength	Cube specimens of size 25 mm were prepared and immersed in acid solution (without any brushing). Compressive strength was tested before acid exposure and at every week of acid exposure, the loading rate being 143 N/s.

mass and thickness of specimens were measured after which they are exposed to 0.5 M citric acid (pH of 1.72). The volume of acid solution to specimen was kept fixed at 7.

Three specimens of the same mix were kept fully immersed in a glass beaker containing acid solution and the beaker is then covered with aluminium foil wrap in order to avoid carbonation and exposure to outside environment as much as possible. Acid solutions were renewed every week to maintain aggressiveness of the acid. Two types of tests were done: with and without brushing to simulate various real-life conditions. Test with brushing (named B28) is useful in studying the alteration kinetics while the study without brushing (named WB28) is essential to investigate the mechanism of degradation. In the method B28, brushing of specimens (with soft nylon brush) was done on a weekly basis to remove the loosely held corroded particles and also to accelerate the testing. Table 3 gives the details of

test methods used to evaluate alteration kinetics. The degradation was stopped after 3 weeks of exposure (by solvent exchange process using isopropanol) and the specimens are stored in sealed zip lock covers inside a vacuum desicccator until further tests to understand the mechanism of degradation. The study with brushing as described above was extended to OPC specimens initially cured for 28 days to analyse its behaviour when exposed to lemon juice solution (≈0.083 M citric acid, pH 1.98) for a period of 6 weeks. In the case of the static test without brushing (WB28), the only difference from the previous test (with brushing) is that no abrasive action is applied in the form of brushing and hence, the corroded layer was preserved for further characterisation.

3 Results and Discussions

3.1 Visual Observations

Citric acid was found to be very aggressive in the cementitious system. A white-coloured salt is precipitated in substantial quantities on specimens immersed in citric acid (Fig. 2) and is confirmed as calcium citrate tetrahydrate ($Ca_3(C_6H_5O_7)_2.4H_2O$) by X-ray diffraction study. This precipitate has low solubility (0.95 g/L at 25 °C), and loosely adhered to the specimen. The salt does not have a protective effect on the matrix due to the high molar volume of the salt, 518.4 cm^3/mol when compared to C–S–H (108–125 cm^3/mol) and Portlandite (33 cm^3/mol). This led to rapid loss of thickness and the aspects of specimens (without brushing) after three weeks of exposure are shown in Fig. 3. It can be noted that the control mix and the mix containing silica fume performed better as the loss of thickness was less when compared to the other mixes. Citric acid is

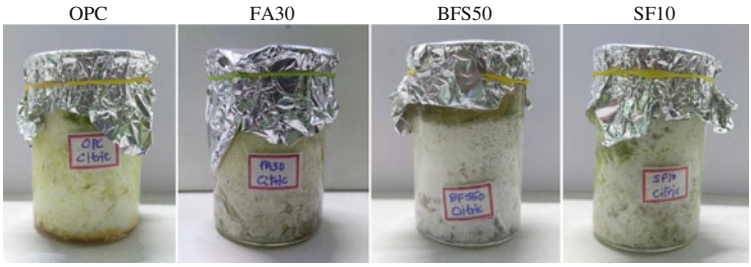

Fig. 2 Solutions after 3 weeks of acid exposure

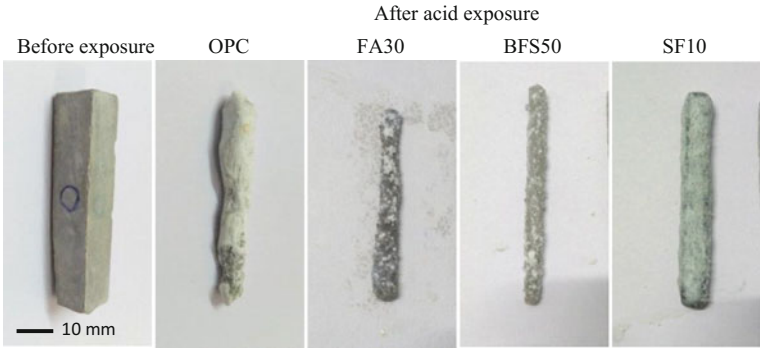

Fig. 3 Specimens before and after acid exposure

Fig. 4 OPC specimens before and after brushing on exposure to lemon juice

polyacidic as they dissociate to give multiple protons at their respective pK_a values of 3.14, 4.76 and 6.40 [6]. The high concentration used (0.5 M), polyacidity of citric acid and the non-protective nature of precipitate formed seems to have increased the aggressiveness of citric acid. According to Koenig and Dehn [7], the higher damaging effect could also be due to the acid buffer action exhibited by these organic acids. Figure 4 shows the specimen before and after brushing, when exposed to the lemon juice solution. The precipitate formation was found to be lesser as the concentration of citric acid was less. Also, the precipitate was not loosely adhered to the matrix as evident from Fig. 4. Apparently, the reduction in thickness was also found to be very less, when compared to 0.5 M citric acid.

3.2 Mass Changes

Mass change is a direct measure of degradation, and hence can be considered as a measure of material resistance against acid attack. The test method with periodic brushing (B28) simulates the flowing conditions of effluents, besides removing the outer degraded layer, thus accelerating the kinetics. Mass changes were calculated with respect to the initial mass (just before acid exposure). A positive value indicates mass gain whereas a negative value indicates mass loss. Exposure to 0.5 M citric acid resulted in mass loss at all ages, for all the mixes as the cementitious materials underwent dissolution to form the precipitate. Among the mixes, the mix containing silica fume (SF10) showed a lower mass loss while the mix containing fly ash (FA30) showed the least resistance as the mass loss was severe. OPC mix exposed to lemon juice (named OPC(L)) showed a small mass gain at initial ages and mass loss at prolonged exposure. However, the mass loss was significantly lesser when compared to 0.5 M citric acid. Hence, it can be inferred that the degradation kinetics in citric acid is highly dependent on its concentration (Fig. 5).

The test method without brushing (WB28) simulates static conditions of effluents. It also preserves the degraded layers for further micro-analytical study. The variation of mass changes without application of brushing is depicted in Fig. 6. It can be noted that the trend in the variation of mass change is similar to the case when brushing is done. The mix containing silica fume (SF10) showed superior resistance to citric acid. The mix containing fly ash (FA30) showed the least resistance while the control mix (OPC) and the mix containing slag (BFS50) exhibited intermediate resistance. It is found that abrasive action in the form of brushing had a negligible impact on kinetics, as the mass changes with and without brushing were comparable. However, the effect of the abrasive action in the form of

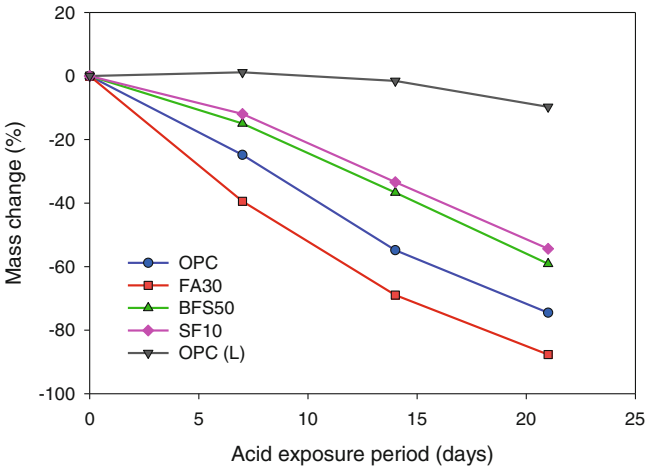

Fig. 5 Mass changes in acid exposure (B28)

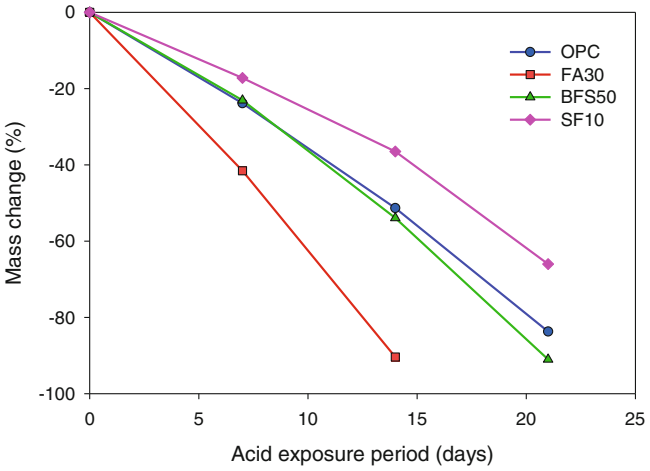

Fig. 6 Mass changes in acid exposure (WB28)

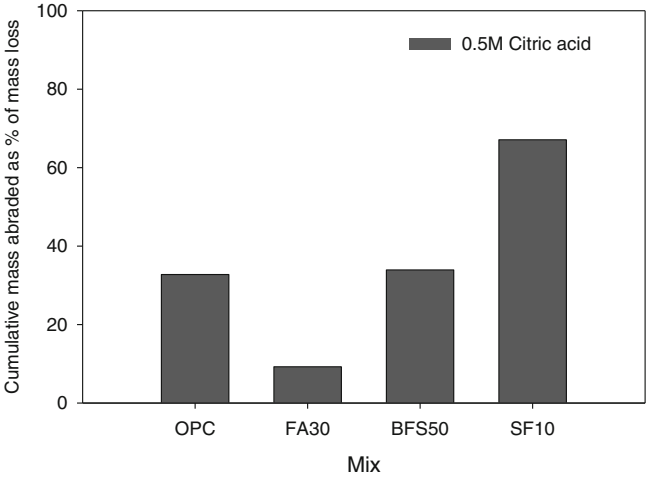

Fig. 7 Effect of abrasion (B28)

brushing will be more pronounced when the specimens are exposed to inorganic/organic acids and when the solubility of the salt formed is protective and less soluble as in the case of gypsum layer formed on specimens exposed to the sulphuric acid solution.

Based on the mass data observed for the testing with brushing (B28), cumulative mass abraded due to brushing and cumulative mass leached were calculated as % of the mass loss of specimens and presented in Figs. 7 and 8 respectively. The precipitate formed is more stable and adhered to the specimen in the case of the mix

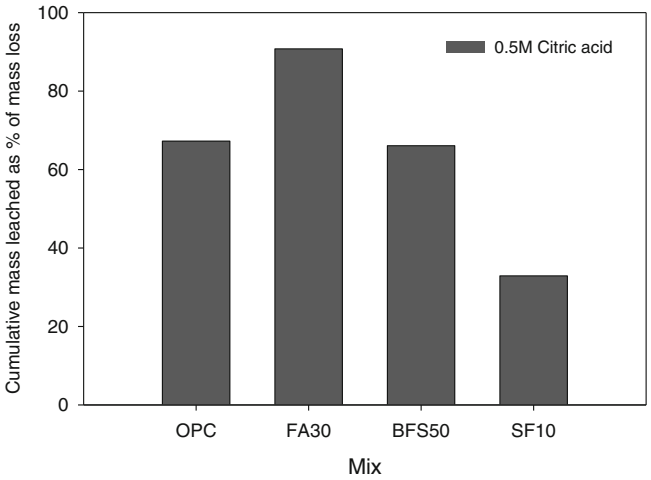

Fig. 8 Effect of leaching (B28)

containing silica fume (SF10) and evidently, abrasion effect was found to be more. Similar behaviour was noticed when OPC specimens are exposed to lemon juice and hence, leaching effect and mass loss was found to be less. In all the other mixes, the precipitate was found to be loosely bound to the matrix offering a little resistance, and it was found to fall from the specimen and got easily deposited in the beakers.

3.3 Changes in pH

The various phases present in the cementitious system reacts with an acid solution, releasing mainly Ca^{2+} and OH^{-} ions to the solution. Acid–base reaction occurs and due to this neutralization process, pH of the acid solution increases with time. Hence, measuring pH on regular basis could be another possible measure of the degradation kinetics as it gives an idea about the hydrogen ion consumption or neutralization capacity of the system. The pH evolution for the testing done with and without brushing is shown in Figs. 9 and 10 respectively. From Figs. 9 and 10, it can be seen that pH decreases with time. However, considering the considerable reduction in mass and surface area of specimens with exposure, it can be concluded that the degradation kinetics is unaffected by the time of exposure and continues to attack the specimen inward. In the case of OPC exposed to lemon juice, pH was found to increase with exposure. A sudden increase in pH after 2 weeks is observed due to the delamination of the adherent thick precipitate layer formed (refer Fig. 4), thus creating a new unattacked surface for leaching to continue at a faster rate thereafter. The hydrogen ion consumption is found to be high in the case of slag

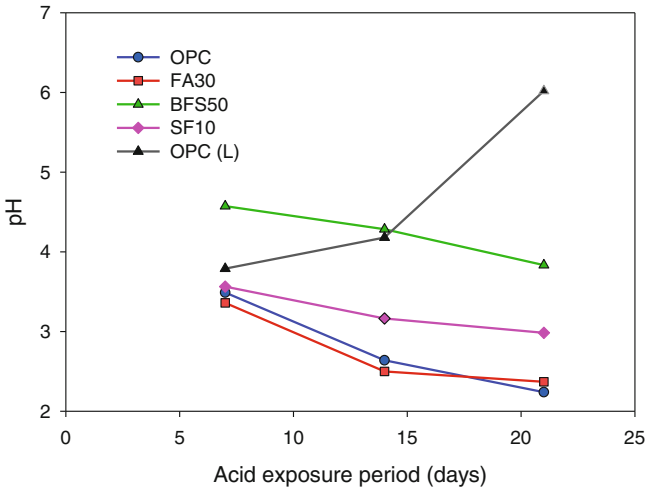

Fig. 9 Changes in pH of the acid solution (B28)

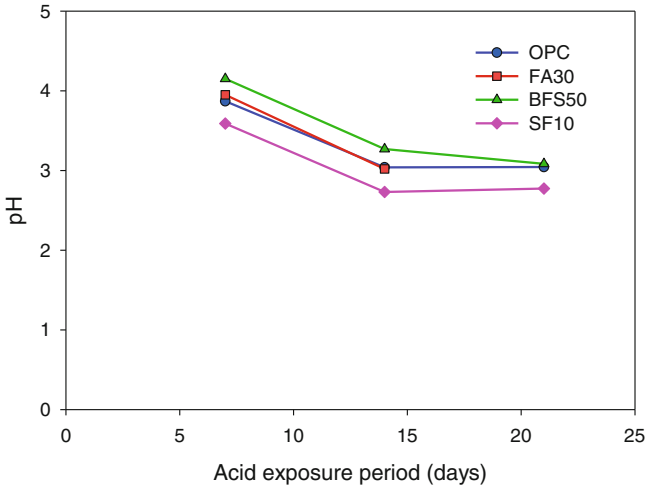

Fig. 10 Changes in pH of the acid solution (WB28)

containing mix (BFS50) for the tests with and without brushing. The pH rise was found to be lowest for SF10 for the test without brushing and this correlates well with the mass loss measurements.

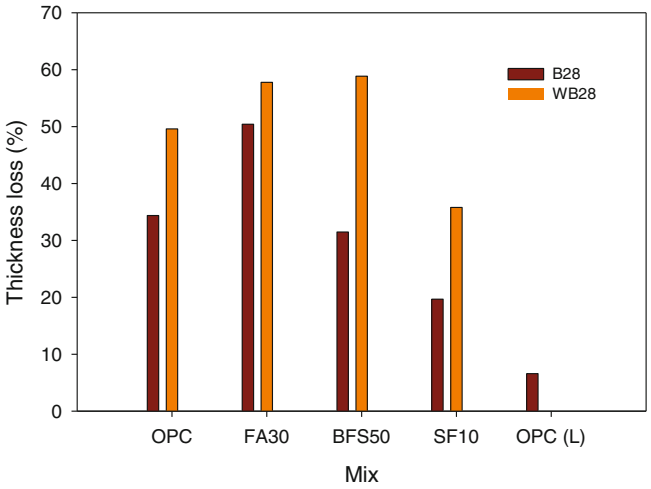

Fig. 11 Changes in thickness on acid exposure

3.4 Thickness Changes

The loss of thickness measured after 3 weeks of exposure is shown in Fig. 11. For FA30, the degradation was severe and hence, thickness reported was at 2 weeks of exposure for the testing without brushing. The order of performance of mixes based on thickness change was found to be in good alignment with mass change measurements.

For the tests with and without brushing, the thickness loss was found to be lesser in the case of the mix containing silica fume (SF10). Contrary to the expectations, the loss of thickness was found to be more when no brushing is involved. In the case of brushing, abrasive action applied in the saturated condition of the specimen could have a protective effect against further leaching. Also, the precipitate was found to be wet as it is a tetrahydrate. This reaffirms to a conclusion that abrasive action need not be applied while testing organic acids where leaching is the predominant process and the salt formed is not protective. These observations have important implications when designing test methods.

3.5 Strength Changes

The variation of the compressive strength of various mixes with acid exposure age is shown in Fig. 12. All the mixes showed a reduction in compressive strength on acid exposure when compared to the strength just before the exposure. This strength reduction is due to the alterations in the microstructure. Portlandite, C–S–H and other hydrates undergo decalcification to form the precipitate and this leads to weakening of the material having an impact in the mechanical properties.

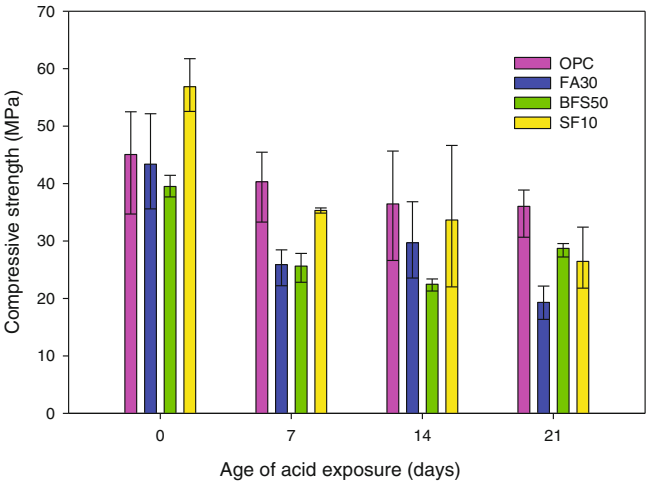

Fig. 12 Strength changes on acid exposure

The strength loss was maximum (more than 50% reduction) for fly ash containing mix (FA30) and minimum for the control mix (OPC). As the degradation has to be limited for the test to be conducted, volume of the solution to specimens was maintained at 4 only. The high variability in strength values observed may be attributed to the smaller size of specimens and the ratio of failure load to testing system capacity being less.

3.6 X-Ray Micro-Tomography

A novel attempt is made to characterize the microstructure of the acid degraded specimens using X-ray computed micro-tomography. Ramaswamy et al. [8] have formulated a test protocol for imaging the cementitious specimens using X-ray tomography. The tomography test set up at IIT Madras used for imaging, v|tome|x s is a versatile high-resolution system. Cubical samples of size approximately 10 mm were cut from the degraded specimens from the end. Solvent exchange process using isopropanol was used for specimen conditioning. The dried specimens were then taken for the imaging.

Figure 13 shows the 2-D cut slice image before and after the degradation (3 weeks); and the 3-D rendered image after the degradation of the various mixes investigated. Black regions in the images refer to the voids, white regions refer to the dense/anhydrous particles and grey coloured regions indicate the various hydrated/deteriorated phases formed.

The specimens after the degradation have clearly shown the mineralogical zonation which consists of an inner core zone, a thin dense transition zone and an

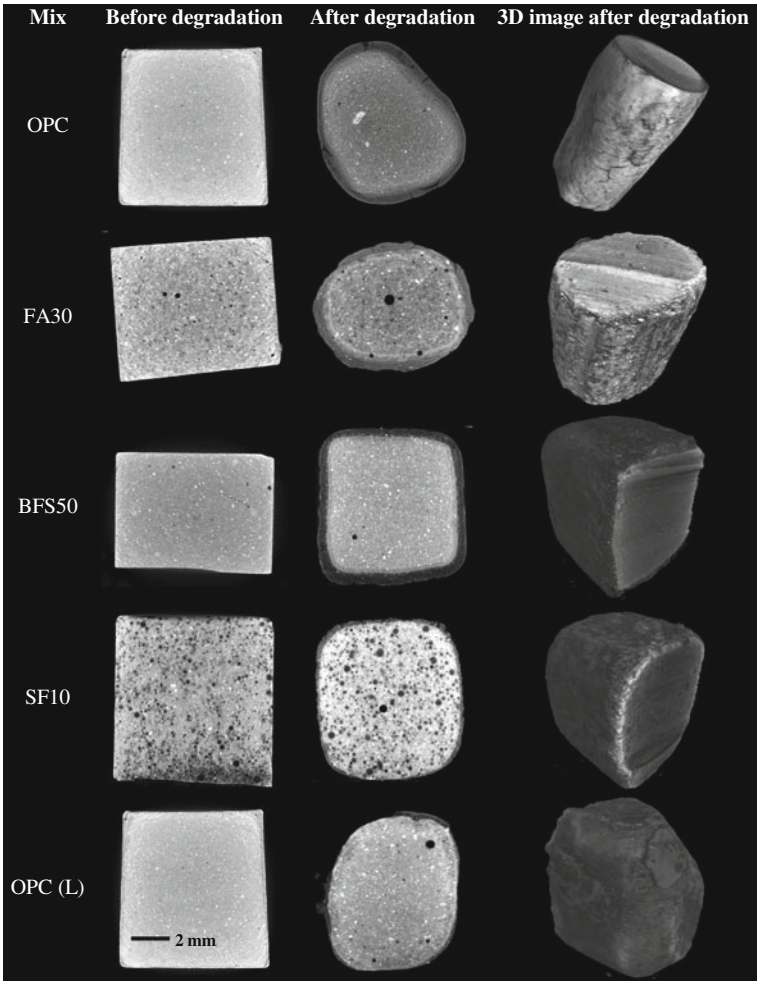

Fig. 13 X-ray tomographic images after acid exposure with brushing (not to scale)

outer degraded zone. The inner core zone is unattacked and the microstructure is very similar to the one before the attack. Transitional zone is seen as a thin dense white layer and this may be ascribed to the formation of aluminium and/or iron-bearing products. The outer zone is severely attacked and was seen only as a thin layer (dark layer with lower grey scale values for pixels), a majority of this zone underwent dissolution and got eroded away due to leaching and brushing. Another observation is that even the anhydrous particles were absent in the outer zone which leads to a conclusion that outer zone is amorphous and even anhydrous particles are unstable. The shape of the specimens was found to be distorted in the mix containing fly ash and control mix. Also, decalcification associated shrinkage cracks were found in the altered zone leading to further deterioration in

these mixes. The dark altered layer was restricted close to the surfaces only and this point out the fact that the salt (precipitate) formed is from outward of the sample. The thickness of the altered layer was found to be lesser in the case of the mix containing silica fume as well as the control mix when exposed to lemon juice. The precipitate formed in these cases was adherent to the matrix but could be removed due to brushing action. However, the altered layer was thicker for other mixes despite brushing which indicates that acid has penetrated to a deeper depth and the degradation is more.

4 Conclusions

In this study, the degradation kinetics of cement-based materials was investigated by developing and performing a static immersion-based-accelerated leaching test on cement paste specimens with and without brushing on exposure to citric acid. A holistic test protocol was presented and the study is one of the first of its kind in India in the area of durability of materials against acid attack. The results showed that citric acid is highly aggressive to cement-based materials as it resulted in strong leaching. The damaging effect was higher when compared to strong inorganic acids. The aggressiveness of citric acid could be attributed to its polyacidity, as they dissociate to give multiple protons at pK_a values. Furthermore, heavy precipitate formation was observed due to the formation of calcium citrate salt. This salt has less solubility and very high molar volume compared to Portlandite and C–S–H gel and thus found to be detrimental to the cement matrix. The performance of binders such as fly ash and slag was found to be ordinary while the mix containing silica fume showed better resistance to citric acid. The ordinary performance of binders could be due to high concentration/low pH of the acid solution and the absence of interfacial transition zone (ITZ) in the paste. A thorough micro-analytical study in conjunction with the methods presented in this paper will throw more light on the better understanding of degradation of cement-based materials in aggressive acidic environments.

References

1. Zivica, V., & Bajza, A. (2001). Acidic attack of cement based materials—A review (Part 1): Principle of acidic attack. *Construction and Building Materials, 15,* 331–340.
2. Pavlik, V. (1994). Corrosion of hardened cement paste by acetic and nitric acids; Part I: Calculation of corrosion depth. *Cement and Concrete Research, 24,* 551–562.
3. Bertron, A. (2013). Methods for testing cementitious materials exposed to organic acids. In M. Alexander, A. Bertron, & N. De Belie, N. (Eds.), *RILEM TC 211—PAE State-of-the-art report: Performance of cement-based materials in aggressive aqueous environments* (pp. 355–387).
4. Larreur-Cayol, S., Bertron, A., & Escadeillas, G. (2011). Degradation of cement-based materials by various organic acids in agro-industrial waste-waters. *Cement and Concrete Research, 41,* 882–892.

5. De Belie, N., Monteny, J., & Taerwe, L. (2002). Apparatus for accelerated degradation testing of concrete specimens. *Materials and Structures, 35,* 427–433.
6. Dyer, T. (2014). *Concrete durability* (pp. 1–420). CRC Press and Taylor & Francis Group.
7. Koenig, A., & Dehn, F. (2016). Main considerations for the determination and evaluation of the acid resistance of cementitious materials. *Materials and Structures, 49,* 1693–1703.
8. Ramaswamy, K. P., Santhanam, M., & Murugan, M. (2015). Characterization of cement paste modified with nano-materials using X-ray computed microtomography. In *3rd International Conference on Modeling and Simulation in Civil Engineering*, pp. 279–289.

Influence of Blended Cement on the Fresh Properties of Self-compacting Concrete Incorporating Recycled Aggregate

Ranganathan Senthamilselvi and Purushothaman Revathi

Abstract Production of self-compacting concrete requires a large amount of powder content, thus demanding the high quantity of cement with one or more admixtures. Using large quantity of cement creates production demand, environmental pollution and leads to high-energy consumption. In view of this aspect, mineral admixtures are used to replace the cement in high volume. On the other hand, the issue of disposal of demolition waste is addressed by recycled aggregate as coarse aggregate in SCC. This study investigates the influence of blended cement on the properties of fresh self-compacting concrete-incorporating RA. SCC with RA mixes is produced with different types and amounts of mineral admixtures. OPC cement, fly ash (FA), silica fume (SF), and ground-granulated blast-furnace slag (GGBS) are used in binary, ternary, and quaternary blends to improve the fresh properties of SCC. Cement is replaced by the above blends with 20, 40, and 60% for all mixtures. Fresh properties of the SCC with RA mixes are tested for slump flow, T 500, V-funnel flow, and L-box tests. The results indicated that when all the blended cement mixtures show improved fresh properties without segregation even at 60% replacement.

Keywords Self-compacting concrete · Recycled aggregate · Fresh properties Blended cement · Mineral admixtures

1 Introduction

Self-Compacting Concrete (SCC) is gaining popularity all over the world due to its self-flowability, which can be placed and compacted under its self-weight without any external vibration [1]. In order to achieve self compaction, a large amount of powder content is required, thus demanding a large quantity of cement with one or more admixtures [2]. Consumption of a large amount of cement severely affects the

R. Senthamilselvi · P. Revathi (✉)
Pondicherry Engineering College, Puducherry, India
e-mail: revathi@pec.edu

A. Rama Mohan Rao and K. Ramanjaneyulu (eds.), *Recent Advances in Structural Engineering, Volume 1*, Lecture Notes in Civil Engineering 11,
https://doi.org/10.1007/978-981-13-0362-3_72

environment severely. In order to reduce energy consumption, CO_2 emission, and production demand, cement is replaced with mineral admixtures in concrete [3]. Mineral admixtures are the by-products of different industries and dumped as waste. Various mineral admixtures such as fly ash (FA), silica fume (SF), ground-granulated blast-furnace slag (GGBS), metakaolin, etc., are used as a cement replacement in SCC. An extensive review of the literature has been carried out to examine the effect of mineral admixtures on the properties of SCC. Proper replacement of cement by suitable mineral admixtures can result in not only economical and ecological benefits but technical benefits as well. It improves the fresh properties of SCC considerably [3–10]. Large quantities of Construction and Demolition (C&D) wastes have been generated annually across the world. The use of C&D waste as a recycled aggregate (RA) in concrete is limited due to its low density and high absorption [11]. Few studies have been conducted using RA in SCC [12–14]. Fresh properties of SCC decreased with the increasing percentage of RA. To overcome these issues, RA is used in saturated surface dry condition (SSD). As a result, RA in SCC enhances the workability and flow properties of concrete, thus reducing the powder demand. Moreover, the fresh properties are influenced due to the small particle sizes of mineral admixtures, which in turn directly influence the fresh, mechanical, and durability performances of concrete. Use of blended cement in SCC is expected to eliminate the drawbacks of the particular mineral admixtures through combining with other superior quality material in order to reduce the overall cost of concrete production. The current knowledge of the fresh properties of blended cement is generally limited to SCC only. Celik [15] utilized high-volume class—F FA/High-volume natural pozzolan and limestone as binary and ternary blends in SCC. The study reveals that both binary and ternary-blended mixes give the better fresh properties. Gesoglu and Ozbay [16] investigated the effects of using FA, GGBFS, and SF as mineral admixtures in binary, ternary, and quaternary blends on the fresh properties of SCC. It is reported that SCC mixtures with blended cement have improved fresh properties without segregation. Guneyisi and Gesoglu [17] studied the properties of SCC with Limestone and GGBS as binary and ternary-blended cement. The study reveals that the use of GGBS in blended cement improves the fresh properties of SCC. Gesoglu et al. investigated the properties of SCC with binary, ternary, and quaternary-blended cement containing FA, GGBS, and SF [18]. It was concluded that the ternary use of PC + FA + GGBS shows the better fresh properties than the other blended mixtures. In view of this, a research program is implemented to study the contribution of binary, ternary, and quaternary blended cement with different mineral admixtures on the fresh properties of SCC with RA as coarse aggregate.

2 Materials

Ordinary Portland Cement (43 Grade) was used for this experimental investigation. Cement was partially replaced with Class F fly ash, Silica fume, and GGBS powders to develop binary, ternary, and quaternary systems. Locally available river sand with 4.75 mm, which is the maximum size and it was used as fine aggregate. Crushed granite obtained from the local quarry was used as NA. The crushed concrete specimens from the laboratory were used as the source of RA. These concrete specimens were crushed manually and subsequently crushed with a lab model jaw crusher and sieved. The aggregate passing in 16 mm sieve and retained on 4.75 mm sieve is used as RA. The nominal size of the natural and recycled coarse aggregates was 16 mm. The physical and mechanical properties of NA and RA were determined in accordance with IS 2386-1963 [19] and presented in Table 1. Potable water available in the college campus was used for the mixes. Polycarboxylic ether-based superplasticizer was used at 1% by weight of powder content, to achieve good workability.

Mix Proportion

In this study, SCC mixes were produced adopting particle packing mix design approach, whose detailed proportions are presented in Table 2. Totally, 22 mixes were designed with w/p of 0.36–0.37 and total powder content used was generally maintained as 570 kg/m^3 of concrete. SCCRA mixtures incorporated binary (PC + FA, PC + GGBS, PC + SF) and ternary (PC + FA + SF, PC + FA + GGBS, PC + GGBS + SF) and quaternary (PC + FA + GGBS + SF) cementitious blends in which a proportion of Portland cement was replaced with the mineral admixtures. The various replacement levels of mineral admixtures considered for SF are 5–15%, for FA are 20–60% and for GGBFS are 20–60% by volume of total powder content. Designed mixes are designated according to the type and the amount of mineral admixtures included.

Testing Methods

Fresh properties of SCC were quantified through slump flow, T 500 slump flow time, J-ring test, V-funnel test, and L-box test. The above tests were performed according to EFNARC guidelines to evaluate the characteristics of SCC such as passing ability, flowability, and segregation resistance. Slump flow and T 500 time test to assess the flowability and the flow rate of SCC in the absence of obstructions. The result is an indication of the filling ability of SCC, and the T 500 time is a

Table 1 Physical properties of aggregate

Sl. no.	Physical properties	Fine aggregate (River sand)	Recycled aggregate (RA)
1.	Specific gravity	2.59	2.27
2.	Bulk density (kg/m^3)	1375	1209
3.	Water absorption (%)	1	7.79
4.	Fineness modulus	3.06	7.24

Table 2 Mix proportions of various blended mixtures

Mix designations	W/P	Water	Cement	FA	GGBS	SF	Fine aggregate	Recycled aggregate		SP dosage (%)
SCCRAFA20	0.36	196	448	73	–	–	788	444	293	4.82
SCCRAFA40	0.36	196	336	146	–	–	788	444	293	4.46
SCCRAFA60	0.37	196	224	219	–	–	788	444	293	4.10
SCCRAGGBS20	0.36	196	448	–	101	–	788	444	293	5.08
SCCRAGGBS40	0.36	196	336	–	203	–	788	444	293	4.62
SCCRAGGBS60	0.37	196	224	–	304	–	788	444	293	4.53
SCC RASF5	0.36	196	532	–	–	20	788	444	293	4.73
SCCRASF10	0.36	196	504	–	–	41	788	444	293	4.67
SCCRASF15	0.37	196	476	–	–	61	788	444	293	4.59
SCCRAFA10S10	0.36	196	448	36	51	–	788	444	293	4.95
SCCRAFA20S20	0.36	196	336	73	101	–	788	444	293	4.72
SCCRAFA30S30	0.37	196	224	109	152	–	788	444	293	4.49
SCCRAFA15SF5	0.36	196	448	55	–	20	788	444	293	4.84
SCCRAFA30SF10	0.36	196	336	109	–	41	788	444	293	4.68
SCCRAFA45SF15	0.37	196	224	164	–	61	788	444	293	4.15
SCCRAS15SF5	0.36	196	448	–	76	20	788	444	293	5.04
SCCRAS30SF10	0.36	196	336	–	152	41	788	444	293	4.89
SCCRAS45SF15	0.37	196	224	–	228	61	788	444	293	4.75
SCCRAFA7.5S7.5SF5	0.36	196	448	27	38	20	788	444	293	4.93
SCCRAFA15S15SF10	0.36	196	336	55	76	41	788	444	293	4.70
SCCRAFA22.5S22.5SF15	0.37	196	224	82	114	61	788	444	293	4.45

measure of the speed of flow. J-ring test is to investigate both the filling ability and the passing ability of SCC. In the V-funnel test, the funnel is filled with the concrete and the time taken by it to flow through the funnel is measured. This test gives the account of the filling capacity of SCC. In the L box test, the test was conducted by removing the gate to allow the flow of concrete through the horizontal part and of the remaining concrete is in the vertical part and then the ratio of h_2/h_1 was determined.

3 Result and Discussion

Slump Flow

Slump flow results of all blended cement with SCCRA are shown in Figs. 1, 2, and 3. The slump flow values of all blended mixtures are within the range of 690–770 mm. As per EFNARC guidelines, binary-blended mixtures are classified SF2, ternary mixes and quaternary mixes are classified as SF_2 and SF_3. These mixtures are suitable for many normal applications and congested reinforcement structures. It is evident from these figures that in all in all cases of blended mixes, the improvement of flowability increased for all replacement levels of mineral admixtures. The result shows that the addition of mineral admixtures such as FA, SF, and GGBS helps in increasing flowability of the mix without segregation even at the 60% replacement ratio. The same trend is observed for all binary, ternary, and quaternary-blended mixes. It is also observed that the binary mix with GGBS and ternary mixes with FA and GGBS shows higher flow value compared to that of other blended mixes at 60% of replacement level. The best combination of various blending with respect to flow is 40% replacement of GGBS, 60% replacement for GGBS for binary blends, 60% of FA & GGBS for ternary blends, and 60% of the quaternary-blended mix. Therefore, it is clear that the binary blends, ternary blends, and quaternary mixes show better stability and flowability of mixes.

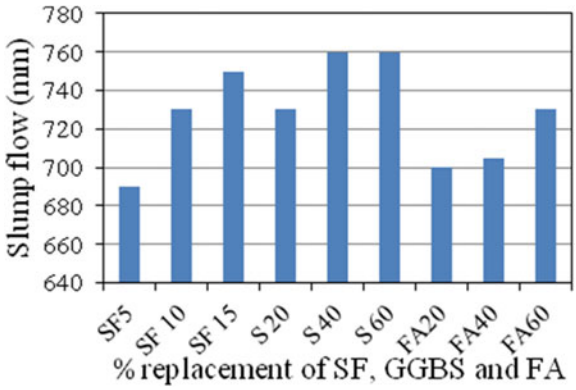

Fig. 1 Effect of binary-blended cement on slump flow

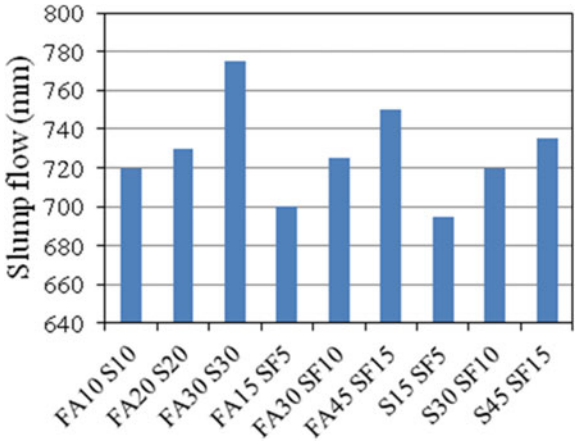

Fig. 2 Effect of ternary-blended cement on slump flow

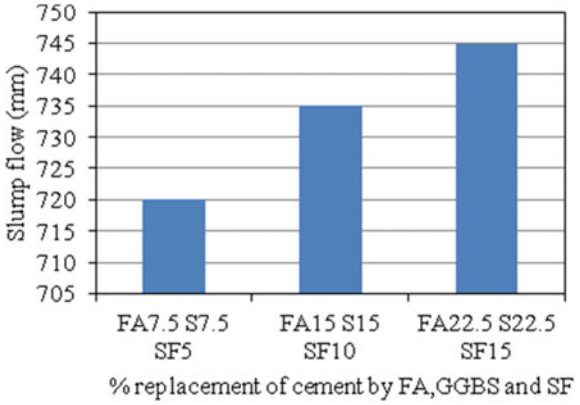

Fig. 3 Effect of quaternary-blended cement on slump flow

T 500 Flow Time

T 500 indicates viscosity of mixture. Shorter time of T 500 is an indication of the better flow capacity, with lower viscosity. As seen in Figs. 4, 5 and 6, T 500 values varied from 0.86 to 1.48 s for binary-blended mixtures, 0.8–1.49 s for ternary-blended mixtures and it is varied from 1.23 to 1.65 s for quaternary-blended mixtures. As per EFNARC guidelines, binary blended, ternary mixes, and quaternary mixtures are classified under VS1. These mixtures are suitable for congested reinforcement structures and it has a better surface finish. As clearly seen in the figures, the use of GGBS and FA in all the blended mixtures shows the effective reduction in the slump flow time. The concretes with SF and 20% of FA in binary mixtures, and all ternary and quaternary-blended mixtures at 20% replacement had a high slump flow time. According to EFNARC specifications and guidelines, the T 500 slump flow time of SCC generally ranges from 2 to 5 s. Hence, the T 500 slump flow times were less than the acceptable range. However, at the time testing,

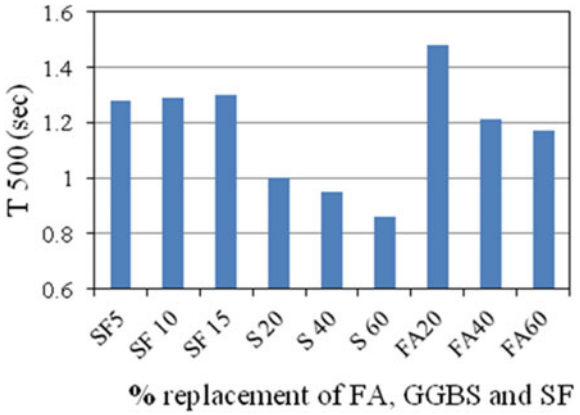

Fig. 4 Effect of binary-blended cement on T 500

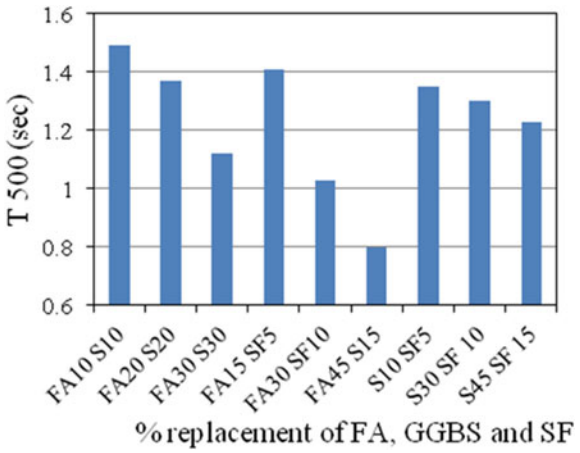

Fig. 5 Effect of ternary-blended cement on T 500

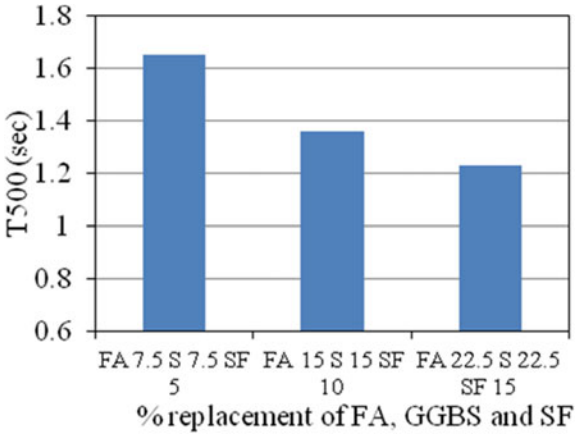

Fig. 6 Effect of quaternary-blended cement on T 500

all the blended mixtures were observed with good flow capacity without any bleeding and segregation. This is mostly due to the increased content of powder and SSD condition of RA.

J-Ring Slump Flow

The slump flow values of J-ring are shown in Fig. 7, 8 and 9. Flow ranges between 610–720 mm, 595–670 mm and 625–640 mm for binary, ternary, and quaternary-blended mixtures are considered acceptable as per EFNARC. It is evident from these figures all the blended mixes having FA and GGBS shows the highest slump value due to its particle size. For all blended mix, no segregation was observed during the tests and indicates satisfactory mix stability and segregation resistance for flow through reinforcement.

V-Funnel Flow

The V-funnel times of different mixes are presented in Figs. 10, 11, and 12. It can be seen from these figures that, V-funnel times for binary, ternary, and quaternary

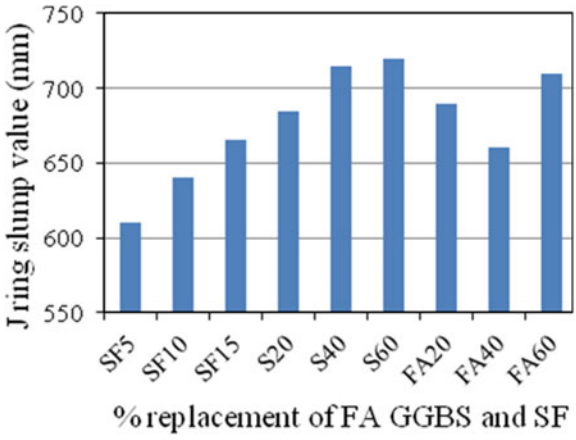

Fig. 7 Effect of binary-blended cement on j-ring slump flow value

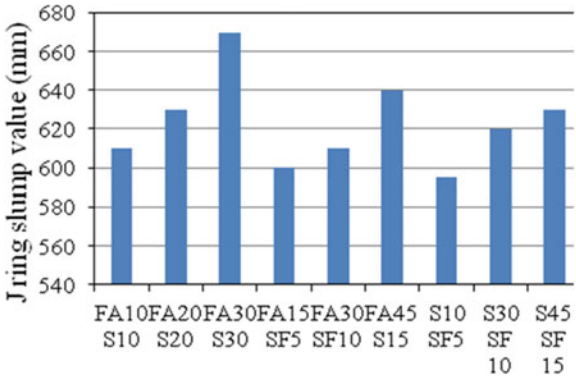

Fig. 8 Effect of ternary-blended cement on J-ring slump flow value

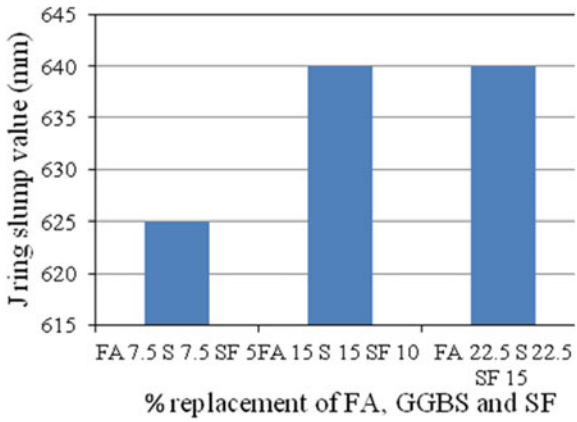

Fig. 9 Effect of quaternary-blended cement on J-ring slump flow

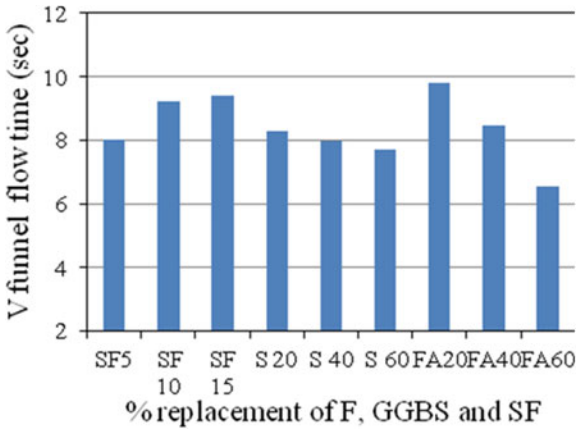

Fig. 10 Effect of binary-blended cement on V-funnel flow time

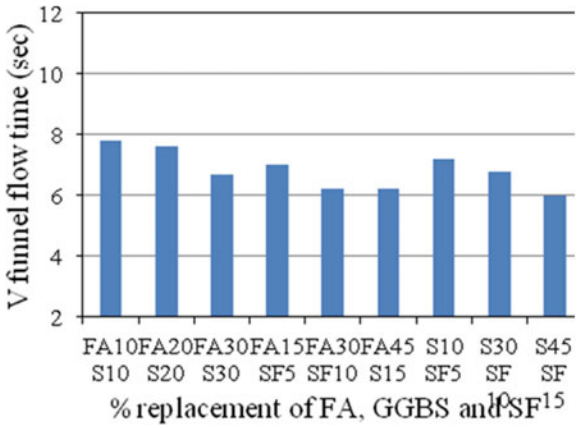

Fig. 11 Effect of ternary-blended cement on V-funnel flow time

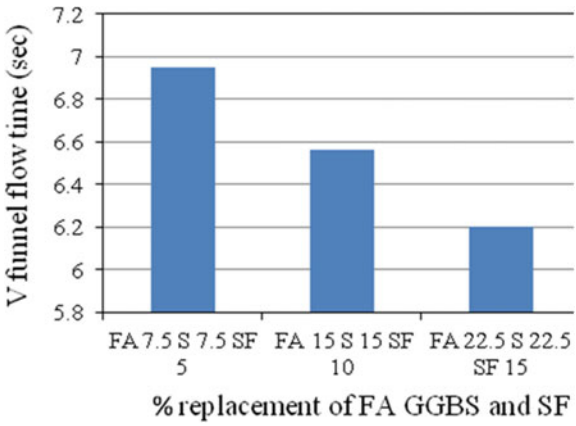

Fig. 12 Effect of quaternary-blended cement on V-funnel flow time

blended mixes are in the range of 6.54–9.8 s, 6–7.8 s, and 6–6.95 s, respectively. The V-funnel flow times of all mixtures satisfy the requirement of EFNARC guidelines. The quantity of mineral admixtures influences the V-funnel flow time of all the SCC mixes. Incorporating the lowest replacement of all blended mixtures in SCC makes it highly flowable with decreased viscosity.

L-Box

The results from the L-box test are shown in the Figs. 13, 14 and 15. The blocking ratio of SCC for all blended mixtures containing FA, GGBS and SF changed from 0.8 to 1.0. It shows the satisfactory blocking ratio as per EFNARC recommendation and all the blended mixtures were under PA 1 category. It is evident from these figures increasing replacement of GGBS and FA content in binary-blended cement shows the increased passing ability. This result was evident in the concrete produced with ternary and quaternary-blended cement. At the same ternary and quaternary blended cement. Also at the time of testing, the authors did not observe

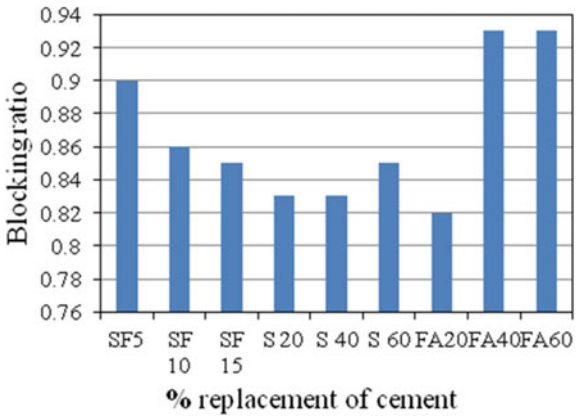

Fig. 13 Effect of binary-blended cement on blocking ratio

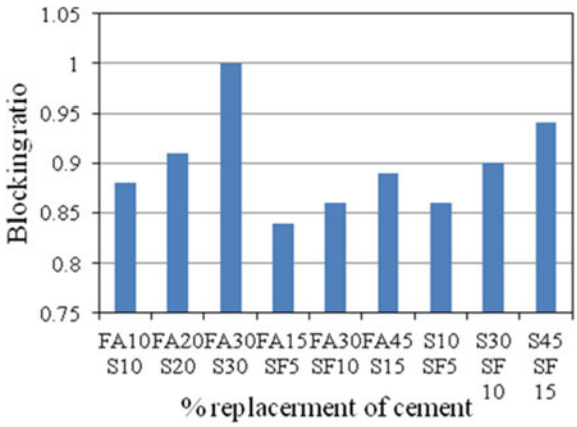

Fig. 14 Effect of ternary-blended cement on blocking ratio

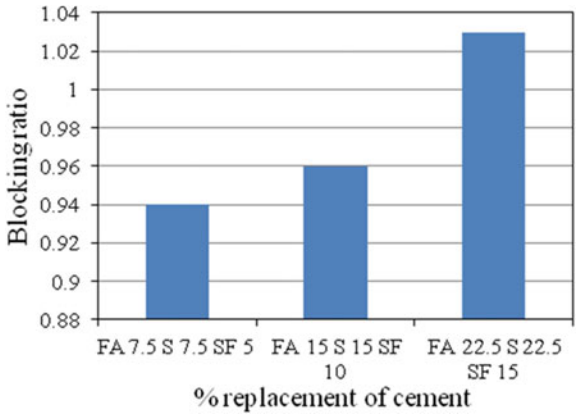

Fig. 15 Effect of quaternary-blended cement on blocking ratio

any tendency of blockage between reinforcement. Hence, it is revealed that all the mixes have good segregation resistance with good filling ability.

4 Conclusions

The following conclusions may be drawn from the experimental results.

1. The result shows that the addition of mineral admixtures such as FA, SF, and GGBS helps in increasing flowability of the mix without segregation even at the 60% replacement ratio. The same trend is observed in the ternary mixes and quaternary mix.

2. The binary mix with GGBS and ternary mixes with FA and GGBS shows higher flow value compared to that of other blended mixes at 60% of replacement level. The best combination of various blending with respect to flow is 20% replacement of S, 40% replacement for S for binary blends, and 60% of FA and S for ternary blends.
3. The filling ability of all blended mixtures increased with the inclusion of FA, GGBS at all replacement levels and with SF at high replacement.
4. Though binary and ternary mixes exhibit good fresh properties, the quaternary blended mixes will be assured to have better mechanical and durability properties of SCC with RA, in addition to its fresh properties.

References

1. Okamura, H. (1997). *Self compacting high –performance concrete* (pp. 50–54). Concrete Int.
2. EFNARC. (2002). *Specification and guidelines for self-compacting concrete*. UK: EFNARC.
3. Ponikiewski, T. (2014). The influence of high-calcium fly ash on the properties of fresh and hardened self and high performance self compacting concrete. *Journal of Cleaner Production, 72*, 212–221.
4. Bouzoubaa, N., & Lachemi, M. Self compacting concrete incorporating high volumes of class F fly ash preliminary results. *Cement and concrete research, 31*, 413–420.
5. Dinakar, P., Babu, K. G., & Santhanam, M. (2008). Durability properties of high volume fly ash self-compacting concrete. *Cement Concrete Composite, 30*(10), 800–886.
6. Yazici, H. (2008). The effect of silica fume and high volume class c fly ash on mechanical properties, chloride penetration and freeze-thaw resistance of self compacting concrete. *Construction and Building Materials, 22,* 456–462.
7. Turk, K., Turgut, P., Karatas, M., & Benil, A. (2010). Mechanical properties of self compacting concrete with silica fume/ flyash. In *9th International Congress on Advances in Civil Engineering*, pp. 27–30.
8. Boukendakdji, O., Kadri EI, H., Kenai, S. (2012). Effects of granulated blast furnace slag and SP type on the fresh property and compressive strength of self-compacting concrete. *Cement and Concrete Composites, 34*(4), 583–590.
9. Venkatasubramani, R. (2013). Performance of self compacting concrete containing different mineral admixtures. *KSCE Journal of Civil Engineering, 17920,* 465–472.
10. Ahmed, S., Adekunle, S. K., Maslehuddin, M., & Azad, A. K. (2014). Properties of self compacting concrete made utilizing alternative mineral fillers. *Construction and Building Materials, 68,* 268–276.
11. Padmini, A. K., Rmamurthy, K., & Mathews, M. S. (2009). Influence of parent concrete on the properties of recycled aggregate concrete. *Construction and Building Materials, 23,* 829–836.
12. Yong, P. L., & Teo. D. C.L. (2009). Utilization of recycled aggregates as coarse aggregate in concrete. *Journal of Civil Engineering, 1*(1), 29–36.
13. Sumanth, R. C., RatnaSai, K. V., & Rathish Kumar, P. (2013). Mechanical and durability properties of self compacting concrete with recycled concrete aggregates. *International Journal of Scientific & Engineering Research, 4*(5), 2229–5518.
14. Tang,W. (2013). Fresh properties of self compacting concrete with coarse recycled aggregate. *Advanced Material Research, 602–604*, 938–942.

15. Celik, K., Meral, C., Mancio, M., Mehta, P. K., & Monteiro, P. J. M. (2014). A comparative study of self-consolidating concretes incorporating high-volume natural pozzolan or high-volume fly ash. *Construction and Building Materials*.
16. Gesogolu, M., & Ozbay, E. (2007). Effects of mineral admixtures on fresh and hardened properties of self-compacting concretes: binary, ternary and quaternary systems. *Materials and Structures, 40,* 923–937.
17. Guneyisi, E., & Gesogolu, M. (2011). Properties of self compacting Portland pozzolana and limestone blended cement concretes containing different replacement of slag. *Materials and Structures, 44,* 1399–1410.
18. EFNARC. (2005). *The European Guidelines for Self Compacting Concrete*.
19. Indian standard Code of Practice for Methods of Test for Aggregates for Concrete IS: 2386 (Part IV)-1963. New Delhi: Bureau of Indian Standards.

Flow Characteristics of Polymer-Modified Sisal Fibre-Reinforced Mortar

Sriraman Priyadharshini and Gudimella Ramakrishna

Abstract Nowadays, incorporation of natural fibres in cement composites is becoming very popular due to several advantageous properties of natural fibres. The natural fibre incorporation into matrix provides varying effects in terms of both negative and positive aspects with respect of fresh characteristics of composites and these effects will resembles in performance of hardened composites. Therefore, it is important to study the fresh behaviour of natural fibre-reinforced matrices and also to proportionate mix parameters before production of fibrous composites. On the other hand, use of polymers in natural fibre plays a vital role in adjusting the negative effects of fibre incorporation. Based on the above facts, the effects of addition of sisal fibre and styrene-butadiene rubber polymer on flow behaviour in 1:3 mortar composite has been investigated in the present study. From the results, it is noticed that the polymer addition into sisal fibre-reinforced cement mortar greatly enhances the fresh behaviour. Also, the flow curves are obtained for various cement mortar mixes containing the polymer contents of 5 and 10% and sisal fibre contents of 0.5, 1, 1.5, 2, 2.5 and 3% respectively. The flow curves can be used to arrive *W/C* ratio for a given flow value, polymer content and fibre content for the various applications of cement mortar.

Keywords Flow · Mix parameters · Mortar · Polymer · Sisal

S. Priyadharshini · G. Ramakrishna (✉)
Department of Civil Engineering, Pondicherry Engineering College,
Puducherry 605014, India
e-mail: grkv10@pec.edu

S. Priyadharshini
e-mail: priya5.sriraman@gmail.com

A. Rama Mohan Rao and K. Ramanjaneyulu (eds.), *Recent Advances in Structural Engineering, Volume 1*, Lecture Notes in Civil Engineering 11,
https://doi.org/10.1007/978-981-13-0362-3_73

1 Introduction

Use of natural fibres in cement/cementitious matrix is gaining vital importance in the field of construction. The major concern on natural fibres among many researchers is because of its abundant availability, economical and eco-friendly nature. Moreover, the environmental issues in manufacturing and disposing of the synthetic fibres are very serious and also pose several health problems. Also, synthetic fibres affords high cost due to more energy consumption during the manufacturing process. Hence, the attention towards natural fibre cement/cementitious composites has been growing and a lot of research works is going on all over the world. Natural fibres, not only proves to be economical and eco-friendly, but also provides several useful technical properties such as light-weight, high impact strength, more toughness, excellent tensile properties, better post-cracking behaviour, etc. [1–3].

Also, natural fibre cement composites show some negative issues on long-term durability due to varying nature of fibre, balling effect in fresh composites, moisture sensitivity, degrading effects under cement medium (i.e. alkaline medium) [4]. These characteristics of natural fibres need some extra care to make such composites to perform in a better way. Several techniques are adopted to improve the properties of natural fibre composites. The various techniques so far adopted are a surface modification of fibres (e.g. coatings to fibre, alkaline treatment, etc.), matrix modification (e.g. Using mineral admixtures, polymer modification) and combined surface and matrix modification [5–12]. The techniques so far mentioned are major aspects of improving the composite properties. On the other hand, there are some minor factors but are very important in improving composite strength and durability. Such minor contributing factors are method of mixing, curing, mix type and various material parameters [4, 9]. The mix proportion and material optimization is the foremost process of achieving good-quality composite product. It is well known that the quality of composites in fresh state resembles its performance at hardened state. The mix with good fresh characteristics will pave way for achieving designed strength and durability. Fresh characteristics of mortar are concerned with several complicated terms namely workability, flowability, consistency, rheology, etc. [13, 14]. These terms are measured by using various tests, viz. mini-slump test, flow test, marsh cone, viscometers and rheometers [15–17]. The literature states that, it is more common to use flow table test for studying the fresh behaviour of mortar [18]. Also, this test proves to be very simple, economical and provides reliable direct results on flow, which, in turn, tells how the mortar is consistent [13]. Also, the term consistency related to the type of application of mortar, thereby arriving the required *W/C* ratio seems to be predominant in proposing adequate mix proportions.

In this investigation, the polymer-modified sisal fibre-reinforced mortar is evaluated for its fresh properties using flow table test. The main aim of this study is to investigate mix parameters and to arrive flow curves for achieving quality mix proportion. The various parameters considered are water–cement ratio, fibre

content, and polymer content and mix type. Also the effect of various sisal fibre content (0.5–3%), SBR polymer content (1–15%) and their interactive effect on flow values for various mixes of 1:3 mortar is thoroughly investigated.

2 Experimental Program

2.1 Materials for Mortar

Ordinary Portland Cement (OPC) of grade 43 confirming to IS 8112-2013, good quality locally available river sand and potable water were used in the preparation of mortar. Natural fibre named sisal fibre available in 300 mm lengths was cut and used an aspect ratio from 125 to 215. Styrene-butadiene rubber (SBR) polymer was used to enhance the properties of mortar mixes and the water content already present in SBR was adjusted with designed *W/C* ratios. The physical properties of all the materials used were provided in Tables 1, 2, 3 and 4.

Table 1 Physical properties of cement (OPC 43 grade)

Sl. no.	Property	Values
1.	Standard consistency (%)	29.5
2.	Initial setting time (min)	120
3.	Final setting time (min)	270
4.	Soundness (mm)	1
5.	Specific gravity	3.15

Table 2 Physical properties of sand

Sl. no.	Property	Values
1.	Specific gravity	2.6
2.	Water absorption (%)	1%
3.	Bulk density (kg/m^3)	1683
4.	Fineness modulus	2.83
5.	Zone	II

Table 3 Physical properties of sisal fibre

Sl. no.	Property	Values
1.	Average length (mm)	2.6
2.	Average diameter (mm)	0.1
3.	Density (g/cm^3)	1.45
4.	Average tensile strength (N/mm^2)	1360
5.	Elongation (%)	7.3
6.	Water absorption (%)	180

Table 4 Physical properties of SBR polymer

Sl. no.	Property	Values
1.	Colour	Milky white
2.	Total solid content (%)	44
3.	Water content (%)	56
4.	pH	10
5.	Specific gravity	1.03

2.2 Mix Proportions

The mix was designed for 1:3 mortar by considering four different mixes, viz. control mix, polymer-modified mortar (PMM) mix, sisal fibre-reinforced mortar (SFM) mix and polymer-modified sisal fibre-reinforced mortar (PMSFM) mix and shown in Table 5. The varying parameters considered were water/cement (*W/C*) ratio, fibre content and polymer content. The mixes were prepared with fibre content (FC) varying from 0.5 to 3% and polymer content (PC) from 1 to 15%. *W/C* ratio has been varied by considering the attainment flow values ranging from 80 to 100%.

2.3 Test Program

The 1:3 mortar mixes were tested for determining the effects of fibre and polymer content on flow characteristics using flow table test confirming to IS 4031: Part-7. The flow table test is performed by placing the mortar sample inside the frustum of cone mould in two layers and each layer is tamped 20 times smoothly with tamping bar and excess mortar is wiped off. Then, remove the mould and operate the machine to offer 25 drops to the placed sample. The flow is measured for the increased base at least for four diameters with equispaced intervals and is expressed as a percentage increase with that of the original base diameter. The flow table test for each mix is performed by increasing *W/C* ratio up to the attainment of aimed flow percentage of 80–100%.

Table 5 Mix proportions of various mixes

Mix	Cement (By parts)	Sand (By parts)	Fibre content (%)	Polymer content (%)
Control	1	3	–	–
PMM	1	3	–	1–15%
SFM	1	3	0.5–3%	–
PMSFM	1	3	0.5–3%	1–15%

3 Results and Discussion

3.1 *Effect of Polymer Content on Flow Characteristics of Mortar*

The effect of different percentages of polymer contents on flow characteristics of mortar for various *W/C* ratios is shown in Fig. 1. The flow curves of PMM falls above the control mortar, confirming that the effect of polymer addition improves the flow characteristics of mortar. In general, increase of PC and *W/C* ratio increases the flow value. However, critically comparing the flow values for each PC shows that the flow increases with increase in PC but the curves with PC of 9, 10 and 11% are overlapped at different *W/C* ratios and also the PC–13% shifts below the PC–15% curve. Therefore, from the above point, it is realized that the selection of low PC with higher flows is also possible. Hence, PC of 13 and 10% are a wise choice instead of 15 and 11%, respectively, for bringing the advantages in achieving required flow at minimum polymer dosages. The improvement in flow with respect to control mortar is compared for flow curve with higher flows. In this aspect, the higher flow is achieved for PC of 13%, showing the increase in flow at *W/C* ratio of 0.45 is around 8.3 times with that of control mortar. Also, the aimed flow percentage of 80–100% is achieved at lower *W/C* ratio for PMM but a flow of only 24.5% attained for control mortar. From this it is clear that the addition of polymer imparts very high flow improvement even at low *W/C* ratios. Almost all flow curves (PC–1 to PC–15%) are noticed to convening closer as *W/C* ratio increases and this implies that the effect of the polymer at higher *W/C* ratios is very less but the effect is vice versa at lower *W/C* ratios. Moreover, increase of PC achieves the flow at very low *W/C* ratios, i.e. the flow starts very earlier for higher PCs when compared with low PCs and control mortar. Therefore, the mixes with very low *W/C* ratio and higher PC impart a mortar to achieve measurable flow.

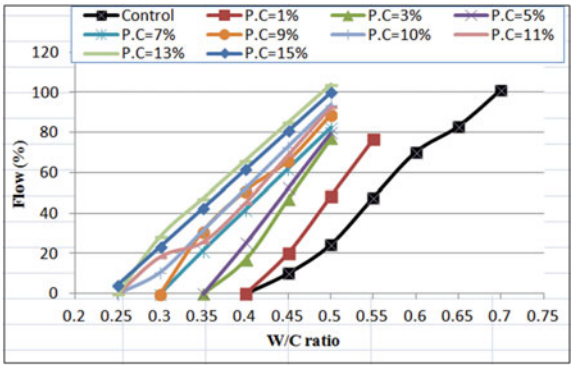

Fig. 1 Flow versus *W/C* ratio for control and PMM mixes

3.2 *Effect of Fibre Content on Flow Characteristics of Mortar*

In Fig. 2, the effect of fibre content on flow characteristics at various *W/C* ratios is shown. From this, it is seen that the flow curves of SFM show opposite trend when compared with PMM curves. Therefore, it is clear that the addition of fibre reduces the flow values when compared with flow of control mortar. Also, increase of FC from 0.5 to 3% shows reduction in flow, but FC of 0.5% illustrates an improved flow from 0.55 *W/C* ratio compared to control mix. This improvement of flow may be due to the minimum FC, which is not sufficient to restrict the flow performance. The percentage reduction of flow for control mortar and SFM at 3% FC is compared and it is evident that the reduction of flow almost ranges from 38 to 75% at various *W/C* ratios. In addition, the flow curves for various FC (0.5–3%) are critically evaluated at constant *W/C* ratio and this depicts that at *W/C* ratio of 0.5, the differences of flow for various FC are very closer than that of flows attained at *W/C* of 0.65 and greater. The difference of flow for 0.5 and 3% ranges from 19.4 to 53.7% between *W/C* ratio 0.5 and 0.65 respectively. Therefore, this may be due to the fact that the fibre used in SSD condition imparts higher flow differences for low-to-high FC at higher *W/C* ratios. Moreover, the flow of control mortar starts at *W/C* ratio of 0.45, SFM at FC between 0.5 and 2.5% starts at 0.5 *W/C* ratios and for FC of 3% the flow begins only at 0.55 *W/C* ratios. From this, it is clear that the water requirement is more for SFM compared to control mortar whereas mix with FC content greater than 2.5% requires still higher *W/C* ratio to attain a measurable flow. Also it is seen that up to *W/C* ratio of 0.6, the flow curves of FC–3% and FC–2% shifts over the flow curves of FC–2.5% and FC–1.5%, respectively, but after *W/C* ratio of 0.6 the curves are vice versa, showing the fibre effect is nonlinear at lower *W/C* ratios whereas shows linear trend at higher *W/C* ratios. Altogether, the attained higher percentage loss in flow for SFM is observed for 3% FC and is compared to control mortar, which seems to be in the range of 75–38% for *W/C* ratios between 0.55 and 0.7.

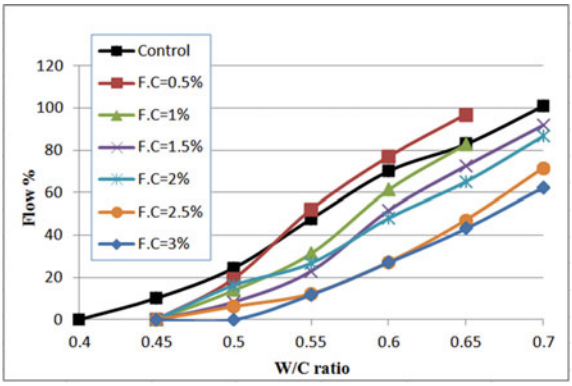

Fig. 2 Flow versus *W/C* ratio for control and SFM mixes

3.3 Comparative Discussion on PMM and SFM Mixes with Flow Curves and Flow Value

The flow curves and flow values obtained for PMM and SFM are compared and critical ranges of varying parameters are presented in this discussion. In Fig. 3, the curves for control mortar, PMM and SFM mixes are correlated. From this, it is clearly seen that the curves of SFM are lying below the control mix and PMM curves are above control mix. Therefore, this confirms that there is a loss in flow is observed for SFM mixes and wide improvement in flow has been noticed for PMM mixes. On the other hand, the PMM attains flow at a very minimum *W/C* ratio of around 0.3 whereas the control and SFM mixes attained the flow only at *W/C* ratios of 0.45 and 0.5 respectively. Hence, the higher water requirement, particularly in SFM, mixes to attain sufficient flow will lead to lower strength, which can be expected to compensate by incorporation of polymer in SFM mortar mixes. The use of SBR polymer in SFM mixes may also contribute to even distribution of fibres throughout the mix and thereby solves the purpose of fibre addition by maintaining uniformity in mixes and reducing the balling effect. Also, it is seen that the PMM curves converge at higher *W/C* ratio but the SFM curves diverge at higher *W/C* ratio. In other words, it is seen that the increase in polymer addition does not shows much effect at higher *W/C* ratios when compared with lower *W/C* ratio but the increase in fibre addition improves flow at higher *W/C* ratios. From Table 6, it is evident that the PMM with *W/C* ratio of 0.45 particularly starts to cover the wide range of mixes than other lower *W/C* ratios by attaining flow for all PCs used. As overall, the *W/C* ratio between 0.35 and 0.45 almost covers major mixes by starts attaining flow in PMM mixes with medium to higher flow percentages. By comparing SFM and PMM, *W/C* ratio of 0.5 starts to cover almost all mixes with various FC and PC by attaining the measurable flow. Moreover, the selection of *W/C* has to be made by compensating the flow loss and flow gain in both PMM and SFM mixes. From the Table 7, it is noticed that the flow value minimized at 0.5 *W/C* ratios for the fibre content from 0.5 to 3% and on the other hand the flow is

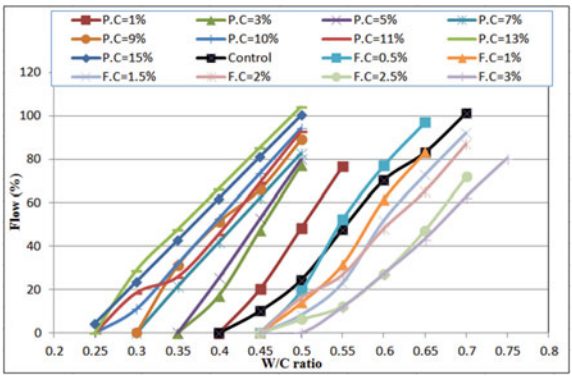

Fig. 3 Comparative flow curves for control, PMM and SFM mixes

Table 6 Flow values in percentage given for Control, PMM and SFM for various *W/C* ratios

W/C ratio	Control mix		SFM-Fibre content (F.C)						PMM-	Polymer content (P.C)						
		0.5%	1%	1.5%	2%	2.5%	3%	1%	3%	5%	7%	9%	10%	11%	13%	15%
0.25	0	0	0	0	0	0	0									4.3
0.3	0	0	0	0	0	0	0						10.9		28.7	23.5
0.35	0	0	0	0	0	0	0				21.5	31.1	31.7	21.8	47.5	42.6
0.4	0	0	0	0	0	0	0		17.2	25.3	41.9	51.2	52.5	45.4	66.3	61.8
0.45	10.2	0	0	0	0	0	0	20.3	47.3	52.6	62.1	66	73.3	69	85.2	81
0.5	24.5	19.4	13.9	8.4	16.3	6.3	0	48.5	77.1	79.8	82.4	88.8	94.1	92.7	104	100.1
0.55	47.8	52.1	31.4	23	26.8	12.4	11.8	76.7								
0.6	70.2	76.9	61.4	51.7	48	27.3	27.1									
0.65	83	96.9	83	72.6	65.2	47.3	43.2									
0.7	101.13	124.2	102	91.9	86.8	71.8	62.5									
0.75	–	149.6	123.3	109.4	100.7	77.2	80.2									

Table 7 Difference in flow value for higher and lower flow values at constant *W/C* ratio for PMM and SFM

W/C ratio	PMM-difference in PC (%)	Difference in flow (%)
0.3	3	17.8
0.35	4	26
0.4	10	49
0.45	12	64.9
0.5	12	55.5
W/C ratio	SFM-difference in FC (%)	Difference in flow (%)
0.5	2.5	19.4
0.55	2.5	40.3
0.6	2.25	49.8
0.65	2.5	53.7
0.7	2.5	61.7
0.75	2.5	69.4

maximized for the *W/C* of 0.45 with respect to various polymer dosages. From this, it is desired to maintain the *W/C* ratio between 0.4 and 0.45 for obtaining measurable flow. Also, the compensation of flow loss in SFM at particular FC will be achieved by adopting a particular range of PC. Furthermore, it is noticed that at lower *W/C* ratio, the flow can be achieved only beyond 10% PC and so selecting lower FC for such mixes will be able to balance the lost flow in SFM. Moreover, the lower PC of 1–5% and higher PC of 7–15% are to be dealt distinctly. It is noticed that the PC of 5% shows better flow among PC below 5% and also PC of 10 and 13% performs superior than other PC. However, the optimum flow at high *W/C* ratios can be achieved by combining lower FC with lower PC and higher PC with higher FC.

3.4 Effect of Fibre–Polymer Interaction on Flow Characteristics of Mortar Using Critical PC

The combined effect of fibre and polymer on flow characteristics of mortar has been studied for the selected PMM mixes based on discussion under Sect. 3.1. The selected PC of 5 and 10% are used to make mortar mixes with all FC employed in SFM mixes and their effects on flow performances are presented in Fig. 4. It is noticed that almost all flow curves of PMSFM falling above the control mortar, illustrating that the polymer addition in SFM improves the flow performance with the chosen PC of 5 and 10% for the mixes having FC from 0.5 to 3%. This improvement in flow is noticed to be about 1.2–4 times and 1.3–5.6 times for mixes produced with PC of 5 and 10%, respectively, for various *W/C* ratios and FCs. Also, it is evident that the flow behaviour seems to be higher with

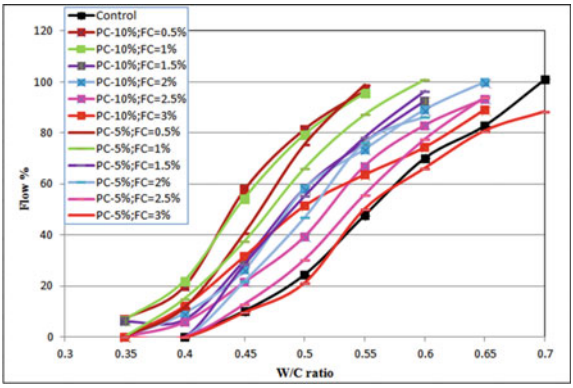

Fig. 4 Flow curves for PMSFM mixes at various *W/C* ratios

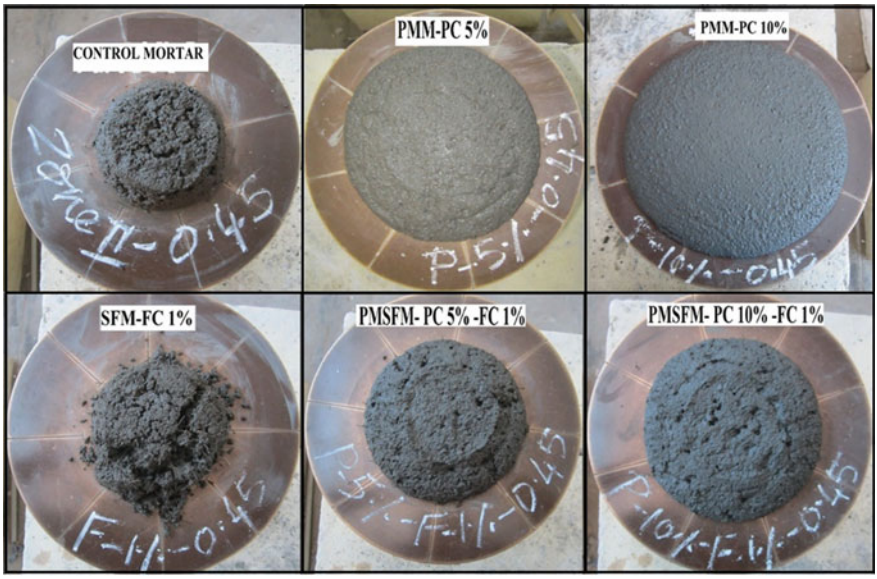

Fig. 5 Flow spread for control, PMM, SFM and PMSFM mixes

decreasing FC and with increasing PC. Moreover, the flow is noticed for constant FC with PC of 5 and 10% and it is observed that the mixes at all FC with 10% of PC performs better than 5% PC with the exception of mix at a FC of 1.5%. Therefore, the flow curves with PC of 5 and 10% with FC of 1.5% almost overlap each other and establish the behaviour of fibre–polymer interaction at FC of 1.5% to be more critical. Moreover, an increase in FC irrespective of PC and *W/C* ratio shifts the flow curves towards the curve of control mortar, implying

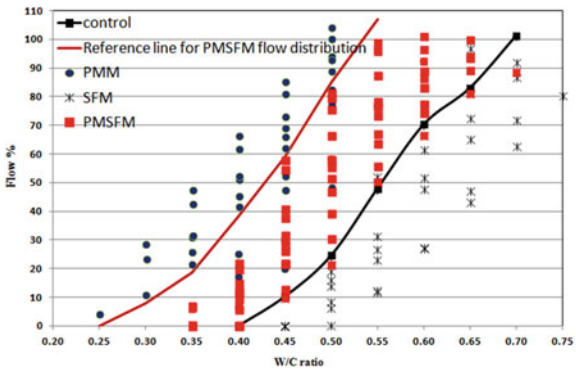

Fig. 6 Flow curve showing a range of distribution of flow for control, PMM, SFM and PMSFM mixes

that mixes with higher FC behave as control mortar even with polymer addition. Anyhow the FC of up to 2.5% with both PC of 5 and 10% offers measurable flow at *W/C* ratio of 0.4, which is earlier than control, showing approximately equal flow only at *W/C* of 0.45. Also, when comparing PMSFM curves with SFM at constant FC, it is possible to observe the compensation of flow loss with minimum water requirement in PMSFM mixes due to polymer interaction. Figures 5 and 6 clearly show the overall flow performances of all the mixes, viz. control mortar, PMM, SFM and PMSFM. The figure depicts that the obtained flow curves of PMSFM are falling between PMM and control mortar mixes. Furthermore, it is accomplished that due to fibre–polymer interaction, the flow gain in PMM and flow loss in SFM are well adjusted and the flow compensation has been noticed for all flow curves with FC from 0.5 to 3% in PMSFM with the selected PC. However, for obtaining better mortar composites, selection of *W/C* ratio has to be made with respect to appropriate flow curve presented and in turn depends on flow requirement and applications of composites.

4 Conclusions

The various useful conclusions were made from the results obtained as follows:

1. Increase in the fibre content decreases the flow value whereas an increase of polymer content and *W/C* ratios increase the flow value as compared with the control mortar.
2. The maximum increase in the flow value of PMM mixes is 8.3 times more than the control mortar for the polymer content of 13%.
3. There is no significant improvement in the flow value is observed beyond 13% polymer content for the chosen *W/C* ratio of 0.25–0.55.
4. The maximum decrease in the flow value of SFM for the fibre content of 3% ranges about 38–75% for the selected *W/C* ratios.

5. In the PMSFM mixes, the improvement in the flow value is about 1.2–4 times at 5% PC and 1.3–5.6 times at 10% PC higher than the control mortar.
6. Due to the addition of SBR polymer in the SFM mixes, the flow values are increased reasonably, with less *W/C* ratios. Also, a uniform distribution of sisal fibres in the mix was observed, while mixing with the polymer.
7. The developed flow curves for various mixes can be used to choose *W/C* ratios for various cement mortar application based on flow value.

Acknowledgements The authors wish to thank the Principal and the Head of the Department, Pondicherry Engineering College for their continuous support and encouragement in respect of undertaking this study. Also, it is acknowledged that the laboratory facilities are provided by the Department of Civil Engineering, Pondicherry Engineering College, Puducherry.

References

1. Ramakrishna, G., & Sundararajan, T. (2005). Impact strength of a few natural fibre reinforced cement mortar slabs: A comparative study. *Cement & Concrete Composites, 27*, 547–553.
2. Kriker, A., Debicki, G., Bali, A., Khenfer, M.M., & Chabannet, M. (2005). Mechanical properties of date palm fibres and concrete reinforced with date palm fibres in hot-dry climate. *Cement & Concrete Composites, 27*, 554–564.
3. Snoeck, D., & De Belie, N. (2012). Mechanical and self-healing properties of cementitious composites reinforced with flax and cottonised flax, and compared with polyvinyl alcohol fibres. *Biosystems Engineering, 111*, 325–335.
4. Gram, H. E. (1983). *Durability of natural fibres in concrete*. Swedish Cement and Concrete Research Institute, S-100 44 Stockholm, CBI Fo 1:83.
5. John, V. M., Cincotto, M. A., Sjostrom, C., Agopyan, V., & Oliveira, C. T. A. (2005). Durability of slag mortar reinforced with coconut fibre. *Cement & Concrete Composites, 27*, 565–574.
6. de Gutie´rrez, R. M., Diaz, L. N., & Delvasto, S. (2005). Effect of pozzolans on the performance of fiber-reinforced mortars. *Cement & Concrete Composites, 27*, 593–598.
7. Mohr, B. J., Biernacki, J. J., & Kurtis, K. E. (2007). Supplementary cementitious materials for mitigating degradation of kraft pulp fiber-cement composites. *Cement and Concrete Research, 37*, 1531–1543.
8. Canovas, M. F., Selva, N. H., & Kawiche.G. M. (1992). New economical solutions for improvement of durability of Portland cement mortars reinforced with sisal fibres. *Materials and Structures, 25*, 417–422.
9. ACI 548.3R-03. (2003). *Polymer-Modified Concrete*. June 17, 2003.
10. Chakraborty, S. Kundu, S. P., Roy, A., Basak, R. K., Adhikari, B., & Majumder, S. B. (2013). Improvement of the mechanical properties of jute fibre reinforced cement mortar: A statistical approach. *Construction and Building Materials, 38*, 776–784.
11. Kundu, S. P., Chakraborty, S., Roy, A., Adhikari, B., & Majumder, S. B. (2012). Chemically modified jute fibre reinforced non-pressure (NP) concrete pipes with improved mechanical properties. *Construction and Building Materials, 37*, 841–850.
12. Chakraborty, S., Kundu, S. P., Roy, A., Basak, R. K., Adhikari, B., & Majumder, S. B. (2013). Polymer modified jute fibre as reinforcing agent controlling the physical and mechanical characteristics of cement mortar. *Construction and Building Materials, 49*, 214–222.
13. Pandya Mithileshdatta, D., Dr. Arora,N. K., Thaker, P., (2012). State of art paper: investigation of workability of cement paste, cement mortar and concrete by various methods. *International Journal of Advanced Engineering Research and Studies, 2*, 16–23.

14. Tattersall, G. H. (1991). *Workability and quality control of concrete*. London: E&FN Spon.
15. Senff, L., Labrincha, J. A., Ferreira, V. M., Hotza, D., & Repette, W. L. (2009). Effect of nano-silica on rheology and fresh properties of cement pastes and mortars. *Construction and Building Materials, 23,* 2487–2491.
16. Park, C. K., Noh, M. H., & Park, T.H. (2004). Park rheological properties of cementitious materials containing mineral admixtures. *Cement and Concrete Research*.
17. Agullo, L., Toralles-Carbonari, B., Gettu, R., & Aguado, A. (1999). Fluidity of cement pastes with mineral admixtures and super plasticizer—A study based on the Marsh cone test. *Materials and Structures, 32,* 479–485.
18. Roel, H. (2009). The adequate measurement of the workability of masonry mortar, Ph.D. report. Katholieke University, Faculty of Engineering Leuven, Beligium.

Steel Fibres as a Partial Shear Reinforcement in Self-compacting Concrete

K. Praveen and S. Venkateswara Rao

Abstract The present study investigates the possibility of replacement of shear reinforcement with steel fibres in Self-Compacting Concrete beams. A total of 12 beams were designed and tested for two grades of SCC, i.e. M30 and M70. The variable parameters in the study apart from grade of concrete are dosage of steel fibres and stirrup spacings. The size of the beam was 100 × 200 × 1200 mm. The clear span of beam, 1100 mm was maintained throughout the study. All the beams were tested under three- point loading with shear span-to-depth ratio $a/d = 2$. The investigation shows that shear strength decreased as spacing of stirrup increased. The test results indicates that the initial crack shear strength increased significantly in the presence of steel fibre and the improvement in ultimate shear strength was also achieved. The present study also proves that steel fibre can reduce the area of shear reinforcement (stirrups) required and that the combination of fibres and stirrups increase the shear strength properties.

Keywords Self compacting concrete · Shear strength · Steel fibers

1 Introduction

When principal tensile stresses within the shear region of a reinforced concrete beam exceed the tensile strength of concrete, diagonal cracks develop in the beam, finally causing failure. The brittle nature of concrete causes the collapse to occur shortly after the formation of the first crack. The addition of steel fibres to concrete mix can bridge the crack propagation and delays the failure of the beam, which can improve the brittle nature of concrete to a more ductile behaviour [1, 2]. Addition of

K. Praveen · S. V. Rao (✉)
Department of Civil Engineering, NIT Warangal, Warangal 5006004, India
e-mail: svrao_civil@yahoo.co.in

K. Praveen
e-mail: praveenkcivil@gmail.com

A. Rama Mohan Rao and K. Ramanjaneyulu (eds.), *Recent Advances in Structural Engineering, Volume 1*, Lecture Notes in Civil Engineering 11,
https://doi.org/10.1007/978-981-13-0362-3_74

steel fibres can also increase the flexural tensile strength of concrete, thereby enchasing the post-cracking behaviour of Reinforced Concrete (RC) member [3].

Of all the different types of failure in concrete, shear failure is a sudden and brittle failure. Addition of steel fibres in concrete, can modify the brittle shear failure mode into a ductile flexural-shear failure. Inclusions of steel fibres can also partially replace conventional shear reinforcement, i.e. stirrups without compromising the strength aspect, thereby significantly reducing the cost and duration of construction [4–6].

The principal parameters that influence shear behaviour of reinforced concrete beam are: shear span-to-effective depth ratio (a/d), concrete compressive strength (f_c), longitudinal tensile reinforcement (ρ_t) and spacing of stirrups (S_v). When fibres are also included, parameters like fibre volume fraction (V_f) or fibre type (material, dimensions shape, etc.), also affect the shear performance of concrete [7, 8].

The main purposes of the present study is (1) To study the mechanical behaviour of steel fibre reinforced self-compacting concrete beams under shear, (2) To study the potential use of steel fibres as partial replacement of stirrups in Self-Compacting Concrete, (3) To investigate the combined effect of stirrups and steel fibres for improvements in initial and ultimate shear strengths and also to check the ductility of Steel Fibre- Reinforced Concrete (SFRSCC).

2 Materials Used

2.1 Cement

Cement used in the present study was 53 grade ordinary Portland cement conforming to IS: 12269-2013 [9]. The specific gravity of cement was 3.14 and specific surface area of 225 m^2/g having initial and final setting time of 45 and 560 min respectively.

2.1.1 Fly Ash

The fly ash used in the experiments was obtained from Ramagundam Thermal Power Station (NTPC) and was sieved by 90 micron sieve and confirmed to IS 3812:1981 [10]. The specific gravity was 2.2 and specific surface area was 450 m^2/g. The fly ash had a silica content of 63.99%, silica + alumina + iron oxide content of 92.7%, pH value 10 and a loss on ignition 2.12.

2.1.2 Fine Aggregate (FA)

The fine aggregate used in the present study was conforming to Zone-2 according to IS: 383-2002 [11]. It was obtained from a nearby river source. The specific gravity was 2.65, while the bulk density of sand was 1.45 g/c.c.

2.1.3 Coarse Aggregate (CA)

Crushed granite was used as coarse aggregate. Coarse aggregates of 20 mm nominal size were obtained from a local crushing unit, which was a well-graded aggregate according to IS: 383-2002 [11]. The specific gravity was 2.8, while the bulk density was 1.5 g/c.c.

2.1.4 Water IS456-2000

Potable water was used in the experimental work for both mixing and curing of specimens.

2.1.5 Silica Fume [12]

It is an amorphous (non-crystalline) polymorph of silicon dioxide, silica. It is an ultrafine powder collected as a by-product of the silicon and ferrosilicon alloy production and consists of spherical particles with an average particle diameter of 150 nm. The main field of application is as pozzolanic material for high-performance concrete. The bulk density of silica fume varies from 130 to 600 kg/m^3. The specific gravity of silica fume is generally in the range of 2.2–2.3. Specific surface area of silica fume typically ranges from 15,000 to 30,000 m^2/kg.

2.1.6 Super Plasticizer (SP)

High-Range Water-Reducing (HRWR) admixture confirming to ASTM C494 [13] commonly called as super plasticizers was used for improving the flow or workability for decreased water–cement ratio without sacrifice in the compressive strength. These admixtures when they disperse in cement agglomerates significantly, decreases viscosity of the paste forming a thin film around the cement particles. In the present investigation, water-reducing admixture CHRYSO FLUID OPTIMA P-77 (poly carboxylic ether based) obtained from Chyrso Chemicals, India was used.

2.1.7 Steel Fibre [14]

Crimped Steel fibre (from Apex Encon Projects Pvt Ltd., New Delhi, India) with nominal diameter of the fibre 0.5 mm and cut length 30 mm with aspect ratio of 60 were used. Tensile strength and modulus of elasticity of this fibre is 850 MPa and 2.1×10^5 MPa.

2.1.8 Tension Reinforcement

TMT bars of 12 and 16 mm diameter of grade Fe 500 confirming to IS: 1786 [15] whose yield strength F_y = 500 N/mm^2 of length 1160 mm were used as tension reinforcement and 6 mm Ø mild steel bars whose yield strength F_y = 290 N/mm^2 was used as stirrups (shear reinforcement) and also for top compression reinforcement.

3 Experimental Programme

In the present study, a total of 12 shear deficient beams were designed and cast for two grades of SCC via M30 and M70. The dimensions of the beam were fixed as 100 × 200 × 1200 mm with a clear span of 1100 mm. All beams were tested under three-point loading. For compressive strength, standard cube moulds of 150 mm × 150 mm × 150 mm made of cast iron were used. For split tensile strength, standard cylinder moulds of 150 mm φ × 300 mm made of cast iron were used. For flexural strength, 100 × 100 × 500 mm of standard prism moulds were used. In the present study, dosage of steel fibres is taken as 0.5% by volume of concrete [16], from our preliminary research work it was found that 0.5% dosage of steel fibres is optimum based on fresh and hardened properties.

Table 1 shows the details of beams with spacing of stirrups and percentage of steel fibre per volume of concrete SCC30-0 beam indicates that Self-Compacting Concrete beam with M30 grade concrete without any shear reinforcement (Stirrups), Similarly, SFRSCC30-180 beam indicates that it is a steel fibrous concrete beam with spacing of stirrups as 180 mm.

Table 1 Details of beams cast

S. No.	Designation	Shear Span-to- depth ratio (*a*/*d*)	Spacing of stirrup's (mm)	Fibre volume fraction (kg/m^3)
1	SCC30-0	2	–	–
2	SFRSCC30-0	2	–	38
3	SCC30-180	2	180	–
4	SFRSCC-180	2	180	38
5	SCC30-360	2	360	–
6	SFRSCC-360	2	360	38
7	SCC70-0	2	–	–
8	SFRSCC70-0	2	–	38
9	SCC70-180	2	180	–
10	SFRSCC70-180	2	180	38
11	SCC70-360	2	360	–
12	SFRSCC-360	2	360	38

3.1 Reinforcement Details in Each Beam

The dimensions and typical reinforcement detail for both grades of SCC M30 and M70 with shear span to depth (*a/d*) ratio 2, are shown in Figs. 1, 2, 3 and 4. The stirrups spacing was varied in the shear span, i.e. 180–360. M30 grade SCC beams consisting of 2–12 mm Ø TMT bars as longitudinal reinforcement, 2–6 mm Ø mild steel bars as top compression reinforcement and two legged 6 mm Ø bar was used as stirrups. Similarly, M70 grade SCC beams consisting of 2–16 and 1–12 mm Ø bars as longitudinal reinforcement, 2–6 mm Ø mild steel bars as top compression reinforcement and two legged 6 mm Ø bar was used as stirrups.

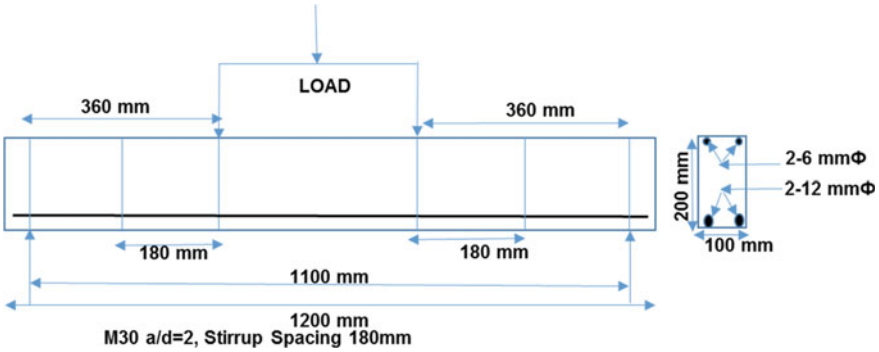

Fig. 1 Details of reinforcement for M30 SCC with *a/d* = 2

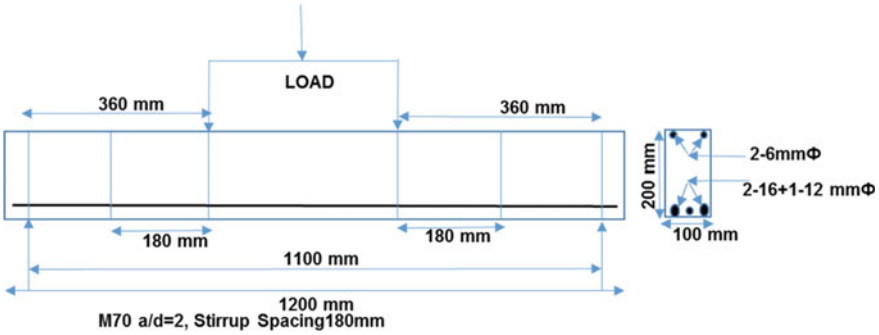

Fig. 2 Details of reinforcement for M70 SCC with *a/d* = 2

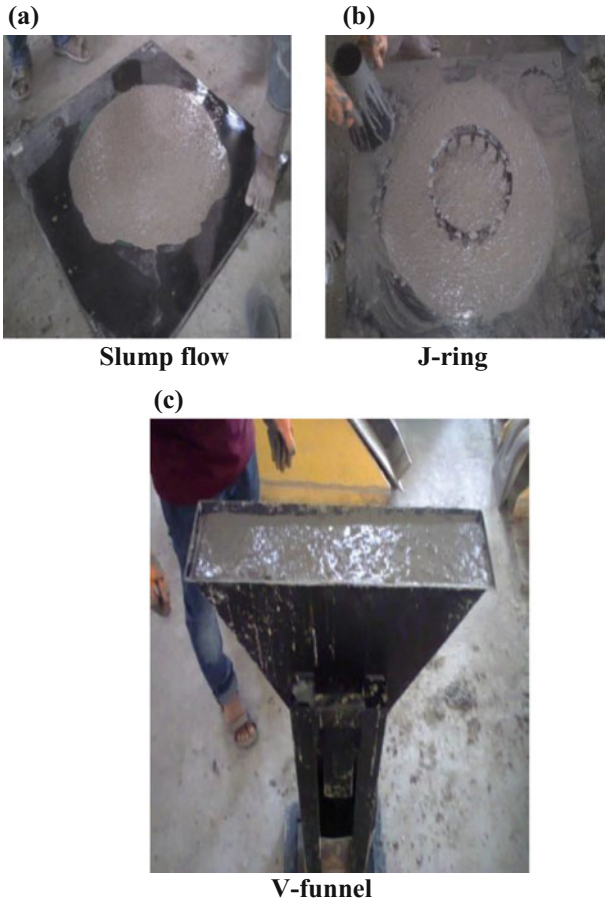

Fig. 3 Some tests on fresh properties of SCC

3.2 Mix Proportions

Self-Compacting Concrete (SCC) mixes were designed by using Rational Mix design method [17], details of mix proportions are presented in the Table 2. Trial mixes were carried out by varying Super Plasticizer dosage and binder content and evaluated the fresh properties as per EFNARC Specifications [18] via, Slump flow, T_{50}, L-Box, V-Funnel, T_5 and *J* ring tests.

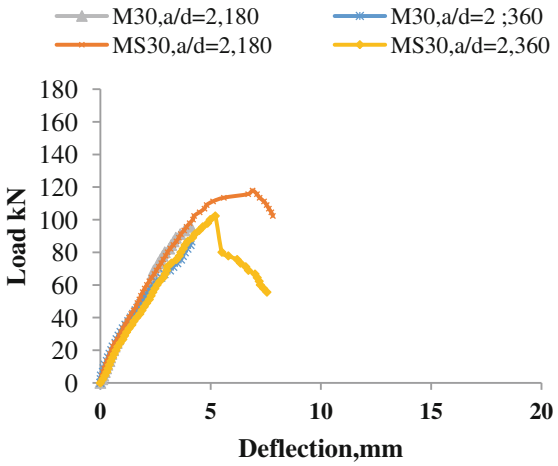

Fig. 4 Load versus deflection for SCC30

Table 2 Mix proportions of M30 and M70 grade SCC

Mix	Cement (kg/m^3)	Fly ash (kg/m^3)	Silica fume (kg/m^3)	CA (kg/m^3)	FA (kg/m^3)	Water (kg/m^3)	SP (kg/m^3)
M30	350	324	0	746	945	203	5.73
M70	600	226	48	780	874	247	6.03

3.3 *Fresh Properties*

The details of Fresh Properties for M30 and M70 grades SCC without and with steel fibre were shown in Table 3. It can be seen from Table 3 that, addition of steel fibres has reduced the flow properties but are satisfying the EFNARC Specifications. Figure 3 shows the various testing methods on workability of SCC.

Table 3 Fresh properties of M30 and M70 grade SCC with and without fibre

	M30		M70	
Dosage of fibres (%)	0	0.5	0	0.5
Slump test (mm)	750	620	720	680
T_{50} slump flow (s)	3	5	2.5	4
V funnel (s)	6	6.58	10.5	11.8
V funnel @ T_5 (min s)	7.5	8.38	12	14
J-ring (s)	3	8	3	7

Table 4 Hardened properties of M30 and M70 grades of SCC at 28 days

	M30			M70		
Dosage of steel fibres (%)	Compressive strength (MPa)	Split tensile strength (MPa)	Flexural strength (MPa)	Compressive strength (MPa)	Split tensile strength (MPa)	Flexural strength (MPa)
0	39.67	4.17	3.98	78.25	5.04	5.34
0.5	48.76	4.34	4.87	86.66	6.85	7.41

3.4 Hardened Properties

The details of hardened properties of M30 and M70 grades of SCC without and with steel fibre at the end of 28 days of curing were shown in Table 4. All the tests were done as per IS: 516-2004 [19] specifications.

4 Results and Discussions

At the end of the required curing period, the beams were tested for three-point loading under the Tinius–Olsen Testing Machine (TOTM) of 2000 kN capacity. The linear variable differential transformers (LVDT) were used to measure the displacement at mid span. From the recorded data, the shear load versus deflection graphs were plotted, initial crack strength and ultimate shear strength were calculated. The toughness and stiffness were evaluated for both fibres and non-fibre concrete beams (Tables 5 and 6).

Table 5 Initial shear and ultimate shear strength values for SCC30

Designation	First crack shear strength (MPa)	Ultimate shear strength (v_u) (MPa)	Deflection (mm)	Toughness (kN/mm)	Stiffness (kN/mm)
SCC30-0	1.60	1.73	3.16	100.83	14.15
SFRSCC30-0	1.98	2.34	5.05	225.60	16.56
SCC30-180	2.03	2.66	4.18	234.27	18.23
SCC30-360	1.76	2.41	4.12	207.43	17.68
SFRSCC30-180	2.29	3.28	6.90	364.1	22.52
SFRSCC30-360	2.16	2.84	5.21	328	20.17

Table 6 Showing initial and ultimate shear strength values for SCC70

Designation	First crack shear strength (MPa)	Ultimate shear strength (v_u) (MPa)	Deflection (mm)	Toughness (kN/mm)	Stiffness (kN/mm)
SCC70-0	1.98	2.41	3.66	197.70	24.61
SFRSCC70-0	2.04	2.55	4.08	228.50	25.55
SCC70-180	2.16	3.21	4.92	365.7	29.17
SCC70-360	2.10	2.60	3.54	212.2	28.07
SFSCC70-180	3.52	4.44	5.90	525.03	36.47
SFSCC70-360	2.41	3.86	5.40	483.46	31.47

4.1 Load Versus Deflection Curves

From the recorded data, load versus deflection curves were plotted, Figs. 4 and 5 show the comparison of load deflection curves of M30 and M70 grade concrete among SCC and SFSCC beams. The SCC30-0 beam without stirrups failed very early after first diagonal crack occurred. SCC30-180 beam with stirrups spacing at 180 mm shows load carrying capacity and brittle failure pattern compared to the SFRSCC30-180, addition of steel fibres has increased the load bearing capacity by 23.25% and also maximum deflection corresponding to ultimate load increased by 65.07%. Similarly, the SCC30-360 beam also shows lower load carrying capacity and brittle failure pattern compared to the beam with steel fibres (SFSCC30-360). With increase in the stirrup spacing from 180 to 360 mm, the ultimate shear strength decreased by 10.37% without fibres and by addition of steel fibres the ultimate shear strength was reduced by 6.7%. This shows that steel fibres will bridge the cracks and increase the shear strength. Similarly, for higher grade

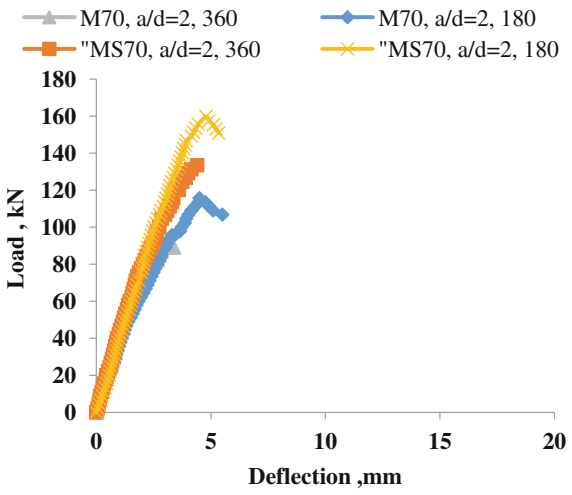

Fig. 5 Load versus deflection for SCC70

concrete (SCC 70), addition of steel fibres has increased the ultimate shear strength by 38.07% and also maximum deflection corresponding to ultimate load increased by 19.91%. From the above observations, it can be concluded that the addition of steel fibres can increase the load carrying capacity and can greatly enhance the ductility and also change the failure pattern of the beam from brittle shear failure to ductile flexural-shear failure. It can be proven that steel fibres can only replace stirrups partially by increasing the stirrup spacing, but not completely replacing the stirrups as shear reinforcement.

5 Details of Tested Beams

A total of 12 beams including 6 Plain and 6 fibre SCC beams have been cast and tested. Figures 6 and 7 show the typical failure pattern of plane and fibrous SCC M30 grade concrete.

Similarly, Figs. 8 and 9 show the failure pattern for plain SCC and fibrous SCC for M70 grade concrete. It was noticed that plain specimen's failed in sudden brittle failure, where as in case of fibrous SCC mode of failure was ductile.

Fig. 6 Failure pattern of SCC30

Fig. 7 Failure pattern of SFRSCC30

Fig. 8 Failure pattern of SCC70

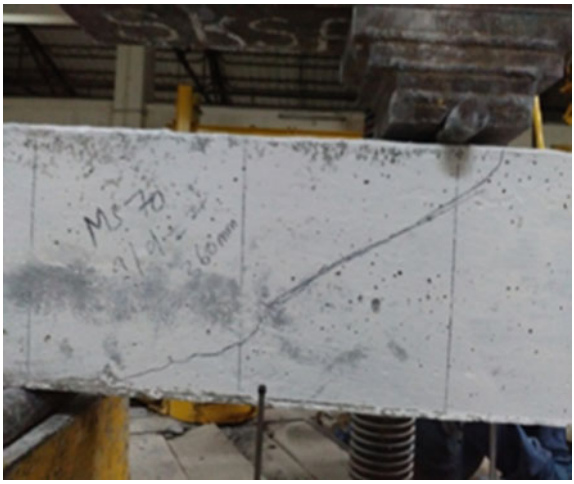

Fig. 9 Failure pattern of SFRSCC70

6 Conclusions from Experimental Study

1. Addition of fibre has modified the failure pattern from brittle shear failure to a ductile flexural-shear failure. There is also an increase in the ultimate shear strength. This shows that steel fibres play a very important role before and after cracking.
2. For an increase of stirrups spacing from 180 to 360 mm for $a/d = 2$, the ultimate shear strength decreased by 15.49% without fibres.
3. In case of M30 grade SCC, addition of fibres enhanced cracking and ultimate shear strength by 19.2 and 23.2%, respectively, and also toughness and stiffness increased by 56.8 and 18.8% respectively.
4. In case of M70 grade SCC, addition of fibres enhanced the cracking and ultimate shear strength by 25.71 and 30.77% respectively.
5. Steel fibres can be used as partial shear reinforcement by increasing the spacing of stirrups thereby reducing the area of shear reinforcement.

References

1. Narayanan, R., & Darwish, I. Y. S. (1987). Use of steel fibers as ear reinforcement. *ACI Structural Journal, 84,* 216–227.
2. Cucchiara, C., Mendola, L. L., & Papia, M. (2004). Effectiveness of stirrups and steel fibres as shear reinforcement. *Cement Concrete Composites, 26,* 777–786.
3. Kwak, Y. K., Eberhard, M., Kim, W. S., & Kim, J. (2002). Shear strength of steel fibre-reinforced concrete beams without stirrups. *ACI Structural Journal, 99*(4), 530–537.
4. Ding, Yining, You, Zhiguo, & Jalali, Said. (2011). The composite effect of steel fibres and stirrups on the shear behaviour of beams using self-consolidating concrete. *Engineering Structures, 33,* 107–117.
5. Kim, K. S., Lee, D. H., Hwang, J. H., & Kuchma, D. A. (2012). Shear behaviour model for steel fiber reinforced concrete members without transverse reinforcements. *Composites Part B, 43*, 2324–2334.
6. Greenough, T., & Nehdi, M. (2008). Shear behaviour of fibre-reinforced self-consolidating concrete slender beams. *ACI Material Journal, 105*(5), 468–477.
7. Tiberti, G., Minelli, F., Plizzari, G. A., & Vecchio, F. J. (2014). Influence of concrete strength on crack development in SFRC members. *Cement Concrete Composites, 45,* 176–185.
8. Cuenca, E., Oviedo, E. J., & Serna, P. (2015). Influence of concrete matrix and type of fiber on the shear behaviour of self-compacting fiber reinforced concrete beams. *Cement and Concrete Composites Part B, 75,* 135–147.
9. IS: 12269-2013. *Indian standard ordinary portland cement, 53 grade—Specification*. Bureau of Indian Standards, New Delhi.
10. IS: 3812 (Part-1)-2003. Indian standard pulverized fuel ash—Specification, Part-1: For use as pozzolana in cement, cement mortar and concrete. Bureau of Indian Standards, New Delhi.
11. IS: 383-1970 (Reaffirmed 2002). *Indian standard specification for coarse and fine aggregates from natural sources for concrete*. Bureau of Indian Standards, New Delhi.
12. IS 15388-2003. *Specification for use silica fume as mineral admixture in cement concrete*. Bureau of Indian Standards, New Delhi.
13. ASTM C494/C494 M-13. (2013). *Standard specification for chemical admixtures for concrete*. ASTM International, West Conshohocken, PA, USA.
14. ASTM A820-01. (2001). *Standard specification for use steel fibers for fiber-reinforced concrete*. ASTM International, West Conshohocken, PA, USA.
15. IS: 1786-2008. *Indian standard high strength deformed steel bars and wires for concrete reinforcement—Specification*. Bureau of Indian Standards, New Delhi.
16. Ponikiewski, T., & Cygan, G. (2011). Some properties of self-compacting concretes reinforced with steel fibres. *Cement Wapno Beton*, CWB-4/2011, 203–209.
17. Rao, S. V., Rao, S. S., Ramaseshu, D., & Kumar, P.R. (2013). Self-compacting concrete—A rational mix design. *Cement Wapno Beton*, CWB-5/2013, pp. 271–280.
18. EFNARC. (2005). Specification and guidelines for self-compacting concrete.
19. IS: 516-1959 (Reaffirmed 2004). *Indian standard methods of tests for strength of concrete*. Bureau of Indian Standards, New Delhi.

On the Toughness Characterization of Fibre- Reinforced Concrete Using Notched Beam Tests

Sujatha Jose and Ravindra Gettu

Abstract The significant benefit of using fibre-reinforced concrete (FRC) is its improved energy absorption capacity, termed as toughness, and the consequent enhanced post-cracking load carrying capacity, which have resulted in applications such as tunnel linings, pavements, industrial floors, etc. There is limited knowledge regarding notched beam testing in India for flexural toughness characterization of FRC though it is prevalent in Europe. In the current work, the flexural behaviour of concrete with different dosages of hooked-ended steel fibres are characterized by centre-point loaded (CPL) notched beam testing, according to the EN 14651:2005 and RILEM TC 162-TDF recommendations. The flexural toughness parameters assessed are based on the load-crack mouth opening displacement (CMOD) curves and load–deflection (δ) curves obtained experimentally. A detailed analysis also revealed that for steel FRC, a good correlation exists between equivalent and residual flexural tensile strength parameters.

Keywords Fibre-reinforced concrete · Flexural toughness · Notched beam test · Crack mouth opening displacement

1 Introduction

The enhanced performance of fibre-reinforced concrete is due to its increased energy absorption capacity during fracture, which is termed as 'toughness'. The main objective of toughness characterization is to measure the effectiveness of the fibres and the resistance offered against crack propagation. The test configuration commonly used for toughness characterization is the bending of prismatic

S. Jose · R. Gettu (✉)
Department of Civil Engineering, Indian Institute of Technology Madras, Chennai 600036, India
e-mail: gettu@iitm.ac.in

S. Jose
e-mail: sujathavin@gmail.com

A. Rama Mohan Rao and K. Ramanjaneyulu (eds.), *Recent Advances in Structural Engineering, Volume 1*, Lecture Notes in Civil Engineering 11,
https://doi.org/10.1007/978-981-13-0362-3_75

specimens. From the fracture mechanics perspective, the notched beam test is mostly recommended for toughness characterization due to its rational analysis [1, 2].

Over the past few decades, extensive research has been carried out on the material properties of FRC. Consequently, based on the state-of-the-art knowledge, FRC is introduced in the fib Model Code 2010 to provide design guidelines for the design of FRC structural elements, at both serviceability and ultimate limit states. In this code, material classification of FRC is based on the flexural toughness parameters with respect to post-cracking tensile strength, determined from bending tests on notched prisms according to EN 14651 [3, 4].

Considering the fact that notched beam test gives a more reliable test data and post-cracking response of FRC, relevant for structural applications, it is proposed as the basis of the present work. The notched beam test with Centre Point Loading (CPL) is performed as per EN 14651:2005 (E) and RILEM TC 162-TDF: Test and design methods of steel fibre-reinforced concrete, Bending Test: Final Recommendations [5, 6].

2 Flexural Toughness Testing Based on the Notched Beam Test

The tests are performed in a closed-loop servo-controlled Controls testing system as shown in Fig. 1. The test control and data acquisition is done through a Controls software interface Advantest. The test is performed initially under load control by increasing the load at a constant rate of 100 N/s up to about 40% of the estimated peak load, and then by changing to crack mouth opening displacement (CMOD) control. However, both deflection and crack mouth opening are measured as shown in Fig. 2. The specimen dimensions are 150 × 150 × 700 mm, and the span is 500 mm. A notch is cut through the width of specimen at mid-span on a face that is

Fig. 1 Experimental setup

Fig. 2 Position of the clip gauge and 2 LVDTs for measuring CMOD and deflections, respectively

perpendicular to the casting direction. Since the crack opening is measured at a distance of y (=3 mm) from the bottom face of the specimen, the value of CMOD has to be corrected as

$$\text{CMOD} = \text{CMOD}_y \frac{h}{h+y} \tag{1}$$

where h is the depth of the specimen (i.e. 150 mm) and CMOD_y is the measured value. For measuring the deflection, two LVDTs are mounted on rigid frames fixed to the either side of the specimen and the tips rest on 1 mm-thick steel plates placed across the notch.

2.1 Notching Procedure

A notch is cut through the width of specimen at mid-span on a face that is perpendicular to the casting face using a water-cooled diamond-edged disc saw. Specimens are rotated 90° over their longitudinal axis and then sawn as shown in Fig. 3. The notch depth adopted for 150 mm deep beam was 25 mm.

1. Top surface during casting
2. Notch
3. Cross-section of test specimen.

h_{sp} is the distance between the tip of the notch and the top of the specimen, in millimetres.

The test specimens are cured for a minimum of 3 days after sawing. Toughness testing is performed at 28 days. The width of the notch is about 3 mm.

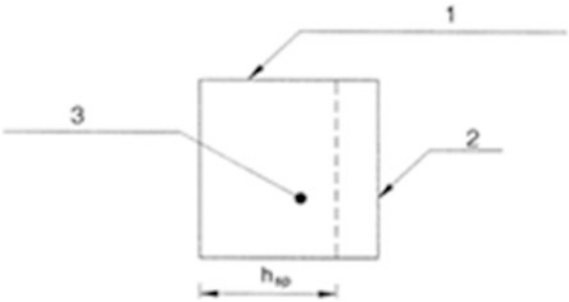

Fig. 3 Position of the notch with respect to the test specimen as cast

2.2 *Flexural Toughness Parameters*

Flexural toughness parameters in are derived from the load–CMOD curves and load–deflection curves. The Limit of Proportionality f^f_{ct} (LOP) and Residual Flexural Tensile Strength (f_R) are the parameters recommended by EN 14651:2005 (E) [3], which are obtained from load–CMOD curve as in Fig. 4. The LOP represents the flexural strength of the composite obtained using the first peak load of the FRC specimen. Residual flexural strength is an estimate of flexural strength retained by FRC after cracking at particular crack widths of 0.5, 1.5, 2.5 and 3.5 mm.

Additionally, the equivalent flexural strength (f_{eq}) has been calculated from the load–δ curve, as recommended by RILEM TC 162-TDF, using the average load over certain deflection ranges as in Fig. 5.

The energy absorption $D_{BZ,2}$(or $D_{BZ,3}$) is equal to the area under the load–deflection curve up to a deflection δ_2 (or δ_3), and is taken to be the sum of the contribution of the plain concrete and that of the fibres ($D^f_{BZ,2}$or $D^f_{BZ,3}$) as in Fig. 5. The two contributions are separated by a straight line connecting the point on the curve corresponding to F_L and the point on the abscissa equal to "δ_L +0.3", where δ_L is the deflection at F_L.

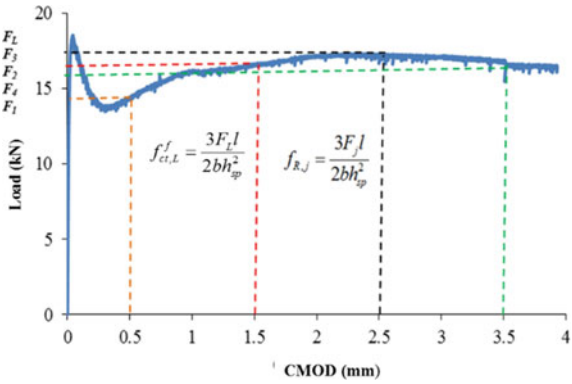

Fig. 4 Estimation of LOP and residual flexural strength from typical load–CMOD curve

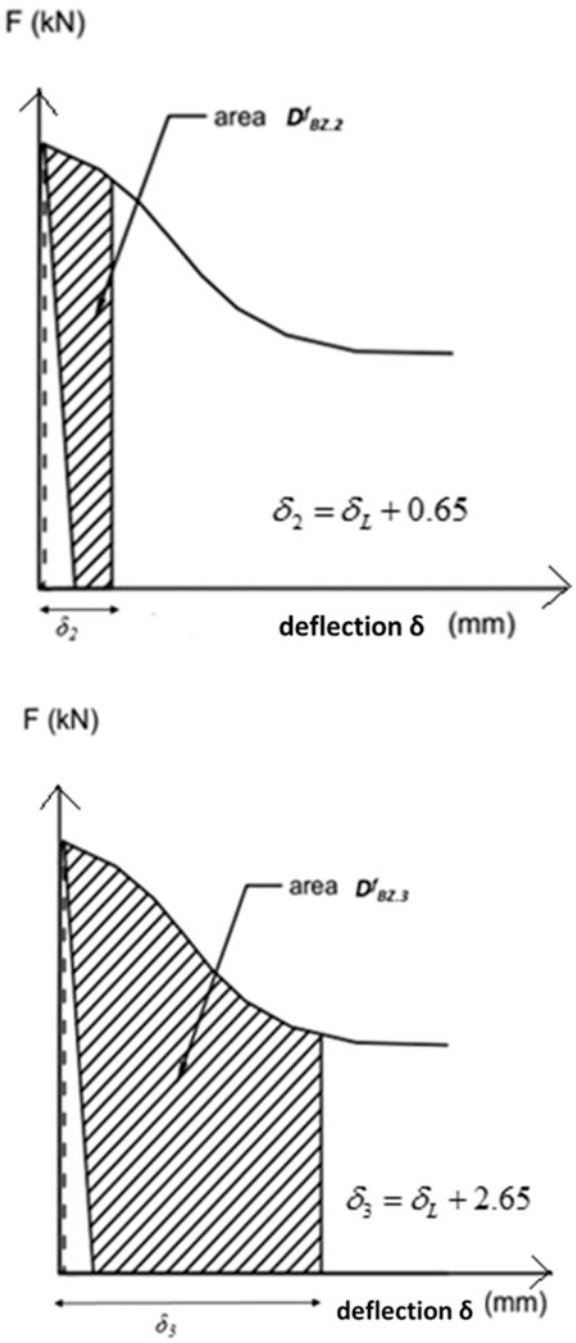

Fig. 5 Estimation of the equivalent flexural strength parameters from the load–deflection curve

The equivalent flexural tensile strengths $f_{eq.\ 2}$ and $f_{eq.\ 3}$ can consequently be determined [6] as

$$f_{eq,2} = \frac{3}{2}\frac{D^f_{BZ,2}}{0.5}\frac{L}{bh^2_{sp}} \tag{2}$$

$$f_{eq,3} = \frac{3}{2}\frac{D^f_{BZ,3}}{2.5}\frac{L}{bh^2_{sp}} \tag{3}$$

3 Experimental Programme

The flexural behaviour of concrete, having 40 MPa design compressive strength (denoted as M40), reinforced with hooked-ended steel fibres was characterized. The fibre details are given in Table 1, as specified by the manufacturer. The nominal mix proportion for the concretes is given in Table 2.

The concrete was mixed for about 3 min after fibre addition. Specimens such as cubes of 150 × 150 × 150 mm and prisms of 150 × 150 × 700 mm, were cast for plain concrete and different dosages of steel fibre-reinforced concretes (SFRC).

Nine prisms were cast, along with nine cubes for each dosage of the mix, and a high-frequency vibrating table was used for compaction of the concrete in moulds. Reference concrete without any fibres was also cast. The specimens were left in the moulds for 24 h after casting, then demoulded and cured for the next 27 days in the mist room. Three days prior to the testing, a notch of 25 mm length was cut across

Table 1 Details of fibre

Type	Specific gravity[a] (g/cc)	Aspect ratio	Tensile strength[a] (MPa)	Fibre dosages (kg/m^3)
Hooked-ended steel fibres	7.8	80	1225	10, 15, 20, 30, 45

[a]Specified by the manufacturer

Table 2 Nominal mix proportions in kg/m^3

Material	Quantity
Cement	380
Fine aggregates	760
5–10 mm coarse aggregates	390
10–20 mm coarse aggregates	700
Water	171

the longitudinal section and the specimen was kept again in the mist room for curing. Flexural tests were performed at the age of 28 days.

4 Results and Discussion

4.1 Fresh Properties

There was a loss in workability due to the addition of fibres with lower slump being obtained. Consequently, a poly-carboxylate (PCE)-based superplasticizer (with a density of 1080 kg/m^3 and solid content of 33%), was used to obtain a reasonable workability to be handled during fabrication. The superplasticizer dosage, by weight of cementitious materials, was increased from 0.19% in plain concrete to 0.4% for 45 kg/m^3 of steel fibres and the slump could be maintained at 100 ± 20 mm. In general, all mixes showed similar trends of workability reduction with an increase in fibre dosage.

4.2 Compressive Strength

Compressive strength tests were conducted on cubes at the ages of 3, 7 and 28 days using a 3 MN capacity Controls compression testing machine; a minimum of three specimens were tested at each age. Note that in the mix designation, M40 denotes the concrete grade, SF denotes the use of steel fibres and the number at the end denotes the fibre dosage in kg/m^3. The compressive strength values along with the standard deviation are given in Table 3, for specimens of different fibre volume fractions.

From Table 3, it can be observed that, the incorporation of steel fibres resulted in an improvement in the compressive strength compared to plain concrete, from 3 to 12% for the fibre dosages of 10–45 kg/m^3. This can be attributed to the bridging of cracks by the fibres, which produces some internal confinement, increasing the

Table 3 Compressive strength of SFRC

Concrete	Compressive strength (MPa) (mean ± standard deviation)		
	At 3 days	At 7 days	At 28 days
M40SF0	22.3 ± 1.2	33.7 ± 0.5	47.1 ± 0.3
M40SF10	22.5 ± 0.8	34.4 ± 0.9	48.4 ± 0.8
M40SF15	23.5 ± 0.7	35.6 ± 1.5	49.2 ± 0.6
M40SF20	26.7 ± 0.8	36.7 ± 1.6	50.4 ± 1.3
M40SF30	27.9 ± 1.3	37.3 ± 0.7	51.5 ± 1.7
M40SF45	28.6 ± 0.4	38.0 ± 0.9	52.8 ± 0.7

compressive strength. The variability of compressive strengths is within the usual range and is not influenced by the type or amount of fibres.

4.3 *Flexural Behaviour of SFRC and Toughness Parameters*

Typical load–CMOD curves for the SFRCs are shown in Fig. 6. For all the mixes it was observed that, the post-peak load-carrying capacity and the area under the load–CMOD curve increase with the fibre dosage, as expected. There is a gradual change from softening- to hardening-type response with an increase in fibre dosage (10–45 kg/m^3), especially at larger deflections (after a CMOD of 0.2 mm). In fact, for the M40SF45 mix, the post-crack load-carrying capacity was even higher than the peak load after a CMOD of 1 mm. For lower dosages of steel fibres (10 and 15 kg/m^3), the softening branch is followed by a region of constant residual load. The typical load–deflection curves of the different mixes, presented in Fig. 7, show similar trends as in the load–CMOD curves. The flexural toughness parameters obtained for all the mixes are given in Table 4, as mean and standard deviation

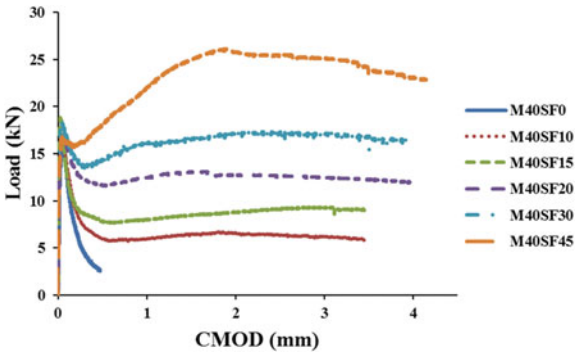

Fig. 6 Typical load–CMOD curves

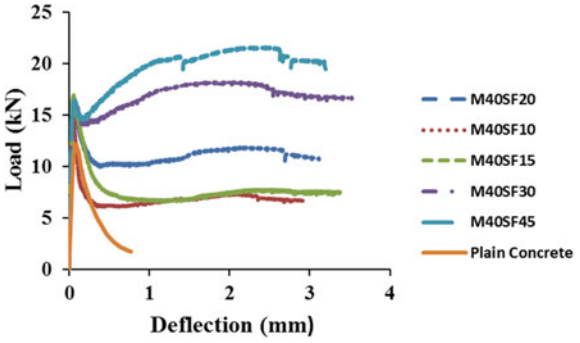

Fig. 7 Typical load–deflection curves

Table 4 Flexural toughness parameters of SFRC

Concrete	LOP, f_{ct}^{f} (MPa)	$f_{R,1}$ @CMOD = 0.5 mm (MPa)	$f_{R,2}$ @CMOD = 1.5 mm (MPa)	$f_{R,3}$ @CMOD = 2.5 mm (MPa)	$f_{R,4}$ @CMOD = 3.5 mm (MPa)	$f_{eq,2}$ (MPa)	$f_{eq,3}$ (MPa)
M40SF0	5.22 ± 0.42	–	–	–	–	–	–
M40SF10	5.33 ± 0.39	2.19 ± 0.18	2.11 ± 0.20	2.13 ± 0.24	2.05 ± 0.29	1.99 ± 0.33	2.04 ± 0.26
M40SF15	5.44 ± 0.45	2.35 ± 0.23	2.48 ± 0.26	2.55 ± 0.29	2.48 ± 0.32	2.09 ± 0.31	2.40 ± 0.21
M40SF20	5.58 ± 0.42	3.40 ± 0.48	3.73 ± 0.53	3.80 ± 0.34	3.68 ± 0.27	3.23 ± 0.55	3.62 ± 0.43
M40SF30	5.38 ± 0.42	4.04 ± 0.61	5.21 ± 0.65	5.54 ± 0.75	5.48 ± 0.75	3.89 ± 0.70	5.03 ± 0.61
M40SF45	5.47 ± 0.41	5.30 ± 0.77	6.70 ± 1.22	6.63 ± 1.55	6.53 ± 1.40	5.29 ± 0.84	6.33 ± 1.19

Table 5 SFRC classification as per *fib Model Code 2010*

Concrete	Class	$f_{R,3k}/f_{R,1k}$	$f_{R,1k}/f_{Lk}$
M40SF10	2b	0.9	0.40
M40SF15	2c	1.0	0.42
M40SF20	2.5e	1.3	0.50
M40SF30	3e	1.4	0.61
M40SF45	4b	0.9	0.80

values. It can be seen that the values of $f_{eq,3}$ and $f_{R,4}$ are higher than $f_{eq,2}$ and $f_{R,1}$, respectively, which indicates that the energy absorption and post-cracking capacity increase at larger crack mouth openings, in the case of SFRC, especially at higher dosages.

Based on the data obtained, the FRC can be classified according to *fib Model Code 2010* in terms of the response at the serviceability limit state (represented by CMOD = 0.5 mm) and at the ultimate limit state (represented by CMOD = 2.5 mm). Note that, in order to take into account the effect of variability of the test specimens, characteristic values of the parameters are considered, i.e. $f_{R,1k.}$ and $f_{R,3k}$. The class of the FRC is denoted with a number followed by a letter: the number is based on the value of $f_{R,1k}$ rounded off to the nearest 0.5 MPa and the letter depends on the ratio $f_{R,3k}/f_{R,1k}$ ratio, as follows:

a. if $0.5 < f_{R,3k}/f_{R,1k} \leq 0.7$
b. if $0.7 < f_{R,3k}/f_{R,1k} \leq 0.9$
c. if $0.9 < f_{R,3k}/f_{R,1k} \leq 1.1$
d. if $1.1 < f_{R,3k}/f_{R,1k} \leq 1.3$
e. if $f_{R,3k}/f_{R,1k} > 1.3$

The FRC is taken to be suitable and can be used at Ultimate Limit State (ULS) if the relationships given in Eqs. (4) and (5) are fulfilled, where f_{Lk} is the characteristic value of the LOP.

$$f_{R,1k}/f_{Lk} \geq 0.4 \tag{4}$$

$$f_{R,3k}/f_{R,1k} \geq 0.5 \tag{5}$$

The classification for the SFRCs tested based on the *fib Model Code2010*, as well as the ratios given in Eqs. (4) and (5) are shown in the Table 5. It can be observed that all the SFRCs considered here have satisfied the restrictions on the minimum residual strength, as given in Eqs. (4) and (5). This becomes relevant in structures with high degree of redundancy, especially when fibres completely replace conventional reinforcement, where a minimum redundancy level is required for the structural member.

4.4 Relationship Between Equivalent and Residual Flexural Tensile Strengths

A linear relationship was found to exist between the equivalent ($f_{eq,2}$ and $f_{eq,3}$) and residual strength parameters ($f_{R,1}$ and $f_{R,4}$), as shown in Figs. 8 and 9, confirming the observations of Barros et al. [7]. Further, the relationships between $f_{eq,2}$ and $f_{R,1}$

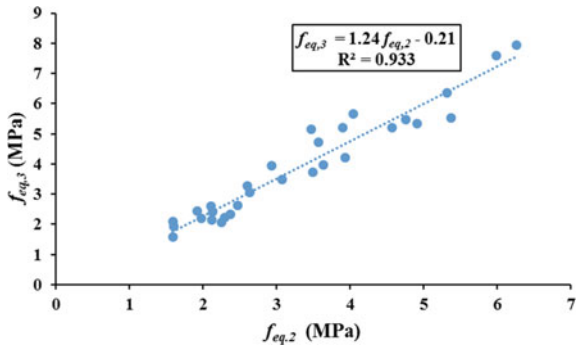

Fig. 8 Relationship between $f_{eq,2}$ and $f_{eq,3}$ of SFRC

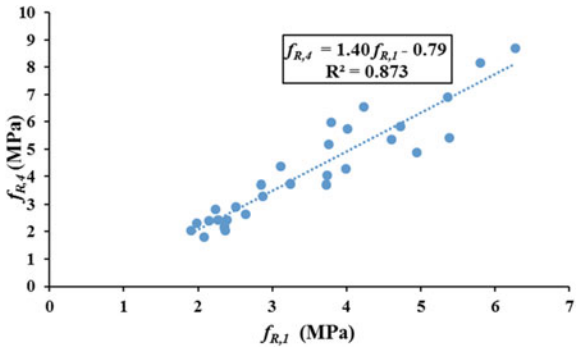

Fig. 9 Relationship between $f_{R,1}$ and $f_{R,4}$ of SFRC

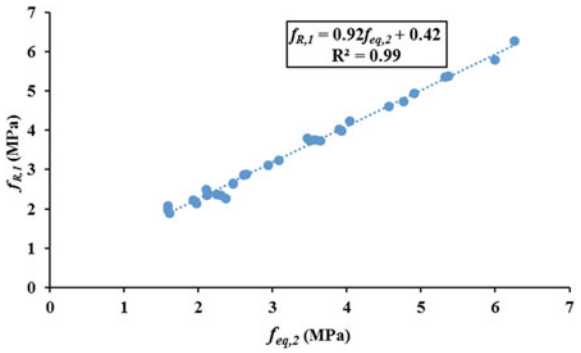

Fig. 10 Relationship between $f_{eq,2}$ and $f_{R,1}$ of SFRC

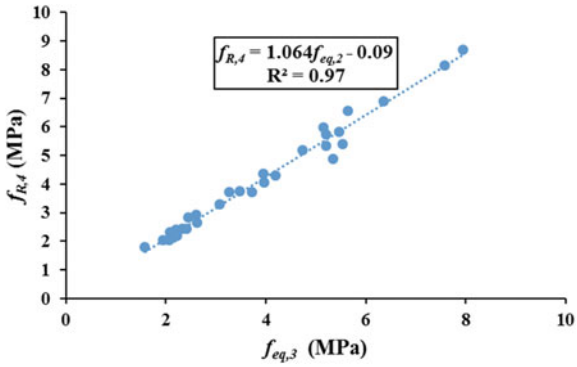

Fig. 11 Relationship between $f_{eq,3}$ and $f_{R,4}$ of SFRC

and between $f_{eq,3}$ and $f_{R,4}$ are represented in Figs. 10 and 11, with good correlation between two sets of parameters, as again obtained by Barros et al. [7].

The present study suggests that approximate values of f_{eq} or f_R can be obtained when the other has been reported.

5 Conclusions

The post-cracking behaviour SFRC was assessed using three-point bending tests on notched specimens for M40 grade of concrete. From the results obtained from the concrete mixes and fibre dosages considered here, the following conclusions can be drawn.

- From the load–CMOD behaviour and load–deflection behaviour of the SFRC from notched beam test, it can be concluded that at large crack openings, the hooked-ended steel fibres are efficient in enhancing the post-crack load-carrying capacity. This is reflected by the higher values seen for $f_{eq,3}$ and $f_{R,4}$ than for $f_{eq,2}$ and $f_{R,1}$.
- A good correlation exists between equivalent and residual flexural tensile strengths parameters of SFRC.

Acknowledgments The authors acknowledge the support of Bekaert Industries, for having provided the fibres used in this study. The help from the staff of the Construction Materials Laboratory of IIT Madras is gratefully appreciated.

References

1. Gopalaratnam, V. S., & Gettu, R. (1995). On the characterization of flexural toughness in fiber reinforced concretes. *Cement & Concrete Composites, 17,* 239–254.
2. Gopalaratnam, V. S., Shah, S. P., Batson, G. B., Criswell, M. E., Ramakrishnan, V., & Wecharatana, M. (1991). Fracture toughness of fiber reinforced concrete. *ACI Materials Journal, 88,* 339–353.
3. *Fib* bulletin 55: *Model Code 2010*, First complete draft, Vol. 1.
4. di Prisco, M., Colombo, M., & Dozio, D. (2013). Fibre-reinforced concrete in *fib* Model Code 2010: principles, models and test validation. *Structural Concrete, 14,* 342–361.
5. Test method for metallic fibre concrete measuring the flexural tensile strength (Limit of Proportionality (LOP), Residual), EN 14651, CEN, Brussels, 2005.
6. RILEM TC 162-TDF. (2002). Test and design methods for steel fibre reinforced concrete—Final recommendations. *Materials and Structures, 35*, 579–582.
7. Barros, J. A. O., Cunha, V. M. C. F., Ribeiro, A. F., & Antunes, J. A. B. (2005). Post-cracking behaviour of steel fibre-reinforced concrete. *Materials and Structures, 38,* 47–56.

Investigations on Aggregate Reactivity in Geopolymer Concrete

B. Singh and G. Ishwarya

Abstract The potential reactivity of sandstone/siliceous aggregates in geopolymer concrete based on fly ash/GGBS composite mixes was assessed in terms of alkali-silica reaction. The mortar bars made as per ASTM C1260 were exposed to 1 M NaOH at 80 °C up to 90 days. The exposed samples were examined for their expansion and petrography. It was observed that the samples expanded less than the threshold of 0.1% at the end of 16 days exposure while its OPC counterpart failed by exceeding the limit. At 90 days, the geopolymer mortars containing composite mixes had expansion in the range of 0.31–0.56% as compared to 0.12% for fly ash-based geopolymers. Evidence of crystalline zeolites, sodium calcium silicate gel and cracks observed under FESEM after 90 days could be responsible for higher expansion. Reduction in alkalinity of solution/dissolved silica from aggregate after 24 h exposure in 1 N NaOH solution indicated innocuous nature of aggregates contrary to the expansion results. It was noted that geopolymer concrete made with high GGBS content exhibited prominent ASR product. It was concluded that siliceous aggregates had less ASR than the sandstone aggregate.

Keywords Geopolymer concrete · Expansion · ASR · Microstructure Aggregate

1 Introduction

In the recent years, geopolymer has received a lot of attention as an alternative to Portland cement (OPC) concrete in civil infrastructures due to its superior properties such as high early compressive strength, low permeability, negligible shrinkage,

B. Singh (✉) · G. Ishwarya (✉)
Polymers, Plastics and Composites Division, CSIR-Central Building Research Institute, Roorkee, India
e-mail: singhb122000@yahoo.com

G. Ishwarya
e-mail: ishwarya@cbri.res.in

A. Rama Mohan Rao and K. Ramanjaneyulu (eds.), *Recent Advances in Structural Engineering, Volume 1*, Lecture Notes in Civil Engineering 11,
https://doi.org/10.1007/978-981-13-0362-3_76

excellent acid and fire resistance and low thermal conductivity [1–3]. However, concerns are often raised on the performance of these new materials in the aggressive chemical environment. It is known that alkali-silica reaction (ASR) is one such factor causing gradual but severe deteriorations of hardened cement concrete structure in terms of its strength loss, cracking and volume expansion [4–6]. It involves the reaction between the hydroxyl ion in the pore solution within the concrete matrix and reactive silica in the aggregate. The extent of dissolution of reactive silica from aggregate depends on a number of factors such as alkalinity of pore solution (threshold 0.20–0.25 M), water–cement ratio, degree of hydration (0.15–0.85 mol/l corresponding to pH values of 13.2–13.9), humidity and temperature. It is also recognized that high calcium content is necessary for concrete expansion by ASR [7]. In geopolymer concrete, the residual alkali after geopolymerization of aluminosilicate is expected to react with reactive silica of the aggregates causing disruption of their siloxane bridges. It is, therefore, desirable to assess the potential reactivity of different types of aggregates and subsequent evolution of their microstructures in geopolymeric environment.

In earlier studies, attempts were made to study ASR in geopolymer concrete using reactive and non-reactive aggregates [8–10]. The alkalis are able to interact in two competitive reactions. In the primary reaction, they are taken up to activate the vitreous component of the aluminosilicates and convert it into a cementitious material, or even form zeolite crystals; but at the same time, they may be involved in a secondary reaction that attacks the aggregate [2]. Garcia-Lodeiro et al. [8] indicated that fly ash-based geopolymers had greater resistance to ASR than the corresponding Portland cement and reported that calcium in the material plays an important role in the expansive nature of gels. Patil and Allouche [9] found that ASR in fly ash-based geopolymer concrete was well below the ASTM-specified threshold because the samples appeared to undergo a densification process during accelerated exposure resulting in reduced permeability and increased mechanical strength. Fernandez-Jimenez and Puertas [10] concluded that alkali-activated slag mortar expanded initially at slower rate than the OPC mortars but monitoring of expansion for longer period will be essential due to formation of sodium and calcium silicate hydrate products with rosette- type morphology in the microstructure. Bakharev et al. [11] found that alkali-activated slag concrete had lower resistance to ASR than that of OPC concrete of similar grade. Till date, there have been no reports available on the potential reactivity of aggregates in geopolymer concrete produced from fly ash–slag composite mix.

In the present study, we aimed at discussing geopolymer pastes based on fly ash/groundgranulated blast furnace slag (GGBS) as binders for producing concrete which can set fast under ambient temperature and be easily adopted in the field similar to OPC concrete [12]. Since aggregates contain some deleterious substances, the knowledge on understanding the reactivity of these aggregates in the geopolymeric alkaline environment is essential for mass utilization. It is expected that un-utilized water-soluble alkalis existing in the geopolymer concrete may cause expansion in the concrete through alkali-silica reaction. Such effect can be assessed by a known method (ASTM C1260) used for cement mortars which is very much applicable to geopolymer concrete as also adopted by other authors [8, 9]. In this

article, the potential reactivity of siliceous and sandstone aggregate in geopolymer concrete using fly ash/GGBS composite mix was investigated under accelerated condition. The exposed mortar bars were assessed for their expansion and microstructural changes. A comparison in the expansion of geopolymer concrete was also made with its corresponding OPC concrete.

2 Experimental

2.1 Materials

Class F fly ash (FA) was collected from Suratgargh super thermal power station, Suratgargh, India (Blaine's surface area 4099 cm^2/g, average Particle size = 39 μm). Chemically, it consists of SiO_2 45.76%, Al_2O_3 22.41%, Fe_2O_3 3.48%, CaO 0.74% and LOI 0.58%. Ground-granulated blast furnace slag (GGBS) was procured from M/s Rashtriya ispat nigam limited, Vishakhapatnam, India (Blaine's surface area—5144 cm^2/g, average Particle size = 14 μm). It consists of CaO 32.23%, SiO_2 27.2%, Al_2O_3 11.85%, Fe_2O_3 0.86%. The fly ash particles were spherical while GGBS particles were angular (Fig. 1). Laboratory-grade sodium hydroxide (97.5% pure) and sodium silicate (Na_2O 8%, SiO_2 27%, H_2O 65% by mass) were used as received. Sandstone (SiO_2 49.9%, Al_2O_3 5.64%, Fe_2O_3 3.35%, CaO 7.04%, MgO 1.68%, $K_2O + Na_2O$ 2.36%) and siliceous type (SiO_2 49.47%, Al_2O_3 8.1%, Fe_2O_3 3.34%, CaO 2.99%, MgO 1.52%, $K_2O + Na_2O$ 2.69%) of aggregates were procured locally.

2.2 Sample Preparation

2.2.1 Preparation of Pastes

Fly ash and GGBS were inter-ground in a ball mill for 5 min in different ratios. The activator solution was prepared with 12 M NaOH and sodium silicate in the ratio of 1:2.5 and kept at room temperature for 24 h before use. The geopolymer pastes

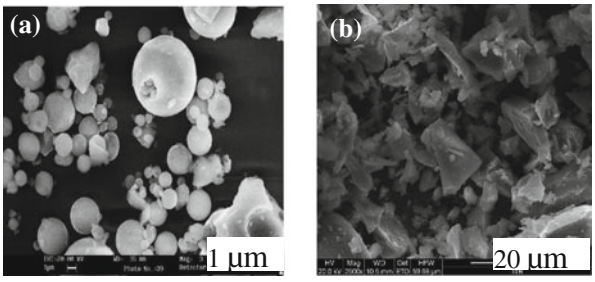

Fig. 1 SEM image **a** fly ash particles **b** GGBS

were optimized varying the fly ash/GGBS mix ratio, activator dosage and liquid–solid ratio. Four binder systems selected for mortar bars are: fly ash geopolymer, fly ash-GGBS geopolymer (80:20, 60:40) and OPC.

2.2.2 Preparation of Mortar Bars

The sandstone aggregates were crushed below 4.75 mm. The mix proportioning of mortar bars was done as per ASTM C1260 using fly ash/GGBS, aggregate and activators. The liquid–solid ratio for geopolymer mortars (GPC) was kept as 0.47. OPC mortar bars were taken as control specimen (w/c, 0.47). The dry components such as fly ash, GGBS and aggregate were first mixed together and then mixed with the activating solution in a Hobart mixer for 2–3 min to obtain homogeneous mix. The resulting mix was cast in a prismatic mould of size 25 × 25 × 285 mm consisting of gauge studs protruding 17.5 mm inside the specimen from both the ends. The cast OPC mortars were demoulded after 24 h and then immersed in water at 80 °C for 24 h. The geopolymer samples were cured at 80 °C for 24 h before being demoulded. The initial length of the demoulded specimens was recorded.

The specimens were immersed in 1 M NaOH at 80 ± 2 °C in an oven up to 90 days. The specimens were monitored at a regular interval of time for visual inspection and change in length.

2.3 Test Methods

The change in length of the mortar bars was measured with the help of a length comparator as per ASTM C490. The samples were placed vertically with the gauge stud at one end pressing against the tip of the dial gauge needle and the gauge stud at the other end resting on the groove of the collar. The length change in the samples was recorded at different periods.

The fractured surface of exposed mortar bars was examined on a FESEM (Quanta 200F). Prior to examination, a thin film of Au/Pd coating was applied on the surface by a sputter coater to render them conductive. The elemental chemical composition was mapped with an EDAX at different locations.

The potential reactivity of sandstone aggregate with NaOH was assessed by chemical method. The sample was digested for 24 h at 80 °C. Reduction in alkalinity and dissolved silica in 1 N NaOH solution were determined in accordance with IS: 2386 (Part VII) [13].

3 Results and Discussion

3.1 Composite Geopolymer Pastes

The geopolymer pastes were optimized as a function of fly ash–GGBS ratio (4:1, 3:1, 2:1), activator dosage (10–30%), water–binder ratio (0.2–0.29), curing temperature (28 & 80 °C) and curing time (7, 28, 56, 90 days) [12]. DSC run under quasi-isothermal mode showed that rate of geopolymerization increased with the increase of activator dosage. The addition of GGBS into the fly ash produced a single heat flow peak and reduced time lag compared to fly ash showing its fast setting time. The optimum strength of geopolymer pastes at 7 days was obtained at a fly ash–GGBS ratio of 2:1, 22% activator dosage and at water–binder ratio of 0.21. It was also found that the compressive strength of room temperature cured samples was higher than the heat cured samples (80 °C) after 28 days.

3.2 Mortars with Sandstone Aggregate

Visually, the surfaces of both OPC and GPC were defect free at the end of 16 days exposure showing no signs of surface fissures, cracks and voids. However, warping in GPC was 51% less than OPC. Contrary to this, at 90 days exposure, the OPC mortars showed white exudates along with pores and hair cracks on their surface. The surface of fly-ash-based GPC was soft and eroded, whereas GPC made with fly ash/GGBS mix appeared harder and less eroded but exhibited thick-white deposits along with large voids and cracks (Fig. 2). It is assumed that low dissolution of Ca from the surface of fly ash/GGBS mix binders in high pH solution favoured their less surface erosion.

Figure 3 shows that expansion of mortar bars increased with increasing exposure time. It was observed that the expansion in GPC mortars at 16 days was less than 0.1% as specified in ASTM C 1260 whereas, OPC mortars expanded beyond the threshold limit. When the exposure period was extended up to 90 days, the expansion in the fly-ash- based geopolymer (0.12%) approached the threshold while fly ash–GGBS composite mixes exhibited expansion in the range of

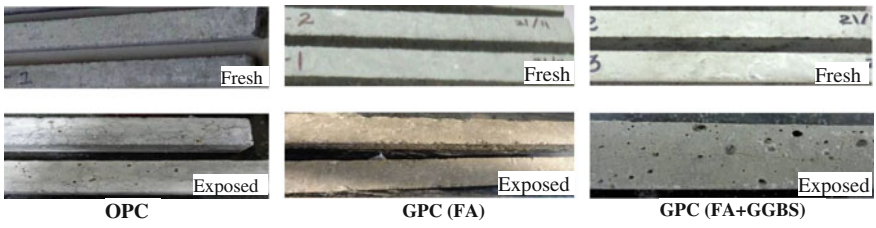

Fig. 2 Fresh and exposed OPC and geopolymer samples (GPC) after 90 days

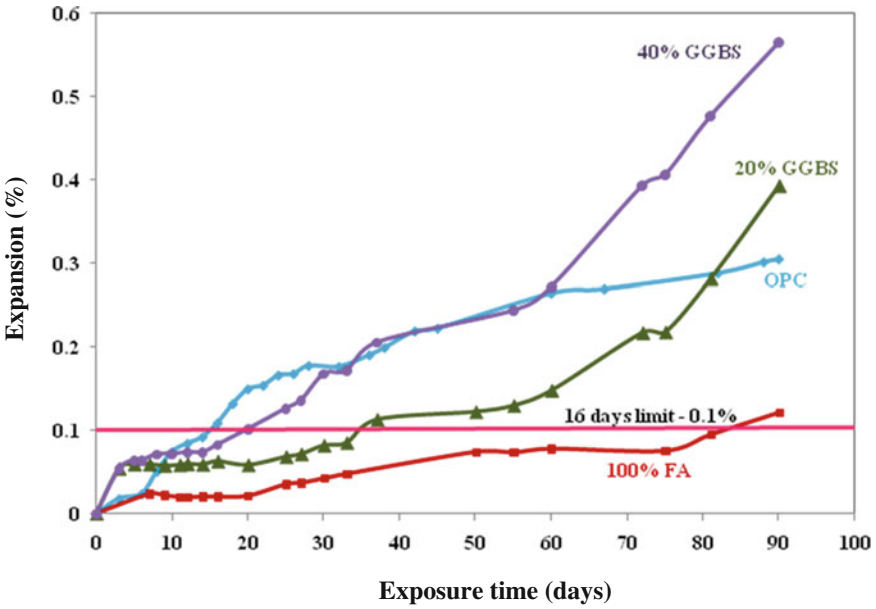

Fig. 3 Expansion of OPC versus geopolymer mortars bars containing coarse aggregates

0.31–0.56%. It was also noted that fly ash-based geopolymer had 60% less expansion than the OPC mortars. Contrary to this, geopolymer mortars made with fly ash–GGBS composite mixes exhibited 23–46% more expansion than the OPC mortars. This can be explained on the basis of unstable co-existence of N-A-S-H and C-S-H gels as a result of exposure at 80 °C for longer periods. In addition to expansion test, the reactivity of aggregates in 1 N NaOH was assessed by fitting the experimental data in the standard curve between the reduction in alkalinity and dissolved silica from aggregate mentioned in the specification (Fig. 4). It was found that the aggregate was falling in the innocuous zone. The reduction in alkalinity was ~50 mmol/litre while silica dissolved from aggregate was ~26 mmol/litre. These values were low because sodium hydroxide might have reacted with carbonate of magnesium or ferrous or certain silicates of magnesium (antegorite). This result was quite contradictory with the expansion and petrographic data wherein ASR reaction evidenced.

Evidence of deterioration in the exposed OPC and GPC was viewed in FE-SEM micrographs. In OPC mortars, a rim of reaction products around the aggregate mainly consisting of sodium, silica and calcium was observed (Fig. 5a). In the vicinity of interface (Fig. 5b), matrix had been converted into jelly-fibrous structure with plenty of voids (90 days). The Ca/Si ratio decreased significantly (from 0.6–1.2 to 0.4) as observed under an EDAX mapping. Sodium existed at a level of ~3% in the matrix suggesting the migration of sodium ions into the specimen during exposure which confirmed the formation of sodium calcium silicate gel

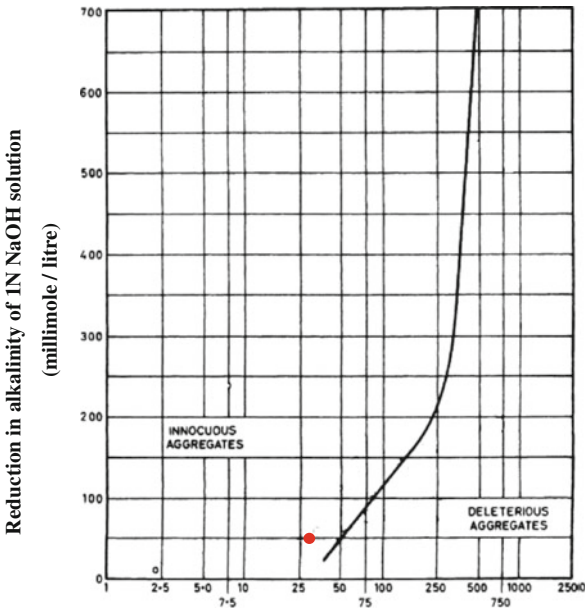

Fig. 4 Illustration of division between innocuous and deleterious aggregates on the basis of reduction in alkalinity test

triggering the ASR. The fly-ash-based GPC showed an intact interface between the paste and the aggregate at the age of 16 days. EDAX mapping indicated that Si/Al (2.27) and Na/Al (0.76) ratios at the interface were nearly comparable to bulk of the matrix (Si/Al = 2.33, Na/Al = 0.53). The ingress of alkali at the initial stage has caused densification of ITZ (Fig. 6a) and matrix by further geopolymerization of unreacted particles, thus causing slight expansion. The growth of crystalline zeolites was viewed in the cavities (Fig. 6b) which play no role in exerting pressure on the structure. The formation of sodium calcium silicate gel appeared to be minimal due to non-availability of adequate calcium in the system. In the case of fly ash/GGBS-based geopolymer (20% GGBS), a clear demarcation between the paste and the aggregate was observed at ITZ (16 days). The Si/Al = 3.99 ratio was higher than that of the bulk matrix (Si/Al = 2.35) probably due to reaction between

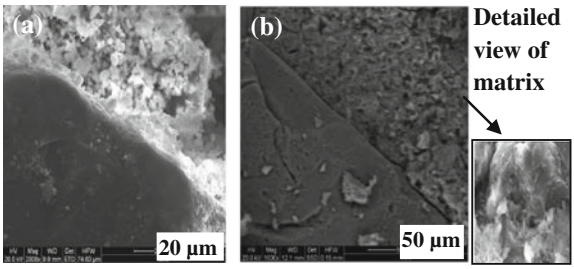

Fig. 5 FESEM images of ITZ of OPC mortars at **a** 16 days **b** 90 days

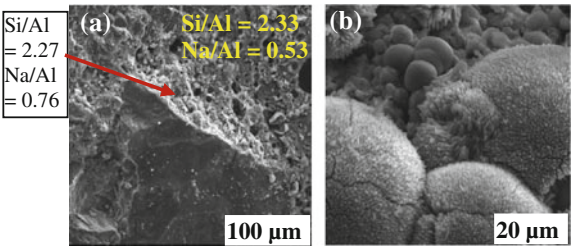

Fig. 6 FESEM images of fly- ash- based GPC mortars showing **a** ITZ at 16 days **b** growth of crystalline zeolites at 90 days

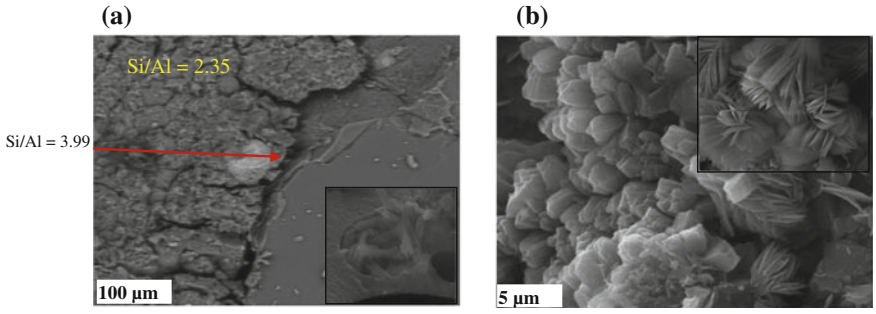

Fig. 7 FESEM images of GPC mortars after 90 days showing **a** 20% GGBS **b** 40% GGBS

reactive silica of aggregate and NaOH. At 90 days exposure, wide cracks at ITZ (Fig. 7a) and the existence of crystalline zeolites in the matrix were evident. When GGBS content was increased up to 40%, the cavities existed in the matrix were filled with the rod-shaped structures (Si/Al = 1.05). A "pseudo rosette"-type zeolitic structure was widely scattered throughout the matrix (Fig. 7b). The presence of excess Ca^{++} ion in the system (from GGBS) had exchanged for sodium ion on silica gel leading to further production of ASR complexes, thus causing severe deterioration.

3.3 Mortar Bars with Siliceous Aggregate

Figure 8 shows expansion of mortar bars as a function of exposure time. At 16 days, both OPC and geopolymer mortars expanded less (0.03–0.07%) than the prescribed limit of the Standard. At 90 days, the expansion in both OPC and geopolymer mortars exceeded the limit as similar to sandstone aggregate system. As observed earlier, the mortars made with composite mix of fly ash and GGBS had higher expansion (0.27–0.35%) than the mortars made with fly ash alone (0.11%).

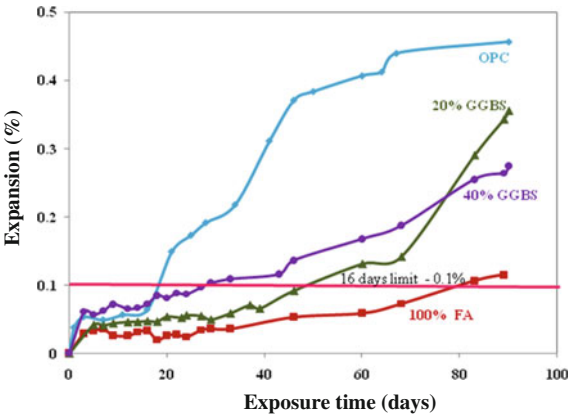

Fig. 8 Expansion of OPC versus geopolymer mortars bars containing siliceous aggregate

It was also observed that geopolymer mortar exhibited less expansion than the OPC mortar (0.46%). This is mainly because of less expansive gel formation following the reaction of NaOH with reactive silica. When compared with sandstone system, the siliceous aggregate was less prone to ASR possibly due to its less reactive silica and also its lower CaO content and higher Al_2O_3 content as determined by chemical analysis. The dissolved aluminium either from the Si–Al networks or unreacted fly ash/GGBS slag may adsorb onto the surface of silica and thus prevented ASR. It is also mentioned that mineralogy of sandstone was mainly quartzite type and soft fragmented. Due to some unstable form, the dissolution of silica was more in sandstone coarse aggregate than the siliceous fine aggregates. Because of this, the expansion in mortar bars containing siliceous aggregate was less than the sandstone aggregate mortars.

SEM micrographs on the fractured surface of mortars were also studied. In OPC samples, ITZ between the paste and aggregate appeared to be intact at 16 days exposure. The reaction product formed at the interface consisted of high silica content (27.59%) and small amount of sodium (1.56%) and calcium (0.53%) showing dissolution of silica from the aggregates. Fly-ash-based geopolymer mortars exhibited large number of cavities in which crystalline zeolites was filled. The specimens did not respond to ASR showing innocuous nature of siliceous aggregate. Mortars made with fly ash–GGBS composite mix (80:20) produced a rim at the interface around the aggregate. As similar to fly ash system, voids were filled with crystalline zeolites showing no stress in the microstructure. Consequently, this has resulted in less expansion. In the case of geopolymer mortar with 40% GGBS, the aggregate was covered with the reaction products. Several gel-type structures were distributed in the matrix and filled the voids (Na = 9.3%, Al = 6.38%, Si = 16.19%, Ca = 3.73%). Because of this gel formation, the mortars exhibited more expansion than those of others systems.

4 Conclusions

The results indicate that geopolymer concretes were less susceptible to the expansive alkali-silica reaction. However, for longer periods, expansion beyond the prescribed limit was observed in the case of fly ash–GGBS composite mix based mortars. It was noted that expansion in geopolymer mortars increased with increasing GGBS content in the fly ash–GGBS mix. The existence of large number of voids, cracks and crystalline zeolitic phases in the microstructure affected the expansion behaviour of geopolymer concrete. The deleterious ASR in geopolymeric environment can be prevented through a dense matrix formation by utilizing/immobilizing dissolved silica in geopolymer and also by involving CaO in the Na/Ca-A-S-H phase formation through ternary binder system.

Acknowledgments This paper forms part of a Supra Institutional Project of CSIR R & D programme (Govt. of India) and is published with the permission of Director, CSIR—Central Building Research Institute, Roorkee (India).

References

1. Davidovits, J. (2005). Green chemistry and sustainable development. In *Proceedings of An International Conference on Geopolymer 2005* (pp. 9–15), Saint-Quentin, France, June, 2005.
2. Provis, J. L., & Van Deventer, J. S. J. (Eds.). (2009). *Geopolymers, structure, processing, properties and application*, (1st ed.). Woodhead Publishing Limited, CRC.
3. Hardjito, D., Wallah, S. E., Sumajouw, D. M. J., & Rangan, B. V. (2004). On the development of fly ash-based geopolymer concrete. *ACI Materials Journal, 101,* 467–472.
4. Swamy, R. N. (Ed.). (1992). *The alkali-silica reaction in concrete*. UK: Blackie and Sons Limited.
5. Bijen, J. M. J. M. (1996). *Blast furnace slag cement for durable marine structures*. Den Bosch, The Netherlands: Stichting Betonprisma, 62.
6. Malek, R. I. A., Roy, D. M. (1983). Effect of slag cements and aggregate type on alkali—Aggregate reaction and its mechanism. In *Alkalies in Concrete, Research and Practice, 6th International Conference* (pp. 223–230).
7. Ichikawa, T. (2009). Alkali-silica reaction, pessimum effects and pozzolanic effect. *Cement and Concrete Research, 39,* 716–726.
8. Lodeiro, I. G., Palomo, A., & Jimenez, A. F. (2007). Alkali-aggregate reaction in alkali activated fly ash mortars. *Cement and Concrete Research, 37,* 175–183.
9. Patil, K. K., & Allouche, E. N. (2013). Impact of alkali silica reaction on fly ash-based geopolymer concrete. *Journal of Materials in Civil Enggineering, 25,* 131–139.
10. Jimenez, A. F., & Puertas, F. (2002). The alkali-silica reaction in alkali-activated granulated slag mortars with reactive aggregate. *Cement and Concrete Research, 32,* 1019–1024.
11. Bakharev, T., Sanjayan, T. G., & Cheng, Y. B. (2001). Resistance of alkali-activated slag concrete to alkali-aggregate reaction. *Cement and Concrete Research, 31,* 331–334.
12. Ishwarya, G. (2013). *Development of geopolymer concrete cured at ambient temperature*, M. Tech thesis. CSIR-Central Building Research Institute (AcSIR), Roorkee, India.
13. IS: 2386. (1963). Methods of test for aggregates for concrete-part VII alkali aggregate reactivity.

Bond Behaviour of Recycled Aggregate Concrete

M. Surya, P. Lakshmy and V. V. L. K. Rao

Abstract This paper discusses the mechanical properties and bond behaviour of recycled aggregate concrete (RAC). The recycled aggregates used were obtained from crushed concrete cubes of 2–3 years old. The properties of the aggregates were studied and a concrete of characteristic compressive strength of 40 MPa was designed. RAC mixes with 50, 75 and 100% coarse-recycled aggregates, viz. R50, R75 and R100 and 20% fly ash were tested, the properties were compared to natural aggregate concrete with and without fly ash, viz. NAC and NAF. Triple mixing method was adopted for mixing of concrete. The mechanical properties were studied at 56 days and the bond behaviour was investigated by performing rebar pull out test. The mechanical properties of the mixes were found to be almost similar for all mixes, except for elastic modulus which decreased with increase in percentage of recycled aggregates. The bond strength of RAC at a slip of 0.025 and 0.25 mm were up to 25% higher and 27% lower than that of NAC and NAF, respectively. However, the bond strength at failure load was found to be almost similar for all the mixes.

Keywords Recycled aggregate concrete · Bond strength · Pull out test
C and D waste

M. Surya (✉)
Structural Engineering Group, CSIR-Central Building
Research Institute, Roorkee 247667, India
e-mail: surya@cbri.res.in

P. Lakshmy · V. V. L. K. Rao
Bridges and Structures Division, CSIR-Central Road
Research Institute, New Delhi 110025, India
e-mail: lakshmyp@crri.nic.in

V. V. L. K. Rao
e-mail: vvlkrao@crri.nic.in

A. Rama Mohan Rao and K. Ramanjaneyulu (eds.), *Recent Advances in Structural Engineering, Volume 1*, Lecture Notes in Civil Engineering 11,
https://doi.org/10.1007/978-981-13-0362-3_77

1 Introduction

The global consumption of construction aggregates, including for road construction, as filling materials and for structural concrete, has increased from 26.8 billion metric tonnes (bmt) in 2011 to 28.7 bmt in 2013 and 48.3 bmt in 2015 [1]. Due to this increased consumption, several sources of natural aggregates (NA) are in decline and the construction industry is at the risk of facing shortage of NA. Use of recycled aggregate (RA) obtained from the construction and demolition waste (CDW) is a techno-economically viable solution for the problem of shortage of aggregates. With the use of CDW for generation of aggregates, the quantity of the same dumped in the landfill is reduced and the use of constructible land as a landfill shall be prevented. However, the use of RA in structural concrete is still limited in use, due to lack of evidence on the efficacy of the RA. Various research studies were and are carried out around the world to investigate the properties of RA and the performance of recycled aggregate concrete (RAC) with respect to mechanical properties and durability, whereas only a few studies have been carried out on the bond strength and structural properties of RAC. This research investigates the bond behaviour of RAC with varying percentage of replacement of NA by RA along with the basic mechanical properties.

2 Literature Review

The earlier studies reported an inferior performance of RA and RAC when compared to NA and NA concrete with respect to mechanical and durability properties [2–19]. However, the same had been found to improve in RAC with the use of SCM, coating of aggregates and adopting double mixing [5] or triple mixing methods [6].

There had been only a few researches on bond of RAC with the steel rebar and the findings reported are as follows. Xiao and Falkner [9] found that RAC exhibited a similar behaviour as NA concrete under rebar pullout testing, with respect to micro slip, residual cracking and load versus slip curve. It was also reported that the mixes with similar compressive strength exhibited equal bond strength. However, the RAC with similar mix proportions exhibited bond strength of up to 6 and 12% lesser than the comparable NA concrete mix when the percentage of RCA replacement were 50 and 100% respectively. Similarly, Butler et al. [10] reported that bond strength of RAC was lesser by 9–11.4% for 30 MPa concrete and by 10.3–11.4% for 50 MPa concrete, when compared to NA concrete of respective strengths.

Kim et al. [11] also reported reduced bond strength of concrete with an increase in the amount of the RA. Based on the study, Eq. (1) was proposed to predict the bond strength of RAC with the quantity of RA replacement.

$$\tau_{r\max} = 0.614\sqrt{f_{ck}}\left[\frac{C_c}{d_b} - 0.55\right] - \left(0.4203e^{0.0172s} + 0.007G\right) \quad (1)$$

where

$\tau_{r\max}$ maximum predicted bond stress of RAC
f_{ck} observed compressive strength of RAC
C_c distance from the deformed steel rebar core to the concrete surface
d_b diameter of deformed steel rebar
S replacement ratio of recycled fine aggregate
G replacement ratio of recycled coarse aggregate

On contrary to the earlier findings, Fathifazl et al. [7] concluded that the type of aggregate does not have any considerable effect on the bond properties of the concrete when equivalent mortar volume method of mix design was adopted.

3 Design Provisions in Standards

CEB-FIP [20] defines bond as the term used to denote the interaction and transfer of force between reinforcement and concrete. Various factors influencing bond slip relations such as cracking, loading, creep and fatigue, rebar surface features, etc., were discussed and suitable anchorage length design procedure has been suggested. The code also suggests a basic bond strength and design bond strength values as given by Eqs. (2) and (3).

The basic bond strength,

$$f_{bd,0} = \eta_1\eta_2\eta_3\eta_4(f_{ck}/25)^{0.5}/\gamma_c \quad (2)$$

where

f_{ck} is the compressive strength of concrete
η_1 is a coefficient representing surface characteristics of rebar
η_2 coefficient based on the casting position of the bar during concreting
η_3 coefficient based on the bar diameter:
η_4 represents the characteristic strength of steel reinforcement

The partial safety coefficient for bond γ_c is taken as 1.5.

The design ultimate bond strength is

$$f_{bd} = (\alpha_2 + \alpha_3)f_{bd,0} - \frac{2P_{tr}}{\gamma_c} < 2.5f_{bd,0} - \frac{0.4P_{tr}}{\gamma_c} < \sqrt[1.5]{f_{ck}}/\gamma_c \quad (3)$$

Table 1 Design values for favourable bond conditions

Concrete grade f_{ck}/rebar grade	M20	M25	M30	M35	M40	M45	M50	M55	≥M60
Plain bars Fe 240	1.0	1.1	1.2	1.3	1.4	1.45	1.5	1.6	1.7
HYSD bars of $\Phi \leq 32$ mm	1.95	2.25	2.7	3.0	3.2	3.4	3.75	4.0	4.3

where

α_2 and α_3 represent the influence of passive confinement from cover (α_2) and from transverse reinforcement (α_3).

P_{tr} is the mean compression stress perpendicular to the potential splitting failure surface at the ultimate limit state; where transverse compression perpendicular to the bar axis acts over a portion of the bond length, bond strength may be increased over that portion. P_{tr} is negative when transverse stress is compressive.

Indian standards like IS 456 [21] and IRC 112 [22] provide a design bond strength value for concrete based on its characteristic compressive strength.

IS 456 [21] consider a design bond stress for design of development length of steel reinforcement. The values of bond stress for plain rebars are considered to be 1.2, 1.4, 1.5, 1.7 and 1.9 N/mm^2, respectively, for concrete of grade M20, M25, M30, M35 and M40 and above. For deformed bars, these values shall be increased by 60% and for bars in compression the values of bond stress shall be increased by 25%. However, it is not to be assumed that the average bond stresses calculated from the pull out tests performed as per IS 2770 [23] have any direct relation to the permissible bond stress given in IS: 456 [21], though these values are arrived at based on the bond slip behaviour of the rebar and concrete.

IRC 112 [22] considers bond as a property dependent on surface pattern of the bar, dimension of the member, and on position and inclination of the rebar with respect to the direction of concreting. The bond strength of concrete is significant in determination of anchorage length of rebar, as per IRC 112 [22]. The design bond strength values are also given for both plain rebar and high yield strength deformed bars as given in Table 1. For unfavourable conditions, these values are multiplied by 0.7.

4 Experimental Study

The experimental studies were carried out in three phases which involved (i) Characterization of materials, (ii) Mechanical properties of the concrete mixes, (iii) Bond strength determination by pull out test.

5 Characterization of Materials

5.1 Aggregates

Crushed granite available in Delhi region was used as coarse natural aggregates (NA). The RA for the present study was obtained by crushing concrete cubes and cylinders that were cast at CSIR-CRRI and various bridge construction sites and tested at CSIR-CRRI. The samples crushed for aggregates were of strength range 35–45 MPa and age between 2 and 3 years and stored in atmospheric conditions after failure. The properties of these aggregates were studied and reported in Table 2 along with the results obtained in earlier studies and acceptance criteria for comparison.

From Table 2, it can be seen that the specific gravity and bulk density of RA used in the present study were lower and water absorption was higher than that of NA. However, the same were found to comply with the acceptance criteria for RA and hover within the range observed in earlier studies. The RA used in the present study was found to have better resistance to impact than the NA and same was observed to be contradictory to the results of the earlier studies. The other mechanical properties of the RA used in the present study, though slightly inferior to that of NA, satisfied the acceptance criteria for RA as well as NA. This, menial performance of RA may be attributed to the porous nature of the adhered mortar and micro cracks and fissures, which could have formed in the aggregates during the manufacturing process of RA.

Table 2 Properties of RA and NA

Property	RA			NA		
	Present study	Earlier studies [2–19]	Acceptance criteria	Present study	Earlier studies [2–19]	Acceptance criteria
Specific gravity	2.501	2.3–2.56	2.5 or more (JIS A 5021 Class H) [24]	2.675	2.5–2.7	2.30–2.90 (ACI EI 07) [27]
Water absorption (%)	2.76	0.9–11.55	3.0 or less (JIS A 5021 – Class H) [24]	0.42	0.2–1.5	2.0 (MORTH) [28]
Abrasion loss (%)	29.27	10–46	40 or less (KS F 2573) [25]	26	12–29	30 (IS 383) [41]
Crushing value (%)	28.87	19.86–36.3	–	27.12	15–28	30 (IS 383) [41]
Impact value (%)	16.04	9.66–35.8	–	21.77	5–22	30 (IS 383) [29]
Bulk density (kg/m^3)	1340	1190–1426	1200 (HB 155: 2002) [26]	1630	1340–1733	1280–1920 (ACI E1-07) [27]

Table 3 Surface parameters of rebars

Property	Observed value
Diameter (mm)	20
Rib height (mm)	1.45
Rib width (mm)	0.2
Rib spacing (mm)	20.8
Rib face angle (°)	45

5.2 Rebar

High-yield strength deformed bars of grade Fe 500 was used. The surface characteristics of the bar are given in Table 3.

5.3 Fine Aggregate

Crushed stone sand available in Delhi region is used as fine aggregate in this study. The specific gravity of the fine aggregates is found to be 2.63 and the water absorption value is obtained as 0.72%. The particle size distribution of the fine aggregate used conformed to the grading curve of Zone I as given in IS 383 [29].

5.4 Concrete Mixes

Five concrete mixes of characteristic compressive strength 40 MPa were made with different percentages of RA, (a) Control concrete with 100% natural aggregate (NAC), (b) Natural aggregate concrete with 100% natural aggregate and fly ash (NAF), (c) RAC with 50% of recycled aggregate and fly ash (R50), (d) RAC with 75% of recycled aggregate and fly ash (R75) and (e) RAC with 100% of recycled aggregate and fly ash (R100).

All the NA concrete mixes were designed as per IS 10262 [30] to achieve a characteristic compressive strength of 40 MPa. In case of RAC mixes, the weight of coarse aggregates was adjusted according to the specific gravity of the aggregates. The specific gravity used for determining the weight of coarse aggregate in RAC are specific gravity of RCA (2.501) for R100 and the specific gravity of the combination of NA and RCA (2.593 and 2.553) for R50 and R75 respectively. The details of mix proportions of the concrete mixes are given in Table 4.

Table 4 Details of mix proportions

Mix designation		NAC	NAF	R50	R75	R100
Cement (kg/m^3)		410	410	410	410	410
Water (kg/m^3)		164	164	164	164	164
Fly ash (kg/m^3)		–	82	82	82	82
Fine aggregate (kg/m^3) (SSD condition)		706	706	706	706	706
Coarse aggregate (kg/m^3) (SSD condition)	NA	1172	1172	568	280	–
	RCA	–	–	568	839	1119
Super plasticizer (percentage by weight of cement)		0.6	0.6	0.6	0.6	0.6
Slump (mm)		65	61	63	62	68

5.5 *Casting and Curing*

The concrete mixes were prepared in a drum mixer of capacity 300 kg. Conventional mixing for NAC and triple mixing method, developed by Kong et al. [6], for NAF and RAC mixes were adopted for the production of concrete. In conventional method, dry mixing of aggregates and cement is carried out first and then the water is added, whereas in triple mixing water is added in two parts. This method of mixing is reported to allow less water near ITZ, making the same more compact contributing to better mechanical and durability properties. The steps involved are as follows: coarse (RCA and NA) and fine aggregates were initially mixed for 15 s. A part of water was then added to the aggregate mixture and mixed for 15 s, and to this wet aggregate the fly ash was added and further mixed for 15 s to facilitate coating of the surface of aggregate with fly ash. Cement was then added to the surface-coated aggregate and the remaining water was added and the mixing was continued for further 60 s. The oiled moulds were filled with concrete in layers and vibrated on a table vibrator. The cast specimens were water cured for 56 days.

5.6 *Mechanical Properties of Concrete Mixes*

The specimens were water cured till the age of test and tested at 56 days for compression, flexure and Young's modulus as per procedure in IS 516 [31] and splitting tensile strength as per IS 5816 [32]. The test results are reported in Table 5, from which it is observed that the compressive strength, split tensile strength and flexural strength of RAC are on par with NAC and NAF while the elastic modulus decreases with increase in percentage of RCA.

Table 5 Mechanical properties of concrete mixes

Mix designation	Compressive strength (MPa)	Split tensile strength (MPa)	Flexural strength (MPa)	Elastic modulus (GPa)
NAC	53.19	3.96	5.35	30.15
NAF	57.77	4.15	5.46	35.20
R50	54.02	3.53	4.78	27.17
R75	54.22	3.63	4.77	26.28
R100	57.33	4.15	5.72	25.03

5.7 Rebar Bond Behaviour

The pull out test has been carried out to determine the bond strength of different concrete mixes in a universal testing machine as shown in Fig. 1 at an age of 56 days. The cube specimens of size 150 mm and deformed high yield strength (HYSD) steel bar of 20 mm diameter were used. The test was performed and the load at a specified slip was recorded until the total slip was 2.5 mm or rebar failure or concrete crushing, whichever occurred first as specified in IS 2770 [23].

During the test it was observed that, NA concrete specimens developed significant measurable cracks on the concrete surface whereas in case of RAC specimens there has been no measurable/significant crack on the concrete surface. On the other hand, a fine powdery material is seen falling from the concrete–rebar interface in the RAC mixes during the test. This may be due to crushing of the adhered mortar (which is porous and comparatively weaker than aggregates) in the RAC mixes as the rebar is pulled which could be preventing transfer of load from the rebar to the

Fig. 1 Pull out test

Fig. 2 Observed crack pattern on specimens after pull out test

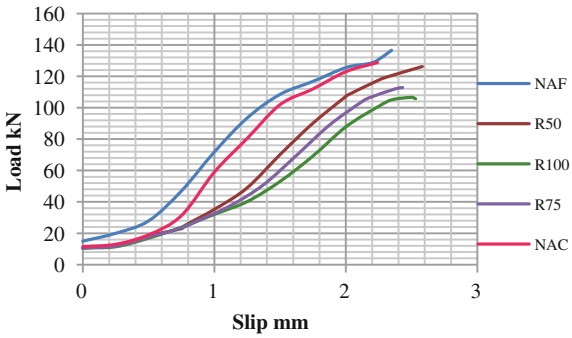

Fig. 3 Comparison of load versus slip curves for the mixes

adjacent concrete. Thus, appearance of crack on concrete surface, which normally happens in the NA mixes, was not found in RAC mixes. Figure 2 shows the crack pattern of specimens after failure.

The effect of this localized crushing of mortar in the interface between RAC and rebar can be observed in the load versus slip curves as shown in Fig. 3. The curve is almost linear initially till a slip of 0.5 mm for all the mixes. However, beyond 0.5 mm slip NAC and NAF mixes displayed comparatively steeper curves than R50, R75 and R100. The steeper curves of NAC and NAF show that the increase in slip is lower for equal increase in load. This indicates that the rate of slip of the bar in RAC specimens is comparatively greater than the rate of slip in NA concrete. This may be because in case of NAC and NAF the slippage of bar is resisted by the

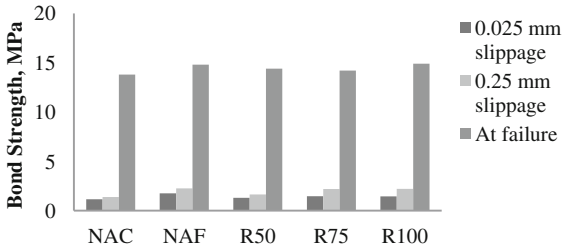

Fig. 4 Variation in bond strength for various mixes

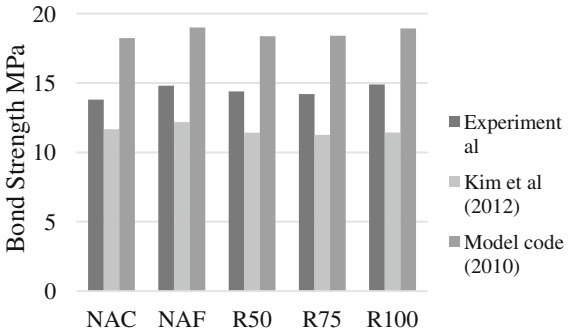

Fig. 5 Comparison of experimental and predicted bond strength

strong rebar–concrete interface and the load is transferred to the adjacent concrete, whereas in the case of RAC mix the rebar–concrete interface becomes weak due to crushing of the mortar at the interface.

The bond strength is determined using the embedded surface area of the bar and load corresponding to a slippage of 0.025, 0.25 mm and at failure. Three specimens have been tested for each mix and the average bond strength is plotted in Fig. 4. It is found from Fig. 4 that the bond strength of RAC at a slip of 0.025 and 0.25 mm were up to 25% higher than that of NAC and 27% lower than that of NAF, respectively.

However, the bond strength at failure load was found to be almost similar for all the mixes with a maximum variation of only 6% when RAC was compared to NAC and NAF.

The results of the present study are similar to the results observed in a study by Xiao and Falkner [9], in which mixes with 100% RA exhibited higher bond strength at failure load and it was concluded that the bond strength of RAC will be similar to the bond strength of NAC when the compressive strength of the mixes are comparable. The same is applicable in the present study as well, as the compressive strength of the mixes are in similar range.

The experimental results compared with the predictions for ultimate bond strength are given in Fig. 5. It is seen that the RAC mixes exhibited a bond strength up to 23% higher than the bond strength predicted by Eq. (1) by Kim et al. [11]. However, all the mixes including NA mixes exhibited a bond strength up to 32%

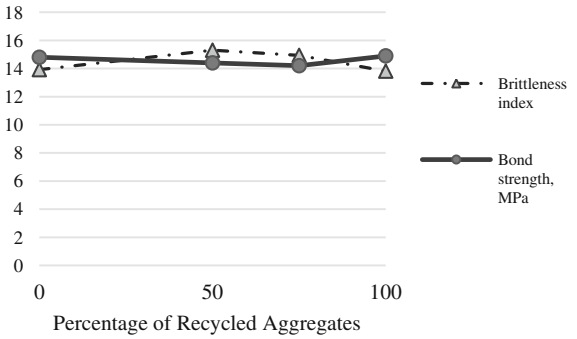

Fig. 6 Variation of brittleness index and bond strength

lesser than that given by the Model Code, 2010 [20]. But the bond strength prediction given in Model Code 2010 is valid for well-confined concrete with a cover greater than five times the diameter, while the specimens used for pull out study had a cover thickness equivalent to three times the bar diameter. Hence, the predictions may not be strictly obliging to the obtained values, but the variation in trend remained similar for both experimental and predicted values.

The bond strength of the concrete is related to its tensile and splitting properties and thus fracture toughness is a significant indicative of bond strength [12]. As the Brittleness index (ratio of compressive strength to split tensile strength) is an important attribute to fracture toughness the obtained ultimate bond strength value and the computed brittleness index against the percentage of RCA are given in Fig. 6. The higher brittleness index indicates more brittle the material is and the vice versa. It is seen from Fig. 6 that the bond strength decreases with increase in brittleness index. This indicates that the brittleness index may be considered as a valid predictor for computation of bond strength of concrete.

6 Conclusions

From the discussions made in the paper following conclusions can be drawn.

- The properties of RCA were menial compared to NA but complied well within the limiting values of the specifications.
- The mechanical properties of RAC were on par with NAC and NAF, except for elastic modulus which decreased with increase in percentage of RCA.
- The bond strengths of RAC mixes were greater than that of NAC and lesser than that of NAF.
- The bond strengths of RAC predicted from the compressive strength values were found to be following a similar trend as that of the experimental values. However, the RAC exhibited up to 23% higher bond strength than the predicted.
- Brittleness index may be considered as a valid predictor for computation of bond strength of concrete.

References

1. Freedonia Group. (2013). *World construction aggregates—Industry study with forecasts for 2015 and 2020*. Cleave Land, USA: Freedonia Group.
2. Rao, M. C., Bhattacharya, S. K., & Barai, S. V. (2011). Influence of field recycled coarse aggregate on properties of concrete. *Materials and Structures, RILEM, 44,* 205–220.
3. Iyer, N. R., Bharatkumar, B. H., Bhashya, V., & Prameettha, J. (2013). Investigation on recycled aggregate concrete with mineral admixture. In *Proceedings of International Workshop on Construction and Demolition (C & D) Waste Recycling*, IIT Madras, Chennai (pp. 75–82).
4. Rao, P., & Madhavi, M. (2013). A study on partially used recycled coarse aggregate cement concrete. *Asian Journal of Civil Engineering (BHRC), 14*(6), 917–933.
5. Otsuki, N., Asce, Miyazato, S., and Yodsudjai, W. (2003, October). Influence of recycled aggregate on interfacial transition zone, strength, chloride penetration and carbonation of concrete. *Journal of Materials in Civil Engineering*, pp. 443–451. (American Society of Civil Engineers, Reston, USA).
6. Kong, D., Lei, T., Zheng, J., Ma, C., Jiang J., & Jiang J. (2010). Effect and mechanism of surface-coating pozzalanics materials around aggregate on properties and ITZ microstructure of recycled aggregate concrete. *Construction and Building Materials, 24*(5), 701–708. (Elsevier, Amsterdam).
7. Fathifazl, G., Abbas, A., Razaqpur, A. G., Isgor, O. B., Fournier, B., & Foo, S. (2009). New mixture proportioning method for concrete made with coarse recycled concrete aggregate. *Journal of Materials in Civil Engineering, 21*, 601–611. (American Society of Civil Engineers, Reston, USA).
8. Kou, S. C., & Poon, C. S. (2010). Properties of concrete prepared with PVA-impregnated recycled concrete aggregates. *Cement Concrete Composites, 32*(8), 645–654. (Elsevier).
9. Xiao, J., & Falkner, H. (2007). Bond behavior between recycled aggregate concrete and steel rebars. *Construction and Building Materials, 21*, 395–401. (Elsevier, Amsterdam).
10. Butler L., West J. S., & Tighe S. L. (2011b). The effect of recycled concrete aggregate properties on the bond strength between RA concrete and steel reinforcement. *Cement and Concrete Research, 41*(10), 1037–1049. (Elsevier, Amsterdam).
11. Kim, Y., Sim, J., & Park, C. (2012). Mechanical properties of recycled aggregate concrete with deformed steel re-bar. *Journal of Marine Science and Technology, 20*(3), 274–280. (Springer).
12. Prince, M., & Singh, B. (2015). Bond behaviour of normal-and high-strength recycled aggregate concrete. *Structural Concrete, 16*(1), 56–70.
13. Rao, M. C., Bhattacharyya, S. K., & Barai, S. V. (2010). Recycled aggregate concrete: A sustainable built environment. In *Proceedings of International Conference on Sustainable Built Environment* (pp 227–233).
14. Somna, R., Jaturapitakkul, C., Chalee, W., & Rattanachu, P. (2012). Effect of water to binder ratio and ground fly ash on properties of recycled aggregate concrete. *Journal of Materials in Civil Engineering, 24*(1), 16–22. (American Society of Civil Engineers, Reston, USA Publications).
15. Padmini, A. K., Ramamurthy, K., & Mathews, M. S. (2009). Influence of parent concrete on the properties of recycled aggregate concrete. *Construction and Building Materials, 23*(2), 829–836.
16. Yong, P. C., & Teo, D. C. L. (2009). Utilisation of recycled aggregate as coarse aggregate in concrete. *UNIMAS E-Journal of Civil Engineering, 1*(1), 1–6.
17. Butler L., West J. S., & Tighe S. L. (2011a). Quantification of recycled concrete aggregate (RA) properties for usage in bridges and pavements: An Ontario case study. In *Proceedings of the 2011 Annual Conference on Innovative Developments in Sustainable Pavements* (17 p.). Organized by the Transportation Association of Canada, Edmonton, Alberta.

18. Xiao, J., Li, J., & Zhang, Ch. (2005). Mechanical properties of recycled aggregate concrete under uniaxial loading. *Cement and Concrete Research, 35*, 1187–1194. (Elsevier, Amsterdam).
19. Casuccio, M., Torrijos, M. C., Giaccio, G., & Zerbino, R. (2008). Failure mechanism of recycled aggregate concrete. *Construction and Building Materials, 22*(7), 1500–1506. (Elsevier, Amsterdam).
20. fib-2010. (2013). *Model code for concrete structures 2010*. Berlin: Ernst & Sohn.
21. IS 456. (2000). *Plain and reinforced concrete—Code of practice*. New Delhi, India: Bureau of Indian Standards.
22. IRC 112. (2011). *Code of practice for concrete road bridges*. New Delhi, India: Indian Roads Congress.
23. IS 2770. (2007). *Methods of testing bond in reinforced concrete*. New Delhi, India: Bureau of Indian Standards.
24. JIS A 5021. (2005). *Japan Industrial Standard—Recycled aggregate for concrete Class H.* Tokyo, Japan: Japan Standards Association.
25. KS F 2573. (1999). *Recycled aggregates for concrete*. Seoul, Korea: Korean Industrial Standards.
26. HB 155. (2002). *Standards Australia. Guide to the use of recycled concrete and masonry materials*. Sydney, Australia.
27. ACI E1–07. (2007). *ACI Committee education bulletin-Aggregates for concrete.* Farmington Hills, USA: American Concrete Institute.
28. MORTH. (2013). *Specifications for road and bridge works*. New Delhi: Indian Road Congress.
29. IS 383. (1997). *Specification for coarse and fine aggregate from natural sources of concrete*. New Delhi, India: Bureau of Indian Standards.
30. IS 10262. (2009). *Concrete mix proportioning—Guidelines.* New Delhi: Bureau of Indian Standards.
31. IS 516. (1999). *Methods of tests for strength of concrete.* New Delhi, India: Bureau of Indian Standards.
32. IS 5816. (1999). *Splitting tensile strength of concrete—Method of test.* New Delhi, India: Bureau of Indian Standards.

Durability and In Situ Performance Evaluation of Sustainable Recycled Aggregate Concrete Using Fluorogypsum as Cementitious Binder

Monalisa Behera, A. K. Minocha, S. K. Bhattacharyya and Rajesh Deoliya

Abstract Enormous industrialization and urbanization have led to the generation of huge quantity of C&D waste, which requires its appropriate utilization or disposal. Keeping these in eyes, construction sector is focusing on sustainable waste management regulations nowadays. Thus, the sustainable future green cities can be possible only by using low-carbon resources, eco-friendly materials and through energy conservation techniques. The goal of this study was to evaluate the durability and in situ performances of concrete made with recycled coarse aggregate (RCA) using fluorogypsum as cementitious binder to replace the cement partially (25%). This leads to a new perspective for achieving green concrete. The quality of RCA and the influence of the replacement ratio were assessed on several parameters such as chloride ion penetration, carbonation and water absorption resistance. The in situ parameters such as ultrasonic pulse velocity (UPV) and rebound hammer number reflected the same behaviour with replacement percentage level of RCA. The UPV values of more than 3600 m/s, showed good-quality concrete. Though, RCA is having potentially inferior quality than natural aggregate (NA), it could be used to produce a structural grade concrete of strength more than 40 MPa. The results with fluorogypsum binder (FB) revealed that though it is having its own binder property, it could not achieve strength up to that with cement replacement. Rather, it can be used as a filling material or as an additive to improve its performance by making its matrix denser.

M. Behera (✉) · A. K. Minocha · R. Deoliya
CSIR-Central Building Research Institute, Roorkee 247667, India
e-mail: monalisabehera7@gmail.com

A. K. Minocha
e-mail: minochaak@yahoo.com

R. Deoliya
e-mail: rdeoliya@gmail.com

S. K. Bhattacharyya
Department of Civil Engineering, Indian Institute of Technology, Kharagpur, Kharagpur 721302, India
e-mail: srimankb@gmail.com

A. Rama Mohan Rao and K. Ramanjaneyulu (eds.), *Recent Advances in Structural Engineering, Volume 1*, Lecture Notes in Civil Engineering 11,
https://doi.org/10.1007/978-981-13-0362-3_78

Keywords Sustainability · Recycled aggregate concrete · Durability
Chloride ion penetration · Carbonation · UPV

1 Introduction

Over the past years, there is a huge demand of natural resources such as aggregates and cement due to the exponential growth in population and the infrastructural development in most of the developing countries like China, India, etc. The increased demand of NA may contribute toward the quarry mining and mining of river bank and contribute towards global warming. Hence, the use of recycled aggregate through the recycling of C&D waste in concrete has become the recent burning topic all over the globe in pursuit of sustainable development. Recycling of C&D waste will provide a breakthrough for turning the economy of developing countries into a circular flow. The use of C&D waste as a substitute of NA not only has the tremendous environmental benefits, but also reduces the social and financial cost. Recently, IS: 383 has permitted to include the use of RCA, iron, steel slag and copper slag among manufacture aggregate to replace the use of natural aggregates (NAs) in its draft revision (March 2015) [1].

The major issues involved in sustainable construction lies with the optimizing usage of natural resources, waste minimization, and innovative usage of industrial by-products by conserving natural minerals and to reduce the emission of greenhouse gasses without sacrificing the safety of structure. The production of cement is extensively energy intensive and contributes 1 ton of CO_2 per ton of its production, which is approximately 7% of the total CO_2 contribution from all sources [2]. The usage of industrial by-products in cement, are becoming popular worldwide in the construction sector to make it less energy intensive and to reduce the greenhouse gas emission. The by-product of hydrofluoric acid industry can be used as a cementitious binder in construction sector, which will significantly reduce the carbon footprint and meet the sustainability requirement.

From the past studies, it is noted that RCA can be utilized for many purposes such as road base material, pavement material and concrete structures. However, the quality assurance is very much essential in its safe and reliable usage for structural purposes. A large number of studies have revealed that RCA is having some inherent negative attributes compared to NAs which limit its mass usage for construction purposes [3, 4]. In consequent to these attributes, the old mortar wrapped around the surface of RCA after crushing is one of the most distinguished aspects in differentiating the quality and properties of RCA over the NA [4–6]. The adhered mortar around RCA is the solely responsible factor for affecting the concrete behaviour [7–9]. Many studies have reported that the inferior properties of RCA have detrimental effect on the physical, mechanical and durability properties of the RAC [10–14].

The objective of this study is to evaluate the durability and in situ performances of RAC at various percentage replacement levels and to correlate these with the

apparent porosity distribution. In addition, the effect of fluorogypsum binder (FB) on the properties of concrete was also studied to evaluate its viability of using as a binding material by replacing cement. The use of industrial by-product (fluorogypsum) in concrete along with RCA for sustainable construction is the main focus of this experimental paper.

2 Availability of Fluorogypsum

In India, more than 300 million tons of industrial by-product such as fly ash, slag, gypsum, red mud, mine tailing are getting generated per annum [15]. Out of these by-products, gypsum waste is a cardinal waste obtained from several industries such as phosphoric acid industry, hydrofluoric acid industry. In India, more than 6.0 million tons of gypsum by-products are produced annually [15]. Fluorogypsum is a waste by-product of hydrofluoric acid industry, available to an extent of 1 million ton per annum. Basically, it is an anhydrite form of gypsum, which is chemically inert. However, it has been used as a binder for producing value added building material by activating its hydration and setting property.

3 Material Properties

The recycled aggregate used in this study was obtained from commercial C&D waste recycling plant crushed through both jaw crusher and impact crusher. The aggregates derived from C&D waste were characterized in accordance with the BIS specifications IS:2386-1963 and IS:383-1970 due to the non-availability of Indian standard specification for the characterization of recycled aggregate. Two different size fractions of 10 and 20 mm were used for both RCA and NA in concrete mix. RCA was used to replace NA at three various replacement levels (0, 50 and 100%). Locally available river sand as fine aggregate (zone-III) confirming to IS-383-1970 and readily available natural coarse aggregates were used. The particle size analysis indicates that the size distribution of RCA lies within specified range of IS: 383, showing a good particle distribution. The fineness modulus of RCA, NA and natural fine aggregate were found to be 6.51, 6.73 and 2.27 respectively. Water absorption of the RCA was 3.95% (20 mm) and 4.07% (10 mm) respectively, which is considerably larger than that of NA which was found to be 0.5%.

Ordinary Portland cement (OPC) of 43 grade, (specific gravity 3.15, specific surface area 3819 cm^2/gm) confirming to IS 8112:1989, is used as binding agent. Additionally, a new binding material, FB was used in this study to partially replace cement up to 25%. FB (specific gravity 2.81, fineness 2875 cm^2/gm) is basically a waste by-product which has been processed to develop its binding property by adding chemical reagents. The content of FB was added to the mix by weight of cement to replace cement. The chemical composition of the binders was determined

Table 1 Chemical composition of the binders

Binder	CaO	SiO_2	Al_2O_3	Fe_2O_3	MgO	SO_3	Na_2O	Cl^-	F^-
Cement	50.40	13.14	2.73	3.27	1.25	2.07	0.18	0.02	–
FB	36.04	0.46	0.18	0.23	0.24	45.50	0.19	0.29	1.32

Table 2 Physical properties of binders

Properties		Cement	FB
Consistency (%)		28.5	22
Initial setting (min)		160	195
Final setting (min)		280	290
pH		12.34	8.5
Mortar strength (MPa)	3 days	20.72	3.67
	7 days	25.23	15.71
	28 days	49.15	21.67
Soundness (mm)		0.5	3

through XRF analysis and reported in Table 1. The required water for a normal consistency and setting times of the binders are assessed in accordance with BIS specifications IS 4031. The results for consistence, setting time, mortar strength and soundness are given in Table 2.

4 Concrete Mix Proportion and Methodology

The proportions of the various components of the concrete mixes were determined as per IS: 10262. The mix proportioning was based on absolute volume method and the aggregates were used in dry condition. The mix design was formulated for control sample to achieve a compressive strength of 40 MPa at 28 days. The minimum value of the *w*/*c* ratio was determined by a preliminary study to assure the desired workability and the required strength. In the present investigation, the free water/binder (*w*/*b*) ratio (0.42) and the quantity of total cementitious substances (390 kg/m^3) were kept constant for all the mixes. To achieve the proper workability, a polyvinyl ether-based high-range superplasticizer was used. Totally, six concrete mix recipes were prepared by taking the combination of type of aggregate and binders and the mix compositions are presented in Table 3. To improve the quality of concrete-containing RCA, two-stage mixing approach (TSMA) [16] was adopted in a little modified manner for the present study. In TSMA, water is added in two stages of equal time interval, in two equal parts. However, in the current investigation, water was added in unequal parts at different time intervals. At first, coarse aggregates of both the sizes were dry mixed and then mixed with one-third

Table 3 Mix proportion details of concrete (kg/m^3)

Mix Notation	Cement	FB	Sand	NA	RCA	SP (%)	*w/c* ratio
REF	390	–	660	1241	–	0.75	0.42
C-R50	390	–	659	619	619	0.75	0.42
C-R100	390	–	660	–	1149	0.75	0.42
F- R0	293	97.5	657	1234	–	0.25	0.42
F-R50	293	97.5	657	617	617	0.25	0.42
F-R100	293	97.5	657	–	1146	0.25	0.42

of the total water in the mixer for around a minute to compensate the initial water absorption of aggregates and in order to make a proper coating of binder around the aggregates. Consequently, the fine aggregate was added and uniformly mixed for 1 min more. Then, the binder was added to the wet aggregates and agitated for around 2 mints to get the aggregates surface-coated with binders. Finally, the balance two-thirds of water premixed with super plasticizer was added to the mix and rotated in the mixer machine for 2–3 min to obtain a uniform mix.

5 Test Methodology

The compressive strength of concrete was determined on 150 mm cube specimen at the age of 7 and 28 days in accordance with IS: 516-1959. Three tests were performed to measure the durability of concrete: the chloride penetration resistance, carbonation resistance and water resistance test in terms of water absorption according to ASTM C 642-06 [17]. The test for chloride ion penetration depth was carried out on 100 mm cubic specimen as per description given by Otsuki et al. [13]. The specimens were immersed in 3.0% by wt. of NaCl solution for the diffusion of chloride ion into the concrete mass for 28 days. The fractured surfaces were sprayed with 0.1 N $AgNO_3$ aqueous solution, which forms a white colour boundary due to the formation of silver chloride indicating the depth of chloride penetration. Similarly, an accelerated carbonation test was carried out on 100 mm cube specimens of size. Only two faces were exposed to CO_2-enriched carbonation chamber with 10% carbon dioxide at 25° C and the relative humidity of 60 ± 5% for 7 days. Non-destructive tests were performed to evaluate the concrete condition to assess the performance of concrete in-place and to determine the presence of voids, cracks, if any. Ultrasonic pulse velocity (UPV) test was conducted as per IS: 13311 (part 1) 1992 and the rebound hammer test was also performed as per IS: 13311(part 2) 1992. The UPV value is mainly related to the density of concrete in terms of quality of concrete. A Schmidt's rebound hammer of N-type was used to evaluate the surface hardness of different concrete specimen.

Table 4 Slump test values of different mixes

Mix	REF	C-R50	C-R100	F- R0	F-R50	F-R100
Slump value (mm)	45	20	15	28	35	9

6 Results and Discussion

6.1 Fresh Properties

Fresh concrete mixes were subjected to the consistency test—slump tests according to IS: 1199-1959. The results of slump test are shown in Table 4. From slump cone test results, slump value decreases drastically with the increment in RCA content irrespective of the binder types. It is mainly associated with the higher initial water absorption features of RCA which absorbs the available free moisture from concrete and more friction due to rough surface of RCA. Furthermore, the increase in the replacement ratio had negative effects on the workability of RAC. Despite that, the influence of cementitious substances on workability was also remarkable. The influence of FG binder also contributes towards lower consistency due to its platy and lathe shape [4].

6.2 Compressive Strength

Figure 1 represents the compressive strength results for all the mixes at 7 and 28 days. The results indicated that the replacement level of RCA and the binder replacement has a strong influence on the compressive strength of concrete for their respective ages. The highest strength was achieved by control concrete 28 days, which was 51.93 MPa. The 28-day strength achieved with 100% RCA was

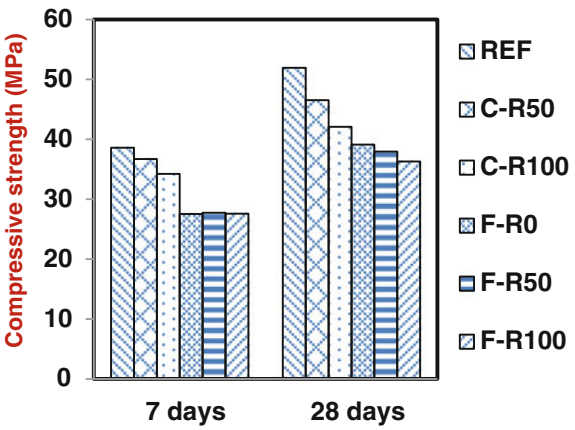

Fig. 1 Compressive strength of mixes at 7 and 28 days

42.07 MPa. The compressive strength thus appeared to be increased with age but with a lesser rate in the latter age than the strength developed in early age. The strength got reduced with the increase in replacement ratio. It was also observed that the rate of 7-day strength development of RAC was higher than the control concrete. The strength at 7 days was found to be 38.59 and 34.22 MPa for control concrete and for concrete with 100% RCA. The higher early strength development in RAC may be attributed to the higher water absorption capacity of RCA which ultimately helps in reducing the effective *w*/*c* ratio. The modified mixing method also would have imparted on RCA in forming better bond with the surrounding matrix and hence, improving the strength. However, a contradictory effect is noticed in the early strength development of concrete made with FB. A significant distinction was noticed in the strength development of concrete made with either NA or RA where FG binder was used as a partial replacement of cement.

The 7-day strength of F-R0 is 28.7% lower than the control concrete. It may be explained on the basis of slower rate of hydration in early strength gain of FG.

From 28-day strength results, it was found that the concrete made with 100% RCA achieved strength more than 40 MPa as the control concrete. Though, it could achieve the characteristics strength of 40 MPa, however, it could not reach to the target strength of control concrete. Thus, there was a decrease of approximately 14.69% in 28-day strength than that of target strength at 100% RCA replacement for pure cement. Similarly, the strength was 18.98% lower than the strength achieved by control concrete at 28 days for OPC with 100% RA respectively. However, the strength reduction rate at 28 days appeared to increase steeply when FB is used as replacement of cement. A reduction in strength is noticed up to 24.69% with NA for the concrete having FB as a partial replacement of cement. Similarly, the strength was reduced up to 30.12% with 100% RA for the concrete made with FB. It was observed that the variation in 28-day compressive strength of FB concrete is nearly similar to each other irrespective of the coarse aggregate replacement ratios.

6.3 Chloride Ion Penetration

Figure 2 illustrates the effect of RCA and the influence of various binders on the chloride ion penetration resistance of various mixes of natural aggregate concrete (NAC) and RAC after an exposure to chloride environment for a period of 28 days. It also represents the influence of partial replacement of various types of cements by FB on the chloride resistance of concrete. As revealed from the figure, there was a reduction in chloride ion penetration resistance of concrete with the subsequent substitution of NA by RCA. The chloride ion penetration depth of control specimen was found to be 5.25 mm. However, after 28-day exposure period, the concrete made with 100% RCA and FB had shown the highest penetration depth than the other concrete. The maximum chloride ion penetration could reach up to 10.54 mm in the mix having 100% RCA and FB as a partial replacement of cement. By using

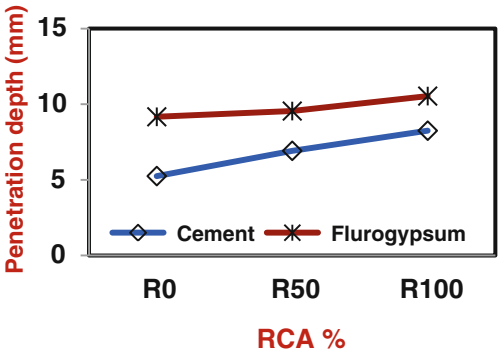

Fig. 2 Chloride ion penetration depth at different RCA replacement levels

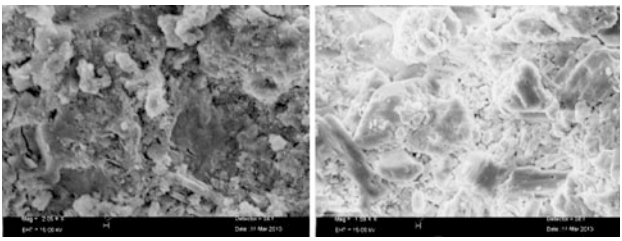

Fig. 3 SEM micrographs of hydration product of cement and FB paste

FB, the chloride ion penetration resistance of mixes is further decreased as compared to using cement. It was found to be two times more than that of control samples. RAC having FB always showed a higher chloride ion penetration depth than that of concrete using cement. This may be attributed to the more porous microstructure of FB concrete as it is also reducing the strength characteristics of concrete. The microstructure of the hydration product of cement and FB paste matrices are shown in Fig. 3. As one can see that the matrix of FB is more porous than that of cement, which facilitates the ingression of chloride ion to a greater depth. To improve the performance of FB, it is needed to improve the hydration process to obtain a denser matrix.

6.4 Water Absorption

The behaviour of pore structure within the concrete was assessed by measuring the water absorption rate of unsaturated specimens by immersing in water. It is a very important parameter for evaluating the pore structure and their connectivity in concrete made with RCA and the results are presented in Table 5. It was observed

Table 5 Water absorption values of different mixes

Mix notation	REF	C-R50	C-R100	F-R0	F-R50	F-R100
Water absorption (%)	3.54	3.80	5.51	4.95	5.24	5.70

that the water absorption value increases with the increase in RCA replacement ratio. The higher porosity of RCA facilitates the higher water absorption of RAC as compared to normal concrete. The water absorption value found to be 5.51%. Hence, there was an increase of water absorption value up to 55% at various replacement level of RCA. The higher water absorption value is attributed to the quantity of adhered mortar present in the RA and its porous nature. It was also observed that water absorption value decreased with the increase in strength. It is due to the dense microstructure which ultimately increases the strength. Despite that, a very prominent influence of binders has been observed on the water absorption characteristics of hardened concrete. There was a significant increase in the water absorption value of concrete with FB. However, the use of FB in concrete resulted in more increase of water absorption. It might be due to the porous microstructure and presence of accessible cracks in FB matrix, obtained from the SEM evidence of the hydration products of paste (Fig. 3).

6.5 *Carbonation*

Keeping the *w*/*c* ratio constant, varying the type of binders and the RCA substitution level, their effect on carbonation depth was analysed upon 7-day period of exposure to carbonation environment and the results are shown in Fig. 4. In control specimens, carbonation occurred only up to 0.3 mm. As a consequence of this, it was difficult to measure and compare the carbonation depth occurred in various concretes. However, an effort was made to measure the carbonation depth of concrete with greater accuracy. Regardless of the binder variation, the RAC showed sufficient resistance to carbonation to occur and did not show proper response towards RA substitution ratio. OPC series did not show any significant difference in

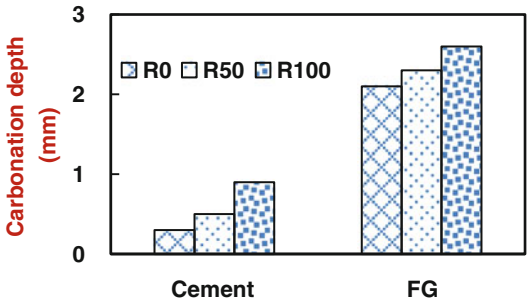

Fig. 4 Carbonation depth in cement and FB at different RCA replacement levels

the carbonation depth at various substitution levels of RCA. A possible reason contributing towards this could be the lower permeability and poor interconnected pore network structure of concrete even if RCAs were used. Moreover, it is seen from the experimental results that carbonation depth increased with the increase in RCA content exhibiting the same trend as in case of water absorption and chloride penetration. However, the FB- containing concrete shows a slight deviation from this trend shown by other concrete suggesting the possibility of different mechanism of carbonation. As expected, it is both NAC and RAC. The replacement of cement by FB facilitated the more diffusion of CO_2 into the hardened concrete irrespective of RCA substitution signifying its more porous microstructure.

6.6 *Ultrasonic Pulse Velocity*

UPV test is a non-destructive in situ test, conducted to ensure the quality of concrete in terms of homogeneity, honeycombing or the presence of internal cracks within the concrete. The UPV test also gives an indirect indication of the coherent porosity of the concrete. The UPV results of all the mixes are illustrated in Fig. 5. The UPV values of all the mixes were found to be more than 3600 m/s, showing a very good quality concrete. The control concrete showed excellent performance with a UPV value of 4636 m/s. However, the UPV values started decreasing with the increase in the replacement level of RCA. Hence, there is a reduction of 5.13% in UPV value at 100% RCA than the control concrete. The higher water absorption of RCA, due to loosely adhered porous mortar is responsible for contributing towards the porosity of concrete. Thus, it affects the transmission of ultrasonic waves in UPV test and results in poor quality concrete. Whereas, the partial replacement of cement with FB resulted in lesser UPV value than concretes made with cement. The lowest UPV value was obtained for concrete made with FB and 100% RCA, which was 4316.17 m/s. In this case, both quality of aggregate and replacement of binder became the limiting parameters. The honeycombing or the presence of internal flaws in the matrix having FG binder or due to the changes in the structure of concrete probably could be added as a contribution towards the

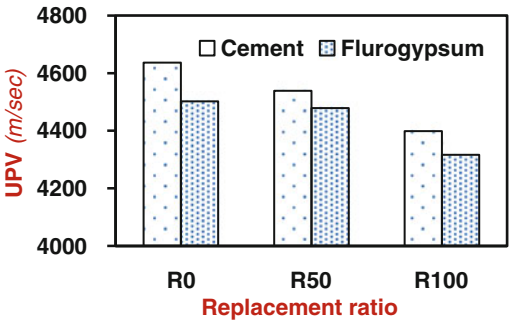

Fig. 5 UPV values at different RCA replacement levels

porosity of concrete. Thus, it resulted in lowering their UPV values to a greater extent, up to 7%. The possible reason could be attributed to the variation in aggregate type and cement type.

6.7 Rebound Hammer Strength

Rebound hammer test is one of the non-destructive tests, performed to evaluate the strength of concrete in terms of surface hardness. The rebound hammer results in terms of rebound indices are shown in Fig. 6. Rebound numbers get influenced by a number of factors such as cement and aggregate, surface condition and moisture content and age of concrete. Fig. 6 shows that the rebound number increases with the increase in strength of concrete and decreases with the increase in replacement level of RCA. The decrease in rebound number may be related to the poorly linked porous mortar attached to RCA surface which increases the porosity of concrete. In addition to this, the same trend was observed with various binder combinations also and it decreased corresponding to their RCA replacement level. However, rebound index reduced drastically in the concrete made of FB. Thus, it shows that the hardness of concrete is reducing when cement is replaced by FB. As per IS: 13311 (part 2) 1992, rebound indices are indicative of the compressive strength of concrete to a limited depth of 30 mm from the surface. So, compressive strength of the core specimen was evaluated after the rebound hammer test in order to establish a relationship between the actual strength and rebound hammer strength. As, the rebound hammer value and UPV value get affected by moisture content of concrete, the increase in moisture content could have increased the UPV value and decreased the rebound number.

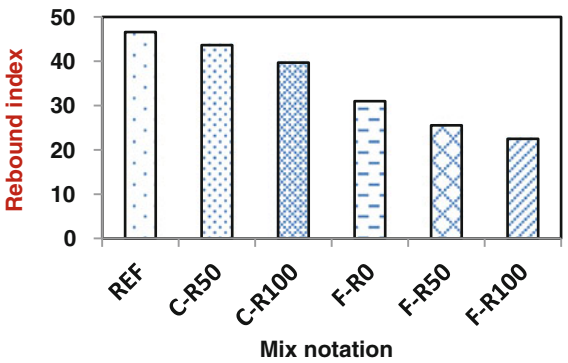

Fig. 6 Rebound hammer value of various mixes

7 Conclusion

This paper addresses the efficient reuse of the RCA derived from C&D waste. The obtained results show that coarse RCA can be used to replace NA up to 100% to achieve a strength value of 40 MPa. The strength reduction was found up to 11% with 100% reduction and 5% with 50% replacement. The chloride ion penetration, carbonation and water absorption resistance decreased with the increase in RCA replacement ratio. However, concrete made with RCA showed good carbonation resistance and better UPV values result of more than 3600 m/s, showing good-quality concrete. The results with FB revealed that though it is having its own binder property, it could not achieve strength up to that with cement replacement as it is having adverse effect on the durability and in situ properties of concrete. Rather, it can be used as a filling material or as an additive or else can be used with other mineral admixture such fly ash to improve its performance by making its matrix denser. RAC with pure cement showed better durability and in situ properties than concrete made with FB as a partial replacement of cement.

References

1. Maullick, A. K. (2016). Viable alternatives to natural fine and coarse aggregate in concrete. In *Proceedings of International Seminar on Emerging Building Materials and Construction Technologies*, March 2016, New Delhi.
2. Malhotra, V. M., & Mehta, P. K. (2008). *High performance high-volume fly ash concrete for building sustainable and durable structures* (3rd ed.). Supplementary Cementing Materials for Sustainable Developments, Ottawa.
3. Etxeberria, M., Vázquez, E., Marí, A., & Barra, M. (2007). Influence of amount of recycled coarse aggregates and production process on properties of recycled aggregate concrete. *Cement and Concrete Research, 37*(5), 735–742.
4. Behera, M., Bhattacharyya, S. K., Minocha, A. K., Deoliya, R., & Maiti, S. (2014). Recycled aggregate from C&D waste & its use in concrete—A breakthrough towards sustainability in construction sector: A review. *Construction and Building Materials, 68,* 501–516.
5. Nixon, P. (1978). Recycled concrete as an aggregate for concrete-a review. *Materials and Structures, 11*(5), 371–378.
6. Hansen, T. C., & Narud, H. (1993). Strength of recycled concrete made from crushed concrete coarse aggregate. *Concrete International, 5*(1), 79–83.
7. Sagoe-Crentsil, K. K., Brown, T., & Taylor, A. H. (2001). Performance of concrete made with commercially produced coarse recycled concrete aggregate. *Cement and Concrete Research, 31*(5), 707–712.
8. Hansen, T. C. (1996). *RILEM REPORT 6. Recycling of demolished concrete and masonry*. Bodmin, UK: E&FN Spon1996.
9. Dhir, R. K., & Jappy, T. G. (Eds.). (1999). *Proceedings of the International Conference on Exploiting Wastes in Concrete*. UK: Thomas Telford.
10. Olorunsogo, F. T., & Padayachee, N. (2002). Performance of recycled aggregate concrete monitored by durability indexes. *Cement and Concrete Research, 32*(2), 179–185.
11. Cui, Z. L., Yang, L. H., & Ohaga, Y. (2006). Durability test investigation on the recycled aggregate concrete. *Science Technology and Engineering, 6*(21), 3516–3519.

12. Levy, S. M., & Helene, P. (2004). Durability of recycled aggregates concrete: A safe way to sustainable development. *Cement and Concrete Research, 34*(11), 1975–1980.
13. Otsuki, N., Miyazato, S., & Yodsudjai, W. (2003). Influence of recycled aggregate on interfacial transition zone, strength, chloride penetration and carbonation. *Journal of Materials in Civil Engineering, 15*(5), 443–451.
14. Kou, S. C., & Poon, C. S. (2012). Enhancing the durability properties of concrete prepared with coarse recycled aggregate. *Construction and Building Materials, 35,* 69–76.
15. Singh, M., & Garg, M. (1999). Cementitious binder from fly ash and other industrial wastes. *Cement and Concrete Research, 29*(3), 309–314.
16. Tam, V. W. Y., Tam, C. M., & Wang, Y. (2007). Optimization on proportion for recycled aggregate in concrete using two-stage mixing approach. *Construction and Building Materials, 21,* 1928–1939.
17. ASTM C 642-06. (2002). *Standard test method for density, absorption, and voids in hardened concrete*. West Conshohocken, USA.

Shear Behaviour of Glass Fibre-Reinforced Geopolymer Concrete

K. Nithyapriya, K. Subramanian, X. John Britto and M. P. Muthuraj

Abstract Experimental investigations were carried out on shear behaviour of geopolymer-reinforced concrete beams with and without fibres. The mix is composed of ternary blend of mineral admixtures, ground-granulated blast furnace slag (GGBS), silica fume, metakaolin and fly ash. In all the mixes, the amount of GGBS is kept constant and other mineral admixtures such as silica fume, metakaolin and fly ash are varied in different proportions. Two concentrations of molarities, namely, 6 and 10 M of NaOH solution are considered in the present study to investigate the shear behaviour of geopolymer concrete beams with and without glass fibres. Several beams were cast for different mixes and the responses were studied under four-point bending static loading. Among the various mixes, it was found that the mix of 10 M, i.e. 70% GGBS + 12% fly ash + 10% silica fume + 8% metakaolin performed well with and without fibres. Many cracks were developed for the case of fibre-incorporated beams signifying the contribution of fibres in terms of higher energy absorption and improved ductility. There is no significant difference is observed in terms of load carrying capacity, first crack load and deflection of 10 M mixes compared to 6 M mixes.

Keywords Geopolymer concrete · Glass fibres · Compressive strength
Flexural loading · Ultimate load · Deflection

K. Nithyapriya (✉) · M. P. Muthuraj
Department of Civil Engineering, Coimbatore Institute
of Technology, Coimbatore 641 014, India
e-mail: nithyapriya83@gmail.com

M. P. Muthuraj
e-mail: m_p_muthuraj@rediffmail.com

K. Subramanian
PSR Engineering College, Sivakasi 626 140, India
e-mail: drkscit@gmail.com

X. John Britto
Department of Civil Engineering, KGISL Institute of Technology,
Coimbatore 641 035, India
e-mail: brittoannai@gmail.com

A. Rama Mohan Rao and K. Ramanjaneyulu (eds.), *Recent Advances in Structural Engineering, Volume 1*, Lecture Notes in Civil Engineering 11,
https://doi.org/10.1007/978-981-13-0362-3_79

1 Introduction

For the construction of buildings, bridges, airport pavements, nuclear containments and other civil infrastructure, the reinforced concrete (RC) is one of the commonly used composite materials. It can be well forecasted that the requirement for RC will enhance many folds in view of expansion of infrastructure in many countries. To produce concrete, Ordinary Portland cement (OPC) is normally employed as primary binder. In the process of production of OPC, it is estimated that about one ton of carbon dioxide (CO_2) liberates for one ton of OPC. It was also found that concrete is less durable under severe environmental conditions.

In the present scenario, it has become necessary and urgent requirement to search for alternate binding materials to reduce CO_2 emission and to preserve natural resources. Geopolymer concretes (GPC) is one of the advanced cementitious concretes, proved to be a potential candidate to replace or supplement the conventional concrete.

It possesses high mechanical and durable properties. Many investigations were carried out on GPC at laboratory level as well as in the field to demonstrate its efficacy [1–6]. The typical mechanism of geopolymerization consists of: (a) dissolution, (b) speciation equilibrium, (c) gelation, (d) reorganization and (e) polymerization and hardening [7]. Pictorially, the process of geopolymerization is shown in Fig. 1 [7]. Many research investigations reported that the behaviour of under-reinforced fly-ash-based geopolymer concrete beams is similar to conventional reinforced concrete beams under flexural loading. The responses considered for comparison include crack width, first crack load, load–deformation relationship, flexural stiffness, failure load, ductility, ultimate load, etc. [8–12].

Mohana and Nagan [13] compared the flexural behaviour of geopolymer-reinforced ferrocement slabs and conventional ferrocement slabs. From the experiment, it was found that the cracking load, yielding load and ultimate load of the geopolymer ferrocement slabs are found to be larger compared to conventional ferrocement slabs. The interesting observation was the geopolymer ferrocement slabs possess higher energy absorption and ductility compared to conventional ferrocement slabs. Maranan et al. [14] investigated the flexural strength and serviceability aspects of beams made up of geopolymer concrete beams and glass fibre-reinforced polymer bars under four-point bending static loading. The effect of bar diameter, anchorage system and reinforcement ratio were also studied and it was noticed that there is no significant effect of bar diameter on the flexural performance of the beams. Hung et al. [15] carried out an extensive review on structural behaviour of geopolymer concrete members such as beams, columns, slabs, panels. From the review, it is highlighted that (i) there is no negative effect of using geopolymer concrete as structural elements in terms of load-carrying capacity and ductility and (ii) standard codes of practice can be used to design the members made up of geopolymer concrete.

In the present study, the shear performance of geopolymer-reinforced concrete beams with and without fibers is carried out.

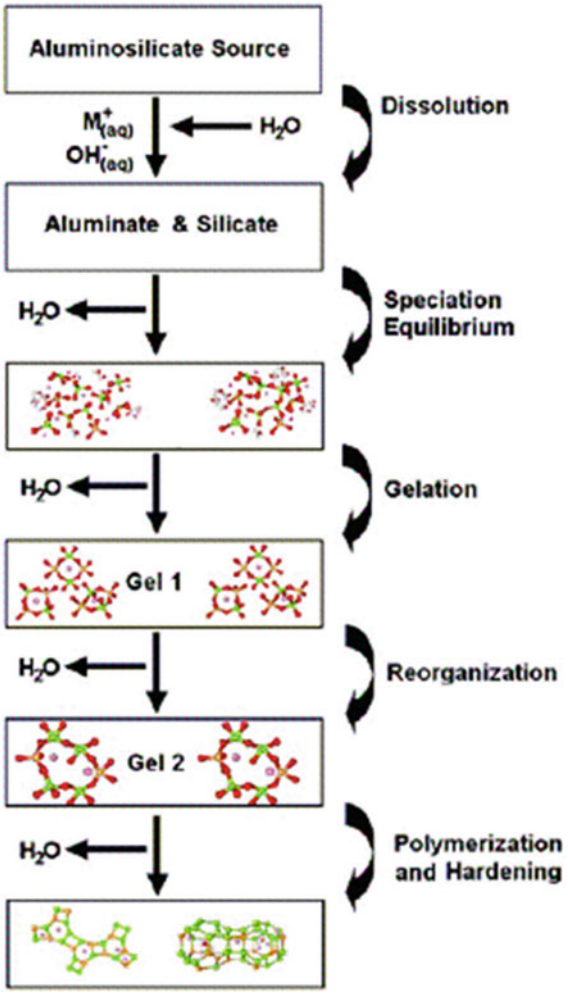

Fig. 1 Concept of geopolymerization [7]

2 Basic Material Characteristics

For the production of geopolymer concrete, various ingredients such as fly ash, ground-granulated blast furnace slag (GGBS), metakaoline, silica fume, sodium silicate, sodium hydroxide, glass fibres, coarse aggregate (12.5 and 20 mm), superplasticizer (Polyheed 997) and water were used. GGBS is procured from JSW Steel Works Ltd., Coimbatore, India. The following norms were considered to arrive at geopolymer concrete mix with and without fibers.

Alkaline liquids/GGBS = 0.3–0.45
Sodium silicate/sodium hydroxide = 2–2.5
Water/GGBS = 0.16–0.24

Table 1 Various material properties

Material	Property	Value
GGBS	Specific gravity Fineness (m^2/kg)	2.2 420
Fly ash	Specific gravity Fineness (m^2/kg)	2.05 415
Silica fume	Specific gravity Fineness (m^2/kg)	2.15 320
Metakaolin	Specific gravity Fineness (m^2/kg)	2.7 432
Sodium Hydroxide	Purity	97%
	Specific gravity	2.13
Sodium Silicate	Purity	98.5%
	Specific gravity	1.53
Coarse aggregate 20 mm	Specific gravity	2.80
	Water absorption in % as per IS 2386	0.35%
Coarse aggregate 12.5 mm	Specific gravity	2.79
	Water absorption in % as per IS 2386	0.30%
Fine aggregate	Specific gravity	2.73
	Water absorption in % as per IS 2386	0.86%
Conforming to Zone II		
Water	Specific gravity	1
Superplasticizer	Specific gravity	1.65

Total aggregate in mass of concrete = 65–85%
Fine aggregate content in total aggregate = 30%
Extra water content = 20% of mass of cementitious material
Superplasticizers = 2% of mass of cementitious material
Various material properties are presented in Table 1.

General description on preparation of geopolymer concrete is given below:

The alkaline activator solution (AAS) is prepared with the combination of sodium hydroxide pellets, sodium silicate solution (SiO_2/Na2O = 2.2), and distilled water. Since lot of heat is generated when sodium hydroxide flakes react with water, the sodium hydroxide solution should be prepared a day before casting. The main function of AAS is to dissolve Si and Al present in the reactive portion of source materials such as FA, GGBS, silica fume and metakaolin and provide a high alkaline liquid medium for condensation polymerization reaction. The aggregates are to be taken out from the mixer and dry mix is to be performed about 2 min after addition of a small quantity of water to prevent the water absorption of aggregates in later stage. Later, all the cementitious materials are added one after the other.

Next, the alkaline activator solution is to be added to the mix and the mixing is to be continued for about 5 min. The required quantity of superplasticizer is mixed with water and then added to the mix during the production of geopolymer

Table 2 Various ingredients used for casting of beams

Mix ID	GGBS (%)	Fly ash (%)	Silica fume (%)	Metakaolin (%)
6M2	70	20	5	5
6M3	70	15	10	5
6M4	70	17	5	8
6M7	70	12	10	8
6M9	70	25	5	0
10M2	70	20	5	5
10M3	70	15	10	5
10M4	70	17	5	8
10M7	70	12	10	8
10M9	70	25	5	0

concrete. In any combination of geopolymer concrete mix, desired degree of workability is to be ensured.

Several trials were made to finalize the mix. The final mix proportion arrived at is 1:0.94:2.2:0.13:0.192 (Cementitious materials: Fine aggregate: Coarse aggregate: Alkaline liquids: Water)

Two concentrations of NaOH (molarities 6 and 10) were considered for the present study. Table 2 presents the details of various ingredients used for casting of geopolymer concrete beams. For all the beams, the percentage of GGBS is fixed as constant, i.e. 70%.

3 Workability Studies

The slump values obtained for the two concentrations of several mixes are given below in the form of table (Table 3). From Table 3, it can be noted that the slump values are varying from 25 to 29 mm for the concentration of 6 M and the highest value is obtained for 6M3 for which the mix proportion is 70% GGBS + 10% silica fume + 5% metakaolin. For the other concentration of 10 M, the slump value for all the combinations is observed to be almost same, i.e. 27 mm (average).

There is no significant variation in slump with the increase in concentration of NaOH.

Table 3 Slump values for the mixes considered

Mix	Slump (mm)	Mix	Slump (mm)
6M2	31	10M2	29
6M3	41	10M3	28
6M4	37	10M4	29
6M7	27	10M7	29
6M9	25	10M9	25

4 Mechanical Properties

Cubes of size 100 mm are cast to determine the compressive strength of various mixes of two concentrations. The compressive strength of various mixes corresponding to the two concentrations is presented in Table 4. The compressive strength values are varied from 61.2 to 71.8 MPa for the case of 6 M concentrations, whereas for the case of 10 M, the values are varied from 64.8 to 79.7 MPa.

The maximum increase in compressive strength between 6 and 10 M is about 10%. From Table 4, it can be observed that the maximum strength is obtained for the cases of 6M7 and 10M7 where in the mix proportion is 70% GGBS + 12% fly ash + 10% silica fume + 8% metakaolin. Figure 2 shows the typical slump test and testing of cube for evaluation of compressive strength.

5 Testing of Beams for Shear

To determine the flexural performance of geopolymer beams, the beams were cast of size 1500 mm × 100 mm × 200 mm (length × width × depth). Some beams were cast with glass fibres by adding at 5% of total volume.

Figure 3 presents the typical reinforcement details for shear tests.

Figure 4 shows casting of typical geopolymer concrete beam. All the specimens were cured at ambient temperature in order to achieve strength gain through the polymerization yielding of Si–Al bonds.

Load is applied incrementally on the beam through hydraulic action till failure. The testing frame has the capacity of 2000 kN. Load has been controlled through a proving ring, which has a capacity of 200 kN. At each incremental load, the deflections were measured by using dial gauges. All the beams were tested under four-point bending.

The responses such as first crack load, corresponding deflection, crack patterns, ultimate load and corresponding deflection were noted for all the beams. To measure curvature of the beams above and below the neutral axis, pellets were fixed at 75 mm distance on either side of the loading point. Figure 5 shows typical test setup including the location of pellets and dial gauges.

Table 4 Compressive strength for the mixes considered

Mix	Compressive strength (MPa)	Mix	Compressive strength (MPa)
6M2	67.2	10M2	71.9
6M3	70.9	10M3	77.3
6M4	70.1	10M4	76.8
6M7	71.8	10M7	79.7
6M9	61.2	10M9	64.8

Fig. 2 Typical slump test on concrete and compressive strength test. **a** Typical Slump test, **b** Testing of a cube for compressive strength

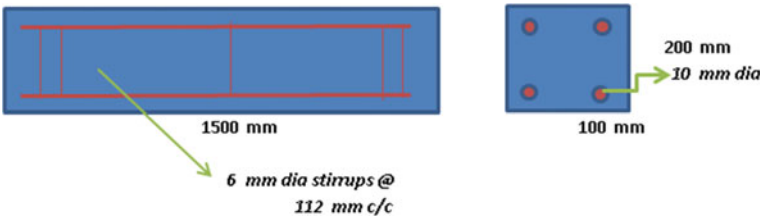

Fig. 3 Reinforcement details for shear test

Fig. 4 Casting of typical geopolymer concrete beam

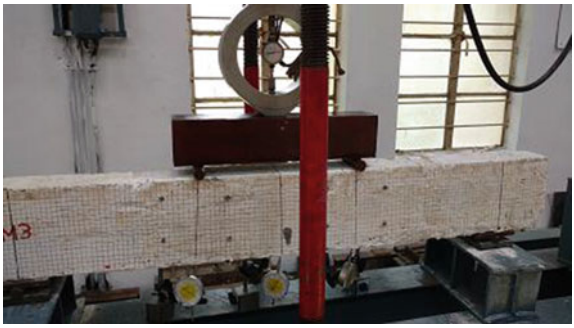

Fig. 5 Typical test setup including the location of dial gauges and pellets

Typical crack pattern of shear beam Without fibres -6M3

Typical crack pattern of shear beam without fibres - 10M4

Fig. 6 Typical crack pattern for a geopolymer beam without fibres

Figure 6 shows the crack pattern of typical geopolymer beam. Table 5 presents the details of first crack load, ultimate load and deflection at ultimate load.

The effect of fibres can be seen clearly in Fig. 7 on the response behavior of geopolymer beams with fibres. There are many multiple cracks compared to the

Table 5 Reponses of tested geopolymer beams

Mix	First crack load (kN)	Ultimate load (kN)	Deflection at ultimate load (mm)
Without fibres			
6M2	18.4	52.5	6.54
6M3	21.4	61.5	6.89
6M4	21.8	62.5	6.91
6M7	24.5	72.1	7.82
6M9	15.9	47.3	6.12
10M2	19.1	54.5	6.61
10M3	21.9	64.8	7.11
10M4	21.7	64.5	7.08
10M7	28.5	78.8	8.45
10M9	17.1	50.3	6.34
With fibres			
6M2	18.1	53.9	6.58
6M3	21.2	62.3	6.97
6M4	21.1	62.7	6.94
6M7	26.7	77.2	8.15
6M9	16.8	49.7	6.38
10M2	18.9	56.4	6.78
10M3	22.9	67.9	8.11
10M4	23.1	68.2	8.24
10M7	28.2	81.2	9.28
10M9	18.2	52.3	6.67

response behavior of beams without fibres (Fig. 6). Figure 7 presents the typical failure behaviour of geopolymer beams with fibres.

The important interpretation can be drawn from nature of failure of beam with fibres is, the beam possess more energy absorption indicating higher ductility compared to the behaviour of beam without fibres. From Table 5, it can be observed that the first crack load occurred at about 25–35% of ultimate load of all the geopolymer beams with and without fibres.

This observation is generally same as for the case of RC beams. The ultimate load varies from 47 to 78 kN for all the mixes without fibres. The vertical deflection is varied from 6.12 to 8.45 mm for all the mixes without fibres. The geopolymer beam with mix 10M7 sustained the maximum load up to 78.8 kN with the corresponding deflection of 8.45 mm.

For the case of beams with fibres, the ultimate load is varied from 49.7 to 81.2 kN and the corresponding deflection is from 6.38 to 9.28 mm.

The increase in maximum load for all the mixes with fibres is about 5% compared to the beams without fibres. But the corresponding deflection is varied by about 10%. The beam containing fibres with mix 10M7 sustained the maximum load of 81.2 kN and the corresponding deflection is 9.28 mm.

Typical crack pattern of shear beam with fibres -10M4

Typical crack pattern of shear beam with fibres -6M9

Fig. 7 Typical crack pattern for a geopolymer beam with fibres

The ultimate load and the corresponding deflections of all the mixes of 10 M are larger by an extent about 5–10% compared to respective mixes of 6 M. This may be due to more polymerization of mineral admixtures. Similarly, about 5–10% increase in ultimate load and deflection is observed for 10 M mixes in comparison with 6 M mixes.

The increase in ultimate load for the case of beams with fibres could be attributed to enhanced compressive strain by the addition of fibres. The extent of increase in deflection may be attributed to the tensile strength of glass fibres.

6 Summary

Experimental investigations were carried out on shear behaviour of glass fibre-reinforced geopolymer concrete beams under shear loading. Geopolymer concrete beams are made up of ternary blend of mineral admixtures, namely, GGBS, silica fume, metakaolin and fly ash. Basic material characteristics of the materials used for the investigation are from the studies. Some beams were cast with and without glass fibres. For all the beams, the amount of GGBS is kept constant, i.e. 70% and other mineral admixtures, namely, fly ash, silica fume and metakaolin are varied in proportion. Along with the mineral admixtures, fine aggregate, coarse aggregate, activator solution and water are used to prepare GPC.

The activator solution is prepared in combination of NaOH with Na_2SiO_3. Two concentrations of NaOH, i.e. 6 and 10 M are considered to the study the behaviour of the beams along with various combinations of mineral admixtures.

The slump and compressive strength were experimentally observed for all the mixes of 6 and 10 M. All the beams were tested under four-point bending static loading under shear loading condition till failure. The responses such as first crack load, ultimate load and the corresponding deflections were monitored during the loading. It was found that the mix 10M7 (70% GGBS + 12% fly ash + 10% silica fume + 8% metakaolin) performed well with and without fibres.

References

1. Guo, X., Shi, H., & Dick, W. A. (2010). Compressive strength and microstructural characteristics of class C fly ash geopolymer. *Cement and Concrete Composites, 32*(2), 142–147.
2. Pacheco-Torgal, F., Moura, D., Ding, Y., & Jalali, S. (2011). Composition, strength and workability of alkali-activated metakaolin based mortars. *Construction and Building Materials, 25*(9), 3732–3745.
3. Shi, X., Collins, F., Zhao, X., & Wang, Q. (2012). Mechanical properties and microstructure analysis of fly ash geopolymeric recycled concrete. *Journal of Hazardous Materials, 237,* 20–29.
4. Hardjito, D., Wallah, S. E., Sumajouw, D. M. J., & Rangan, B. V. (2004). On the development of fly ash-based geopolymer concrete. *ACI Materials Journal, 101,* 467–472.
5. Sumajouw, D. M. J., Hardjito, D., Wallah, S. E., & Rangan, B. V. (2007). Fly-ash based geopolymer concrete: Study of slender columns. *Journal Materials Science, 42,* 3124–3130.
6. Fernandez-Jimenez, A. M., Polomo, A., & Lopez-Hombrados, C. (2006). Engineering properties of alkali-activated fly ash concrete. *ACI Materials Journal, 103,* 251–257.
7. Duxson, P., Fernandez-Jimenez, A., Provis, J. L., Lukey, G. C., Palomo, A., & Deventer, J. S. J. V. (2007). Geopolymer technology: The current state of the art. *Journal of Materials Science, 42*(9), 2917–2933.
8. Dattatreya, J. K., Rajamane, N. P., Sabitha, D., Ambily, P. S., & Nataraja, M. C. (2011). Flexural behaviour of reinforced geopolymer concrete beams. *International Journal of Civil and Structural Engineering, 2*(1), 138–159.

9. Yost, J. R., Radlinska, A., Ernst, S., Salera, M., & Martignetti, N. J. (2013). Structural behavior of alkali activated fly ash concrete. Part 2: structural testing and experimental findings. *Materials and Structures, 46,* 449–462.
10. S. Kumaravel, & Thirugnanasambandam, S. (2013). Flexural behaviour of reinforced low calcium fly ash based geopolymer concrete beam. *Global Journal of Researches in Engineering, 13*(8).
11. Kumaravel, S., Thirugnanasambandam, S., & Jeyasehar, C. A. (2014). Flexural behavior of geopolymer concrete beams with GGBS. *IUP Journal of Structural Engineering, 7*(1), 45–54.
12. Wanchai, Y. (2014). Application of fly ash-based geopolymer for structural member and repair materials. *Advances in Science and Technology, 92,* 74–83.
13. Mohana, R., & Nagan, S. (2013). An experimental investigation on the flexural behavior of geopolymer ferrocement slabs. *Journal of Engineering and Technology, 3*(2), 97–103.
14. Maranan, G. B., Manalo, A. C., Benmokrane, B., Karunasena, W., & Mendis, P. (2015). Evaluation of the flexural strength and serviceability of geopolymer concrete beams reinforced with glass-fibre-reinforced polymer (GFRP) bars. *Engineering Structures, 101,* 529–541.
15. Mo, K. H., Alengaram, U. J., & Jumaat, M. Z. (2016). Structural performance of reinforced geopolymer concrete members: A review. *Construction and Building Materials, 120,* 251–264.

Part V
Mitigation of Structures Against Natural Hazards

The Effect of Macroroughness in Front of Building for Tsunami Pressure Dissipation—A Numerical Study

D. Ghosh, A. K. Mittal, S. K. Bhattacharyya and S. Behera

Abstract Ocean surge may create a serious damage to coastal buildings. The surge may be generated due to high tide, storms or even from tsunami. The damage on buildings depends on shielding characteristics of the objects near the buildings. The shielding can be provided by placing small barrier or blocks in front of the considered building. It is difficult to estimate the loading on this building due to interference between waves and barrier. Wave pressure on building is numerically evaluated for the presence of macroroughness elements (small obstructions) placed in tandem arrangement in front of building. Computational Fluid Dynamics (CFD) technique is adopted for the simulation of tsunami-like solitary wave impact on macroroughness and building. Realizable k-ε turbulence model is applied for turbulence modelling. Volume of Fluid (VOF) method is adopted to track the free surface movement of the flow. Wave is generated with the help of sudden discharge control at the inlet of an open channel. Wave characteristics are validated with the reported experimental results. Two types of wave height are considered in the study to evaluate the dependence between wave height and pressure on building. The results reveal that for wave height less than the building height, the placement of macroroughness is quite effective but if the wave height is more than the building height, the wave pressure reduction is not so significant.

Keywords Tsunami impact · Macroroughness · CFD · VOF model

D. Ghosh · A. K. Mittal · S. Behera
CSIR-Central Building Research Institute, Roorkee 247667, India

S. K. Bhattacharyya (✉)
Department of Civil Engineering, Indian Institute of Technology Kharagpur, Kharagpur 721302, India
e-mail: bsri@civil.iitkgp.ernet.in

A. Rama Mohan Rao and K. Ramanjaneyulu (eds.), *Recent Advances in Structural Engineering, Volume 1*, Lecture Notes in Civil Engineering 11,
https://doi.org/10.1007/978-981-13-0362-3_80

1 Introduction

Tsunami is commonly generated due to movement of underwater earth crust. Tsunami wave travels at hundreds of kilometres an hour in the deep ocean and as they approach towards the land, the shallow water causes them to slow down and increase in height, which is known as shoaling effect of tsunami. Three parameters responsible for magnitude of tsunami induced pressure are: (1) inundation depth, (2) flow velocity and (3) flow direction. These parameters mainly depend on: (a) tsunami wave height and wave period (b) coast topography and (c) roughness of the coastline. Therefore, it is difficult to estimate pressure induced on coastal structures during tsunami. The impact of tsunami-induced forces on coastal protection structures, viz. breakwaters, seawalls, etc., have been analysed and clarified by different researchers to a certain degree. Different strategies to protect buildings against the tsunami wave surge are also studied. But it is very difficult to design the building considering those strategies, because no guidelines are readily available in this regard. Macroroughness in front of building can be used as effective strategies for wave pressure dissipation. Before estimation of tsunami pressure on building, it is important to calculate the run-up and inundation of tsunami wave. Goseberg et al. [1] studied the effect of macroroughness elements on tsunami run-up and inundation experimentally and numerically. Investigation of tsunami inundation is also carried out through an urban waterfront modelling and it is observed that the macroroughness elements can reduce the wave speed up to 40% [2]. Tsunami force estimation on building model with different configurations is also carried out by others [3–5]. Recently an experimental study is carried out [6] to investigate the effect of symmetrically placed macroroughness on coastal structures and it is observed that properly configured macroroughness can be used as an effective tsunami pressure dissipation strategy. Experimentations are very costly and time consuming. Therefore, numerical modelling can be an alternative and less time-consuming method for the investigation.

Numerical modelling of tsunami impact on building or any coastal structures is not reported by many researchers. Some of the studies are listed here. Ref. [7] studied dam break wave (i.e. single long wave) impact on tall structure using smooth particle hydrodynamics method. Two-dimensional RANS turbulence modelling is also carried out [8] to investigate the effect of impinging and overtopping of tsunami waves over an impermeable sea wall. Modelling of tsunami impact on rectangular shaped structure using smoothed particle hydrodynamics has been studied [9]. Therefore, it is observed that modelling of tsunami wave and its impact on building or structures is an emerging area and only a few studies have been reported.

2 Problem Descriptions

In the present study, tsunami impact on building and macroroughness elements has been simulated using CFD technique. The wave pressure reduction on building due to presence of macroroughness in front of building is also quantified in this paper.

Two following cases are studied:

(a) Reference building (without any obstruction) model
(b) Presence of macroroughness in front of building model.

The study is carried out for two types of solitary waves with constant period.

Wave type 1: Wave height (0.135 m or 0.45H) which is less than the building height (300 mm or H).

Wave type 2: Wave height (0.380 m or 1.27H) which is more than the building height (300 mm or H).

3 Numerical Modelling

ANSYS commercial software on unsteady 3D Reynolds-averaged Navier–Stokes (RANS) model is used to describe this flow. Realizable k-ε turbulence model is employed for the turbulence modelling. In order to simulate two-phase (air and water) flow, Volume of Fluid (VOF) technique is used. The free surface is detected using this. The Pressure-Implicit with Splitting of Operators (PISO) algorithm is used for pressure– velocity coupling. The stability and accuracy of the model is enhanced by keeping Courant Number below 0.25, which resulted in a time step between 0.001 and 0.01 s. Two phases (air and water) domain are created and involved governing equations are solved using VOF, which is a surface tracking technique applied to a fixed Eulerian mesh which is generally used for two or more immiscible fluids where the position of the interface between the fluids is of interest. The fluids in both phases are Newtonian, viscous and isothermal. A single set of momentum equations is shared by two fluids, and the volume fraction of each of the fluids in each computational cell is tracked throughout the domain. Since, time-accurate transient behaviour of the VOF solution is required to track the free surface motion of water, time-dependent with the geometric reconstruction interpolation scheme is used. The VOF formulation depends on the fact that fluids (or phases) are not interpenetrating and in a control volume, the sum of volume fractions of all phases equals to unity. The fields for all variables and properties are shared by the phases and represent volume-averaged values corresponding to the volume fraction of each of the phases at each cell location. Thus, the variables and properties in any given cell are representative of any of the phases, or representative of a mixture of the phases, depending upon the volume fraction values. Therefore, if qth fluid's volume fraction in the cell is denoted as α_q, then $\alpha_q = 1$: when cell is completely full, $\alpha_q = 0$: when cell is completely empty and for $0 < \alpha_q < 1$ it

contains interfaces of qth fluid and one or more other fluids. Based on the local value of α_q, the appropriate properties and variables are assigned to each control volume within the domain.

3.1 Governing Equations

The governing equations can be written as follows [10]:

Continuity equation:

The continuity equation is used for the volume fraction of one of the phases to track the interface between the phases. For the qth phase, this equation has the following form:

$$\frac{\partial}{\partial t}(\alpha_q \rho_p) + \nabla.(\alpha_q \rho_p \vec{v}_q) = 0 \tag{1}$$

where $\vec{v}$ is the velocity vector and ρ is the density. The volume fraction equation is not solved for the primary phase; the primary-phase volume fraction is computed based on the following constraint:

$$\alpha_q + \alpha_p = 1 \tag{2}$$

The properties appearing in the transport equations are determined by the presence of the component phases in each control volume. The density in each cell is given by

$$\rho = \alpha_q \rho_q + (1 - \alpha_q)\rho_p \tag{3}$$

And the viscosity of each cell is given by

$$\mu = \alpha_q \mu_q + (1 - \alpha_q)\mu_p \tag{4}$$

Volumes of fraction equations are evaluated using explicit time discretization scheme. The volume fractions of each phase are interpolated using Geometric Reconstruction Scheme (an interface reconstruction scheme).

Momentum Equation:

A single momentum equation is solved throughout the domain, and the resulting velocity field is shared among the phases. The momentum equation is dependent on the volume fractions of all phases through the properties ρ and μ as shown below.

$$\frac{\partial}{\partial t}(\rho\vec{v}) + \nabla.(\rho\vec{v}\vec{v}) = -\nabla p + \nabla.\left[\mu(\nabla\vec{v} + \nabla\vec{v}^T)\right] + \rho\vec{g} \tag{5}$$

where $\vec{v}$ = velocity vector, ρ = density, μ = viscosity and g = gravitational constant.

Turbulence Modelling:

During free surface flows, a high-velocity gradient at the interface between the two fluid surfaces result in high turbulence. Therefore, accurate modelling of turbulence is required. Realizable $k-\varepsilon$ turbulence model is used for the simulation of free surface flow, where k is the turbulence kinetic energy and its dissipation rate is ε. In case of realizable model expression for the normal Reynolds stress in an incompressible strained mean flow is obtained by combining the Boussinesq relationship and eddy viscosity equation:

$$\overline{u^2} = \frac{2}{3}k - 2v_t\frac{\partial U}{\partial x} \tag{6}$$

where $v_t = \mu_t/\rho$, when the strain is large enough to satisfy $\frac{k}{\varepsilon}\frac{\partial U}{\partial x} > \frac{1}{C_\mu} \approx 3.7$; the normal stress, $\overline{u^2}$, which by definition is positive quantity.

Transport Equations for the realizable $k-\varepsilon$ model are as follows.

Turbulence kinetic energy (k)

$$\frac{\partial}{\partial t}(\rho k) + \nabla.(\rho\vec{v}k) = \nabla\left[\left(\mu + \frac{\mu_t}{\sigma_k}\right)\nabla k\right] + G_k - \rho\varepsilon \tag{7}$$

and dissipation rate ε is

$$\frac{\partial}{\partial t}(\rho\varepsilon) + \nabla.(\rho\vec{v}\varepsilon) = \nabla\left[\left(\mu + \frac{\mu_t}{\sigma_k}\right)\nabla\varepsilon\right] + \rho C_1 S\varepsilon - \rho C_2\frac{\varepsilon^2}{k + \sqrt{v\varepsilon}} \tag{8}$$

where $C_1 = \max\left[0.43, \frac{\eta}{\eta+5}\right]$, $\eta = S\frac{k}{\varepsilon}$, $S = \sqrt{S_{ij}S_{ij}}$ and the generation of turbulent kinetic energy, G_k due to mean velocity gradient is computed from,

$$G_k = -\rho\overline{u_i'u_j'}\frac{\partial u_j}{\partial x_i} \tag{9}$$

The eddy viscosity is computed from

$$\mu_t = \rho C_\mu\frac{k^2}{\varepsilon} \tag{10}$$

The model constants are $C_2 = 1.9$; $\sigma_k = 1.0$; $\sigma_\varepsilon = 1.2$ and $C_\mu = \frac{1}{A_0 + A_s\frac{kU_*}{\varepsilon}}$, where $U_* \equiv \sqrt{S_{ij}S_{ij} + \tilde{\Omega}_{ij}\tilde{\Omega}_{ij}}$, $\tilde{\Omega}_{ij} = \Omega_{ij} - 2\varepsilon_{ijk}\omega_k$ and $\Omega_{ij} = \bar{\Omega}_{ij} - 2\varepsilon_{ijk}\omega_k$, where $\bar{\Omega}_{ij}$ is the

mean rate of rotation tensor viewed in a rotating reference frame with the angular velocity $\bar{\omega}_k$. The constants A_0 and A_s are given by $A_0 = 4.04$, $A_s = \sqrt{6}\cos\phi$, where $\phi = \frac{1}{3}\cos^{-1}(\sqrt{6}W)$, $W = \frac{S_{ij}S_{jk}S_{ki}}{\tilde{S}^3}$, $\tilde{S} = \sqrt{S_{ij}S_{ij}}$, $S_{ij} = \frac{1}{2}(\frac{\partial u_j}{\partial x_i} + \frac{\partial u_i}{\partial x_j})$.

3.2 Geometry

The scaled model of 1:50 is used in the numerical modelling. The building is as per geometric scale and velocity is as per Froude number. Table 1 shows the building model dimensions and prototype dimensions. Velocity of wave and wave height are also mentioned for both the cases.

The dimensions of the numerical domain are fixed according to the experimental facility of earlier research [11]. The domain is also optimized for numerical domain requirement. The dimensions of various portion of tank, channel and building are described below and shown in Fig. 1.

Table 1 Model and prototype dimensions

Details	Model (1:50)	Prototype
Height of building	0.3 m	15 m
Width of building	0.25 m	12.5 m
Length of building along the direction of wave	0.15 m	7.5 m
Dimension of macror oughness	1 m × 1 m × 1m	0.02 m × 0.02 m × 0.02 m
Generated wave height	0.38 and 0.135 m	19 and 6.75 m
Wave velocity	2.76 m/s	10.74 m/sec (Froude Scale)

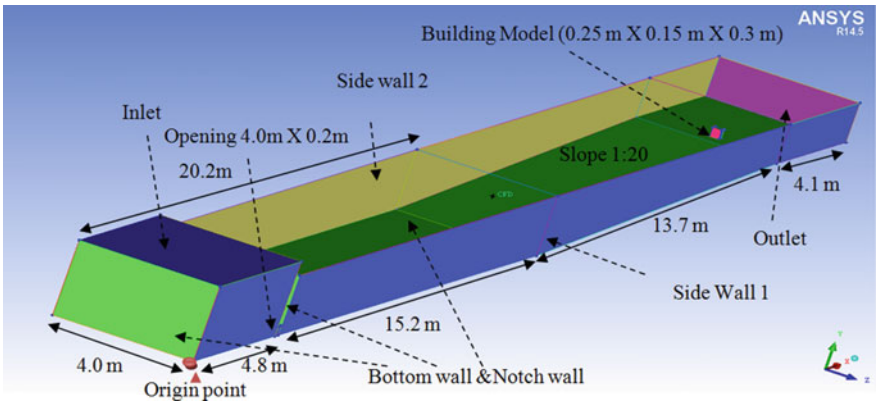

Fig. 1 Details of numerical domain and its different part name

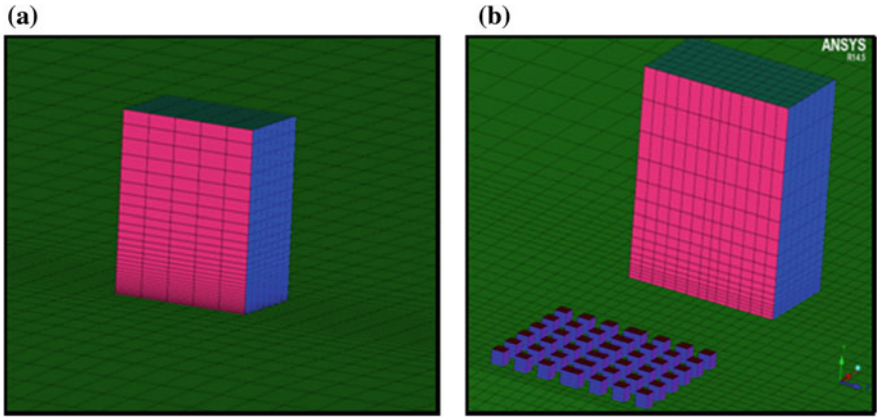

Fig. 2 **a** Building without any macroroughness **b** macroroughness present in front of building

Hexahedral type of mesh of variable sizes is used in entire numerical domain and near wall treatment is provided around the wall boundary (Fig. 2). The mesh convergence study is also carried out to find the optimum numbers of cell requirement. Approximately 20×10^5 numbers of hexahedral cells are employed for the creation of each numerical domain. The strategies for wave dissipation, employed in the study are shown in Fig. 2.

3.3 Boundary Conditions

Inlet is considered as a mass flow inlet, where a certain amount of water discharge is applied (see Fig. 1). Outlet and top of the channel is considered as pressure outlet and hydraulic diameter is mentioned. Bottom wall, notch wall and building walls are considered as no slip wall, non-penetrating (Fig. 1) and wall functions are employed for the turbulent quantities. Sidewalls are considered as symmetric. Initially, the tank and certain height of the channel (up to 0.66 m) are kept filled with water as an initial condition. The wave is generated by application of sudden discharge in the inlet of the tank which is controlled through a user-defined command.

4 Results

Wave generation in the numerical wave channel and wave movement at the different instances of time are shown in Fig. 3. At 10th second of the simulation, wave is in the verge of impacting the structure. Bore-like wave front is observed.

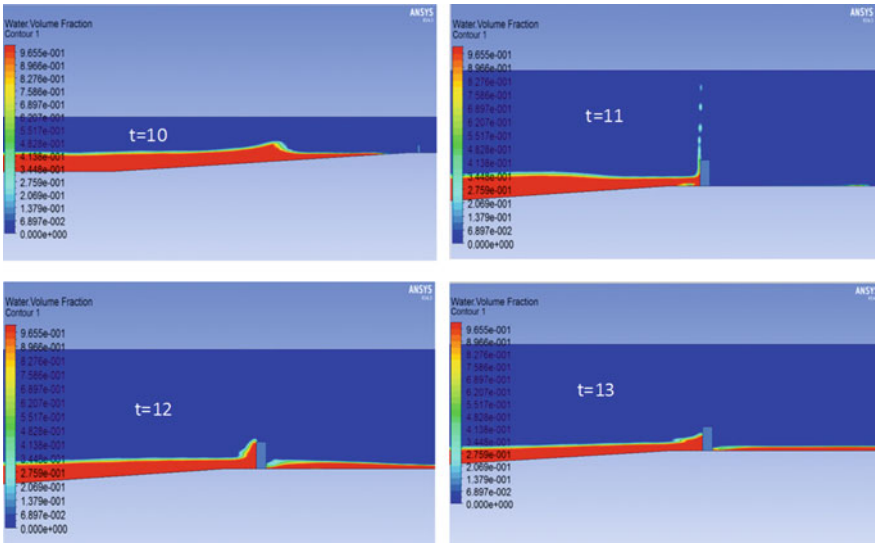

Fig. 3 Movement of wave at different instant of time for a particular wave condition

Overtopping of water over the building is observed at 11th second. Water line is observed at the back of the building at 12th second. At 13th second, water height is reduced and rundown is started.

4.1 Validation of Wave Velocity and Wave Profile

The average velocity of the wave at any particular instant is measured by dividing distance travelled with time taken by the wave to cross a particular distance. The average wave velocity = 34.375/13 = 2.644 m/sec, which has 3.89% error as compared to shallow wave velocity computed using $\sqrt{gD}$ formula. The non-dimensional wave amplitude and non-dimensional time can be represented by following equations.

$$\eta* = \eta/h_0 \tag{11}$$

$$t* = t\sqrt{(g/h_0)} \tag{12}$$

where η* is the normalized wave amplitude, η is surface elevation of the wave, h_o is the initial level of the water. t* = non-dimensional time and g = gravitational constant.

Figure 4 shows the validation of wave profile at 15th m of the channel location. The numerical results are in fair agreement with theoretical Boussinesq equation, Synolakis [12] experimental results, and University College London

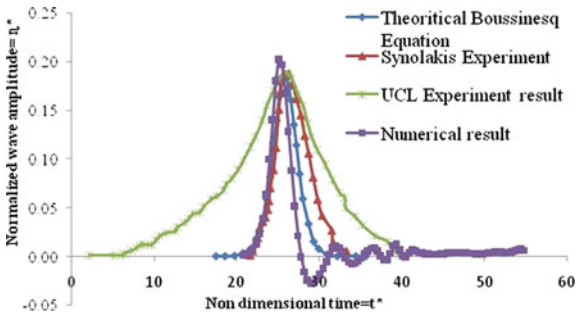

Fig. 4 Validation of wave profile

(UCL) experimental results [11]. The horizontal axis represents the non-dimensional time and vertical axes represent the normalized wave amplitude.

4.2 Wave Pressure Reduction

Numerical results show the reduction of wave pressure on building due to the presence of macroroughness. Wave conditions for Wave type 1 and Wave type 2 are different; therefore, the individual wave takes different time to reach up-to building from generation point. Wave type 1 takes 13 s while Wave type 2 takes 10 s to reach the building as shown in Figs. 5a and 7a. Pressure profile on building is also higher for Wave type 2 (Figs. 5b and 7b). But in presence of macroroughness, the wave motion is delayed by one second as shown in Figs. 6a and 8a. Therefore, the wave velocity reduces and thereby pressure profile also reduces as shown in Figs. 6b and 8b. Low-pressure zone and formation of vortices are observed in the gap between the obstructions and the building. A low-pressure zone is also observed at the top of the obstructions. Figure 8 shows that due to high amplitude of wave (Wave type 2), water is crossing the obstruction without changing its flow pattern and pressure reduction is not significant.

Quantification of the pressure reduction on the object building due the presence of macroroughness has been carried out. The plots of pressure reduction along height of building with and without obstructions are shown in Figs. 9, 10 and 11. The obstructions reduce 46% of maximum pressure for Wave type 2 and 62% of

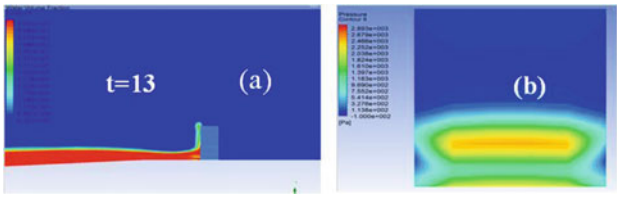

Fig. 5 **a** Volume fraction contour **b** pressure contour on building for Wave type 1

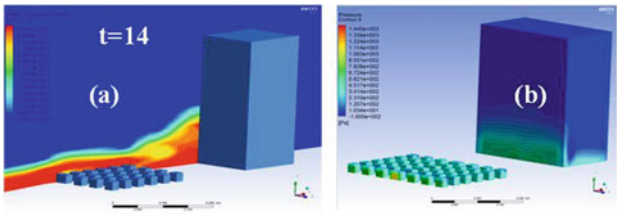

Fig. 6 **a** Volume fraction contour **b** pressure contour on building for Wave type 1

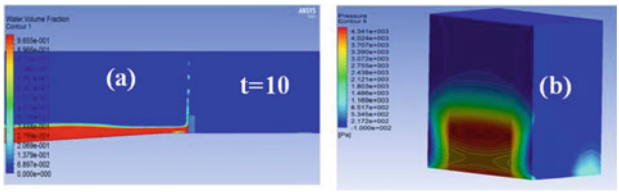

Fig. 7 **a** Volume fraction contour **b** pressure contour on building for Wave type 2

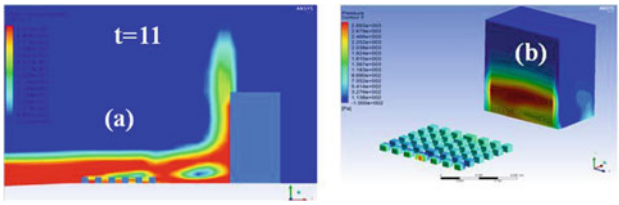

Fig. 8 **a** Volume fraction contour **b** pressure contour on building for Wave type 2

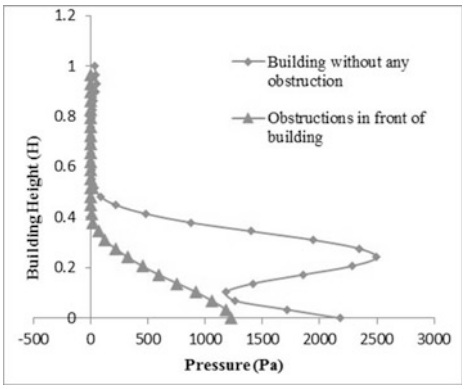

Fig. 9 Pressure distribution throughout the height of the building for Wave type 1

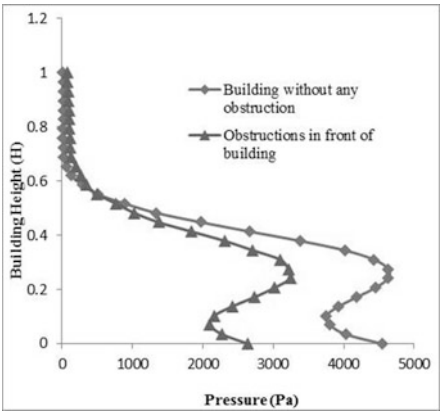

Fig. 10 Pressure distribution throughout the height of the building for Wave type 2

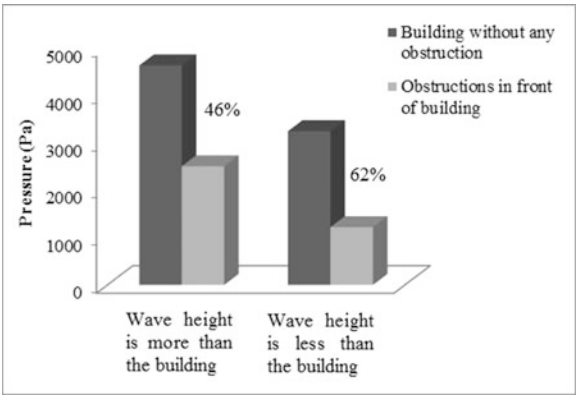

Fig. 11 Comparison of maximum water pressure reduction for different wave conditions

pressure for Wave type 1. It is interesting to observe that the pressure distributions are of similar patterns along the building height with or without obstruction in case of Wave type 2, however, this not the case for Wave type 1. This may be due to efficiency of the obstructions in reducing the hydrodynamic pressure component for smaller wave only. Therefore, the macroroughness are more effective for smaller wave height than larger wave height.

5 Conclusions

i. The strategy to place macroroughness in front of building is most effective when wave height is less than the building height (Wave type 1). It reduces pressure up to 62% whereas for wave height is more than the building height (Wave type 2) the reduction is 46%.

ii. For Wave type 2, the reduction in the pressure is less may be because macroroughnessess are not able to reduce the hydrodynamic contribution of wave pressure.
iii. Considerable amount of negative pressure is observed around the macroroughness elements which may lead to uplift of the elements. Scouring around these obstructions will also be an issue to be addressed. Therefore, special care is to be taken while designing these elements.

References

1. Goseberg, N., & Schlurmann, T. (2010). Numerical and experimental study on tsunami run-up and inundation influenced by macro roughness elements. In *Proceedings of the International Conference on Coastal Engineering*, 32 (pp. 1–12).
2. Rueben, M., Holman, R., Cox, D., Killian, J., & Stanley, J. (2011). Optical measurements of tsunami inundation through an urban waterfront modeled in a large-scale laboratory basin. *Coastal Engineering, 58*(3), 229–238.
3. Lindt, W., Gupta, R., Garcia, R., & Wilson, J. (2009). Tsunami bore forces on a compliant residential building model. *Engineering Structures, 31,* 2534–2539.
4. Triatmadja, R., & Nurhasanah, A. (2012). Tsunami force on buildings with openings and protection. *Journal of Earthquake and Tsunami, 6*(4), 1–17.
5. Aguíñiga, F., Jaiswal, M., Sai, J., Cox, D., Gupta, R., & van de Lindt, J. (2013). Experimental study of tsunami forces on structures. *Coastal Hazards*, 111–118.
6. Thomas, S., M., Killian, J., & Bridges, K. (2015). Influence of macroroughness on tsunami loading of coastal structures. *Journal of Waterway, Port, Coastal, and Ocean Engineering, 141*(1), 1–14.
7. Gomez-Gesteira, M., & Dalrymple, R. A. (2004). Using a 3D SPH method for wave impact on a tall structure. *Journal of Waterway, Port, Coastal, and Ocean Engineering, 130*(2), 63–69.
8. Hsiao, T., & Lin, C. (2010). Tsunami-like solitary waves impinging and overtopping an impermeable seawall: Experiment and RANS modeling. *Coastal Engineering, 57,* 1–18.
9. St-germain, P., Nistor, I., Townsend, R., & Shibayama, T. (2014). Smoothed-particle hydrodynamics numerical modeling of structures impacted by tsunami bores. *Journal of Waterway, Port, Coastal, and Ocean Engineering, 140*(1), 66–81.
10. ANSYS FLUENT: Version 14.5. 64 bit. (2013). Southpointe, 275 Technology Drive Canonsburg, PA 15317, USA.
11. Rossetto, T., Allsop, W., Charvet, I., & Robinson, D. I. (2011). Physical modelling of tsunami using a new pneumatic wave generator. *Coastal Engineering, 58,* 517–527.
12. Synolakis, C. E. (1986). *The runup of long waves*, Ph. D. thesis. California Institute of Technology, USA.

Performance of Base-Isolated Building Frame for Extreme Earthquakes

M. Bhandari, S. D. Bharti, M. K. Shrimali and T. K. Datta

Abstract Seismic design codes all over the world specify the concept of two-level earthquakes, one extreme earthquake (maximum credible earthquake) and other is design-level earthquake. Base-isolated buildings designed for design-level earthquake should be checked for their performances in the extreme-level earthquake. While under design-level earthquake, the framed structure remains in the elastic range but sufficient inelastic excursion may take place in the isolated frame in the extreme earthquake. The present study deals with the inelastic behavior of base-isolated frame subjected to an extreme level far-field and near-field earthquakes. Inelastic behavior of the structure is studied for different response parameters like base shear, top story displacement, isolator displacement, the formation of plastic hinges. A numerical study elucidates that for extreme level, the building goes highly into inelastic state in near-field earthquakes as compared to far field earthquakes.

Keywords Base isolation · Maximum credible earthquake · Inelastic excursion
Near-field earthquake · Far-field earthquake

M. Bhandari · S. D. Bharti · M. K. Shrimali (✉)
National Center for Disaster Mitigation and Management, Malaviya National Institute of Technology, Jaipur 302017, India
e-mail: shrimalimk@gmail.com

M. Bhandari
e-mail: man2301@yahoo.co.in

S. D. Bharti
e-mail: sdbharti@gmail.com

T. K. Datta
Department of Civil Engineering, Indian Institute of Technology Delhi, New Delhi 110016, India
e-mail: tushar_k_datta@yahoo.com

A. Rama Mohan Rao and K. Ramanjaneyulu (eds.), *Recent Advances in Structural Engineering, Volume 1*, Lecture Notes in Civil Engineering 11,
https://doi.org/10.1007/978-981-13-0362-3_81

1 Introduction

Base isolation technique is widely accepted and applied successfully all over the world. It has also been adopted in some codes for designing base-isolated buildings. Base-isolated structures offer minimum base shear and floor accelerations such that minimum energy is pumped into the structure. Though base-isolated structure remains in the elastic state for design0level earthquakes but it can go into inelastic phase up to some extent for extreme-level earthquakes. Also, different types of earthquakes may lead to different inelastic behaviors of the structure.

For the same PGA (peak ground acceleration), the structure is highly susceptible to near-field earthquakes as compared to far-field earthquakes. When the distance between the site and fault is less than 20 km, site experiences near-field earthquake which consists of major portion of faults energy in the form of pulses [1, 2]. These pulses tend to have maximum Fourier spectrum in limited periods whereas far-field earthquakes have maximum Fourier spectrum in wide range of periods. Near-field earthquakes are associated with two major effects namely, directivity effect and fling step effect [3].

When the direction of propagation of rupture is aligned toward the site or having a small angle between them and when the velocity of fault rupture is close to shear wave velocity of the site, then it is called forward directivity effect [4]. Fling step effect is accompanied by permanent ground displacement resulting from tectonic deformations. It produces large amplitude unidirectional velocity pulse and a monotonic step in displacement time history [5, 6].

Structural responses of base-isolated buildings have been studied by a number of researchers. Base isolation is effective in near-fault earthquake but eventually increases the story drift. Formation of hinges is found in structure and inelasticity is more in lower story level [7]. High initial isolator stiffness excites higher modes which increase floor accelerations [8]. Large displacements and high floor accelerations are produced due to lead rubber bearing isolator subjected to near-field earthquakes [9]. Properly designed isolation system can reduce floor accelerations and column stress. Also, the variation in structural and isolator damping have very less effect on peak acceleration and deflection [10]. The flexibility of superstructure increases the superstructure acceleration but did not significantly affect the bearing displacements [11]. Time history analyses is conducted on a 2-story reinforced concrete shear wall structure seismically isolated using unbonded rectangular fiber-reinforced elastomeric isolator FREI and with the fixed base. Investigation on the influence of near-fault and far-fault earthquakes with consideration of soil–structure interaction on the maximum response of SDOF system [12] is performed. A comprehensive parametric study conducted on the inelastic seismic response of seismically isolated RC frame building designed for gravity loads only with different isolation systems [13]. Investigated on inter-story drift and floor acceleration demands is carried out in buildings subjected to near-fault ground motions by considering simplified building and ground motion [14]. Interstory drift ratio is compared by conducting nonlinear time history analysis to assess the damage caused by near fault and far-fault ground motions [15].

Well-designed and constructed structures for design-level earthquakes can also be damaged up to great extent for some type of earthquakes [16]. This creates a scope to investigate the structures for extreme levels so that their inelastic demands can be identified and necessary measures can be taken in order to cope up with the excess deformation levels.

To this end, present work in directed toward the assessment of base-isolated structure for its nonlinear behaviour under near-field and far-field earthquakes at an extreme level. Time history analysis is simulated for 10- story-reinforced concrete frame which is isolated with the lead rubber bearing subject to different types of earthquakes scaled to PGA of 0.4 g. Inelastic behavior is depicted by comparing different response parameters for fixed base and base-isolated frame.

2 Building Details

The building which has been considered for the study is square building consisting of 3 bays in each direction of 5 m width each whose plan view is shown in Fig. 1 and loading is shown in Fig. 2. Further, all the building details are given in Table 2.

3 Analysis and Design

A frame in *x*-direction is considered for analysis and design. The distribution of the floor loads on the frame is calculated by considering the tributary areas of the slab. Dead load value is calculated as 22 and 23 kN/m for roof beams and floor beams, respectively, live load value is calculated as 3.75 and 6.25 kN/m for roof beams and floor beams. The frame is modeled and analyzed in SAP 2000 software. The design

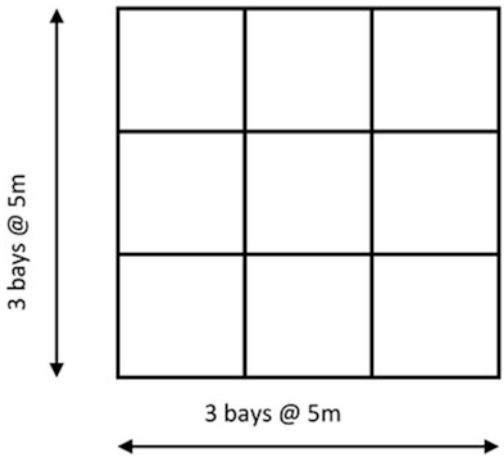

Fig. 1 Building plan

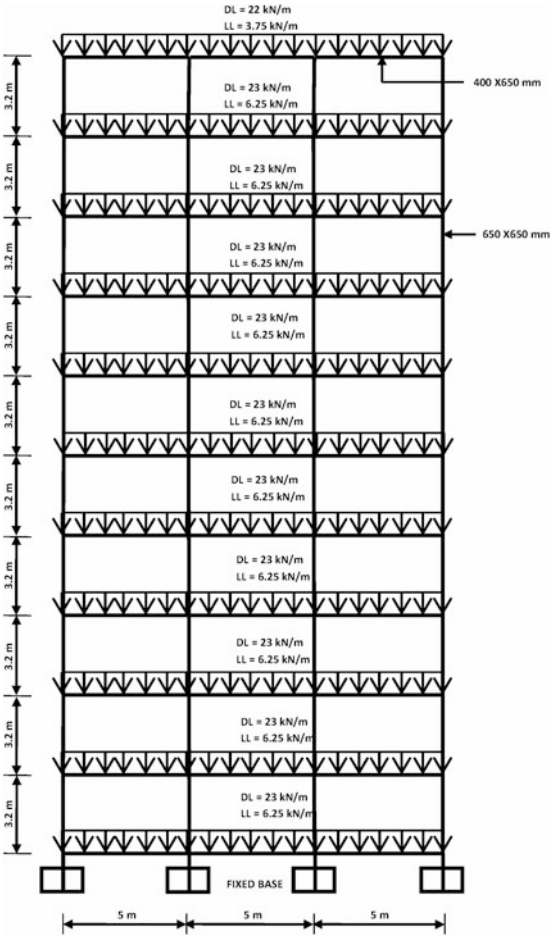

Fig. 2 Loading details

of the frame is done by considering seismic loads as governed by Indian Code 1893–2002.

Base isolator properties used for analysis are given in Table 1 with bilinear curve shown in Fig. 3. The isolators are designed according to the method proposed by Datta [17].

FEMA 356 default hinges in SAP 2000 are inserted to model the nonlinear hinges in the frame. Force–deformation behavior of plastic hinge is described by 5 points A, B, C, D, E as shown in Fig. 4. Three performance levels are shown in force–deformation relationship labeled as IO, LS, CP as immediate occupancy, life safety, collapse prevention whose default plastic hinge rotation values are defined in FEMA 356 for the various section, material, and design parameters.

Time history analysis of frame is done for different sets of far-field and near-field earthquakes in SAP 2000 for both fixed base and base-isolated condition.

Table 1 Properties of isolator

Parameters	Values
K_{eff} Effective stiffness	713 kN/m
K_1 Initial stiffness	5419 kN/m
β_{eff} Effective damping	0.1
γ Post yield stiffness ratio	0.10
F_Y Yield force	59.61 kN
K_v Vertical stiffness	200,687 kN/m

Table 2 Building details

No. of storeys	10
No. of bays in *x*-direction	3
No. of bays in *x*-direction	3
Floor height	3.2 m
Parapet height	1.5 m
Slab thickness	150 mm
Brick wall thickness	230 mm
Grade of concrete	M40
Grade of steel	Fe415
Density of concrete	25 kN/m^3
Density of brick	20 kN/m^3
Size of columns	650 × 650 mm
Size of beams	400 × 650 mm
Terrace water proofing	1.5 kN/m^2
Floor finish	0.5 kN/m^2
Live load on floor	2.5 kN/m^2
Live load on roof	1.5 kN/m^2
Seismic design code	IS 1893
Seismic zone	v
Building frame type	SMRF
Importance factor	1
Soil type	medium

A comparative study is also done for the analysis results on different parameters both for far-field and near-field earthquakes.

4 Ground Motion Database

Earthquake records which are used in this study have been taken from PEER Strong Motion Database, University of California (Berkeley). All the records have been normalized and scaled to 0.4 g in order to perform time history analysis. All the relevant properties of records like PGA (peak ground acceleration), PGV (Peak ground velocity), PGD (peak ground displacement) are given in Table 3.

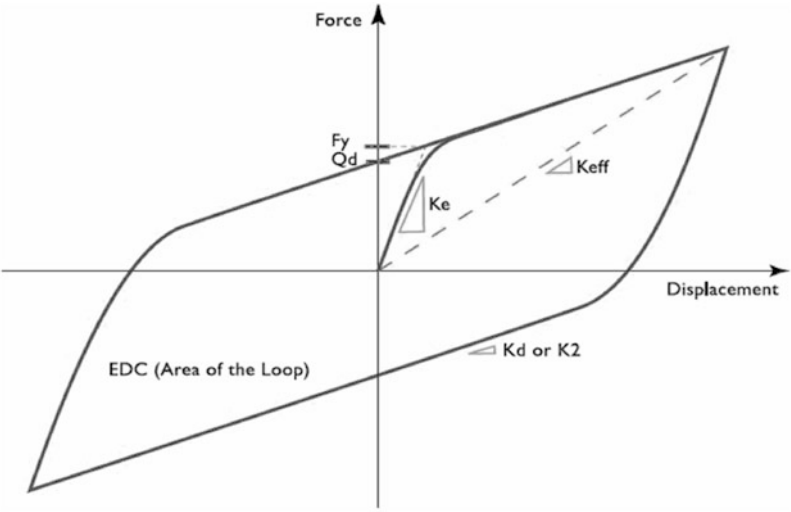

Fig. 3 Bilinear curve of isolator

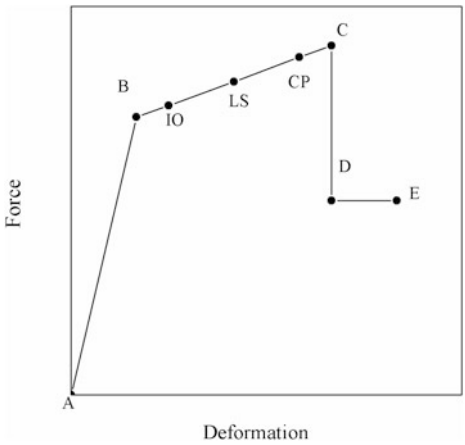

Fig. 4 Force–deformation relationship of plastic hinge

5 Numerical Study

In the present study, the seismic response is obtained by performing time history analysis of 10-story building frame subjected to set of near-field and far-field earthquakes. The seismic response is calculated both for fixed base and base-isolated conditions. Response parameters which are considered are base shear, top story absolute acceleration, maximum story drift, peak top floor displacement, RMS (root means square) value of top floor and first floor, isolator displacement.

Table 3 Ground Motion Records

S. No.	Year	Earthquake	M_w	Station	Component	PGA (g)	PGV (cm/s)	PGD (cm)
Far-field records								
1.	1992	Landers	7.3	Cool water	SCE STATION 23	0.42	42.35	13.84
2.	1978	Tabas	7.4	Ferdows	L	0.093	5.4	2.24
Near-field records (Forward directivity effect)								
3.	1992	Erzincan	6.69	Erzinkan	EW	0.5	64.32	21.91
Near-field records (Fling step effect)								
4.	1999	Chi–Chi	7.6	TCU 068	N	0.46	263.25	430.2

Table 4 shows the comparison of different response quantities for far-field and near-field earthquakes scaled to 0.4 g (extreme level) for fixed base (FB) and base-isolated (BI) condition. It can be clearly seen that there is maximum 71% reduction in base shear for far-field earthquake (LANDERS) and the maximum of 59% for near-field directivity effect (ERZINCAN) and 18% reduction in base shear in the case of near-field fling step (CHI–CHI). This indicates the poor performance of base isolation system in earthquakes having fling step effect but for the far field and earthquake with directivity effect, the base isolation efficacy is high to reduce the base shear.

Base isolation is effective in reducing the maximum story drift to 84 and 71% for far-field and near-field with directivity effect earthquakes but there is only 28% reduction in case of near-field fling step effect earthquake. Also, high value of story drift of 48 mm for near-field fling step effect leads to high level of stresses even in base- isolated structure. Maximum top floor displacement reaches to 265 and 962 mm for near-field earthquakes with directivity effect and fling step effect, but for far-field earthquake the value is only 118 mm which is quite acceptable for base-isolated structure. Far-field earthquake and near-field earthquake produces the fair amount of isolator displacement of 96 and 215 mm, which is acceptable for extreme earthquakes but near-field earthquake with fling step effect demands 702 mm of isolator displacement which leads to the complete failure of the isolation system.

The inelastic performance of building frame is investigated by prediction of plastic hinge formation in fixed base (FB) and base-isolated (BI) subjected to near-field and far-field earthquakes. Plastic hinges are formed against different performance levels.

Only B-level hinges are formed as shown in Fig. 5a, b for (Landers) in fixed base and base-isolated frame, showing the minimum damage to the structure as the number of hinges which were formed are only 21. It is observed from Fig. 5c, d that for the Chi–Chi earthquake with fling step effect have the maximum number of hinges having severe damage up to E level for fixed base and there is a reduction of inelasticity in base-isolated condition but still, the structure goes into the high

Table 4 Response parameters

Earthquake	Building type	Base shear (Kn)	Top storey absolute acceleration (m/sec2)	Maximum storey drift (mm)	Peak top floor displacement (mm)	Peak first floor displacement (mm)	RMS of top floor displacement (mm)	RMS of first floor displacement (mm)	Isolator displacement (mm)	Nonlinear hinges					
										B	IO	LS	CP	D	E
Landers	FB	1422	5.06	20.88	132.9	8.8	35.22	2.48		94	0	0	0	0	0
(Far filed)	BI	421	1.93	3.41	118.9	98.9	27	19.06	95.58	21	0	0	0	0	0
	Reduction	*70.39%*	*61.86%*	*83.67%*	*10.53%*										
Tabas	FB	1148	5.7	6.51	48.7	4	13.65	1.12		73	0	0	0	0	0
(Far filed)	BI	290	1.4	2.51	56.13	37.5	14.58	9.62	35.13	6	0	0	0	0	0
	Reduction	*74.74%*	*75.44%*	*61.44%*	*−15.26%*										
Erzinkan	FB	1644	6.28	23.97	143.21	11.76	80.74	7.04		108	0	0	0	0	0
(Near field)	BI	680	1.65	6.96	265.3	222.11	75.52	64.25	215	40	0	0	0	0	0
Directivity effect															
	Reduction	*58.64%*	*73.73%*	*70.96%*	*−85.25%*										
Chi– Chi	FB	2060	4.96	67.8	384.27	48.92	182.33	27.7		72	21	15	0	8	5
(Near field)	BI	1704	2.04	48.75	962.51	750.98	184	140	702	67	20	3	0	0	0
Fling step															
Effect	*Reduction*	*17.28%*	*58.87%*	*28.1%*	*−150.48%*										

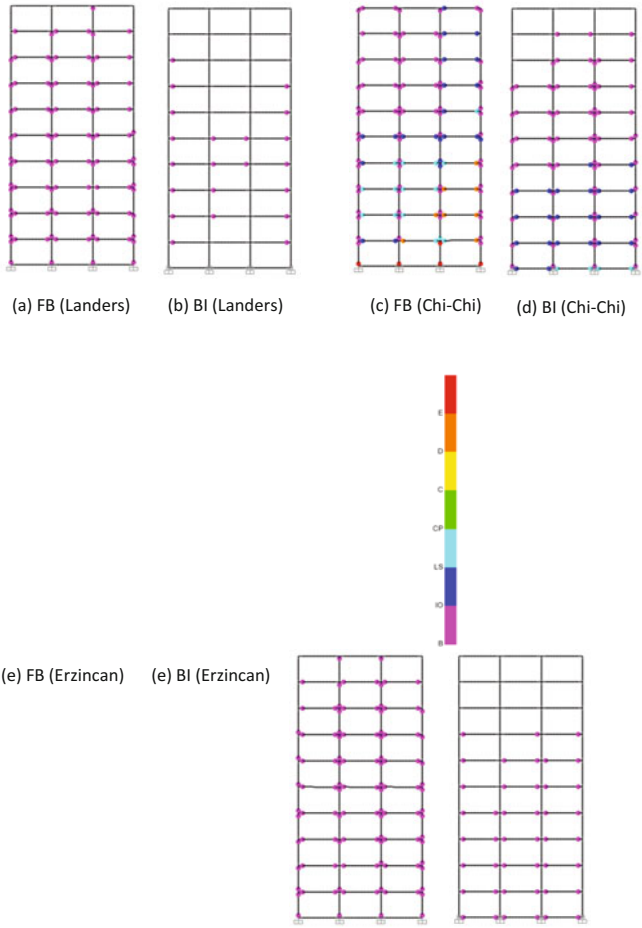

Fig. 5 Plastic hinge formation

inelastic state. For Erzinkan, the hinge formation is only up to B level forming 40 hinges for base-isolated case showing less damage as compared to fling step effect.

Force–deformation loops for different types of earthquakes are shown in Fig. 6. It can be clearly observed in the case of far-field earthquake (landers) that there are a large number of loops which are placed centrally and the force–deformation curve is wide enough which indicates large amount of energy dissipation. Near-field earthquake with directivity effect produces less loops which are distributed along the whole force–deformation cycle because of less dissipation of energy. Also, the force–deformation curve is less wider as compared to far-field earthquake. On the other hand, very few cycles have occurred in case of near-field fling step effect earthquake (Chi–Chi) having narrow force–deformation curve which clearly shows very low efficacy to dissipate the earthquake energy.

Fig. 6 Force–deformation curves

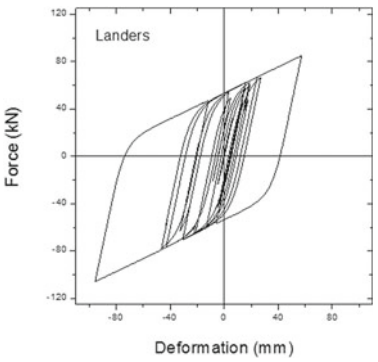

(a) Far field (landers)

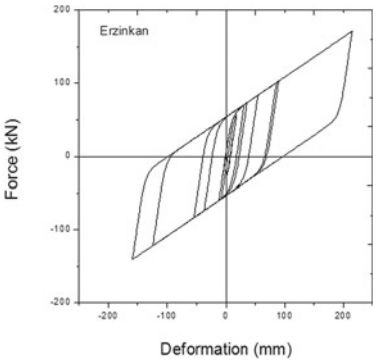

(b) Near field field (landers)

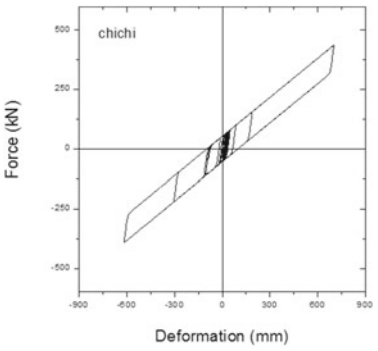

(c) Near field (chichi)

6 Conclusion

Base-isolated frame of 10 stories is analyzed in order to evaluate its performance under extreme earthquakes scaled to 0.4 g PGA. Three different types of earthquakes are used likely, far field, near field with directivity effect and near field with

fling step effect. Different response quantities of base-isolated structure are compared with fixed base structure which draws following conclusions:

1. It is seen from the numerical study that under extreme earthquake the base-isolated frames can sufficiently get into the inelastic range.
2. Most of the plastic hinges remain in the initial stage, i.e., B for far-field and near-field (directivity effect) but the frame has undergone in high level of inelasticity under near- field (fling step) earthquake.
3. There is sufficient reduction in base shear of about 60–70% (remains nearly equal to design level earthquake) except in near field.
4. Effective reduction in story drift of about 70–80% is observed but for near-field (fling step) earthquake reduction is only 28%.
5. At isolator level for near field, (fling step) earthquake base isolation acts as inappropriate system as it demands high isolator displacement which seems to be very difficult to accommodate and can result in complete failure of the system.

References

1. Heydari, M., & Mousavi, M. (2015). The comparison of seismic effects of near-field and far-field earthquakes on relative displacement of seven-storey concrete building with shear wall. *Current World Environment, 10*(1), 0–46.
2. Zade, M, T., & Najafi, L. H. (2008). Assessing seismic behavior of eccentrically braced frames (EBFs) due to near-field ground motions. In *The 14th World Conference on Earthquake Engineering.* Beijing, China.
3. Somerville, P. G., et al. (1997). Modification of empirical strong ground motion attenuation relations to include the amplitude and duration effects of rupture directivity. *Seismological Research Letters, 68*(1), 199–222.
4. Kalkan, E., & Kunnath, S. K. (2006). Effects of fling step and forward directivity on seismic response of buildings. *Earthquake Spectra, 22*(2), 367–390.
5. Hall, J. F., et al. (1995). Near-source ground motion and its effects on flexible buildings. *Earthquake Spectra, 11*(4), 569–605.
6. Li, S., & Xie, L.-L. (2007). Progress and trend on near-field problems in civil engineering. *Acta Seismologica Sinica, 20,* 105–114.
7. Providakis, C. (2008). Pushover analysis of base-isolated steel–concrete composite structures under near-fault excitations. *Soil dynamics and earthquake Engineering, 28*(4), 293–304.
8. Sharma, A., & Jangid, R. (2009). Behaviour of Base-Isolated Structures with High Initial Isolator Stiffness. *World Academy of Science, Engineering and Technology, International Journal of Civil, Environmental, Structural, Construction and Architectural Engineering, 3* (2), 49–54.
9. Jangid, R., & Kelly, J. (2001). Base isolation for near-fault motions. *Earthquake Engineering and Structural Dynamics, 30*(5), 691–707.
10. Fan, F.-G., et al. (1991). Performance analysis of aseismic base isolation systems for a multi-story building. *Soil Dynamics and Earthquake Engineering, 10*(3), 152–171.
11. Matsagar, V. A., & Jangid, R. (2004). Influence of isolator characteristics on the response of base-isolated structures. *Engineering Structures, 26*(12), 1735–1749.

12. Davoodi, M., et al. (2012). Effects of near-field and far-field earthquakes on seismic response of SDOF system considering soil structure interaction. In *15th World Conference on Earthquake Engineering.* Lisbon, Portugal.
13. Cardone, D., Flora, A., & Gesualdi, G. (2013). Inelastic response of RC frame buildings with seismic isolation. *Earthquake Engineering and Structural Dynamics, 42*(6), 871–889.
14. Alonso-Rodríguez, A., & Miranda, E. (2015). Assessment of building behavior under near-fault pulse-like ground motions through simplified models. *Soil Dynamics and Earthquake Engineering, 79,* 47–58.
15. Akkar, S., Yazgan, U., & Gülkan, P. (2005). Drift estimates in frame buildings subjected to near-fault ground motions. *Journal of Structural Engineering, 131*(7), 1014–1024.
16. Elnashai, A. (2000). Analysis of the damage potential of the Kocaeli (Turkey) earthquake of 17 August 1999. *Engineering Structures, 22*(7), 746–754.
17. Datta, T. K. (2010). *Seismic analysis of structures*. Wiley.

Analytical Seismic Fragility Analysis of Existing Building Frame in Northeast India

S. Mukherjee, S. Ghosh, S. Ghosh and S. Chakraborty

Abstract The analytical seismic fragility analysis (SFA) of a typical mid-rise steel building frame considered to be located in the Guwahati city of Northeast India is presented in the performance-based earthquake engineering (PBEE) framework. The approach starts with a detailed probabilistic seismic hazard analysis (PSHA) of the Guwahati city to obtain hazard curve parameters. Subsequently, nonlinear time history analyses (NLTHA) are carried out to obtain displacement demand model parameters for the example frame. For dynamic analysis, a representative ground motion bin is prepared judiciously. As the recorded accelerograms in the region is limited, the bin is formed with recorded as well as artificially and synthetically generated data. The structural capacities at various limit states are obtained from random pushover analysis (RPA). With the estimated seismic hazard, demand and capacity parameters, fragility curves are generated for different performance levels. The annual probability of failure is finally estimated based on the seismic hazard and the fragility curves.

Keywords Northeast India · Probabilistic seismic hazard analysis
Steel frame building · Nonlinear dynamic and pushover analysis
Seismic fragility analysis

S. Mukherjee · S. Ghosh · S. Ghosh · S. Chakraborty (✉)
Department of Civil Engineering, Indian Institute of Engineering Science and Technology, Shibpur, Howrah 711103, India
e-mail: schak@civil.iiests.ac.in

S. Mukherjee
e-mail: subhojit27@rediffmail.com

S. Ghosh
e-mail: gh.swarup@gmail.com

S. Ghosh
e-mail: gh13shyamal@gmail.com

A. Rama Mohan Rao and K. Ramanjaneyulu (eds.), *Recent Advances in Structural Engineering, Volume 1*, Lecture Notes in Civil Engineering 11,
https://doi.org/10.1007/978-981-13-0362-3_82

1 Introduction

The Northeast (NE) India, comprising of the States of Arunachal Pradesh, Assam, Manipur, Meghalaya, Mizoram, Nagaland, Sikkim and Tripura, is one of the seismically most active regions of the world. The region has experienced 18 large earthquakes ($M \geq 7$) during the last hundred years including the great earthquakes of Shillong (1897, $M = 8.7$) and Assam–Tibet border (1950, $M = 8.7$). The region marks the boundary between Indian and Eurasian plates. The complex tectonic and geological set up of the region cause plate movements in different directions. Due to the highly oblique continental convergence of the northward-moving Indian plate at the rate of 20 + 3 mm/year, earthquakes of magnitudes 8 and above have occurred in the past and may recur. But the big concern is that with the present state of the art knowledge it is not possible to predict when, where and how it will occur. Moreover, there has been a phenomenal increase in the population density and infrastructural development programmes in the region. These factors are further increasing the vulnerability of human population and structures to earthquakes. Thus, it becomes essential to assess the status of seismicity in the NE region realistically for an urgent and sustained mitigation measure.

A significant amount of research conducted on the subject and the subsequent advancements in the understanding and knowledge of earthquake-resistant structural design provided a better recognition of the need for Seismic vulnerability assessment (SVA) and retrofit of older existing buildings. The recent development of performance-based earthquake engineering (PBEE) in the context of probabilistic seismic response analysis of structures is believed to open a new way for SVA of structures considering parameter uncertainty. In fact, seismic fragility analysis (SFA) has emerged as an integrated platform for SVA in a probabilistic framework to quantify seismic risk during the life-cycle of a structure.

Though, the development in the field of SVA at international level is exhaustive [1, 2]; same is not the case for NE region. The studies on seismic hazard analysis of the NE region are notable [3, 4]. However, the studies on the seismic safety of existing structures are very scarce and limited to simplified evaluation in deterministic framework [5, 6]. Thus, realistic SFA of existing structures of the NE region for an urgent and sustained mitigation measure has become important.

The present study deals with analytical SFA of a typical mid-rise moment resisting steel building frame located in the Guwahati city of NE India. The approach starts with a detailed Probabilistic Seismic Hazard Analysis (PSHA) considering the seismicity around 300 km radius around the city to estimate the seismic hazard parameters corresponding to the desired hazard level. Subsequently, the nonlinear time history analyses (NLTHA) are carried out to obtain the displacement demand model and the demand parameters are calculated accordingly for the example frame. For NLTHA, a representative ground motion bin corresponding to the specified hazard level for the location of the structures is necessary. As the recorded accelerograms in the NE region is very scarce, the present study is limited to use of eight numbers of recorded accelerograms. And, to supplement the limited

recorded input, the accelerogram data are further generated artificially and synthetically so that statistically meaningful study can be performed for seismic demand analysis. Eight numbers of accelerograms are generated artificially and matched with IS code (IS 1893: 2000) specified pseudo-acceleration response spectrum for seismic Zone V and for rock and hard soil site corresponding to 5% damping. Another eight numbers are synthetically generated by stochastic point source modelling, identifying the most vulnerable source for the specific hazard level for the city. The structural capacities at various limit states are obtained from the random pushover analysis (RPA) of the considered frame. Finally, with the knowledge of the seismic hazard parameters, demand and capacity parameters, the analytical seismic fragility expression is obtained in the context of PBEE and fragility curves are generated corresponding to different structural limit states namely the immediate occupancy (IO), life safety (LS) and collapse prevention (CP). Annual probability of failure of the example frame is also estimated based on the seismic fragility and hazard data obtained by PSHA corresponding to specified hazard level.

2 Fundamental of Seismic Risk Analysis

The fundamental of seismic risk analysis procedure is to calculate the probability of exceeding a structural limit state. It is basically a time-dependent structural reliability analysis problem in which the limit state of interest is the difference between seismic demand and capacity. It can be mathematically expressed as

$$Z(\mathbf{X_C}, \mathbf{X_D}, t) = C(\mathbf{X_C}, t) - D(\mathbf{X_D}, t) \tag{1}$$

In the above, $\mathbf{X_C}, \mathbf{X_D}$ are the variables governing the capacity and demand and t is the time parameter. The computation of probability that the limit state function is negative represents the seismic risk of the structure, i.e.

$$P_f = \int_{Z<0} f_Z(\mathbf{X}) \mathrm{d}Z \tag{2}$$

where $\mathbf{X}$ is an 'n' dimensional vector having variables involving seismic demand and capacity, $f_Z(\mathbf{X})$ is the joint probability density function (pdf) of the involved random variables. The exact computation of the above is often computationally demanding. In fact, the joint pdf of $f_Z(\mathbf{X})$ is hardly available in closed form. Various approximations are usually adopted to obtain the probability of exceeding different limit states of damage for a response parameter under a specific seismic intensity measure. This is customarily termed as SFA. The SFA by PBEE in the probabilistic framework can be performed by two approaches: (i) Analytical fragility based on probabilistic seismic demand and capacity model and

(ii) Simulation-based fragility based on nonlinear PBEE using random field theory and statistical simulation. Considering the focus of the present study, the analytical SFA is presented here.

3 Analytical Seismic Risk Analysis

The problem of seismic risk evaluation for a structure at a site is to obtain the failure limit state probability, $P_{\mathrm{LS}} = P[D \geq C]$, i.e. the exceedance of the structural demand value (D) to its capacity (C). In order to determine P_{LS}, the equation can be decomposed into parts with respect to an interface variable using the concept of total probability theorem [7]. Considering the spectral acceleration (S_{a}) as the interface variable, the decomposition can be obtained as

$$\begin{aligned} P_{\mathrm{LS}} = P[D \geq C] &= \sum_{x} P[D \geq C | S_{\mathrm{a}} = x].P[S_{\mathrm{a}} = x] \\ &= \int_{x} F_R(x).|d\lambda_{S_{\mathrm{a}}}(x)| \end{aligned} \tag{3}$$

The problem of calculating the limit state probability in Eq. (3) involves solution of two problems. The first term in the integral represents the conditional limit state probability for a given level of ground motion intensity which is the seismic fragility, $F_R(x)$. The second problem is to estimate the spectral acceleration hazard for the location, which can be estimated from PSHA. For this, a detailed PSHA is carried out in the present study, considering the seismicity around the site from historical earthquake data. Evaluations of these are briefly discussed in the following subsections.

3.1 Spectral Acceleration Hazard, $P[S_{\mathrm{a}} \geq x]$

The spectral acceleration hazard at a site is based on evaluating the pdf of a random parameter Z, representing the strong ground motion parameter at a site due to all the earthquakes expected to occur during a specified exposure period in the region around the site. The peak spectral velocity, PSV(T) for a time period T is considered as the ground motion parameter here for PSHA. If, $q(z|M_jR_i)$ denotes the probability that a given PSV(T) of amplitude 'z' at a site will be exceeded during an event of magnitude M_j occurring at a source element R_i, the annual average occurrence rate of earthquakes $\lambda(z)$ can be obtained as:

$$\lambda(z) = \sum_{i=1}^{I} \sum_{j=1}^{J} q(z|M_j R_i) n(M_j R_i) \tag{4}$$

The quantity $n(M_j R_i)$ in the above equation is the annual rate of occurrence of the (M_j, R_i) event. The estimated value of the PSV(T) amplitude for a particular M_j and R_i combination will be $\log[\mathrm{PSV}'(T)] + \varepsilon(T)$, $\varepsilon(T)$ is the error residual term obtained from the attenuation model [4]. The probability that the estimated value of $\mathrm{PSV}'(T)$ will be greater than a specific value 'z' can be obtained as, $\varepsilon(T) > \log[z] - \log[\mathrm{PSV}'(T)]$. Based on the normal distribution assumption of the residuals $\varepsilon(T)$, the cumulative distribution function (CDF) can be obtained as

$$p(\varepsilon(T)) = \frac{1}{\sigma(T)\sqrt{2\pi}} \int_{-\infty}^{\varepsilon(T)} \mathrm{e}^{-\frac{1}{2}\left(\frac{x-\mu(T)}{\sigma(T)}\right)^2} \mathrm{d}x \tag{5}$$

Thus, the term $q(z|M_j R_i)$ can be obtained as $1 - p(\varepsilon(T))$, where $p(\varepsilon(T)) = \Phi(\varepsilon(T))$. Assuming that $\lambda(z)$ is the average occurrence rate of a Poisson process, the probability of exceeding z during an exposure period of Y years can be obtained as

$$P[\mathrm{PSV}(T)] = 1 - \exp\{-\lambda(z).Y\} \tag{6}$$

The CDF is obtained for a specified exposure period (50 years herein) using Eq. (4) in Eq. (6) with the knowledge of $n(M_j R_i)$ around the site and an attenuation model. The details of those calculations may be seen in [4].

The steel frame taken up for the case study (detailed in Sect. 5) is considered to be located in the Guwahati city. Based on the procedure outlined above, the PSV hazard is obtained and converted to PSA hazard by multiplying its ordinates with $2\pi/T$. Figure 1a shows the peak spectral acceleration (PSA) hazard curve (in terms of 'g') for horizontal motions, for T = 1.0 s, Y = 50 years. Figure 1b shows the uniform hazard spectra (UHS) obtained for 10% probability of exceedance in 50 years. The hazard curve is approximated in the region of interest by a power-law relationship [7]:

$$\begin{aligned} \lambda_{\mathrm{IM}}(x) &= P[\mathrm{IM} \geq x] \\ &= 1 - \exp\left[-(x/u)^{-k}\right] \approx (x/u)^{-k} \approx k_0 x^{-k} \end{aligned} \tag{7}$$

where u and k are the scale and shape parameter, respectively, and $k_0 = u^k$. Drawing a tangent line to the hazard curve (Fig. 1a) at the point of interest (i.e. points corresponding to p = 0.1, Y = 50 years), the slope and intercept of the tangent are obtained which provides the values of the parameters k_o and k. These are estimated as 0.0004 and −2.72, respectively. Thus, the power-law model of PSA hazard for

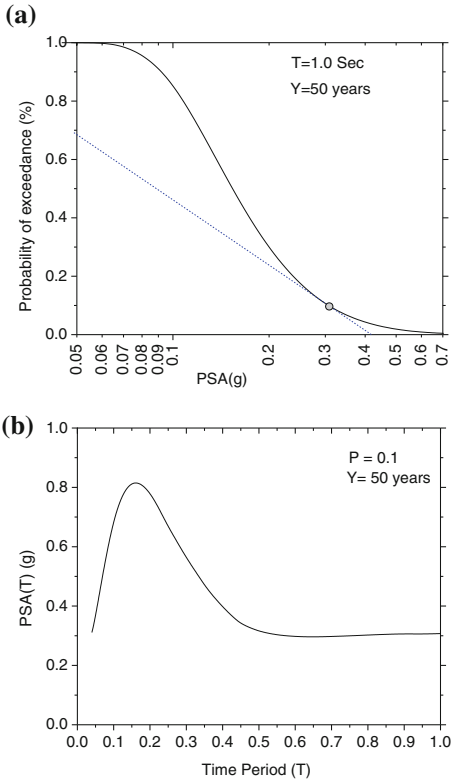

Fig. 1 **a** Hazard curve for $T = 1.0$ s and exposure period of 50 years. **b** Uniform hazard spectra for 10% probability of exceedance in 50 years

Guwahati city is obtained as $\lambda_{\mathrm{IM}}(x) = 0.0004x^{-2.72}$ for $T = 1.0$ s, $p = 0.1$ and $Y = 50$ years (i.e. 475 years of return period).

3.2 *Damage Fragility* $P[D \geq C|S_{\mathrm{a}} = x]$

The next problem is to calculate the conditional failure probability of seismic demand reaching or exceeding random structural capacity given a specific value of seismic intensity, i.e. $F_R(x) = P[D \geq C|S_{\mathrm{a}} = x]$. Assuming structural capacity is log-normal with uncorrelated D and C, following the fundamentals of first order reliability analysis method, the damage fragility (probability of failure) can be obtained as

$$F_R(x) = \Phi\left[-\frac{\ln m_{\mathrm{C}} - \ln m_{\mathrm{D}}}{\sqrt{\beta_{\mathrm{C}}^2 + \beta_{\beta_{\mathrm{D}|S_{\mathrm{a}}}}^2}}\right] = \Phi\left[\frac{\ln m_{\mathrm{D}|S_{\mathrm{a}}} - \ln m_{\mathrm{C}}}{\sqrt{\beta_{\mathrm{D}|S_{\mathrm{a}}}^2 + \beta_{\mathrm{C}}^2}}\right] \tag{8}$$

Here $F_R(x)$ is the fragility that the median demand will reach or exceed the median capacity for a specified value of $S_a = x$, m_C is the median capacity and β_C is its log-normal standard deviation (SD). For a given level of intensity S_a there will be variability in displacement based demand due to randomness in seismic phenomenon. A functional relationship is conveniently introduced between the spectral acceleration and the median, m_D of the demand variable. In general, the conditional median of D for $S_a = x$ can be expressed as

$$m_{D|S_a}(x) = g(x) \tag{9}$$

Assuming that the demand parameters are log-normally distributed, the above conditional probabilistic model can be represented as

$$D = m_{D|S_a}(x).\varepsilon \tag{10}$$

In which ε is a log-normal random variable with median equal to unity and conditional logarithmic SD $\sigma_{\ln \varepsilon} = \beta_{D|S_a}$. A power-law relationship can be readily obtained between the median demand and spectral acceleration as:

$$m_{D|S_a}(x) = a.x^b \tag{11}$$

where, 'a' and 'b' are the regression parameters and can be obtained by probabilistic seismic demand analysis methods, e.g. cloud analysis (CA), strip method or incremental dynamic analysis method. In the present study, the CA method is used to obtain the median relationship which is further detailed in the case study section.

Now, substituting Eq. (11) in Eq. (8) yields

$$\begin{aligned} F_R(x) &= \Phi\left[\frac{\ln(ax^b) - \ln m_C}{\sqrt{\beta_{D|S_a}^2 + \beta_C^2}}\right] \\ &= \Phi\left[\frac{\ln x - \ln(m_C/a)^{1/b}}{\frac{1}{b}\sqrt{\beta_{D|S_a}^2 + \beta_C^2}}\right] = \Phi\left[\frac{\ln(x/m_R)}{\beta_R}\right] \end{aligned} \tag{12}$$

where, m_R and β_R are the median and dispersion of the damage fragility defined as $m_R = (m_C/a)^{1/b}$ and $\beta_R = \frac{1}{b}\sqrt{\beta_{D|S_a}^2 + \beta_C^2}$. The log-normal SD of capacity, $\beta_C = \sqrt{\beta_{CR}^2 + \beta_{CU}^2}$, where β_{CR} represents the effect of structural uncertainty propagation obtained through RPA of the considered structure for different performance level. While β_{CU} arises from the assumption of structural modelling. Due to the non-availability of specific information on epistemic uncertainty (β_{CU}), it is considered to be 0.2 in the present study [8].

3.3 Analytical Seismic Risk

Once the conditional failure probability $F_R(x)$ is obtained from Eq. (12), the analytical expression can be readily obtained to estimate the seismic risk. By substituting Eqs. (7) and (12) in Eq. (3) and carrying out the integral, the failure limit state probability, P_{LS} can be obtained as

$$\begin{aligned} P_{\mathrm{LS}} &= P[D \geq C] = \sum_x P[D \geq C | S_{\mathrm{a}} = x].P[S_{\mathrm{a}} \geq x] \\ &= \int_x F_R(x).|d\lambda_{S_{\mathrm{a}}}(x)| = \lambda_{\mathrm{IM}}(m_R) \exp\left(\frac{1}{2}k^2\beta_R^2\right) \\ &= \lambda_{\mathrm{IM}}(m_R) \exp\left[\frac{1}{2}\frac{k^2}{b^2}\left(\beta_{\mathrm{D}|S_{\mathrm{a}}}^2 + \beta_{\mathrm{C}}^2\right)\right] \end{aligned} \tag{13}$$

The above displacement based explicit format to obtain annual limit state frequency can be directly used by substituting the values of m_R and β_R in Eq. (13) and the use of the hazard curve relation as describe by Eq. (7).

4 Selection of Ground Motion Bin

The analytical SFA in the framework of PBEE as described in the previous section largely hinges on proper evaluation of structural demand parameters through nonlinear response history analysis. The most acceptable form for NLTHA of SFA of structures corresponds to the use of recorded accelerograms. However, due to the limited availability of recorded accelerograms specific to the hazard level for the focused region, the choice of natural ground motions here is limited to eight numbers. Thus, eight numbers of accelerograms are generated artificially and another eight numbers are synthetically generated identifying the most vulnerable M_j and R_i combination for the specific hazard level of the location under consideration. These are briefly discussed in the following.

The eight natural records are selected from the past earthquake data in the region which covers a surface wave magnitude range from 6.0 to 8.0 and epicentral distance within 300 km for rock site. For the disaggregation study, a target hazard level is identified and contribution of each source is calculated by finding out the probability of exceedance of the target hazard level for each of the sources. Due to limited resources of recorded accelerograms in the region, the accelerogram records are also selected from Northern Himalayan earthquakes corresponding to similar subsoil sites (available in the COSMOS virtual data centre). The earthquakes with an epicentral range within 10 km are avoided due to the possibility of directivity pulse effect.

The artificial accelerograms are generated compatible with the acceleration response spectra for rock and hard soil for 5% damping [9]. The power spectral density (PSD) function is obtained following Kaul [10] and the accelerograms are generated accordingly following the methodology proposed by Gasparini and Vanmarcke [11]. Defining a vector of amplitudes and simulating different arrays of phase angles, the stationary stochastic process is obtained with the same general aspect but with different characteristics. These amplitudes are calculated using the PSD and the random phase angles are generated in the interval of 0–2π. Further, to simulate the transient nature of the earthquakes, the steady-state motions are multiplied by a deterministic envelope function [12].

The stochastic ground motion model as proposed by Boore [13] is used for generation of synthetic acceleration time histories. Following this, eight accelerograms are generated for different magnitudes between 6.0 and 8.0 and epicentral range within 300 km. Figure 2a compares actual and one typical simulated acceleration spectra for Loharghat Station (closest to the Guwahati City) and Fig. 2b is the associated synthetic accelerogram generated for M_w = 6.0 and R = 150 km and focal depth = 15 km.

5 Case Study: A Six-Storey Steel Frame

A two-bay steel moment frame as shown in Fig. 3 considered to be located in the Guwahati city is undertaken for the numerical elucidation of the analytical SFA and seismic risk evaluation procedure. The structural analysis is performed by using SAP 2000 software. The grade of steel is Fe250 having expected yield stress of 275 MPa. The beams and columns are modelled with lumped plasticity at their ends. The nonlinear hinges are assigned at the beam and column ends. The beams are modelled with moment hinges (M3) whereas the columns are modelled with axial-moment (P-M3) hinges. Auto hinges are assigned at beam and column ends according to tables of FEMA 356 [14]. The NLTHA is carried out by Hilber–Huges–Taylor integration scheme. The mass and stiffness proportional damping, i.e. Rayleigh's damping is considered as 2% for the first two modes.

The NLTHA of the frame is carried out for the 24 numbers of ground motion inputs and the maximum interstory drift (ISD) values are obtained for each of ground motion input representing the structural demands D. The power-law relationship conveniently constructed between the median maximum ISD and spectral acceleration values and the regression parameters 'a' and 'b', obtained by the cloud analysis. For the considered building frame the power-law relationship between the median demand and spectral acceleration is obtained as: $m_{\mathrm{D}}(x) = 1.713.x^{0.828}$, $\beta_{\mathrm{D}|S_{\mathrm{a}}} = 0.263$.

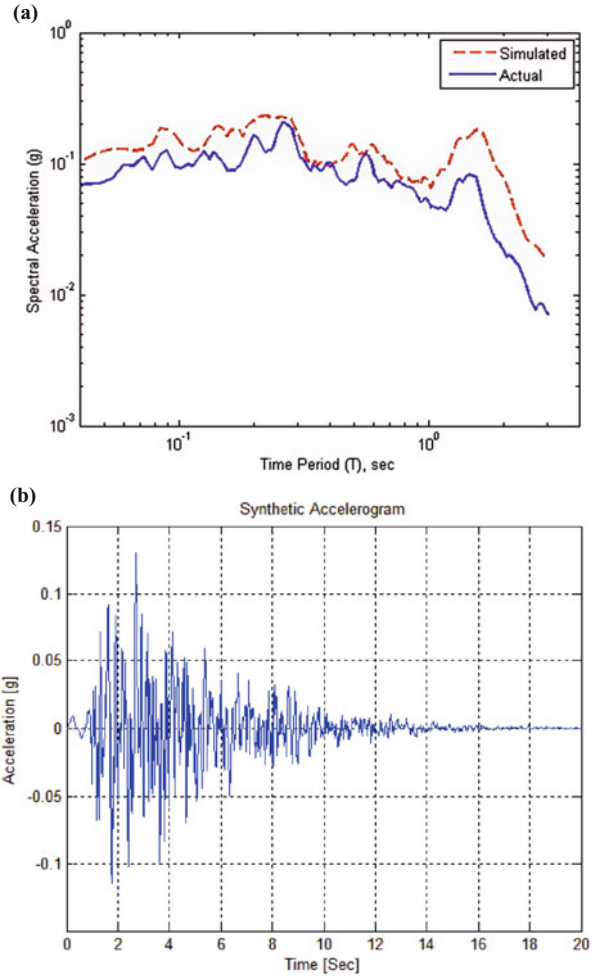

Fig. 2 **a** Acceleration spectra for actual and simulated accelerogram for Loharghat Station. **b** Generated accelerogram from the modified Fourier spectrum

The RPA is performed to obtain the probabilistic seismic capacity of the frame. For the present study, four structural parameters are considered to be random as detailed in Table 1. With the assumed distribution types of the parameters, random samples are generated using Latin Hypercube Sampling (LHS) with reduced correlation. With the generated 100 sets of random parameters and the maximum ISD values are calculated corresponding to each limit state. The three structural limit states or performance levels, i.e. IO, LS and CP as per FEMA 356 are considered for seismic risk evaluation. The median capacity values (m_C) and the associated SD (β_C) are obtained accordingly and are depicted in Table 2.

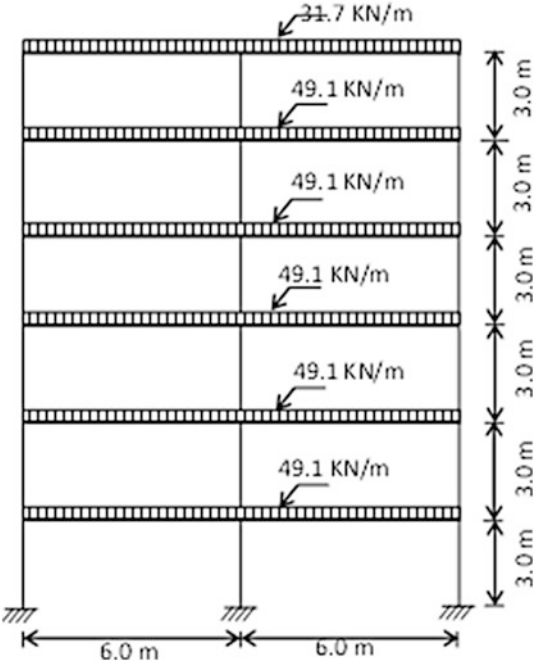

Fig. 3 Elevation of the two-bay steel frame

Table 1 The properties of the random parameters

Uncertainty source	pdf	COV
Dead load	Normal	0.07
Live load	Normal	0.10
Steel yield strength	Log-normal	0.1
Steel elastic modulus	Log-normal	0.02

Table 2 The median capacity and associated SD

Parameter	IO	LS	CP
m_C (%)	0.65	0.7	1.04
β_C	0.06	0.07	0.10

With these parameters, the fragility curves corresponding to all the three limit states are obtained for the considered frame and shown in Fig. 4. With the knowledge of the fragility and hazard curve the annual failure probability, corresponding to the spectral acceleration hazard level of 10% probability of exceedance in 50 years, is calculated from Eq. (13) and are shown in Table 3 for different performance limit states.

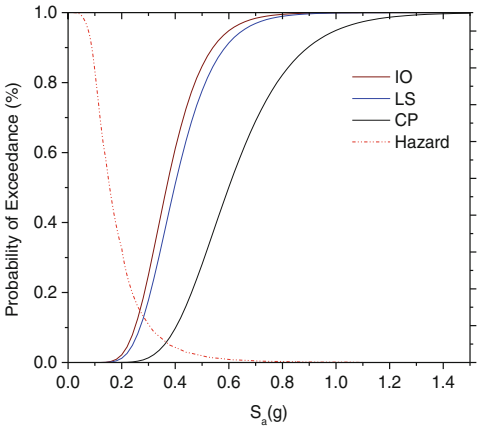

Fig. 4 The seismic fragility curves corresponding to different limit states

Table 3 The annual probability of failure for different performance limit states

Limit state	P_{LS}
IO	0.0071
LS	0.0058
CP	0.0020

6 Discussion and Conclusions

The analytical SFA of steel frame located in the Guwahati city of the NE India is performed in the framework of PBEE and the associated seismic risks are estimated for different limit states. From the fragility curves, it is observed that the structure is associated with high probability of failure for IO limit state corresponding to the spectral acceleration hazard level (i.e. 0.3*g*) at fundamental period of the structure. However for LS and CP limit state, the performance of the structure is rather satisfactory. The hazard value corresponding to 10% probability of exceedance in 50 years as obtained from the PSHA at the fundamental period is close to the hazard value as specified by the Indian code, i.e. 0.36*g*. Hence the spectral acceleration hazard level considered for the present analysis may be regarded as the representative of the IS code specified hazard level. Based on the observations it may be opined that a steel moment frame building located in NE India with the moderate fundamental period when designed according to the IS code guidelines is most likely to perform beyond its elastic range, i.e. beyond IO level when subjected to the IS code specified hazard level. This clearly indicates the need for a more detailed study on nonlinear seismic performance evaluation of structures located in the NE India.

Acknowledgements The financial support received in TSD Scheme No. DST/TSG/STS/2012/45, 21.1.13 from the DST, Govt. of India (for the project entitled 'Seismic vulnerability …. special emphasis to North Eastern Region') for this work is gratefully acknowledged.

References

1. Kwon, O. S., & Elnashai, A. S. (2006). The effect of material and ground motion uncertainty on the seismic vulnerability curves of RC structure. *Engineering Structures, 28*(2), 289–303.
2. Lu, D., Yu, X., Jia, M., & Wang, G. (2014). Seismic risk assessment for a reinforced concrete frame designed according to Chinese codes. *Structure and Infrastructure Engineering, 10* (10), 1295–1310.
3. Nath, S. K., Thingbaijam, K. K. S., & Raj, A. (2008). Earthquake hazard in Northeast India—A seismic microzonation approach with typical case studies from Sikkim Himalaya and Guwahati city. *Journal of Earth System Science, 117*(S2), 809–831.
4. Das, S., Gupta, I. D., & Gupta, V. K. (2006). A probabilistic seismic hazard analysis of Northeast India. *Earthquake Spectra, 22*(1), 1–27.
5. Pathak, J. (2008). Earthquake vulnerability assessment of Guwahati urban centre. In *The 14th World Conference on Earthquake Engineering*, Beijing, China.
6. Sarkar, P., Patir, B. K., & Menon, D. (2004). Survey and Assessment of seismic safety of multistoreyed buildings in Guwahati, India. In *13th World Conference on Earthquake Engineering*, Vancouver, Canada.
7. Jalayer, F. (2003). *Direct probabilistic seismic anaysis: Implementing non-linear dynamic assessments* (Ph.D. thesis). Department of Civil and Environmental Engineering, Stanford, CA.
8. Wen, Y. K., Ellingwood, B. R., Veneziano, D., & Bracci, J. (2003). *Uncertainty modeling in earthquake engineering*, MAE Project FD-2 Report. USA: Mid-America Earthquake Center.
9. IS 1893 (Part 1). (2002). *Indian standard criteria for earthquake resistant design of structures, part 1: general provisions and buildings* (5th revision). New Delhi: Bureau of Indian Standards.
10. Kaul, M. K. (1978). Stochastic characterization of earthquakes through their response spectrum. *Earthquake Engineering & Structural Dynamics, 6,* 497–509.
11. Gasparini, D. A., & Vanmarcke, E. H. (1976). *SIMQKE, a program for artificial motion generation, user's manual and documentation*, Publication R76-4. Cambridge, Massachusetts: MIT Press.
12. Saragoni, G. R., & Hart, G. C. (1974). Simulation of artificial earthaquakes. *Earthquake Engineering & Structural Dynamics, 2,* 249–268.
13. Boore, D. M. (2003). Simulation of ground motion using the stochastic method. *Pure and Applied Geophysics, 160*, 635–676.
14. Federal Emergency Management Agency (FEMA). (2000). *Prestandard and commentary for the seismic rehabilitation of buildings*, Rep. No. 356—FEMA, Washington, DC.

Seismic Vulnerability Assessment of Open Ground Storey Buildings

G. V. Rama Rao, N. Gopalakrishnan and K. Sathish Kumar

Abstract Open Ground Storey (OGS) in multistoried buildings is meant for a parking space within a building plan. These buildings have reduced stiffness at the ground storey due to absence of in-fill walls. The abrupt change in the stiffness of the open ground storey compared to the stories at the top result in huge seismic displacement demand, to be borne by the ground storey itself. Conflict demand between seismic safety and functional requirement, and moreover huge number of OGS buildings in urban areas in India, necessitates the seismic vulnerability assessment of OGS buildings. In the present paper, a simplified procedure to assess the level of severity of OGS building is developed using plastic hinge concept. The simplified procedure is validated with the shake table experiment conducted on three-storey model OGS building. The simplified procedure will help to identify the urgency for repair and rehabilitation of OGS buildings.

Keywords Open ground storey · Seismic vulnerability assessment
Shake table · Soft storey

1 Introduction

Urban residential buildings of a special class have been and are being built in India, which has open ground stories and are built with prescriptive dimensions without proper seismic design. The number of such buildings in the country runs in lakhs, and such buildings are located in urban areas of moderate to severe seismic zones of

G. V. Rama Rao (✉) · K. Sathish Kumar
CSIR-Structural Engineering Research Centre, Chennai 600113, India
e-mail: ramarao@serc.res.in

K. Sathish Kumar
e-mail: ksk@serc.res.in

N. Gopalakrishnan
CSIR-Central Building Research Institute, Roorkee 247667, India
e-mail: director@cbri.res.in

A. Rama Mohan Rao and K. Ramanjaneyulu (eds.), *Recent Advances in Structural Engineering, Volume 1*, Lecture Notes in Civil Engineering 11,
https://doi.org/10.1007/978-981-13-0362-3_83

the country. A number of these buildings are being built simply and not being designed as per sound practices of earthquake-resistant design. Past earthquakes worldwide (including the events in India during the past two decades) have shown that these structures are vulnerable. Open Ground Storey (OGS) structures are reinforced concrete frames consisting of beams and columns with in-fill walls made of masonry available only in the top stories and left open (without in-fill) at the ground storey. Functionally, these are built for the purpose of parking of vehicles. These structures characterized by the vertical stiffness irregularities cause the discontinuity in force and displacement flow and causes excessive displacement demands from the ground floor during seismic actions. Damage of such structures is concentrated in the ground floor and none of the other elements show any sign of significant damage.

Street parking is difficult in many urban areas, where the available road widths are small. Hence, between the municipal authorities and architects, a solution was achieved to take motorized vehicles off the road, and move them to the ground storey of the buildings. To a large extent, this has helped to overcome the parking problem. Having parking in the ground storey is not a concern, but removing all masonry walls in the ground storey and leaving the exposed slender 230 mm wide columns, is the crux of the matter. Removing all in-fill masonry walls in the ground storey makes the whole building flexible and weak in that storey. It is important to sensitize the general public (stake holders), approving agencies and construction contractors about the high vulnerability of these classes of structures to lateral seismic loadings. Along with that, existing municipal and urban rules that govern the construction of new apartment buildings in India also tempt the builder to choose parking space within the building, make highly vulnerable situation.

IS 1893(Part 1): 2002 [1] defines soft storey, as one in which the lateral stiffness is less than 70% of that in the storey above or less than 80% of the average lateral stiffness of the three stories above. Because of such a configuration, more seismic force is attracted in the ground storey level and the displacement demand has to be realized fully from the ground storey. A high level of ductility (with associated damage and in-elastic rotations) is expected from axially loaded compressive members, which are incapable of giving such a demand (columns). P-Δ effects, Secondary moments are generated in these columns due to their large deformation resulting in lack of stability. Due to all these reasons, the damage is sudden, catastrophic and without warning.

The usual way to address and solve the soft storey is to avoid, by introducing the in-fills in the soft storey. However, IS 1893(Part-1): 2002 [1] suggests the columns and beams of the soft storey are to be designed for 2.5 times the storey shears and moments calculated under seismic loads specified in the other relevant clauses. But this may not solve the full problem, as displacement demands are not satisfied by the above suggestion. Addition of shear walls throughout the height of the building will solve the problem. After retrofit, it is necessary to check the displacement behaviour through proper nonlinear analysis.

Internationally, quite a number of literature on the performance and retrofit of open ground storey structures emanate from Turkey and Greece [2]. References [3]

and [4] explain the behaviour of soft storey buildings. References [5] and [6] discuss the strengthening options for soft storey buildings. But there is not much published guidance on how to carry out a quick assessment of soft storey buildings. Reference [7] proposed a fast and simple seismic risk-assessment procedure for vulnerable urban building stocks. A performance score for determining the risk priorities of buildings is proposed. Statistical correlations have been obtained for measuring the sensitivity of damage to the assigned performance score by employing a database consisting of 454 damaged buildings surveyed after the 1999 Düzce earthquake in Turkey. This study highlighted the presence of soft storey and heavy overhangs significantly influence the seismic vulnerability of the building. Reference [8] presented a review of the available methods for Rapid Visual Screening (RVS) of RC-frame buildings and proposes a RVS method for RC-frame buildings in India based on systematic studies on damage data of the 2001 Bhuj earthquake. This study also highlighted the significance of soft storey.

OGS buildings stock is the majority of the class of buildings in Indian urban places, which are highly vulnerable to earthquake. The conflict between the demand of seismic safety and the functional requirement to provide a parking space within a building plan necessitates the seismic vulnerability assessment of the OGS buildings. Due to the huge stock of OGS buildings, a simplified and quick methodology to assess the severity is very much necessary. In the present paper, a simplified procedure to assess the level of severity of OGS building is developed using plastic hinge concept. The plan symmetrical OGS building is represented into an SDOF system as an inverted pendulum with a heavy mass at the top such that the entire deformation of the structure is felt only by the OGS columns. Displacement Demand–Capacity Ratio (DCR) is used to evaluate the severity of the risk of an OGS building for local seismic hazard and can be calculated as a ratio of displacement demand to displacement capacity. The value of DCR larger than one indicates that the building requires retrofit to avoid the soft storey mechanism. If the DCR is more than 1, it indicates that the building requires retrofit to avoid the soft storey failure mechanism, and precisely it indicates that urgent detailed evaluation is required before decides its vulnerability.

The simplified procedure is validated with the nonlinear static analysis and the shake table experiment conducted on three storey model OGS building. The proposed simplified procedure will help to identify the urgency for repair and rehabilitation of OGS buildings.

2 Simplified Procedure for Assessment of Open Ground Storey Buildings

A simplified procedure to assess the level of severity of OGS building is developed using plastic hinge concept. The main assumption in this procedure is that the whole structure behaves as a single degree of freedom system as an inverted

pendulum with a heavy mass at the top such that the entire elastic deformation of the structure is felt only by the OGS columns. Further, the columns in the OGS are rotationally restrained at top of the stilt floor and at the foundation level. They are free to translate at top of the stilt floor only. The displacement demand–capacity ratio is used to evaluate the severity of the risk of an OGS building for local seismic hazard. The displacement demand–capacity ratio is calculated using yield and ultimate curvature of the representative column section in the open ground storey. The moment and curvature at yield and ultimate for the representative column can be obtained using section analysis by using modified mander's model [9] for confined concrete and suitable model for steel reinforcement. As the OGS column bent in double curvature the force at it yield will be yield moment divided by half of the height of the column. A check should be made to avoid premature shear failure; the yield (or ultimate) force should be lower than the shear strength of column.

As the representative column is free to translate at top of the stilt floor only, the yield displacement (Δ_y) of the soft storey representative column can be calculated using the yield curvature (ϕ_y) by the following expression Eq. (1).

$$\Delta_y = \frac{\phi_y h^2}{6} \tag{1}$$

where h is the height of the open ground storey. The displacement capacity (Δ_u) of the soft storey is the sum of yield displacement and the plastic displacement due to post-yield plastic rotation of the soft storey columns and it can be worked as the function of the ultimate curvature (ϕ_u) and yield curvature, plastic hinge length and total height of the open ground storey.

$$\Delta_u = (\phi_u - \phi_y) l_p (h - l_p) + \frac{\phi_y h^2}{6} \tag{2}$$

Plastic hinge length (l_p) can be estimated using expressions given in the literature or it can be assumed that it is half the depth of the section. Displacement ductility capacity (μ) of the overall structure is derived from the ductility of soft storey columns and can be estimated using Eq. (3).

$$\mu = \frac{6(\phi_u - \phi_y) l_p (h - l_p)}{\phi_y h^2} + 1 \tag{3}$$

The seismic demand on the soft storey building for the local seismicity can be estimated using IS 1893(Part-1): 2002 [1] by assuming total displacement demand of OGS columns are equal to their elastic displacement demand ($R = 1$), such that the equal displacement rule applies and not equal energy rule. The time period of the structure can be estimated from the total stiffness of the columns in open ground storey and the total mass of the above structure. The stiffness can be calculated using the above-estimated force and displacement at yield. The force demand can be obtained by multiplying the mass with the horizontal acceleration (A_h)

correspond to Maximum Considered Earthquake (MCE) obtained from the spectrum given IS 1893 for a corresponding calculated time period of the building. The force demand to yield force is similar to response reduction factor, which should be less than the available displacement ductility capacity. The displacement demand (Δ_d) can be calculated using Eq. (4).

$$\Delta_d = \frac{1}{4\pi^2}\frac{A_h}{f^2} \tag{4}$$

where the 'f' is the natural frequency of the building, which is inverse of the time period of the building (T). The displacement Demand Capacity Ratio (DCR) is used to evaluate the severity of risk of an OGS building for local seismic hazard and is given in Eq. (5).

$$\text{DCR} = \frac{\Delta_d}{\Delta_u} < 1.0 \tag{5}$$

The DCR above one indicates that the building requires retrofit to avoid the soft storey mechanism; precisely it indicates that urgent detailed evaluation is required before decides its vulnerability.

3 Validation of Proposed Simplified Procedure

The proposed simplified procedure is validated with shake table experiment conducted on a three storey model OGS building and the pushover analysis made on typical multistoried building model using SAP software. In order to understand the importance of soft storey effect and ductile detailing, a half-scale model of three-storey RC building with soft storey is constructed and tested on 4 m × 4 m, 30T shake table at Advanced Seismic Testing and Research Laboratory (ASTaR Lab), CSIR-Structural Engineering Research Centre, India. The building is three storied with a total height of 4.8 m, two bays in X-direction and single bay in Y-direction. Storey height of the specimen at each floor is 1.6 m. The RC building is OGS frame having in-fills at higher floors and kept open at the ground floor. Non-ductile detailing is incorporated by means of large stirrup spacing (6 mm ϕ @ 150 mm c/c) and 90° hook. The dimensions of beam and column are 150 × 150 mm. The reinforcement details are for column 4#12 mm ϕ, 6 mm ϕ stirrups @ 150 mm c/c, with 90° hook (weak column) and for beam 4#16 mm ϕ, 6 mm ϕ stirrups @ 150 mm c/c, with 90° hook (strong beam). The slab thickness is 100 mm and base is a raft foundation, which is used for connect the model to shake table. Figure 1 shows the shake table test of OGS model frame. Materials used are M 25 grade concrete and Fe 415 steel. The additional mass of 1200 kg has been added on each floor to represent an equivalent live load. The length of the beam in

Fig. 1 Shake table test of OGS model frame

shorter direction is 2 m. The length of the continuous beam in longer direction is 3 m (bay width is 1.5 m). Displacement and Acceleration at each floor level is measured.

The earthquake time history compatible to response spectrum given in Indian standard code of practice IS-1893(Part 1): 2002 [1] for soft soil spectrum is used and it is modified by considering frequency scaling of $\sqrt{2}$ by similitude law for the half-scale model of reinforced concrete frame. The earthquake time history is

applied in a longer direction (uni-axial excitation), progressively increasing the acceleration levels (PGA levels) and the response is measured. Reference [10] has given details of experimental programme and results. OGS behaviour is clearly depicted wherein the drift value is very high for the ground storey compared to the second and third storey. The test building failed at a maximum peak ground acceleration value of 7.99 m/s^2 (0.814 g). The corresponding response acceleration value at the third storey level is 11.44 m/s^2, with an amplification of 1.43. Maximum base shear is 116.48 kN. The RC-frame model has undergone a maximum displacement of 48.75 mm at third storey level at final failure stage.

The force and displacement capacities of the reinforced concrete model frame are determined analytically using the developed simplified procedure. The force and displacement capacity of the experimental OGS reinforced concrete model frame building is calculated. Based on the concrete grade, reinforcement detailing, cross section and the weight (axial load) of the reinforced concrete frame model, the following moment–curvature values are determined, using a section analysis. Yield Moment (M_y) is 13.17 kN-m, Ultimate moment (M_u) is 13.58 kN, Yield curvature (ϕ_y) is 0.000048 rad/mm and Ultimate curvature (ϕ_u) is 0.000275 rad/mm. l_p is taken as D/2 (D-depth of column). Total displacement capacity, $\Delta = \Delta_y + \Delta_p =$ 46.55 mm. The force capacity and the maximum displacement obtained from the shake table experiment is 11.65 t as against 11.075 t from the simplified method and 48.75 mm as against 46.55 mm from the simplified method respectively. Table 1 shows the validation of simplified procedure with shake table test of OGS model frame.

Also, the simplified procedure is validated with the nonlinear static analysis conducted on five-storey OGS building using SAP software. Pushover analysis is done for better understanding the behaviour of soft storey buildings using SAP software. A five storied building is modelled in SAP 2000 software (Fig. 2). Beams and columns are modelled as 3D frame elements. The material properties of concrete and steel rebar including unit weight, modulus of elasticity, Poisson's ratio, shear modulus, characteristic compressive strength, yield stress and ultimate stress has been provided. Beams and columns are then assigned the respective cross-section dimensions, materials and reinforcement.

A design is made using IS 456: 2000 [11]. Rigid beam–column joints have been modelled by giving end length offsets to the frame elements. To take into account the structural effect of slabs, diaphragm constraint has been assigned at each floor level. The brick in-fill is modelled as equivalent diagonal compression strut elements. Rigid joints connect the beams and columns, but pin joints at the beam-to-column junctions connect the equivalent struts. The considered building

Table 1 Validation of the simplified procedure with shake table test of OGS model frame

	Experiment	Simplified procedure
Displacement capacity	48.75 mm	46.55 mm
Force capacity	11.65 ton	11.07 ton

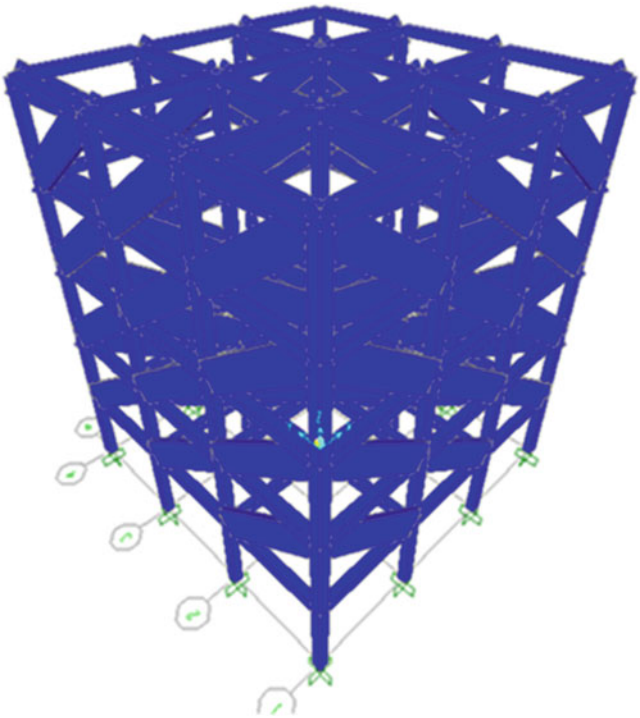

Fig. 2 Five-storey OGS building—SAP model

Table 2 Validation of the simplified procedure with nonlinear static analysis

	Pushover analysis	Simplified procedure
Displacement capacity	95.2 mm	98 mm
Force capacity	106 ton	120 ton

model is identical in plan, consisting of 3 bays in both *X*-direction and *Y*-direction with a bay width of 4 m. The storey height is 3 m. Dead load and live loads are applied as gravity loading. Table 2 shows validation of simplified procedure with the nonlinear static method. The proposed simplified procedure fairly gives good matching in case of plan symmetrical buildings.

4 Parametric Study Using Prescriptive Dimensions

A parametric study is carried out considering the prescriptive reinforcements and dimensions of ground floor columns of the OGS buildings in India. The study made for stilt+1 storey building to stilt+4. The column sizes are varied between 230 and 450 mm, commonly used, and are considered as prescriptive dimensions. The reinforcement is varied between 1 and 2%, which is also considered based on prescriptive reinforcement used for various dimensions of the column. The height of the OGS is considered as 3 and 2.4 m cases. Axial load on OGS columns are calculated approximately by assuming 4 m bay width in both directions. The material and other data are considering prevailing site conditions. Two cases of shear reinforcements are considered, these are confined case and unconfined case. Detailed as per IS 13920: 1993 [12] codal provisions, is considered as the confined case. Non-compliant shear reinforcement with 90-degree hooks is considered as the unconfined case. The study made for various zones and by varying the soil type.

The displacement Demand–Capacity Ratio (DCR) is used to evaluate the severity of risk of an OGS building for local seismic hazard. Typical outcome from the study is given in Figs. 3, 4, 5 and 6, the dashed line above DCR indicates the OGS building is vulnerable. Ductile detailing plays a role in controlling the soft storey mechanism. Figures 3 and 4 for soft storey building with 230 mm × 230 mm column in zone V and zone II respectively. Figures 5 and 6 for soft storey

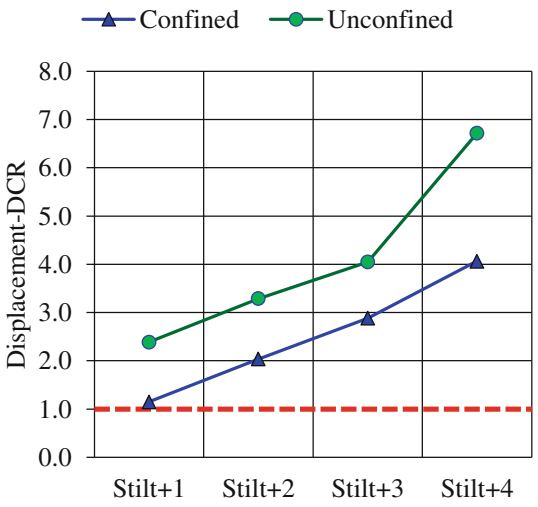

Fig. 3 Soft storey building with 230 × 230 mm column —zone–V

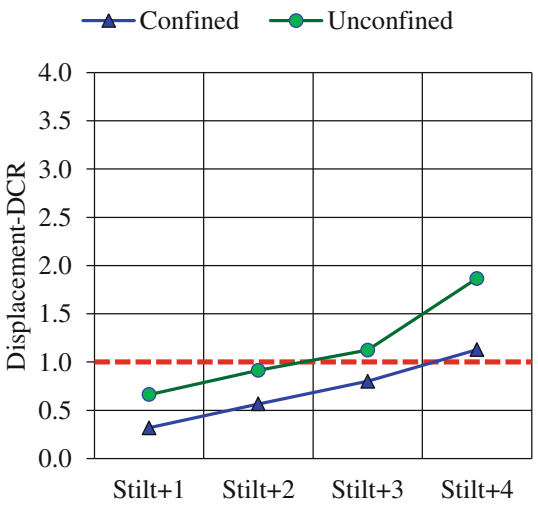

Fig. 4 Soft storey building with 230 × 230 mm column —zone–II

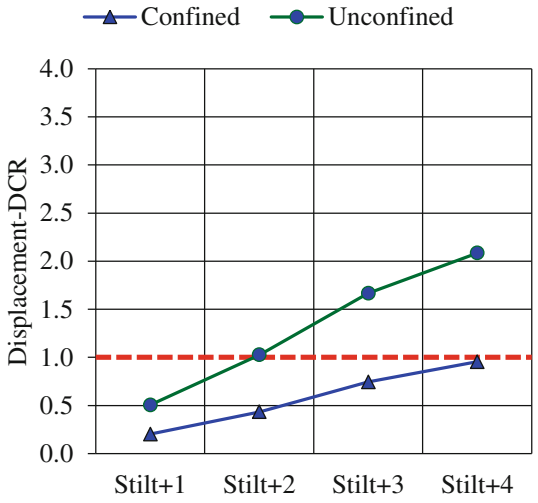

Fig. 5 Soft storey building with 450 × 450 mm column —zone–V

building with 450 mm × 450 mm column in zone V and zone II respectively. This parametric study is made on an assumed building for the purpose to show the effect of zone location and ductile detailing. These cannot be directly applicable to the other buildings.

Fig. 6 Soft storey building with 450 × 450 mm column —zone–II

5 Summary

OGS buildings are highly vulnerable to earthquake, since it is conflict demand from the function requirement point and a huge stack of OGS buildings existed in Indian urban places, makes the assessment and retrofit is a major challenge. In this paper, a simplified procedure to assess the level of severity of OGS building is proposed using plastic hinge concept. The simplified procedure is validated with the non-linear static analysis and the shake table experiment conducted on three-storey model OGS building. The simplified procedure will help to identify the urgency for repair and rehabilitation of OGS buildings.

Acknowledgements We thank and acknowledge Dr. N. Lakshmanan, Former Director, CSIR-SERC, for his immense help and valuable guidance. The authors record their sincere thanks for the excellent cooperation rendered by the staff of Advanced Seismic Testing and Research Laboratory, CSIR-SERC, Chennai.

References

1. IS 1893 (Part 1): 2002. Indian Standard criteria for earthquake resistant design of structures. *Bureau of Indian Standards*, New Delhi, India.
2. Arslan, M. H., & Korkmaz, H. H. (2007). What is to be learned from damage and failure of reinforced concrete structures during recent earthquakes in Turkey? *Engineering Failure Analysis, 14*(1), 1–22.
3. Chopra, A. K., Clough, D. P., & Clough, R. W. (1973). Earthquake resistance of buildings with a soft first story. *Earthquake Engineering and Structural Dynamics, 1*(4), 347–355.

4. Arlekar, J. N., Jain, S. K. & Murty, C. V. R. (1997). Seismic response of RC frame buildings with soft first storeys. In *Proceedings of the Golden Jubilee Year Conference on Natural Hazards in the Urban Habitat,* New Delhi, pp. 13–24.
5. Kaushik, H. B., Rai, D. C., & Jain, S. K. (2009). Effectiveness of some strengthening options for masonry-infilled RC Frames with open first storey. *Journal of Structural Engineering, ASCE, 135*(8), 925–937.
6. Sahoo, D. R., & Rai, D. C. (2013). Design and evaluation of seismic strengthening techniques for reinforced concrete frames with soft ground story. *Engineering Structures, 56,* 1933–1944.
7. Sucuoğlu, H., Yazgan, U., & Yakut, A. (2007). A screening procedure for seismic risk assessment in urban building stocks. *Earthquake Spectra, 23*(2), 441–458.
8. Jain, S. K., Mitra, K., Kumar, M., & Shah, M. (2010). A screening procedure for seismic risk assessment in urban building stocks. *Earthquake Spectra, 26*(3), 709–729.
9. Mander, J. B., Priestley, M. J. N., & Park, R. (1988). Theoretical stress strain model for confined concrete. *Journal of structural Engineering, ASCE, 114*(8), 1804–1826.
10. Muthumani, K., Gopalakrishnan, N., Sathish Kumar, K., Sreekala, R., & Rama Rao, G. V. (2011). *Assessment of methodologies for seismic performance evaluation of structures*, *SERC Research Report, MLP 142–12*.
11. IS 13920. (1993). Indian Standard Ductile detailing of reinforced concrete structures subjected to seismic forces—Code of practice. *Bureau of Indian Standards*, New Delhi, India.
12. IS 456. (2000). Indian Standard plain and reinforced concrete—Code of practice. *Bureau of Indian Standards*, New Delhi, India.

Cyclic Behavior of Retrofitted-Reinforced Concrete Coupling Beams

Romanbabu M. Oinam, P. C. Ashwin Kumar, Dipti Ranjan Sahoo and Kaushik Maran

Abstract Coupling beams are utilized in shear walls to connect one shear wall to another. A high amount of reinforcement is required in these beams to resist the forces developed during a seismic event. Generally, the main reinforcements in a coupling beam are provided in a diagonal manner but due to the high reinforcement content, the constructability and construction time management becomes an issue. Past earthquakes and experimental studies on coupling beams have shown that these members are subjected to high shear forces and it becomes imperative that the members should have adequate shear reinforcement. To reduce the reinforcement concentration and enhance the ductility of coupling beam, an experiment was conducted on two coupling beam specimens, (a) reinforced concrete specimen with the double-beam-type reinforcement arrangement, and (b) steel fiber-reinforced concrete specimen with again the double-beam-type reinforcement arrangement. Both beams were geometrically identical and were subjected to a reversed-cyclic loading up to 6% lateral drift. The steel fiber-reinforced concrete specimen showed higher resistance than the reinforced concrete specimen. The failure patterns

R. M. Oinam
Department of Civil Engineering, National Institute of Technology, Warangal 506004, India
e-mail: romanbabu@nitw.ac.in

P. C. Ashwin Kumar
Department of Earthquake Engineering, Indian Institute of Technology, Roorkee 247667, India
e-mail: pcashwin.feq2018@iitr.ac.in

D. R. Sahoo (✉) · K. Maran
Department of Civil Engineering, Indian Institute of Technology Delhi, New Delhi 110016, India
e-mail: drsahoo@civil.iitd.ac.in

K. Maran
e-mail: kaushikmaran93@gmail.com

A. Rama Mohan Rao and K. Ramanjaneyulu (eds.), *Recent Advances in Structural Engineering, Volume 1*, Lecture Notes in Civil Engineering 11,
https://doi.org/10.1007/978-981-13-0362-3_84

observed in steel fiber-reinforced specimen showed distributed microcracks, whereas the reinforced concrete specimen showed wider and fewer numbers of cracks.

Keywords Reinforced concrete · Steel fiber · Coupling beam · Shear force Ductile

1 Introduction

The lateral load resistance of the reinforced concrete coupled shear walls is greatly affected by the response of their coupling beams. Coupling beams tie the individual shear wall and convert the lateral load resisting response from an individual wall flexural action to an axial compression–tension couple between two walls. Thus, for the satisfactory performance of coupled shear walls, it is imperative that the coupling beam has adequate strength and ductility under large cyclic displacements. Paulay [1] highlighted the inadequacy of the conventional longitudinal beam reinforcements in coupling beams and a subsequent study by Paulay and Binney [2] demonstrated the advantage of having higher ductility by providing diagonal reinforcement in coupling beams. Other alternatives to achieve higher ductility in coupling beam have also been investigated, namely, "rhombic" reinforcement detail in coupling beams [3, 4], diagonally reinforced coupled beams with alternate confinement detail [5], steel and hybrid steel–concrete composite coupling beams [6], use of double-beam coupling beam reinforcement detailing [7] and use of high-performance fiber-reinforced concrete [8, 9]. However, these alternatives have not been implemented widely due to issues related to performance, constructability and fewer numbers of studies. Hence, it is the diagonal reinforcement detailing as shown in Fig. 1, which is widely used in coupling beams to achieve enhanced lateral load resisting performance. As it is evident from Fig. 1, the provision of diagonal reinforcement with the column-type transverse reinforcement to confine each diagonal reinforcement poses great difficulty in terms of constructability and construction time management. This has been the main motivation for the alternative studies as mentioned above. Similarly, this study investigates the provision of double-beam reinforcement arrangement with the fiber reinforcement to enhance the ductility and to avoid reinforcement congestion in the coupling beam. Experimental investigation was carried out on two coupling beam specimens, (a) Reinforced concrete (RC) specimen with double-beam-type reinforcement arrangement, and (b) Steel Fiber-Reinforced Concrete (SFRC) specimen with again the double-beam-type reinforcement arrangement. The hysteresis response, energy dissipation capacity and stiffness degradation response of both the specimen were studied to highlight the advantage of using fiber-reinforced double-beam-type reinforcement in coupling beam.

Fig. 1 Diagonal reinforcement detailing in coupling beam

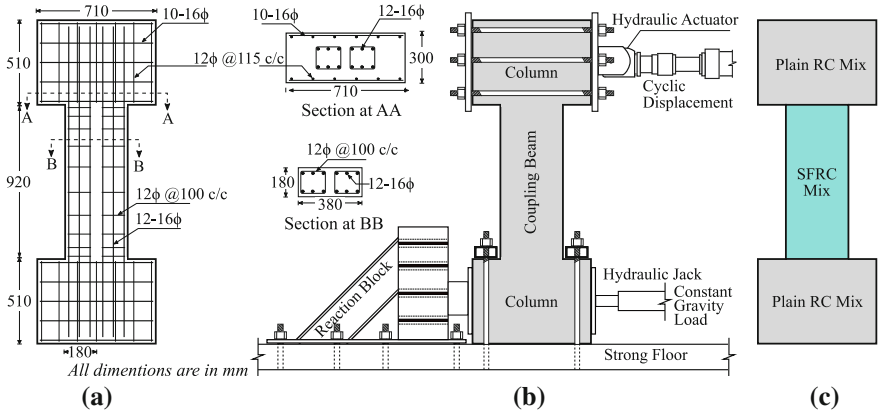

Fig. 2 **a** The reinforcement detailing of coupling beams, **b** details of test setup and **c** location of SFRC

2 Experimental Programs

The details of the test specimen, material properties and loading history are discussed in the following sections. The dimensions and the reinforcement details of the coupling beams are as shown in Fig. 2a. The dimensions and the reinforcement detailing of both RC and SFRC specimen was kept the same. The region of the SFRC in the test specimen is as shown in Fig. 2c.

2.1 Material Properties

Ordinary Portland cement (OPC) was used in the preparation of cement concrete used in the casting of the test specimens. Natural sand confirming to Zone-II was

used as fine aggregates [10]. The maximum size of coarse aggregates used in concrete was limited to 12.5 mm as the use of 20 mm aggregates lead to workability issues. This was also done to limit the nominal cover to 15 mm. Concrete mix was designed for a characteristic cube compressive strength of 25 MPa which resulted in a target mean cube compressive strength of 31.6 MPa as per Indian Standard IS: 10262-1982 [10] code provisions. The design mix proportion for the cement concrete was taken as 1.0:2.6:2.3 (cement: sand: coarse aggregate) for a water–cement ratio of 0.45 and a compaction factor of 0.9. End-hooked steel fibers of 60 mm length and 0.75 mm diameter (i.e. fiber aspect ratio = 80) were used into the concrete mix of the SFRC specimen. The specified tensile yield strength of steel fibers was 1100 MPa. Usually, the increase in fiber content reduces the workability of concrete and ACI Committee 318-08 [11] recommends a minimum fiber content of 0.75% to be used in the concrete construction. Although higher fiber content has been used in different research applications [12–16], a fiber content of 1% has been used in the SFRC specimen in this study [17]. To achieve better workability, superplasticizer of 0.5% volume/volume of water was used in the mixing of SFRC.

The average 28-day compressive strength of plain concrete was 35.39 MPa, which was slightly higher than the target mean strength of 31.6 MPa. In case of SFRC, the 28-day compressive strength was found to be 39.5 MPa. This showed a minor increase of about 10% in the compressive strength of SFRC as compared to the plain concrete.

Thermomechanically treated (TMT) steel reinforcement bars were used as both longitudinal reinforcement and transverse stirrups in both the specimens. The minimum specified values of yield stress, ultimate stress, and elongation of TMT bars are 500 MPa, 545 MPa and 12.0%, respectively. Since these bars do not exhibit a definite yield point, the 0.2% proof stress values was considered as the yield stress. Sufficient development length of reinforcement bars was provided at the required locations.

2.2 Test Setup

Servo-hydraulic actuator of 250 kN capacity and stroke length of 125 mm was used to apply the cyclic lateral displacements at one side of the column level of the specimen. The actuator was supported by a reaction frame, which was firmly held to the laboratory strong floor. Figure 2b shows the test setup along with specimen used in this study. The specimens were firmly attached to the strong floor at the bottom column level using high-strength bolts to prevent their possible vertical movements under the lateral loading. Figure 2b shows the details of the attachment of the actuator with the test specimens. Additional supports were also placed at the bottom column level using hydraulic jack, which provided a constant gravity load and a lateral support system to restrict the horizontal movement.

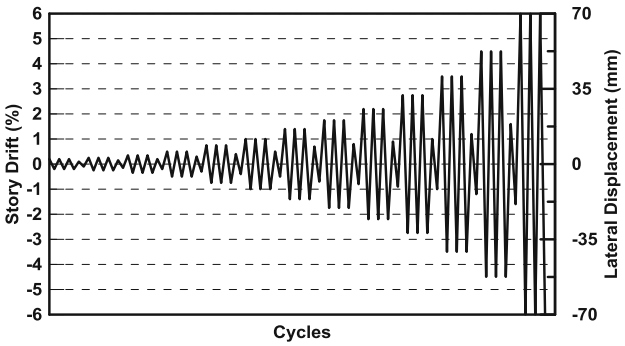

Fig. 3 Imposed displacement profile on specimens

2.3 Loading Protocol

Test specimens were subjected to gradually increasing reversed cyclic lateral displacements in addition to a constant gravity load. Displacement history as specified in ACI Committee 374.1-05 [18] was used for the slow-cyclic testing of specimens in this study. This displacement history consists of drift cycles of 0.20, 0.35, 0.50, 0.75, 1.10, 1.40, 1.75, 2.20, 2.75, 3.50, 4.50, and 6.0% (Fig. 3). Story drift (or drift ratio) may be defined as the ratio of the roof displacement to the height of the story measured from the top of footing to the centerline of the beam. Each displacement cycle was repeated for three times at any drift ratio and then, followed by a single drift cycle of the smaller magnitude. With the help of the hydraulic jack, 10% of column capacity was applied to the lower column face constantly. Figure 2b shows the test setup of coupling beam, which indicates the location of application of gravity load and cyclic displacement load.

3 Results

Two tests, namely, slow load control test and slow-cyclic displacement control test, were carried out on the test specimens. Slow load control test was conducted to determine the initial stiffness of specimen, whereas the slow-cyclic displacement control test was carried out to study the overall behavior under the action of lateral loading condition. The results of these tests are discussed in the following sections.

3.1 Hysteresis Response

Figure 4a, b shows the comparison of experimental results in terms of hysteresis loop and backbone curve of both specimens. The maximum load resisted by RC

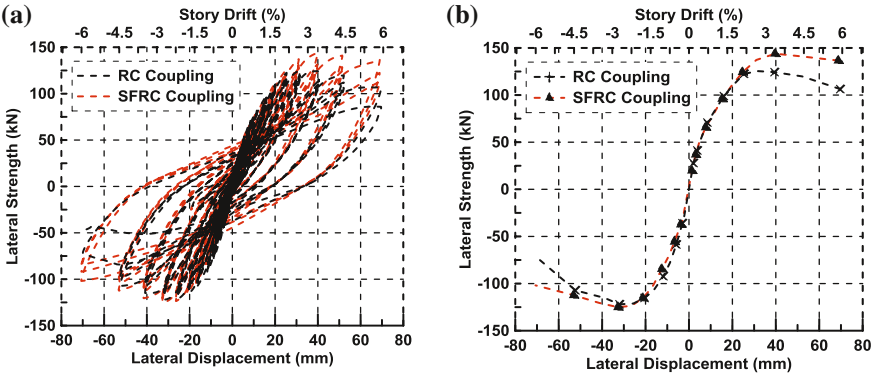

Fig. 4 Comparison of experimental results **a** hysteresis and **b** backbone curve

specimen was 125.4 and 122.1 kN in pull and push directions respectively. First microcrack in the RC specimen appeared on the coupling beam face at 0.35% lateral drift level. Most of the microcracks were observed near beam and column joints, however, at higher drift level, major cracks were concentrated near the bottom of the coupling beam. Up to 1.0% drift level, flexural behavior was observed; however, just after the starting of 1.4% drift-level major cracks appeared on coupling beam face vertically. At 2.2% drift level, maximum peak load of specimen was observed; after this drift level, load degradation was observed up till the end. Maximum lateral drift resisted by this specimen was 6.0%.

SFRC specimen resisted a maximum lateral load of 143.9 and 125.1 kN in pull and push directions respectively. At 0.35% drift level, few microcracks were observed near upper and bottom end of coupling beam. Later, most of the existing microcracks expanded at higher drift level under flexural action, and this flexural nature continued up to 1.4% drift level. First shear crack was observed at 1.75% drift level while for the RC specimen it was observed at 1.4% drift.

3.2 Stiffness Degradation

The effective lateral stiffness (K_{eq}) in each drift cycles was obtained as the ratio of the lateral load resisted by the specimens to the corresponding displacement values observed in both pull and push directions as per FEMA 356, 2000 [19]. The equation to calculate effective lateral stiffness is given in Eq. (1). Figure 5 shows a comparison of effective lateral stiffness degradation of both specimens. Initial and final stiffness of RC specimen was 13.2 and 1.28 kN/mm respectively; while for the SFRC specimen it was 12.0 and 1.7 kN/mm, respectively. SFRC specimen had a bit lower initial stiffness compared to RC specimen; however, SFRC specimen had higher final stiffness value.

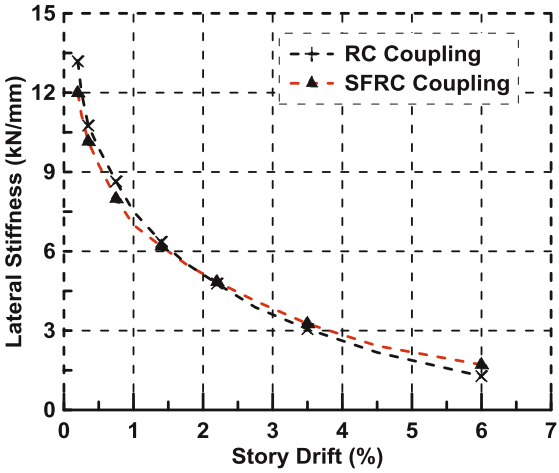

Fig. 5 Stiffness degradation curve

There was the absence of severely damaged in SFRC specimen while RC specimen observed severe damage at the end of the experiment Fig. 7; this can be related to the observation of higher final stiffness in SFRC specimen. However, both specimens had a very close value of effective lateral stiffness at all intermediate drift level.

$$K_{\text{eq}} = (F^{+} - F^{-})/(\Delta^{+} - \Delta^{-}) \tag{1}$$

where F^{+} and F^{-} are the peak positive and negative force, Δ^{+} and Δ^{-} are the peak positive and negative displacement of hysteresis loop.

3.3 Energy Dissipation

Figure 6 shows the cumulative energy dissipated by the RC and SFRC test specimen. There is minor variation in the energy dissipation capacity of the two test specimens in the initial story drifts. However, at higher drift level, the SFRC specimen showed slightly higher energy dissipation capacity. The peak cumulative energy attained by the RC specimen was 21.98 kNm, whereas the SFRC specimen attained a maximum value of 23.58 kNm at 6% lateral drift level. The variation is only 7%.

3.4 Final Damaged State

Figure 7 shows the final damaged state of the test specimens. As it is evidently clear, the RC specimen underwent heavy damage. The concrete at the bottom of the coupling beam in the RC specimen had spalled off leaving the main reinforcement

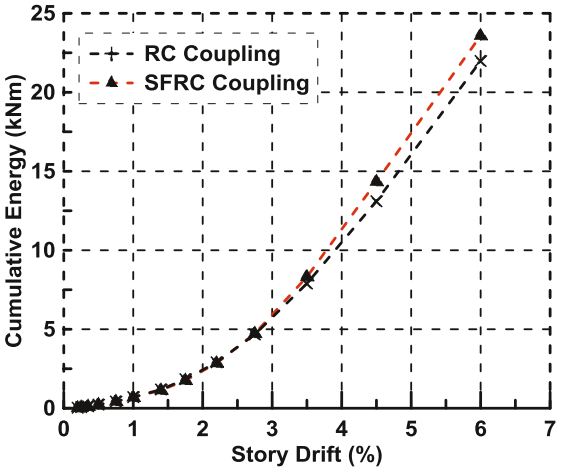

Fig. 6 Cumulative energy dissipation of specimens

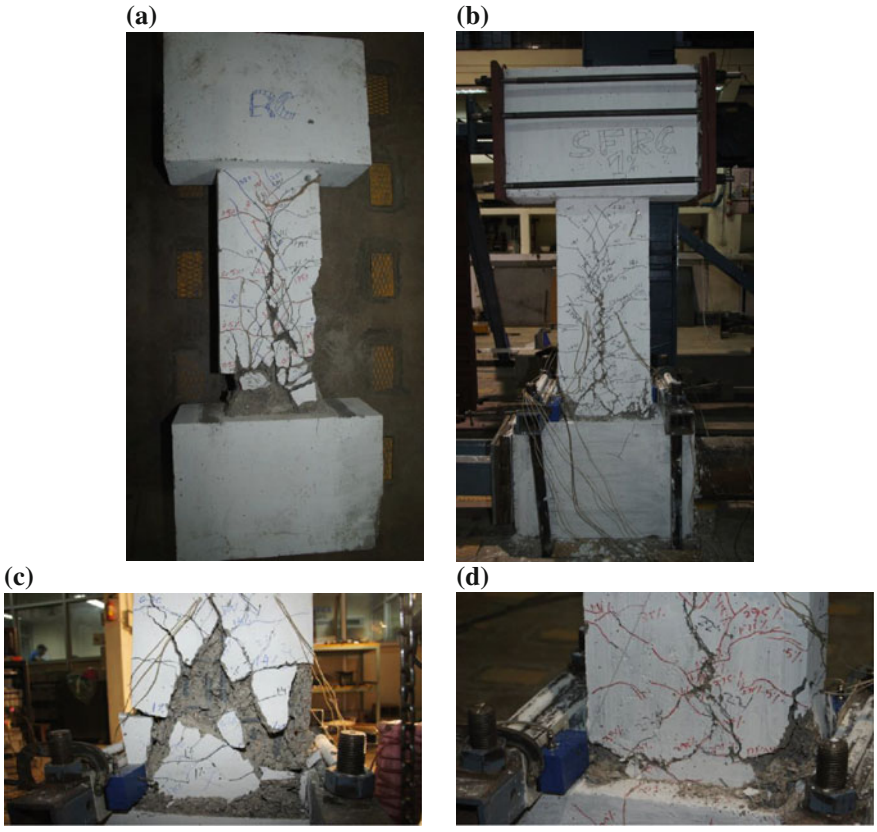

Fig. 7 Damaged state of the test specimen at the end of the experiment

visible. The major crack in the specimen developed along the region in between the double-beam reinforcement arrangement. The possible reason for this can be attributed to the relative motion between the two beams of the double-beam coupling beam arrangement. Additionally, no shear reinforcement was provided in the interface region of the double beams. The major crack in the SFRC specimen also developed in the same region. However, the width and the extent of the crack were much smaller than what was observed in the RC test specimen. Distributed microcracks, more in numbers were also visible in the SFRC specimen but the damage intensity was much lower. The RC specimen underwent greater crushing and cracking in comparison to the SFRC specimen, which was held together due to the bridging action of the steel fibres present.

4 Conclusions

An experimental investigation was carried out on two geometrically identical coupling beam specimens (i.e., RC and SFRC) under the displacement-controlled slow-cyclic loading. The main parameters studied were the hysteretic response and lateral stiffness. Based on this study, the following conclusions can be drawn:

- Both SFRC and RC specimen attained the 6% drift level. However, in terms of the crack width, lateral strength and initiation of reinforcement yielding the SFRC specimen performed better than the RC specimen.
- The SFRC beam was able to withstand a greater peak load of 143.9 kN as compared to the RC beam which could only withstand 125.4 kN. The SFRC beam performed 14.8% better in this aspect.
- The number of cracks in the SFRC members was more in number but was minor and was distributed more or less uniformly in the stressed region of the specimen, showing the bridging action of the steel fibers.
- The failure pattern for both specimens was observed at the mid-region, in between the double-beam arrangement.
- The double-beam reinforcement arrangement proves to be an effective alternative in place for the diagonally reinforced coupling beam.

Acknowledgements The authors are thankful to the Structural Engineering laboratory staffs of the Department of Civil Engineering, IIT Delhi for their help in casting and testing of specimens.

References

1. Paulay, T. (1971). Coupling beams of reinforced concrete shear walls. *Journal of the Structural Division, ASCE, 97*(ST3), 843–861.
2. Paulay, T., & Binney, J. R. (1974). Diagonally reinforced coupling beams of shear walls. *Shear in Reinforced Concrete American Concrete Institute Structural Journal*, *SP-42*, 579–598.

3. Shiu, K. N., Barney, G. B., Fiorato, A. E., & Corley, W. G. (1978). Reversing load tests of reinforced concrete coupling beams. In *Central American Conference on Earthquake Engineering—Conferencia Centroamericana de Ingenieria Siemica*, pp. 239–249.
4. Galano, L., & Vignoli, A. (2000). Seismic behavior of short coupling beams with different reinforcement layouts. *American Concrete Institute Structural Journal, 97*(6), 876–885.
5. Fortney, P. J., Rassati, G. A., & Shahrooz, B. M. (2008). Investigation on effect of transverse reinforcement on performance of diagonally reinforced coupling beams. *American Concrete Institute Structural Journal, 105*(6), 781–788.
6. Harries, K. A., Gong, B., & Shahrooz, B. M. (2000). Behavior and design of reinforced concrete, steel, and steel-concrete coupling beams. *Earthquake Spectra, 16*(4), 775–799.
7. Hajyalikhani, P., & Chao, S. H. (2014). Experimental study on seismic performance of reinforced concrete coupling beams with double beam reinforcement layout. In *Tenth U.S. National Conference on Earthquake Engineering*, pp. 21–25.
8. Canbolat, B. A., Parra-Montesinos, G. J., & Wight, J. K. (2005). Experimental study on seismic behavior of high-performance fiber-reinforced cement composite coupling beams. *American Concrete Institute Structural Journal, 102*(1), 159–166.
9. Lequesne, R., Parra-Montesinos, G., & Wight, J. K. (2013). Seismic behavior and detailing of high-performance fiber-reinforced concrete coupling beams and coupled wall systems. *Journal of Structural Engineering*, *139*(SP-2), 1362–1370.
10. IS:10262. (2009). *Concrete mix proportioning-guidelines*. New Delhi: Indian Standard.
11. ACI 318-08. (2008). *Building code requirements for structural concrete and commentary*. Farmington Hills, MI: American Concrete Institute.
12. Sahoo, D. R., & Sharma, A. (2014). Effect of steel fiber content on behavior on concrete beams with and without shear stirrups. *American Concrete Institute Structural Journal, 111* (5), 1157–1166.
13. Oinam, R. M., Sahoo, D. R., & Sindhu, R. (2014). Cyclic response of non-ductile rc frame with steel fibers at beam-column joints and plastic hinge regions. *Journal of Earthquake Engineering, 18*(6), 908–928.
14. Chao, S. H., Pareek, T., & Sahoo, D. R. (2011). Effect of fiber reinforced concrete in members with highly-complex stress fields. In *High Performance Fiber Reinforced Cement Composites (HPFRCC 6), International Workshop*, June 20–22, pp. 213–220, Ann Arbor, MI.
15. Sahoo, D. R., Flores, C. A., & Chao, S. H. (2012). Behavior of steel fibers reinforced concrete deep beams with openings. *American Concrete Institute Structural Journal, 109*(2), 193–204.
16. Sahoo, D. R., & Chao, S. H. (2010). Use of steel fiber reinforced concrete for enhanced performance of deep beams with large opening. In *ASCE Structural Congress/North American Steel Construction Conference (NASCC)*. September 22–25, pp. 1981–1990, Orland, Florida.
17. Sahoo, D. R., Maran, K., & Kumar, A. (2015). Effect of steel and synthetic fibers on shear strength of RC beams without shear stirrups. *Construction and Building Materials, 83,* 150–158.
18. ACI, Committee, 374.1-05. (2006). *Acceptance criteria for moment frames based on structural testing and commentary—An ACI standara*. Farmington Hills, MI: American Concrete Institute.
19. FEMA 356. (2000). *Prestandard and commentary for the seismic rehabilitation of buildings*. Washington, D. C.: Federal Emergency Management Agency.

Part VI
Structural Health Monitoring

Nonlinear System Identification of Breathing Crack Using Empirical Slow-Flow Model

J. Prawin and A. Rama Mohan Rao

Abstract Most of the existing SHM damage detection methodologies are based on the changes in the system parameters estimated by the linear model fitted to the structure. However, real-life structures exhibit nonlinearity even in their healthy state due to complex joints, interfaces, etc. Nonlinear identification and damage identification are very challenging inverse engineering problems. In this paper, a nonlinear system identification methodology using empirical Slow-Flow Model has been presented. A dynamical system described by slowly varying amplitudes and phases is obtained through performing partition between slow and flow dynamics of the system using the well known complexification-averaging technique. By using the theoretical link between the measured instantaneous parameters through Hilbert transform and slow-flow equations of a system, the system parameters are identified using the classical least square procedure. A numerical simulation study has been conducted on a beam with breathing crack to demonstrate the effectiveness of the proposed algorithm.

Keywords Nonlinear system · Hilbert transform · Slow-flow model
Breathing crack

1 Introduction

Damage sometimes manifests itself as the introduction of nonlinearity into a linear system. The damage that introduces nonlinearity into structures includes post-buckled structures (duffing nonlinearity), fatigue or breathing cracks (bilinear stiffness effect), and rattling joints (impacting systems with discontinuities).

J. Prawin (✉) · A. Rama Mohan Rao
AcSIR, CSIR-Structural Engineering Research Centre, Taramani, Chennai 600113, India
e-mail: prawinpsg@gmail.com

A. Rama Mohan Rao
e-mail: arm2956@yahoo.com

A. Rama Mohan Rao and K. Ramanjaneyulu (eds.), *Recent Advances in Structural Engineering, Volume 1*, Lecture Notes in Civil Engineering 11,
https://doi.org/10.1007/978-981-13-0362-3_85

Damage detection can be significantly enhanced if one accounts for nonlinear characteristics of the structure during extraction of damage sensitive feature [1–4].

A complete list of nonlinear identification techniques developed is very exhaustive and hence to give a reasonable flavor of the range of techniques developed a few of them, with a reasonable success, are mentioned here. The comprehensive list of techniques includes time-series models [5], reverse path spectral methods [6], describing function [7], Volterra and Wiener series [8], adaptive Volterra filter [9], meta-heuristic algorithms [10], time–frequency analysis [11, 12] and so on.

In this paper, a nonlinear system identification method based on correspondence between the analytical and empirical slow-flow equation of the dynamics of the systems is presented. This nonlinear system identification technique using empirical slow-flow model requires only input–output measurement and need not know about the type of nonlinearities present in the system. A numerical simulation study has been carried out on a beam with breathing crack and investigations carried out in this paper clearly indicate that the empirical slow-flow method is an effective scheme for nonlinear parameter estimation even with noisy measurements.

2 Nonlinear System Identification Using Empirical Slow-Flow Model

The slow-flow-based system identification technique (SFMI) is based on multiscale dynamic partitions and the direct analysis of the measured time history response without any knowledge about the system [13]. It partitions the system response in terms of slow and fast components. Generally, a time history response of a structure is composed of a number of well-separated dominant frequency components called fast frequencies of the response and slow dynamic components that are represented by the slowly varying modulations of the fast-frequency components.

The slow-flow model of a nonlinear system provides a good approximation to the original dynamic system and also it governs the long-term behavior of the response. The reduced slow-flow model is easier to analyze than the traditional equations of motion and its parameters such as slowly varying amplitudes and phases provide clear-cut information about the characteristics of the system than the original time history response. This is usually performed by Complexification-Averaging (Cx-A) technique [14].

On the other hand, Hilbert transform to the actual time history response can be applied in order to obtain the instantaneous parameters such as instantaneous amplitude and instantaneous phase/instantaneous frequency. These can be easily related to the slow-flow model parameters obtained analytically through complexification-averaging technique from which the system parameters can be obtained.

3 Complexification-Averaging (Cx-A) Technique

The actual time history response is decomposed into slow and fast dynamics components using the Complexification-Averaging (Cx-A) technique

The Complexification-Averaging Method (CX-A) basically involves the following four steps:

(i) complexification of the equations of motion
(ii) partition of the dynamics into slow and fast component
(iii) averaging of the fast-varying terms and
(iv) extraction of the slow-flow variables from the averaged system.

In order to demonstrate the method, a nonlinear single degree of a system exhibiting a polynomial form of nonlinearity up to fourth order is considered.

$$\begin{aligned} &\ddot{x} + c\dot{x} + k_1 x + k_2 x^2 + k_3 x^3 + k_4 x^4 = 0 \\ &\text{with} \quad x(0) = X,\ \dot{x}(0) = 0, m = 1 \end{aligned} \tag{1}$$

For complexification, complex change of variable $\Psi(t) = \dot{x}(t) + \mathrm{j}\omega x(t)$ is carried out

$$x = \frac{\Psi - \Psi'}{2\mathrm{j}\omega}; \quad \dot{x} = \frac{\Psi - \Psi'}{2}; \quad \ddot{\mathrm{x}}(\mathrm{t}) = \dot{\Psi} - \mathrm{j}\omega\frac{\Psi - \Psi'}{2} \tag{2}$$

where superscript $'$ indicates complex conjugate.

The equation of motion (Eq. 1) in terms of complex variable (Eq. 2) can be written as

$$\begin{aligned} &\dot{\Psi} - \mathrm{j}\omega\frac{\Psi + \Psi'}{2} + c\frac{\Psi + \Psi'}{2} + k_1\frac{\Psi - \Psi'}{2\mathrm{j}\omega} + k_2\left(\frac{\Psi - \Psi'}{2\mathrm{j}\omega}\right)^2 \\ &+ k_3\left(\frac{\Psi - \Psi'}{2\mathrm{j}\omega}\right)^3 + k_4\left(\frac{\Psi - \Psi'}{2\mathrm{j}\omega}\right)^4 = 0 \end{aligned} \tag{3}$$

The second step of the partitioning of the dynamics $\Psi(t) = \varphi(t)\mathrm{e}^{\mathrm{j}\omega t}$ into slow, $\varphi(t)$, and fast, $\mathrm{e}^{\mathrm{j}\omega t}$, components having a single frequency with modulated amplitude and phase is performed.

By averaging out the fast-frequency component, $\mathrm{e}^{\mathrm{j}\omega t}$, Eq. (3) is transformed into Eq. (5) with the help of Eq. (4) by eliminating higher order terms (square-, cubic-, and fourth-order terms)

$$\dot{\Psi} = \dot{\varphi}\mathrm{e}^{\mathrm{j}\omega t} + \varphi\mathrm{j}\omega\mathrm{e}^{\mathrm{j}\omega t} \tag{4}$$

$$\dot{\varphi} + \mathrm{j}\omega\frac{\varphi}{2} + c\frac{\varphi}{2} - \frac{\mathrm{j}k_1\varphi}{2\omega} + \frac{k_2}{2\omega^2}|\varphi|\varphi - \frac{3\mathrm{j}k_3}{8\omega^3}|\varphi|^2\varphi - \frac{k_4}{4\omega^4}|\varphi|^3\varphi = 0 \tag{5}$$

On carrying out the third step of CX-A, the equation of motion represents an approximation to the actual dynamics. After averaging, the corresponding envelope and phase variables will be extracted by rewriting the variable $\varphi(t)$ in polar form, $\varphi(t) = a(t)\mathrm{e}^{\mathrm{j}\beta(t)}$ as

$$\dot{a} + \mathrm{j}a\dot{\beta} + \frac{\mathrm{j}\omega a}{2} + \frac{ca}{2} - \frac{\mathrm{j}k_1 a}{2\omega} + \frac{k_2 a^2}{2\omega^2} - \frac{3\mathrm{j}k_3 a^3}{8\omega^3} - \frac{k_4 a^4}{4\omega^4} = 0 \tag{6}$$

The real and the imaginary parts of Eq. (6) are

$$\dot{a} + \frac{ca}{2} + \frac{k_2 a^2}{2\omega^2} - \frac{k_4 a^4}{4\omega^4} = 0 \tag{7a}$$

$$\dot{\beta} + \frac{\omega}{2} - \frac{k_1}{2\omega} - \frac{3k_3 a^2}{8\omega^3} = 0 \tag{7b}$$

The boundary conditions can be determined by

$$\varphi(t) = a(t)\mathrm{e}^{\mathrm{j}\beta(t)} \tag{8}$$

$$\Psi(t) = \varphi(t)\mathrm{e}^{\mathrm{j}\omega t} = \dot{x}(t) + \mathrm{j}\omega x(t) \tag{9}$$

Hence $\beta(t) = \pi/2$ and $a(0) = X\omega$

On solving the real and the imaginary part (Eq. 7), the slow-flow parameters can be obtained as

$$a(t) = X\omega e^{\left[-\frac{ct}{2} - \frac{k_2 t^2}{2\omega^2} + \frac{k_4 t^4}{4\omega^4}\right]} \tag{10a}$$

$$\beta(t) = \frac{3k_3 X^2}{8\omega c}(1 - e^{-ct}) - \left(\frac{\omega}{2} - \frac{k_1}{2\omega}\right)t + \frac{\pi}{2} \tag{10b}$$

Therefore, Eqs. (10a) and (10b) are the approximate and simplified slow-flow equations of the considered dynamical system. The system response predicted by the Cx-A method can be written in general form as

$$x(t) = \frac{a(t)}{\omega}\sin(\omega t + \beta(t)) \tag{11}$$

which shows that the total phase variable is $\theta = \omega t + \beta(t)$;

The slow-flow model of the system after performing Cx-A is given by

$$\begin{aligned} x(t) &= \frac{a(t)}{\omega}\sin(\omega t + \beta(t)) \\ \text{where } a(t) &= X\omega e^{\left[-\frac{ct}{2} - \frac{k_2 t^2}{2\omega^2} + \frac{k_4 t^4}{4\omega^4}\right]} \\ \text{and} \quad \beta(t) &= \frac{3k_3X^2}{8\omega c}(1 - e^{-ct}) - \left(\frac{\omega}{2} - \frac{k_1}{2\omega}\right)t + \frac{\pi}{2} \end{aligned} \tag{12}$$

It is recommended to use the sub- and super-harmonics instead of frequency 'ω' during partitioning for systems exhibiting strong nonlinearities to improve the predictive capacity of the Cx-A model.

4 Numerical Study—Breathing Crack Problem

A cantilever beam with a breathing crack is considered as an example as shown in Fig. 1. The breathing crack introduces bilinear stiffness effect corresponding to the opening and closing state. The equation of motion (bilinear oscillator) of the beam with a breathing crack can be written as

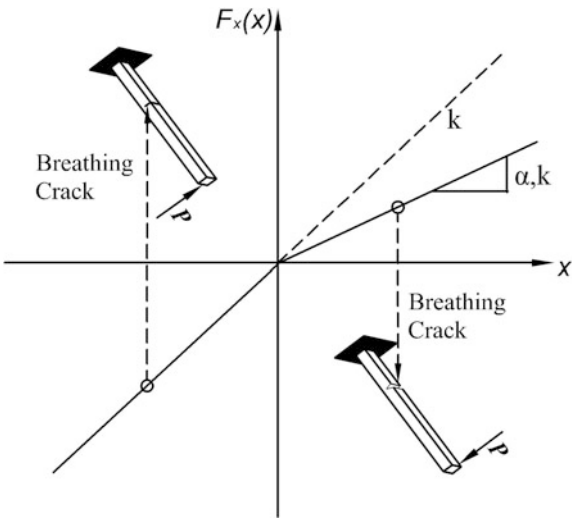

Fig. 1 Cantilever beam with breathing crack

$$m\ddot{x}(t) + c\dot{x}(t) + g[x(t)] = f(t);\ g(x) = \begin{cases} \alpha kx & x \geq 0 \\ kx & x < 0 \end{cases} \tag{13}$$

where $g(x)$ is the restoring force and m, k, c, and f are the mass, stiffness, damping, and force respectively. The stiffness ratio α is defined as the ratio of squares of the cracked frequency to uncracked frequency. It lies in the range $0 \leq \alpha \leq 1$. The bilinear frequency ω_B of the undamped free vibration of bilinear oscillator [15] is given by

$$\omega_B = \frac{2\omega_0\omega_1}{(\omega_0 + \omega_1)} = \frac{2\sqrt{\alpha}}{(1+\sqrt{\alpha})}\omega_0 \tag{14}$$

where ω_0 and ω_1 are the natural frequencies of the uncracked and cracked beam, respectively, k and k' ($k' = \alpha k$) are the stiffness of the uncracked and cracked states of the beam.

In the present work, the bilinear nature of the beam with a breathing crack is approximated by an amplitude dependent polynomial model of order 4 using the Weierstrass Approximation theorem [16]. Then a slow-flow model is established for the approximated polynomial system through Cx-A technique and its slowly varying parameters are determined.

The Weierstrass approximation theorem states that: "*If f(x) is a continuous real-valued function on [a, b] and if any ε > 0 is given, then there exists a polynomial P(x) on [a, b] such that |f(x)-P(x)| < ε for all x ε [a, b]. Since the restoring force g(x) is a continuous function of displacement x, it can be well approximated by a polynomial.*"

The restoring force of the fourth-order-approximated polynomial-type nonlinear system is given by

$$\begin{aligned} m\ddot{x}(t) + c\dot{x}(t) + \hat{g}[x(t)] &= f(t) \text{ with } \hat{g}[x(t)] \\ &= g_0 + c_1 kx + c_2 kx^2 + c_3 kx^3 + c_4 kx^4 \end{aligned} \tag{15}$$

where g_0 indicates the constant term and can be neglected when no static force is applied to the structure and k indicates the uncracked stiffness and $c_1 kx$ represents the linear component and the additional higher order terms indicate the nonlinear components of the approximated polynomial nonlinear system. The coefficients, c_1, c_2, c_3, c_4 are evaluated by minimizing the error function E between the actual and approximated polynomial nonlinear system using the above-mentioned Weierstrass approximation theorem in the domain $[-X, X]$ as

$$E(c_1, c_2, c_3, c_4) = \int_{-X}^{X} g[x(t)] - \hat{g}[x(t)]\}^2 \mathrm{d}x; \tag{16}$$

$$\frac{\partial E}{\partial c_i} = 0, \quad \text{for } i = 1, 2, 3, 4 \tag{17}$$

By applying the above equation, the coefficients are obtained [17, 18] as

$$c_1 = \frac{(1+\alpha)}{2}, \quad c_2 = -\frac{105(1-\alpha)}{128X}, \quad c_3 = 0, \quad c_4 = \frac{105(1-\alpha)}{256X^3} \tag{18}$$

The actual system equation of motion is given by

$$\ddot{y}(t) + 23.5619\dot{y}(t) + 3.5e4\underbrace{(0.75)}_{\alpha} y(t) = 0; \quad y_0 = 0.25; \quad \dot{y}_0 = 0 \tag{19}$$

where α is the stiffness ratio varying between 0 and 1 such that $\alpha = 1$ for $x(t) < 0$ and $\alpha < 1$ for $x(t) \geq 0$. Further, the system can be idealized as a system with polynomial terms having coefficients up to fourth order depending on the value of the stiffness ratio, as discussed earlier.

$$\begin{aligned} &\ddot{y}(t) + 23.5619\dot{y}(t) + 3.5e04c_1 y(t) + 3.5e04c_2 y^2(t) \\ &\quad + 3.5e04c_3 y^3(t) + 3.5e04c_4 y^4(t) = 0 \end{aligned} \tag{20}$$

The value of X is chosen as 2e-4 for this problem.

The system parameters considered are m = 1, c = 23.5619 Ns/m, k = 3.5e4. The time history responses are measured using Runge–Kutta integration scheme. The natural frequency of the system is found to be 30 Hz. The nonlinear system response will exhibit sub- and super-harmonics of excitation frequency into addition to the fundamental harmonic.

The displacement time history response obtained using Runge–Kutta (RK) integration scheme and the corresponding power spectrum (PSD) of the actual system are shown in Fig. 2. The white Gaussian noise in the form of signal to noise ratio (SNR = 50) is added to the time history response before processing. It can be observed from Fig. 2b that the spectrum exhibits peaks at the excitation frequency and at second and fourth-order super-harmonic resonances. This clearly indicates the presence of nonlinearity in the structure.

Hilbert Transform (HT) on the displacement time history response can be applied to obtain the instantaneous amplitude and instantaneous frequency. The Hilbert transform of response $x(t)$ can be defined as

$$\bar{x}(t) = \mathrm{HT}(x(t)) = \frac{1}{\pi}\mathrm{PV}\int_{-\infty}^{\infty} \frac{x(\tau)}{t-\tau}\mathrm{d}\tau \tag{22}$$

where PV indicates the principal Cauchy value. The corresponding analytical signal $z(t)$ is then given by

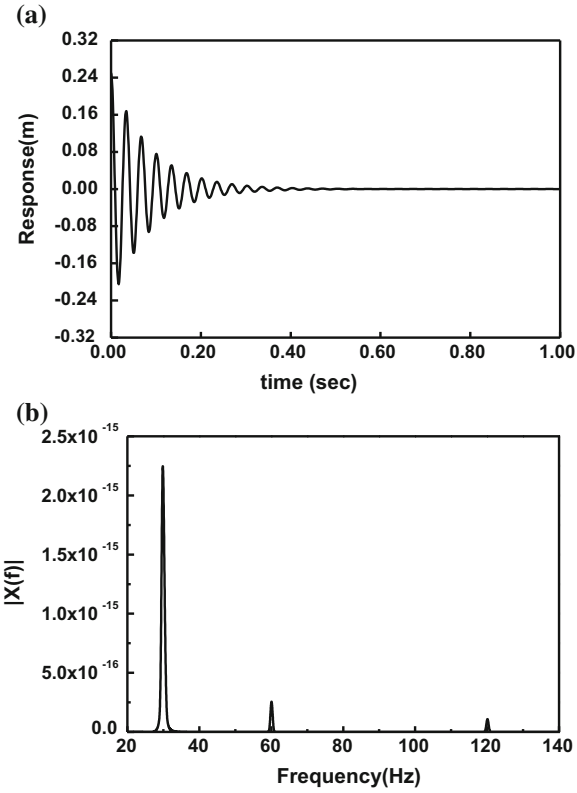

Fig. 2 **a** Displacement time history response; **b** power spectrum of breathing crack problem

$$z(t) = x(t) + \mathrm{i}\bar{x}(t) = A(t)\mathrm{e}^{\mathrm{i}\theta(t)} \tag{23}$$

$$A(t) = \left[\left([x(t)]^2 + [\bar{x}(t)]^2\right)\right]^{1/2} \tag{24a}$$

$$\omega(t) = \frac{\mathrm{d}\theta(t)}{\mathrm{d}t}; \quad \theta(t) = \tan^{-1}\frac{\bar{x}(t)}{x(t)} \tag{24b}$$

where $A(t)$ is instantaneous amplitude, $\theta(t)$ is the phase angle and $\omega(t)$ is the instantaneous frequency.

The instantaneous parameters (i.e., instantaneous amplitude and instantaneous frequency) obtained using HT of time history response is shown in Fig. 3a, b respectively. Once the instantaneous parameters are obtained through the Hilbert transform, it can be easily related to the slow-flow equations of the system.

Through Slow-Flow Model Identification, the instantaneous phase given in Eq. (10b) after eliminating k_3 (i.e. $c_3 = 0$) becomes

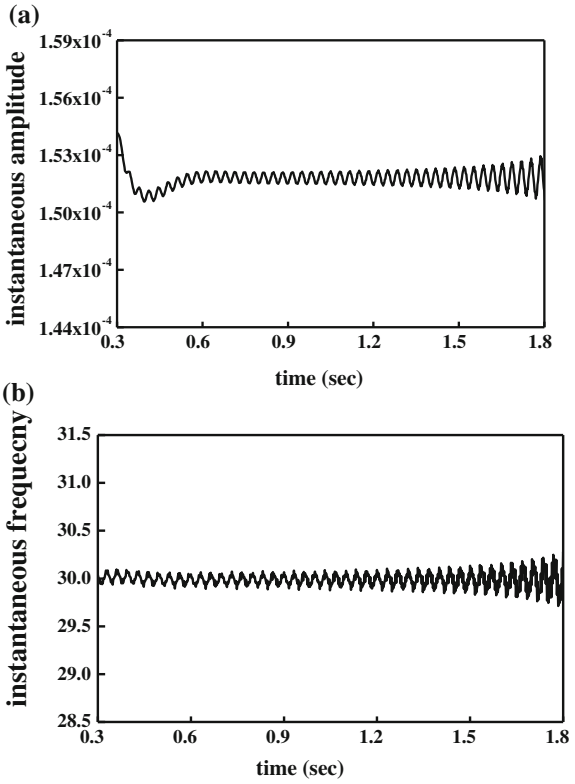

Fig. 3 HT of response **a** instantaneous amplitude **b** instantaneous frequency

$$\beta(t) = -\left(\frac{\omega}{2} - \frac{k_1}{2\omega}\right)t + \frac{\pi}{2} \tag{25}$$

The slow-flow instantaneous phase equation (Eq. 25) obtained through complexification-averaging and the Hilbert transform (Eq. 24) are compared. As the system frequency and mass are known a priori, the time-dependent linear stiffness coefficient k_1 can be estimated. A single value of k_1 is then estimated using the least square procedure. The final single value of k_1 is then related to stiffness ratio α and then the value is determined.

Further, the instantaneous amplitudes given in Eqs. (10a) and (24a) are compared and the system damping parameter is estimated using the least square procedure.

The identified system parameters are shown in Table 1. It can be verified from Table 1 that the parameters obtained using slow-flow model compare well with the actual parameters even with measurement noise. The extension of the slow-flow model formulations to multi-degree of freedom is rather straightforward and Hilbert–Huang Transform (HHT) is used instead of HT for instantaneous parameter extraction. The advantage of the slow-flow model technique is that it is applicable

Table 1 System identification by SFMI

Parameters	Stiffness	Damping	Stiffness ratio
Actual	3.5e4	23.5619	0.8
Slow-flow model	3.4816e4	23.3291	0.8003
Model (SNR50)	3.5024e4	23.5	0.798

for both linear and nonlinear systems which might include systems with smooth and non-smooth nonlinearities

5 Conclusion

In this paper, the physics-based interpretation of instantaneous parameters derived using Hilbert transform and the slow-flow equation of the dynamics of the system is demonstrated. Based on the correspondence between the HT approach and slow-flow model, a nonlinear system identification strategy using the empirical slow-flow model in the time domain is presented. The analysis is based on input–output response measurements of the system and is applicable for both smooth and non-smooth nonlinear systems. The Hilbert transform approach gives sharper frequency and time resolutions compared to other time–frequency decomposition and helps in accurate estimation of instantaneous parameters for strongly nonlinear systems.

The extension of the approach to multi-degree of freedom is rather straightforward and Hilbert–Huang transform needs to perform on the time history response instead of Hilbert transform.

Numerical investigations have been carried out to verify the presented empirical slow-flow model for nonlinear parameter estimation by solving a beam with a single-edged breathing crack problem. Numerical studies presented in this paper clearly indicate that the proposed identification strategy using slow-flow model can identify nonlinear coefficients accurately even with noisy measurements.

Acknowledgements This paper is being published with the permission of the director, CSIR-Structural Engineering Research Centre, Chennai.

References

1. Kerschen, G., Worden, K., Vakakis, A. F., & Golinval, J. C. (2006). Past, present and future of non-linear system identification in structural dynamics. *Mechanical Systems and Signal Processing, 20,* 505–592.
2. Bornn, Luke, Farrar, C. R., & Park, Gyuhae. (2011). Damage detection in initially nonlinear systems. *International Journal of Engineering Sciences, 48,* 909–920.

3. Worden, K., & Tomlinson, G. R. (2001). Nonlinearity in structural dynamics: Detection, identification, and modeling. Institute of Physics Press.
4. Prawin, J., Rao, A. R. M., & Lakshmi, K. (2015). Nonlinear identification of structures using ambient vibration data. *Computers & Structures, 154,* 116–134.
5. Billings, S. A. (2013). *Severely nonlinear systems, nonlinear system identification: NARMAX methods in the time-frequency and spatio-temporal domains*. New York: Wiley.
6. Josefsson, A., Magnevall, M., Ahlina, K., & Broman, G. (2012). Spatial location identification of structural nonlinearities from random data. *Mechanical Systems and Signal Processing, 27,* 410–418.
7. Aykan, M., & Özgüven, H. N. (2013). Parametric identification of nonlinearity in structural systems using describing function inversion. *Mechanical Systems and Signal Processing, 40,* 356–376.
8. Schetzen, M. (1980). *The Volterra and Wiener theories of non-linear systems*. New York: Wiley.
9. Prawin, J., & Rao, A. R. M. (2017). Nonlinear identification of MDOF systems using Volterra series approximation. *Mechanical Systems and Signal Processing, 84,* 58–77.
10. Prawin, J., Rao, A. R. M., & Lakshmi, K. (2016). Nonlinear parametric identification strategy combining reverse path and hybrid dynamic quantum particle swarm optimization. *Nonlinear Dynamics, 84*(2), 797–815.
11. Feldman, M. (2011). *Hilbert transform applications in mechanical vibration*. New York: Wiley-Interscience.
12. Prawin, J., & Rao, A. R. M. (2015). Time-frequency analysis for nonlinear identification of structures. *Journal of Structural Engineering, 42*(1), 40–48.
13. Kerschen, G., & Vakakis, A. F. (2008). Toward a fundamental understanding of the Hilbert-Huang transform in nonlinear structural dynamics. *Journal of Vibration and Control, 14,* 77–105.
14. Lee, Y. S., Vakakis, A. F., Bergman, L. A., Michael, D., & Farland, M. C. (2011). A time domain nonlinear system identification method based on multiscale dynamic partitions. *Meccanica, 46*(4), 625–649.
15. Peng, Z. K., Lang, Z. Q., Billings, S. A., & Lu, Y. (2007). Analysis of bilinear oscillators under harmonic loading using nonlinear output frequency response functions. *International Journal of Mechanical Sciences, 49*(11), 1213–1225.
16. Jeffreys, H., & Jeffreys, B. S. (1988). *Methods of mathematical physics*. Cambridge, England: Cambridge University Press.
17. Prawin, J., & Rao, A. R. M. (2016). Development of polynomial model for cantilever beam with breathing crack. *Procedia Engineering, 144,* 1419–1425.
18. Surace, C., Ruotolo, R., & Storer, D. (2011). Detecting nonlinear behaviour using the Volterra series to assess damage in beam-like structures. *Journal of Theoretical and Applied Mechanics, 49,* 905–926.

Analytical Investigations on Structural Damage Identification Using Torsional Wave Propagation

K. Varun Kumar, T. Jothi Saravanan, N. Gopalakrishnan and K. M. Mini

Abstract Damage identification of the concrete pile element through torsional wave propagation technique is studied in this paper. Concrete pile foundations are often prevalent in all engineering structures and their safety is paramount for obviating the failure. Damage detection and estimation in a substructure is difficult because the visual image of the substructure and its condition is not acknowledged and, therefore, the state of the structure or foundation can be inferred solely through its static and dynamic response which is usually carried out by using Pile Integrity Testing (PIT), includes axial wave propagation approach. This paper explores a novel idea on damage identification of the concrete pile element through torsional wave propagation technique using analytical study. Structural damage is induced in the concrete pile elements by varying the cross-sectional area along the length and the position of the damage is also varied. Analytical simulations are performed using Abaqus dynamic explicit analysis under pulse-echo configuration method. The effect of reduction of area (or an increase of area) causes a reduction in stiffness, as well as mass and thus torsional impedance, is not altered to a great extent. In the case of uniform wave propagation, the transient pulse is preserved and the response is quiet and hence the damage identification is very easy when compared to dispersive flexural wave propagation. Hence, the elapsed time of the reflected pulse can be a simple indicator of the location of the damage.

K. Varun Kumar · K. M. Mini (✉)
Department of Civil Engineering, Amrita School of Engineering,
Coimbatore 641112, India
e-mail: k_mini@cb.amrita.edu

K. Varun Kumar
e-mail: kvkg124@gmail.com

T. Jothi Saravanan
Department of Civil Engineering, The University of Tokyo, Tokyo 1138654, Japan
e-mail: tjs.saravanan@gmail.com

N. Gopalakrishnan
CSIR-Central Building Research Institute, Roorkee 247667, Uttarakhand, India
e-mail: gnramana68@gmail.com; ng@cbri.res.in

A. Rama Mohan Rao and K. Ramanjaneyulu (eds.), *Recent Advances in Structural Engineering, Volume 1*, Lecture Notes in Civil Engineering 11,
https://doi.org/10.1007/978-981-13-0362-3_86

Keywords Wave propagation · Structural health monitoring · Damage detection Pulse-echo method · Abaqus

1 Introduction

Structural Health Monitoring (SHM) is the practice of monitoring the structure over its lifetime to detect the changes in the structural properties that may indicate a reduction in the performance. SHM process involves observation of a system over time using periodically sampled dynamic response measurements from an array of sensors, the extraction of damage-sensitive features from these measurements, and the statistical analysis of these features so as to determine the current state of system health [1]. SHM is an emerging technology which has its application in various fields like aerospace, buildings, bridges, offshore structures, underground structures, ships and many more industries [2–5]. The damage is defined as changes to the material and/or geometric properties of a structural system, including changes to the boundary conditions and system connectivity, which in turn affect the system's performance. Damage detection is carried out by monitoring the structure [6], nondestructive testing (NDT) [7], and damage prognosis [8].

Among all NDT tools, wave propagation tools play a vital role in identifying the damage. It is a transient dynamic phenomenon resulting from short duration loadings like gust, birds hit, tool drops, etc., which have very high-frequency content. The dynamic characteristics of the structures at high frequency are well understood with the help of wave propagation studies. Wave propagation-based automatic SHM techniques are widely adopted in the nuclear and aerospace industry. But, these techniques are not in a well-matured state of development for civil engineering structures. Hence, enough importance is to be given in these areas of research so that an automatic alert and warning system can be designed for critical and important civil engineering structures.

Damage identification using the response of wave propagations are discussed [9–13]. This is based on the assumption that the damages or discontinuities disturb the propagation of the waves in a structure. Wave propagation techniques are very effective because the wave travels for long range and depends on operating frequency, elastic properties of the material, material thickness, and density. Damage identification using spectral finite element method is discussed in some literature [14, 15].

Pile foundation not only transfers load but also enables the construction activities in low bearing capacity soils and controls the level of soil settlement. The integrity of the pile is directly related to the safety of the super-structure. So, there is a need for monitoring the health and safety of pile from time to time. Early damage identification can provide a possibility of finding and repairing the defects. The concept of wave propagation involves dynamic impedance and whenever a wave confronts a changing impedance (due to loss of stiffness or mass addition), a reflecting wave is produced with the total strain energy forked as reflected as well as refracted portions. The ratio of reflected wave to the incident wave is managed by

the impedance change and hence the position of the damage could be evaluated. Many researchers used conventional finite element method for damage identification and still need to be explored. This paper deals with damage identification of a concrete pile element using torsional wave propagation approach and is studied through numerical simulations using Abaqus dynamic explicit analysis under pulse-echo configuration method. In particular, detection of damage in form of discontinuity of cross-section is identified by analyzing wave speeds and reflections from the recorded velocity signals.

2 Basics of Wave Propagation

When a structure is subjected to dynamic loads, it will experience the stresses of varying degrees of severity depending upon the magnitude of the load and its duration. If the variation of the load is of larger duration (order of seconds), the intensity of the load felt by the structure will be lower and such problems come under the category of structural dynamics. For those problems, two parameters, namely, natural frequency and normal mode shapes are significant. The main difference between wave propagation and classical structural dynamics arises due to higher frequency content in the primary case. Wave propagation is a transient phase of dynamic response before the ongoing wave and the incoming wave superimpose over each other to give a standing wave pattern. The ratio of reflected wave to the incident wave is controlled by the change in the impedance and hence the position of the damage and its magnitude could be quantified. Hence, wave propagation mechanics becomes handy for damage detection and diagnosis. Wave propagation through a prismatic bar element can be derived and the second-order partial differential equation which governs the process can be written as

$$V_{\mathrm{p}}^2 \frac{\partial^2 u}{\partial x^2} - \frac{\partial^2 u}{\partial t^2} = 0 \tag{1}$$

$$V_{\mathrm{p}} = \sqrt{\frac{EA}{\rho A}} = \sqrt{\frac{E}{\rho}} \tag{2}$$

where u, x are displacement and coordinate in the longitudinal (axial) direction, V_{p} is phase velocity in axial direction and E, ρ, A: modulus of elasticity, mass density, and area of the rod (bar) element. Similarly, the velocity of the shear wave, V_{s} (also represented as 'c') is given by

$$V_s = \sqrt{\frac{G}{\rho}} \tag{3}$$

where G is the modulus of rigidity.

Modulus of elasticity and modulus of rigidity are related by the equation

$$E = 2G(1+\mu) \tag{4}$$

where 'μ' represents a number called Poisson's ratio given to the particular material.

By substituting Eq. (4) in (3), the velocity of the shear wave is given by

$$V_s = \sqrt{\frac{G}{\rho}} = \sqrt{\frac{E}{2(1+\mu)\rho}} \tag{5}$$

3 Analytical Investigation

A simplified model of five pile elements, namely, No damage pile, pile 1, pile 2, pile 3, and pile 4 with different cross-sectional enlargements and decrements at different locations have been analyzed using Abaqus dynamic explicit analysis under pulse-echo configuration method. The modeling of pile elements in Abaqus is shown in Fig. 1. All the pile elements are having a length of 6 m. No damage pile is of size 0.2 × 0.2 m along the full length.

The description of all the pile elements is as follows:

- Pile 1: The depth of the specimen-1 is 0.1 m for the center 1 m length (reduction in *c/s* area)
- Pile 2: The depth of the specimen-2 is 0.1 m for the center 1 m length from 1 m from the toe (reduction in *c/s* area)
- Pile3: The depth of the specimen-3 is 0.3 m for the center 1 m length (increase in *c/s* area)
- Pile 4: The depth of the specimen-4 is 0.3 m for the center 1 m length from 1 m from the toe (increase in *c/s* area)

The grade of the concrete and steel used for modeling in Abaqus is M20 and Fe415 respectively. Poisson's ratio is assumed as 0.15 for concrete. The load is applied at the corner ends of the face so as to create torsion wave in the pile element. The loading of the pile element is shown in Fig. 2. The reflected waves from the damages or defects or toe are sensed by the sensors present at the head of the pile. The speed of the wave calculated from Eq. (5) is found to be 1965 m/s.

3.1 Pulse-Echo Method

In this method, the head of the pile is given as load at the corner ends, and the sensor is located at the head. The input excitation of the pile element is shown in

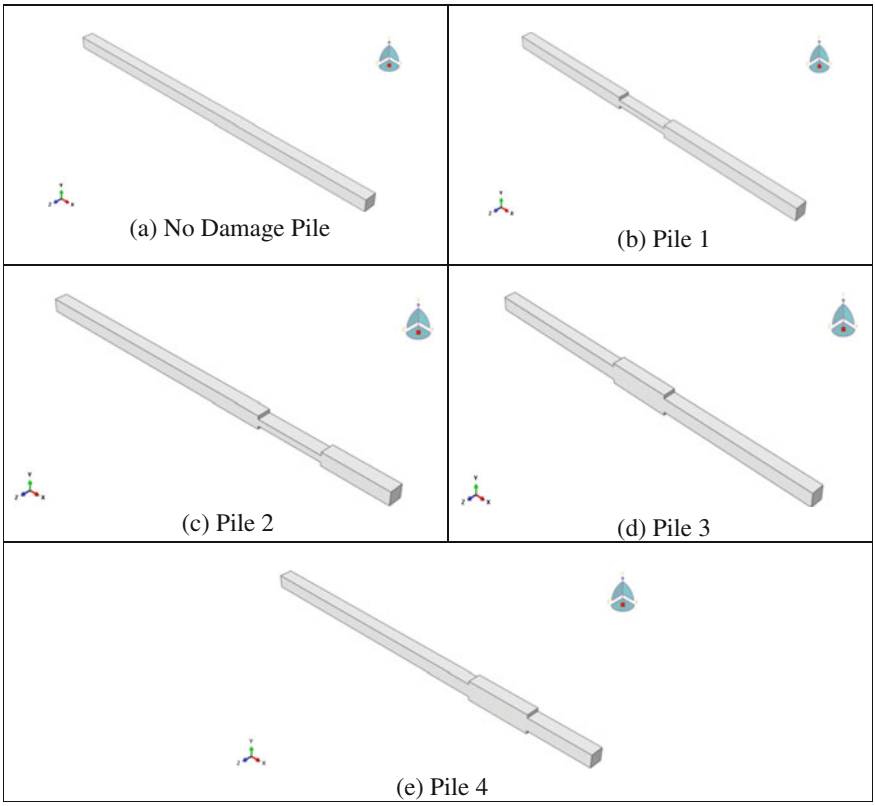

Fig. 1 3D view of the pile elements modeled in Abaqus

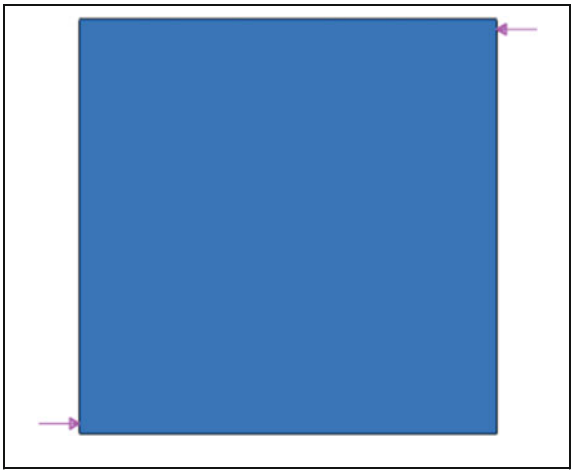

Fig. 2 Loading of the pile element

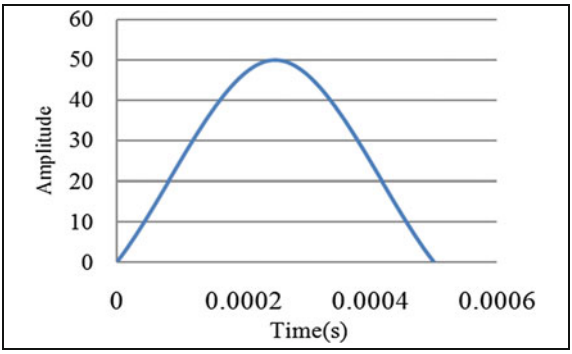

Fig. 3 Input excitation

Fig. 3. When the pile element is loaded, downward compressive waves are generated which travels with a velocity (c) along the pile and reflects from damages or defects or toe. When this initial wave encounters a change in the c/s (structural discontinuity) at a depth 'x', it reflects an upward traveling wave and it is observed at a time which is equal to twice the distance between the pile head and change in c/s divided by the velocity of the wave ($2x/c$).

The sensor which is located at the head of the pile senses the waves and the velocity time profiles are noted down for the whole duration.

4 Results and Discussions

The velocity–time profiles obtained in pulse-echo method are presented in Fig. 4. The location of the damages calculated based on the reflected times and wave velocity are tabulated in Table 1.

In Fig. 4b–c, after the initial damage there is a decrement in the c/s at some distance and thus the wave travels upwards, after 1 m length again the c/s increases and thus the wave travels in the downward direction. Similarly, in Fig. 4d–e after the initial damage there comes the increment in the c/s at some distance and thus the wave travels downwards, after 1 m length again the c/s decreases and thus the wave travels in the upward direction. From Table 1, for no damage pile, the end of the pile (toe) is identified as 5.92 m, but the actual length is 6 m. Similarly, all other damages of the remaining piles are identified accurately with ± 0.15 m precision.

5 Conclusions

In this paper, damage identification of a pile element using torsional wave propagation technique is studied through analytical testing (using pulse-echo configuration method) by Abaqus dynamic explicit analysis. The location of the damage is

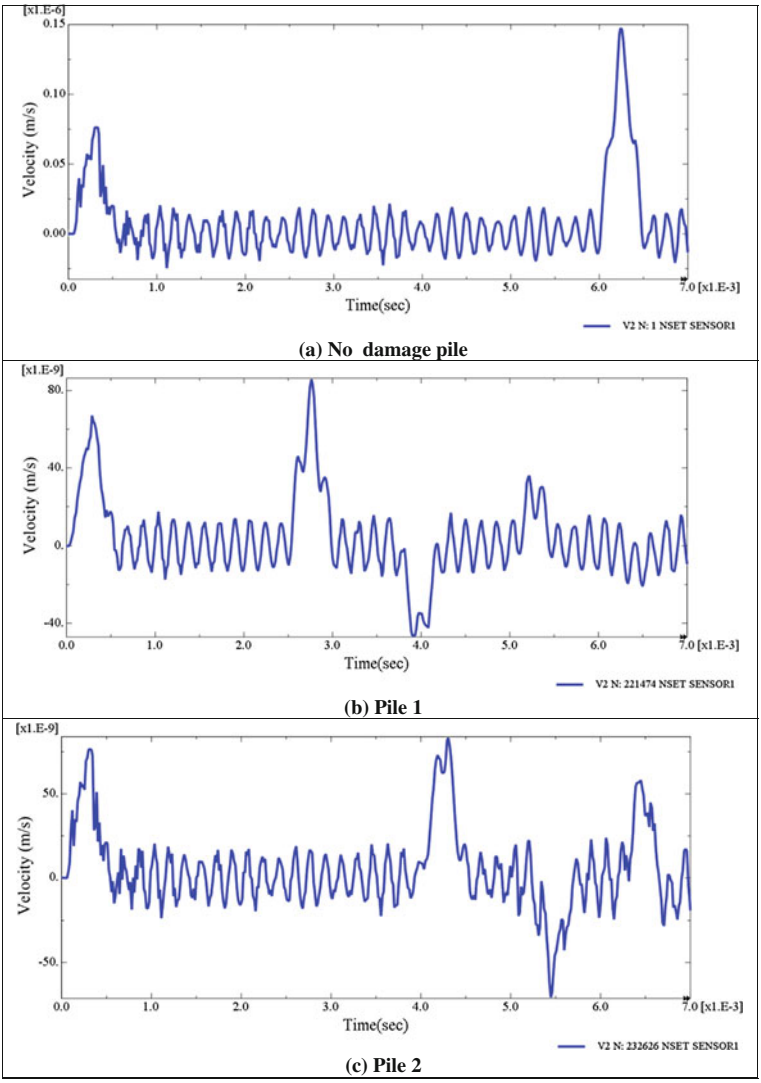

Fig. 4 Velocity–time profile for pulse-echo configuration method

identified by the wave scattering from elements of impedance change. The wave scattering denotes both wave reflection (coming back to the source) and wave refraction (going away from the source). In specific, the damages are detected by analyzing the wave reflections and velocity of the wave. The increase in the magnitude of the reflected pulses with increasing damage can be calibrated to quantify the damage magnitude. Pulse shape being preserved in the reflected pulses in the un-damaged prismatic pile, coming out of the analytical study illustrates the

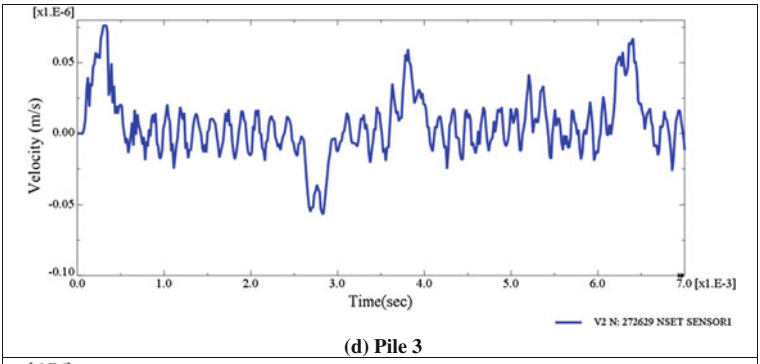

(d) Pile 3

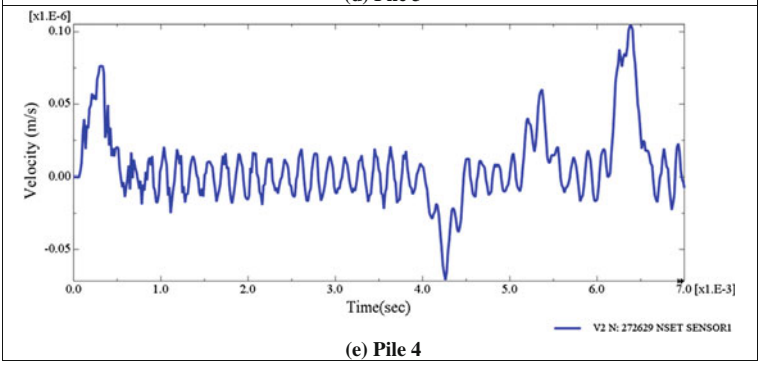

(e) Pile 4

Fig. 4 (continued)

Table 1 Damage locations identified by pulse-echo method

Specimen name	Incident (ms)	Damage reflection 1 (ms)	Location (m)	Damage reflection 2 (ms)	Location (m)	Toe reflection (ms)	Location (m)
No damage Pile	0	–	–	–	–	6.03	5.92
Pile 1	0	2.56	2.51	3.72	3.64	6.20	6.09
Pile 2	0	4.05	3.97	5.19	5.09	6.14	6.03
Pile 3	0	2.58	2.53	3.65	3.58	6.15	6.04
Pile 4	0	4.03	3.95	5.13	5.04	6.13	6.02

phenomenon of uniform wave propagation. So, the proposed method is suitable and compatible for damage detection. It is suggested that the presented approach shall be suitable for exact damage detection, as the impedance around the structural discontinuity varies and so does the energy of propagating and reflecting waves.

References

1. Farrar, C. R., & Worden, K. (2007). An introduction to structural health monitoring. *Philosophical Transactions of the Royal Society, A365,* 303–315.
2. Mickens, T., Schulz, M., Sundaresan, M., Ghoshal, A., Naser, A., & Reichmeider, R. (2003). Structural health monitoring of an aircraft joint. *Mechanical Systems and Signal Processing, 17,* 285–303.
3. Mufti, A. A. (2002). Structural health monitoring of Canadian civil engineering structures. *Structural Health Monitoring, 1,* 89–103.
4. Koh, B., & Dyke, S. (2007). Structural health monitoring for flexible bridge structures using correlation and sensitivity of modal data. *Computers & Structures, 85,* 117–130.
5. Nihols, J. (2003). Structural health monitoring of offshore structures using ambient excitation. *Applied Ocean Research, 25,* 101–114.
6. Bently, D. E., & Hatch, C. T. (2003). *Fundamentals of rotating machinery diagnostics*. New York, USA: ASME Press.
7. Shull, P. J. (2002). *Nondestructive evaluation theory, techniques, and applications*. New York, USA: Marcel Dekker Inc.
8. Farrar, C. R., & Lieven, N. A. J. (2007). Damage prognosis: The future of structural health monitoring. *Philosophical Transactions of the Royal Society, A 365,* 623–632.
9. Gan, C., Wei, Y., & Yang, S. (2014). Longitudinal wave propagation in a rod with variable cross-section. *Journal of Sound and Vibration, 333,* 434–445.
10. Gan, C., Wei, Y., & Yang, S. (2014) Longitudinal wave propagation in a multi-step rod with variable cross section. *Journal of Vibration and Control*. https://doi.org/10.1177/1077546314531806.
11. Saravanan, T. J., Rao, N. P., & Gopalakrishnan, N. (2015). Experimental and numerical investigation on longitudinal wave propagation in rod with structural discontinuity. *Journal of Structural Engineering (India), 42*(1), 1–7.
12. Yang, Z., Radzienski, M., Kudela, P., & Ostachowicz, W. (2016). Two-dimensional modal curvature estimation via Fourier spectral method for damage detection. *Composite Structures, 148,* 155–167.
13. Ostachowicz, W. (2008). Damage detection of structures using spectral finite element method. *Computers & Structures, 86,* 454–462.
14. Gopalakrishnan, S., & Doyle, J. F. (1995). Spectral super-elements for wave propagation in structures with local non uniformities. *Computer Methods in Applied Mechanics and Engineering, 121,* 77–90.
15. Saravanan, T. J., Gopalakrishnan, N., & Rao, N. P. (2016). Detection of damage through coupled axial–flexural wave interactions in a sagged rod using the spectral finite element method. *Journal of Vibration and Control*. https://doi.org/10.1177/1077546316630855.

Damage Assessment in Composites Using Frequency Discrimination of Acoustic Emission Signals

Sanjay Sengupta, Aloke Kumar Datta and Pijush Topdar

Abstract For assessment of damages in real time for the layered composite plates, which have gained wide acceptance in weight-sensitive engineering structures, acoustic emission (AE) signals captured at different locations of the plate can be used. For such structures, damages such as delamination, matrix cracking, fibre failure, etc., which may not be detected visually can be identified by discrimination of the frequency content of the response AE signals and can be used for structural health monitoring purpose. In this study, an attempt is made to utilise frequency content of the AE response caused due to the damage as a discriminating factor for determining different modes of failures in multi-layered composite plates using Finite Element (FE) technique. Numerical examples are solved. The results show that the source frequency has a telling effect on the frequency content of the response signals which can be used for discrimination of flexural, i.e. out-of-plane and extensional, i.e. in-plane modes.

Keywords Acoustic emission · Structural health monitoring · Finite element Frequency content

1 Introduction

Assessment of damages in real time is crucial for safety and reliability of every engineering structure. In recent years layered composites like fibre-reinforced laminated composite (FRLC) plates have gained wide acceptance in

S. Sengupta
Dr. B.C. Roy Engineering College, 713206 Durgapur, India
e-mail: sanswati2004@gmail.com

S. Sengupta · A. K. Datta (✉) · P. Topdar
National Institute of Technology, 713209 Durgapur, India
e-mail: dattarec@yahoo.com

P. Topdar
e-mail: topdar72@yahoo.co.uk

A. Rama Mohan Rao and K. Ramanjaneyulu (eds.), *Recent Advances in Structural Engineering, Volume 1*, Lecture Notes in Civil Engineering 11,
https://doi.org/10.1007/978-981-13-0362-3_87

weight-sensitive engineering structures. Damages such as delamination, matrix cracking, fibre failure, etc., which may not be detected visually, can occur in composite plates. Interestingly, such damages emit acoustic waves that travel through the material as flexural plate wave and extensional plate wave. Analysis of such acoustic emission (AE) signals, captured at different locations of the plate, can be used for structural health monitoring (SHM) of the composite structures [1]. There are instances in the literature where the frequency of AE signals is used to identify failure modes of plates. Literature reveals that a number of researchers have attempted to utilise frequency content of AE signals as a discriminating factor for damage assessment [2–4]. However, such studies are limited to isotropic and single-layer anisotropic plates where the responses are obtained from experiments.

In this work, an attempt is made to utilise frequency content of the AE response caused due to the damage as discriminating factor for determining different modes of failures in multi-layered composite plates using Finite Element (FE) technique, where single-layer anisotropic plate is only a special case. Modelling such layered plates is challenging as material properties may vary from one layer to another across the plate-thickness and transverse shear stress continuity at the interface of two consecutive layers of different materials must be maintained while modelling the in-plane displacement fields. To address this difficulty, a generalised refined plate theory (RPT) as proposed by Cho and Parmerter [5] is used to model the displacement field. A four-node higher order C^1 continuous element [6] is used such that the structural behaviour of the plates, as mentioned earlier, under simulated AE source can be predicted realistically. This RPT is 2D FE approach and is very generic in nature as it can accommodate variation in material property in any direction, variety of boundary conditions, thickness ratios and aspect ratios of the plate. The effect of source frequency in the response is studied through solving different numerical examples using finite element method for anisotropic and layered composites using a software code that is specifically developed to implement the present formulation. Fast Fourier Transform (FFT) is used on the time domain displacement response to get the frequency domain response. Results are presented for single-layer anisotropic and multi-layered composite plates for assessment of damages due to simulated high-frequency forcing functions in the frequency domain. The results show that the source frequency has a telling effect on the frequency content of the response signals which can be used for discrimination of flexural, i.e. out-of-plane and extensional, i.e. in-plane mode.

2 Mathematical Formulations

A mathematical model is proposed which is very generic in nature and computationally efficient as suggested by Cho and Parmerter [5] for this study. The basis of AE technique in damage detection has been elaborated in the paper. In this technique, structural damage is studied in real time. Signal generated due to damage developed is considered in the present modelling. However, due to non-availability

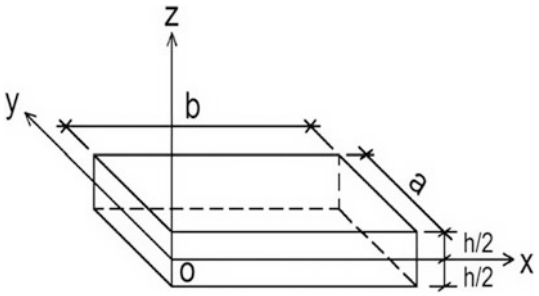

Fig. 1 3D view of the plate along with axis system

of exact signal corresponding to a particular type of damage in a structure, researcher normally adapts the signal generated by pencil lead break which is widely available in the literature. Here to make the study little bit realistic and to develop workable model an example signal, i.e. sinusoidal signal having high frequency has been considered. The 3D view of the plate considered for analysis is shown in Fig. 1. Displacements at the reference plane (mid-plane of the plate) along x axis, y axis and z axis are represented as u, v and w respectively. The variation of in-plane displacements across the plate thickness is expressed as a combination of linearly varying zigzag component and a cubically varying continuous component. The transverse displacement is taken to be constant over the plate thickness. A rectangular element having four nodes at its four corners is used considering eight degrees of freedom $u, v, w, w_{,x}, w_{,y}, w_{,xy}, \gamma_x, \gamma_y$ at each node. The field variables u, v, γ_x *and* γ_y are approximated by bi-linear interpolation functions whereas the transverse displacement w is approximated by bi-cubic interpolation function.

The Hamilton's variation principle of dynamics is applied to get the equation of motion of the system. For an element, if $\{\delta\}$ is the nodal displacement vector, considering the effect of damping, the equation of motion for an element may be expressed as

$$[M_e]\left\{\ddot{\delta}\right\} + [C_e]\left\{\dot{\delta}\right\} + [K_e]\{\delta\} = \{R\} \tag{1}$$

The element-level mass matrix $[M_e]$, damping matrix $[C_e]$ and stiffness matrix $[K_e]$ and load vector $\{R\}$ for all the elements can be computed and assembled together to form the system-level mass matrix $[M]$, damping matrix $[C]$, stiffness matrix $[K]$ and load vector $\{F\}$ for the entire structure. The equation of motion for the system may be expressed as

$$[M]\left\{\ddot{\Delta}\right\} + [C]\left\{\dot{\Delta}\right\} + [K]\{\Delta\} = \{F\} \tag{2}$$

where $\{\Delta\}$ is the global displacement vector for the entire plate. The governing equation of dynamic response, i.e. (Eq. 2) can be solved by direct time integration scheme following Newmark's β method, which is an explicit time integration technique [7].

The model proposed in this case is a linear model. The present simulated study is free from nonlinearity phenomena as well as noise. However, the formulation is very general in nature which can incorporate the effect of the above factors. The time domain responses are simply transformed from time domain to frequency domain using Fast Fourier Transform (FFT). The emphasis is given on the total energy content in the frequency data for discrimination rather than the peaks of the FFT data.

3 Numerical Examples and Discussion

3.1 Preliminary Remarks

Numerical examples are solved, where the damage is simulated by a forcing function of high frequency. A sinusoidal function having a frequency of 100 and 500 kHz is considered for the purpose where the duration of the force is 150 μs following Eaton et al. [4]. To obtain the flexural AE waveforms, the forcing function is applied out of the plane, i.e. in the transverse direction of the plate and to obtain the extensional AE waveforms the forcing function is applied along in-plane direction in all cases. Rectangular plate geometry is used with simply supported boundary condition along all the edges. Displacement, velocity and acceleration at initial time were considered as zero. Damping is not considered. The time step used for a solution using Newmark's-β method is taken as 0.164 μs and the value of α and ψ are taken as 0.25 and 0.50 respectively.

3.2 Example 1

To validate the present model, initially, a lamina of AS4/3502 graphite/epoxy of size 0.254 × 0.1524 × 0.00254 m is considered. The material properties used as reported by Prosser et al. [3] and are as follows:

Density: 1550 kg/m^3,

C_{11} = 147.1 GPa, C_{12} = 4.11 GPa, $C_{13} = C_{12}$
C_{22} = 10.59 GPa, C_{23} = 3.09 GPa, $C_{33} = C_{22}$
C_{44} = 3.75 GPa, C_{55}: 5.97 GPa, $C_{66} = C_{55}$

The source is positioned at x = 0.0508 m and y = 0.0762 m. The responses are obtained at a distance 0.0762 m from the source along the longer side of the plate, i.e. along x-direction. The frequency responses to 100 and 500 kHz sinusoidal driving pulses in the out-of-plane directions are shown in Fig. 2. The frequency responses to similar driving pulses in the in-plane direction are presented in Fig. 3.

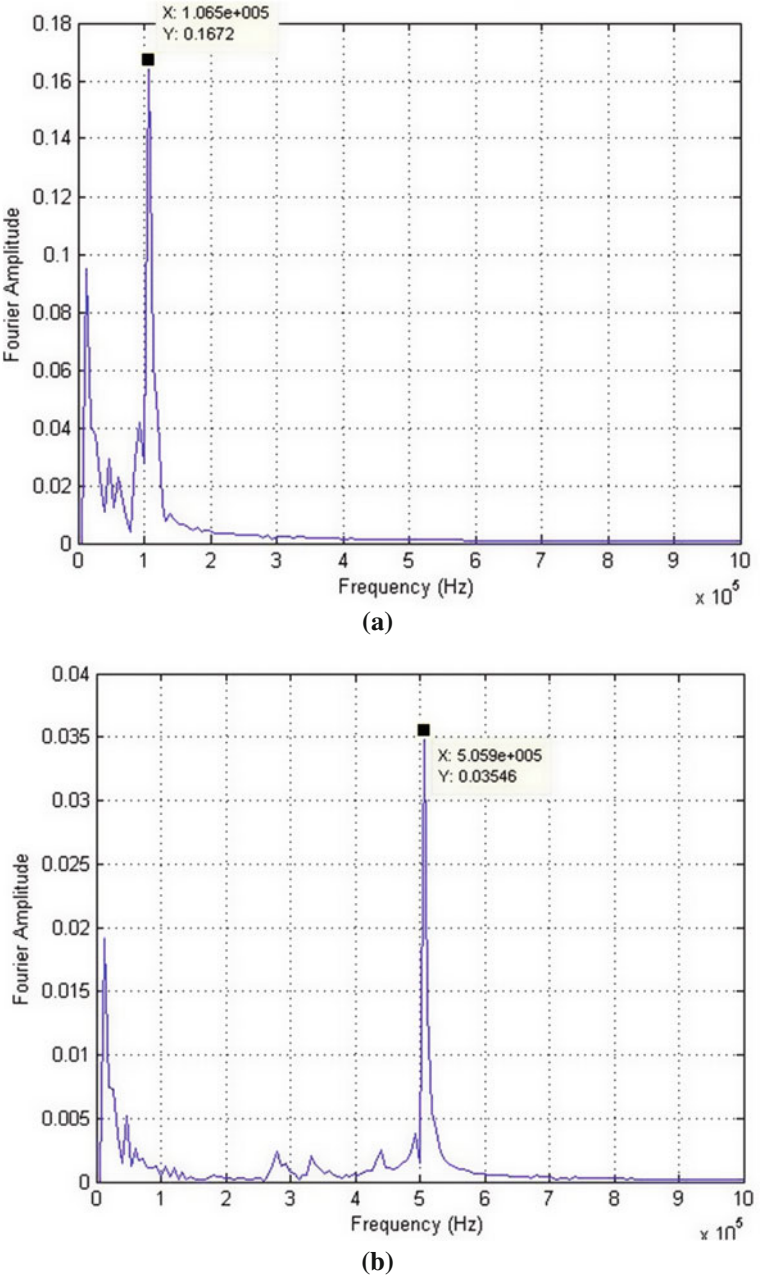

Fig. 2 FFT data of displacement response due to out-of-plane AE source causing flexural or asymmetric mode. **a** 100 kHz frequency sinusoidal source and **b** 500 kHz frequency sinusoidal source

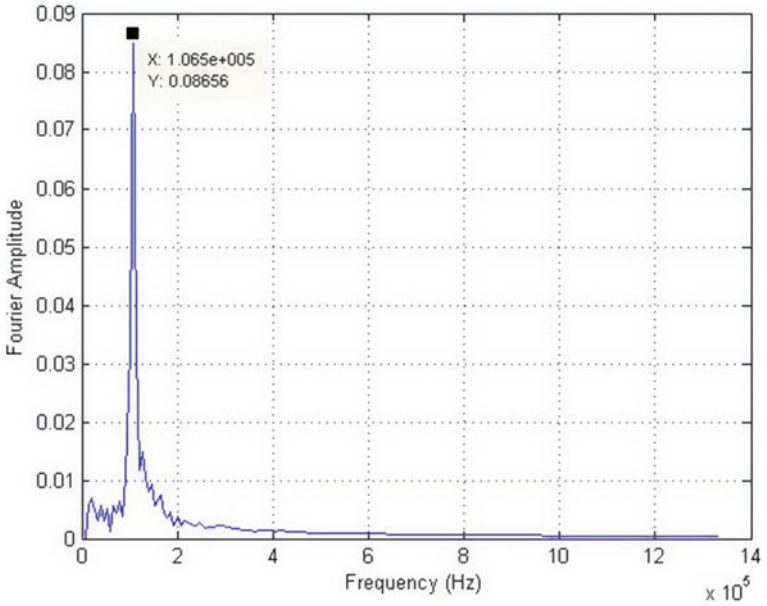

(a)

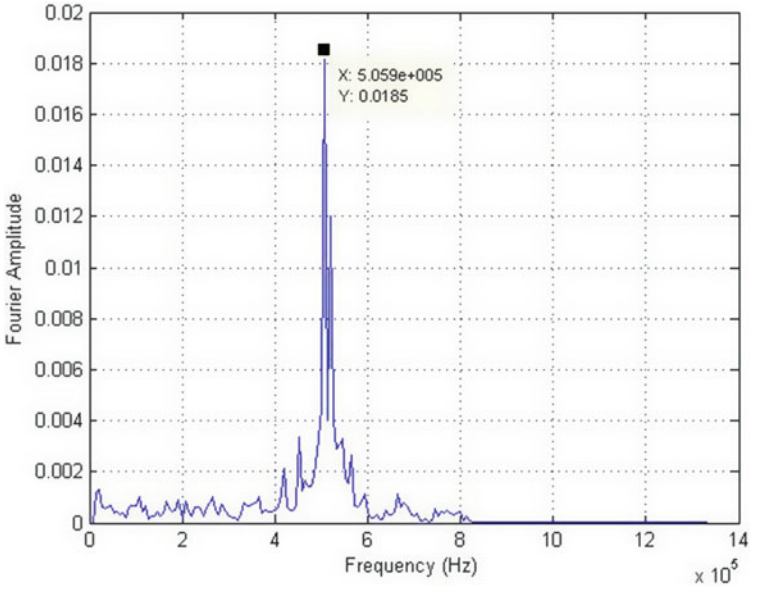

(b)

Fig. 3 FFT data of displacement response due to in-plane AE source causing extensional or symmetric mode. **a** 100 kHz frequency sinusoidal source and **b** 500 kHz frequency sinusoidal source

The response to 100 kHz driving pulse shows that most of the energy is contained below 100 kHz. As the frequency of the driving pulse increases to 500 kHz, the frequency content of the response expands to higher frequencies. However, with 500 kHz driving pulse, it is observed that most of the energy is contained within 500 kHz and very little energy is seen above 600 kHz. It is also observed from the above figures that for 100 or 500 kHz driving pulse, the flexural or asymmetric mode contains more energy below 100 kHz than that of the extensional or symmetric mode. The findings match favourably with those obtained from experiments in Ref. [4]. Hence, it is apparent that by discrimination of the frequency contents of a response signal, the failure mode of damage may be assessed.

3.3 Example 2

In the previous examples, the present model is validated for single-layered anisotropic material. In this example, the present model is used to further study the two-layer composite plate [0/90] of graphite/epoxy. The plate dimension and material properties are same as in Example 1.

The source is positioned at $x = 0.0508$ m and $y = 0.0762$ m. The flexural or asymmetric mode AE waveforms are obtained at a distance 0.0762 and 0.127 m from the source along the longer side of the plate, i.e. along x-direction due to simulated out of plane 100 and 500 kHz sinusoidal pulse.

The frequency responses to 100 kHz sinusoidal driving pulse in the out-of-plane directions, i.e. the frequency responses of the flexural AE waveforms are shown in Fig. 4. Figure 4a shows a response at 0.0762 m from source and Fig. 4b shows the same at 0.127 m from source.

The frequency responses to 500 kHz sinusoidal driving pulse in the out-of-plane directions, i.e. the frequency responses of the flexural AE waveforms are shown in Fig. 5. Figure 5a shows a response at 0.0762 m from source and Fig. 5b shows the same at 0.127 m from source.

For the multi-layer plate, it is also observed that due to 100 kHz pulse the most of the energy for the frequency responses is contained below 100 kHz. This is true both for the responses at 0.0762 m (near filed) and 0.127 m (far filed). For 500 kHz driving pulse, it is observed that for the near field almost no energy is contained at the level of 500 kHz and beyond 500 kHz. For the far field, some energy is found to be contained in the region of 500 kHz. However, the amplitudes are very low compared to the near-field response. Moreover, for the flexural AE waveforms, it can be observed that energy content in the response due to 100 kHz driving pulse is much higher than that of the energy content observed for 500 kHz driving pulse. Hence, it is apparent that by discrimination of the frequency contents of response signals, an idea can be obtained about the frequency content of the driving pulse.

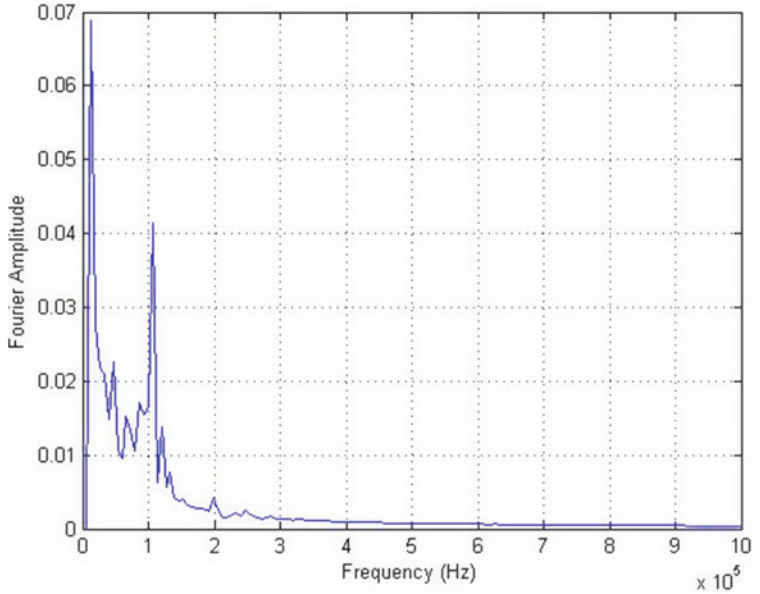

(a)

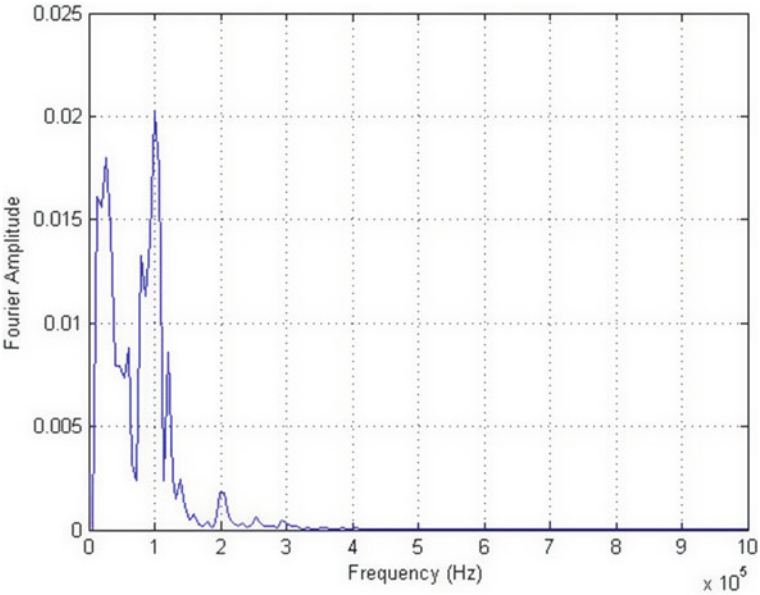

(b)

Fig. 4 FFT data of displacement response due to out of plane AE source causing flexural or asymmetric mode due to 100 kHz sinusoidal source. **a** 0.0762 m from source and **b** 0.127 m from the source

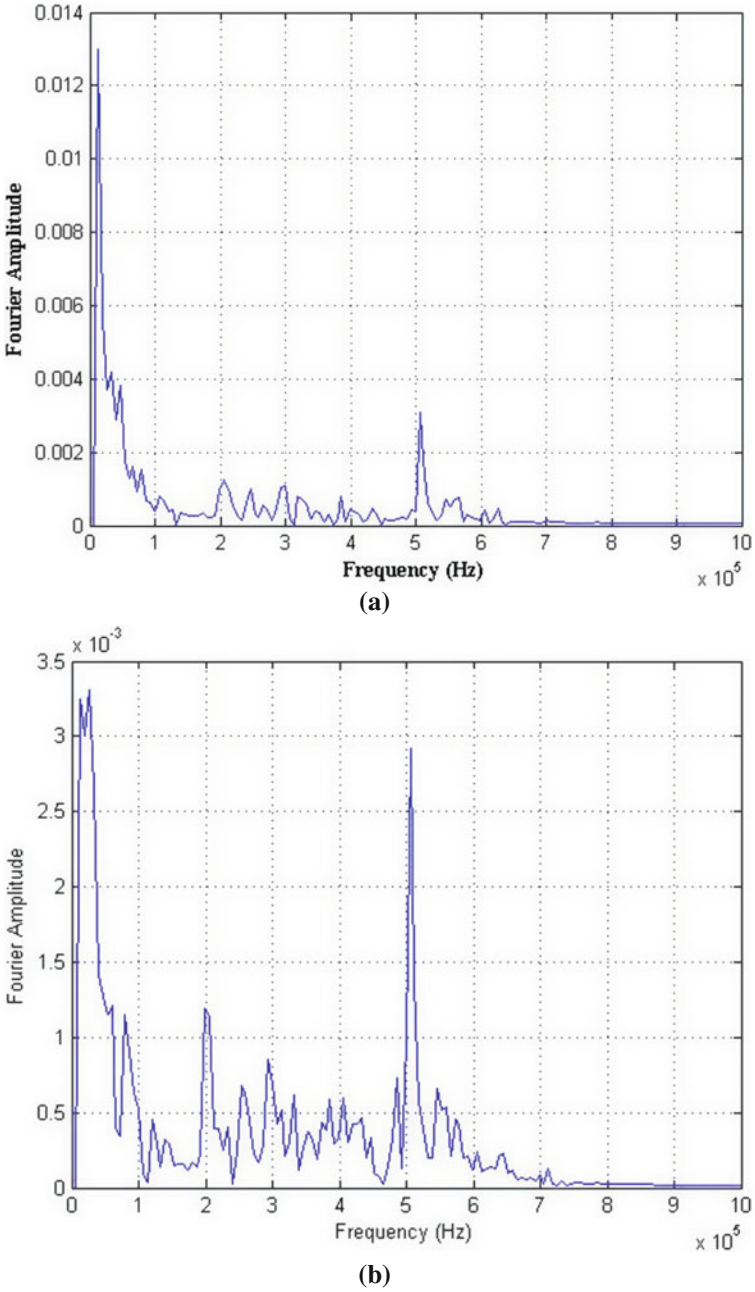

Fig. 5 FFT data of displacement response due to out of plane AE source causing flexural or asymmetric mode due to 500 kHz sinusoidal source. **a** 0.0762 m from source and **b** 0.127 m from the source

3.4 Example 3

In Example 2, the present model is used to study the two-layer composite plate [0/90] of graphite/epoxy for flexural or out-of-plane AE response. In this example, the present model is used to study the extensional or symmetric mode AE response. The plate dimension and material properties are kept same as in Example 2.

The source is positioned at $x = 0.0508$ m and $y = 0.0762$ m. The extensional/symmetric AE waveforms are obtained at a distance 0.0762 and 0.127 m from the source along the longer side of the plate, i.e. along x-direction due to simulated in-plane 100 and 500 kHz sinusoidal pulse.

The frequency responses to 100 kHz sinusoidal driving pulse in the in-plane directions, i.e. the frequency responses of the extensional AE waveforms are shown in Fig. 6. Figure 6a shows a response at 0.0762 m from source and Fig. 6b shows the same at 0.127 m from source.

The frequency responses to 500 kHz sinusoidal driving pulse in the out-of-plane directions, i.e. the frequency responses of the extensional AE waveforms are shown in Fig. 7. Figure 7a shows a response at 0.0762 m from source and Fig. 7b shows the same at 0.127 m from source.

For the multi-layer plate, it is also observed that due to 100 kHz pulse most of the energy for the frequency responses is contained below 100 kHz. This is true both for the responses at 0.0762 m (near filed) and 0.127 m (far filed). However, it is observed that the amplitudes are much lesser than that of the flexural AE waveforms.

For 500 kHz driving pulse, it is observed that for the near field as well as for the far filed some energy is contained in the 500 kHz zone. However, beyond 500 kHz not much energy is found. The energy content is found to be quite less than that of the flexural AE waveforms and extensional AE waveforms due to 100 kHz in-plane driving pulse.

From the above, it can be said that the frequency response due to extensional AE waveforms contain much less energy than the flexural AE waveforms for multi-layer composite plates. Also, due to the change of the nature of the driving pulse, i.e. the source the frequency responses are changing and thus frequency response has a telling effect on the discrimination of damages which causes AE.

The available results in existing literature, e.g. the experimental work done by Eaton et al. [4] depicts a similar trend as is obtained from the present mathematical model.

4 Concluding Remarks

Acoustic emission (AE) can be used for in-service structural health monitoring of composite structures. Composite material components are approximated as plate-like structures due to their laminated nature. In this work, an attempt has been

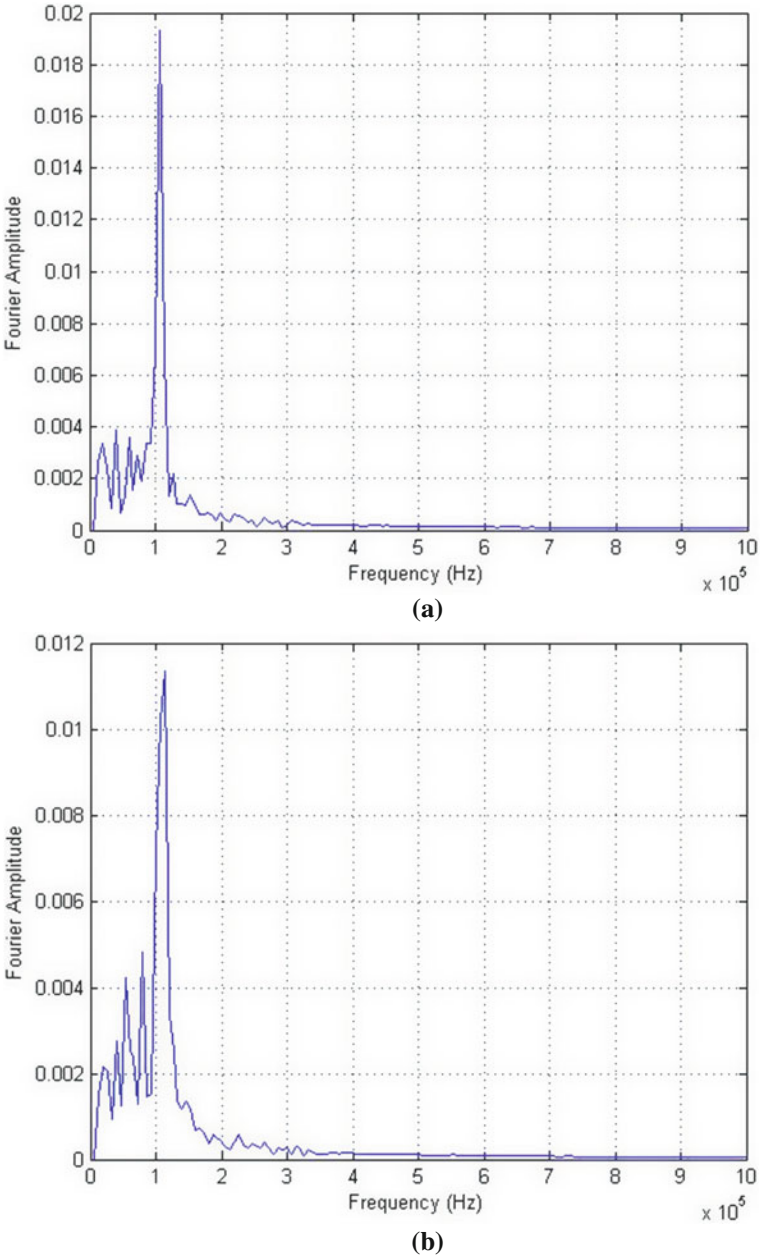

Fig. 6 FFT data of displacement response due to out of plane AE source causing extensional or symmetric mode due to 100 kHz sinusoidal source. **a** 0.0762 m from source and **b** 0.127 m from the source

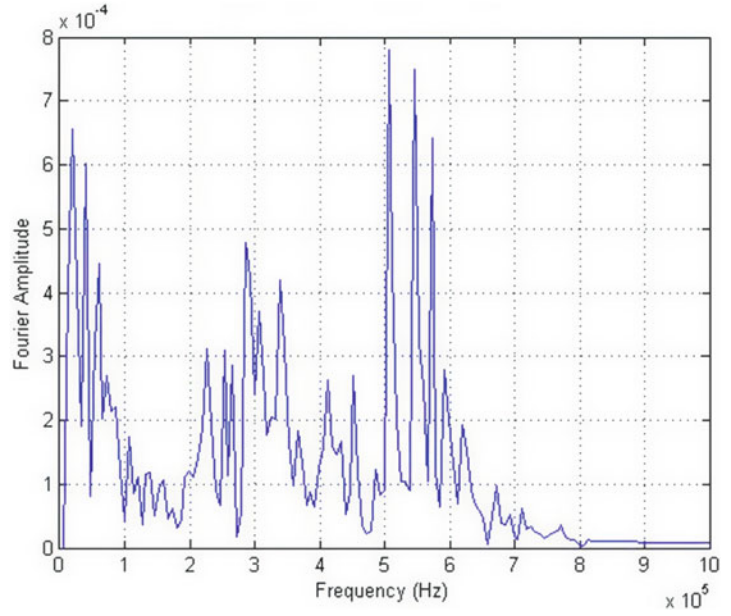

Fig. 7 FFT data of displacement response due to out of plane AE source causing extensional or symmetric mode due to 500 kHz sinusoidal source. **a** 0.0762 m from source and **b** 0.127 m from the source

made to utilise frequency content of the response caused due to AE signals as discriminating factor for determining different modes of failures in composites. A generalised refined plate theory is used for modelling. Single-layer anisotropic as well as multi-layer composite plates are studied under different high-frequency AE like out of plane and in-plane simulated pulse. Frequency responses are obtained and compared to discriminate the simulated damage condition.

The response to 100 kHz driving pulse shows that most of the energy is contained below 100 kHz. As the frequency of the driving pulse increases to 500 kHz, the frequency content of the response expands to higher frequencies. However, with 500 kHz driving pulse, it is observed that most of the energy is contained within 500 kHz and very little energy is seen above 600 kHz. For 100 or 500 kHz driving pulse, the flexural or asymmetric mode contains more energy below 100 kHz than that of the extensional or symmetric mode.

The results show that the source frequency has a telling effect on the frequency content of the response signals which can be used for discrimination of flexural, i.e. out of plane and extensional, i.e. in-plane mode. The present formulation is very general in nature and can, after minor modifications, incorporate the effect of nonlinearity and noise.

References

1. Sengupta, S., Datta, A. K., & Topdar, P. (2015). Structural damage localisation by acoustic emission technique: A state of the art review. *Latin American Journal of Solids and Structures, 12,* 1565–1582.
2. Bohse, J. (2000). Acoustic emission characteristics of micro-failure processes in polymer blends and composites. *Composites Science and Technology, 60,* 1213–1226.
3. Ramirez-Jimenez, C. R., Papadakis, N., Reynolds, N., Gan, T. H., Purnell, P., & Pharaoh, M. (2004). Identification of failure modes in glass/polypropylene composites by means of the primary frequency content of the acoustic emission event. *Composites Science and Technology, 64,* 1819–1827.
4. Eaton, M., Holford, K., Featherston, C., & Pullin, R. (2007). Damage in carbon fibre composites: The discrimination of acoustic emission signals using frequency. *Journal of Acoustic Emission, 25,* 140–148.
5. Cho, M., & Parmerter, R. R. (1993). Efficient higher order plate theory for general lamination configuration. *AIAA Journal, 31*(7), 1299–1308.
6. Topdar, P., Sheikh, A. H., & Dhang, N. (2007). Vibration characteristics of composites/sandwich laminates with piezoelectric layers using a refined hybrid plate model. *International Journal of Mechanical Sciences, 49,* 1193–1203.
7. Bathe, K. J. (1996). *Finite element procedures*. Prentice Hall.

Handling Environmental and Operational Variations in Structural Health Monitoring

K. Lakshmi and A. Rama Mohan Rao

Abstract Handling environmental and operational variability is currently the major challenge in successfully implementing the structural health monitoring techniques on real structures especially civil structures like bridges. Even though several methods are proposed in the literature to handle the environmental variability, it still remains an active area of research. In this paper, we present a damage diagnostic technique capable of handling environmental variability is presented. The method proposed is based on time series and we combine time series (AR-ARX) model with cointegration techniques to isolate the effects of environmental and operational variability in the measured acceleration time history signals. Numerical and experimental verification of the proposed algorithm is presented in this paper.

Keywords Damage diagnostic techniques · Structural health monitoring
Environmental variability · Cointegration · AR-ARX model

1 Introduction

From past two decades, researchers around the globe have paid great attention towards the development of a variety of damage diagnostic techniques for structural health monitoring due to their significance in the safety assessment of engineering structures. Majority of earlier damage diagnostic techniques are mainly focused on evaluating damage features from modal properties of the structures like natural frequency, modal curvatures, modal flexibility, modal strain energy, frequency response functions, Ritz vectors, etc., [1]. Even though most of these techniques work well during numerical simulations and lab-level experimentation, they found to be ineffective for practical implementation on real structures under variable

K. Lakshmi (✉) · A. Rama Mohan Rao
CSIR-Structural Engineering Research Centre, Taramani, Chennai 600113, India
e-mail: lakshmik@serc.res.in

A. Rama Mohan Rao
e-mail: arm2956@yahoo.com

A. Rama Mohan Rao and K. Ramanjaneyulu (eds.), *Recent Advances in Structural Engineering, Volume 1*, Lecture Notes in Civil Engineering 11,
https://doi.org/10.1007/978-981-13-0362-3_88

operational and environmental conditions. This is mainly due to the fact that the damage features are often masked by these environmental and operational variabilities. In view of this, signal processing techniques like multivariate analysis [2], time series models [3–5], time–frequency and time scale analysis [6], can be tuned to handle the environmental and operational variability are gaining popularity. The other major advantage of these time series and time–frequency models are that they are highly adaptive for implementation on wireless smart sensor networks (WSSN). The changes in operational and environmental conditions [7] is highly profound in the context of civil infrastructure monitoring programs, as the measured structural responses of a structure in operational condition are exposed to daily and seasonal variations, due to the wind, temperature loading and operational loadings (i.e. traffic loads on bridges). In such cases, any changes in the structural responses due to the occurrence or the progression of damage can be easily masked by the nonstationary dynamic and quasi-static responses exhibited due to the presence of the variability.

As it is considered to be intuitive that the temperature variability is capable of changing the material property of a structure, the effects due to temperature on the measured dynamical structural responses have been discussed in several studies. In order to isolate the changes due to temperature from the damage, at present, two approaches are being followed. The first approach employs a physics-based model to predict the response of healthy (baseline) structure over its operational range under various environmental conditions. However, reliable physics-based models are often very difficult or impossible to obtain for complex structures. Alternatively, a data-driven model can be created through experimental measurements of the baseline structure. However, this requires a very large database to create a model valid under various operational and environmental conditions. The second approach tries to measure the factors concerned with operational/environmental variations such as wind speed, moisture levels, temperature, live loads, as well as the structural response at various locations. Parameterization of the normal condition of the structure in terms of a function of different operational and environmental conditions is performed. Popularly, novelty detection procedures can be employed with such parameterized model to detect the deviations of the measured structural responses from the normal condition that corresponds to the appropriate operational and environmental conditions.

In this paper, we propose an output-only damage diagnostic technique for detecting and locating the damage on the structure by combining time series model with the cointegration technique. The cointegration technique [8] is used in the proposed damage diagnostic algorithm to handle the environmental and/or operational variability. The effectiveness of the proposed damage diagnostic algorithm is verified through numerical simulation studies considering environmental variability as well as experimental studies conducted in the lab simulating environmental variability.

2 Handling Environmental Variability Combining Time Series Models with Cointegration

2.1 Cointegration Technique

In most of the techniques proposed for SHM, the features obtained from the responses of the system under observation, are tested to determine whether significant changes in the features extracted are related to damage or not. As mentioned, operational and environmental variability or other nonstationary influences can indicate significant changes in the features extracted that are not due to damage. Recently, cointegration from econometrics [9] was proposed as a viable solution to handle the problems associated with environmental variability. 'Cointegration', is defined as a property of a multivariate nonstationary time series. If an arbitrary linear combination, $a_1x_1(t) + \ldots + a_nx_m(t)$, of a m-dimensional time series exhibits stationarity, then the said m-dimensional time series is said to be cointegrated. The coefficients form a 'cointegrating vector' and the combination is called a 'cointegrating relation'. Multiple cointegrating relations are possible among the variables. The approach used for the analysis is adopted mainly based on the Johansen's procedure [10], which is capable of finding the cointegrating vector that results in the stationary combination of the variables.

It can be noted that the "degree of nonstationarity" of the cointegrated time series is same. The "degree of nonstationarity" is otherwise known and understood as the "order of integration" of the time series. By the process of differencing, a time series which is nonstationary is integrated to form a stationary one. The order of integration is found to be the number of differences required to become stationary and it can be estimated by a stationarity test. To test the stationarity, the Augmented Dickey–Fuller (ADF) test [11] is used. The ADF test procedure uses the least-squares methods to estimate the parameters in Eq. (1) for the process x_i and the difference operator, Δ.

$$\Delta x(t) = \delta x(t-1) + \sum_{j=1}^{p-1} a_j \Delta x(t-j) + \tilde{\varepsilon}(t) \tag{1}$$

Then null hypothesis $\delta = 0$ is tested using the test statistic:

$$t_\delta = \frac{\hat{\delta}}{\sigma_\delta} \tag{2}$$

where the least-squares estimate of δ is $\hat{\delta}$ and σ_δ is the variance of the parameter estimate, with critical values, similar to conducting a t-test. The hypothesis is said to be rejected at the level η, if $t_\delta < t_\eta$, where t_η is the critical value. If the hypothesis gets accepted, then it can be understood that the root of the time series is unity and is I(1). And if the hypothesis gets rejected, the test is repeated for $\Delta x(t)$ and now, if

the hypothesis is accepted, then $x(t)$ becomes an I(2) nonstationary sequence. This process is continued till the order of integration of the time series is found. If the model is to be extended for deterministic trends or shifts, it is required to employ additional test statistics and hypotheses. After confirming the order of integration of the interested variables, cointegration analysis is carried out using the variables of the same order. The Johansen procedure [10], is popularly used to obtain the possible linear combination of the variables which are 'most' stationary, for few set of nonstationary variables. This process uses the maximum likelihood argument to obtain the estimation of the cointegrating vectors for I(1) variables. The Johansen procedure is a complex theory and is not discussed here in detail. However, the essential steps to carry out the Johansen procedure are discussed for completion. The Johansen procedure starts with the fitting of the variables of interest to a Vector Auto-Regressive (VAR) model, of the following form:

$$\begin{aligned}\{x(t)\} = [C_1]\{x(t-1)\} + [C_2]\{x(t-2)\} \\ + \cdots + \left[C_p\right]\{x(t-p)\} + \{\tilde{\varepsilon}(t)\}\end{aligned} \tag{3}$$

where p, the most suitable model order, is obtained by an Akaike Information Criterion(AIC) or from any of the similar procedures. The cointegrating vectors are present in the matrix $[\xi]$ in the vector error correction model (VECM) as follows

$$\{z_0(t)\} = [\omega][\xi]^T\{z_1(t)\} + [\Psi]\{z_2(t)\} + \{\varepsilon(t)\} \tag{4}$$

where $\{z_0(t)\} = \{\Delta x(t)\}, \{z_1(t)\} = \{x(t-1)\}$, $\{z_2(t)\} = \{\{\Delta x(t-1)\}^{\mathrm{T}}$, $\{\Delta x(t-2)\}^{\mathrm{T}}, \{\Delta x(t-p)\}^{\mathrm{T}}, \{D_T\}^{\mathrm{T}}\}^T$ $[\Psi] = [[A_1], [A_2], \ldots, [A_{p-1}], [\Phi]]$, $\{D_{\mathrm{T}}\}^{\mathrm{T}}$ is a deterministic trend term. It should be noted that the following regression residuals $\{r_0(t)\}$ and $\{r_1(t)\}$ are to be evaluated first, to find $[\xi]$,

$$\{Z_0(t)\} = [M_1]\{Z_2(t)\} + \{r_0(t)\} \tag{5}$$

$$\{\mathrm{Z}_1(t)\} = [M_2]\{\mathrm{Z}_2(t)\} + \{r_1(t)\} \tag{6}$$

Once the residuals are found, then the product moment matrices are defined as

$$\left[K_{jk}\right] = \frac{1}{N}\sum_{t=1}^{N}\left\{r_j(t)\right\}\left\{r_k(t)\right\}^T \quad j,k = 0,1 \tag{7}$$

At last, the cointegrating vectors are obtained from the generalized eigenvalue problem, of the moment matrices, as follows:

$$\left(\lambda'[K_{11}] - [K_{10}][K_{00}]^{-1}[K_{01}]\right)\{v\} = 0 \tag{8}$$

The eigenvectors corresponding to the largest eigenvalue become the cointegrating vector that results in the best stationarity state, out of combining the original

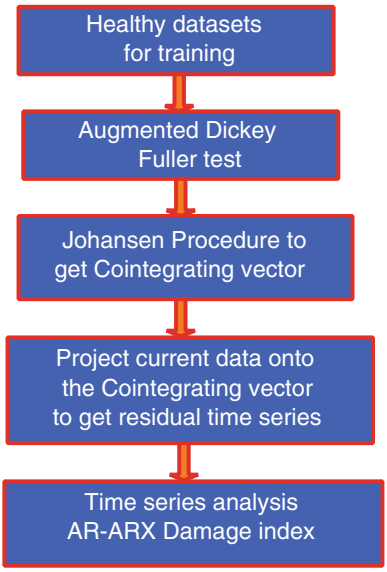

Fig. 1 Flowchart of the proposed technique using cointegration to handle environmental variability

variables. More details on cointegration can be found in Refs. [9, 10]. The implementation of the cointegration technique in practice for SHM involves the establishment of the cointegrating vectors using data from the undamaged structure during the training period. When a new data arises, it is projected on the cointegrating vector obtained earlier and observed for the stationarity of the combination. On introduction of any damage, this stationarity is lost and the combination becomes nonstationary. This gives the time instant of damage and time series analysis is carried out using AR-ARX model on the data after damage to find the spatial location of damage. The complete damage detection process combining time series models with cointegration is shown in Fig. 1.

2.2 *Time Series Analysis*

Once the time series is cointegrated, it becomes stationary and free from environmental and operational effects but preserves all the damage features. Subsequently, AR-ARX model is used for damage diagnostics of the cointegrated time series $x(t)$. For an acceleration time series $x(t)$ of each channel in the subsets of reference data, an AR model is constructed with 'P' AR terms as

$$x(t) = \sum_{j=1}^{p} \phi_{xj} x(t-j) + e_x(t) \tag{9}$$

where ϕ denotes the AR coefficients and e_x denotes the prediction errors. With an assumption that the error $e_x(t)$, between the measurement and the prediction

obtained by AR model is primarily due to the external unknown input, an ARX model is used to reconstruct the input–output relationship between $e_x(t)$ and $x(t)$ as follows.

$$x(t) = \sum_{i=1}^{a} \alpha_i x(t-i) + \sum_{j=1}^{b} \beta_j e_x(t-j) + \varepsilon_x(t) \tag{10}$$

where $\varepsilon_{\boldsymbol{x}}(\boldsymbol{t})$ indicates the prediction error of the ARX(a, b) model fitted to the $e_x(t)$ and $x(t)$ pair.

Now, the accuracy of ARX(a, b) model, estimated in Eq. (10), is investigated in reproducing the input/output relationship of $e_y(t)$ and a current data subset, $y(t)$.

$$\varepsilon_y(t) = y(t) - \sum_{i=1}^{a} \alpha_i y(t-i) + \sum_{j=1}^{b} \beta_j e_y(t-j) \tag{11}$$

where $e_y(t)$ is considered to be an approximation of the system input estimated from Eq. (9) for a current data subset. α_i and β_j coefficients are related to $x(t)$ and obtained from Eq. (10).

The probability density function (PDF) curves are constructed using the residual errors obtained from ARX model for the time series data at each node and they follow a Gaussian distribution. Further, the PDF curve constructed using the residual errors obtained for the time history data measured at a node near the damage location is found to be more dispersed than the corresponding time history data before damage. Similarly, the peak of the PDF curve related to data with structural damage is also much lesser in comparison with healthy PDF curve. The details of PDF curves drawn for time history data at a typical node with the structure both in healthy state and also with damage is shown in Fig. 2. The

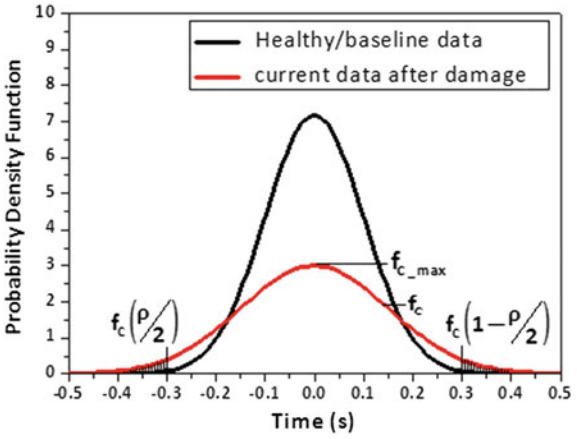

Fig. 2 PDFs of residual errors of healthy and damage data from a sensor near an arbitrary damage location

difference in the PDF curves is exploited to arrive at a damage index. The damage index is defined as

$$\text{DI\_PDF} = \frac{f_{c(1-\rho/2)} = -f_{c(\rho/2)}}{f_{c\_max}} \tag{12}$$

3 Numerical Studies

3.1 Simply Supported Beam

The simply supported beam girder, with a span of 6 m as shown in Fig. 3 is considered as a numerically simulated example to verify the effectiveness of the cointegration in handling the environmental variability. The generated baseline data is divided into 80 subsets and varied levels of measurement noise (i.e. SNR values varying between 40 and 60) is added to each subset of data to simulate the noise and other uncertainties in the measurements. A random temperature in the range of −15 to 50 °C is simulated while generating the baseline subset data. Each subset of baseline data consists of 500 samples. The healthy data generated is partitioned into 30 subsets. These subsets (signals) are with varying levels of noise, environmental conditions and also obtained with random input excitation. Similarly, 30 current data subsets (i.e. 15 s data) are generated with varied temperature, operational loads and measurement noise. The current data is a combination of the data from a healthy structure and the data with simulated damage on the structure in predefined elements. Hypothetical damage scenarios are simulated by reducing the stiffness of 4th element by 25%, after obtaining 20,000 samples of current data (i.e. after 10 s). Out of 30 current subsets, last 10 subsets are considered to be obtained from the structure after damage.

Initially, the healthy data subsets are subjected to the Augmented Dickey–Fuller test and then to the Johanson's procedure to obtain the cointegrating vector. This is the training phase and the current data subsets are employed in the testing phase to diagnose the damage. The first cointegrating vector obtained from the training phase is projected onto the current data subsets to purge of the environmental and operational variability. This produces a cointegrated time series vector which must be stationary. Figure 4 shows the cointegrated vector of a training data subset (500 samples) and a current data subset (500 samples) from the healthy structure. From the figure, it can be observed that the cointegrated time series of the current

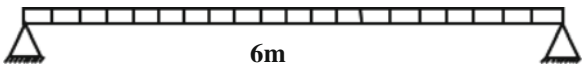

Elastic Modulus = 205 GPa ; Cross sectional Area = 0.225m^2 ;
Mass Density = 7850 Kg/m^3; Moment of Inertia = 0.000562 m^4

Fig. 3 Simply supported beam

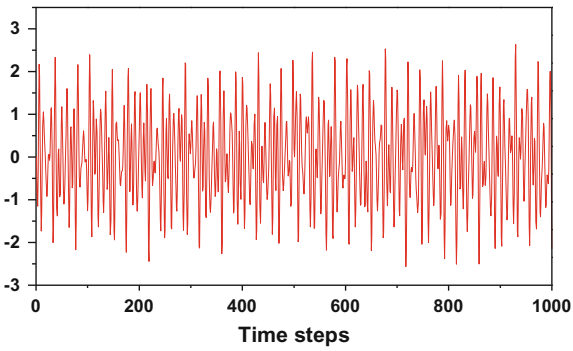

Fig. 4 Cointegrated residual of a healthy current data

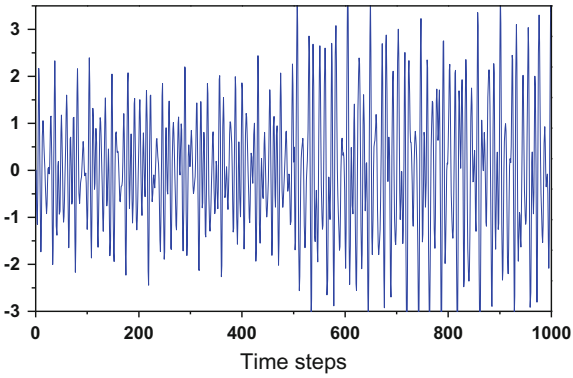

Fig. 5 Cointegrated residual of current data with damage

data subset is stationary and follows a similar trend of the training data subset. When the 21st subset is subjected to damage detection, the cointegrated time series of the current data subset departs from that of the training subset indicating the presence of damage. This is shown clearly in Fig. 5. The time instant of damage can be obtained from the index number of the subset which is being investigated for damage.

Once the presence of damage is indicated, the time series analysis is performed after normalisation [4] of data to evaluate the damage index of every sensor using AR-ARX model errors. The PDF-based damage index described in the earlier section is employed to determine the spatial location of damage. Figure 6a, b show the damage index of the subset when diagnosed with and without the cointegration procedure to handle the environmental variability respectively. The damage indices are shown in Fig. 6, clearly, indicating the spatial location of damage as element number 4.

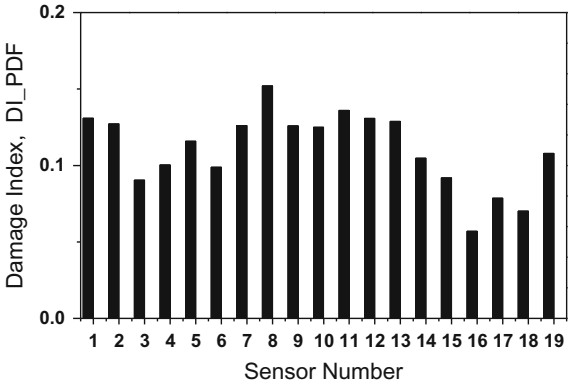

(a) Without cointegration

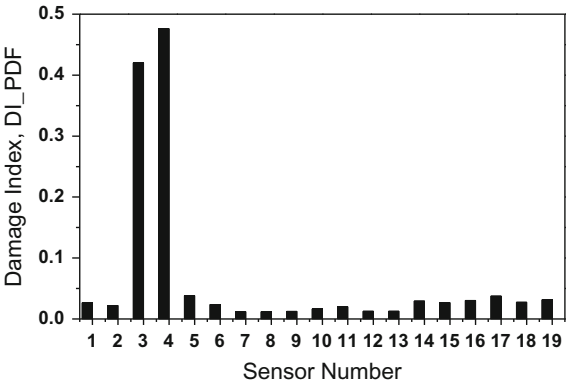

(b) With Cointegration

Fig. 6 Damage indices obtained using time series model with and without cointegration

4 Experimental Verification

Laboratory experimental studies in CSIR-Structural Engineering Research Centre (SERC) are carried out to validate the ability of the proposed damage diagnostic algorithm. The test structure considered is a simply supported RCC beam with dimensions: span length-3000 mm, Width-165 mm and Depth-200 mm and is shown in Fig. 7. The beam is instrumented with 16 MEMS accelerometers, placed spatially at equal distances along the beam to obtain acceleration time history data. In order to simulate the ambient vibration on the beam, a hydraulic actuator, applying the random and harmonic loadings at the centre of the beam is used. The loading frequencies, as well as amplitude, is varied during each set of measurements to simulate operational variability. Similarly, in order to simulate the environmental variability, small masses are randomly placed on the beam for each set of measurements. Damage in the form of a crack is inflicted at one- third of a span of the beam from the left support and after collecting time history measurements,

Fig. 7 Experimental setup for the verification of the proposed damage diagnostic algorithm

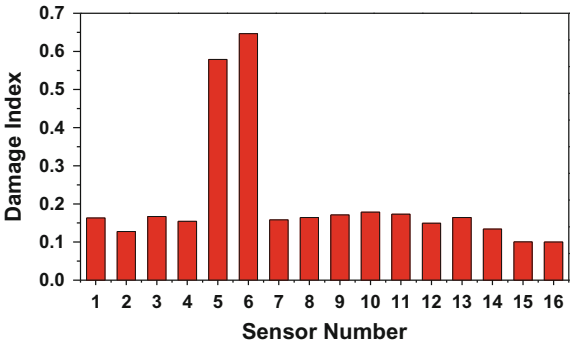

(a) Single damage scenario

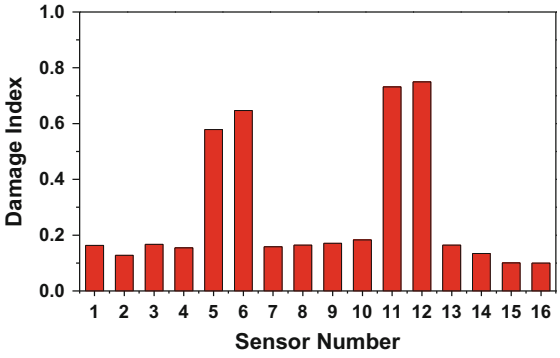

(b) Multiple damage scenario

Fig. 8 Damage indices of single and multiple damage scenarios of the simply supported RCC beam

another damage is inflicted at one-third of the beam from right support. The damage indices obtained using the proposed damage diagnostic technique for both the single and multiple damage scenarios are shown in Fig. 8. From Fig. 8, it can be

seen that the cointegration purges the effect of the environmental variability and enables the damage index DI_PDF to locate single as well as multiple damages effectively.

5 Conclusion

In this paper, a novel damage diagnostic technique, combining cointegration with AR-ARX model to handle environmental and operational variability is presented. The proposed damage diagnostic algorithm is verified using both numerically simulated examples as well as using experimental results. The studies presented in this paper clearly indicated that the proposed technique is effective in identifying the time instant as well as the spatial location of damage and it can handle the measurement noise apart from environmental and operational variability quite effectively.

Acknowledgements This paper is being published with the permission of the Director, CSIR-Structural Engineering Research Centre (SERC), Chennai.

References

1. Doebling, S. W., Farrar, C. R., & Prime, M. B. (1998). A summary review of vibration-based damage identification methods. *Shock Vibration Digest, 30*(2), 91–105.
2. Rama Mohan Rao, A., Lakshmi, K., & Dhanya, V. (2012). Damage diagnostic technique for structural health monitoring using POD and self-adaptive differential evolution algorithm. *Computers and Structures, 106–107*, 228–244.
3. Sohn, H., & Farrar, C. R. (2001). Damage diagnosis using time series analysis of vibration signals. *Smart Material Structures, 10*(3), 446–451.
4. Lakshmi, K., & Rama Mohan Rao, A. (2015). Damage identification technique based on time series models for LANL and ASCE benchmark structures. *Journal of Non-destructive Testing and Condition Monitoring, 57*(10), 580–588.
5. Lakshmi, K., & Rama Mohan Rao, A. (2014). A robust damage-detection technique with environmental variability combining time-series models with principal components. *Nondestructive Testing and Evaluation, 29*(4), 357–376.
6. Rama Mohan Rao, A., & Lakshmi, K. (2015). Damage diagnostic technique combining POD with time-frequency analysis and dynamic quantum PSO. *Meccanica*, 50, 1551–1578.
7. Worden, K., Farrar, C. R., Manson, G., & Park, G. (2007). The fundamental axioms of structural health monitoring. *Proceedings of the Royal Society A: Mathematical, Physical and Engineering Science, 463*(2082), 1639.
8. Worden, K., Cross, E. J., Antoniadou, I., & Kyprianou, A. (2014). A multiresolution approach to cointegration for enhanced SHM of structures under varying conditions—An exploratory study. *Mechanical Systems and Signal Processing, 47*(1–2), 243–262.

9. Engle, R., & Granger, C. (1987). Co-integration and error-correction: Representation, estimation, and testing. *Econometrica, 55,* 251–276.
10. Johansen, S. (1995). Likelihood-based inference in cointegrated vector autoregressive models. USA: Oxford University Press. ISBN 0198774508.
11. Dickey, D. A., & Fuller, W. A. (1979). Distribution of the estimators for autoregressive time series with a unit root. *Journal of the American Statistical Association, 74*(366), 427–431. ISSN 0162-1459.

Influence of Curing on Acoustic Emission Characteristics of Plain Concrete Subjected to Uniaxial Compression

Richa Priyadarshi, Isha Narsaria, K. P. Sreejaya and R. Vidya Sagar

Abstract Acoustic emissions (AE) released during the uniaxial compression testing of cylindrical plain concrete specimens were analysed to study the fracture process by the computation of *b*-value of Gutenberg–Richter relation. Also, the influence of curing of plain concrete on AE characteristics like energy and cumulative count has been studied. The *b*-value decreased suddenly at $\sim$96% of failure stress. Also, the lateral shift towards left was observed in *b*-value based on the concrete compressive strength. The cumulative AE count at different stages of loading can be useful to study the crack propagation. Also, the crack pattern emerged on the test specimen near the peak stress was analysed using the locations of the AE events recorded. At the time of ultimate failure, shear cracks were observed.

Keywords Concrete · Compressive strength · Fracture · Non-destructive testing Crack pattern

R. Priyadarshi · I. Narsaria
Department of Civil Engineering, BITS Pilani, 333 031 Pilani, India
e-mail: f2014793@pilani.bits-pilani.ac.in

I. Narsaria
e-mail: f2014490@pilani.bits-pilani.ac.in

K. P. Sreejaya
Department of Civil Engineering, GEC, 680 009 Thrissur, India
e-mail: sreejayakp@gmail.com

R. Vidya Sagar (✉)
Department of Civil Engineering, I.I.Sc, 560 012 Bangalore, India
e-mail: rvsagar70@gmail.com

A. Rama Mohan Rao and K. Ramanjaneyulu (eds.), *Recent Advances in Structural Engineering, Volume 1*, Lecture Notes in Civil Engineering 11,
https://doi.org/10.1007/978-981-13-0362-3_89

1 Introduction

Concrete is a quasi-brittle material. It is widely used in the construction of many structures like bridges, dams, buildings, etc. There is a necessity to monitor and assess the performance as well as the safety of concrete structures. AE monitoring technique is one of the powerful methods to study fracture process in concrete structures [1]. It is important to understand the initiation of internal cracks in concrete and their propagation with increasing load.

Acoustic emission is the phenomena where transient elastic waves are generated by the rapid release of energy from localized sources within a material under stress. It is the process of emission and propagation of stress waves generated from local irreversible changes in the material. In concrete, during fracture process, the AE energy will be released in the form of stress waves which propagate in the material. These stress waves can be detected on the surface of the material by mounting piezoelectric transducers which convert the mechanical waves into electrical signals. AE occurs at locations where there is a chance of new permanent deformations developed due to high stresses.

The AE monitoring method is one of the non-destructive testing (NDT) methods in which the recorded parameters of AE wave can be utilized for detecting damage in concrete structures.

b-value analysis is used to process and interpret the AE data obtained from the monitoring of a structure. It is used to study the fracture process of the concrete and measure the severity of a damage.

According to Gutenberg–Richter empirical relation [G–R relation] as shown in Eq. (1), the *b*-value is defined as the log-linear slope of the frequency–magnitude distribution of the earthquakes [2, 3].

$$\log_{10} N = a - bM \tag{1}$$

where M is Richter magnitude of the earthquakes; N is the number of earthquakes having a magnitude greater than M, a and b are constants. *b*-value is an important parameter used to study the occurrence of earthquakes and is widely used in seismology [1].

Analogous to the occurrence of earthquakes, frequency of waves having higher amplitude AE is less and low-amplitude AE waves are more during fracture process in concrete. *b*-value can also be computed in the case of AE monitoring technique. Based on the extent of damage in the concrete structure, AE signals of different amplitude are generated by micro or macrocracks. Microcracks having small amplitude are generated in large number, whereas macrocracks having larger amplitude are lesser in number. The G–R relation can be modified in case of AE technique as shown in Eq. (2)

$$\log_{10} N = a - b\left(\frac{A_{\mathrm{dB}}}{20}\right) \tag{2}$$

where N is the incremental frequency (i.e., the number of AE events or hits with an amplitude greater than the threshold amplitude, a and b are constants. b-value is defined as the 'log-linear slope of the frequency–amplitude distribution' of AE [2]. When a reinforced concrete (RC) beam is subjected to flexure, it undergoes both compressive and tensile stresses. If the strain in the tension steel exceeds the allowable limit, then the crack propagates from the tension zone to the compression zone. Hence, the study of fracture of concrete in compression is required. Parametric study of Acoustic Emission is important to establish a relation between the failure mechanism with various AE parameters. The damage severity can be assessed based on following relations: (1) Significant changes in AE parameters during various stages of cracking namely, initiation, propagation and coalescence of cracks (2) Nature of crack (microcrack and macrocrack) to assess the severity of damage, especially post ultimate load (3) Brittleness of concrete (4) Mode of failure of the material (Shear or tensile).

2 Experimental Program

2.1 Materials and Test Specimens

Uniaxial compression tests were conducted using cylindrical concrete specimens (150 mm dia X 300 mm height) on 7th, 14th and 28th day. 10 concrete specimens were designed for M25 according to IS 10262:2009. The concrete mixture proportion details are given in Table 1. Specimens were cast and later cured at the room temperature.

Table 1 Concrete mixture proportions (kg/m^3)

Property		
Cement (53 Grade; OPC)		426
Coarse aggregate	12.5 mm	455
	20 mm	682.6
Fine aggregate		612.6
Water		192
Water/binder ratio		0.45
Compressive strength (MPa)	7th day	27
	14th day	28.25
	28th day	33.4

2.2 Test Setup

Compression tests were conducted under displacement control at a rate of 0.002 mm/s using servo-controlled hydraulic testing machine of capacity 1200 kN. Simultaneously, the various AE parameters were recorded using an 8 channel PC-based AE system (Spartan of PAC, USA). The test setup is shown in Fig. 1.

2.3 AE Monitoring System

A 8-channel AE monitoring system was used to record the released AE. Resonant-type AE sensors (57 kHz) were mounted on the specimen. An equilateral triangular grid layout of AE sensors is used as shown in Fig. 2a, b. The AE threshold was set at 39 dB with floating value of 6 dB. The sensors were mounted in a triangular grid so that the whole specimen can be covered and the detected signals do not overlap hence, minimizing the error.

3 Results and Discussion

3.1 AE-Based b-Value Analysis

Uniaxial compressive tests were carried out on a group of 3 similar and identical specimens each on 7th, 14th and 28th day. AE-based *b*-value was calculated by using Eq. (2). A group of 100 hits was taken to reduce the computation effort. *b*-value has an inverse relation with the amplitude of the AE signal detected as discussed. On superimposing the *b*-value versus time graph with load versus time graph, a pattern can be observed which explains the fracture mechanism in concrete. It is shown in Fig. 3.

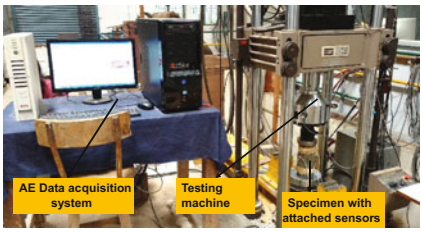

Fig. 1 Experimental setup in Structures laboratory, Civil Engineering Department, IISc Bangalore

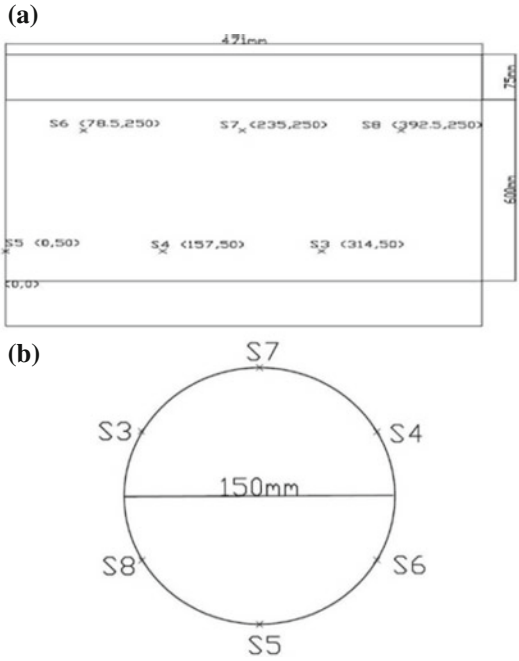

Fig. 2 **a** View of the cylindrical specimen showing the position of the sensors. **b** Top view of the cylindrical specimen mounted with AE sensors. [S3 to S8 indicates sensors]

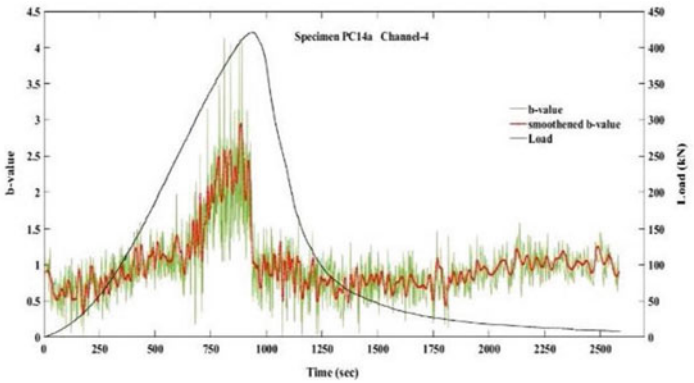

Fig. 3 Variation of *b*-value with time [tested on 14th day; *b*-value is smoothened by taking the mean of five and overlapped in the same plot]

In the initial stages of loading, a gradual increase in *b*-value is observed varying from 0.5 to 4 which encounters a sudden drop at ∼96% of the peak load. On further increase in loading until the final collapse of the specimen, the variation of *b*-value is only from 1.0 to 1.5. A high *b*-value arises due to low-amplitude hits in

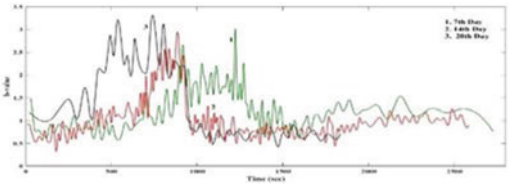

Fig. 4 Variation of *b*-value with the curing

large number representing new crack formation and slow crack growth, whereas a low *b*-value indicates faster or unstable crack growth accompanied by relatively high amplitude AE [4]. The crack growth is characterized by coalescence of microcracks. After the peak load is attained, macrocracks are visible resulting in low *b*-values.

The similar pattern of decrease in *b*-value is observed for 7th-day and 28th-day specimen as in 14th-day specimen. Through Fig. 4, a relation between *b*-value with the age of concrete has been tried to establish. A shift in *b*-value curve towards left is observed due to change in the compressive strength of concrete. As brittleness of concrete increases with the curing period, less high-energy AE events are generated, hence lower *b*-value after the peak load is observed.

The shifting of the time for attainment of peak stress indicates the increase in the brittleness of the concrete [5]. It can be observed that the concrete of age 7th day is more ductile in nature while the concrete age of 28 days is more brittle as shown in Fig. 5.

The time at which the specimen failed for 7th-, 14th- and 28th- day test was 2733 s, 2600 s and 1818 s respectively. The 7th-day concrete is capable of bearing less stress than 28th-day concrete but it can bear it for longer period of time due to its ductile nature. The dotted line in the Fig. 5 indicates the 14th-day response, which shows lesser softening than the former one. As 28th-day concrete is more brittle in nature, it attained the peak stress before the other two and showed a

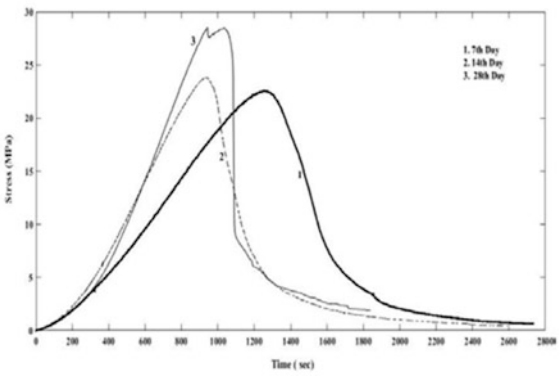

Fig. 5 Variation of compressive strength with curing period

sudden decrease in the post-peak region. It is observed that when the concrete is more brittle, softening of concrete after post peak is less. Though Fig. 5 does not establish any new result but it confirm previously known facts.

3.2 Analysis of Cumulative AE Counts

AE count is the number of threshold crossings of an AE signal. On ageing, the cumulative count is found to shift towards left as stress level changes. It indicates that as macrocracking is more in the brittle material upon loading, it results in higher cumulative AE count.

The AE count recorded during the test can be divided into three phases namely (i) silent period, (ii) swift growth period and (iii) surge period (Fig. 6a, b, c) on the basis of change of slope of the cumulative count with time.

In silent period, AE counts are very less in number due to the occurrence of microcracks. The cracks are stable as the coarse aggregates prevent the formation of macrocracks. Also, the rate of change of the cumulative count is very small. In swift growth period, due to increase in stress, number of AE counts also increased but not significantly. It can be distinguished from the silent period by considering the change in the slope of the graph. While in the surge period, as the peak stress is reached, number of AE count has increased suddenly. Duration of surge period is increased with the age of concrete as the concrete has become more brittle.

The cumulative AE count increased with the age of the concrete due to increase in the strength of the concrete. It can be observed from Fig. 6a–c that as brittleness of concrete increased, duration of surge period decreased and rate of increment of counts increases. As near to peak load, microcracks coalesces to form macrocrack, less number of high amplitude AE are emitted and rate of threshold crossing reduced. At peak stress predominantly macrocracks are present, surge period increases with ageing of concrete. Also, it is observed from Fig. 6c is that even after reaching peak stress at t = 934 s, the specimen resist more stress. The reason may be due to aggregate inter-locking. The slope of the cumulative AE count also changed twice once at t = 934 s and other at t = 1050 s, strengthening the occurrence of surge period. It shows that on attaining ultimate load, there is an increase in AE count.

3.3 Variation of AE Energy

AE energy can be defined as the total elastic transient energy released by an emission event. AE energy is more sensitive to amplitude and duration of an AE signal than AE count. Also, it is less dependent on frequency and threshold of AE signal. It can be considered a better measure to interpret the magnitude of the source rather than counts. Figure 7a, b, c, shows the variation of AE energy released with

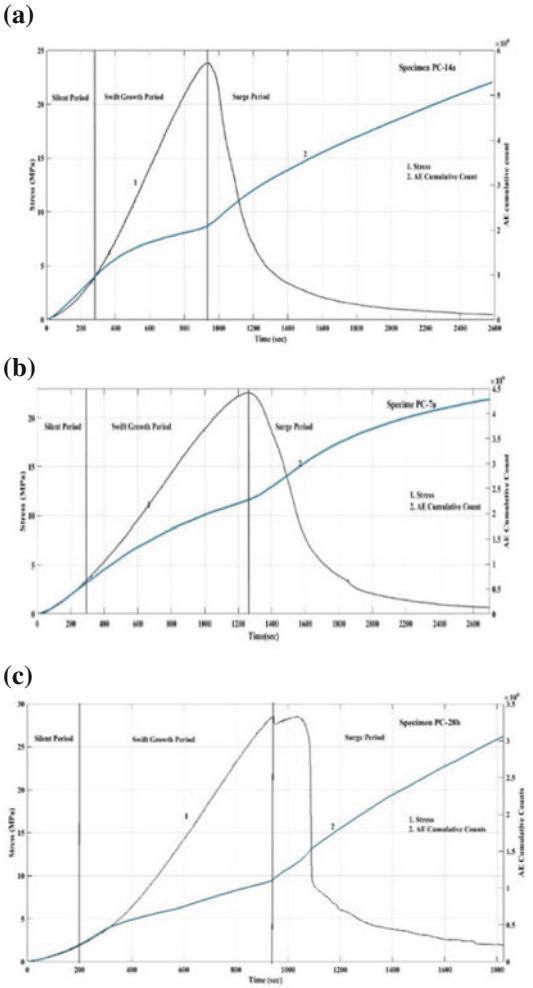

Fig. 6 Variation of cumulative AE count on **a** 7th day, **b** 14th day, **c** 28th day

time and the stress applied. All the three graphs depict that there is no significant AE energy present before the peak stress, hence the formation of microcracks.

Considering the distribution of AE energy over time of 28th day as shown in Fig. 7, there is a sharp increase of AE energy which indicates the formation of macrocracks (shear cracks) with a tremendous energy of 22,274 V^2-s. At this instant, microcracks have coalesced leading to the opening of microcracks. Also there is a difference between the initial AE energy of 1.0873e–03 V^2-s, close to zero and ultimate AE energy 22,274 V^2-s. Also, it is clear that higher AE energy of signals indicates the onset of critical cracks. Hence, the AE energy can be used to assess the severity of a damage.

Table 2 shows the variation of cumulative AE energy with the curing period. AE energy with higher values could be related to brittle fracture, whereas a lower value

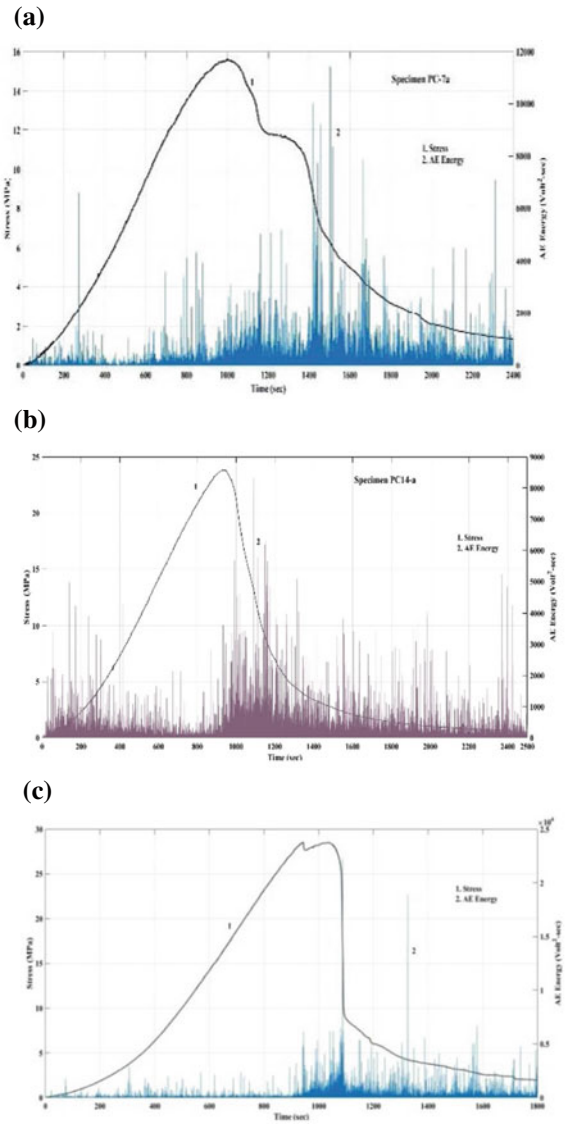

Fig. 7 Variation of AE energy with time on **a** 7th day, **b** 14th day, **c** 28th day

Table 2 AE energy recorded at various curing periods

Curing period (days)	Cumulative AE energy (V^2-s)
7	12005363
14	16448577
28	17752361

of AE energy indicates propagation of stable ductile crack. From Table 2, an increase in the cumulative AE energy with curing period of the concrete can show the increase in brittleness of the concrete with its curing period.

The amount of AE energy released depends on the size of the crack formed and crack propagation. The AE amplitude is proportional to the area of new surface formed and crack velocity. If the crack occurring is a sudden discrete one, it produces high amplitude signal than a slow creeping advance of the crack tip. Up to peak stress, the AE released is low compared to that released after the peak stress. The predominance of sudden discrete cracks can be assessed near to peak stress.

3.4 Crack Pattern

Identification of cracking mode can be studied based on the AE parameters like rise angle (RA) and average frequency (AF). The rise angle is the ratio between rise time and peak amplitude. Rise time is the time required to reach peak amplitude after the first threshold crossing. AF is the ratio of AE count and peak amplitude. The cracking mode can be identified based on the above parameters.

Mode-I fracture is dominated by tensile cracks. In the initial parts of loading, longitudinal waves propagate in concrete test specimen since they are fast. Tensile cracks are characterized by low RA and high AF. They are also appeared as vertical cracks, while shear cracks are diagonal in nature and having high rise angle and low average frequency. Mode-II cracks are characterized as shear cracks.

Shear cracks are expected to cause global failure. As delay is there in attaining maximum energy, shear cracks occur in later stages [3]. Due to the formation of vertical and diagonal cracks, plain concrete fails. It can be observed from Fig. 8 that post peak time period has a shear crack formation.

Figure 8 shows the event location on the longitudinal section of the specimen PC-14b, after peak stress is reached, as observed in the AEwin software. The analysis has been done by replaying the data of the events recorded by all the channels on plotting X-Y position graph during selected time intervals. In the initial stages of loading, vertical tensile cracks were formed. The development of diagonal

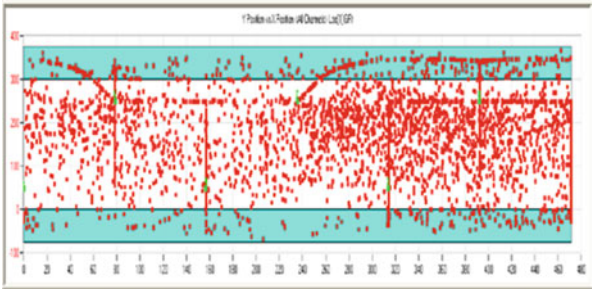

Fig. 8 Post peak (1050–2000 s)

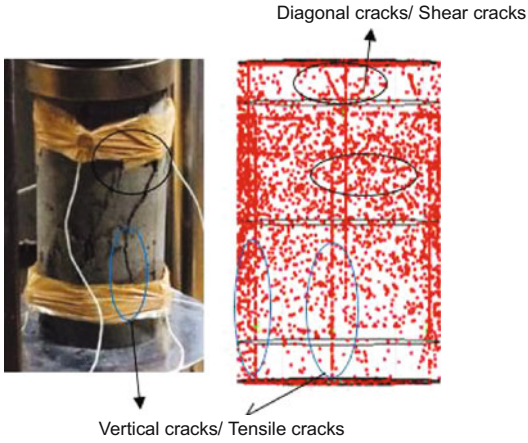

Fig. 9 Crack pattern observed in the experiment

shear cracks was observed after some time. The ultimate failure occurred due to the formation of shear cracks in the specimen under uniaxial compression.

Figure 9 shows the comparison between the crack pattern observed on the test specimen and the crack pattern obtained by plotting x, y and z-position of the events recorded by the sensors mounted on the specimen. The graph has been plotted using PAC AEwin Software by replaying the recorded AE data. It replicates the cracks observed during the test on the test specimen and AE event locations.

The cracks enclosed by black circle both on the specimen after the test and the graph shows the diagonal or the shear cracks. The cracks enclosed by a blue circle show the vertical or the tensile cracks. A similar pattern of diagonal and vertical cracks is observed which justifies the observed and calculated results of the dislocations occurring on the specimen.

4 Conclusions

This paper presents an analysis of concrete specimen under uniaxial compression by acoustic emission method.

1. *b*-value was found to drop suddenly indicating unstable and faster crack growth near to peak load whereas high *b*-value indicates large number of small AE hits causing stable and slower propagation of crack. As concrete becomes brittle on ageing less high-energy AE events are generated hence lower *b*-value after peak load, causing the *b*-value plot to shift laterally (Fig. 4).
2. As high AE energy signals indicate onset of critical cracks, formation of macrocracks near to peak stress can be observed from Fig. 7. Thus the severity

of the damage can be assessed from the AE energy released during Acoustic Emission testing.

3. Lower AE energy indicates stable ductile crack propagation. For brittle fracture, AE energy will be high causing audible crackling noise. On ageing AE energy is found to increase. Hence a shift is observed in cumulative AE energy from 7th day to 28th day (Table 2).
4. Through the AE cumulative count versus time plot, it can be said that the crack formation in concrete can be divided into three phases, namely silent period, swift growth period and surge period on the basis of the rate of change of slope. Also, the duration of surge period increases with the age of concrete due to the accumulation of stress.
5. Different modes of failure namely, tensile and shear failure can be observed on the specimen in the form of vertical and diagonal cracks respectively. Also, the same can be verified by plotting x and y coordinates of events detected by the AE sensors mounted on the specimen.

References

1. Grosse, C. U., & Ohtsu, M. (2008). *Acoustic emission testing* (1st ed.). Berlin, Heidelberg: Springer.
2. Rao, M. V. M. S., & Lakshmi, K. J. P. (November 2005). Analysis of b-value and improved b-value of acoustic emissions accompanying rock fracture. *Current Science, 89*(9).
3. Colombo, S., Main, I. G., & Forde, M. C. (2003). Assessing damage of reinforced concrete beam using *b*-value analysis of acoustic emission signals. *Journal of Materials in Civil Engineering, 15*(3), 280–286.
4. Vidya Sagar, R. (2016). Importance of acoustic emission *b*-value in the study of fracture process in reinforced concrete structures. In V. E. Souma, J. Bolendar & E. Landis (Eds.) *Proceedings of FraMCos-9 Conference*. https://doi.org/10.21012/fc9.040.
5. Haneef, T. K., Kumari, Kalpana, Mukhopadhyaya, C. K., Rao, P. B. C., & Jaya kumar, T. (2013). Influence of flash and curing on cracking behavior of concrete by acoustic emission technique. *Construction and Building Materials, 23,* 342–350.

Size-Dependent Wave Propagation Response in Nanoscale Beams Using Spectral Finite Element Method Incorporating Surface Energy Effects

N. Khandelwal and S. Kapuria

Abstract In this paper, 1D spectral finite element (SFE) formulation is developed for studying wave propagation response of nanoscale beams, considering the Gurtin-Murdoch continuum model accounting for surface energy effects. The numerical results obtained from the developed SFE for beam static deflection and natural frequencies are compared with the analytical results available in the literature. Numerical results for wave propagation analysis in beams for tone burst signal and impulse signal are also presented, considering surface energy effect, and compared with the beam theory without the surface energy effects. It is observed that nanoscale beam wave response shows a significant influence of the surface energy effect, which also explains the size-dependent behaviour.

Keywords Wave propagation · Spectral finite element · Root mean square deviation

1 Introduction

Dynamic analysis of the engineering structures is governed by either low-frequency loading or high-frequency loading. High-frequency loading comes under the category of wave propagation [1]. The frequency content in the high-frequency loading can vary in the range of KHz to GHz and many modes participate in the analysis of wave propagation response. To capture the effect of every mode of structure in high-frequency loading, finite element meshing of the structure should be very dense and size of each element should be in the order of the wavelength of

N. Khandelwal (✉) · S. Kapuria
Department of Applied Mechanics, IIT Delhi, 110016 New Delhi, India
e-mail: nitinnitin128@gmail.com; khandelwalnitin128@gmail.com

S. Kapuria
e-mail: kapuria@serc.res.in

S. Kapuria
CSIR-Structural Engineering Research Centre, 600113 Taramani, Chennai, India

A. Rama Mohan Rao and K. Ramanjaneyulu (eds.), *Recent Advances in Structural Engineering, Volume 1*, Lecture Notes in Civil Engineering 11,
https://doi.org/10.1007/978-981-13-0362-3_90

the signal. This results in large system size even for 1D structure, hence conventional FEM becomes time consuming when applied to high-frequency excitation problems [2] and not helpful for online structural health monitoring which demands for short computation time.

Spectral finite element method (SFEM) is a numerical method that has evolved in recent years, to solve high-frequency loading problems. The SFEM is a computational technique that basically combines two different numerical techniques that is spectral methods and the finite element method (FEM). Two types of approaches are used in SFEM. The first one is based on the frequency domain defined by Bescos and Narayanan [3] and the second one is in the time domain given by Patera [4]. The SFEM proposed by Beskos and Narayanan [3] is basically the FEM formulated in the frequency domain. In Beskos and Narayanan [3] approach, the time domain solution obtained from frequency domain involve inverse Laplace transform. The use of Laplace transform for solution of wave equation is limited because of difficulty in performing inverse transformation which makes complex structures difficult to solve by this approach and the application of this approach in the wave propagation analysis of anisotropic and inhomogenous structure has not been well documented in the available literature [1]. The SFEM, proposed by Patera [4], is a weighted residual method like the conventional FEM and discretize the whole structure into small elements. However, it uses high-order interpolation functions with a numerical integration rule known as a nodal quadrature, where integration points coincide with nodal points. Kudela et al. [2] use the Patera [4] approach to solve wave propagation modelling in 1D structures. In Komatitsch et al. [5, 6] extend the same approach to 2D and 3D fully anisotropic media.

Application of nanoscale beams is most commonly found in NEMS-based sensor and actuator devices. These NEMS devices contribute to the wide diversity of applications such as sensors, medical diagnostics, displays, and data storage [7]. Dynamic analysis is highly important for design and manufacturing of nanoelectromechanical system (NEMS). The behaviour of nanoscale beams is size dependent, which cannot be modelled by classical beam theory. It has been reported that the size-dependent behaviour can be essentially influenced by the surface energy effect, which is prominent in the nanoscale.

Incorporation of surface energy into the continuum mechanics was first proposed by Gurtin and Murdoch [8]. In their study, the surface was assumed as zero thickness deformation membrane fully bonded to the bulk material of the structure. The equilibrium and generalized Young–Laplace equations and own constitutive relations were used. Lim and He [9] developed a model based on the Gurtin–Murdoch continuum theory to analyse the nonlinear deformation of a thin nanoscale film under bending. Liu and Rajapakse [10] presented a generalized mechanistic model, incorporating surface energy effects based on Gurtin-Murdoch continuum theory, for thick and thin nanoscale beam. Their work presents analytical solutions for the static response under different loading and boundary conditions, as well as the solution of free vibrations of such beams. From their study, it was concluded that classical beam theory are not suitable for modelling beams with higher surface residual stress and surface elastic moduli. Liu et al. [11] presented a 1D finite

element modelling of beams accounting surface energy effect based on Gurtin-Murdoch theory.

In this paper, Galerkin-type SFE is developed for obtaining the wave propagation response of nanoscale Timoshenko beams considering the surface energy effect. It employs the model developed by Liu and Rajapakse [10] based on Gurtin-Murdoch surface elasticity theory. SFEM second approach proposed by Patera has been used for beam modelling. Wave propagation response is analysed under the different type of high-frequency loading (tone burst signal and Impulse signal). The results are compared with those obtained without the surface energy effect.

2 Spectral Finite Element Method

There are two techniques, h refinement and p refinement, which are used in conventional FEM to solve high-frequency loading problems.

In h refinement techniques, the number of elements used for discretization is increased, while the order of interpolation polynomial remains fixed within each element, but as the number of element increases, the computation time also increases, making this approach inconvenient for the high-frequency loading problems. In p refinement techniques, the number of elements used for discretization remains same while the polynomial interpolation order increases within each element to improve the accuracy of finite element method. Conventional FEM uses a set of local shape functions within each element defined by Lagrange interpolation polynomial having evenly spaced nodes. As the order of Lagrange interpolation polynomial, having evenly distributed nodes, increases, oscillations arise near the ends of the interpolation domain [12] making the p refinement technique unsuitable for high-frequency loading problem. Definition of ith Lagrange interpolation polynomial is given by Eq. (1) which exhibit a property define by Eq. (2), where δ_{ij} denotes Kronecker delta.

$$\psi_i(\xi) = \frac{(\xi - \xi_1)\ldots(\xi - \xi_{i-1})(\xi - \xi_{i+1})\ldots(\xi - \xi_{p+1})}{(\xi_i - \xi_1)\ldots(\xi_i - \xi_{i-1})(\xi_i - \xi_{i+1})\ldots(\xi_i - \xi_{p+1})} \tag{1}$$

$$\psi_i(\xi_j) = \delta_{ij} \tag{2}$$

This oscillation problem can be removed by SFEM. The SFE formulation for the stiffness and mass matrix is similar as conventional FE formulation [2], only change lies in the shape functions. Shape functions within an element are defined by Lagrange interpolation polynomial ψ, as defined in the case of conventional FE, but it consists of unevenly distributed nodes. These unevenly distributed nodes are obtained using the roots of the first derivative of the Legendre polynomials [12], defined in Eq. (3), over the interval of the ξ axis, subjected to the constraints that the first node is placed at $\xi_1 = 1$ and the last node is placed at $\xi_{r+1} = 1$, where r is

Table 1 Node locations and their weightage

Node no.	Node location	Node weightage
1.	−1.0000	0.0357
2.	−0.8717	0.2107
3.	−0.5917	0.3411
4.	−0.2092	0.4125
5.	0.2092	0.4125
6.	0.5917	0.3411
7.	0.8717	0.2107
8.	1.0000	0.0357

the order of the Legendre polynomial. The main reason for adopting the roots of the derivative of the Legendre polynomials is that the values of interpolation functions are guaranteed to vary in the range [−1, 1], independent of the order of the polynomial [12].

$$(1-\xi^2)L_r'(\xi)=0 \tag{3}$$

where $L_r'(\xi)$ is the first derivative of Legendre polynomial of order r.

Nodal quadrature weights w_i are defined from Eq. (4).

$$w_i=\frac{2}{p(p-1)[L_{p-1}(\xi_i)]^2} \quad i\in 1,\ldots,p, p=P+1 \tag{4}$$

Lagrange polynomial, having unevenly spaced nodes, when combined with nodal quadrature integration rule leads to diagonal form of mass matrix which reflect in the reduction of complexity and cost of algorithm [2].

In this paper, 8-noded spectral element is used within the formulation whose node locations and weightage is given in Table 1.

3 Spectral Finite Element Formulation of Beams Considering Surface Energy Effect

Consider a beam as shown in Fig. 1 having A and S as area and perimeter of cross section respectively. Surface energy model used in the formulation is based on the Gurtin-Murdoch theory [8].

Surface of the beam is assumed as zero thickness elastic membrane fully adhere to its bulk. Bulk material of the beam is governed by assuming plane stress condition with σ_{xx}, σ_{zz}, σ_{xz} as non-zero stress and ε_{xx}, ε_{zz}, ε_{xz} as non-zero strain. Surface of the beam is governed by generalized Young–Laplace equations.

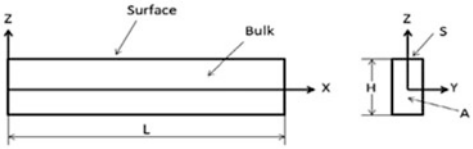

Fig. 1 Geometry of rectangular beam and its coordinate system

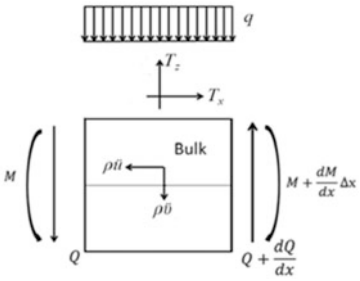

Fig. 2 Free body diagram of a beam element

$$\tau_{xx} = \tau_0 + (2\mu_0 + \lambda_0)u_{,x} \quad \text{and} \quad \tau_{zx} = \tau_0 v_{,x} \tag{5}$$

where τ_0 is the unconstrained residual surface stress on the surface, and μ_0 and λ_0 are the Laplace surface constants, which can be determined experimentally from an atomistic model.

The free body diagram of beam element having length as Δx is shown in Fig. 2 subjected to arbitrary distributed transverse load q. M and Q denote the internal moment and the shear force respectively. $T_i = \sigma_{ij} n_j$ are the contact traction force to provide the interaction between surface and bulk material of beam.

The bending moment and vertical forces equilibrium equations for beam element imposing Timoshenko theory is given by Eqs. (6) and (7) (see [11]).

$$G\kappa A(v_{,xx} + \phi_{,x}) + \tau_0 s^* v_{,xx} - q(x) = (\rho A + \rho_0 s^*)\ddot{v} \tag{6}$$

$$\begin{aligned}[EI + (2\mu_0 + \lambda_0)I^*]\phi, xx + \frac{2\upsilon I\tau_0}{H} v_{,xxx} \\ - G\kappa A(v_{,x} + \phi) = (\rho I + \rho_0 I^*)\ddot{\phi} + \frac{2\upsilon I\rho_0}{H}\ddot{v}_{,x}\end{aligned} \tag{7}$$

where E is the Young modulus, I is the area moment of inertia, υ is the Poisson's ratio, ρ is the mass density of the bulk and κ is the shear correction factor. v and ϕ are the transverse and angular displacement of the beam an ρ_0 is the mass density of surface. $I^* = \int z^2 \mathrm{d}s$ is the perimeter moment of inertia, and $s^* = \int \mathrm{d}s$. In case of beams with a rectangular cross section of depth $2\ h$ and width b, these relations are defined as given by Eq. (8).

$$\begin{aligned} I &= 2bh^3/3, \quad & I^* &= 2bh^2 + 4h^3/3 \\ S^* &= 2b, & H &= 2h \end{aligned} \tag{8}$$

If the surface effects are not taken into the consideration (i.e. μ_0, λ_0, ρ_0 and τ_0 are zero), then Eqs. (6) and (7) reduce to the governing equations of the classical beam theory. On applying the Galerkin approach in Eqs. (6), (7), by using $\bar{v}$ and $\bar{\phi}$ as assumed weight functions, lead to the weighted residual statement given by Eq. (9).

$$\begin{aligned} &\int_0^L \{(G\kappa A(v_{,xx} + \phi_{,x}) + ([EI + (2\mu_0 + \lambda_0)I^*]\phi_{,xx} + \tau_0 s^* v_{,xx} \\ &\quad -q(x))\bar{v} + \frac{2\upsilon I\tau 0}{H} v_{,xxx} - G\kappa A(v_{,x} + \phi))\bar{\phi}\Big\} \mathrm{d}x \\ &= \int_0^L \left\{(\rho A + \rho_0 I^*)\ddot{\phi} + \frac{2\upsilon I\rho_0}{H}\ddot{v}_{,x})\bar{\phi}\right\} \mathrm{d}x \end{aligned} \tag{9}$$

On applying integration by parts rule to Eq. (9) results in the weak formulation as given by Eq. (10).

$$\begin{aligned} &\int_0^L \left\{G\kappa A(v_{,x} + \phi)(\bar{v}_{,x} + \bar{\phi}) + [EI + (2\mu_0 + \lambda_0)I^*]\phi_{,x}\,\bar{\phi}_{,x}\right. \\ &\quad \left. + \frac{2\upsilon I\tau 0}{H} v_{,xx}\,\bar{\phi}_{,x} + \tau_0 s^* v_{,x}\,\bar{v}_{,x} + q(x)\bar{v}\right\} dx - (Q\bar{v} + M\bar{\phi})\Big|_0^L \\ &= \int_0^L \left\{(\rho A + \rho_0 s^*)\ddot{v}\bar{v} - ((\rho I + \rho_0 I^*)\ddot{\phi} + \frac{2\upsilon I\rho_0}{H}\ddot{v}_{,x})\bar{\phi}\right\} \mathrm{d}x \end{aligned} \tag{10}$$

where shear force (Q) and bending moment (M) can be expressed as

$$\begin{aligned} Q^T &= G\kappa A(v_{,x} + \phi) + \tau_0 s^* v_{,x} \\ M^T &= [EI + (2\mu_0 + \lambda_0)I^*]\phi_{,x} + \frac{2\upsilon I\tau 0}{H} v_{,xx} \end{aligned} \tag{11}$$

To simplify the formulation, assume weight function $\bar{v}$ and $\bar{\phi}$ the same as v and ϕ respectively.

Elemental stiffness matrixes are obtained from the left-hand side of Eq. (10).

$$\mathbf{K}^{\mathrm{e}} = \mathbf{K}_1^e + \mathbf{K}_2^e + \mathbf{K}_3^e + \mathbf{K}_4^e \tag{12}$$

where

$$\begin{aligned}
\mathbf{K}_1^e &= \int_0^L G\kappa A\left(\frac{\mathrm{d}v}{\mathrm{d}x}+\phi\right)\left(\frac{\mathrm{d}v}{\mathrm{d}x}+\phi\right)\mathrm{d}x \\
\mathbf{K}_2^e &= \int_0^L [EI+(2\mu_0+\lambda_0)I^*]\frac{\mathrm{d}\phi}{\mathrm{d}x}\frac{\mathrm{d}\phi}{\mathrm{d}x}\mathrm{d}x \\
\mathbf{K}_3^e &= \int_0^L \frac{2\upsilon I\tau_0}{H}\frac{\mathrm{d}^2v}{\mathrm{d}x^2}\frac{\mathrm{d}\phi}{\mathrm{d}x}\mathrm{d}x \\
\mathbf{K}_4^e &= \int_0^L \tau_0 s^*\frac{\mathrm{d}v}{\mathrm{d}x}\frac{\mathrm{d}v}{\mathrm{d}x}\mathrm{d}x
\end{aligned} \tag{13}$$

Elemental mass matrices are obtained from the right hand side of Eq. (10):

$$\mathbf{M}^{\mathrm{e}} = \mathbf{M}_1^e + \mathbf{M}_2^e + \mathbf{M}_3^e \tag{14}$$

where

$$\begin{aligned}
\mathbf{M}_1^e &= \int_0^L [\rho A+\rho_0 s^*]\left(\frac{\mathrm{d}^2v}{\mathrm{d}t^2}\right)v\mathrm{d}x \\
\mathbf{M}_2^e &= \int_0^L [\rho I+\rho_0 I^*]\left(\frac{\mathrm{d}^2\phi}{\mathrm{d}t^2}\right)\phi\mathrm{d}x \\
\mathbf{M}_3^e &= \int_0^L \frac{2\upsilon I\rho_0}{H}\left(\frac{\mathrm{d}^3v}{\mathrm{d}x\,\mathrm{d}t^2}\right)\phi\mathrm{d}x
\end{aligned} \tag{15}$$

For an element subjected to a transverse load $q(x)$, the force vector becomes

$$\mathbf{F}^e = \int_0^L q(x)\,v\,\mathrm{d}x \tag{16}$$

To derive the desired form of stiffness and mass matrix using the SFE method for the beam considered in the formulation, 8-noded spectral element is used with two degree of freedom per node (v and ϕ) as shown in Fig. 3.

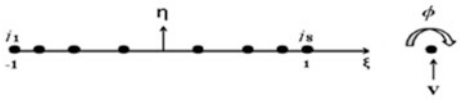

Fig. 3 8-noded spectral beam element

The element nodal displacement vector is

$$v^e = [v_1 \ \phi_1 \ v_2 \ \phi_1 \ \ldots . \ v_8 \ \phi_8]^T \tag{17}$$

The element generalized displacements v and ϕ are interpolated, using same interpolation functions ψ_i (i = 1, 2, … , 8), within each element as

$$\begin{Bmatrix} v \\ \phi \end{Bmatrix} = \begin{bmatrix} \psi_1 & 0 & \psi_2 & 0 & \ldots & \psi_8 & 0 \\ 0 & \psi_1 & 0 & \psi_2 & \ldots & 0 & \psi_8 \end{bmatrix} [v_1 \ \phi_1 \ldots v_8 \ \phi_8]^T \tag{18}$$

The element generalized displacements v and ϕ and its derivatives can be independently written as

$$v = \mathbf{N}_1(x)v^e \quad \frac{\mathrm{d}v}{\mathrm{d}x} = \mathbf{B}_1(x)v^e \quad \frac{\mathrm{d}^2v}{\mathrm{d}x^2} = \mathbf{B}_{11}(x)v^e \tag{19}$$

$$\phi = \mathbf{N}_1(x)v^e \quad \frac{\mathrm{d}\phi}{\mathrm{d}x} = \mathbf{B}_1(x)v^e \quad \frac{\mathrm{d}^2\phi}{\mathrm{d}x^2} = \mathbf{B}_{11}(x)v^e \tag{20}$$

Substitute Eqs. (19)–(20) into Eqs. (13)–(16), map the spectral element (Ω_e) from the x-axis to the standard domain λ = [− 1, 1] of the parametric ξ axis, and applying nodal quadrature integration rule will result in the elemental stiffness, mass matrix and force vector in the following form as shown in Eqs. (21)–(23).

In Eq. (21)–(22), formulation is shown for only first term of elemental stiffness and mass matrix, formulation for other terms can be obtained in the same way.

Elemental stiffness matrix as

$$\begin{aligned} \mathbf{K}_1^e &= \int_0^L (\mathbf{B}_1(x)v^e + \mathbf{N}_2(x)v^e)^T [G\kappa A](\mathbf{B}_1(x)v^e + \mathbf{N}_2(x)v^e)\mathrm{d}x \\ &\approx \sum_{i=1}^{8} w_i (\mathbf{B}_1(\xi_i)v^e + \mathbf{N}_2(\xi_i)v^e)^T [G\kappa A](\mathbf{B}_1(\xi_i)v^e + \mathbf{N}_2(\xi_i)v^e) \det(J(\xi_i)) \end{aligned} \tag{21}$$

Elemental mass matrix as

$$\begin{aligned} \mathbf{M}_1^e &= \int_0^L (\mathbf{N}_1(x)\ddot{v}^e)^T [\rho A + \rho_0 s^*](\mathbf{N}_1(x)v^e)\mathrm{d}x \\ &\approx \sum_{i=1}^{8} w_i (\mathbf{N}_1(\xi_i)\ddot{v}^e)^T [\rho A + \rho_0 s^*](\mathbf{N}_1(\xi_i)v^e) \det(J(\xi_i)) \end{aligned} \tag{22}$$

Elemental force vector as

$$\begin{aligned}\mathbf{F}^e &= \int_0^L (N_1(x)v^e)^T q(x)\,\mathrm{d}x \\ &\approx \sum_{i=1}^{8} w_i (N_1(\xi_i)v^e)^T q(\xi_i)\det(J(\xi_i))\end{aligned} \tag{23}$$

where w_i is nodal quadrature weights and J is the jacobian associated with the mapping from the element Ω_e to the reference domain λ. The assembly of element stiffness matrix, mass matrix and nodal force vector yield the global equilibrium equation as

$$\mathbf{M}\ddot{\mathbf{X}} + \mathbf{K}\mathbf{X} = \mathbf{F} \tag{24}$$

where **M, K**, **F**, **X** are global stiffness matrix, global mass matrix, nodal force vector and displacement vector respectively. Newmark-beta scheme is used to solve the Equilibrium Eq. (24). Initial displacements, initial velocities and damping are assumed to be zero in the numerical simulations.

4 Numerical Results

4.1 Validation of Spectral Finite Element Formulation

To verify the accuracy of spectral finite element formulation in the surface energy model, static transverse deflections (v) and natural frequencies of Al beam are computed and these compared with the analytical results presented by Liu and Rajapakse [11]. Bulk material properties and surface parameters for an Al beam are taken from Liu and Rajapakse [11] is presented in Table 2. Beam was assumed as a homogenous and an isotropic having geometric parameters: Length (L) = 50 nm, Width (b) = 3 nm, and depth $(2\ h)$ = 6 nm. Solutions are presented for cantilever beam under end point load (P). The normalized deflection $V_P^E = v/P$ for Al beam with surface model and classical theory is shown in Fig. 4.

First four natural frequencies corresponding to different modes also has been calculated for Al cantilever and compared with those presented by Liu and Rajapakse [11]. These frequencies are presented in Table 3. From Fig. 4 and

Table 2 Material properties

Material	E (GPa)	υ	μ (N/m)
Al	90	0.23	−5.4251
λ_o (N/m)	τ_o (N/m)	ρ (Kg/m^3)	ρ_o (Kg/m^3)
3.4939	0.5689	2.7×10^3	5.46×10^{-7}

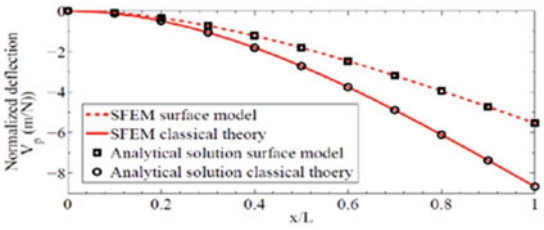

Fig. 4 Comparison of Normalized deflection under point load between SFEM method and analytical result presented by Liu and Rajapakse [11]

Table 3 Natural frequencies of Al nano-beam

Method	Frequency (GHz)		
	Mode 1	Mode 2	Mode 3
SFEM (Surface)	2.619	12.605	31.290
Analytical (Surface)	2.620	12.600	31.240
SFEM (Classical)	2.214	13.075	33.797
Analytical (Classical)	2.210	13.050	33.740

Table 3, it is clear that developed SFE method completely agree with the analytical results presented by Liu and Rajapakse [11]. It is found that there is an increase in the natural frequency of the system for the first mode when accounting surface energy effect in contrast to classical theory because stiffness contributions due to the surface elasticity is higher than the bulk bending stiffness (*EI*) of the system while for higher modes the bulk bending stiffness becomes the dominant factor.

4.2 Wave Propagation Analysis Using Spectral Finite Element Formulation

In order to analyse wave propagation in beam based on the proposed method, two examples are carried out by using two different transverse force excitation signals at the tip of the cantilever beam, tone burst pulse signal and impulse signal. To observe the surface effect in the wave propagation analysis of the beam, the length of beam considered here varies from nanoscale to milliscale. Al beam has been considered for analysis having bulk and surface properties same as defined earlier.

4.2.1 Wave Propagation Analysis Using Tone Burst Pulse Signal

Cantilever beam is subjected to a five-cycle tone burst excitation at frequency F_s, which varies according to the length of beam, and is shown in Fig. 5. Tone burst pulse was generated using Hanning window modulated with sinusoidal signal. In Fig. 5, T_e = a*T_{Li}, F_s = F_{Li}*(1/a), where a, is the ratio of the length of beam (L) to the reference length of beam (L_i) termed as normalized length ratio. T_{Li} and F_{Li} are

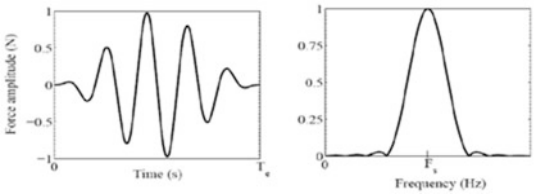

Fig. 5 Tone burst pulse signal in time and frequency domain

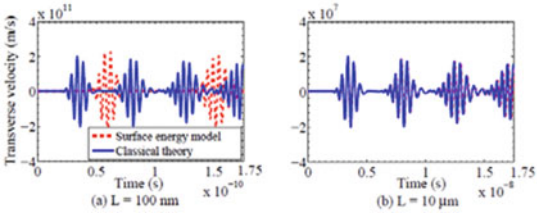

Fig. 6 Comparison of transverse velocity at mid-point of the beam of length: **a** 100 nm, **b** 10 μm under five-cycle tone burst excitation

time duration of a Hanning window and central frequency, respectively, at reference beam length (L_i). Time window of the analysis also varies according to length of beam given as $TT = a*T_s$, where T_s is the time window of the analysis used in reference length of beam (L_i). Step time (Δt) of the analysis, for different beam, is taken as $\Delta t = (T_s/100)$ s. Wave propagation analysis has been done by considering the reference beam length (L_i) as 100 nm. The width and depth of beam depend on the length of the beam as $L/100$ and $L/100$ respectively. Pulse signal parameter considered at reference length (L_i) are $T_{Li} = 2.5 \times 10^{-11}$ s, $F_{Li} = 20 \times 10^{10}$ Hz and $T_s = 17.5 \times 10^{-11}$ s respectively.

Figure 6 show the comparison between the classical beam theory and the surface energy model, at the mid-point of the beam, for different length of beam. The results have been compared at various lengths of the beam varying from nanoscale to milliscale.

In Fig. 6, at beam length 100 nm and 10 μm, four wave packet appears for classical theory: starting from left, first wave packet corresponds to the excited signal and second wave packet is reflection of first wave packet from the clamp end of the beam, third wave packet is the reflection of second wave packet from free end and last packet is the reflection of third packet from clamped end, while in surface energy model, for beam length 100 nm, only two wave packets appear, and at the beam length 10 μm, four wave packets appear which suggest that group velocity of wave signal at nanoscale in surface energy model is lesser in comparison to the group velocity in classical theory. All these wave packets in wave propagation are obtained corresponding to the first mode. Figure 7 has been plotted between Root mean square deviation (RMSD) of transverse velocity in surface energy model with respect to classical theory and normalized length ratio, at mid-point of the beam. It can be seen from Fig. 7 that as the length of beam increases, the effect of the surface energy decreases. It is suggesting that the surface energy effect is more significant at the nanoscale.

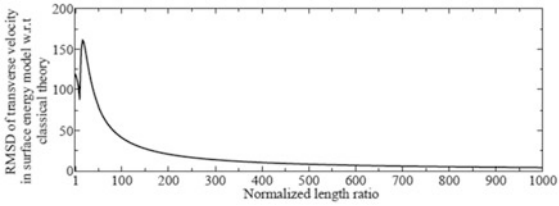

Fig. 7 RMSD of transverse velocity as a function of normalized length ratio

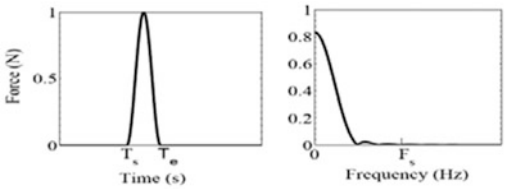

Fig. 8 Impulse force excitation signal

4.2.2 Wave Propagation Analysis Using Impulse Signal

Cantilever beam is also excited with an impulse signal, whose pulse duration varies for the different length of the beam, is shown in Fig. 8. In Fig. 8, $T_s = a*Ts_{Li}$ and $T_e = a*Te_{Li}$ are the loading and unloading time of impulse signal, respectively, for different lengths of beam (L); Ts_{Li}, Te_{Li} are the loading and unloading time of impulse signal, respectively, used in the case of reference beam length (L_i). $TT = a*TT_{Li}$ is the total time window of the analysis used for beam length (L); TT_{Li} is the total time window of the analysis used in case of reference beam length (L_i). In the case of impulse signal, wave propagation analysis has been done by considering the beam reference length (Li) as 400 nm. Width and depth of the beam depend on the length of the beam as $L/100$ and $L/1000$ respectively. Pulse signal parameter considered at reference length are $Ts_{Li} = 16 \times 10^{-11}$ s, $Te_{Li} = 24 \times 10^{-11}$ Hz and $TT_{Li} = 320 \times 10^{-11}$ s respectively.

Figure 9 shows the comparison between the classical beam theory and the surface energy model for transverse velocity at free end of the beam. The results have been compared at various lengths of the beam varying from nanoscale to milliscale.

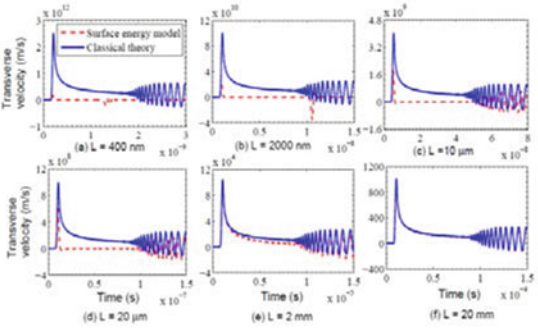

Fig. 9 Comparison of transverse at free end of the beam of various lengths (L) in impulse loading

5 Conclusion

A spectral finite element formulation, considering the surface energy effect, has been derived from Galerkin weightage residual method to investigate the wave propagation effect in the beam. The Spectral finite element formulation is verified by the analytical results under static loading and free vibration cases presented by Liu and Rajapakse [11]. Finally, wave propagation study in beam has been carried out, by taking into account the surface energy effect and the result thus obtained were compared with classical theory. From the study, it was found that surface energy effect is more significant at nanoscale and surface effect reduces, as the length of beam increases. It is difficult to make general conclusion about the critical length, after which classical theory and surface energy model give the same result, because critical length is not fixed and it varies according to the type of loading applied. The SFEM model developed in this paper provide an efficient tool for the design of nanoscale devices.

References

1. Gopalakrishnan, S., Chakraborty, A., Mahapatra, D. R. (2007). *Spectral finite element method: Wave propagation, diagnostics and control in anisotropic and inhomogeneous structures*. Germany: Springer Science & Business Media.
2. Kudela, P., Krawczuk, M., & Ostachowicz, W. (2007). Wave propagation modelling in 1d structures using spectral finite elements. *Journal of Sound and Vibration, 300*(1), 88–100.
3. Beskos, D. E., & Narayanan, G. V. (1983). Dynamic response of frameworks by numerical laplace transform. *Computer Methods in Applied Mechanics and Engineering, 37*(3), 289–307.
4. Patera, A. T. (1984). A spectral element method for fluid dynamics: Laminar flow in a channel expansion. *Journal of Computational Physics, 54*(3), 468–488.
5. Komatitsch, D., Barnes, C., & Tromp, J. (2000). Simulation of anisotropic wave propagation based upon a spectral element method. *Geophysics, 65*(4), 1251–1260.
6. Komatitsch, D., Martin, R., Tromp, J., Taylor, M. A., & Wingat, B. A. (2001). Wave propagation in 2-d elastic media using a spectral element method with triangles and quadrangles. *Journal of Computational Acoustics, 9*(02), 703–718.
7. Craighead, H. G. (2000). Nanoelectromechanical systems. *Science, 290*(5496), 1532–1535.
8. Gurtin, M. E., & Murdoch, A. I. (1975). A continuum theory of elastic material surfaces. *Archive for Rational Mechanics and Analysis, 57*(4), 291–323.
9. Lim, C. W., & He, L. H. (2004). Size-dependent nonlinear response of thin elastic films with nano-scale thickness. *International Journal of Mechanical Sciences, 46*(11), 1715–1726.
10. Liu, C., & Rajapakse, R. K. N. D. (2010). Continuum models incorporating surface energy for static and dynamic response of nanoscale beams. *IEEE Transactions on Nanotechnology, 9*(4), 422–431.
11. Liu, C., Rajapakse, R. K. N. D., & Phani, A. Srikantha. (2011). Finite element modeling of beams with surface energy effects. *Journal of Applied Mechanics, 78*(3), 031014.
12. Pozrikidis, C. (2005). *Introduction to finite and spectral element methods using MATLAB*, Florida: CRC Press

Reconstruction of Faulty Sensor Data in Time Domain

A. Rama Mohan Rao, K. Lakshmi and Harshil Khimesara

Abstract The reliability and consistency of structural health monitoring system will be compromised due to lack of reliable data at crucial nodes. It may be due to sensor faults or due to non-placement of sensors at some inaccessible points. Several research efforts are made towards sensor fault diagnosis. In this paper, we propose a method for reconstruction of the faulty sensor data or at nodes where sensors are not placed due to inaccessibility, but still crucial for structural health assessment. The proposed data reconstruction technique makes use of the empirical mode decomposition technique being popularly used during Hilbert–Huang transformation. Numerical studies have been carried out to evaluate the proposed reconstruction method.

Keywords Structural health monitoring · Sensor fault · Empirical mode decomposition · Intermittency criteria · Measurement noise · Data reconstruction

1 Introduction

The civil engineering structures like bridges are exposed to varied levels of impact loads during their service life and the structural degradation takes place due to ageing. Hence structural health monitoring (SHM) systems are being deployed on important structures for continuous online monitoring and integrity assessment. SHM typically uses the data (typically acceleration time history) obtained from the sensors placed spatially on the structure to detect abnormal changes in the structural condition. To ensure consistent and reliable monitoring of these civil structures,

A. Rama Mohan Rao (✉) · K. Lakshmi · H. Khimesara
CSIR-Structural Engineering Research Centre, Taramani, Chennai 600113, India
e-mail: arm2956@yahoo.com

K. Lakshmi
e-mail: lakshmik@serc.res.in

H. Khimesara
e-mail: harshil8@yahoo.com

A. Rama Mohan Rao and K. Ramanjaneyulu (eds.), *Recent Advances in Structural Engineering, Volume 1*, Lecture Notes in Civil Engineering 11,
https://doi.org/10.1007/978-981-13-0362-3_91

we must ensure that sensor network installed on the structure must operate accurately. However, during continuous online structural health monitoring, the accuracy and also dependability of these sensor networks can be affected due to malfunctioning of some sensors in the network, environmental impacts and also due to harsh weather conditions. In order to overcome this, several sensor fault diagnostic techniques have been proposed in the literature based on principal component analysis [1], null subspace-based technique [2], MMSE algorithm [3], modal filters [4], etc. Apart from them, techniques based multi-level concept and also employing meta-heuristic algorithms [5, 6] that are suitable for fast detection and isolation are also reported in the literature. Once the faulty sensors are isolated, we need to reconstruct the data at these faulty locations in order to correctly interpret using various advanced signal processing techniques or feature extraction methods. Apart from this due to economic reasons, in order to bring down the cost of SHM, we may place sensors rather sparsely than actually required and also we may skip placing sensors at important places due to lack of accessibility. Hence, sensor data reconstruction is a very critical component in the SHM.

2 Previous Work

Using the concept of transmissibility, a method for reconstruction of response at inaccessible spatial locations of a structure is proposed by Ribeiro et al. [7]. From the known responses at accessible spatial locations of the structure, a transmissibility matrix can be formulated for reconstructing the responses at unknown locations. However, we need to know responses at a minimum number of spatial locations in order to form transmissibility matrix and reconstruct the responses at locations of our interest [8]. A method is proposed by Kammer [9] to extrapolate the signals measured at accessible locations to locations which are not accessible. However, here we need to perform a free vibration test to record the responses at convenient spatial locations on the structure and also at inaccessible points. Both due to time as well economic considerations, it rather difficult to perform such tests on a practical civil engineering structure which are spatially large. Law [10] has proposed a technique in the frequency domain using transmissibility to reconstruct the dynamic response either in full structure or a substructure. Since this method works in the frequency domain, the reconstructed data in frequency domain need to be converted into the time domain by using inverse Fourier transform. The truncation errors during transformation effect the accuracy of reconstruction and apart from this it involves additional computational burden.

In the present work, we propose a technique for reconstruction of dynamic response using empirical mode decomposition (EMD) [11, 12] and also using finite element model of the structure. We make use of the dynamic time history responses measured at spatial locations which are accessible and also ensure that the sensor placed is not faulty. We decompose the measured time history response into IMFs using EMD. These IMFs represent the modal time history responses at the chosen

spatial location. We arrive at the modal responses at any spatial locations, where the sensor is faulty by making use of the IMFs obtained from measured responses and a simple transformation function derived using the mode shapes of the structure.

In contrast to the earlier studies using the transmissibility concept, we can perform all the computations in the time domain using the proposed reconstruction algorithm. Since we use an improved version of EMD with intermittency and a simple transformation equation at modal level, the proposed technique is computationally very effective. Hence this can be effectively employed for real-time continuous health monitoring. Apart from this, this technique can be used for various dynamic response reconstructions based on the different types of sensor measurements, i.e. dynamic displacement or dynamic strain, if displacement transducers or strain gauges are employed on the structure.

3 Empirical Mode Decomposition

Empirical mode decomposition as its name suggests is an empirical method. The aim of this method is to decompose the complicated (nonlinear and/or nonstationary) time history response signal into a series of oscillating components obeying some basic properties, called intrinsic mode functions (IMFs). The basic principle here is to decompose any signal $x(t)$ into a set of band-limited functions, which are zero mean oscillatory components called the IMFs. Each IMF satisfies two basic criteria: (1) In the whole data set, the number of extrema and the number of zero crossings are same or differ at most by one; and (2) at any point, mean value defined by the local maxima and the envelope defined by the local minima is zero. EMD is realised through an empirical process called sifting. The sifting process works as follows: we first identify the local maxima and minima of the measured time history response $x(t)$ and use cubic spline interpolation to connect these points in order to generate upper and lower envelopes. We later compute the mean of the upper and lower envelopes and subtract from the time history $x(t)$. The difference between the original time history and the mean value, c_1, is called the first IMF, if it satisfies the two basic criteria discussed above. We repeat the same sifting process on the new time history obtained after subtracting the C_1 component from the original time history data in order to generate the second IMF. This process is repeated to generate the IMFs till the residue becomes a monotonic function or less than specified convergence level. We can reconstruct the original time history $x(t)$ by summing up all the IMFs and the final residue.

$$x(t) = \sum_{j=1}^{n} C_j(t) + r_n(t) \tag{1}$$

4 Empirical Mode Decomposition with Intermittency

The conventional sifting process discussed in the earlier section has limitations and generally will not produce IMFs, which should ideally be the complete, adaptive and almost orthogonal decomposition of the original time history signal. The main reason for this is that the spline fitting process involved in sifting generates large swings near the ends of the signal. These swings propagate inside and corrupt the whole signal resulting in generating poor IMFs during sifting process. This will be predominant especially when low-frequency components are present in the signal. Apart from this, in the signals with closely spaced frequency components, the modal perturbation phenomena are too prominent to be ignored and it results in the bad sifting of EMD. The IMFs thus generated will generally cover more than one modal frequency and can also have some pseudo-components. In order to overcome these limitations, several EMD techniques are proposed in the literature and EMD with intermittency criteria is popular among them.

Initially, EMD with intermittency criteria was proposed by Huang et al. [12] to locate the intermittent components of the signal. Alternatively, an approach was proposed by Gao et al. [13] using the Teager–Kaiser energy operator to locate the intermittent components of the signal. Subsequently, several other researchers have investigated on improving the EMD for generating IMFs. Since our objective is to generate the IMFs and to ensure that each of the IMF generated, represent the individual modal response, we have implemented the EMD with intermittency criteria in a different form as given below.

Our objective in the present work is to decompose the response signal into IMFS such that each IMF represents one single modal response. In order to accomplish this, we impose an intermittent frequency f_i in the sifting process in order to ensure that each of the IMFs generated to represent the modal response and contains only one frequency component. We use a bandpass filter during the sifting process to remove all the frequency components which are lower or greater than f_i from an IMF. We can obtain the frequency components related to each resonant frequency of the structure using FFT. The dominant frequency band covered in the Fourier spectrum (i.e. corresponding to participating modal components of the structure) will be partitioned into several (say m) subdomains. The centre of each subdomain represents the resonant frequency f_j^0 with the upper lower limits of each subdomain (i.e. f_j^u and f_j^l ($j = 1, 2, \ldots, m$) are defined as $(1 \pm 5\%) f_j^0$. Accordingly, the resonant frequency band covered in Fourier spectrum will be divided into m subdomains as follows:

$$\Omega_j = \left\{ |f| f_i \leq f \leq f_{j+1} \right\} j = 1, 2, \ldots, m \tag{2}$$

The original signal which is a wideband signal is filtered into a number of narrowband signals by using bandpass filter by considering the boundaries of each subdomain as the sweep starting and sweep-ending frequency.

Each of the IMF contains the frequency components of the original signal and is almost an orthogonal representation of the signal. Therefore, it will have a relatively good correlation with the original signal. Therefore, we use a selection criterion based on the correlation coefficient, μ_i, (i = 1, 2, …, n), of each of the 'n' IMFs with the signal. In order to preserve some of the real IMFs with low amplitude, we normalise the signal and also the IMFs before computing the correlation coefficients. In order to differentiate the true IMFs from pseudo IMFs, we use the correlation coefficients with a threshold η is defined as

$$\eta = \max(\mu_i)/\kappa \quad (i = 1, \ldots, n) \tag{3}$$

where κ is an assumed empirical factor and should be greater than 1.0. We retain the IMFs, if $\mu_i \geq \eta$, otherwise, we eliminate by adding to the residue. The main objective here is to guarantee that the selected IMFs include all the resonant modes to be extracted and have no pseudo-components. In the present work, κ is assumed as 10.0. Apart from this, we use the signal extension method employing time series to eliminate the end effects of IMFs generated. Due to the paucity of space, the complete details are not furnished in this paper.

5 Modal-Level Transformation and Superposition

The dynamic equilibrium equation for n-degrees of freedom system with its mass and stiffness and damping matrices represented by M, K and C, respectively, can be written as

$$\begin{aligned} &M\ddot{U} + C\dot{U} + KU = F(t) \\ &\text{with } U(0) = 0 \text{ and } \dot{U}(0) = 0 \end{aligned} \tag{4}$$

where U, $\dot{U}$, $\ddot{U}$ are the displacement, velocity and acceleration vectors respectively. $F(t)$ is the force vector. By solving the associated eigenvalue problem, we can obtain the mode shape matrix, ϕ of size $n \times n$. We can use finite element analysis with mass, stiffness and damping matrices obtained using model updating. Alternatively, we can obtain the modes shapes employing operational modal analysis techniques with measured time history responses of the structure. Once the mode shape matrix is obtained. We can construct the following transformation equation to estimate the missing modal time history response.

$$\delta_{iu}(t) = \frac{\phi_{iu}}{\phi_{im}} \delta_{im}(t) \tag{5}$$

where $\delta(t)$ is the modal time history response and subscript i stands for mode shape number. While subscript m refers to the spatial location (degrees of freedom) at which the response is measured and u refers to the unmeasured spatial location,

where the time history response need to be reconstructed. Using Eq. (5), the modal time history response $\delta_{iu}(t)$ at any unmeasured location can be computed using the modal time history response at measured location. The modal time history response at any measured location can be obtained from the IMFs generated using empirical mode decomposition. Once all the modal time history responses at the unmeasured spatial location are computed using the transformation equation given in (5), we can compute the time history response through modal summation procedure. It may be noted that the procedure outlined here is simple and efficient and depends rather heavily on the effectiveness of the EMD procedure.

It should be mentioned here that the proposed method is not suitable to reconstruct dynamic responses if the structure is excited by periodic external forces. For the excitation force, which has a deterministic frequency (such as periodic excitation), the frequency component from the excitation will be dominant during the excitation duration. Since the proposed method is based on a simple transformation and is extrapolating mode shape based on the frequency distribution in Fourier spectra, this may not account for the contributions from these frequency components as they are not associated with any mode. However, for stochastic excitations, such as vibrations induced by ambient wind and earthquakes, the forces are considered to be random. Even for such cases, the proposed method is expected to reconstruct dynamic responses pretty accurately.

6 Numerical Studies

The effectiveness of the proposed response reconstruction technique using empirical mode decomposition and also its accuracy is investigated by solving several numerical examples. In this paper, we present the studies carried out on a simply supported beam. Even though experimental verification of the proposed technique has been carried out, it is not presented here due to the paucity of space. The accuracy of the proposed method is investigated using several influencing parameters like measurement noise, sensor numbers, sensor location, and also damping. Mean squared error (MSE) and mean relative error (RE) are the two metrics employed in the present work to evaluate the accuracy of the proposed method and they are defined as

$$\mathrm{MSE}(\ddot{x}) = \frac{1}{m} \sum_{t=1,2,\ldots m} [\ddot{x}^a(t) - \ddot{x}^r(t)]^2 \tag{6}$$

$$\text{mean RE}(\ddot{x}) = \frac{1}{m} \sum_{t=1,2,\ldots m} \left| \frac{\ddot{x}^a(t) - \ddot{x}^r(t)}{\ddot{x}^r(t)} \right| \tag{7}$$

where 'm' refers to the number of samples (or time steps) in the acceleration time history response and superscripts 'a' and 'r' refer to the actual and reconstructed time history responses.

Fig. 1 Simply supported beam girder

A simply supported beam girder, shown in Fig. 1, is considered as the numerical example to demonstrate the effectiveness of the proposed method of response reconstruction. The girder has a span of length 10 m and cross-Section 0.3 m × 0.6 m. The modulus of elasticity and density of the material of the beam are 34,500 N/mm^2 and 2400 kg/m^3 respectively. The Raleigh damping for first and second modes are considered as 0.01 and 0.01 respectively. The beam is idealised using 20 beam elements for the present investigations. The first five natural frequencies of the system are 8.785, 35.142, 79.072, 140.583 and 219.196 Hz. A random load is applied at node 12 of the beam.

In order to test the accuracy of the proposed method, it is assumed that there is no sensor at node-8 and we require to compute the acceleration time history response at node-8 using the measured time history response at node-12. The time history response of node-12 is subjected to EMD with intermittency criteria in order to obtain modal time history responses. For this problem, we have considered four IMFs for reconstructing the time history response at node-8. Figure 2 shows the theoretical time history response at node-8 and also the reconstructed time history response. It can be observed that the reconstructed time history response is correlating very well with the theoretical response. Mean squared error (MSE) and mean relative error (RE) are the two metrics employed to evaluate the performance of the proposed reconstructing algorithm. The mean square error is found to be 0.00254 and the relative error is found to be 0.0128, which appears to be pretty good. The Fourier spectra of the theoretical (true) as well as reconstructed data is shown in Fig. 3.

In order to investigate the effect of measurement noise on the performance of the proposed response reconstruction method, we add white Gaussian noise of 5% to the acceleration time history data of the reference node at 12 and the reconstructed time history data for node-7 is shown in Fig. 4. It can be observed from the plots

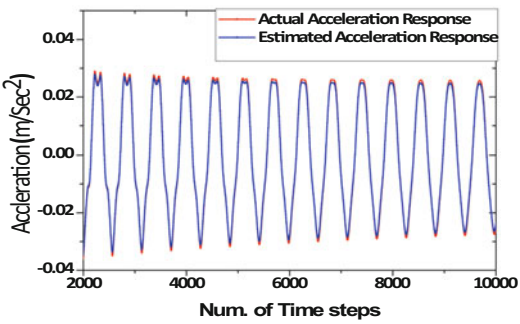

Fig. 2 Reconstructed acceleration time history response of simply supported beam at node-8 using the response at node-12

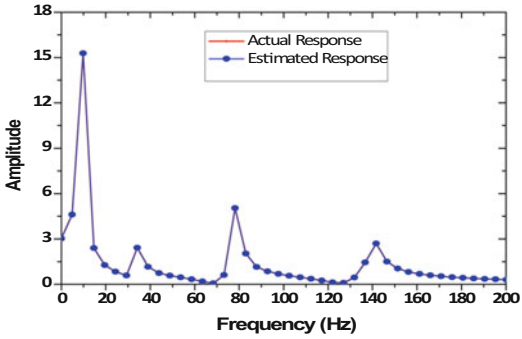

Fig. 3 Fourier spectra of reconstructed acceleration time history response of simply supported beam at node-8

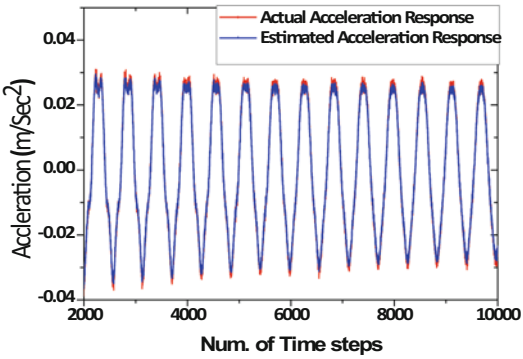

Fig. 4 Reconstructed acceleration time history response of simply supported beam at node-7 using the response at node-12 with measurement noise as 5%

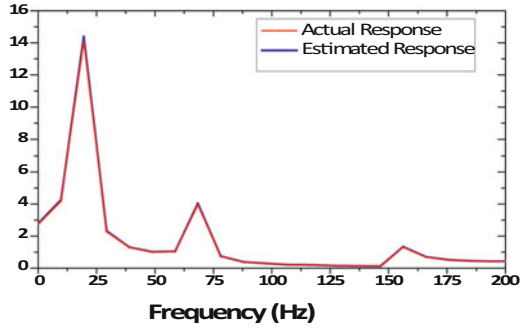

Fig. 5 FFT spectra of node-7: reconstructed and theoretical response with 5% noise

shown in Fig. 4 that the proposed reconstruction algorithms work well even in the presence of measurement noise. The Fourier spectra comparisons are shown in Fig. 5. The mean square error and the relative error recorded for varied levels of measurement noise are presented in Table 1. We can observe from the results presented in Table 1 that the mean square error (MSE) is within 0.15 and mean relative error (RE) is within 0.10 even when the measurement noise is 10%.

Table 1 MSE and mean relative error of reconstructed time history response at node-8 using measured response at node-12 with varied noise levels

Noise (%)	0	2	5	10
MSE	0.00214	0.00354	0.00426	0.00788
Mean RE	0.0112	0.0208	0.0418	0.0967

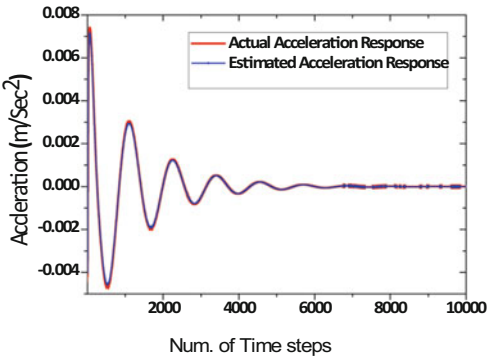

Fig. 6 Reconstructed acceleration time history response of simply supported beam at node-3 using the response at node-12 with damping as 10%

In order to investigate the performance of the proposed reconstruction algorithm with a high level of damping, 10% of damping is considered. The reference node is considered as 12 and the node-3, which close to the support is considered for reconstruction of the time history. The reconstruction of acceleration time history is evaluated using the proposed algorithm for node-3 and the reconstructed results are compared with theoretical time history response and the details are furnished in Fig. 6. The amplitude of the measured acceleration signal reduces rapidly due to the induced high damping ratio as shown in Fig. 6. Good correlation of the reconstructed and theoretical time history responses can be observed. Therefore, it can be concluded that the proposed response history reconstruction approach can work effectively for the cases where the damping ratios are high. For this test case, the mean square error is found to be 0.000426 and the relative mean error is found to be 0.00162.

Predicting the time history response near the mid-span of the simply supported beam from measurements taken near the support may be more difficult. In order to investigate the influence of the sensor location on the proposed method, the measurements were taken near the support (i.e., node-2) are used to reconstruct the acceleration time history responses near the mid-span, i.e. node-10. Four IMFs have been used for reconstructing the dynamic responses. The true acceleration time history responses near the mid-span, i.e. at node-10 and reconstructed responses using the measurements at a node (node-2) near the support are shown in Fig. 7. It can be observed from Fig. 7 that there is good agreement between the reconstructed response and the true time history response.

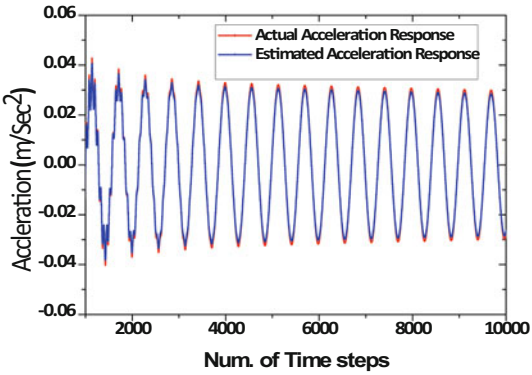

Fig. 7 Reconstruction of acceleration time history response at node-10 using the time history response at node-2

However, in a real situation, each acceleration sensor may have an intrinsic measurement noise and this noise is independent of the actual measured time history responses of the target system. Therefore, the signal-to-noise ratio of a sensor is likely to vary with the spatial location of the structure. In view of this, spatial locations on a structure where the responses are with relatively low amplitude, i.e. measured response from an accelerometer placed closer to the support of the beam likely to have low signal-to-noise ratio when compared to the signal measured from the accelerometer close to the mid-span. This is due to the fact that noise will be same in both cases, but the signal amplitude makes the difference. Signal-to-noise ratio (SNR) measured at a node close to the supports will obviously be much smaller than the signal of the node near the mid-span of simply supported beam. In order to simulate this on the responses obtained from simply supported beam, a Gaussian pulse process with a standard deviation of 1.20 is generated and are added to the responses at all sensor locations. Using this noise-corrupted signals, efforts are made to reconstruct the signal at mid-span, i.e. at node-10 using the signal at node-2 using the proposed algorithm. The reconstructed results found to be totally different from the actual response. The details could not be presented here figuratively due to the paucity of space. As mentioned earlier, this is due to low signal to noise ratio of the sensor near the support when compared to the sensor at mid-span. Hence, it may be concluded that it is certainly difficult to reconstruct the responses at a spatial location where the signal is expected to be with high amplitude using the signal with low amplitude. This needs to be kept in mind while choosing the responses to use for reconstruction. We will encounter similar sort of problems if we choose the signal from a sensor which is placed at nodes of the structure. The reconstructed results may be inaccurate as the responses obtained at nodal points of the structure will not be able to capture all the excited modes.

7 Conclusions

In this paper, we present a dynamic time history response reconstruction technique using empirical mode decomposition technique and also performing a simple transformation using modal responses and finally the response is reconstructed using the modal responses at the desired node, where the response time history is sought. We use EMD with intermittency criterion to avoid mode mixing in generated IMFs and also the signal extension method using time series in order to eliminate the issues related to end effects while generating IMFs. Numerical simulation studies have been carried out by solving a simply supported beam girder to demonstrate the effectiveness of the proposed method. The major advantage of the proposed method is that we use the measured time history responses directly in the time domain. Hence we do not need to perform inverse transformations unlike the other classical methods developed using transmissibility concept. This will help in minimising the errors associated with inverse FFT and also reduces the computational cost. Influence of sensor locations, high damping and the influence of measurement noise on the accuracy of the reconstructed responses using the proposed method are investigated in detail. Numerical studies presented in this paper clearly indicate that the proposed method can produce accurate results for signal even with high damping and also measurement noise.

Acknowledgements This paper is being published with the permission of the Director, CSIR-Structural Engineering Research Centre (SERC), Chennai.

References

1. Kerschen, G., De Boe, P., Golinval, J. C., & Worden, K. (2005). Sensor validation using principal component analysis. *Smart Materials and Structures, 14,* 36–42.
2. Rama Mohan Rao, A., Kasireddy, V., Gopalakrishnan, N., & Lakshmi, K. (2015). Sensor fault detection in structural health monitoring using null subspace-based approach. *Journal of intelligent materials and structures., 26*(2), 172–185.
3. Kullaa, J. (2010). Sensor validation using a minimum mean square error estimation. *Mechanical Systems and Signal Processing, 24,* 1444–1457.
4. Friswell, M. I., & Inman, D. J. (1999). Sensor validation of smart structures. *Journal of Intelligent Material Systems and Structures, 10,* 973–982.
5. Rama Mohan Rao, A., Lakshmi, K., & Krishnakumar, S. (2014). A sensor fault detection algorithm for structural health monitoring using adaptive differential evolution. *International Journal for Computational Methods in Engineering Science and Mechanics, 15,* 282–293.
6. Rama Mohan Rao, A., Lakshmi, K., & Krishna Kumar, S. (2012). Sensor fault detection in large sensor networks using PCA with a multi-level search algorithm. *Structural Durability and Health Monitoring, 8*(3), 271–293.
7. Ribeiro, A., Silva, J., & Maia, N. (2000). On the generalisation of the transmissibility concept. *Mechanical Systems and Signal Processing, 14*(1), 29–36.
8. Jacquelin, E., Bennani, A., & Hamelin, P. (2003). Force reconstruction: Analysis and regularization of a deconvolution problem. *Journal of Sound and Vibration, 265*(1), 81–107.

9. Kammer, D. C. (1997). Estimation of structural response using remote sensor locations. *Journal Guidance Control Dynamics, 20*(3), 501–508.
10. Law, S. S., Li, J., & Ding, Y. (2010). Structural response reconstruction with transmissibility concept in the frequency domain. *Mechanical Systems and Signal Processing, 25*(3), 952–968.
11. Huang, N. E., & Shen, S. S. (2005). *Hilbert–huang transform and its applications*. World Scientific Publishing Co Inc.
12. Huang, N. E., Shen, Z., Long, S. R., Wu, M. C., Shih, H. H., Zheng, Q., et al. (1998). The empirical mode decomposition and Hilbert spectrum for nonlinear and nonstationary time series analysis. *Proceedings of Royal Society, 454*(1971), 903–995 (London) (Series A).
13. Gao, Y., Ge, G., Sheng, Z., & Sang, E. (2008). Analysis and solution to the mode mixing phenomenon in EMD. *Congress on Image and Signal Processing, 5,* 223–227.

A Novel Method for Vibration-Based Damage Detection in Structures Using Marginal Hilbert Spectrum

Timir Baran Roy, Srishti Banerji, Soraj Kumar Panigrahi, Ajay Chourasia, Lucia Tirca and Ashutosh Bagchi

Abstract This vibration-based method for Structural Health Monitoring (SHM) utilizes the dynamic response of a structure measured using a set of sensors to identify the modal properties and potential structural damage. Signal processing tools are widely used for analyzing and diagnosing these response signals. Change in the dynamic characteristics of a structure can provide an indication of damage. However, a direct comparison of the vibration signals or modal properties at different periods of time may not be sufficient to identify the damages and their locations. Therefore, it is important to analyze the vibration signals to extract the morphologies of the changes in these response signals and correlate them with the types, location and magnitude of structural damage. In the proposed method of damage detection, first, the response signals are decomposed into intrinsic mode functions (IMF) using empirical mode decomposition (EMD) technique. Those IMFs are then processed with Hilbert–Huang transform (HHT) to obtain their corresponding Hilbert spectra, which allows the estimation of the time-varying instantaneous properties of those response signals. Then a marginal Hilbert spec-

T. B. Roy · L. Tirca · A. Bagchi (✉)
Department of Building Civil and Environmental Engineering, Concordia University, 1455 de Maisonneuve Blvd. W, Montreal, QC H3G 1M8, Canada
e-mail: ashutosh.bagchi@concordia.ca

T. B. Roy
e-mail: timirbaranju@gmail.com

L. Tirca
e-mail: tirca@encs.concordia.ca

S. Banerji
Department of Civil and Environmental Engineering, Michigan State University, 428 South Shaw Lane, East Lansing, MI 48823, USA
e-mail: srishti.banerji@gmail.com

S. K. Panigrahi · A. Chourasia
CSIR-Central Building Research Institute, Roorkee 247667, Uttarakhand, India
e-mail: panigrahi1111@yahoo.com

A. Chourasia
e-mail: ajaycbri@gmail.com

A. Rama Mohan Rao and K. Ramanjaneyulu (eds.), *Recent Advances in Structural Engineering, Volume 1*, Lecture Notes in Civil Engineering 11,
https://doi.org/10.1007/978-981-13-0362-3_92

trum (MHS)-based technique has been applied on the Hilbert spectrum coefficients to calculate associated damage indices (DI). The proposed method was tested using experimental tests conducted on a cantilever steel beam prototype at the CBRI laboratory, Roorkee, India, and a three-storey steel frame at Concordia University, Canada. The damage locations were determined by comparing the DIs of the damaged steel beam and frame with that of the corresponding baseline (undamaged) structures.

Keywords Structural health monitoring (SHM) · Damage detection
Intrinsic mode functions (IMF) · Empirical mode decomposition (EMD)
Marginal Hilbert spectrum (MHS) · Damage indices (DI)

1 Introduction

Structural Health Monitoring (SHM) implies real-time monitoring of structures to detect damages arising from the changes in the structural behavior. The structural response parameters, such as strain, acceleration, etc., are measured using different sensors installed at the critical locations in the structures. SHM constitutes of set of processes including data acquisition, data processing, damage-sensitive features extraction and decision making for damage localization and severity assessment. Due to the complexity of the raw structural response data acquired from the sensors, meaningful diagnosis is important, which requires efficient tools, like signal processing. Acquired data from the structure is usually nonlinear and nonstationary. Various damage detection algorithms including mode shape curvature, damage detection based on flexibility matrix, wavelet transform, Hilbert–Huang transform, neural network, machine learning, data mining are used in SHM.

Hilbert–Huang Transform (HHT) is considered to be the only method which can be used for processing the structural responses by truly preserving their nonlinear and nonstationary features [1]. Earlier studies have shown the applicability of this method in simple structures, and its application in civil engineering structures needs further exploration. This paper proposes and validates damage indices based on Marginal Hilbert Spectrum (MHS) and Normalized Cumulative Marginal Hilbert Spectrum (NCMHS) curves developed by using HHT [1]. The details of the methods and damage indices are explained in the following sections. Two case studies have been considered for this research; the first one is an experimental prototype of a cantilever steel beam tested at CBRI laboratory, Roorkee, India and the second one is a prototype of a three-storey steel frame tested at Concordia University, Canada. In these cases, the data were acquired at different sampling rates, and damage was simulated at various locations by changing the stiffness and/or mass. The results show that the method can effectively detect damages and locate their positions.

1.1 Background

Developed by Huang et al. [2], the Empirical Mode Decomposition (EMD) method is based on the concept of signal decomposition into different Intrinsic Mode Functions or Oscillations (IMFs) [2]. This adaptive approach can be applied to any time-history signal for decomposition without energy leakage or loss of signal. Performing Hilbert transform on IMFs, instantaneous parameters as functions of time such as amplitudes and frequencies are obtained that provide identification of fundamental nonlinear and nonstationary features of a vibration signal [3].

The IMFs represent the oscillation mode of the structural response data and have to satisfy two necessary conditions: (1) the number of extrema and the number of zero crossings must be either equal or different at most by one in the entire data set under consideration; and (2) at any point, the mean value of the envelope defined by the local maxima and the envelope by the local minima is zero [3].

The original signal can be reconstructed as the sum of all the IMFs. The next step is to apply the Hilbert transform to obtain the analytic signal $Z(t)$, which can be defined as [3]

$$Z(t) = X(t) + \mathrm{i}Y(t) = a(t)\mathrm{e}^{i\,\theta(t)} \tag{1}$$

where $X(t)$ is the response time series signal and $Y(t)$ is the Hilbert transform of $X(t)$.

This determines the instantaneous amplitude, phase and frequency of the signal as follows [3]:

$$\text{Amplitude, } A(t) = \left(X^2 + Y^2\right)^{0.5} \tag{2}$$

$$\text{Phase, } \theta(t) = \arctan(Y(t))/(X(t)) \tag{3}$$

$$\text{Frequency, } \omega(t) = (\mathrm{d}\theta(t))/\mathrm{d}t \tag{4}$$

The Hilbert–Huang Transform (HHT) plot is defined using these instantaneous parameters in time–frequency plane with amplitude contoured on it. This distribution is known as the Hilbert Spectrum, $H(\omega,\ t)$. Further, Marginal Hilbert Spectrum (MHS), $h(\omega)$ is described as [3]

$$h(\omega) = \int_0^T H(\omega, t)\ \mathrm{d}t \tag{5}$$

where T is the total data length.

1.2 Damage Detection Method

MHS shows the total amplitude contribution from each frequency component of the signal. The amplitude of MHS is dependent on the input energy of the system. For damage detection in the structure under different scenarios, consistency of MHS amplitude is necessary before and after damage. In order to achieve this, Normalized Marginal Hilbert Spectrum (NMHS) curve is constructed by normalizing the MHS curve and removing the effect of varying input energy [1]. The NMHS curves represent the energy distribution between vibrating modes of the structure which change with damage. The NMHS curve is plotted utilizing discrete sensor data which is nonsmooth in nature. As suggested by Ghazi et al. [1], the cumulative sum of a curve represents its smoothness and monotonically increasing function while preserving its energy and physics [1]. Such a curve is easier to be dealt with, mathematically. The cumulative curve of MHS is termed as Cumulative Marginal Hilbert Spectrum (CMHS). Again, it requires normalization for the sake of consistent input energy criteria for damage detection. The resulting curve is Normalized Cumulative Marginal Hilbert Spectrum (NCMHS) curve. The damage indices are calculated in this paper utilizing NCMHS curves with their applications which are discussed in the rest of the sections [4].

1.3 Damage Indices

Damage indices are calculated at different sensor locations providing a measure of level of damage at those locations. The damage indicators are higher within the proximity of the damage. The detection of damage metrics are based on the discrepancies from the responses of the intact structure [4]. The peaks of NMHS curve represent the dominant frequency components in the structural response signal which undergo shifting when subjected to damage. This change in the distribution of NMHS curves is captured in Damage Index. Damage Index based on NCMHS is used in the present work to testify its accuracy and applicability which is represented as [4]

$$\text{Damage Index} = \left(\sum |\text{Area between damaged and undamaged NCMHS}|\right) / (\text{Area of undamaged NCMHS}) \tag{6}$$

The areas between the NCMHS curves of the undamaged and damaged scenarios of the structure depict the energy transfer between the vibrating modes with its variation due to damage. This ratio is always less than unity. So in order to increase the prominence of the damage index, the values are magnified by a constant factor depending on the dataset [4].

2 Case Study

For the present work, two different structures have been chosen as case study problems, a steel cantilever beam and a three-storey steel frame, which are described in the following:

2.1 Cantilever Steel Beam Prototype

The HHT method is tested on a cantilever steel beam prototype of length 1.02 m, which was tested at the CBRI laboratory, Roorkee, India. The details of geometry and dimensions are shown in Fig. 1, and its properties are presented in Table 1.

The beam was instrumented with 5 wireless sensors as shown in Fig. 2. Both forced and ambient vibration test were performed. To simulate the damage, a known mass was added, instead of reducing the stiffness. The position of the added mass was changed to simulate different scenarios of damage. In forced vibration test, the beam was excited using an impact hammer by striking the beam at different points to capture all the major modes of vibration. The sampling rate of the sensors was chosen to be 256 Hz. Table 2 shows different modal frequencies determined from the test before adding the additional mass to simulate damage to the beam.

The instrumentation scheme for the beam is shown in Fig. 2. The beam is instrumented with acceleration sensors at five locations as shown in Fig. 2. Two damage locations are considered for this beam; one is at 0.75 m from the fixed end and the other is 0.415 m from the fixed end.

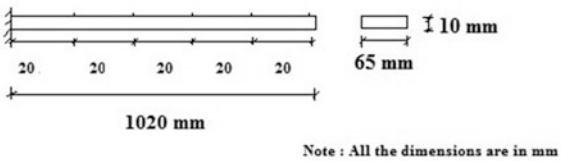

Fig. 1 Beam section details

Table 1 Properties of the beam section

Material properties and dimensions	
Length (mm)	1020
Width (mm)	65
Thickness (mm)	10
Elastic modulus (MPa)	2.10×10^5
Density (kg/m^3)	7.800×10^3
Poisson's ratio (v)	0.3

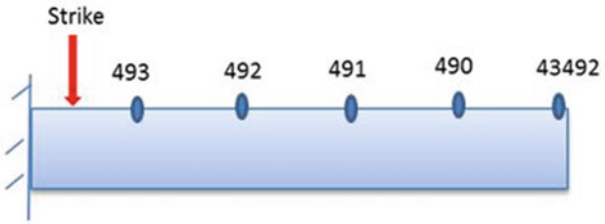

Fig. 2 Sensor locations in the beam prototype

Table 2 Modal frequencies of the intact beam

First three modes	
First	7.23 Hz
Second	44.53 Hz
Three	126.11 Hz

In the first case, the damage was simulated by assigning 50 g mass at 0.75 m from the fixed end and in the second case the damage was simulated by using 50 g mass at 0.415 m from the fixed end.

2.2 Frame Structure Prototype

A small-scale frame structure, made of galvanized steel, as shown in Fig. 3, was built for experimental study at Structures Laboratory, Concordia University, Canada for damage detection. The steel frame is fixed to the base using concrete to depict it as a three-storey structure model. Its geometry and dimensions are presented in Table 3. This frame structure was instrumented with wireless sensors to record the vibration data (acceleration) at three different points at the storey level under undamaged and damaged scenarios. The frame was struck at the top using an impact hammer in order to study its vibration characteristics [5]. The test was repeated for vibration along both the horizontal axes (long and short). Since the stiffness is same in both directions, the vibration properties were found to be almost identical in both directions.

The first three modal frequencies obtained from the sensor data are shown in Table 4.

Each level of the frame is rectangular in shape and bolted with the angle section columns in all four directions. Two bolts at each corner were used with a total of eight bolts for one level.

To induce damage at a particular level, all the eight bolts were loosened as shown in Fig. 4. Two damage scenarios were considered, “D1” or Damage 1 at the top floor and “D2” signifying Damage 2 s in the middle floor. The frame consists of three levels

Fig. 3 Frame structure

Table 3 Frame structure

Dimensions of the frame prototype	
Height	1.40 m
Length	0.60 m
Width	0.27 m

Table 4 Modal frequencies of the intact frame

First three modes	
First	8 Hz
Second	37.5 Hz
Three	94 Hz

Fig. 4 Damage scenario in frame structure [5]

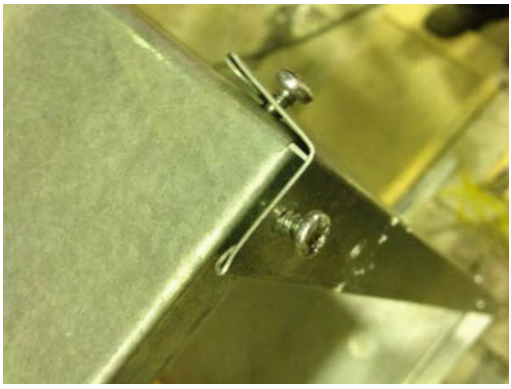

portraying a building with three floors. The wireless sensors were placed at the center of each floor to record the vibration data. "Microstrain" Wireless G-Link Accelerometers were used for data collection at a sampling rate of 512 Hz.

3 Results and Discussion

The aim of this study is to localize damage accurately without any loss of nonlinear and nonstationary features of the structural response. Damage metrics calculated from NMHS and NCMHS curves capture the effect of damage at each sensor location. Damage detection is achieved by comparing the NMHS and NCMHS curves of damage scenarios with that of intact structural condition. The location with the highest value of damage index signifies the location of structural damage.

The damage indices and their detection results are demonstrated in this section. The first step for Hilbert–Huang transform is to decompose the response signal into

Fig. 5 IMFs of the intact structure; **a** beam and **b** frame

(a)

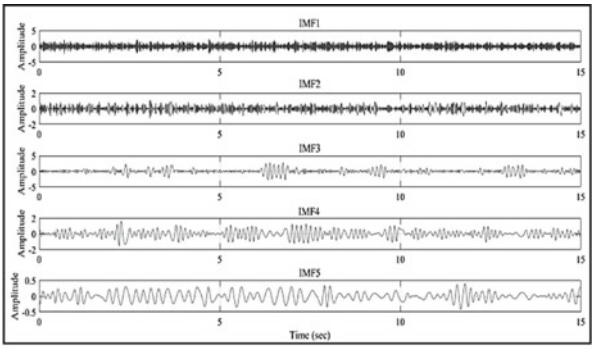

IMFs at 491 sensor data for intact structure

(b)

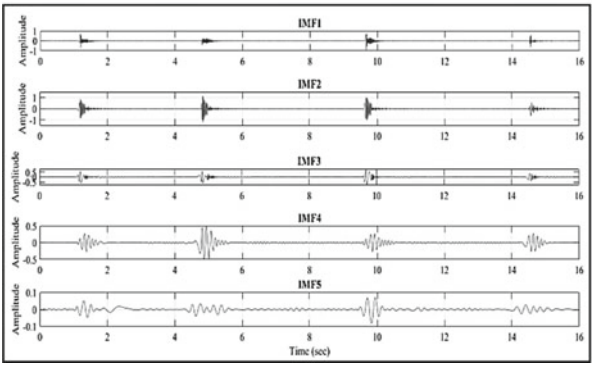

IMFs of the top floor sensor data for intact structure

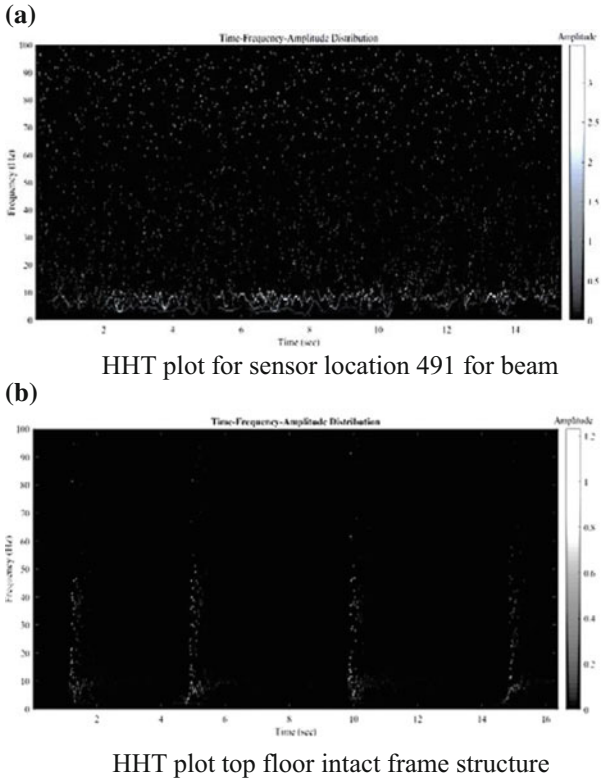

Fig. 6 HHT plot

its IMFs by EMD, as shown in Fig. 5 [2]. The IMFs of sensor location 491 for the beam and top floor sensor for the frame for the intact state are shown in Fig. 6. The IMFs are mono-component signals which admit well-behaved Hilbert transform providing the amplitude and frequency variation with respect to time shown in the HHT plot Fig. 6. The time integral of HHT provides the MHS curve, which is a measure of the amplitude contribution from each frequency value. It is the cumulative amplitude over the distribution in a probabilistic sense.

The cumulative function smoothens the MHS curve, and by normalizing its cumulative sum, it maintains a consistent input energy in the structural system. NCMHS plots for both the intact and damaged structures at the sensor location 491 for the beam and D1 damage condition for the frame are shown in Fig. 7.

Finally, the damage indices have been calculated by comparing the areas under the NCMHS curves in both the cases. Damage indices for the beam model in both the cases are shown in Table 5.

Damage indices for the frame structure in both the damage cases are shown in Table 6.

(a)

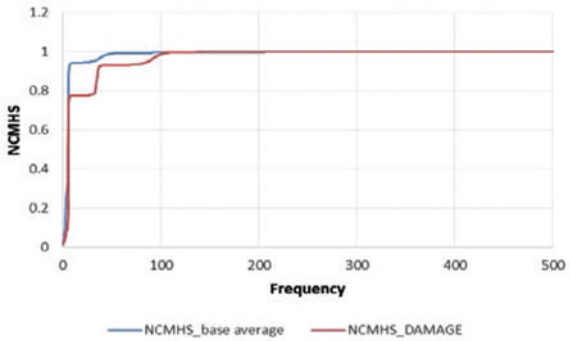

NCMHS comparison for the beam prototype

(b)

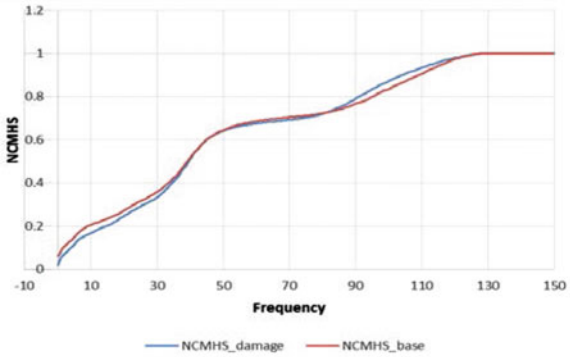

NCMHS comparison for the frame prototype

Fig. 7 NCMHS comparison for the intact and damaged structures

Table 5 Damage indices for the beam

Damage indices for damage location 0.415 m	
493	0.95
492	1.15
491	1.27
490	0.85
43,492	0.75
Damage indices for damage location 0.75 m	
493	0.74
492	0.85
491	1.40
490	1.37
43,492	0.91

Table 6 Damage indices for the frame structure

Damage indices for top floor damage	
Floor 1	1.11
Floor 2	3.70
Floor 3	4.52
Damage indices for the middle floor damage	
Floor 1	1.21
Floor 2	1.34
Floor 3	0.97

4 Conclusions

The fundamental objective of this research is to examine and utilize HHT technique for observing nonlinear and nonstationary information of a structure. The HHT method preserves the nonlinear and nonstationary components of a response signal. The EMD procedure disintegrates the signal into Intrinsic Mode Functions (IMFs) which admit well-behaved Hilbert Transform to estimate components like frequency and amplitude of the signal. The cumulative amplitude contribution of frequencies in the signal is measured by marginal Hilbert spectrum curves. The energy distribution changes with damage in the structure. The differences in area under the curves between the Normalized Cumulative Marginal Hilbert Spectrum (NCMHS) of the intact and the damaged structure generate the damage metric. This method is accurate to detect and localize damage. The test results indicate that the proposed method is feasible and effective. Also, development of computational effort, application of HHT on full-scale structures, improved signal processing tools; damage sensitive features for multi-damage scenarios represent future challenges.

Acknowledgements The authors acknowledge the support of the IC-IMPACTS Network in Canada and Department of Science and Technology (DST) in India under the India–Canada Collaborative Research Program. Thanks are also due to Dr. Sourav Kumar Mukhopadhyay, Postdoctoral Researcher at Concordia University, Canada for careful review of the paper.

References

1. Ghazi, R. M., & Büyüköztürk, O. (2015). Damage detection with small data set using energy-based nonlinear features. *Structural Control Health Monitoring, 23*(2), 333–348.
2. Huang, N. E., Shen, Z., Long, S. R., Wu, M. C., Shih, H. H., Zheng, Q., et al. (1998). The empirical mode decomposition and the Hilbert spectrum for nonlinear and non-stationary time series analysis. *Proceedings of the Royal Society of London, 454,* 903–995.
3. Dhengyun, H., Ding, Y. (2013). Marginal Hilbert spectrum based on EMD reconstruction and its application in fault diagnosis of cooling tower. In *Intelligent System Design and Engineering Applications (ISDEA)*, Third International Conference on 2013 Jan 16, IEEE (pp. 926–929).

4. Ghazi, R. M., & Buyukozturk, O. (2014). Assessment and localization of active discontinuities using energy distribution between intrinsic modes. In *Structural Health Monitoring, 5*, 1–9. Cham: Springer.
5. Banerji, S. (2016). *Vibration-based monitoring and damage detection of structures using wireless sensors* (M.A.Sc. thesis). Department of Building Civil and Environment Engineering, Concordia University.